NASA/CP-1999-209690/PT3

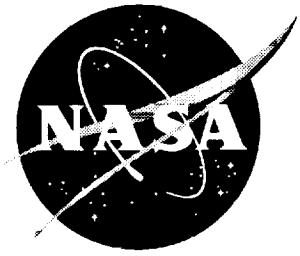

First NASA/Industry High-Speed Research Configuration Aerodynamics Workshop

Edited by
Richard M. Wood
Langley Research Center, Hampton, Virginia

December 1999

The NASA STI Program Office . . . in Profile

Since its founding, NASA has been dedicated to the advancement of aeronautics and space science. The NASA Scientific and Technical Information (STI) Program Office plays a key part in helping NASA maintain this important role.

The NASA STI Program Office is operated by Langley Research Center, the lead center for NASA's scientific and technical information. The NASA STI Program Office provides access to the NASA STI Database, the largest collection of aeronautical and space science STI in the world. The Program Office is also NASA's institutional mechanism for disseminating the results of its research and development activities. These results are published by NASA in the NASA STI Report Series, which includes the following report types:

- TECHNICAL PUBLICATION. Reports of completed research or a major significant phase of research that present the results of NASA programs and include extensive data or theoretical analysis. Includes compilations of significant scientific and technical data and information deemed to be of continuing reference value. NASA counterpart of peer-reviewed formal professional papers, but having less stringent limitations on manuscript length and extent of graphic presentations.

- TECHNICAL MEMORANDUM. Scientific and technical findings that are preliminary or of specialized interest, e.g., quick release reports, working papers, and bibliographies that contain minimal annotation. Does not contain extensive analysis.

- CONTRACTOR REPORT. Scientific and technical findings by NASA-sponsored contractors and grantees.

- CONFERENCE PUBLICATION. Collected papers from scientific and technical conferences, symposia, seminars, or other meetings sponsored or co-sponsored by NASA.

- SPECIAL PUBLICATION. Scientific, technical, or historical information from NASA programs, projects, and missions, often concerned with subjects having substantial public interest.

- TECHNICAL TRANSLATION. English-language translations of foreign scientific and technical material pertinent to NASA's mission.

Specialized services that complement the STI Program Office's diverse offerings include creating custom thesauri, building customized databases, organizing and publishing research results . . . even providing videos.

For more information about the NASA STI Program Office, see the following:

- Access the NASA STI Program Home Page at ***http://www.sti.nasa.gov***

- Email your question via the Internet to help@sti.nasa.gov

- Fax your question to the NASA STI Help Desk at (301) 621-0134

- Telephone the NASA STI Help Desk at (301) 621-0390

- Write to:
  NASA STI Help Desk
  NASA Center for AeroSpace Information
  7121 Standard Drive
  Hanover, MD 21076-1320

NASA/CP-1999-209690/PT3

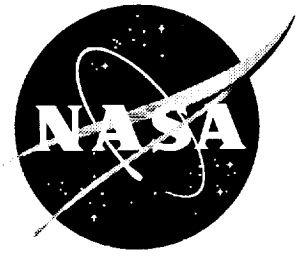

First NASA/Industry High-Speed Research Configuration Aerodynamics Workshop

Edited by
Richard M. Wood
Langley Research Center, Hampton, Virginia

Proceedings of a workshop held at
Langley Research Center,
Hampton, Virginia
February 27–29, 1996

National Aeronautics and
Space Administration

Langley Research Center
Hampton, Virginia 23681-2199

December 1999

Available from:

NASA Center for AeroSpace Information (CASI)
7121 Standard Drive
Hanover, MD 21076-1320
(301) 621-0390

National Technical Information Service (NTIS)
5285 Port Royal Road
Springfield, VA 22161-2171
(703) 605-6000

PREFACE

This publication is a compilation of documents presented at the First NASA/Industry High-Speed Research Configuration Aerodynamics Workshop held on February 27-29, 1996, at NASA Langley Research Center. The purpose of the workshop was to bring together the broad spectrum of aerodynamicists, engineers, and scientists working within the Configuration Aerodynamics element of the HSR Program to collectively evaluate the technology status and to define the needs within Computational Fluid Dynamics (CFD) Analysis Methodology, Aerodynamic Shape Design, Propulsion/Airframe Integration (PAI), Aerodynamic Performance, and Stability and Control (S&C) to support the development of an economically viable High-Speed Civil Transport (HSCT) aircraft. To meet these objectives, papers were presented by representatives from NASA Langley, Ames and Lewis Research Centers, Boeing, McDonnell Douglas, Northrop-Grumman, Lockheed-Martin, Vigyan, Analytical Services, Dynacs, and RIACS.

The workshop was organized in 12 sessions as follows:

- Introduction/Overviews
- Overviews
- PAI I
- PAI II
- Analysis and Design Optimization Methods
- Experimental Methods
- Design Optimization - Applications I
- Design Optimization - Applications II
- Design Optimization - Applications III/Validation
- Reynolds Number Effects
- Stability and Control
- High Lift

Appreciation is expressed to the individuals at NASA Langley, NASA Ames, McDonnell Douglas, and Boeing who developed the structure and content of the workshop; to the session chairs and speakers who contributed to the technical quality; and to the many individuals who contributed to the administration and logistics of the workshop. A list of attendees is included in this document.

Richard M. Wood
NASA Langley Research Center

CONTENTS

*Part 1 is presented under separate cover.

†Part 2 is presented under separate cover.

Session 6

Session 7

Session 8

Part 3

Session 9

Session 10

Session 11

Session 12

ATTENDEES

Abdol-Hamid, Khaled S.	Analytical Services & Materials, Inc.
Adams, Bill	NASA Langley Research Center
Agrawal, Shreekant	McDonnell Douglas Aerospace
Allen, Jerry M.	NASA Langley Research Center
Antani, Tony	McDonnell Douglas Aerospace
Applin, Z.	NASA Langley Research Center
Baker, Timothy J.	Princeton University
Bard, William	Northrop Grumman Corporation
Bauer, Steve	NASA Langley Research Center
Beach, H. Lee	NASA Langley Research Center
Bencze, Daniel P.	NASA Ames Research Center
Bharadvaj, Bala	McDonnell Douglas Aerospace
Bobbitt, Percy J.	Eagle Aeronautics, Inc.
Burner, A. W.	NASA Langley Research Center
Bushnell, D.	NASA Langley Research Center
Buttrill, C.	NASA Langley Research Center
Calloway, R. L.	NASA Langley Research Center
Campbell, James F.	NASA Langley Research Center
Campbell, Richard L.	NASA Langley Research Center
Capone, Francis J.	NASA Langley Research Center
Cappuccio, Gelsomina	NASA Ames Research Center
Carlson, John R.	NASA Langley Research Center
Chaney, Steve	Boeing
Chu, J.	NASA Langley Research Center
Clark, Roger	McDonnell Douglas Aerospace
Cliff, Susan E.	NASA Ames Research Center
Coen, P.	NASA Langley Research Center
Compton, W.	NASA Langley Research Center
Conner, Roy S.	Boeing Commercial Airplane Group
Covell, P.	NASA Langley Research Center
DeBonis, Jim	NASA Lewis Research Center
Deere, Karen A.	NASA Langley Research Center
Dollyhigh, S.	NASA Langley Research Center
Domack, C.	NASA Langley Research Center

Driver, Cornelius ..... Eagle Aeronautics, Inc.
Dudley, Mike ..... NASA Ames Research Center
Dwoyer, D. ..... NASA Langley Research Center
Dwyer, William P. ..... Northrop Grumman ATDC
Erickson, G. ..... NASA Langley Research Center
Flamm, J. ..... NASA Langley Research Center
Fox, Mike C. ..... Vigyan, Inc.
Frink, Neal ..... NASA Langley Research Center
Gerhardt, Heinz A. ..... Northrop Grumman Corporation
Ghaffari, Farhad ..... NASA Langley Research Center
Gibson, Berry T. ..... Lockheed Martin Aeronautical Systems
Gilbert, W. P. ..... NASA Langley Research Center
Glaab, Lou ..... Lockheed Martin
Goldberg, Perry ..... McDonnell Douglas Aerospace
Goodsell, Aga ..... NASA Ames Research Center
Graber Ed ..... NASA Lewis Research Center
Green, L. ..... NASA Langley Research Center
Hager, James ..... McDonnell Douglas Aerospace
Hahne, David ..... NASA Langley Research Center
Hamner, Marvine ..... McDonnell Douglas Aerospace
Harris, Roy V. ..... NASA Langley Research Center
Hartwich, Peter ..... McDonnell Douglas Aerospace
Hefner, J. ..... NASA Langley Research Center
Henderson, W. ..... NASA Langley Research Center
Hicks, Ray ..... NASA Ames Research Center/MCAT
Holloway, Paul F. ..... NASA Langley Research Center
Hoyle, David ..... McDonnell Douglas Aerospace
Jameson, A. ..... Princeton University
Joslin, Ronald D. ..... NASA Langley Research Center
Kandula, Max ..... Dynacs Engineering Co.
Kammerly, G. ..... NASA Langley Research Center
Kennelly, Jr., Robert A. ..... NASA Ames Research Center
Keyes, Sandy ..... NASA Langley Research Center
Krist, Steve ..... NASA Langley Research Center
Kubiatko, Paul ..... McDonnell Douglas Aerospace
Kulfan, Robert M. ..... Boeing Commercial Airplane Group

Kuruvila, G. ..... McDonnell Douglas Aerospace
LaBozzetta, Walt ..... McDonnell Douglas Aerospace
Lawrence, Scott ..... NASA Ames Research Center
Leavitt, Lawrence D. ..... NASA Langley Research Center
Lessard, Wendy B. ..... NASA Langley Research Center
Luckring, J. ..... NASA Langley Research Center
Ludas, Kevin ..... McDonnell Douglas Aerospace
Malone, Michael B. ..... Northrop Grumman
Mason, Charlie ..... Lockheed Martin
McMillin, S. Naomi ..... NASA Langley Research Center
Midea, Tony ..... NASA Lewis Research Center
Naik, Dinesh ..... Vigyan/NASA Langley Research Center
Narducci, Robert ..... McDonnell Douglas Aerospace
Nelms, Pres ..... NASA Ames Research Center
Nelson, Chester P. ..... Boeing Commercial Airplane Group
Owens, L. ..... NASA Langley Research Center
Ozoroski, L. ..... NASA Langley Research Center
Pao, S. Paul ..... NASA Langley Research Center
Parikh, Paresh ..... TSAB/NASA Langley Research Center
Peavey, Charles C. ..... Northrop Grumman
Plencner, Bob ..... NASA Ames Research Center
Pirzadeh, Shahyar ..... Vigyan
Princen, Norm ..... McDonnell Douglas Aerospace
Putman, Lawrence E. ..... NASA Langley Research Center
Re, R. ..... NASA Langley Research Center
Reuther, James ..... NASA Ames Research Center/RIACS
Rivers, Melissa B. ..... NASA Langley Research Center
Saladino, Anthony J. ..... Dynacs Engineering Co.
Sawyer, W. C. ..... NASA Langley Research Center
Schuster, Ernie ..... McDonnell Douglas Aerospace
Shieh, Chih Fang ..... McDonnell Douglas Aerospace
Shields, B. ..... NASA Langley Research Center
Shin, Jaiwon ..... NASA Lewis Research Center
Siclaris, Michael J. ..... Northrop Grumman
Smith, Brian ..... NASA Ames Research Center
Phillip, T. ..... NASA Ames Research Center

A Computational/Experimental Study of Two Optimized Supersonic Transport Designs and the Reference H Baseline

Susan E. Cliff, Timothy J. Baker, Raymond M. Hicks, and James J. Reuther

1 Abstract

Two supersonic transport configurations designed by use of non-linear aerodynamic optimization methods are compared with a linearly designed baseline configuration. One optimized configuration, designated Ames 7-04, was designed at NASA Ames Research Center using an Euler flow solver, and the other, designated Boeing W27, was designed at Boeing using a full-potential method. The two optimized configurations and the baseline were tested in the NASA Langley Unitary Plan Supersonic Wind Tunnel to evaluate the non-linear design optimization methodologies. In addition, the experimental results are compared with computational predictions for each of the three configurations from the Euler flow solver, *AIRPLANE*. The computational and experimental results both indicate moderate to substantial performance gains for the optimized configurations over the baseline configuration. The computed performance changes with and without diverters and nacelles were in excellent agreement with experiment for all three models. Comparisons of the computational and experimental cruise drag increments for the optimized configurations relative to the baseline show excellent agreement for the model designed by the Euler method, but poorer comparisons were found for the configuration designed by the full-potential code.

2 Introduction

The High Speed Research (HSR) program was chartered to develop and evaluate non-linear aerodynamic optimization methods. New methods were sought to design advanced configurations with substantial improvements in the aerodynamic efficiency of supersonic transports designed by classical linear methods. The Boeing Reference H configuration was used as the starting baseline geometry to evaluate the design methodologies and determine if non-linear methods can improve the performance of linear-based designs. The Reference H configuration was designed by Boeing Aircraft Corporation using linear based optimization methods, and has been shown experimentally to have performance characteristics indicative of a good linear design. Although non-linear methods have been used for several years to design configurations operating at transonic speeds where the non-linear effects are large, this study represents one of the first applications of non-linear optimization methods to supersonic transport design.

Two different non-linear optimization methods were used to redesign the Reference H configuration with the objective of improving the aerodynamic performance at the supersonic cruise Mach number. The first method was developed at NASA Ames Research Center using an Euler flow solver coupled to a unconstrained quasi-Newton optimization algorithm [1, 2]. The second method was developed at the Boeing Aircraft Company and used a full-potential flow solver coupled to an constrained optimization code [3]. For each of the optimized designs, the wing camber and twist were modified while the planform and thickness distributions remained the same as those of the Reference H configuration. The entire fuselage camber of the Boeing W27 configuration was modified, whereas only the forebody camber was changed on the Ames 7-04 design. The geometries resulting from the two optimization methods were very different, but both were predicted to have better performance than the baseline.

An unstructured tetrahedral mesh generator capable of modeling complete aircraft was used in conjunction with an Euler flow solver to evaluate the performance of the optimized configurations. The two codes together are called *AIRPLANE*. The *AIRPLANE* code has been extensively evaluated on numerous configurations, and has been shown to provide accurate and reliable results. *AIRPLANE* was used as part of the design process at Ames to provide the differences in the surface pressures and forces between the complete configuration, and the wing/body configuration. The differences in the lower surface pressures with and without nacelles from the *AIRPLANE* solutions were added to the wing/body pressures computed within the optimization code, by interpolating the pressures from *AIRPLANE* onto the nodes of the wing/body grid used during optimization. This provided a method of incorporating the effects of the diverters and nacelles on the wing lower surface in

the computations during optimization. *AIRPLANE* was also used to evaluate the complete configurations of the intermediate and final designs obtained at Ames and Boeing.

This report compares the *AIRPLANE* computational results with experimental data for the final designs of the two optimized configurations and the baseline Reference H configuration. The performance increments of the optimized configurations relative to the baseline, and the performance differences of the configurations with and without nacelles and diverters will be shown.

3 Experimental Models and Instrumentation

Wind tunnel models of the two optimized configurations were manufactured to the 1.675% scale of an existing model of the baseline Reference H configuration. The models were made primarily of stainless steel, with aluminum fore- and aft-bodies. A single set of aluminum nacelles was used on all models including the baseline to eliminate nacelle manufacturing tolerance from becoming an issue in determining drag increments between models. Individual diverters were manufactured to fit the different wing lower surfaces of each model. The fuselage of the existing baseline model was truncated a short distance from the wing trailing edge and bored to accept a balance/sting assembly. The optimized models were truncated at the same location, and bored to accept the same balance. It was very important that the same balance be used with all models, to eliminate the possibility of any discrepancies in the data resulting from different balances. The optimized models were primarily force models, instrumented with only enough pressures for base and cavity corrections to the balance data. These pressure taps were located within the balance cavity, on the base of the truncated fuselage, and on the base of the nacelles. The baseline model had 177 static pressure ports that were not used for this test.

The models were tested in the Langely Unitary Plan Supersonic Wind Tunnel (UPWT), at a Reynolds number of 4.0 million per foot at Mach 2.4. The three models were tested with transition disks attached near the leading edges of the model surfaces to promote transition from laminar to turbulent flow to simulate flight boundary layer characteristics. The circular disks were 0.010 inches in height and placed 0.10 inches apart on the fuselage and nacelle surfaces, and 0.20 inches apart along the highly swept leading edge of the wing for more uniform spacing. The disks were located 0.4 inches from the wing leading edge, 1.0 inch from the fuselage nose, and 0.875 inches from the nacelle leading edge. Transition was verified by use of a sublimating chemical during the wind tunnel test. Installation photographs of the three configurations are shown in Figs 1-3.

4 Mesh Generation Issues and Computational Requirements

All computations were carried out with the *AIRPLANE* code [4, 5]. *AIRPLANE* uses a vertex based finite volume method to solve the Euler equations on an unstructured tetrahedral mesh. The mesh generator employs a Delaunay triangulation algorithm [6, 7] to create a tetrahedral mesh throughout the flowfield. *AIRPLANE* has proven to be very reliable and capable of handling a variety of complex geometries. It has been used extensively in several supersonic transport studies [8, 9, 10].

Unstructured tetrahedral meshes were developed for all three configurations with and without nacelles and boundary layer diverters. The configurations were meshed in a modular fashion so that components could easily be removed or interchanged, and meshes for different configurations could be generated in a straightforward manner. The breakdown of the components for the baseline Reference H configuration are shown in Fig 4. The thin boundary layer diverters made it challenging to obtain high quality surface meshes in the region where the diverters attach to the wing lower surface. In order to obtain grids with accurate surface representation, each nacelle and diverter comprised one component in the data set, where the diverter is extended through the upper surface of the wing, and contains a portion of the upper wing surface (seen in the upper surface view of the figure). Accurate grids in the nacelle/diverter/wing region could successfully be obtained with the nacelles and diverters as one component. In addition, the nacelle/diverter assembly could be easily removed to generate a mesh for the wing/body configuration. The inboard wing and middle portion of the fuselage comprised one component which was later split into two components for the Ames 7-04, and Boeing W27 configurations to more easily obtain accurate surface triangulations along the intersection between the wing and fuselage. Accurate surface triangulations near intersections of adjoining components were easily obtained since *AIRPLANE* contains logic which does not allow different components to triangulate together except at the intersection between components. The mid and outboard portion of the wing were treated as separate components split along the sides of the extended diverter in a streamwise cut to the wing leading edge. The forward fuselage, and aft fuselage/horizontal tail were also defined as separate components, but could just as well have been combined to form a single component together with the mid-fuselage/inboard wing. Individual

vertical tail and yahuddi components were used to take advantage of the logic within the *AIRPLANE* code to provide accurate intersections between fuselage components.

The computations required approximately 1,000 iterations to achieve 4 orders of magnitude reduction of the average residual at Mach 2.4. The computations were carried out on an IBM SP2 and a Cray YMP, both located at Ames. The SP2 computer system consists of 160 IBM 590 processors running in parallel. The parallelized version of the *AIRPLANE* code has been shown to give linear speed up [11] as the number of processors is increased. Converged solutions for these cases (1,000 iterations) were achieved in under 25 minutes using 64 nodes with meshes of approximately 459,000 points and 2.77 million tetrahedral cells. The solutions on a single processor on the Cray-YMP required approximately 3 hours for the same number of iterations. The exceptional speed-up in computational time on the SP2 permitted computations of full polars to be obtained within a reasonable turnaround time.

5 Corrections Applied to Computational Results

Several corrections were made to the computed axial force coefficients to compare the inviscid computations with the experimental data. A flat plate skin friction coefficient was calculated for the model scale and wind tunnel Reynolds number and added to the axial force coefficients computed with *AIRPLANE*. The same skin friction coefficient values were used for all three configurations. These values were 0.006314 for wing/body computations, and 0.007196 for wing/body/nacelle computations. The skin friction of the diverters was negligible and was not added. The drag associated with the trip disks used to promote transition from laminar to turbulent flow in the wind tunnel was also applied to the computations. This value was estimated for the Langley UPWT test using the data from a trip drag study on the baseline Reference H configuration in the NASA Ames 9x7 Foot Supersonic Wind Tunnel. The results of this study showed that 2.0 counts of drag were attributed to the trip disks on a 2.7% scale model with 0.01 in. trip disk height at Mach 2.4, and Reynolds number of 3 million.

The accuracy of this number is questionable since it depends upon the overall accuracy of the drag measurements in the test. This value could be in error by 20 percent, since the repeatability of the data from the 9x7 test was approximately 0.25 to 0.5 count. To estimate a trip drag for the 1.675% scale model, the 2.0 counts were multiplied by the ratio of the model scales (0.027/.01675) to obtain 3.2 counts. This value was added to the computed axial force coefficients of all configurations. The final correction was a scaling of the flat plate skin friction values obtained for the baseline configuration by the ratio of the wetted areas of each optimized configuration to that of the baseline. The full scale wetted areas for the three configurations were 1.459 million sq in, 1.456 million sq in, and 1.467 sq in, for the baseline, Ames 7-04, and Boeing W27 configurations, respectively. The corrections are summarized below:

RefH

W/B	$0.006314 + 0.00032 = 0.006634$
$W/B/N$	$0.007196 + 0.00032 = 0.007516$

Ames7 − 04

W/B	$0.006314(1.45617/1.45932) + 0.00032 = 0.006620$
$W/B/N$	$0.007196(1.45617/1.45932) + 0.00032 = 0.007500$

BoeingW27

W/B	$0.006314(1.46695/1.45932) + 0.00032 = 0.006667$
$W/B/N$	$0.007196(1.46695/1.45932) + 0.00032 = 0.007554$

These values were added to the axial force coefficients obtained from *AIRPLANE* and the lift and drag were computed by rotating the body axis forces (normal and axial) by the angle of attack to obtain the wind axis forces (lift and drag).

Other corrections could have been made, such as obtaining different trip drag values with and without nacelles, or adding the skin friction for the diverters, but these differences are probably less than 1/10 of a count and are not measurable; the short term repeatability of the data obtained in the Langley UPWT was approximately 1.0 count.

6 Qualitative Results

The computed surface pressure coefficients for the three configurations are shown in isometric, front, and side views in Figs 5-7. The *AIRPLANE* solutions were obtained at Mach 2.4, and a lift coefficient of 0.12. The angles of attack needed to obtain a CL of 0.12 were; 4.25 degrees for the baseline and Ames 7-04 configurations, and 6.25 degrees for the Boeing W27 configuration. The two degree increase in angle of attack needed to attain a CL of 0.12 for the Boeing W27 configuration, was due to a drooped leading edge and lower wing incidence

(compare front views of Figs 5-7). At a quick glance, the pressure contours on the lower surface look similar for the three configurations (compare isometric views in Figs 5-7). The most noticeable difference is seen on the fuselage near the inboard wing leading edge. The Ames 7-04 configuration exhibits more uniform pressures in this region with more positive pressure than the Boeing W27 configuration, which should result in more lift in this region. A large increase in the forebody camber of the Ames 7-04 configuration is evident in the side views of the configurations (compare Fig 5 with Figs 6-7). A previous forebody camber optimization study, using the method developed at Ames, found that increased camber reduced the cruise drag and increased the pitching moment at zero lift on the Reference H configuration. Those results provided some assurance that the increased fuselage camber of the Ames 7-04 configuration would have similar performance benefits.

Both methods of modifying the wing camber and twist during optimization resulted in surface waviness (seen in the isometric views) on the two optimized configurations. The surface of the Boeing W27 configuration is more wavy than the Ames 7-04 configuration, and is seen in both the chordwise and spanwise directions, whereas the Ames configuration waviness is primarily in the spanwise direction. The assumption in the Ames design is that configuration waviness in the streamwise direction is more likely to increase form drag than in the spanwise direction, since the flow is predominately chordwise. The lack of smoothness in the spanwise direction for the Ames configuration results from localized modifications in the spanwise direction. The waviness could be reduced by using less wing defining sections, but this would limit the design space. The gradient information for inviscid flow (the partial derivatives with respect to the design variables) may not be accurate enough to detect small changes in the forces related to surface waviness. The surfaces of the final designs from both optimization methods were smoothed prior to model construction and the *AIRPLANE* evaluations. The amount of surface waviness which can be tolerated needs to be studied to determine criteria for acceptable levels of surface waviness.

Planform views of the *AIRPLANE* upper and lower surface pressures for the optimized configurations are shown in Figs 8-9. The upper surface oblique shock is notably stronger on the Ames 7-04 configuration than on the Boeing W27, but since the drag of the Ames 7-04 configuration is less than the Boeing W27 configuration, the lower induced drag of the Ames 7-04 configuration may offset the increased wave drag from the stronger oblique shock. The lower surface Cp's of the Boeing W27 configuration change rapidly near the leading edge of the wing, due to a cusp on the lower surface. The waviness in the Boeing W27 lower wing surface is reflected in the pressure coefficients.

An enlarged view near the nacelles and diverters of the Ames 7-04 configuration is shown in Fig 10. Diligent care and effort were required to obtain the accurate surface grids shown in this figure. The outboard sides of the diverters, which can be seen in this view, are extremely thin and their height compares with that of the boundary layer thickness at the inlet for the flight Reynolds number. This severe geometric constraint made it challenging to obtain the necessary level of surface accuracy for these configurations. The surface is colored by the computational pressure coefficient at the cruise flight condition: M=2.4, CL = .12. The high pressures resulting from the nacelle shocks on the wing lower surface are evident in the figure. The lower surface pressures between the nacelles with the nacelle/diverter component removed are shown in Fig 11. A increase in pressure on the lower surface is seen from the combined effects of the inboard and outboard nacelle shocks. The inboard nacelle shock strikes the lower portion of the fuselage. The increased pressures on the upper portion of the fuselage are from the trailing wing shock. Colored contour lines of the same pressure coefficient are displayed against the surface of the Ames 7-04 configuration in Fig 12.

7 AIRPLANE Force and Moment Predictions

The aerodynamic force and moment coefficients predicted by *AIRPLANE* for all three configurations with and without nacelles and diverters are shown in Figs 13-18. The plots of lift coefficient versus angle of attack are shown in Figs 13 and 14. The Boeing W27 configuration requires a two degree increase in angle of attack to attain a lift coefficient comparable to the baseline Ref H and Ames 7-04 configurations. The computations of the configurations with nacelles and diverters result in a 0.01 increase in lift coefficient compared with wing/body results due to the added lift from the high pressures of the nacelle shocks on the wing lower surface. The Ames 7-04 configuration requires a slightly lower angle of attack to attain lift coefficients comparable to the baseline configuration. Both optimized configurations are predicted to have more positive pitching moments than the baseline configuration which should reduce the trim drag of the aircraft (Fig 15). Drag polars are shown in Figs 16-18. An increase in drag associated with the nacelles and diverters is evident for the complete polar shown in Fig 16. This drag increase is primarily due to the skin friction of the nacelles, which accounts for approximately nine drag counts. An enlarged polar near zero lift is shown in Fig 17. The three wings can be easily compared in this figure. The Ames 7-04 configuration is predicted to have less drag than the W27 or Ref H configurations with and without nacelles and diverters. The Ames 7-04 configuration has approximately a 2

to 3 drag count improvement over the baseline, whereas the Boeing W27 has a 0 to 2 drag count improvement near zero lift. The polars are shown for lift coefficients near the design in Fig 18. The *AIRPLANE* results for the Ames 7-04 configuration show a 6.8 count improvement for the wing/body, and a 5.7 count improvement with nacelles and diverters compared with the baseline. The Boeing W27 configuration is predicted to have a 4.0 count improvement for the wing/body, and a 4.5 count improvement with nacelles and diverters.

8 Experimental Results: Wing/body

The experimental force and moment coefficients for the two optimized and baseline wing/body configurations are shown in Figs 19-24. Three repeat runs are plotted with the same line type, and without symbols, for each of the three configurations. The two degree shift in the lift curve predicted by *AIRPLANE* for the Boeing W27 configuration is also seen in the experimental results (compare Figs 14 and 20). Approximately 0.03 degrees angle of attack scatter band width is seen in the repeat runs (Fig 20). An error in angle of attack of this magnitude can result in a drag coefficient error of approximately 0.5 count at a lift coefficient of 0.1 and a Mach number of 2.4.

The pitching moment data shows the same relative trends that were predicted by *AIRPLANE*, with the optimized configurations having more positive moments than the baseline configuration. The experimental pitching moment data will be compared with the *AIRPLANE* computations in a later section of this report.

The drag polar near zero lift (Fig 23) shows that the Ames 7-04 configuration has less drag than the other configurations for lift coefficients greater than zero. The performance of the Boeing W27 configuration is poorer than the baseline for lift coefficients less than 0.08. The *AIRPLANE* wing/body results, Fig 17, showed similar trends. However, the lift coefficients at which the optimized configurations begin to outperform the baseline are approximately 0.015, and 0.05 for the Ames 7-04 and Boeing W27 configurations, respectively (compare Figs 17 and 23). Performance improvements of the optimized configurations near the design lift coefficient are seen in the partial drag polars shown in Fig 24. The experimental results for the Ames 7-04 model show a 6.5 count drag reduction relative to the baseline. This substantial performance improvement is in excellent agreement with the predicted 6.8 counts from the *AIRPLANE* computations (compare with Fig 18). The experimental performance improvement of the Boeing W27 relative to the baseline is smaller than expected, only 1.3 counts, compared with a 4.0 count improvement predicted by *AIRPLANE*. Disagreement between *AIRPLANE* and experiment will be discussed in later sections of this report. The three repeat runs in Fig 24 show some scatter in the drag for all three models. For example, 0.75 counts scatter is seen for the baseline model at CL of 0.12, and a 0.60 counts scatter for the 7-04 configuration at CL of 0.105. This will later be shown to be associated with scatter in the angle of attack data.

9 Experimental Results: Wing/Body/Nacelle/Diverter

The experimental force and moment coefficients for the optimized and baseline configurations with nacelles and diverters are shown in Figs 25-30. The drag results shown in Figs 28-30 validate the use of non-linear methods for the design of realistic supersonic transport configurations. The Ames 7-04 configuration shows improvement over the baseline for nearly all positive lift coefficients, with the largest improvement near the cruise lift coefficient. The experimental results at cruise show that the Ames 7-04 model has a 5.4 drag count reduction compared to the baseline. These experimental results of the complete Ames 7-04 model are in excellent agreement with the *AIRPLANE* computations which predicted a 5.7 count improvement. The performance gains are over a wide range of lift coefficients increasing the significance of the performance benefits of this design.

The Boeing W27 performance gains are greater with nacelles and diverters; the data shows a 2.0 drag count improvement, whereas only 1.3 counts were attained for the wing/body configuration. The *AIRPLANE* results also predicted a performance gain for the complete W27 configuration relative to the baseline. The improvement over the baseline begins at nearly the same lift coefficient (CL = 0.08) as the wing/body configuration. The scatter in the experimental data, for the three repeat runs, is nearly one count for all configurations (Fig 30). The difference in the computational and experimental results are much larger for this configuration.

10 AIRPLANE vs Experiment: Reference H

The *AIRPLANE* results for the baseline Reference H configurations with and without nacelles and diverters are compared with experiment in Figs 31-36. The *AIRPLANE* computations are plotted with symbols and experiment without symbols, since the computational data is sparser than the experimental data, and it would be difficult to see the small difference in repeat runs if the experimental data were plotted, as is typically done,

with symbols. The computational lift curves correlate well with the experimental data (Figs 31-32). The comparisons are slightly better for the complete configuration at the larger lift coefficients. This may be due in part to the smaller angle of attack required for the complete configuration compared with the wing/body model, for a fixed lift coefficient, since attached flow is more likely at lower angles of attack.

The pitching moment comparisons (Fig 33) are typical for an inviscid code. The computations predict more stability and nose down pitching moment than experiment. The computational and experimental results both show a more gradual pitch up for the complete configuration than the wing/body. The addition of the nacelles and diverters also result in a more negative CMo than the wing-body results, as would be expected from the increased lift on the aft portion of the wing from the nacelle shock waves impinging on the wing lower surface.

The comparisons of the drag polar near zero lift show excellent agreement between the *AIRPLANE* results and experiment (Figs 34 and 35). All computations shown are within 0.25 counts of experiment. The results near cruise (Fig 36) show a 1.3 and a 1.5 count difference between computation and experiment for the wing/body and wing/body/nacelle/diverter configurations, respectively.

11 AIRPLANE vs Experiment:Ames 7-04

The computational/experimental comparisons for the Ames optimized model with and without nacelles and diverters are shown in Figs 37-42. The lift curves (Figs 37-38) correlate very well; the *AIRPLANE* curves exhibit a small positive shift in CLo indicating a small increase in effective camber for the Ames 7-04.

The pitching moment comparisons (Fig 39) show similar trends as was shown for the baseline, with the computations showing more stability and nose down moments near cruise. Less pitch up is again observed for the configuration with nacelles and diverters.

The Ames 7-04 wing/body and complete configuration computational results presented in Fig 41 both slightly over predict the drag by approximately 1.3 counts at zero lift, but near a lift coefficient of approximately 0.08 the computations agree precisely with experiment. The results at cruise (Fig 42) show a 1.6 and a 1.9 drag count difference between *AIRPLANE* and experiment for the wing/body and complete configurations, respectively.

12 AIRPLANE vs Experiment:Boeing W27

AIRPLANE and experiment are compared for the Boeing W27 configurations in Figs 43-48. The lift curve correlation is good (Figs 43-44). The moment data comparisons show the increased stability of the computations relative to experiment, similar to that shown for the baseline and Ames 7-04 models. The *AIRPLANE* drag polar near zero lift (Fig 47) shows excellent agreement with experiment. The wing/body computations match experiment very well for lift coefficients less than 0.04, but the curves begin to separate at larger lift coefficients. The wing/body/nacelle/diverter drag data comparisons show less than 0.25 counts difference near zero lift. The curves diverge at larger lift coefficients with approximately a 2.0 count difference at a CL of 0.08.

Poor correlations are shown near cruise in Fig 48. The increments between computation and experiment show a 3.5 and 4.3 drag count difference for the wing/body and complete configurations, respectively. This discrepancy in drag may be due in part to separation on this model, or some other viscous phenomenon not modeled in the Euler computations. The experimental angle of attack measurements will be shown to be a source of error in the wind-axis force coefficients. Normal and axial force coefficients for the wing/body and complete configurations will be compared in the following section to eliminate any error associated with the measurement of the experimental angle of attack.

13 Body Axis Force coefficients Comparisons

The computational and experimental normal and axial force coefficients are compared for the the optimized and baseline wing/body configurations in Figs 49-50. Notice that the experimental repeat runs have very little scatter in the data, whereas the wind-axis data showed scatter of approximately 1.0 drag count. This indicates that the scatter in the experimental drag polars was due to inaccuracies in the angle of attack measurements.

The computational and experimental correlations of the normal versus axial force curves are very good for all configurations. Even the curvature of the Ames 7-04 axial force curves is accurately predicted by *AIRPLANE*. The shape of the Ames 7-04 axial force curves indicate somewhat desirable characteristics for this design, since the largest reduction in axial force occurs near the design lift coefficient, and the gradual curvature indicates that the improvement will be realized off-design. The cruise normal force and lift coefficients are not greatly different since the design angle of attack is only 4.50 degrees. The axial force coefficients are significantly lower

for the Boeing W27 configuration than the other configurations. However, one cannot compare the cruise performance characteristics of the models using the axial force data since the angle of attack needed to attain the same lift coefficient is approximately two degrees larger for the W27 than that required for the other models. The net effect is that at cruise the Boeing W27 configuration is superior to the baseline, but still has more drag than the Ames model. The plot is enlarged near a normal force coefficient of 0.12 in Fig 50. The differences in the axial force coefficient at CN of 0.12 are 0.0, 0.75, and 1.25 axial forces counts for the baseline, Ames 7-04, and Boeing W27 configurations respectively. This represents a significant improvement over the comparisons for the wing/body wind-axis data, those increments were: 1.3, 1.6, and 3.5 drag counts for the baseline, Ames 7-04, and Boeing W27 configurations, respectively. The better computational/experimental correlations for the body-axis force coefficients and the absence of scatter in the experimental repeat runs clearly indicates that the inaccuracies in the experimental angle of attack are responsible for a large portion of the drag discrepancies between *AIRPLANE* and experiment for the Boeing W27 configuration. The reason that the scatter in the angle of attack for W27 is greater than that for 7-04 is not clear.

The body-axis correlations for the configurations with nacelles and diverters are shown in Fig 51-52. The baseline and Boeing W27 *AIRPLANE* results were obtained with the diverter truncated at the trailing edge of the wing resulting in a rearward facing step. The aft portion of the actual diverter was smoothly closed with a ramp tangent to the upper surface at the trailing edge of the wing, provided this resulted in a ramp which intersected the nacelle.

Modeling the aft portion of the diverter with a step as opposed to the ramp used on the wind tunnel models will later be shown to account for only 0.3 drag counts. The computed axial force data for the complete configurations correlate well with experiment. The plot (Fig 52) near a normal force coefficient of 0.12 shows increments of approximately 1.4, 0.86, and 2.8 axial force counts for the baseline, Ames 7-04, and Boeing W27 configurations, respectively. There is again substantially less differences in the body-axis comparisons than the wind-axis comparisons, which were: 1.5, 1.3, and 4.3 drag counts for the baseline, Ames 7-04, and Boeing W27 configurations, respectively.

14 Experimental Data Recomputed Using the Computational Angle of Attack

Since the experimental angle of attack measurements have been identified as a source of error in the experimental drag measurements, the computational angle of attack can be used to recompute the experimental lift and drag coefficients using this angle and the experimental normal and axial force coefficients. This will allow comparisons to be made of the computational and experimental drag polar data with consistent angle of attack values and show the importance that angle of attack makes to the drag and lift coefficients.

The experimental drag polar for the Boeing W27 wing/body configuration was recomputed using the angle of attack computed by *AIRPLANE* at the experimental lift coefficient. The original experimental data and the *AIRPLANE* computation are compared with the re-computed experimental data using the computational angle of attack in Figs 53-54. The computational and experimental data correlations remain largely the same at low lift coefficients, but the discrepancy between *AIRPLANE* and experiment using the computational angle of attack is significantly reduced at larger lift coefficients. The enlarged view of the results near the design lift coefficient (Fig 54) show that the computational and experimental data are within 1.5 drag counts, instead of the 3.5 count increment that was obtained with the original wind tunnel data.

The results for the Ames 7-04 wing/body configuration are presented in Figs 55-56. The comparison of the experimental data using the computed alpha is nearly indistinguishable from the *AIRPLANE* results (Fig 55). The results near the design lift coefficient (Fig 56) show that computational data is nearly coincident with the recomputed experimental data, whereas the original results had approximately 1.6 counts discrepancy.

The baseline Reference H wing/body comparisons of the experimental data using the CFD angle of attack and *AIRPLANE* are shown in Figs 57 and 58. The computational data now coincides with the recomputed experimental data (Fig 57). The increment between the computational data and the recomputed experimental data is now within approximately 0.5 count near cruise, whereas the original data had a 1.5 count discrepancy with the *AIRPLANE* computations.

The experimental results using the *AIRPLANE* computational angle of attack for the optimized and baseline wing/body configurations are compared in Figs 59-60. The polar near the cruise lift coefficient (Fig 60) shows that the Boeing W27 configuration has a 2.5 drag count improvement relative to the baseline, whereas the original experimental data showed a 1.3 count improvement. The Ames 7-04 configuration has nearly the same performance improvement as with the original data. This indicates that the experimental angle of attack measurements may be worse for the Boeing W27 model. If the Boeing W27 has regions of separated flow, it might be evident in the experimental colored oil flow pictures presented in Fig 61. The upper surface flow on the Ames 7-04 and Boeing W27 models at cruise conditions, M=2.4, CL = 0.12, are shown. Oblique shocks

on the upper surface of both optimized configurations were predicted by *AIRPLANE* (see Figs 8-9). The shocks begin near the root and lie nearly parallel to the mid-wing leading edge. This shock extends to the wing trailing edge near the outboard side of the outboard nacelle on the Ames 7-04 model, whereas the oblique shock on the Boeing W27 is weaker and does not extend to the trailing edge. These shocks can be seen in the experimental oil flow photographs by the change in flow direction of the oil. They appear to be positioned in nearly the same location as predicted by *AIRPLANE*, and appear to have the relative strengths that were predicted for the configurations (compare Fig 61 with Figs 8-9). The lack of oil on the inboard wing panels near the side of body indicates that the flow has separated in this region on both configurations. This could be caused by a vortex formed at the root leading edge of the wing or could be due to the flow separating at the trailing edge or a combination of both. The photographs alone are not sufficient to positively determine the flow phenomena of the configurations.

15 Ames 7-04 vs Baseline: Wing/Body Comparisons

The data presented in this and the next three sections were shown in the previous sections, without overlaying the the computational and experimental data for the optimized and baseline configurations. The previous sections were focused on the increments between the computational and experimental data. However, a computational tool like *AIRPLANE* has two functions. One function is to determine the aerodynamic characteristics of a given configuration, which is usually accomplished by comparing the computational and experimental force and moment coefficients. The second and equally important function of a CFD method is to predict the performance effects due to a design change to any aircraft component. This and the following three sections are focused on the performance increments, obtained with *AIRPLANE* and experiment, between the optimized and baseline configurations.

Computational and experimental comparisons of the Ames 7-04 and baseline wing/body configurations are shown in Figs 62-67. The computational and experimental lift curves show a small increase in lift curve slope for the Ames 7-04 configuration relative to the baseline configuration. This change in slope could be attributed to more vorticity on the Ames 7-04 model than the baseline configuration. The computational/experimental correlations of the lift curves of both configurations are good, but the slope of the computational curves are larger than experiment (Figs 62-63).

The computational and experimental data both show that the Ames configuration has more positive pitching moments than the baseline configuration. The computational and experimental moment curves appear rotated about the point of zero lift. The rotation of the computational moment data is in the expected direction for an inviscid code. The pitching moment increments between the Ames 7-04 and baseline configurations are nearly the same for computation and experiment. This indicates that *AIRPLANE* is capable of accurately predicting the moment changes from camber and twist, but over estimates the stability.

The computational and experimental drag polars are rotated near zero lift for the Ames 7-04 configuration (Fig 66). The computational data indicates that the Ames 7-04 has less drag than the baseline for lift coefficients greater than 0.02, whereas the experimental data indicates that the Ames 7-04 model performs better for lift coefficients greater than 0.0. Overall, the computational and experimental drag increments between the Ames 7-04 and baseline configurations correlate well. Experiment shows that the two configurations have equivalent drag at zero lift, whereas *AIRPLANE* shows a 1.0 count performance penalty for the baseline. The computational and experimental performance increments as well as the absolute drag level of the two configurations are identical for lift coefficients between 0.07 and 0.10 (Fig 66). At CL 0.12, the *AIRPLANE* computations show a 6.8 count improvement of the Ames configuration relative to the baseline whereas experiment shows a 6.5 count gain (Fig 67).

16 Boeing W27 vs Baseline: Wing/Body Comparisons

Computational and experimental force and moment data for the Boeing W27 and baseline wing/body configurations are presented in Figs 68-73. The computational and experimental increments in lift coefficient between the two configurations correlate well, both show a two degree increase in angle of attack required for the Boeing W27 to attain the CL of the baseline (Fig 69). *AIRPLANE* predicts a very small increase in lift curve slope for both configurations relative to experiment. Because this increase in lift curve slope is nearly the same for the two configurations, the computational and experimental lift coefficient increments correlate well for the full range of angles of attack.

The pitching moment data increments are not as well predicted as for the Ames configuration (compare Fig 71 with Fig 65). *AIRPLANE* predicted a less positive shift in moment than was obtained experimentally, the difference in the increments is 0.005. The Baseline computational/experiment correlations are better than for

W27.

The computational and experimental performance increments of the W27 configuration relative to the baseline configuration are in excellent agreement near zero lift coefficient. (Fig 72). *AIRPLANE* shows a 3.0 count performance penalty for the W27, and experiment shows a 3.25 count penalty. The correlations begin to deteriorate rapidly for lift coefficients above 0.04. At cruise, *AIRPLANE* predicts a 4.0 count improvement and the experimental data shows 1.3 counts (Fig 73). The experimental measurements of the angle of attack were identified and discussed previously as a primary source of these discrepancies.

17 Ames 7-04 vs Baseline: Wing/Body/Nacelle/Diverter Comparisons

Computational and experimental comparisons of the Ames 7-04 and baseline configurations with nacelles and diverters are shown in Figs 74-79. The baseline and Ames 7-04 configurations have very similar lift curves, and the experiment/*AIRPLANE* correlations are good. *AIRPLANE* has a slightly larger lift curve slope than experiment for the Ames 7-04 configuration, but predicts nearly the same slope as experiment for the baseline configuration (Fig 75). The overprediction of the Ames configuration lift curve slope, results in an increment in CL of 0.004 for *AIRPLANE*, and 0.0022 for experiment near cruise. The pitching moment increments between the Ames 7-04 and baseline configurations are nearly equal for the computations and experiment (Fig 76). The stability is again overpredicted by *AIRPLANE*. The drag increments of the Ames 7-04 relative to the baseline for lift coefficients between 0.05 and 0.125 are nearly the same for *AIRPLANE* and experiment (Figs 78 and 79). However, the increments at zero lift are approximately 1.3 counts for *AIRPLANE* , whereas experiment shows approximately a 0.5 counts increment; both experiment and *AIRPLANE* predict the the poorer performance of the 7-04 configuration relative to the baseline at this condition. The increments at cruise are predicted to be 5.7 counts from *AIRPLANE* , and 5.4 counts from experiment.

18 Boeing W27 vs Baseline: Wing/Body/Nacelle/Diverter Comparisons

Computational and experimental comparisons of the Boeing W27 and baseline configurations with nacelles and diverters are shown in Figs 80-85. The angle for zero lift for the complete W27 configuration is 0.10 deg. larger for *AIRPLANE* than experiment. Note that the experimental measurements may not be accurate as discussed earlier. The moment comparisons in Fig 82, indicate that *AIRPLANE* does not predict the extent of pitch-up shown in the experimental results for either configuration. Pitch-up begins at a lower lift coefficient for the W27 configuration than for the baseline, which may indicate more separation on the W27 configuration than the baseline at and above cruise lift. The drag coefficient increments are in poor agreement with experiment (Figs 84-85). The *AIRPLANE* computations show larger performance improvements for the W27 relative to the baseline for nearly all lift coefficients. The correlation of the computational and experimental performance increments worsen with increasing lift.

19 Nacelle Orientation: Performance Effects

Upon the completion of the design optimization process, it was necessary to attach the nacelles to the optimized wing lower surface, without loss of performance. In previous studies [8, 10] it has been shown that this can be accomplished by maintaining the height of the baseline Ref H diverter at the leading and the trailing edge corners. These three points are identified on the diverter/wing intersection of the baseline configuration, and then projected vertically onto the optimized wing surface. The projected points on the optimized wing surface are then used as targets to aid in the alignment of the nacelle/diverter on the optimized configuration. The baseline nacelle/diverter assembly is moved such that the leading and trailing edge points on the baseline diverter/wing intersection nearly match the projected points on the optimized wing. After moving the nacelles and diverters using this method, the diverter height is again equal to the boundary layer thickness at the leading edge, with minimum height at the trailing edge, as with the baseline configuration. A new diverter/wing intersection is then derived for the optimized configuration by vertically projecting the nacelle/diverter intersection onto the optimized wing.

This method was initially used to attach the nacelles of the optimized wind tunnel models. But, the possibility of channel flow between the nacelle and wing was considered, since the distance between the wing and nacelle were not equal on the inboard and outboard sides of the diverter. However, this was not a concern on the original Ref H configuration which had unequal diverter sides. But, the possibility of channel flow could easily be eliminated on the optimized configurations by rolling the nacelles about their centerline, to achieve a more equal heights along the sides of the diverters, resulting in the nacelles being nearly perpendicular to the lower surface. An aft view of the nacelle/diverter region of the *AIRPLANE* surface grid for the Ames 7-04

configuration with the nacelles/diverters in the original and modified orientations is shown in Fig. 86. The inboard side of both diverters is shorter than the outboard side when the nacelles are in the original orientation. The nacelle and diverters were rotated about the center of the nacelle until the sides of the diverter were of equal height when measured at the middle of the diverter side. This resulted in the diverter/wing intersection shifting inboard from the original intersection, as is seen in the planform view of the Ames 7-04 configuration in Fig 87. Note that the inboard intersections have moved more than the outboard, reflecting a greater orientation change for the inboard nacelle.

The *AIRPLANE* aerodynamic characteristics for the Ames 7-04 with the nacelles in the original orientation are compared with the nacelles placed nearly normal to the wing lower surface in Fig 88. Almost no discernible differences can be seen in the lift and moment curves. But, approximately a 0.3 count drag penalty is shown for the new orientation. The penalty is attributed to the nacelles not being oriented in this position during optimization.

The Boeing W27 configuration was also evaluated using *AIRPLANE* with the original nacelle orientation and the nacelles rolled approximately normal to the lower surface. An aft view of the nacelle/diverter region of the Boeing W27 configuration with the nacelles/diverters in their original position (top) and aligned normal to the lower surface (bottom) is shown in Fig. 89. The non-equal sides of the inboard nacelle can be seen in the figure. The nacelle appears to have larger differences in the heights of the sides of the diverter than for the Ames 7-04. This is because when the nacelle is moved using the 3-point method an optimization process takes place. It is usually only possible to exactly match one of the three projected surface points which is chosen to be the leading edge of the diverter, the other two trailing corner points are as closely aligned as possible. This can result in different heights of the diverter at the trailing corners on the optimized configurations relative to the baseline. The greater differences in diverter heights results in larger shift of the diverter-wing intersections for the Boeing W27 (Fig 90) than for the Ames 7-04 configuration (Fig 87).

The *AIRPLANE* aerodynamic characteristics for the different nacelle orientations on the Boeing W27 are shown in Fig 91. Again, there is no discernible differences in the lift and moment curves. However, there is approximately a 0.3 count drag improvement for the new orientation. The performance improvement is attributed to the nacelles being oriented in this position during optimization.

20 Aft Modeling of Diverters: Performance Effects

The aft portion of the diverter was modeled in *AIRPLANE* in two ways. The first way, and easiest to grid, was to truncate the aft portion of the diverter at the trailing edge of the wing. This results in a rearward facing step, which would cause separation in the wind tunnel, but since *AIRPLANE* is an inviscid code, the forces from this region would be inaccurate. Fortunately, the base of the diverter is fairly small, so the drag increment should be small. The second method of modeling diverter closure was to add a ramp tangent to the upper surface trailing edge of the wing, provided the resulting ramp intersected the nacelle. This method was used to smoothly close the diverters on the wind tunnel models.

The *AIRPLANE* surface grid, colored by the surface normal, with truncated and ramped diverters are shown for the Ames 7-04 and Boeing W27 configurations in Figs 92 and 93, respectively. The changes to the aerodynamic coefficients of the Ames 7-04 and Boeing W27 configurations are shown in Figs 94 and 95, respectively. Both configurations show no difference in the lift and moment coefficients, the drag coefficient is reduced by approximately by a third of a count for the ramped diverters, compared with the truncated, stepped diverters. This difference is small enough that the diverter could be truncated in *AIRPLANE* computations for intermediate designs evaluations to expedite the grid generation process.

21 Computational Pressure Distributions: Spanwise Cuts

A planform view of the *AIRPLANE* lower surface pressures for the Ames 7-04 configuration is shown in Fig 96. The streamwise and spanwise cut locations are superimposed on the lower surface pressures to identify the source of shocks when studying the wing/body pressure distributions in the following figures where the flow from the nacelles causes rapid changes in the wing pressures. Spanwise pressure distributions and geometry for the two optimized and baseline configurations are shown in Figs 97-106. The geometrical cuts are taken for the three configurations, without angle of attack changes. The conditions were: Mach 2.4, CL = 0.12. The computational angle of attack for the baseline and Ames 7-04 models was 4.25 degrees, whereas the the Boeing W27 configuration was 6.25 degrees.

The first section with constant axial dimension begins to cut through the leading edge of the wing (Fig 97). The Boeing w27 geometry is very different from the baseline and Ames configurations. The wing incidence and/or fuselage camber has resulted in the large geometrical shift shown. A lower surface cusp in the Boeing

W27 is also evident in the figure. The pressure distributions for the two optimized configurations show more lift than the baseline. It is somewhat surprising that the large geometrical differences in the optimized configurations have similar pressure distributions at this station. The next station (Fig 98) shows that the optimized configurations produce more lift, and possibly thrust, near the wing leading edge than the baseline configuration. The Boeing W27 configuration has considerable droop at this station, which is partly responsible for a larger angle of attack to attain the design CL than the baseline or Ames models. The Ames 7-04 configuration continues to have more leading edge lift at x=1730 than the Boeing W27 configuration. The wavy surface of the Boeing W27 configuration is seen in both the geometry and pressure distributions in Figs 98 and 99.

The oblique shock on the upper surface is seen in the pressure distributions in Figs 100-104. The shock is clearly stronger for the Ames 7-04 than the Boeing W27 or baseline configurations. The cut at x=2350 (Fig 104) intersects only the outboard nacelle. The geometry shows the outer portion of the nacelle and diverter for reference to the geometrical shape computed, but only the pressures on the lower wing surface are shown. The increase in pressures from the outboard nacelle shocks are seen in the lower surface pressures. The next two stations cut through both nacelles (Figs 105 and 106). In these figures, it is apparent that only lower surface pressures are shown, since pressures are not shown in the region of the diverters. These stations show increased pressures on the lower surfaces of the optimized wings resulting from the nacelle shocks. This increase in pressure results in lift which may provide thrust or a reduction in drag if the pressures act on a aft facing surface.

Streamwise pressures and geometry are shown in Figs 107-113. The first station, near the wing root, shows the increased lift in the leading edge region. The pressures have small oscillations near the leading edge, due to scalloping of leading edge resulting from the unstructured grid generator connecting closest points, and the slicing routine to sample the unstructured data set. These oscillations are most severe on the Boeing W27 configuration. The enlarged leading edge of W27 in Fig 108 shows a lower surface cusp and non-smooth geometry, resulting from the CAD definition of the configuration. This cusp and the leading edge droop result in fairly rapid changes in the lower surface pressures near the leading edge (Figs 109 and 110). A large change in pressures is seen aft of the lower surface shocks from the combined nacelle shocks (Fig 111). The optimized models have higher pressures in this region resulting more lift. The Boeing W27 configuration is reflexed upward in this region, which should result in thrust or reduced drag. Whereas the Ames 7-04 model is not reflexed up in this region. The Ames optimization procedure did not allow the the trailing edge to reflex upward.

22 Concluding Remarks and Summary Figures

The two optimized configurations were found to have superior performance characteristics relative to the baseline Reference H configuration. The experimental lift/drag ratio (L/D) of the two optimized configurations and the baseline wing/body and complete configurations are shown in Figs 114 and 115, respectively. The Ames 7-04 wing/body configuration has a substantial improvement relative to the baseline, whereas the Boeing W27 configuration shows a lessor improvement than the Ames model (Fig 114). The improvements are over a broad range of lift coefficients with the maximum at the design CL. The improvements in L/D are realized with nacelles and diverters present, but the improvement is less for the Ames model, and greater for the Boeing W27 configuration relative to the wing/body increments (compare Figs 115 with 114).

Excellent drag correlations between *AIRPLANE* and experiment were found for the Ames 7-04 and baseline configurations, but poorer correlations were obtained for the Boeing W27 model. A bar chart of the drag count increments between *AIRPLANE* and experiment at the cruise lift coefficient is shown for the two optimized and baseline configurations in Fig 116. The increments at zero lift are shown in Fig 117. The results are better at zero lift than at CL = .12.

The experimental data was shown to have scatter in the angle of attack measurements and drag coefficient measurements. The short term repeatability scatter band width was found to be approximately 1 drag count.

The experimental axial and normal force coefficient measurements showed no discernible differences in the short term repeat runs. Therefore the angle of attack measurements were deemed responsible for the 1 count scatter in the drag data.

The axial force correlations between *AIRPLANE* and experiment were found to be better than the drag correlations, providing further evidence of inaccurate experimental angle of attack measurements.

The computational and experimental performance increments for the Ames 7-04 model with and without nacelles and diverters were found to correlate well. However, the correlation is poorer for the Boeing W27 models, owing in part to the inaccurate experimental angle of attack measurements. These increments, defined as the difference in drag of the baseline from each optimized configuration, are shown for *AIRPLANE* and

experiment in Fig 118.

Excellent nacelle/diverter installation drag correlations between *AIRPLANE* and experiment were obtained for the baseline and two optimized configurations. The installation drag was the least for the Boeing W27 configuration. The changes in drag due to nacelle installation are shown in a bar chart in Fig 119.

The computational and experimental drag correlations for the three models was greatly improved when the experimental data was re-computed using the angle of attack obtained from the *AIRPLANE* computations. This further substantiates the claim that the experimental angle of attack measurements are not of the accuracy needed to obtain accurate drag data. The change in drag counts between *AIRPLANE* and the re-computed experimental data are shown in Fig 120.

The *AIRPLANE* performance effects of modeling the aft portion of the diverter with a rearward facing step; truncated at the trailing edge of the wing, and a extending the diverter with a ramp tangent to the upper surface trailing edge angle, resulted in only in a third of a count difference in drag coefficient. The drag was less for the ramped diverter for all configurations.

References

[1] Reuther, J. — Practical design optimization of wing/body configurations using the Euler equations *AIAA paper 92-2633*, 1992.

[2] Gill, P.E. , Murray, W. and Wright, M.H. — Practical optimization, *Academic Press*, 1981.

[3] Young, D.P. , Huffman, W.P. , Melvin, R.G. , Bieterman, M.B. , Hilmes, C.L. , and Johnson, F.T. — Inexactness and global convergence in design optimization, *5th AIAA/USAF/NASA/ISSMO Symposium on Multidisciplinary Analysis and Optimization*, Panama City, Florida, AIAA Paper 94-4286, September 1994.

[4] Jameson, A. , Baker, T.J. and Weatherill, N.P. — Calculation of inviscid transonic flow over a complete aircraft, *AIAA 24th Aerospace Sciences meeting* , Reno, AIAA Paper 86-0103, January 1986.

[5] Jameson, A. and Baker, T.J. — Improvements to the aircraft Euler method, *AIAA 25th Aerospace Sciences meeting* , Reno, AIAA Paper 87-0452, January 1987.

[6] Baker, T.J. — Three dimensional mesh generation by triangulation of arbitrary point sets, *AIAA 8th Computational Fluid Dynamics Conference* , AIAA Paper 87-1124-CP, Hawaii, June 1987

[7] Baker, T.J. — Automatic mesh generation for complex three-dimensional regions using a constrained Delaunay triangulation, *Eng. Comp.* , Vol. 5, pp. 161–175 (1989)

[8] Cliff, S.E. , Reuther, J.J. , Baker, T.J. , Mann, M.J. and Hicks, R.M. —Supersonic wing design by numerical optimization with superimposed nacelle pressures, *Proc. NASA Workshop on Propulsion Airframe Integration*, Cleveland, Ohio, October 1993

[9] Cliff, S.E. , Baker, T.J. and Hicks, R.M. — Design and computational/experimental analysis of low sonic boom configurations, *Proceedings of High Speed Research: 1994 Sonic Boom Workshop*, NASA/CP-1999-209699, December 1999.

[10] Cliff, S.E. and Baker, T.J. — Nacelle integration studies for HSCT Configurations using *AIRPLANE*. Unpublished.

[11] Jameson, A. , Cliff, S.E. ,Thomas, S.D. , Baker, T.J. and Cheng, W. — Supersonic transport design on the IBM parallel system SP2, *Proc. Computational Aerosciences Workshop* , Sunnyvale, CA, March 1995.

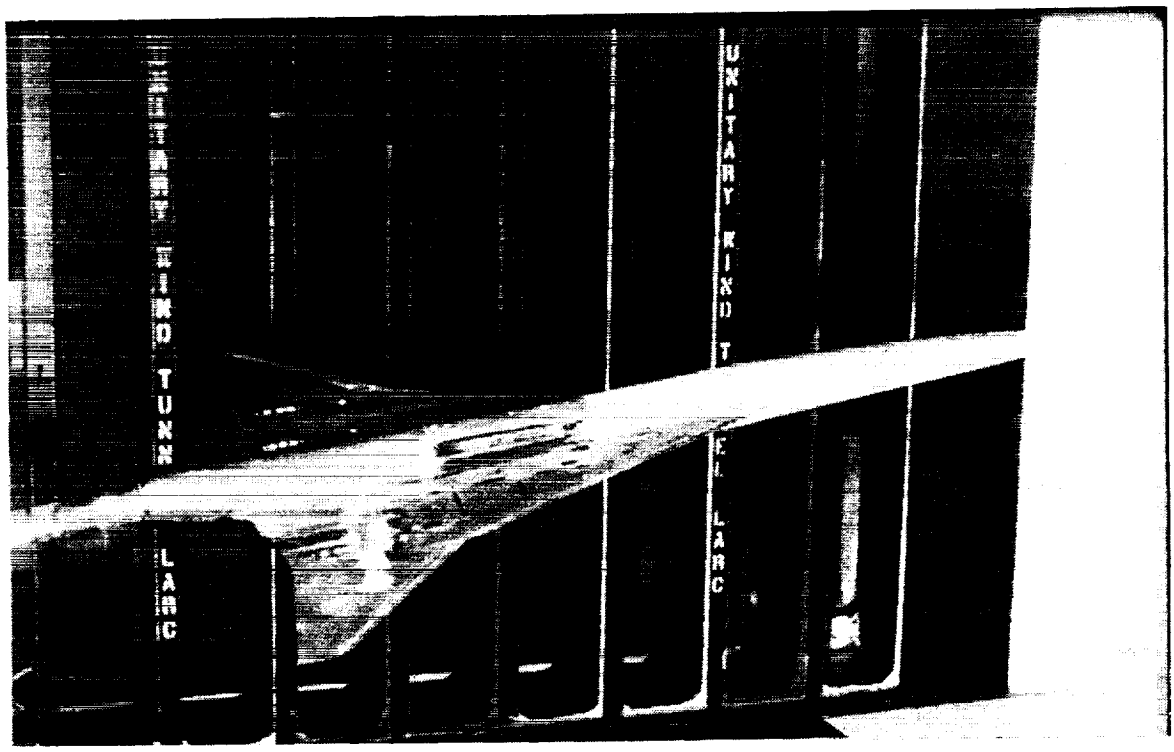

Fig 1. Photograph of the Baseline Reference H model installed in the Langley Unitary Plan Supersonic Wind Tunnel.

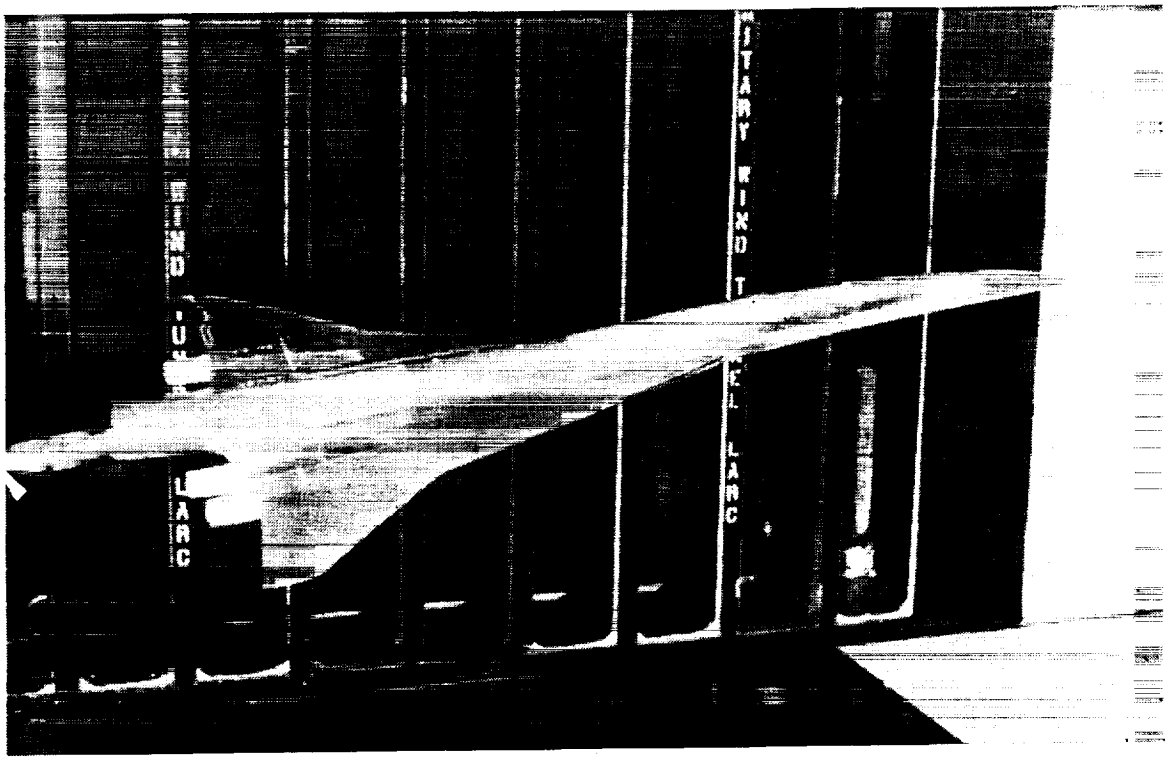

(a) Upper Surface

Fig 2. Photograph of the Ames 704 model installed in the Langley Unitary Plan Supersonic Wind Tunnel.

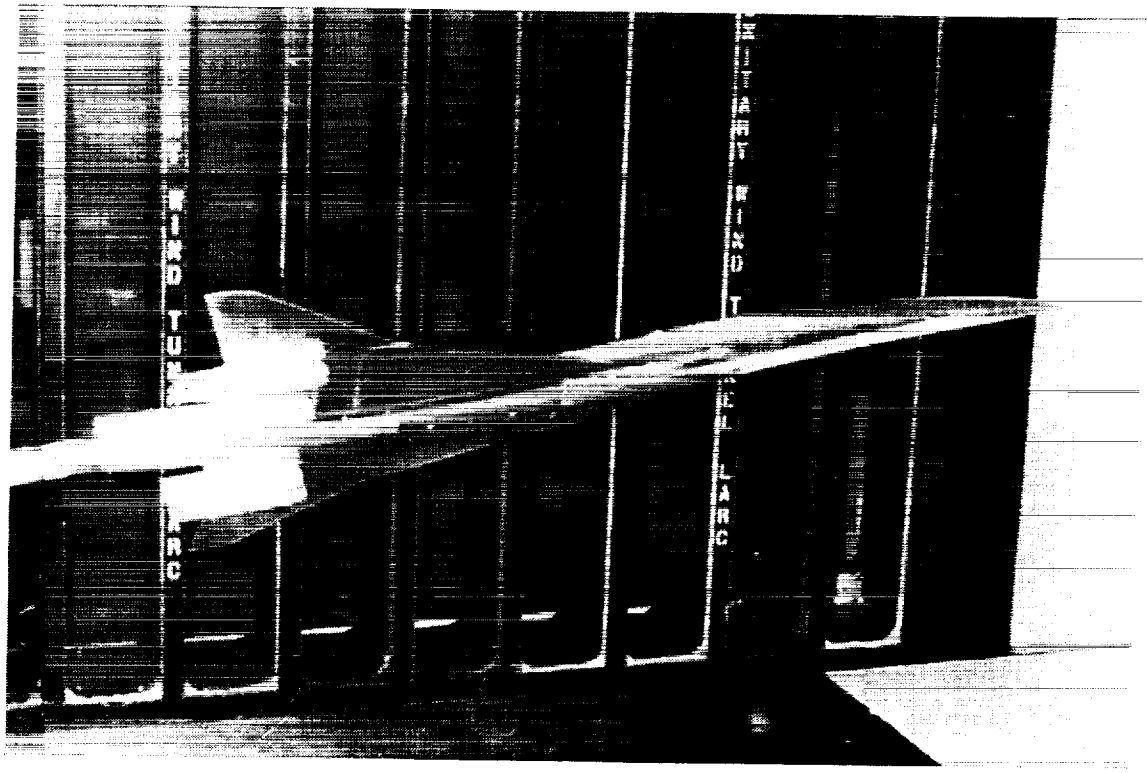

(b) Lower Surface

Fig 2. Concluded.

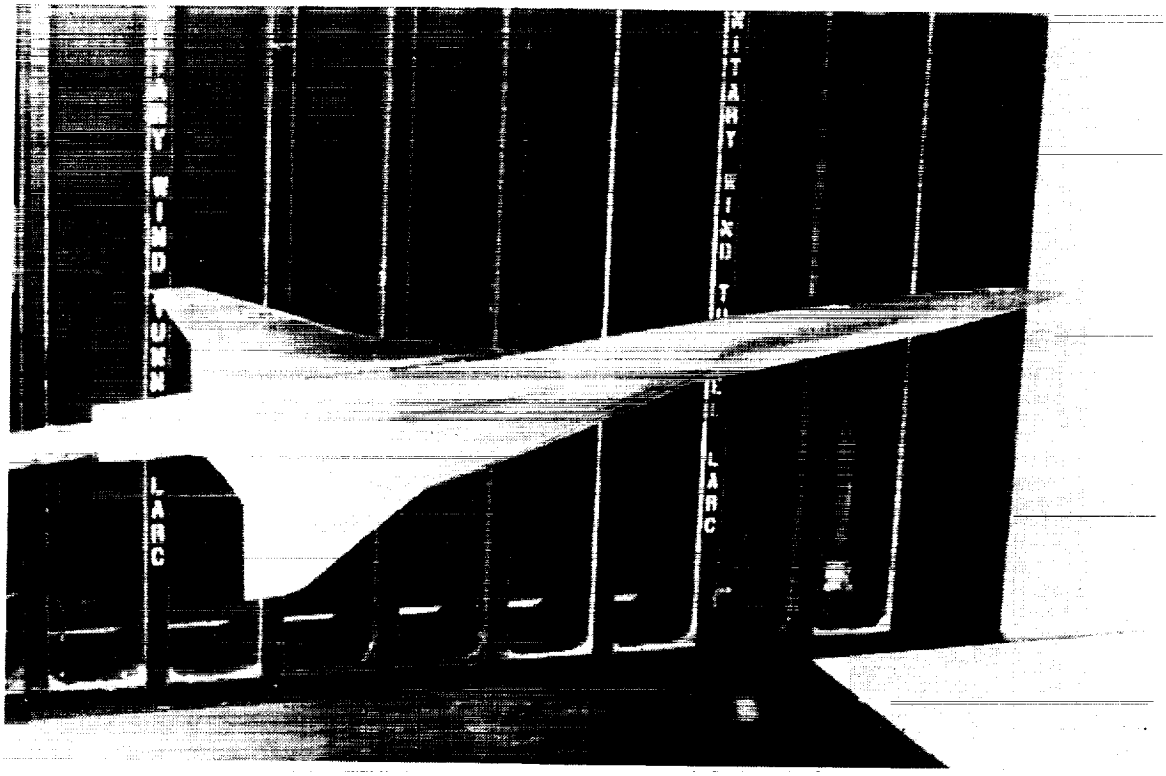

Fig 3. Photograph of the Boeing W27 model installed in the Langley Unitary Plan Supersonic Wind Tunnel.

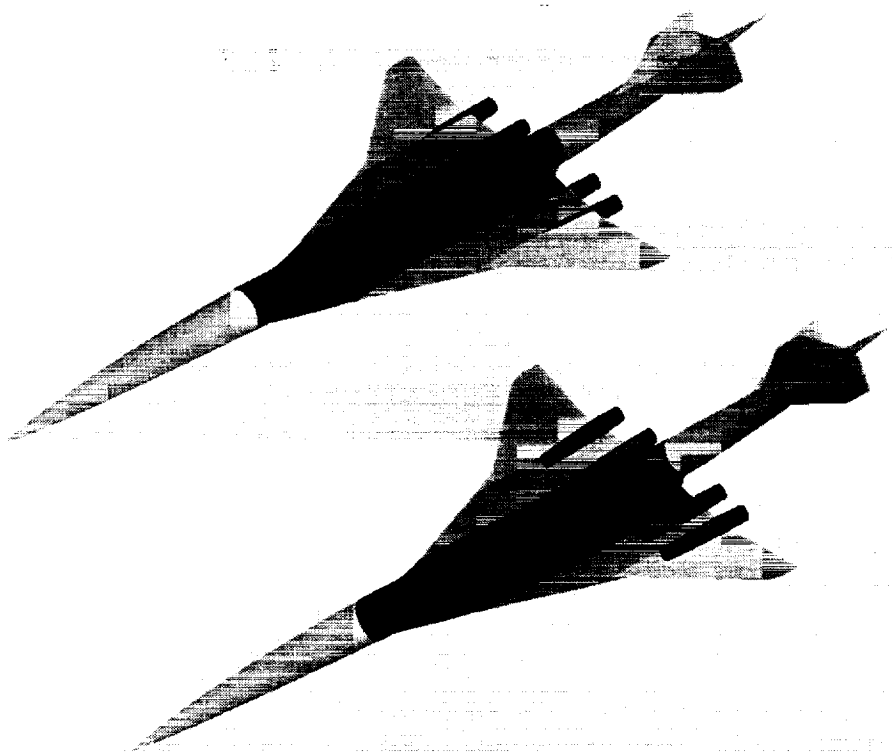

Fig 4. Component breakdown of the Baseline Reference H Configuration used for AIRPLANE.

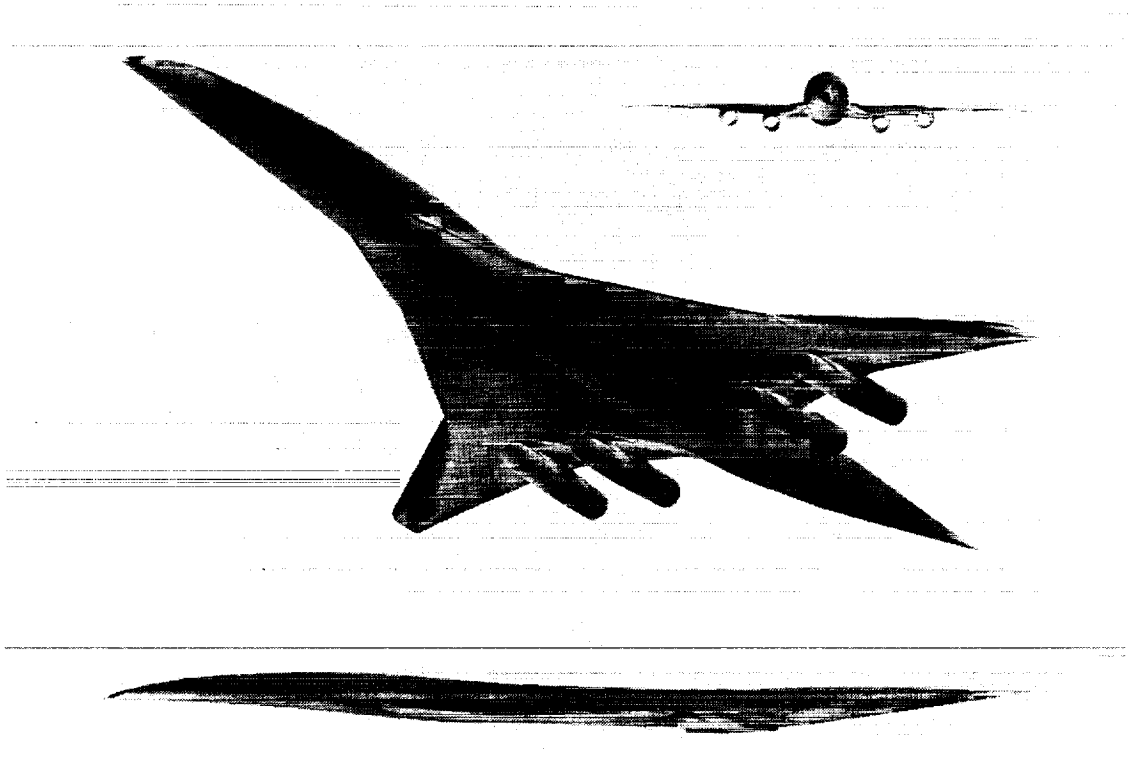

Fig 5. AIRPLANE surface pressure coefficients for the Ames 704 configuration, M=2.4, CL = 0.12, alpha = 4.25 degrees.

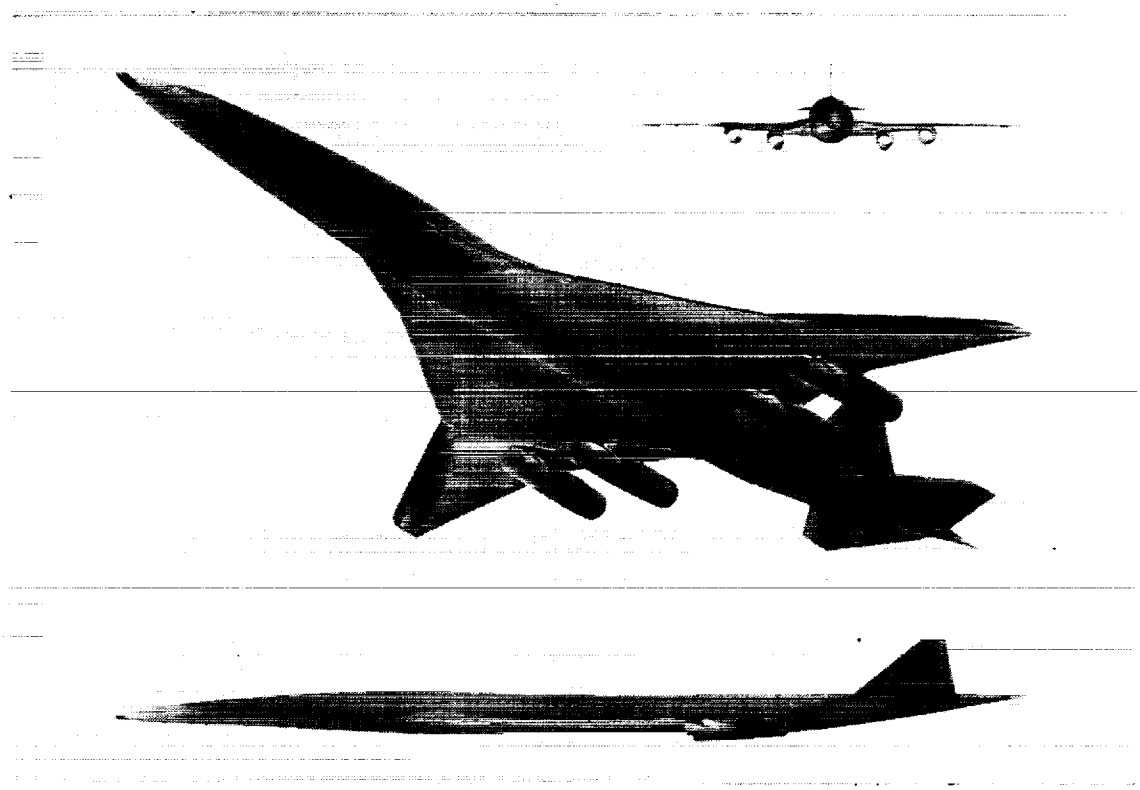

Fig 6. AIRPLANE surface pressure coefficients for the baseline Ref H configuration, M=2.4, CL = 0.12, alpha = 4.25 degrees.

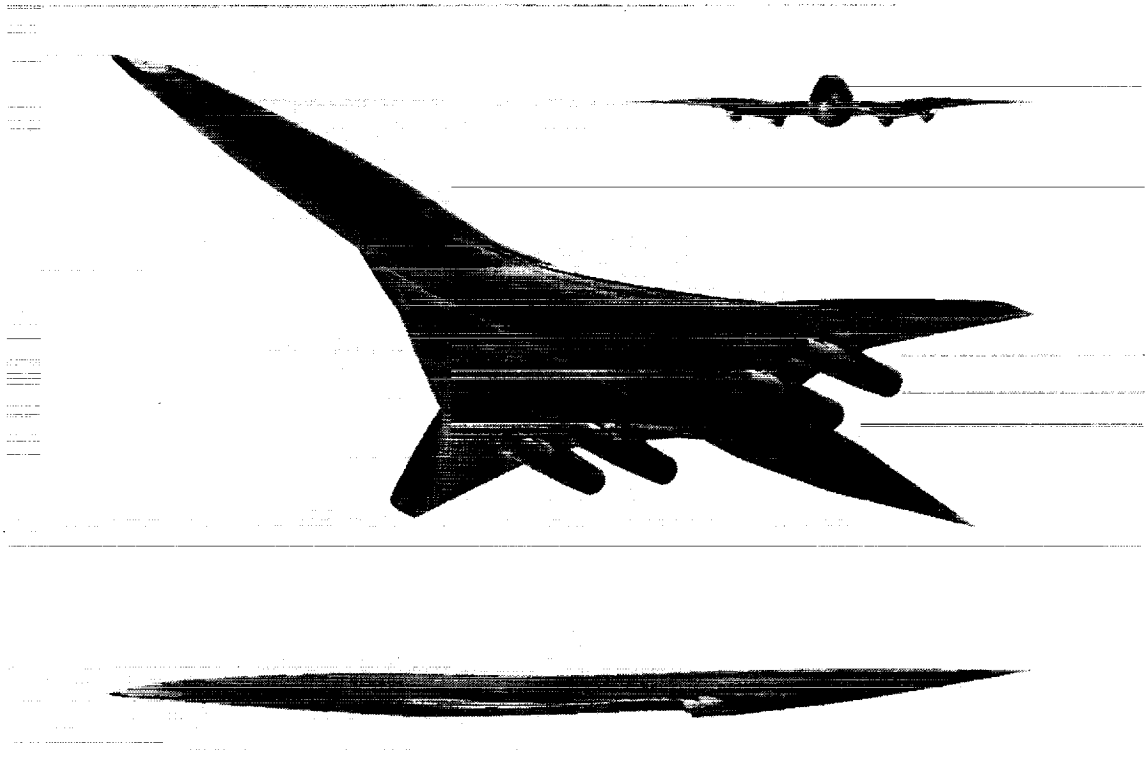

Fig 7. AIRPLANE surface pressure coefficients for the Boeing W27 configuration, M=2.4, CL = 0.12, alpha = 6.25 degrees.

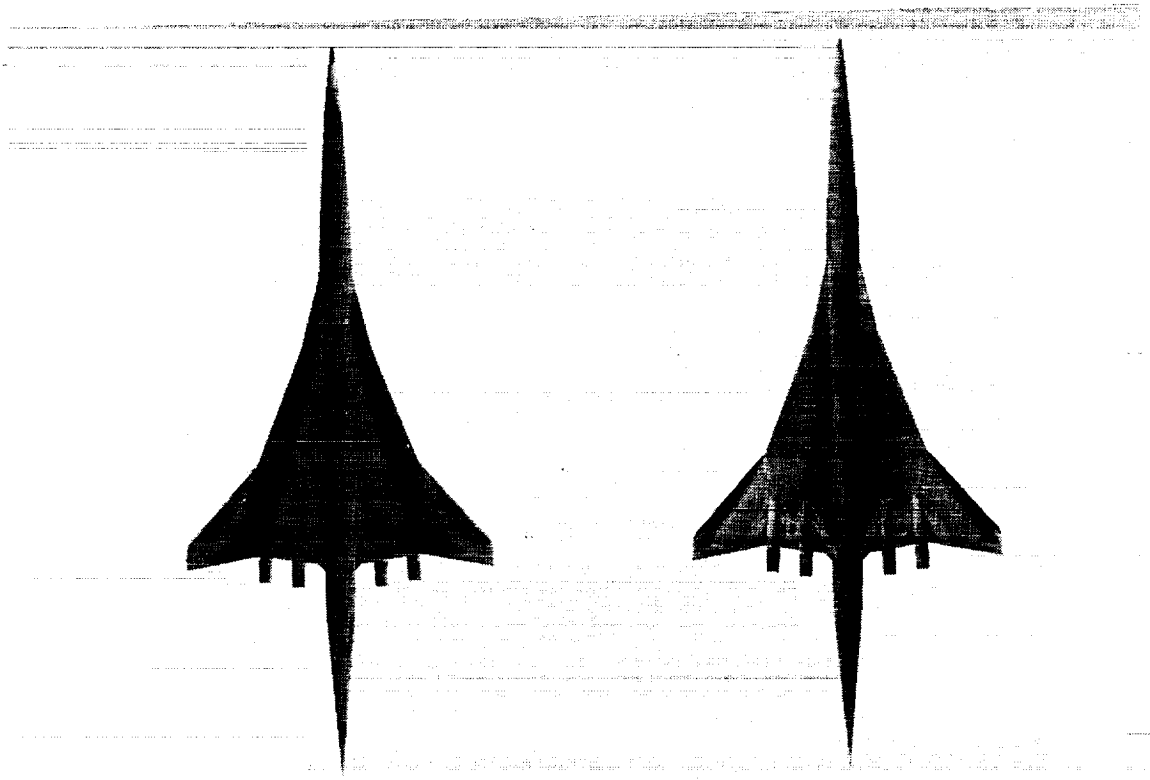

Fig 8. Planform views of the AIRPLANE surface pressure coefficients for the Ames 704 configuration, M=2.4, CL=0.12, alpha=4.25 degrees.

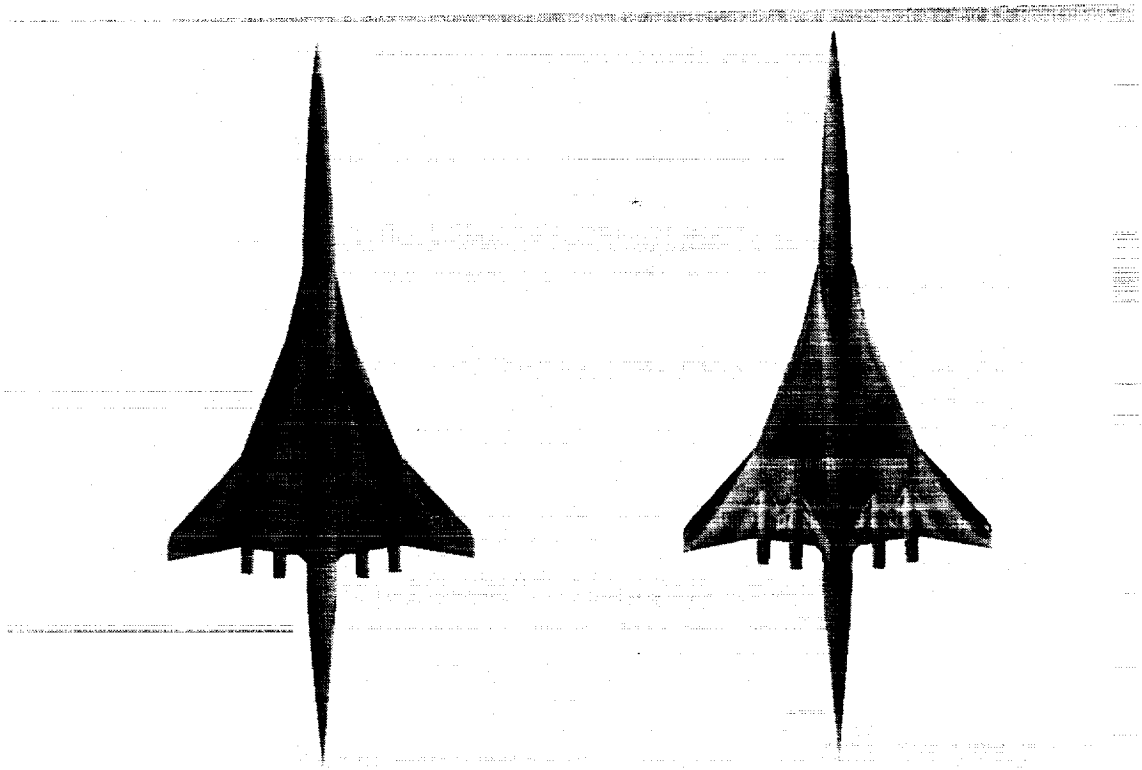

Fig 9. Planform views of the AIRPLANE surface pressure coefficients for the Boeing W27 configuration, M=2.4, CL=0.12, alpha=6.25 degrees.

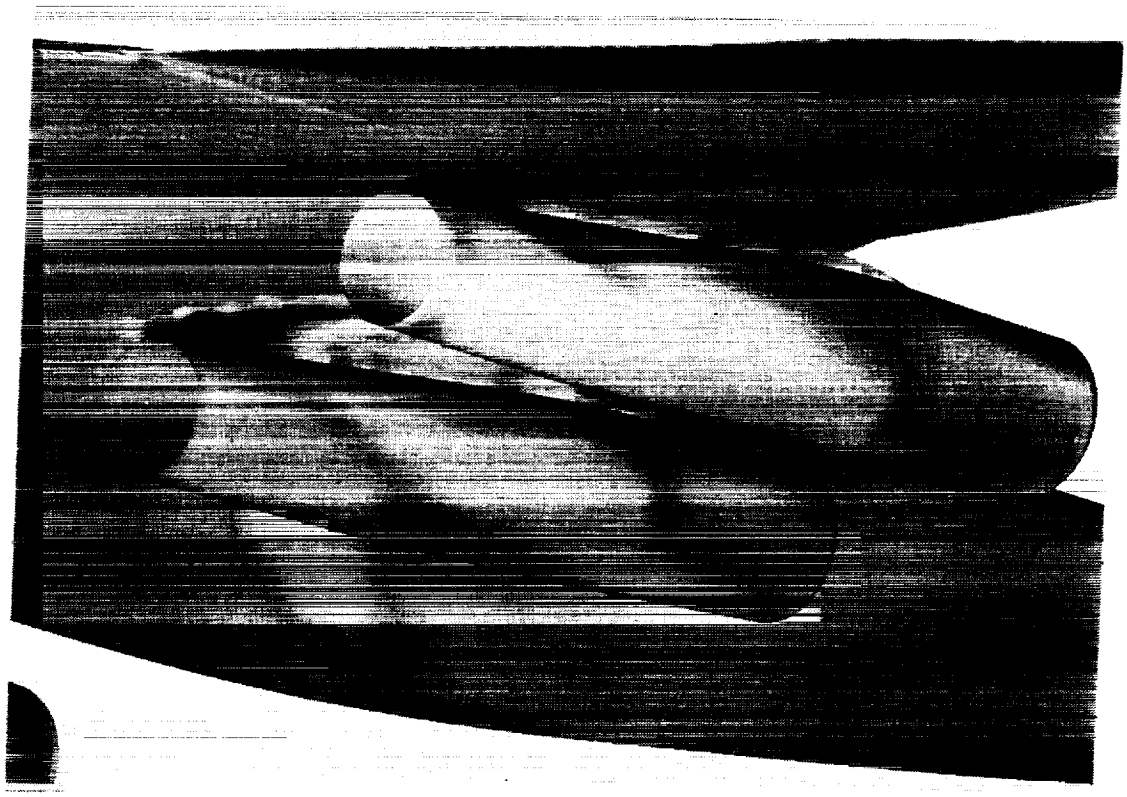

Fig 10. AIRPLANE surface pressure coefficients near the nacelles and diverters of the Ames 704 configuration, M=2.4, CL=0.12.

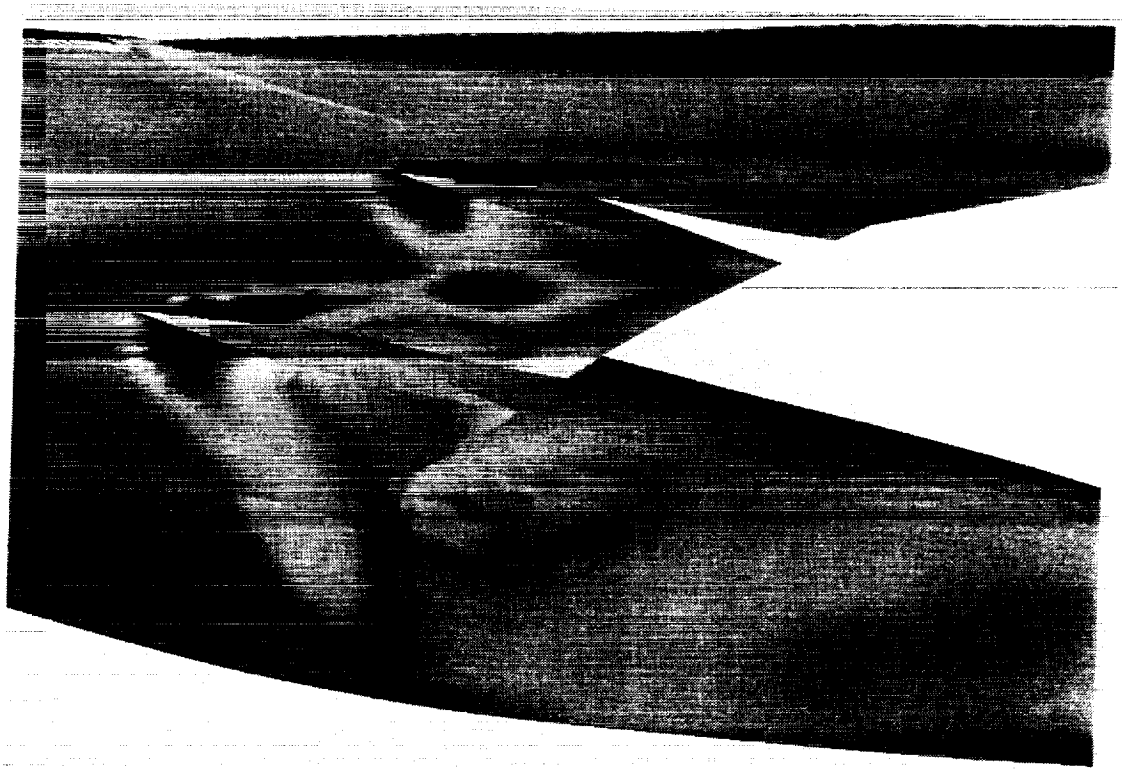

Fig 11. AIRPLANE lower surface pressure coefficients without the nacelles and diverters for the Ames 704 configuration, M=2.4, CL=0.12.

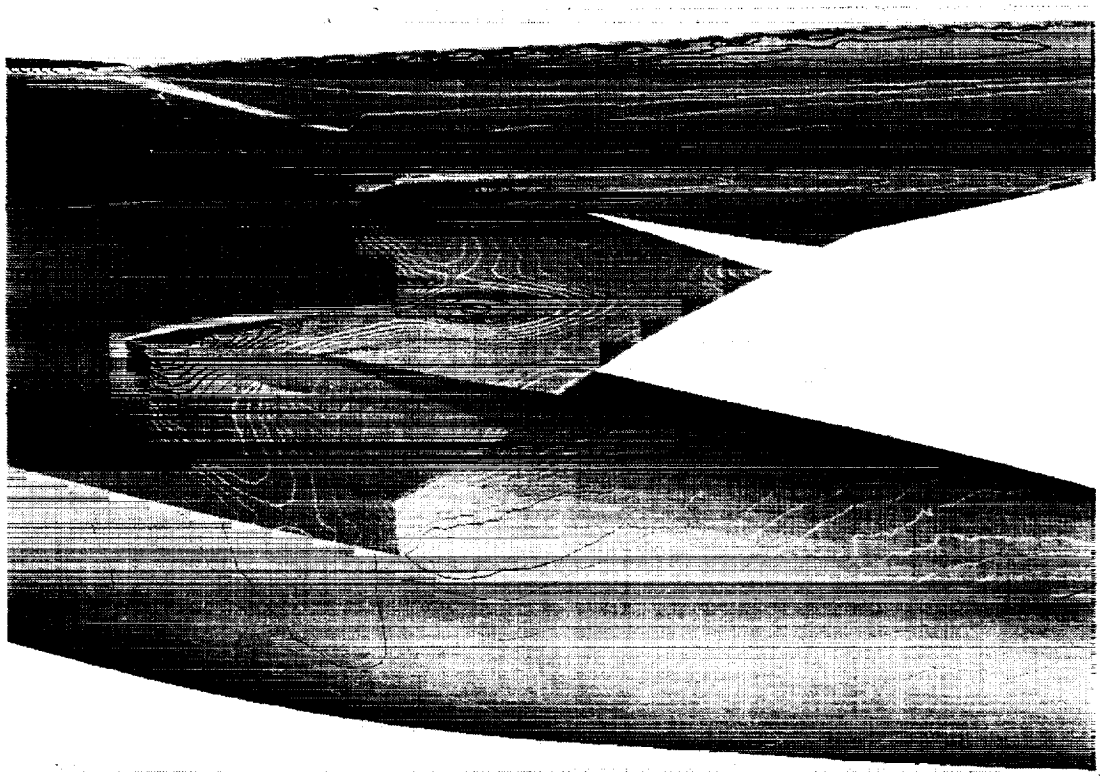

Fig 12. AIRPLANE lower surface pressure coefficient contours lines without the nacelles and diverters for the Ames 704 configuration, M=2.4, CL=0.12.

SYMBOL	CONFIGURATION	MACH	RN	RUN	Data Type
—○—	W27 W/B AIRPLANE	2.40	4.000	1	AIRPLANE
—□—	704 W/B AIRPLANE	2.40	4.000	1	AIRPLANE
—◇—	REF H W/B AIRPLANE	2.40	4.000	1	AIRPLANE
·····○·····	W27 W/B/N/D AIRPLANE	2.40	4.000	1	AIRPLANE
·····□·····	704 W/B/N/D AIRPLANE	2.40	4.000	1	AIRPLANE
·····◇·····	REF H W/B/N/D AIRPLANE	2.40	4.004	1	AIRPLANE

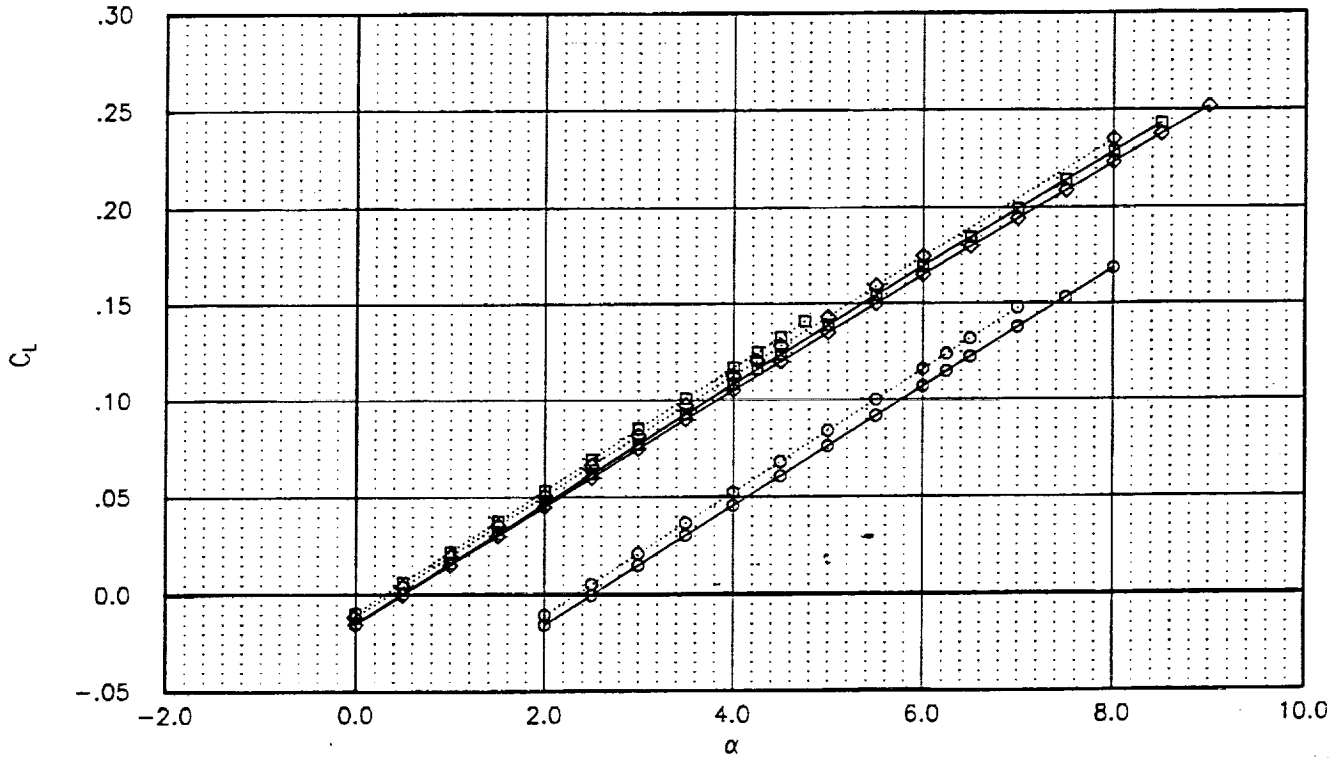

Fig 13. AIRPLANE W/B and W/B/N/D aerodynamic force and moment coefficients for Ref H baseline and optimized configurations

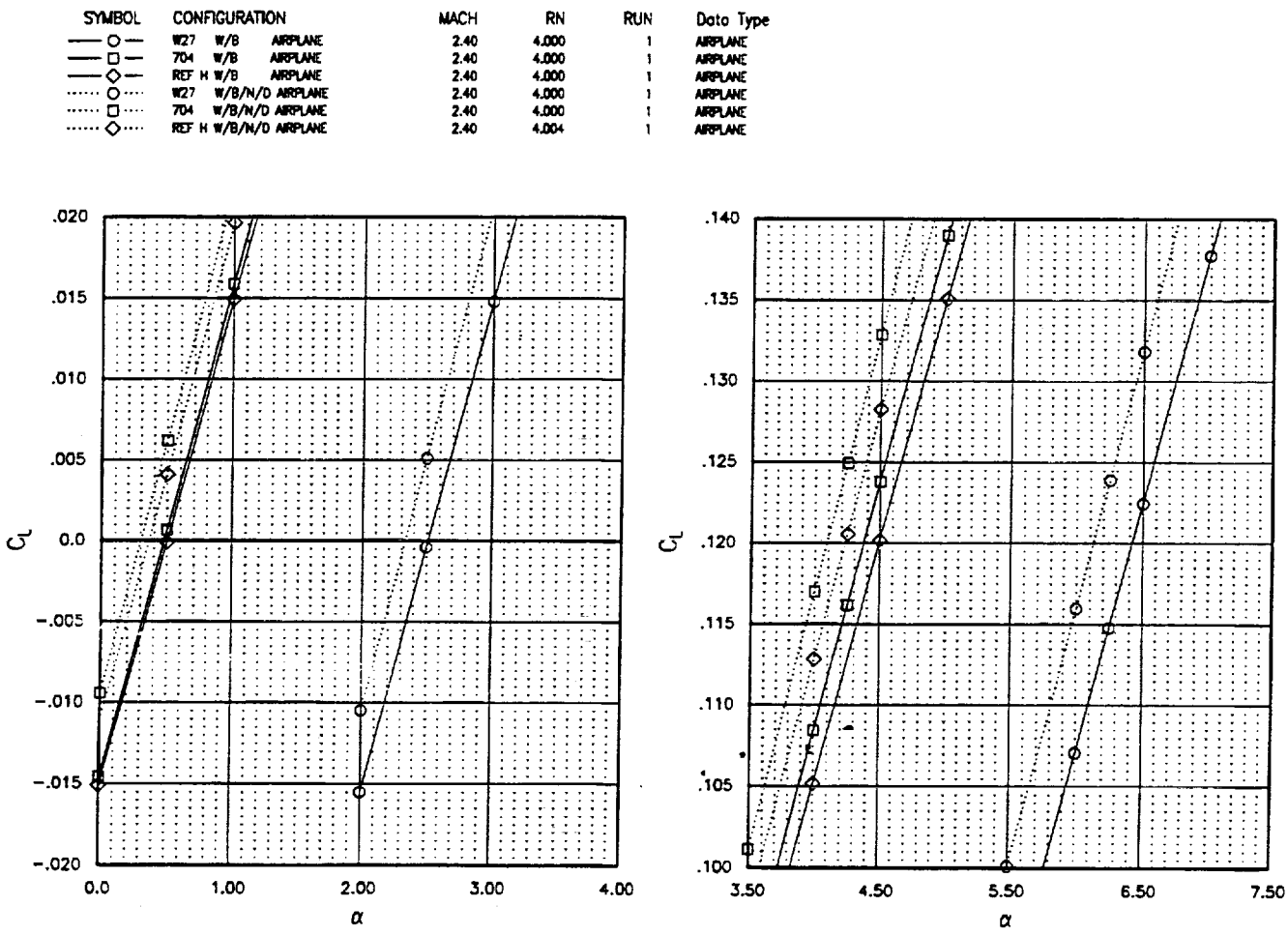

Fig 14. AIRPLANE W/B and W/B/N/D aerodynamic force and moment coefficients for Ref H baseline and optimized configurations

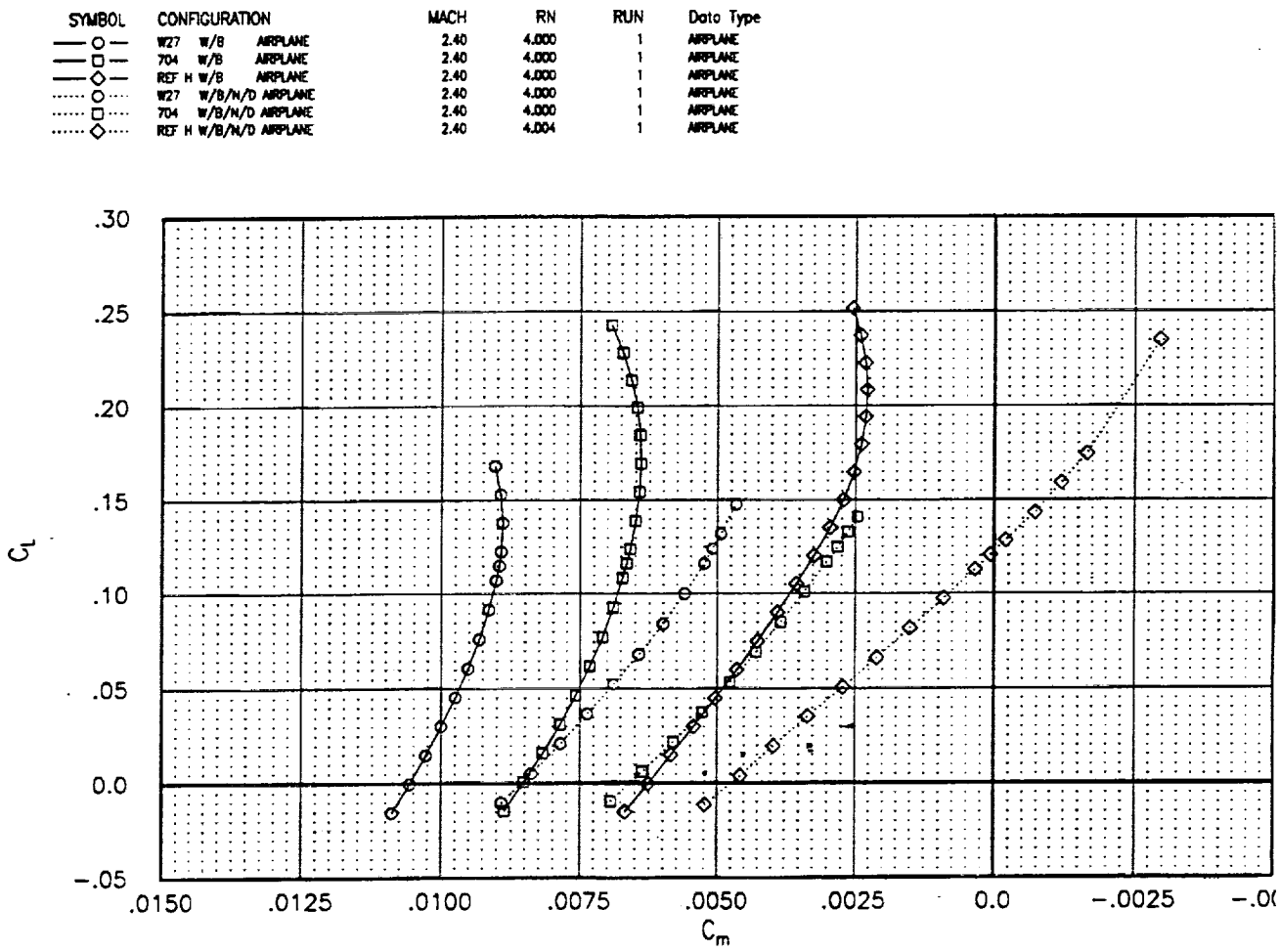

Fig 15. AIRPLANE W/B and W/B/N/D aerodynamic force and moment coefficients for Ref H baseline and optimized configurations

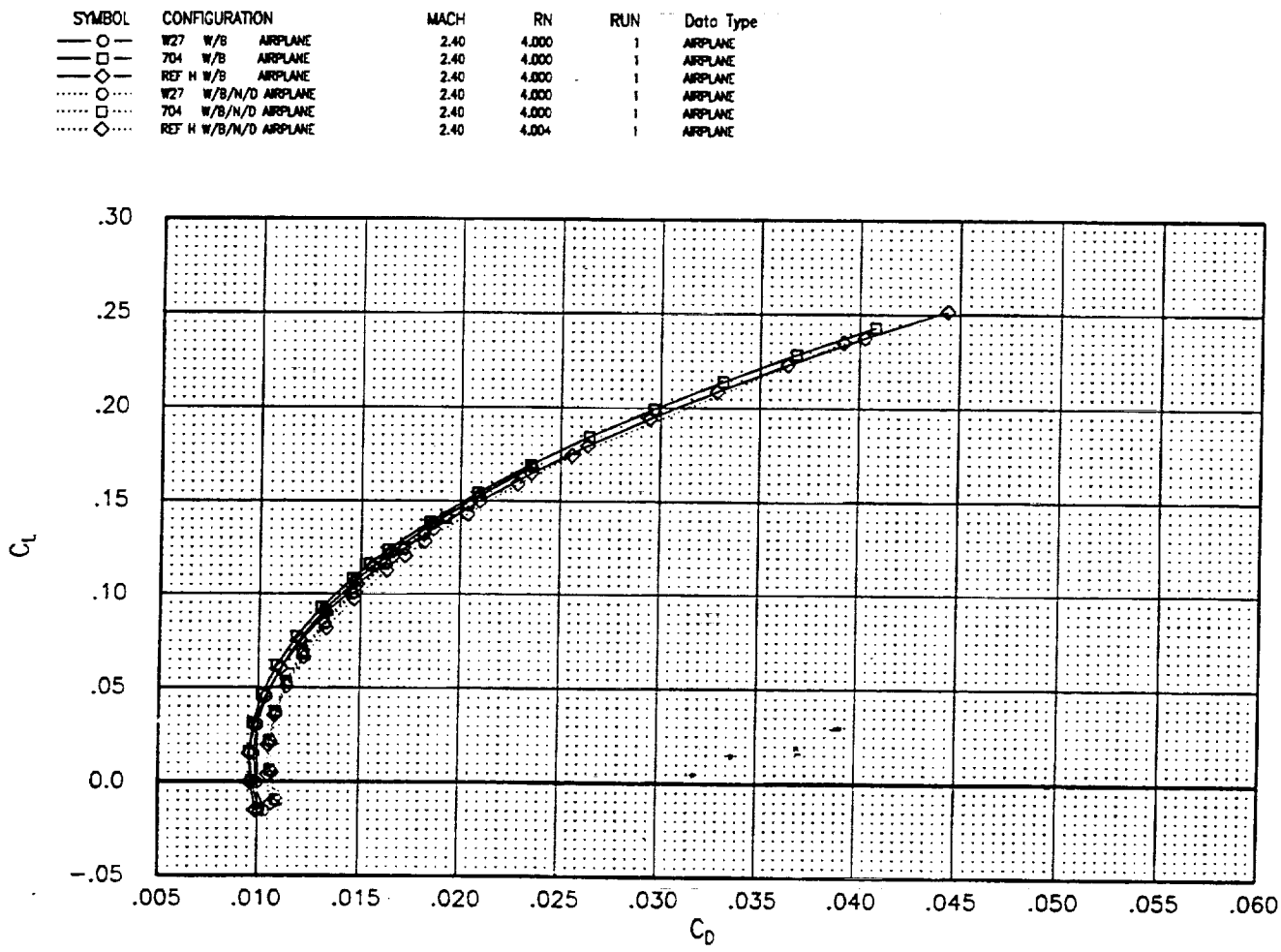

Fig 16. AIRPLANE W/B and W/B/N/D aerodynamic force and moment coefficients for Ref H baseline and optimized configurations

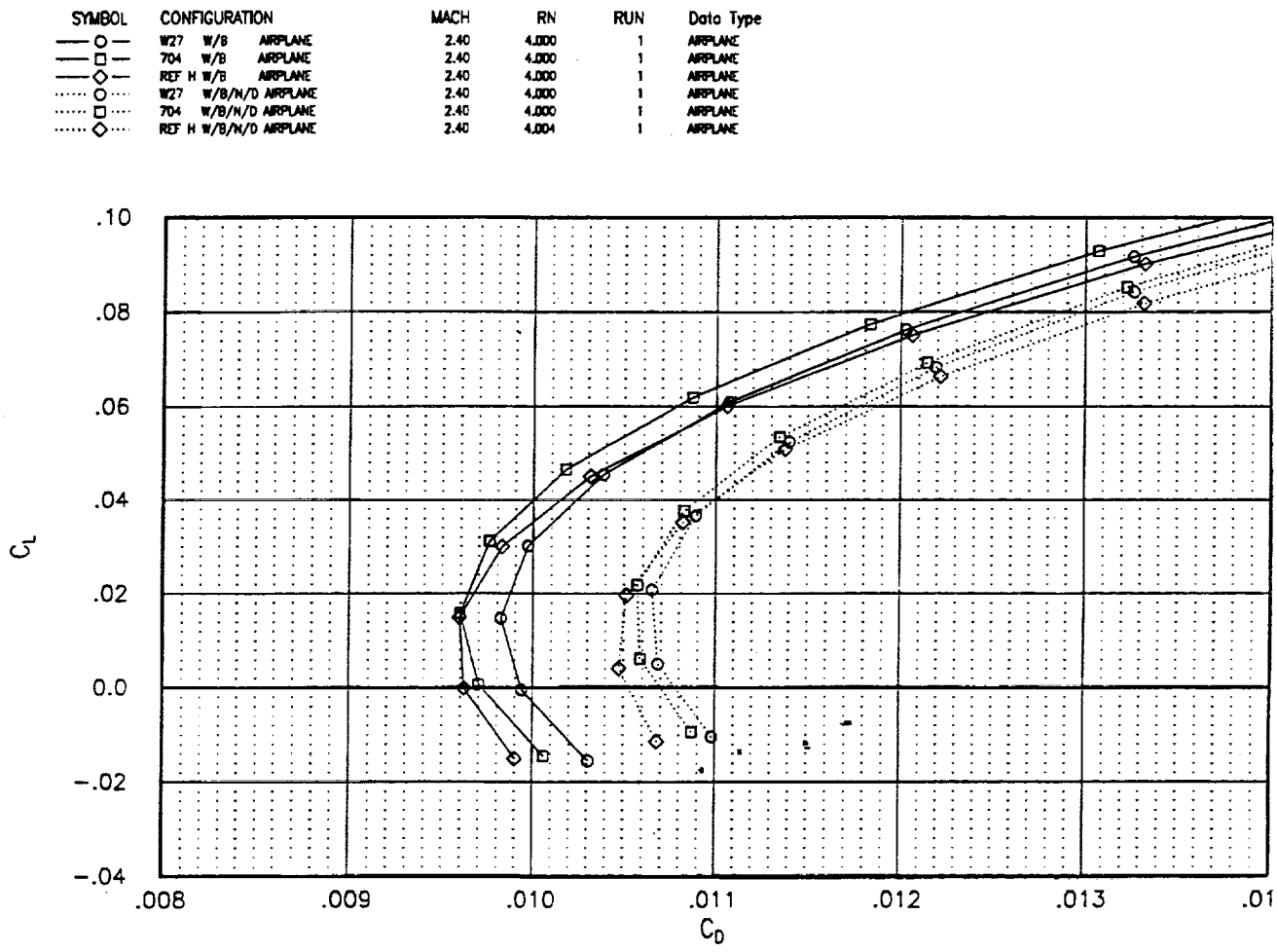

Fig 17. AIRPLANE W/B and W/B/N/D aerodynamic force and moment coefficients for Ref H baseline and optimized configurations

SYMBOL	CONFIGURATION	MACH	RN	RUN	Data Type
—○—	W27 W/B AIRPLANE	2.40	4.000	1	AIRPLANE
—□—	704 W/B AIRPLANE	2.40	4.000	1	AIRPLANE
—◇—	REF H W/B AIRPLANE	2.40	4.000	1	AIRPLANE
·····○·····	W27 W/B/N/D AIRPLANE	2.40	4.000	1	AIRPLANE
·····□·····	704 W/B/N/D AIRPLANE	2.40	4.000	1	AIRPLANE
·····◇·····	REF H W/B/N/D AIRPLANE	2.40	4.004	1	AIRPLANE

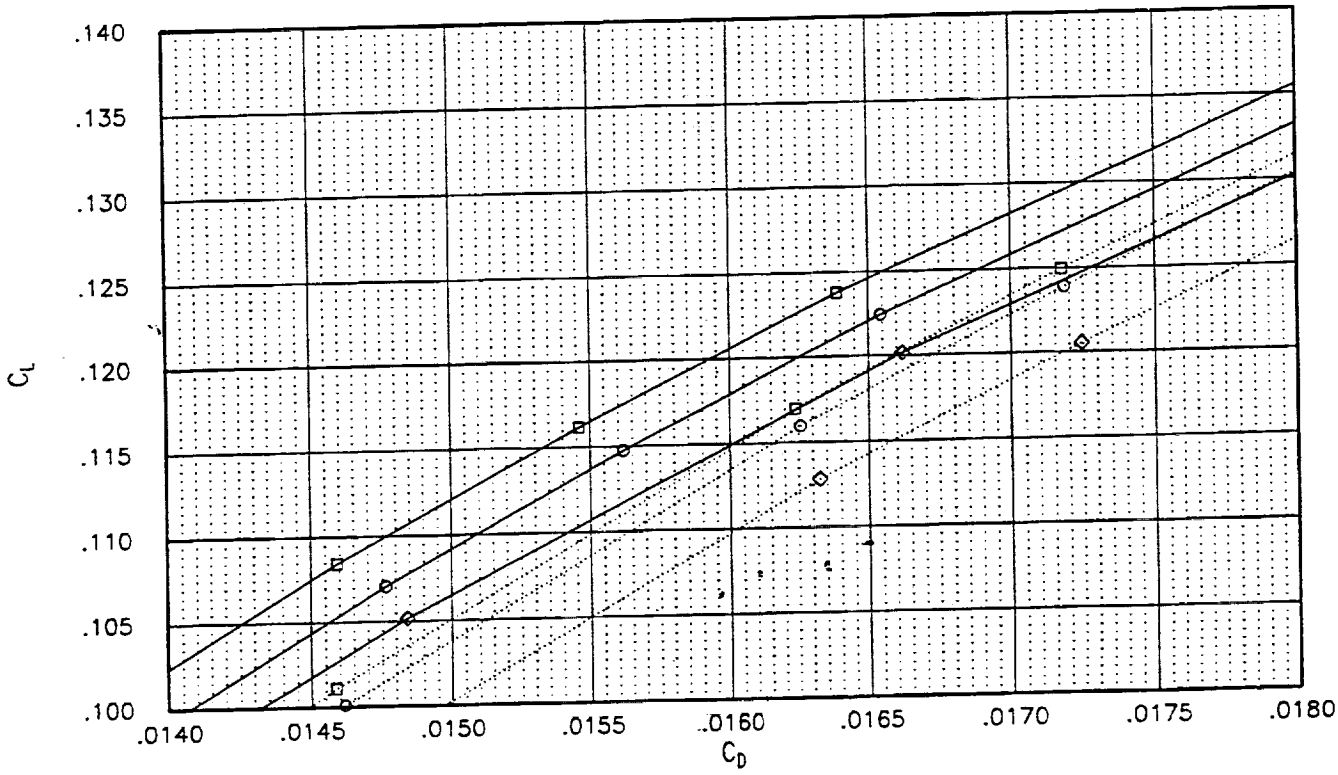

Fig 18. AIRPLANE W/B and W/B/N/D aerodynamic force and moment coefficients for Ref H baseline and optimized configurations

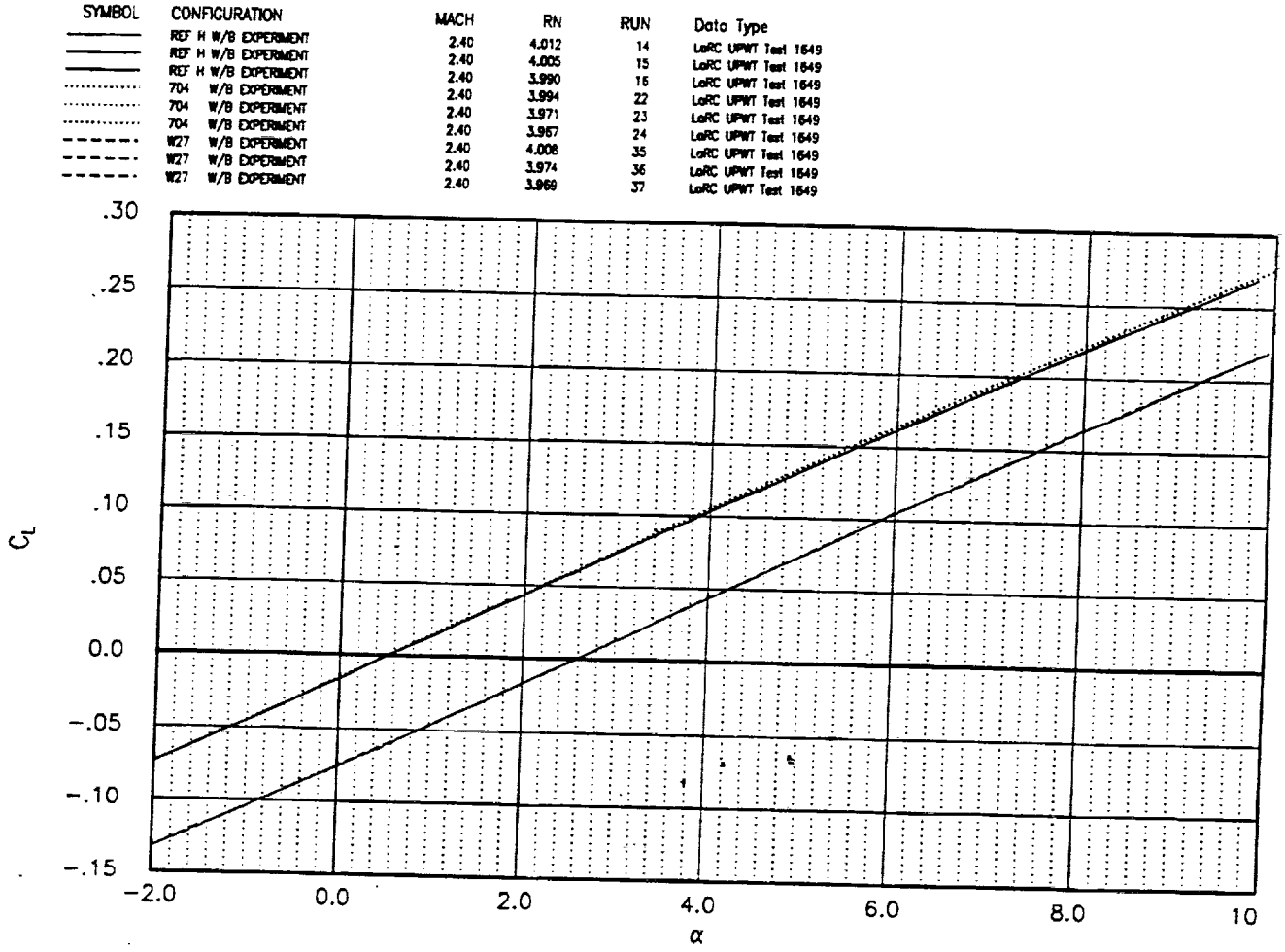

Fig 19. Experimental aerodynamic force and moment coefficents for Reference H basline and optimized wing/body configurations.

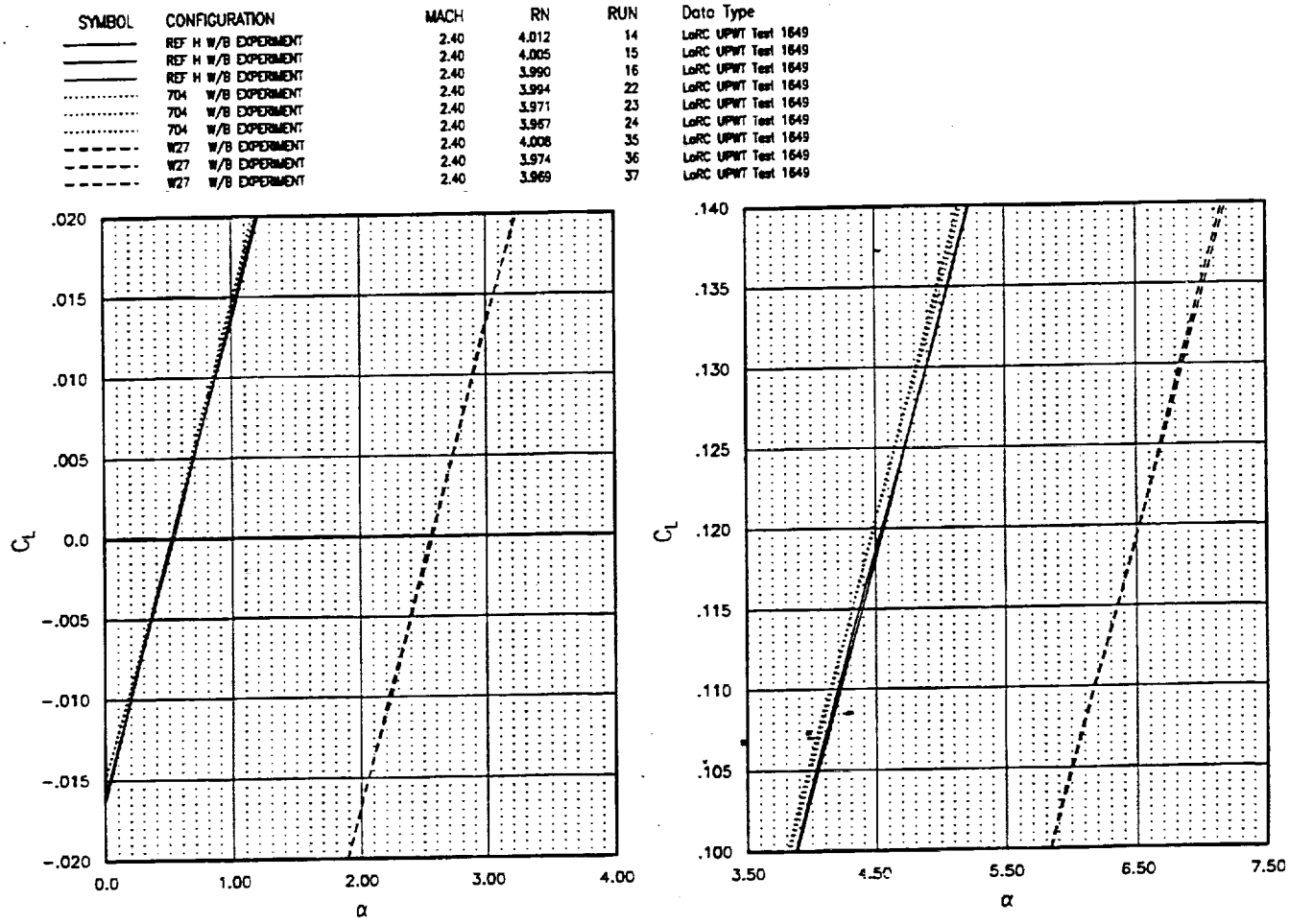

Fig 20. Experimental aerodynamic force and moment coefficents for Reference H basline and optimized wing/body configurations.

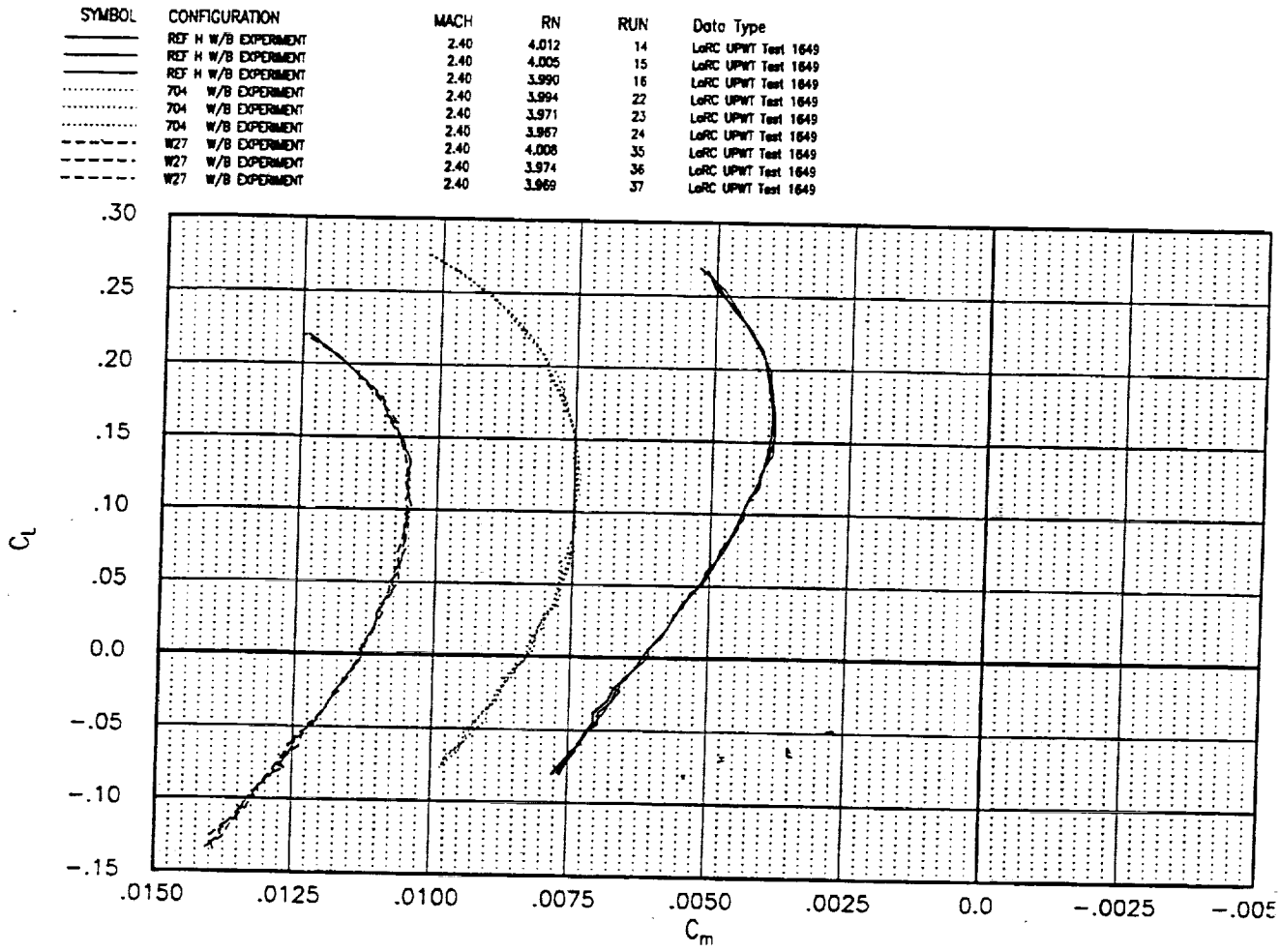

Fig 21. Experimental aerodynamic force and moment coefficents for Reference H basline and optimized wing/body configurations.

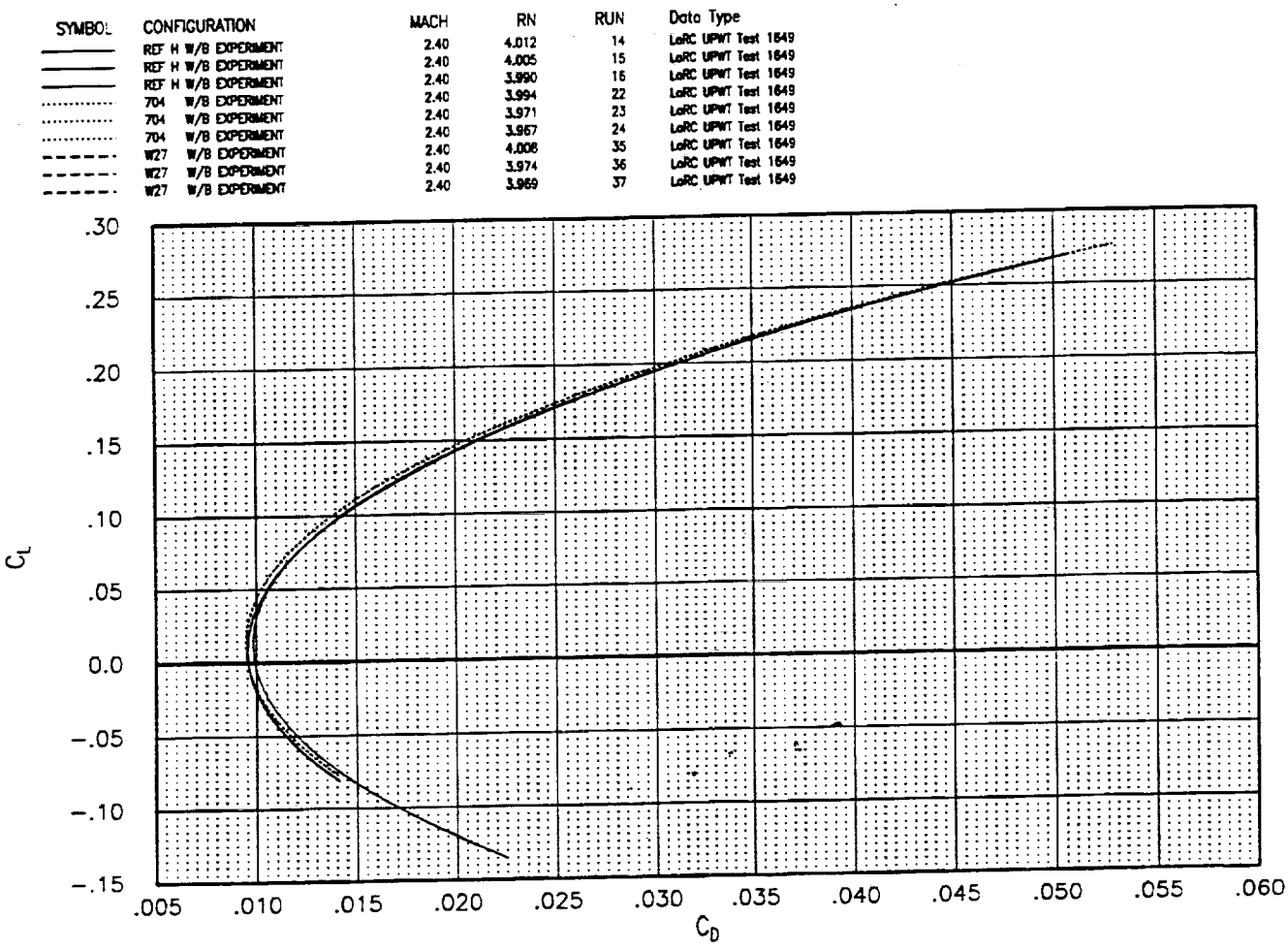

Fig 22. Experimental aerodynamic force and moment coefficents for Reference H basline and optimized wing/body configurations.

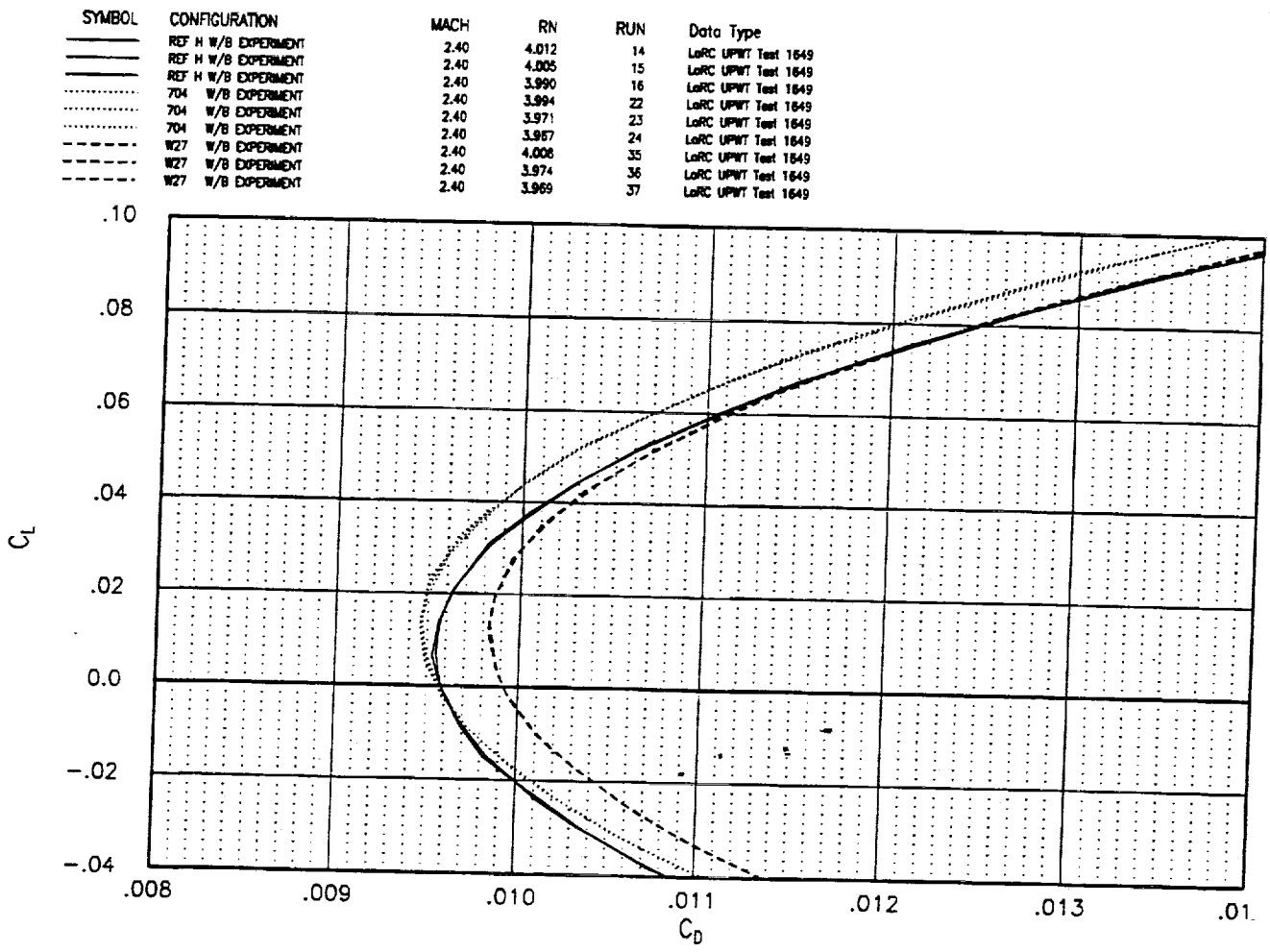

Fig 23. Experimental aerodynamic force and moment coefficents for Reference H basline and optimized wing/body configurations.

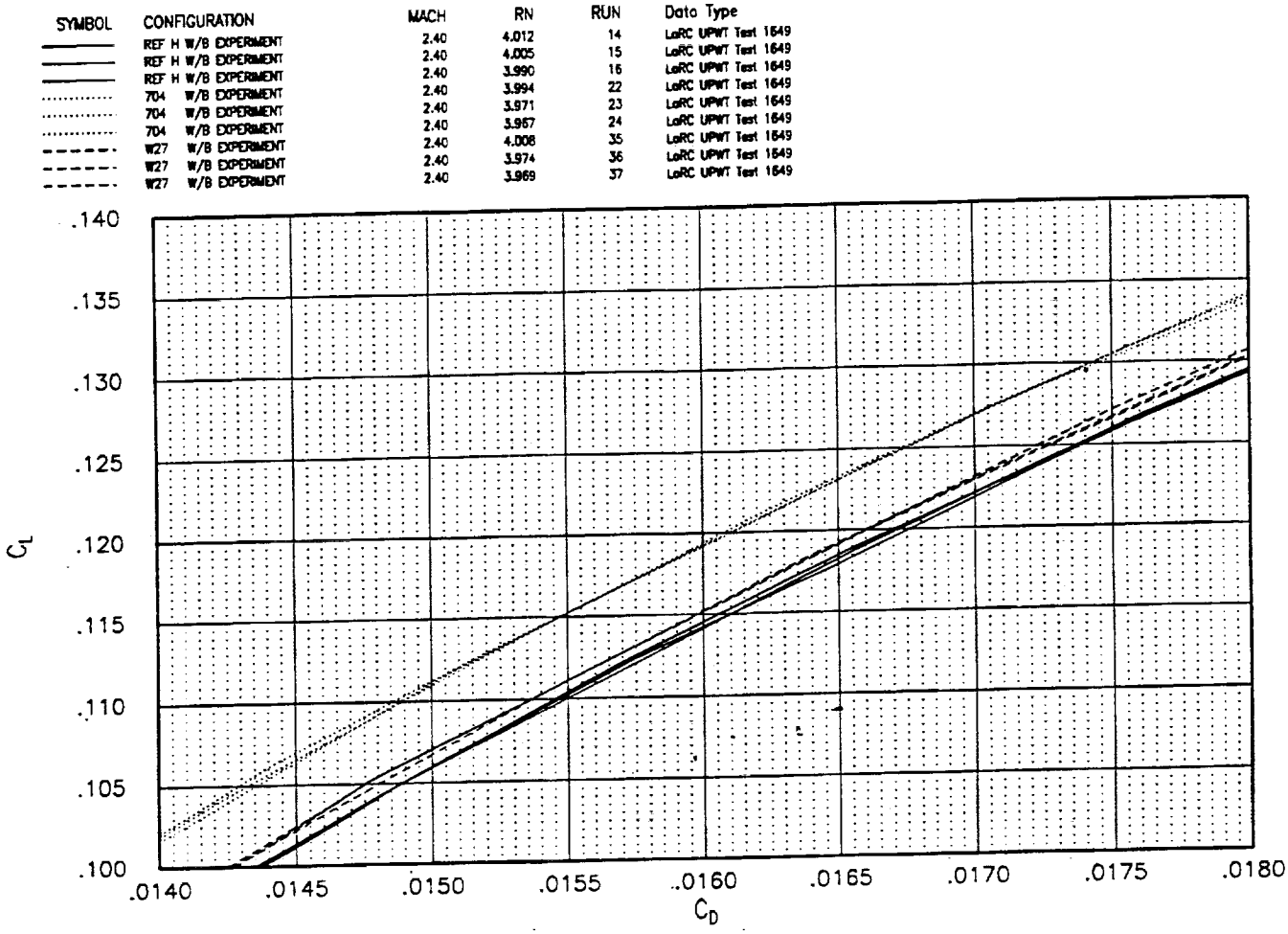

Fig 24. Experimental aerodynamic force and moment coefficents for Reference H basline and optimized wing/body configurations.

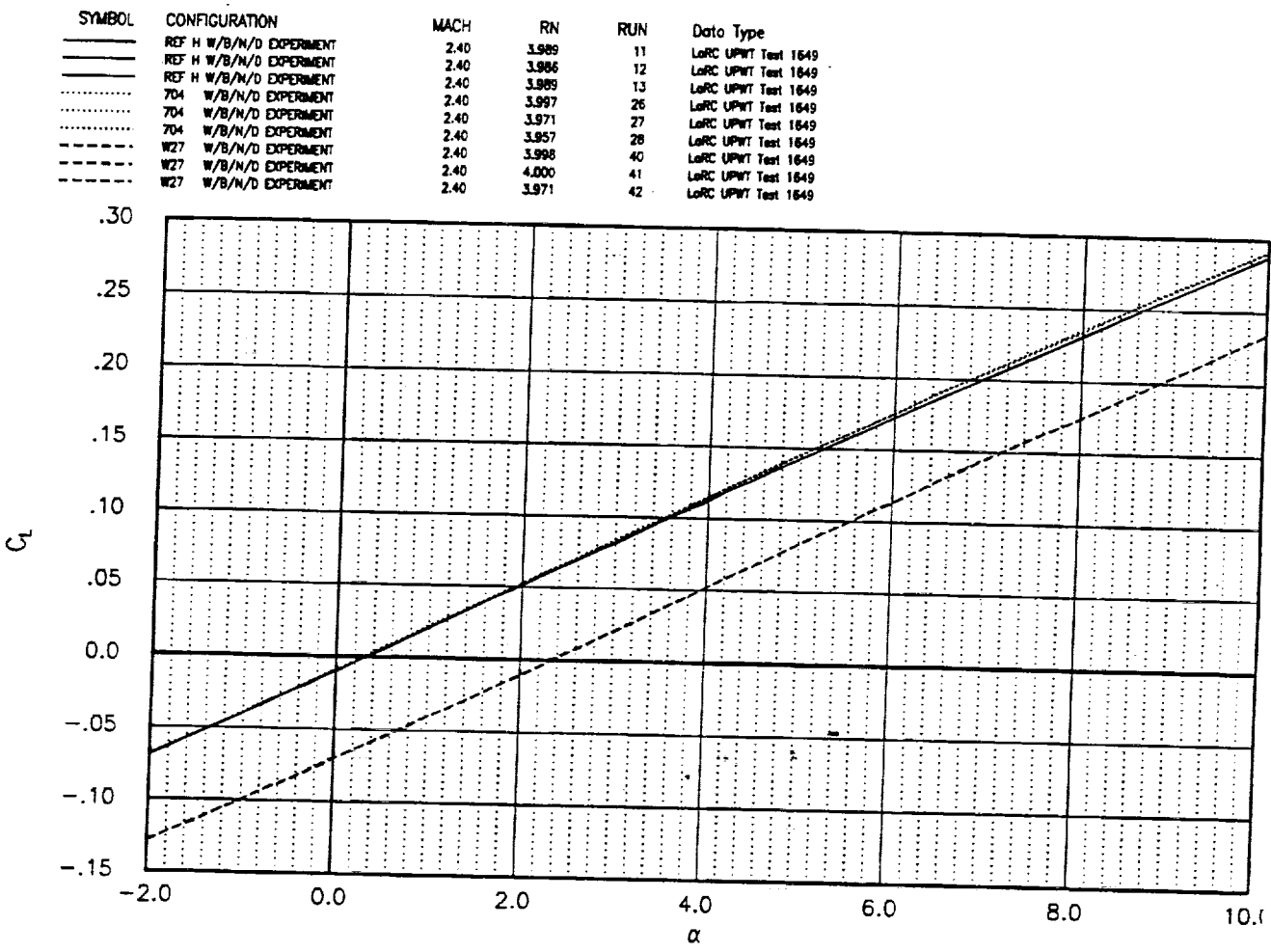

Fig 25. Experimental aerodynamic force and moment coefficients for Ref H baseline and optimized wing/body/nacelle/diverter configurations.

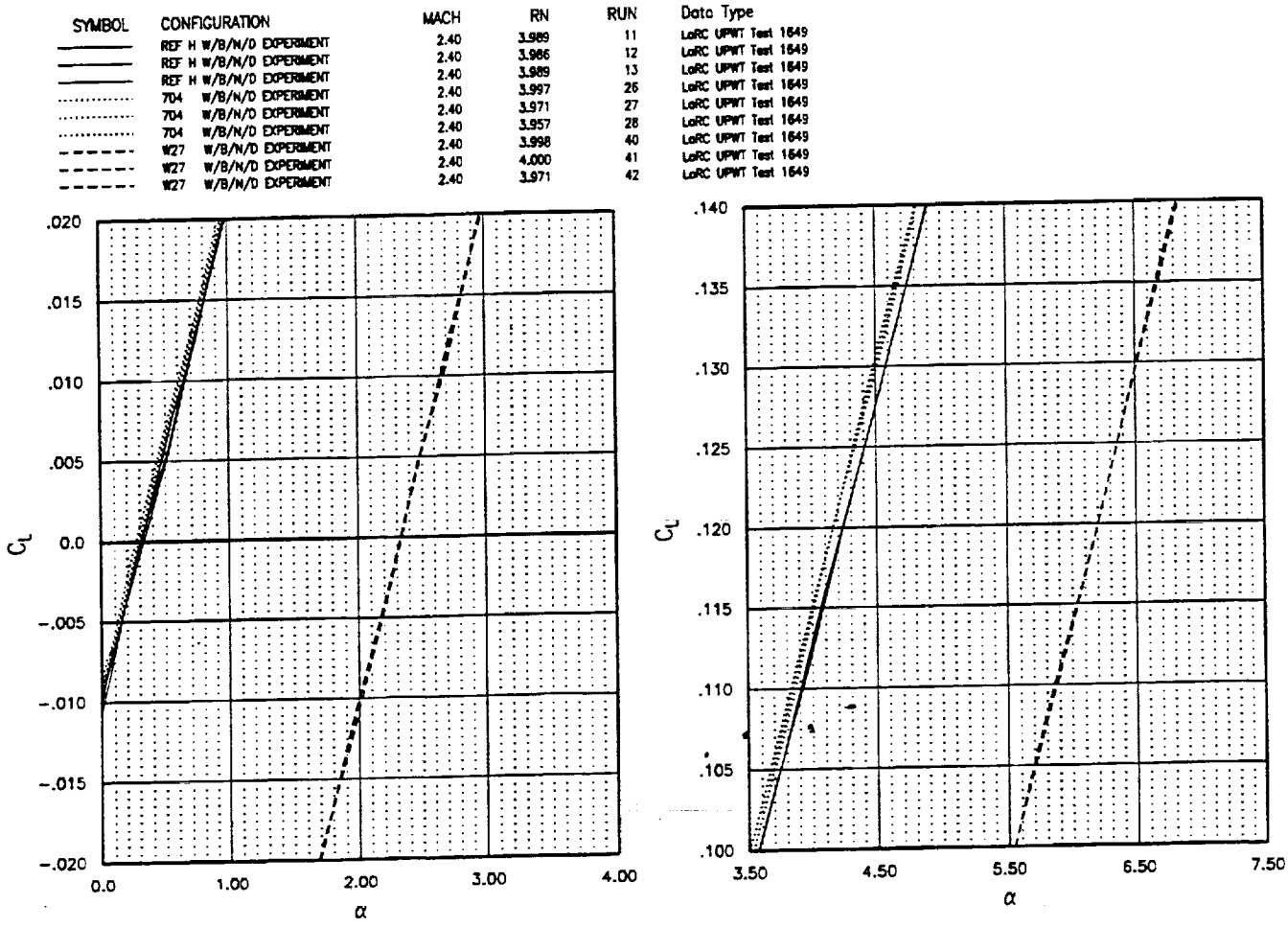

Fig 26. Experimental aerodynamic force and moment coefficients for Ref H baseline and optimized wing/body/nacelle/diverter configurations.

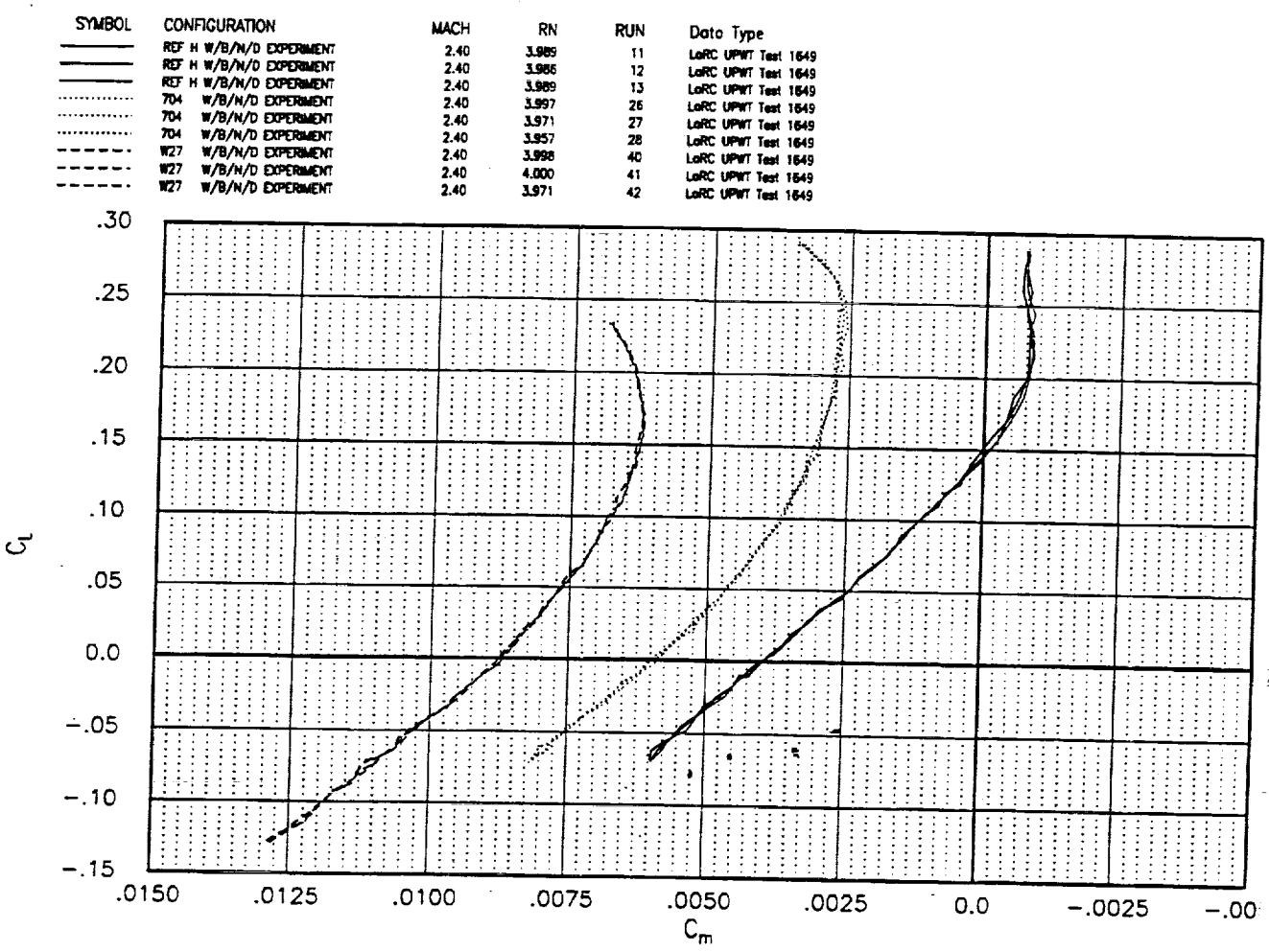

Fig 27. Experimental aerodynamic force and moment coefficients for Ref H baseline and optimized wing/body/nacelle/diverter configurations.

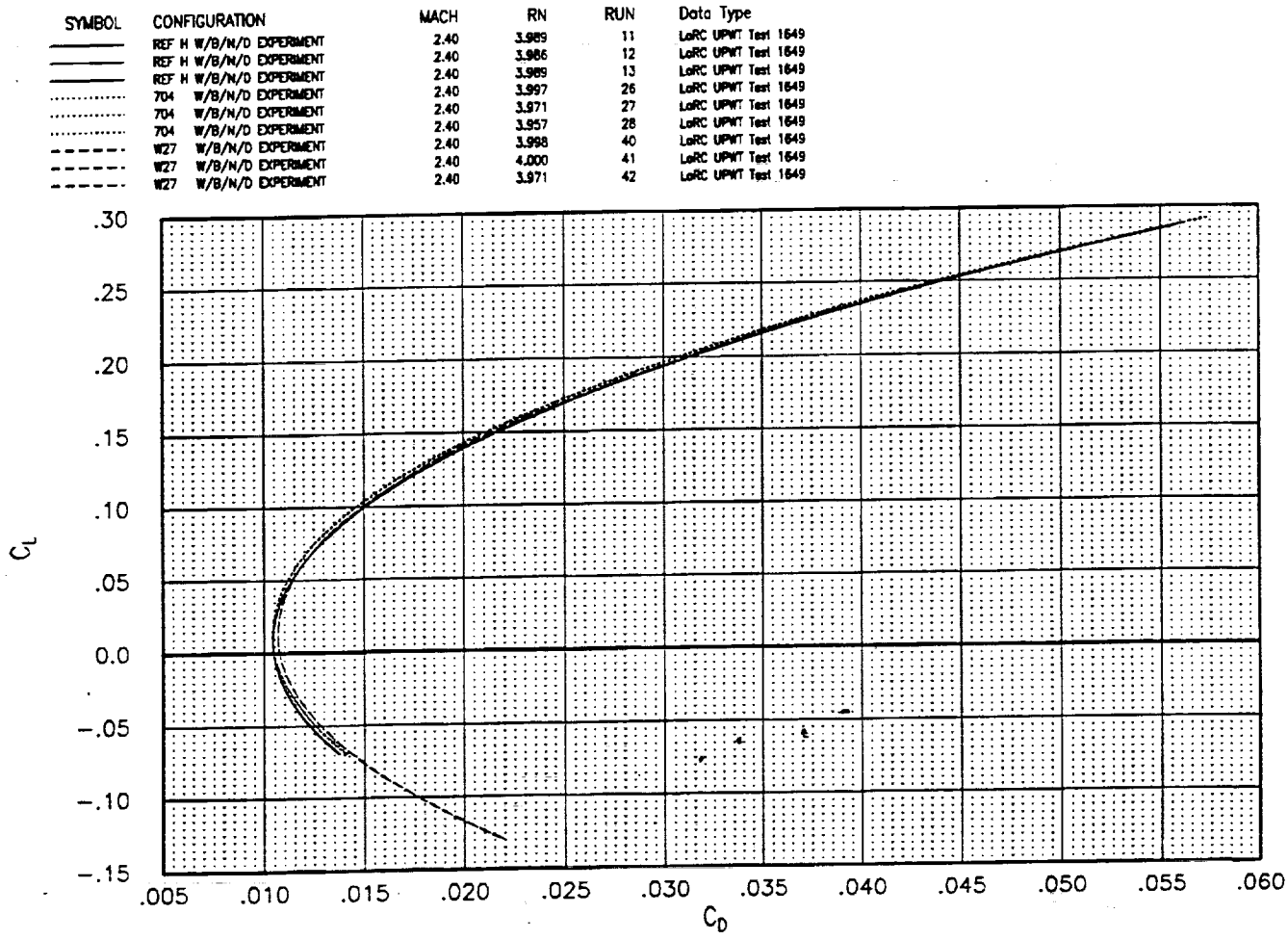

Fig 28. Experimental aerodynamic force and moment coefficients for Ref H baseline and optimized wing/body/nacelle/diverter configurations.

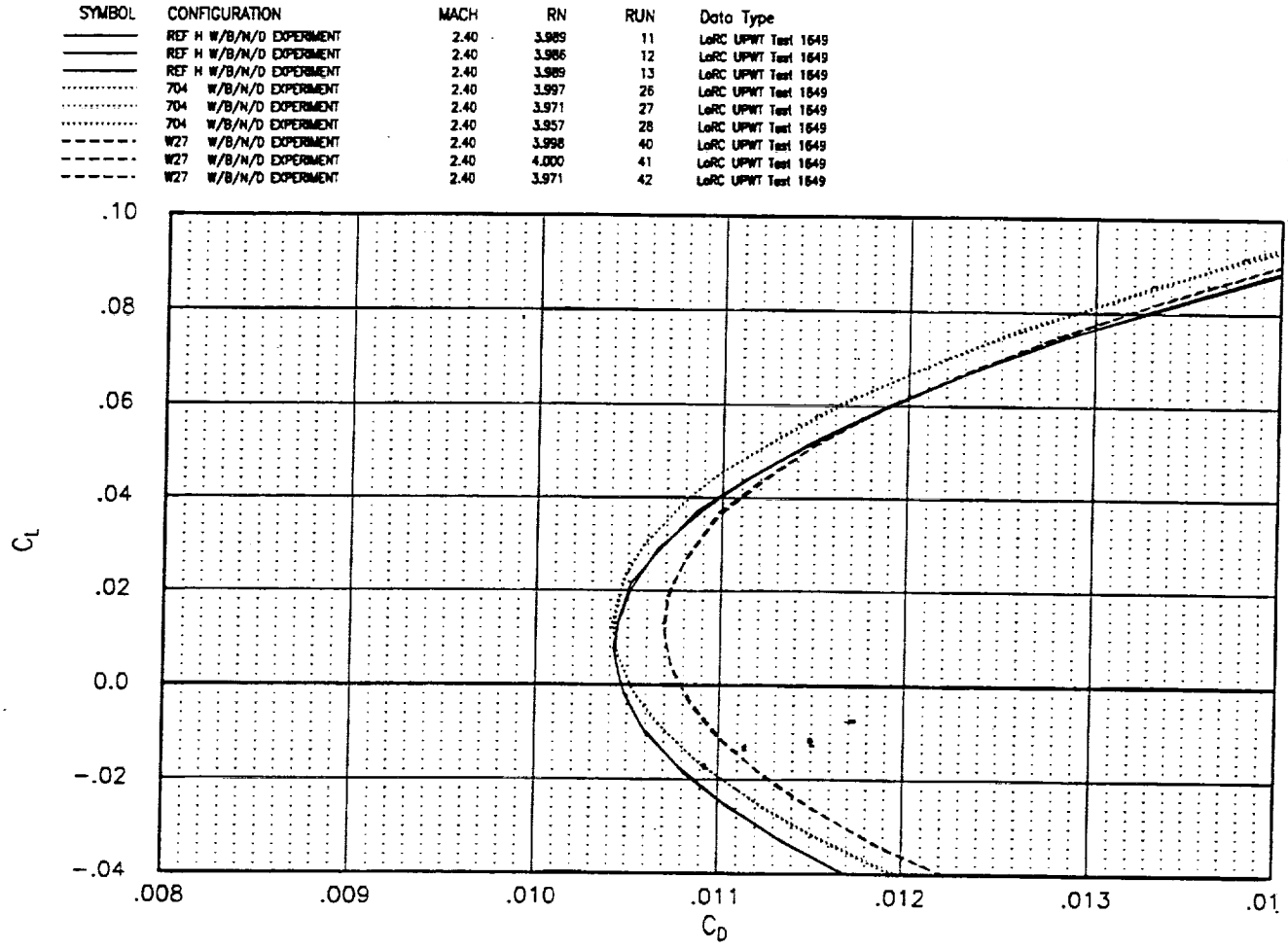

Fig 29. Experimental aerodynamic force and moment coefficients for Ref H baseline and optimized wing/body/nacelle/diverter configurations.

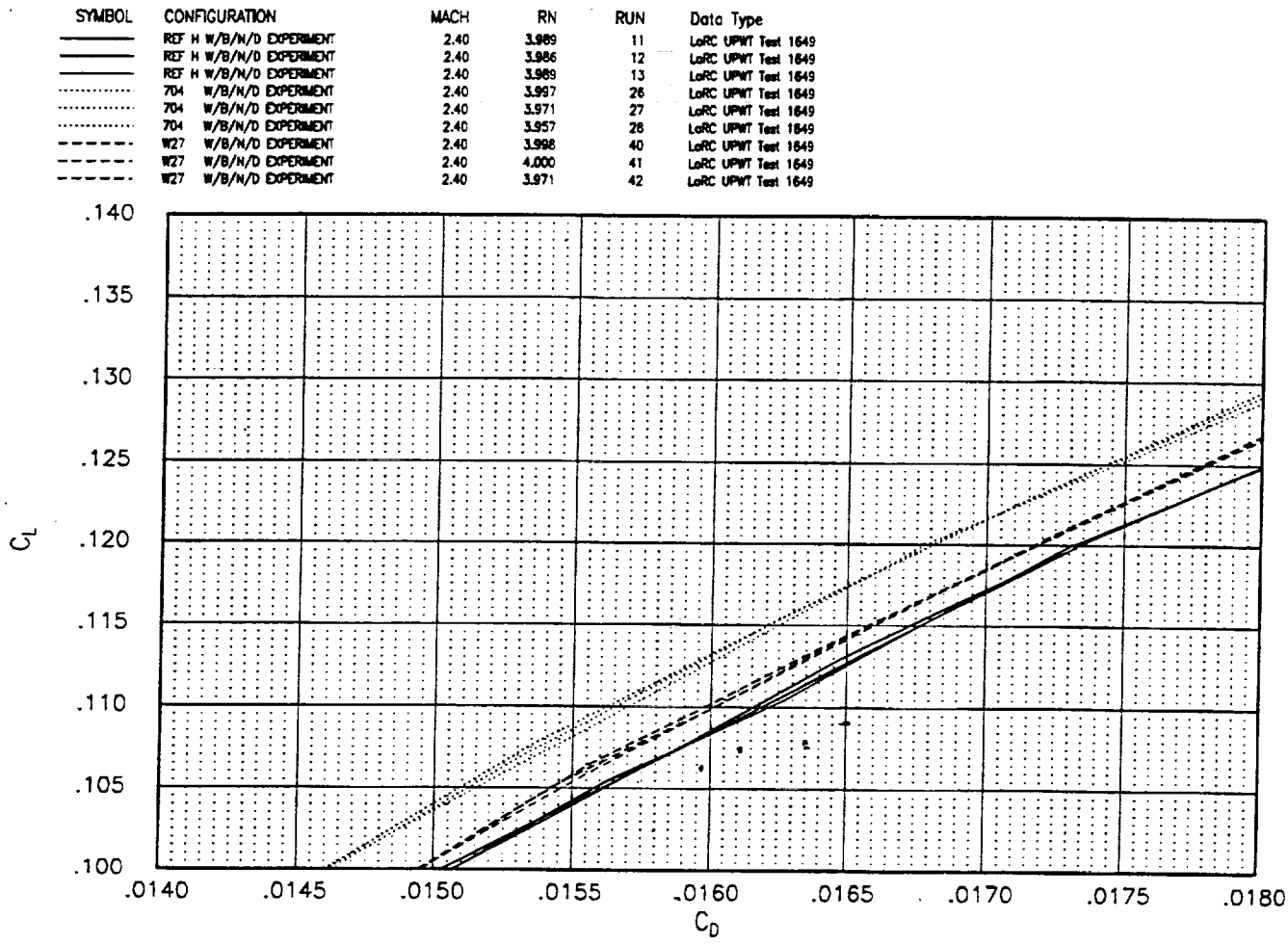

Fig 30. Experimental aerodynamic force and moment coefficients for Ref H baseline and optimized wing/body/nacelle/diverter configurations.

SYMBOL	CONFIGURATION	MACH	RN	RUN	Data Type
———	REF H W/B/N/D EXPERIMENT	2.40	3.989	11	LaRC UPWT Test 1649
———	REF H W/B/N/D EXPERIMENT	2.40	3.986	12	LaRC UPWT Test 1649
———	REF H W/B/N/D EXPERIMENT	2.40	3.989	13	LaRC UPWT Test 1649
····O····	REF H W/B/N/D AIRPLANE	2.40	4.004	1	AIRPLANE
- - - - - -	REF H W/B EXPERIMENT	2.40	4.012	14	LaRC UPWT Test 1649
- - - - - -	REF H W/B EXPERIMENT	2.40	4.005	15	LaRC UPWT Test 1649
- - - - - -	REF H W/B EXPERIMENT	2.40	3.990	16	LaRC UPWT Test 1649
— - □ —	REF H W/B AIRPLANE	2.40	4.000	1	AIRPLANE

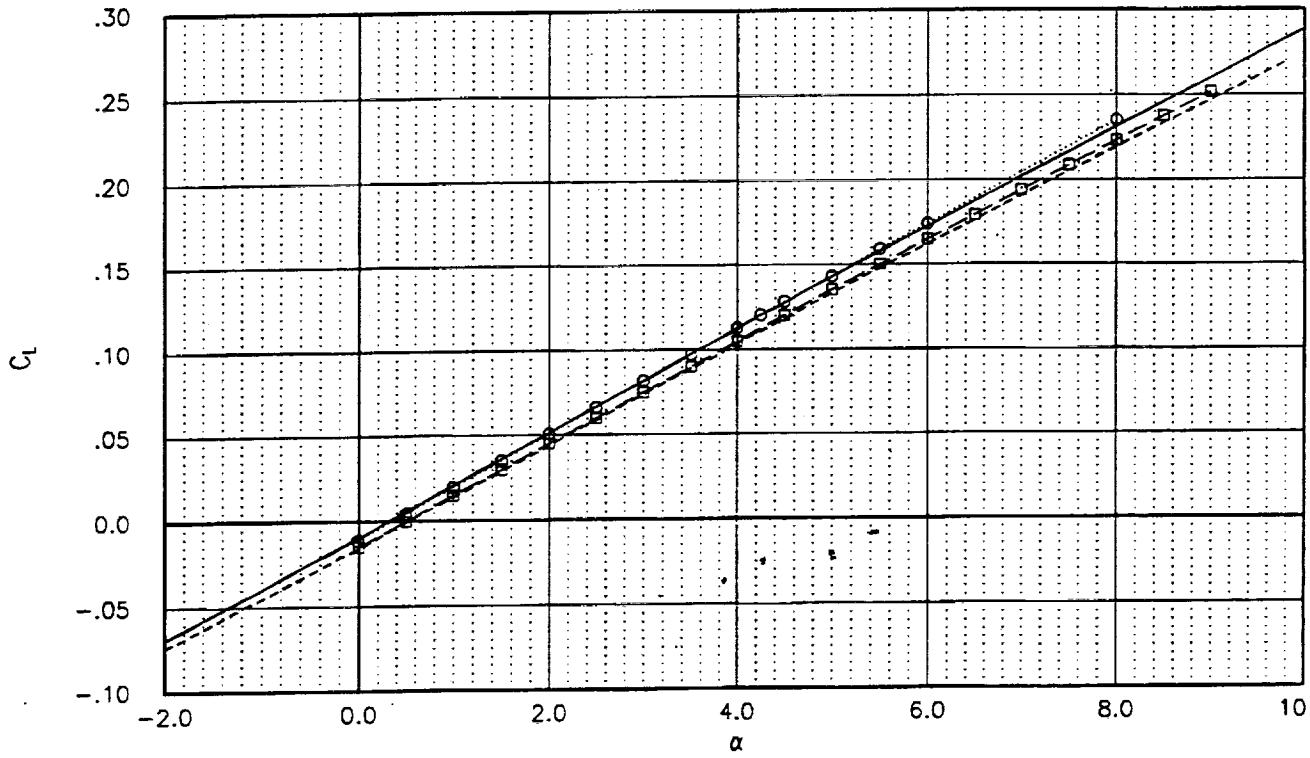

Fig 31. AIRPLANE force and moment coefficients of Ref H W/B (CAi = 0.006634) and W/B/N/D (CAi = 0.007516) compared with wind tunnel data.

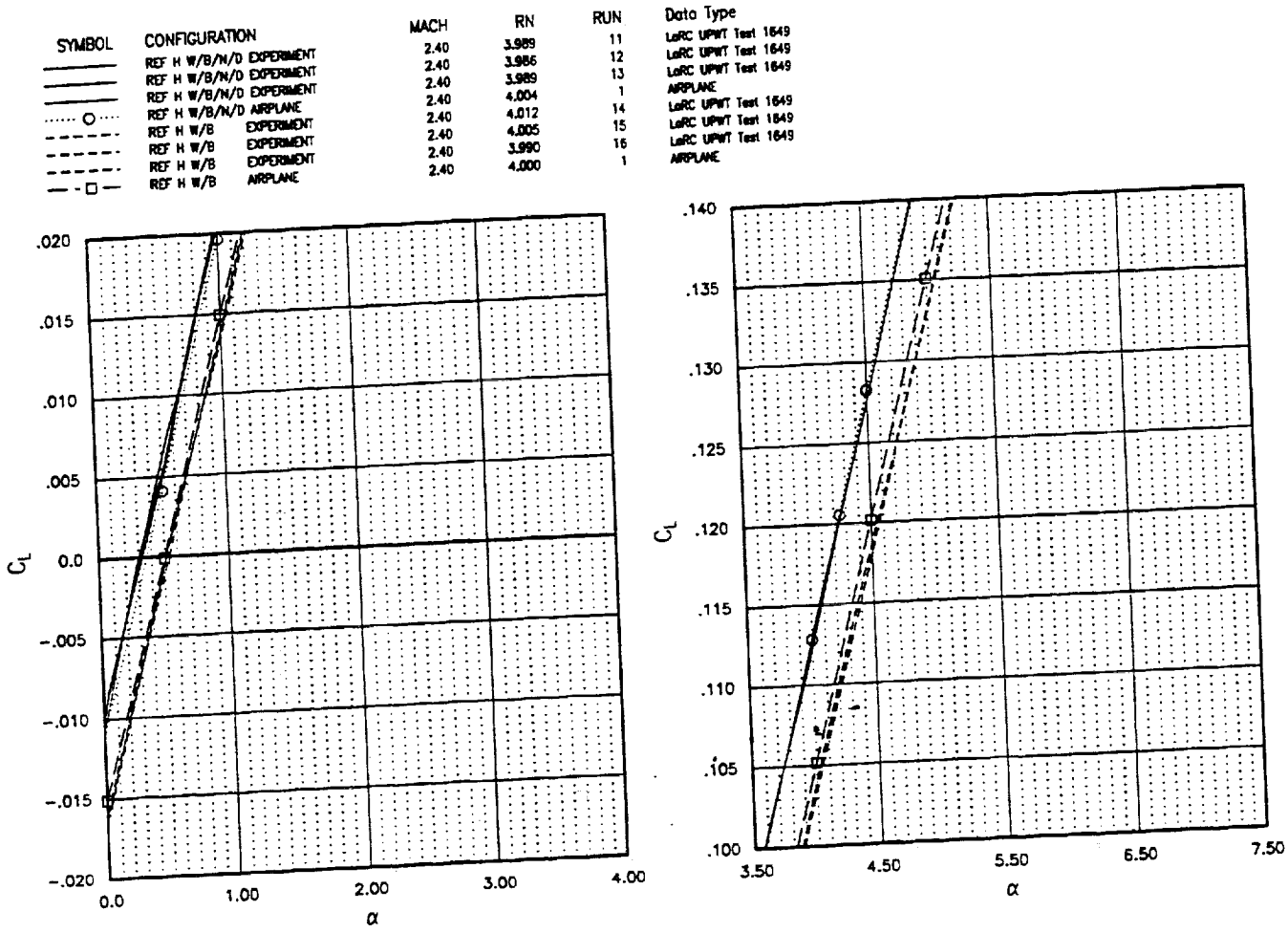

Fig 32. AIRPLANE force and moment coefficients of Ref H W/B (CAi = 0.006634) and W/B/N/D (CAi = 0.007516) compared with wind tunnel data.

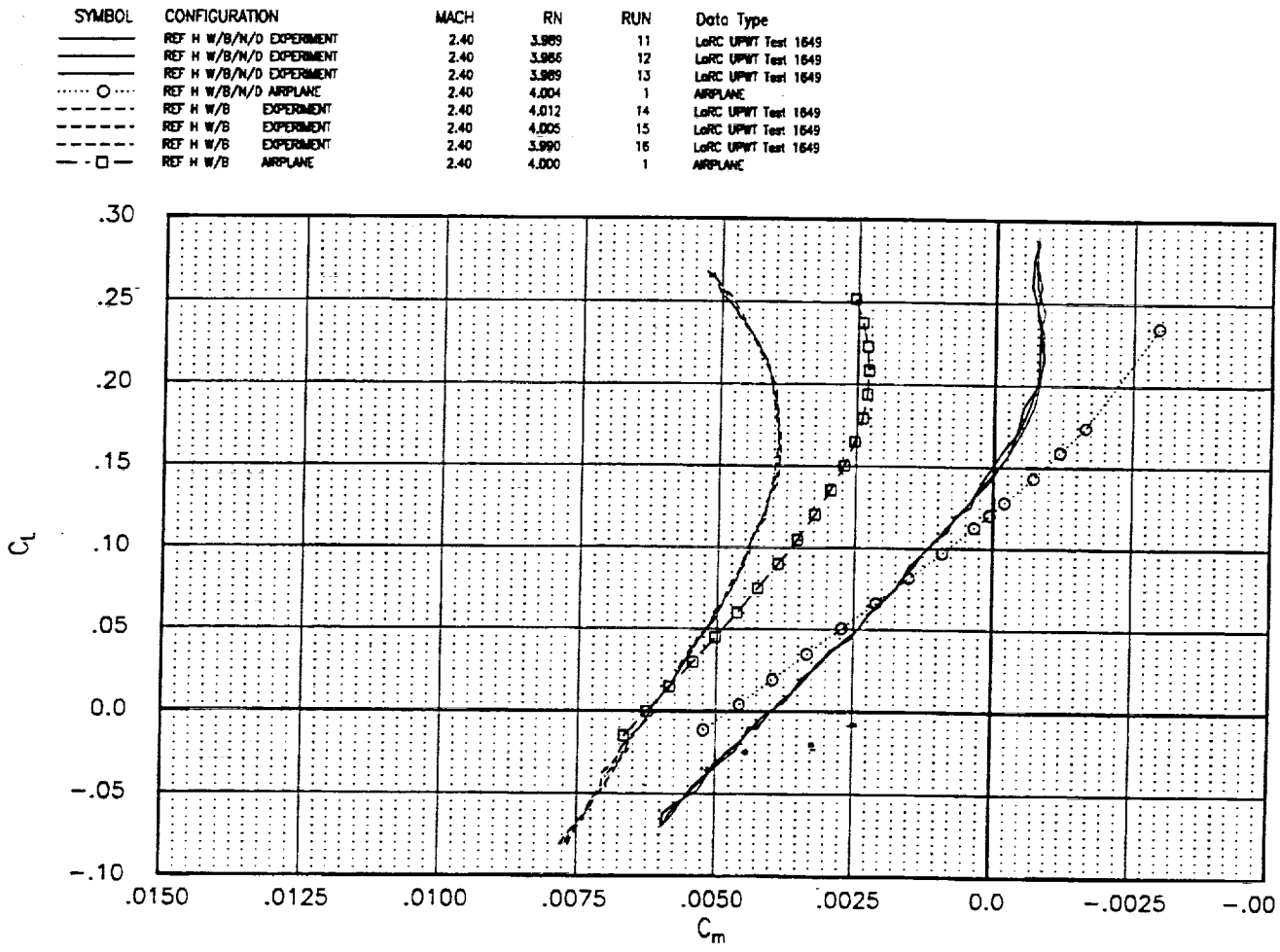

Fig 33. AIRPLANE force and moment coefficients of Ref H W/B (CAi = 0.006634) and W/B/N/D (CAi = 0.007516) compared with wind tunnel data.

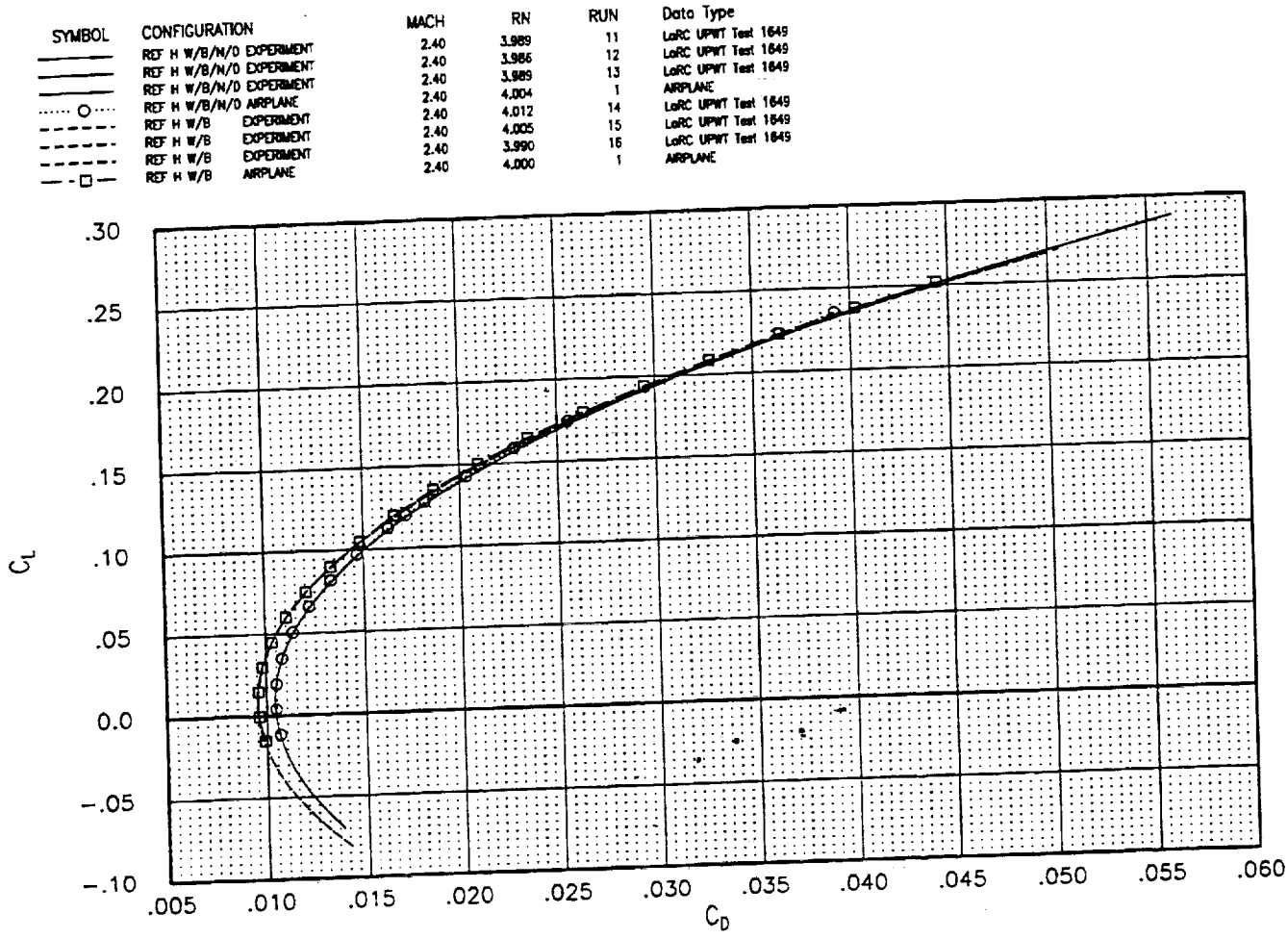

Fig 34. AIRPLANE force and moment coefficients of Ref H W/B (CAi = 0.006634) and W/B/N/D (CAi = 0.007516) compared with wind tunnel data.

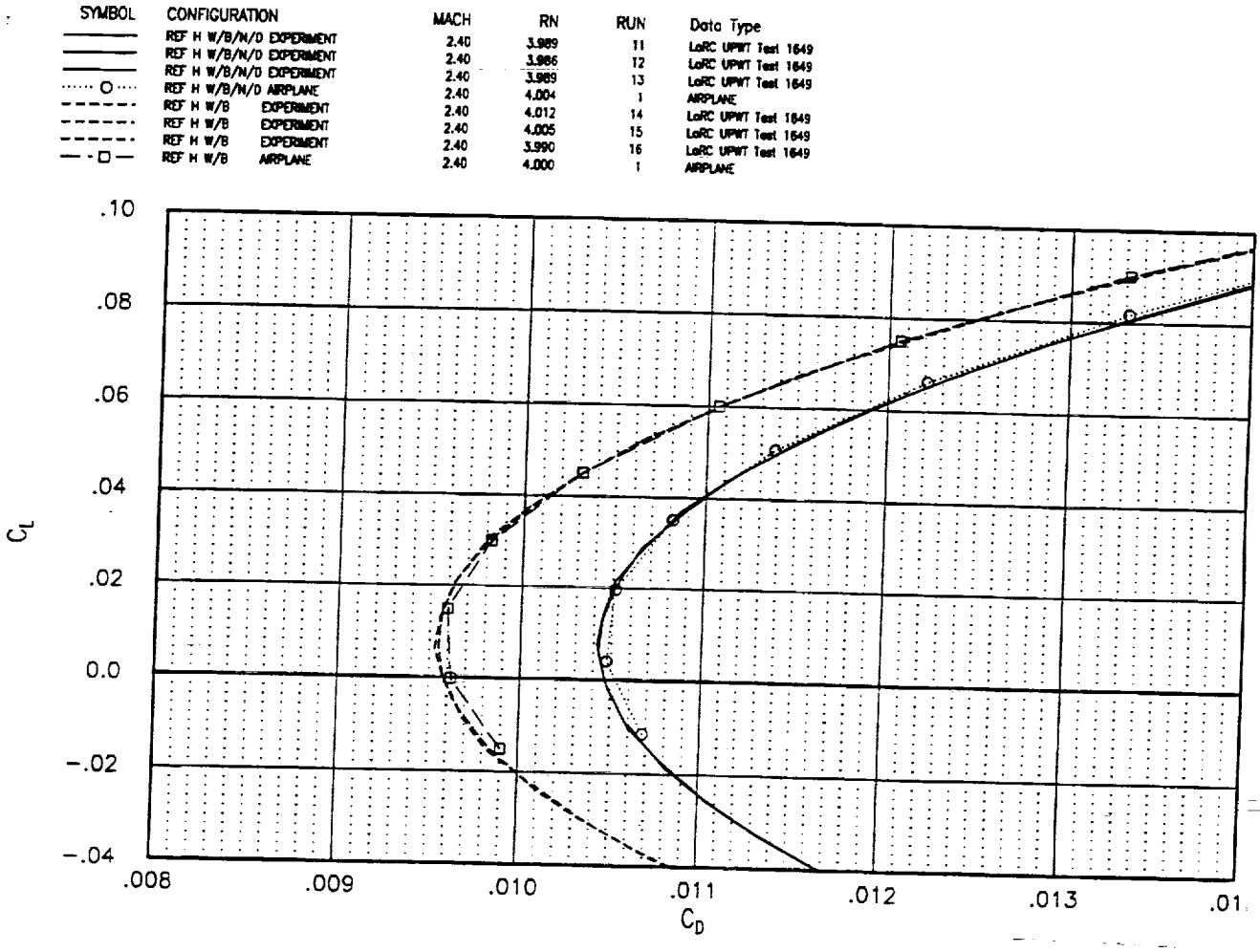

Fig 35. AIRPLANE force and moment coefficients of Ref H W/B (CAi = 0.006634) and W/B/N/D (CAi = 0.007516) compared with wind tunnel data.

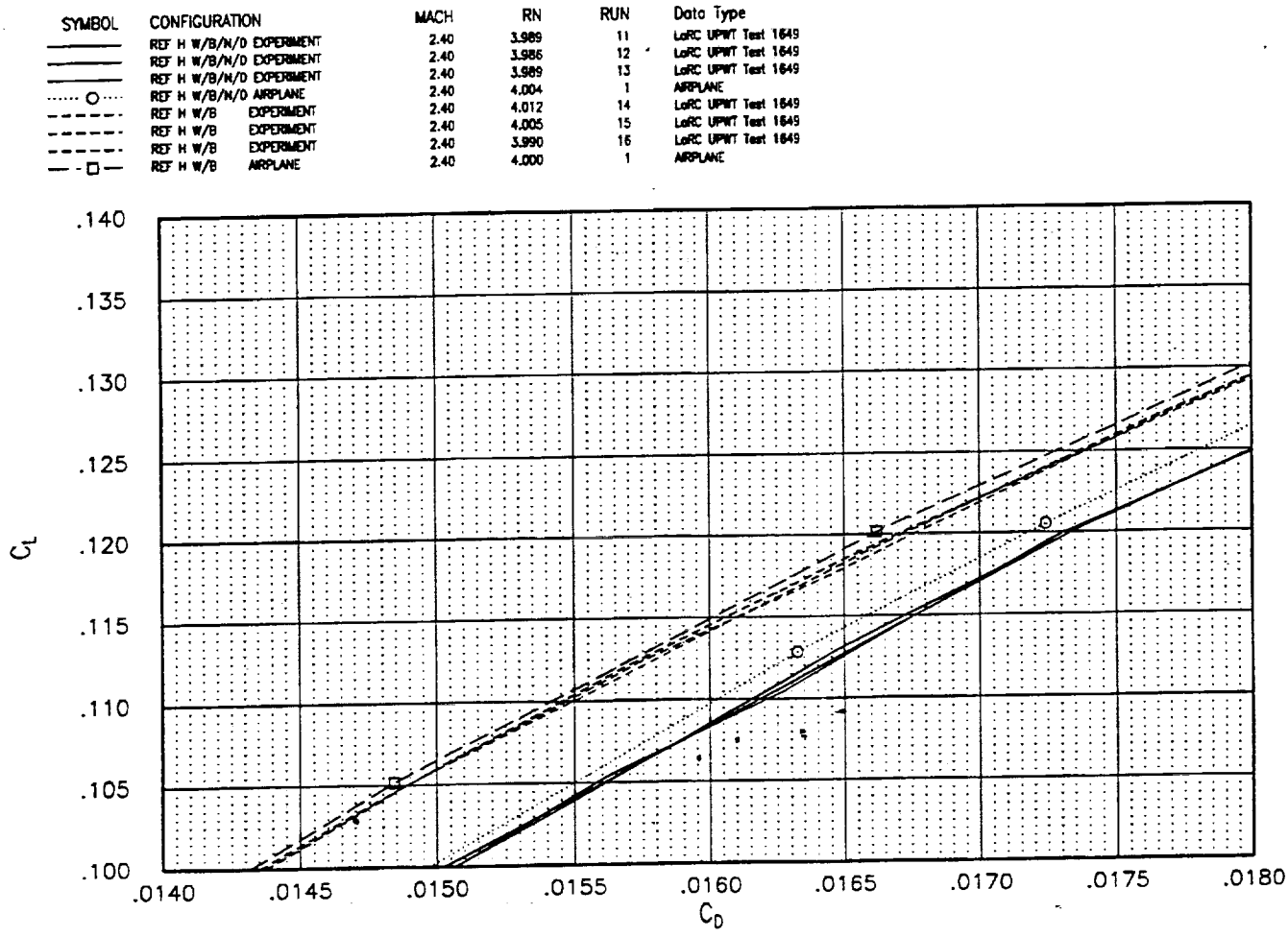

Fig 36. AIRPLANE force and moment coefficients of Ref H W/B (CAi = 0.006634) and W/B/N/D (CAi = 0.007516) compared with wind tunnel data.

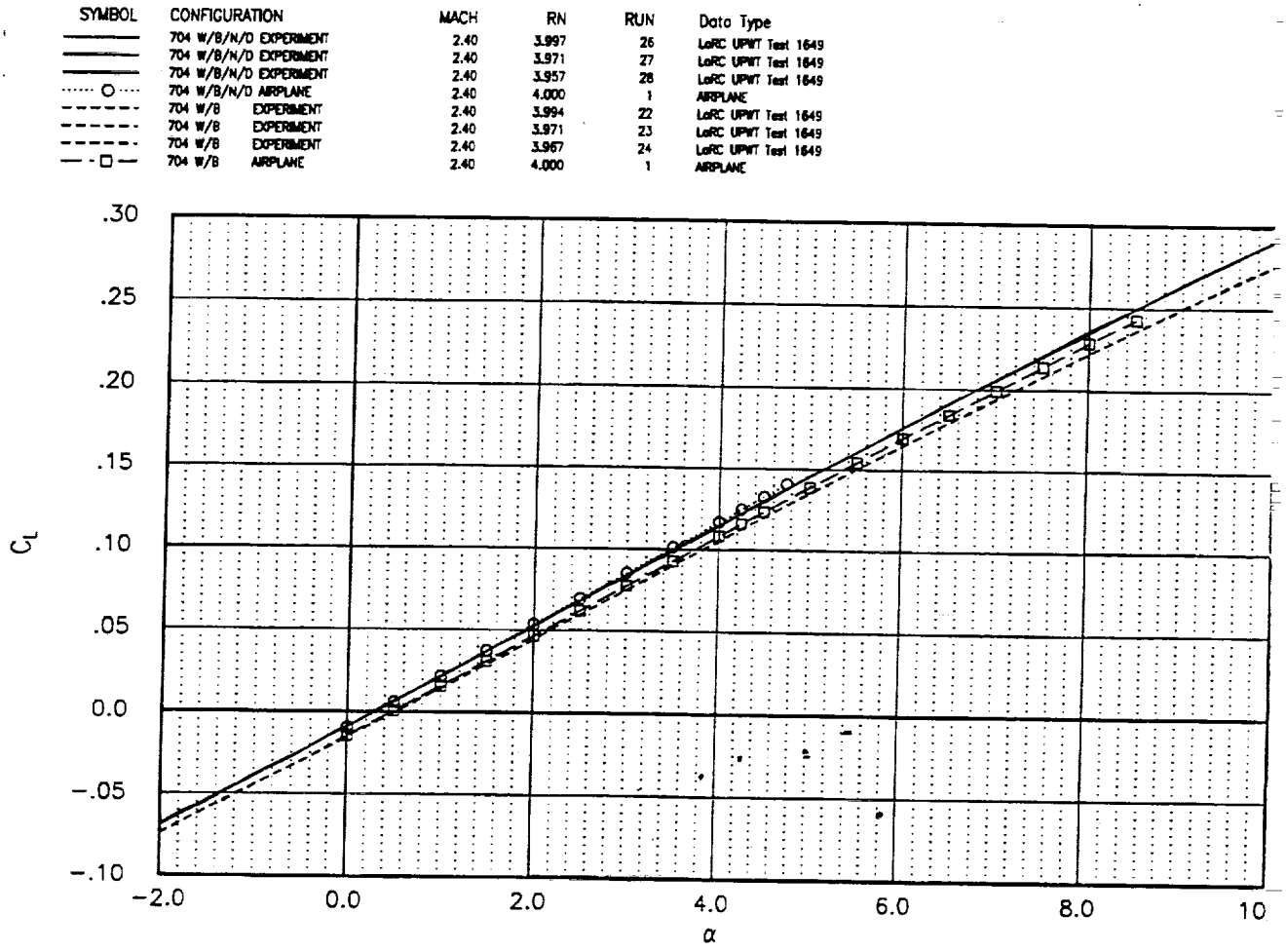

Fig 37. AIRPLANE force and moment coefficients of Ames 7-04 W/B (CAi = 0.006620) and W/B/N/D (CAi = 0.007500) compared with wind tunnel data.

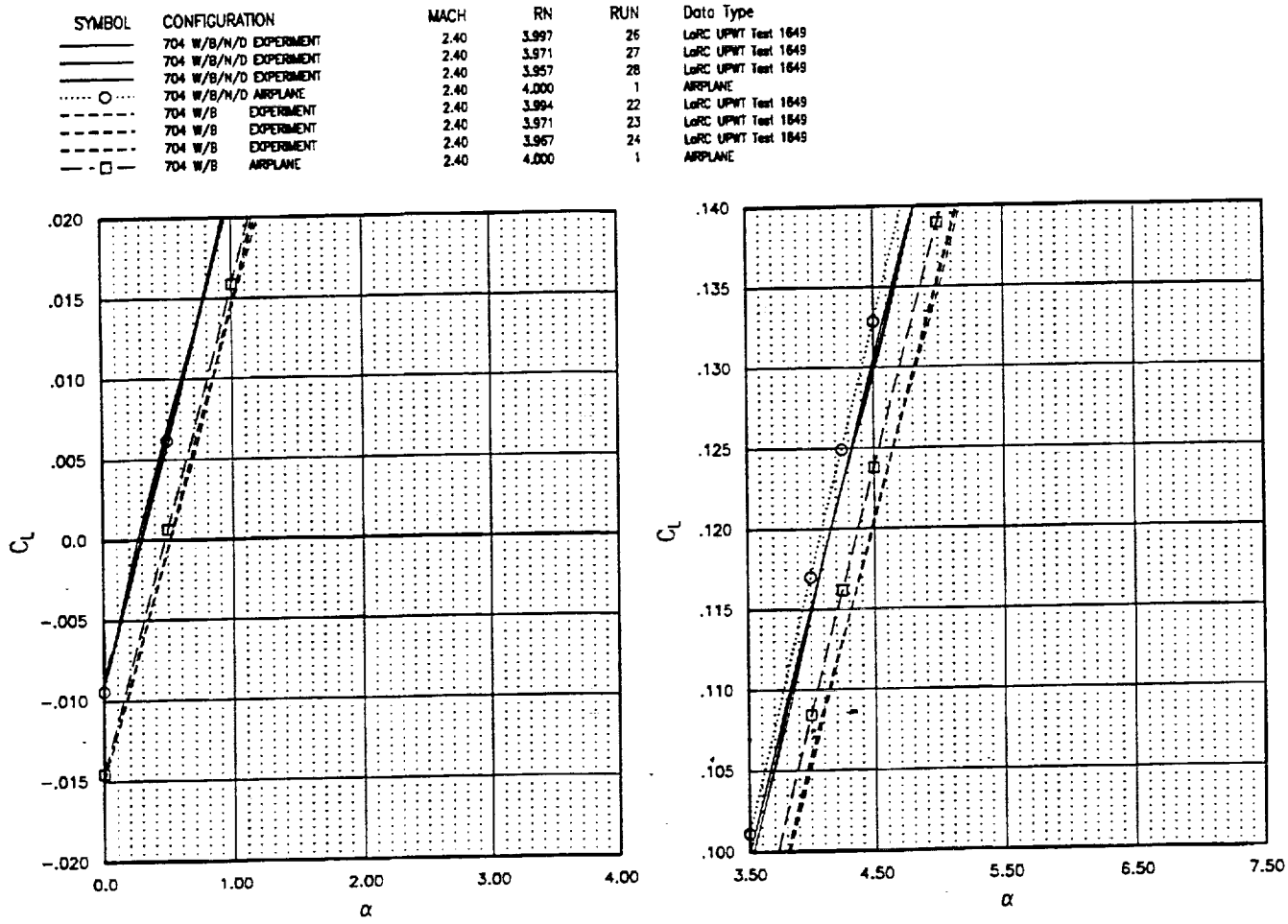

Fig 38. AIRPLANE force and moment coefficients of Ames 7-04 W/B (CAi = 0.006620) and W/B/N/D (CAi = 0.007500) compared with wind tunnel data.

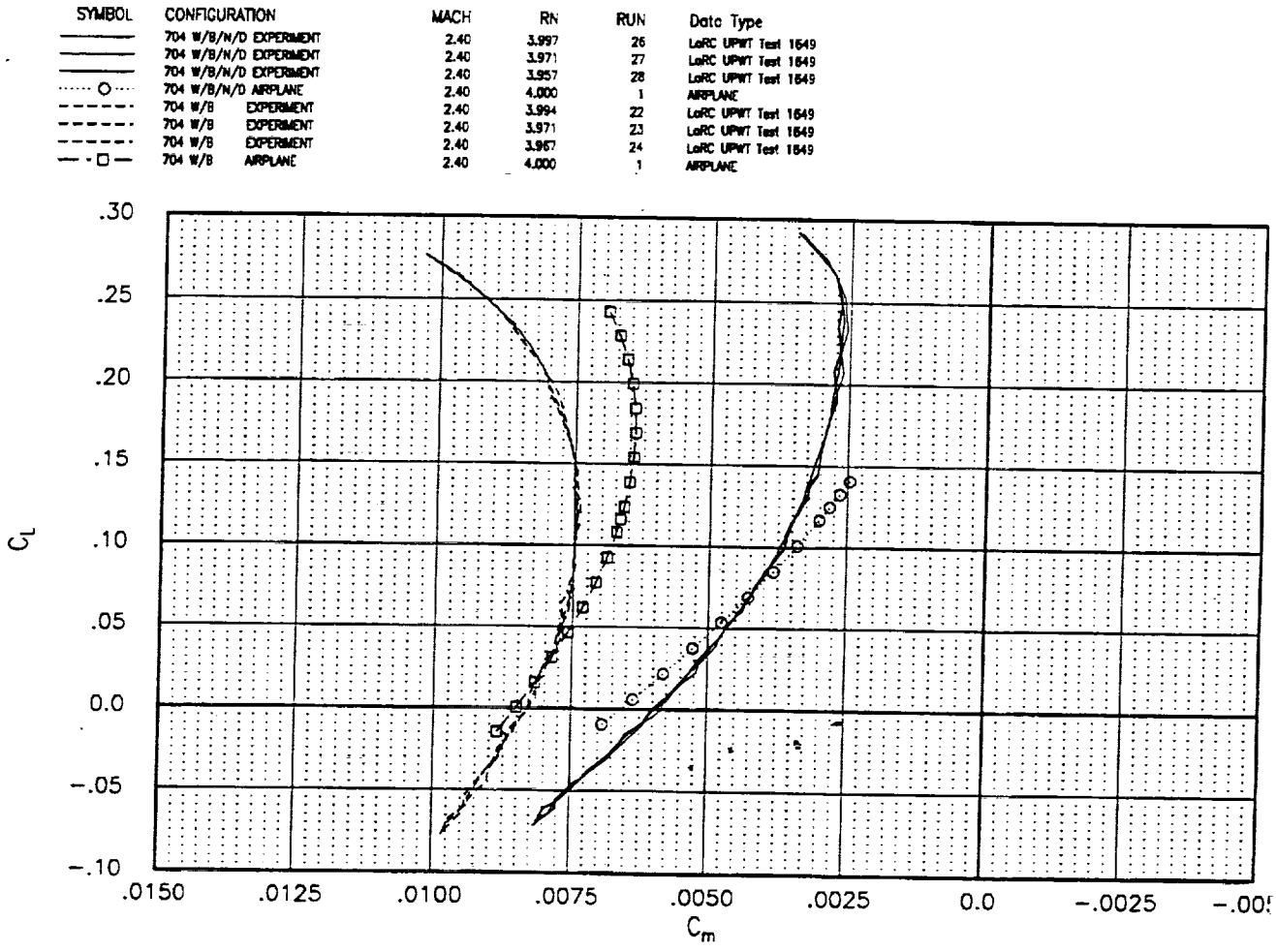

Fig 39. AIRPLANE force and moment coefficients of Ames 7-04 W/B (CAi = 0.006620) and W/B/N/D (CAi = 0.007500) compared with wind tunnel data.

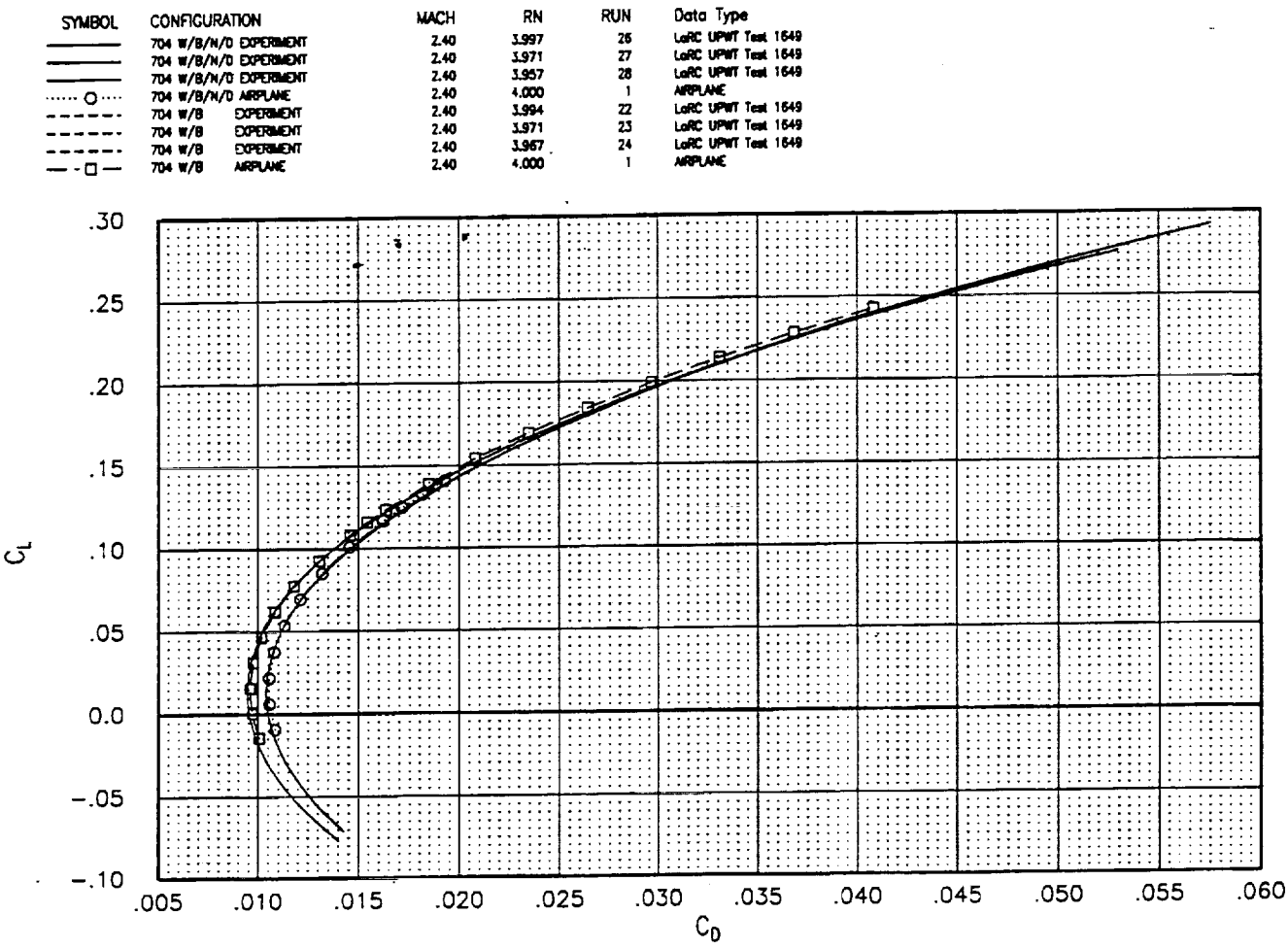

Fig 40. AIRPLANE force and moment coefficients of Ames 7-04 W/B (CAi = 0.006620) and W/B/N/D (CAi = 0.007500) compared with wind tunnel data.

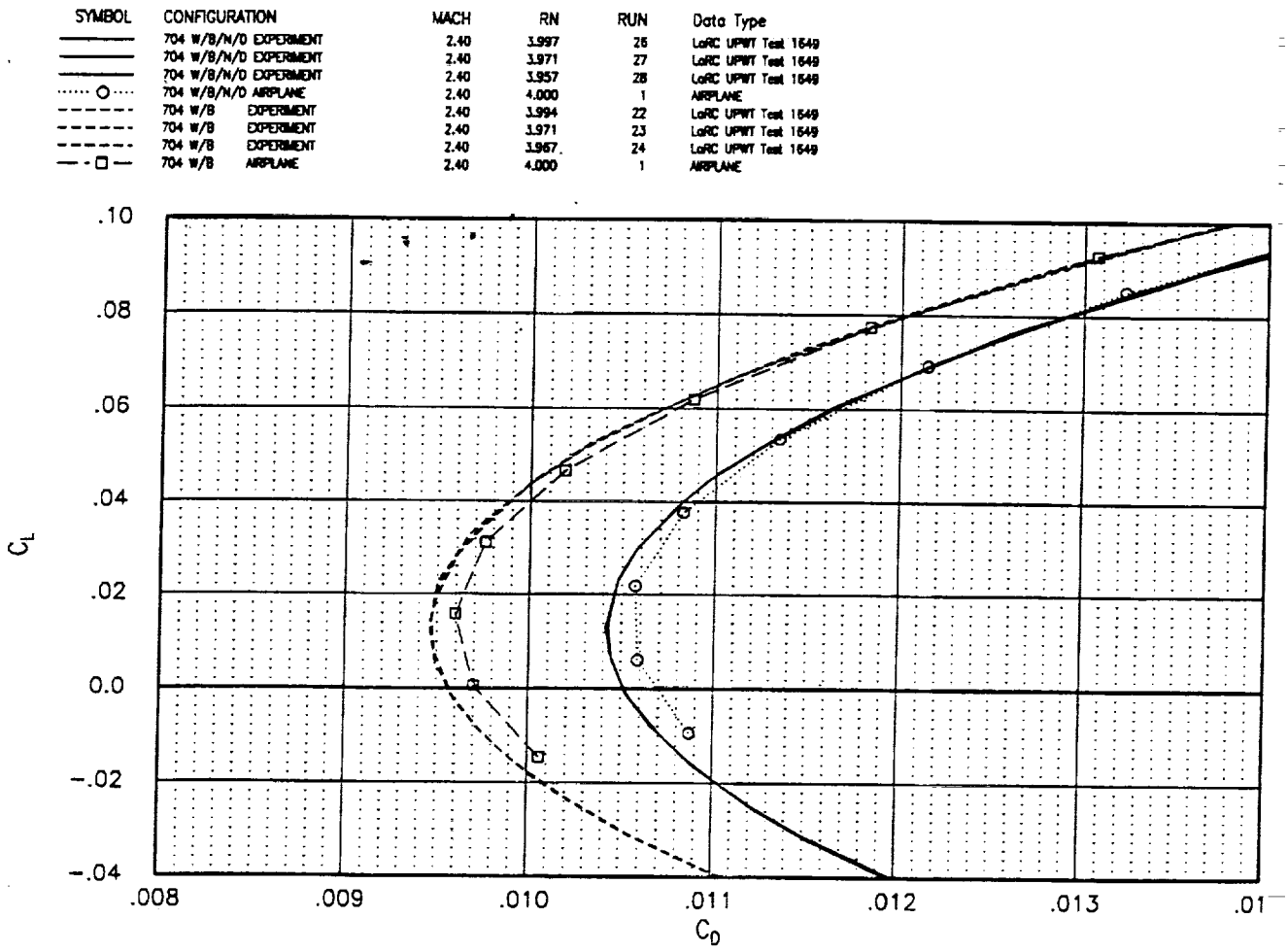

Fig 41. AIRPLANE force and moment coefficients of Ames 7-04 W/B (CAi = 0.006620) and W/B/N/D (CAi = 0.007500) compared with wind tunnel data.

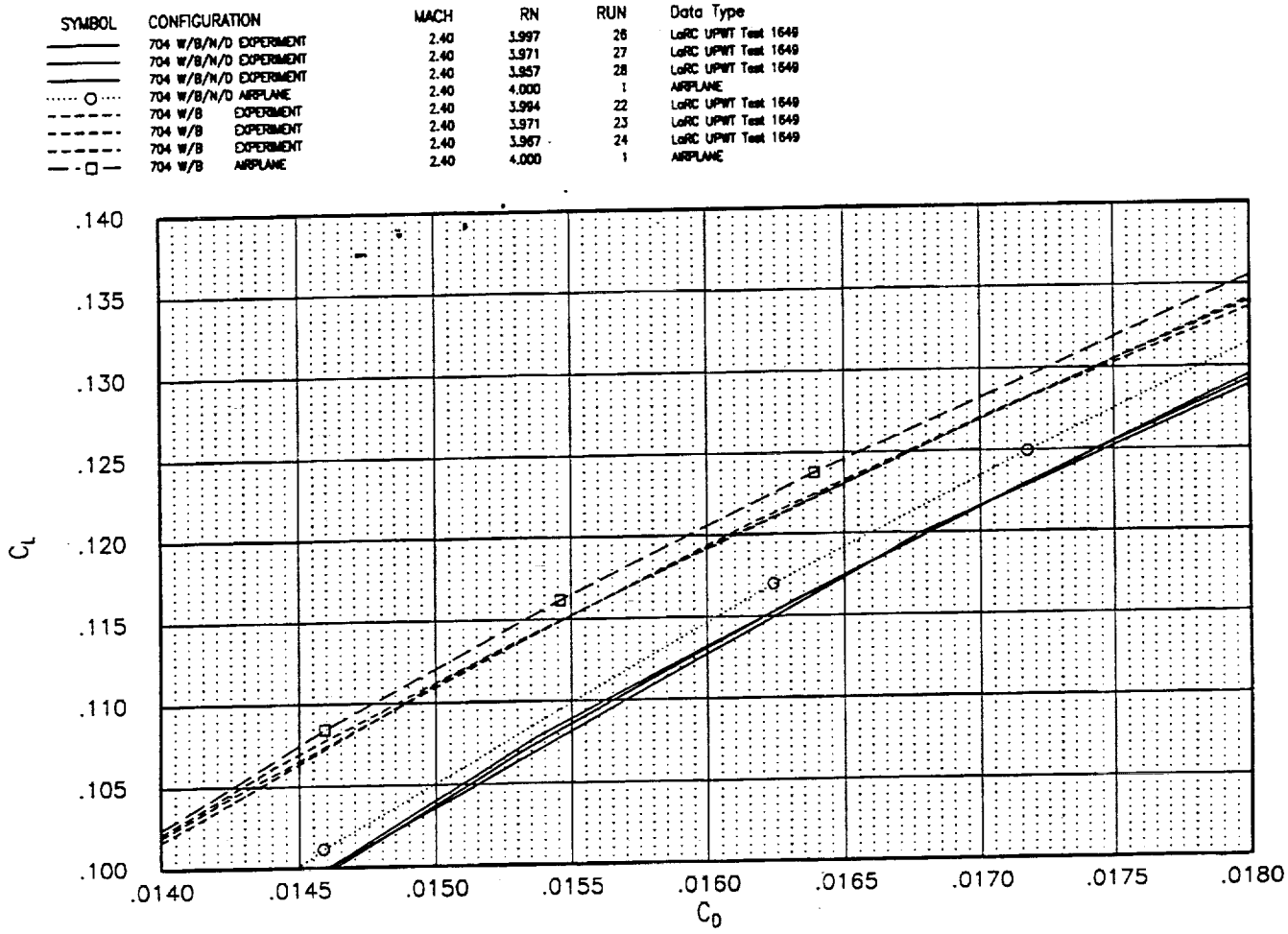

Fig 42. AIRPLANE force and moment coefficients of Ames 7-04 W/B (CAi = 0.006620) and W/B/N/D (CAi = 0.007500) compared with wind tunnel data.

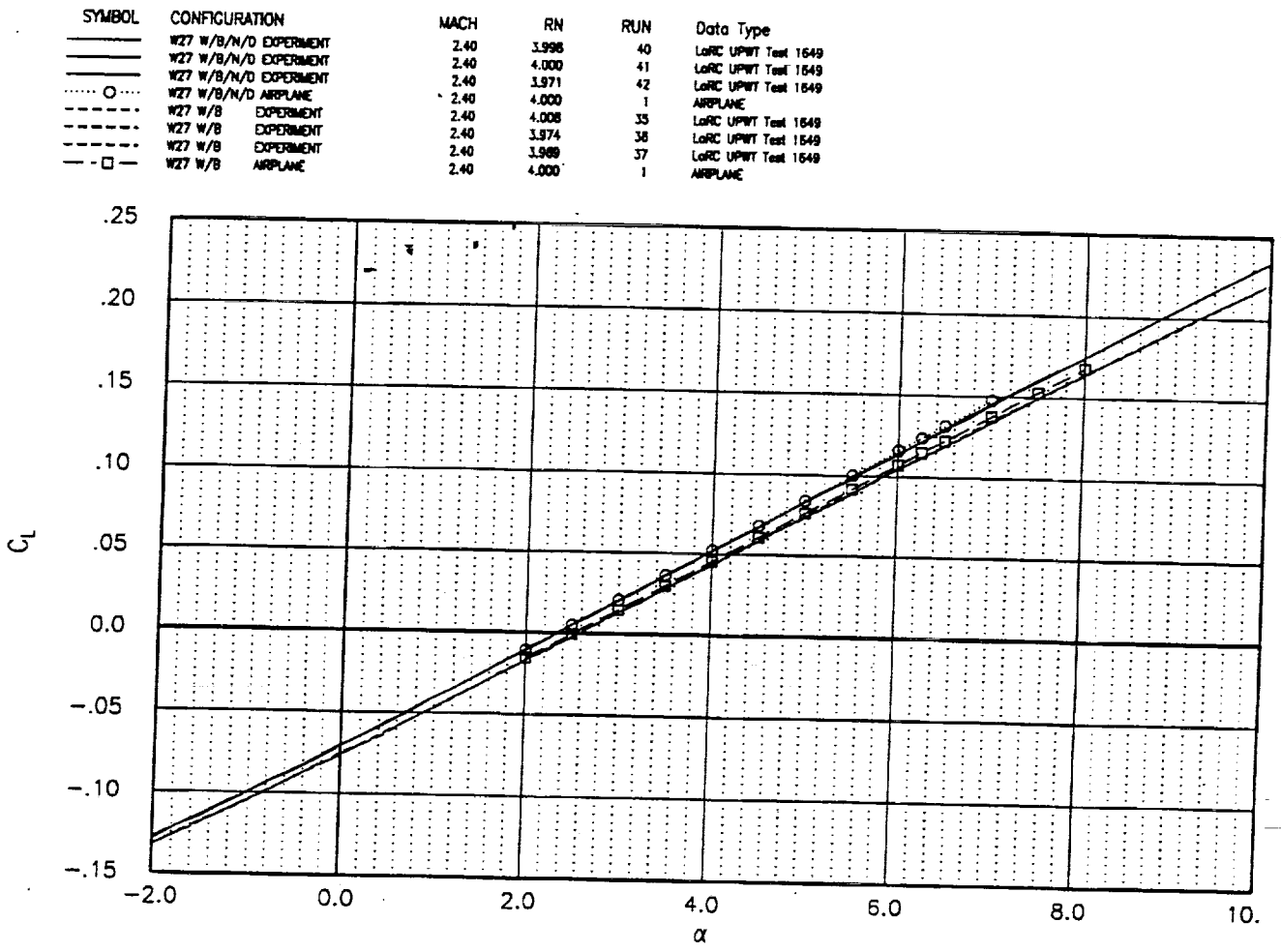

Fig 43. AIRPLANE force and moment coefficients of Boeing W27 W/B (CAi = 0.006667) and W/B/N/D (CAi = 0.007554) compared with wind tunnel data.

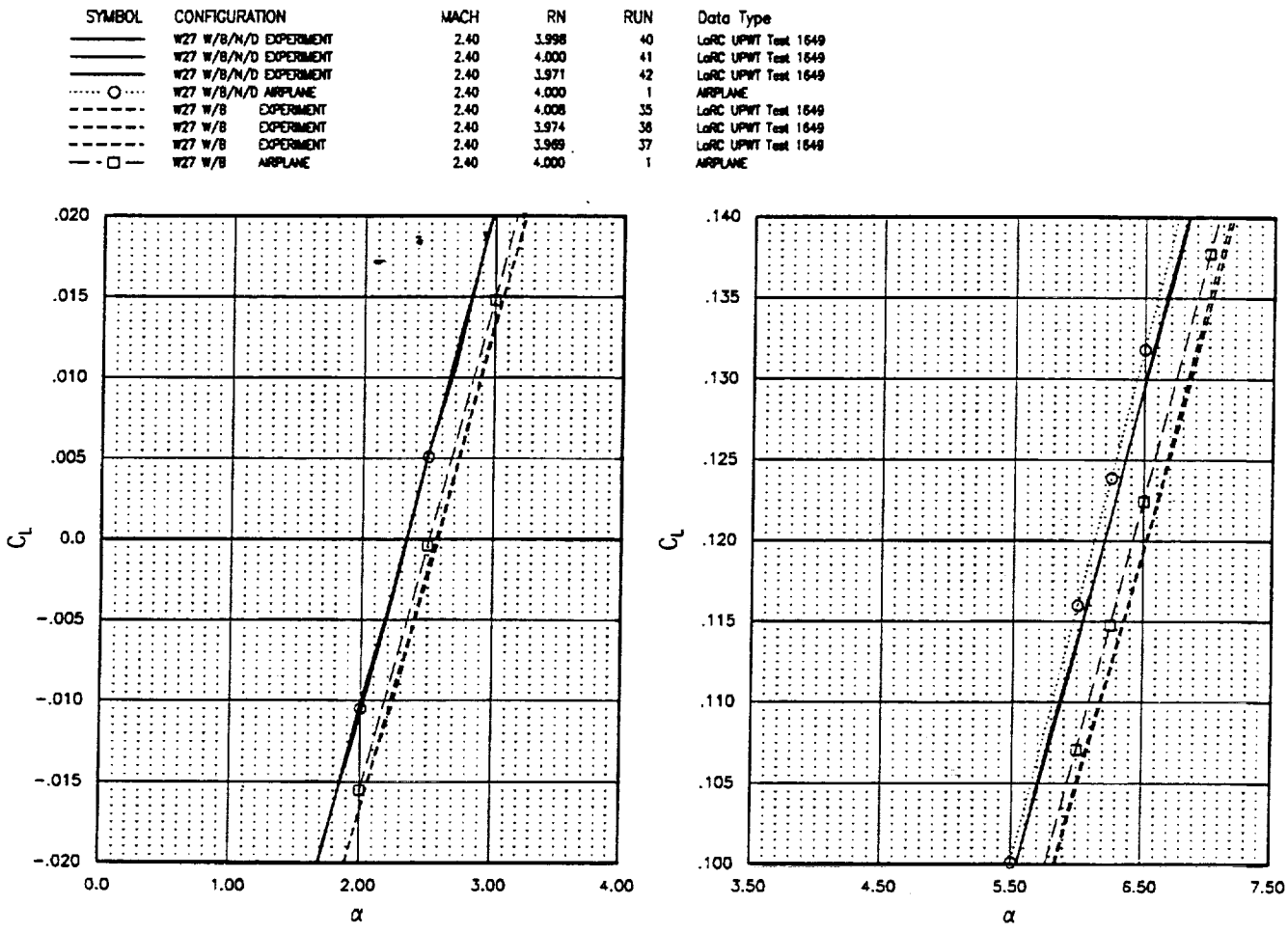

Fig 44. AIRPLANE force and moment coefficients of Boeing W27 W/B (CAi = 0.006667) and W/B/N/D (CAi = 0.007554) compared with wind tunnel data.

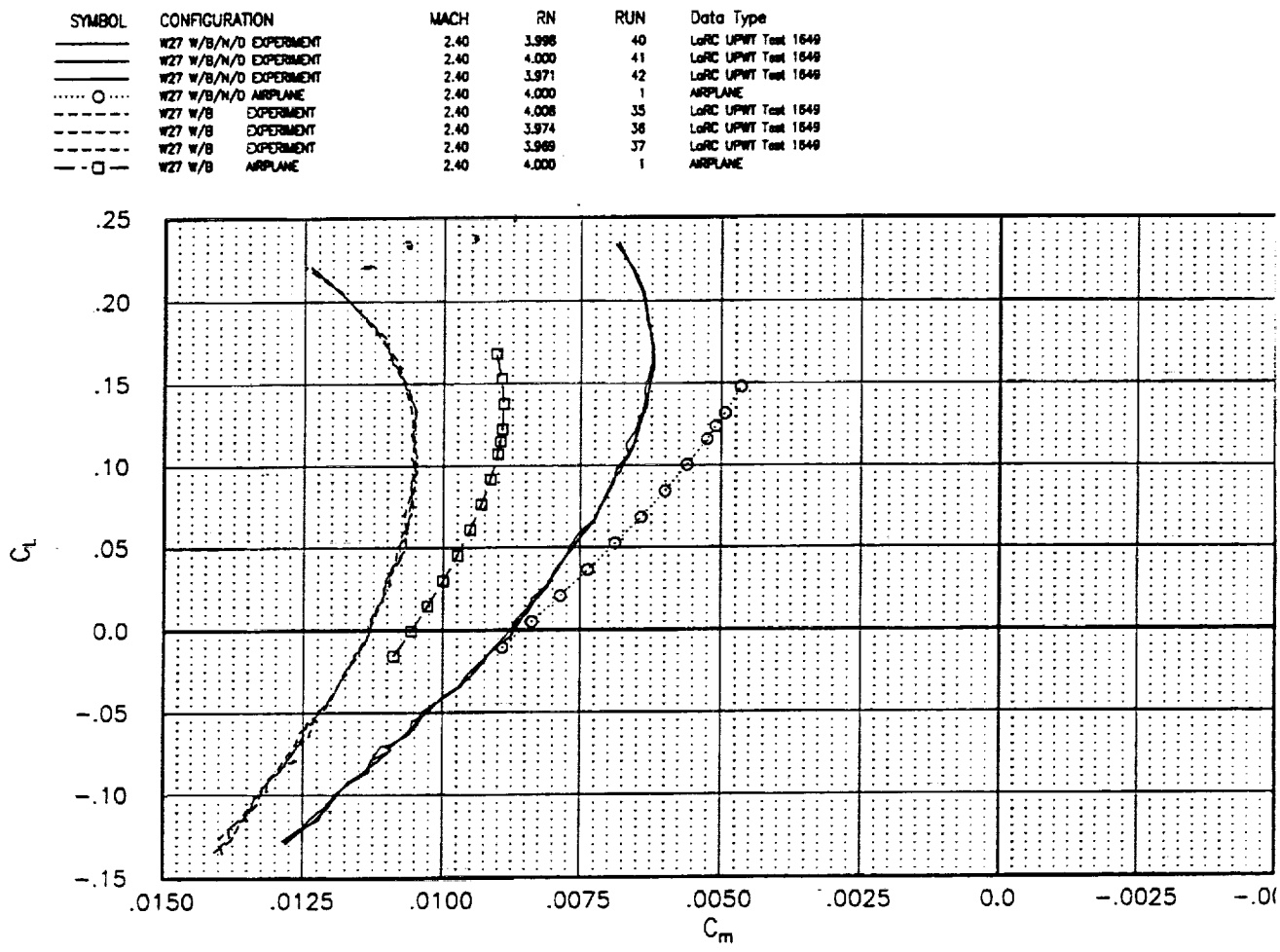

Fig 45. AIRPLANE force and moment coefficients of Boeing W27 W/B (CAi = 0.006667) and W/B/N/D (CAi = 0.007554) compared with wind tunnel data.

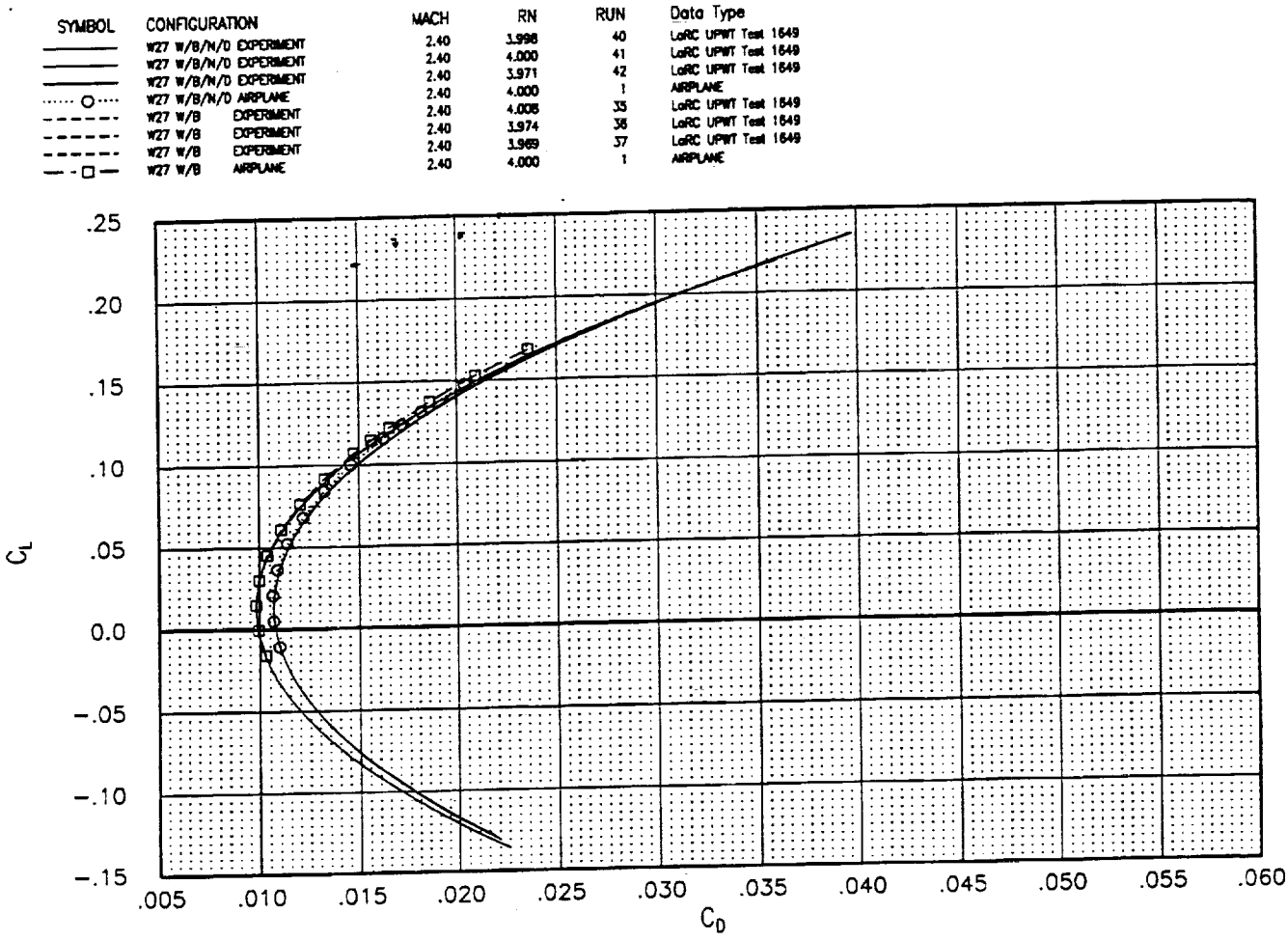

Fig 46. AIRPLANE force and moment coefficients of Boeing W27 W/B (CAi = 0.006667) and W/B/N/D (CAi = 0.007554) compared with wind tunnel data.

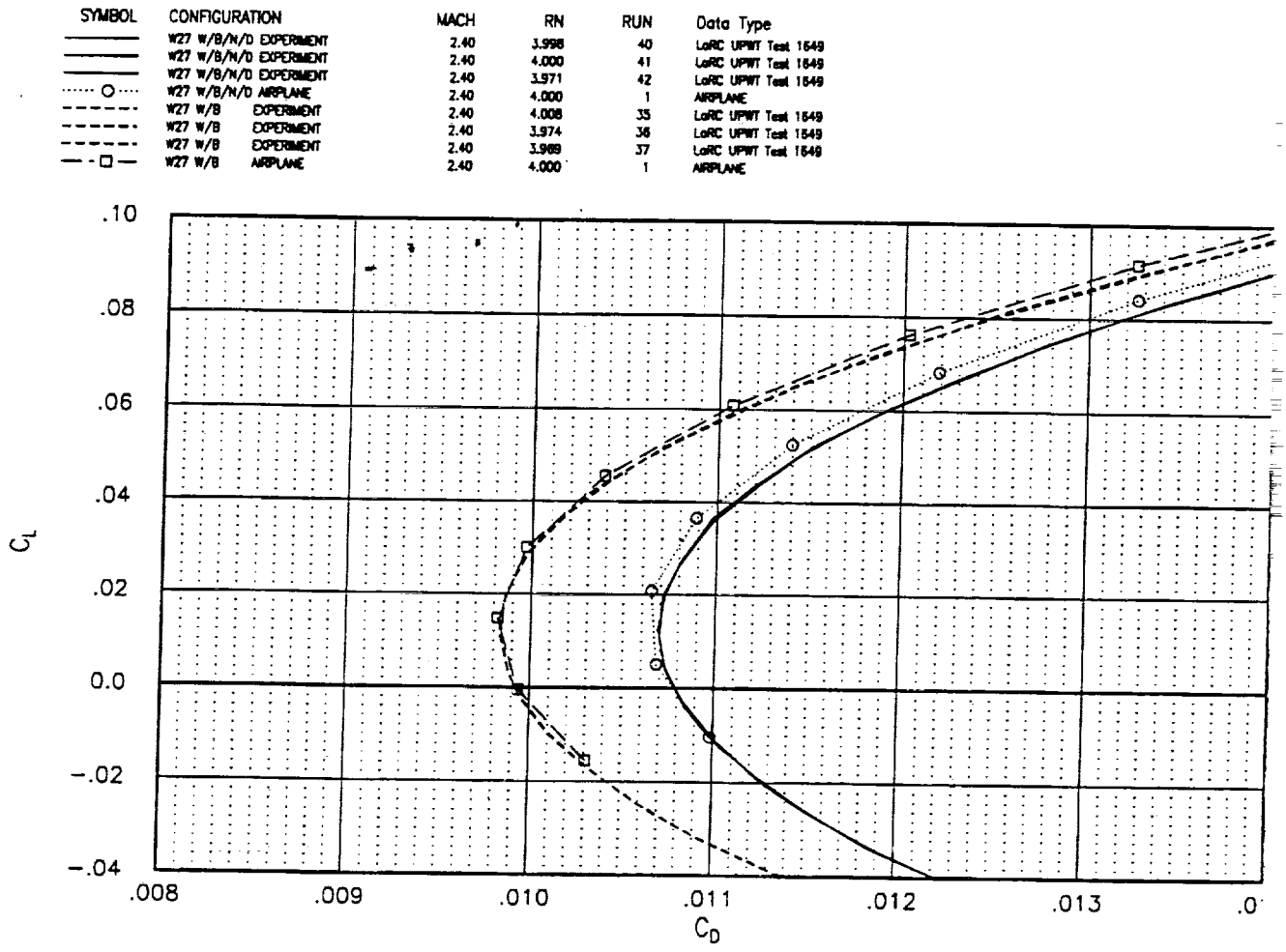

Fig 47. AIRPLANE force and moment coefficients of Boeing W27 W/B (CAi = 0.006667) and W/B/N/D (CAi = 0.007554) compared with wind tunnel data.

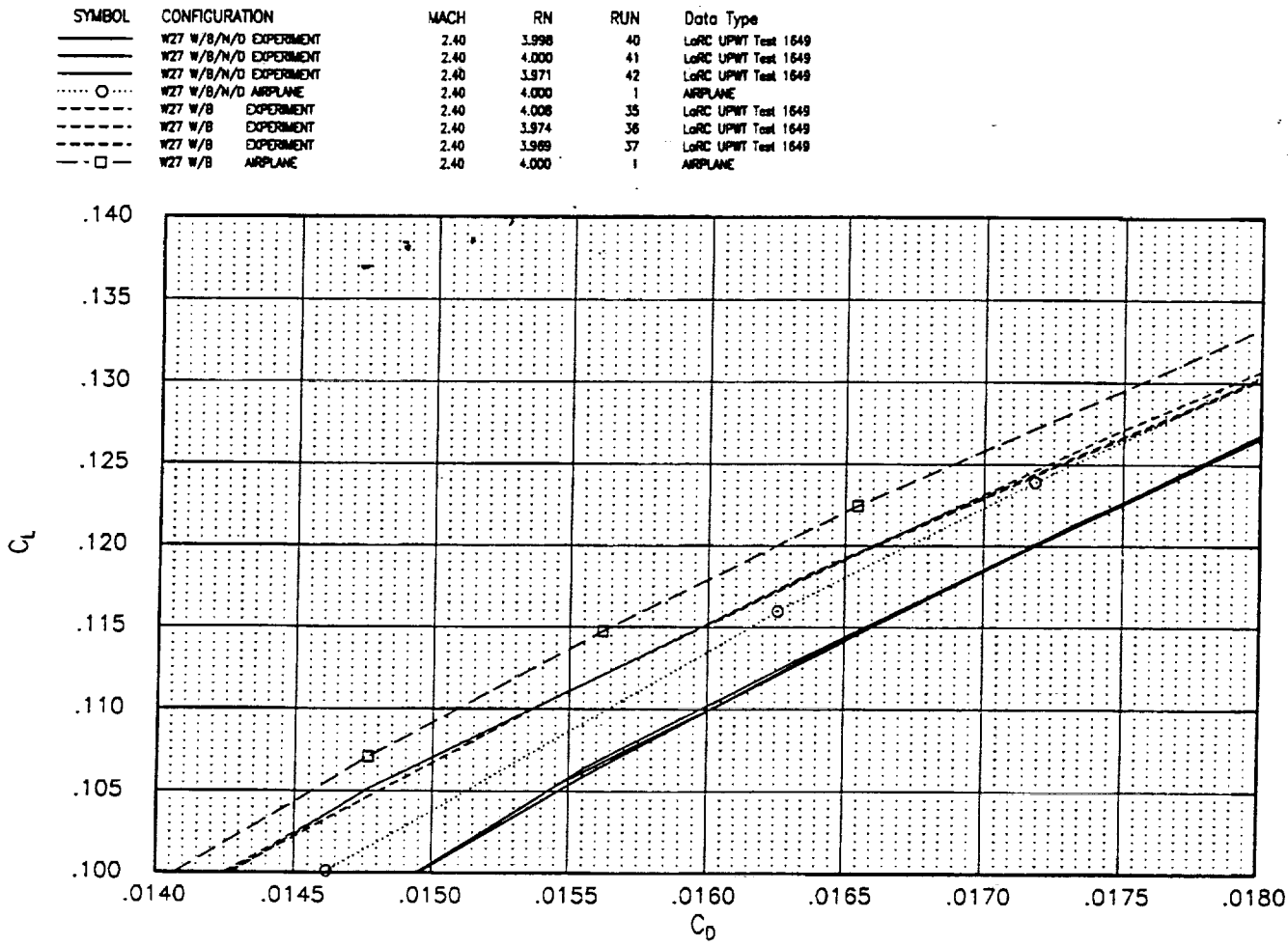

Fig 48. AIRPLANE force and moment coefficients of Boeing W27 W/B (CAi = 0.006667) and W/B/N/D (CAi = 0.007554) compared with wind tunnel data.

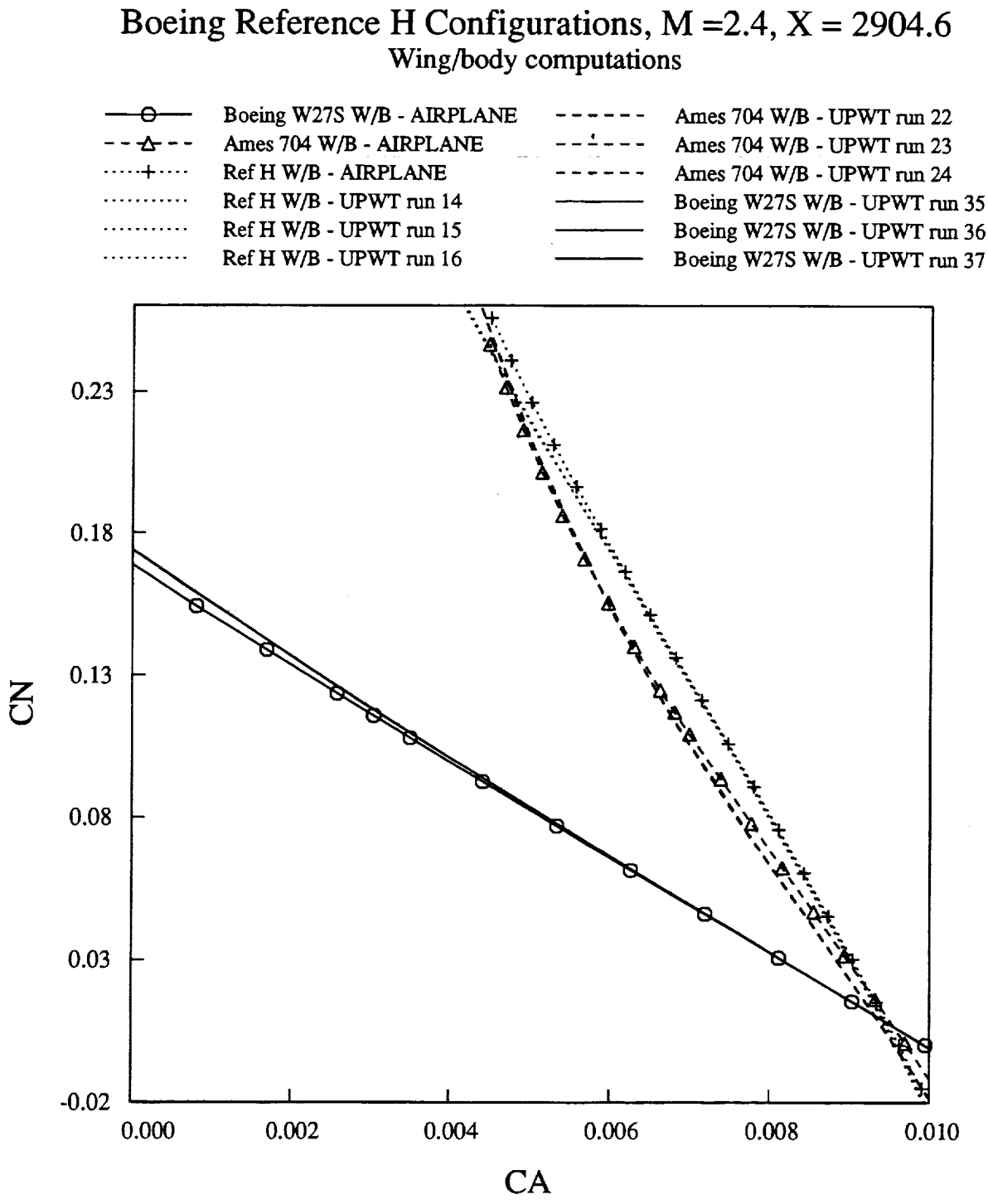

Fig 49. AIRPLANE and experiment body-axis coefficients for the wing/body baseline and optimized configurations, M=2.4.

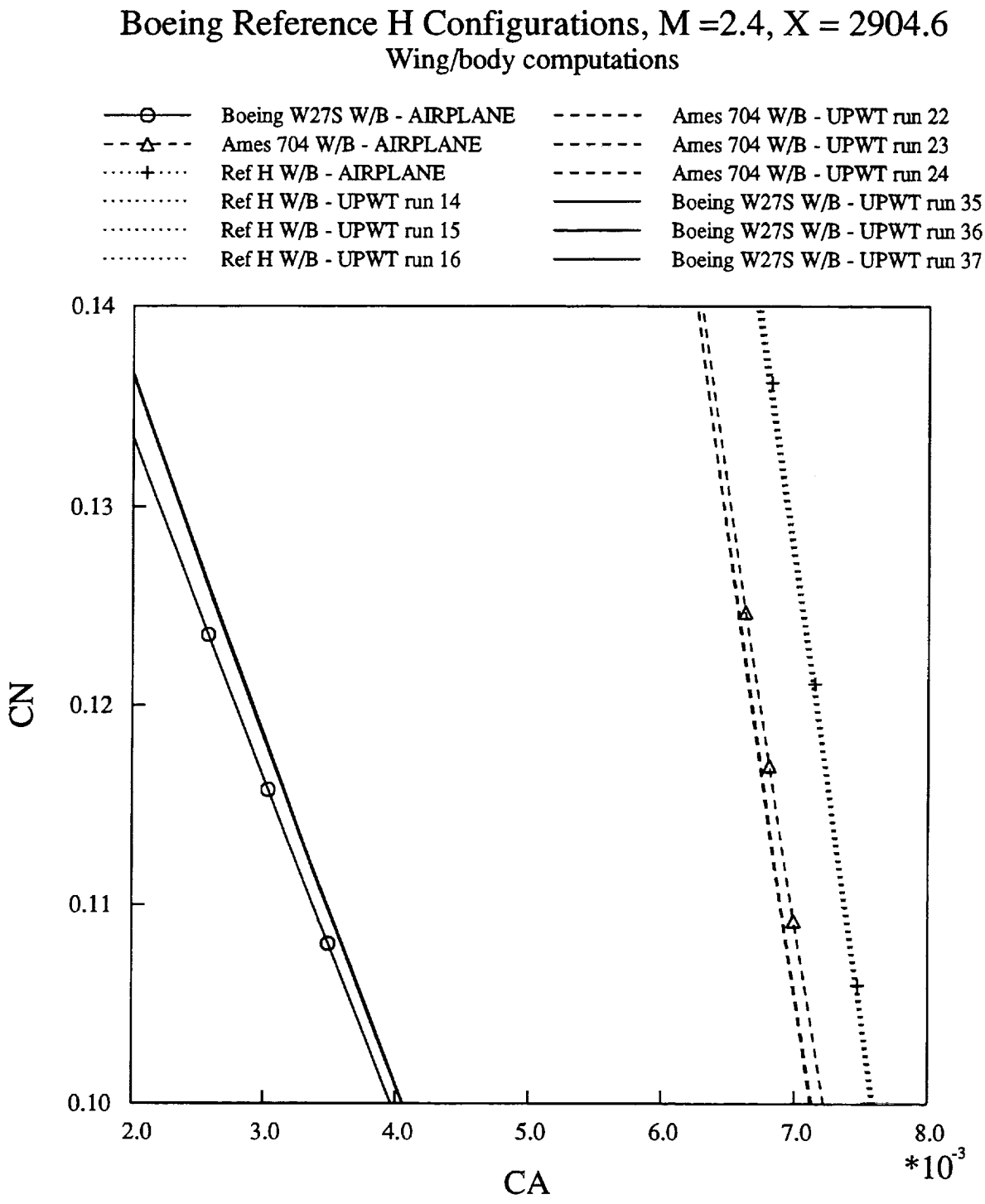

Fig 50. AIRPLANE and experiment body-axis coefficients for the wing/body baseline and optimized configurations near CN=0.12, M=2.4.

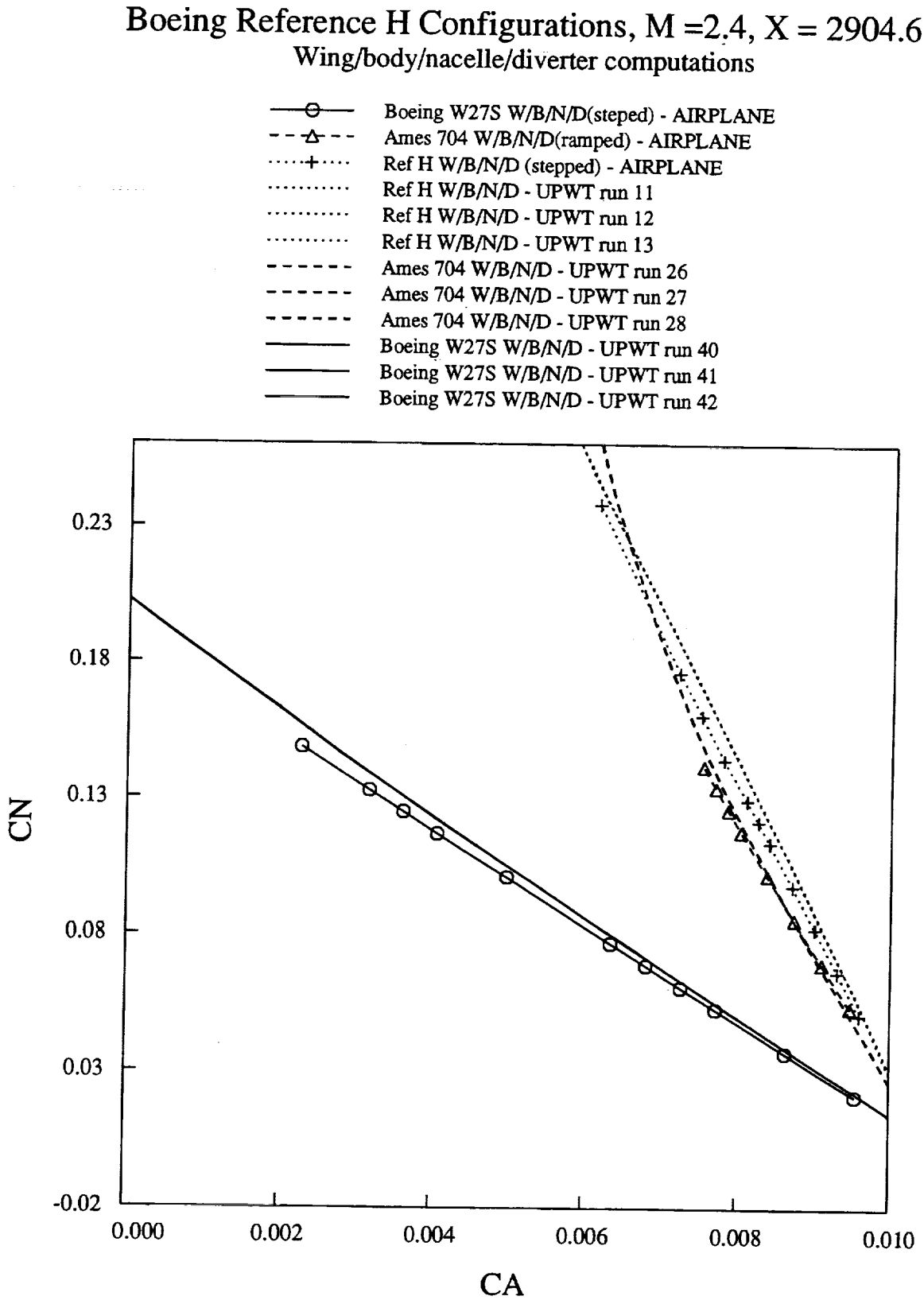

Fig 51. AIRPLANE and experiment body-axis coefficient for the complete baseline and optimized configurations, M=2.4.

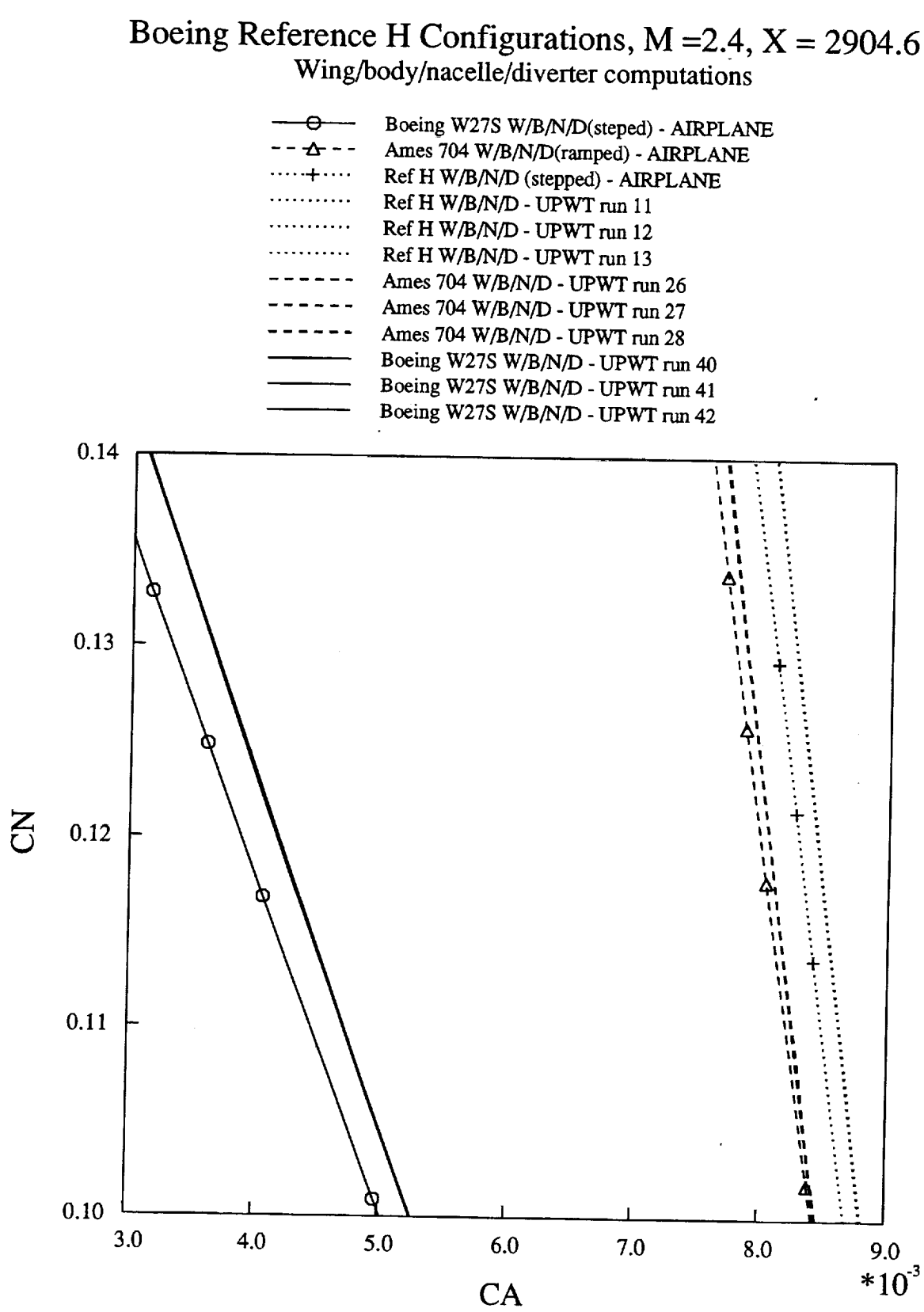

Fig 52. AIRPLANE and experiment body-axis coefficient for the complete baseline and optimized configurations near CN=0.12, M=2.4.

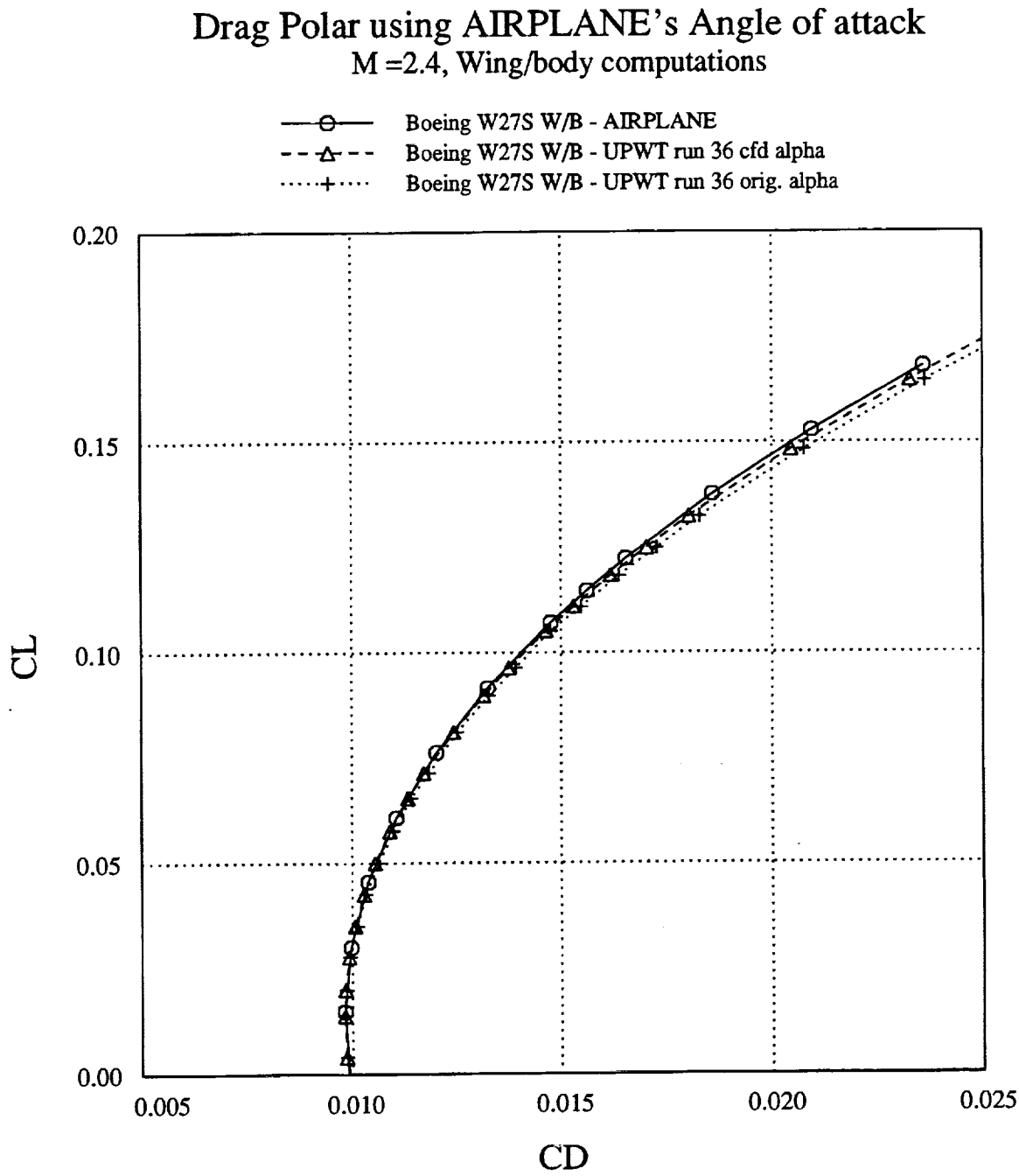

Fig 53. Experimental drag polar of the W27 wing/body configurations recomputed using CFD's angle of attack, and compared with original experimental data and AIRPLANE computations at M=2.4.

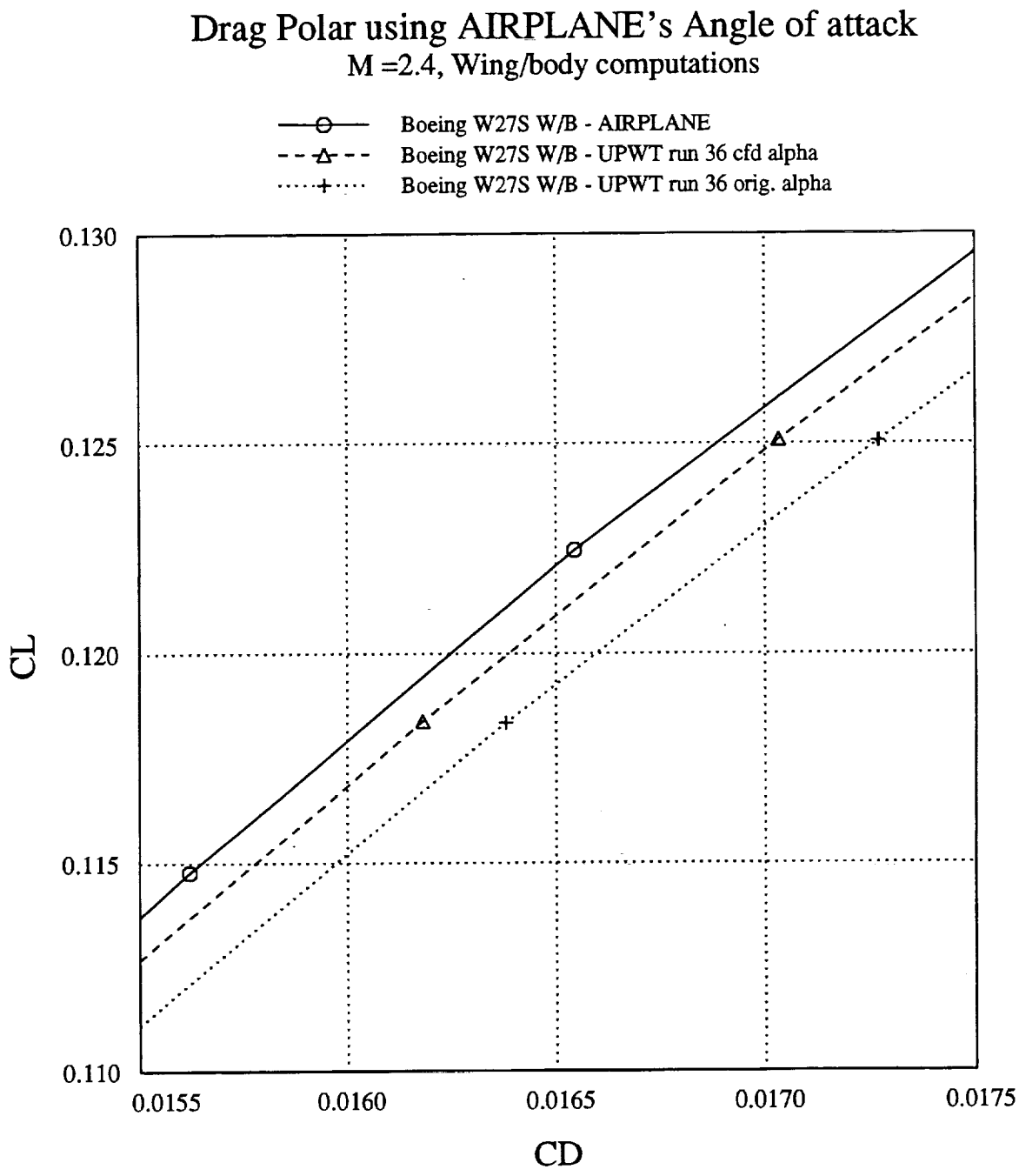

Fig 54. Experimental drag polar of the W27 wing/body configurations recomputed using CFD's angle of attack, and compared with original experimental data and AIRPLANE computations near cruise lift at M=2.4.

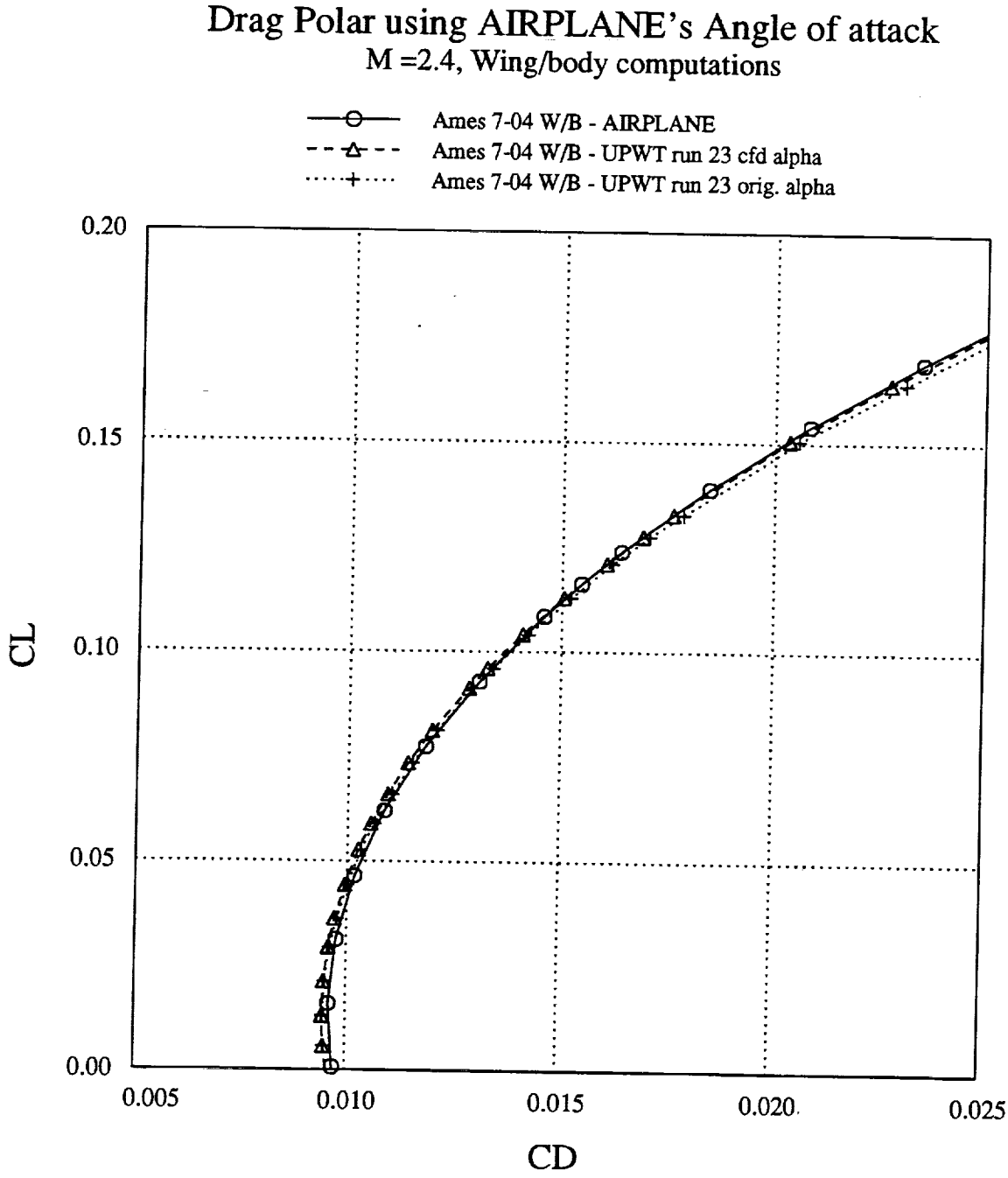

Fig 55. Experimental drag polar of the 704 wing/body configurations recomputed using CFD's angle of attack, and compared with original experimental data and AIRPLANE computations at M=2.4.

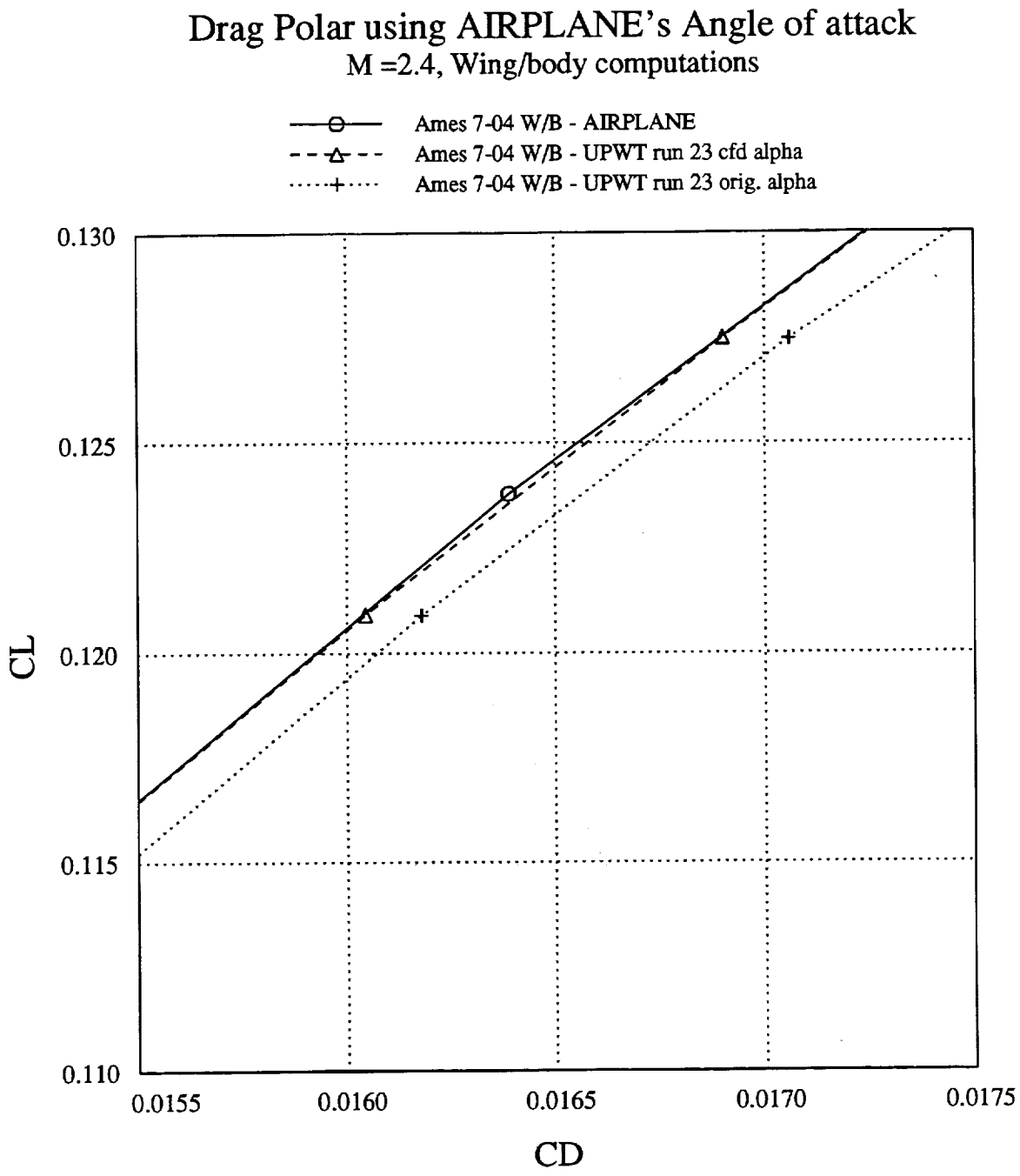

Fig 56. Experimental drag polar of the 704 wing/body configurations recomputed using CFD's angle of attack, and compared with original experimental data and AIRPLANE computations near cruise lift at M=2.4.

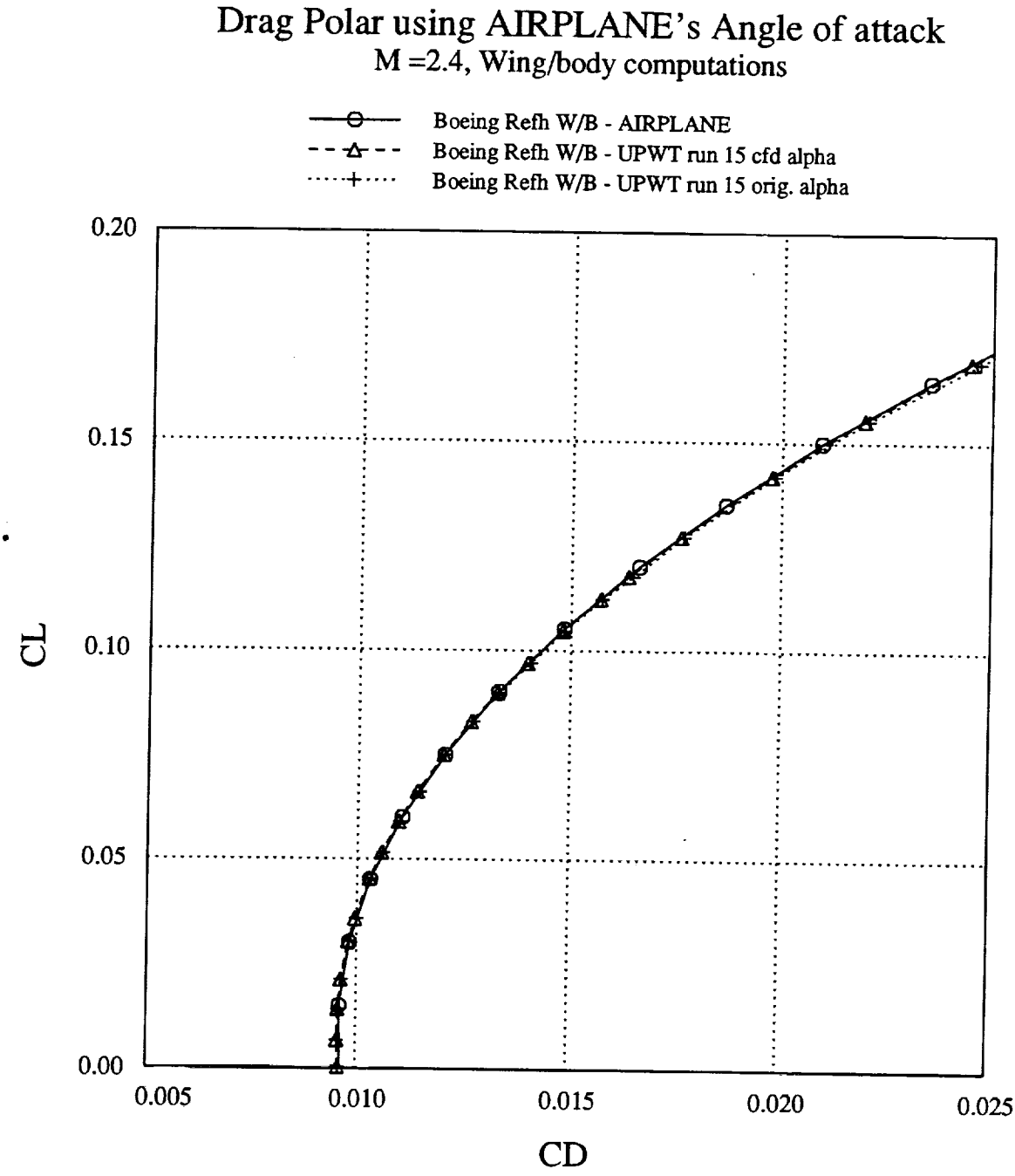

Fig 57. Experimental drag polar of the Ref H wing/body configurations recomputed using CFD's angle of attack, and compared with original experimental data and AIRPLANE computations at M=2.4.

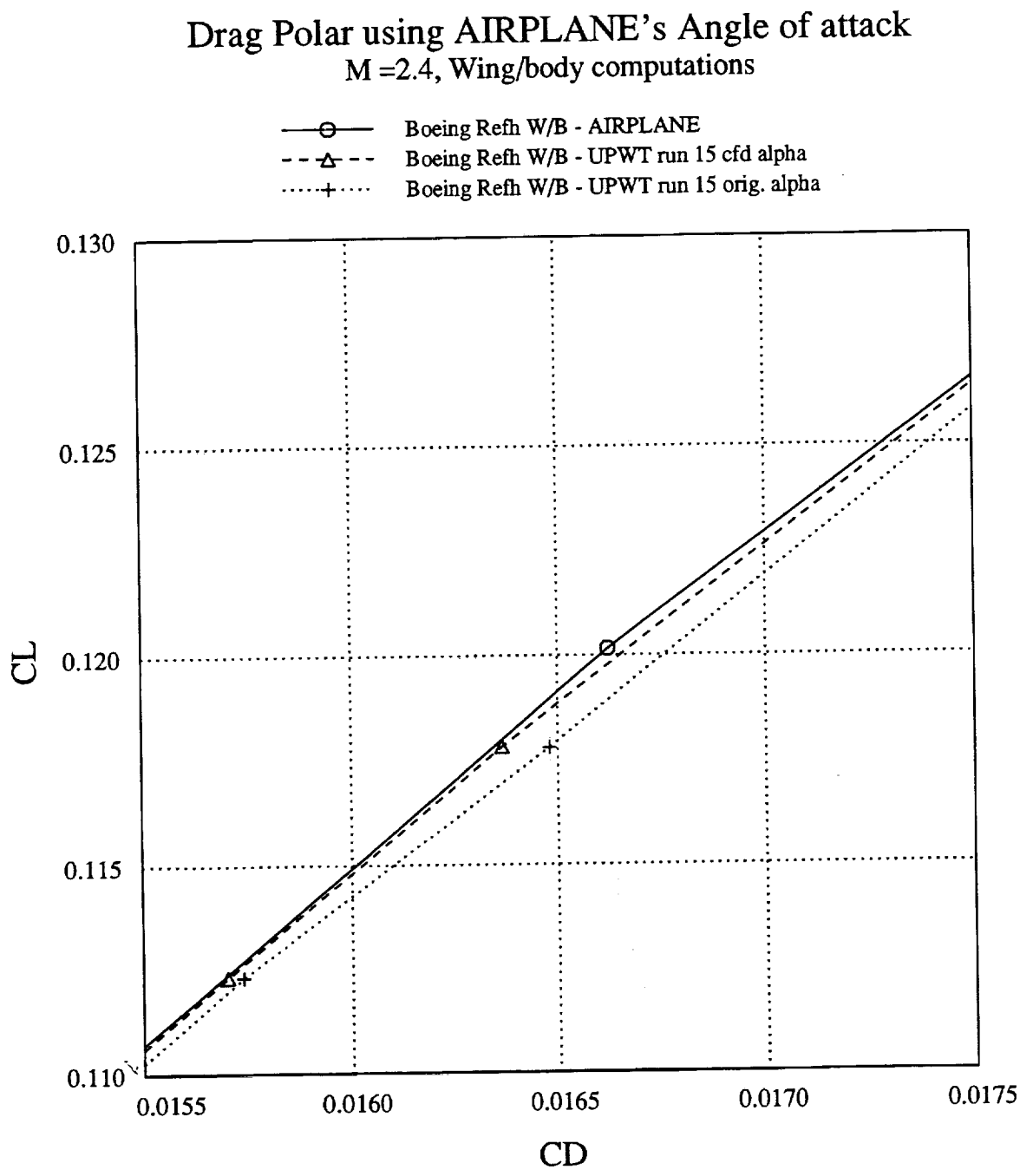

Fig 58. Experimental drag polar of the Ref H wing/body configurations recomputed using CFD's angle of attack, and compared with original experimental data and AIRPLANE computations near cruise lift at M=2.4.

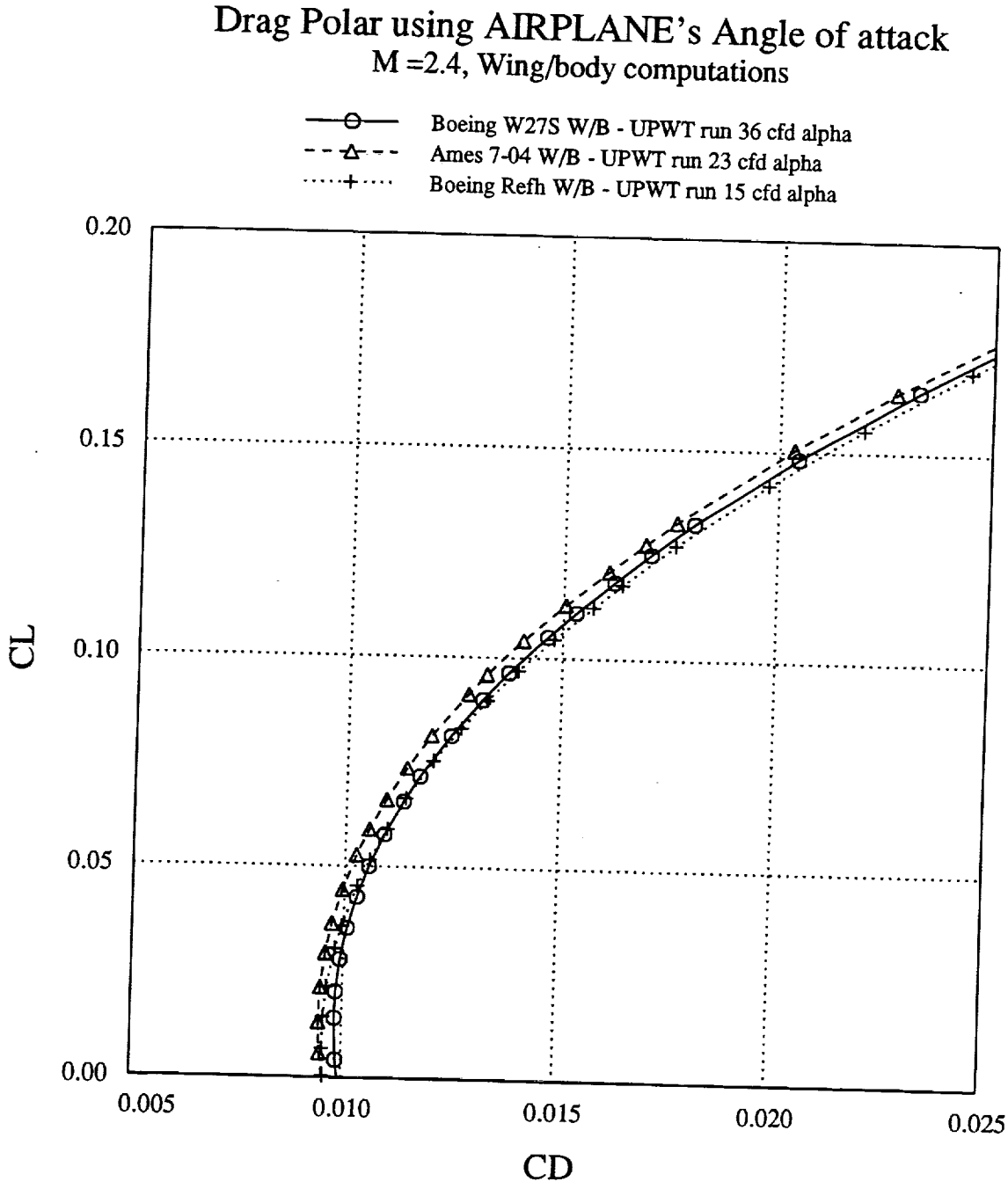

Fig 59. Experimental drag polar of the baseline and optimized wing/body configurations using CFD's angle of attack, M=2.4.

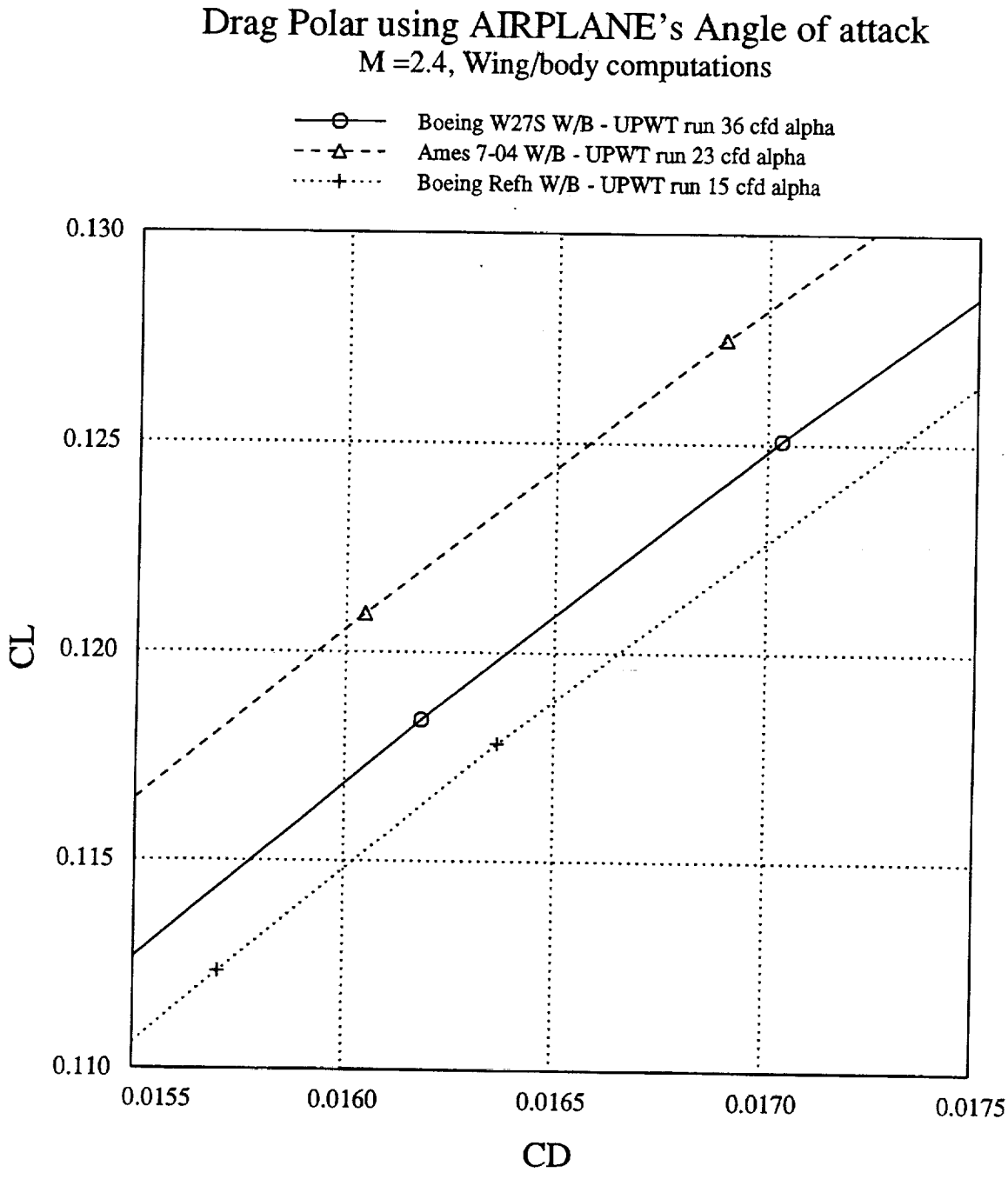

Fig 60. Experimental drag polar of the baseline and optimized wing/body configurations using CFD's angle of attack near cruise lift, M=2.4.

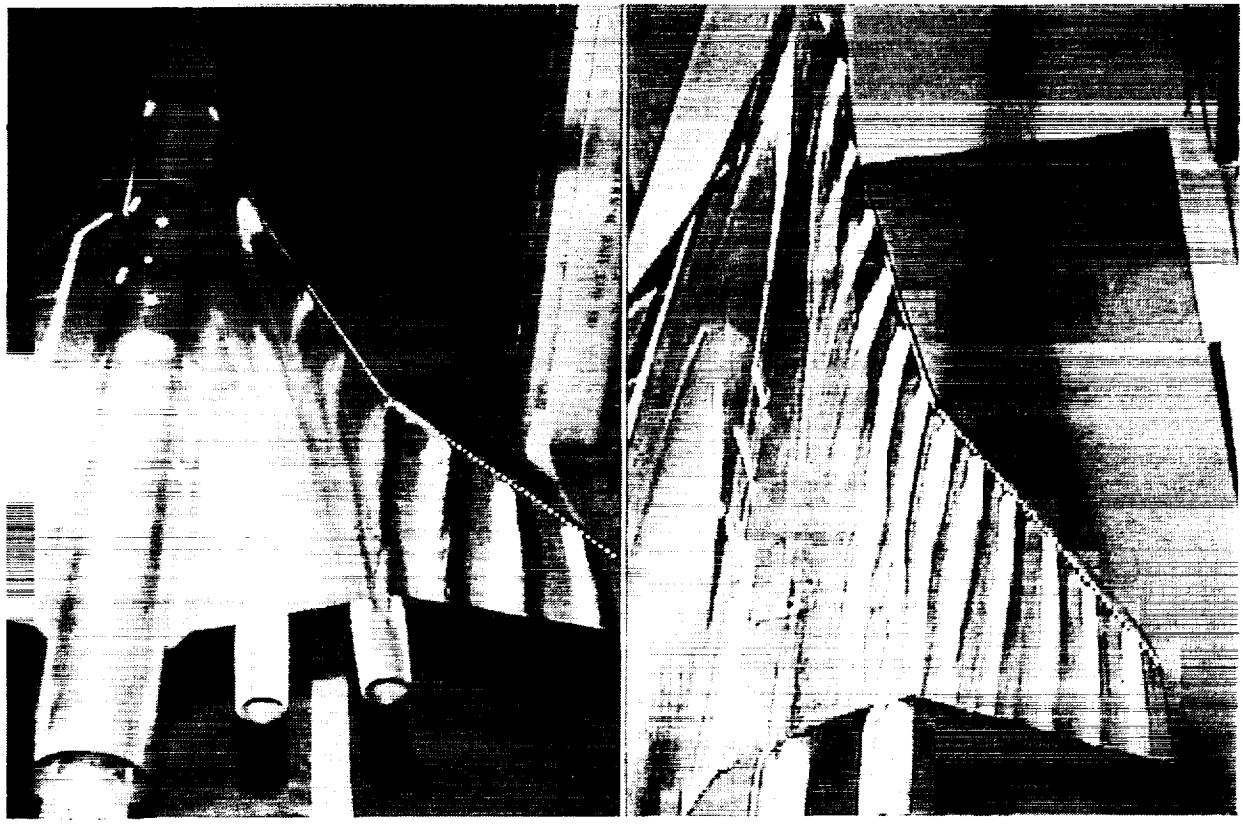

Fig 61. Experimental colored oil flow photographs of the 704 and W27 configurations at cruise, M=2.4, CL=0.12.

SYMBOL	CONFIGURATION	MACH	RN	RUN	Data Type
———	REF H W/B EXPERIMENT	2.40	4.012	14	LaRC UPWT Test 1649
———	REF H W/B EXPERIMENT	2.40	4.005	15	LaRC UPWT Test 1649
———	REF H W/B EXPERIMENT	2.40	3.990	16	LaRC UPWT Test 1649
····· O ·····	REF H W/B AIRPLANE	2.40	4.000	1	AIRPLANE
- - - - - -	704 W/B EXPERIMENT	2.40	3.994	22	LaRC UPWT Test 1649
- - - - - -	704 W/B EXPERIMENT	2.40	3.971	23	LaRC UPWT Test 1649
- - - - - -	704 W/B EXPERIMENT	2.40	3.967	24	LaRC UPWT Test 1649
— - □ —	704 W/B AIRPLANE	2.40	4.000	1	AIRPLANE

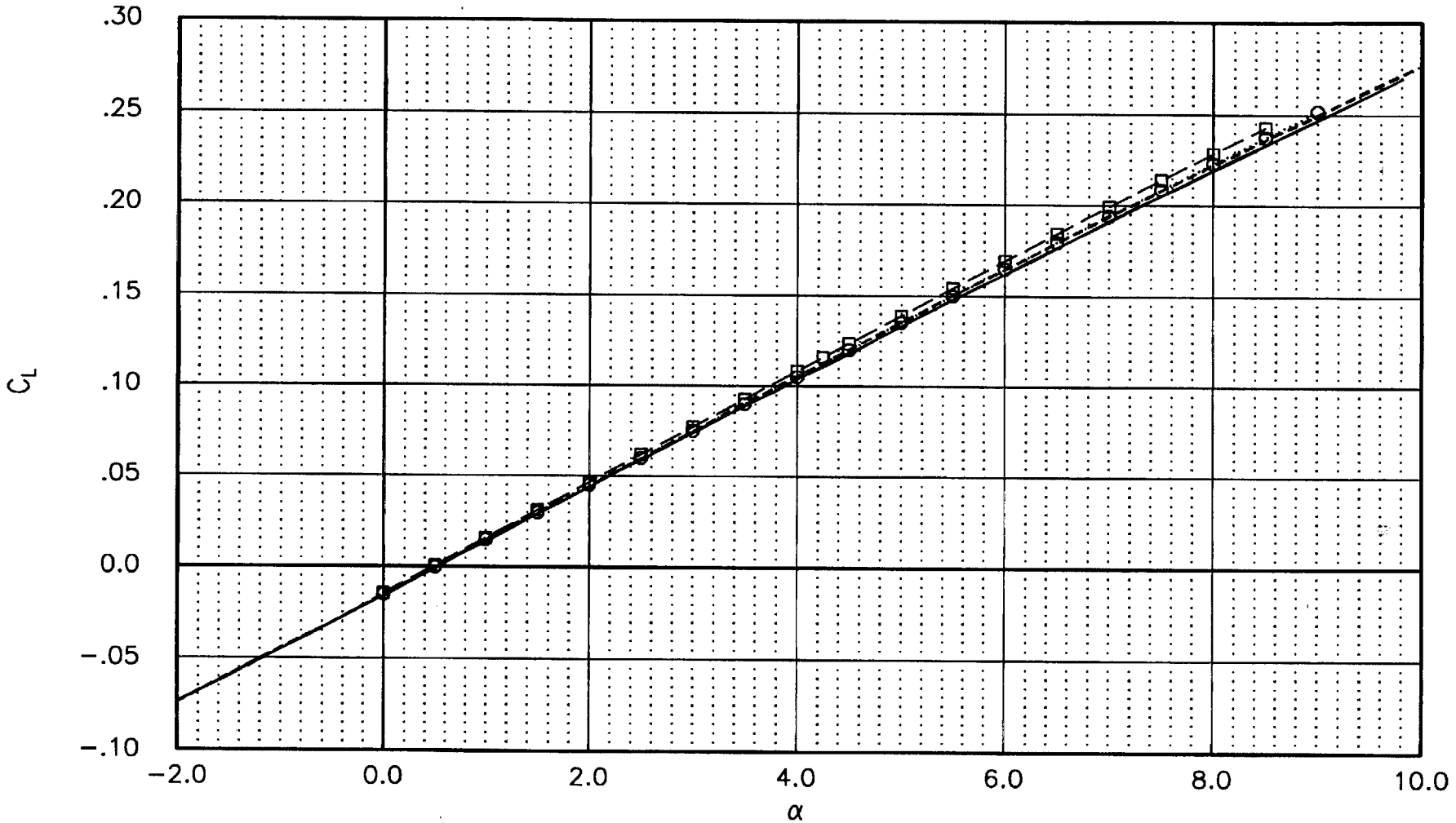

Fig 62. AIRPLANE force and moment coefficients of Ref H W/B (CAi = 0.006634) and Ames 7-04 W/B (CAi = 0.006620) compared with wind tunnel data.

SYMBOL	CONFIGURATION	MACH	RN	RUN	Data Type
———	REF H W/B EXPERIMENT	2.40	4.012	14	LaRC UPWT Test 1649
———	REF H W/B EXPERIMENT	2.40	4.005	15	LaRC UPWT Test 1649
———	REF H W/B EXPERIMENT	2.40	3.990	16	LaRC UPWT Test 1649
····O····	REF H W/B AIRPLANE	2.40	4.000	1	AIRPLANE
- - - - -	704 W/B EXPERIMENT	2.40	3.994	22	LaRC UPWT Test 1649
- - - - -	704 W/B EXPERIMENT	2.40	3.971	23	LaRC UPWT Test 1649
- - - - -	704 W/B EXPERIMENT	2.40	3.967	24	LaRC UPWT Test 1649
— - □ —	704 W/B AIRPLANE	2.40	4.000	1	AIRPLANE

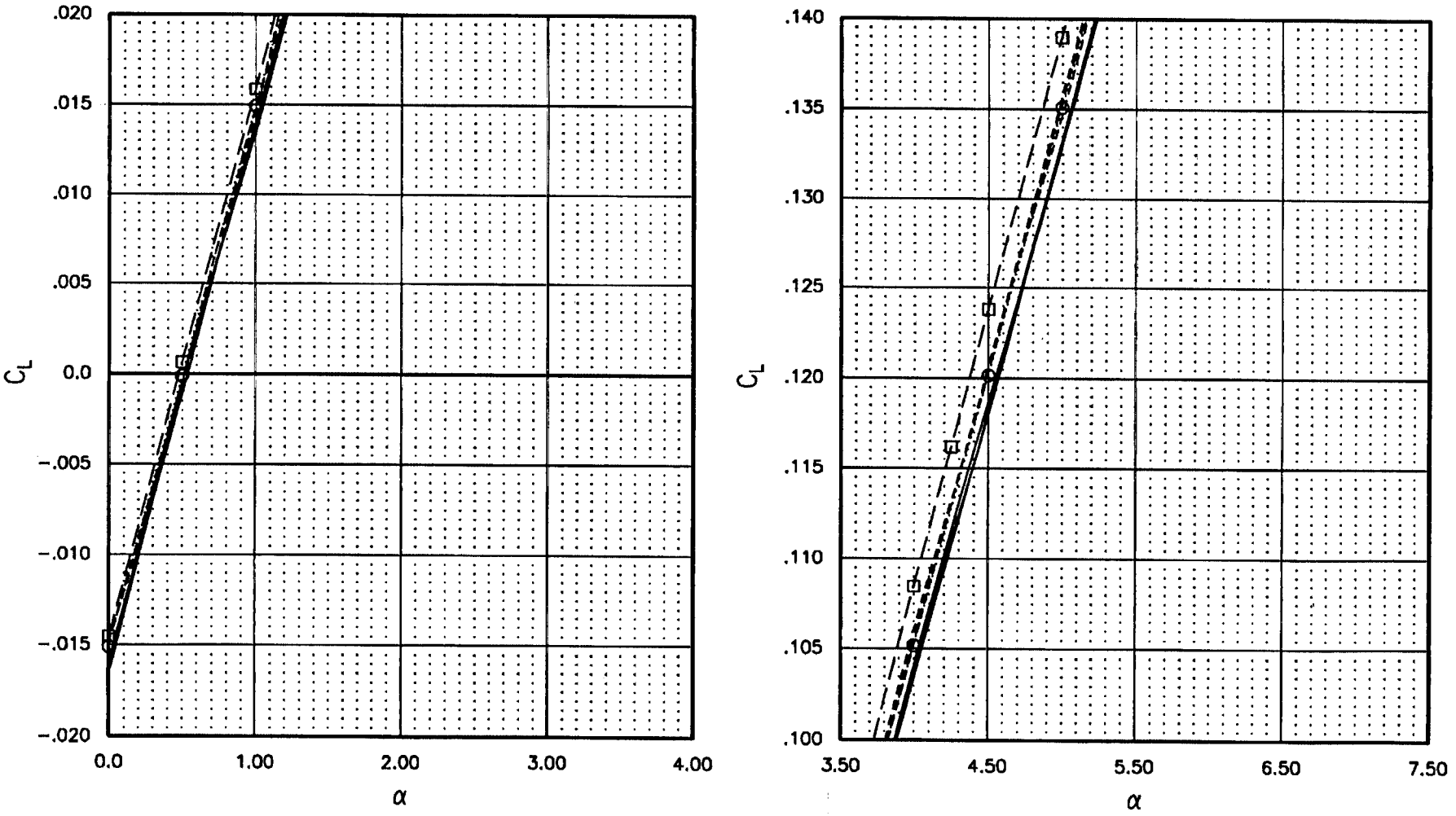

Fig 63. AIRPLANE force and moment coefficients of Ref H W/B (CAi = 0.006634)

SYMBOL	CONFIGURATION	MACH	RN	RUN	Data Type
———	REF H W/B EXPERIMENT	2.40	4.012	14	LaRC UPWT Test 1649
———	REF H W/B EXPERIMENT	2.40	4.005	15	LaRC UPWT Test 1649
———	REF H W/B EXPERIMENT	2.40	3.990	16	LaRC UPWT Test 1649
····O····	REF H W/B AIRPLANE	2.40	4.000	1	AIRPLANE
- - - - - -	704 W/B EXPERIMENT	2.40	3.994	22	LaRC UPWT Test 1649
- - - - - -	704 W/B EXPERIMENT	2.40	3.971	23	LaRC UPWT Test 1649
- - - - - -	704 W/B EXPERIMENT	2.40	3.967	24	LaRC UPWT Test 1649
—-□—	704 W/B AIRPLANE	2.40	4.000	1	AIRPLANE

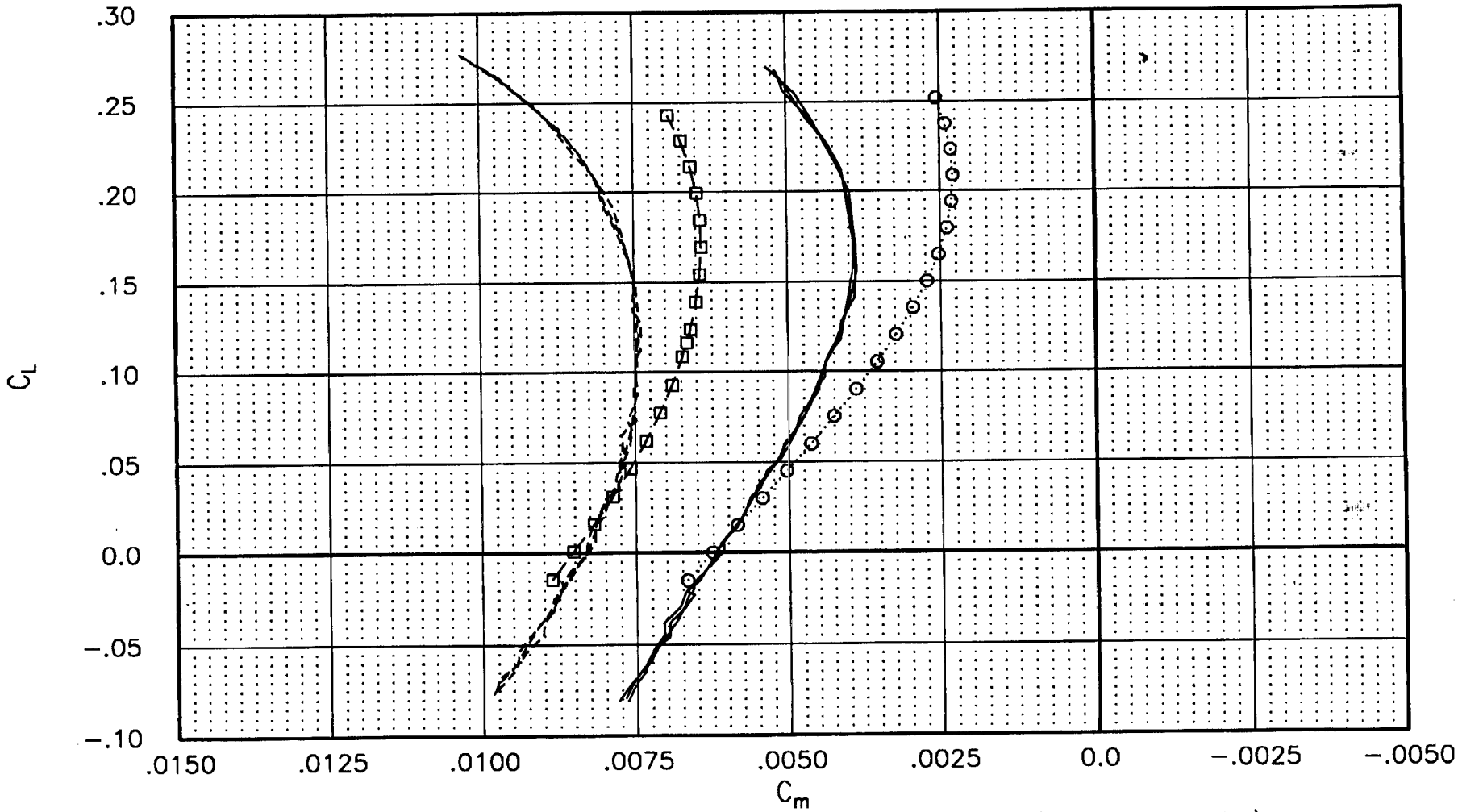

Fig 64. AIRPLANE force and moment coefficients of Ref H W/B (CAi = 0.006634) and Ames 7-04 W/B (CAi = 0.006620) compared with wind tunnel data.

SYMBOL	CONFIGURATION	MACH	RN	RUN	Data Type
———	REF H W/B EXPERIMENT	2.40	4.012	14	LaRC UPWT Test 1649
———	REF H W/B EXPERIMENT	2.40	4.005	15	LaRC UPWT Test 1649
———	REF H W/B EXPERIMENT	2.40	3.990	16	LaRC UPWT Test 1649
····O····	REF H W/B AIRPLANE	2.40	4.000	1	AIRPLANE
- - - - -	704 W/B EXPERIMENT	2.40	3.994	22	LaRC UPWT Test 1649
- - - - -	704 W/B EXPERIMENT	2.40	3.971	23	LaRC UPWT Test 1649
- - - - -	704 W/B EXPERIMENT	2.40	3.967	24	LaRC UPWT Test 1649
— - □ —	704 W/B AIRPLANE	2.40	4.000	1	AIRPLANE

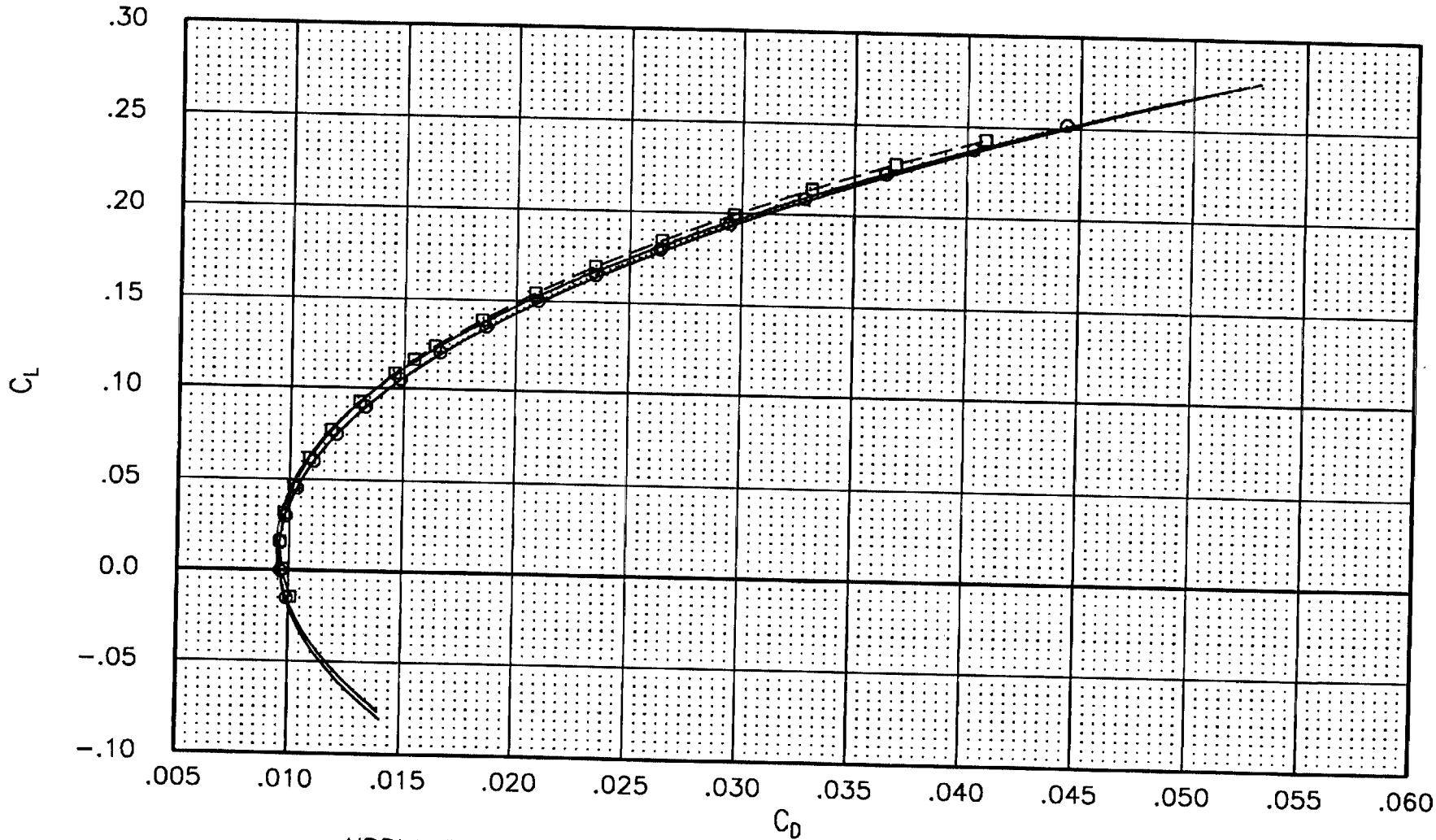

Fig 65. AIRPLANE force and moment coefficients of Ref H W/B (CAi = 0.006634) and Ames 7-04 W/B (CAi = 0.006620) compared with wind tunnel data.

SYMBOL	CONFIGURATION	MACH	RN	RUN	Data Type
———	REF H W/B EXPERIMENT	2.40	4.012	14	LaRC UPWT Test 1649
———	REF H W/B EXPERIMENT	2.40	4.005	15	LaRC UPWT Test 1649
———	REF H W/B EXPERIMENT	2.40	3.990	16	LaRC UPWT Test 1649
····O····	REF H W/B AIRPLANE	2.40	4.000	1	AIRPLANE
- - - - -	704 W/B EXPERIMENT	2.40	3.994	22	LaRC UPWT Test 1649
- - - - -	704 W/B EXPERIMENT	2.40	3.971	23	LaRC UPWT Test 1649
- - - - -	704 W/B EXPERIMENT	2.40	3.967	24	LaRC UPWT Test 1649
—-□—	704 W/B AIRPLANE	2.40	4.000	1	AIRPLANE

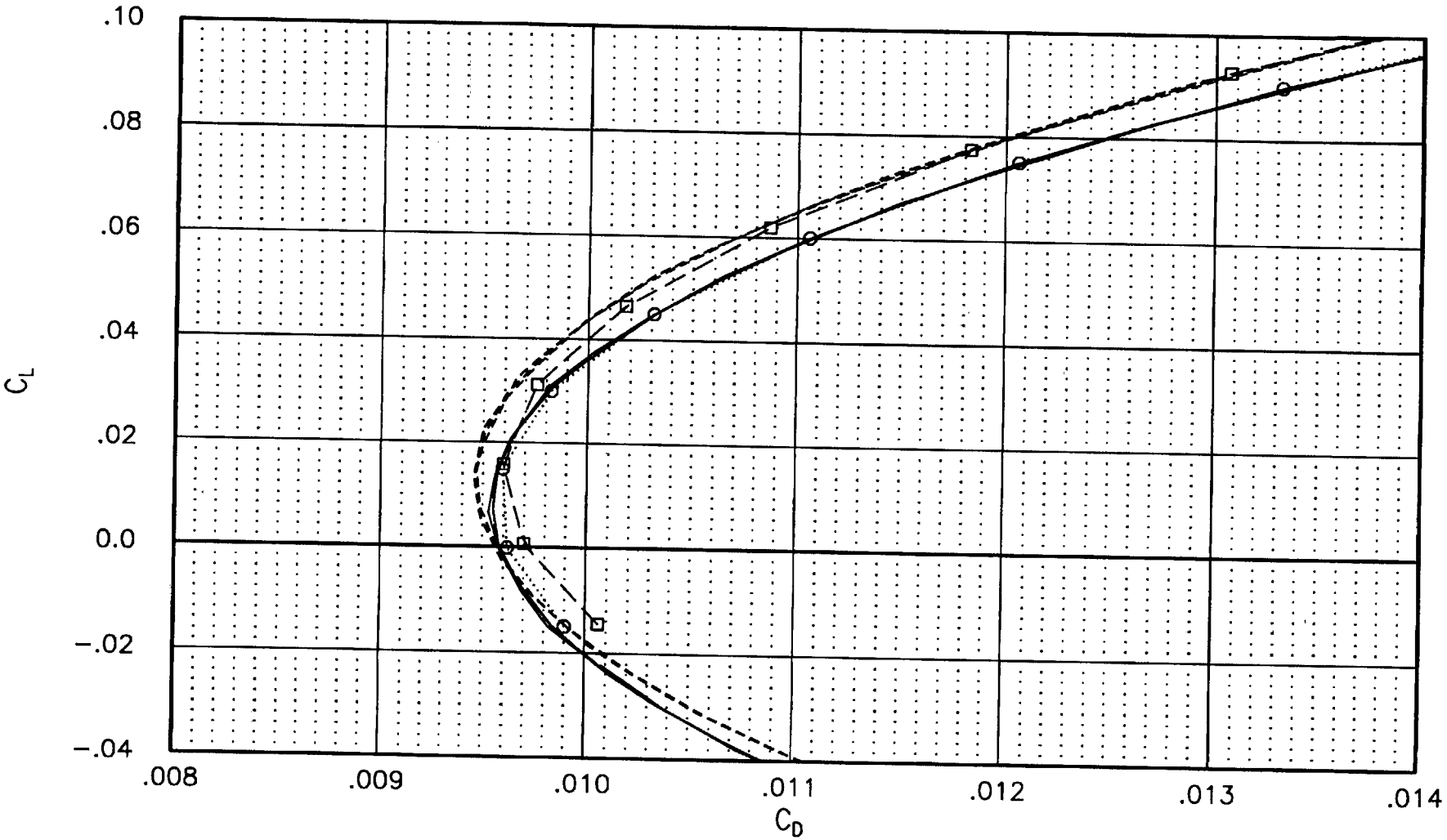

Fig 66. AIRPLANE force and moment coefficients of Ref H W/B (CAi = 0.006634) and Ames 7-04 W/B (CAi = 0.006620) compared with wind tunnel data.

SYMBOL	CONFIGURATION	MACH	RN	RUN	Data Type
———	REF H W/B EXPERIMENT	2.40	4.012	14	LaRC UPWT Test 1649
———	REF H W/B EXPERIMENT	2.40	4.005	15	LaRC UPWT Test 1649
———	REF H W/B EXPERIMENT	2.40	3.990	16	LaRC UPWT Test 1649
····· O ·····	REF H W/B AIRPLANE	2.40	4.000	1	AIRPLANE
- - - - - -	704 W/B EXPERIMENT	2.40	3.994	22	LaRC UPWT Test 1649
- - - - - -	704 W/B EXPERIMENT	2.40	3.971	23	LaRC UPWT Test 1649
- - - - - -	704 W/B EXPERIMENT	2.40	3.967	24	LaRC UPWT Test 1649
— - □ —	704 W/B AIRPLANE	2.40	4.000	1	AIRPLANE

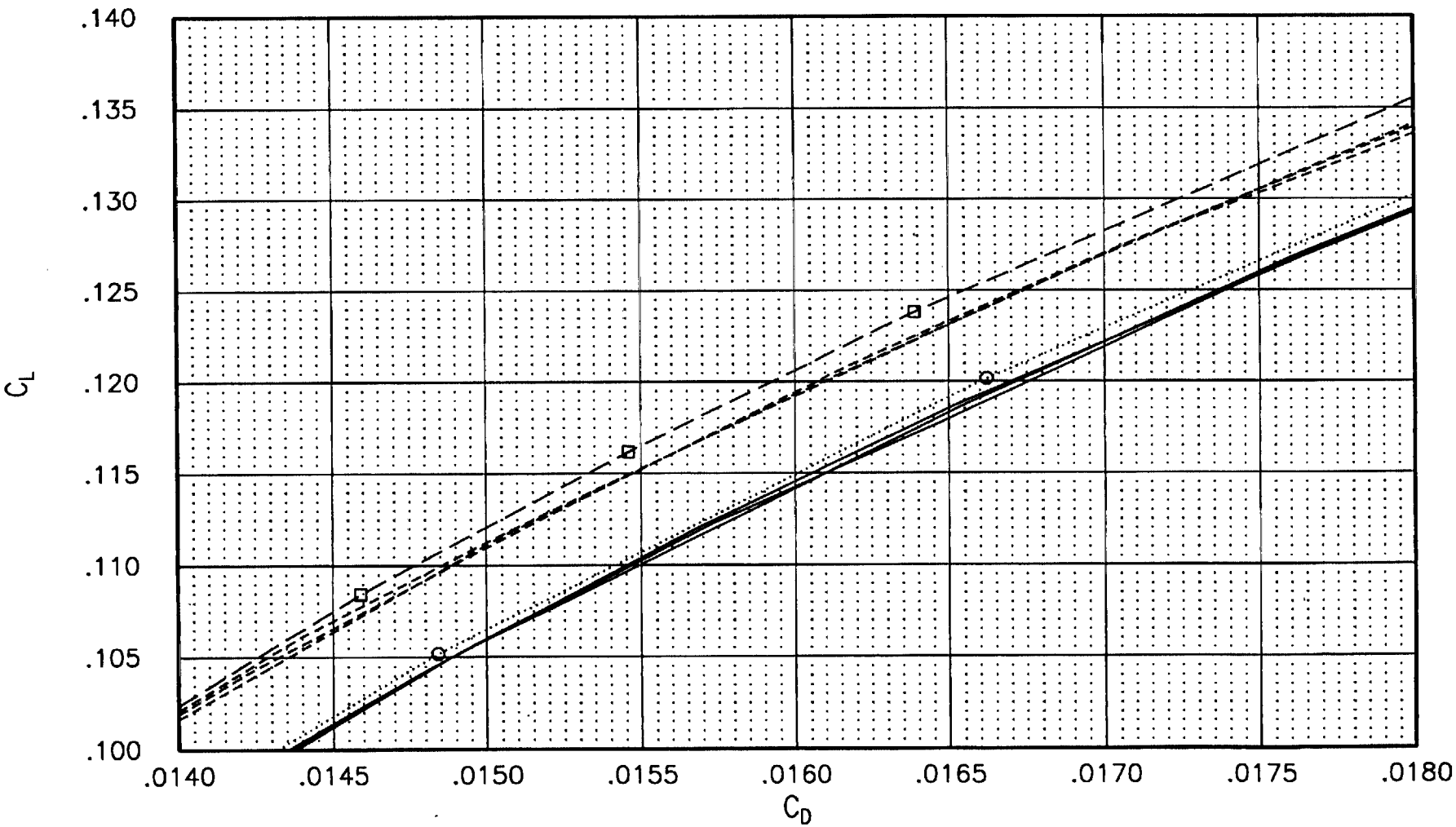

Fig 67. AIRPLANE force and moment coefficients of Ref H W/B (CAi = 0.006634)

SYMBOL	CONFIGURATION	MACH	RN	RUN	Data Type
———	REF H W/B EXPERIMENT	2.40	4.012	14	LaRC UPWT Test 1649
———	REF H W/B EXPERIMENT	2.40	4.005	15	LaRC UPWT Test 1649
———	REF H W/B EXPERIMENT	2.40	3.990	16	LaRC UPWT Test 1649
····O····	REF H W/B AIRPLANE	2.40	4.000	1	AIRPLANE
- - - - - -	W27 W/B EXPERIMENT	2.40	4.008	35	LaRC UPWT Test 1649
- - - - - -	W27 W/B EXPERIMENT	2.40	3.974	36	LaRC UPWT Test 1649
- - - - - -	W27 W/B EXPERIMENT	2.40	3.969	37	LaRC UPWT Test 1649
— - □ —	W27 W/B AIRPLANE	2.40	4.000	1	AIRPLANE

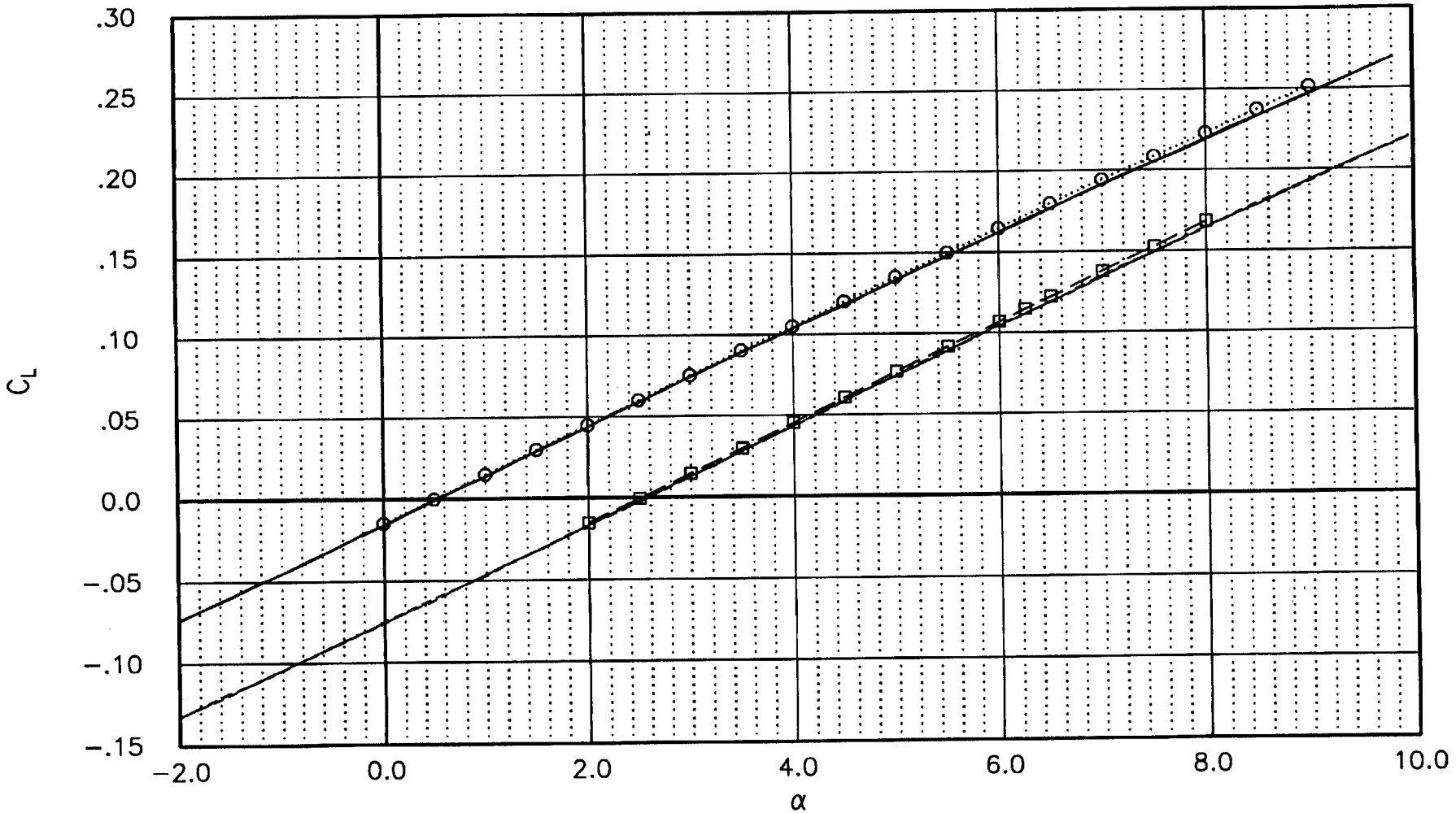

Fig 68. AIRPLANE force and moment coefficients of Ref H W/B (CAi = 0.006634) and Boeing W27 W/B (CAi = 0.00667) compared with wind tunnel data.

SYMBOL	CONFIGURATION	MACH	RN	RUN	Data Type
———	REF H W/B EXPERIMENT	2.40	4.012	14	LaRC UPWT Test 1649
———	REF H W/B EXPERIMENT	2.40	4.005	15	LaRC UPWT Test 1649
———	REF H W/B EXPERIMENT	2.40	3.990	16	LaRC UPWT Test 1649
·····O·····	REF H W/B AIRPLANE	2.40	4.000	1	AIRPLANE
- - - - -	W27 W/B EXPERIMENT	2.40	4.008	35	LaRC UPWT Test 1649
- - - - -	W27 W/B EXPERIMENT	2.40	3.974	36	LaRC UPWT Test 1649
- - - - -	W27 W/B EXPERIMENT	2.40	3.959	37	LaRC UPWT Test 1649
— - □ —	W27 W/B AIRPLANE	2.40	4.000	1	AIRPLANE

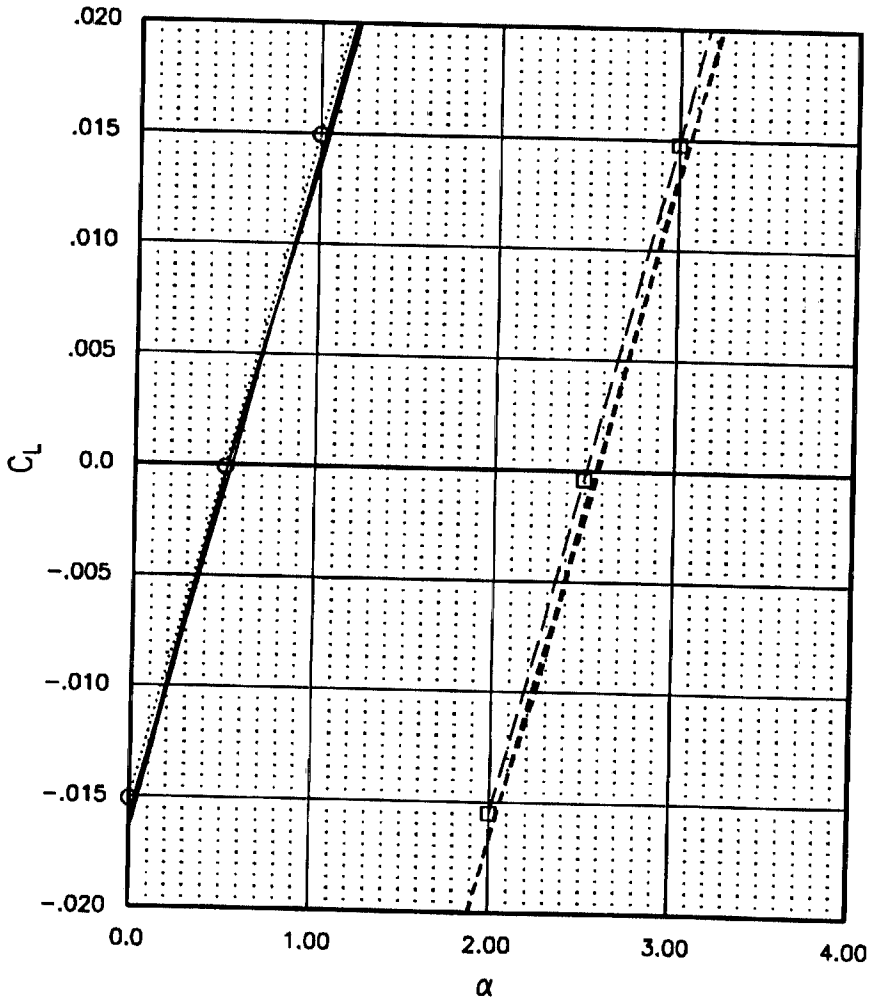

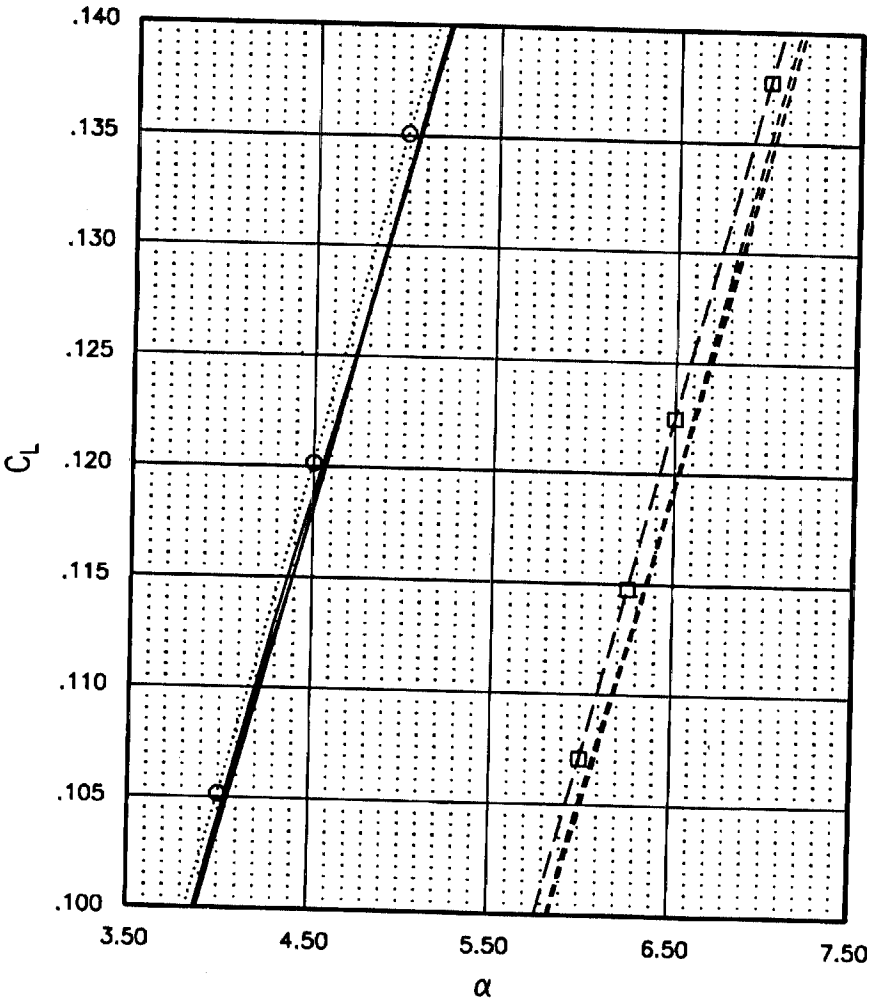

Fig 69. AIRPLANE force and moment coefficients of Ref H W/B (CAi = 0.006634)

SYMBOL	CONFIGURATION	MACH	RN	RUN	Data Type
———	REF H W/B EXPERIMENT	2.40	4.012	14	LaRC UPWT Test 1649
———	REF H W/B EXPERIMENT	2.40	4.005	15	LaRC UPWT Test 1649
———	REF H W/B EXPERIMENT	2.40	3.990	16	LaRC UPWT Test 1649
····· O ·····	REF H W/B AIRPLANE	2.40	4.000	1	AIRPLANE
- - - - - -	W27 W/B EXPERIMENT	2.40	4.008	35	LaRC UPWT Test 1649
- - - - - -	W27 W/B EXPERIMENT	2.40	3.974	36	LaRC UPWT Test 1649
- - - - - -	W27 W/B EXPERIMENT	2.40	3.969	37	LaRC UPWT Test 1649
— - □ —	W27 W/B AIRPLANE	2.40	4.000	1	AIRPLANE

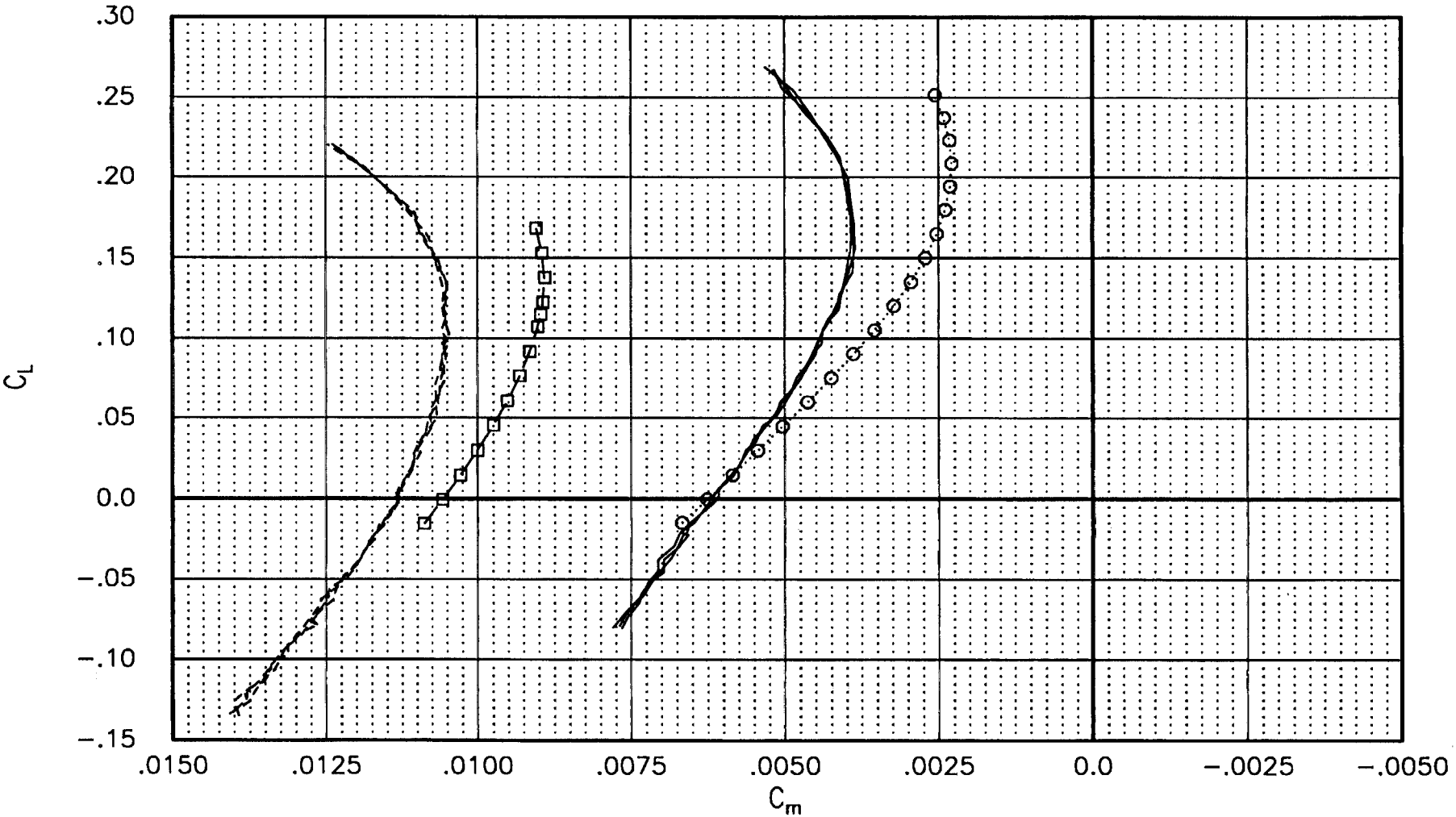

Fig 70. AIRPLANE force and moment coefficients of Ref H W/B (CAi = 0.006634) and Boeing W27 W/B (CAi = 0.00667) compared with wind tunnel data.

SYMBOL	CONFIGURATION	MACH	RN	RUN	Data Type
———	REF H W/B EXPERIMENT	2.40	4.012	14	LaRC UPWT Test 1649
———	REF H W/B EXPERIMENT	2.40	4.005	15	LaRC UPWT Test 1649
———	REF H W/B EXPERIMENT	2.40	3.990	16	LaRC UPWT Test 1649
····· O ·····	REF H W/B AIRPLANE	2.40	4.000	1	AIRPLANE
- - - - - -	W27 W/B EXPERIMENT	2.40	4.008	35	LaRC UPWT Test 1649
- - - - - -	W27 W/B EXPERIMENT	2.40	3.974	36	LaRC UPWT Test 1649
- - - - - -	W27 W/B EXPERIMENT	2.40	3.969	37	LaRC UPWT Test 1649
— - □ —	W27 W/B AIRPLANE	2.40	4.000	1	AIRPLANE

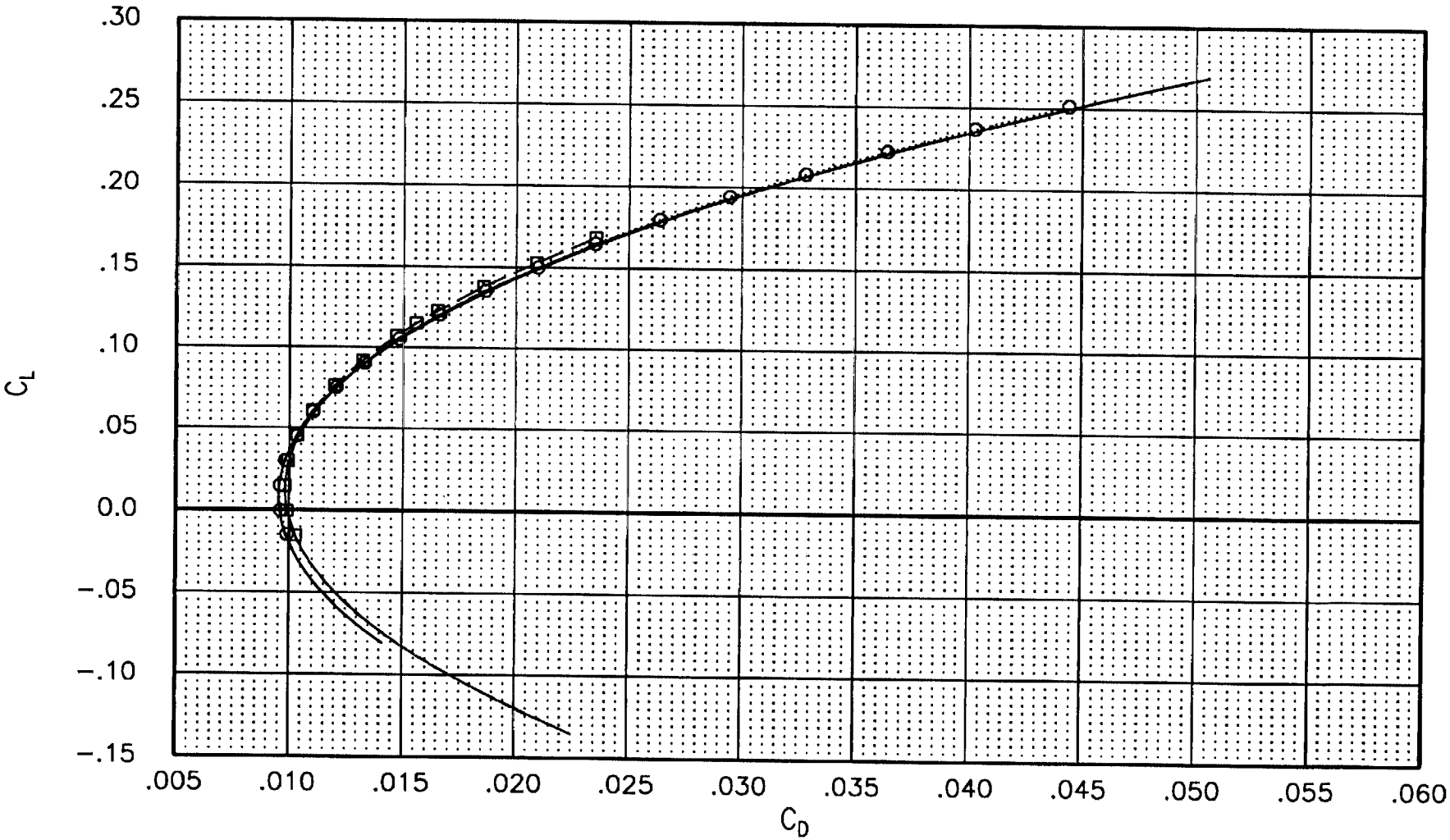

Fig 71. AIRPLANE force and moment coefficients of Ref H W/B (CAi = 0.006634)

SYMBOL	CONFIGURATION	MACH	RN	RUN	Data Type
———	REF H W/B EXPERIMENT	2.40	4.012	14	LaRC UPWT Test 1649
———	REF H W/B EXPERIMENT	2.40	4.005	15	LaRC UPWT Test 1649
———	REF H W/B EXPERIMENT	2.40	3.990	16	LaRC UPWT Test 1649
····· O ·····	REF H W/B AIRPLANE	2.40	4.000	1	AIRPLANE
- - - - - -	W27 W/B EXPERIMENT	2.40	4.008	35	LaRC UPWT Test 1649
- - - - - -	W27 W/B EXPERIMENT	2.40	3.974	36	LaRC UPWT Test 1649
- - - - - -	W27 W/B EXPERIMENT	2.40	3.969	37	LaRC UPWT Test 1649
— - □ —	W27 W/B AIRPLANE	2.40	4.000	1	AIRPLANE

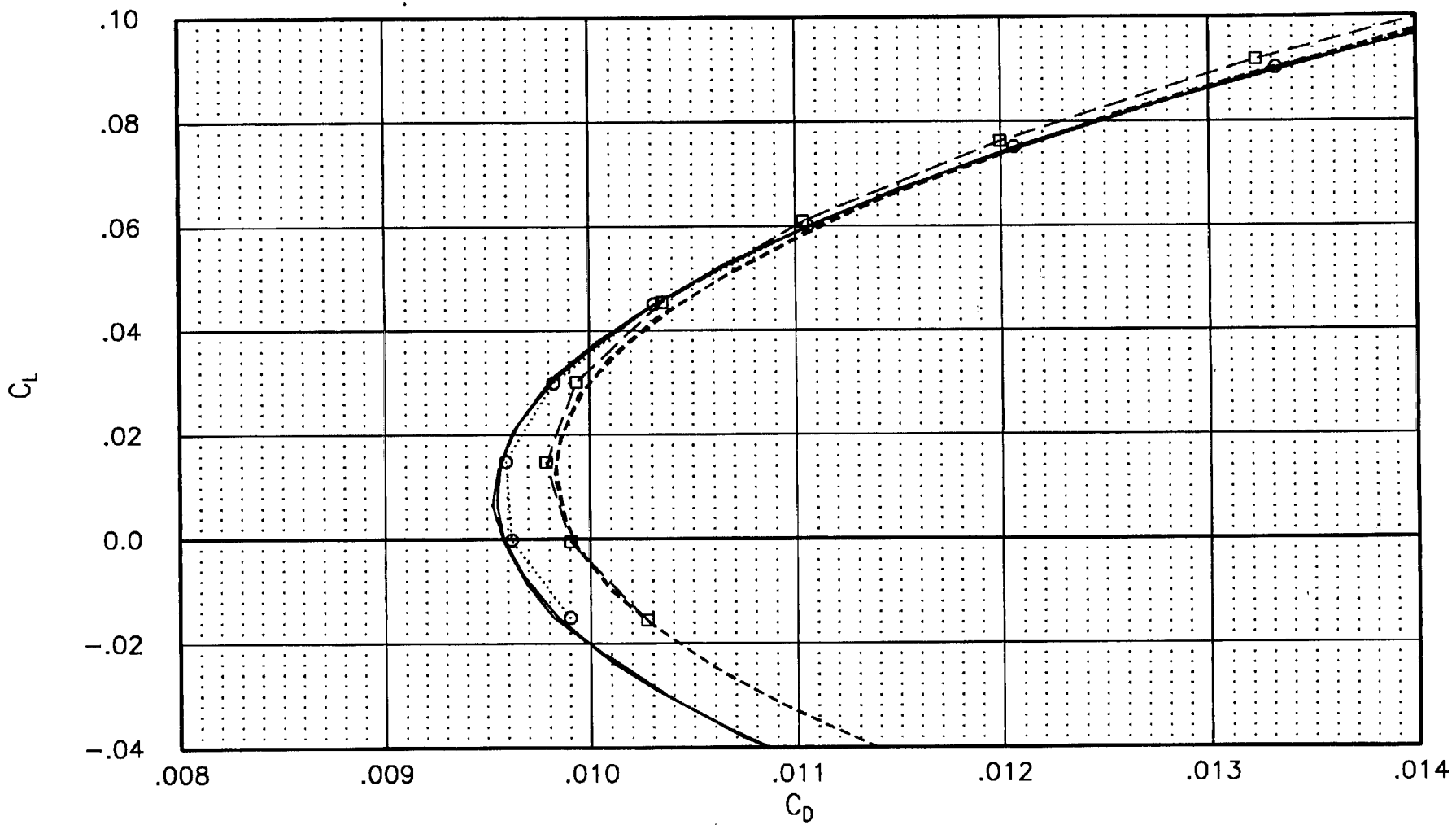

Fig 72. AIRPLANE force and moment coefficients of Ref H W/B (CAi = 0.006634) and Boeing W27 W/B (CAi = 0.00667) compared with wind tunnel data.

SYMBOL	CONFIGURATION	MACH	RN	RUN	Data Type
———	REF H W/B EXPERIMENT	2.40	4.012	14	LaRC UPWT Test 1649
———	REF H W/B EXPERIMENT	2.40	4.005	15	LaRC UPWT Test 1649
———	REF H W/B EXPERIMENT	2.40	3.990	16	LaRC UPWT Test 1649
·····O·····	REF H W/B AIRPLANE	2.40	4.000	1	AIRPLANE
- - - - -	W27 W/B EXPERIMENT	2.40	4.008	35	LaRC UPWT Test 1649
- - - - -	W27 W/B EXPERIMENT	2.40	3.974	36	LaRC UPWT Test 1649
- - - - -	W27 W/B EXPERIMENT	2.40	3.969	37	LaRC UPWT Test 1649
— - □ —	W27 W/B AIRPLANE	2.40	4.000	1	AIRPLANE

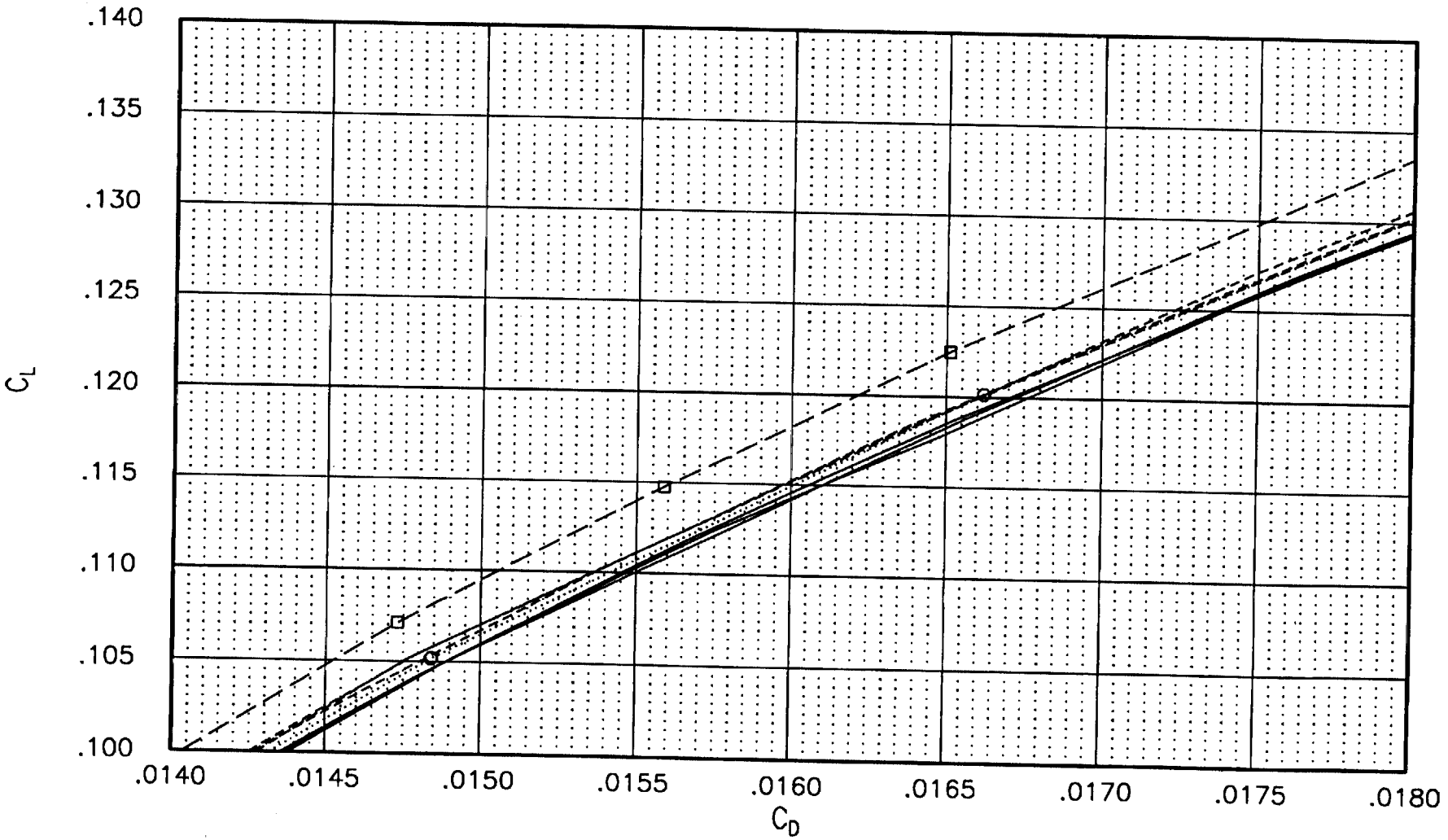

Fig 73. AIRPLANE force and moment coefficients of Ref H W/B (CAi = 0.006634)

SYMBOL	CONFIGURATION	MACH	RN	RUN	Data Type
———	REF H W/B/N/D EXPERIMENT	2.40	3.989	11	LaRC UPWT Test 1649
———	REF H W/B/N/D EXPERIMENT	2.40	3.986	12	LaRC UPWT Test 1649
———	REF H W/B/N/D EXPERIMENT	2.40	3.989	13	LaRC UPWT Test 1649
····O····	REF H W/B/N/D AIRPLANE	2.40	4.004	1	AIRPLANE
- - - - - -	704 W/B/N/D EXPERIMENT	2.40	3.997	26	LaRC UPWT Test 1649
- - - - - -	704 W/B/N/D EXPERIMENT	2.40	3.971	27	LaRC UPWT Test 1649
- - - - - -	704 W/B/N/D EXPERIMENT	2.40	3.957	28	LaRC UPWT Test 1649
— - □ —	704 W/B/N/D AIRPLANE	2.40	4.000	1	AIRPLANE

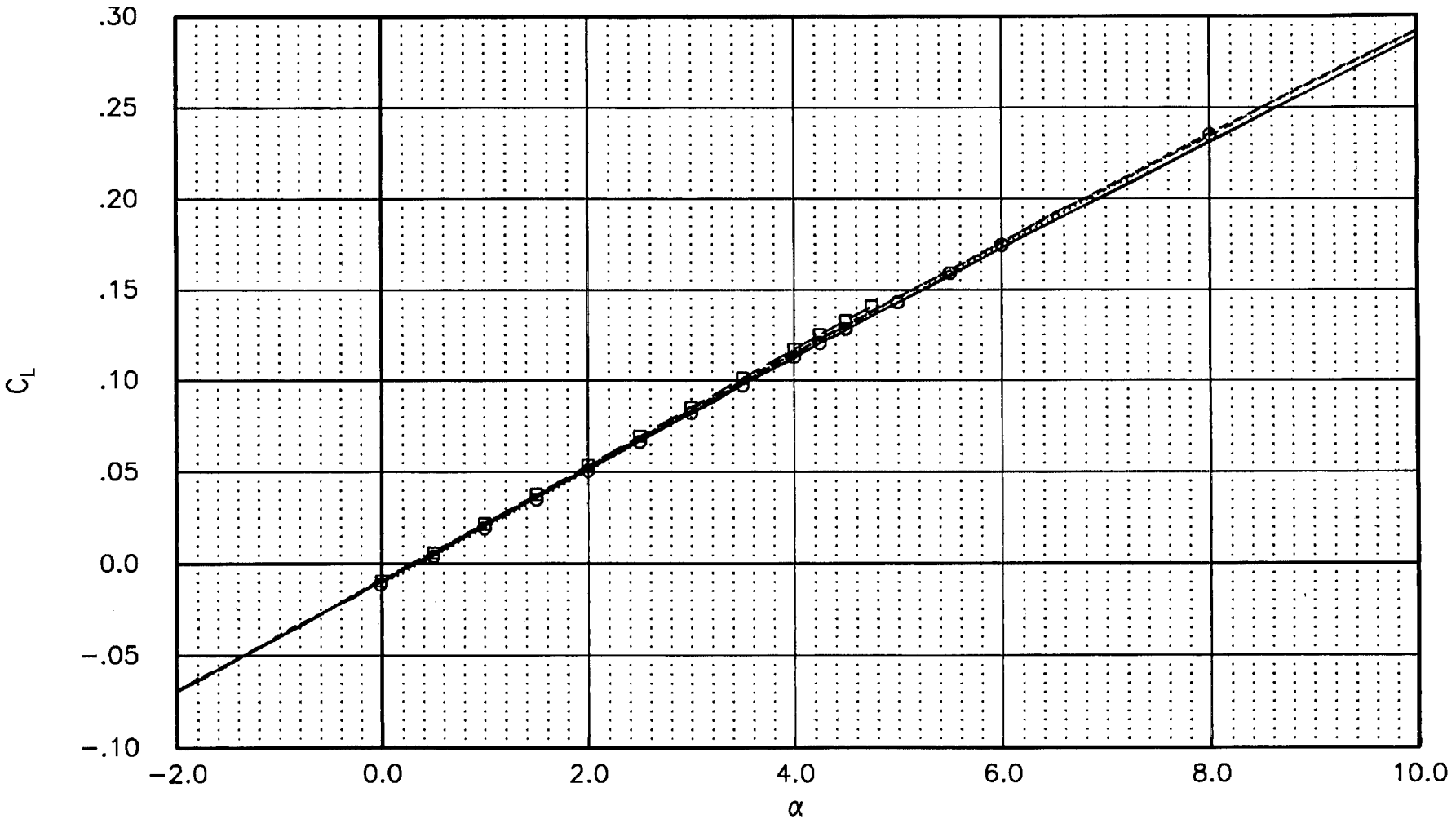

Fig 74. AIRPLANE force and moment coefficients of Ref H W/B/N (CAi = 0.007516) and Ames 7-04 (CAi = 0.0075) compared with wind tunnel data.

SYMBOL	CONFIGURATION	MACH	RN	RUN	Data Type
———	REF H W/B/N/D EXPERIMENT	2.40	3.989	11	LaRC UPWT Test 1649
———	REF H W/B/N/D EXPERIMENT	2.40	3.986	12	LaRC UPWT Test 1649
———	REF H W/B/N/D EXPERIMENT	2.40	3.989	13	LaRC UPWT Test 1649
····O····	REF H W/B/N/D AIRPLANE	2.40	4.004	1	AIRPLANE
- - - - -	704 W/B/N/D EXPERIMENT	2.40	3.997	26	LaRC UPWT Test 1649
- - - - -	704 W/B/N/D EXPERIMENT	2.40	3.971	27	LaRC UPWT Test 1649
- - - - -	704 W/B/N/D EXPERIMENT	2.40	3.957	28	LaRC UPWT Test 1649
—-□—	704 W/B/N/D AIRPLANE	2.40	4.000	1	AIRPLANE

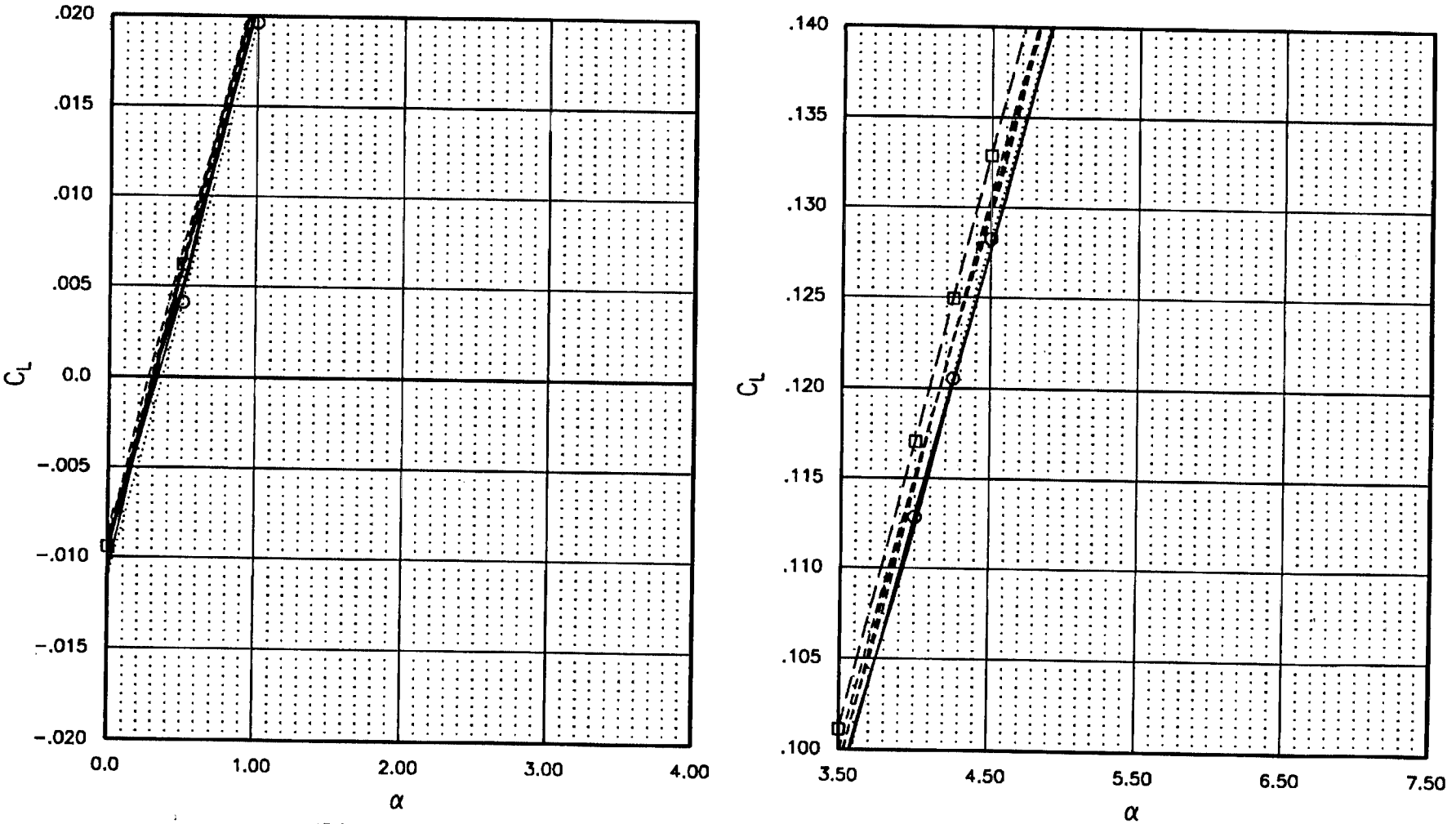

Fig 75. AIRPLANE force and moment coefficients of Ref H W/B/N (CAi = 0.007516) and Ames 7-04 (CAi = 0.0075) compared with wind tunnel data

SYMBOL	CONFIGURATION	MACH	RN	RUN	Data Type
———	REF H W/B/N/D EXPERIMENT	2.40	3.989	11	LaRC UPWT Test 1649
———	REF H W/B/N/D EXPERIMENT	2.40	3.986	12	LaRC UPWT Test 1649
———	REF H W/B/N/D EXPERIMENT	2.40	3.989	13	LaRC UPWT Test 1649
····· O ·····	REF H W/B/N/D AIRPLANE	2.40	4.004	1	AIRPLANE
- - - - - -	704 W/B/N/D EXPERIMENT	2.40	3.997	26	LaRC UPWT Test 1649
- - - - - -	704 W/B/N/D EXPERIMENT	2.40	3.971	27	LaRC UPWT Test 1649
- - - - - -	704 W/B/N/D EXPERIMENT	2.40	3.957	28	LaRC UPWT Test 1649
— - □ —	704 W/B/N/D AIRPLANE	2.40	4.000	1	AIRPLANE

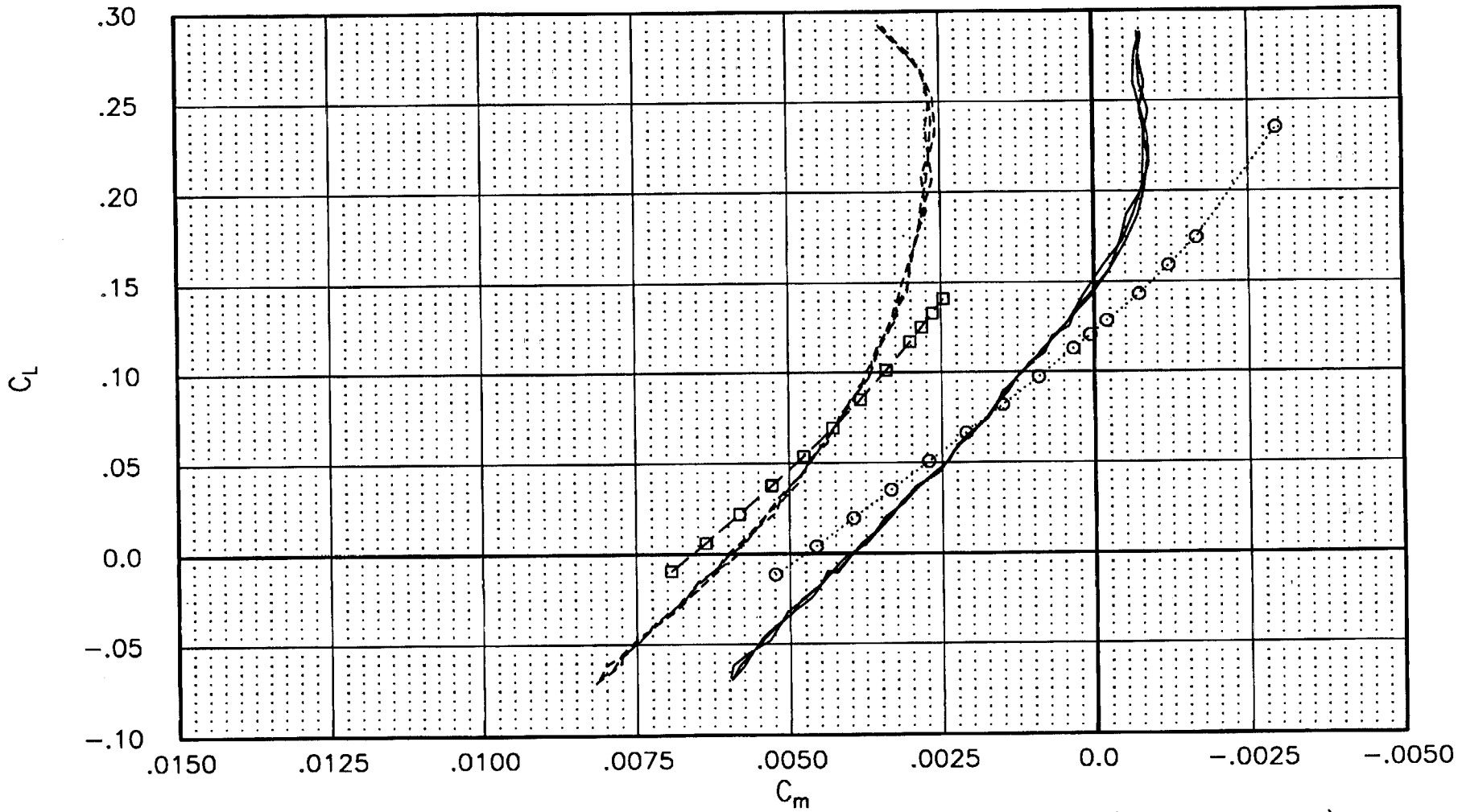

Fig 76. AIRPLANE force and moment coefficients of Ref H W/B/N (CAi = 0.007516) and Ames 7-04 (CAi = 0.0075) compared with wind tunnel data.

SYMBOL	CONFIGURATION	MACH	RN	RUN	Data Type
———	REF H W/B/N/D EXPERIMENT	2.40	3.989	11	LaRC UPWT Test 1649
———	REF H W/B/N/D EXPERIMENT	2.40	3.986	12	LaRC UPWT Test 1649
———	REF H W/B/N/D EXPERIMENT	2.40	3.989	13	LaRC UPWT Test 1649
····O····	REF H W/B/N/D AIRPLANE	2.40	4.004	1	AIRPLANE
- - - - -	704 W/B/N/D EXPERIMENT	2.40	3.997	26	LaRC UPWT Test 1649
- - - - -	704 W/B/N/D EXPERIMENT	2.40	3.971	27	LaRC UPWT Test 1649
- - - - -	704 W/B/N/D EXPERIMENT	2.40	3.957	28	LaRC UPWT Test 1649
—-□—	704 W/B/N/D AIRPLANE	2.40	4.000	1	AIRPLANE

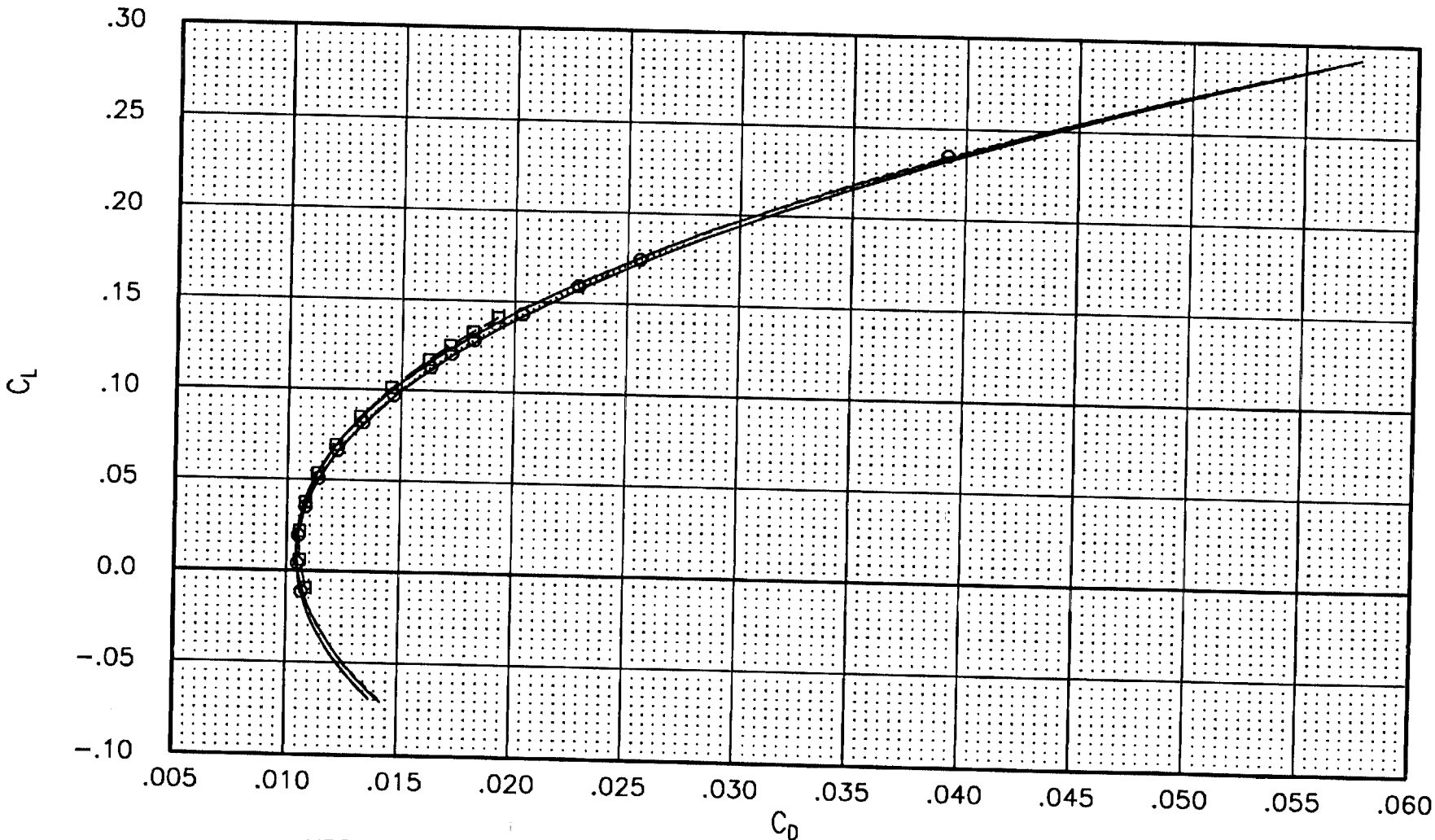

Fig 77. AIRPLANE force and moment coefficients of Ref H W/B/N (CAi = 0.007516)

SYMBOL	CONFIGURATION	MACH	RN	RUN	Data Type
———	REF H W/B/N/D EXPERIMENT	2.40	3.989	11	LaRC UPWT Test 1649
———	REF H W/B/N/D EXPERIMENT	2.40	3.986	12	LaRC UPWT Test 1649
———	REF H W/B/N/D EXPERIMENT	2.40	3.989	13	LaRC UPWT Test 1649
····O····	REF H W/B/N/D AIRPLANE	2.40	4.004	1	AIRPLANE
- - - - -	704 W/B/N/D EXPERIMENT	2.40	3.997	26	LaRC UPWT Test 1649
- - - - -	704 W/B/N/D EXPERIMENT	2.40	3.971	27	LaRC UPWT Test 1649
- - - - -	704 W/B/N/D EXPERIMENT	2.40	3.957	28	LaRC UPWT Test 1649
— -□—	704 W/B/N/D AIRPLANE	2.40	4.000	1	AIRPLANE

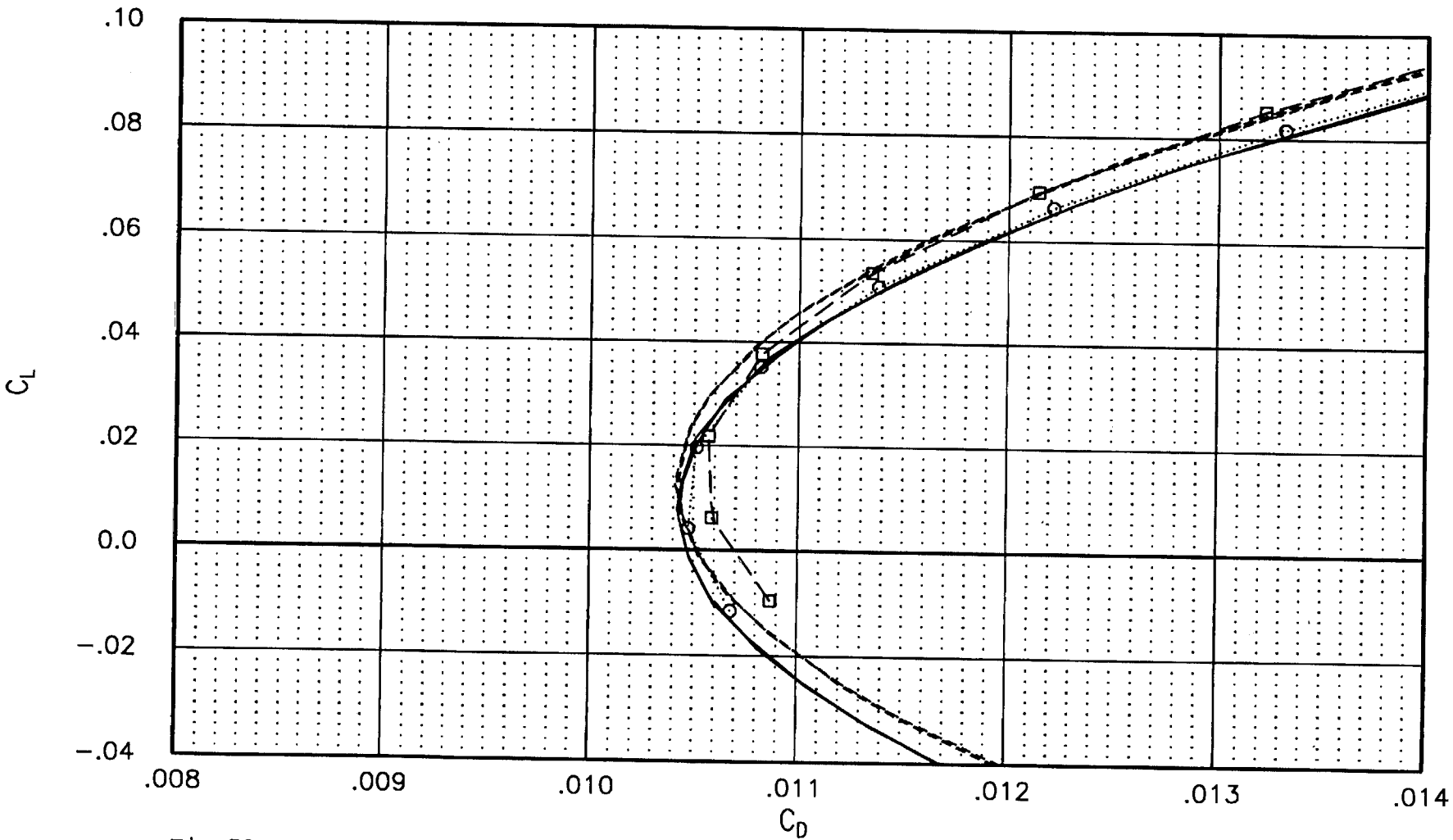

Fig 78. AIRPLANE force and moment coefficients of Ref H W/B/N (CAi = 0.007516) and Ames 7-04 (CAi = 0.0075) compared with wind tunnel data.

SYMBOL	CONFIGURATION	MACH	RN	RUN	Data Type
———	REF H W/B/N/D EXPERIMENT	2.40	3.989	11	LaRC UPWT Test 1649
———	REF H W/B/N/D EXPERIMENT	2.40	3.986	12	LaRC UPWT Test 1649
———	REF H W/B/N/D EXPERIMENT	2.40	3.989	13	LaRC UPWT Test 1649
····· O ·····	REF H W/B/N/D AIRPLANE	2.40	4.004	1	AIRPLANE
- - - - - -	704 W/B/N/D EXPERIMENT	2.40	3.997	26	LaRC UPWT Test 1649
- - - - - -	704 W/B/N/D EXPERIMENT	2.40	3.971	27	LaRC UPWT Test 1649
- - - - - -	704 W/B/N/D EXPERIMENT	2.40	3.957	28	LaRC UPWT Test 1649
— - □ —	704 W/B/N/D AIRPLANE	2.40	4.000	1	AIRPLANE

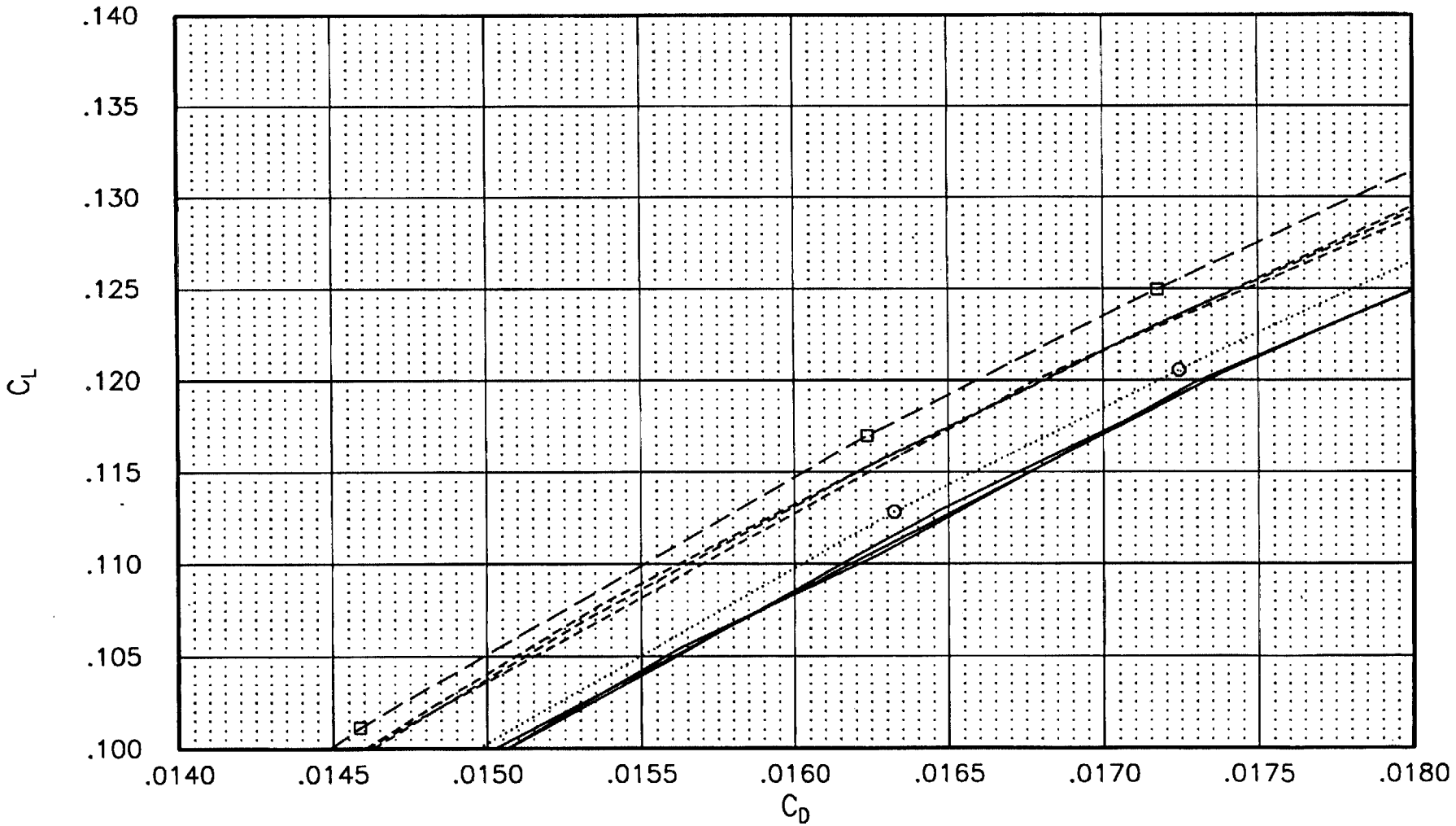

Fig 79. AIRPLANE force and moment coefficients of Ref H W/B/N (CAi = 0.007516)

SYMBOL	CONFIGURATION	MACH	RN	RUN	Data Type
———	REF H W/B/N/D EXPERIMENT	2.40	3.989	11	LaRC UPWT Test 1649
———	REF H W/B/N/D EXPERIMENT	2.40	3.986	12	LaRC UPWT Test 1649
———	REF H W/B/N/D EXPERIMENT	2.40	3.989	13	LaRC UPWT Test 1649
····· O ·····	REF H W/B/N/D AIRPLANE	2.40	4.004	1	AIRPLANE
- - - - - -	W27 W/B/N/D EXPERIMENT	2.40	3.998	40	LaRC UPWT Test 1649
- - - - - -	W27 W/B/N/D EXPERIMENT	2.40	4.000	41	LaRC UPWT Test 1649
- - - - - -	W27 W/B/N/D EXPERIMENT	2.40	3.971	42	LaRC UPWT Test 1649
— - □ —	W27 W/B/N/D AIRPLANE	2.40	4.000	1	AIRPLANE

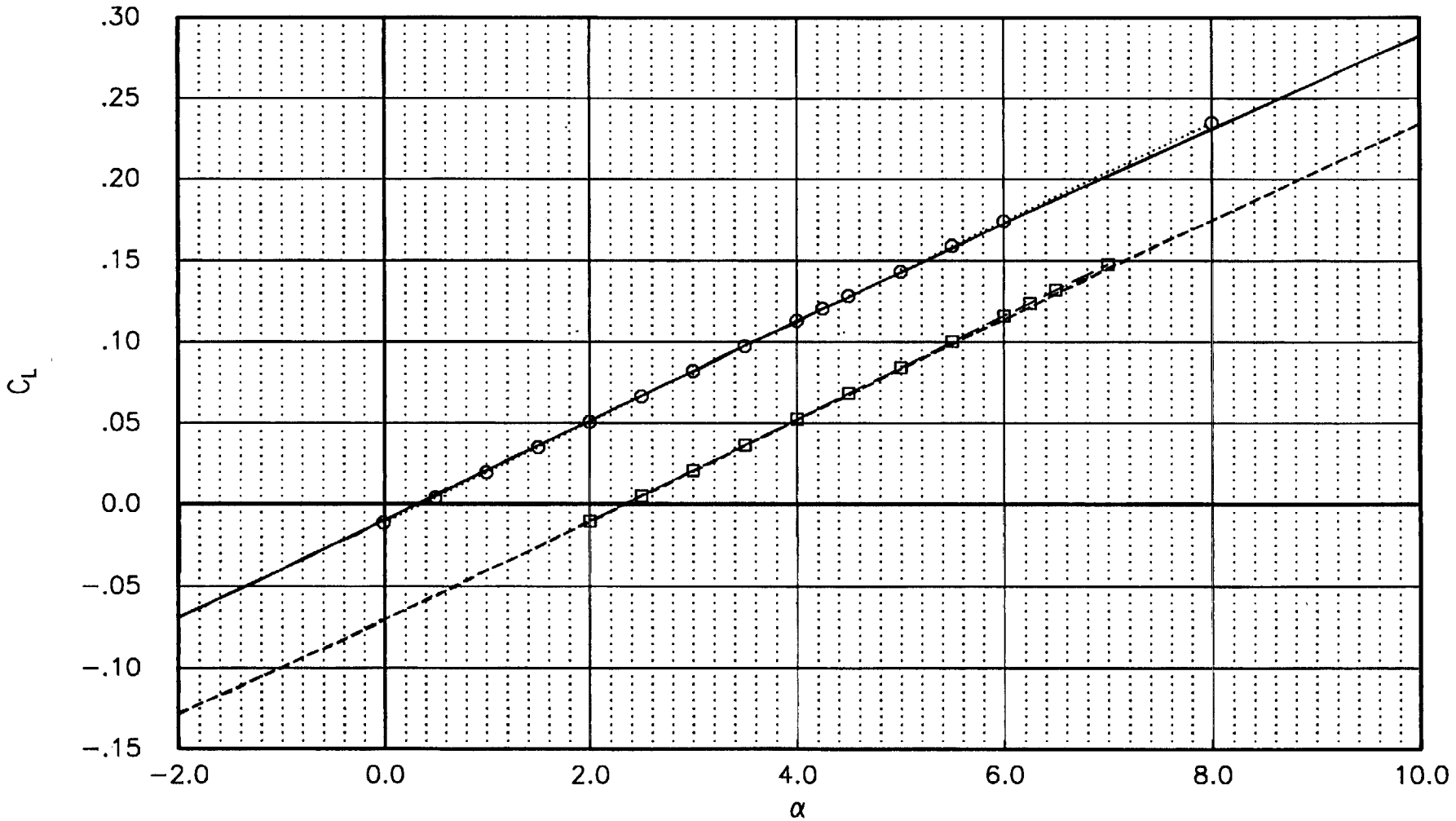

Fig 80. AIRPLANE force and moment coefficients of Ref H W/B/N (CAi = 0.007516) and Boeing W27 (CAi = 0.007554) compared with wind tunnel data.

SYMBOL	CONFIGURATION	MACH	RN	RUN	Data Type
———	REF H W/B/N/D EXPERIMENT	2.40	3.989	11	LaRC UPWT Test 1649
———	REF H W/B/N/D EXPERIMENT	2.40	3.986	12	LaRC UPWT Test 1649
———	REF H W/B/N/D EXPERIMENT	2.40	3.989	13	LaRC UPWT Test 1649
····O····	REF H W/B/N/D AIRPLANE	2.40	4.004	1	AIRPLANE
- - - - -	W27 W/B/N/D EXPERIMENT	2.40	3.998	40	LaRC UPWT Test 1649
- - - - -	W27 W/B/N/D EXPERIMENT	2.40	4.000	41	LaRC UPWT Test 1649
- - - - -	W27 W/B/N/D EXPERIMENT	2.40	3.971	42	LaRC UPWT Test 1649
— - □ —	W27 W/B/N/D AIRPLANE	2.40	4.000	1	AIRPLANE

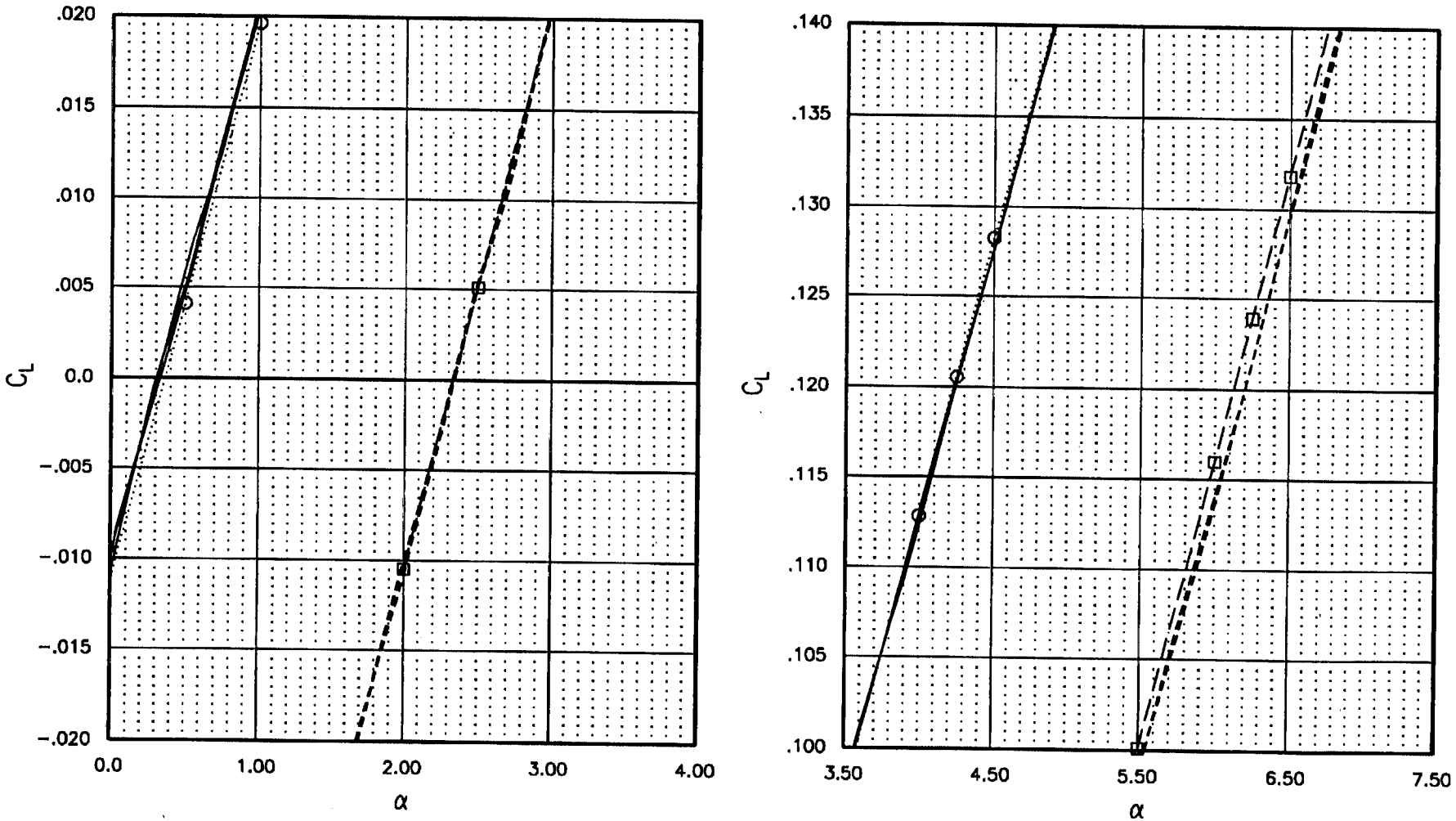

Fig 81. AIRPLANE force and moment coefficients of Ref H W/B/N (CAi = 0.007516) and Basic W27 (CAi = 0.007554) compared with wind tunnel data

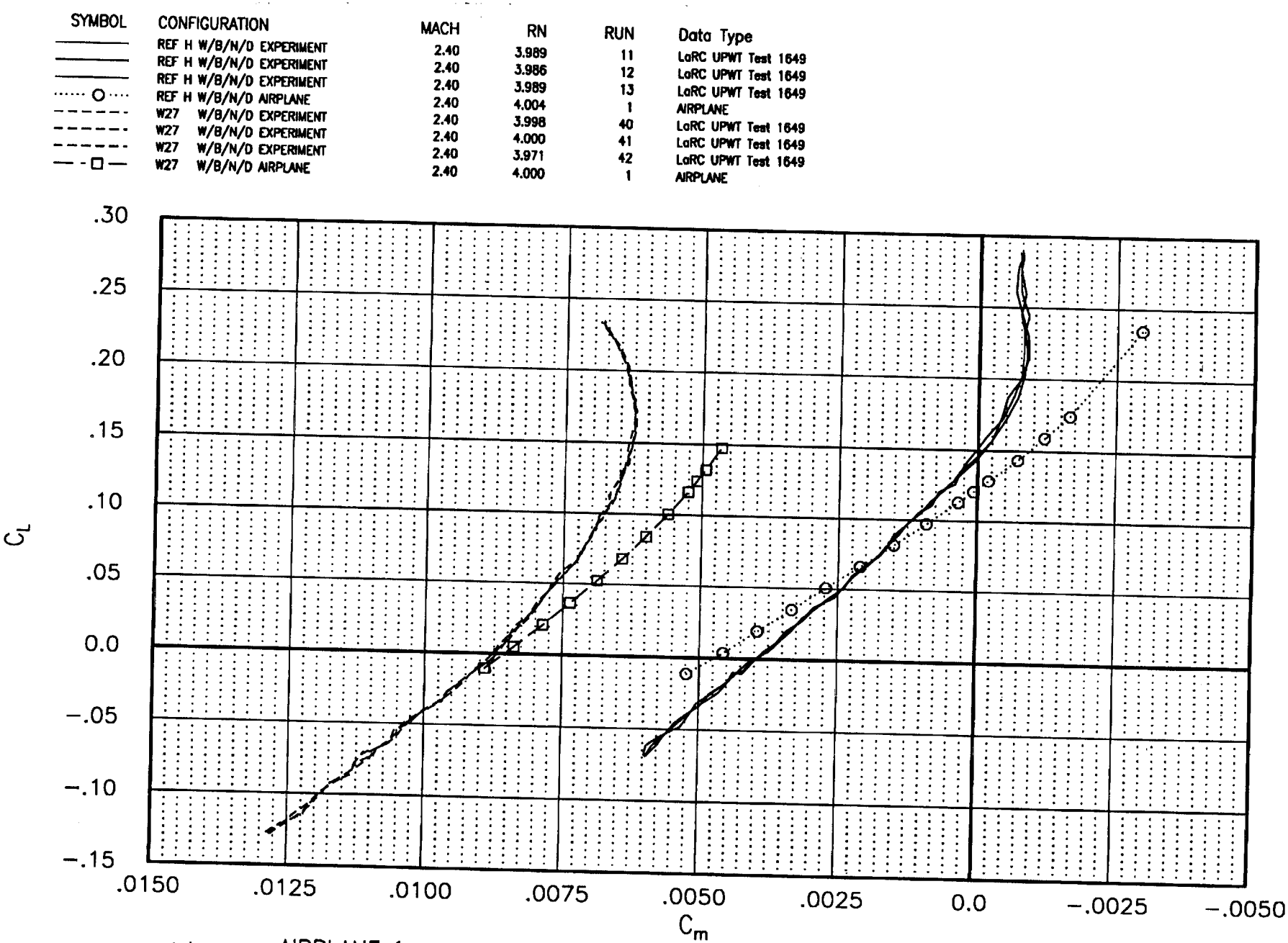

Fig 82. AIRPLANE force and moment coefficients of Ref H W/B/N (CAi = 0.007516) and Boeing W27 (CAi = 0.007554) compared with wind tunnel data.

SYMBOL	CONFIGURATION	MACH	RN	RUN	Data Type
———	REF H W/B/N/D EXPERIMENT	2.40	3.989	11	LaRC UPWT Test 1649
———	REF H W/B/N/D EXPERIMENT	2.40	3.986	12	LaRC UPWT Test 1649
———	REF H W/B/N/D EXPERIMENT	2.40	3.989	13	LaRC UPWT Test 1649
····· O ····	REF H W/B/N/D AIRPLANE	2.40	4.004	1	AIRPLANE
- - - - - -	W27 W/B/N/D EXPERIMENT	2.40	3.998	40	LaRC UPWT Test 1649
- - - - - -	W27 W/B/N/D EXPERIMENT	2.40	4.000	41	LaRC UPWT Test 1649
- - - - - -	W27 W/B/N/D EXPERIMENT	2.40	3.971	42	LaRC UPWT Test 1649
— - □ —	W27 W/B/N/D AIRPLANE	2.40	4.000	1	AIRPLANE

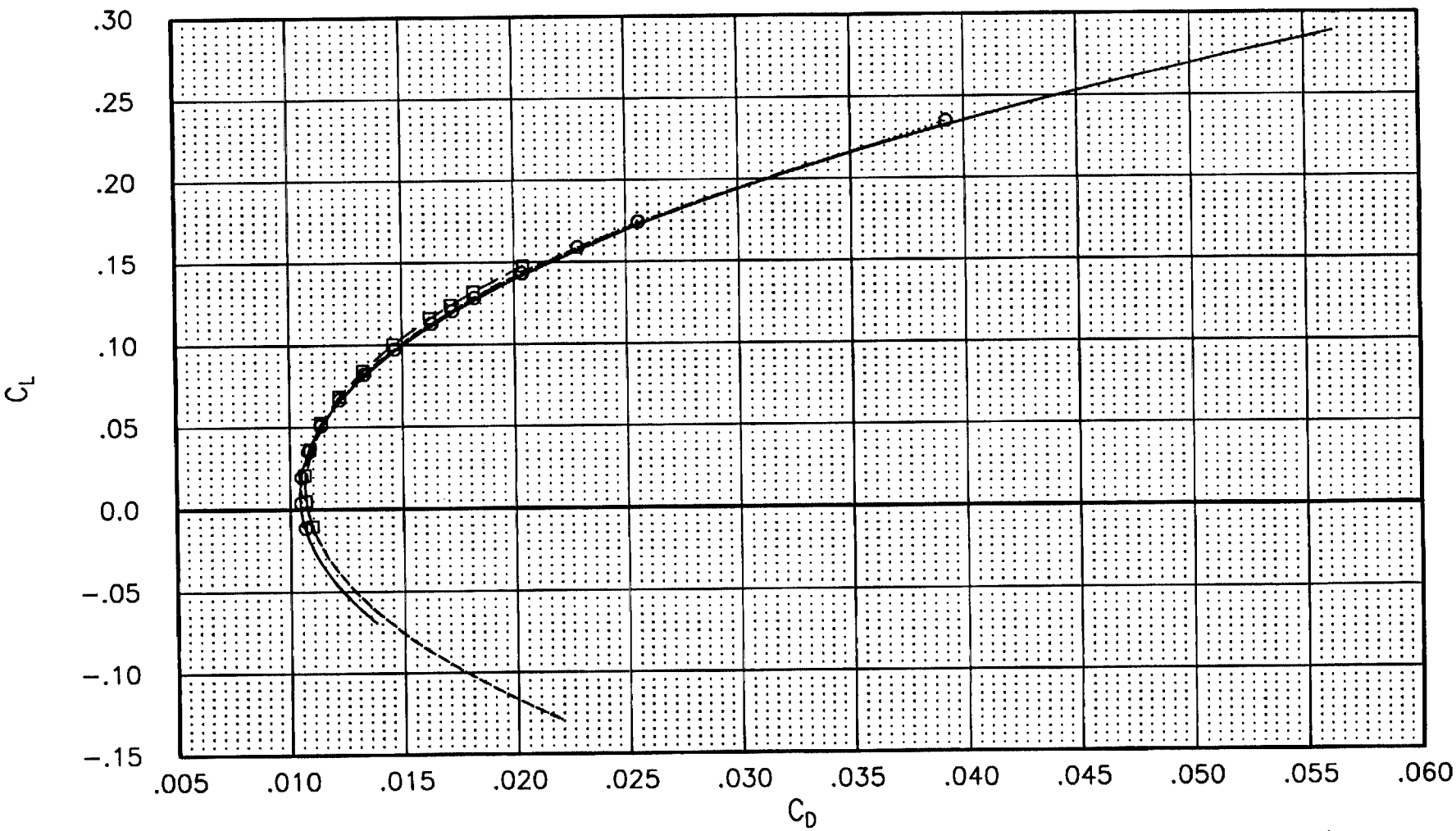

Fig 83. AIRPLANE force and moment coefficients of Ref H W/B/N (CAi = 0.007516)

SYMBOL	CONFIGURATION	MACH	RN	RUN	Data Type
———	REF H W/B/N/D EXPERIMENT	2.40	3.989	11	LaRC UPWT Test 1649
———	REF H W/B/N/D EXPERIMENT	2.40	3.986	12	LaRC UPWT Test 1649
———	REF H W/B/N/D EXPERIMENT	2.40	3.989	13	LaRC UPWT Test 1649
····· O ·····	REF H W/B/N/D AIRPLANE	2.40	4.004	1	AIRPLANE
- - - - - -	W27 W/B/N/D EXPERIMENT	2.40	3.998	40	LaRC UPWT Test 1649
- - - - - -	W27 W/B/N/D EXPERIMENT	2.40	4.000	41	LaRC UPWT Test 1649
- - - - - -	W27 W/B/N/D EXPERIMENT	2.40	3.971	42	LaRC UPWT Test 1649
— - □ —	W27 W/B/N/D AIRPLANE	2.40	4.000	1	AIRPLANE

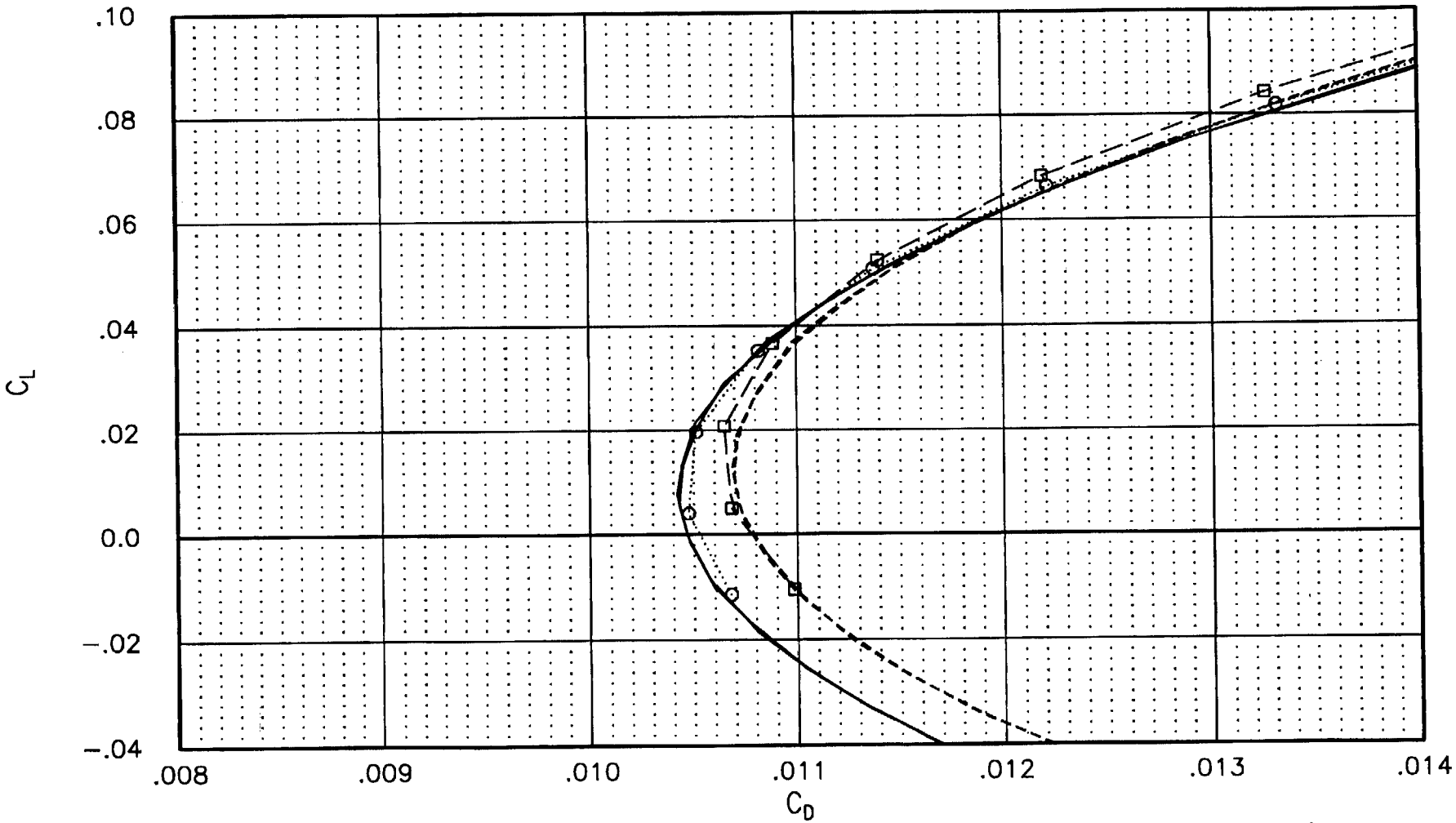

Fig 84. AIRPLANE force and moment coefficients of Ref H W/B/N (CAi = 0.007516) and Boeing W27 (CAi = 0.007554) compared with wind tunnel data.

SYMBOL	CONFIGURATION	MACH	RN	RUN	Data Type
———	REF H W/B/N/D EXPERIMENT	2.40	3.989	11	LaRC UPWT Test 1649
———	REF H W/B/N/D EXPERIMENT	2.40	3.986	12	LaRC UPWT Test 1649
———	REF H W/B/N/D EXPERIMENT	2.40	3.989	13	LaRC UPWT Test 1649
·····O·····	REF H W/B/N/D AIRPLANE	2.40	4.004	1	AIRPLANE
- - - - - -	W27 W/B/N/D EXPERIMENT	2.40	3.998	40	LaRC UPWT Test 1649
- - - - - -	W27 W/B/N/D EXPERIMENT	2.40	4.000	41	LaRC UPWT Test 1649
- - - - - -	W27 W/B/N/D EXPERIMENT	2.40	3.971	42	LaRC UPWT Test 1649
— - □ —	W27 W/B/N/D AIRPLANE	2.40	4.000	1	AIRPLANE

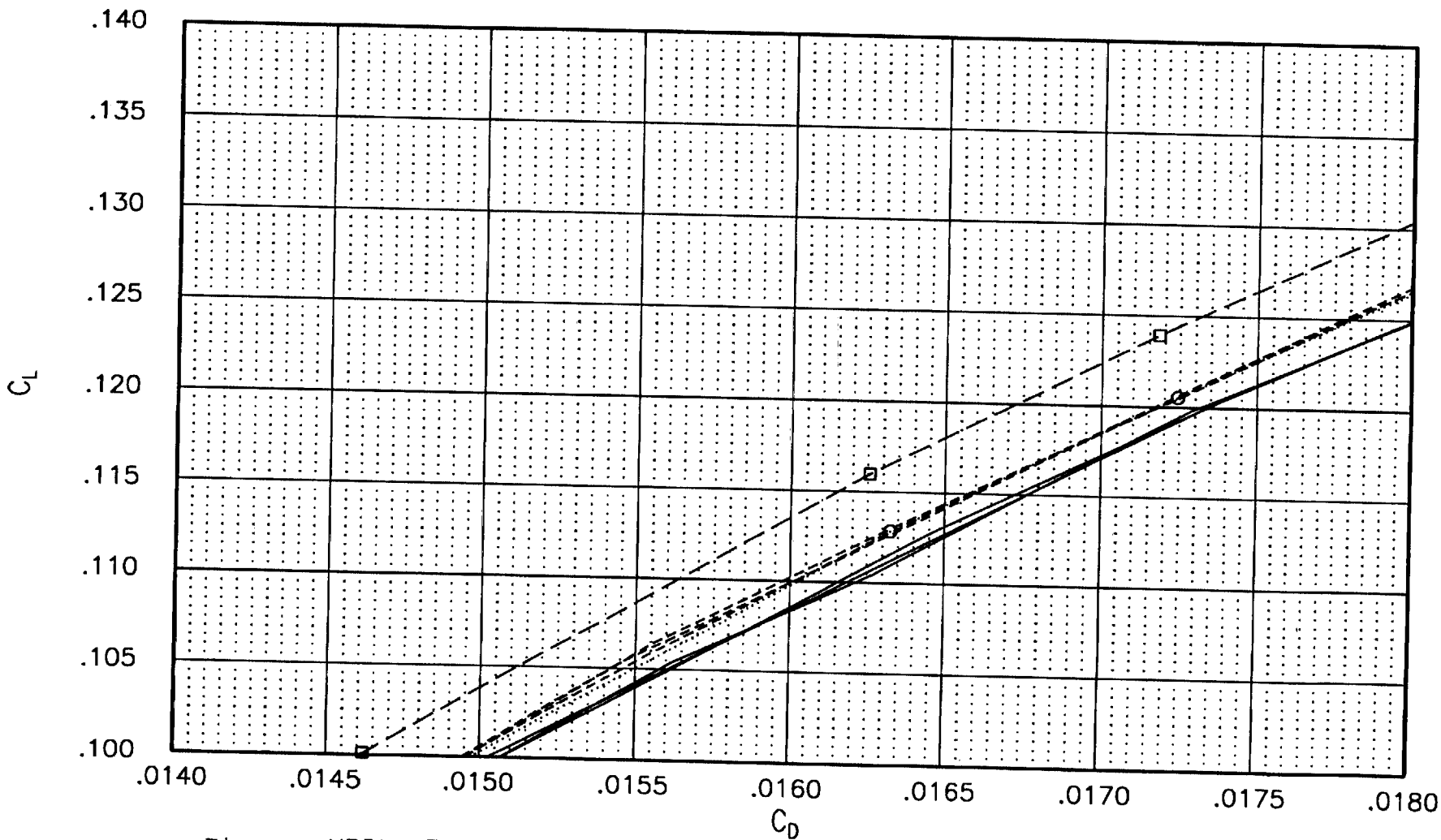

Fig 85. AIRPLANE force and moment coefficients of Ref H W/B/N (CAi = 0.007516)

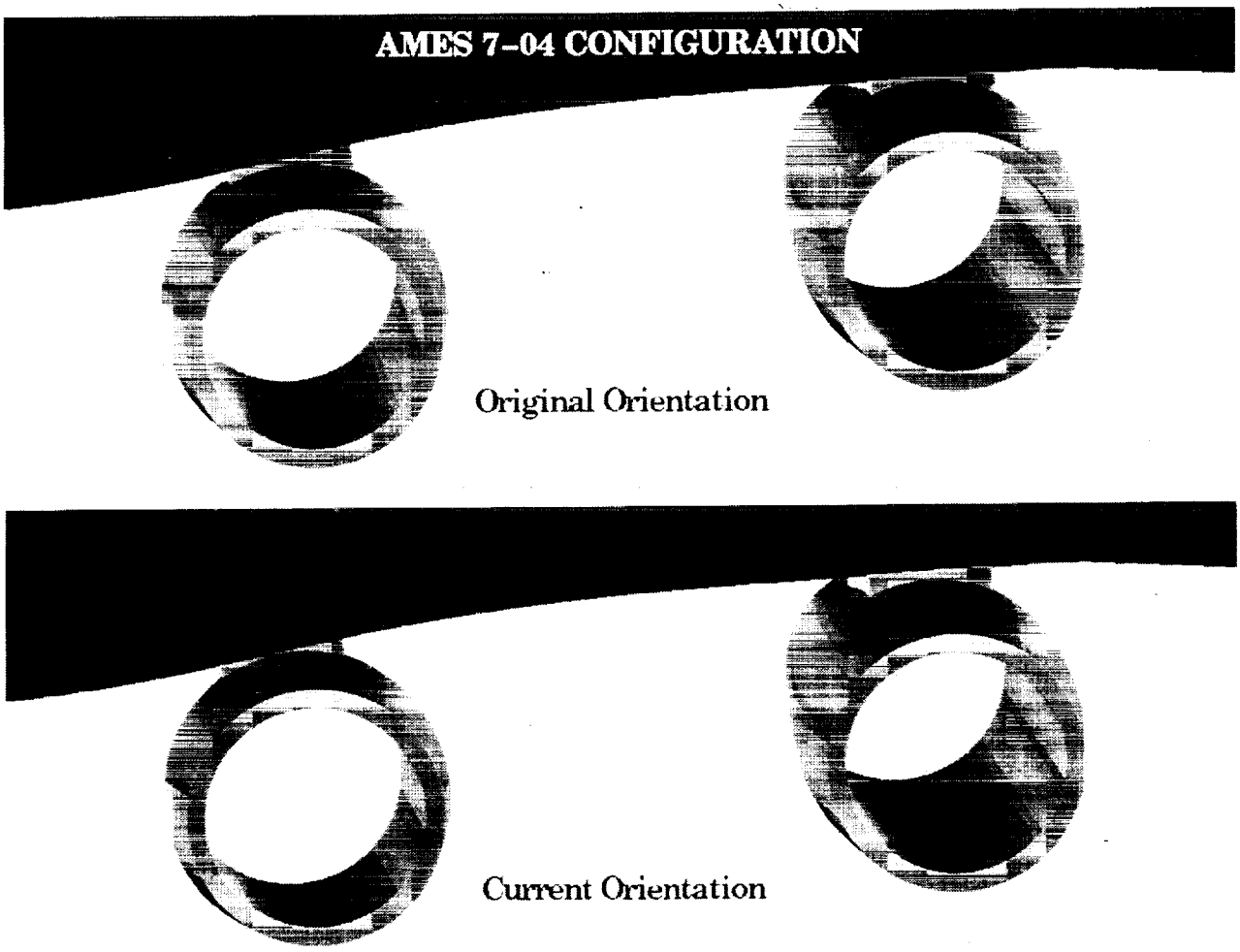

Fig 86. AIRPLANE surface grid for the Ames 704 configuration with the nacelles/diverters in the original and modified orientations.

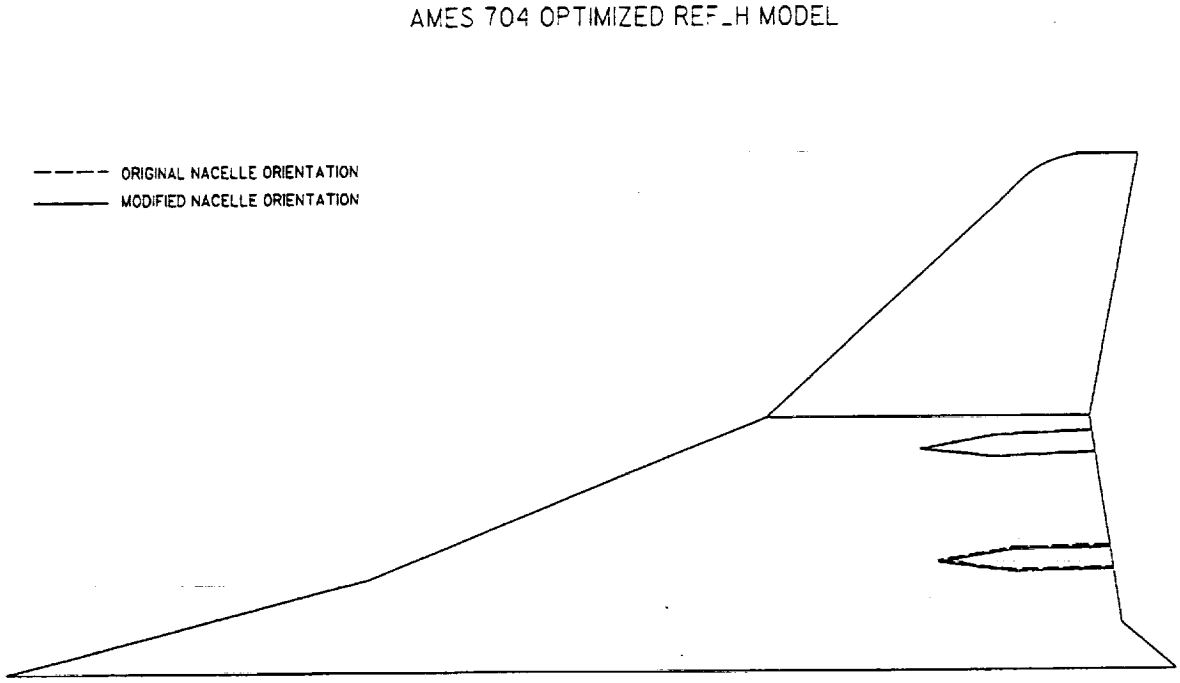

Fig 87. Diverter/wing intersections for the Ames 704 configuration in planform view for the nacelle/diverters in the original and modified orientations.

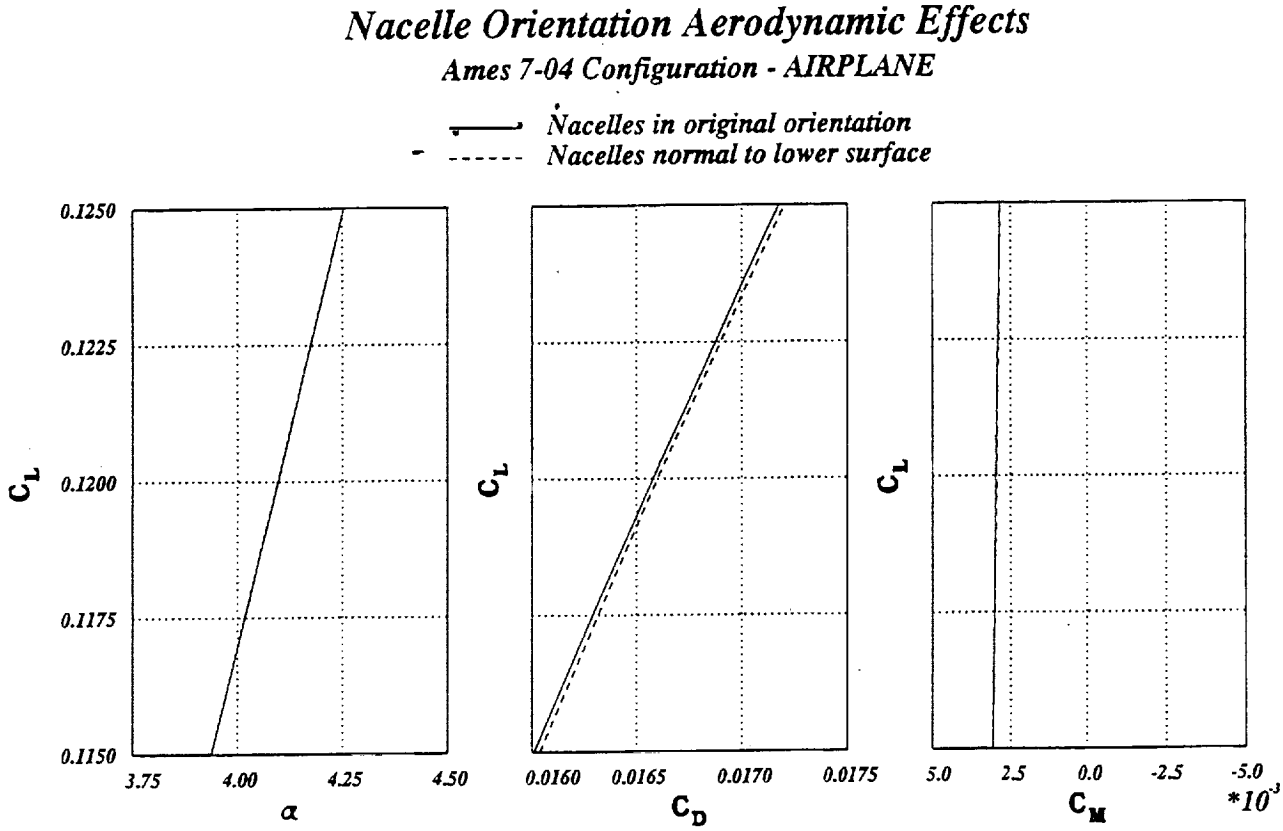

M = 2.40

Fig 88. AIRPLANE aerodynamic characteristics for the Ames 704 with the nacelles/diverters in the original and modified orientations, M=2.4.

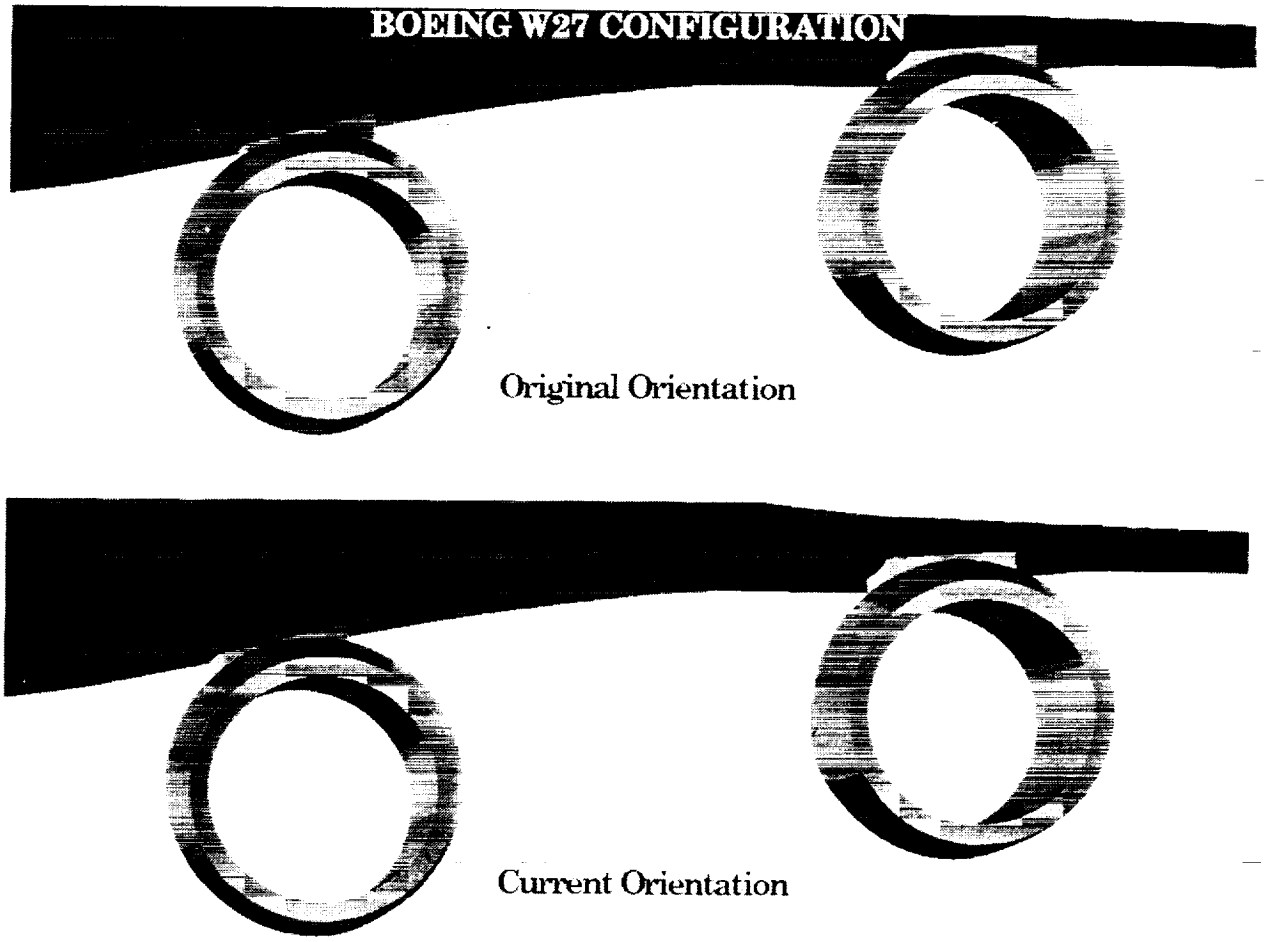

Fig 89. AIRPLANE surface grid for the Boeing W27 configuration with the nacelles/diverters in the original and modified orientations.

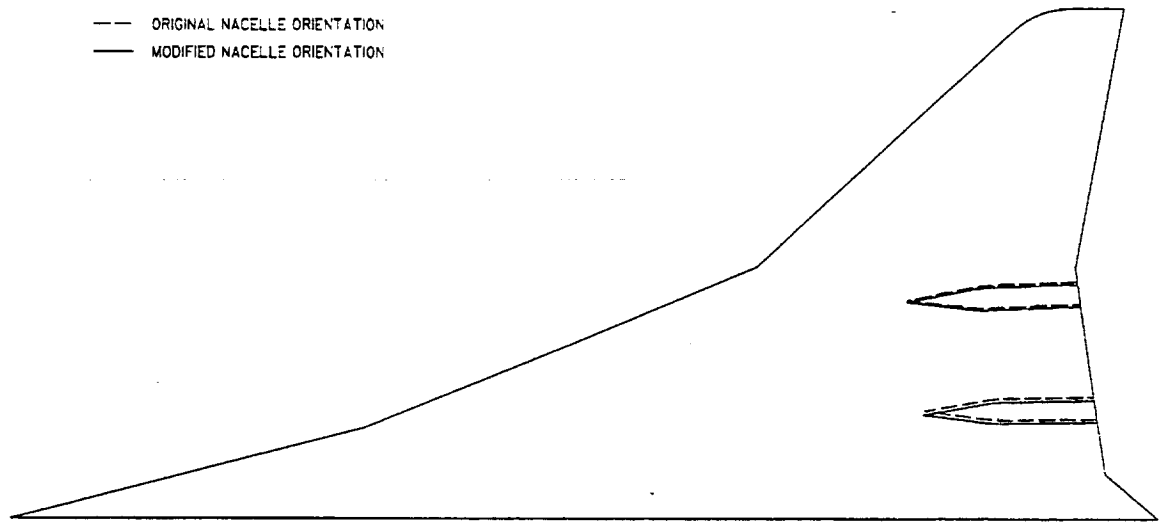

Fig 90. Diverter/wing intersections for the Boeing W27 configuration in planform view for the nacelle/diverters in the original and modified orientations.

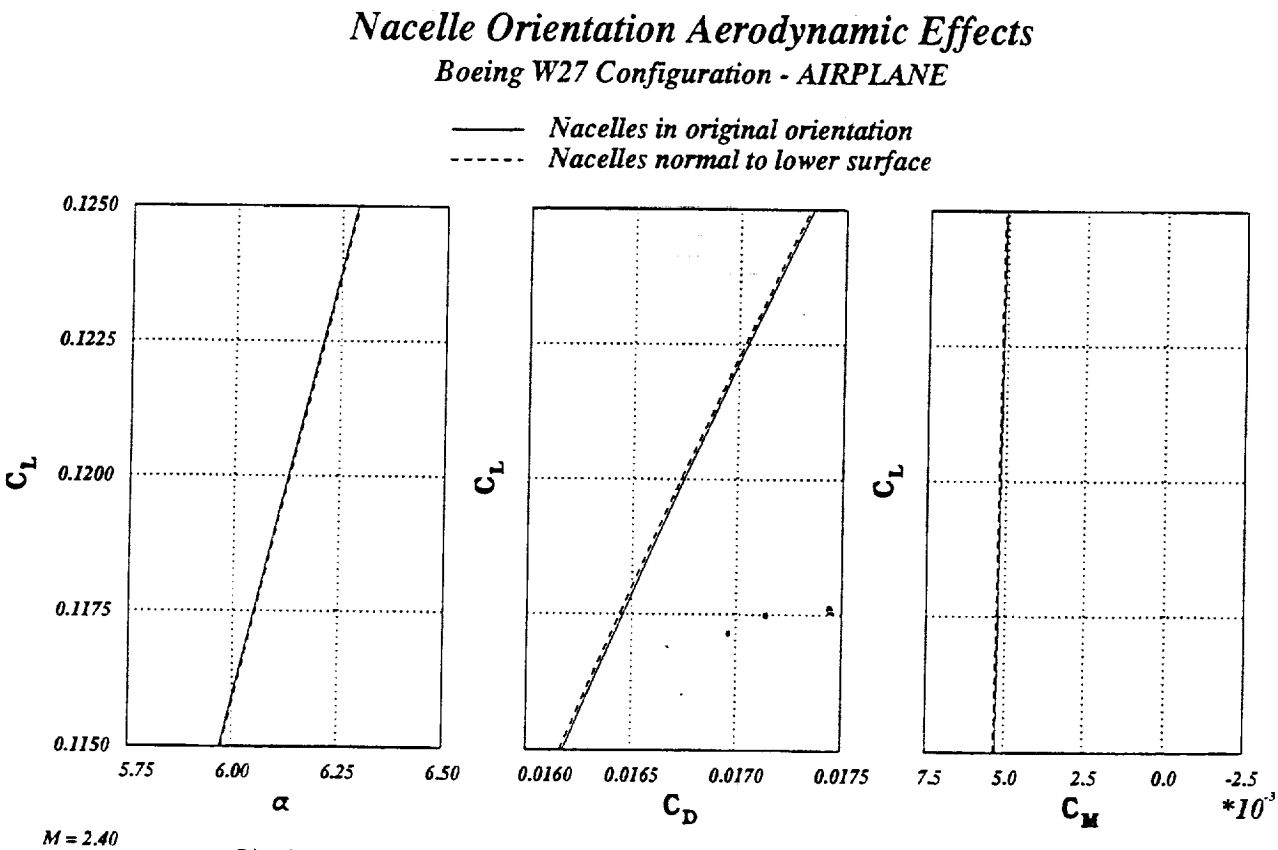

Fig 91. AIRPLANE aerodynamic characteristics for the Boeing W27 with the nacelles/diverters in the original and modified orientations, M=2.4.

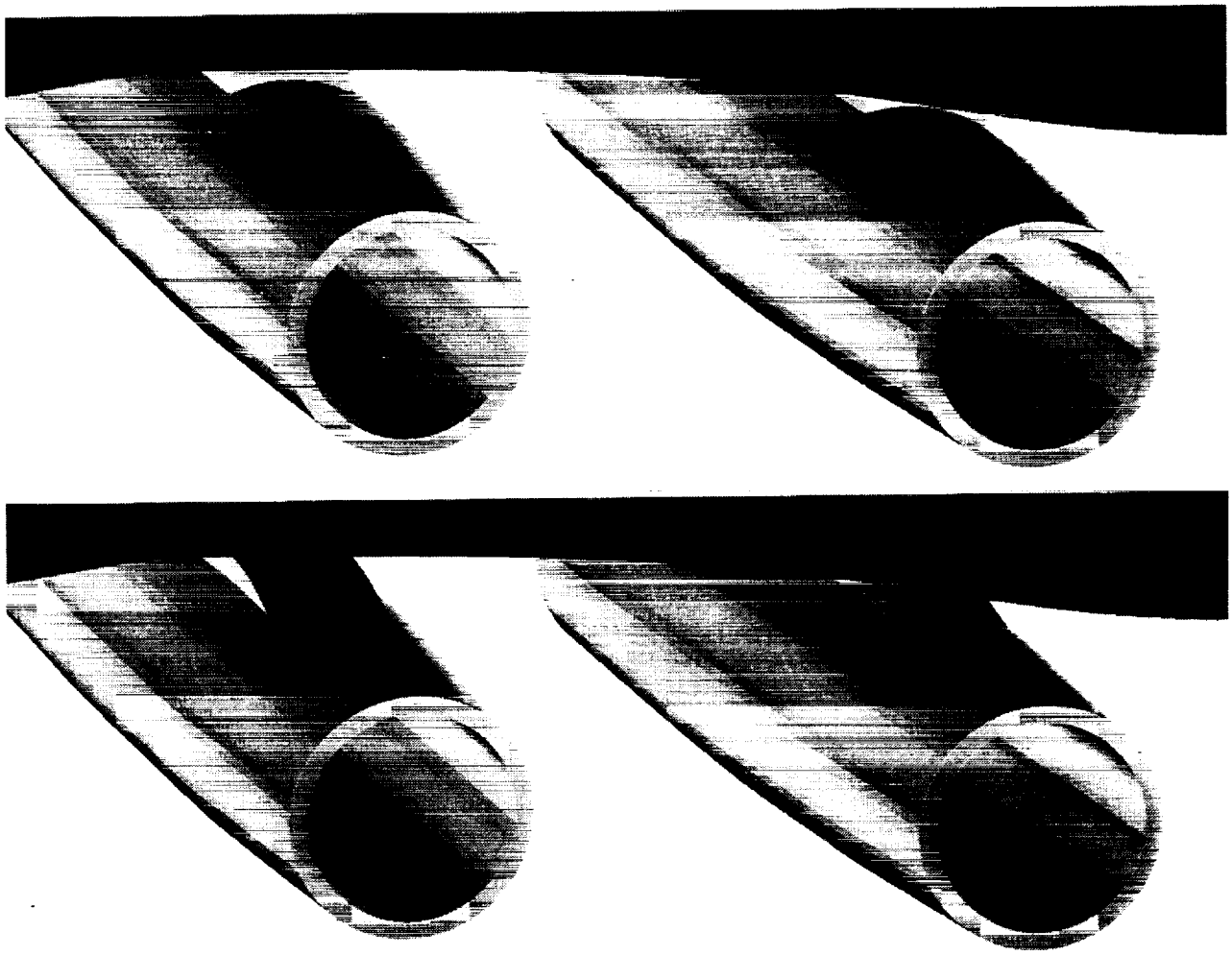

Fig 92. AIRPLANE surface grid, colored by surface normal, with truncated and ramped diverters for the Ames 704 configuration.

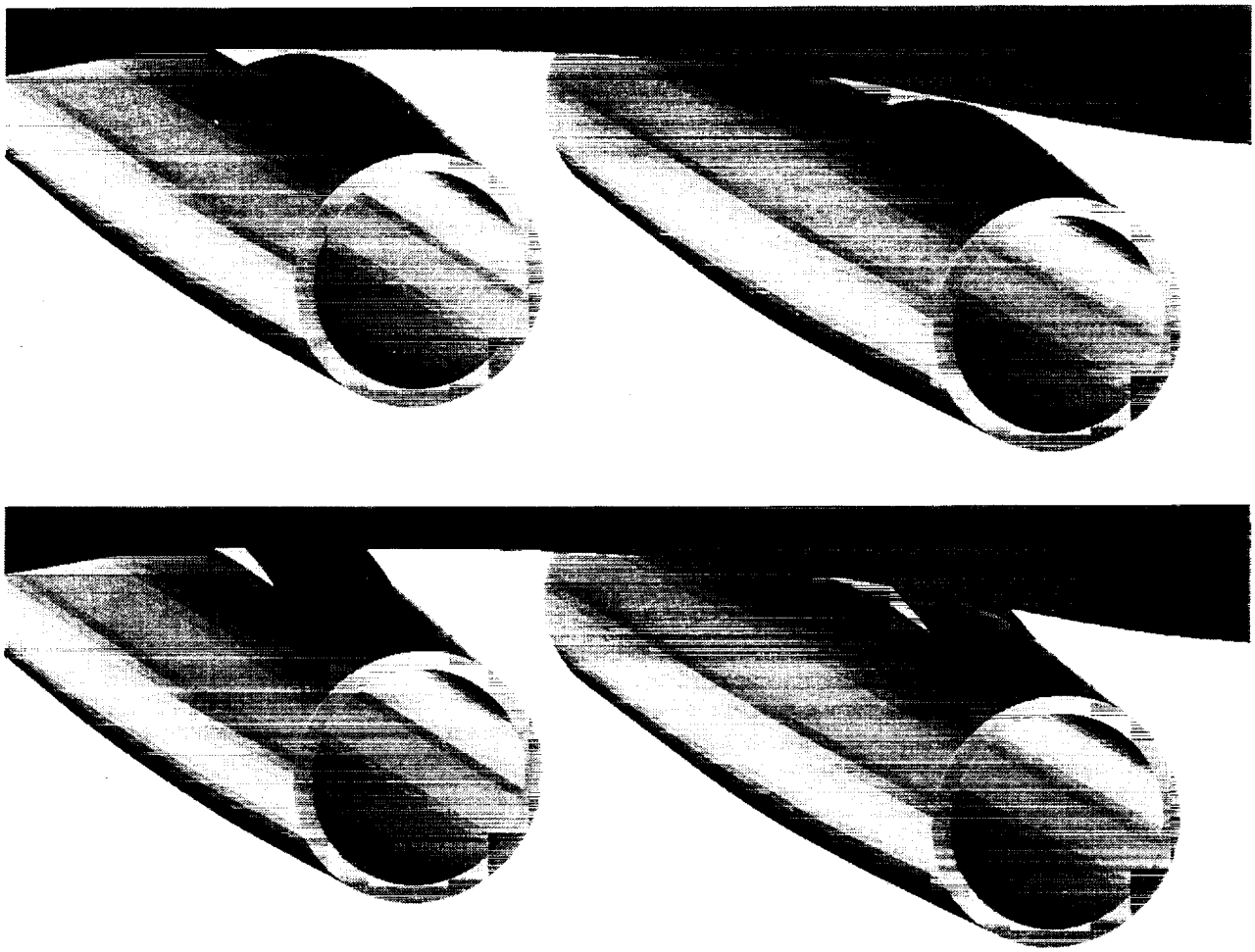

Fig 93. AIRPLANE surface grid, colored by surface normal, with truncated and ramped diverters for the Boeing W27 configuration.

Nacelle Diverter Fairing Aerodynamic Effects

Ames 7-04 Configuration - AIRPLANE

——— *nacelle/diverter fairing modeled with a step*
------ *nacelle/diverter fairing modeled with a ramp*

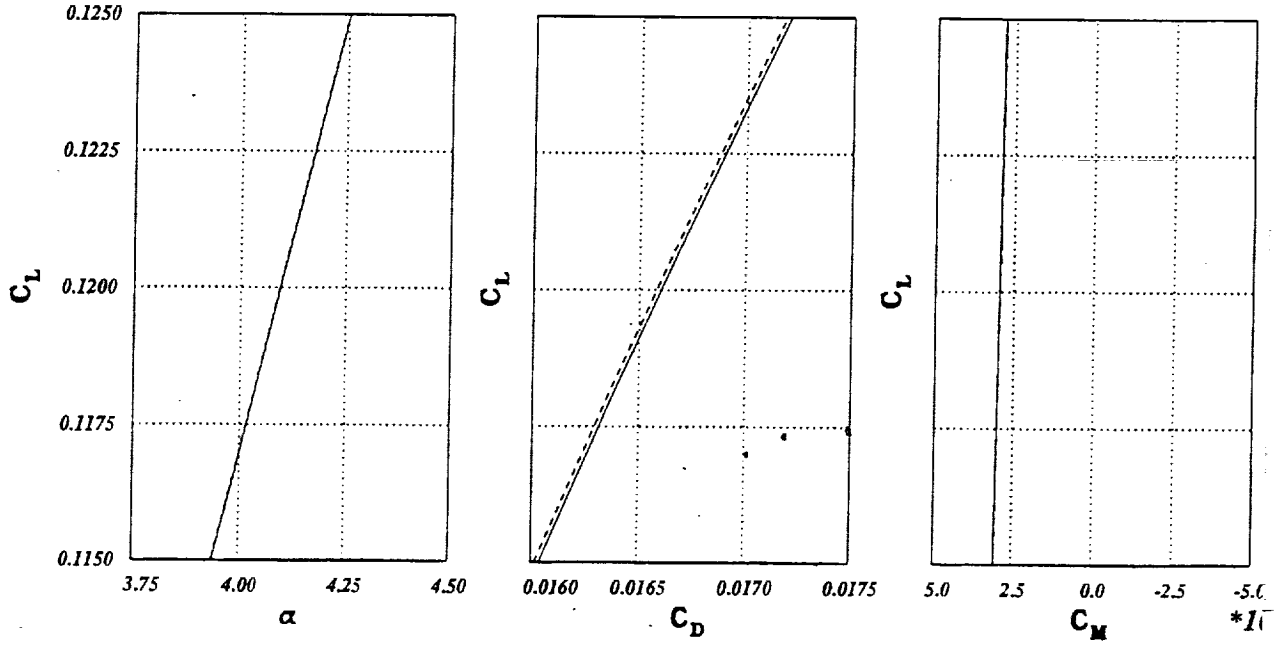

M = 2.40

Fig 94. AIRPLANE aerodynamic characteristics of the Ames 704 configuration with stepped and ramped diverter, M = 2.4.

Boeing W27 Configuration - AIRPLANE

——— *nacelle/diverter fairing modeled with a step*
------ *nacelle/diverter fairing modeled with a ramp*

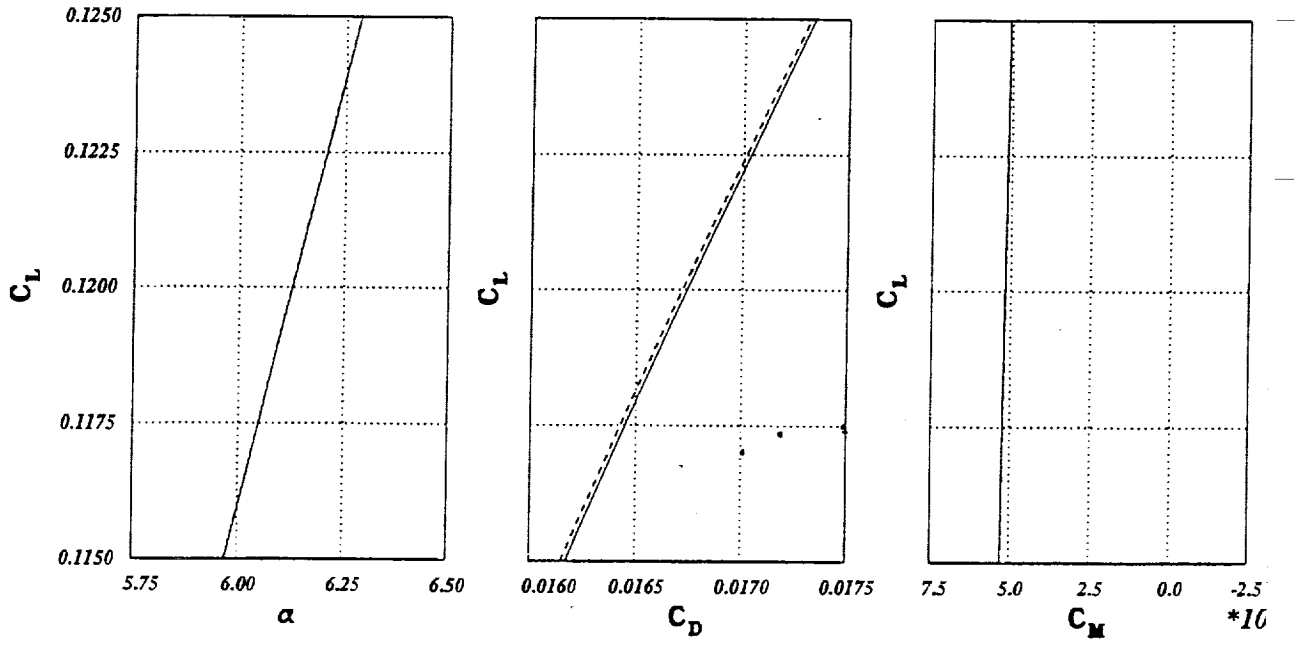

M = 2.40

Fig 95. AIRPLANE aerodynamic characteristics of the Boeing W27 configuration with stepped and ramped diverter, M = 2.4.

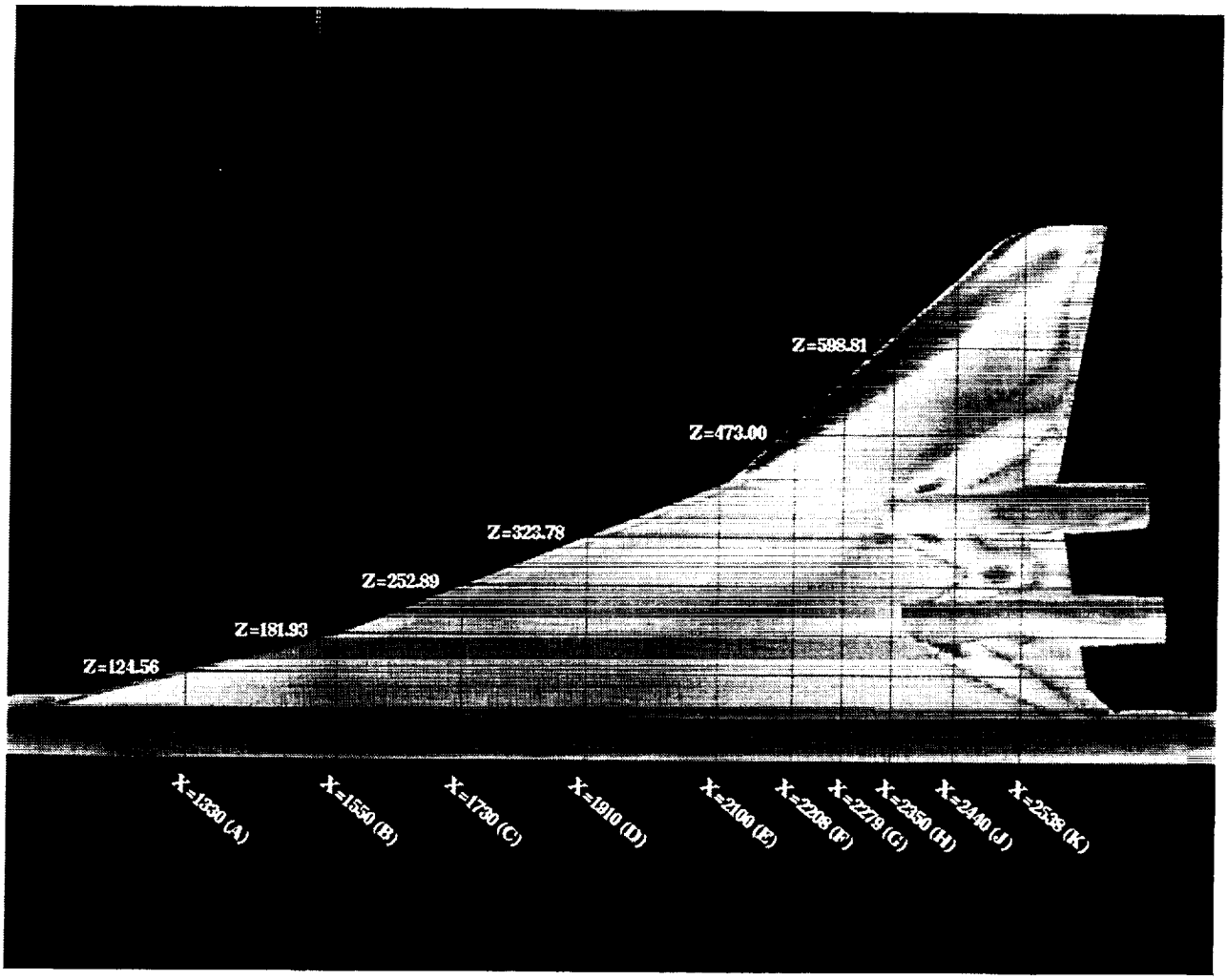

Fig 96. AIRPLANE lower surface pressure for the Ames 704 configuration with streamwise and spanwise cut locations superimposed, M=2.4, CL=0.12.

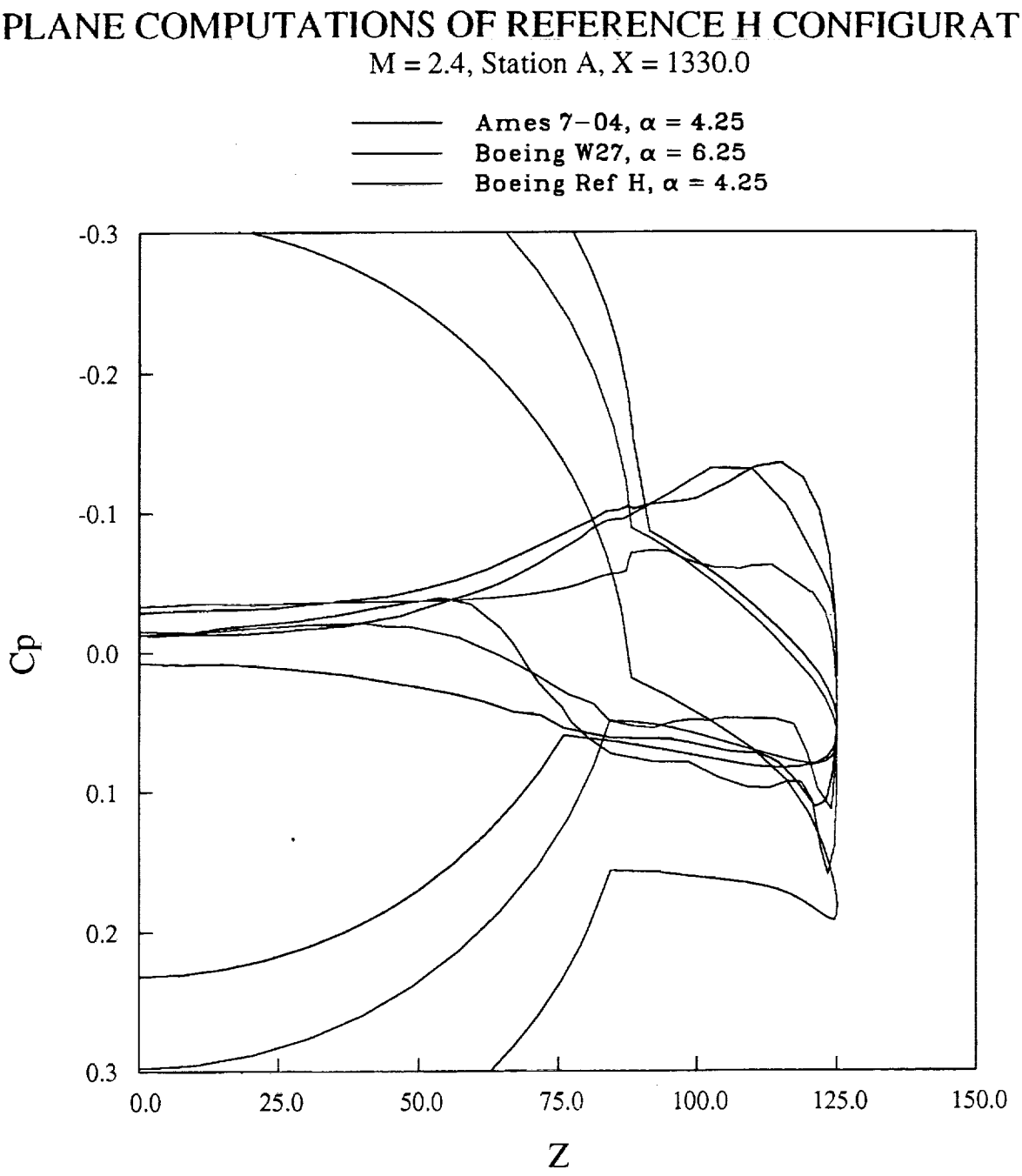

Fig 97. AIRPLANE pressure distributions and geometry for the baseline and optimized configurations, X=1330, station A, M=2.4, CL=0.12

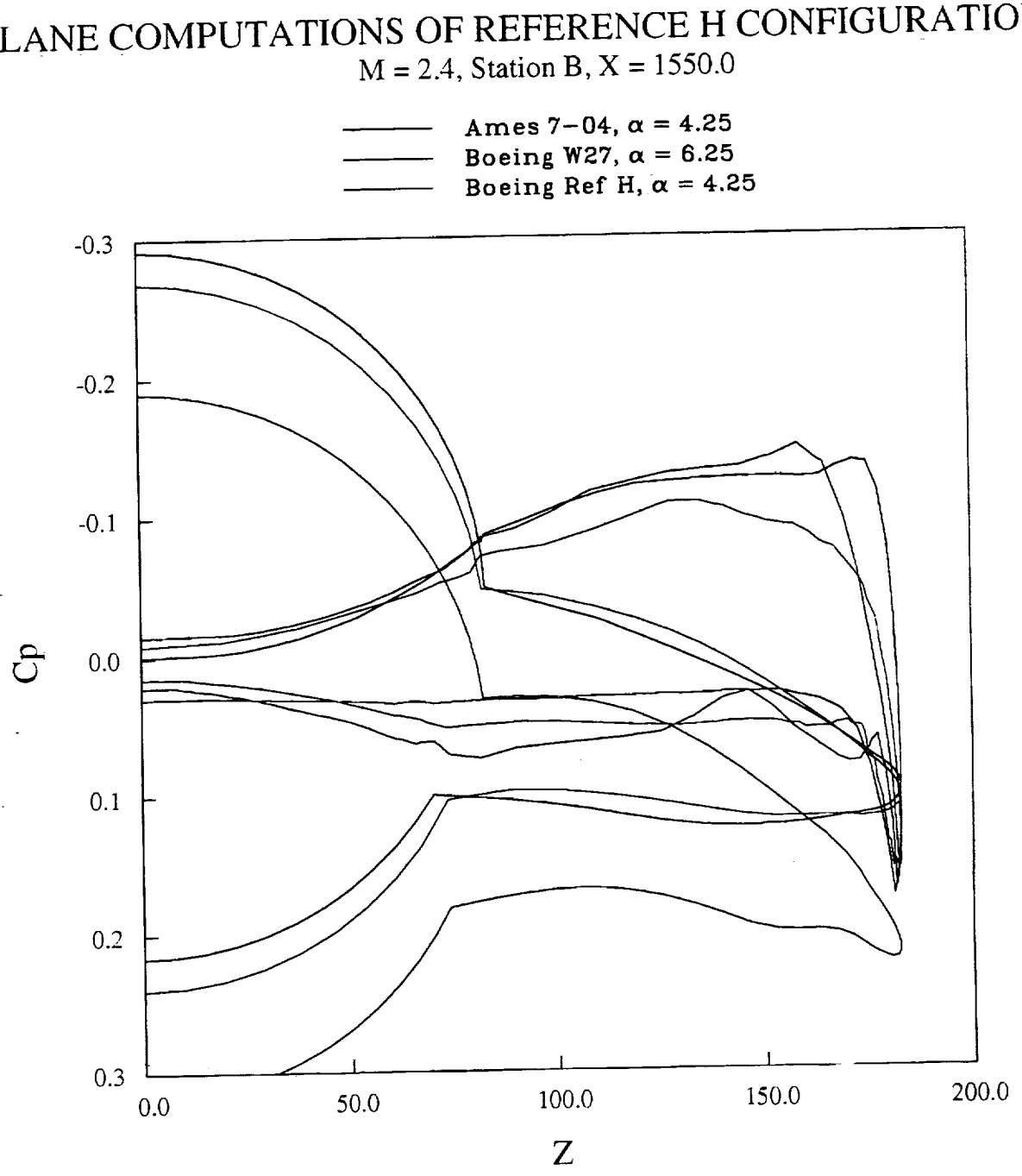

Fig 98. AIRPLANE pressure distributions and geometry for the baseline and optimized configurations, X=1550, station B, M=2.4, CL=0.12.

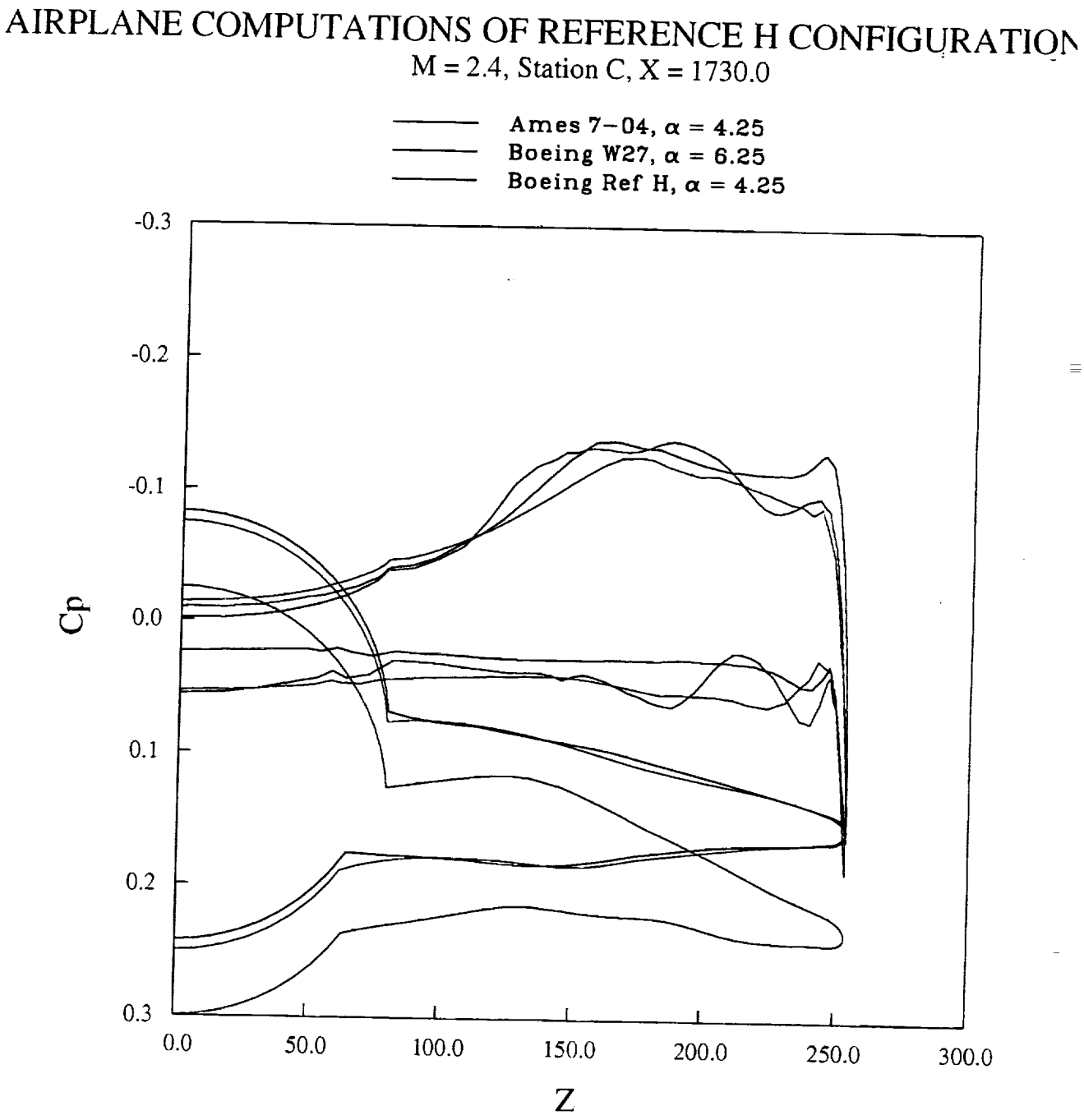

Fig 99. AIRPLANE pressure distributions and geometry for the baseline and optimized configurations, X=1730, station C, M=2.4, CL=0.1

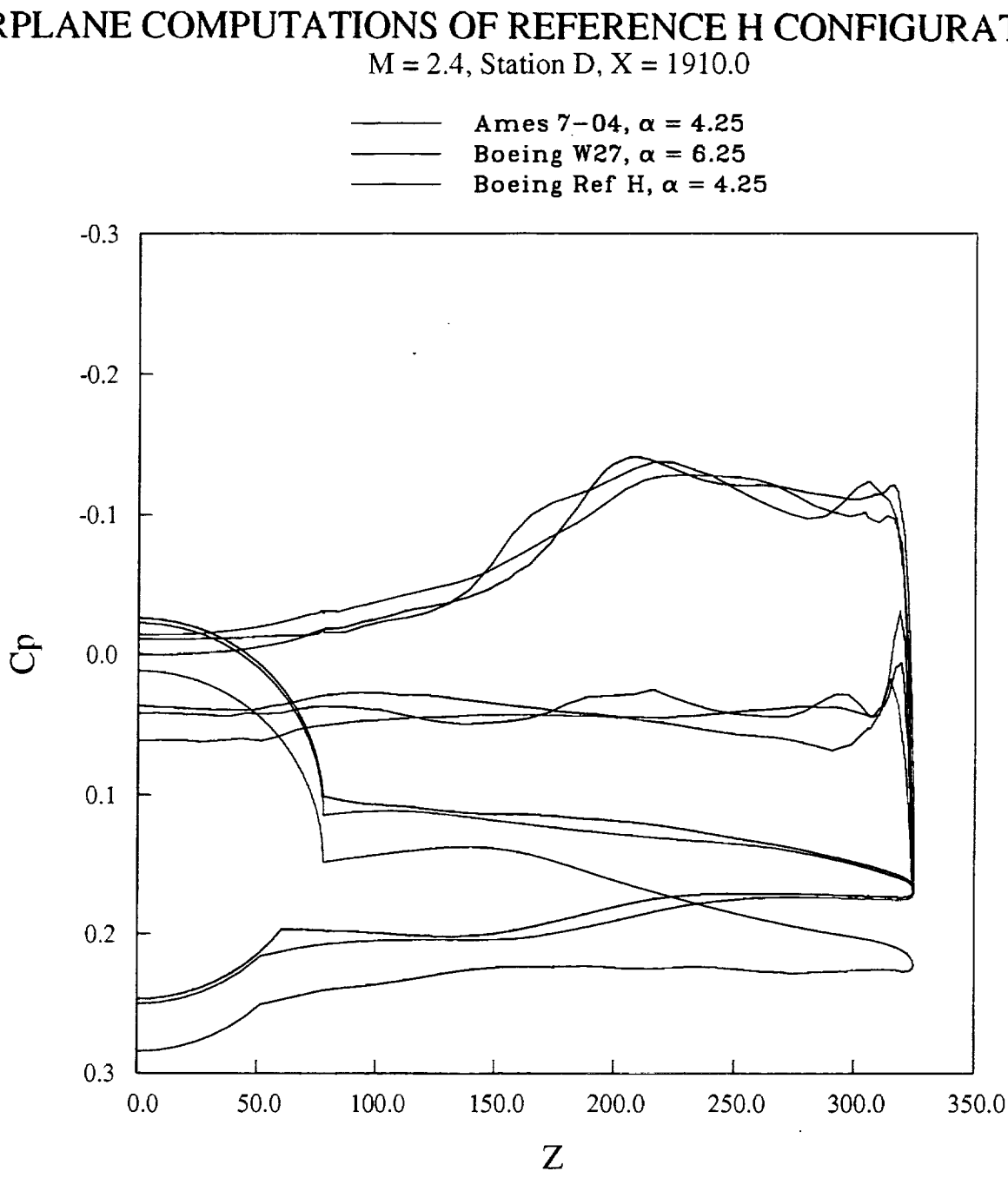

Fig 100. AIRPLANE pressure distributions and geometry for the baseline and optimized configurations, X=1910, station D, M=2.4, CL=0.12.

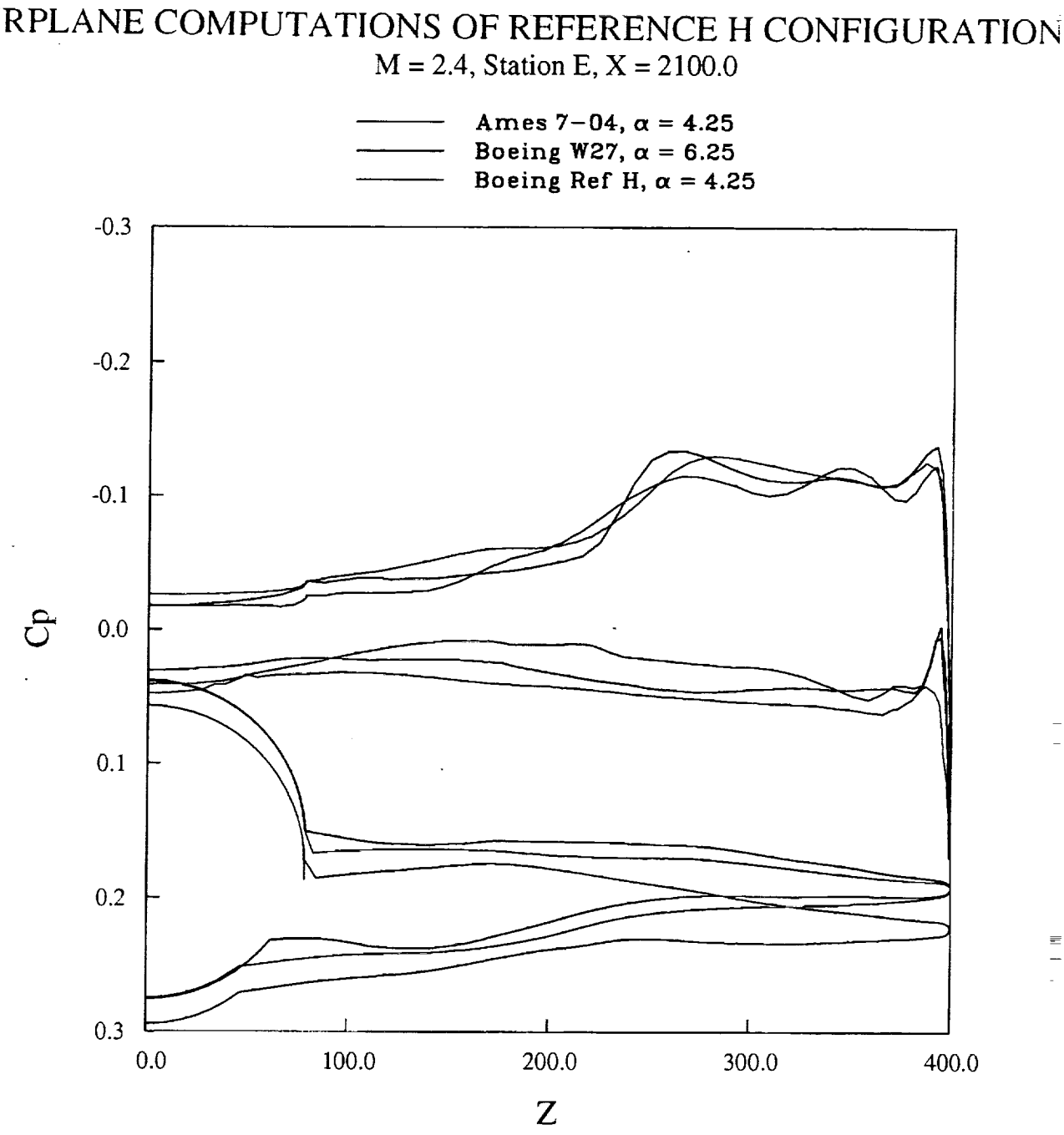

Fig 101. AIRPLANE pressure distributions and geometry for the baseline and optimized configurations, X=2100, station E, M=2.4, CL=0.12.

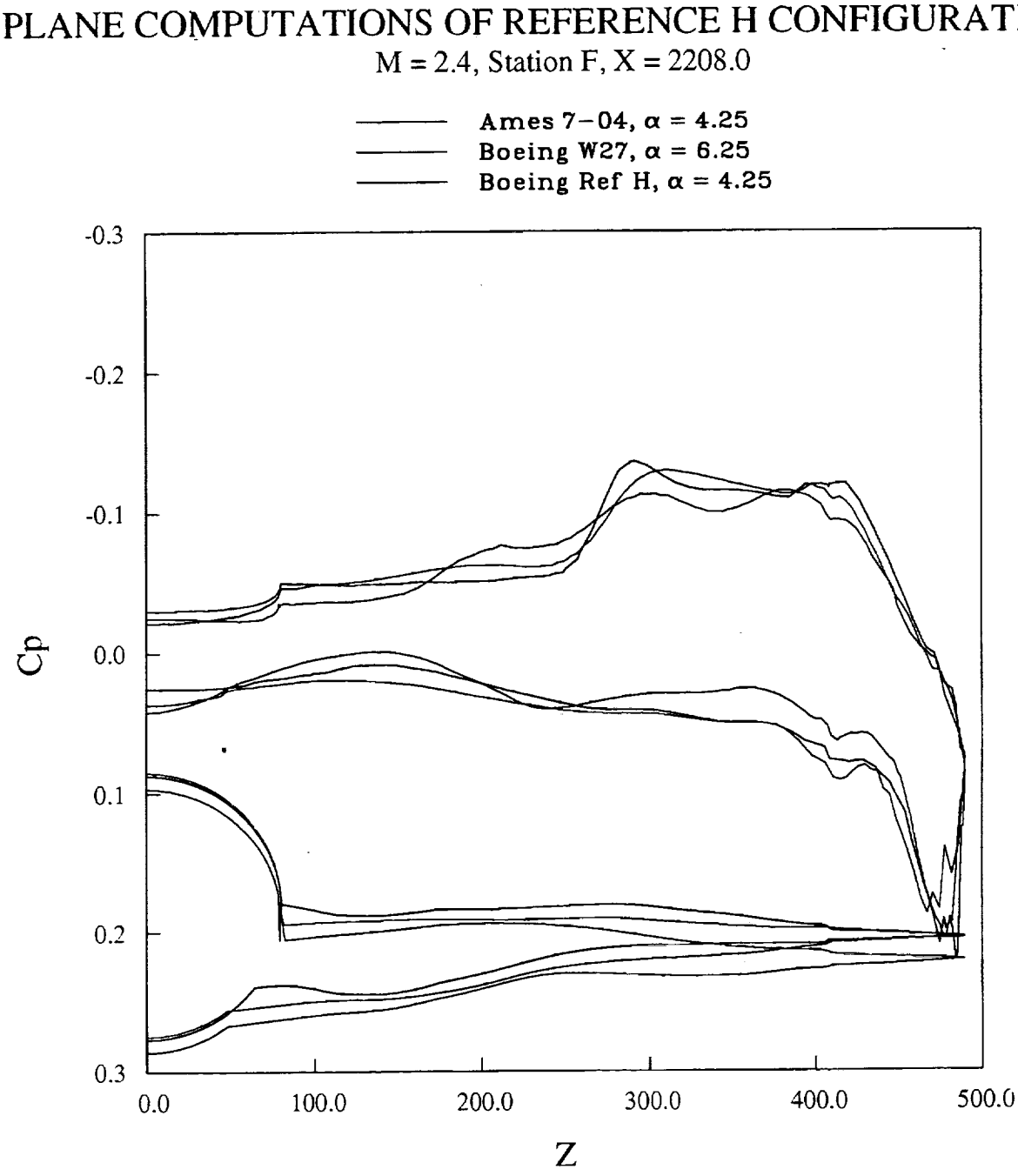

Fig 102. AIRPLANE pressure distributions and geometry for the baseline and optimized configurations, X=2208, station F, M=2.4, CL=0.12.

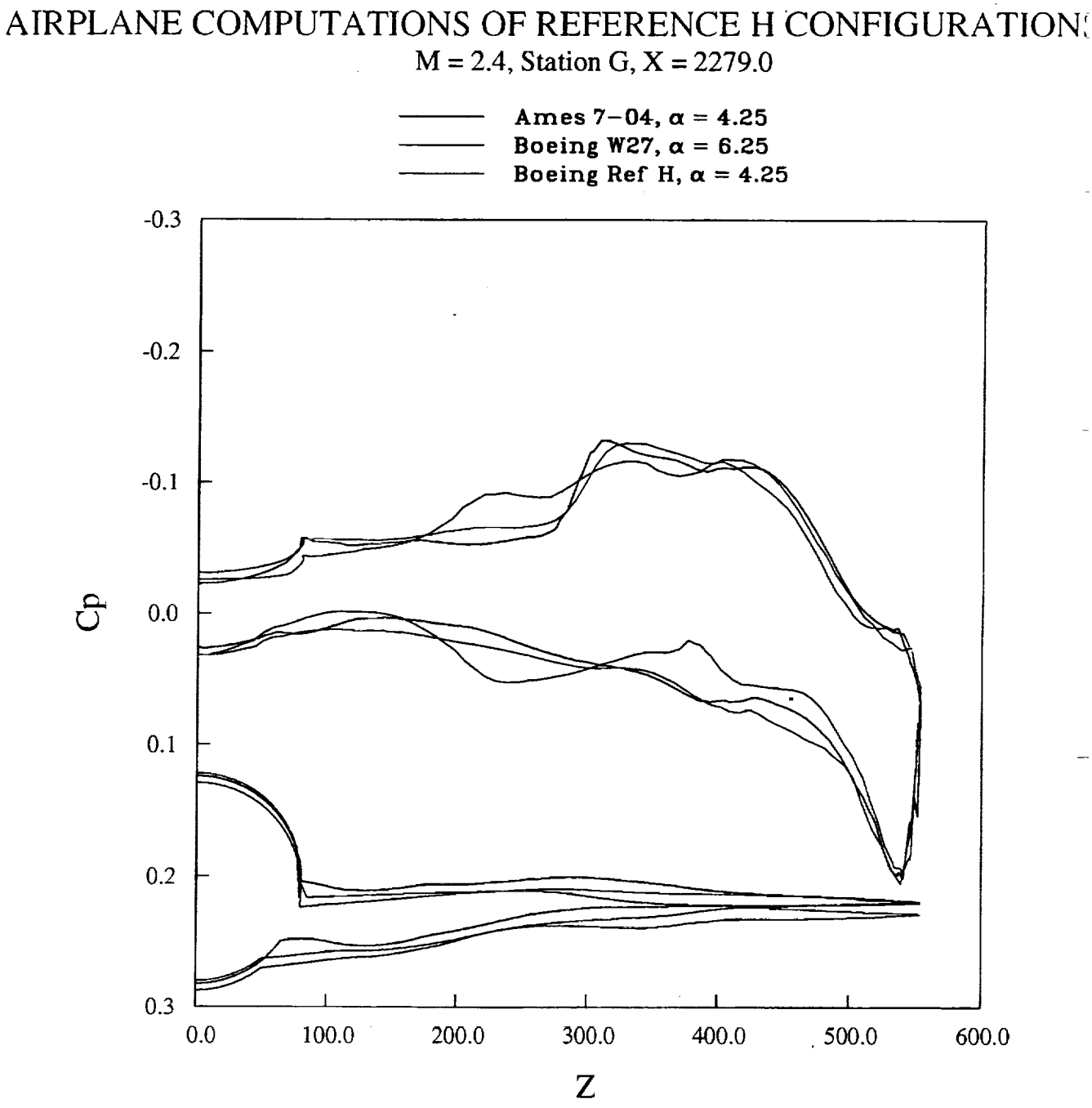

Fig 103. AIRPLANE pressure distributions and geometry for the baseline and optimized configurations, X=2279, station G, M=2.4, CL=0.12

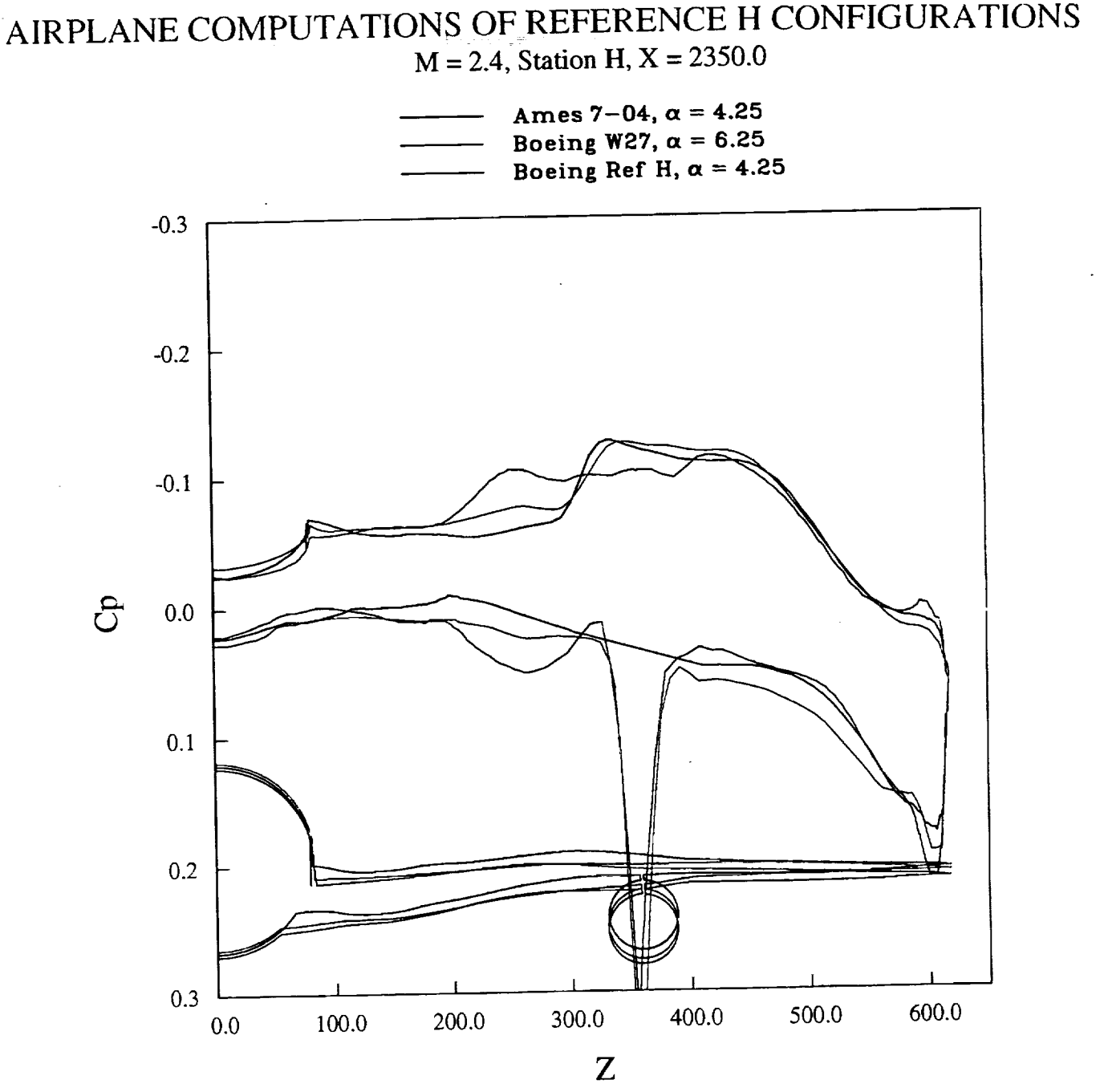

Fig 104. AIRPLANE pressure distributions and geometry for the baseline and optimized configurations, X=2350, station H, M=2.4, CL=0.12.

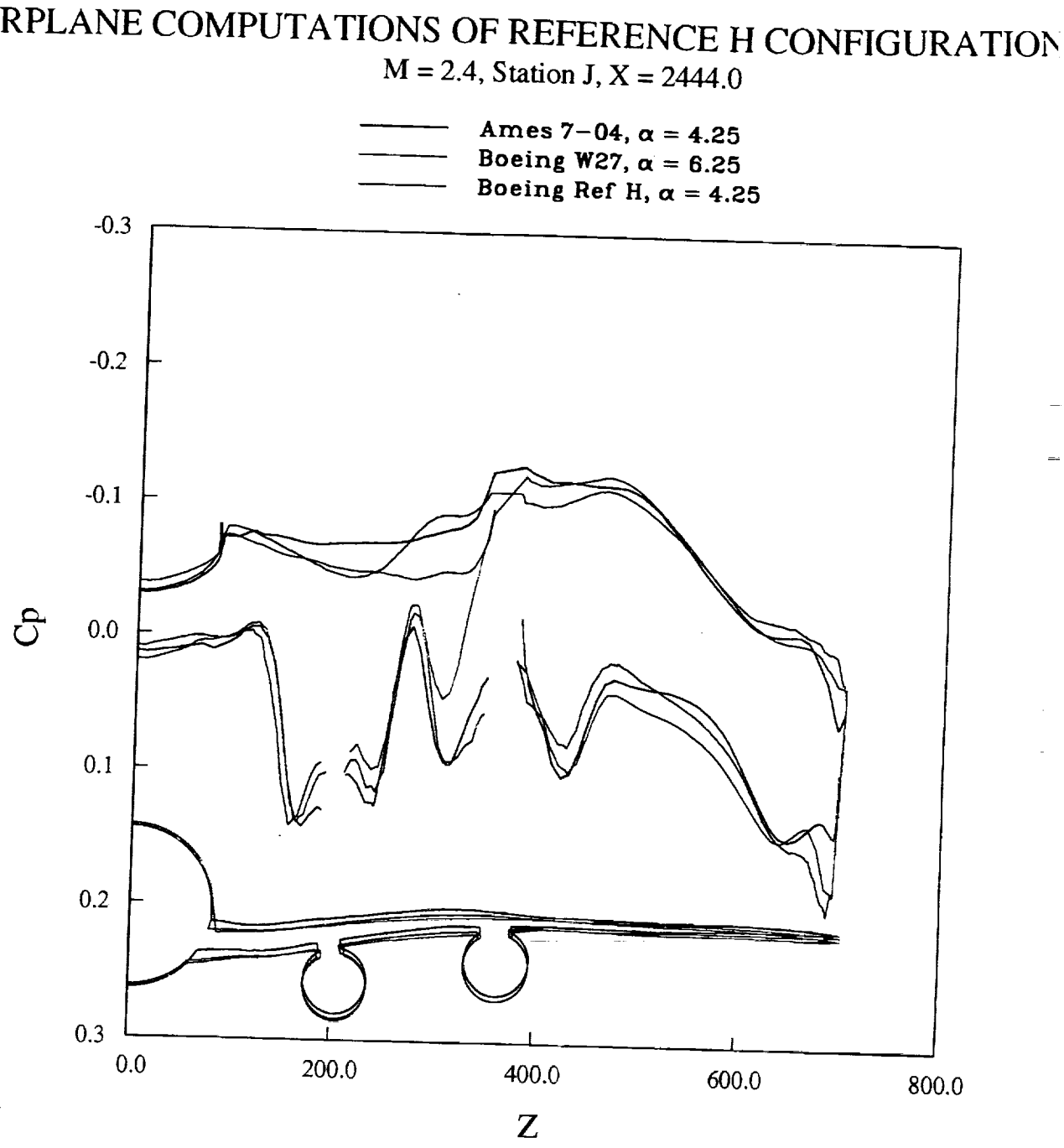

Fig 105. AIRPLANE pressure distributions and geometry for the baseline and optimized configurations, X=2444, station J, M=2.4, CL=0.12

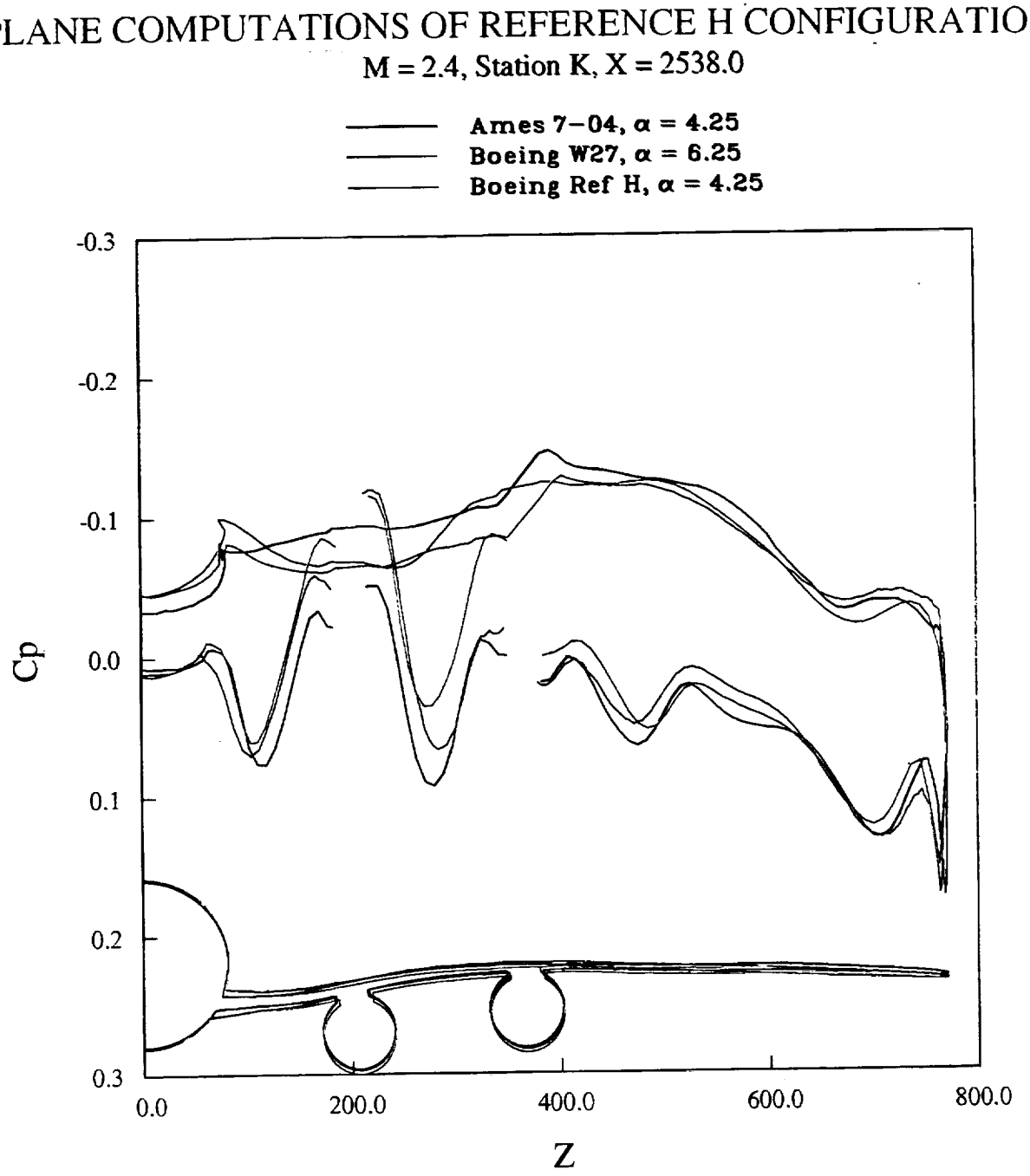

Fig 106. AIRPLANE pressure distributions and geometry for the baseline and optimized configurations, X=2538, station K, M=2.4, CL=0.12.

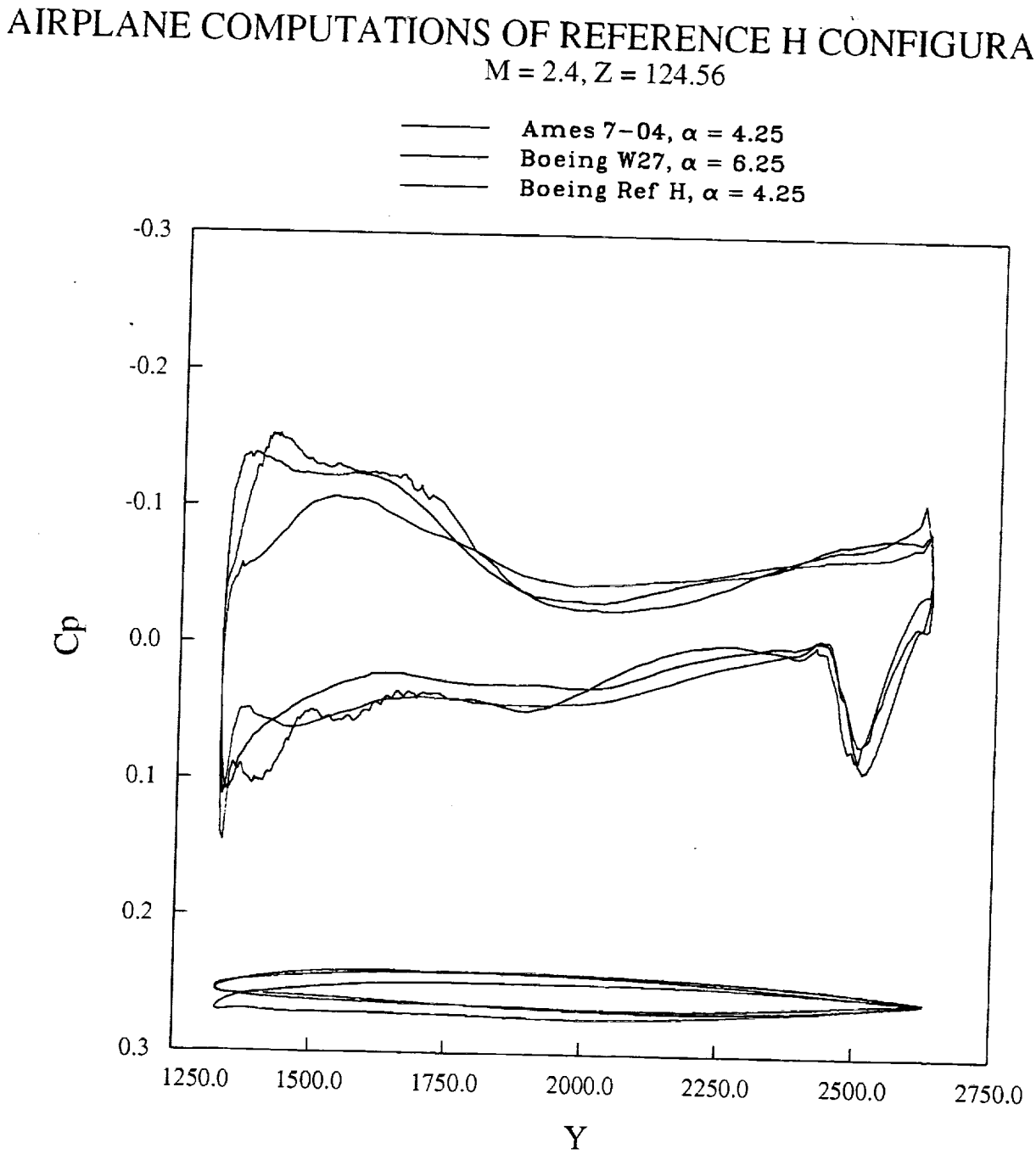

Fig 107. AIRPLANE pressure distributions and geometry for the baseline and optimized configurations, Z=124.56, M=2.4, CL=0.12.

AIRPLANE COMPUTATIONS OF REFERENCE H CONFIGURATIONS

M = 2.4, Z = 124.56

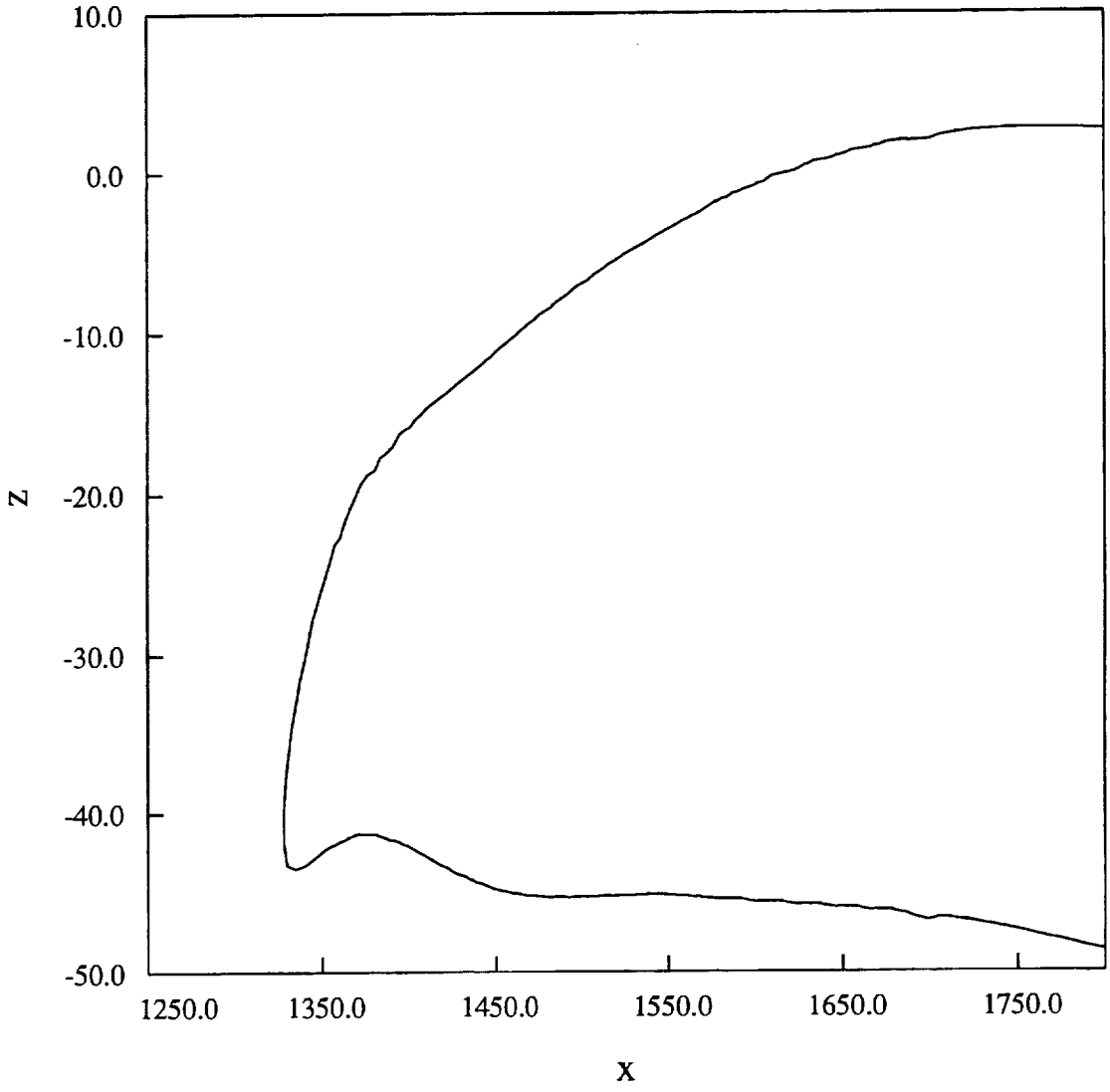

Fig 108. Leading edge of the Boeing W27 geometry.

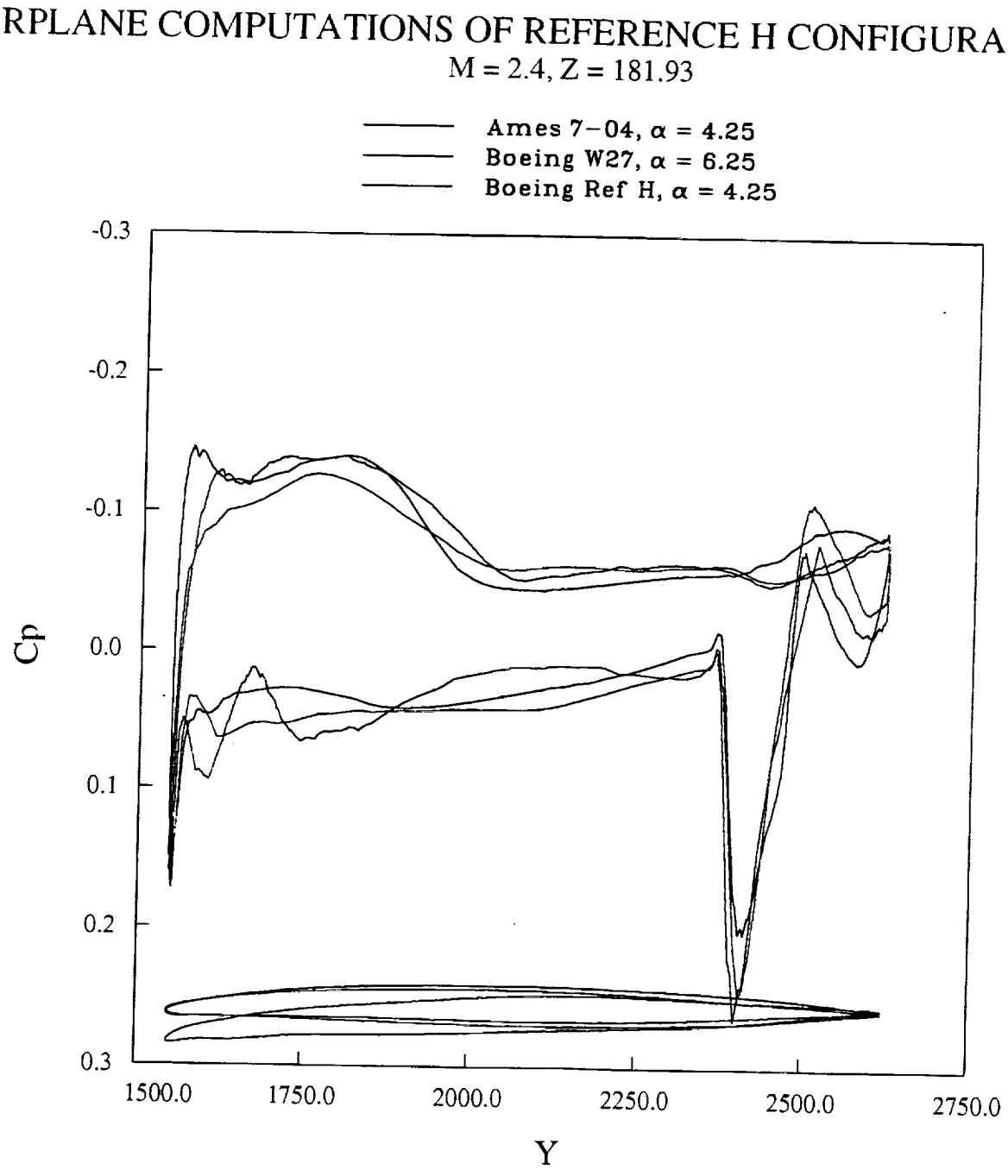

Fig 109. AIRPLANE pressure distributions and geometry for the baseline and optimized configurations, Z=181.93, M=2.4, CL=0.12.

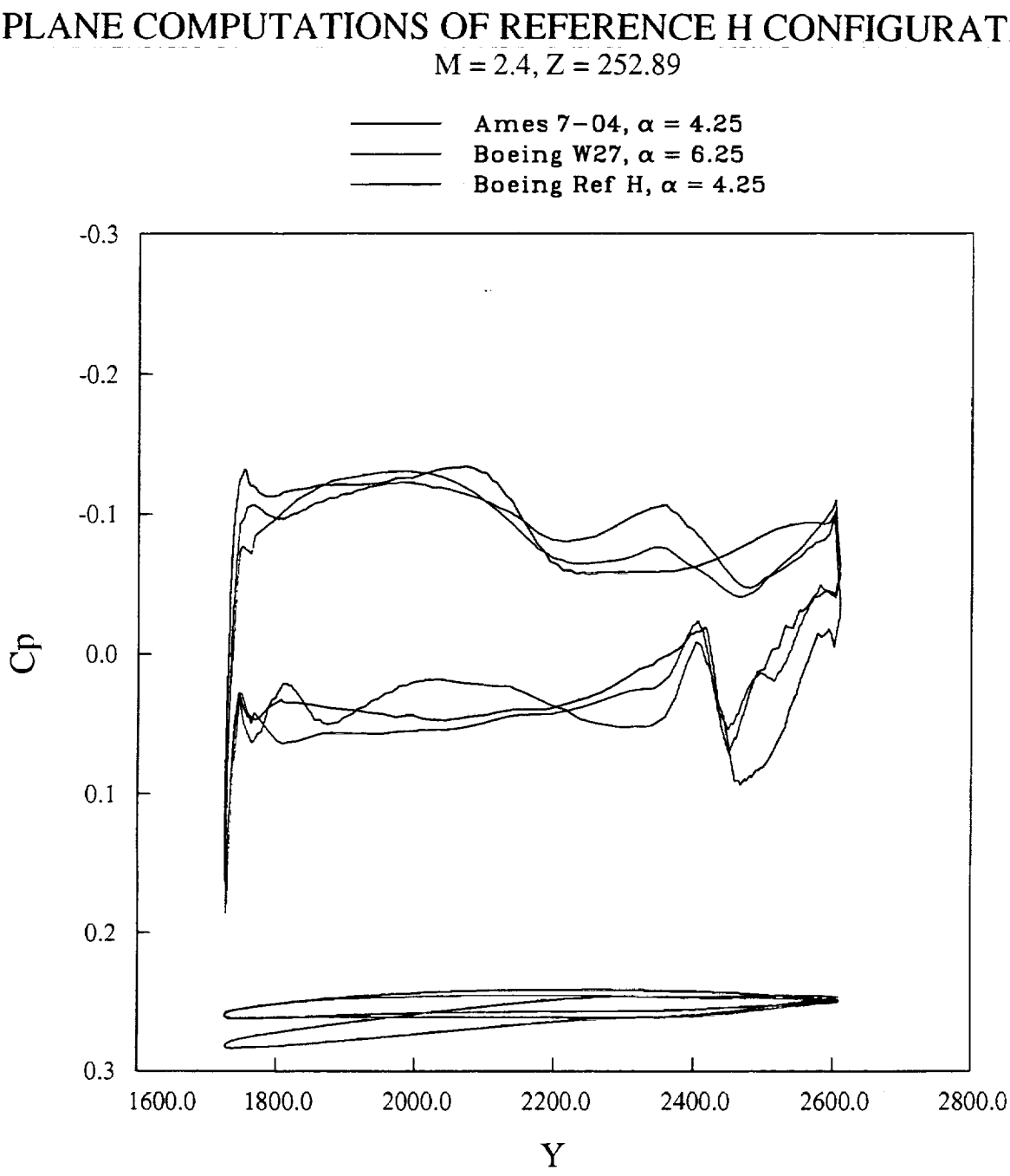

Fig 110. AIRPLANE pressure distributions and geometry for the baseline and optimized configurations, Z=252.89, M=2.4, CL=0.12..

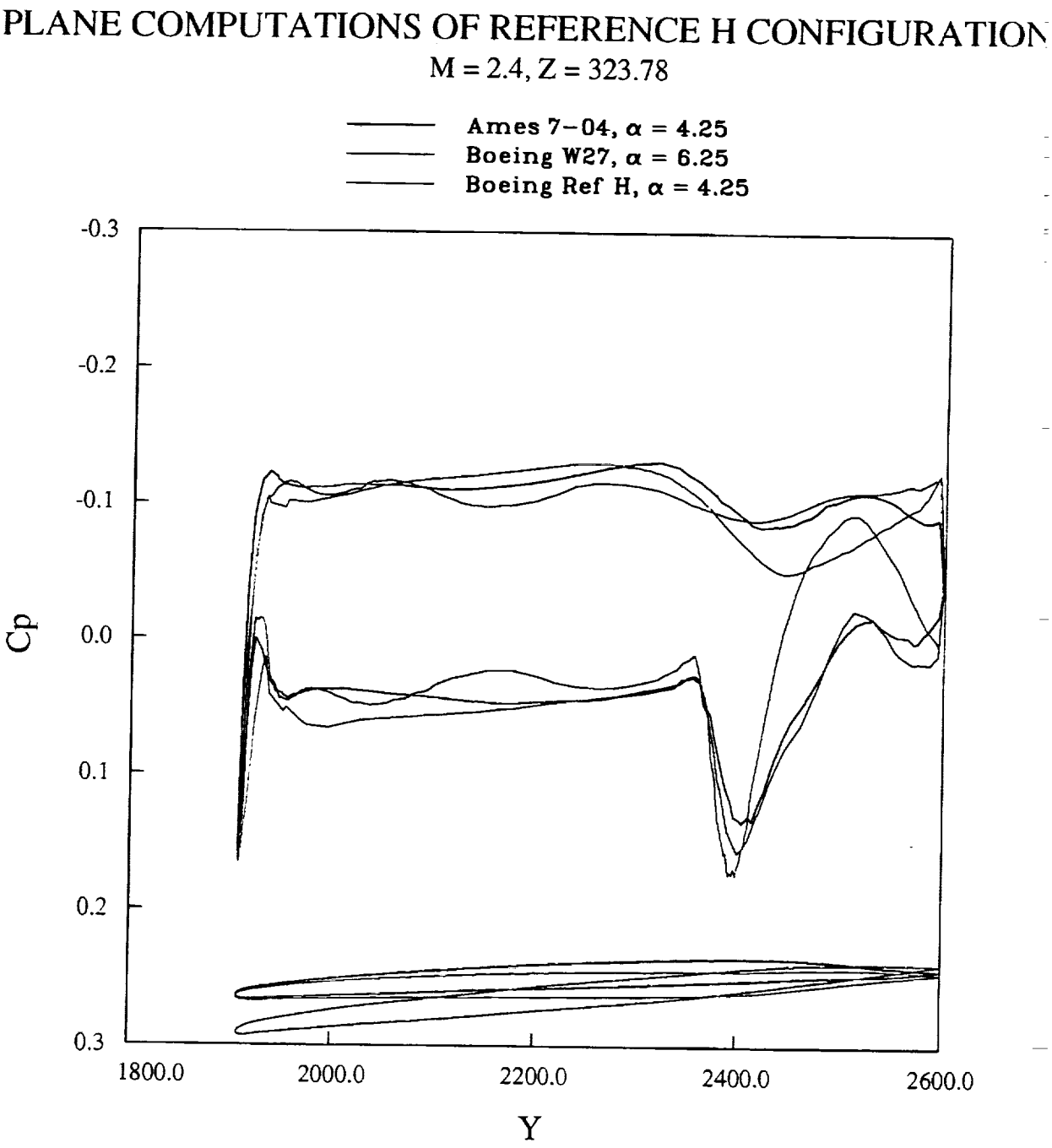

Fig 111. AIRPLANE pressure distributions and geometry for the baseline and optimized configurations, Z=323.78, M=2.4, CL=0.12.

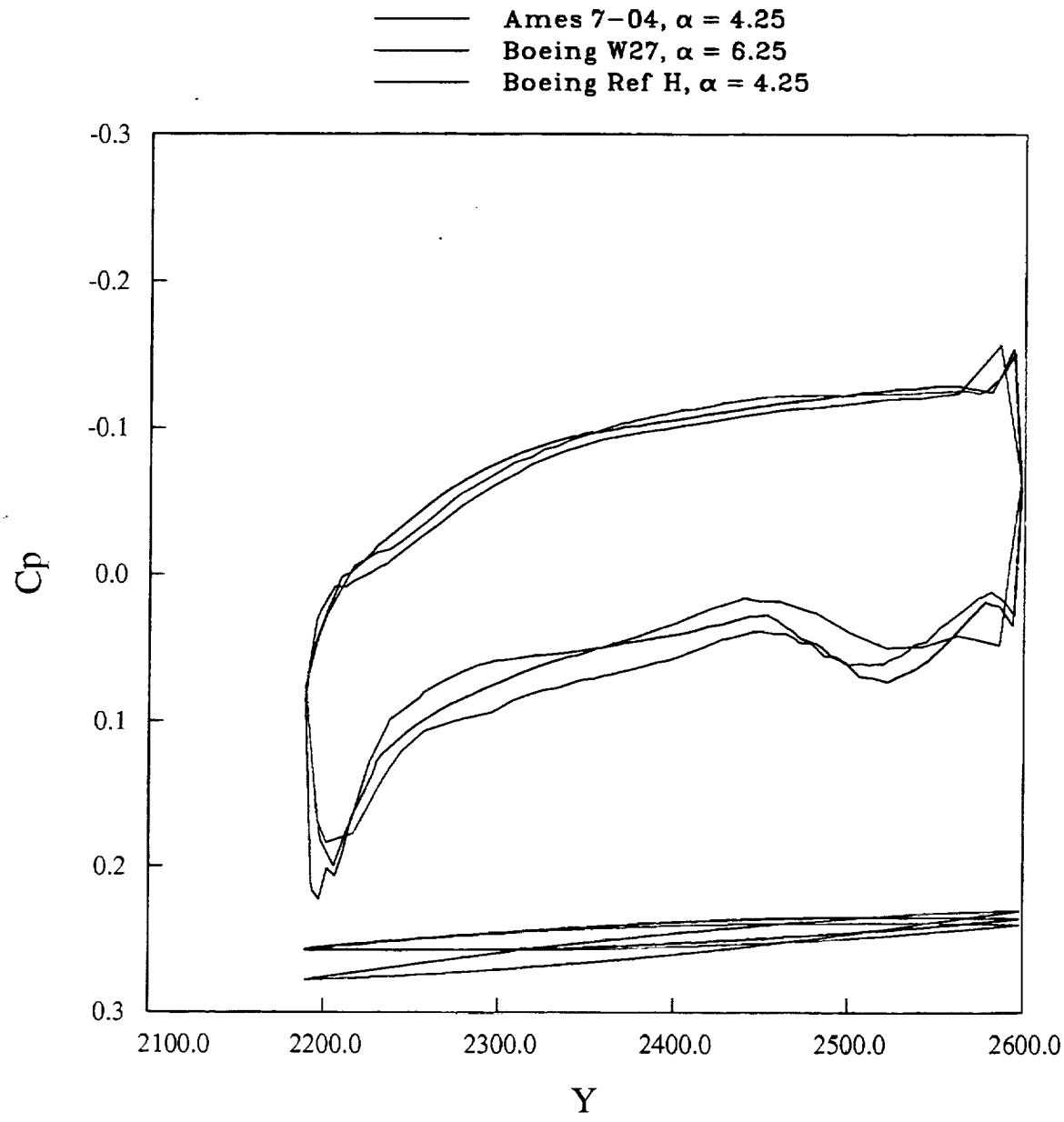

Fig 112. AIRPLANE pressure distributions and geometry for the baseline and optimized configurations, Z=473.00, M=2.4, CL=0.12.

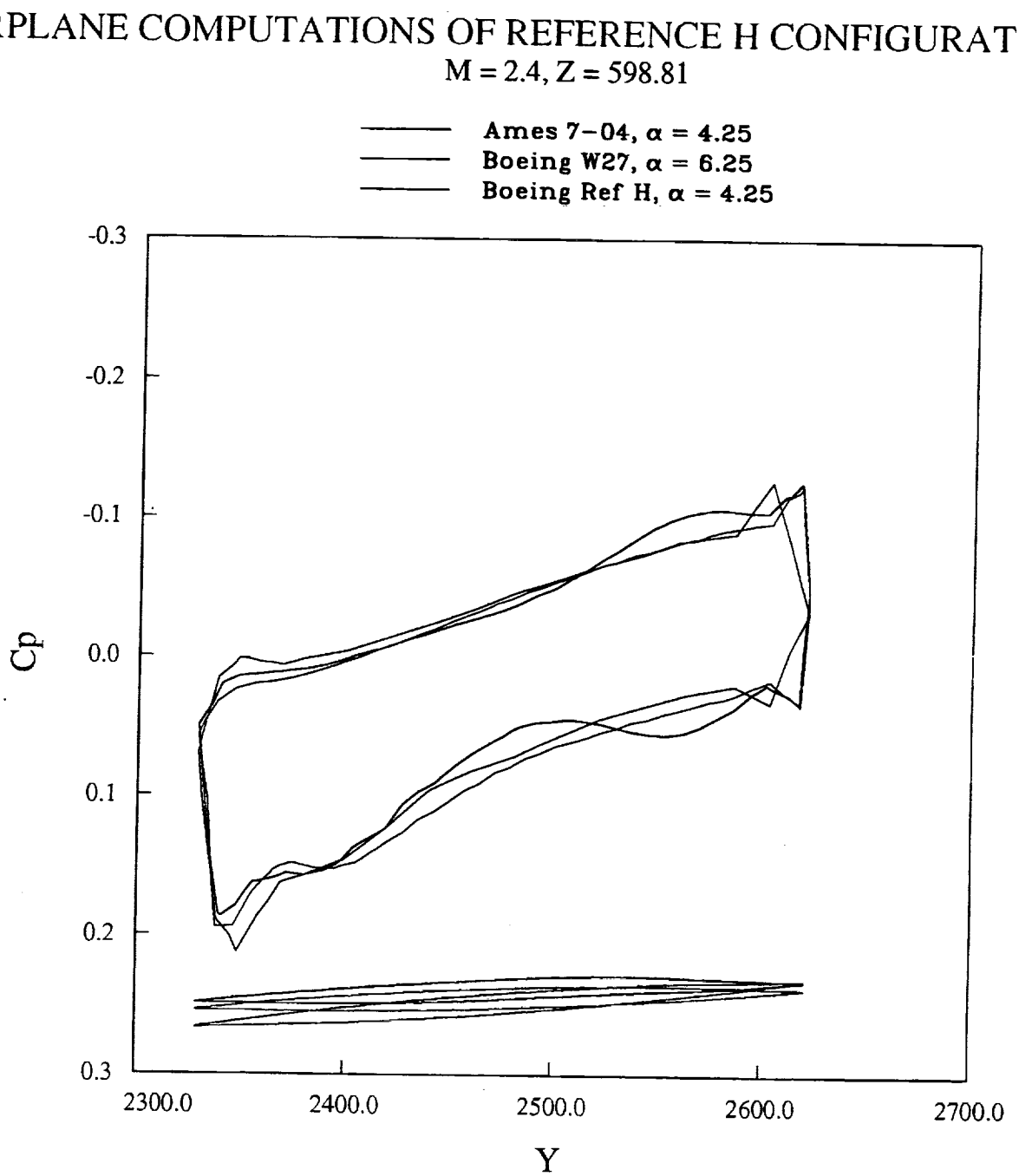

Fig 113. AIRPLANE pressure distributions and geometry for the baseline and optimized configurations, Z=598.81, M=2.4, CL=0.12.

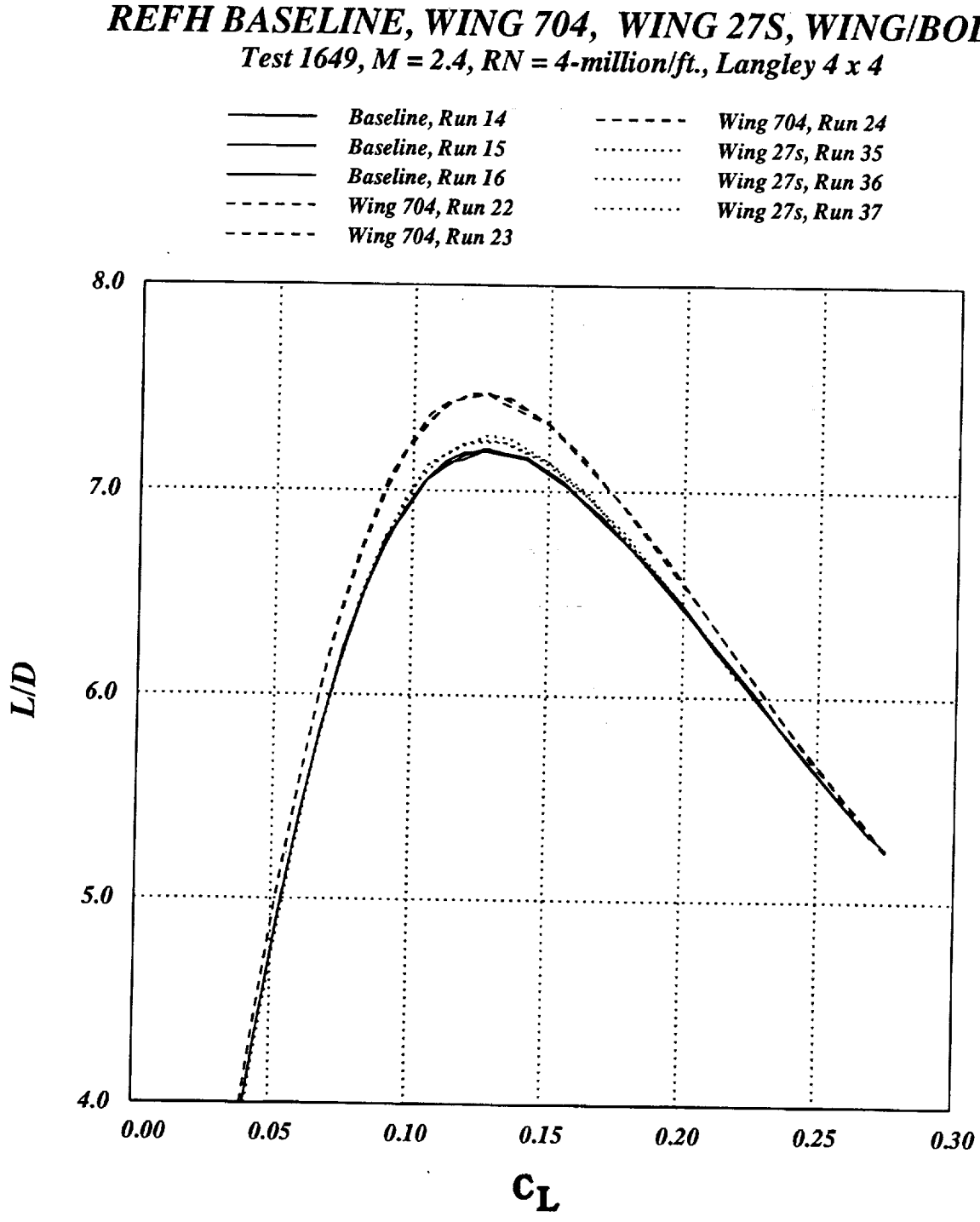

Fig 114. Experimental lift/drag ratio of the two optimized and the baseline wing/body configurations, M=2.4, RN=4-million/ft.

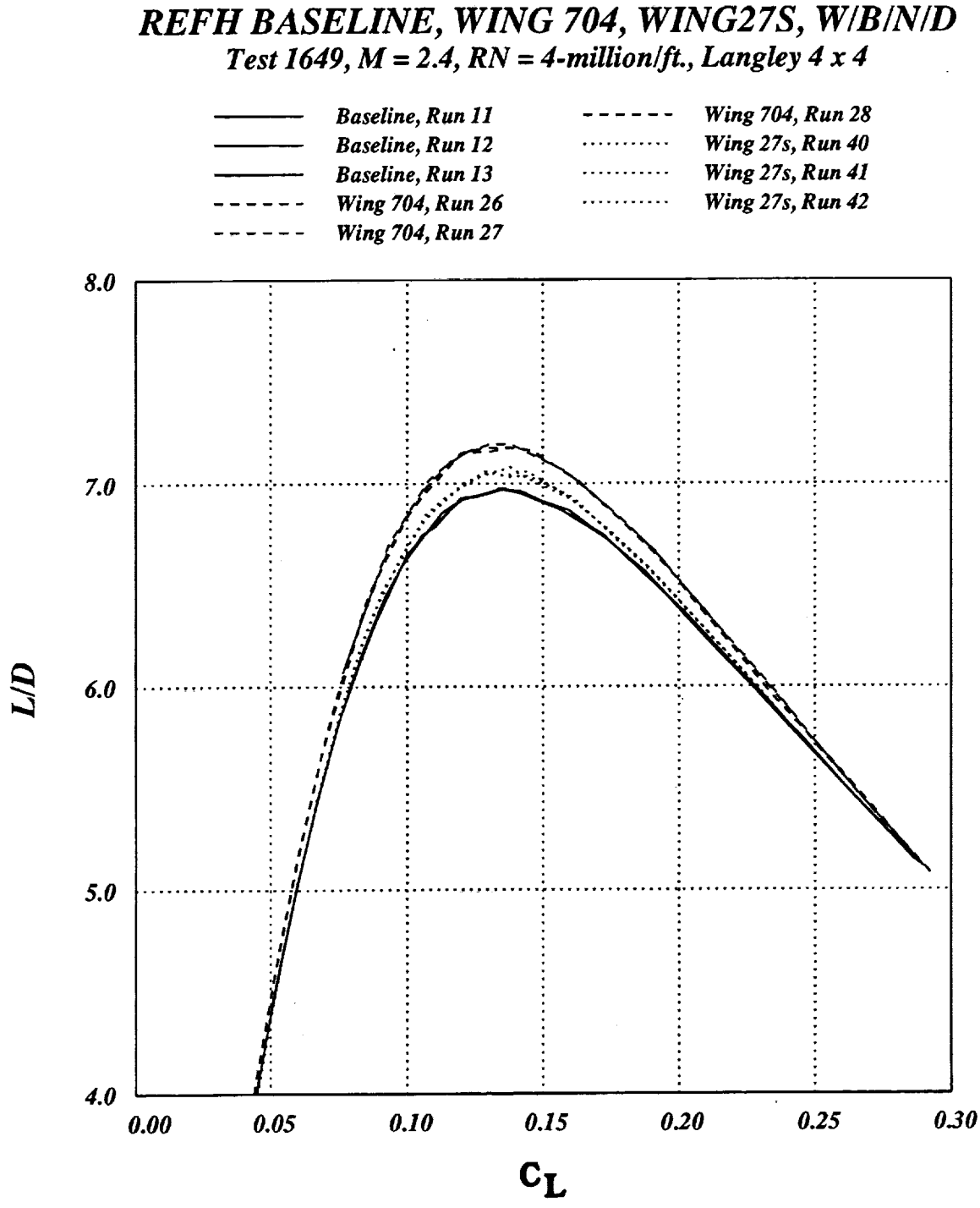

Fig 115. Experimental lift/drag ratio of the two optimized and the baseline complete configurations, M=2.4, RN=4-million/ft.

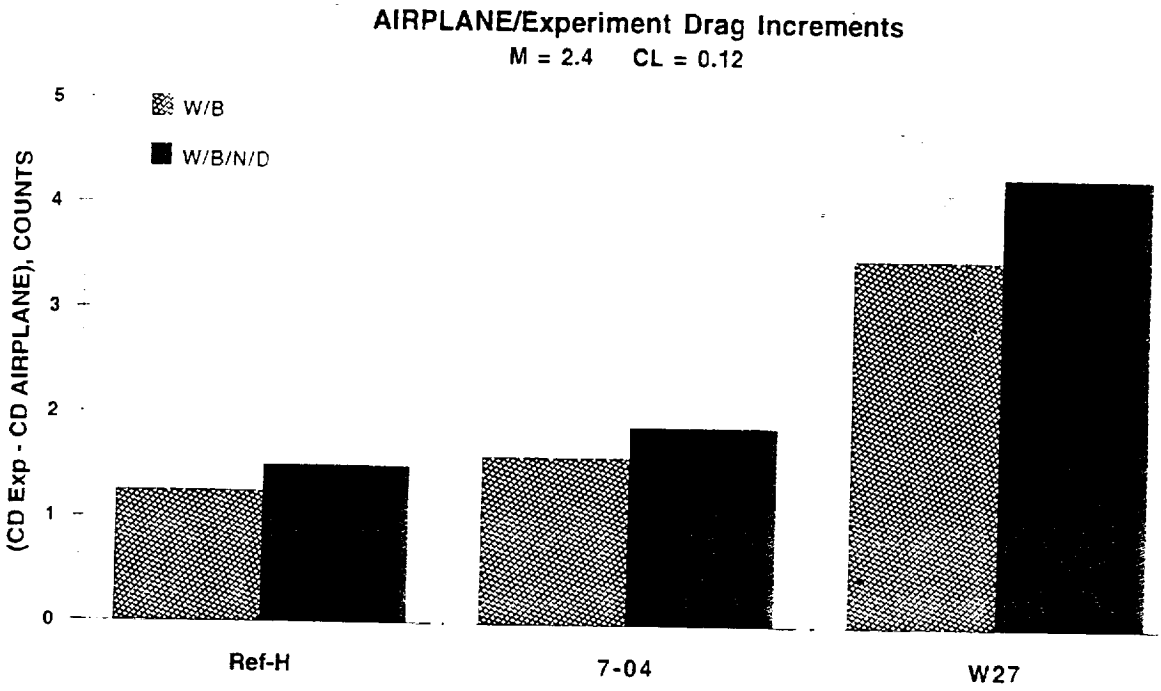

Fig 116. Drag increments between AIRPLANE and experiment at cruise lift for the two optimized and baseline configurations.

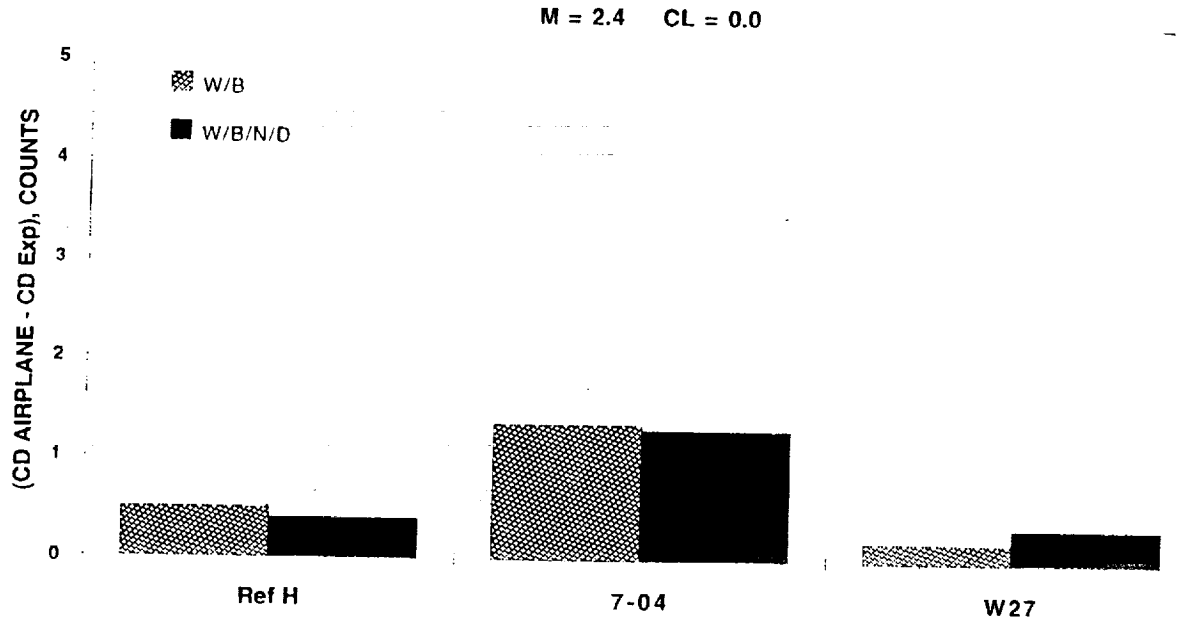

Fig 117. Drag increments between AIRPLANE and experiment at zero lift for the two optimized and baseline configurations.

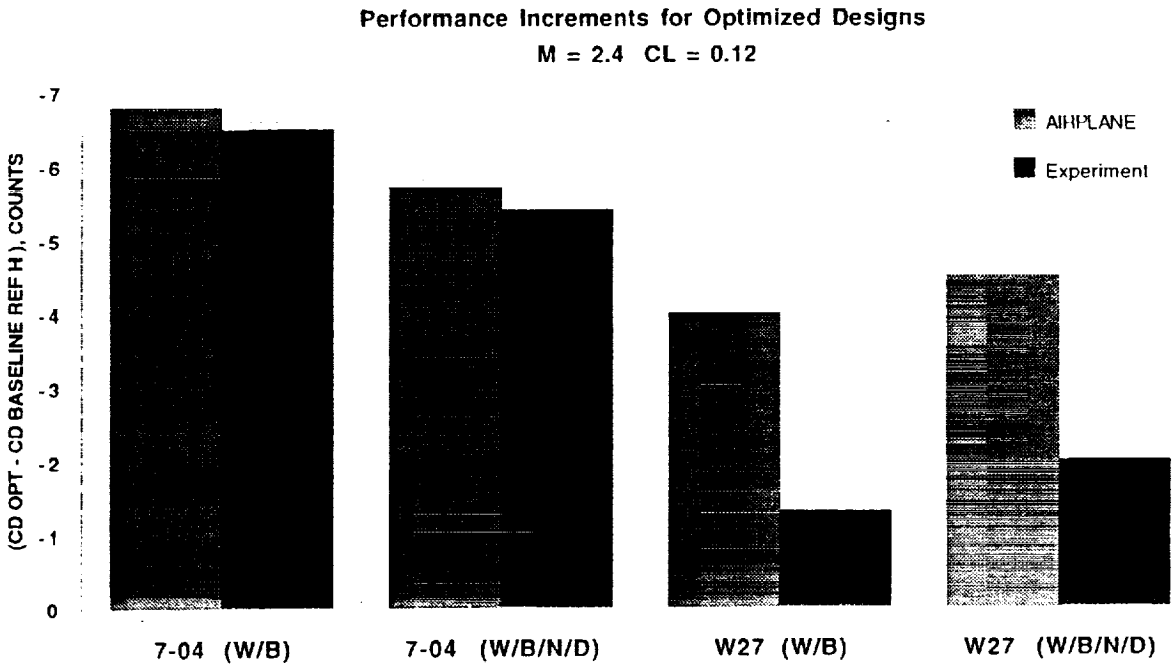

Fig 118. Performance increments of the optimized configurations compared with the baseline for AIRPLANE and experiment at cruise lift.

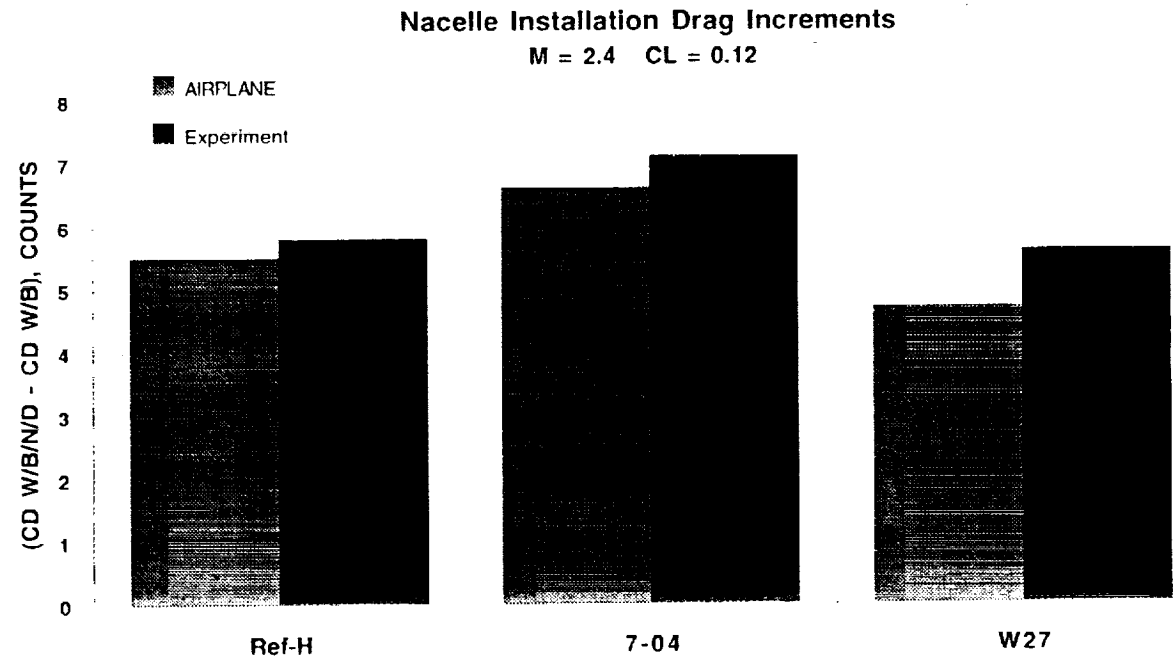

Fig 119. Drag increments due to nacelle installation for the two optimized and baseline configurations at cruise lift.

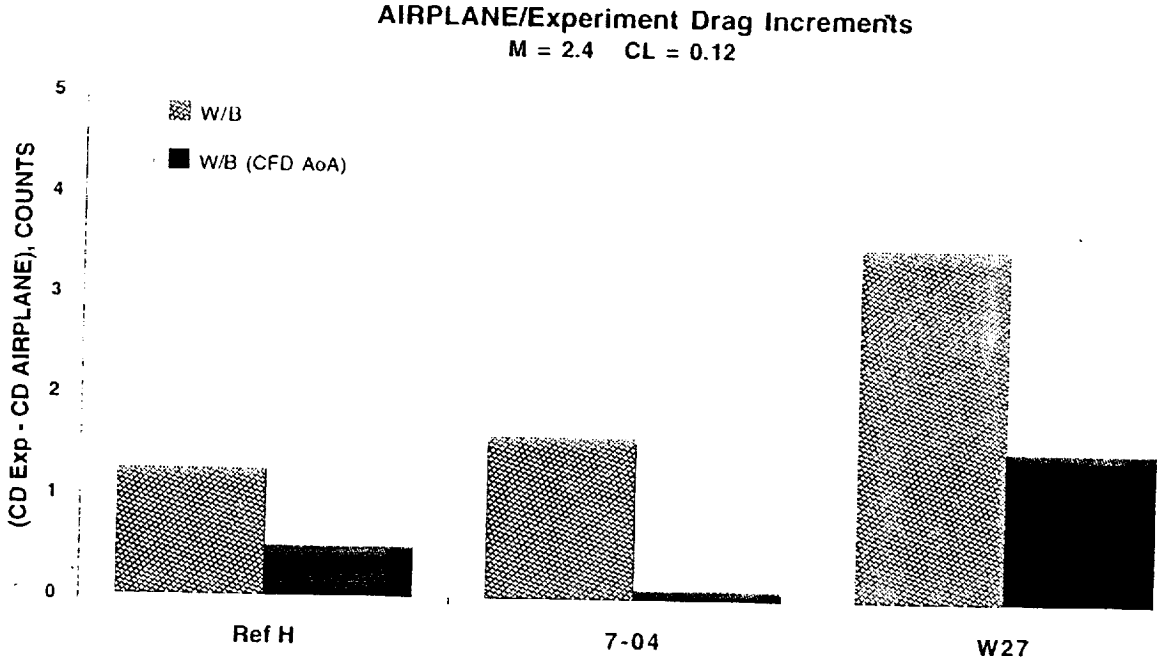

Fig 120. Drag increments between AIRPLANE and the re-computed experimental data at cruise lift for the two optimized and baseline configurations.

Update to the "*Summary of Langley Unitary Test 1649 and its Implications on Validity of Viscous and Inviscid Analyses*" Presentation in the HSR Aero. Config. Workshop

S. Yaghmaee
Boeing Commercial Airplane Group
Seattle Washington

The present report is meant to update the TLNSMB calculated results reported in the first NASA/Industry Configuration Aerodynamics Workshop held at NASA Langley Research Center. The update arises from the erroneous inclusion of the forces on the aft–body section of the configurations when comparing the results to the experimental data. Although, this update has little impact on the incremental data, it does considerably improve the agreement in the absolute lift and drag levels. In particular, the calculated drag level is now within a count of experimental data when corrected for the trip drag.

The enclosed report is intended to replace the report submitted in the workshop.

Summary of Langley Unitary Test 1649 and its Implications on Validity of Viscous and Inviscid Analyses

S. Yaghmaee and K.M. Mejia
Boeing Commercial Airplane Group
Seattle Washington

The primary objective of the NASA Langley UPWT Test 1649 was to provide accurate data for the validation of computational optimization and design methodology, in particular the validation of the non–linear inviscid methods available in the late calendar year 1994 as applied to Reference H configuration by Boeing and NASA Ames. A secondary objective was to reduce the uncertainty with the effect of outboard leading edge, trailing edge, and the body base bluntness on measured forces. The data was to be provided for wing/body and wing, body, nacelle, and diverter configurations.

The test was successful in producing accurate force data. The polar for baseline Reference H was repeated within 0.5 count of drag relative to earlier entries. For the current entry, the polars were repeatable to within 0.5 counts of drag. The sharpening of the baseline reference H configuration shaved a count of drag at cruise. The Boeing W27S configuration showed a 0.2 count of drag reduction for wing/body configuration at cruise, compared to 4.9 counts of drag reduction for Ames 704 configuration. The photos of sublimation runs, although of poor quality, validate transition. The results are disappointing with respect to the configuration designed by Boeing's inviscid methodology. However, a pretest viscous analysis compares very well with the experiment.

The Boeing methodology consists of an inviscid full–potential TRANAIR optimization followed by a viscous validation analysis. In the design of W27S configuration the viscous STUFF, a space marching Parabolized Navier–Stokes code, was used in the pretest validation. Due to shortcoming of STUFF code in modeling configurations with nacelle and diverter, it was decided to validate the TLNSMB multiblock thin layer Navier–Stokes code. The ability to model more complex configurations with TLNSMB, allows a consistent evaluation of drag increments due to various components. The TLNSMB calculations for wing/body configurations, predicted the experimental drag increment within a 0.5 counts in the lift range of interest, which is within experimental uncertainty band. The STUFF calculated increments, however, are within one count of the experimental data. In addition, the CPU time per modeling is reduced by switching form STUFF to TLNSMB code.

The inviscid analysis in the nonlinear TRANAIR optimization can lead to geometries with severe viscous/inviscid interaction at the wing/body juncture flow. The interaction can significantly reduce the anticipated drag benefit of the optimized geometry. However, a viscous analysis of the optimized geometry can validate the drag benefit with a high level of confidence. Furthermore, a viscous inspired constraint on optimization, such as a limit on the magnitude of spanwise velocity, may help inviscid optimizer avoid potential pitfalls.

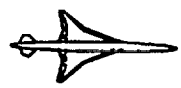

Objective

- Summarize the Unitary Test 1649.
- Cross–Validate Experimental Results with Viscous and Inviscid Computational Tools.

Objective

To summarize the Langley unitary test 1649 and cross–validate the data with viscous and inviscid computational results.

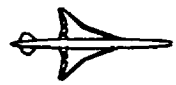

Objective of Langley Unitary Test 1649

- **Provide Accurate Data for the Validation of Computational Optimization and Design Methodologies.**
- **Particularly, The validation of Nonlinear Inviscid Methods Available in 1994.**
- **Reduce Uncertainty about the Effect of OB LE and Trailing Edge Bluntness.**

Objective of Langley Unitary Test 1649

To provide accurate data for the validation of computational optimization and design methodologies. In particular, the validation of nonlinear inviscid methods available in 1994. A secondary objective was to reduce the uncertainty about the effects of outboard leading edge, entire trailing edge, and body base bluntness on the measured forces and moments.

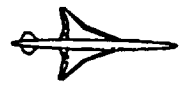

Configurations Tested

Wing/Body and Wing/Body/Nacelle/Diverter for the Following Geometries

- The Baseline Reference H
- Ames 704
- Boeing W27S
- Sharpened Reference H

Configurations Tested

The baseline Reference H configuration tested earlier.
The NASA Ames optimized configuration 704.
The Boeing optimized configuration W27S.
The baseline Reference H model had a blunter outboard leading edge, entire trailing edge,and the body base relative to other configurations. The Reference H model was sharpened to specifications and tested to remove uncertainty about the effects of bluntness on the incremental data.

All the geometries except for the last were tested with and without axisymmetric nacelle/diverter combination.

Experimental Setup

- A 1.675% Model of all Configurations
- Model Sting Mounted with Internal Balance
- Trip Strip with Dot Height of 0.009" and Spacing of 0.2"
- Mach No. of 2.4 and Model Reynolds No. of 4 Million per foot

Experimental Setup

The models were 1.675% scale of the tested configurations. Models were sting mounted with internal balance. Trip strips with dot height of 0.009" and spanwise spacing of 0.2" was used on the wing. The flow conditions were Mach 2.4 and model Reynolds number of 4 million per foot. The Reynolds number per mean aerodynamic chord was 5.7636 million.

Data Taken

- Forces and Moments
- Pictures of Sublimation Runs to Validate Boundary Layer Transition by the Trip Strip
- Pictures of Surface Streamlines from Colored Oil Flow Runs.

Data Taken

The forces and moments from the internal balance. Primarily interested in drag polars.

Two type of flow visualization were done. First, sublimation to inspect the effectiveness of the trip strip to trigger transition and establish turbulent boundary layer. Second, colored oil flow to display the surface streamlines. The photo of the visualization were used to form a photo–cd album.

Test to Test Repeatability

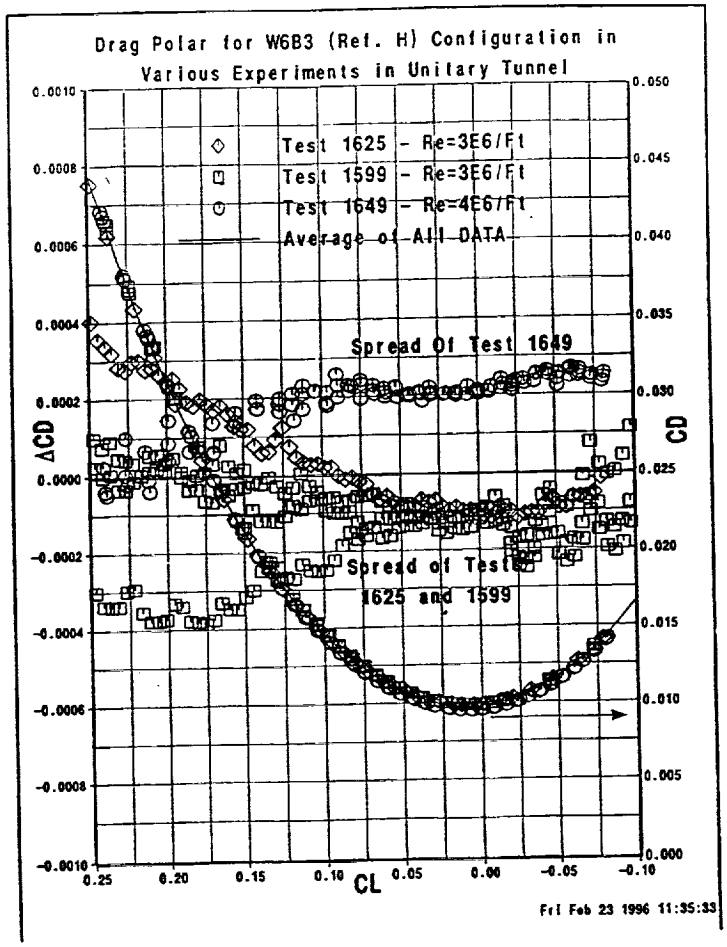

Test to Test Repeatability

The Figure shows the drag polars for baseline Reference H configuration at three tunnel entries(right ordinate). The repeated runs at all tunnel entries are merged to form a single polar. The spreads, defined as deviation at constant lift, of individual runs form the all inclusive polar are also shown(left ordinate). A positive increment indicates a lower drag value for the particular test.

The drag level for test 1649 is consistently lower than other entries by 3 counts.

The entries 1625 and 1599 are at 3 million per Ft. while 1649 is at 4 million per Ft.. This accounts for an estimated 3.5 counts. Thus, the current entry repeats earlier entries to a fraction of a count of drag when corrected for Reynolds number difference.

Lift Repeatability

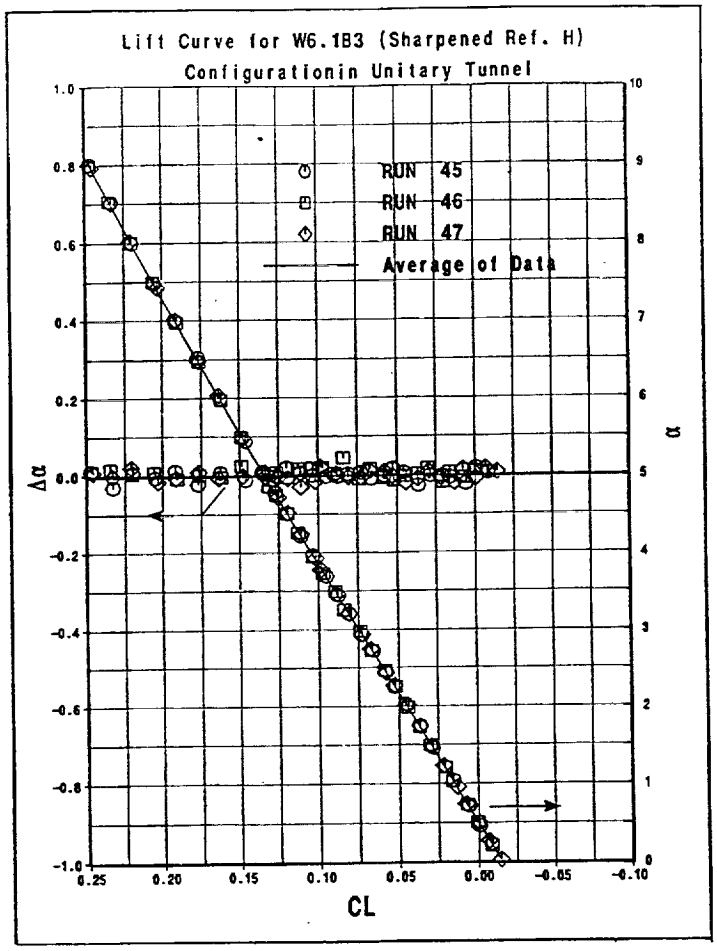

Lift Repeatability

This figure shows repeated and average lift curve for Reference H configuration in the 1649 tunnel entry (right ordinate). The spread of data from the average, defined as deviations at constant lift, is also shown (left ordinate). The angle of attack is seen to repeat itself within 0.025^{o}.

Lift Repeatability, *Cntd.*

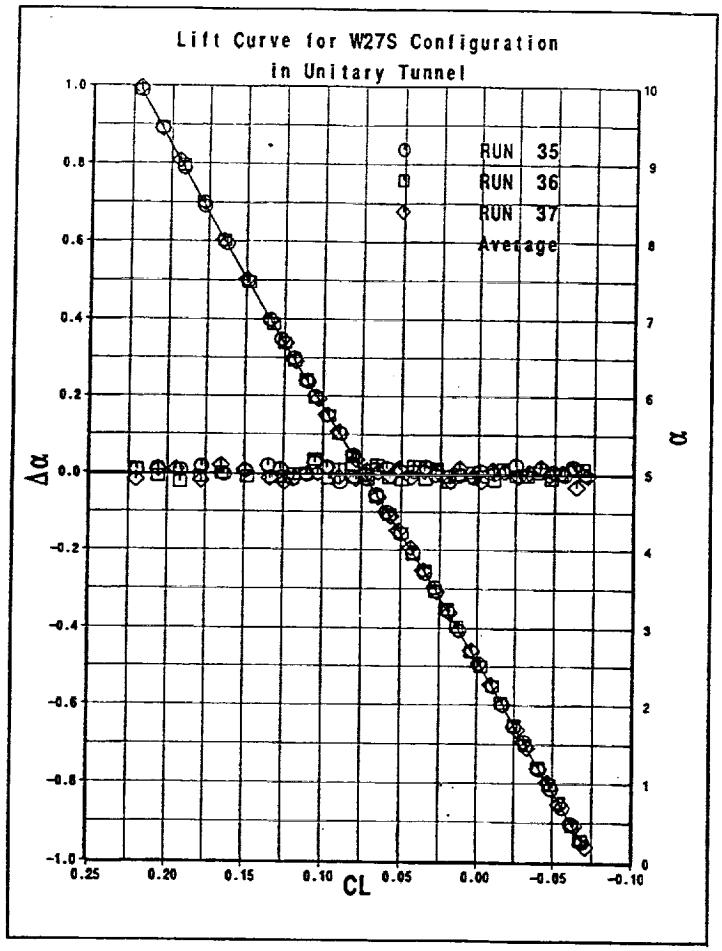

Lift Repeatability, *continued*

This figure shows repeated and average lift curve for W27S configuration in the 1649 tunnel entry (right ordinate). The spread of data from the average, defined as deviations at constant lift, is also shown (left ordinate). The angle of attack is seen to repeat itself within 0.025^{o}.

Lift Repeatability, *Cncld.*

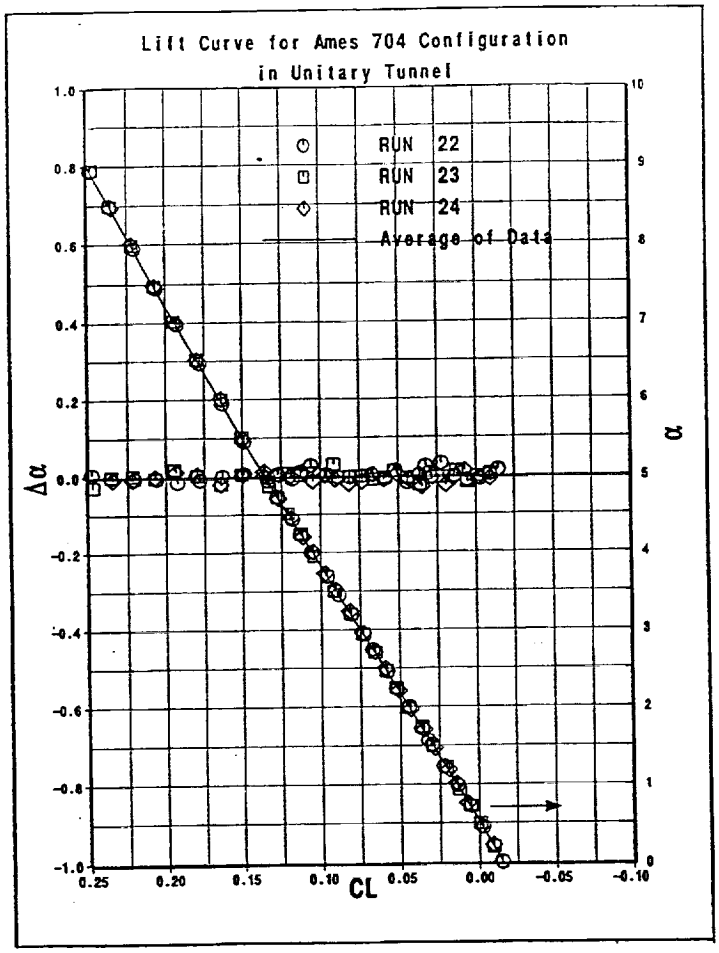

Lift Repeatability, *concluded*

This figure shows repeated and average lift curve for Ames 704 configuration in the 1649 tunnel entry (right ordinate). The spread of data from the average, defined as deviations at constant lift, is also shown (left ordinate). The angle of attack is seen to repeat itself within 0.025^{o}.

Polar Repeatability

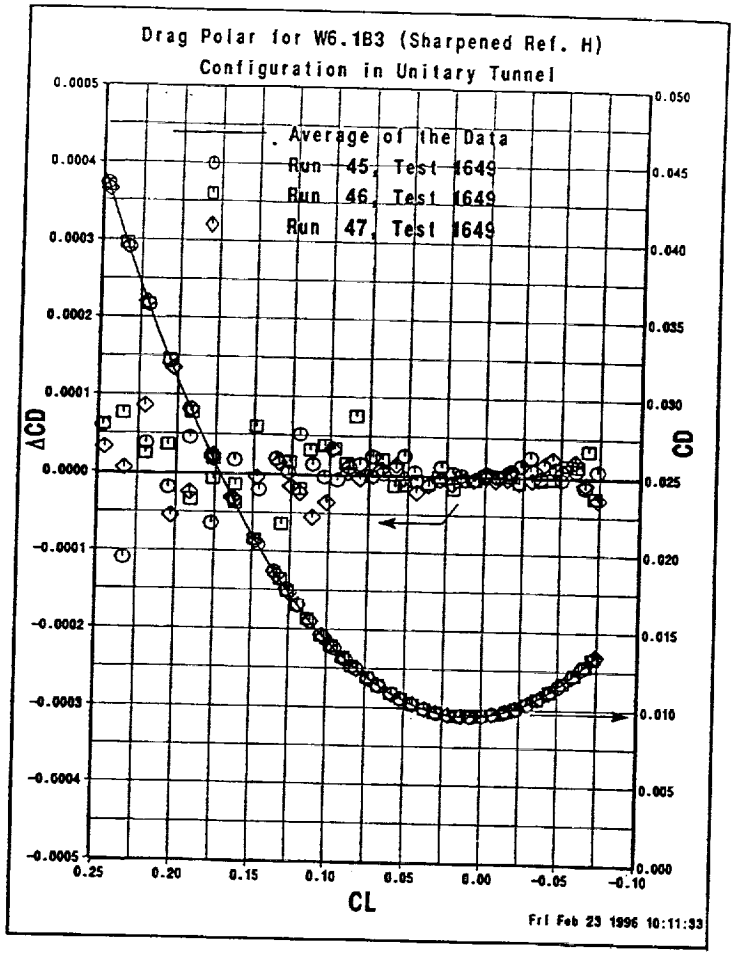

Polar Repeatability

This figure shows repeated and average drag (right ordinate) polar for sharpened Reference H configuration in the unitary 1649 tunnel entry. The spread of data from average (left ordinate), defined as deviation at constant lift, is also shown (left ordinate). The drag shows a spread of half a count for lift range of interest.

Polar Repeatability, *Cntd.*

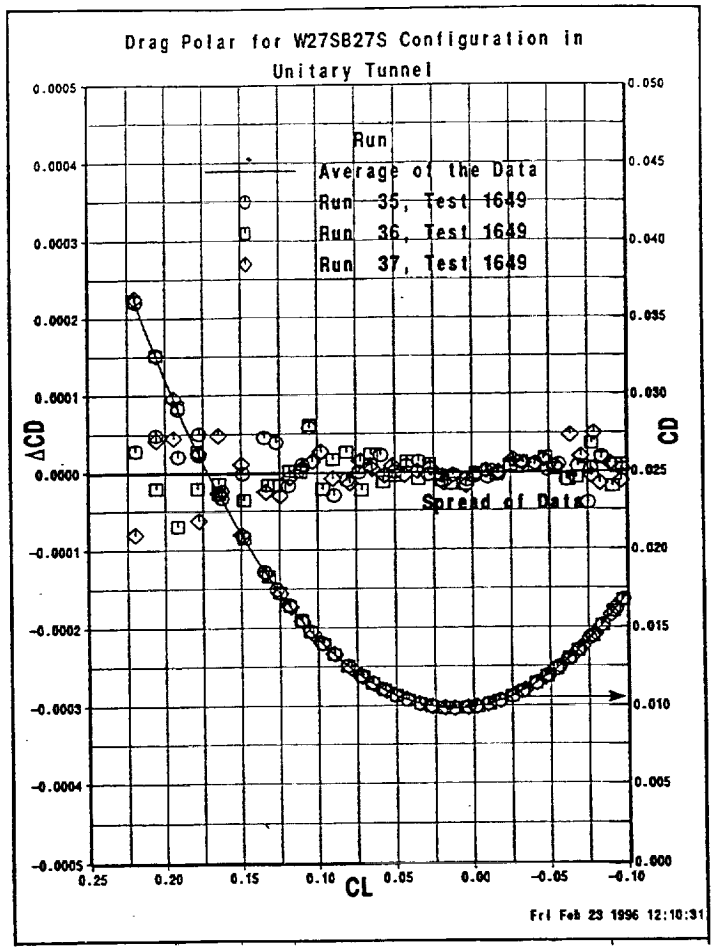

Polar Repeatability, *continued*

This figure shows repeated and average drag (right ordinate) polar for sharpened W27S configuration in the unitary 1649 tunnel entry. The spread of data from average (left ordinate), defined as deviation at constant lift, is also shown (left ordinate). The drag shows a spread of half a count for lift range of interest.

Polar Repeatability, *Cncld.*

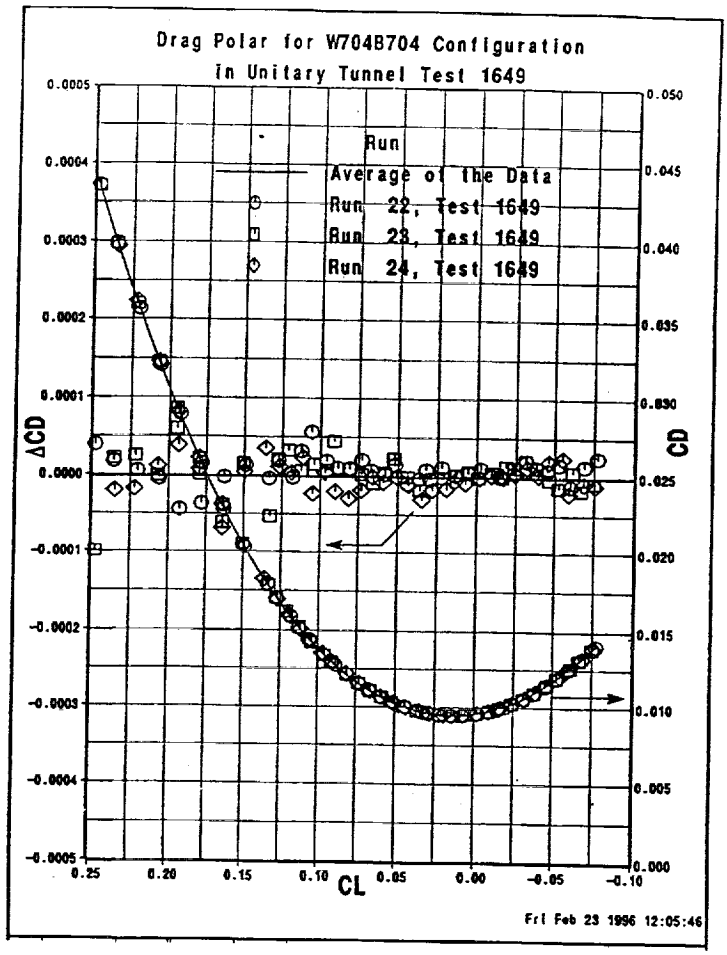

Polar Repeatability, *concluded*

This figure shows repeated and average drag (right ordinate) polar for sharpened Ames 704 configuration in the unitary 1649 tunnel entry. The spread of data from average (left ordinate), defined as deviation at constant lift, is also shown (left ordinate). The drag shows a spread of half a count for lift range of interest.

Sharpening Increment

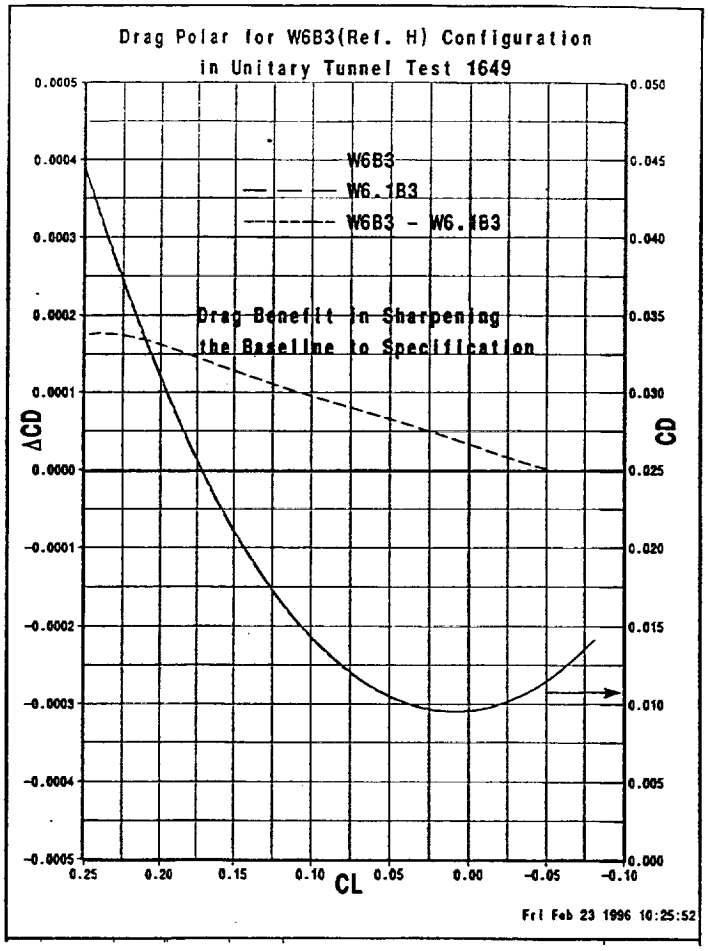

Sharpening Increment

The figure shows the drag polar for the baseline Reference H and the Ref. H sharpened to specifications (right ordinate). Also shown is drag benefit at constant lift due to sharpening (left ordinate). A positive value represents a drag improvement. The drag benefit is seen to increase linearly with lift and at cruise is one count.

Ref. H Sublimation Run

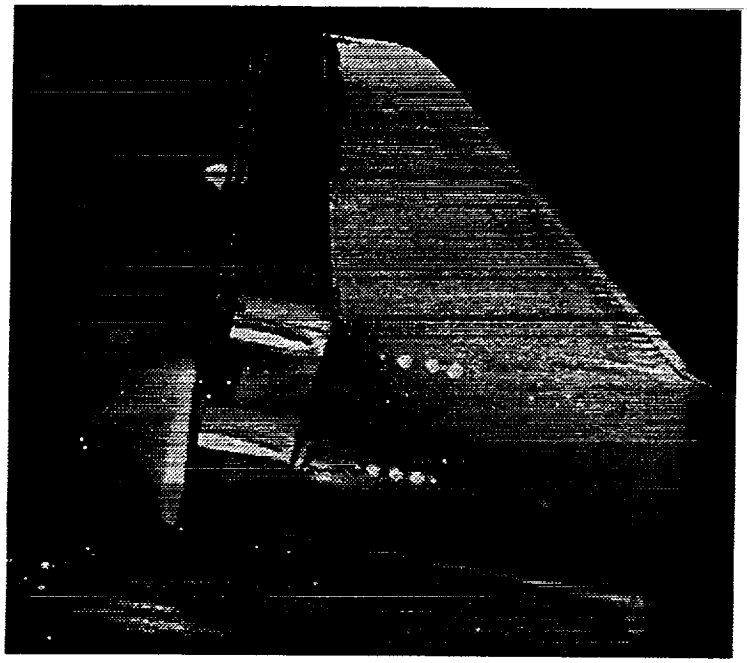

Ref. H Sublimation Run

This photo shows the sublimation run for the upper surface of the outboard wing of Ref. H configuration. The effect of the trip strip is accentuated by removal of one dot. The photo strongly suggests that the boundary layer on that part of surface is tripping. There are no clear picture of sublimation for the other segments of the wing, however, the engineers who staffed the test reported successful transition for all configurations.

W27S Sublimation Run

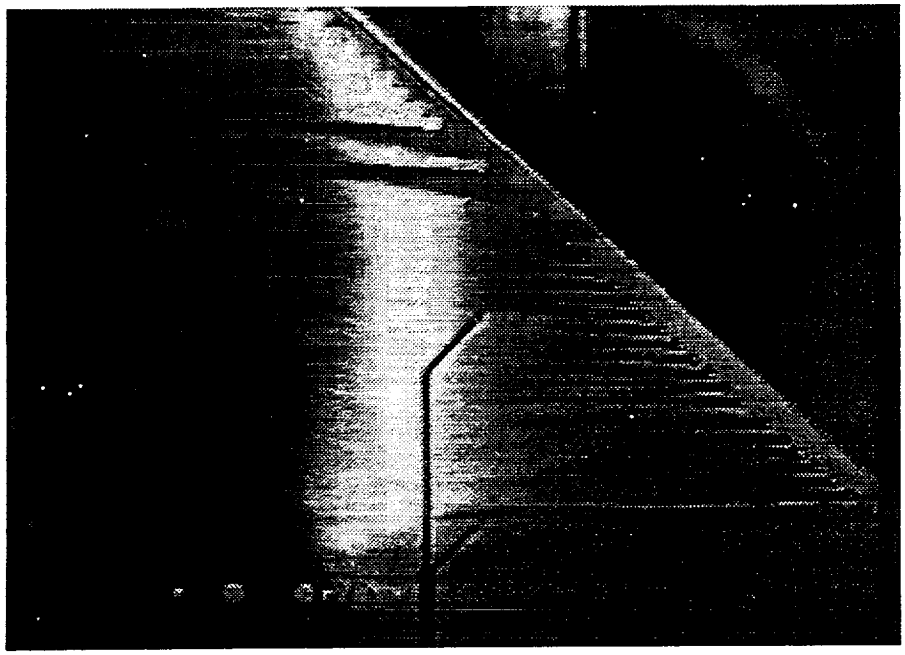

W27S Sublimation Run

This photo shows the sublimation run for the upper surface of the outboard wing of W27S configuration. The effect of the trip strip is accentuated by removal of one dot. The photo strongly suggests that the boundary layer on that part of surface is tripping. There are no clear picture of sublimation for the other segments of the wing, however, the engineers who staffed the test reported successful transition for all configurations.

Ames 704 Sublimation Run

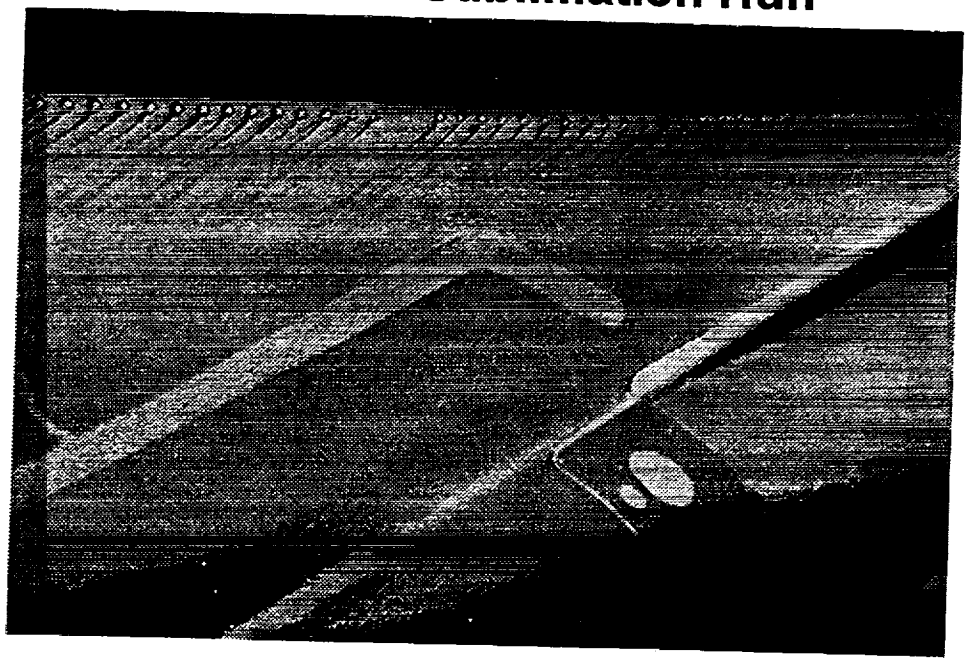

Ames 704 Sublimation Run

This photo shows the sublimation run for the upper surface of the outboard wing of Ames 704 configuration. The effect of the trip strip is accentuated by removal of one dot. The photo strongly suggests that the boundary layer on that part of surface is tripping. There are no clear picture of sublimation for the other segments of the wing, however, the engineers who staffed the test reported successful transition for all configurations. The was some concern about transition on the inboard upper surface of this configuration.

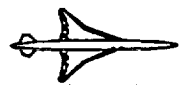

Analysis Tools

- **Earlier Design Used TRANAIR Inviscid Optimization with Viscous Validation with STUFF Code.**
- **The New Procedure is to Replace the STUFF Code with TLNSMB for Viscous Validation.**

Analysis Tools

In the previous design which led to W27S configuration, TRANAIR was used as the inviscid optimization code and the STUFF code as the viscous validation tool. The TLNSMB code will replace the STUFF code in the viscous validation process.

STUFF Calculations

- Developed by Molvic and Merkle for Modeling of Supersonic and Hypersonic Flows.
- Utilizes a 3D Finite Volume Space Marching TVD Scheme to Integrate the PNS Equations.
- Used in Pre–test Viscous Estimation of Wing/Body Configuration by G.A. Blom of BCAG.
  - Baldwin–Lomax Turbulence Model
  - Planes of 156 Circumferential by 60 Normal Cells

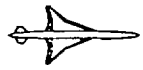

Sample STUFF Grid and Solution

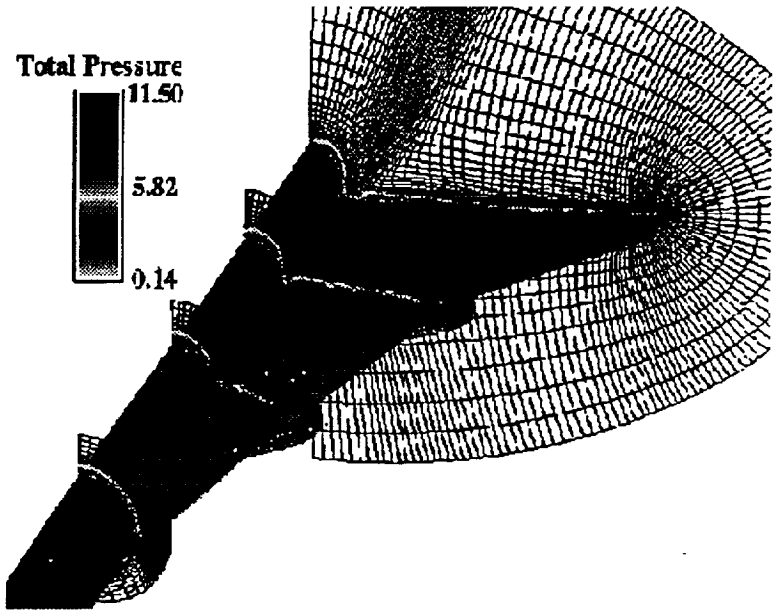

Sample STUFF Grid and Solution

This figure shows a portion of planar PNS grid, at several streamwise stations, colored by the value of total pressure. Regions of low total pressures highlight the boundary layer.

TLNSMB Code

- Multi-Block Thin Layer Navier-Stokes Solver Developed by V. Vatsa
- Utilizes Implicit Residual Smoothing, Multigrid, and Mesh Sequencing to Enhance Convergence.
- Less CPU time than STUFF Calculation
- Preferred BCAG NS Code
- Allows a Consistent Approach to the Evaluation of Drag Increments.
- Improves the Physics Relative to PNS Codes.

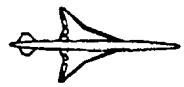

TLNSMB Calculations

- The Field Was Divided into Four Blocks.
- Each Block Was Discretized with "H" Grid.
- There Was a Total of Nearly Two Million Cells.
- Turbulent Flow Modeling with the Spalart–Allmaras Model
- Calculations were Performed with the Assistance of T.J. Kao and N.J. Yu.

Surface Streamlines, W27S

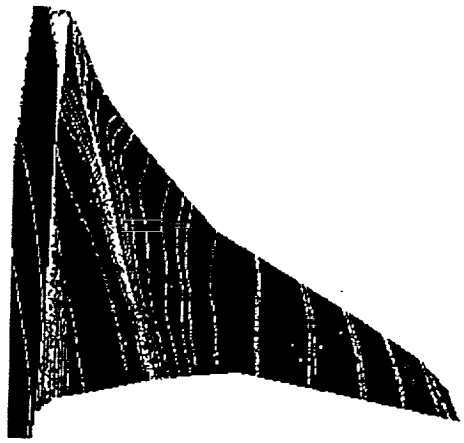

Surface Streamlines, W27S

This figures show experimental and computational surface streamlines for W27S configuration, where excellent qualitative agreement is observed.

Surface Streamlines, Ames 704

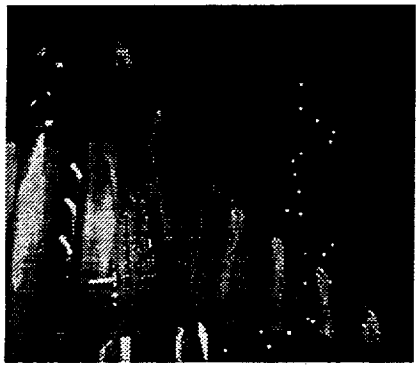

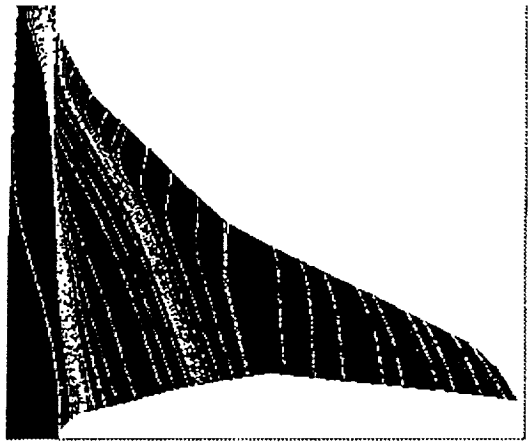

Surface Streamlines, Ames 704

This figures show experimental and computational surface streamlines for Ames 704 configuration, where excellent qualitative agreement is observed.

Lift Level Validation, Ref. H

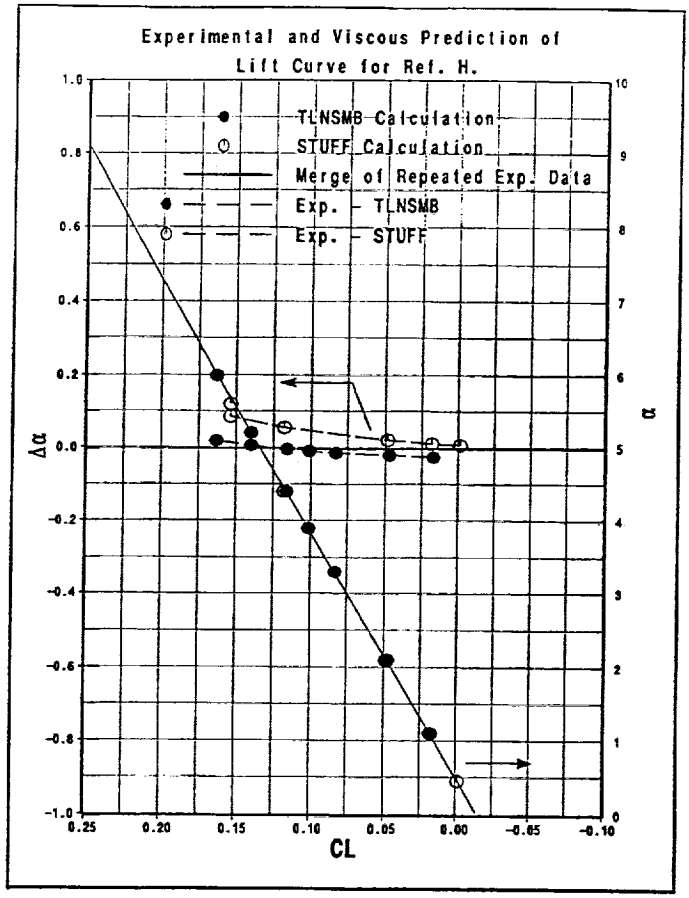

Lift Level Validation, Ref. H

This figure shows the experimental(solid line) and calculated (symbols) lift curves (right ordinate). The open symbols are viscous STUFF and the solid symbols are viscous TLNSMB results. Also shown on the plot is the difference in angle attack between experimental and calculated curves at constant lift (left ordinate). The TLNSMB calculations show a difference within ±0.02 degrees of experimental angle of attack, and is almost zero at cruise lift. The STUFF calculations show a difference of 0.05° at cruise lift.

Lift Level Validation, W27S

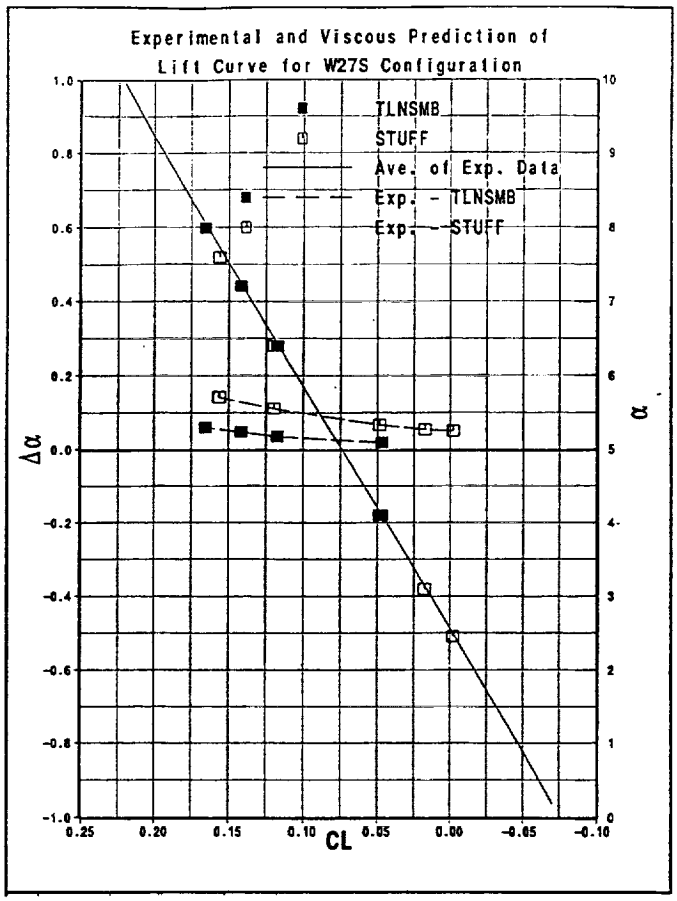

Lift Level Validation, W27S

This figure shows the experimental(solid line) and calculated (symbols) lift curves (right ordinate). The open symbols are viscous STUFF and the solid symbols are viscous TLNSMB results. Also shown on the plot is the difference in angle attack between experimental and calculated curves at constant lift (left ordinate). The TLNSMB calculations show a difference of 0.03^{o} at cruise lift. The STUFF calculations show a difference of 0.09^{o} at cruise lift.

Lift Level Validation, Ames 704

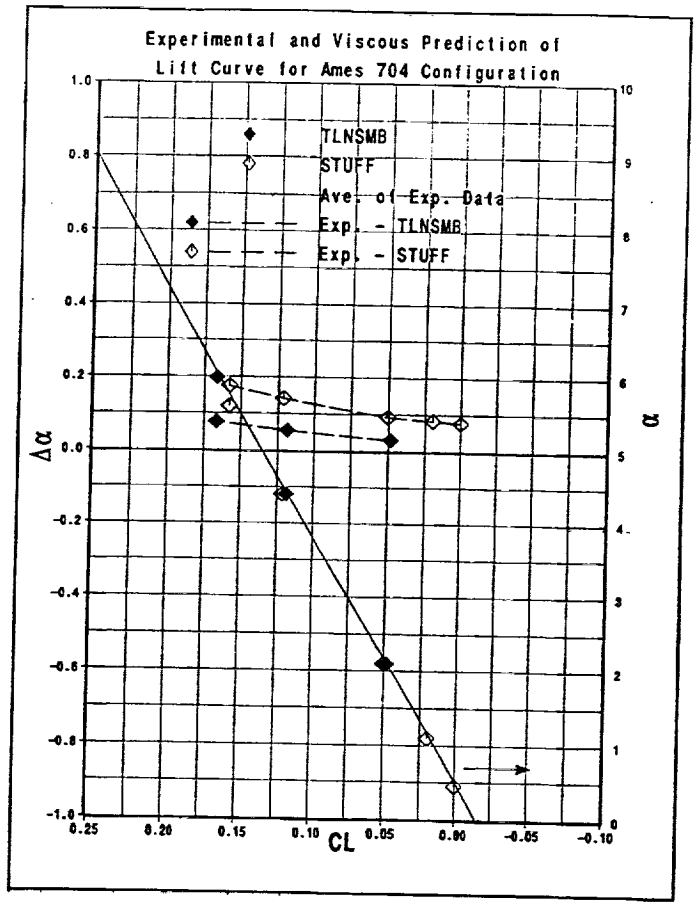

Lift Level Validation, Ames 704

This figure shows the experimental(solid line) and calculated (symbols) lift curves(right ordinate). The open symbols are viscous STUFF and the solid symbols are viscous TLNSMB results. Also shown on the plot is the difference in angle attack between experimental and calculated curves at constant lift (left ordinate). The TLNSMB results show a difference of 0.05^{o} at cruise lift. The STUFF results show a difference of 0.13^{o} at cruise lift.

Drag Level Validation, Ref. H

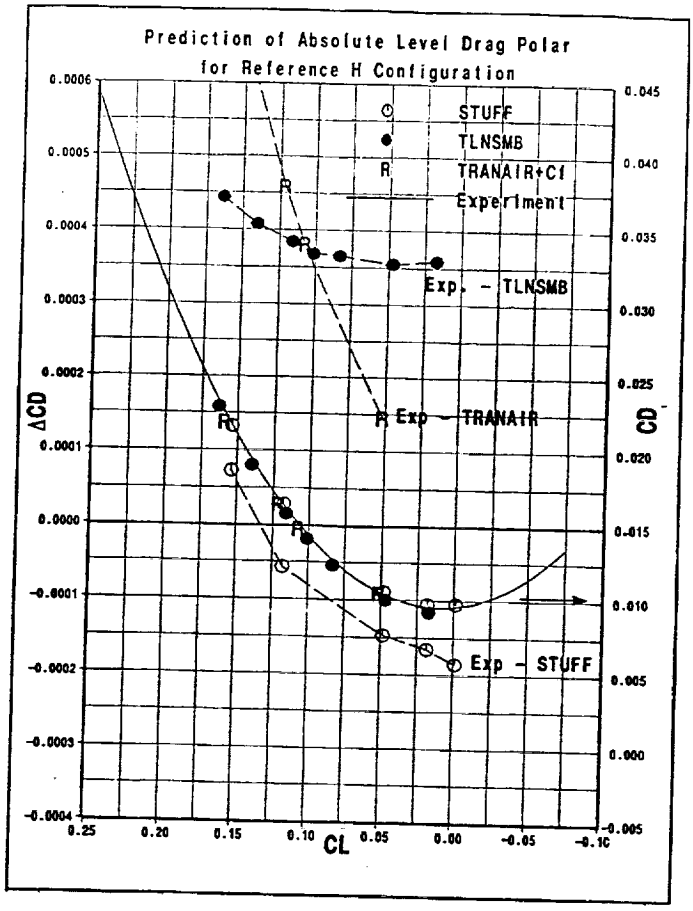

Drag Level Validation, Ref. H

This figure shows the experimental(solid line) and calculated (symbols) drag polars. The open symbols are viscous STUFF and the solid symbols are viscous TLNSMB results. The symbol "R" shows Inviscid TRANAIR plus flat plate skin friction. Also shown on the plot are the differences in drag between experimental and calculated curves at constant lift (left ordinate) for all codes. The adjusted TRANAIR results underpredict the drag. The TLNSMB results underpredict the drag within 3.75 counts of drag for lifts levels up to 0.12 (cruise for wing/body is at 0.107). The trip drag, estimated to be between 1 and 3 counts, is a large part of the difference between TLNSMB and experiment. The STUFF code overpredicts the drag by 0.75 count at cruise lift.

Drag Level Validation, W27S

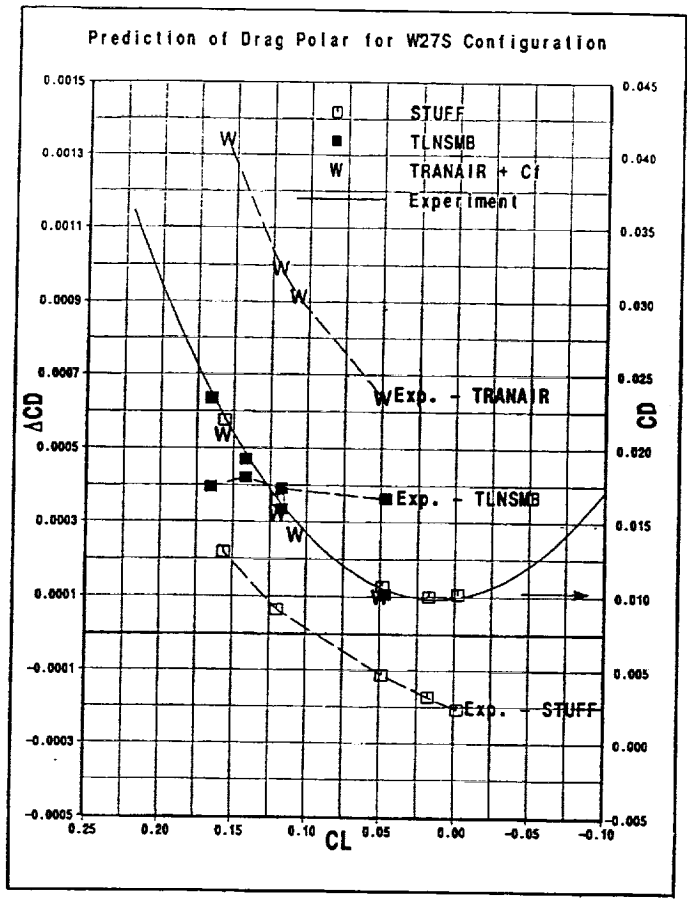

Drag Level Validation, W27S

This figure shows the experimental(solid line) and calculated (symbols) drag polars. The open symbols are viscous STUFF and the solid symbols are viscous TLNSMB results. The symbol"W" shows Inviscid TRANAIR plus flat plate skin friction. Also shown on the plot are the differences in drag between experimental and calculated curves at constant lift (left ordinate) for all codes.. The adjusted TRANAIR results underpredict the drag by a considerably larger value compared to Ref. H. The TLNSMB results underpredict the drag by 3.9 counts at cruise lift. The STUFF results underpredict the drag by 0.75 counts at cruise lift.

Drag Level Validation, Ames 704

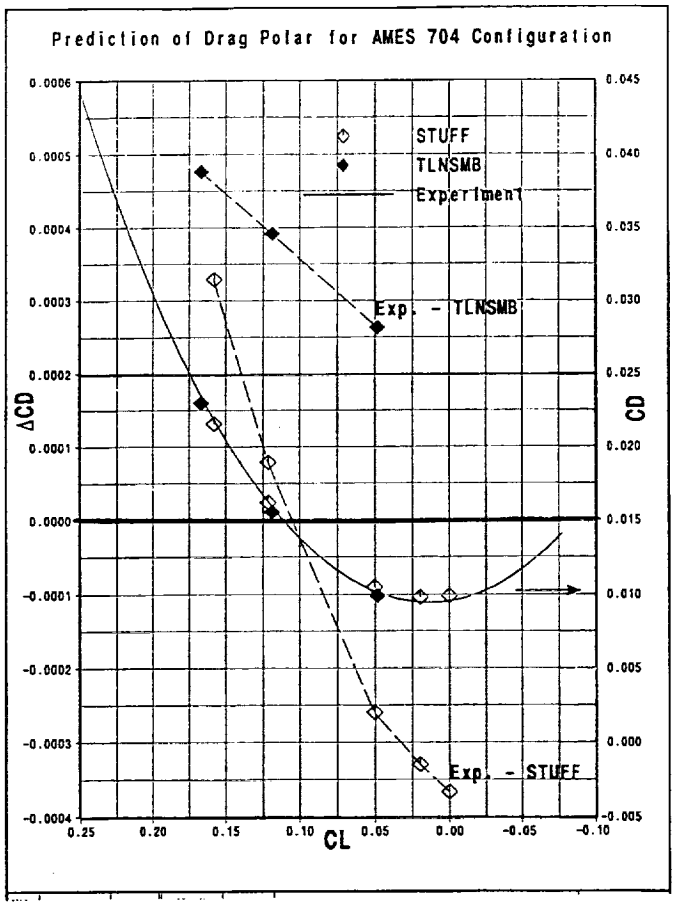

Drag Level Validation, Ames 704

This figure shows the experimental(solid line) and calculated (symbols) drag polars. The open symbols are viscous STUFF and the solid symbols are viscous TLNSMB results. Also shown on the plot are the differences in drag between experimental and calculated curves at constant lift (left ordinate) for all codes. The TLNSMB results underpredict the drag by 3.75 counts at cruise lift. The STUFF results exactly predict the drag at cruise lift.

Drag Increment Validation

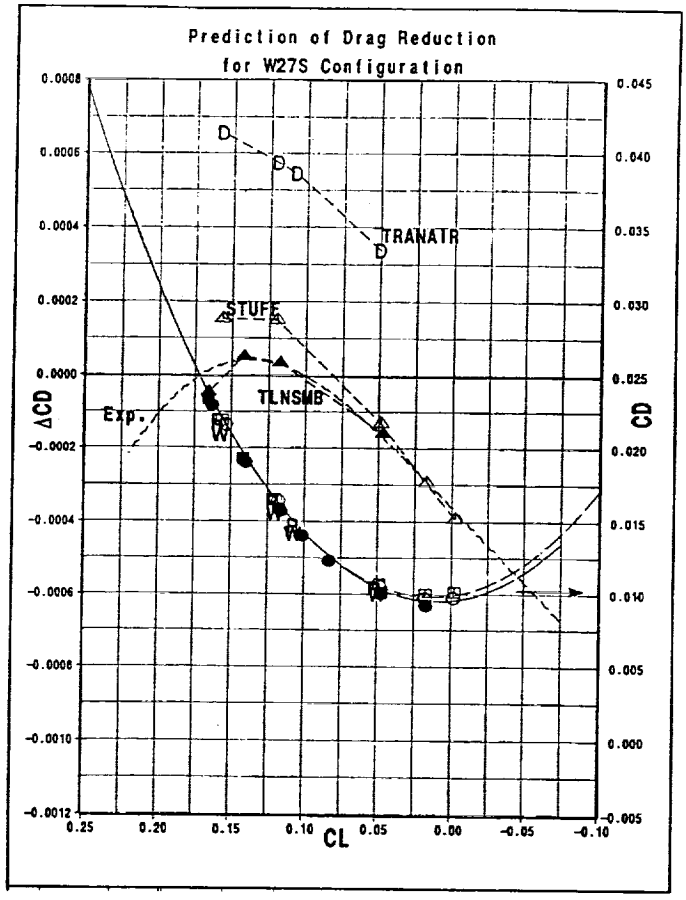

Drag Increment Validation

This figure shows the experimental(solid line) and calculated (symbols) drag polars for W27S and Ref. H wing/body configurations. The open symbols are viscous STUFF and the solid symbols are viscous TLNSMB results. The symbol"W" shows Inviscid TRANAIR plus flat plate skin friction. Also shown on the plot are the calculated and experimental increment in drag between W27S and Ref. H. A positive value is drag reduction. The experimental data show a drag improvement of 0.2 count at cruise lift. The TRANAIR results overestimate the drag benefit of W27S. The TLNSMB code is within 0.1 count of the experimental increment for lifts levels upto 0.15 which includs the cruise point. The STUFF code has similar agreement as TLNSMB for lift levels upto 0.05, however, at cruise STUFF results overestimate the drag benefit by a count .

Drag Increment Validation, *Cncld.*

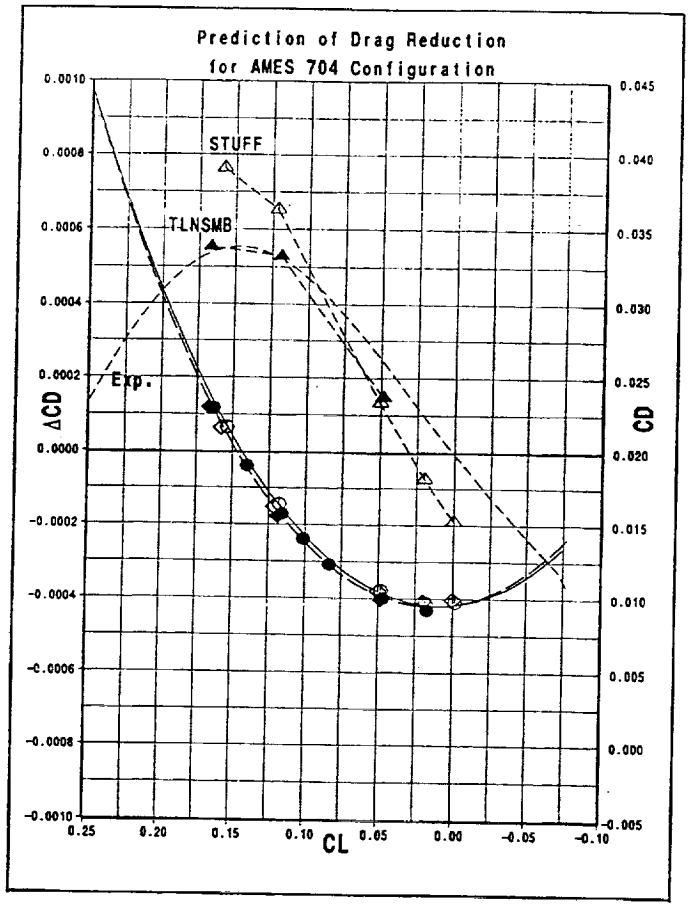

Drag Increment Validation, *concluded*

This figure shows the experimental(solid line) and calculated (symbols) drag polars for Ames 704 and Ref. H for wing/body configurations. The open symbols are viscous STUFF and the solid symbols are viscous TLNSMB results. Also shown on the plot are the calculated and experimental increments in drag between Ames 704 and Ref. H. **A positive value is drag reduction.** The experimental data show a drag improvement of 4.9 counts at cruise lift. The TLNSMB calculated increment is generally within a 0.2 counts of the experimental value. At lower lift value the agreement deteriorates to one count at CL of 0.05. At the cruise point, the TLNSMB calculated increment is 4.5 counts. The STUFF calculated increment is generally within 2 counts of the experimenal value. At cuise, STUFF estimates a 5.3 count drag reduction.

TRANAIR Calculated Cp, Ref. H

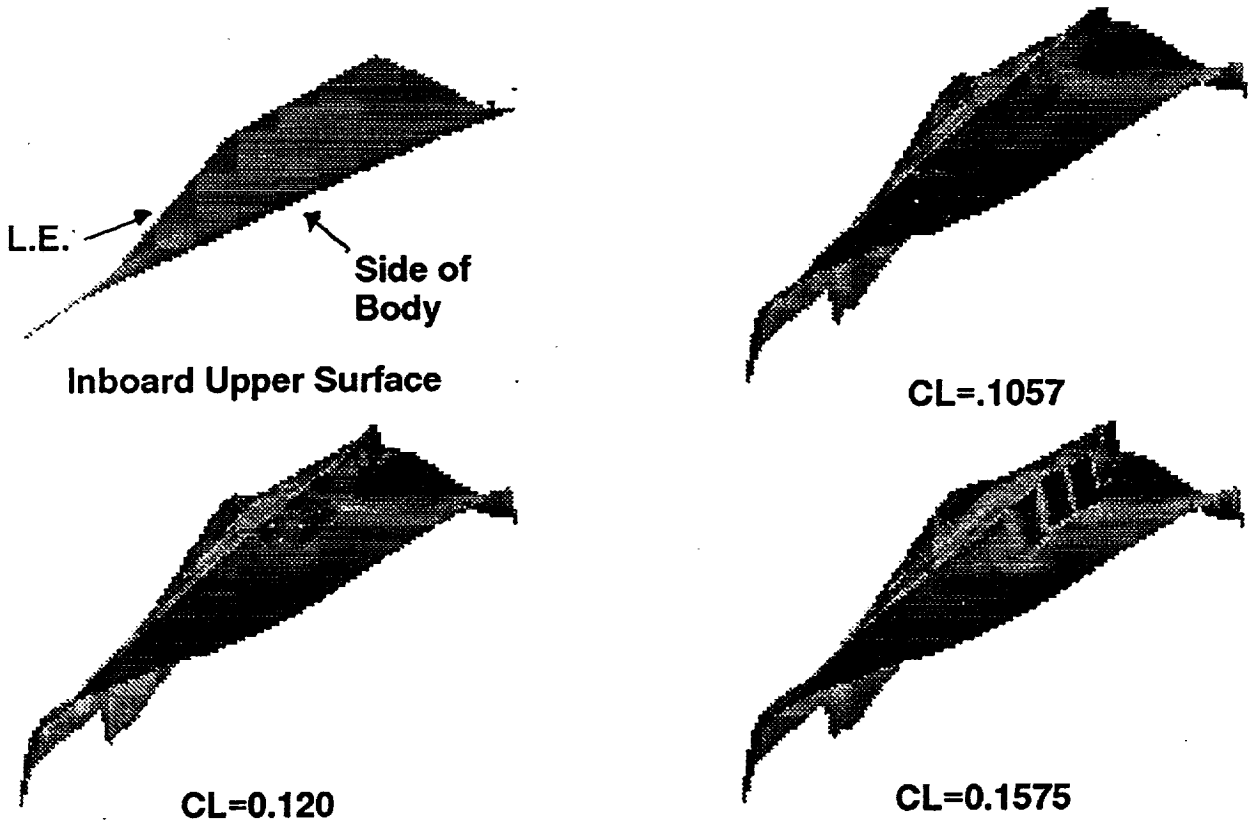

TRANAIR Calculated Cp, Ref. H

The figures show the inboard wing upper surface geometry (top left), where the side of body and the leading edge have been labeled. The other plots show the "–Cp" distribution imposed on the planform of the geometry. A section cut of this surface creates the familiar Cp vs. X plot. The leading edge expansion and the shock wave are easily identifiable. The shock wave is seen to become stronger with increasing lift.

TRANAIR Calculated Cp, W27S

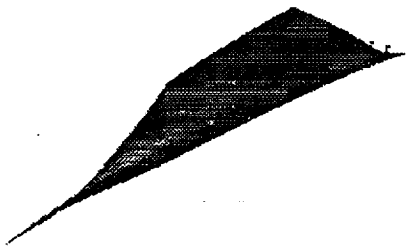

a) Inboard Upper Wing Surface

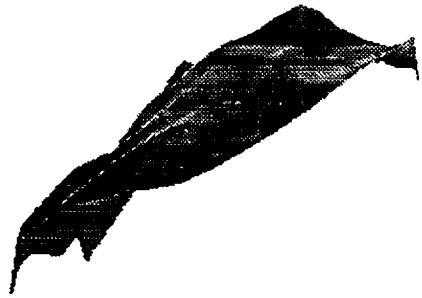

b) Pressures at Cl=0.1075

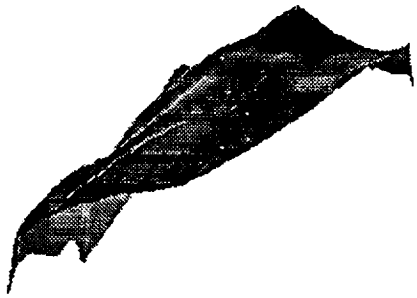

c) Pressures at Cl=0.120

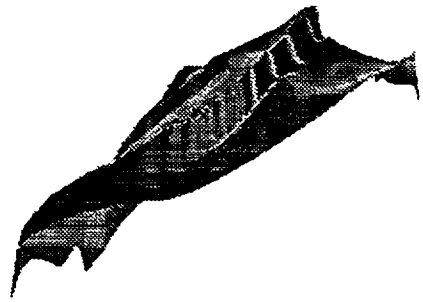

d) Pressures at Cl=0.1575

TRANAIR Calculated Cp, W27S

The figures show the inboard wing upper surface geometry (top left). The other plots show the "–Cp" distribution imposed on the planform of the geometry. A section cut of this surface creates the familiar Cp vs. X plot. The leading edge expansion and the shock wave are easily identifiable. At the highest lift level a strong shock is clearly identifiable. At lower lift levels,a sequence of two weak shocks is observed. This double shock structure is not present in the viscous calculation. This suggest that the corner boundary layer and the double shock wave strongly interact, that led to viscous losses.

TRANAIR Calculated Cross Flow

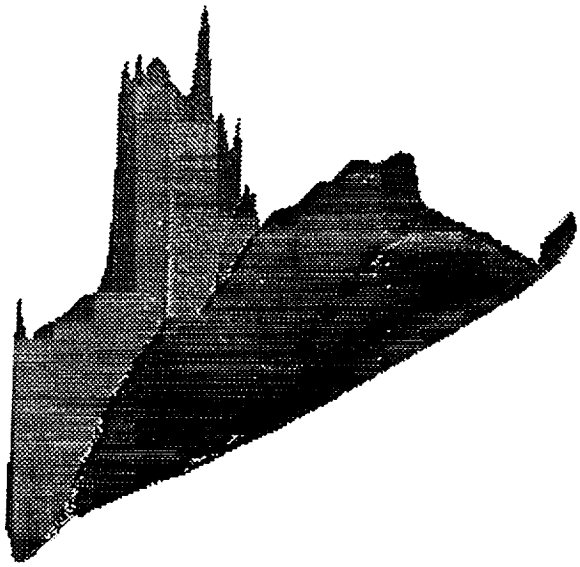

Reference H

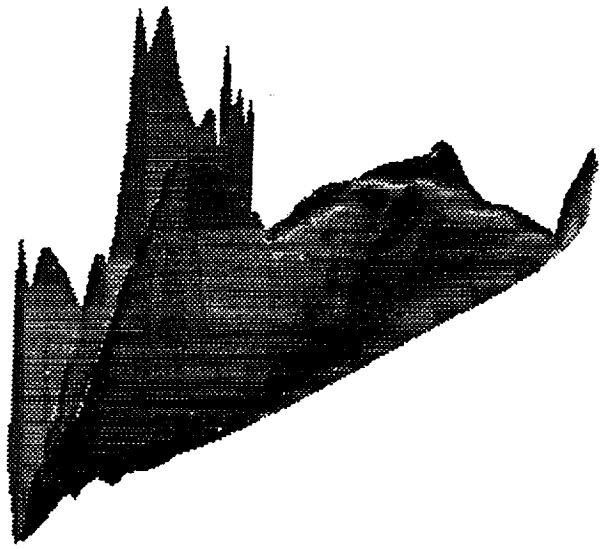

W27S

TRANAIR Calculated Cross Flow

The figures show the magnitude of the spanwise velocity distribution imposed on the planform of the inboard upper surface wing geometry for Reference H and W27S geometries. This component of velocity clearly stands out at the side of body for the W27S configuration, suggesting that it maybe a suitable candidate to be limited via a constraint on optimization.

TRANAIR Calculated Peak Cross Flow

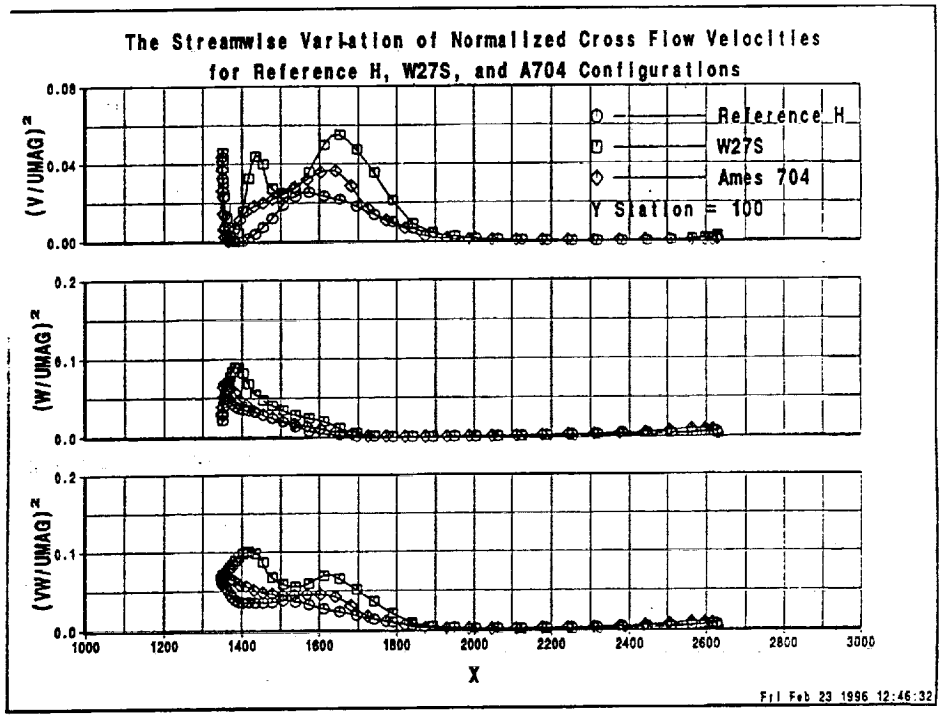

TRANAIR Calculated Peak Cross Flow

The figures show the streamwise variation of normalized magnitudes squared of spanwise, vertical, and total cross flow velocities at Wing Buttock Line of 130 inches. This section corresponds to the location of peak cross flow shown in the previous plot. The data shown are for Reference H, W27S, and Ames 704 configuration. The spanwise velocity for W27S configuration has two maxima, while the Ref. H and Ames 704 have a single maximum. The magnitude of the spanwise velocity for W27S at peak locations is higher than the maxima for the other two configurations. The normal component of velocity shows a well behaved variation for all configurations. The total cross flow velocity variations are dominated by spanwise component of velocity. The magnitude of spanwise component of velocity was chosen to form a constraint.

Conclusions, Experiment

- The Unitary 1649 Test Objective Was Met.
- Polar is Repeatable to 0.5 Count of Drag Relative to Earlier Entries.
- The Lift Curve is Repeatable to within 0.05^{o} in Incidence.
- The Polar is Repeatable to within 0.5 Counts of Drag.
- Sharpening OB L.E. , T.E., and Body Base Shaved a Count of Drag at Cruise.
- Boeing's W27S Showed 0.2 Count Drag Reduction at Cruise for Wing/Body Configuration.
- Ames 704 Showed 4.9 Counts Drag Reduction at Cruise for Wing/Body Configuration.

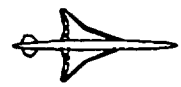

Conclusions, Computational

- Inviscid Optimization May Lead to Severe Viscous/Inviscid Interaction at Wing/Body Juncture.
- A Limit on Spanwise Velocity Magnitude may be a Simple and Effective Viscous Inspired Constraint.
- Viscous Analysis for Wing/Body Configurations Compares Very Well with the Experiment.
- TLNSMB Predicts the Increments Better Than STUFF.
- Lift Curve is within 0.05^{o} in Incidence of Exp. Data.
- Drag Polars is within 3 Counts of Exp. Data.
- Drag Increment is Generally within 0.5 Counts of Exp. Data.

Supersonic Aerodynamic Design Improvements of an Arrow-Wing HSCT Configuration Using Nonlinear Point Design Methods

Eric R. Unger
James O. Hager
Shreekant Agrawal

McDonnell Douglas Aerospace
Long Beach, California

First NASA/Industry HSR Configuration Aerodynamics Workshop
February 27-29, 1996
NASA Langley Research Center, Hampton, VA

This paper is a discussion of the supersonic nonlinear point design optimization efforts at McDonnell Douglas Aerospace under the High-Speed Research (HSR) program. The baseline for these optimization efforts has been the M2.4-7A configuration which represents an arrow-wing technology for the High-Speed Civil Transport (HSCT). Optimization work on this configuration began in early 1994 and continued into 1996. Initial work focused on optimization of the wing camber and twist on a wing/body configuration and reductions of 3.5 drag counts (Euler) were realized. The next phase of the optimization effort included fuselage camber along with the wing and a drag reduction of 5.0 counts was achieved. Including the effects of the nacelles and diverters into the optimization problem became the next focus where a reduction of 6.6 counts (Euler W/B/N/D) was eventually realized. The final two phases of the effort included a large set of constraints designed to make the final optimized configuration more realistic and they were successful albeit with a loss of performance.

Outline

- Background
- Design methods
- The Opt5 design effort
- The Opt5-A and Opt6 design efforts
- Conclusions

The presentation of this material is broken down into five major categories. The first of these is the background of MDC's wing design optimization efforts and the objectives of the efforts as related to the HSR plan. Next there is a quick look at MDC's current optimization system (MDO3D) which is similar in format to the various tools used for the optimization efforts. The next two sections are focused on the results of the study with the bulk of the material focused on the M2.4-7A Opt5 configuration which was tested in NASA Langley's UPWT supersonic 4' tunnel (the results of which will be presented later by Robert Narducci). Finally, some conclusions from the study will be presented that will summarize the optimization results to date.

Objectives

- Conduct systematic applications of the emerging non-linear aerodynamic design optimization methods to the M2.4-7A Arrow-wing configuration
- Conduct performance assessments of the M2.4-7A Arrow-wing configurations
- Define HSR HSCT geometry for wind-tunnel test verification

This effort was concerned with the development of methods to be used in optimization tasks in aerodynamic design and integration studies. The objective of this HSR effort was to adapt, assess, validate, and select nonlinear CFD methods in the application of supersonic cruise point design optimization of HSCT configurations. The results of this study were then to be used to make recommendations on methods most suitable for the HSCT design activities along with a configuration to be used for a wind-tunnel test.

MDC Arrow-Wing Design History

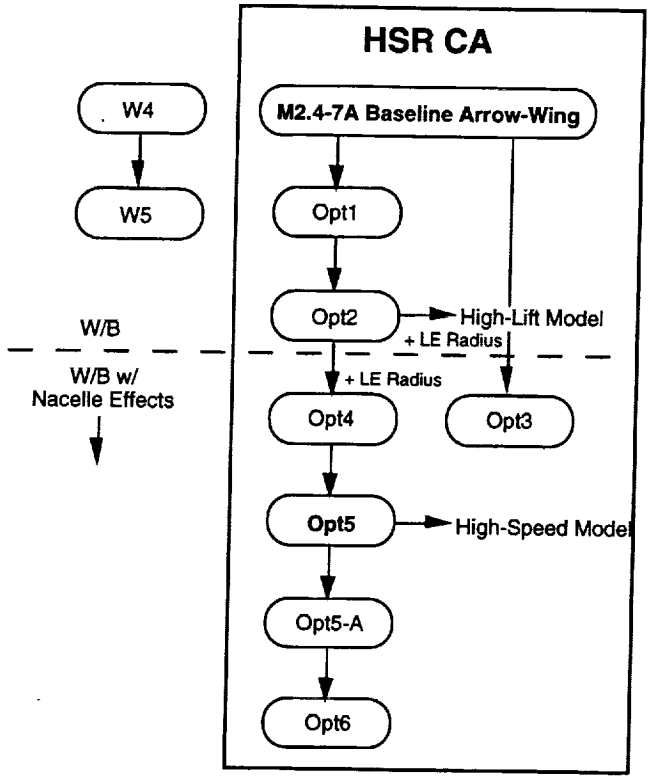

Improvements (wrt baseline):

Opt1: 3.5 cnts (Euler W/B)
Opt2: 5.0 cnts (Euler W/B)
Opt3: 3.5 cnts (Euler W/B/N/D)
Opt4: 6.0 cnts (Euler W/B/N/D)
Opt5: 2.5 cnts (Euler W/B)
4.5 cnts (N-S W/B)
6.6 cnts (Euler W/B/N/D)
Opt5-A: 6.0 cnts (Euler W/B/N/D)
Opt6: 6.5 cnts (Euler W/B/N/D)

The history of MDC's optimization efforts is shown in this chart. It began as a collaborative effort with NASA Ames Research Center in the optimization of the W4 configuration which represented the technology for a high-speed transport developed in the late 1970's. The outcome of the optimization effort was the W5 configuration which yielded a significant reduction in supersonic cruise drag over the W4 configuration, verified through wind-tunnel tests. The success of this initial effort provided the confidence for it to be applied to the HSR Configuration Aerodynamics (CA) design efforts at MDA.

The baseline configuration for the new studies was the M2.4-7A arrow-wing which represents a full configuration, not just a technology demonstrator. Wing/body optimization on this configuration began early 1994 and yielded the Opt1 configuration. The wing camber and twist were the only design variables active at this time while camber design for the fuselage had to wait until the Opt2 configuration. The Opt1 design yielded an improvement of 3.5 counts (W/B Euler) and the Opt2 yielded an improvement of 5.0 counts (W/B Euler). Note that a high-lift wind-tunnel model was built utilizing the Opt2 configuration with the addition of a much larger leading-edge radius.

Early in the Fall of 1994, wing/body optimization with nacelle/diverter effects began. The initial design for this effort was started from the M2.4-7A baseline while another configuration was initiated with the Opt2 configuration. The outcome of these efforts was the Opt3 and Opt4 configurations. The Opt4 showed considerably better performance, a 6.0 count drag reduction versus a 3.5 count reduction, despite the fact that a much larger leading-edge radius was also placed on this design. From the Opt4 configuration, another design optimization was performed (with updated nacelle effects), and the Opt5 configuration was generated and lofted for the high-speed wind-tunnel model. This configuration yielded about a 6.6 count reduction in drag over the baseline.

The final two configurations generated were the Opt5-A design which tested the impact of realistic fuselage/cabin constraints, and the Opt6 design which included these new constraints, but also allowed for some thickness variation on the wing.

Three-View of MDA HSCT M2.4-7A Configuration

- Cruise Mach no. = 2.4
- Range = 5000 n.m.
- 300 passengers
- MFTF nacelles
- Landing gear fairing

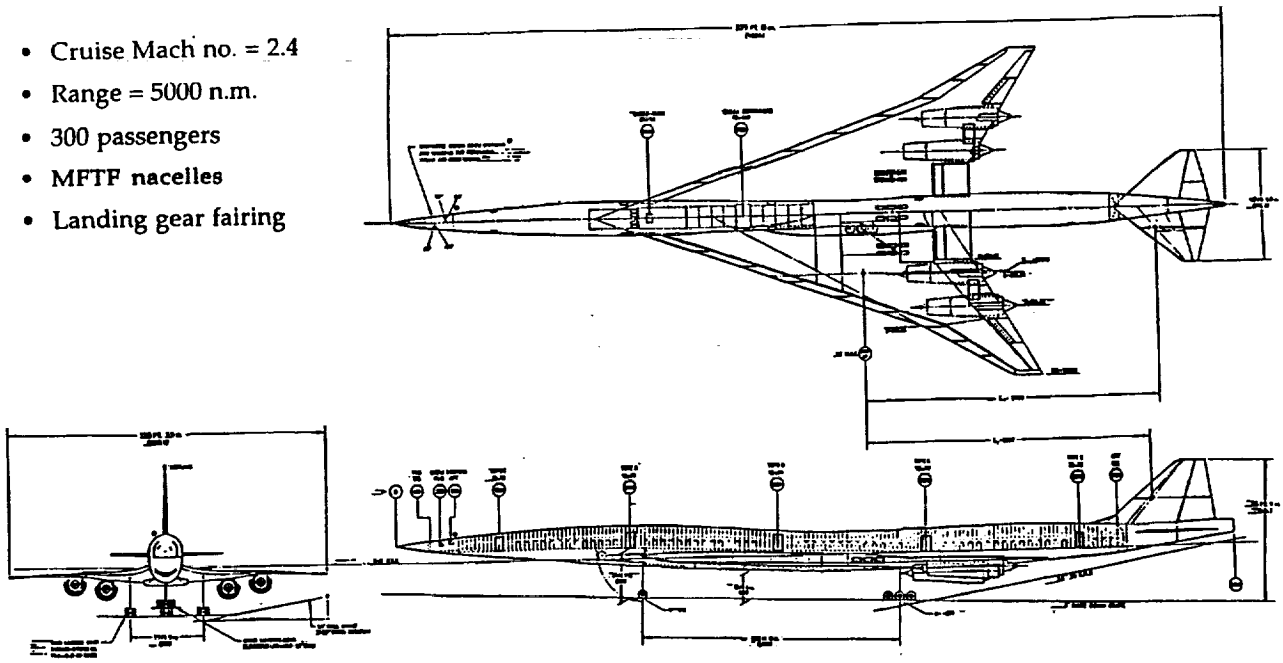

The MDA M2.4-7A configuration layout is shown. This aircraft is a full configuration that meets the mission requirements by holding 300 passengers and having a range of 5000 *nm*. This configuration uses very large mixed-flow turbofan (MFTF) engine nacelles which dominate the flow characteristics on the lower surface of the wing (the Boeing Ref. H configuration uses much smaller nacelles). Note that this configuration does have a significant landing-gear fairing on the lower portion of the wing that was not included in the optimization efforts due to the optimization analysis capabilities present at that time. The results of this optimization follow.

MDC M2.4-7A Wing Optimization

Opt5 Configuration Design

- **FLO67(WBGRID)/QNMDIFF Euler design code with nacelle effects, optimization of all variables at once (started at Opt4)**
- **Camber**
  - 4 distinct variables per span station, 7 stations on the wing (entire wing)
  - 8 distinct design variables on the fuselage
  - perturbations linearly lofted between design stations
- **Twist**
  - 1 design variable per span station, 8 stations on the wing
  - trailing edge fixed
  - perturbations linearly lofted between design stations
- **Constraints**
  - lift and pitching moment coefficients
  - cabin height
  - planform nearly fixed

This slide shows the details and background of the previously mentioned Opt5 configuration. This design used the FLO67(WBGRID)/QNMDIFF Euler design code with optimization of all variables simultaneously. The focus of this particular design was a second iteration of the wing and fuselage camber optimization with the effects of nacelles and diverters included. This design used the Opt4 configuration as a starting point and placed constraints on the cabin height and on the lift and pitching moment (as was the case with the Opt4 configuration). Note that the constraint of the pitching moment was not very strict and there was a moderate shift of the C_{M0} curve as a result of the optimization.

Lift Coefficients for the Baseline and Optimized M2.4-7A Wing/Body Configurations

CFL3D, M_∞=2.4, Forces Integrated to FS3280

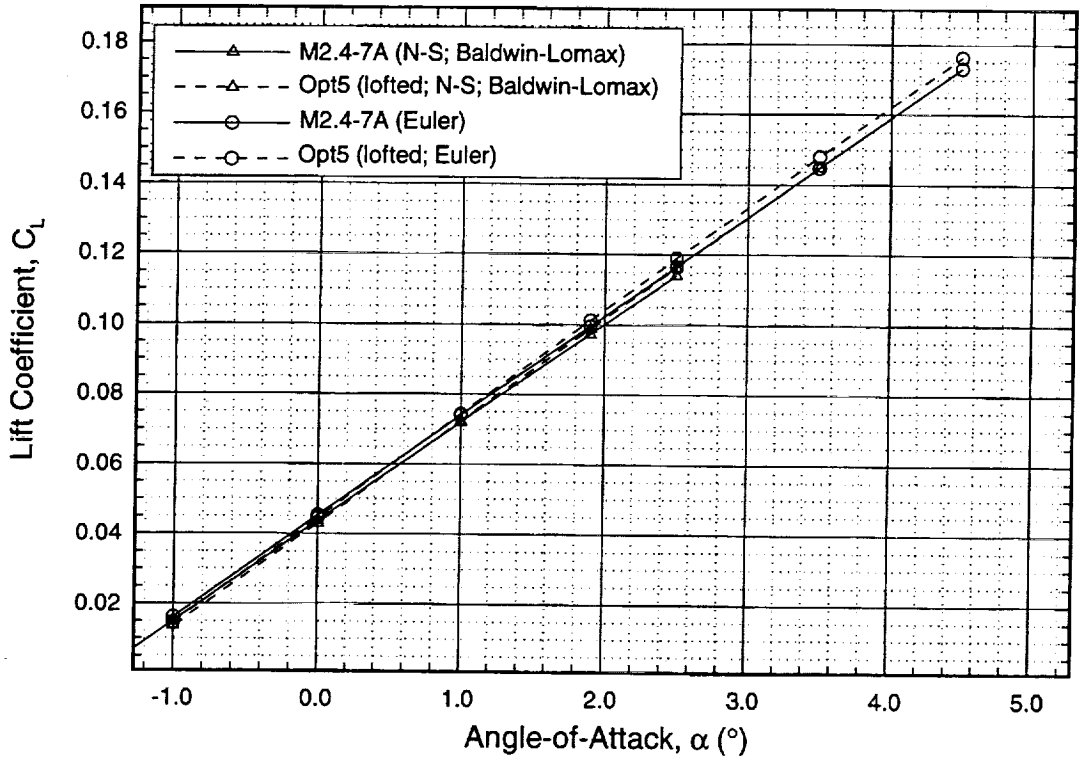

Lift curves from CFL3D Euler and Navier-Stokes analysis of the M2.4-7A Baseline and Opt5 (lofted) wing/body configurations are shown. For both the Euler and Navier-Stokes analysis, the slope of the lift curve has been for the Opt5. At this time, the driving mechanism for this phenomenon is still not fully understood, although the increased leading-edge suction of the optimized configurations may play a significant role. As expected, the Navier-Stokes analysis on both configurations yielded a lower lift curve slope than the corresponding Euler analysis.

Drag Polars for the Baseline and Optimized M2.4-7A Wing/Body Configurations

CFL3D, M_∞=2.4, Re_c=4.1x10^6, Forces Integrated to FS3280

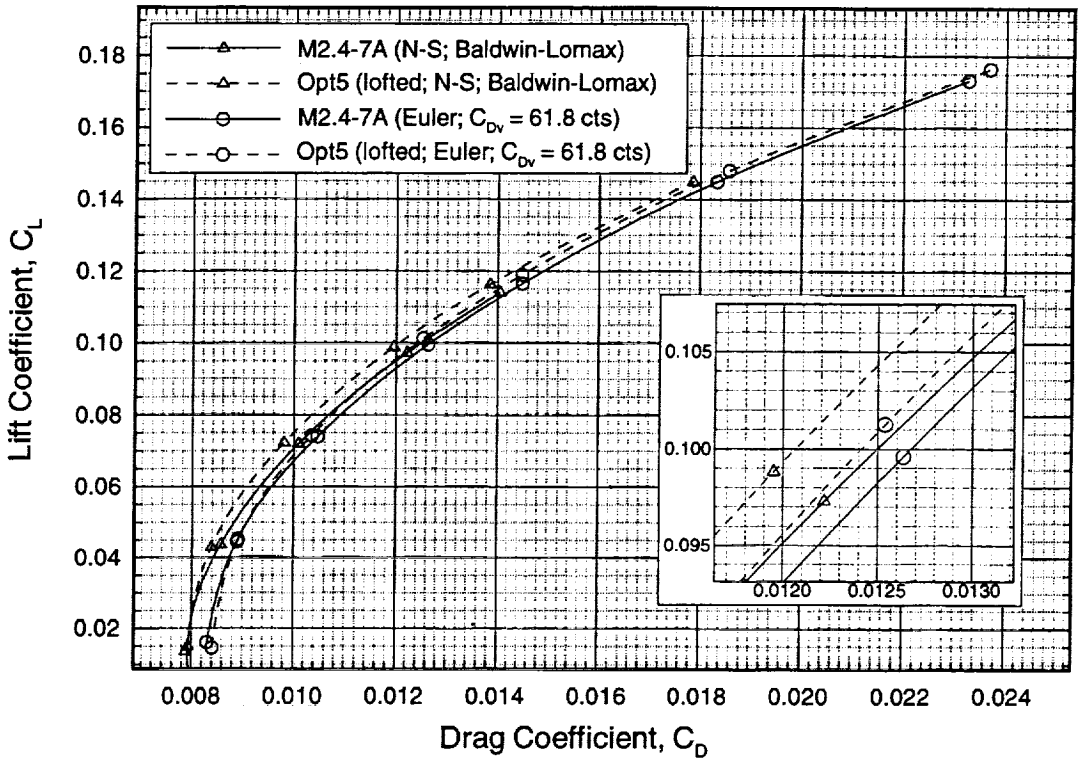

Drag polars from CFL3D Euler and Navier-Stokes analysis of the M2.4-7A Baseline and Opt5 (lofted) wing/body configurations are shown. With Euler analysis, the optimized configuration shows a 2.5 count reduction in cruise drag (C_L=0.10) over the baseline M2.4-7A design when the forces are integrated to x=3280" (note that this is with a flat-plate skin friction estimate of 61.8 counts for each configuration). With Navier-Stokes analysis, there is an unexpected result that gives a cruise drag reduction of about 4.5 counts for the optimized configuration. This increase in the drag difference between the two configurations is due to a reduction in friction drag (see next slide) for the optimized configuration despite the fact that this configuration has more wetted surface area than the baseline. Note that a separate flat-plate skin friction estimate for the Opt5 configuration actually predicts more friction drag (62.5 counts) than that of the baseline.

Friction Drag for the Baseline and Optimized M2.4-7A Wing/Body Configurations

CFL3D, M_∞=2.4, Re_c=4.1x10^6, Forces Integrated to FS3280

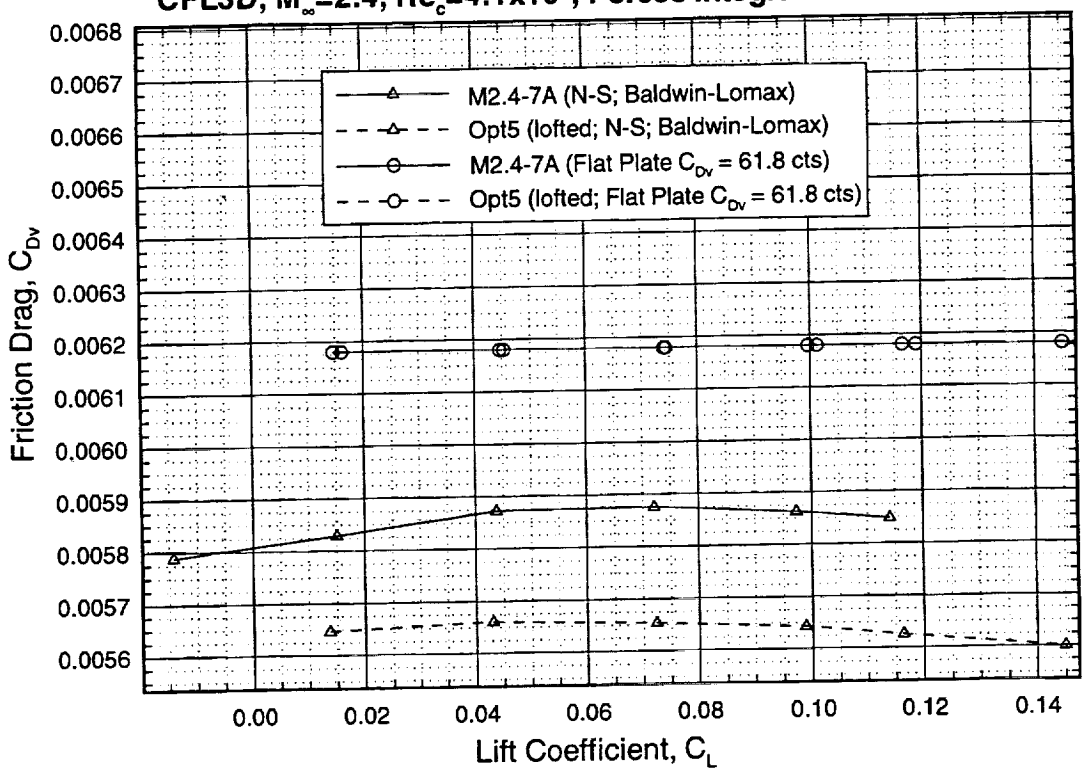

Friction drag from CFL3D Navier-Stokes analysis of the M2.4-7A Baseline and Opt5 (lofted) wing/body configurations are shown. As previously mentioned, there is a reduction in friction drag of about 2 counts for the optimized configuration (although not shown here, this result also holds true for a Reynolds number of 2.0x10^6/ft). The present explanation for this reduction is that the optimized configuration has a considerably larger region of an adverse pressure gradient (near the wing leading edge) than the M2.4-7A Baseline configuration. Note that the flat-plate skin friction estimate (Re_c=4.1x10^6) is considerably higher than the Navier-Stokes predictions.

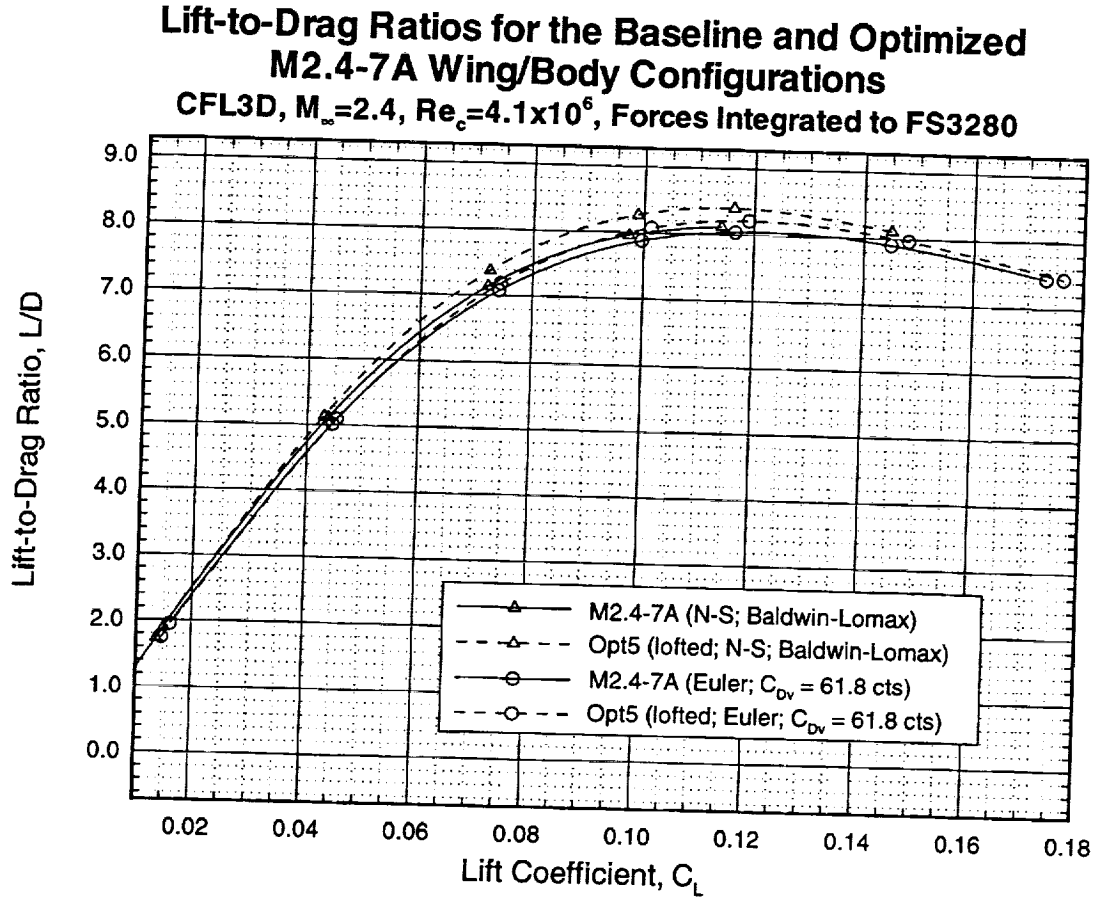

Lift-to-drag ratio curves from CFL3D Euler and Navier-Stokes analysis of the M2.4-7A Baseline and Opt5 (lofted) wing/body configurations are shown. Once again, the performance gains in the optimized configuration are clearly shown. Note that the C_L at $(L/D)_{max}$ is somewhat less for both Euler analyses due to the poor estimation of friction drag from flat-plate analysis.

Pitching Moments for the Baseline and Optimized M2.4-7A Wing/Body Configurations

CFL3D, M_∞=2.4, Re_c=2x10^6, Forces Integrated to FS3280

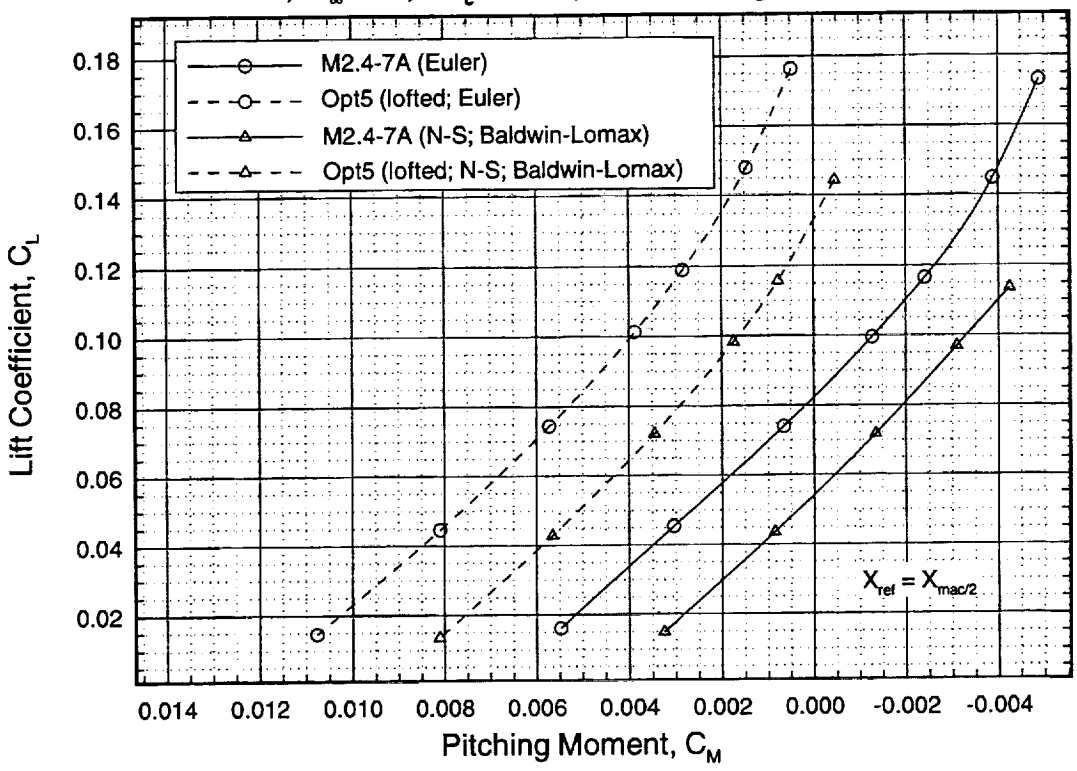

Pitching moment coefficients from CFL3D Euler and Navier-Stokes analysis of the M2.4-7A Baseline and Opt5 (lofted) wing/body configurations are shown. As previously mentioned, the constraint on the pitching moment was not strictly enforced and we see considerable shifting in the curves (although we see very little change in shape). For both the Euler and Navier-Stokes analyses, the optimized configuration generates more nose-up pitching moment which is generally considered good as it requires the tail to produce more lift for trim.

Comparison of Pressure Distributions from CFL3D Navier-Stokes Calculations for the M2.4-7A Baseline and the Opt5 Wing/Body Configurations (Re_c=4x10^6, Baldwin-Lomax)

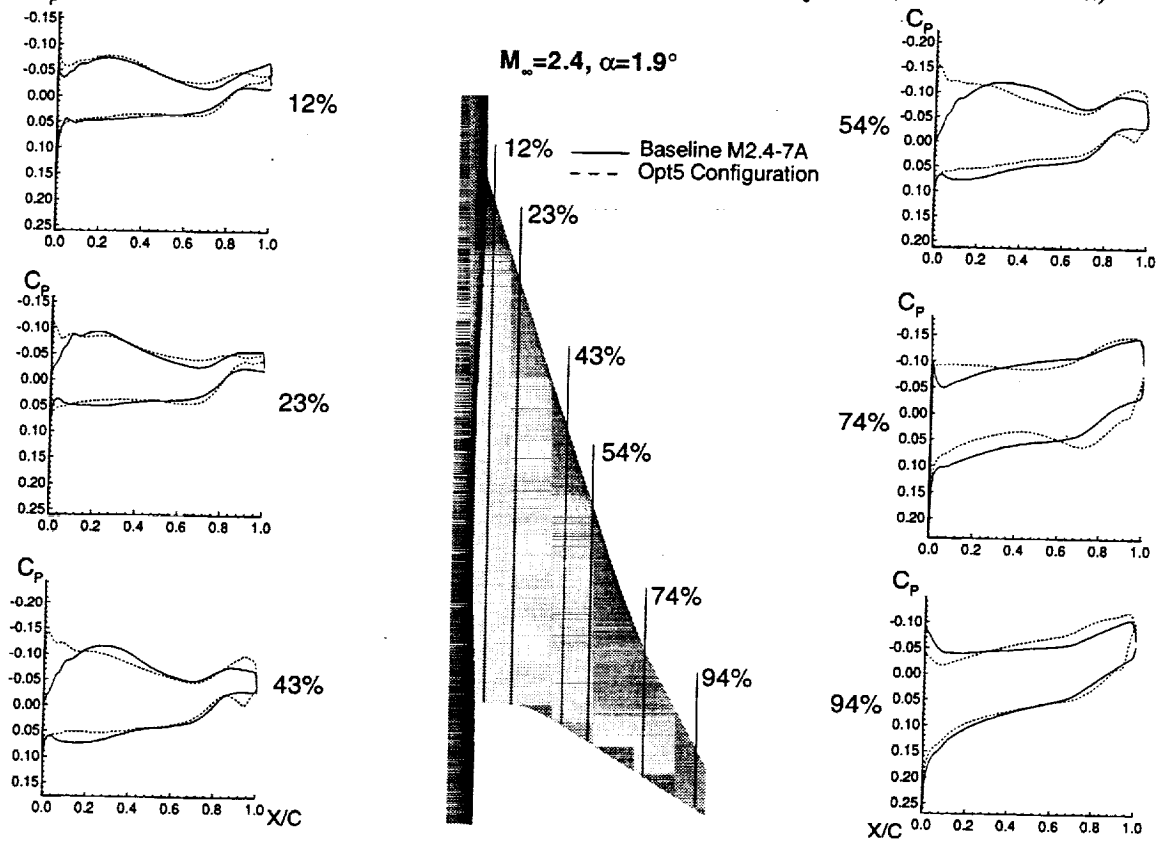

Pressure distributions from CFL3D Navier-Stokes analysis on the M2.4-7A Baseline and Opt5 (lofted) wing/body configurations are shown. The optimized configuration has much higher loading at the leading edge and a generally more even pressure distribution on the upper surface. Note that the optimized configuration also exhibits a much larger region of an adverse pressure gradient over the inboard portion of the wing. This adverse gradient has the effect of lowering the local skin friction for the configuration. Too much of an adverse gradient would lead to flow separation, although none is present for these cases.

Local Drag Contours on the Baseline M2.4–7A Wing/Body Configuration

CFL3D Navier–Stokes, Baldwin–Lomax

M_∞=2.4; α=1.9°; Re_c=4.1x10^6

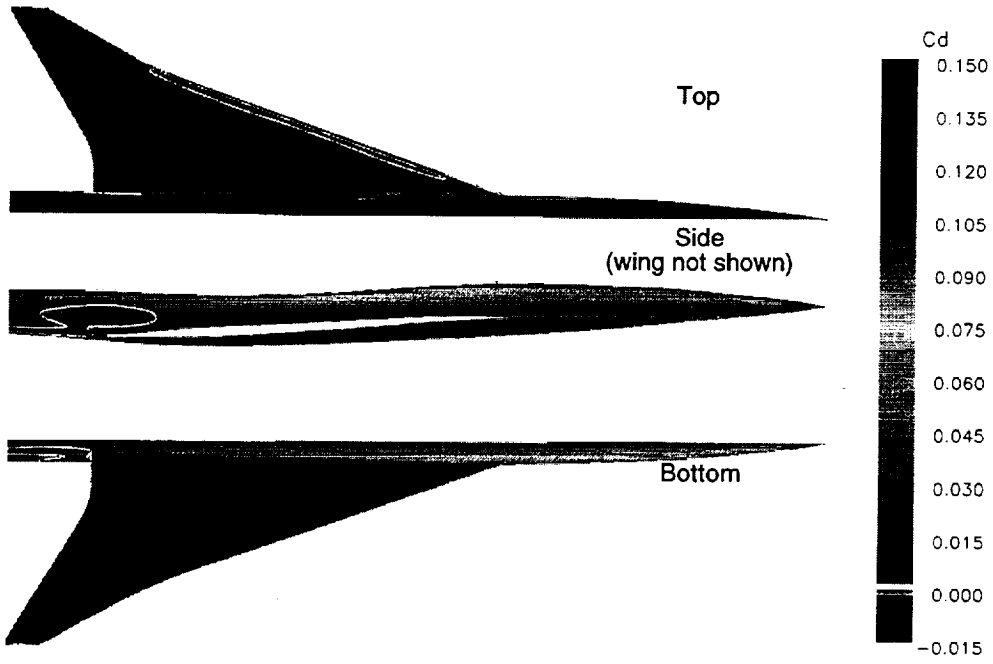

Local drag contours on the M2.4-7A Baseline configuration are shown. The purpose of this slide is to illustrate regions of the wing/body surface where a large (or small) amount of drag exists. Of the most interest for these optimization efforts are the regions of negative drag (thrust) that occur near the leading-edge of the wing. A white contour line marks the boundary of the thrusting region for this and the following contour plots. This line indicates that the thrusting region for the baseline configuration occupies a narrow band very near the wing leading edge that extends from the wing/body junction to the wing break. This leading-edge thrust is caused by low pressure flow acting over forward facing surfaces. Generally, any improvements in leading-edge thrust will increase the overall performance of the aircraft. Therefore, we would hope that any optimization effort would increase the size and intensity of leading-edge thrust. Also note that there is a small region of thrust on the body surface near the wing trailing edge. Please see the next slide for a similar plot of the optimized configuration.

Local Drag Contours on the M2.4–7A Opt5 Wing/Body Configuration

CFL3D Navier–Stokes, Baldwin–Lomax

M_∞=2.4; α=1.9°; Re_c=4.1x10^6

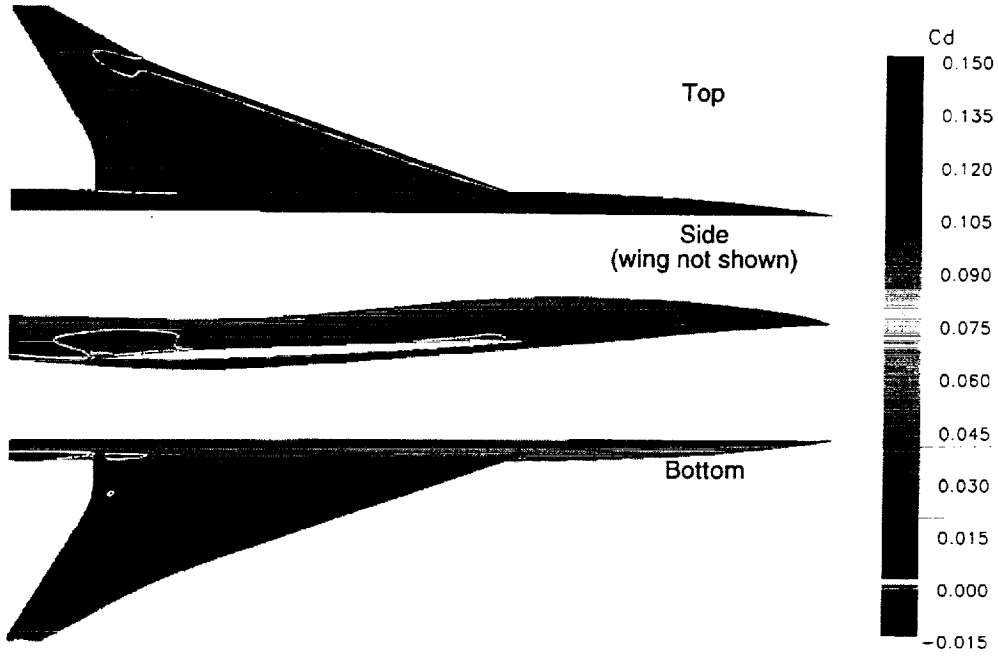

Local drag contours on the M2.4-7A Opt5 configuration are shown. This slide is a follow-on to the previous one and demonstrates that the optimization process did in fact increase both the size and intensity of the thrusting portion of the wing. One can see that the leading-edge thrust is even closer to the wing leading edge and extends from the wing/body junction to beyond the wing break, where a small region extents almost to the wing midchord. It is also clear that the intensity of the thrust is greater on the optimized configuration (although this may be difficult to see on a black-and-white reproduction). The small thrusting region on the body near the wing trailing edge is still present on the optimized configuration and it is slightly larger than before. If one also looks at the lower-wing surface on the optimized configuration, it appears that the drag on the leading edge (lower surface) has been slightly reduced.

Lift Coefficients for the Baseline and Optimized M2.4-7A Wing/Body/Nacelle/Diverter Configurations

CFL3D, Euler, M_∞=2.4, Forces Integrated to FS3280

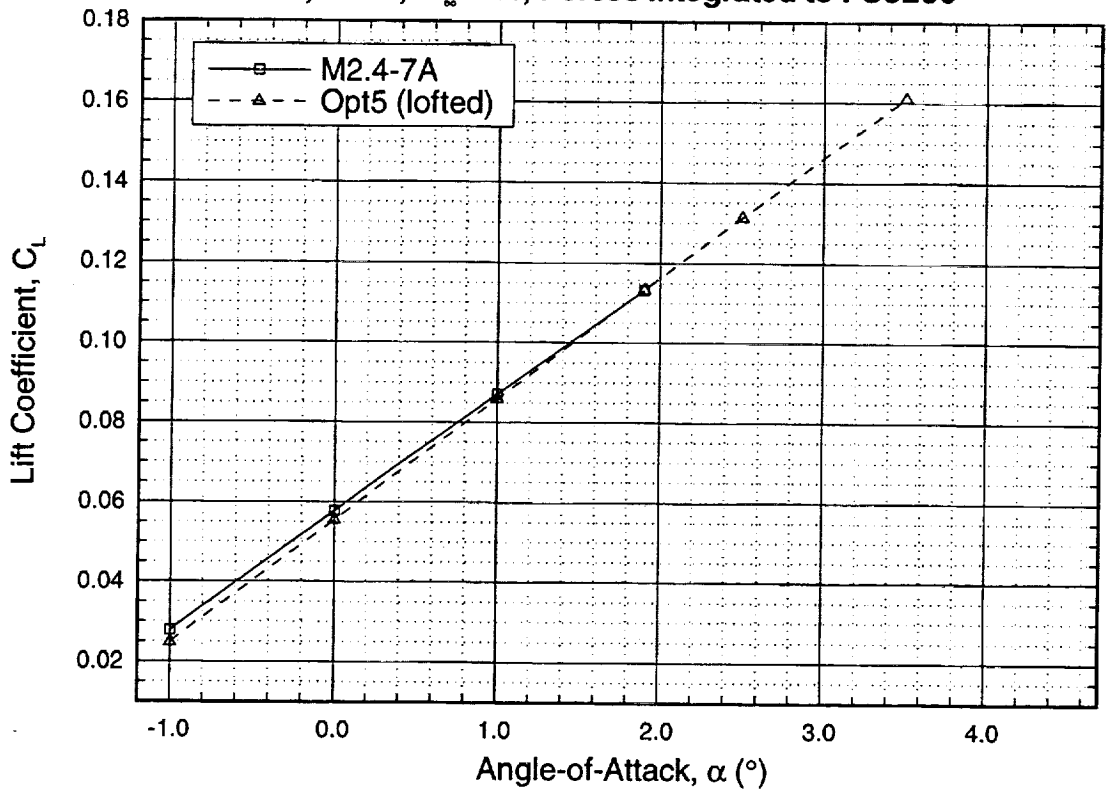

Lift curves from CFL3D Euler analysis of the M2.4-7A Baseline and Opt5 (lofted) wing/body/nacelle/diverter configurations are shown. As with the wing/body analysis case, the slope of the lift curve is larger for the Opt5. Once again, the driving mechanism for this phenomenon is still not fully understood, although the increased leading-edge suction of the optimized configurations may play a significant role.

Pressure Drag Polars for the Baseline and Optimized M2.4-7A Wing/Body/Nacelle/Diverter Configurations

CFL3D, Euler, M_∞=2.4, Forces Integrated to FS3280

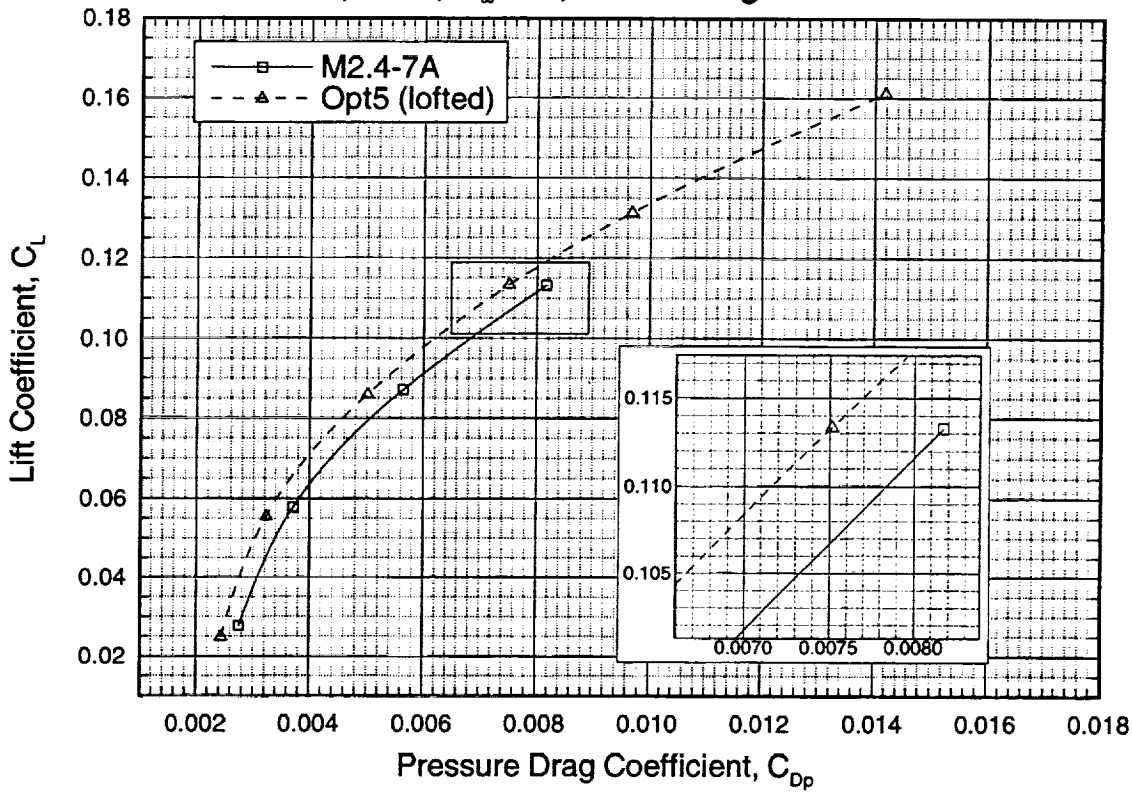

Pressure drag polars from CFL3D Euler analysis of the M2.4-7A Baseline and Opt5 (lofted) wing/body/nacelle/diverter configurations are shown. The optimized configuration shows a 6.6 count reduction in cruise pressure drag (C_L=0.11) over the baseline configuration when the forces are integrated to x=3280'.

Pressure Distributions for the Baseline and Opt5 M2.4-7A Wing/Body/Nacelle/Diverter Configurations

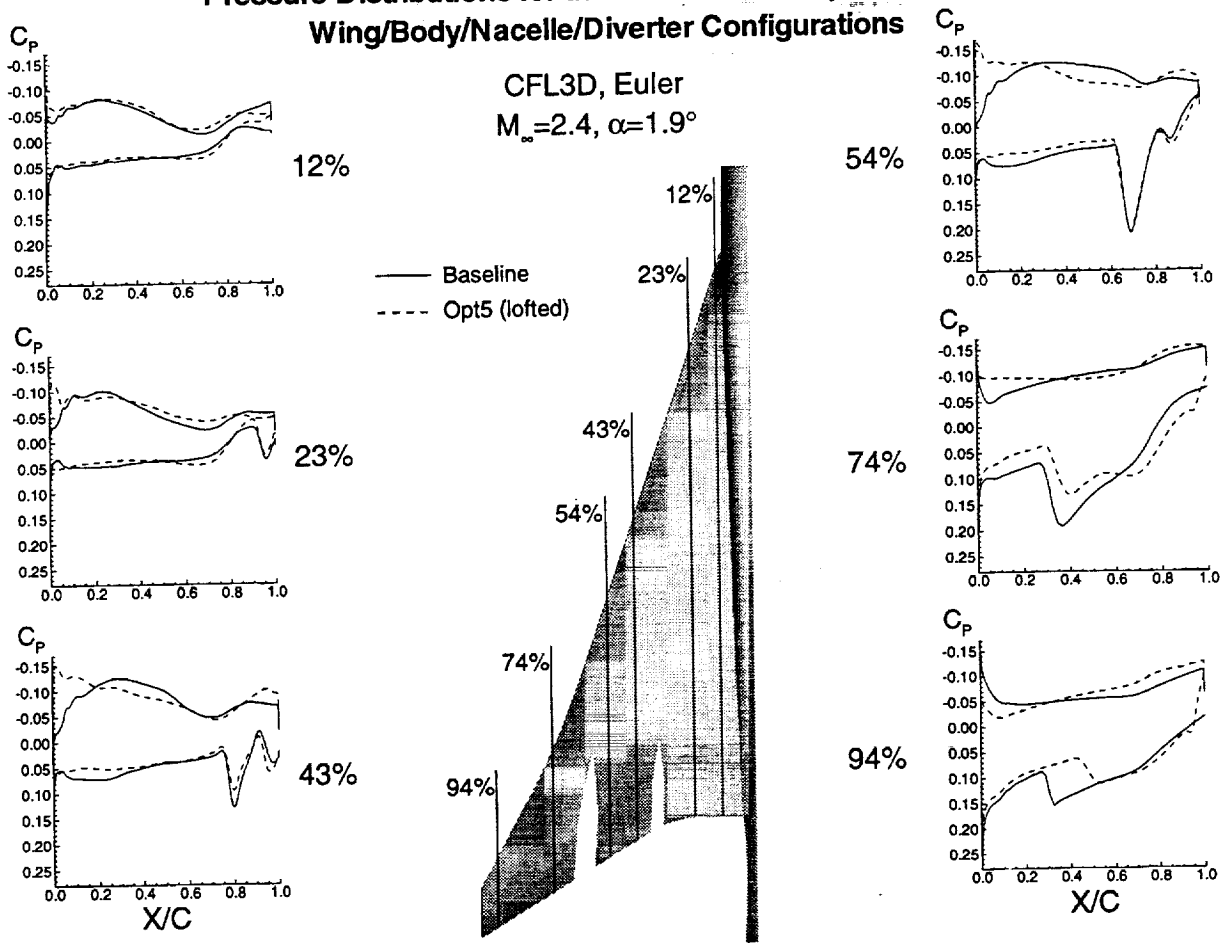

Pressure distributions from CFL3D Euler analysis on the M2.4-7A Baseline and Opt5 (lofted) wing/body/nacelle/diverter configurations are shown. The optimized configuration has much higher loading at the leading edge and a generally more even pressure distribution on the upper surface. Note that the large expansion that was seen on the wing/body analysis of the Opt5 configuration on the lower surface near the trailing edge is not as evident on the inboard section. The strength of the outboard nacelle/diverter shock was reduced mainly by reducing the diverter height. This reduced height was possible because the optimized wing/body allowed an improved nacelle integration. Note that the upper surface flow is unaffected by the presence of the nacelles and diverters (as it should be) thus preserving the increased adverse pressure gradient region shown in the wing/body configuration solutions. Therefore, there is good reason to believe that the reduction in skin friction indicated by the wing/body Navier-Stokes analysis would also hold true for the wing/body/nacelle/diverter configuration.

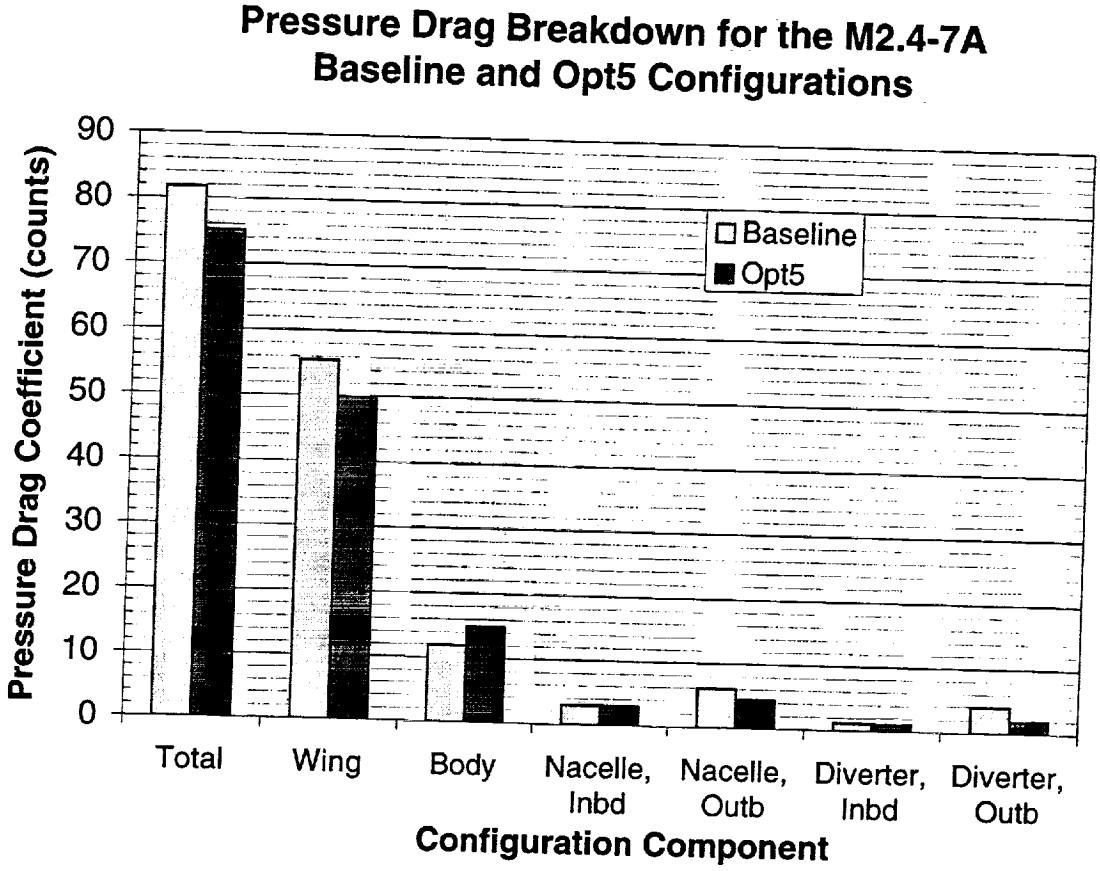

A pressure drag breakdown for M2.4-7A Baseline and Opt5 configuration are shown. Such a breakdown is useful to determine where the optimization process made improvements and design trade-offs. As indicated in the slide, the optimizer removed almost 6 counts of drag from the wing alone, and surprisingly, the body gained about 3 counts of drag. This is clearly a trade-off where fuselage performance was sacrificed to further improve the wing. The case also illustrates how important it is to optimize the wing and the fuselage simultaneously. Also shown in the slide is the fact that the drag on the inboard nacelle and diverter was virtually unchanged while the drag on the outboard nacelle and diverter decreased by about 3.5 counts. Note that the drag reduction on the outboard diverter can mostly be attributed to the manual shortening of that diverter height which was possible due to the favorable modifications of the wing lower surface.

Optimization of Wing and Fuselage with Fuselage Constraints

- **Opt5-A Configuration Design (Fuselage Deck Modification)**
- **FLO67(QGRID)/ADS Euler design code with nacelle effects, optimization of all variables at once (started at Opt5 design)**
- **Camber**
  - 5 distinct variables per span station, 7 stations on the wing (entire wing)
  - 9 distinct design variables on the fuselage
  - perturbations linearly lofted between design stations
- **Twist**
  - 1 design variable per span station, 8 stations on the wing
  - trailing edge fixed
  - perturbations linearly lofted between design stations
- **Constraints**
  - lift and pitching moment coefficients
  - deck angles, cabin and cargo bay heights
  - spanwise wing surface curvature

Beyond Opt5, the first optimization study, Opt5-A, was focused on studying the impact of much more realistic constraints on the fuselage deck. The initial design for this study was the M2.4-7A Opt5 configuration and the optimization took place utilizing the FLO67-based design code with the QGRID grid generator and the ADS optimizer. The design variables for this case were wing twist and camber (although only the twist alone results will be presented here), fuselage camber, deck placement variables, and wing plunge. The constraints for this case consisted of lift and pitching moment limitations, fuselage deck angles, cabin and cargo bay heights, and spanwise wing curvature. The constraints on wing curvature were put in place when initial results gave unacceptable geometries.

Illustration of Fuselage Deck Layout Constraints

(M2.4-7A Configuration)

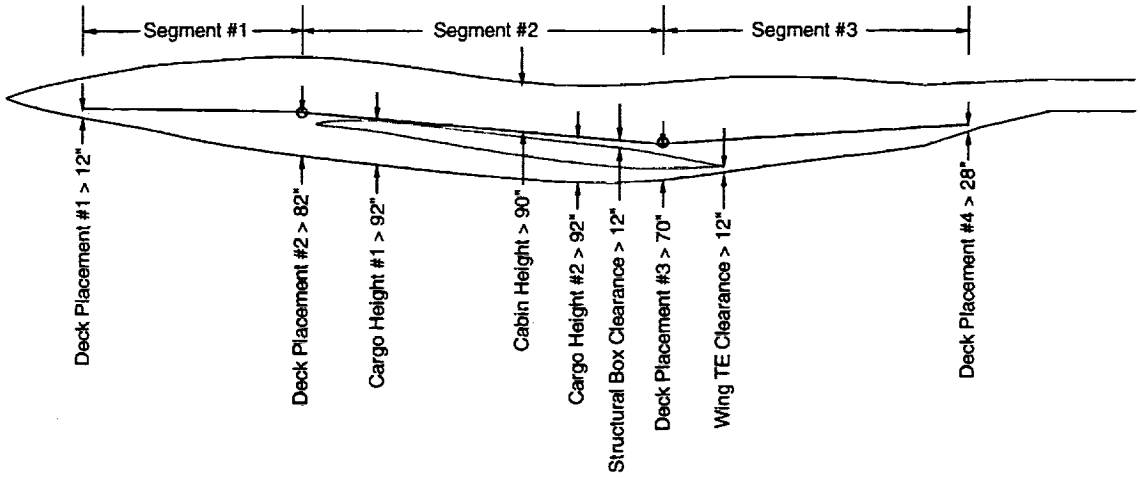

o Denotes deck break locations

All deck angles must be < 2.0° (w.r.t. WRP)

Vertical dimensions not to scale

A graphical representation of the fuselage constraints is shown.

Impact of Fuselage Constraints on Design

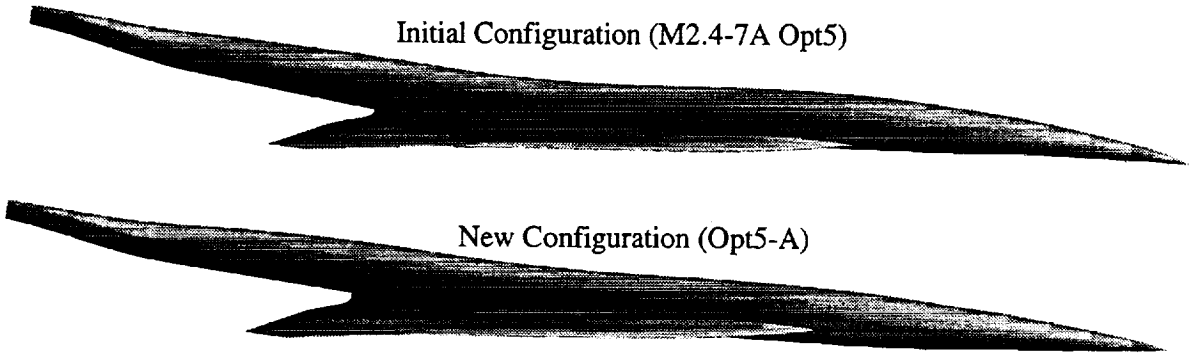

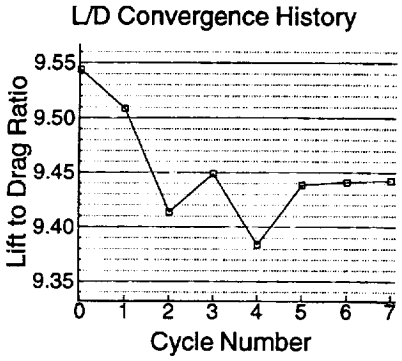

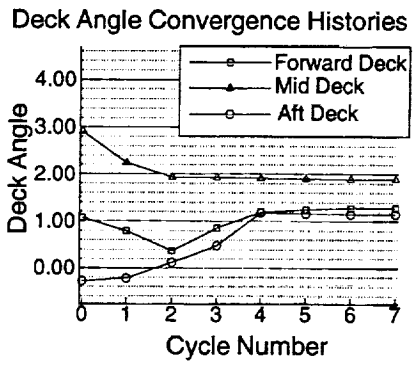

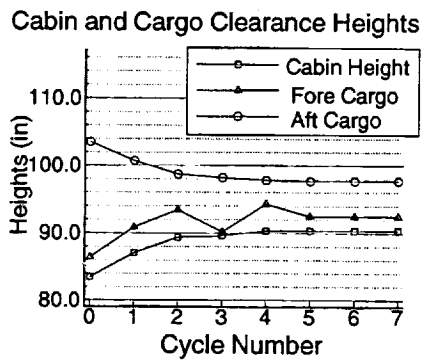

The details for the Opt5-A optimization are shown. The lower three plots illustrate the convergence of the objective function and the most critical constraints. Note that all of the constraints are satisfied by the fifth cycle and that the objective function (L/D) smooths out at that point. The upper figure shows the significant impact of the new fuselage deck constraints on the final design. Unfortunately, a 1% loss of performance in supersonic cruise L/D was required to meet the constraints on the fuselage.

Thickness Optimization of Wing and Fuselage

Opt6 Configuration Design (Wing Thickness Modification)

- **FLO67(QGRID)/ADS Euler design code with nacelle effects, optimization of all variables at once (started at Opt5-A design)**
- **Camber & Thickness**
  - Used Hick's functions & polynomial shape functions
  - 5 distinct variables per span station, 7 stations on the wing (entire wing)
  - 9 distinct design variables on the fuselage
  - perturbations linearly lofted between design stations
- **Twist**
  - 1 design variable per span station, 7 stations on the wing
  - trailing edge modified with 7 design variables along wing
  - perturbations linearly lofted between design stations
- **Constraints**
  - lift and pitching moment coefficients
  - deck angles, cabin and cargo bay heights
  - forward door clearance
  - spanwise wing surface curvature

The second optimization study in this effort, Opt6, was focused on studying the impact of allowing the wing thickness to be modified during optimization. The initial design for this study was the M2.4-7A Opt5-A configuration and the optimization took place utilizing the FLO67-based design code with the QGRID grid generator and the ADS optimizer. The design variables for this case were wing twist, camber, and thickness, along with fuselage camber and area distribution, deck placement, and wing plunge. The constraints for this case consisted of all the constraints (full deck) for the Opt5-A configuration plus the addition of wingbox area limitations.

Comparison of Lift Coefficients for the Optimized M2.4-7A Wing/Body Configurations

FLO67 Results with Forces Integrated to the Fuselage End; w/ Nacelle Effects; 193x33x33; M_∞=2.4

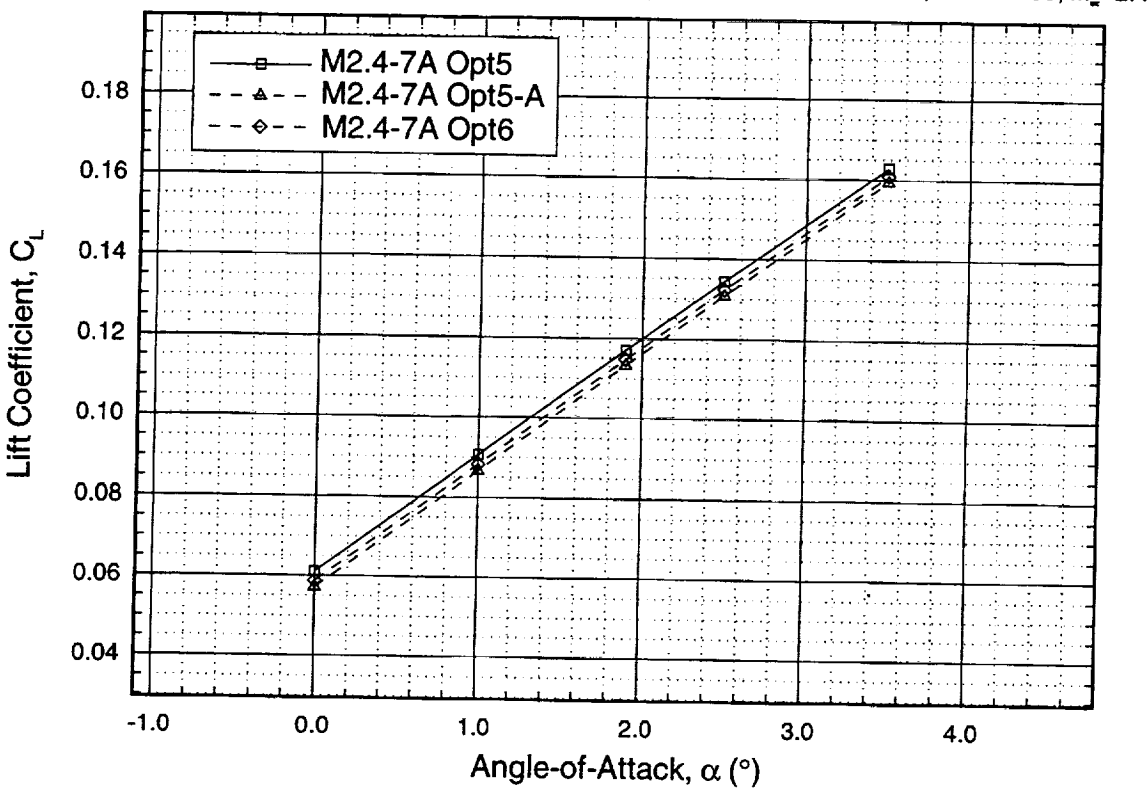

Lift curves from FLO67 Euler analysis for the M2.4-7A optimized wing/body configurations (with nacelle/diverter effects) are shown. The Opt5 configuration has the highest lift of the three for a given angle-of-attack while the Opt5-A has the lowest. At the cruise condition of C_L = 0.11, there is a spread of 0.2 deg. between the three curves although all of them have an angle-of-attack less than 1.9 deg. (the baseline value). There is no change in lift curve slope between the configurations.

Comparison of Drag Polars for the M2.4-7A Optimized Wing/Body Configurations

FLO67 Results with Forces Integrated to the Fuselage End; w/ Nacelle Effects; 193x33x33; M_∞=2.4

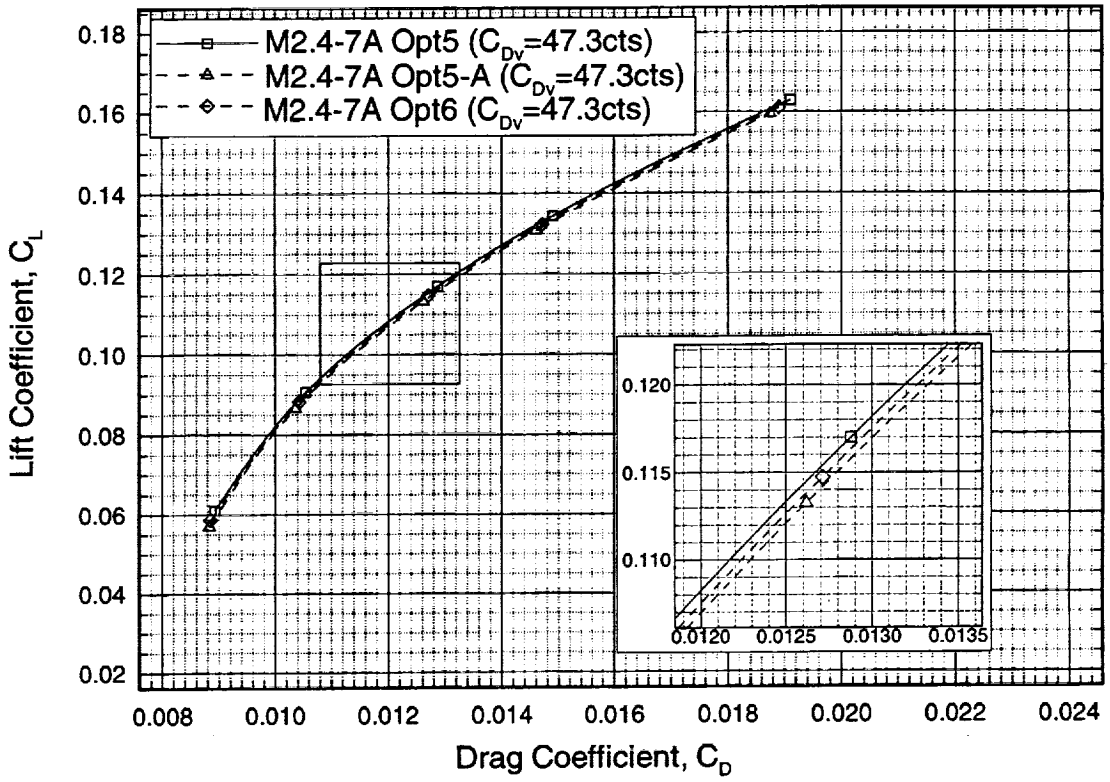

Drag polars from FLO67 Euler analysis (with flat-plate skin friction) for the M2.4-7A optimized wing/body configurations (with nacelle/diverter effects) are shown. The Opt5 configuration has the lowest drag of the three for a given lift coefficient although all have significantly less drag than the baseline configuration. At the cruise lift coefficient of 0.11, the spread between the curves is 1.5 counts. The disappointing results for the Opt6 configuration yielded only a 0.6 count drag improvement over the Opt5-A design.

Comparison of Lift-to-Drag Ratios for the Optimized M2.4-7A Wing/Body Configurations

FLO67 Results with Forces Integrated to the Fuselage End; w/ Nacelle Effects; 193x33x33; M_∞=2.4

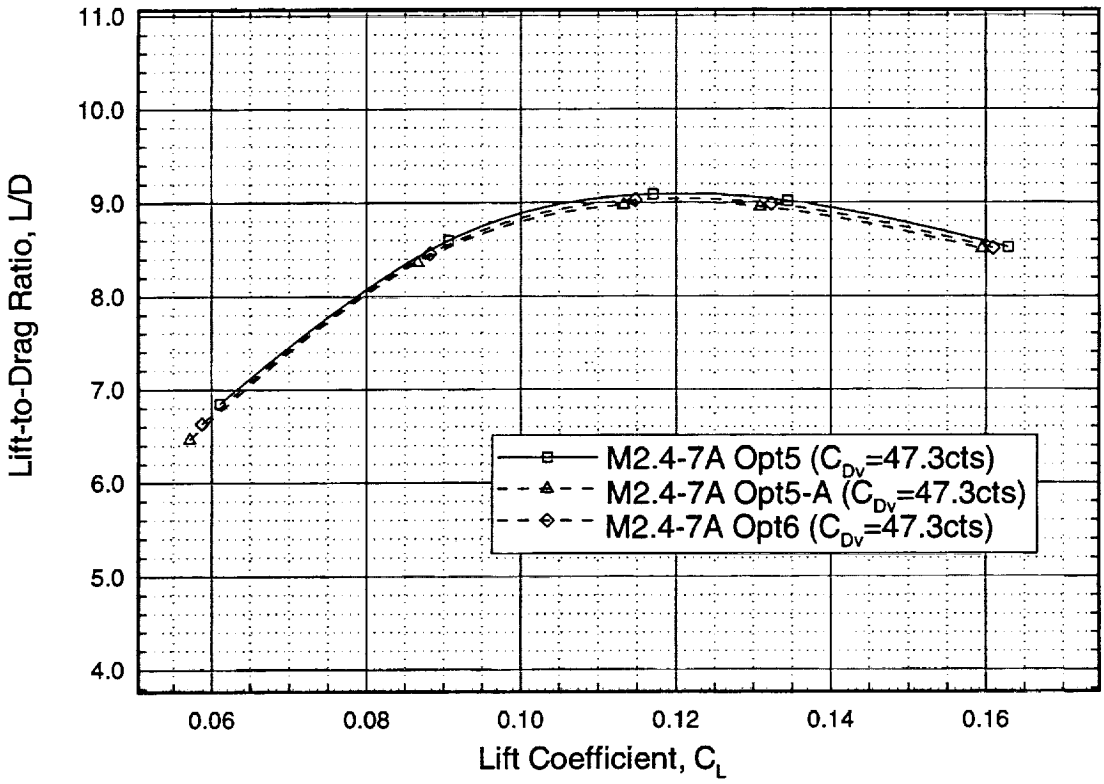

Lift-to-drag ratios from FLO67 Euler analysis (with flat-plate skin friction) for the M2.4-7A optimized wing/body configurations (with nacelle/diverter effects) are shown. As expected, the Opt5 has the highest L/D and the Opt5-A the lowest. All of the configurations show relatively flat response near $(L/D)_{max}$ which seems to occurs at a C_L of approximately 0.12.

Comparison of Pitching Moments for the Optimized M2.4-7A Wing/Body Configurations

FLO67 Results with Forces Integrated to the Fuselage End; w/ Nacelle Effects; 193x33x33; M_∞=2.4

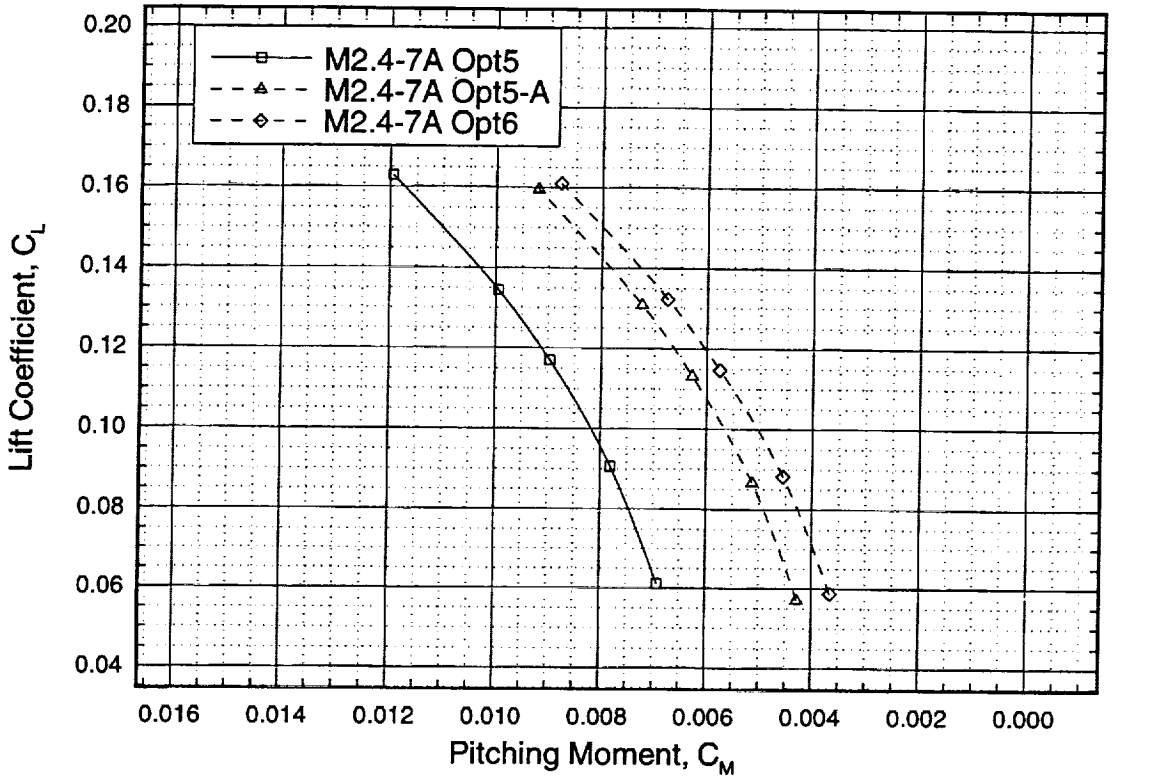

Due to the loose constraints placed on the pitching moments during optimization, there is a significant shift in pitching moment between the three configurations. Note that only a shift in the curves has taken place between the configurations and the slopes are maintained.

X-Cut Comparison of the Baseline and Design Geometries

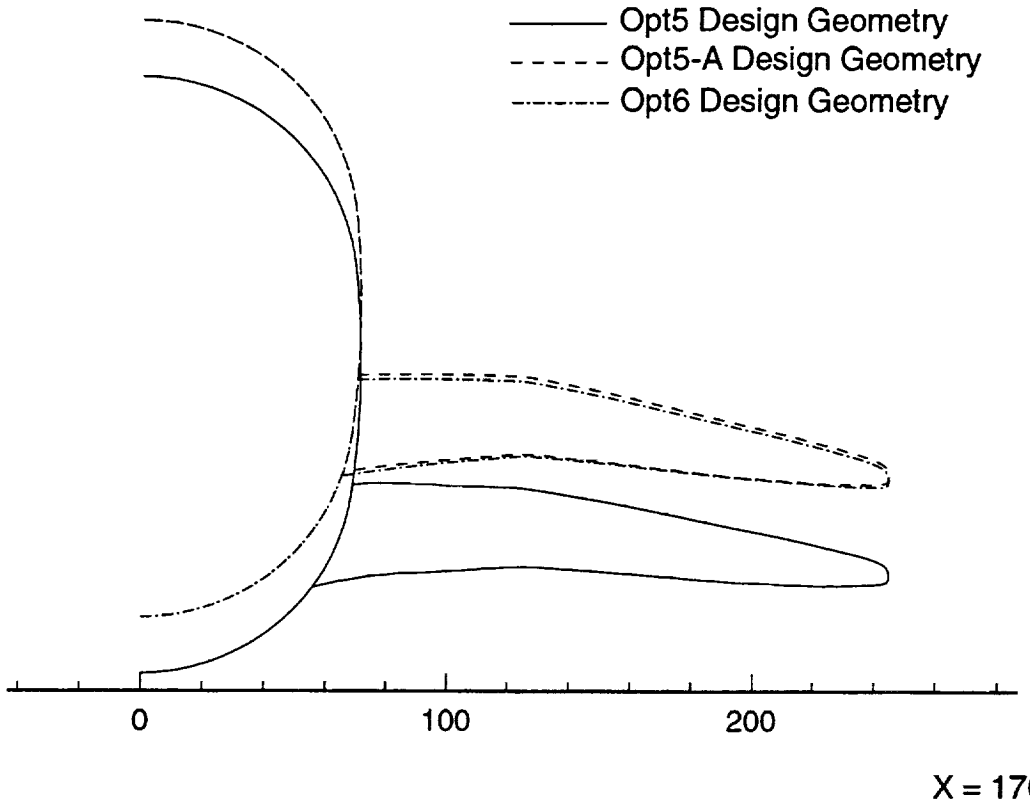

Cross-sectional cuts at constant fuselage (X) stations and constant butt-line stations (Y) are shown in the next several slides for the Opt5, Opt5-A, and Opt6 configurations. The first chart shows the geometries at X=1700". Note that there is a considerable shift in wing position for the Opt5-A configuration and very little for the Opt6 (with respect to the Opt5-A).

X-Cut Comparison of the Baseline and Design Geometries

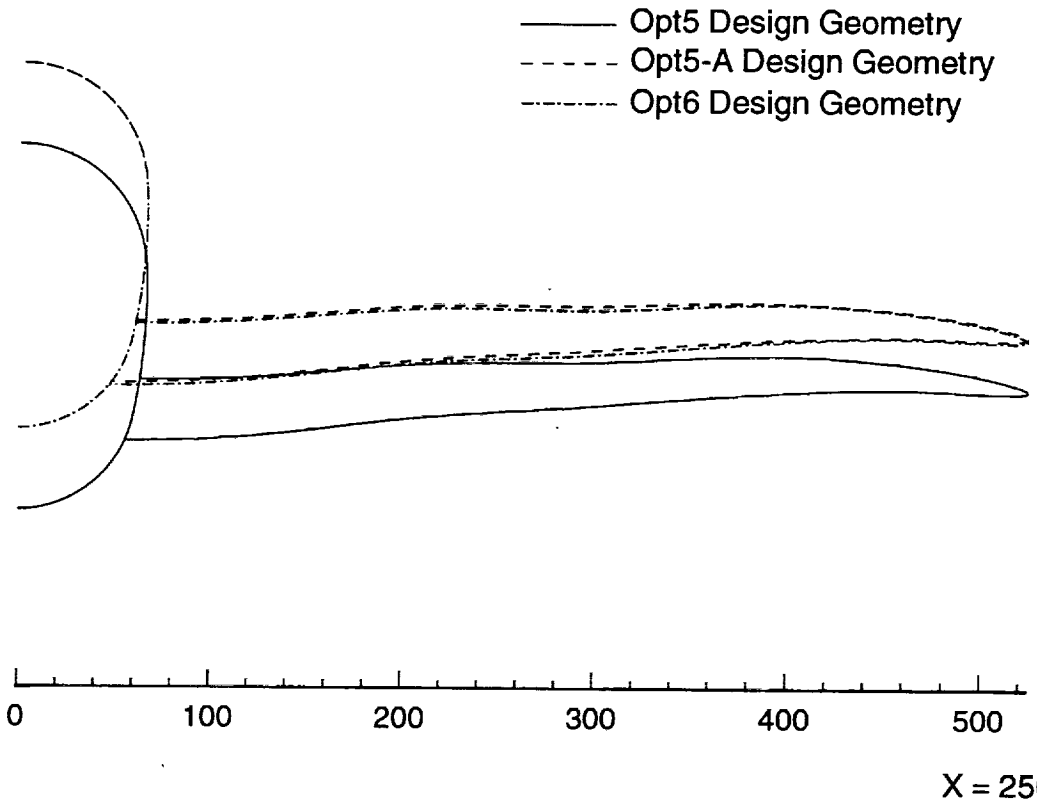

Once again, there is a significant shift in the wing position between the Opt5 and Opt5-A configurations. The Opt6 configuration shows only marginal changes in the wing geometry. The general shape of the wings however appears to be unchanged.

Y-Cut Comparison of the Design Geometries

——— Opt5 Design Geometry
- - - - - Opt5-A Design Geometry
-.-.-.-.- Opt6 Design Geometry

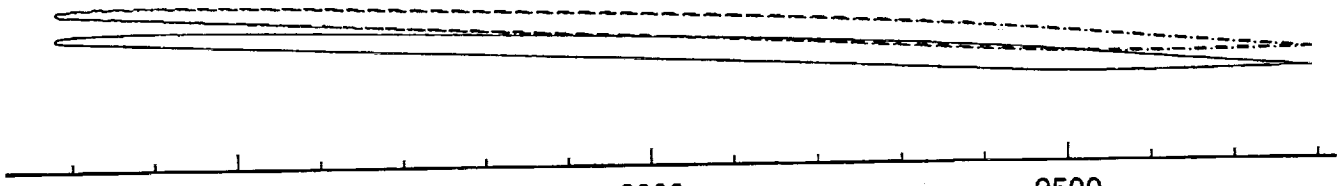

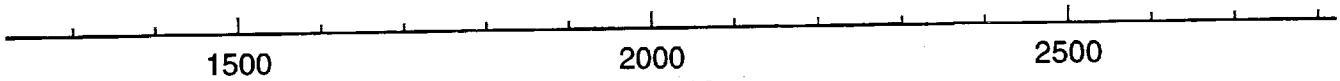

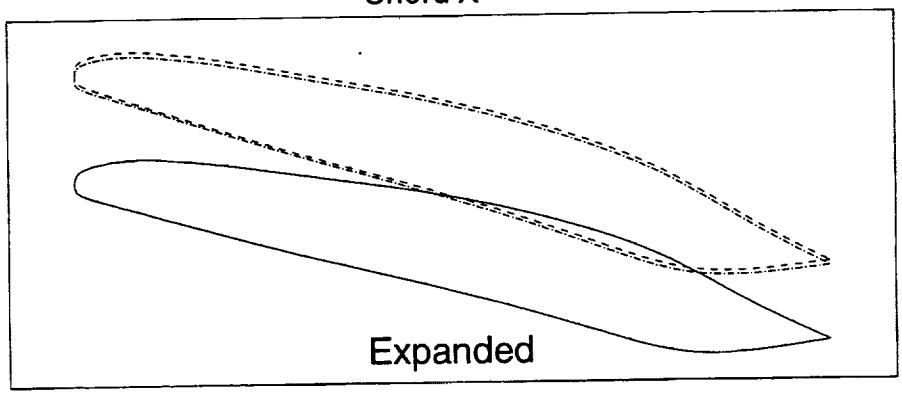

Cut at Y = 100"

This slide shows an airfoil cut for the Opt5, Opt5-A, and Opt6 configurations at Y=100". The differences between the Opt5-A and Opt6 cuts appear to be mostly camber changes with very little thickness differences apparent. Note a somewhat awkward leading-edge curvature of the geometries in the expanded scale.

Y-Cut Comparison of the Design Geometries

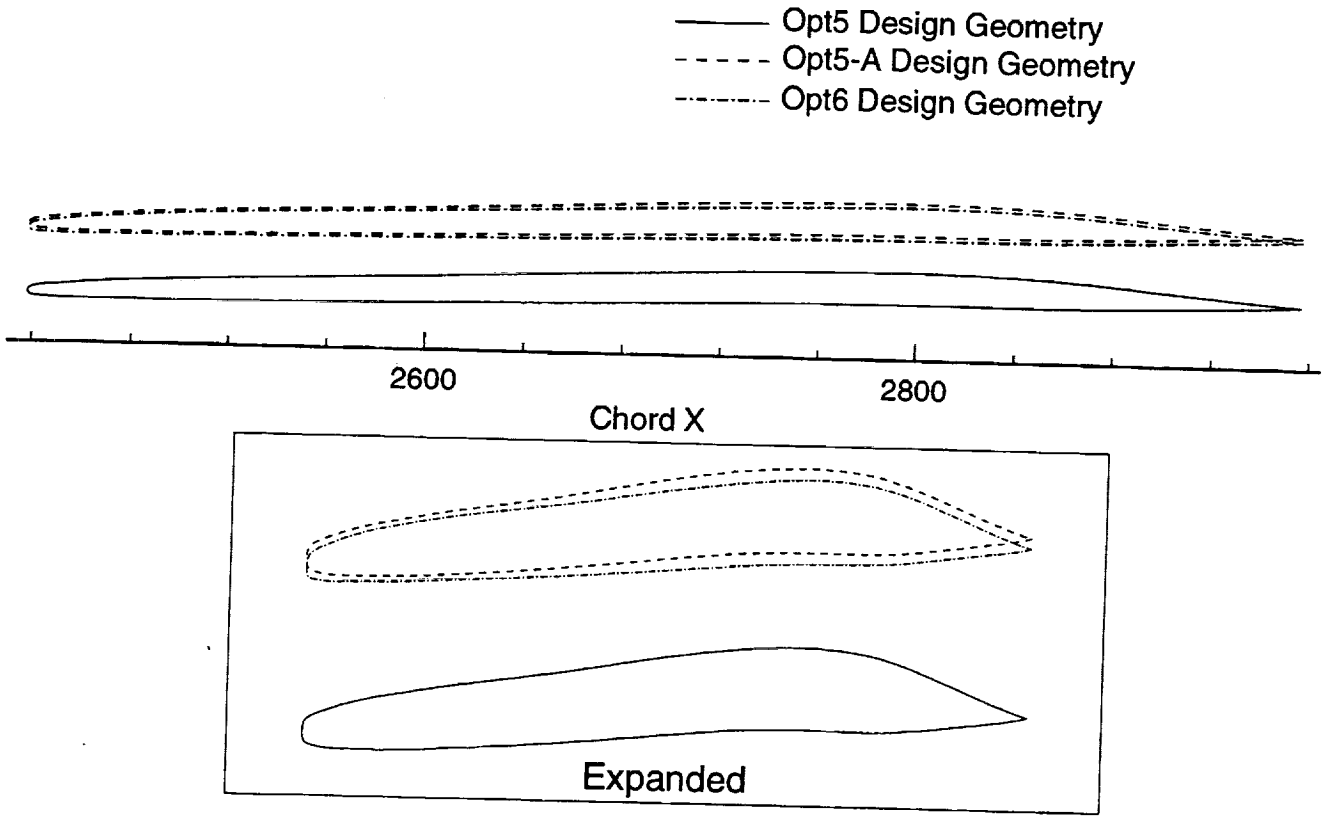

Cut at Y = 500"

In this cut, there are more significant camber/twist differences between the Opt5-A and Opt6 configurations (especially near the trailing edge). However, the thickness differences are slight.

Y-Cut Comparison of the Design Geometries

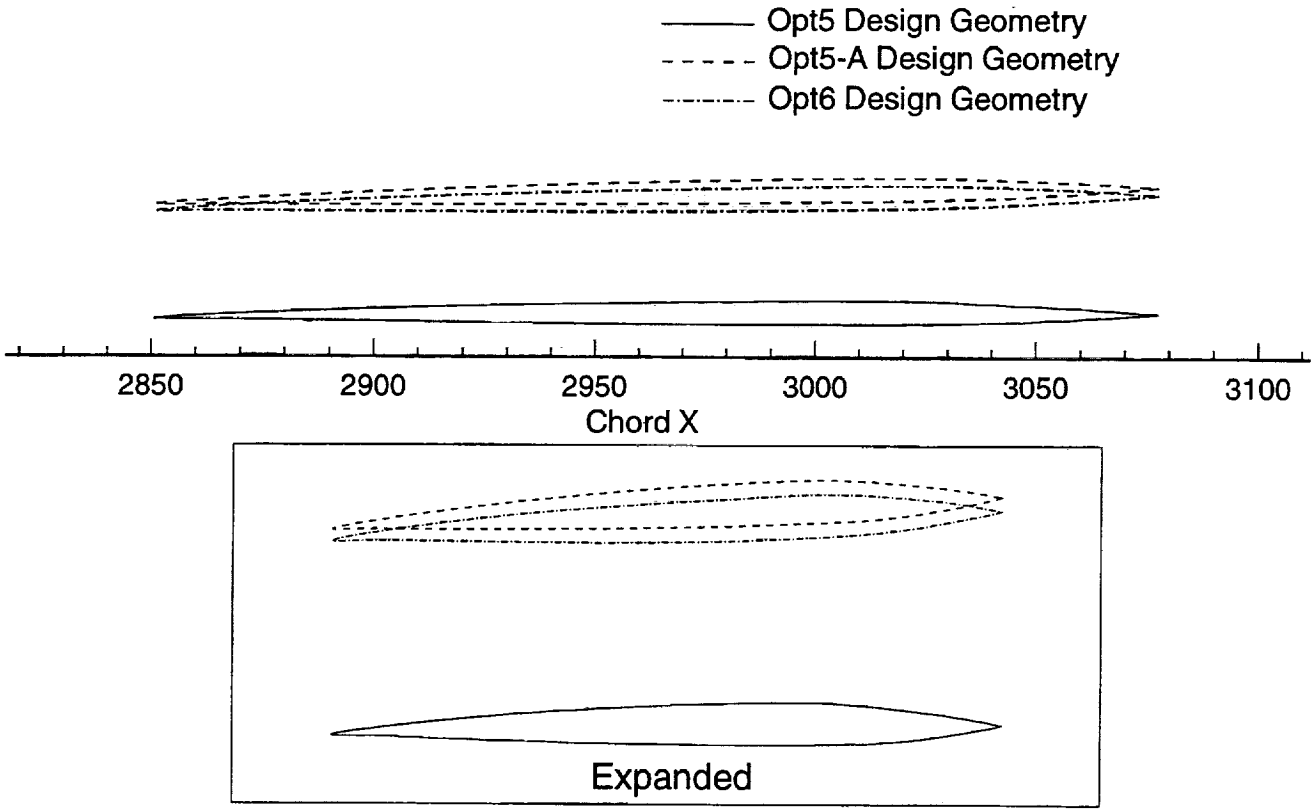

Cut at Y = 700"

As before, this cut has more significant camber/twist differences between the Opt5-A and Opt6 configurations (especially near the trailing edge). However, the thickness differences are very small.

Summary and Conclusions

- The M2.4-7A Opt5 (lofted) wing/body configuration showed a 2.5 count (Euler) and a 4.5 count (N-S) reduction in supersonic cruise drag over the Baseline M2.4-7A.
- The M2.4-7A Opt5 (lofted) wing/body/nacelle/diverter configuration showed a 6.6 count (Euler) and 8.6 count (estimated N-S) reduction in supersonic cruise drag over the Baseline M2.4-7A.
- Fuselage deck constraints caused a 1.0% reduction in cruise performance for a highly constrained camber and twist design (Opt5-A configuration).
- Including the effects of thickness design variables has yet to produce significant improvements in cruise performance. The best design to date that includes deck constraints and thickness design variables is still 0.5% under the performance of the Opt5 configuration.

Detailed CFL3D analyses have revealed a 2.5 count (Euler) and a 4.5 count (N-S) reduction in cruise drag for the Opt5 wing/body configuration along with a 6.6 count reduction (Euler) for the Opt5 wing/body/nacelle/diverter configuration and an estimated 8.6 count reduction for N-S analysis. The application of realistic fuselage/deck constraints had a negative impact on the performance resulting in a 1% loss of supersonic cruise performance. The inclusion of thickness effects has not significantly improved the design to date (0.5%) although investigations are currently underway to rectify this situation.

Experimental Investigation of a Point Design Optimized Arrow Wing HSCT Configuration

R.P. Narducci, P. Sundaram, S. Agrawal, S. Cheung, A.E. Arslan, G.L. Martin
McDonnell Douglas Aerospace
Long Beach, California 90807-5309

The M2.4-7A Arrow Wing HSCT configuration was optimized for straight and level cruise at a Mach number of 2.4 and a lift coefficient of 0.10. A quasi-Newton optimization scheme maximized the lift-to-drag ratio (by minimizing drag-to-lift) using Euler solutions from FLO67 to estimate the lift and drag forces. A 1.675% wind-tunnel model of the Opt5 HSCT configuration was built to validate the design methodology. Experimental data gathered at the NASA Langley Unitary Plan Wind Tunnel (UPWT) section #2 facility verified CFL3D Euler and Navier-Stokes predictions of the Opt5 performance at the design point. In turn, CFL3D confirmed the improvement in the lift-to-drag ratio obtained during the optimization, thus validating the design procedure.

A data base at off-design conditions was obtained during three wind-tunnel tests. The entry into NASA Langley UPWT section #2 obtained data at a free stream Mach number, M_∞, of 2.55 as well as the design Mach number, M_∞=2.4. Data from a Mach number range of 1.8 to 2.4 was taken at UPWT section #1. Transonic and low supersonic Mach numbers, M_∞=0.6 to 1.2, was gathered at the NASA Langley 16 ft. Transonic Wind Tunnel (TWT).

In addition to good agreement between CFD and experimental data, highlights from the wind-tunnel tests include a trip dot study suggesting a linear relationship between trip dot drag and Mach number, an aeroelastic study that measured the outboard wing deflection and twist, and a flap scheduling study that identifies the possibility of only one leading-edge and trailing-edge flap setting for transonic cruise and another for low supersonic acceleration.

Acknowledgments

Mina Cappuccio	(ARC)	Paul Kubiatko	(MDA)
Susan Cliff		Bret Leonhardt	
Raymond Hicks		John Morgenstern	
Robert Kennelly		Pete Wilcox	
James Reuther			
Jim Sedowski			
A.B. Blair	(LaRC)	Tim Kariya	(Vigyan)
Al Burner			
Dan Cler			
Tom Mills			
Floyd Wilcox			
Langley Technicians			

More than 11 weeks of total testing was done on the Opt5 model at the UPWT and 16 ft. TWT facilities. McDonnell Douglas Aerospace wishes to thank all those who supported the tests.

Wind-Tunnel Test Objectives

- Validate the aerodynamic design improvements predicted by non-linear CFD
- Develop an experimental database for the Arrow Wing HSCT configuration
- Obtain aerodynamic characteristics for different wing-flap deflections in the transonic flow regime

The primary objective of the test was to validate the non-linear point-design methodology used at McDonnell Douglas to obtain the Opt5 configuration from the linearly optimized baseline M2.4-7A. The methodology was validated by confirming the aerodynamic improvements predicted by non-linear CFD codes. In addition to obtaining data at the design point, a database for the Arrow Wing HSCT configuration was established at off-design Mach numbers. A third objective was to obtain aerodynamic characteristics for different wing-flap deflections in the transonic flow regime.

Outline

- Model description
- Test log
- Supersonic testing (UPWT)
  - Trip drag study
  - Comparison to CFD
  - Aeroelastic study
- Transonic testing (16 ft. TWT)
  - Transonic drag rise
  - Flap effectiveness
- Summary of important findings

This presentation begins with a description of the 1.675% scale Opt5 model used in the tests. Following this, a general overview of the Opt5 entries into the Langley UPWT and 16 ft. TWT test facilities will be given. To begin the presentation of data gathered during the tests, a detailed trip study showing trip drag as a function of Mach number will be given. Next, CFD comparisons at design and off-design Mach numbers will be shown. This includes an aeroelastic study showing the effects of outboard wing deflection and twist on lift. Transonic data from Langley's 16 ft. TWT facility is presented next. This includes the transonic drag rise and leading-edge and trailing-edge flap effectiveness. The presentation is concluded with a summary of important findings of the Opt5 wind-tunnel tests.

Model Description

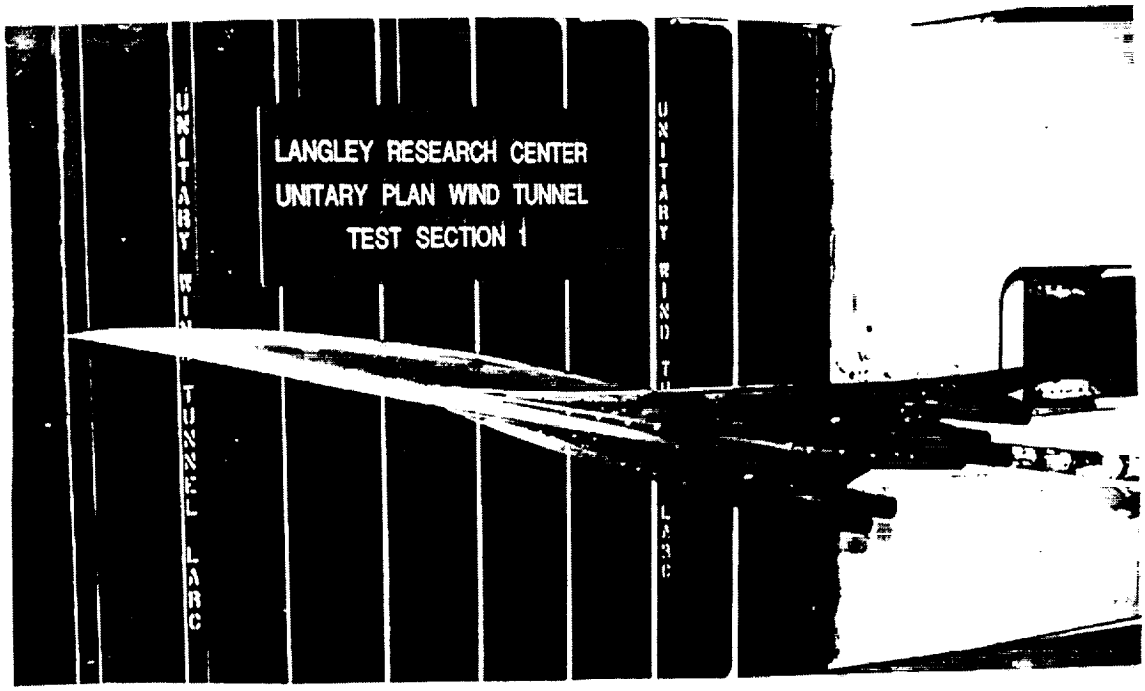

The model is a 1.675% scale of the McDonnell Douglas optimized M2.4-7A W/B/N/D configuration (Opt5). The model, sized for testing in the NASA Langley UPWT section #2, is 4.578 ft. long and spans 2.149 ft. The fuselage is 2.2 in. shorter than the full geometry to accommodate the balance and sting within the model. The internal nacelle geometry is cylindrical to simplify the mass flow assessment and is sized to match the mass flow at the design condition.

The wing is fabricated from stainless steel and covers an area of 2.511 ft^2. It has a faired leading-edge break at 70% semi-span and a faired trailing-edge break at 30% semi-span. The wing has two leading-edge flaps and three trailing-edge flaps. Flaps are deflected by replacing flap pieces to accommodate the desired flap setting. The inboard leading-edge flap may be deflected 0° or 10° and the outboard leading-edge flap may be deflected 0°, 5°, 10°, 15°, or 20°. The leading-edge deflections are smoothly faired from inboard to outboard and thus only certain combinations of the inboard and outboard leading-edge flap deflections can be made. The trailing-edge flaps may be deflected 0°,3°, 6°, or 10°.

During the tests, 85 static pressure orifices were functional. Fifty-six taps were located on the leading-edge and trailing-edge flaps and were only functional with 0° flap deflections.

Opt5 1995 Test Log

	UPWT Section #2	UPWT Section #1	16 ft. TWT
Date	June 12 - June 30 (3 Weeks)	Aug 3 - Aug 30 (4 Weeks)	Sept 20 - Oct 20 (4.5 Weeks)
Configurations	W/B & W/B/N/D	W/B & W/B/N/D	W/B & W/B/N/D Flaps
Mach	2.4, 2.55	1.8 - 2.4	0.3 - 1.2
Re_c	4.12×10^6	4.12×10^6	2.0×10^6 - 4.0×10^6
Measurements	Force, Moment, Pressure	Force, Moment, Pressure	Force, Moment, Pressure
Flow Visualization	Oil flow Sublimation	Oil flow Sublimation Schlieren	Oil flow Sublimation
Studies	Trip drag Aeroelastic	Trip drag	Trip drag Flap deflections

Nearly 11 weeks of total testing was done on the Opt5 model at the UPWT and 16 ft. TWT facilities. Opt5 entry in the Langley UPWT sections #2 and #1 occurred June 12 to June 30, 1995 and August 3 to August 30, 1995, respectively. Testing in the 16 ft. TWT facility occurred between September 20 and October 20, 1995.

Tunnel experiments obtained force, moment, and pressure data for both wing/body (W/B) and wing/body/nacelle/diverter (W/B/N/D) configurations. At selected flow conditions, colored oil flow visualization tests were performed to gain insight into the flow physics. In addition, sublimation runs were performed to assist in understanding the boundary layer transition. During the Opt5 entry into test section #1, Schlieren photographs were taken to visualize the shock structure.

NASA Langley UPWT Facility

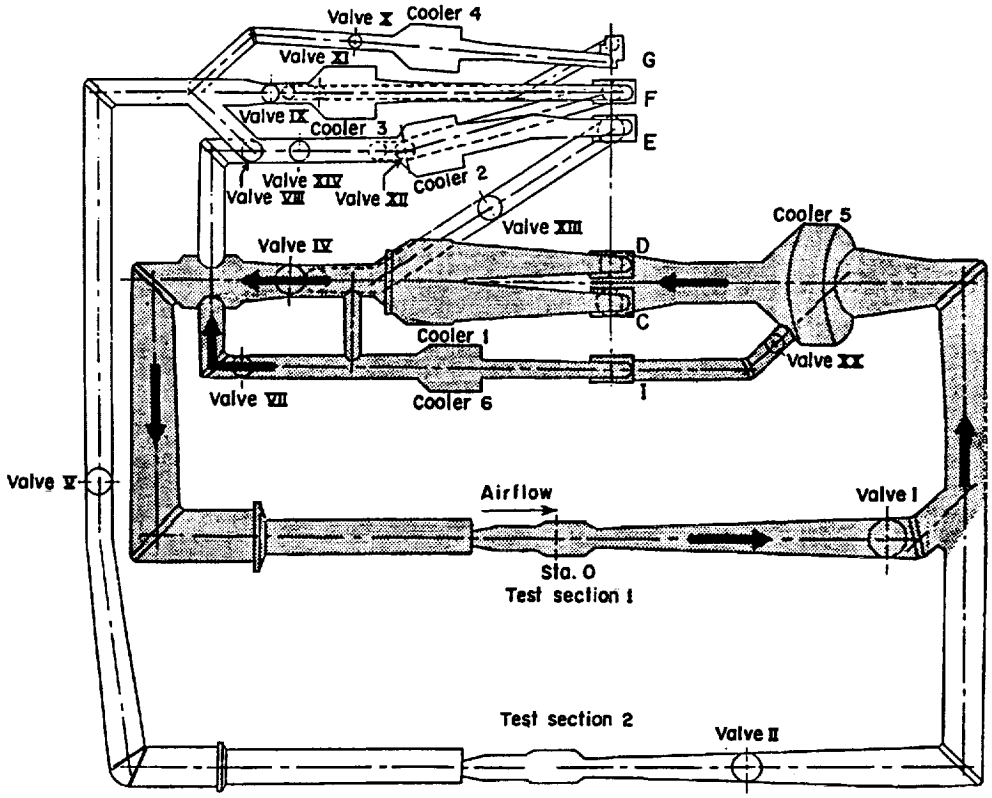

The NASA Langley UPWT is a fan driven, closed circuit, continuous flow, pressurized wind tunnel. Tunnel total pressure can be varied from 3 psia to 150 psia. It has two test sections, both 4 ft. x 4 ft. in cross-section and 7 ft. long. Test section #2 has a Mach number range from 2.29 to 4.63. Tunnel operation for test section #1 occurs in two modes. One mode covers a Mach number range of 1.46 to 2.16; the second mode covers the range from 2.36 to 2.87.

NASA Langley 16 ft. TWT Facility

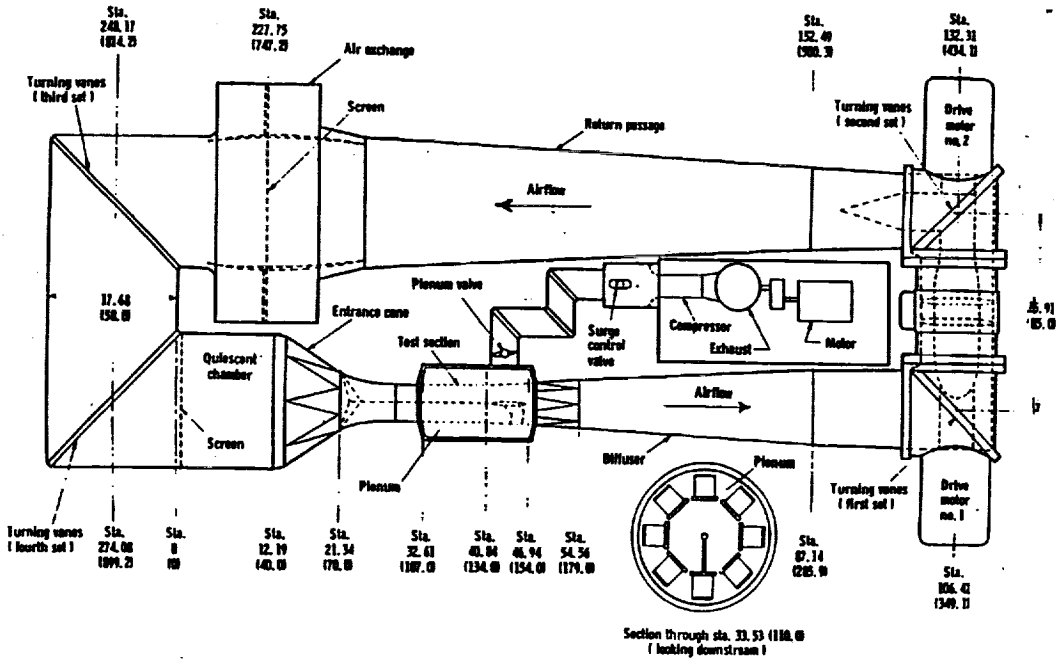

The NASA Langley 16 ft. TWT is a fan driven, closed circuit, single return, continuous flow atmospheric wind tunnel. The test section is octagonal in shape and is approximately 15.5 ft. in diameter. The test section is slotted to reduce reflected shock interference and wall boundary layer effects. For transonic flow the test section is 22 ft. long; for supersonic flow the test section length is 8 ft. long. The Mach number range for this tunnel is 0.3 to 1.2.

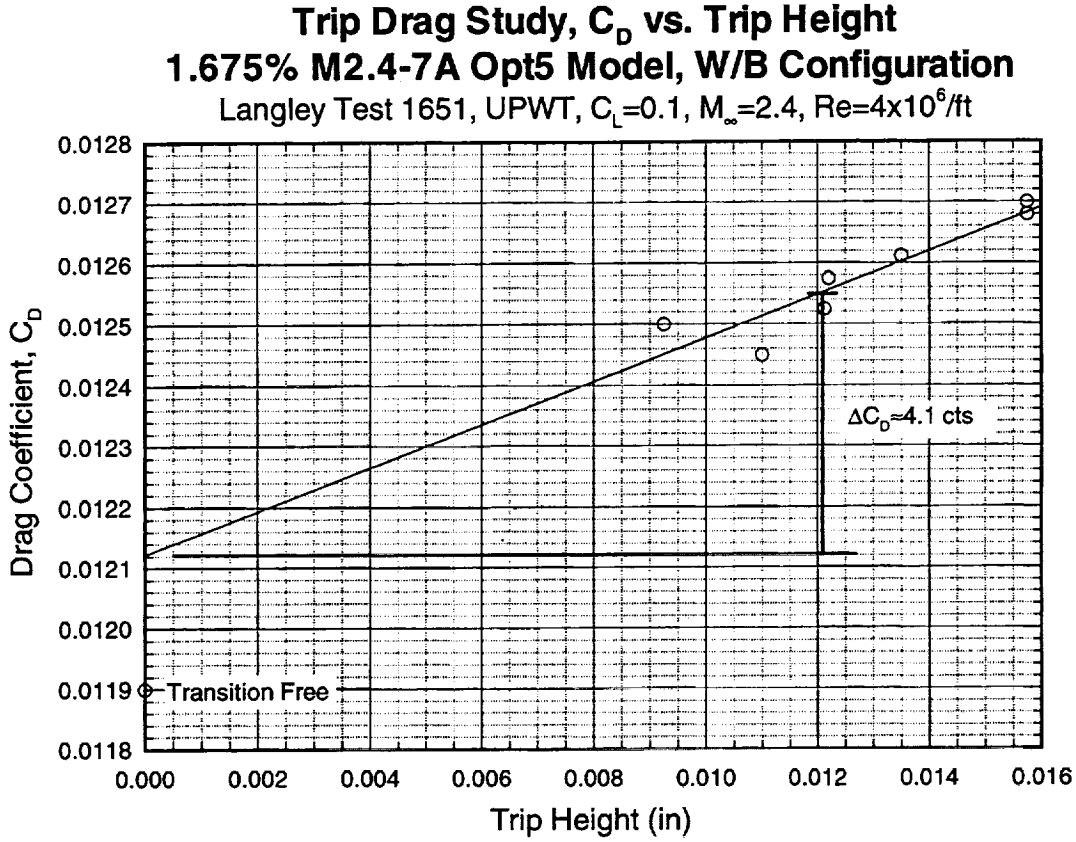

Tunnel conditions are usually such that the flow over the model is inherently part laminar and part turbulent. To more accurately model the turbulent flight conditions, thin, circular disks were used to trip the boundary layer. Along the upper surface and lower wing surfaces, these disks were placed 0.4" behind the leading edge; a ring of disks was placed on the fuselage 1" from the nose; on the inner and outer surfaces of the nacelles, disks were placed 0.875" from the nacelle leading edge. The distances were chosen to be consistent with previous Reference H wind-tunnel tests.

While these disks are useful to trip the boundary layer, their presence is felt in the drag measurements. The objective of the trip drag study is to separate the additional drag due to the presence of the disks from the total drag measurement.

The trip drag variation with respect to the disk height near the cruise condition for M_∞=2.4 is shown. The change in drag due to the disks is estimated by fitting a linear curve through data points measured at different disk heights and extrapolating the curve to a disk height of 0". The difference between the drag at a particular disk height and the extrapolated value at height = 0" is the drag due to the disks.

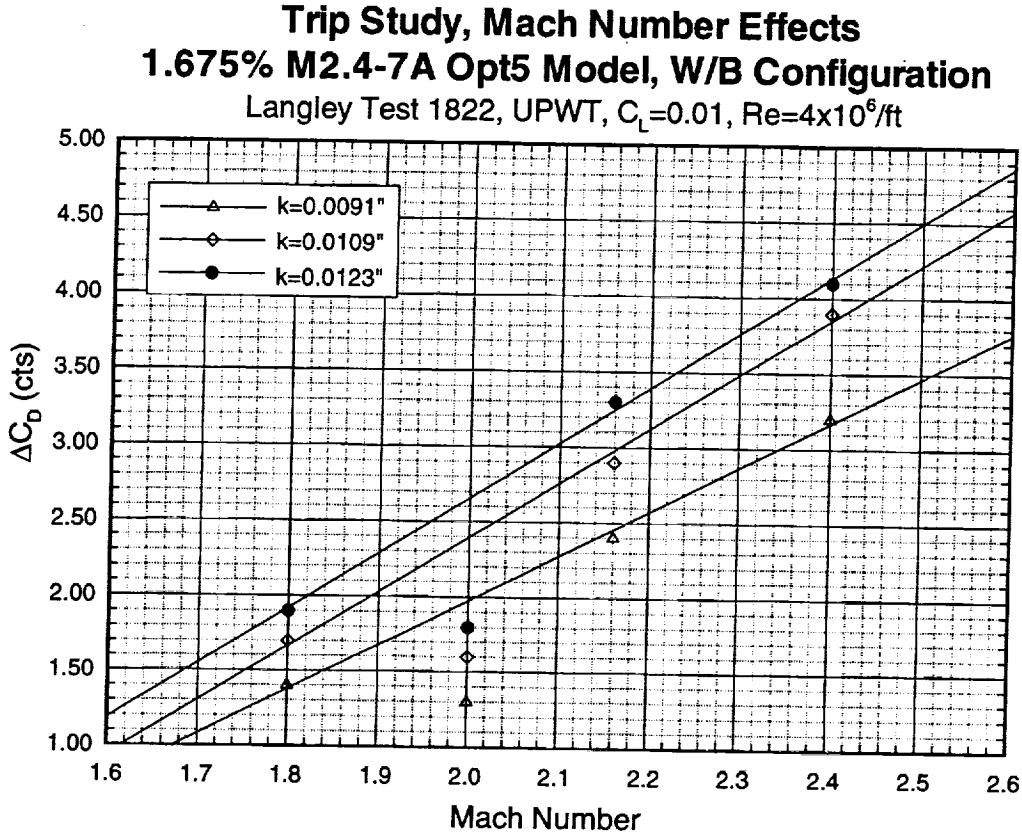

Trip drag as a function of Mach number for the three disk heights are shown. Off-design Mach number data is taken from UPWT section #1. Also included on the chart are data compiled from section #2 for M_∞=2.4. The fit to the data excluded the information measured at M_∞=2.0 due to the non-repeatability of the data. The amount of trip drag subtracted from the recorded data is done according to the fitted line. The trip drag correction is governed by

$$\Delta C_D = -3.8994 + 2.9824 M_\infty, \quad k = 0.0091"$$
$$\Delta C_D = -4.8842 + 3.6404 M_\infty, \quad k = 0.0109"$$
$$\Delta C_D = -4.7105 + 3.6842 M_\infty, \quad k = 0.0123"$$

for $1.8 \leq M_\infty \leq 2.4$. Much of the data was gathered with a disk height of 0.0123". The corrections are summarized below.

Mach Number	ΔC_D (cts)
1.8	1.92
2.0	2.66
2.16	3.25
2.4	4.13

Sublimation Flow Visualization

1.675% M2.4-7A Opt5 Model, W/B Configuration

M_∞=2.0, α=2.0°, Re=4.0x10^6/ft., Upper Surface

To check the transition of the boundary layer, sublimation runs were made. For these runs, a mixture had to be made immediately prior to the runs. The sublimation mixture consisted of 25 grams of fluorine powered per 1 quart of Genesolv 2004. The sublimation material was applied to the model using an airless sprayer yielding a very even coat. A turbulent boundary layer would cause the material to sublime away.

At M_∞=2.0 and the cruise angle-of-attack of 2.0°, the material sublimed off the model aft of the transition disks. Shown above is a close-up near the leading-edge of the upper surface. A lone disk clearly shows a wedge of turbulent flow transitioned by the disk (height = 0.0091").

Shock Impingement Calculation

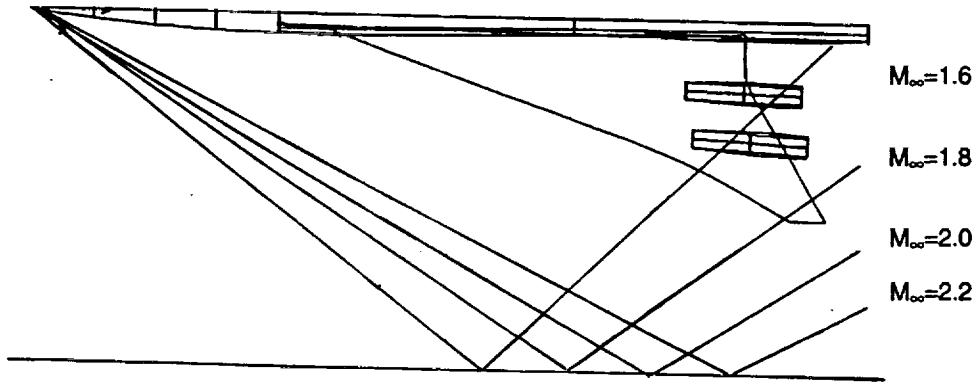

The 1.675% model was originally sized for M_∞=2.4 flow inside the UPWT section #2. At lower supersonic Mach numbers, the shock off the nose weakens and the angle between the shock wave and the model's centerline increases. At M_∞=1.6 and some angles-of-attack at M_∞=1.8, the shock reflects off the wall and strikes the model in the aft section. Shown above is a schematic of the shock wave reflections. Shock angles are computed using shock relation tables found in NASA TR 1135.

Schlieren Photograph

1.675% M2.4-7A Opt5 Model, W/B Configuration

M_∞=1.6, α=0.32°, Re=4.0x10^6/ft.

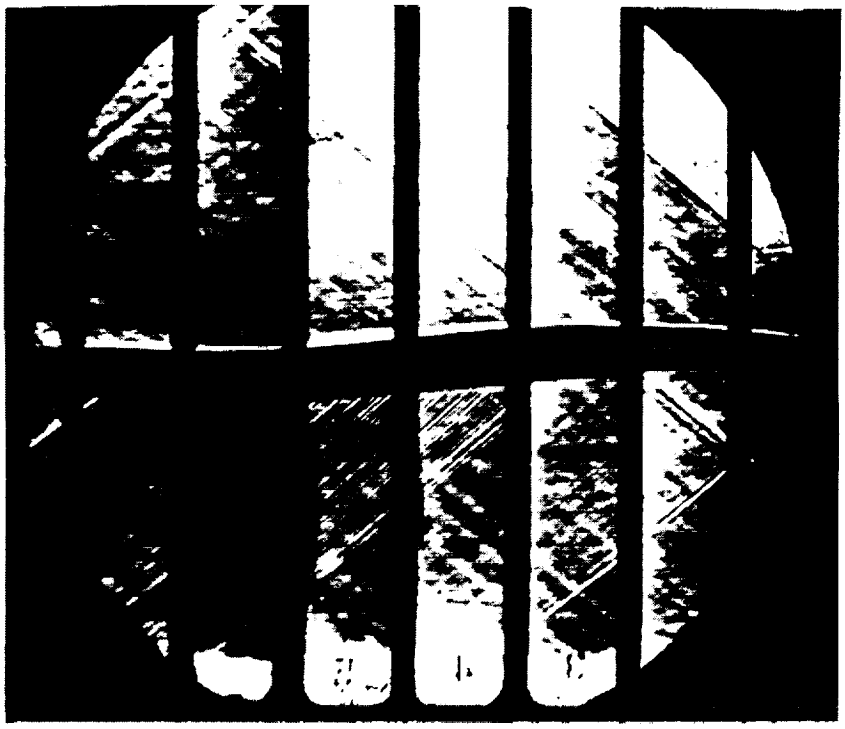

Supersonic flow visualization using Schlieren is an essential aspect of supersonic wind-tunnel testing. This method of flow visualization provides the shock patterns in the flow field. The picture above shows a Schlieren photograph of the flow over the W/B configuration at M_∞=1.6 and α=0.32°. Clearly shown here are the shocks from the nose and wing reflecting off the wall and impinging on the aft section of the model.

Comparison of Predicted and Experimental Lift Curves M2.4-7A Opt5, 1.675% Model, W/B Configuration

CFL3D and Langley Test 1651, UPWT, M_∞=2.4, Re=4x10^6/ft

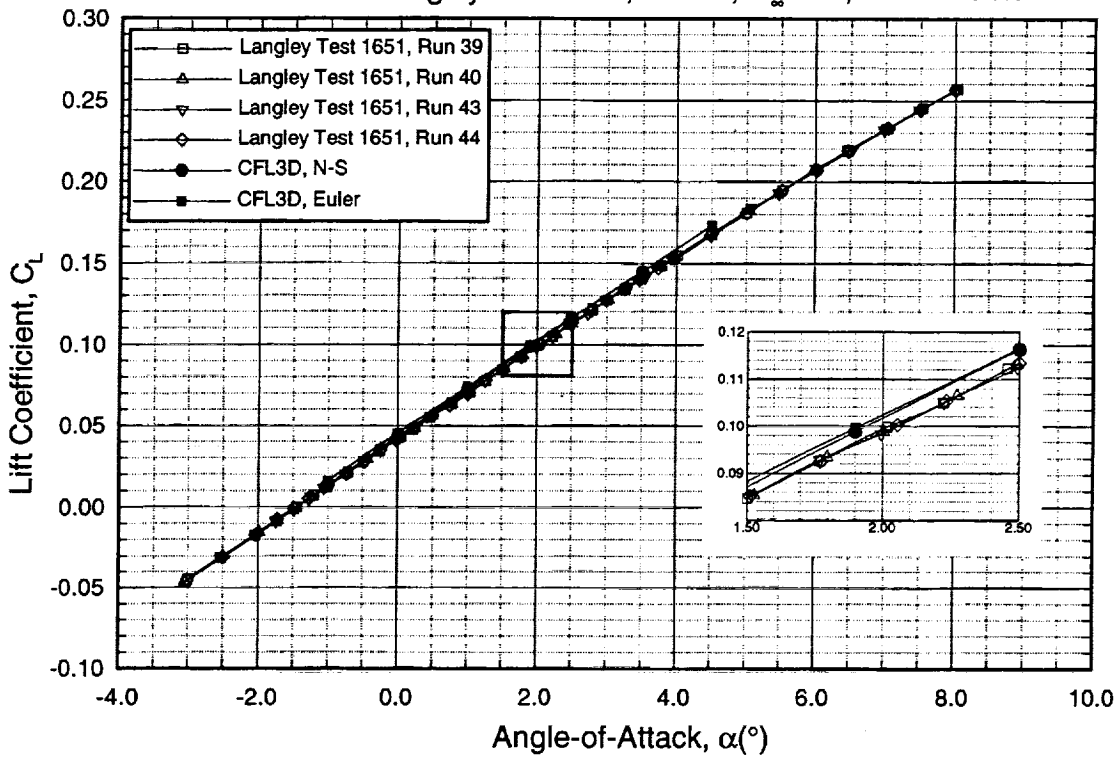

Having established an approximation to trip drag it is now possible to validate the MDA non-linear design methodology by verifying CFD prediction methods with the experimental data. While optimization of the M2.4-7A baseline was performed using FLO67 as the analysis tool, improvements to the design were quantified using CFL3D. The following chart shows CFL3D Euler and Navier-Stokes lift predictions closely matching experimental data from UPWT section #2 for the Opt5 W/B configuration at the design Mach number and Reynolds number of 4 million/ft. The CFD solutions slightly over predict the lift-curve slope. The Navier-Stokes calculations were performed using the Baldwin-Lomax turbulence model. Sublimation runs showed the boundary layer to be fully tripped.

Comparison of Predicted and Experimental Drag Polars
M2.4-7A Opt5, 1.675% Model, W/B Configuration

CFL3D and Langley Test 1651, UPWT, M_∞=2.4, Re=4x10^6/ft

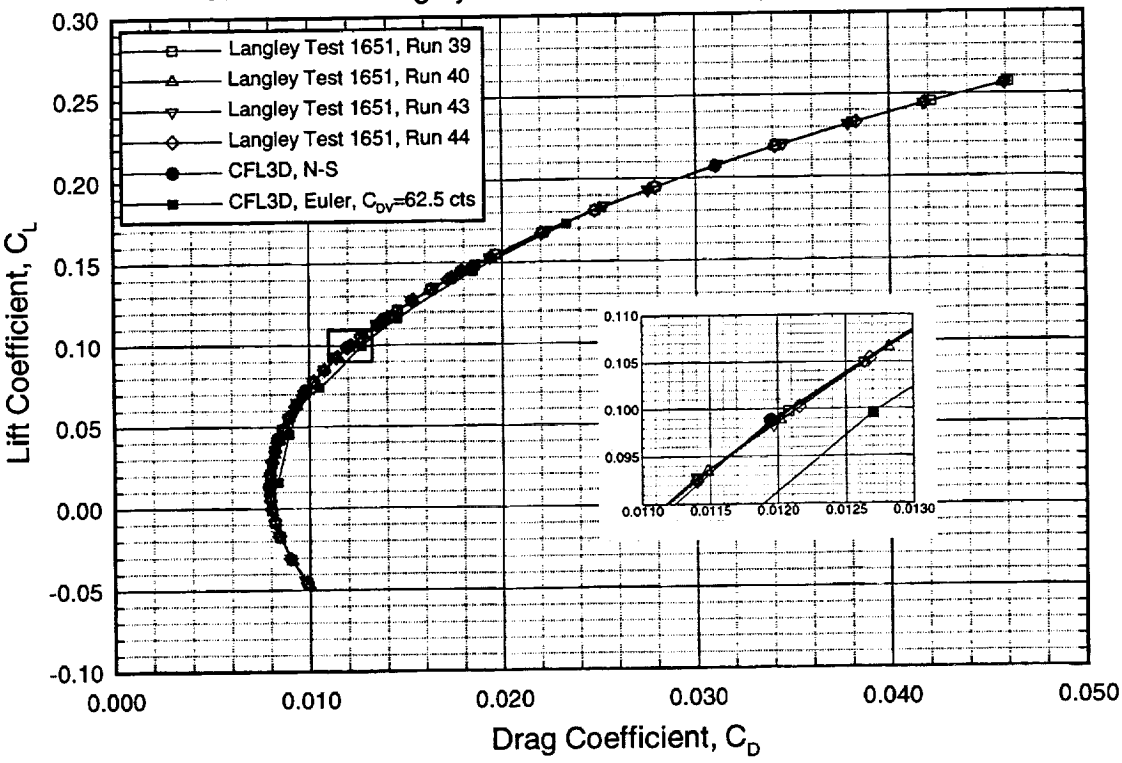

This plot shows a comparison of CFL3D Euler and Navier-Stokes predicted drag polars to experimental data taken at the cruise Mach number and Reynolds number of 4 million/ft. The Navier-Stokes solutions, computed with the Baldwin-Lomax turbulence model, agree very well at the cruise C_L of 0.1 and are within 0.5 counts at the minimum drag condition. As the trip study showed, the installation of trip dots (height=0.0122") produced 4.1 counts of drag at M_∞=2.4. This drag is subtracted from the experimental data in this chart. A flat-plate skin friction, C_{DV}, value of 62.5 counts has been added to the Euler solution. By comparing the Euler drag values with the Navier-Stokes drag values, it can be seen that the difference occurs in the skin friction estimation.

Comparison of Predicted and Experimental L/D Curves
M2.4-7A Opt5, 1.675% Model, W/B Configuration

CFL3D and Langley Test 1651, UPWT, M_∞=2.4, Re=4x10^6/ft

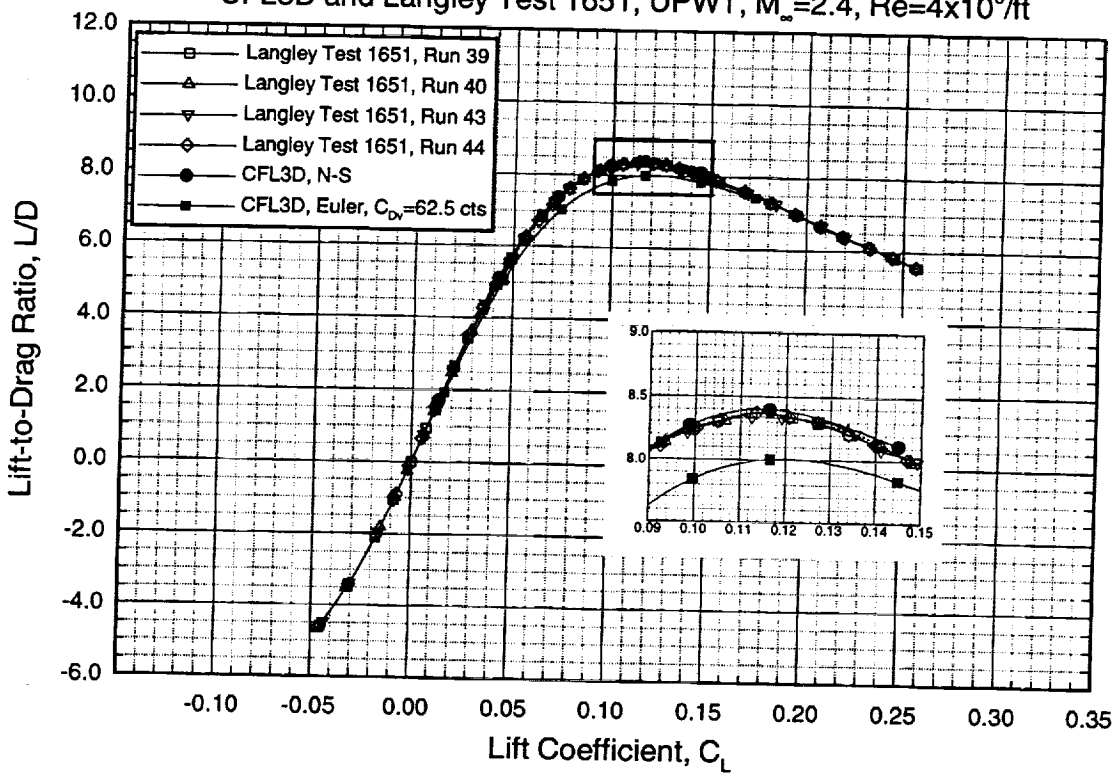

Shown above is an excellent agreement between the CFL3D Navier-Stokes solutions and the experimental data. As in the previous chart, a trip drag value of 4.1 counts has been subtracted out of the experimental data. The Euler solutions, with 62.5 counts of flat-plate skin friction added in, under predicts the maximum L/D value by approximately 5%. Differences between the Navier-Stokes and Euler drag values occur in the skin friction prediction.

Comparison of Predicted and Experimental Lift Curves M2.4-7A Opt5, 1.675% Model, W/B/N/D Configuration

CFL3D and Langley Test 1651, UPWT, M_∞=2.4, Re=4x10^6/ft

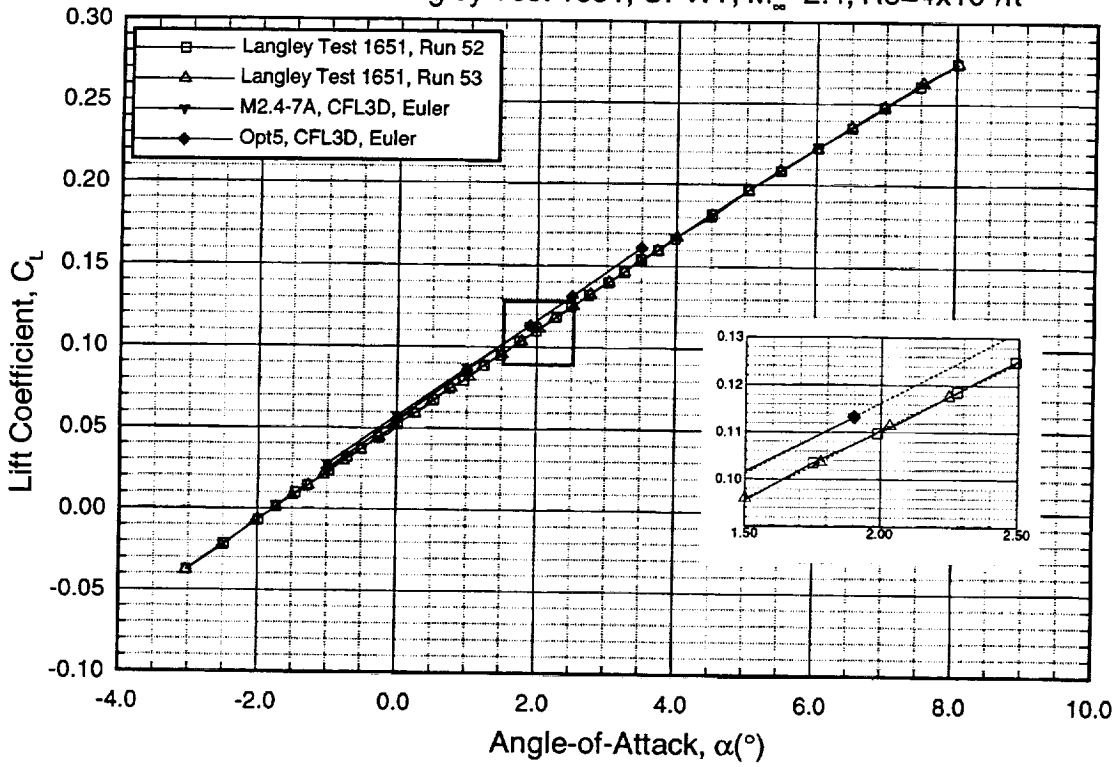

In addition to verifying the Navier-Stokes W/B predictions, Euler W/B/N/D predictions were compared to experimental data. Navier Stokes predictions for the W/B/N/D are currently not available. This figure shows that the Euler W/B/N/D solutions slightly overpredict the lift-curve slope.

In addition, this plot shows a comparison to Euler solutions for the M2.4-7A baseline W/B/N/D configuration. While the Euler predictions for the Opt5 W/B/N/D show a slight increase in lift-curve slope over the baseline, experimental measurements show a slight decrease compared to the CFD predicted baseline slope.

Comparison of Predicted and Experimental Drag Polars
M2.4-7A Opt5, 1.675% Model, W/B/N/D Configuration

CFL3D and Langley Test 1651, UPWT, M_∞=2.4, Re=4x10^6/ft

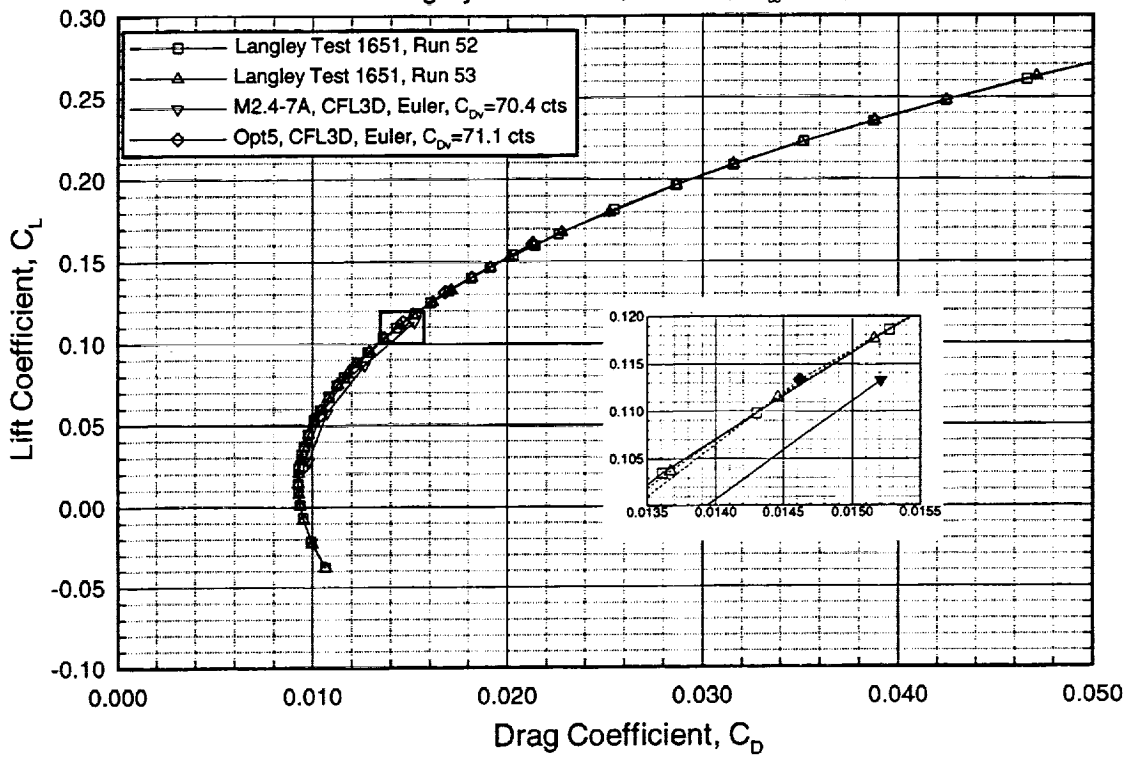

This drag polar shows the excellent comparison between CFL3D Euler W/B/N/D solutions and two short-term repeat experimental runs. The CFD-predicted baseline M2.4-7A drag polar is included as a reference. Flat-plate skin friction drag was added to the Euler solutions in the amount of 70.4 and 71.1 counts for the baseline M2.4-7A and Opt5 configurations, respectively.

This plot also shows the improvement in the optimized W/B/N/D configuration over the baseline M2.4-7A configuration. At the cruise C_L of 0.11, the total improvement is approximately 6 counts. However, contrary to flat-plate skin friction predictions, Navier-Stokes comparisons between the baseline and Opt5 W/B configuration shows that the Opt5 has less skin friction than the baseline by approximately 2 counts. This would suggest an even larger improvement between the baseline and the optimized Arrow Wing.

Comparison of Predicted and Experimental L/D Curves M2.4-7A Opt5, 1.675% Model, W/B/N/D Configuration

CFL3D and Langley Test 1651, UPWT, M_∞=2.4, Re=4x10^6/ft

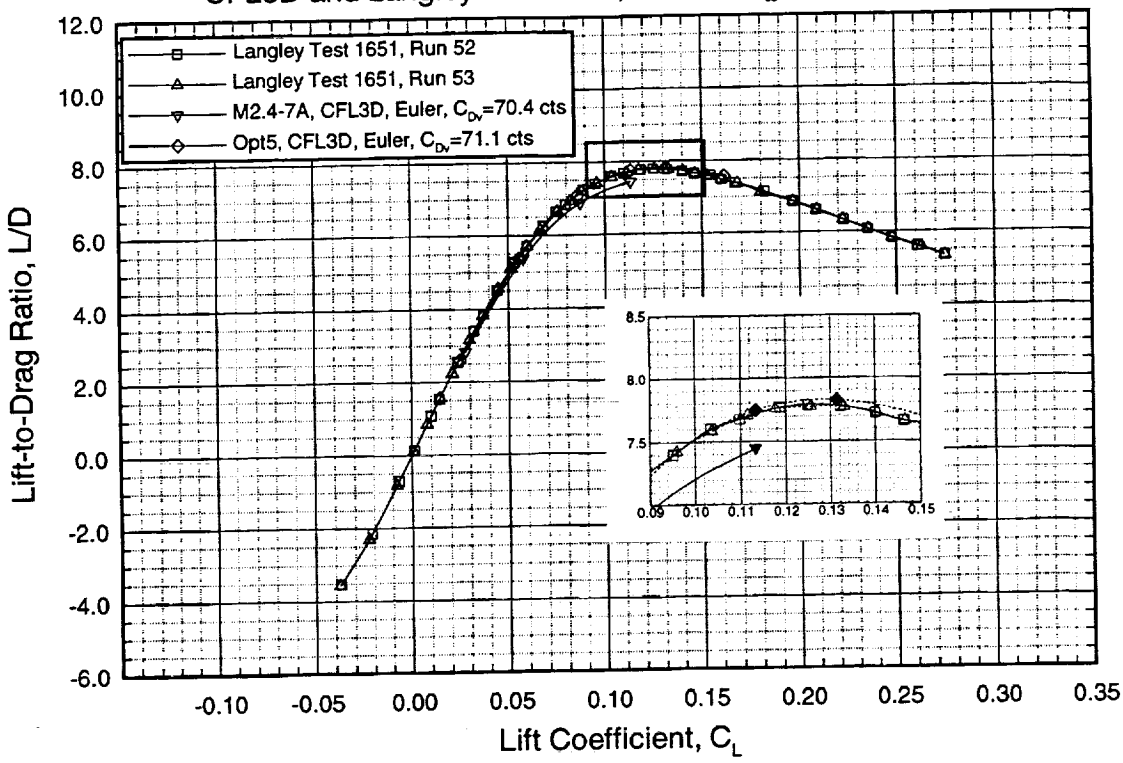

This figure shows the improvement in L/D of the optimized M2.4-7A over the baseline as predicted by CFL3D and verified by experimental data. As in the previous figure, flat-plate skin friction drag was added to the Euler solutions in the amount of 70.4 and 71.1 counts for the baseline M2.4-7A and Opt5 configurations, respectively.

Predicted and Experimentally Determined Drag Reduction of the Opt5 Configuration

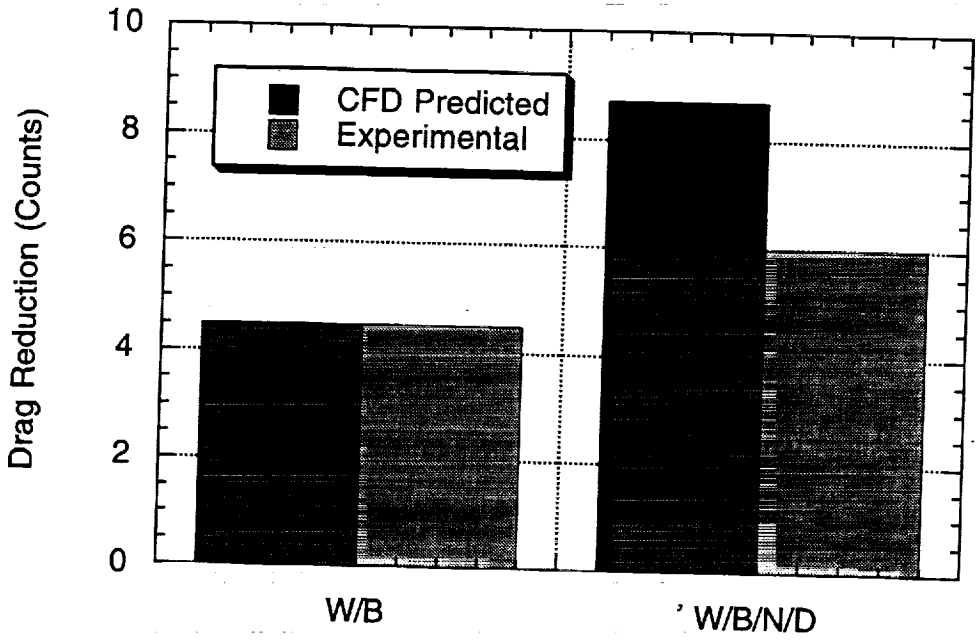

* Comparisons made to CFD predicted drag values of baseline M2.4-7A

CFD predictions of the W/B compared well to force, moment and pressure data gathered during the Opt5 entry in the UPWT section #2. The data shows an appreciable drag reduction over the baseline linear design. The experimental W/B/N/D data shows 6 counts of drag reduction over the CFD-predicted linear theory design. CFL3D Euler predictions with flat-plate skin friction corrections shows a similar 6 count improvement. However, as mentioned on the previous page, Navier-Stokes comparisons between the baseline and Opt5 W/B configuration shows the Opt5 to have 2 counts less skin friction. The less accurate, flat-plate theory predicts the Opt5 design to have an additional 0.7 counts of skin friction. We expect the Navier-Stokes-predicted 2 count reduction in skin-friction to translate from the W/B to the W/B/N/D configuration. Thus, at best an 8.7 count improvement will be observed between the baseline M2.4-7A and the Opt5 W/B/N/D. The actual improvement between the Opt5 and baseline designs will be determined after the experimental evaluation of the baseline M2.4-7A. Nevertheless, the tests clearly proved that the present non-linear optimization scheme works well.

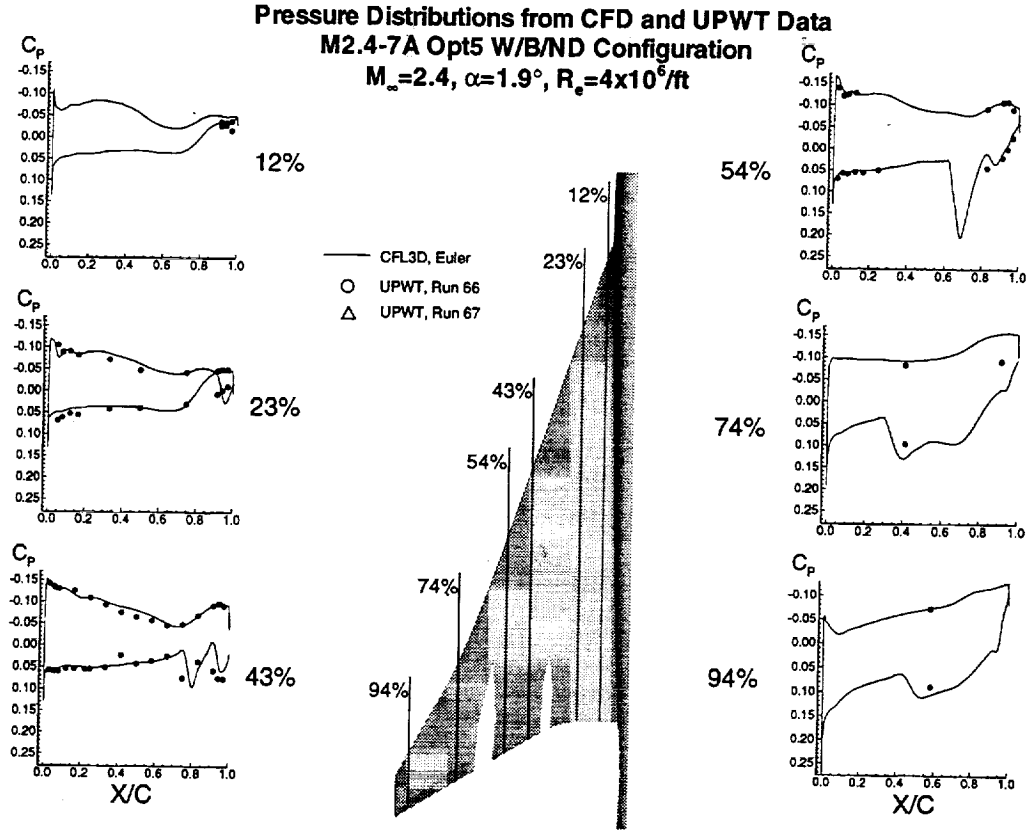

Shown above are pressure distributions that compare CFL3D Euler results to the test data at M_∞=2.4 and α=1.9°. The results are considered fairly good considering that viscous effects are not modeled in the prediction. The predicted nacelle shocks are generally upstream and stronger than the measured (which is expected from the Euler analysis).

Comparison of Predicted and Experimental Drag Polars
1.675% M2.4-7A Opt5, Model, W/B Configuration

Langley Test 1651 & 1822, UPWT, M_∞=1,8, 2.0, 2.16, 2.4, Re=4x10^6/ft

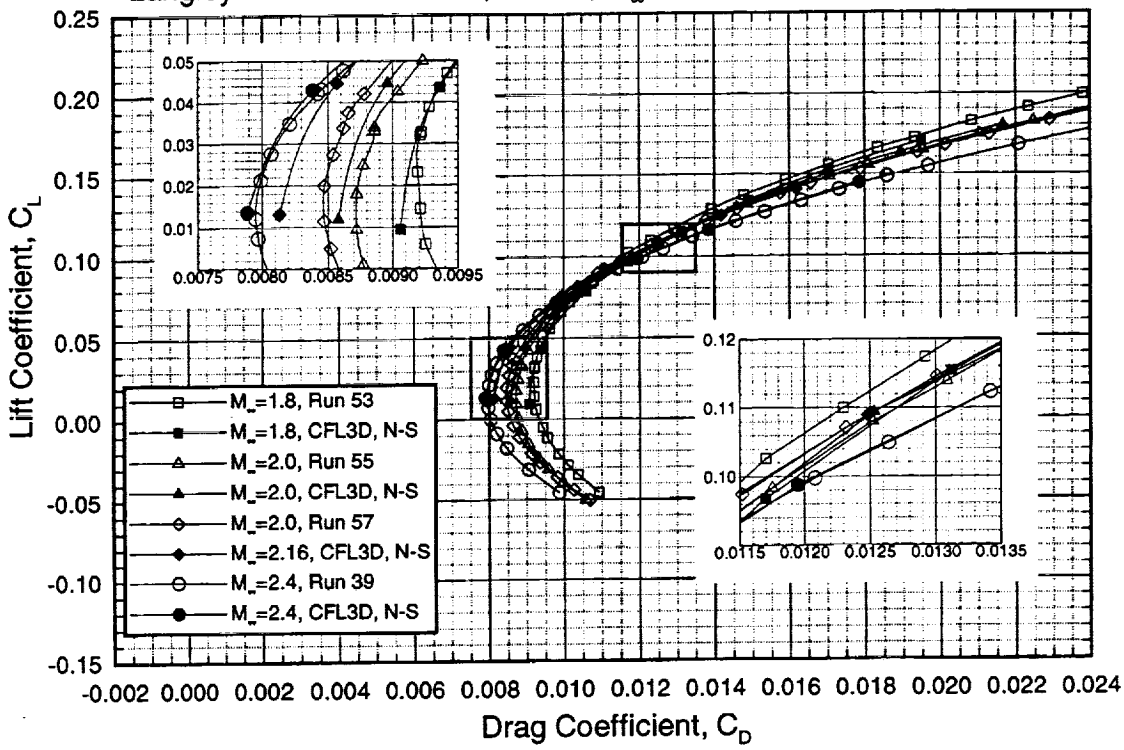

Wind-tunnel data from UPWT test section #1 was used to validate CFL3D Euler and Navier-Stokes solutions at off-design Mach numbers. In this figure, Navier-Stokes solutions using the Baldwin-Lomax turbulence model are compared to experimental data. The wind-tunnel model had trip dots installed to trip the boundary layer and the appropriate trip drag has been removed from the experimental data. At M_∞=1.8 and 2.0, the Navier-Stokes solutions under predict the minimum drag by one count. At M_∞=2.16, the Navier-Stokes solutions under predict the minimum drag by 3 counts. For reference, the cruise Mach number polar is added to the plot.

CFL3D N-S Streamlines

1.675% M2.4-7A Opt5 Model, W/B Configuration

M_∞=2.4, α=4.49°, Re=4.0x10^6/ft.

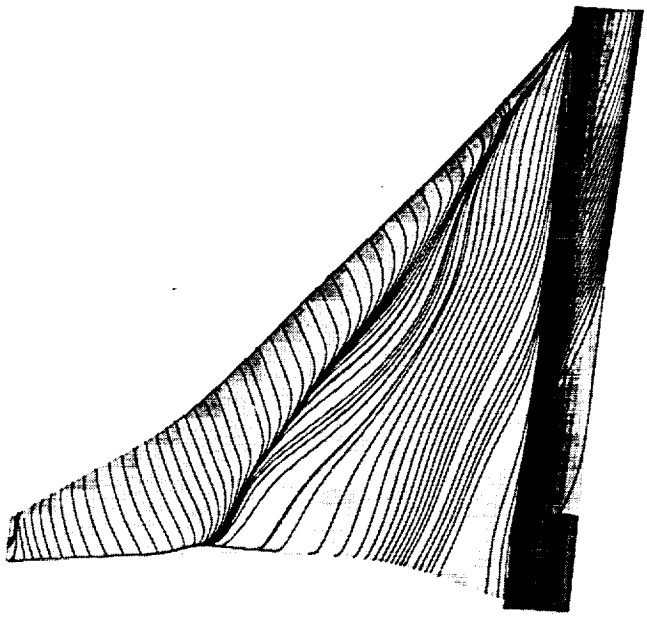

Pictured above are surface streamlines generated from a Navier-Stokes solution using CFL3D at M_∞=2.4 and α=4.49°. Similar patterns exist between the CFD solution and the colored oil flow picture taken during the Opt5 entry in test section #1 (viewed on the next page).

Oil Flow Visualization

1.675% M2.4-7A Opt5 Model, W/B Configuration

M_∞=2.4, α=4.49°, Re=4.0x10^6/ft.

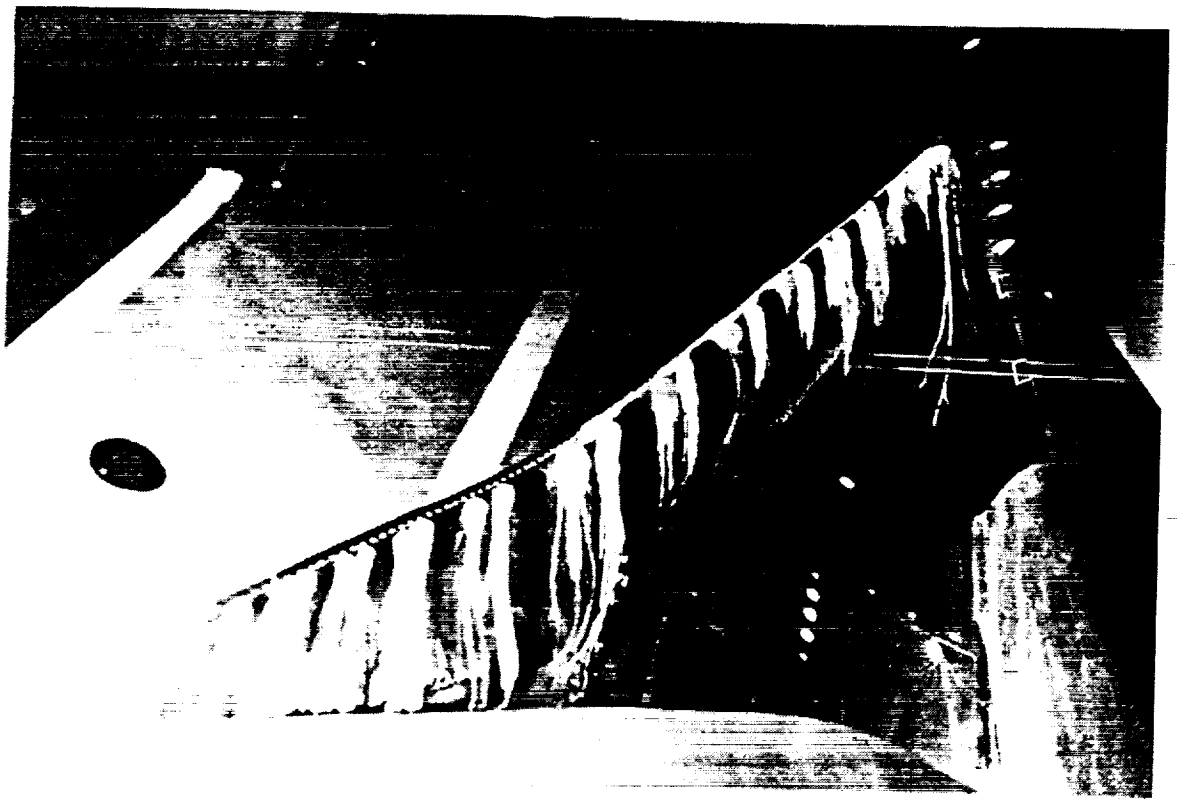

Surface oil flow visualization is an effective way to understand the overall behavior in the neighborhood of the model surface. This also provides an easy method to visualize separated flow, vortex flow and shocks.

For supersonic oil flow visualization, the recommended paint mixture consists of 2 tubes of colored oil paints, 2 to 3 tablespoons of Tempora paint, and a sufficient amount of 10 to 90 weight motor oil to achieve a consistancy similar to whipped cream. The oil paint mixture was applied to the model aft of the transition disks with a syringe in the form of dots approximately 1/8" to 1/4" in diameter.

The picture above maps the streamlines for the condition M_∞=2.4 and α=4.49° on the upper surface. On the inboard section of the upper wing, we see a large section of the wing where the paint had not spread. Here the flow had turned outboard indicating that a vortex was generated from the W/B junction.

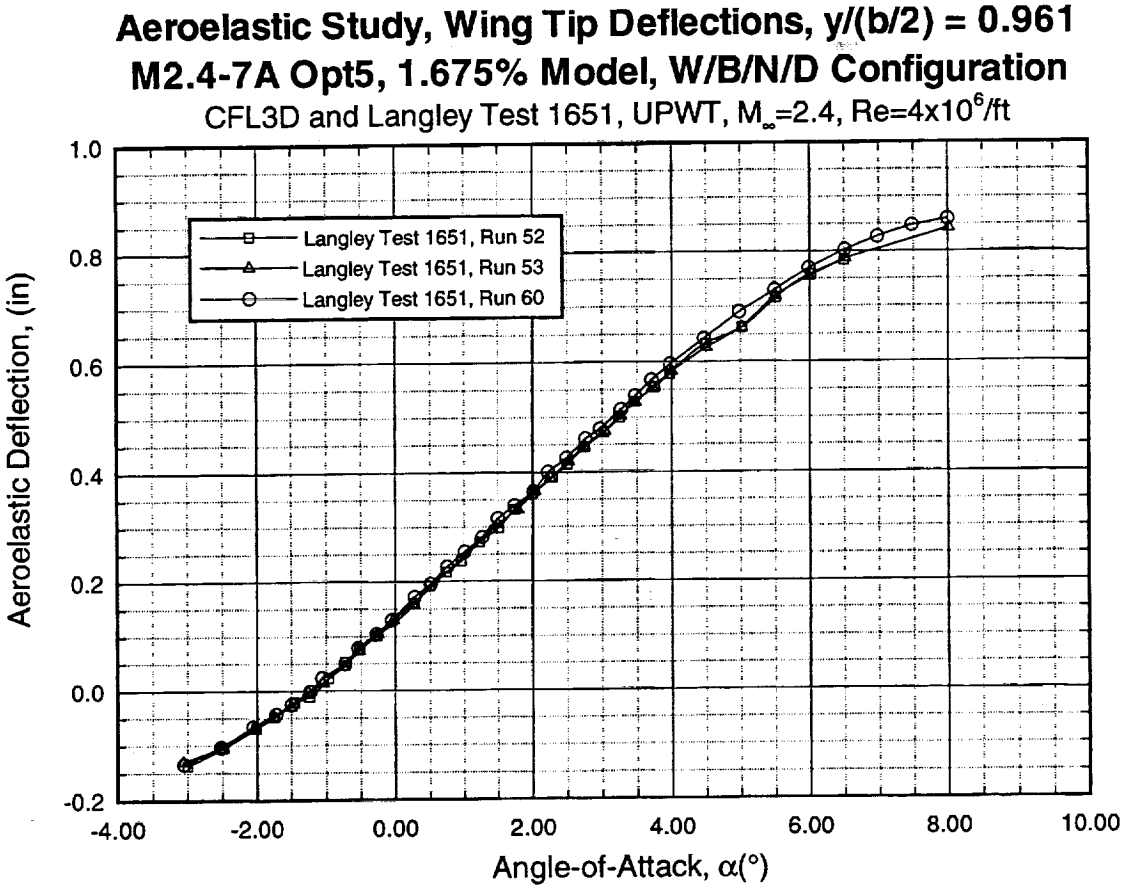

An attempt was made to measure the real-time aeroelastic deflections on the wing tips of the model. A prototype system developed by NASA Langley involves tracking targets placed on the wings with a digital camera. Two rows of four reflective tape targets (0.001" thick, 0.125" to 0.25" dia.) were placed on the wing upper surface at 84% and 96% semi-span, equally spaced from 25% to 90% chord. The camera recorded the position of the disks prior to and during the run. Results indicated a wing tip deflection of approximately 0.35" at the cruise C_L, Re=4 million/ft., and M_∞=2.4.

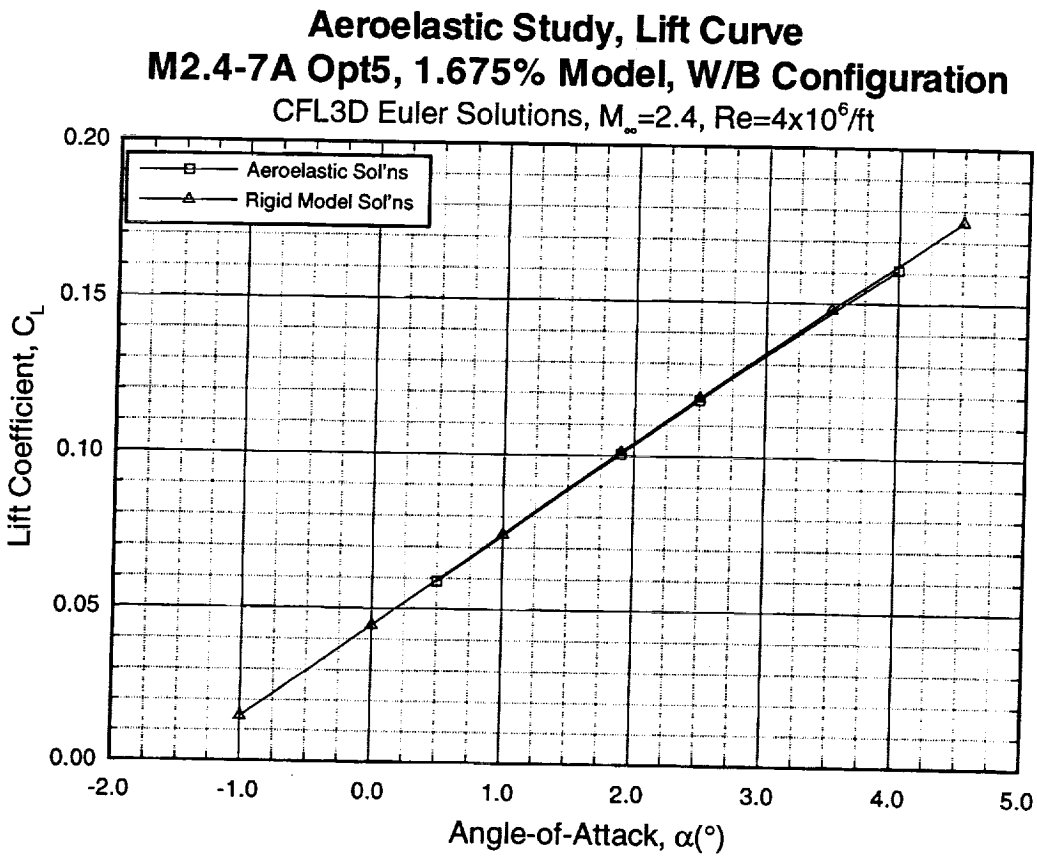

The following chart shows an effort to quantify the aeroelastic effects using CFD. In this comparison CFL3D Euler predictions with aeroelastic deflections are compared to CFL3D Euler predictions of a rigid model. The Euler solutions represented by the square symbols in the figure are obtained with geometries having deflected wing tips representative of the deflections observed in the previous chart. There is a slight loss of lift noticeable at the higher angles-of-attack since the outboard wing section provides only a small portion of the lift. A more in-depth study is currently underway at MDA.

Data Highlights of Tests in 16 ft. TWT

- Established an Arrow Wing data base at transonic and low supersonic speeds; captured drag rise
- Concluded optimal flap settings of 10°/15°/3°* for M_∞=0.95 and 0°/5°/3° for M_∞=1.1

* x°/y°/z° indicates x° inboard leading-edge flap deflection, y° outboard leading-edge flap deflection, and z° trailing-edge flap deflection

The test began with an assessment of the flow angularity in the wind tunnel. A trip drag study was performed next using nominal disk height of 0.006", 0.008", and 0.011" on the W/B/N/D configuration. A transition-free run concluded the trip-drag assessment. Flow visualization using the sublimation technique was used to identify fully transitioned flow. Force and moment data were taken next for the W/B/N/D configuration with several leading-edge and trailing-edge flap settings. The pressure tubes were then hooked-up to obtain pressure data. Following this, the pressure hook-ups were removed to obtain accurate force and moment data at the optimal flap settings for $(L/D)_{max}$ at M_∞=1.1 and M_∞=0.95. During the test, colored oil flow visualization tests were also performed to gain insight into the flow physics.

During the test, the tunnel ran primarily at Mach numbers of 0.6, 0.8, 0.9, 0.95, 1.1, and 1.2. A small number of runs was obtained at Mach 0.3 to compare with future low-speed wind-tunnel data. In addition, a small number of runs at M_∞= 0.975, 1.01, and 1.05 was performed to capture the drag rise; however, shock reflection interference occurred at these Mach numbers. Reynolds number per foot was maintained between 3 and 4 million. The angle-of-attack ranged from -3.0° to 8.0° with $\Delta\alpha$=0.5° and from -1.0° and 1.0° with $\Delta\alpha$=0.25°.

Highlights from the 16 ft. TWT test include capturing of the drag rise and establishment of flap settings for the Opt5 design at M_∞=0.95 and 1.1.

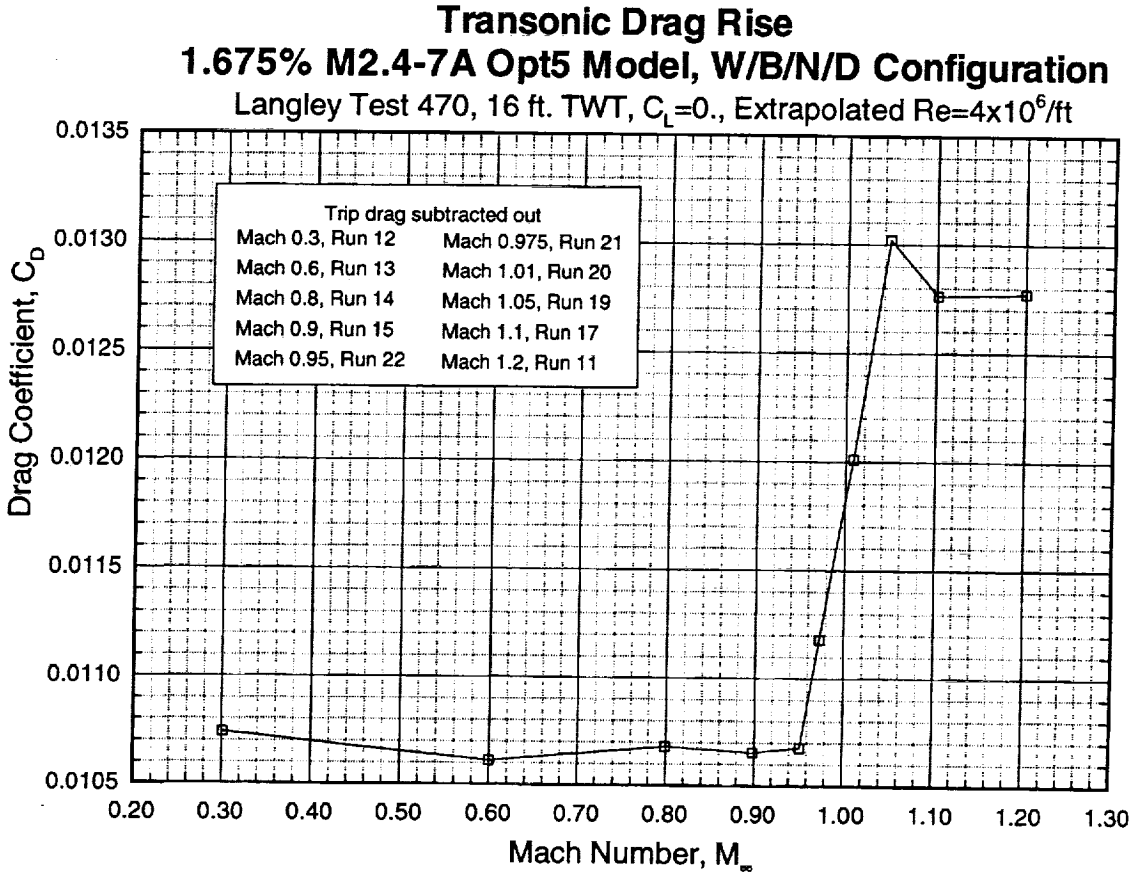

Shown below is the transonic drag rise, Mach number versus drag coefficient. Since the Reynolds numbers at the lower Mach numbers were less than 4 million/ft., the drag coefficients at these Mach numbers have been extrapolated to the corresponding drag value at Re=4 million/ft. based on a flat-plate correction.

Best L/D for Subsonic and Low Supersonic Mach Numbers
1.675% M2.4-7A Opt5 Model, W/B/N/D Configuration

Langley Test 470, 16 ft. TWT, C_L=0.21 at Tunnel Reynolds Numbers

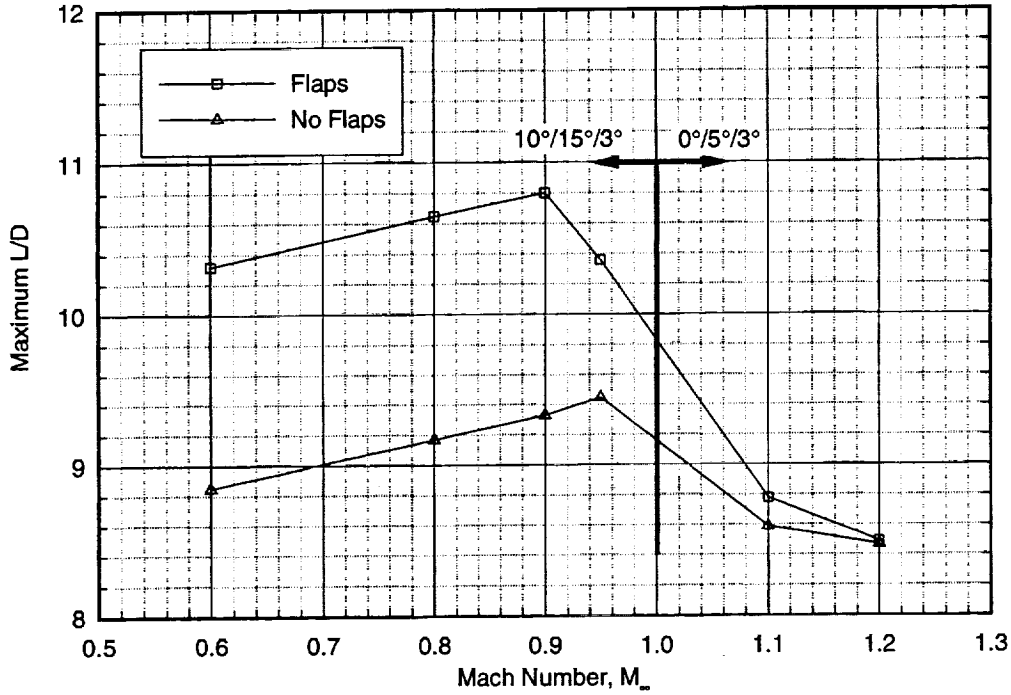

Maximum L/D data, shown above, suggests that only one flap setting may be needed for subsonic cruise (10°/15°/3°), and one for low supersonic cruise (0°/5°/3°). The Opt5 configuration was tested at transonic and low supersonic Mach numbers with several leading-edge and trailing-edge flap deflections. At the transonic Mach numbers, the maximum L/D was obtained with an inboard leading-edge deflection of 10°, outboard leading-edge deflection of 15° and trailing-edge deflection of 3° (10°/15°/3°). At low supersonic Mach numbers, the optimal setting for the maximum L/D was found to be 0°/5°/3°. At these speeds the inboard leading-edge flap was found to be ineffective. The maximum L/D data, shown above, suggests that only one flap setting may be needed for subsonic cruise and one for low supersonic acceleration condition.

Summary and Conclusions

- M_∞=2.4 and 2.55 tested in UPWT section #2
- M_∞=1.6 through 2.4 tested in UPWT section #1
- M_∞=0.3 through 1.2 tested in 16' transonic wind tunnel
- Good agreement between CFD and test data
- Achieved at least 6 counts of drag reduction for W/B/N/D configuration in the UPWT section #2
- Validated the supersonic cruise point design optimization methodology used at MDA

The 1.675% model of the M2.4-7A Opt5 geometry was successfully tested at the UPWT section #2 and section #1 as well as the 16 ft. TWT. Data at a series of Mach numbers between 0.3 and 2.55 has been obtained. Good agreement between CFD and experimental data at the design Mach number confirmed that the design methodology used to obtain the optimized M2.4-7A Opt5 configuration is effective. At least six counts of drag reduction for the W/B/N/D configuration was obtained over the linear theory-based design.

Summary and Conclusions
(Con't)

- Established a linear relationship between trip drag correction and Mach number
- Established one flap setting for transonic cruise and one for low supersonic acceleration

Experiments in the UPWT test section #1 and 16 ft. TWT also validated CFD prediction at off-design conditions. A trip drag study was done with the data obtained and a linear relationship was found between the trip drag penalty and Mach number. At transonic and low supersonic acceleration, a series of flap settings was investigated. It was found that only one flap setting for transonic cruise and another for supersonic acceleration was needed.

Initial Results of Reynolds Number Testing at LaRC's NTF Using the 2.2% Reference H Model

Marvine Hamner, Engineer Scientist/Specialist, McDonnell Douglas Aerospace
Lewis R. Owens, Jr., Aerospace Engineer, NASA Langley Research Center
Dr. Richard A. Wahls, Aerospace Engineer, NASA Langley Research Center

To develop full scale flight performance predictions an understanding of Reynolds number effects on HSCT-class configurations is essential. A wind tunnel database utilizing a 2.2% scale Reference H model in NASA Langley Research Center's National Transonic Facility is being developed to assess these Reynolds number effects. In developing this database temperature and aeroelastic corrections to the wind tunnel data have been identified and are being analyzed. Once final corrections have been developed and applied, then pure Reynolds number effects can be determined. In addition, final corrections will yield the data required for CFD validation at q = 0.

Presented in this report are the results of seven tests involving the wing/body configuration. This includes summaries of data acquired in these tests, uncorrected Reynolds number effects, and temperature and aeroelastic corrections. The data presented herein illustrates the successes achieved to date as well as the challenges that will be faced in obtaining full scale flight performance predictions.

Initial Results of Reynolds Number Testing at LaRC's NTF Using the 2.2% Reference H Model

Marvine Hamner, Engineer Scientist/Specialist, McDonnell Douglas Aerospace
Lewis R. Owens, Jr., Aerospace Engineer, NASA Langley Research Center
Dr. Richard A. Wahls, Aerospace Engineer, NASA Langley Research Center

With grateful acknowledgment of all the other researchers at NASA, The Boeing Company, and McDonnell Douglas Aerospace that have contributed to this testing.

This presentation is the successful result of the collaboration of NASA, Boeing, and McDonnell Douglas researchers in planning and testing an HSCT-class configuration under a wide variety of conditions. It focuses on the wing/body configuration. The full configuration including aftbody and tails is discussed in other papers included in this conference which specifically address issues such as; aftbody closure, and high Reynolds number stability and control characteristics. Ongoing seal development work will enhance the acquisition of high quality performance data on the full configuration.

Presentation Outline

- Overall Test Objectives
- Model/Configurations Definition
- Summary of Tests Completed
- NTF Operating Envelopes and Conditions
- Initial, Uncorrected Test Results
  - Data Repeatability
  - Reynolds Number Effects
- Corrections to Data
  - Temperature Effects
  - Aeroelastic Effects
- Initial, Corrected Test Results
- Summary, Conclusions, and Recommendations
- Appendices:
  - Pressure Data Acquired
  - Force/Moment Data Acquired
  - Linear Aeroelastic Data Acquired

Overall NTF Test Objectives

- **Develop full scale performance predictions.**
- **Obtain data for CFD validation.**
- **Obtain other data relevant to determining Reynolds number effects on an HSCT-class configuration.**

To develop full scale performance predictions an understanding of Reynolds number effects on HSCT-class configurations is essential. A wind tunnel database utilizing a 2.2% scale Reference H model in NASA Langley Research Center's National Transonic Facility is being developed to assess these Reynolds number effects. In developing this database temperature and aeroelastic corrections to the wind tunnel data have been identified and are being analyzed. Once final corrections have been developed and applied, then 'pure' Reynolds number effects can be determined. In addition, application of these final corrections will yield the data required for CFD validation at q=0.

Model/Configurations Definition

Wing: Reference H wing (76/68.5/48)

Flap deflections available:

	LE	TE
Baseline	**0/0**	**0/0**
Transonic	**0/10**	**0/3**
High Lift	**30/30**	**10/10**
	30/30	**0/20**
	30/30	**20/20**
	50/50	**30/30**

Body: Fuselage truncated at station 60.8150

Complete fuselage

Nacelles: Axisymmetric

The 2.2% scale Reference H model used for testing at the NTF includes:

- wing - with various flap deflections representing high-speed and high-lift configurations
- fuselage
- axisymmetric nacelles
- vertical tail - with and without rudder deflection
- horizontal tail - with various stabilizer deflections

The truncated fuselage is run on the straight sting and the complete fuselage on the lower swept strut. Trips normally applied include the forebody ring and nacelle internals. Wing trips will be developed as part of the boundary layer transition study during 1996.

Model/Configurations Definition
Cont.

Vertical Tail: Undeflected rudder
Rudder deflected to 30° (TE left)

Horizontal Tail: Undeflected elevator with stabilizer incidence of i_H=0, +/-2, +/-5, +/-10, -15
Elevator deflected to 30° (TE down) with stabilizer incidence of i_H=-15

Trips: Forebody ring
Nacelle internal

Sting: Straight sting
Lower swept strut (LSS)

Test	Test Date	Test Type	Configs	Objective
NTF057	7/93	P	W/B: Baseline High Lift (a)	(1) Longitudinal Pressure Data
NTF060	12/93	F	W/B: Baseline High Lift (a) Transonic	(1) Longitudinal Force/Moment Data
NTF063	5/94	P/F	W/B/N: Baseline High Lift (b) Transonic	(1) Longitudinal Pressure and Force/Moment Data with and without Nacelles
NTF067	12/94	P/F	W/B/N: Baseline High Lift (b) Transonic	(1) Lateral/Directional Data (2) Transition and Simulated Frost Data
NTF070	4/95	P/F	Full Config: High Lift(b) Transonic	(1) Seal Study (1) Longitudinal and Lateral/Directional Data
NTF073	6/95	F	Full Config: High Lift(b) Transonic	(1) Seal Study (1) Stability and Control Data
NTF078	1/96	P/F	W/B/N: Baseline High Lift (c) Transonic	(1) Longitudinal Data on Additional High-Lift Configurations (1) Detailed Aeroelastics Data (2) Mini-Tufts Data

P = Pressure W = Wing N = Nacelles
F = Force B = Body

(a) High Lift 30/30 0/20
(b) High Lift 30/30 20/20
(c) High Lift 30/30 10/10
High Lift 50/50 30/30

(1) Primary Objectives
(2) Secondary Objectives

In order to understand Reynolds number effects on HSCT type planforms, seven tests have been completed in Langley Research Center's National Transonic Facility, the NTF. These tests span a period of two and one-half years. The model used in these tests has been the 2.2% scale Reference H model.

A variety of data have been acquired during these tests including: pressure data, force/moment data, simulated frost effects, and transition data by sublimating chemicals. The chord Reynolds number range for the transonic configuration/conditions is from 10-120 million. The chord Reynolds number range for the high-lift configuration/conditions is from 4-90 million.

The conditions required to obtain these chord Reynolds numbers involve temperatures that range from +120° to -250°, with total pressures from ambient to 6 atm. Dynamic pressures range from 150 psf to 2700 psf. In order to assess aeroelastic effects, multiple conditions have been run at the same chord Reynolds number.

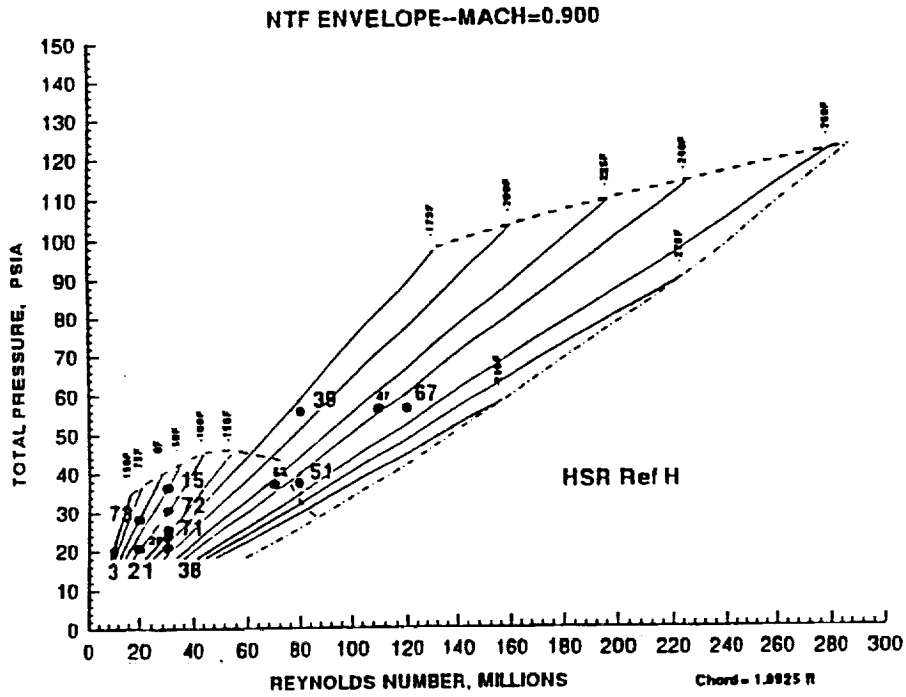

NTF Operating Envelopes:

These figures show the NTF operating envelope for Mach = 0.9 and Mach = 0.3. Rows of numbers across the respective operating envelopes represent conditions at constant q/E and varying chord Reynolds numbers, where E is Young's modulus. Columns of numbers represent conditions at constant chord Reynolds numbers and varying q/E. It should be noted that at the lower and upper bounds on the Reynolds number range only a limited number of conditions can be run, thus only a limited amount of data can be acquired for aeroelastic corrections. No attempt has been made to run conditions along constant temperature lines.

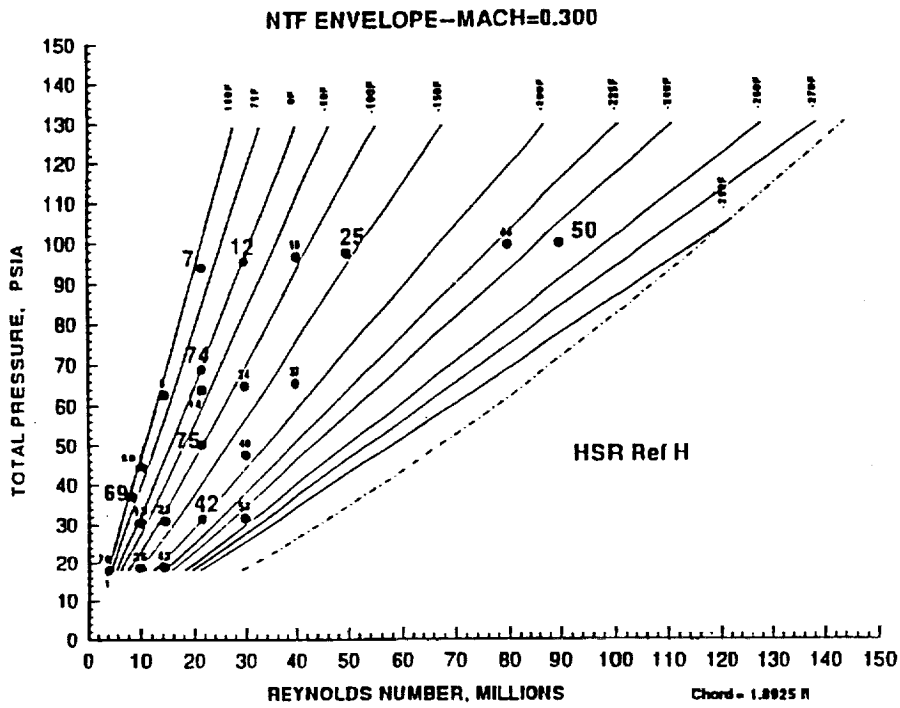
NTF ENVELOPE--MACH=0.300
TOTAL PRESSURE, PSIA
REYNOLDS NUMBER, MILLIONS
HSR Ref H
7
12
25
50
74
75
69
42
0 10 20 30 40 50 60 70 80 90 100 110 120 130 140 150

2.2% Reference H Flaps Up Configuration (Wing/Body)

Mach=0.9 Reynolds Nr.=30.0 Million

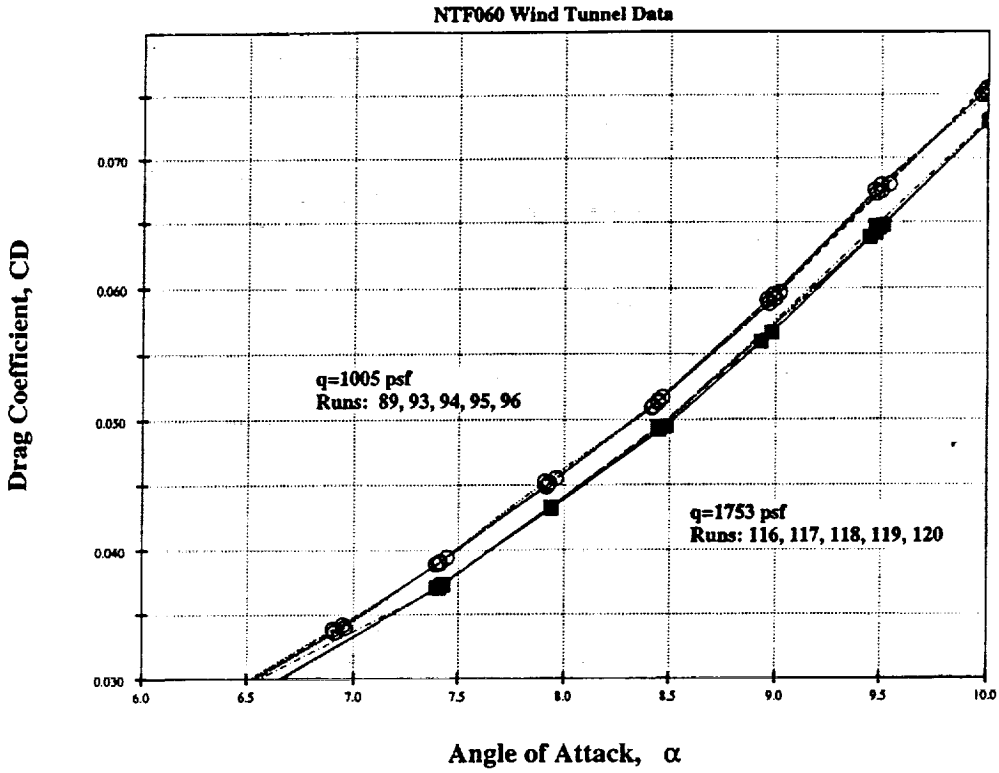

Data Repeatability:

This set of figures illustrates two things. First the overall data repeatability, including the degradation in repeatability at low q conditions. Second it illustrates data repeatability at the end point conditions, that is, at the highest q condition and at the lowest q condition of the linear aeroelastic correction. As can be seen from these figures a correction for aeroelastics is required.

This figure is a plot of repeat runs at high q (q = 1753 psf) and low q (q = 1005 psf) dynamic pressure conditions for Mach=0.9 using the baseline, wing/body, configuration. The difference between the high q and low q runs is quite evident and illustrates the need to calculate a meaningful increment for aeroelastic effects.

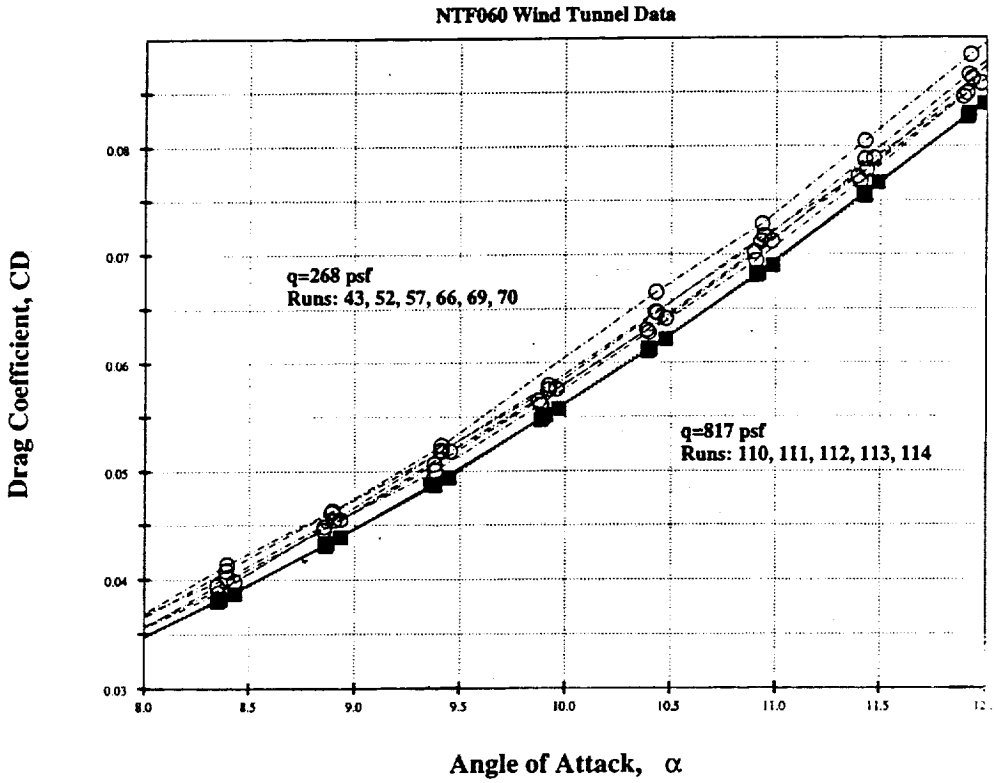

Data Repeatability:

This figure is a plot of repeat runs at high q (q = 817 psf) and low q (q = 268 psf) dynamic pressure conditions for Mach=0.3, again using the baseline, wing/body configuration. The variation in repeatability between the high q and low q runs is quite evident and illustrates the need to acquire repeat runs at low q conditions (q < 600 psf per the HSR NTF Research Guide) in order to calculate a meaningful increment for aeroelastic effects. A band of approximately 40 drag counts results from the natural scatter in the data at low q conditions for the baseline configuration.

Low q conditions are run for Mach = 0.3, baseline and high-lift configurations in order to extend the Reynolds number range to low Reynolds numbers. This is due to the facility constraints as seen before on the NTF operating envelopes.

2.2% Reference H Flaps Up Configuration (Wing/Body)

Mach = 0.9 Reynolds Nr. = 30.0 Million

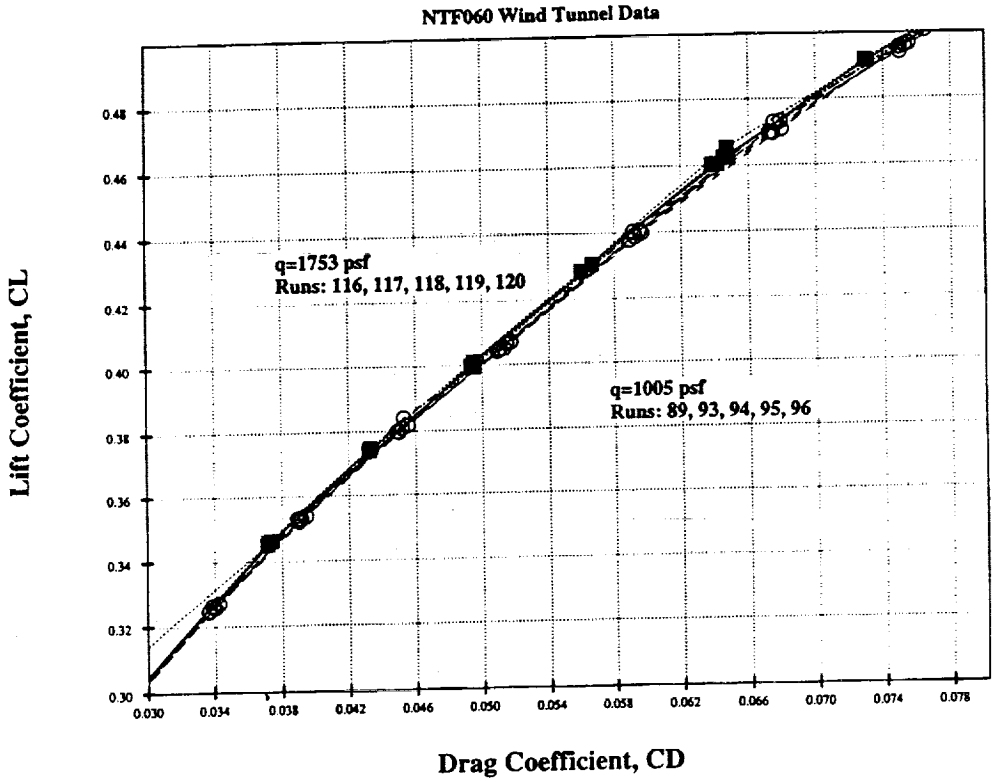

Data Repeatability:

This figure is another plot of the same repeat runs for the Mach=0.9 case at high q (q = 1753 psf) and low q (q = 1005 psf) dynamic pressure conditions. It shows an expanded view of the drag polars from these repeat runs. Again, the difference between the high q and low q runs is quite evident in the polar rotation and illustrates the need to calculate a meaningful increment for aeroelastic effects.

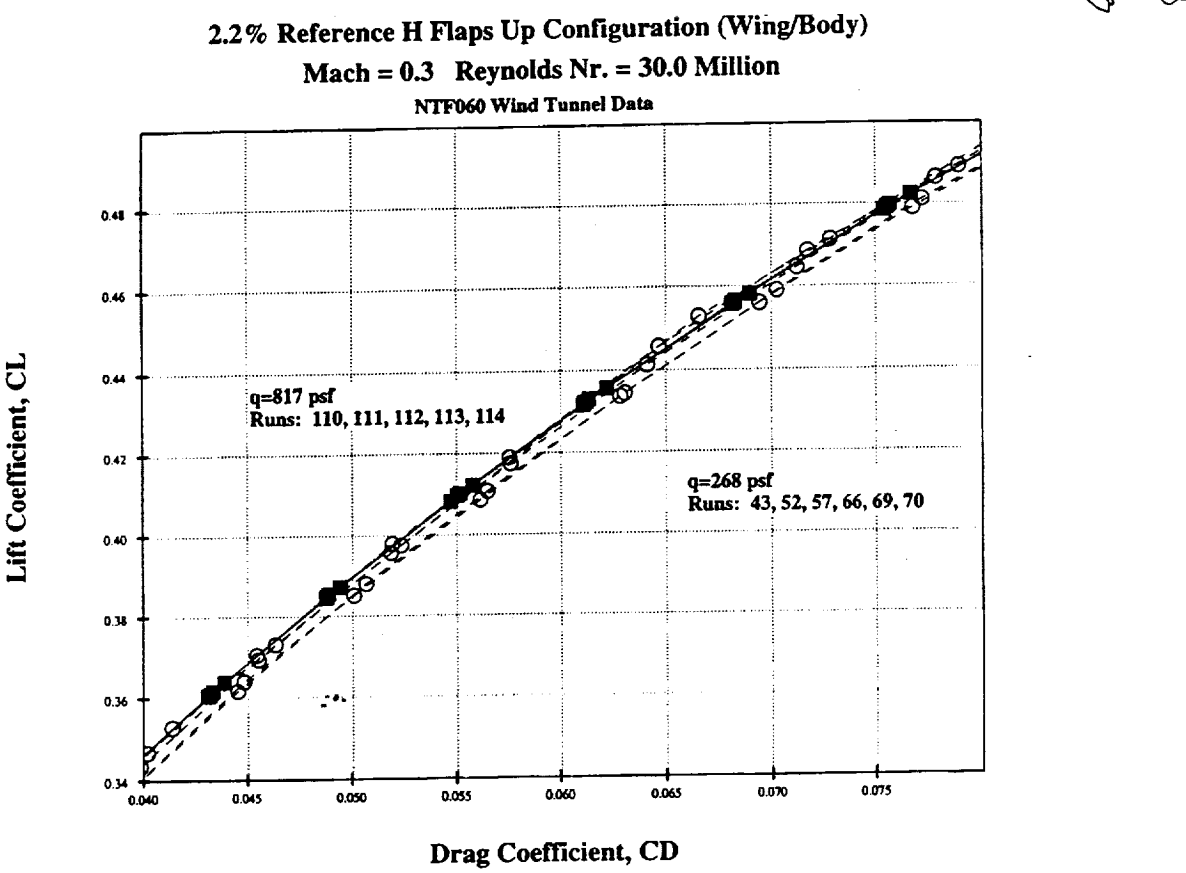

Data Repeatability:

This figure is another plot of the same repeat runs for the Mach=0.3 case at high q (q = 817 psf) and low q (q = 268 psf) dynamic pressure conditions. It shows an expanded view of the drag polars from these runs. The variation in repeatability between the high q and low q runs is quite evident again, illustrating the need to acquire repeat runs at low q conditions (q < 600 psf per HSR NTF Research Guide) in order to calculate a meaningful increment for aeroelastic effects. Once again, the polar rotation apparent indicates the need to understand aeroelastic effects.

EFFECT OF BALANCE ACCURACY ON COEFFICIENTS

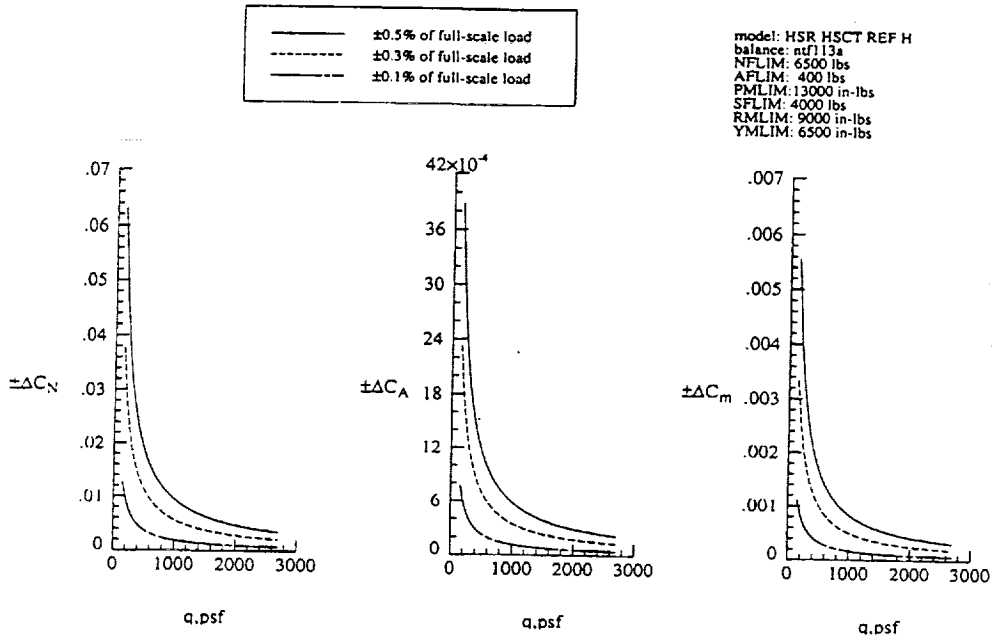

Data Repeatability:

This figure is a plot illustrating the effect of balance accuracy on balance coefficients. The cause of the degradation in repeatability for low q conditions is clearly evident.

Reynolds Number Effect on Drag Coefficient without Aeroelastic or Temperature Corrections

Mach=0.9 Transonic Configuration (Wing/Body/Nacelles)

NTF067 Wind Tunnel Data

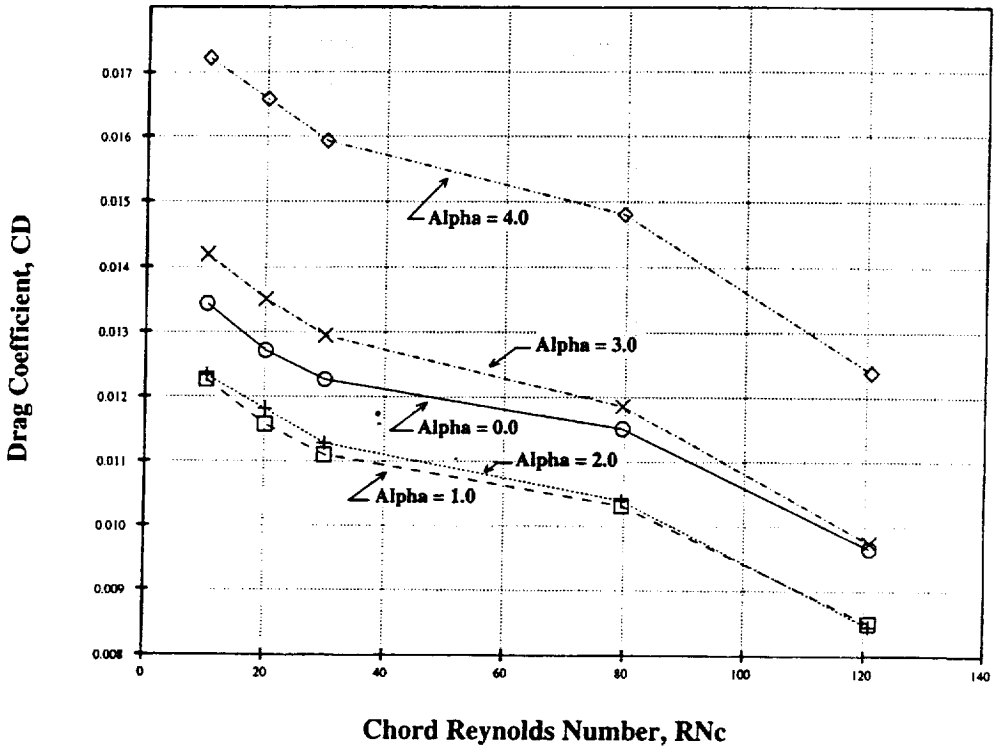

Reynolds Number Effects without Aeroelastic or Temperature Corrections:

The following figures illustrate Reynolds number effects without any additional corrections other than the normal corrections applied by the facility. The points shown are the averages of repeat runs for each condition. The data has been independently verified to be within the normal repeatability of HSCT testing in the NTF. No boundary layer control was employed when this data was acquired. Each point, or condition, represents a different combination of pressure and temperature.

This figure illustrates the uncorrected Reynolds number effect for the Mach = 0.9, baseline configuration. At angles of attack ranging from 0° to 3° there is an approximately 40 count uncorrected increment in drag due to Reynolds number effects over the Reynolds number range from 10 to 120 million. As the angle of attack increases the uncorrected increment in drag due to Reynolds number also increases.

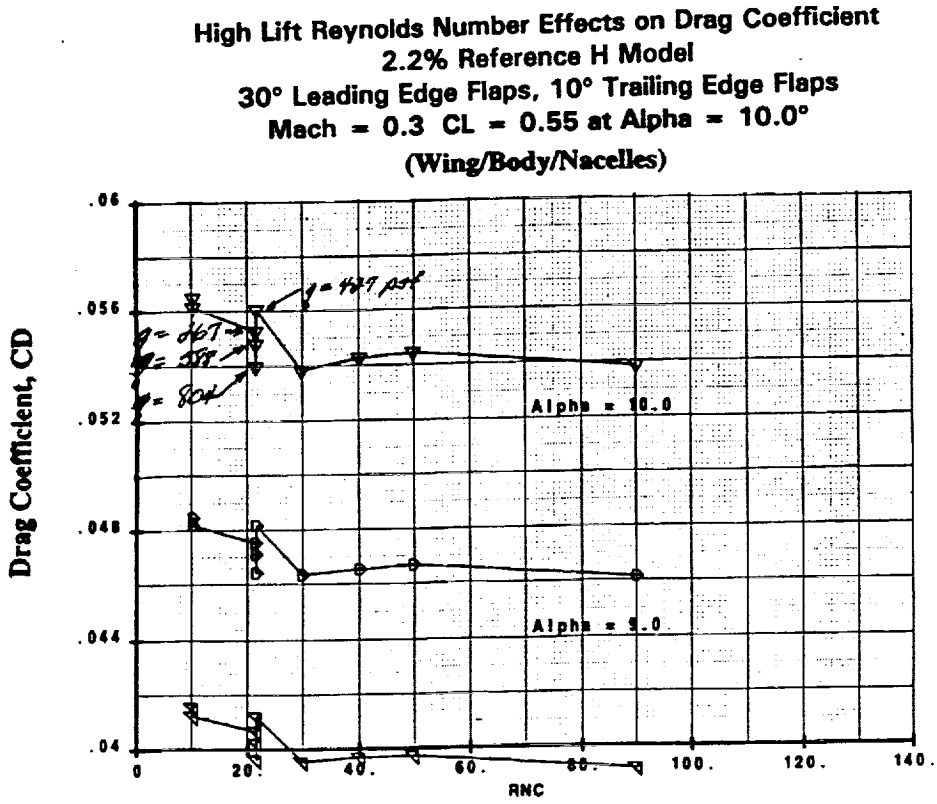

Reynolds Number Effects without Aeroelastic or Temperature Corrections:

This figure illustrates the uncorrected Reynolds number effect for the Mach = 0.3, high-lift configuration. Also shown on this figure are the data at various dynamic pressures for a Reynolds number of 21.6 million. It appears from this data that the aeroelastic correction could be the same magnitude as the increment due to Reynolds number effects.

Additionally, the trend in the Reynolds number effects does not appear to be linear. As has been noted, no boundary layer control was used during data acquisition. As discussed in "Boundary Layer Transition in the NTF - HSR Experience and Plans," there is significant laminar flow at low Reynolds numbers. It has been postulated that this will account for the non-linear behavior in several trends discussed in this paper. The ongoing boundary layer transition study and the boundary layer control defined by that study will be used to assess these ideas and data.

Data Corrections

Temperature Effects

Aeroelastic Effects

To obtain 'pure' Reynolds number effects

For CFD validation

Corrections identified to obtain pure Reynolds number effects:

1) Temperature effects.

An assessment of the change in wing area with changing temperature has yielded a small correction to force/moment data. During the boundary layer transition study this year an attempt will be made to assess the effect of changing temperature on boundary layer stability.

2) Aeroelastic effects.

Data has been acquired to assess the aeroelastic, or q, effects on the Reference H model in the NTF. The changes in force/moment data with increasing q are the result of the bending and untwisting of the wing with increasing loads. Assessment of q effects will allow extrapolation of data to q=0 for CFD validation and a correction to data taken at various dynamic pressures to obtain 'pure' Reynolds number effects.

Effect of Thermal Expansion

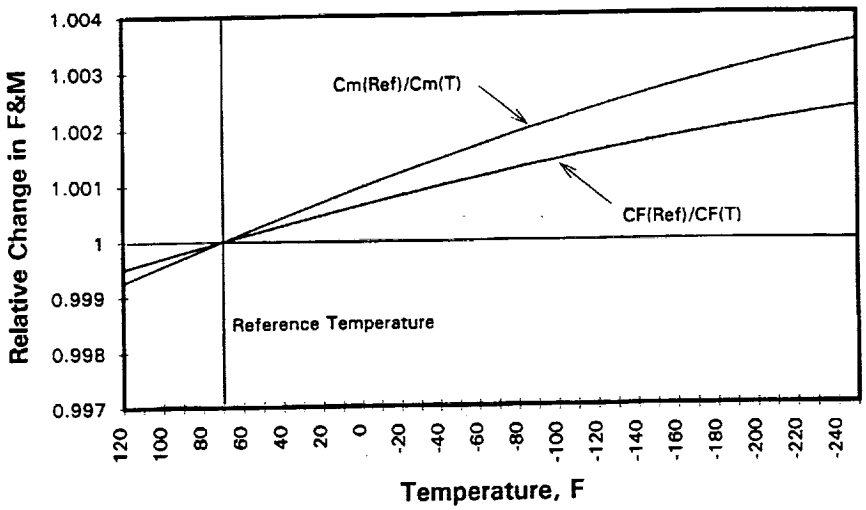

$$Forces: C_{F_{REF}} = \frac{C_{F_T}}{[1+\hat{\alpha}(T-T_{REF})]^2}$$

$$Moments: C_{M_{REF}} = \frac{C_{M_T}}{[1+\hat{\alpha}(T-T_{REF})]^3}$$

$$\hat{\alpha} = 3.5x10^{-9}T + 4.52x10^{-6} \frac{in}{in - °F}$$

Temperature Effects:

As the total temperature decreases the model undergoes thermal contraction resulting in a measurable change in area. This thermal effect has been modeled and is shown in the figure above. This figure includes the change in both forces and moments.

Raw Data for Aeroelastic Correction to Drag Coefficient

Mach=0.9 RNc=30.0 Million Transonic Configuration (Wing/Body/Nacelles)

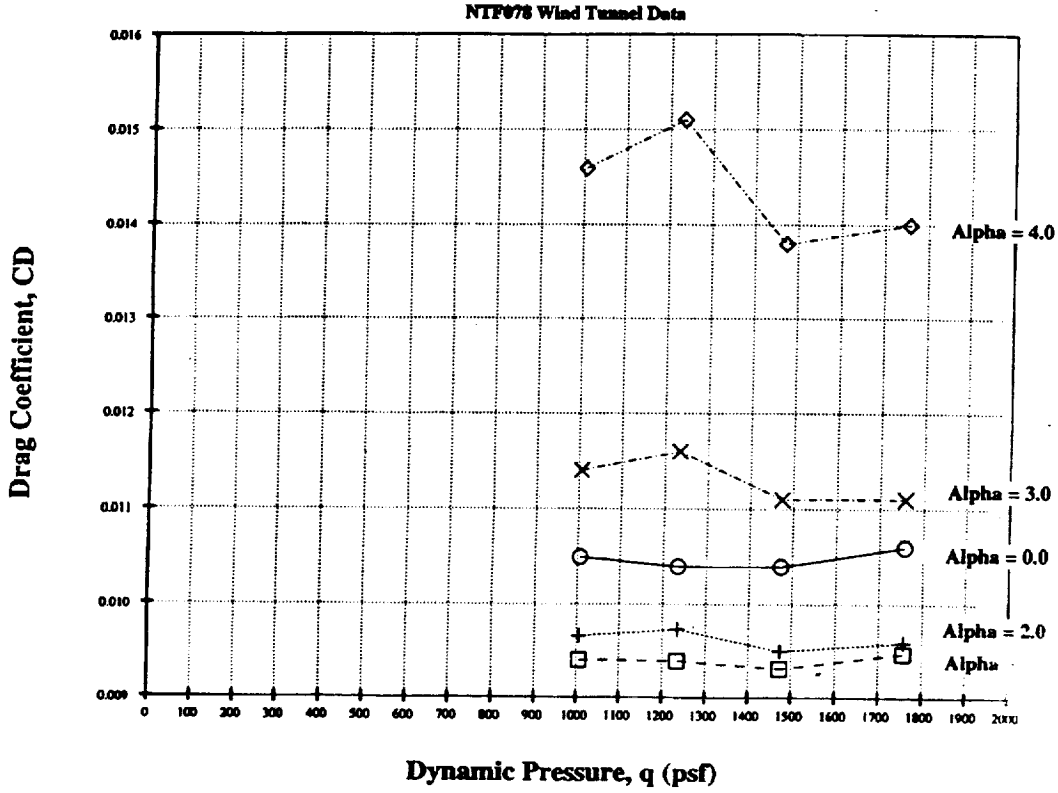

Aeroelastic Effects:

The next set of figures illustrates data acquired and increments computed for aeroelastic effects. Initially two conditions were run at constant chord Reynolds numbers providing a simple linear correction for aeroelastic effects. With the maturing program, additional data has been acquired to assess the non-linearity of the aeroelastic effects.

This figure illustrates the variation in drag across the range of dynamic pressures tested for the Mach = 0.9, transonic configuration. Results from the latest NTF test, NTF078, are shown in this figure. The points shown in this figure do not include repeat runs for each condition. The data has been independently verified to be within the normal repeatability of HSCT testing in the NTF. No boundary layer control was employed when this data was acquired. Each point, or condition, represents a different combination of pressure and temperature.

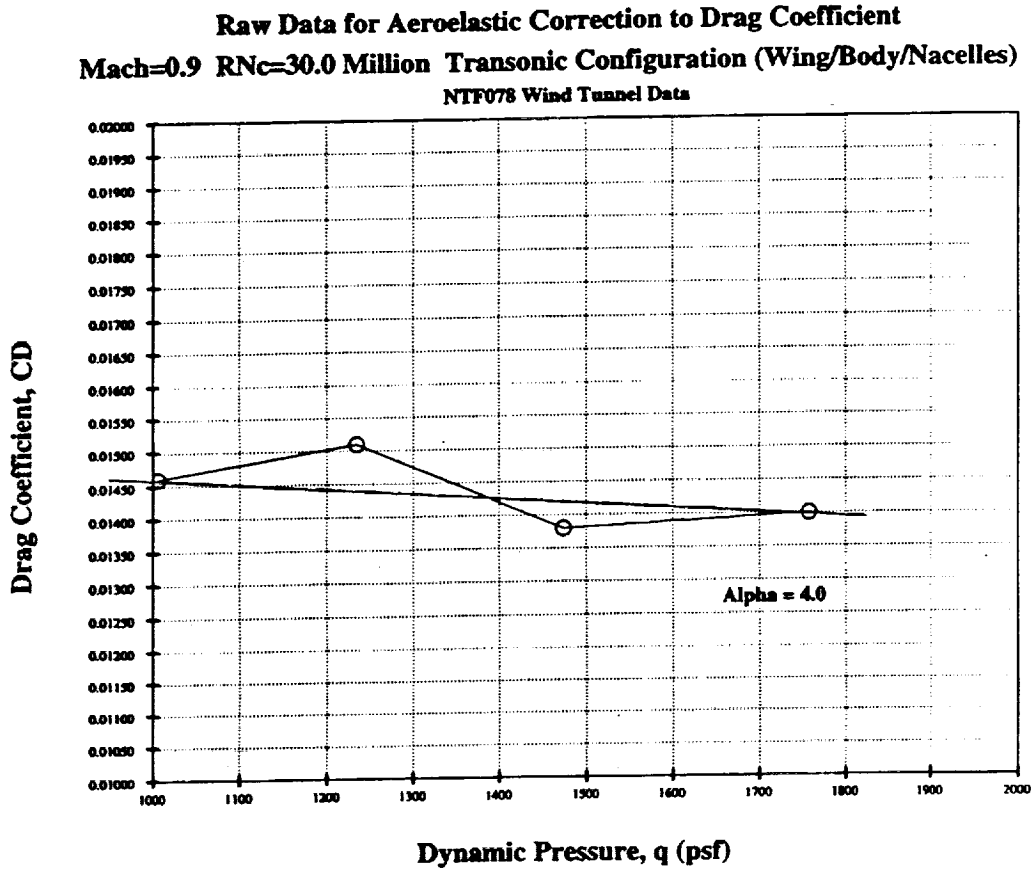

Aeroelastic Effects:

At low angles of attack the aeroelastic correction to the high-speed data is within the normal repeatability of the high-quality, high-speed performance data acquired. As with Reynolds number effects, aeroelastic effects also increase with increasing angle of attack. At 4° angle of attack there appears to be approximately 6 counts of drag difference between 1000q and 1800q.

Raw Data for Aeroelastic Correction to Drag Coefficient

Mach=0.3 RN=21.6 Million High-Lift Configuration (Wing/Body/Nacelles)

NTF078 Wind Tunnel Data

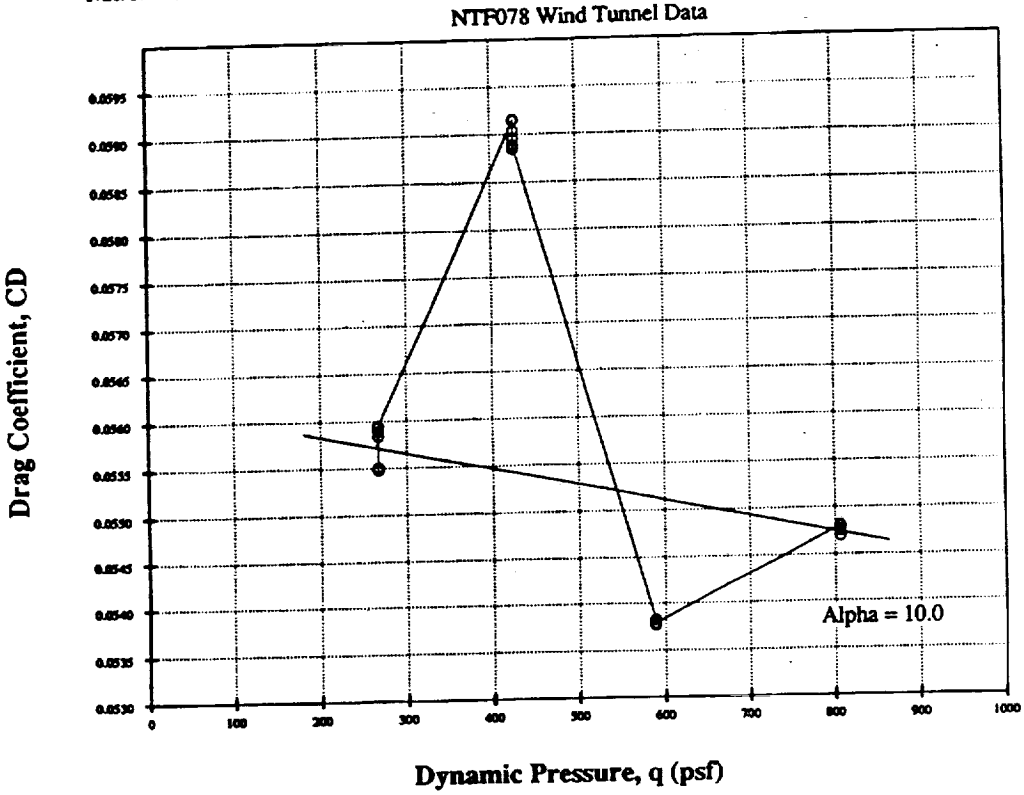

Aeroelastic Effects:

This figure illustrates the variation in drag across the range of dynamic pressures tested for the Mach = 0.3, high-lift case. Results from the latest NTF test, NTF078, will be used to assess non-linearity in the aeroelastic corrections and are shown in this figure. The linear correction, represented by the solid line from the highest q condition through the lowest q condition, is 10 to 12 counts at this angle of attack.

All points taken at a each condition are shown in this figure. No boundary layer control was employed when this data was acquired. Each condition represents a different combination of pressure and temperature.

Raw Data for Aeroelastic Correction to Drag Coefficient

Mach=0.3 RNc=21.6 Million Flaps Up Configuration (Wing/Body/Nacelles)

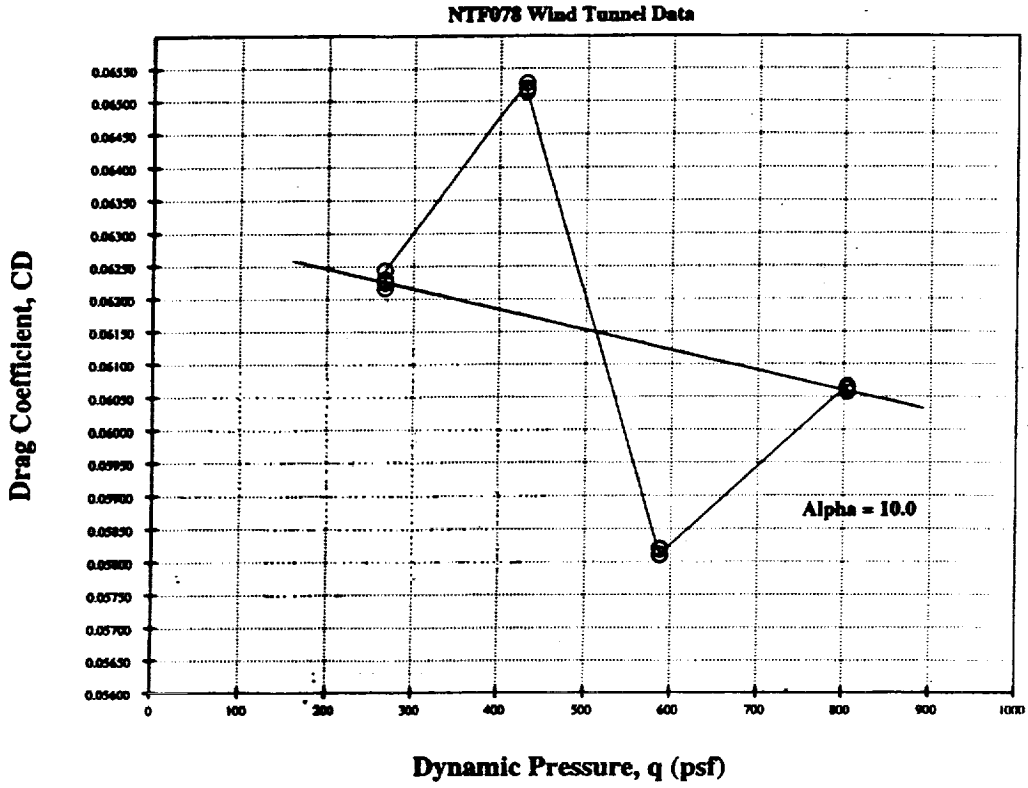

Aeroelastic Effects:

This figure illustrates the variation in drag across the range of dynamic pressures tested for the Mach = 0.3, baseline case. Results from the latest NTF test, NTF078, will be used to assess non-linearity in the aeroelastic corrections and are shown in this figure. The linear correction, represented by the solid line from the highest q condition through the lowest q condition, is 16 to 17 counts at this angle of attack. The higher level of drag shown in this figure, compared to the drag level for the high-lift configuration, reflects the leading-edge separation and vortex formation present at this angle of attack for this configuration.

All points taken at a each condition are shown in this figure. No boundary layer control was employed when this data was acquired. Each condition represents a different combination of pressure and temperature.

Reynolds Number Effect on Drag Coefficient

Mach=0.9 Transonic Configuration (Wing/Body/Nacelles)

NTF067 Wind Tunnel Data

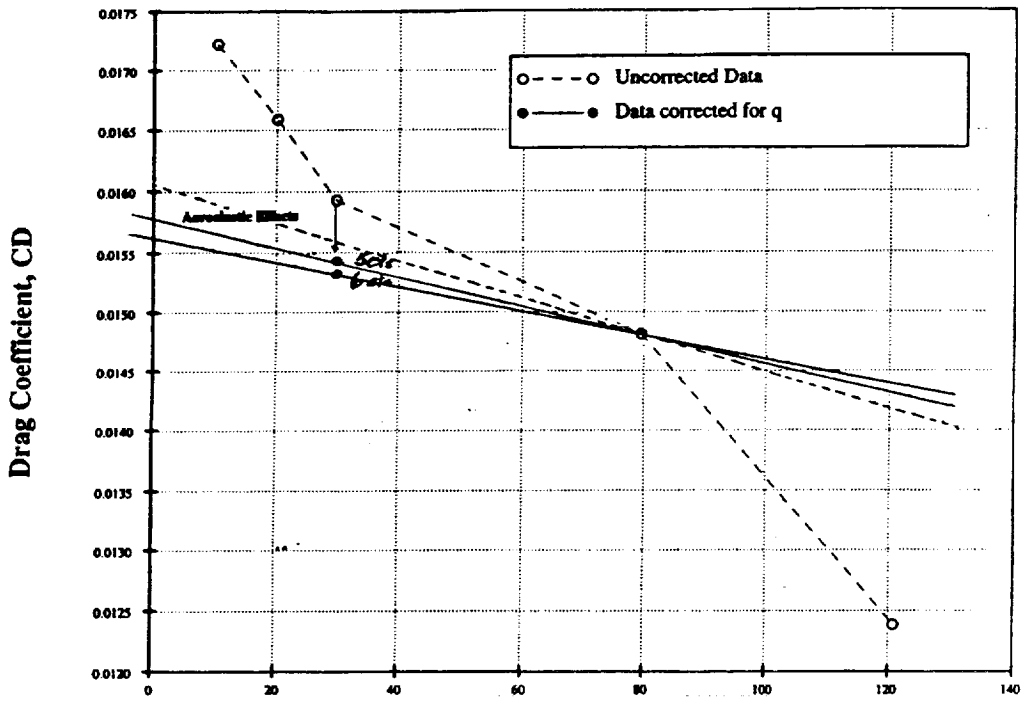

Chord Reynolds Number, RNc

Reynolds Number Effects:

An estimate of the Reynolds number benefit for the transonic configuration can be made using the following assumptions and extrapolating the data as shown in the figure above.

Assumptions:

1) The wing is fully turbulent at a Reynolds number of 80 million.

2) The aeroelastic correction is about 6 counts between dynamic pressures ranging from 1000 psf to 1800 psf.

3) The temperature correction is insignificant from the 30 million Reynolds number to the 80 million Reynolds number conditions in this case.

Solid lines have been drawn illustrating the Reynolds number effect on drag coefficient extrapolated from wind tunnel data at 30 million and 80 million Reynolds numbers with both a 5 count and a 6 count aeroelastic correction applied. A dashed line has been drawn illustrating the theoretical Reynolds number effect extrapolated from an anchor point at the 80 million Reynolds number condition. As can be seen in this figure there is a difference between the Reynolds number effect derived from wind tunnel data and the effect predicted by theory. It can be seen from the two solid lines that a very small change in the aeroelastic correction would make a large change in the Reynolds number effect derived from wind tunnel.

Reynolds Number Study

2.2% Reference H, W/B Baseline Configuration, Mach = 0.9

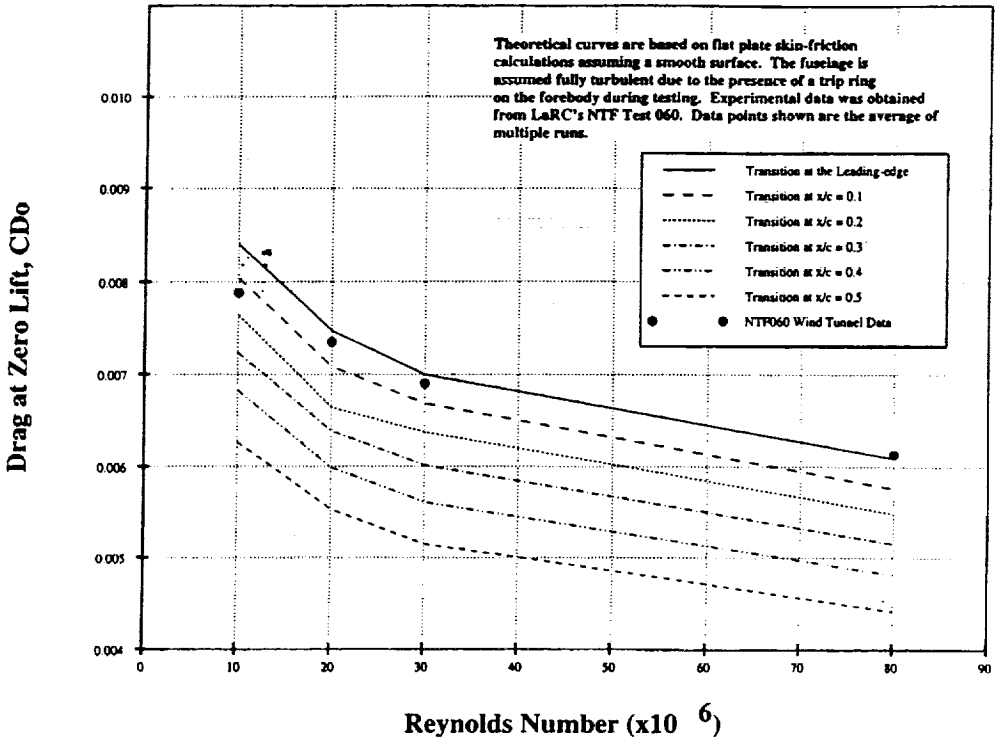

This figure illustrates the study which serves as the basis of the theoretical Reynolds number effect shown in the previous slide for the Mach=0.9 case. It appears that theory predicts a slightly larger Reynolds number effect than appears in the wind tunnel data.

High Lift Reynolds Number Effects on Drag Coefficient
2.2% Reference H Model
30° Leading Edge Flaps, 10° Trailing Edge Flaps
Mach = 0.3 CL = 0.55 at Alpha = 10.0°
(Wing/Body/Nacelles)

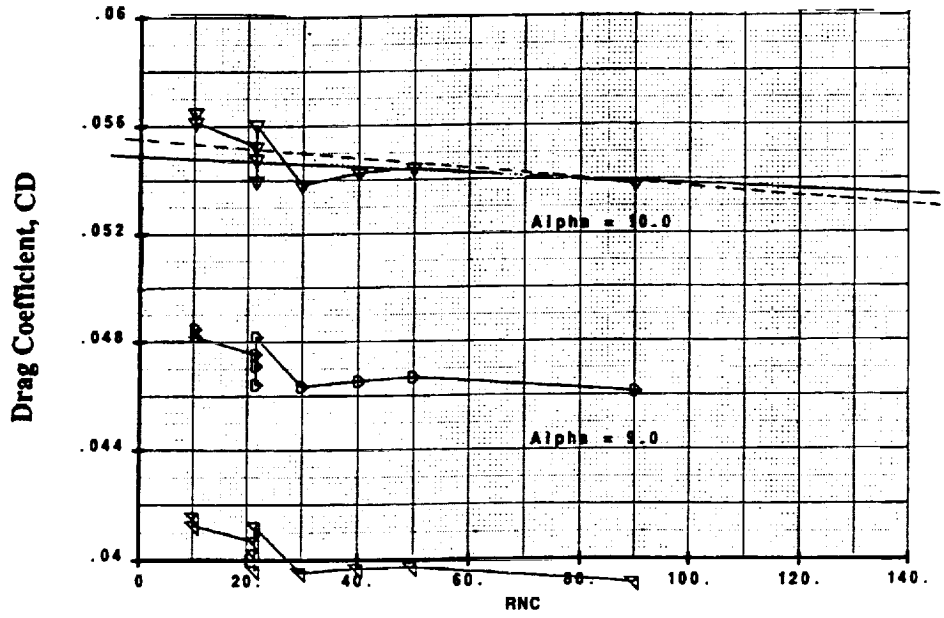

Reynolds Number Effects:

An estimate of the Reynolds number benefit for the high-lift configuration can be made using the following assumptions and extrapolating the data as shown in the figure above.

Assumptions:

1) The wing is fully turbulent at a Reynolds number above 50 million.

2) The aeroelastic correction is not significant between 800q and 850q so no correction is required to data at and above the 30 million Reynolds number condition.

3) The temperature correction is very small at the 90 million Reynolds number condition.

A solid line has been drawn illustrating the Reynolds number effect on drag coefficient extrapolated from wind tunnel data between 50 million and 90 million Reynolds numbers. A dashed line has been drawn illustrating the theoretical Reynolds number effect extrapolated from an anchor point at the 90 million Reynolds number condition. Again, this figure shows that there is a difference between the Reynolds number effect derived from wind tunnel data and the effect predicted by theory. As before, it should be noted that a very small change in the aeroelastic correction would make a large change in the Reynolds number effect derived from wind tunnel.

Reynolds Number Study
2.2% Reference H, W/B Baseline Configuration, Mach = 0.3

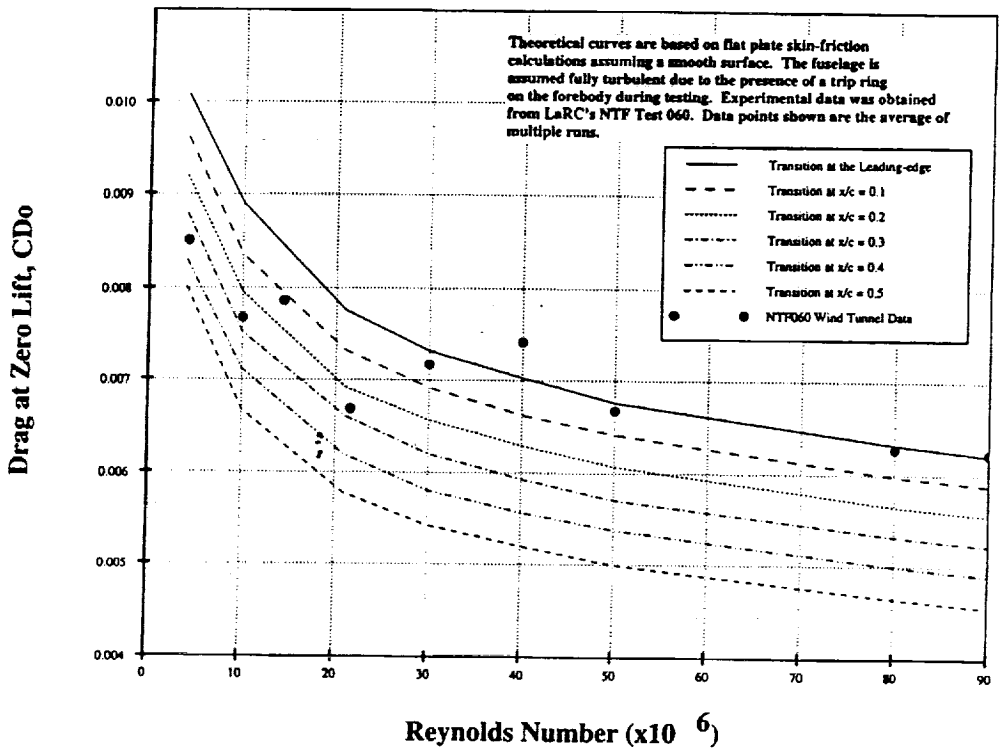

This figure illustrates the study which serves as the basis of the theoretical Reynolds number effect shown in the previous slide for the Mach=0.3 case. As in the Mach=0.9 case, it appears that theory predicts a slightly larger Reynolds number effect than appears in the wind tunnel data.

Summary

- **A significant database exists for the 2.2% Reference H model, including various configurations under a wide range of conditions.**
- **Data corrections developed and being assessed include:**
  - **Temperature effects**
  - **Linear aeroelastic effects**
  - **Non-linear aeroelastic effects**

The charts shown before indicate the data that has been acquired to develop data corrections and ultimately determine Reynolds number effects. This data represents a substantial wind tunnel database on the 2.2% scale Reference H model acquired in the NTF. As has been discussed, this data was acquired over a wide range of conditions.

An initial assessment of the Reynolds number effect for the high-speed and high-lift configurations has been made.

Conclusions

- **Data corrected for temperature effects and linear aeroelastic effects shows a smaller Reynolds number effect than theory predicts for both the transonic and high-lift configurations.**

The initial assessment of the Reynolds number effect on drag coefficient has been made for the transonic and high-lift configurations. This assessment indicates that there is a difference between theoretical predictions and fully corrected wind tunnel data. However, a slight change in the aeroelastic correction to the wind tunnel data would result in a substantial change to overall Reynolds number effects extrapolated from this data.

Concerns over the boundary layer state, laminar versus turbulent, ultimately leading to variations in separation and vortex shedding tend to the conclusion that to obtain Reynolds number effects the model must be adequately tripped. That is, to get meaningful, understandable data the experiment must be adequately controlled.

Recommendations

- **A significant amount of time is needed to analyze the existing database including non-linear aeroelastic effects.**
- **On completion of the boundary layer transition study in 1996, select Reynolds number and aeroelastic conditions should be repeated with boundary layer control in place to obtain final Reynolds number effects on performance data.**
- **On completion of the seal development, select Reynolds number and aeroelastic conditions should be repeated on the full configuration including aftbody and tails, with boundary layer control in place.**

A significant effort will be required to analyze the database acquired on this model. Because of the large effect of small changes to data corrections, and the apparent non-linearity of the aeroelastic correction, this effort will be an essential part of understanding the Reynolds number effects that appear in this data.

Results of the boundary layer study during 1996 will include the extent of laminar flow and free transition on the 2.2% Reference H at a variety of Reynolds numbers. This information will be used to develop "trip(s)" for the high-speed and high-lift configurations in order to better control testing of this model.

Ongoing seal development will allow acquisition of "high quality" performance data to complete the wind tunnel database on the full configuration including aftbody and tails.

Pressure Data:

Configuration		Mach	Reynolds Nr.	Test
Baseline	W/B	0.20	30	57
		0.30	4.2, 10.0,[a] 14.4, 21.6, 30.0, 40.0, 50.0, 80.0, 90.0	57
		0.40	30	57
		0.50	30	57
		0.60	7.7, 10.0, 21.6, 30.0, 50.0, 80.0, 90.0, 110.0	57
		0.90	10.3,[a] 20.0, 30.0, 70.0, 80.0	57
		0.95	10.5, 20.0, 30.0, 80.0	57
		0.98	10.6, 20.0, 30.0, 80.0	57
		1.10	15.0, 20.0, 30.0, 76.8	57
High Lift	W/B [d]	0.30	4.2, 10.0, 14.4, 21.6, 30.0, ------, ------, 80.0, 90.0	57
		0.60	7.7, 10.0, ------, 30.0, ------, ------, 90.0, 110.0	57
	W/B [b]	------	------	
	W/B/N [b]	0.30	4.2,[a,f,r] 10.0,[a,b,f] ------, 21.6,[a,f,r] 30.0,[a,b,f] ------, ------, ------, 90.0,[a,b,f]	63, 67
Transonic	W/B	0.90	10.3, ------, 30.0, ------, 80.0	63
	W/B/N		10.3,[a,p] 20.0,[a,p] 30.0,[a,b] ------, 80.0[a,b]	63, 67
	W/B	0.95	10.5, ------, 30.0, 80.0	63
	W/B/N		10.5,[a,p] 20.0,[a,p] 30.0,[a,b] 80.0[a,b]	63, 67
	W/B	0.98	10.6, ------, 30.0, 80.0	63

NOTES:
- [a] with and without conventional wing trip (test 67)
- [__*] run with conventional wing trip only (test 67)
- [a] with and without forebody trip ring
- [d] no forebody trip ring
- [f] yawed runs completed for this condition
- [p] inboard trailing-edge flaps undeflected
- [b] all trailing edge flaps deflected
- [f] frost runs
- [r] trailing-edge flap rake

Data Acquired - pressure data:

The objective in this testing was to obtain performance data leading to Reynolds number effects for use in extrapolating from wind tunnel test to full scale flight conditions. This testing is required for a variety of configurations representing transonic cruise and high-lift flap schedules on an HSCT-class model. The following figure illustrates the pressure data acquired on configurations without the aftbody and tails. Chord Reynolds numbers are listed for the data acquired. Dashed lines illustrate gaps in the database, or configurations/conditions where data has not been acquired.

For a constant Mach number, Reynolds number can be changed by changing temperature and/or pressure. Combinations of total temperature, total pressure, Mach number, and dynamic pressure are referred to as conditions. The chord Reynolds numbers shown in this figure each have a different condition. These conditions were shown in the previous slide on the operating envelopes.

Force/Moment Data:

Configuration		Mach	Reynolds Nr.	Test
Baseline	W/B	0.20	------	60
		0.30	4.2, 10.0, 14.4, 21.6, 30.0, 40.0, 50.0, 80.0, 90.0	60
		0.40	------	60
		0.50	------	60
		0.60	7.7, ------, 21.6, 30.0, ------, 80.0, ------, 110.0	60
		0.80	10.3	60
		0.90	10.3, 20.0, 30.0, 70.0, 80.0	60
		0.92	10.3	60
		0.95	10.5, 20.0, 30.0, 80.0	60
		0.98	10.6, 20.0, 30.0, 80.0	60
	W/B/N	0.20	-------	
		0.30	4.2, (10,*) ------, 21.6, (30,*) ------, ------, ------, 90.0	63
		0.40	-------	
		0.50	-------	
		0.60	7.7, ------, ------, ------, ------, ------, ------, ------	63
		0.80	10.3	63
		0.90	10.3,* (20,*) 30.0,* ------, 80.0	63
		0.92	10.3	63
		0.95	10.5, ------, 30.0, 80.0	63
		0.98	10.6, ------, 30.0, 80.0	63

NOTES:
- * with and without conventional wing trip (test 67)
- (__*) run with conventional wing trip only (test 67)
- # no forebody trip ring
- c with and without forebody trip ring
- β yawed runs completed for this condition
- α inboard trailing-edge flaps undeflected
- δ all trailing-edge flaps deflected

Data Acquired - force/moment data for Reynolds number effects:

In addition to pressure data, high quality force and moment data has been acquired. "High quality" refers to data acquired without pressure lines crossing the balance and when the balance has been properly conditioned.

The following figure illustrates the high quality force and moment data acquired at various chord Reynolds numbers for the baseline configuration without aftbody and tails. Dashed lines illustrate gaps in the database, that is, conditions where data has not been acquired.

Force/Moment Data:

Configuration		Mach	Reynolds Nr.	Test
High Lift	W/B [a]	0.30	4.2, ------, 14.4, 21.6, 30.0, 40.0, 50.0, 80.0, 90.0	60
		0.60	------	
	W/B [b]	0.30	4.2, ------, ------, 21.6, ------, ------, ------, ------, 90.0	63
	W/B/N [b]	0.30	4.2, ------, ------, 21.6,[β] 30.0,[β] 40.0,[β] 50.0,[β] 80.0,[β] 90.0[β]	63, 67
Transonic	W/B	0.90	10.3, 20.0, 30.0, ------, 80.0	60,63
	W/B/N		10.3,[*β] 20.0,[*β] 30.0,[*β] ------, 80.0[*β] 120.0	63, 67
	W/B	0.95	10.5, 20.0, 30.0, 80.0	60,63
	W/B/N		10.5,[*β] 20.0,[*β] 30.0,[*β] 80.0[*β]	63, 67
	W/B	0.98	10.6, 20.0, 30.0, 80.0	60,63
	W/B/N		10.6, ------, ------, 80.0	63

NOTES:
- * with and without conventional wing trip (test 67)
- (___*) run with conventional wing trip only (test 67)
- [a] no forebody trip ring
- [o] with and without forebody trip ring
- [β] yawed runs completed for this condition
- [a] inboard trailing-edge flaps undeflected
- [b] all trailing-edge flaps deflected

Data Acquired - force/moment data for Reynolds number effects:

The following figure illustrates the high quality force and moment data acquired for the high-lift and transonic configurations without aftbody and tails. As before, the chord Reynolds numbers are listed for data acquired. Dashed lines illustrate gaps in the database, that is, conditions where data has not been acquired.

Force Data Acquired for Aeroelastic Cor ection

Configuration	Mach	RN(x10e-6)	q (condition n	Runs (>800q)
Baseline W/B	0.3	4.2	*153(1)*	
		10	*159(26)*	
		14.4	160(43)*, 264(2	
		21.6	267(42)*, 804(	11
		30	268(53)*, 817(1	110,111,112,113,114
		40	*826(18)*	108
		50	*832(25)*	82
		80	*841(45)*	75
		90	*843(50)*	47,49,63,64,65
	0.6	7.7	*535(2)*	
		10		
		21.6	*557(34)*	
		30	561(46)*, 834(29)	
		50		
		80	*1789(60)*	
		90		
		110	*1800(61)*	
	0.9	10.3		
		20	*966(3), 993(21)*	
		30	1005(38), 1753(15)	
		70	*1795(62)*	
		80	*1798(51)*	
	0.95	10.5		
		20	*1018(4), 1047(19)*	
		30	1059(36), 1756(63)	
		80	*1800(56)*	
	0.98	10.6		
		20	*1047(5), 1076(17)*	
		30	1089(33), 1757(64)	
		80	*1800(57)*	

*Low q conditions with only 1 run

Data Acquired - force/moment data for aeroelastic corrections:

This figure illustrates the force and moment data acquired for linear aeroelastic corrections on the baseline configuration. Bold numbers specify q (psf) for the multiple conditions run at a constant chord Reynolds number. It also lists the high q data (q > 800 psf) acquired for this configuration in plain type. The asterisks denote low q conditions (q < 600 psf) where only one run exists.

Force Data Acquired for Aeroelastic Correction

Configuration	Mach	RN(x10e-6)	q (condition nr.)	Runs (>800q)
High Lift W/B (a)	0.3	4.2	*153(1)*	
		10		
		14.4	160(43)*, 284(23)*	
		21.6	267(42)*, 804(7)	145,146,147,148,149,150
		30	268(53)*, 817(12)	129,130,131,132,133,134
		40	*826(18)*	127
		50	*832(25)*	153
		80	*841(45)*	177
		90	*843(50)*	166,167,168,169,175,176
High Lift W/B (b)	0.3	4.2	*153(1)*	
		10		
		14.4		
		21.6	*267(42)*	
		30		
		40		
		50		
		80		
		90		
High Lift W/B (b)	0.3	4.2	*153(1)*	
		10		
		14.4		
		21.6	*267(42)*	
		30		
		40		
		50		
		80		
		90	*843(50)*	

*Low q conditions with only 1 run
(a) inboard trailing-edge flaps undeflected
(b) all trailing-edge flaps deflected

Data Acquired - force/moment data for aeroelastic corrections:

This figure illustrates the force and moment data acquired for linear aeroelastic corrections on the high-lift configuration. As before, bold numbers specify q (psf) for the multiple conditions run at a constant chord Reynolds number. It also lists the high q data (q > 800 psf) data acquired for this configuration in plain type. Again, the asterisks denote low q conditions where only one run exists. Data acquired at Reynolds numbers of 30 million and greater all have dynamic pressures above 800 psf. A plot of this data is included in this presentation.

Force Data Acquired for Aeroelastic Correction

Configuration	Mach	RN(x10e-6)	q (condition nr.)
Transonic W/B	0.9	10.3	*966(3)*
		20	*993(21)*
		30	1005(38), 1753(15)
		80	*1798(51)*
	0.95	10.5	*1018(4)*
		20	*1047(19)*
		30	1059(36), 1756(63)
		80	*1800(56)*
	0.98	10.6	*1047(5)*
		20	*1076(17)*
		30	1089(33), 1757(64)
		80	*1800(57)*
Transonic W/B/N	0.9	10.3	*966(3)*
		20	
		30	*1005(38)*
		80	*1798(51)*
	0.95	10.5	*1018(4)*
		20	
		30	
		80	*1800(56)*
	0.98	10.6	*1047(5)*
		20	
		30	
		80	*1800(57)*

Data Acquired - force/moment data for aeroelastic corrections:

This figure illustrates the force and moment data acquired for linear aeroelastic corrections on the transonic configuration. As before, bold numbers specify q (psf) for the multiple conditions run at a constant chord Reynolds number. The lowest dynamic pressures used in acquiring transonic data have been greater than 900 psf. This high q data is listed in plain type.

HSCT Ref-H Transonic Flap Data Base: Wind-Tunnel Test and Comparison with Theory

Paul M. Vijgen
Boeing Commercial Airplane Group
Seattle, WA 98124-2207

Abstract

In cooperation with personnel from the Boeing ANP Laboratory and NASA Langley, a performance test was conducted using the Reference-H 1.675% model ("NASA Modular Model") without nacelles at the NASA Langley 16-Ft Transonic Tunnel. The main objective of the test was to determine the drag reduction achievable with leading-edge and trailing-edge flaps deflected along the outboard wing span at transonic Mach numbers (M = 0.9 to 1.2) for purpose of preliminary design and for comparison with computational predictions. The obtained drag data with flap deflections for Mach numbers of 1.07 to 1.20 are unique for the Reference-H wing. Four leading-edge and two trailing-edge flap deflection angles were tested at a mean-wing chord-Reynolds number of about 5.7 million.

An outboard-wing leading-edge flap deflection of 8° provides a 4.5 percent drag reduction at M = 1.2 (C_L = 0.2), and much larger values at lower Mach numbers with larger flap deflections. The present results for the baseline (no flaps deflected) compare reasonably well with previous Boeing and NASA Ref-H tunnel tests, including high-Reynolds number NTF results. Viscous CFD simulations using the OVERFLOW thin-layer N.S. method properly predict the observed trend in drag reduction at M = 1.2 as function of leading-edge flap deflection. Modified linear theory properly predicts the flap effects on drag at subsonic conditions (Aero2S code), and properly predicts the absolute drag for the 4° and 8° leading-edge deflection at M = 1.2 (A389 code).

Ref-H Transonic Flap Data Base *

Approach

- **Wind-tunnel test in NASA Langley 16-Ft Transonic Tunnel**
- **Comparison of wind-tunnel data with theory and CFD predictions**
- **Analysis of Reynolds-number effects on transonic flap data with N.S. method (Dynacs)**

* **HSR Configuration Aerodynamics FY1995 Contract Deliverable - Task 3 (Configuration Evaluation, Subtask 4.3.1.2)**

Approach to Development of Ref-H Transonic Flap Data Base

The approach followed to develop a transonic flap data base for the Reference-H planform is centered along three complementary paths. Using the Ref-H NASA Modular Model, an experimental data set was obtained for various flap settings in the Langley 16-Ft transonic wind tunnel. The new data set is compared with available other Ref-H wind-tunnel tests, mostly for the baseline (cruise) configuration with undeflected flaps. As part of the pre-test predictions and the post-test analysis both modified-linear theory predictions as well as viscous CFD solutions were obtained at the conditions of the 16-T entry. Finally, the effect of increasing Reynolds number on the effect of flaps was studied using the N.S. method.

Ref-H Transonic Flap Data Base

Motivation

- **Transonic drag rise can be a significant factor in engine sizing and selection**
- **For sized airplane, 1 count drag reduction at transonic / low-supersonic speeds can imply 2,000 lbs reduction in MTOW**
- **Previous SST wind-tunnel data indicate significant drag reduction with leading-edge flaps at low-supersonic speeds**
- **At high subsonic speeds, recent Ref-H NTF test with outboard flaps showed significant drag reduction with LE10°/TE3° outboard flaps**

Motivation

Reduction of high drag at the transonic "pinch" can favorably affect total weight of the sized aircraft, among other effects. From previous SST wind-tunnel test, significant drag reduction was obtained with leading-edge deflections on the outboard wing panel at low supersonic speeds. A recent test in the NTF (test 63) with the Ref-H geometry showed the potential of large high-subsonic drag reduction with both leading-edge and trailing-edge flap deflection on the outboard wing panel. Prior to this test, no low-supersonic data was available on outboard-wing leading-edge flaps effects for the Ref-H geometry.

HSCT High-Speed Technology (pmv5727)
Ref-H Transonic Flap Data Base

Ref-H Transonic Flap Data Base

Presentation Outline

- **Langley 16-Ft transonic test with outboard flaps**
- **Comparison with previous tests (baseline and subsonic flaps)**
- **Comparison with CFD and modified-linear theory**
- **Concluding remarks**

Outline of Paper

The paper presents the indicated main topics.

Objectives of Ref-H Transonic Flap Test

- Develop outboard flap data base at transonic speeds using NASA's 1.675% Modular Controls Model in NASA- Langley 16-Ft Tunnel
- Determine drag reduction achievable with leading- and trailing-edge flaps deflections on outboard wing
- Verify transition trips and assess possible flap hinge-line separation due to low-Reynolds number
- Compare new test results with previous Ref-H tests
- Evaluate predictive (design) capability of codes using the new data set

---

Objectives of Ref-H Transonic Flap Test

The objectives of the Boeing-supported performance test with the NASA Modular Controls Model in the Langley 16-Ft Transonic Tunnel were to generate a data base for design of outboard flaps of an Reference-H like HSCT configuration to reduce drag in the transonic "drag pinch", to determine the magnitude (and sign) of drag reduction and to obtain a sufficient number of repeat polars to assess the quality of the test and to allow comparison with previous Reference-H tests. If the data base is of sufficient quality, the set can be used for calibration of existing modified-linear theory methods and recent viscous CFD overset codes. Since prior to this test no supersonic Ref-H data existed with flap deflections, it was desirable to obtain as much flow visualization results as possible to contribute to understanding of the flow mechanisms underlying the drag reduction.

1.675% Ref-H Modular Model in LaRC 16-Ft Tunnel

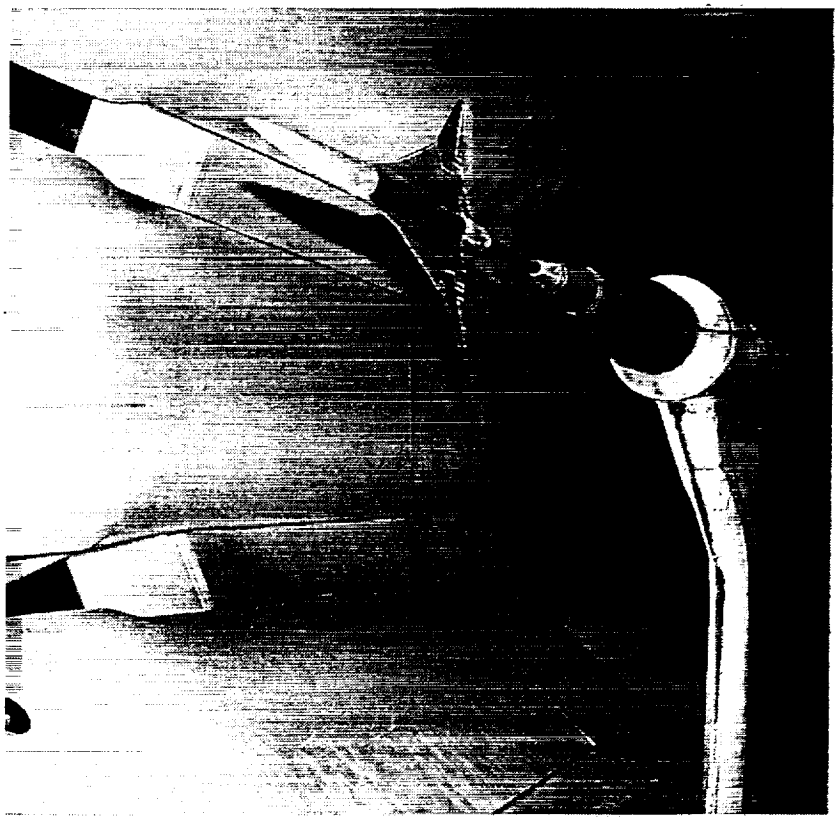

The picture shows the relative size of the NASA 1.675% Reference-H Modular Model in the 16-Ft tunnel. (The model is rolled at a 90° orientation for purpose of recording oil-flow visualization results after a run.)

The data indicated no discernable effect of the model-wall reflection shock on the balance forces at Mach numbers exceeding M = 1.07.

16-T Testing Requirements and Constraints

- From 1993 Boeing test of Ref-H cruise geometry in 16-T tunnel, 3 repeat runs were planned to achieve +/- 1.5 counts drag accuracy
- ITD decided two weeks before entry that test time would be restricted to 25% of total 16-T test with Modular Model
- Allotted test time (7 prime shifts) barely enough to obtain minimum set of force data assuming 1993 productivity
- 16-T competed for power-drive train with NTF and competed for power with the UPWT during test
- Achieved test matrix smaller than planned
- Adverse balance-temperature effect discovered during present test, further reducing number of usable polars
- Only minimum (oil) flow visualization was obtained. No trip-drag data and trip effectiveness information obtained

Testing Requirements and Constraints, Achieved Test Matrix and Productivity

Not until 2 weeks prior to start of the test was a decision obtained from the ITD on the amount of run time allocated for the present performance test using the Modular-Controls model. Assuming the productivity (installation, polars per hour and data reduction) achieved in the 1993 Boeing test (T457) with another 1.675% Ref-H model, a pretest matrix was developed. Based on the T457 results, a minimum of three back-to-back repeat runs was planned to obtained the desired drag accuracy (at least +/- 1.5 counts).

A significant constraint of testing in the 16-Ft tunnel is the competition for power train with the NTF (in cryogenic mode) for power late at night and in the morning, as well as for power with the Unitary UPWT complex in day time.
Only a minimal set of force, moment, and colored-oil flow visualization data could be acquired during the occupancy-fixed test window. The number of repeat runs is smaller than desired for some flap settings. During this test, it was discovered that a severe temperature gradient existed over the balance beams during the initial supersonic runs of the day. Inspection of the data affected by this gradient shows that generally a significant change in drag occurred. In the present analysis, the affected polars have been discarded, resulting in a further reduction of available polars.

Finally, limited oil-flow visualization was conducted instead of the originally planned transition sublimation in an attempt to determine whether hinge-line separation could be the cause for the observed trend in drag reduction with increasing leading-edge flap deflection. Quality of the oil-flow visualization achieved in the present test is marginal due to limited time available to adjust the oil/paint mixture for the present conditions.

1.675% Ref-H NASA Modular Model

Outboard Panels with Fixed LE-Flap Deflection

Flap Deflections

LE - 0°, 4°, 8° and 10°
TE - 0° and 3°

(No nacelles installed for transonic-flap performance test)

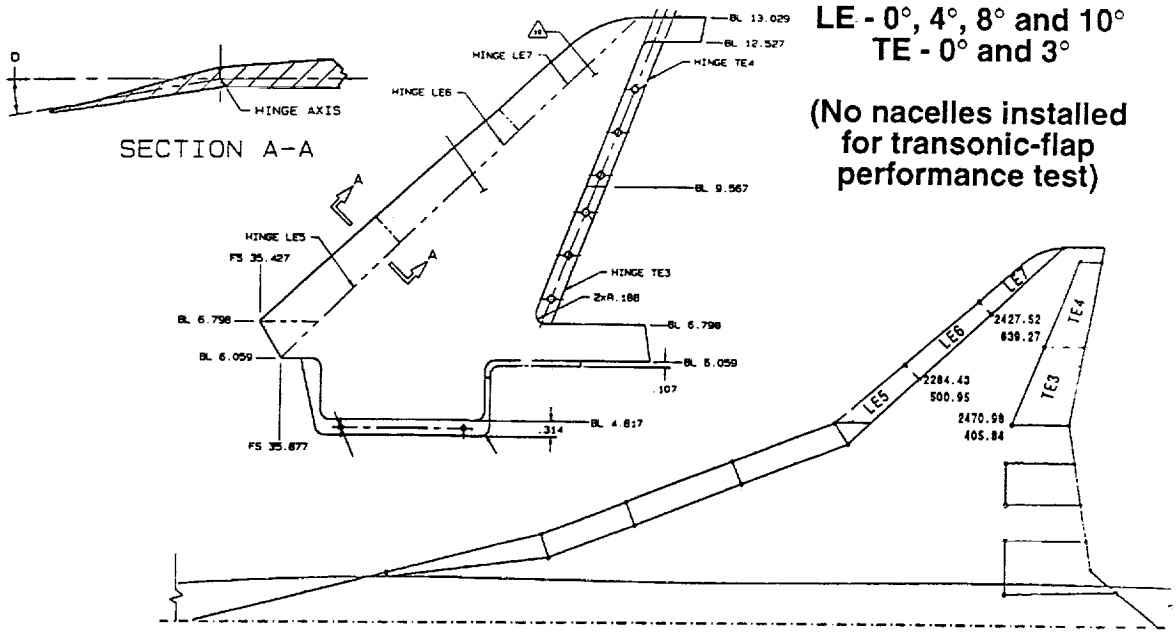

Model

The model tested in the present performance study was the NASA Modular-Controls Model, a 1.675% scale model of Boeing's Reference-H geometry with truncated aft body and without nacelles. In the present Leading-Edge Flap Test (LEFT) supported by Boeing, only leading-edge and trailing-edge deflections of the outboard wing were investigated. (Normal-to-hingeline flap-deflections angles tested are indicated) No nacelles were installed during the LEFT test to alleviate CFD modelling requirements and eliminate nacelle-flow interference scale-effect issues.

A similar 1.675% Reference-H model (Boeing Model 1873) was tested in the same 16-T tunnel in 1993 (Test 457) but in the cruise configuration only. Fairing with dental filler of gaps for interchangeable wing tips (with different leading-edge flaps) and trailing-edge flaps was required and the trailing-edge wing/fuselage junction had a break to allow inboard trailing-edge flap deflections for the Modular Model.

Boundary-layer transition dots were applied to the fuselage and the wing leading-edge surfaces following standard trip-sizing methods (based on the highest Mach number tested here), and are identical to the layout in the previous 16-Ft Test 457 with the Reference-H geometry.

16-T Tunnel Conditions, Flap Geometries Tested and Data Repeatability Achieved

- **Mach numbers: 0.90, 0.95, 0.98, 1.07, 1.10 and 1.20**
- **M.a.c. Reynolds number: 5.7 million**
- **Outboard-wing flap deflections* tested:**
  - **Leading-edge flaps 0°, 4°, 8° and 10°**
  - **Trailing-edge flaps 0° and 3°**
- **Excluding data affected by balance temperature gradient, drag repeatability is at best +/- 2.5 counts near C_L = 0.2 across tested Mach range**

* **Deflections are normal to hingeline**

HSCT High-Speed Technology (pmv5727)
Ref-H Transonic Flap Data Base

16-T Tunnel Conditions, Flap Geometries Tested and Data Repeatability

The figure indicates the tunnel conditions of the present test, and the flap settings tested during the short entry.

Analysis of the available data, and comparison with the merged and curve fitted (least-squares approximation) polars for each configuration at each Mach number indicated that the repeatability of the data is at best +/- 2.5 counts near C_L = 0.2 (i.e., approximate operating condition). The polars likely affected by the balance temperature gradient problem were not included in the data analysis.

In this paper, the curve-fitted data sets are shown in the comparisons with earlier tests and with predictions. Also, detailed wind-tunnel results are presented here only for M = 0.90 and M = 1.20, however, the results are intermediate Mach numbers are summarized.

Effect of Flap Deflection on Lift and Moment M = 0.90

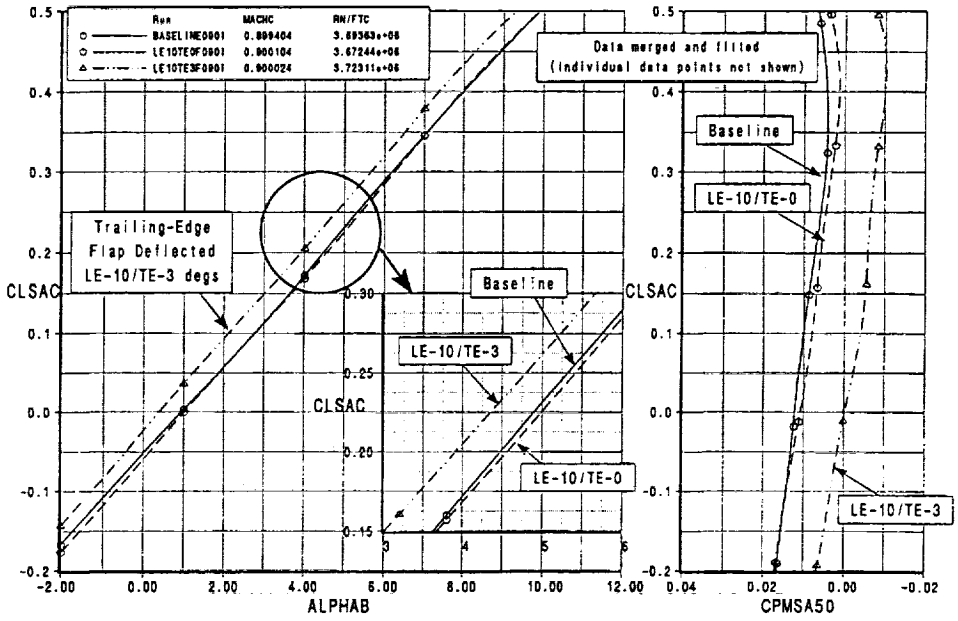

HSCT High-Speed Technology (pmv5
Ref-H Transonic Flap Data

Effect of Flaps on Lift and Pitching Moment at M = 0.90.

At subsonic conditions (M = 0.90), the present results indicate only small reductions in lift and small changes in pitching moment as the leading-edge flap angle is increased from 0° to 10°. As expected, the change in camber at subsonic speeds due to deflection of the trailing-edge flap to 3° increases the lift for given angle of attack, and increases the nose-down pitching moment (leading-edge deflected at 10°).

Effect of Leading-Edge Flaps on Drag
M = 0.90

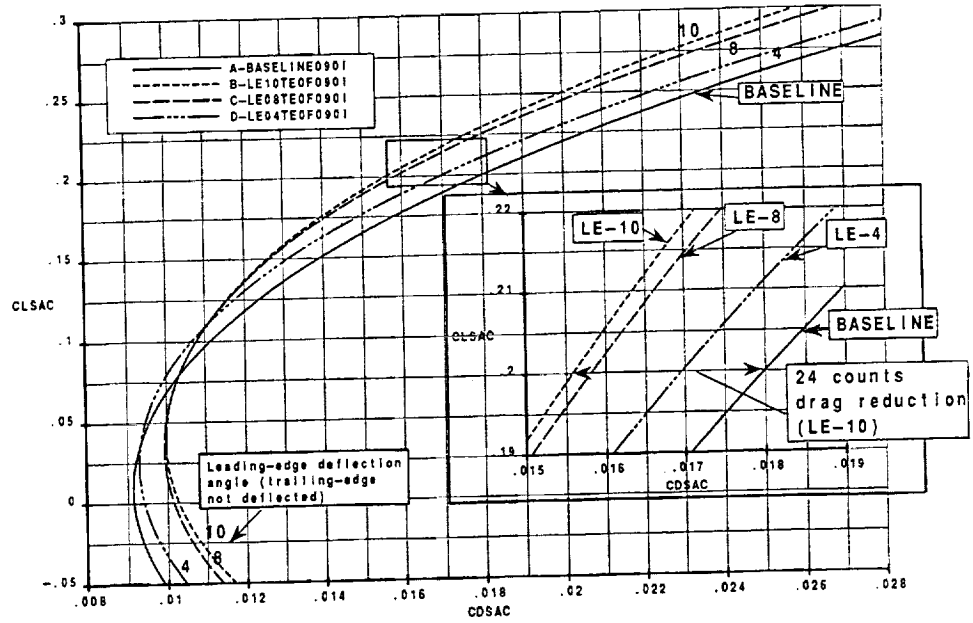

HSCT High-Speed Technology (pmv5727)
Ref-H Transonic Flap Data Base

Effect of Leading-Edge Flap Deflection on Drag at M = 0.90.

The effect of leading-edge flap deflection on drag is very significant at subsonic conditions. At C_L = 0.2, a drag reduction of 24 counts was measured with the highest flap angle available in this test (10°), i.e., a reduction of about 15 percent compared to the baseline wing. The drag benefit progressively reduces with reduced flap angle, as well as with reduced angle of attack. The present subsonic data suggests that the 10° leading-edge deflection provides about the maximum drag reduction at C_L = 0.2. (The crossover points between 8° and 10° occurs near C_L = 0.15.) At higher C_L's, further drag reduction may be possible with leading-edge deflections above 10°.

HSCT High-Speed Technology (pmv5727)
Ref-H Transonic Flap Data Base

Effect of Trailing-Edge Flaps on Drag M = 0.90 (Leading-edge flaps at 10°)

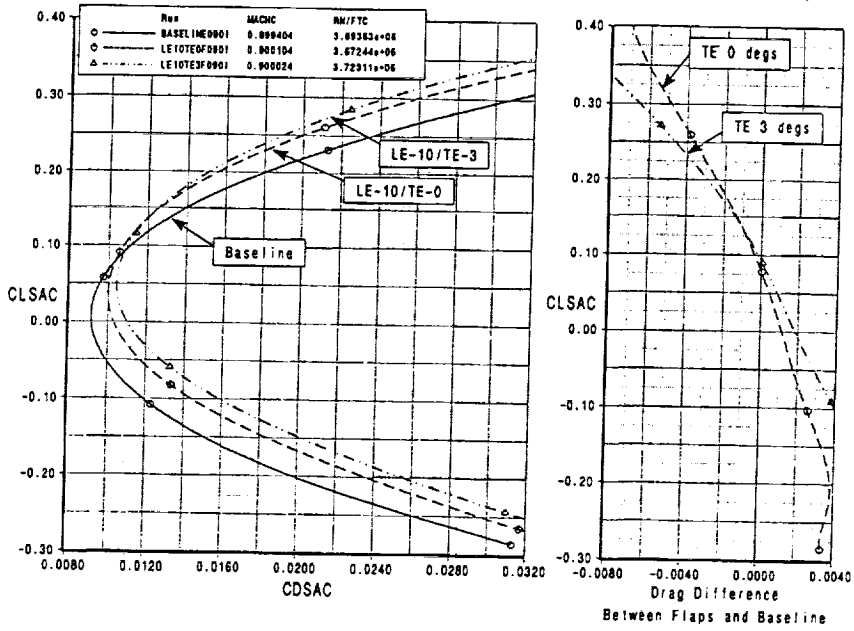

HSCT High-Speed Technology (pmv57
Ref-H Transonic Flap Data Ba

Effect of Trailing-Edge Flaps on Drag at M = 0.90 (Leading-Edge Flap at 10°)

From previous tests in the NTF with both leading-edge and trailing-edge deflections, a significant increment in drag reduction was expected when the trailing flap is deflected by 3°. At C_L = 0.2, an additional drag reduction of about 5 counts is achieved in the present test by deflecting the trailing-edge flap. Note that the crossover point is near C_L = 0.15, suggesting that larger drag benefits may be achieved at C_L's above 0.2 with higher trailing-edge deflections.

Effect of Leading-Edge Flaps on Lift and Moment M = 1.20

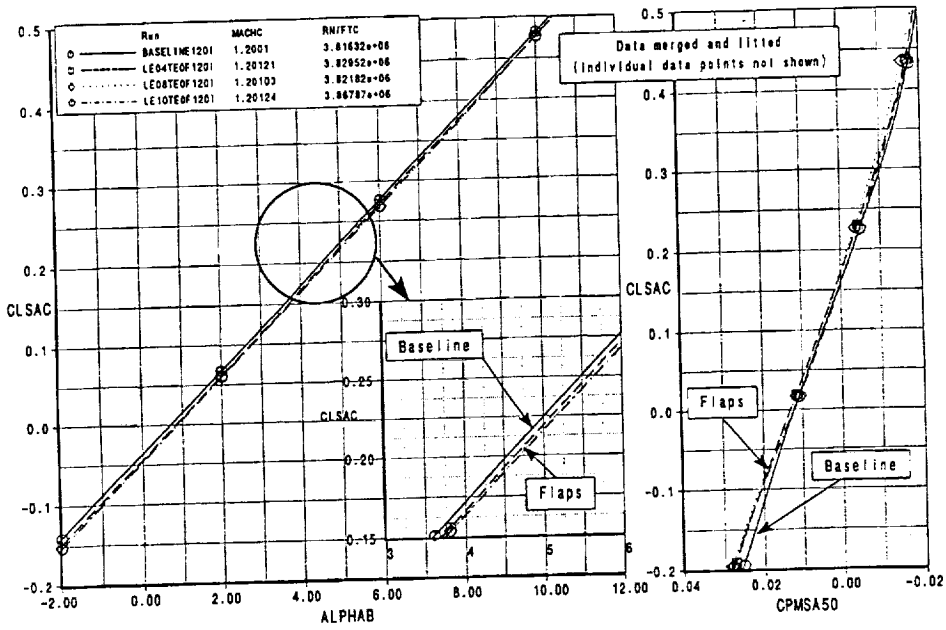

HSCT High-Speed Technology (pmv5727)
Ref-H Transonic Flap Data Base

Effect of Leading-Edge Flaps on Lift and Pitching Moment at M = 1.20.

Also at supersonic conditions (M = 1.20), the present results indicate only small reductions in lift and very small changes in pitching moment as the leading-edge flap angle is increased. Note that the normal-to-the-leading-edge Mach number is still subsonic at M = 1.20 (the highest Mach number tested here).

Effect of Leading-Edge Flaps on Drag M = 1.20

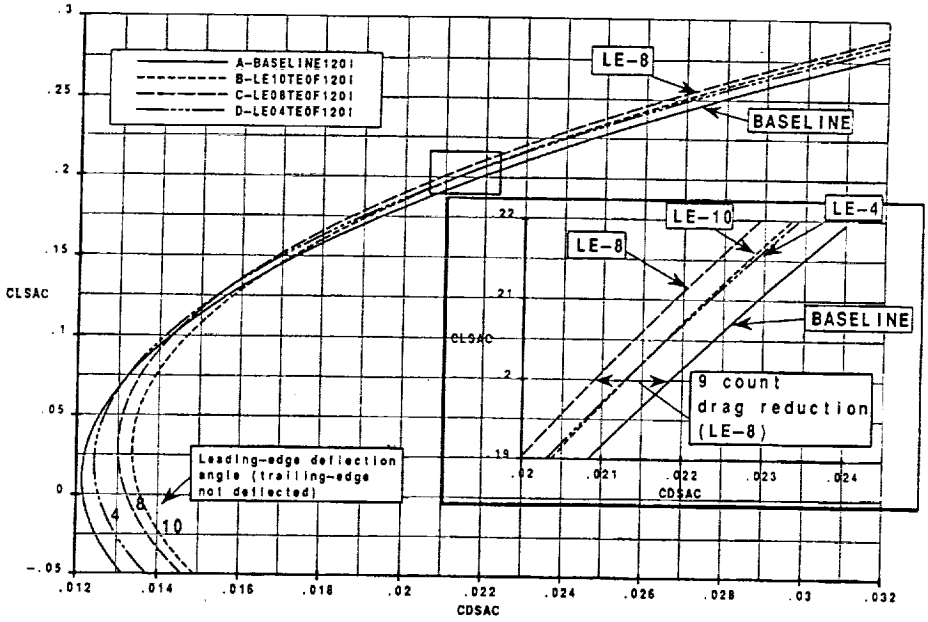

HSCT High-Speed Technology (pmv5727)
Ref-H Transonic Flap Data Base

Effect of Leading-Edge Flaps on Drag at M = 1.20.

The effect of leading-edge flap deflection on drag is different in comparison to the subsonic results. First, the magnitude of the drag reduction at $C_L = 0.2$ is smaller, however, a significant reduction of 9.4 counts (i.e., about 4.5 percent of total drag) is obtained for the 8° flap deflection. Second, in the C_L range of interest, the 10° flap achieves the same drag reduction as the 4° flap setting, i.e., about 6 counts. The rather sharp reduction in drag with a relatively small increase in flap setting (from 8° to 10°) suggested that possibly flap hinge-line separation contributed to this phenomenon. Available oil-flow visualization was of too low quality to conclusively exclude hinge-line separation. Post-test OVERFLOW viscous CFD analyses reveal that hinge-line separation is not expected until higher angles of attack at the Reynolds number of the test[1].

[1] M. Kandula and R. Sheckler, "CFD Methodology Adaptation - Analysis Methods Validation," Dynacs Engineering, Renton, in HSR Configuration Aerodynamics Final Review FY95, Boeing HSCT High-Speed Aerodynamics, Dec. 1995. (See paper in this Session.)

Effect of Flap Deflection on Lift/Drag Ratio
(C_L = 0.2, Re_c = 5.7 million)

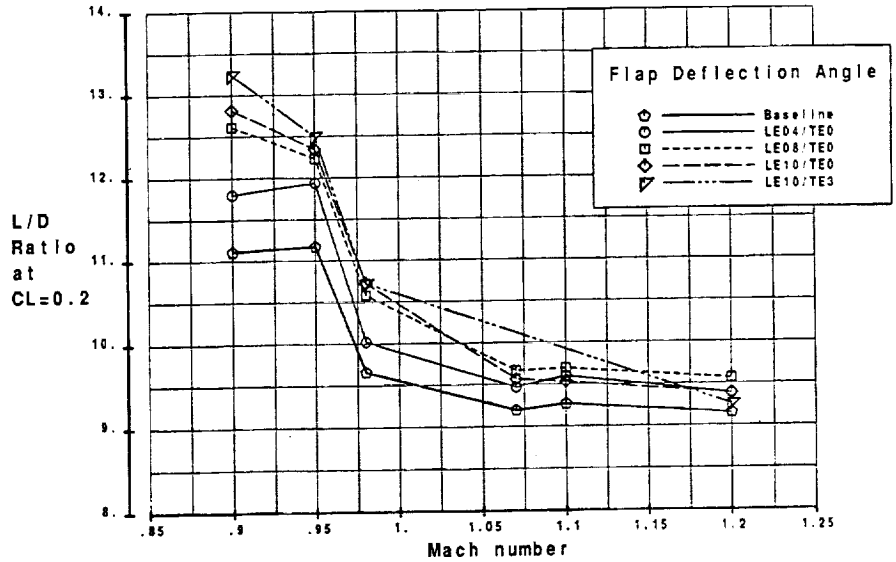

HSCT High-Speed Technology (pmv5727)
Ref-H Transonic Flap Data Base

Effect of Flap Deflection on Lift-to-Drag Ratio

The figure presents the measured L/D ratio with the various leading- and trailing-edge deflections tested at C_L = 0.2 across the range of test Mach numbers. At M = 0.90, L/D is 13.3 for the LE-10°/TE-3° configuration. The figure illustrates the rather sharp reduction in drag benefit due the higher flap setting as the Mach number is increased from 0.95 to 0.97 due to the rapid increase in wave drag.
As soon as the freestream Mach number becomes supersonic, the drag benefit with outboard flaps reduced to order 5 - 10 counts and L/D drops to about 9.2 for the cruise configuration. L/D = 9.6 for the LE-8°/TE-0° flap setting at M = 1.20. Note that the 10° leading-edge deflection has the same performance as the 4° flap at all supersonic Mach numbers tested, whereas the 8° deflection has the largest benefit at these conditions.

In contrast to the results at M = 0.90, a drag *penalty* occurs due to the trailing-edge flap deflection compared to a leading-edge deflection only. At C_L = 0.2, the penalty is about 5 counts due to trailing-edge flap. However, compared to the baseline undeflected wing, there is still a small net increase in L/D (about 3 counts drag reduction).

HSCT High-Speed Technology (pmv5727)
Ref-H Transonic Flap Data Base

Relative Effect of Flap Deflection on Lift/Drag Ratio
(C_L = 0.2, Re_c = 5.7 million)

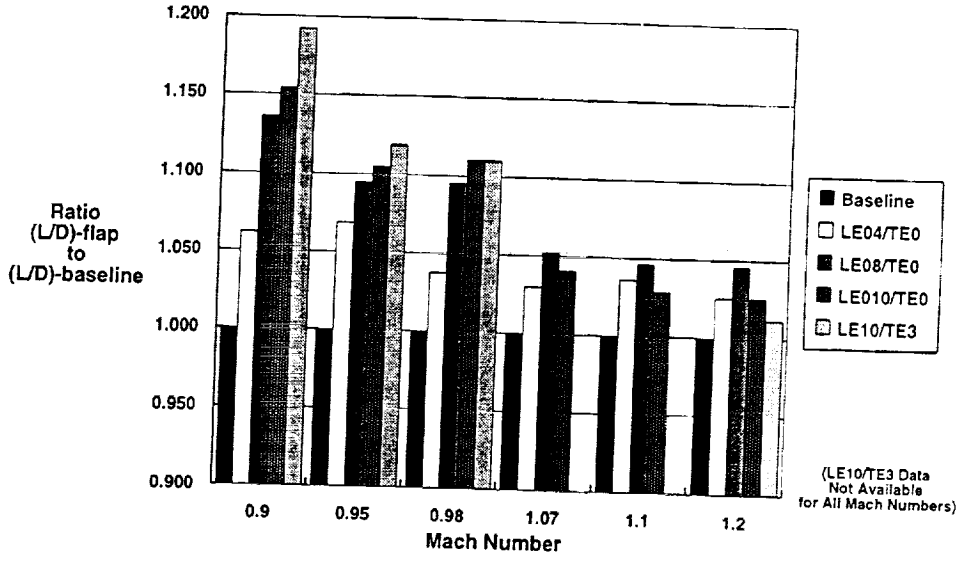

HSCT High-Speed Technology (pmv572
Ref-H Transonic Flap Data Ba

Relative Effect of Flap Deflection on Lift-to-Drag Ratio

The absolute L/D data in the previous figure are shown here relative to the L/D value for the baseline geometry at each Mach number. The relative impact of each flap setting across the Mach-number range tested is apparent.

Comparison with Previous Ref-H Wind-Tunnel Tests

- **Baseline model has been tested at transonic speeds in several facilities:**
  - Ames 11-Ft Test ARC198 (2.7% model; Re = 4.8 million)
  - Boeing BSWT Test 630 (1.675% model; Re = 10.7 million)
  - Langley 16-Ft Test 457 (1.675% model; Re = 5.7 million)
  - Langley NTF Test 060 (2.2% model; Re = 30 million used here)
- **Model with 10° leading-edge and 3° trailing-edge flaps has been tested in NTF (Test 063)**
- **Turbulent flat-plate skin-friction correction is applied to previous data**

Comparison with Previous Ref-H Wind-Tunnel Tests

The current data set for the Ref-H Modular-Model is compared with available Reference-H baseline data obtained in the indicated previous tests. All comparison data are for the nominally identical Reference-H Wing/Body loft lines.

Because the data with the NTF models were obtained without transition trip dots, NTF data at a chord-Reynolds number of 30 million (and a dynamic pressure of 1000 psfa) was used. At this Reynolds number, the flow over the highly-swept wing is expected to become turbulent close to the leading edge. The NTF drag data used here has been corrected for aero-elastic effects by K. Mejia of Boeing. The lift and pitching-moment data from the previous test presented here are not corrected for changes in Reynolds number.

The drag data from previous tests were corrected by applying a constant drag increment across the C_L range obtained from comparing the wetted-area skin-friction drag at the conditions of the previous test (Reynolds number and total temperature) with those of the present test. The skin-friction corrections were obtained from the fully-turbulent analysis routine in the A389 program. Finally, in the comparisons shown, the present data as well as the previous results have not been corrected for trip drag.

Drag Comparison with Previous Ref-H Baseline Tests M = 0.90

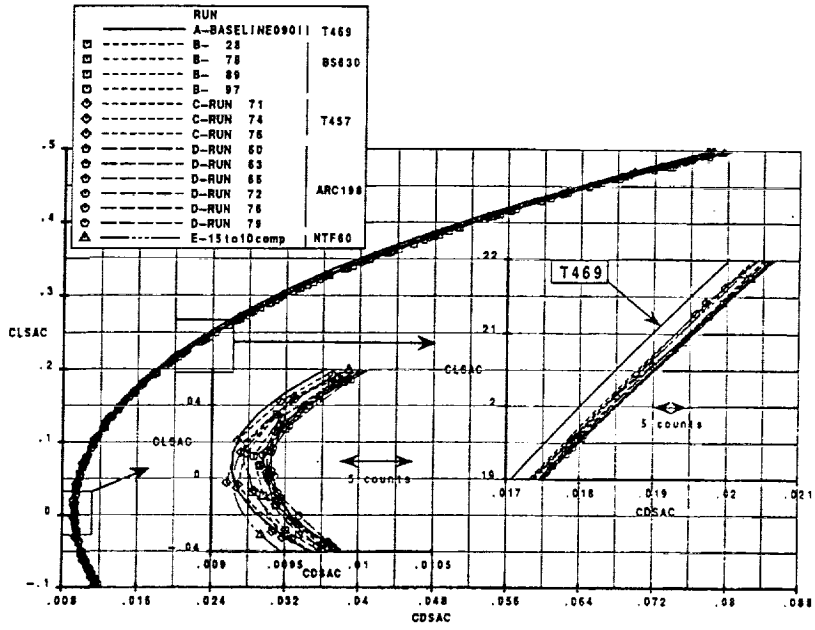

HSCT High-Speed Technology (pmv57
Ref-H Transonic Flap Data E

Drag Comparison with Previous Ref-H Baseline Tests at M = 0.90

Drag comparisons are first presented for the non-cryogenic subsonic tests with the Reference-H baseline wing. Both lift and moment repeat very well in the range of C_L of interest between the T457 and the ARC198 tests. Drag comparisons indicate that the present baseline wing is about 3 - 4 counts lower in drag than the other test at C_L = 0.2, whereas the zero-lift drag is about 2 counts lower.

NTF60 / 63 Drag Comparison (Baseline and Flaps) M = 0.90

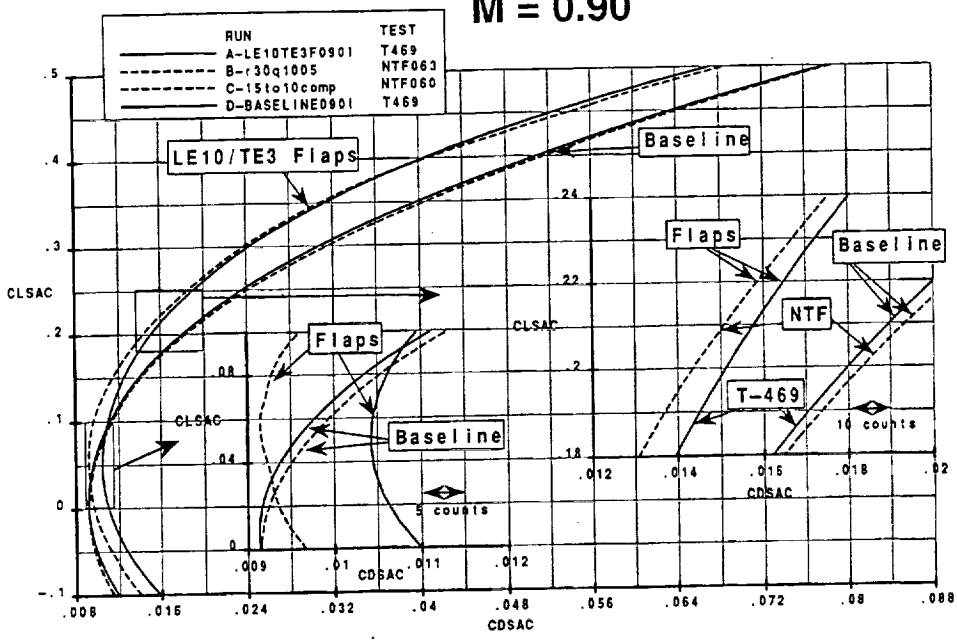

HSCT High-Speed Technology (pmv5727)
Ref-H Transonic Flap Data Base

Drag Comparison with Previous Ref-H NTF Tests at M = 0.90

The drag results for the baseline wing in the NTF test 60 (cryogenic mode) show the same (corrected) zero-lift drag coefficient and about a 3 counts higher drag than the present test at C_L = 0.2. The drag results for the flapped wing (leading-edge 10° / trailing-edge 3°) in the NTF test (063) show a much lower (corrected) zero-lift drag, while the drag coefficient at C_L = 0.2 is about 8 counts lower than the present test. As a consequence, the drag reduction with leading-edge 10° / trailing-edge 3° flap is about 11 counts larger in the NTF tests than obtained in the present test.

Lift and Moment Comparison with Previous Baseline Tests M = 1.20

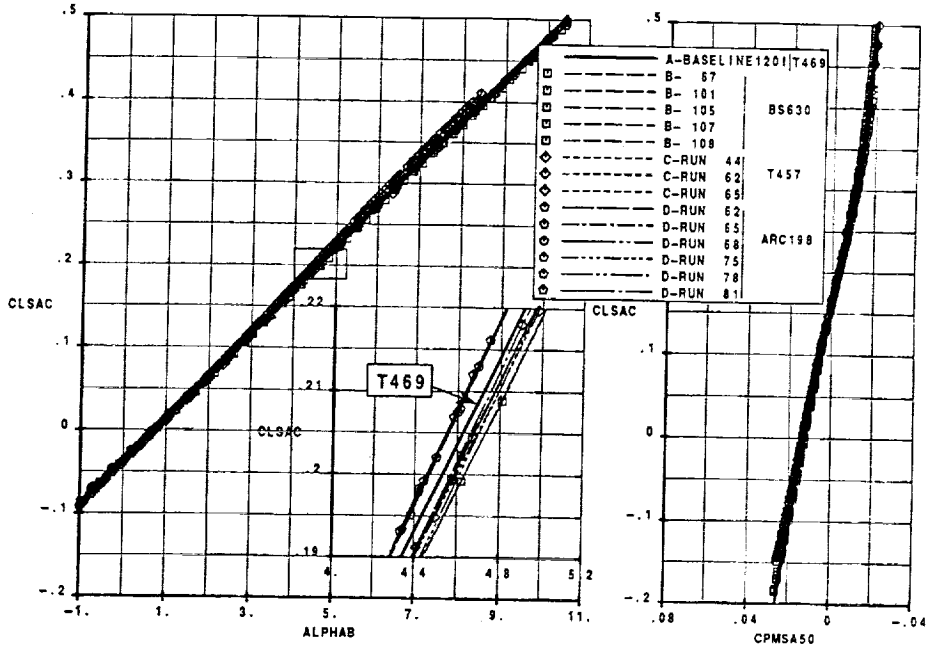

HSCT High-Speed Technology (pmv5727
Ref-H Transonic Flap Data Bas

Lift and Pitching-Moment Comparison with Previous Baseline Tests at M = 1.20

At supersonic speeds (M = 1.20 shown here), good agreement can be observed in lift and pitching-moment characteristics with the three comparison tests indicated in the C_L range of interest.

Drag Comparison with Previous Baseline Tests M = 1.20

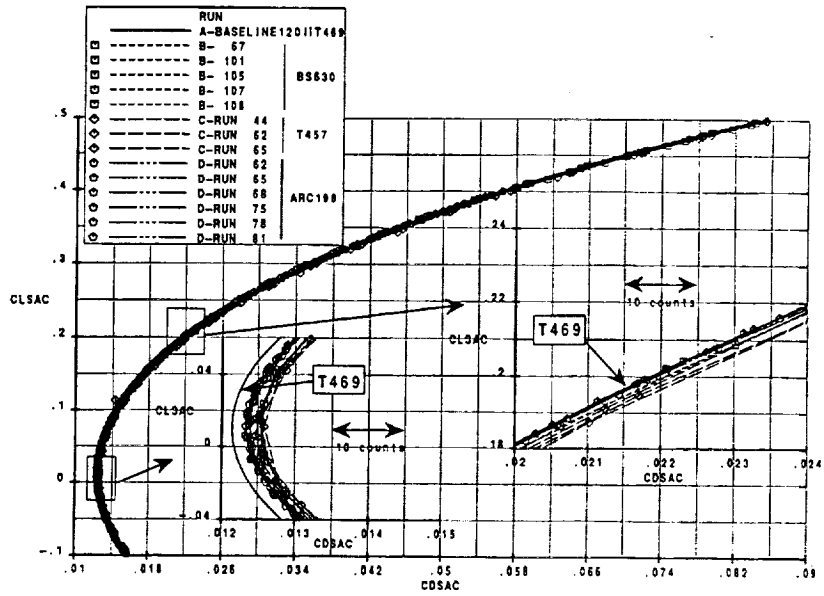

HSCT High-Speed Technology (pmv5727)
Ref-H Transonic Flap Data Base

Drag Comparison with Previous Baseline Tests at M = 1.20

The drag comparison at M = 1.20 indicate that at C_L = 0.2 good to excellent agreement is obtained for the baseline geometry with the previous tests in the BSWT and Ames tunnels. The drag variation with the previous 16-T test (T457) is within the experimental uncertainty of the data sets.
Similar to the observation at M = 0.90, the zero-lift drag coefficient is lower in the present test. At M = 1.20, C_{Dmin} is about 3 - 5 counts lower. It is possible that the size of the transition-trip dots in the present test are closer to the lower tolerance estimated from the hand-book method, accounting for a (small) reduction in zero-lift drag across the Mach range.

The observed agreement between the current data set and previous Ref-H baseline data in the lift range of interest indicates that the present data is consistent with earlier supersonic results.

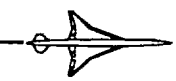

Summary of Comparison with Previous Ref-H Tests

- Lift and moment data are very similar across Mach range tested
- Baseline C_{Dmin} is 2 - 5 counts lower than in previous (skin-friction corrected) tests across Mach range.
  - Possible causes are tripping effects, small number of repeat runs and Modular-Model loft shape
- The present test with LE10°/TE3° flaps has higher C_{Dmin} than (corrected) NTF063 results
- Drag at C_L = 0.2 is within 2- 5 counts at M = 0.90
- Drag at C_L = 0.2 is within 1 counts at M = 1.20

Summary of Comparison with Previous Ref-H Tests

The slide summarizes the observations made from the above discussion of the comparison with previous Ref-H tests in different tunnels.

Comparison with Theory/CFD Predictions

Approach

- Evaluate predictive capability of analysis methods for flap design
- Evaluate measured drag trends with leading-edge flaps at M = 1.20

Methods

- Modified-Linear Theory
  - Aero2S subsonic method (with A389 skin-friction model)
  - A389/A080 supersonic method
- CFD
  - OVERFLOW N.S. code

Comparison with Linear Theory/CFD Predictions

The present data set is compared next with results from modified-linear theory as well as with CFD viscous simulations at the conditions of the 16-Ft wind tunnel. The purpose of the comparison is twofold. First, the prediction capability of these design and analysis tools can be evaluated for their application to transonic flap design. Secondly, the prediction tools may allow further understanding of the measured trends in drag with increasing flap deflection at M = 1.20.

At subsonic speeds, the modified-linear theory method by Carlson et al. (Aero2S) is applied for lift-dependent drag[1]. The viscous drag is obtained from the turbulent skin-friction module in A389[2] to allow buildup of drag polars. At supersonic speeds, the modified-linear theory methods by Middleton et al (A389/A80[3]) are used. The estimation of attainable leading-edge suction is partly based on previous in-house wind-tunnel correlations at low supersonic Mach numbers.

Viscous OVERFLOW[4] overset-grid flow solutions for several of the present geometries have been obtained at Boeing by S. Chaney (for the baseline) and at DYNACS[5] (for the flapped geometries) at both subsonic and supersonic conditions. Code grid convergence and detailed N.S. flow results are discussed in detail in the paper by Dynacs[5].

It is noted that the drag polars obtained from both linear theory and OVERFLOW were curve fitted. (The acutal OVERFLOW data points are also indicated with symbols.)

1 H. Carlson and K. Walkley, "A Computer Program for Wing Subsonic Aerodynamic Performance Estimates Including Attainable Thrust and Vortex Lift Effects," NASA CR-3515, 1982.

2 W. Middleton and J. Lundry, "A System for Aerodynamic Design and Analysis of Supersonic Aircraft," Parts 1 (General Description and Theoretical Development) and 2 (User's Manual), NASA CR-3351 and CR-3352, Dec. 1980.

3 T. Byron and D. Olson, "Zero-Lift Wave Drag Program," Boeing Report D183-10030-1, 1971.

4 P. Buning et al., "OVERFLOW/F3D User's Manual, Version 1.6ap, NASA Ames Res. Center, Moffett Field, March 1994.

5 M. Kandula and R. Sheckler, "CFD Methodology Adaptation - Analysis Methods Validation," Dynacs Engineering, Renton, in HSR Configuration Aerodynamics Final Review FY95, Boeing HSCT High-Speed Aerodynamics, Dec. 1995. (See also paper in this Session.)

Comparison Lift and Moment Test Data with Predictions

M = 0.90, R_c = 5.7 million (Baseline and LE10°/TE3° Flaps)

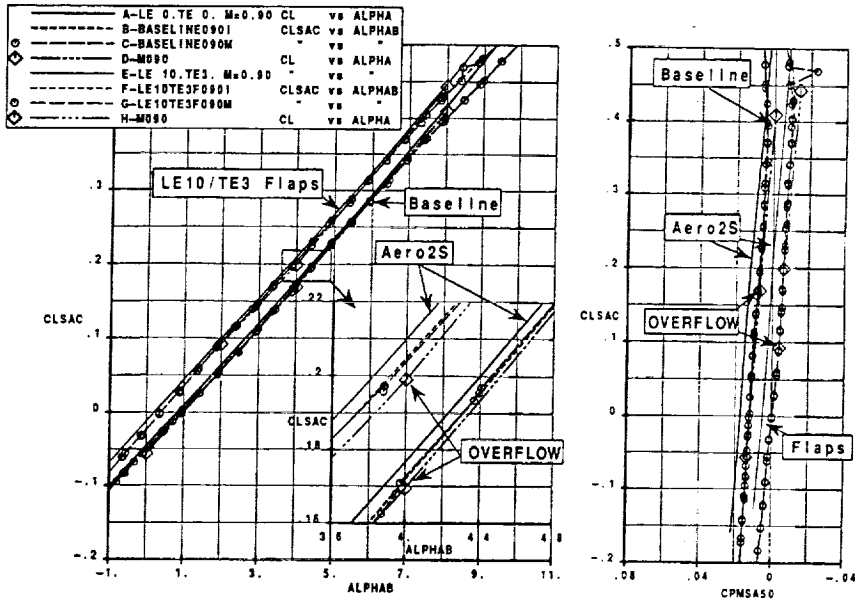

HSCT High-Speed Technology (pmv572
Ref-H Transonic Flap Data Ba

Comparison Lift and Moment Test Data with Predictions (M = 0.90)

Linear theory generally predicts the lift-curve slope for C_L's in the operating range properly for the baselin and the LE-10°/TE-3° geometry, but lift is overpredicted at a given angle of attack. OVERFLOW properl predicts $C_{L\alpha}$ for both configurations, and slightly underpredicts lift for the flapped wing. (For α's above 8 the extent of vortex separation on the outboard wing may be underpredicted by the CFD result[1]). Aero2 overpredicts the pitching moment, while OVERFLOW properly predicts C_M at lower C_L. Overall, both code properly predict the shift in lift and moment due to flap deflections at subsonic conditions.

1 M. Kandula and R. Sheckler, "CFD Methodology Adaptation - Analysis Methods Validation," Dynacs Engineering, Renton, in HSR Configuration Aerodynamics Final Review FY95, Boeing HSCT High-Speed Aerodynamics, Dec. 1995. (See also paper in this Session.)

Comparison Drag Test Data with Predictions

M = 0.90, R_c = 5.7 million (Baseline and LE10°/TE3° Flaps)

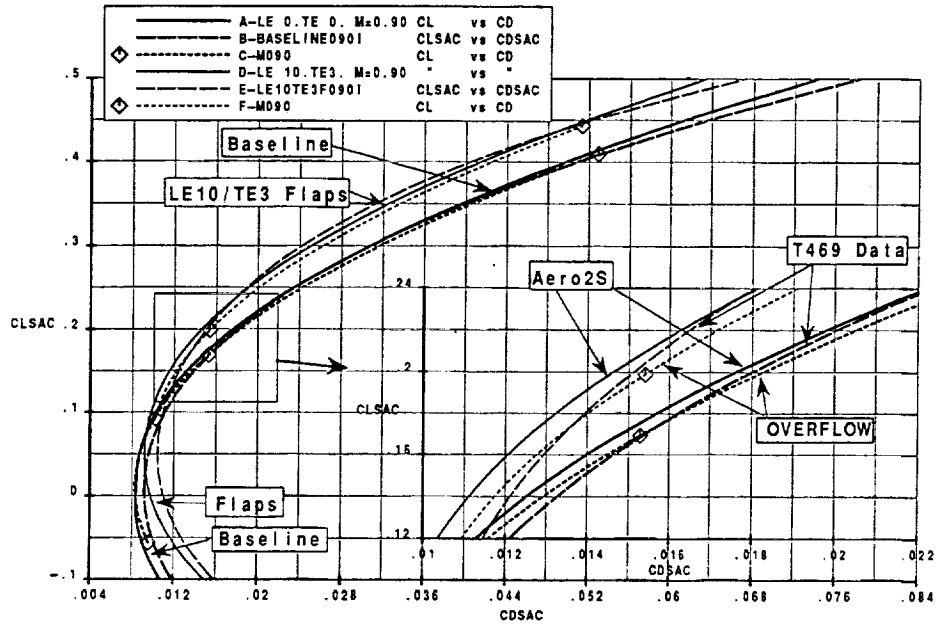

HSCT High-Speed Technology (pmv5727)
Ref-H Transonic Flap Data Base

Comparison Drag Test Data with Predictions (M = 0.90)

The modified-linear method Aero2S underpredicts drag for the baseline at C_L = 0.2 within 4 counts of the experimental data. The OVERFLOW calculation at α = 4° (C_L = 0.165) exactly predicts the measured drag. The curvefit through the OVERFLOW data points overpredicts drag by 2 count at C_L = 0.2, and provides a similar estimate of zero-lift drag in comparison to the flat-plate estimate. (Note that the CFD-data curvefit probably exaggerates this $C_{D_{min}}$ underprediction.) For the LE-10°/TE-3° flap configuration, Aero2S again underpredicts measured drag at C_L = 0.2 by about 4 counts. As a consequence, Aero2S predicts the magnitude of drag reduction due to leading-edge flap deflection with very good agreement. OVERFLOW overpredicts drag for the flapped geometry by a similar amount as the baseline, also resulting in proper prediction of the flap effect.

Summary Subsonic Flap Drag Prediction Capability
M = 0.90, R_c = 5.7 million

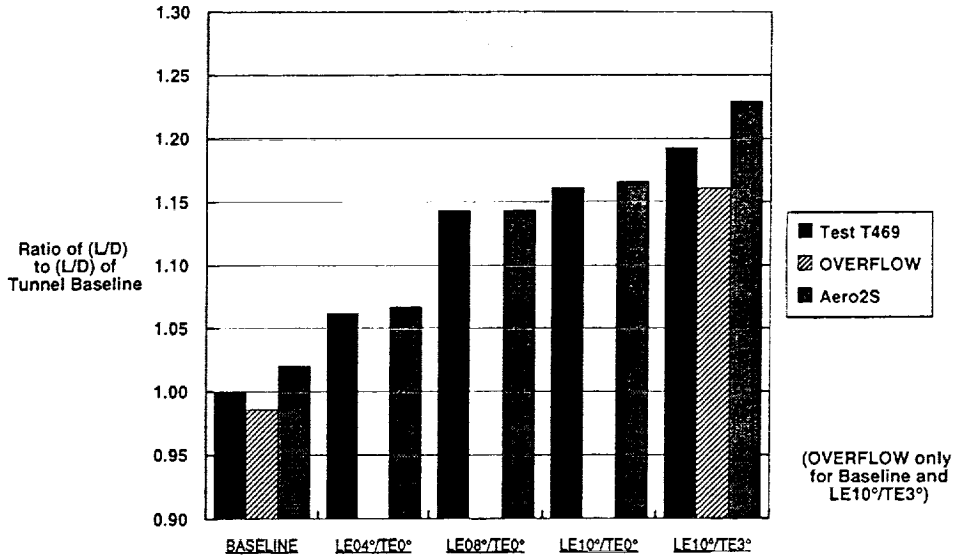

Note: Drag Changes Are Relative to Baseline in T469 Test

HSCT High-Speed Technology (pmv57
Ref-H Transonic Flap Data B

Summary Subsonic Flap Drag Prediction Capability (M=0.90)

The figure summarizes the L/D predictions from Aero2S at C_L = 0.2 for all tested configuration an OVERFLOW results available for the baseline and the LE-10°/TE-3° flap configurations. The measured L/ value of the baseline in the present 16-T test (T469) was used to non-dimensionalize the measured c predicted L/D for the other configurations. The linear method accurately predicts the absolute drag of th geometries with only leading-edge deflection. Both methods predict the measured improvement in L/D wit flaps at C_L = 0.2 to within 2 -3 percent.

OVERFLOW results[1] for the LE-10°/TE-3° case at NTF Reynolds number of 30 million show that the extent of leading-edge flap hinge-line separation (at C_L = 0.2) and lower-surface flap separation (at C_L = 0.1) have a much smaller extent in comparison to the 16-T predictions. Both viscous-flow phenomena would contribute to the relatively large deviation of the T469 results for LE-10°/TE-3° with the already discussed NTF data (with skin-friction correction).

1 M. Kandula and R. Sheckler, "CFD Methodology Adaptation - Analysis Methods Validation," Dynacs Engineering, Renton, in HSR Configuration Aerodynamics Final Review FY95, Boeing HSCT High-Speed Aerodynamics, Dec. 1995. (See also paper in this Session.)

HSCT High-Speed Technology (pmv5727)
Ref-H Transonic Flap Data Base

Comparison Lift and Moment Tunnel Data with Predictions

M = 1.20, R_c = 5.7 million (Baseline and LE08°/TE0° Flaps)

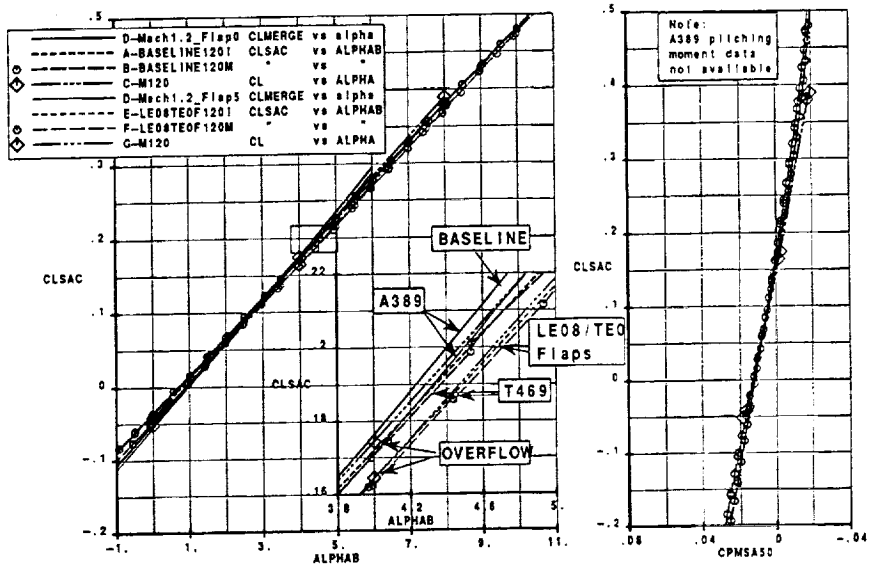

HSCT High-Speed Technology (pmv5727)
Ref-H Transonic Flap Data Base

Comparison Lift and Moment Tunnel Data with Predictions (M = 1.20)

Lift-curve slope overestimation by the inviscid linear-theory method A389 is as expected. The OVERFLOW method properly predicts the slope and magnitude of lift and pitching moment at M = 1.20 near C_L = 0.2. At higher C_L's, OVERFLOW overpredicts the pitching moment as well as the lift. Simulated oil-flow visualization from OVERFLOW at α = 8° indicates a large region of trailing-edge separation over the outboard wing[1] . Larger separation than predicted could explain the differences observed in the figure. (Note that no flow visualization was obtained in the present test at this high angle of attack.)

[1] M. Kandula and R. Sheckler, "CFD Methodology Adaptation - Analysis Methods Validation," Dynacs Engineering, Renton, in HSR Configuration Aerodynamics Final Review FY95, Boeing HSCT High-Speed Aerodynamics, Dec. 1995. (See also paper in this Session.)

Comparison Drag Tunnel Data with Predictions
M = 1.20, R_c = 5.7 million (Baseline and LE08°/TE0° Flaps)

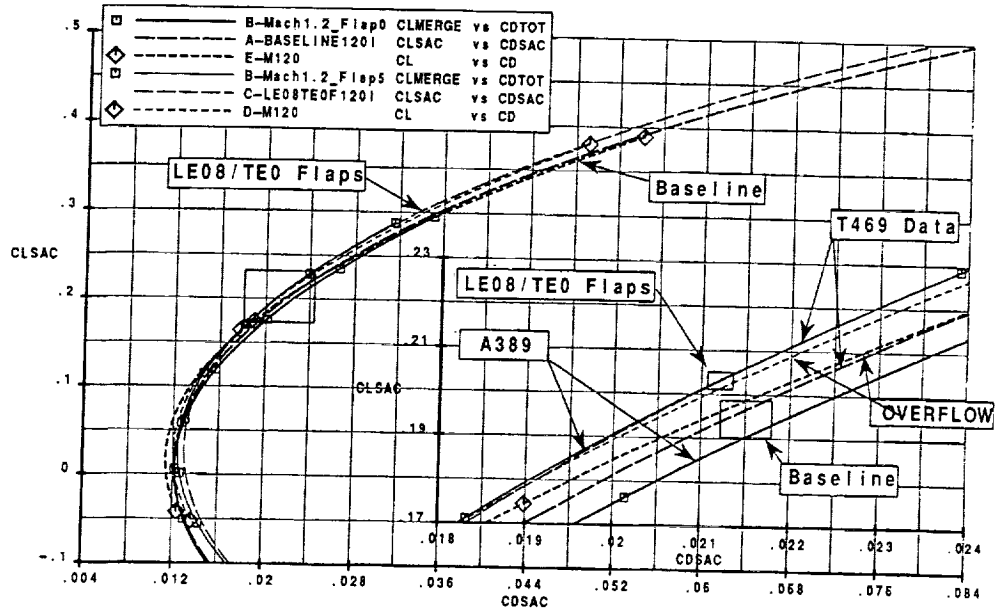

HSCT High-Speed Technology (pmv5727)
Ref-H Transonic Flap Data Base

Comparison Drag Tunnel Data with Predictions at M=1.20 (Baseline and LE-8°/TE-0° Flaps)

Modified linear theory overpredicts the baseline-wing drag at C_L = 0.2 by about 7 counts, but provides a good estimate for zero-lift drag. The OVERFLOW simulations underpredicts baseline drag at CL = 0.2 by about 5 counts. Also at C_L = -0.05, OVERFLOW predicts a lower drag. In contrast to the results for the baseline, the linear method correctly predicts the drag at C_L = 0.2 for the LE-8°/TE-0° flap configuration (which showed the largest measured drag reduction) to within the experimental scatter. The fact that the baseline wing drag is overpredicted by A389 explains the larger pre-test expectation concerning flap benefits at M = 1.20. The OVERFLOW prediction at C_L = 0.20 is again well within experimental scatter, whereas the drag near C_L = -0.05 is again underpredicted.

HSCT High-Speed Technology (pmv5727)
Ref-H Transonic Flap Data Base

Comparison Tunnel Drag Data with Predictions

M = 1.20, R_C = 5.7 million (Baseline and LE10°/TE0° Flaps)

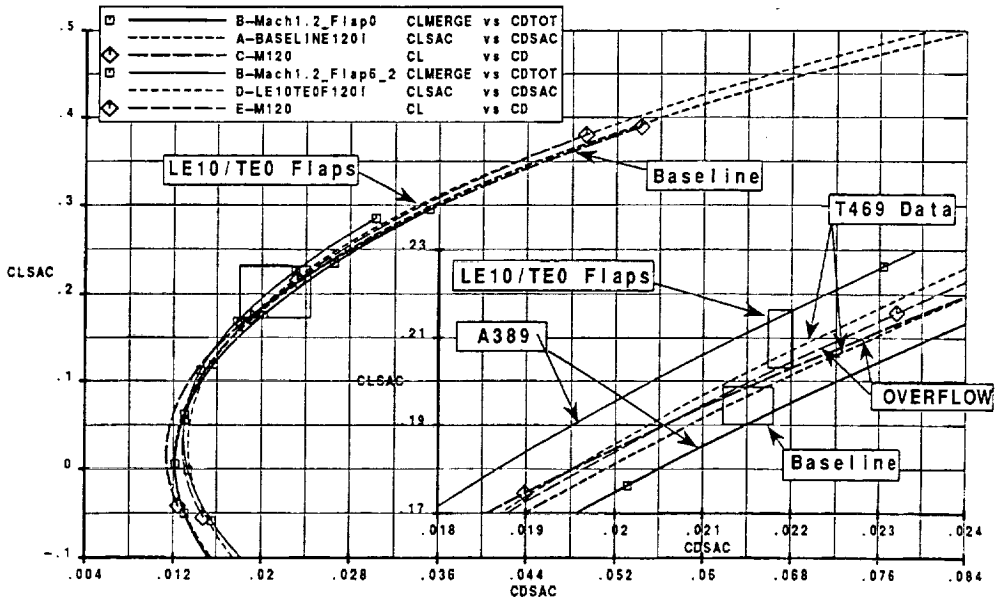

HSCT High-Speed Technology (pmv5727)
Ref-H Transonic Flap Data Base

Comparison Drag Tunnel Data with Predictions at M=1.20 (Baseline and LE-10°/TE-0° Flaps)

The experimental results indicate that the increase in leading-edge flap deflection from 8° to 10° result in a relative large drag increase at M = 1.20. The modified-linear theory prediction underpredicts the drag at C_L = 0.2 by about 8 counts for the 10° deflection. The OVERFLOW computations for the LE-10°/TE-0° flap configuration predict the absolute drag of the experiment again to within 1 count at C_L = 0.2. (Excellent agreement is also obtained at higher lift (C_L = 0.37), while at C_L = -0.05 the drag is again underpredicted.) In other words, OVERFLOW properly predicts the adverse drag trend with increased leading-edge deflection above 8°.

Summary Supersonic Flap Drag Prediction Capability
M = 1.20, R_c = 5.7 million

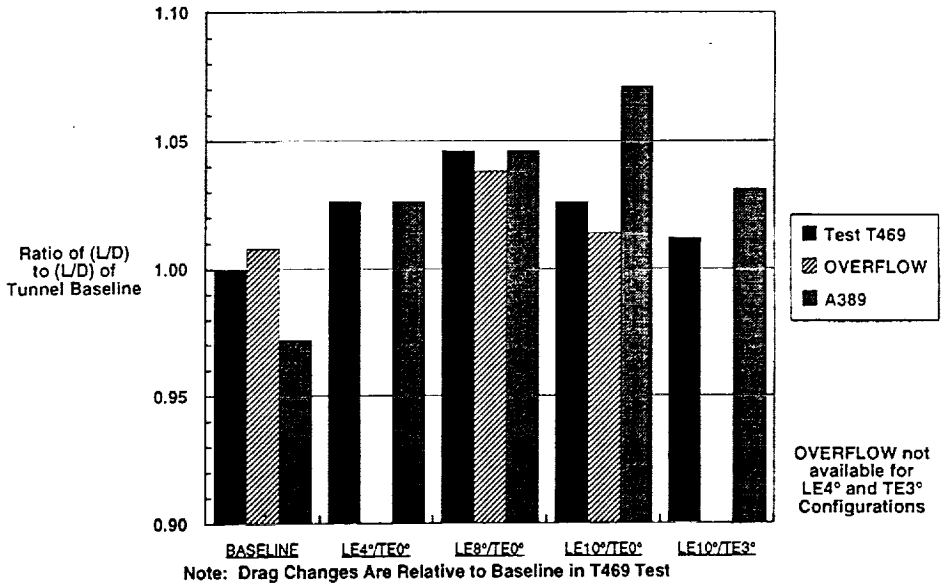

Note: Drag Changes Are Relative to Baseline in T469 Test

Summary Supersonic Flap Drag Prediction Capability (M=1.20)

The figure shows that the L/D prediction by A389 for the LE-4°/TE-0° configuration is as good as the L 8°/TE-0° geometry. (As before, the measured L/D value of the baseline in the present 16-T test (T469) used to non-dimensionalize the measured or predicted L/D for the other configurations.) The adverse tre in drag with trailing-edge flap deflection at supersonic speed is properly captured by A389. The differenc between test data and A389 predictions at the present low supersonic conditions for the LE-10° geome suggest that the modified-linear theory model cannot completely account for the changes as well magnitudes of the local upflow angles along the outboard wing panel. However, the fact that A389 prope predicted the drag for the "optimum" LE-8°/TE-0° configuration also suggests that the method can be us *a-posteriori* after the optimum flap angle has been determined from experiment or CFD.

The figure reiterates that OVERFLOW properly predicts the measured adverse trend in drag with the 1 leading-edge flap as compared to the 8° flap. However, the magnitude of L/D benefits with flaps predict by OVERFLOW is smaller than measured. Analysis of OVERFLOW pressure-distribution data over t flapped outboard wing shows that for the LE-8°/TE-0° geometry the attachment line is on the flap low surface while at LE-10°/TE-0° the attachment line is on the flap upper surface[1]. The resulting pressure pe on the LE-8° flap results in a much larger flap normal force and offers a drag reduction through increas leading-edge suction. OVERFLOW simulated surface oil-streamline results were used to interpret t marginal oil-flow visualization obtained during this test at M = 1.20. As OVERFLOW did not predict fl hinge-line separation at C_L = 0.2, it appears that the reduced performance for LE-10° is not caused leading-edge flap hinge-line separation, but by the flap pressure distribution as dominated by flap deflecti angle and local upwash angle on the outboard wing panel.

[1] M. Kandula and R. Sheckler, "CFD Methodology Adaptation - Analysis Methods Validation," Dynacs Engineering, Renton, in HSR Configuration Aerodynamics Final Review FY95, Boeing HSCT High-Speed Aerodynamics, Dec. 1995. (See also paper in this Session.)

Conclusions - 16-Ft Ref-H Flap Test

- Obtained minimum set of Ref-H performance data for four LE and two TE outboard flap settings at transonic speeds. Supersonic data with flaps is unique for Ref-H geometry
- Subsonic drag reduction with 10° leading- and 3° trailing-edge deflection is 29 counts (19% reduction; M = 0.90). (L/D = 13.3 at C_L = 0.2)
- Supersonic drag reduction with 8° leading-edge deflection is 9 counts (4.5% reduction; M = 1.20). (L/D = 9.6 at C_L = 0.2)
- Present supersonic results are in good agreement with previous Ref-H baseline data at C_L = 0.2

Conclusions - 16-Ft Wind-Tunnel Flap Test

The main objective of the Reference-H outboard-flap test was achieved. A minimum set of performance data was obtained for four leading-edge (0°, 4°, 8°, and 10°) and two trailing-edge flap (0° and 3°) settings at transonic speeds. The supersonic data is unique for the Reference-H geometry.

The 8° leading-edge flap deflection offered a 9 counts reduction in drag (4.5 percent of total drag) at M = 1.20 and C_L = 0.2. In contrast to the pre-test linear-theory prediction, the larger deflection of 10° resulted in a much reduced benefit than the 8° setting at supersonic speeds.
A large improvement in efficiency is obtained by deflecting the outboard leading-edge flaps at subsonic speeds. A drag reduction of 29 counts (19-percent reduction) with the 10° leading-edge and 3° trailing-edge setting was measured. At supersonic speeds, such trailing-edge deflection for the 10° leading-edge setting increased drag (at C_L near 0.2), however, a small net drag reduction relative to the baseline wing was maintained.

The minimal test time allotted for this performance test, combined with rather low productivity, resulted in cancellation of planned transition-trip verification, and precluded additional repeat polars and more extensive oil-flow results. Nevertheless, the supersonic data obtained in this test with the baseline wing is consistent with previous Ref-H results from tests in others tunnels near C_L = 0.2.

Conclusions - Comparison with Theory

- Predictive capability of modified linear theory is good at subsonic conditions (C_L = 0.2). Drag levels and trends are predicted well
- At supersonic conditions, the linear method properly predicts the drag for smaller flap settings but overpredicts the optimum flap angle
- Predictive capability of OVERFLOW N.S. method is good both at subsonic and supersonic speeds. OVERFLOW properly predicts relative performance of LE-8° vs. LE-10° flaps at M = 1.20
- The N.S. method predicts no leading-edge hinge-line separation at C_L = 0.2 and M = 1.20

HSCT High-Speed Technology (pmv57
Ref-H Transonic Flap Data B

Conclusions - Comparison with Theory

Comparison results of the new data set with modified-linear theory and with viscous N.S. simulations wer presented. The modified linear-theory method Aero2S properly predicted the drag levels as well as th trend due to flap deflection at subsonic speeds. The supersonic modified linear-theory method A38 overpredicted the drag of the baseline, and underpredicted the LE 10° deflection, resulting in a prete: expectations biased towards the 10° flap setting. Nevertheless, the A389 method properly predicts the dra for the LE-4° and LE-8° flap setting in the CL range of interest.
The N.S. method OVERFLOW properly predicted the measured trends with leading-edge flap deflection supersonic speeds. The method captured the larger drag reduction for the LE-8° setting as compared the LE-10° configuration at M = 1.20. Finally, the OVERFLOW results indicate that the likely cause for th measured trend is not leading-edge hinge-line separation at the wind-tunnel Reynolds number but significant change in pressure distribution over the leading-edge flap between the LE-8° and LE-1(settings.

Final Remarks

- Together with higher Reynolds number CFD solutions by Dynacs*, current test results provide a data base on flap effects at transonic speeds for Ref-H like geometry
- Recommend to use present flap data base to alleviate drag pinch at low-supersonic Mach numbers
- Flap surface-pressure measurements and improved oil-flow visualization data are needed to further validate CFD predictions at M = 1.20
- Tripping issues of flow over leading-edge flaps on outboard panels with low sweep need to be verified

* See Dynacs paper in this workshop session

Final Remarks

Together with higher Reynolds-number OVERFLOW simulations, the present test results provide a data base on transonic flap effects for Ref-H like HSCT geometries. It is recommended to apply the present data base to alleviate as much as possible the transonic drag "pinch" at high subsonic and low supersonic Mach numbers. The data presented here suggest a possible flap schedule to minimize drag from M = 0.90 to 1.20. Also, it is possible that improved definition of the leading-edge flap design space can further enhance the drag benefits of outboard flaps at low-supersonic speeds. Based on the present results, such optimization should utilize CFD methods.

In possible future additional wind-tunnel testing with flaps at low-supersonic speeds, it is recommended to obtained surface-pressure measurements with deflected leading-edge flaps to validate the CFD predictions. Particularly, verification of the predicted large changes in leading-edge flap pressure distribution with small variation in flap angle is of interest.

Additional high-resolution oil-flow visualization is needed to evaluate available detailed computational surface-flow fields, particularly at off-design angles of attack were flow separation is predicted by the CFD method.

Finally, future experimental work needs to address transition-trip effectiveness (and drag) on leading-edge flaps along low-moderately-swept outboard wing panels.

Assessment of Ref. H HSCT Transonic Flap and Reynolds Number Effects with the OVERFLOW Code

Max Kandula and Ross Sheckler
Dynacs Engineering Company, Inc.
Renton, WA 98058

Transonic flap effects on the aerodynamic performance of Ref. H HSCT wing/body configuration have been analyzed using the OVERFLOW thin-layer Navier-Stokes code. Flap deflection effects at freestream Mach numbers M=0.9 (10/3 deg LE/TE at Re=5.8E6 and 30E6 based on the mean aerodynamic chord, and M=1.2 (10/0 deg and 8/0 deg LE/TE at Re=5.8E6) for a range of angle of attack alpha= 0 to 8 deg are investigated. The predictions from the CFD analysis are correlated with the NTF (M=0.9 at Re=30E6) and LaRC-16T (M=1.2 at Re=5.8E6) wind tunnel data. Surface grids are generated using Gridgen-2D elliptic grid generator in conjunction with GRIDTOOL for database projection. Volume grids are developed with the HYPGEN hyperbolic grid generator. The volume grid communication is carried out using the PEGSUS code based on Chimera overlapping scheme. Flow solutions are obtained with OVERFLOW code (central-differencing option) with the Baldwin-Barth one-equation turbulence model.

Boeing HSCT High Speed Aerodynamics provided the baseline (flaps-up 0/0 deg LE/TE) CFD results and the wind tunnel data presented here. In general the OVERFLOW Navier-Stokes CFD computations correlated well with the NTF and LaRC-16T data for forces, drag polar and pitching moments. The computed drag at low alpha is in general underpredicted, while the computed pitching moment at high alpha deviates appreciably from the data. Calculations for the 10/3 deg flaps at M=0.9 and Re=5.8E6 and 30E6 have indicated that the main effect of Re on the 10/3 deg flaps is seen on the wing upper surface downstream of the the hinge lines. For Re=5.8E6, a separation is noted on the upper surface downstream of the hinge line whereas no separation is observed at higher Reynolds number. The OVERFLOW calculations for the 10/0 deg and the 8/0 deg flaps at M=1.2 correlate well with the LaRC-16T data which show that in the range of alpha=3 to 8 deg, the 8/0 deg flap performs better than the 10/0 deg flaps relative to the baseline case.

Objectives

- Validate Predictions of Transonic Flap Effects with OVERFLOW Code
  - Generate Surface & Volume grids, and Obtain Solutions
  - Correlate with NTF & LaRC-16T Data
    - » Assess Flap Deflection Effect
    - » Assess Reynolds Number Effect
  - Assess Euler vs. Navier-Stokes Solutions
- Develop Multi-point Design Capability

The objective of this task is to validate predictions of transonic flap effects on the aerodynamic performance of Ref. H wing/body configuration using OVERFLOW thin-layer Navier-Stokes code. In particular the predictions from CFD for flap deflection and Reynolds number effects on forces and moments will be correlated with NTF (National Transonic Facility at NASA Langley) and LaRC-16T (pressure tunnel at NASA Langley) data. Also Euler solutions will be assessed with regard to the lift and pressure drag by a comparison with Navier-Stokes solution, so that the feasibility of considering a combination of Euler and Navier-Stokes solutions for application to a multi-point design capability can be examined.

Flap & Flow Conditions

- Transonic Flaps 10/3 deg, M=0.9
  - Re=10E6,30E6, 80E6 (NTF)
  - Re=5.8E6 (LaRC-16T)
- Transonic Flaps 10/0 deg, M=1.2
  - Re=5.8E6 (LaRC-16T)
  - Re=11E6 (BSWT)
- Transonic Flaps 8/0 deg, M=1.2
  - Re=5.8E6 (LaRC-16T)

CFD analysis is conducted for the transonic flap and flow conditions at freestream Mach numbers of M=0.9 (high subsonic) and M=1.2 (low supersonic) for which wind tunnel data are available. The available data are those from NTF and LaRC-16T wind tunnels. At M=0.9, the 10/3 deg LE/TE flaps are analyzed at Reynolds number Re=30E6 and Re=80E6 (NTF data, 2.2% scale), and at Re=5.8E6 (LaRC-16T data, 1.675 % scale). The quantity Re is based on Mean Aerodynamic Chord (MAC) of 1032.24 in. The NTF data were obtained in 1993 and 1994 (NTF-60 for flaps up and NTF 63 for flaps down). The LaRC data were obtained in 1995. At M=1.2, both the 10/0 deg LE/TE and 8/0 deg LE/TE flap deflections are analyzed at Re=5.8E6.

Approach

- Surface Grids: *GRIDGEN-2D*
  - Database Projections: *GRIDTOOL*
- Volume Grids: *HYPGEN*
- Volume Grid Communication:
  - Chimera Overlapping (*PEGSUS*)
- Flow Solutions: *OVERFLOW*
  - Baldwin-Barth 1-Eqn. Turbulence Model
  - Reynolds Number Restarts

The approach to conducting the CFD analysis using OVERFLOW code is as follows. Existing surface grids from Boeing are used for components other than the inboard/outboard wing transition, and the outboard wing with the deflected flaps. Surface grids are generated using GRIDGEN-2D code (elliptic grid generator). In the surface grids generated using GRIDGEN, there is found some mismatch between the surface grid and the database. This is primarily due to the inability of GRIDGEN to constrain the surface grid to the database when elliptic grids are to be generated when spanning multiple data networks. Thus the surface grids from GRIDGEN are made to conform to the database by projecting them onto the database using GRIDTOOL. The volume grids are constructed using HYPGEN hyperbolic code. Volume grid communication is established by chimera overlapping scheme with PEGSUS code. The flow solutions are obtained with OVERFLOW thin-layer Navier-Stokes code with Baldwin-Barth one-equation turbulence model. Reynolds number restarts are also considered.

Surface Grid For Wing/Body Configuration

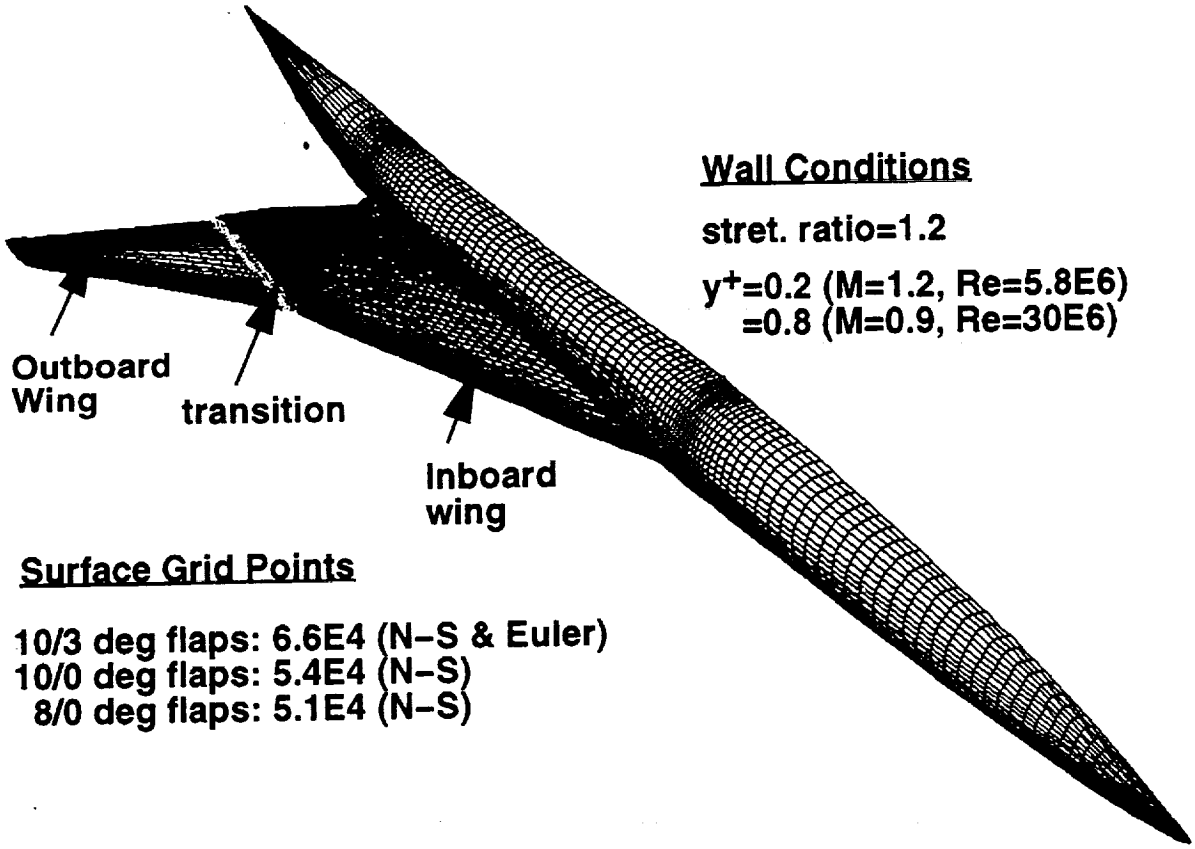

Existing surface grids are used for the fuselage, the collar grid, and the inboard wing. These grids were obtained from Steve Chaney of Boeing. New surface grids are thus generated only for the inboard/outboard wing transition region, and for the outboard wing. The database for the outboard wing geometry for the 10/3 deg flaps is obtained from Boeing in IGES format. For the 10/0 deg flaps, the surface grids are constructed on the basis of an overlap approach, where the 10/3 deg flap grids and the 0/0 deg flap (baseline flaps-up) grids are overlapped to provide the 10/0 LE/TE flap grids. For the 8/0 deg flaps, the outboard wing geometry is generated using Boeing AGPS software. A C-H grid topology is used for the wing and the wake regions. The grid is clustered near the leading and the trailing edges, the wing tip, and near the hinge lines to facilitate flow resolution. The total number of surface grid points are 6.6E4 for the 10/3 deg flaps, 5.4E4 for the 10/0 deg flaps, and 5.1E4 for the 8/0 deg flaps.

Surface Grid Detail (10/3 deg LE/TE)

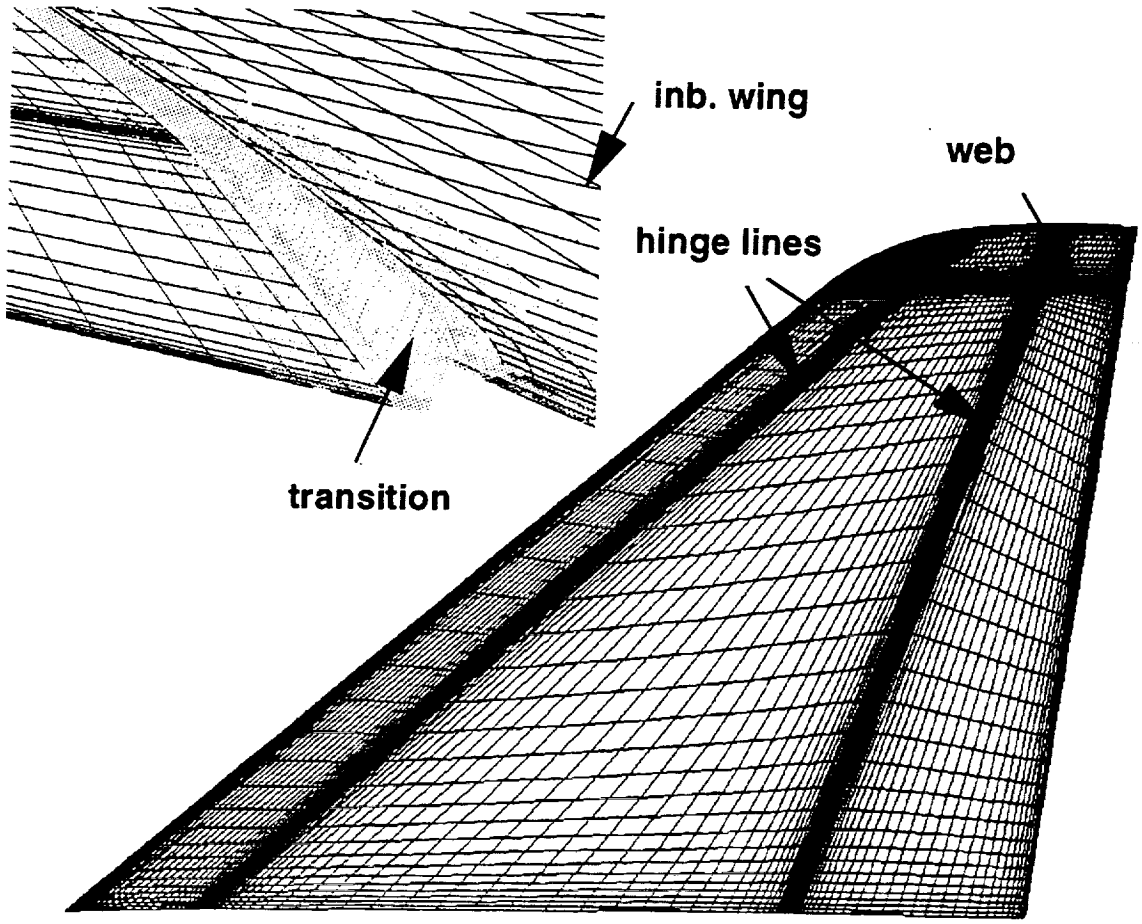

A more detailed view of the surface grid for the 10/3 deg flaps is shown in this figure, indicating hinge line locations and the web regions.

Volume Grid For Wing/Body Configuration

Volume Grid Points

10/3 deg: 5.0E6 (N–S), 3.3E6 (Euler)
10/0 deg: 4.4E6 (N–S)
8/0 deg: 3.5E6 (N–S)

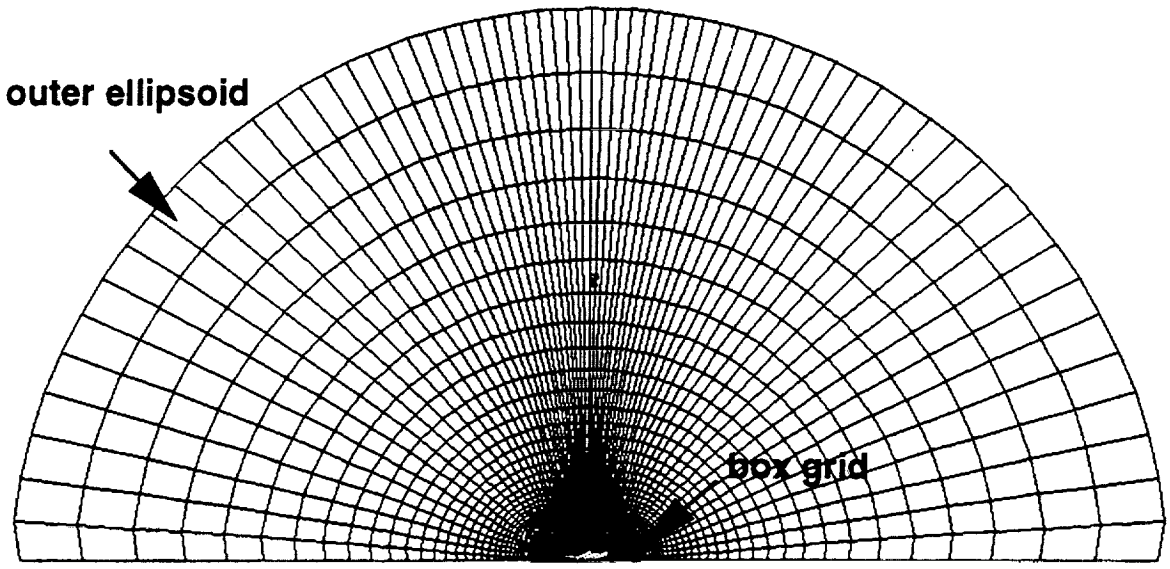

This figure shows the volume grid detail for the wing/body configuration. The rectangular box grid enclosing the wing/body and the outer ellipsoidal grid are obtained from Steve Chaney of Boeing. For the 10/3 deg flap case, the volume grid dimensions are: fuselage (134x93x71), inboard wing (289x36x61), inboard/outboard wing transition (281x45x61), outboard wing (306x81x61), collar (271x23x61), box (217x53x66) and ellipsoid (65x40x31). In general for the Navier-Stokes solutions, 61 grid points are considered in the surface normal direction. For the Navier-Stokes solution, the total number of grid points are 5.0E6 for the 10/3 deg flaps, 4.4E6 for the 10/0 deg flaps, and 3.5E6 for the 8/0 deg flaps. In the case of 10/3 deg flaps, the volume grids for the Euler grids are built using the same surface grids as for the viscous solution, but with reduced number of grid points in the surface normal direction (41 for Euer, and 61 for viscous), resulting in total grid points of 3.3E6 for the Euler solution.

The first grid cell size off the wall is taken as 0.001 in (full scale) for all Navier-Stokes solutions except for the 8/0 deg flaps. This results in values of y^+=0.2 for the case of M=1.2 and Re=5.8E6, and y^+=0.8 for the case of M=0.9 and Re=30E6. The volume grid for the 8/0 deg flaps is specifically designed for viscous solution at Re=5.8E6 only, and contained the first cell size off the wall as 0.003 in. Also it has reduced number of points in the wall normal direction for the inboard wing and the collar grid (about 45 points), thus resulting in a reduced number of total grid points compared to the 10/3 deg and 10/0 deg flaps. In the case of Euler solution, the first grid cell distance from the wall is taken as 0.025 in. A stretching ratio of about 1.2 is considered near the wall in order to minimize truncation errors.

Ref. H Transonic Flaps (10/3 deg); M=0.9
Surface Pressure Coefficient (OVERFLOW)

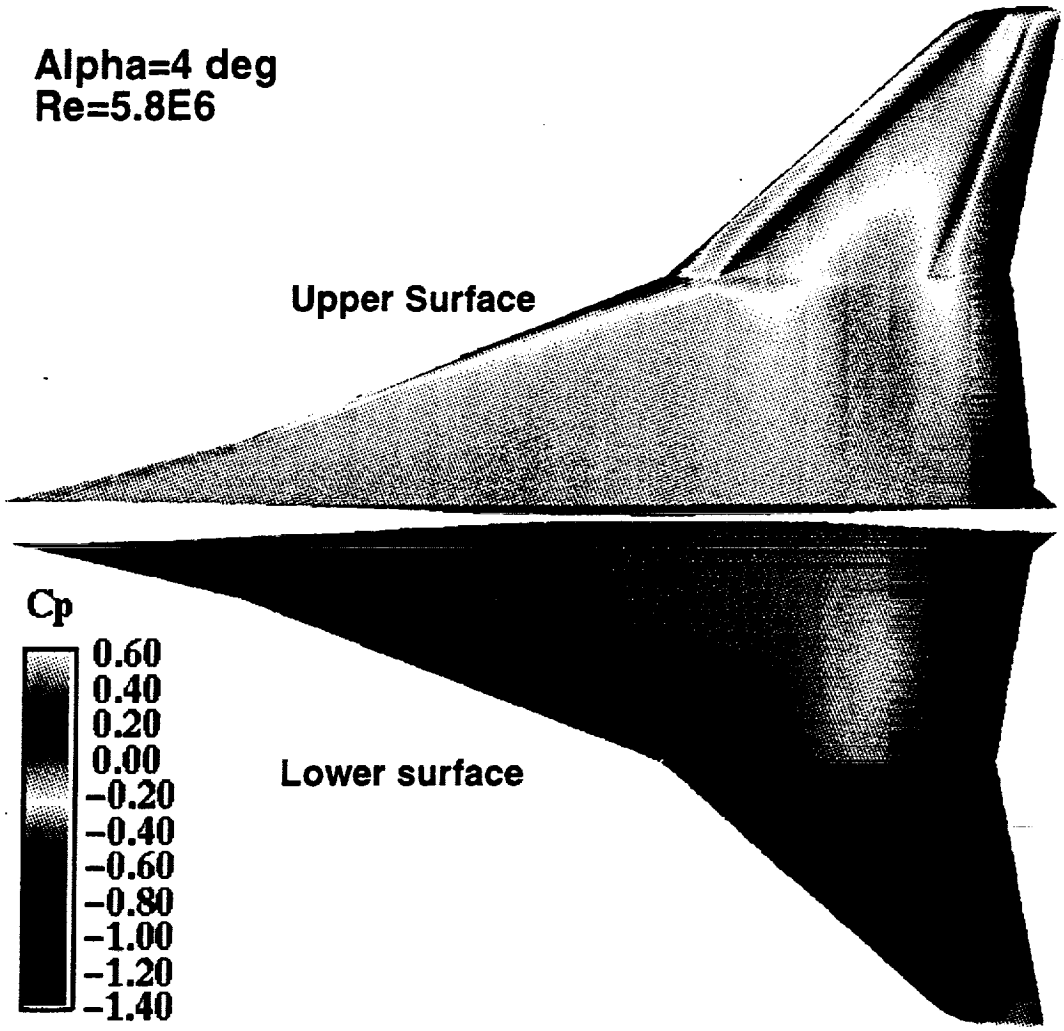

The next several figures illustrate the flap deflection effect on the aerodynamic performance of the wing/body configuration with the 10/3 deg flaps at M=0.9 and Re=5.8E6 along with comparisons with the LaRC-16 ft tunnel data. The tunnel dynamic pressure is q=700 psf at M=0.9. The baseline CFD solutions were obtained from Steve Chaney of Boeing. Paul Vijgen of Boeing provided the wind tunnel data.

This figure depicts the surface pressure coefficient for alpha=4 deg. At alpha=4 deg, the attachment line is on the lower surface of the outboard wing, and a vortex separation of small extent is noted on the upper surface leading edge. A discrete pocket of high pressure region is noted in the mid-chord region near the wing tip. The leading edge vortex on the inboard wing upper surface is wider and more clearly visible compared to that for alpha=2 deg. The surface pressure coefficient distribution on the wing lower surface is seen to be more uniform.

Ref. H Transonic Flaps (10/3 deg); M=0.9
Surface Streamlines (OVERFLOW)

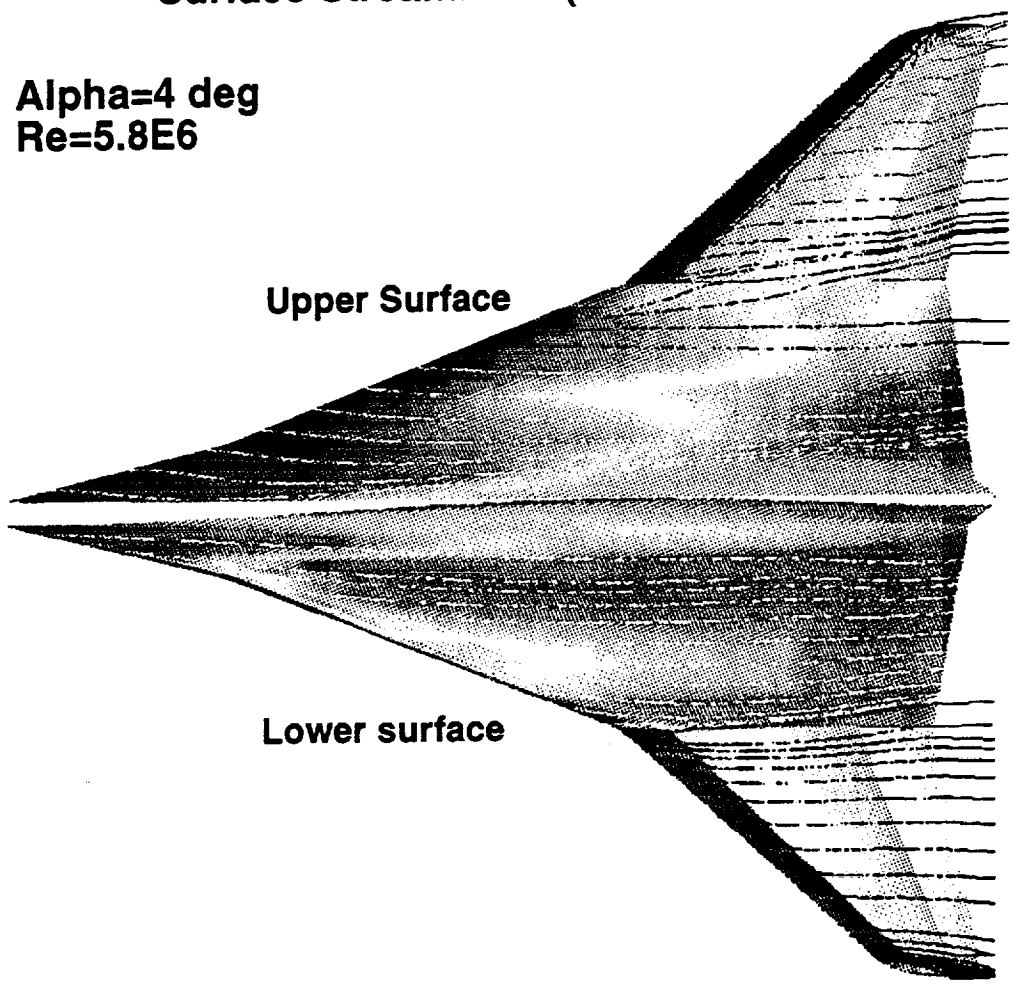

A separation region is noted downstream of the upper surface hinge line. In the case of alpha=4 deg, the chordwise extent of separation is larger than that at alpha=2 deg. The reattachment line near the upper surface leading edge is evident. Spanwise flow on the outboard wing upper surface is beginning to appear.

Ref H Transonic Flaps (10/3 deg); M=0.9
Surface Streamlines (OVERFLOW)

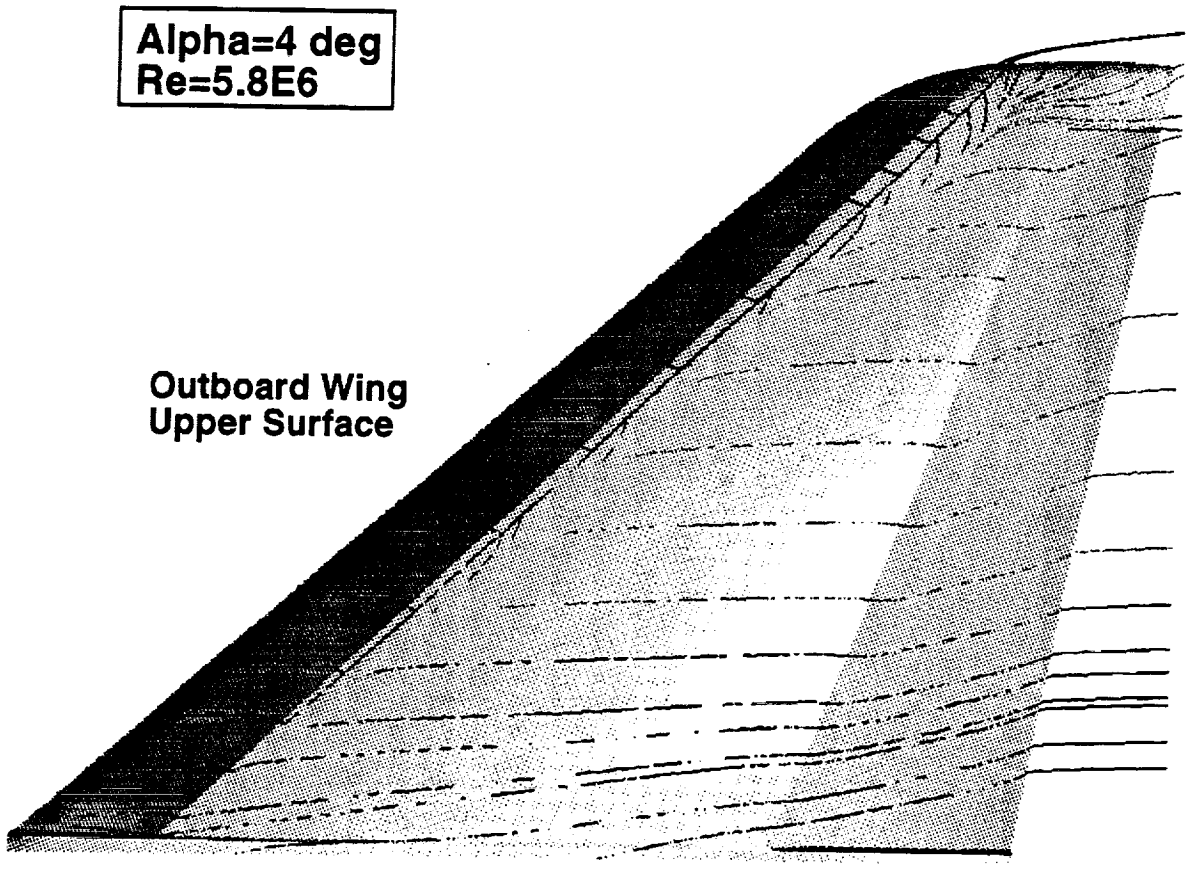

--- see previous page text---

Ref. H Transonic Flaps (10/3 deg); M=0.9
Surface Streamlines (OVERFLOW)

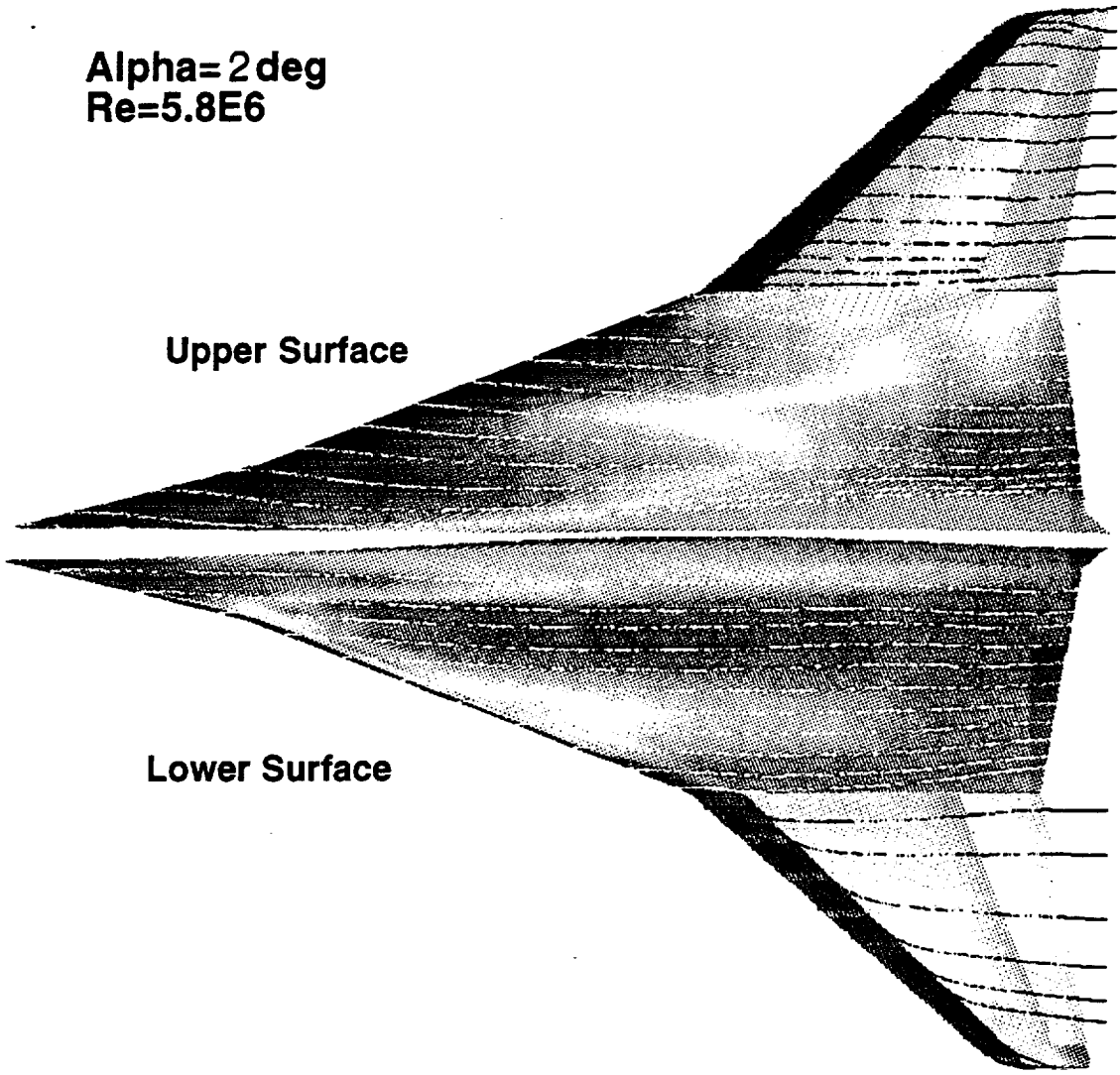

Displayed in this figure are the surface streamlines at alpha=2 deg and Re=5.8E6. The flow is attached near the leading edge, and a significant leading edge vortex separation is noted on the lower surface of the leading edge flap. A small extent of separation is noted downstream of the upper surface hinge line along the whole span of the outboard wing. The flow is primarily streamwise.

Ref. H Transonic Flaps (10/3 deg); M=0.9
Surface Streamlines (OVERFLOW)

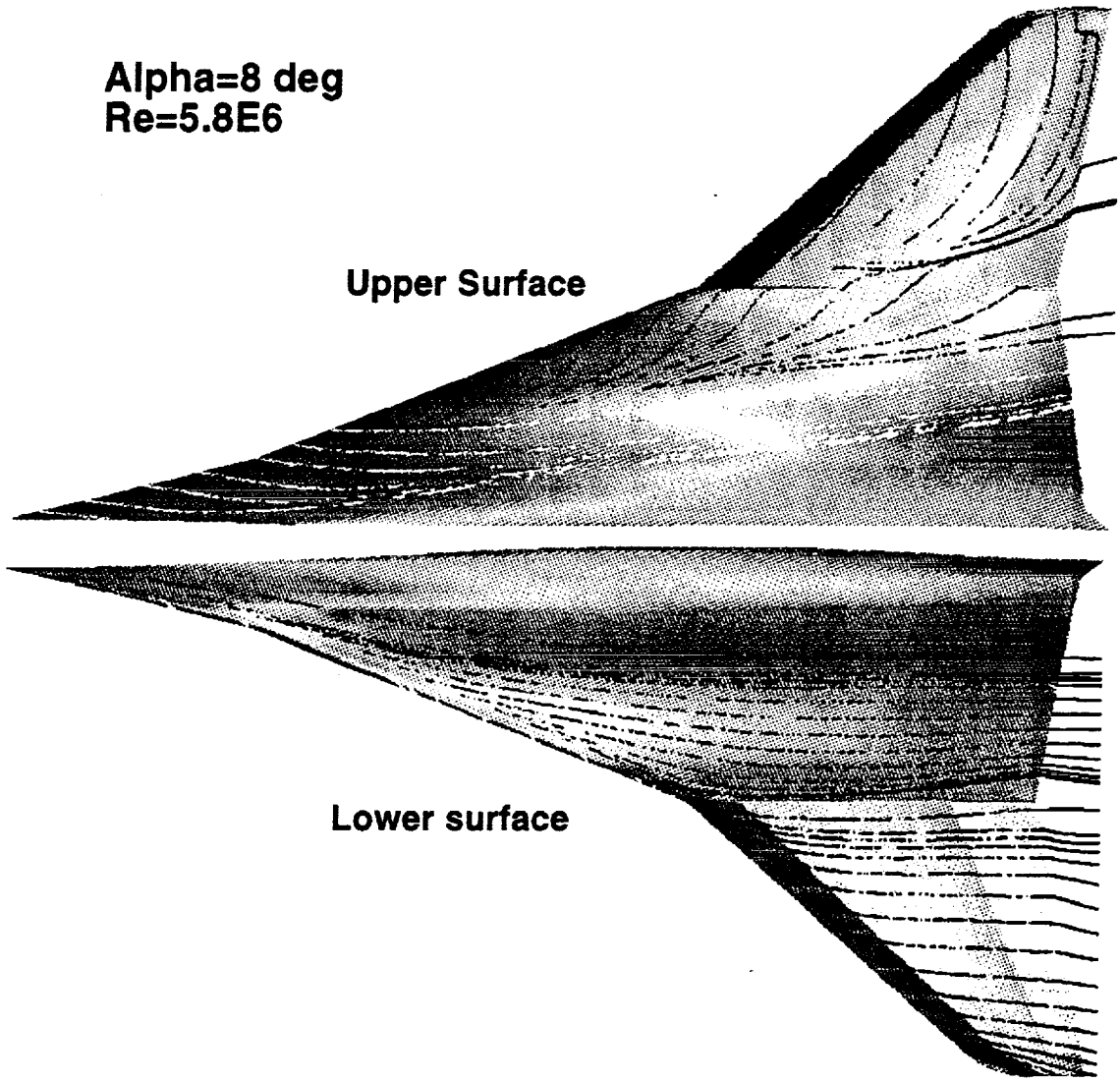

At alpha=8 deg, vortex separation is noted on the leading edge flap along with significant spanwise flow.

Ref. H Transonic Flaps (10/3 deg); M=0.9, Alpha=4 deg Streamlines (OVERFLOW)

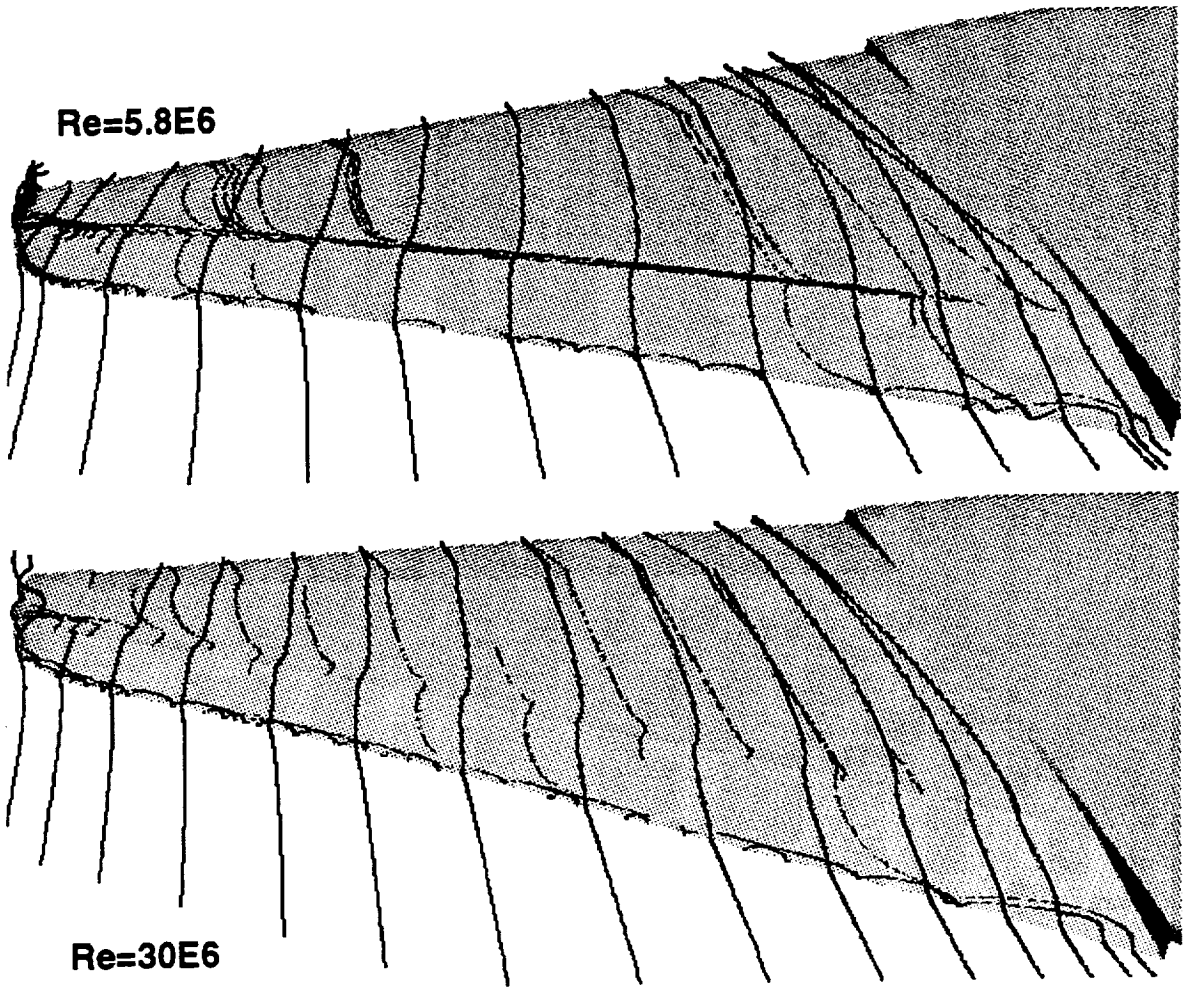

This figure displays a comparison of the streamlines on the outboard wing upper surface for the 10/3 deg flaps at alpha=4 deg for Re=5.8E6 and 30E6. In both the cases, the flow is primarily streamwise, and a small leading edge vortex region is observed. While a narrow region of separation downstream of the leading edge flap hinge line is noted at Re=5.8E6, no hinge line separation is observed at Re=30E6.

Ref. H Transonic Flaps (10/3 deg LE/TE); M=0.9, Alpha=4 deg

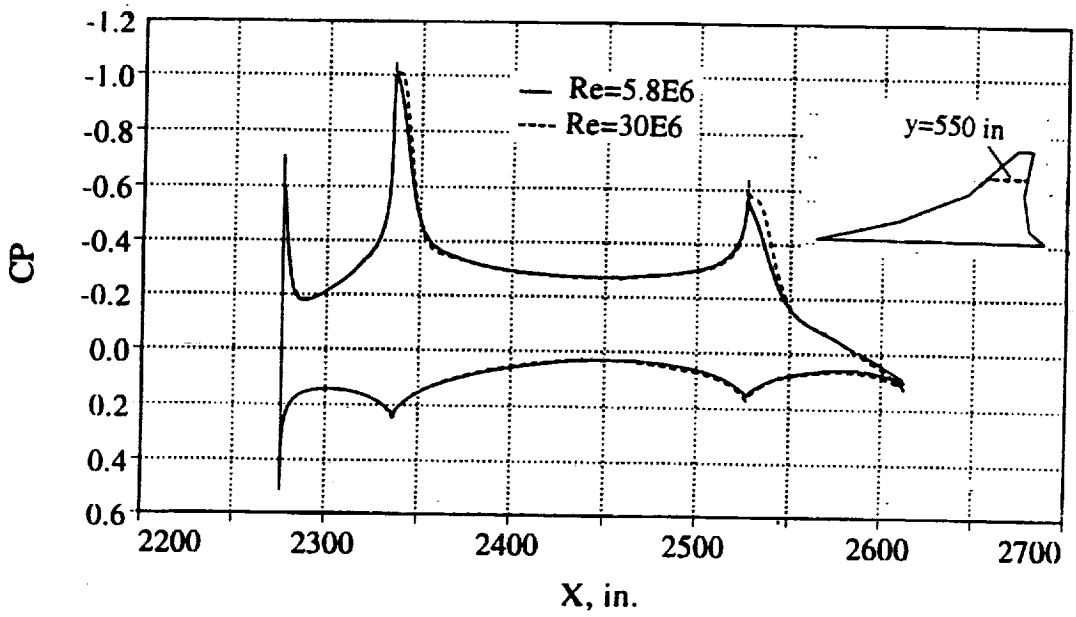

This figure shows the effect of Reynolds number on the chordwise CP distribution at alpha=4 deg. Reynolds number effects are confined locally to regions downstream of the hinge lines on the wing upper surface.

In the calculations, the flow over the entire wing surface is considered turbulent, and Baldwin-Barth one equation turbulence model is employed. The LaRC-16T model (1.675% scale, Re=5.8E6) is tripped, while the NTF model (2.2% scale, Re=30E6) is untripped. Referring to the computed surface streamlines and drag polars for Re=5.8E6 and 30E6, we find that for the 10/3 deg flaps at alpha=4 deg (close to the design CL of 0.25 at M=0.9) OVERFLOW shows hinge line separation and an overprediction of drag by about 4 counts Re=5.8E6, while at Re=30E6 it shows no hinge line separation (except near the tip region) and an underprediction of drag by about 5 counts. The existence of hinge line separation at Re=5.8E6 and the absence of hinge line separation at Re=30E6 as indicated by OVERFLOW is seen to signify the effect of Reynolds number on the computed flowfield. Reynolds number effects on the chordwise CP distribution are manifest at all angles of attack considered. While Reynolds number effects are confined locally to regions downstream of the hinge lines on the wing upper surface, global effects of Reynolds number are observed at alpha=2 deg and 8 deg.

Ref. H Transonic Flaps (10/3 deg LE/TE); M=0.9, Alpha=2 deg

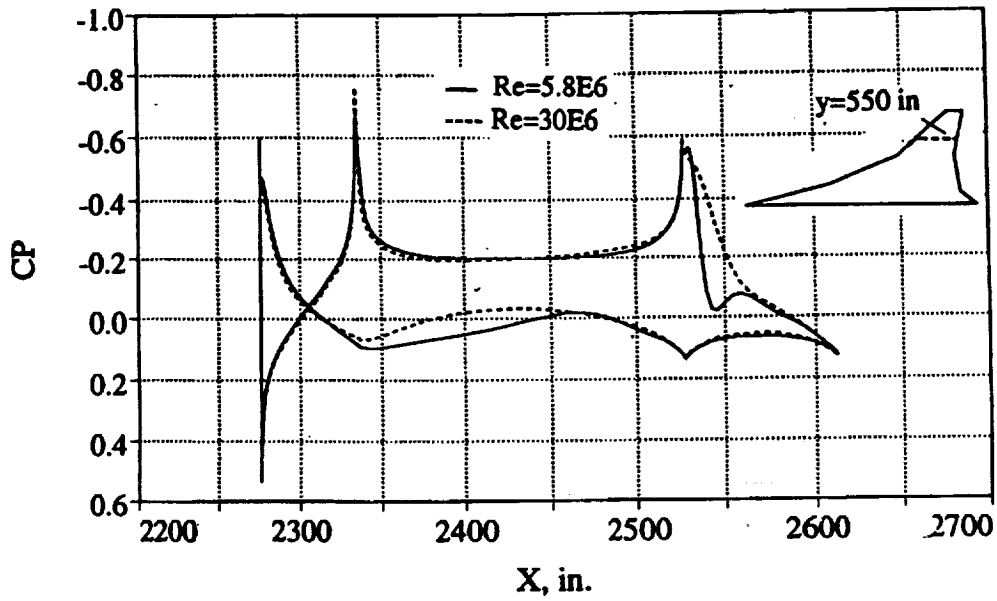

---see previous page text---

Ref. H Transonic Flaps (10/3 deg LE/TE); M=0.9, Alpha=8 deg

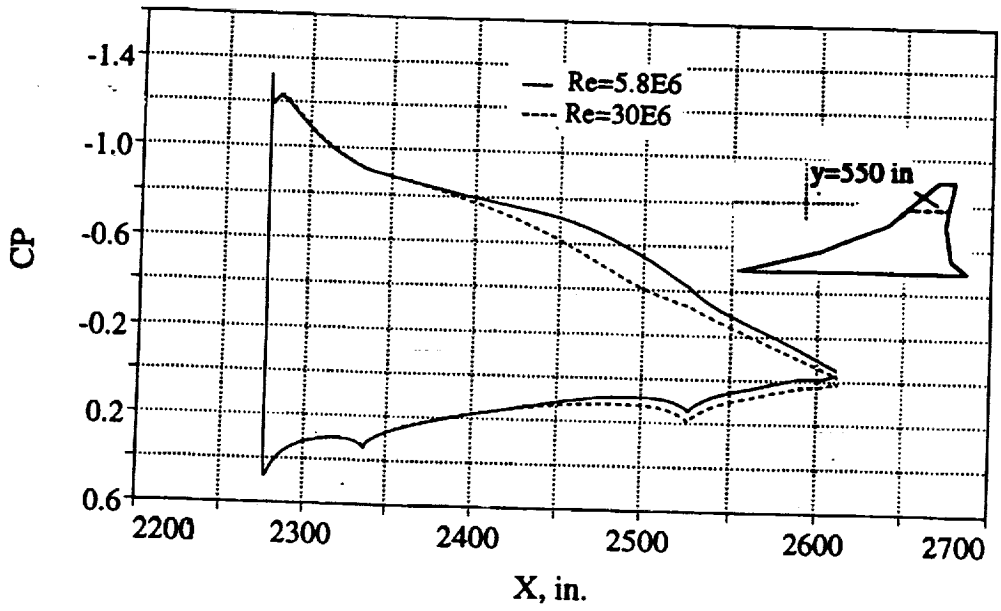

---see previous page text---

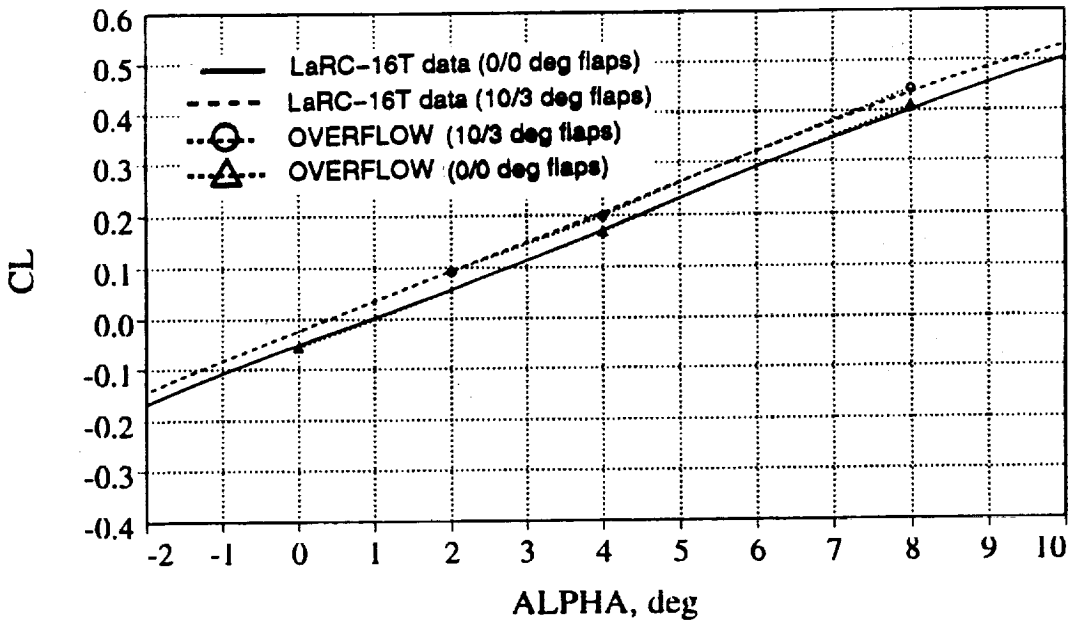

This figure demonstrates the flap effects on CL-alpha curve at Re=5.8E6. The flap increments in CL predicted by OVERFLOW are seen to be close to those indicated by the wind tunnel data in the range of alpha=0 to 8 deg. The incremental CL due to the 10/3 deg flaps relative to the baseline flaps-up case is seen to be nearly uniform in the range of alpha from 2 to 8 deg. Beyond about alpha=8 deg, the flap effect on CL tends to decline, which is perhaps due to significant leading edge vortex separation that results in a diminished effect of camber on CL.

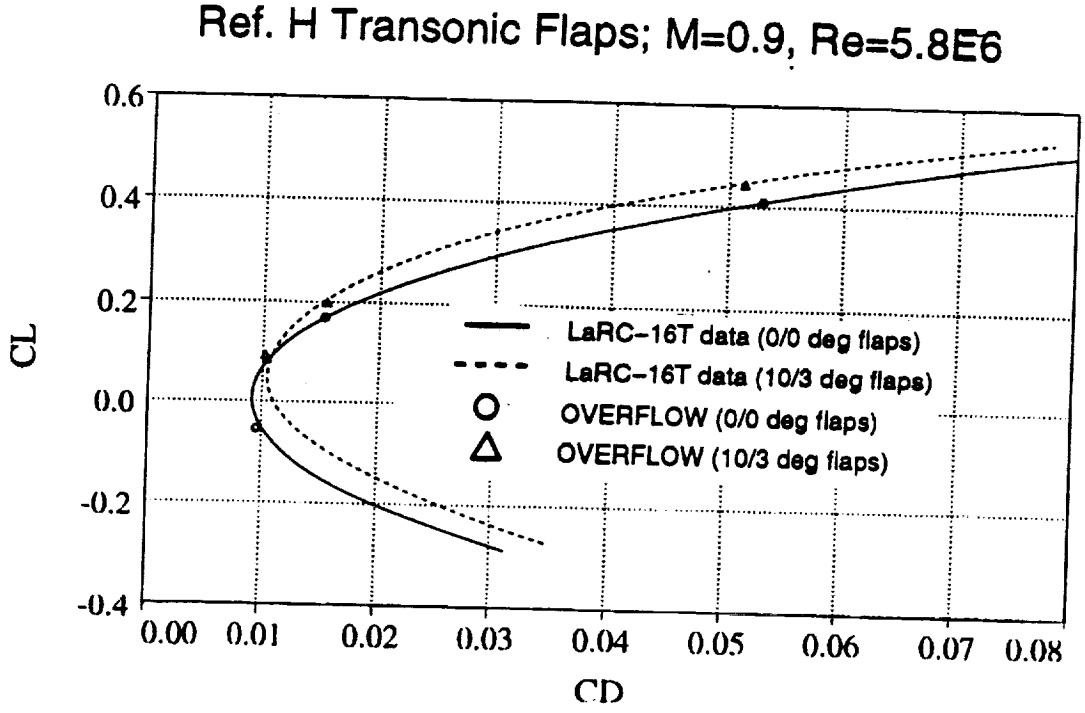

The flap effect on the drag polar at Re=5.8E6 is presented in the next two figures. The value of CD_{min} for the 10/3 deg flaps is higher than that for the flaps-up case due to camber drag, and occurs at CL≈0.05 while the CD_{min} for the flaps-up case is seen at CL≈0. The cross-over of the two polars due to the polar shift is observed at CL≈0.1, beyond which the 10/3 deg flap results in a reduced drag relative to the baseline case at constant CL.The CFD solutions show good correlation with the measured polars for both the flaps-up (0/0 deg) and flaps-down (10/3 deg) cases except at alpha=0 and 2 deg. At low alpha the drag is underpredicted for both the flaps-up and the flaps-down cases. This inaccuracy is perhaps related to the occurrence of leading vortex separation on the wing lower surface at low alpha, for which the 1-equation Baldwin-Barth turbulence model may be inaccurate.

The viscous drag is found to be relatively insensitive to changes in alpha over the range considered.

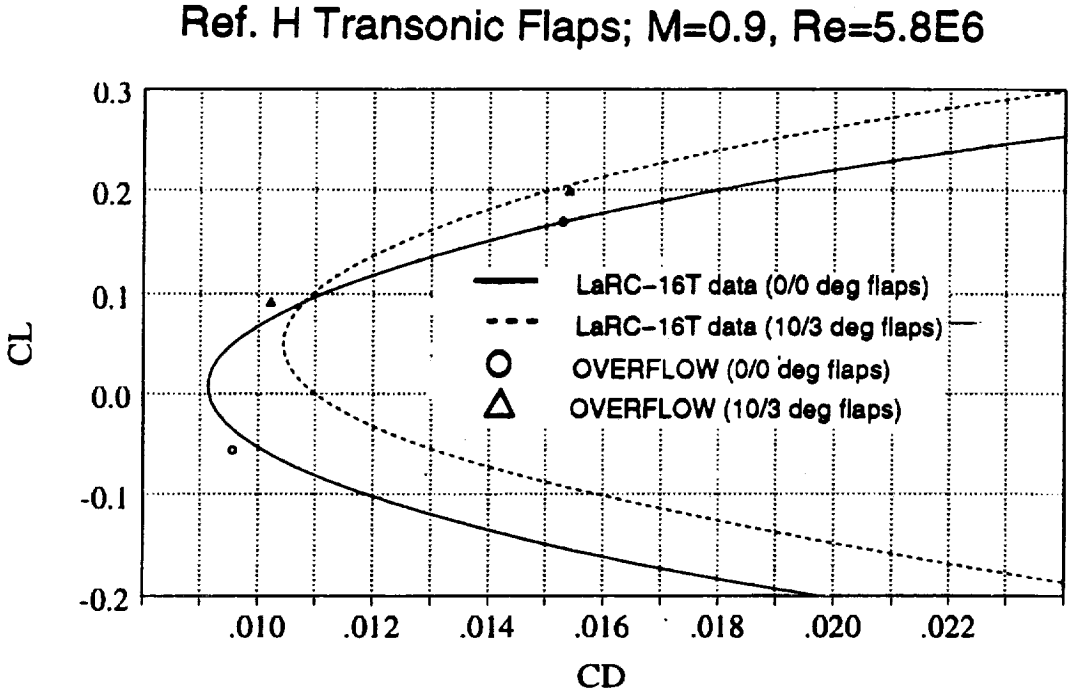

For the 10/3 deg LE/TE flap at M=0.9 at alpha=4 deg and Re=5.8E6, the CFD solution underpredicts the drag by about four counts. At the transonic design CL=0.2, the data show a drag reduction of 29 counts (19% improvement in L/D) at M=0.9 with the 10/3 deg LE/TE flap.

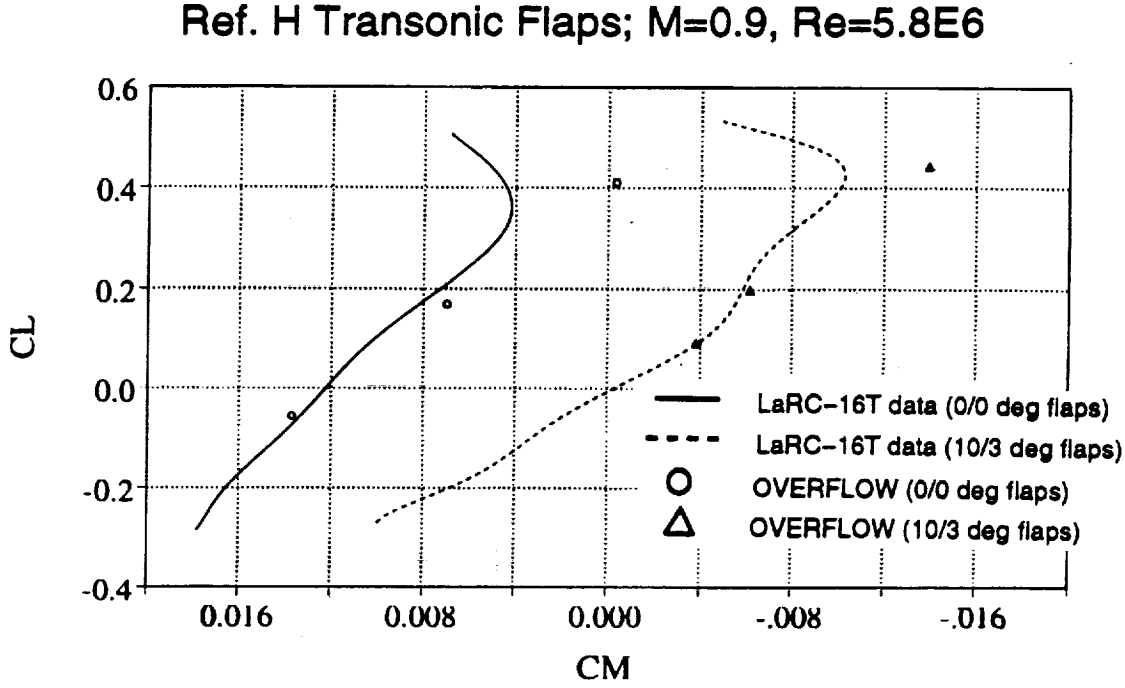

A comparison of the flap effect on the CL-CM variation at Re=5.8E6 is reported in this plot. The agreement between the CFD result and the data is good, except at alpha=8 deg where we find appreciable deviation for both the flaps-up and the flaps-down cases. At alpha=8 deg, OVERFLOW predicts more nose-down pitching moment than the data indicate. The departure between the CFD and the data for CM at alpha=8 deg is perhaps due to the large scale vortex separation and spanwise flow on the outboard wing upper surface, for which the Baldwin-Barth one-equation turbulence model may be in error.

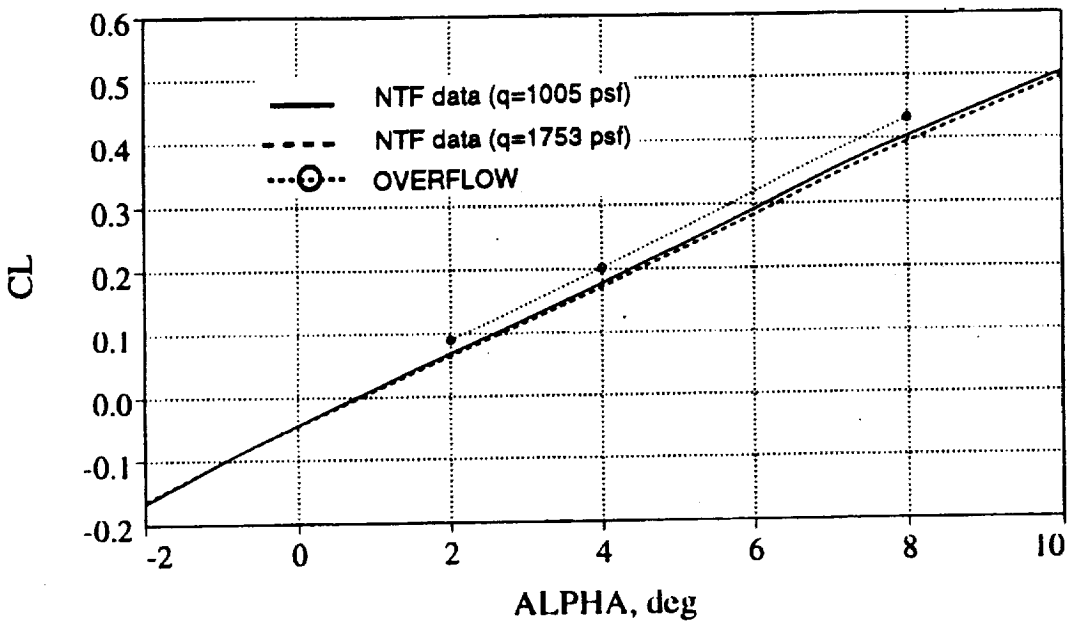

The next several figures show a comparison of the CFD solution with the NTF data at M=0.9 at a Reynolds number Re=30E6 (q=1005 psf and 1753 psf). The results for Re=30E6 are obtained based on a restart from the solution for Re=5.8E6, rather than starting from a freestream initial condition. The force coefficients and drag polars will be compared to the NTF data at Re=30E6 at two dynamic pressures q=1005 psf and 1753 psf to assess aeroelastic effects.

This figure shows the CL-alpha variation at Re=30E6. The CFD solution shows values of CL higher than the data. If a linear aeroelastic correction is applied (extrapolated to q=0 psf), the agreement would be closer.

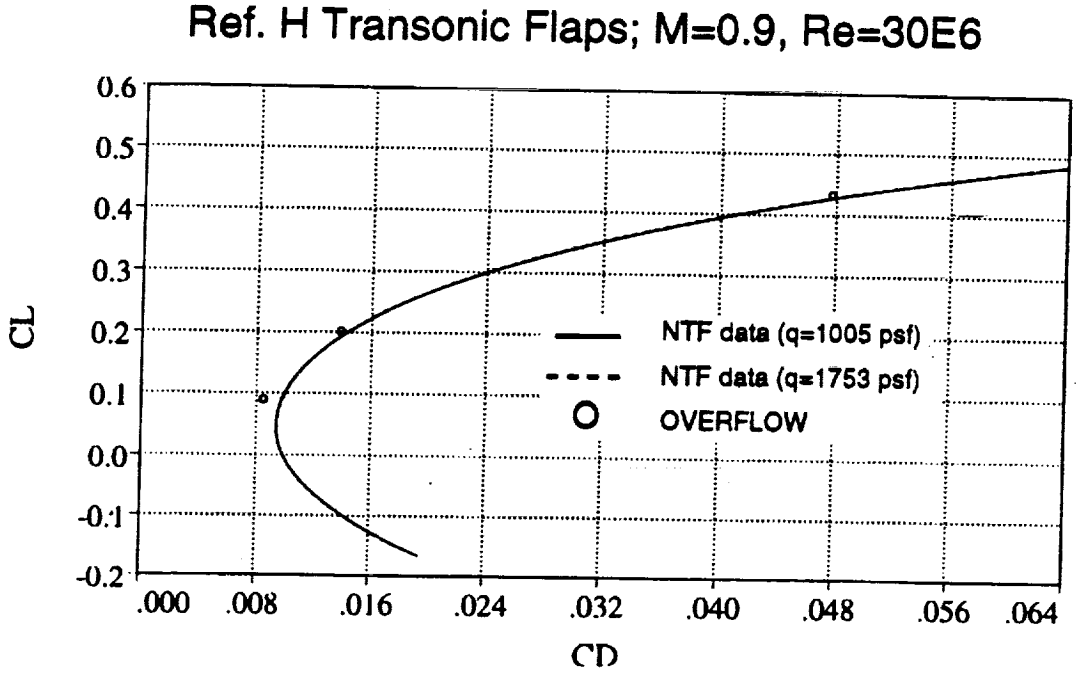

The next two figures display a comparison of the measured drag polar with the CFD result at Re=30E6. The measured aeroelastic effect on the drag polar is seen to be small. This is due to a situation where both CL and CD are changed due to aeroelastic effect in such a way (an increase in CL and a decrease in CD) that the polar shape is relatively less effected. The correlation at higher angles of attack (alpha=4 and 8 deg) is seen to be better relative to that at alpha=2 deg, where the drag is off by about 12 counts. This underprediction of drag is similar to that noted at Re=5.8E6.

The pressure drag is found to be relatively independent of Reynolds number (Re=5.8E6 and Re=30E6) except at low alpha (alpha=2 deg).

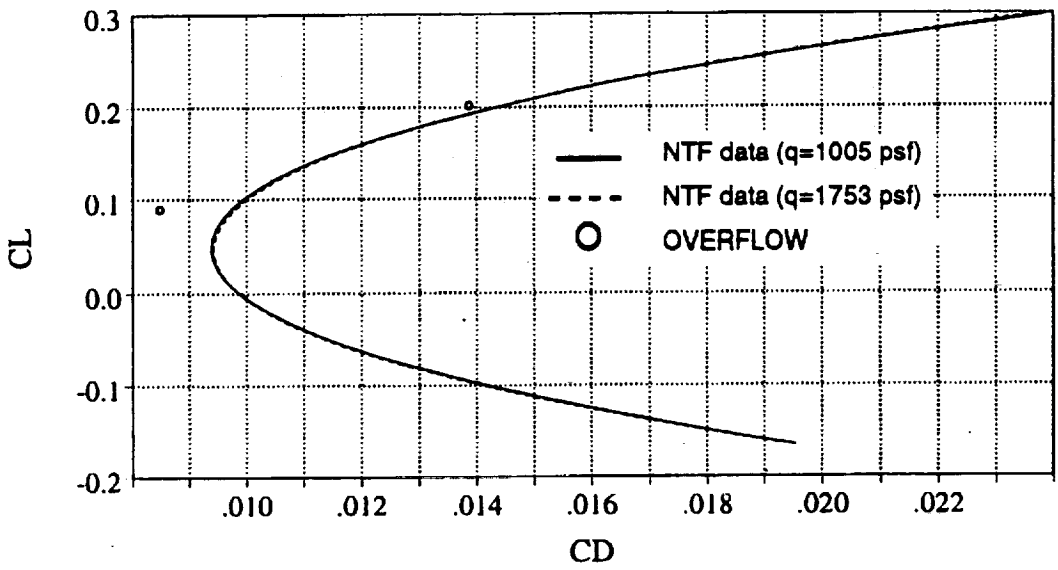

--- see previous page text---

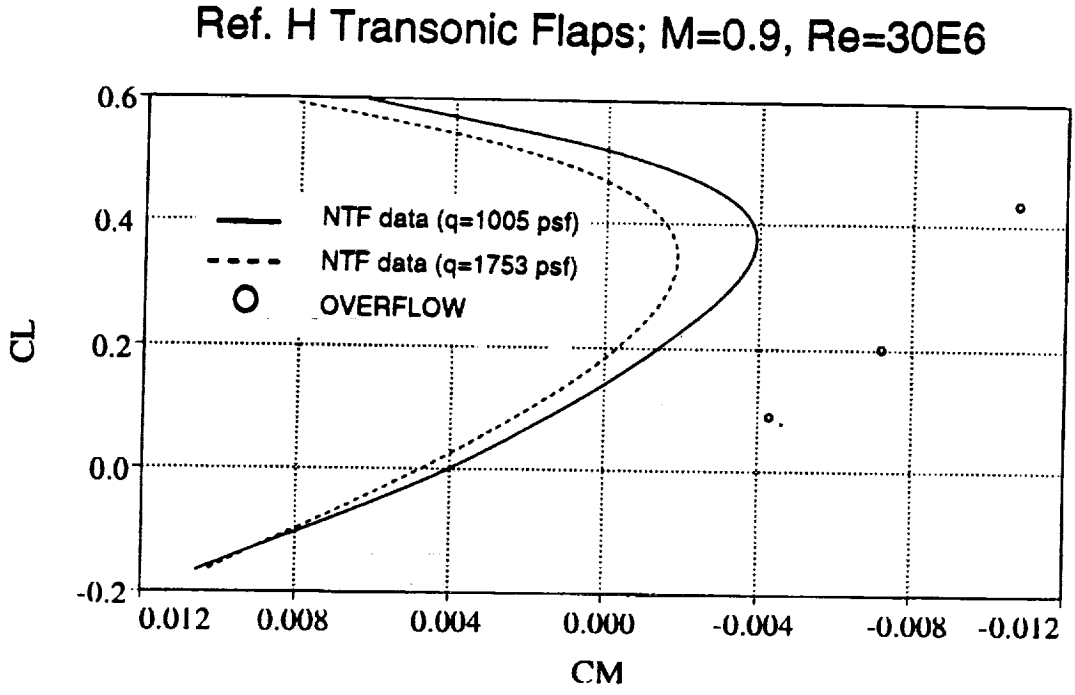

The pitching moment comparison at Re=30E6 shown in this figure suggests that the CFD values deviate considerably from the data, although the trends are similar. The agreement would be closer if aeroelastic corrections were taken into account. The deviation is pronounced at alpha=8 deg. Leading edge vortex and predominant spanwise flow on the upper surface are noted at alpha=8 deg.

Ref. H Transonic Flaps (10/3 deg LE/TE); M=0.9, Re=30E6 & Euler

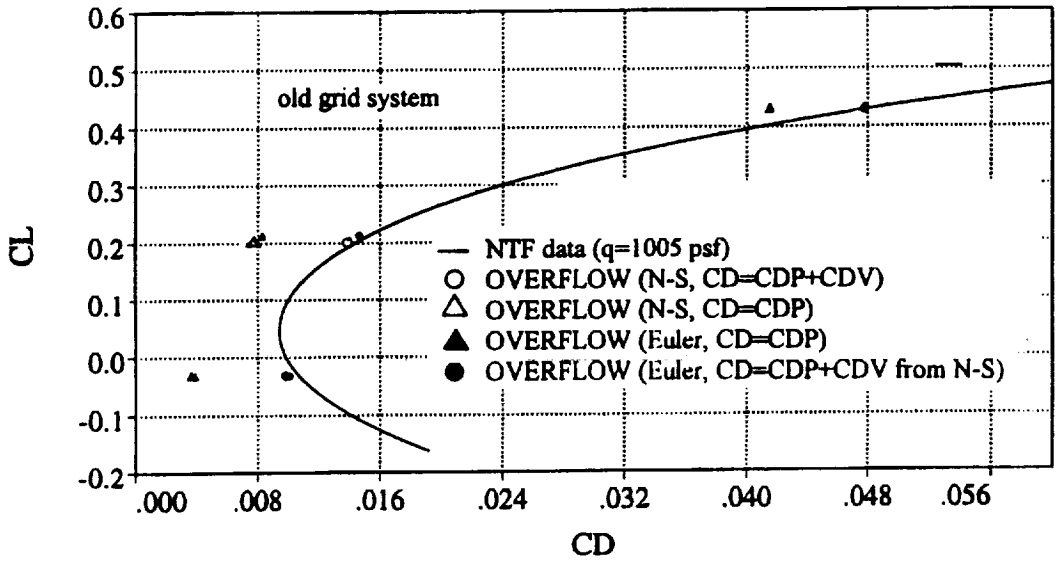

A comparison of Euler solution with the Navier-Stokes solution (Re=30E6) for the drag polar of the 10/3 deg flaps configuration based on the old grid system (with some geometric mismatch) is demonstrated in this figure. The results show that CL and the pressure drag CD from the Euler solution are close to those given by the Navier-Stokes solution. This suggests the acceptability of Euler solutions in predicting the lift and the pressure drag in the range of alpha considered.

Ref. H Transonic Flaps (10/0 deg); M=1.2
Surface Pressure Coefficient (OVERFLOW)

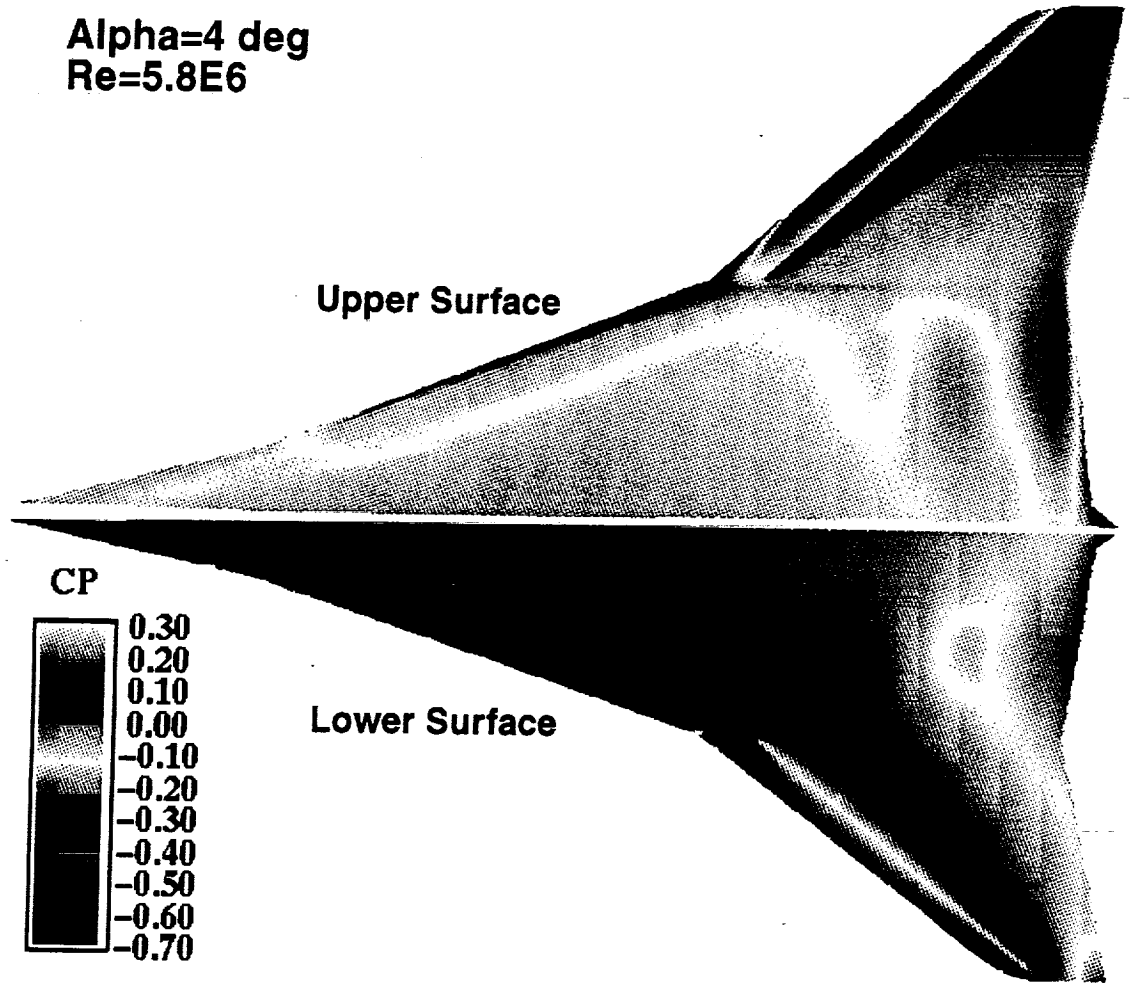

OVERFLOW CFD solutions are generated for transonic flaps at M=1.2 for alpha=0, 4, 5 and 8 deg for the 10/0 deg and 8/0 deg flaps at a Reynolds number of 5.8E6. The CFD results for the flaps up case were generated by Steve Chaney of Boeing. Paul Vijgen of Boeing provided the wind tunnel data. Oil flow visualization data are available at alpha=4.6 deg corresponding to design CL of 0.2 at M=1.2.

The next several figures show the effects of flap delection at M=1.2 and Re=5.8E6, indicating the results for the 10/0 deg and the 8/0 deg flaps. This figure presents the surface CP for the 10/0 deg flap configuration at alpha=4 deg. The attachment line is on the upper surface of the leading edge. A comparison of this result with the CP distribution for the 10/3 deg flap (M=0.9, alpha=4 deg, Re=5.8E6) provides the following. On the inboard wing upper surface, a leading edge vortex is observed as in the case of 10/3 deg flaps at M=0.9. Downstream of the leading edge hinge line on the upper surface of the outboard wing, there is seen a conical band of gradual compression, with its vertex emanating from the inboard end of the hinge line

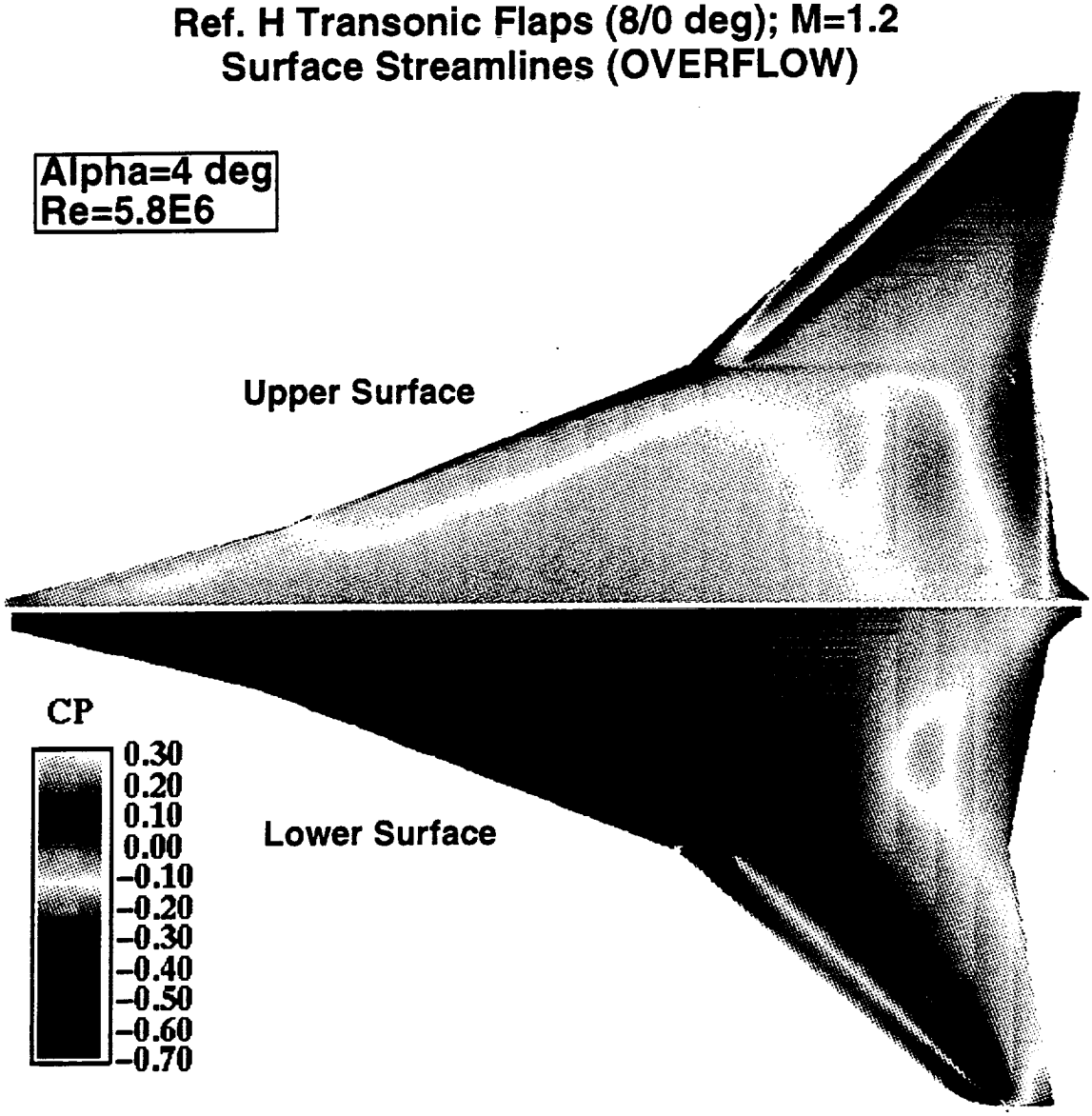

This figure presents the surface CP for the 8/0 deg flap configuration at alpha=4 deg and Re=5.8E6. The attachment line is at the leading edge.

Ref. H Transonic Flaps (10/0 deg); M=1.2
Surface Streamlines (OVERFLOW)

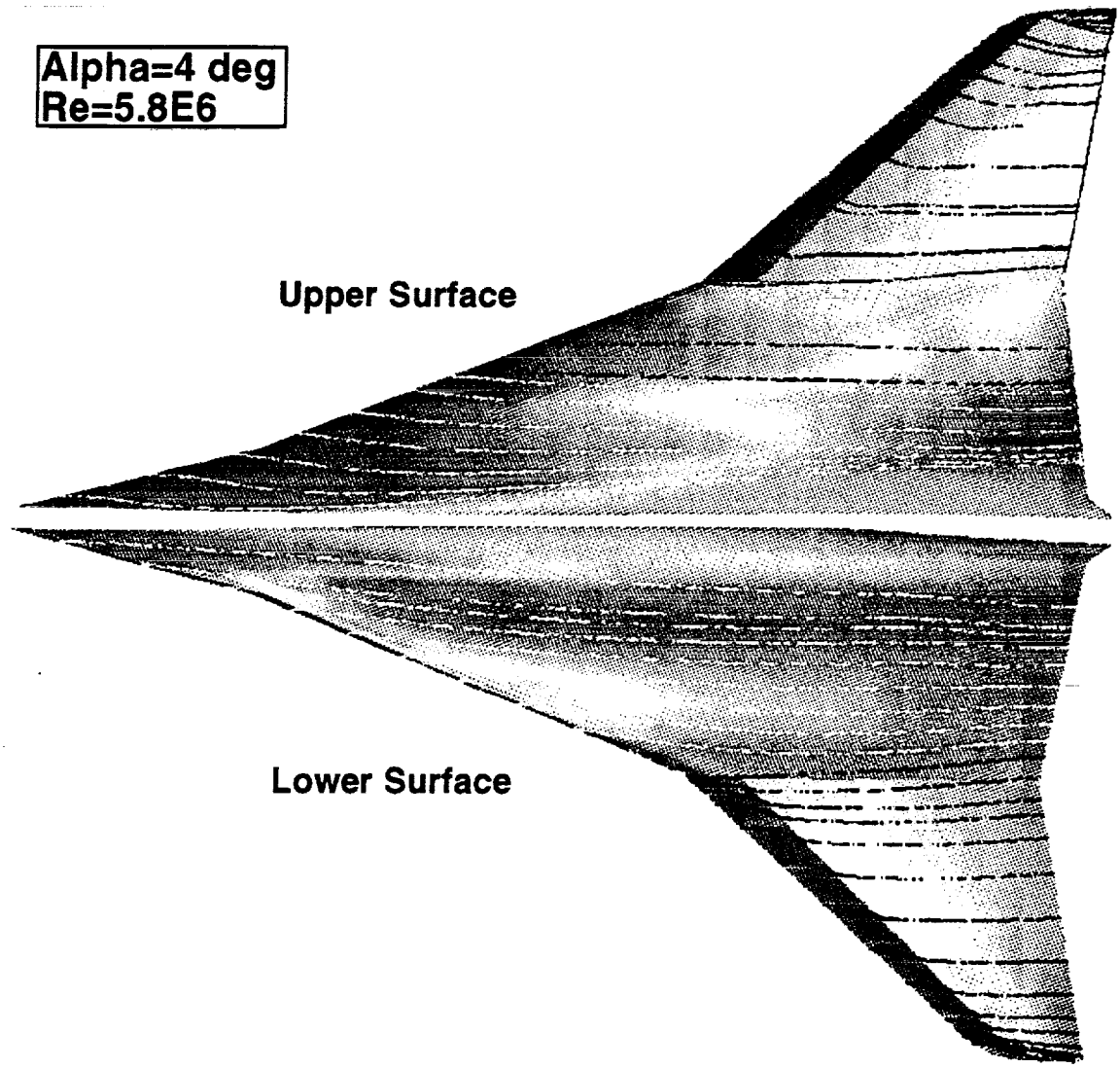

This figure presents the surface streamline for the 10/0 deg flap configuration at alpha=4 deg. On the inboard wing , a vortex originates near the leading edge. There appears to be no flow separation except near the trailing edge. These results are in accord with wind tunnel oil flow visualization taken at alpha=4.6 deg. The flow is primarily streamwise.

Ref. H Transonic Flaps (8/0 deg); M=1.2
Surface Streamlines (OVERFLOW)

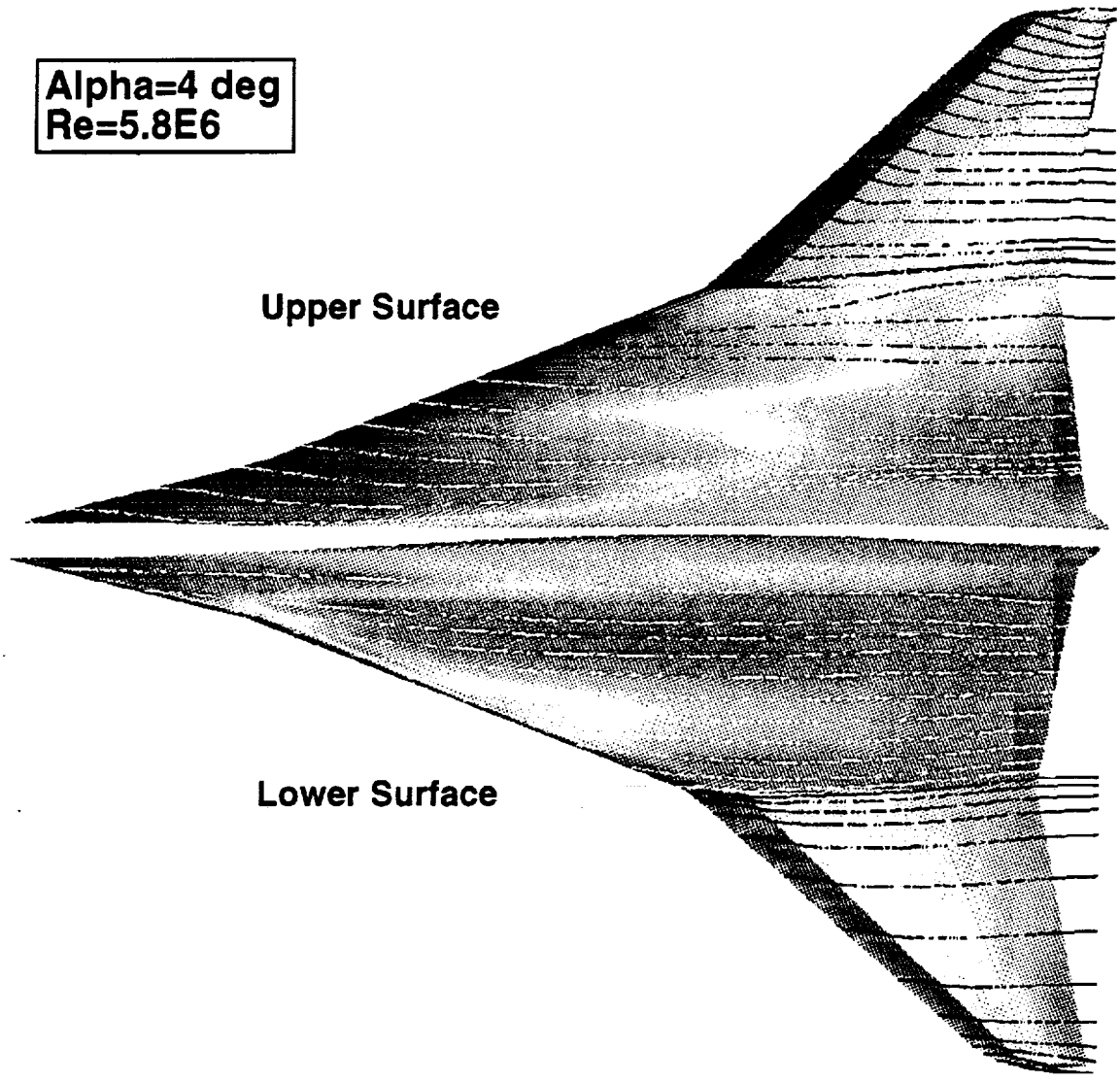

This figure presents the surface streamline for the 10/0 deg flap configuration at alpha=4 deg. On the inboard wing , a vortex originates near the leading edge. There appears to be no flow separation except near the trailing edge. These results are in accord with wind tunnel oil flow visualization taken at alpha=4.6 deg. The flow is primarily streamwise.

Ref H Transonic Flaps (8/0 deg); M=1.2
Surface Streamlines (OVERFLOW)

Alpha=4 deg
Re=5.8E6

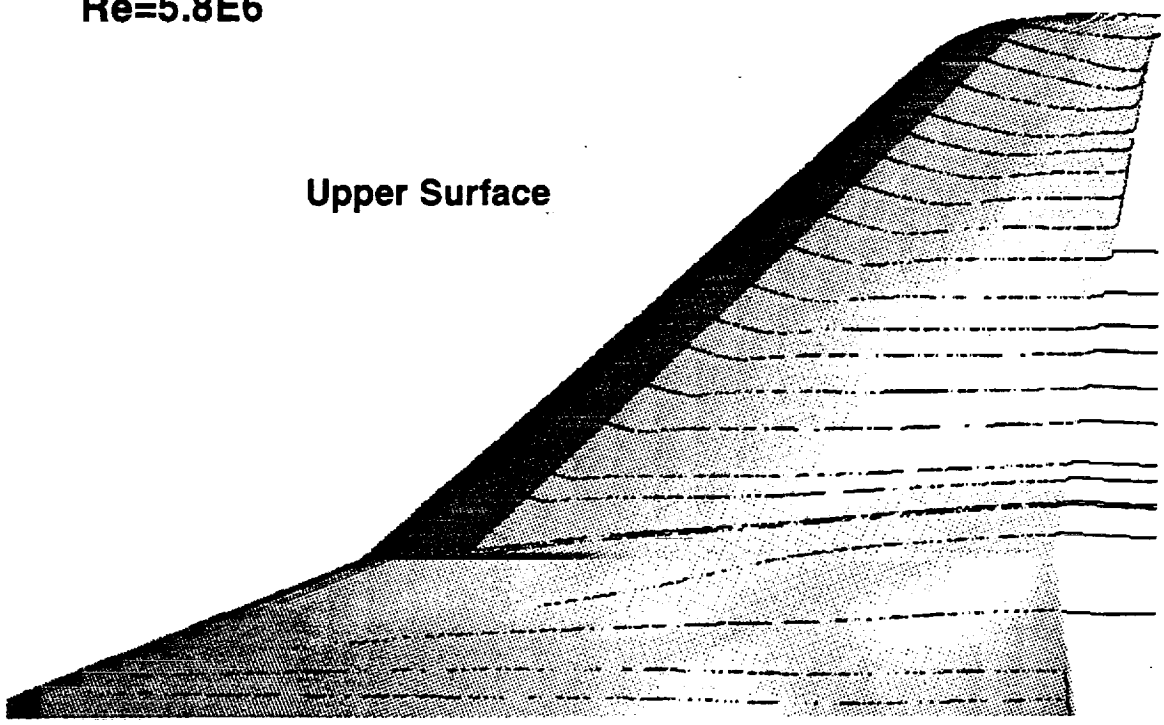

--- see previous page text---

Ref.H Transonic Flaps (8/0 deg); M=1.2
Upper-Surface Streamlines (16-Ft Tunnel Oil-Flow)

Alpha~4 deg
Re~5.8E6

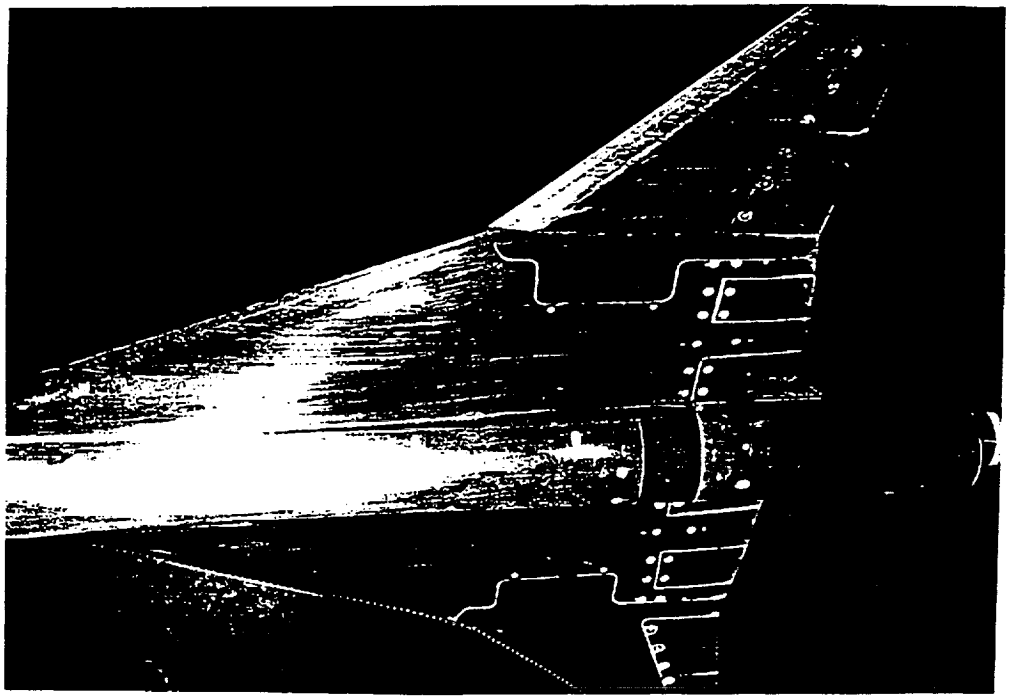

Oil-dot flow visualization for the 8°/0° flap configuration is shown at alpha about 4°. Oil dots were applied ahead of the transition trip dots on the inboard wing. Absence of oil streaklines in the mid section of the onboard wing indicates the presence of a leading-edge vortex in this region. No leading-edge flap hinge-line separation is observed.

Ref. H Transonic Flaps; M=1.2, Alpha=4 deg, Re=5.8E6

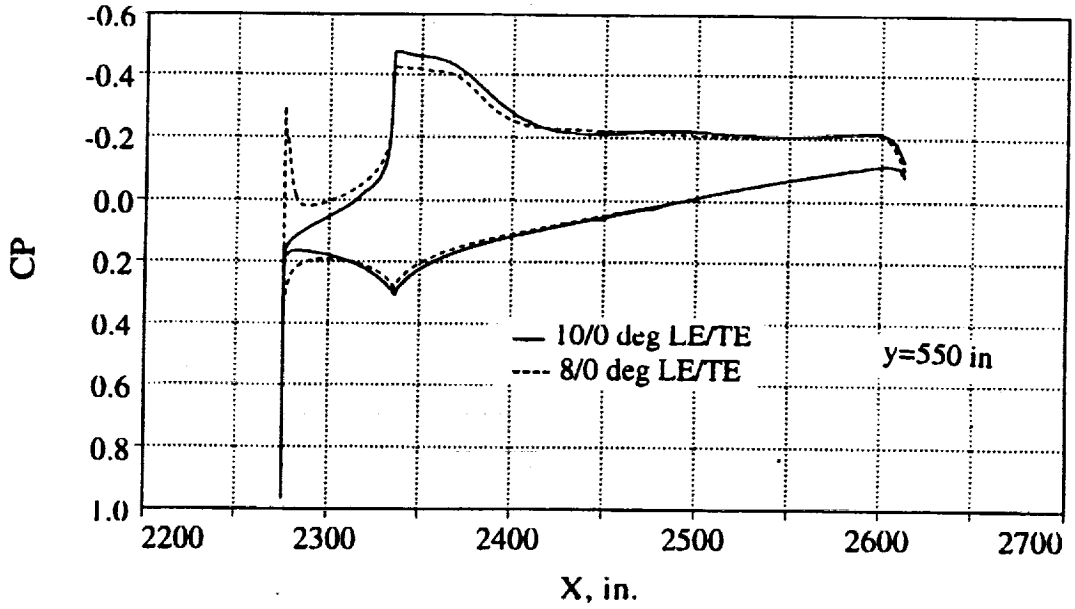

This figure displays a comparison of the chordwise CP distributions for the 10/0 deg and the 8/0 deg flaps at y=550 in for alpha= 4 deg. For alpha=4 deg, the attachment line is on the upper surface for the 10/0 deg flap, and is at the leading edge for the 8/0 deg flap case. This notable difference in CP distribution near the leading edge of the 10/0 deg and the 8/0 deg flaps at alpha=4 deg explains the main difference in performance of the the two flap configurations. The results show that the main difference in CP for the two flap configurations occurs on the upper surface.

Ref. H Transonic Flaps (10/0 deg); M=1.2
Surface Streamlines (OVERFLOW)

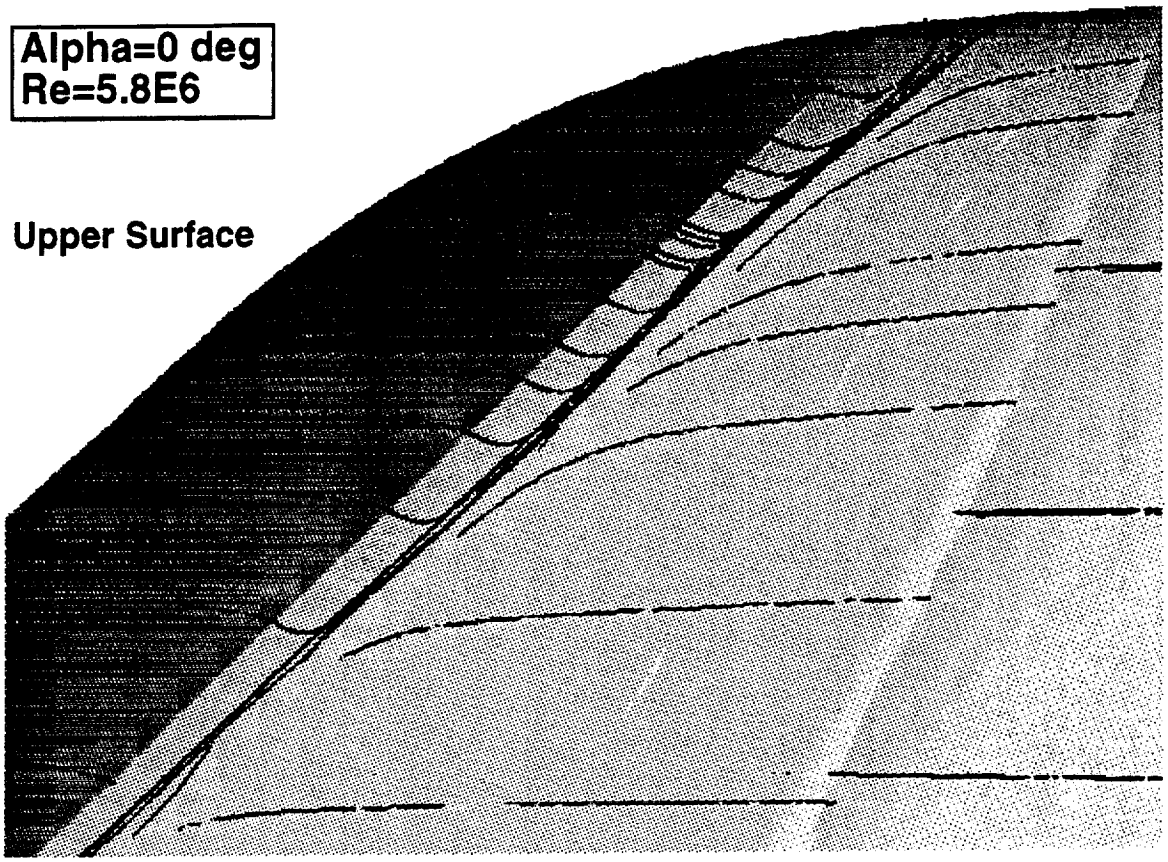

The surface streamlines for the 10/0 deg flap configuration at alpha=0 deg are sketched in this plot. For the 10/0 deg flap at alpha=0 deg, a boundary layer separation is indicated on the upper surface downstream of the hinge line of the leading edge flap. Similar streamline distributions are seen for the 8/0 deg flaps at alpha=0 deg.

Ref. H Transonic Flaps (8/0 deg); M=1.2
Surface Streamlines (OVERFLOW)

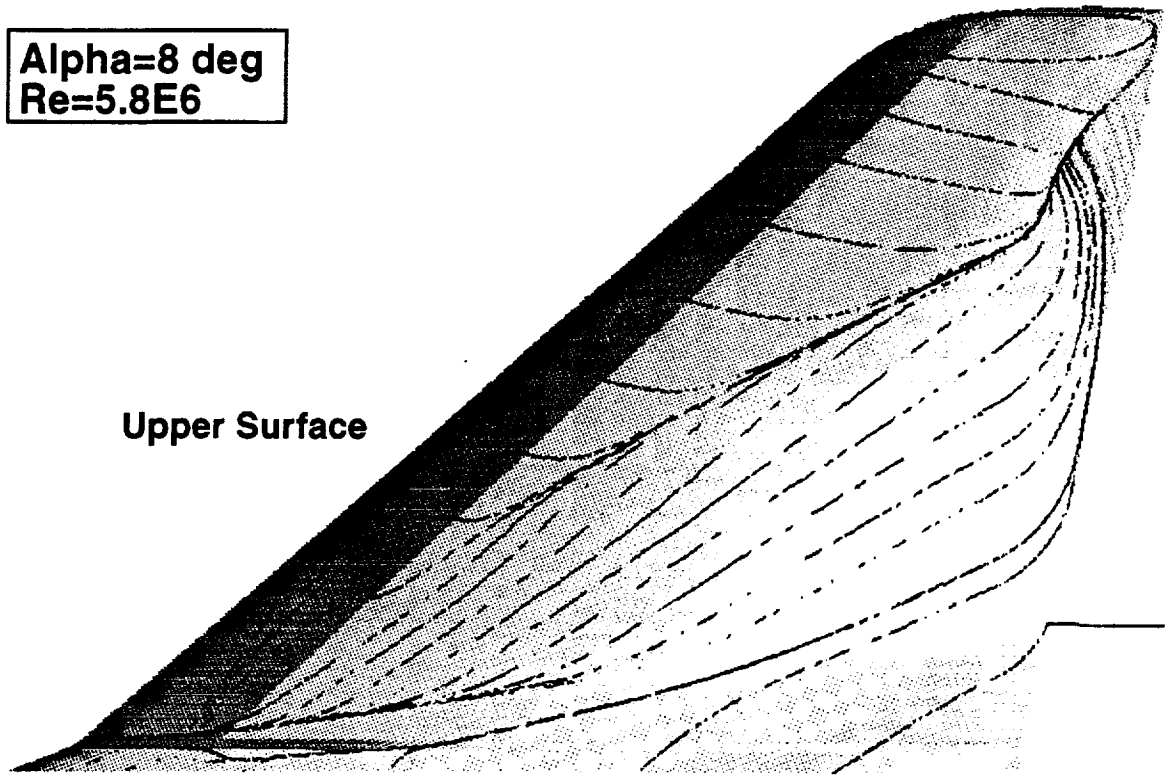

This figure presents the surface streamlines for the 10/0 deg flap configuration at alpha=8 deg. Here we note leading edge vortex separation and a trailing edge separation on the upper surface of the outboard wing. Similar streamline pattern is observed for the 10/0 deg flap at alpha=8 deg. The streamline patteren at M=1.2 is different from that for the 10/3 deg flap at M=0.9 and alpha=8 deg.

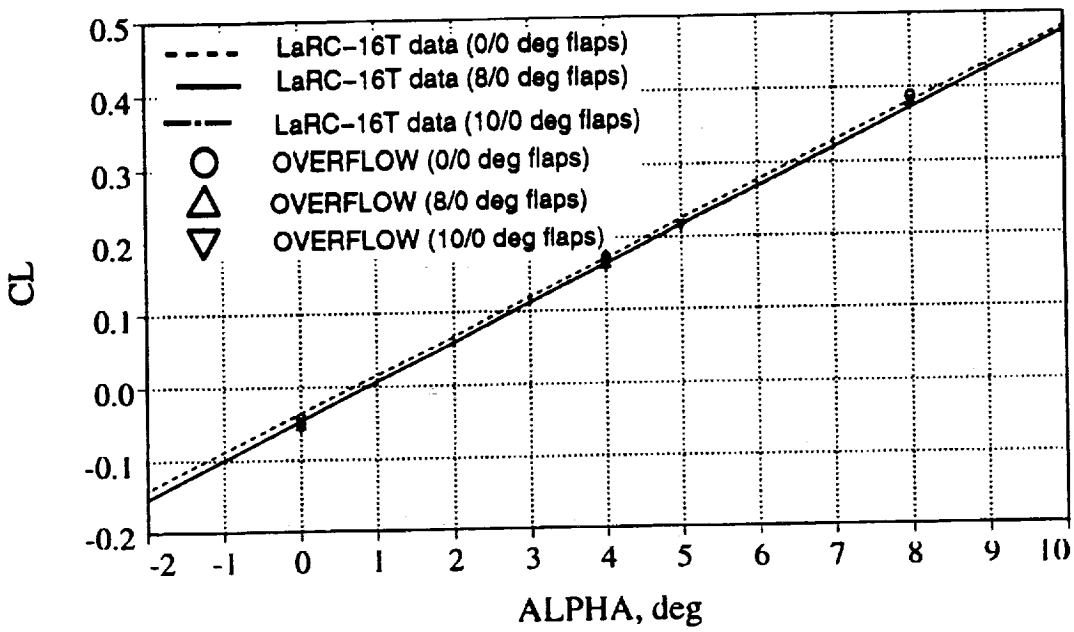

A comparison of the force and moment coefficients for the 10/0 deg and the 8/0 deg flaps with the LaRC-16T data is summarized in the next several figures, where results for the baseline case (flaps up, 0/0 deg) are also included. This figure displays a comparison of CL-alpha curves for the 10/0 deg and the 8/0 deg flaps at Re=5.8E6. The measured CL values for the 8/0 deg and the 10/0 deg case are very close (indistinguishable in the scale of this plot), and are less than the flaps-up values. Predictions from CFD agree with the data. The trend is opposite to that at M=0.9 (10/3 deg flaps) where the flaps result in an increased lift, and is indicative of the transonic effects.

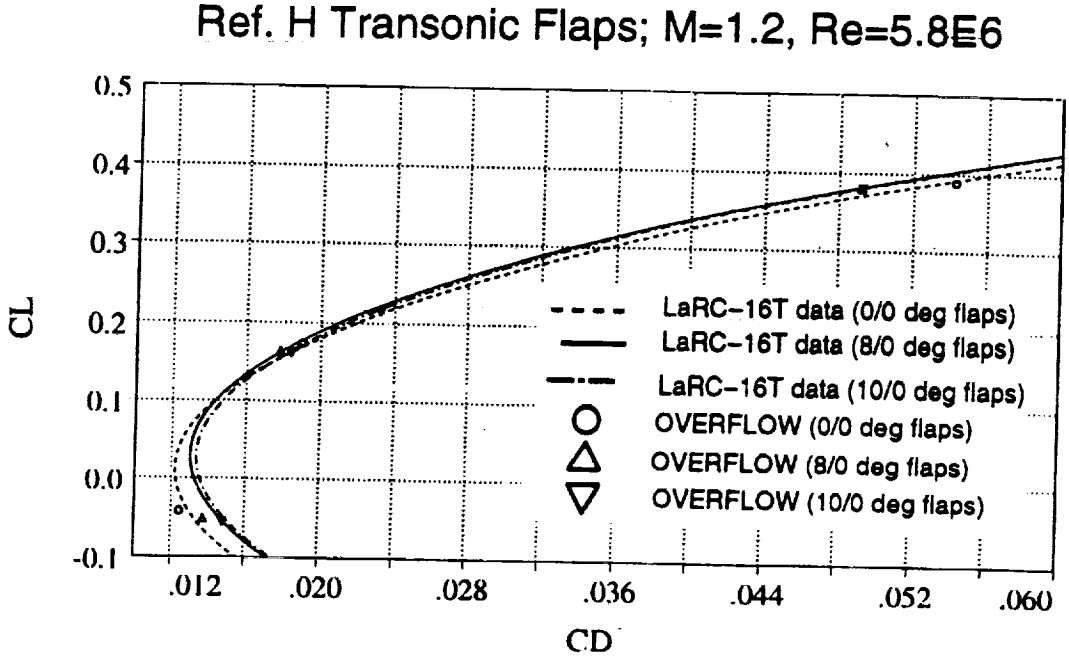

The drag polar comparisons for the 8/0 deg and the 10/0 deg flaps are shown in the next two figures. These results suggest that the CFD computations are able to demonstrate the improved performance of the 8/0 deg flap relative to the 10/0 deg flap. At low alpha, the drag is seen to be somewhat underpredicted for both the flaps up and the flaps down cases. The viscous drag is found to be relatively insensitive to changes in alpha over the range considered.

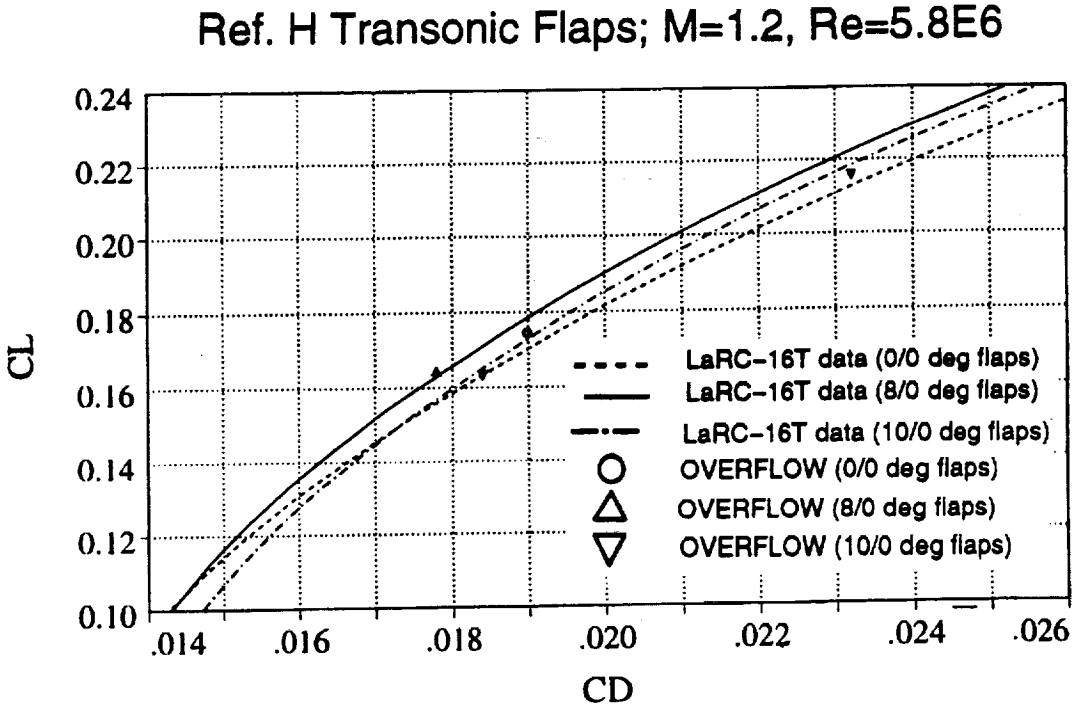

At M=1.2, the 10/0 deg LE/TE flap reduced the drag by about nine counts at the transonic design CL of 0.2 (a 4.5% reduction in L/D relative to cruise geometry, ie. flaps-up case). A higher leading edge flap setting of 10 deg results in a sharply reduced drag benefit at M=1.2. The drag benefit of 4.5 counts obtainable with the 10/0 deg LE/TE flap at M=1.2 is considerably smaller than the drag benefit of 29 counts obtainable with the 10/3 deg LE/TE flap at M=0.9.

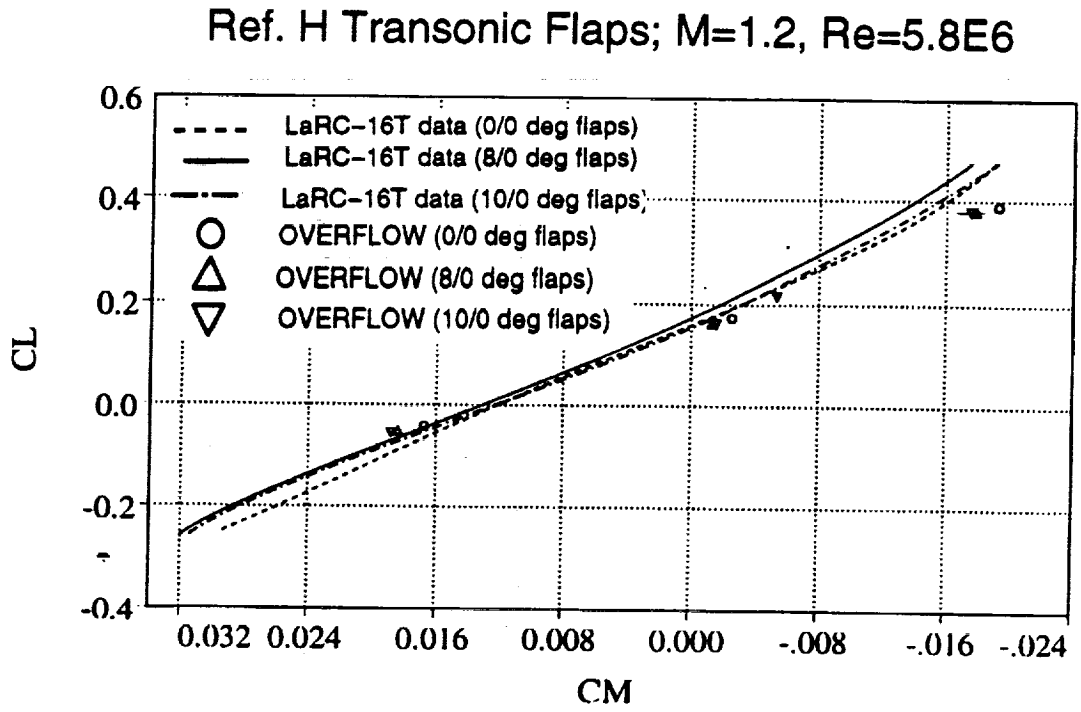

This figure presents a comparison of CL-CM curve at M=1.2 and Re=5.8E6 for the 10/0 deg and the 8/0 deg flaps. At alpha=8 deg, the deviation between the CFD and the data for CM is appreciable, as observed for the 10/3 deg flaps at M=0.9.

Ref. H Transonic Flaps (10/0 deg LE/TE); M=1.2, Alpha=5 deg

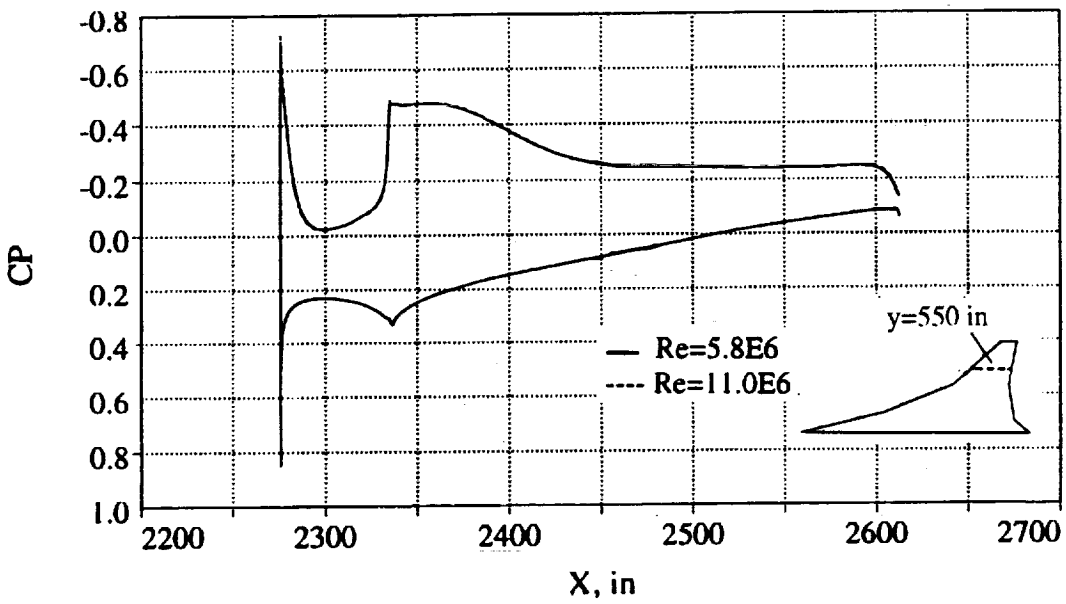

At alpha=5 deg, a trailing edge separation line is observed on the upper surface, as in the case of alpha=4 deg.. The surface streamline pattern is in general similar to the case of alpha=4 deg, except that the reattachment region near the leading edge on the upper surface is of larger extent at alpha=5 deg. This figure displays the Reynolds number effect (Re=5.8E6 and 11E6) on the chordwise CP distribution at alpha=5 deg. The Reynolds number of 11E6 corresponds to the proposed test Reynolds number of the Boeing Supersonic Wind Tunnel (BSWT). Only at the leading edge is there seen to be some effect of Reynolds number on the CP distribution. The flow expansion at the leading edge upper surface is larger at higher Reynolds number. The lift coefficient and the pressure drag are unchanged with Re (CL=0.216, CDP=0.0153), but the viscous drag coefficient (CDV) decreased from 79 counts at Re=5.8E6 to 70 counts at Re=11E6. The solution for Re=11E6 was obtained using restart from the solution at Re=5.8E6.

Ref. H Transonic Flaps (10/0 deg LE/TE); M=1.2, Alpha=5 deg

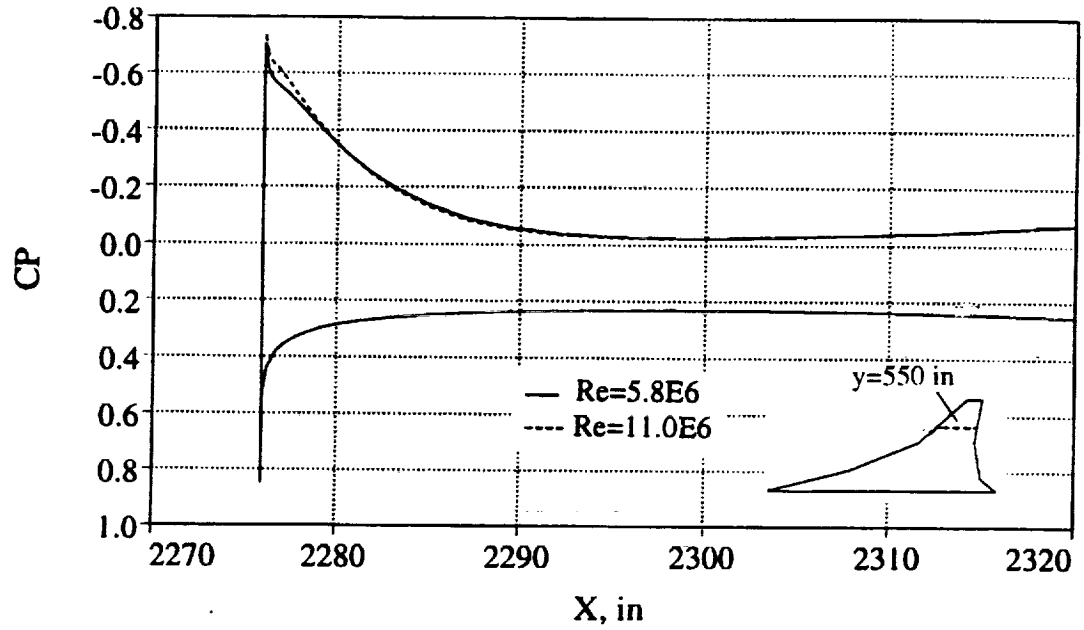

---see previous page text---

Conclusions

- Overflow Predictions Correlated Well with NTF & LaRC-16T Data
- Flap & Reynolds Number Effects are Accurately Described
- Euler solutions are acceptable for lift & drag
- Reynolds Number Restarts Provided Significant Savings (75%)
- Drag at Low Angle of Attack is Underpredicted
- Pitching Moment Prediction at High Angle of Attack is Less Accurate
- Aeroelastic Effects Need to be Assessed with Greater Accuracy

In general OVERFLOW Navier-Stokes CFD computations correlated well with the NTF and LaRC-16T data for forces, drag polar and pitching moments. Although limited data are available for CP on the inboard wing, the computed CP agreed well with the data. The surface streamlines also compared well with the oil flow data (M=1.2 for 10/0 and 8/0 flaps at Re=5.8E6). The flap and Reynolds number effects are accurately described. The Reynolds number restarts provided significant savings in CPU time compared to fresh start in several cases with a moderate range of Re variation (a factor of about three). The Euler solutions compare well with the Navier-Stokes solutions for the lift coefficient and the pressure drag. Since the viscous drag is seen to be relatively independent of the angle of attack, the total drag can be reasonably estimated by adding the viscous drag from the Navier-Stokes solution to the pressure drag from the Euler solutions. Thus a combination of Navier-Stokes solutions, Euler solutions, and Reynolds number restarts appear to be a powerful procedure for application to multi-point design. However, deviations are noted between the theory and the data at low and high alpha. The computed drag at low alpha is in general underpredicted. Also the pitching moment predictions is less accurate at high alpha. The aeroelastic effects present in the NTF data need to be assessed with greater accuracy so that OVERFLOW rigid-body computations can be accurately compared.

Turbulence Model Comparisons and Reynolds Number Effects Over a High-Speed Aircraft at Transonic Speeds

by
Melissa B. Rivers
Richard A. Wahls
NASA Langley Research Center
Hampton, VA 23681

This paper gives the results of a grid study, a turbulence model study, and a Reynolds number effect study for transonic flows over a high-speed aircraft using the thin-layer, upwind, Navier-Stokes CFL3D code. The four turbulence models evaluated are the algebraic Baldwin-Lomax model with the Degani-Schiff modifications, the one-equation Baldwin-Barth model, the one-equation Spalart-Allmaras model, and Menter's two-equation Shear-Stress-Transport (SST) model. The flow conditions, which correspond to tests performed in the NASA Langley National Transonic Facility (NTF), are a Mach number of 0.90 and a Reynolds number of 30 million based on chord for a range of angle-of-attacks (1 degree to 10 degrees). For the Reynolds number effect study, Reynolds numbers of 10 and 80 million based on chord were also evaluated. Computed forces and surface pressures compare reasonably well with the experimental data for all four of the turbulence models. The Baldwin-Lomax model with the Degani-Schiff modifications and the one-equation Baldwin-Barth model show the best agreement with experiment overall. The Reynolds number effects are evaluated using the Baldwin-Lomax with the Degani-Schiff modifications and the Baldwin-Barth turbulence models. Five angles-of-attack were evaluated for the Reynolds number effect study at three different Reynolds numbers. More work is needed to determine the ability of CFL3D to accurately predict Reynolds number effects.

Wireframe Surface Grids of C-O and O-C Topologies

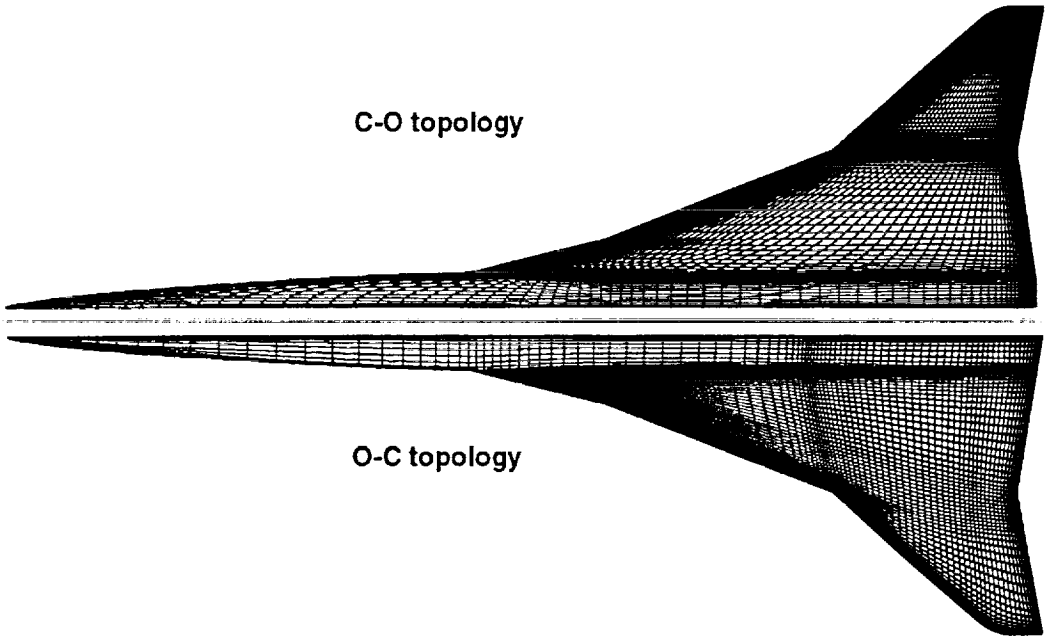

The grid generated about the NTF 2.2% HSR Reference H baseline geometry was created using the GRIDGEN grid generation package. This figure shows the surface grid of the first two grids generated for the NTF 2.2% HSR geometry. The first was a two block grid with an O-C topology with a 5 inch full scale transition from blunt to sharp leading edge at the crank location on the wing. This grid had 105 points in the streamwise direction, 177 points in the spanwise direction and 81 points normal to the surface in the first block, which defines the wing/body configuration; the second block, which defines the sting, had 49 points in the streamwise direction, 177 points in the spanwise direction, and 81 points normal to the surface. The total number of grid points was 2207898. The normal spacing adjacent to the surface was $5x10^{-5}$ over the entire surface. The surface spacing distribution corresponds to a nondimensional y^+ value of approximately 1.6. The farfield boundary extends to 20$\bar{c}$ in the circumferential and upstream directions and the second block extends approximately 20$\bar{c}$ downstream of the first block.

The second grid used was a single block grid with a C-O topology also with a 5 inch full scale transition from blunt to sharp wing leading edge at the crank; this grid defines both the wing/body configuration and the sting. This grid had 133 points in the streamwise direction, 249 points in the spanwise direction and 81 points in the normal direction. The total number of grid points was 2682477. The normal spacing was $5x10^{-5}$ over the entire surface. The surface spacing distribution corresponds to a nondimensional y^+ value of approximately 1.00. The farfield boundary extends to 20$\bar{c}$ in the circumferential, upstream, and downstream (of the wing/body configuration) directions.

Wireframe Surface Grids of C-O topology 1" Wedge and 5" Wedge

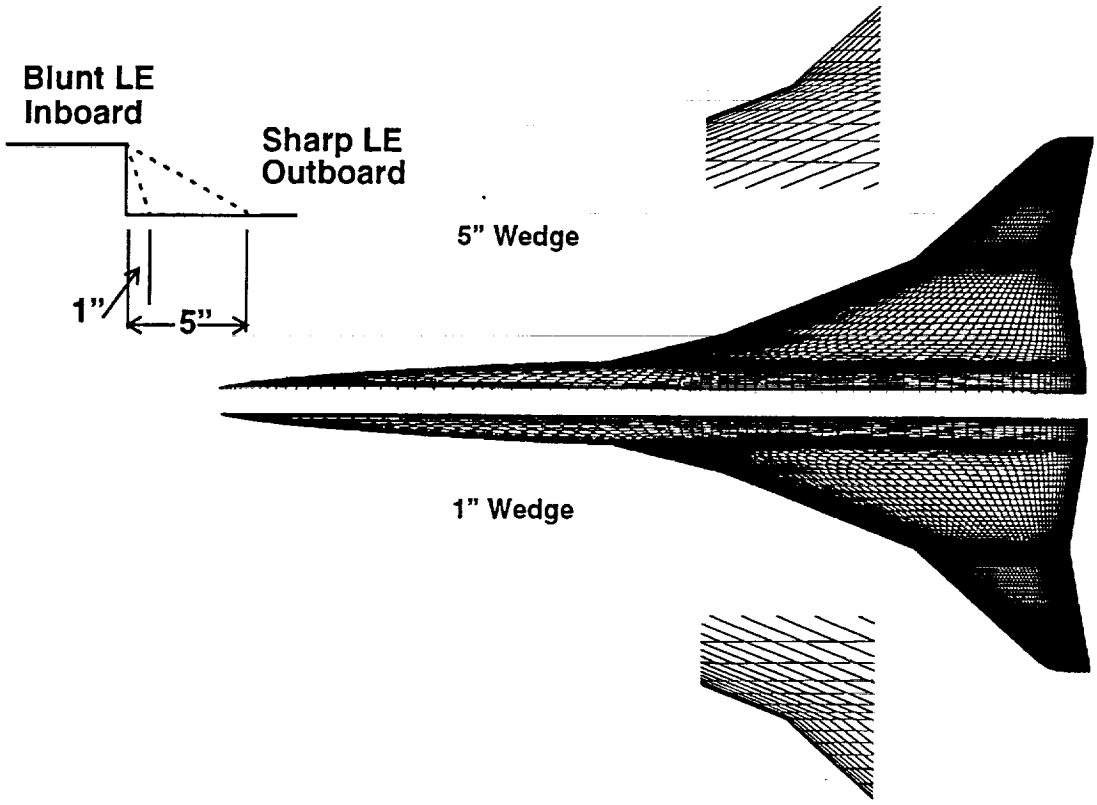

The wind tunnel model had a discontinuity between the sharp wing leading edge and the blunt wing leading edge. In attempt to computational model this discontinuity, a third grid was generated which was identical to the second grid (C-O topology) with the exception of a 1 inch, rather than 5 inch full scale, geometric transition region between the blunt and sharp wing leading edges at the crank.This figure shows the differences in the surface grids of the C-O grid on the wing with a 5 inch full scale transition from blunt to sharp wing leading edge and the C-O grid on the wing with a 1 inch full scale transition from blunt to sharp wing leading edge. The sketch shows where the geometric wedge is on the wing and what is meant by 1 inch versus 5 inch full scale geometric transition from blunt to sharp wing leading edge.

C-O Topology Volume Grid for the NTF 2.2% HSR Geometry

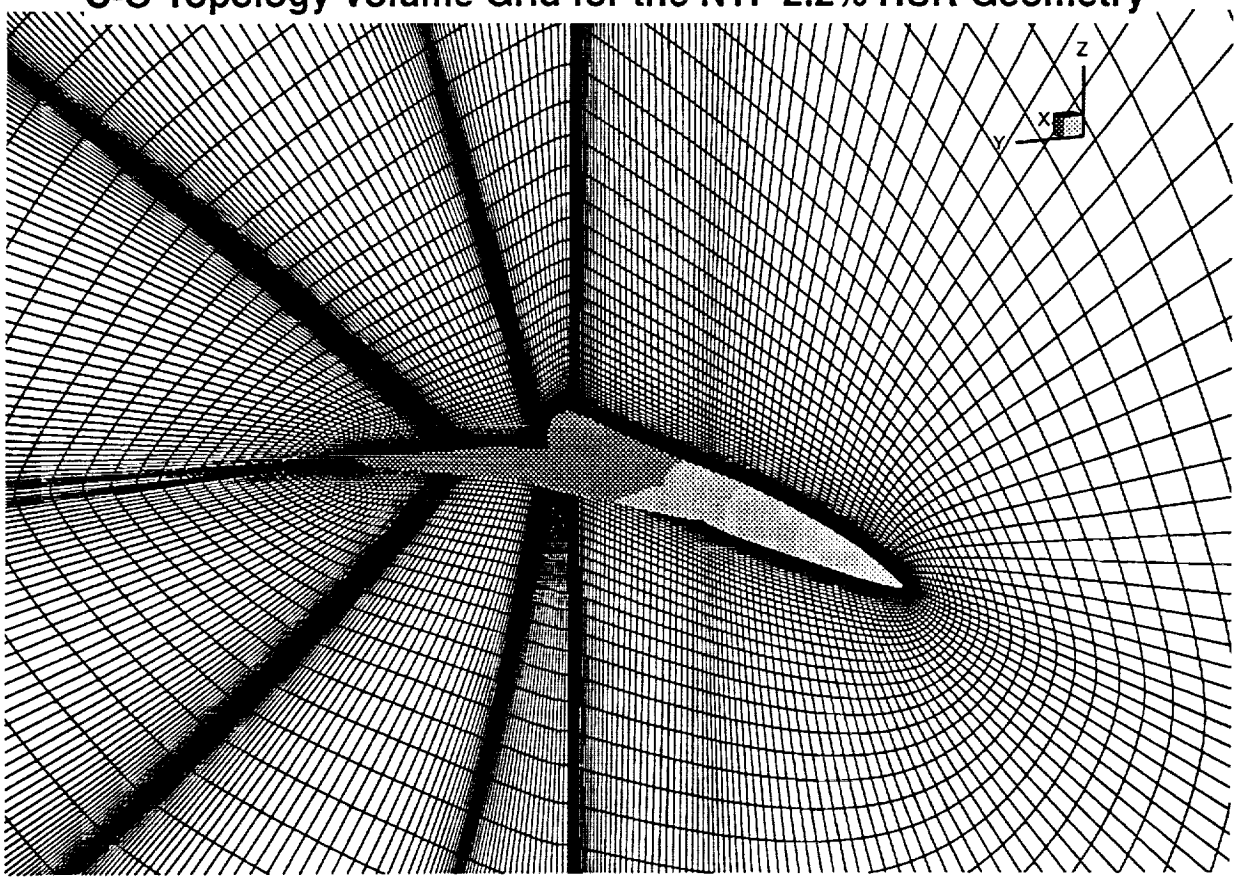

This is the volume grid for the C-O grid topology with a 1 inch full scale transition from blunt to sharp wing leading edge.

Spanwise Pressure Stations on the Wing of the NTF 2.2% HSR Geometry

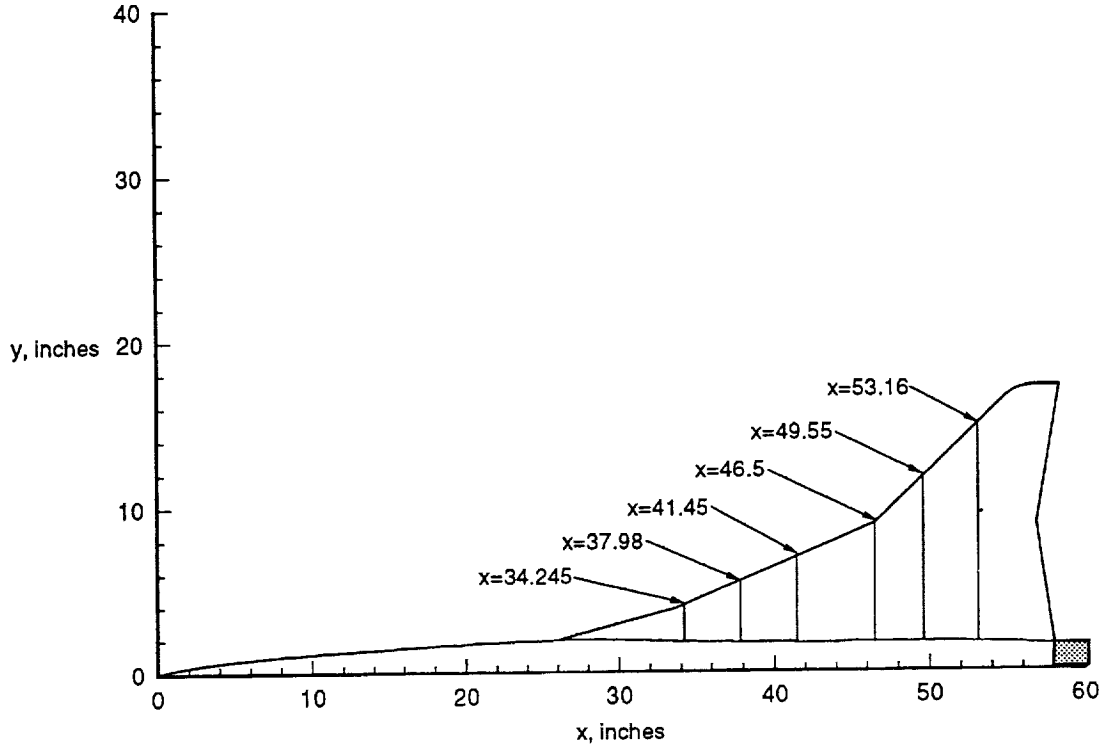

This figure shows the location of the six spanwise pressure rows on the wing of the NTF 2.2% HSR geometry. The shaded area is part of the metric model, but not part of the computational model.

Surface Pressure Comparison of O-C and C-O Grid Topology Results, M=0.90, α=5.0 deg, Re_c=30x10^6, Spalart-Allmaras Turbulence Model

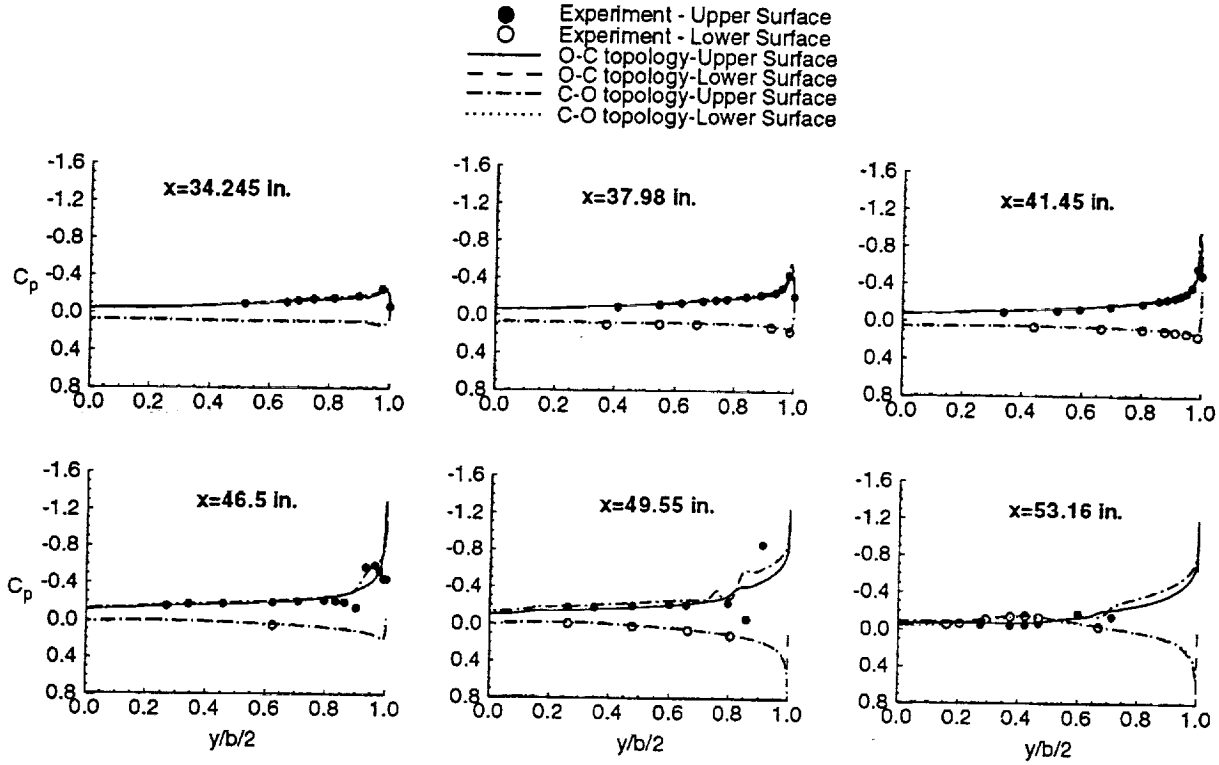

A grid study was performed using these three grids in an effort to determine which grid gave the best comparisons with the experimental data. All of the runs made for this grid study were performed at a M=0.90, Re_c=30x10^6, and at an angle-of-attack of 5 degrees. These runs were all made with CFL3D using the Spalart-Allmaras turbulence model. This figure shows the pressure distributions at the six spanwise stations on the wing of the NTF 2.2% HSR geometry for the C-O topology versus the O-C topology. As shown in this figure, the C-O topology agrees better with the experimental values than the O-C topology, most notably at the crank of the wing and on the outboard wing panel.

Surface Pressure Comparison of 1" and 5" Full-Scale Wedge Results, M=0.90, α=5.0 deg, Re_c=30x10^6, Spalart-Allmaras Turbulence Model

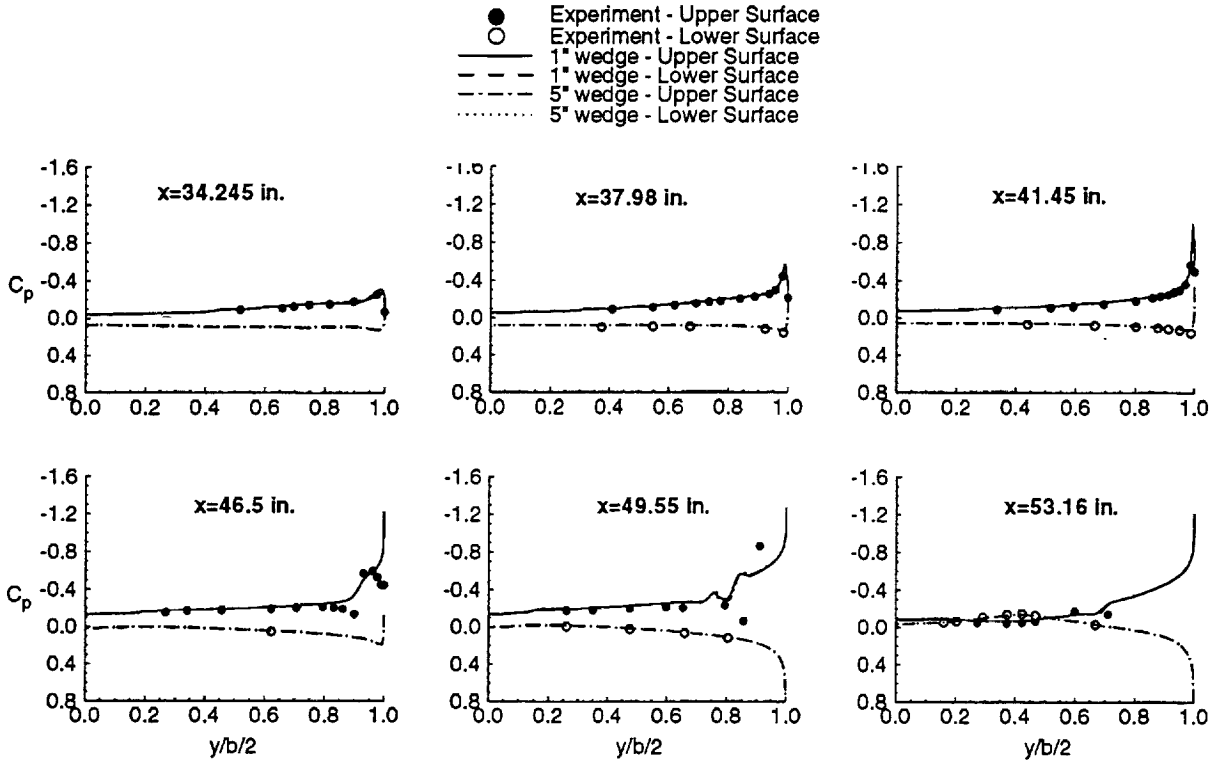

This figure shows the pressure distributions at the six spanwise pressure stations on the wing of the NTF 2.2% HSR geometry for the 1 inch full-scale wedge versus the 5 inch full-scale wedge at a Mach number of 0.90, a Reynolds number of 30 million and at an angle-of-attack of 5.0 deg. As shown in the figure, the wedge size does not have a significant effect on the pressure distributions.

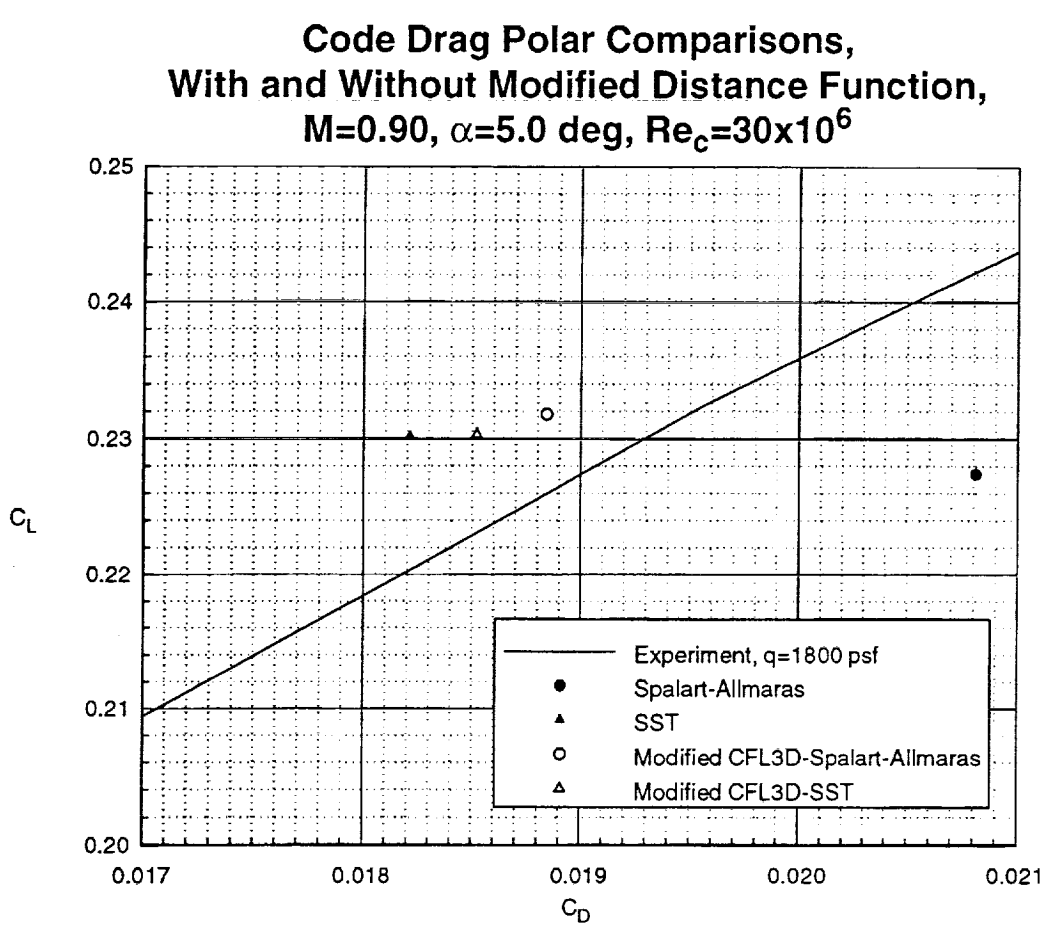

During the course of this study, an important modification was made to the CFL3D Navier-Stokes code. A change was made in the calculation of the minimum distance function. The new minimum distance function was calculated by interpolating to the nearest point on the body rather than just picking the nearest body cell-center point. This modification effected the results of the Spalart-Allmaras and SST turbulence models. The modifications made to the code did not significantly effect the pressure distributions of either the Spalart-Allmaras turbulence model or the Menter's SST turbulence model. However, as shown in this figure, the modification did effect the forces for both the Spalart-Allmaras and the SST turbulence model calculations. For the Spalart-Allmaras case, the lift is increased by approximately 0.004 and the drag is decreased by approximately 20 drag counts, which is closer to matching the experimental value. For the Menter's SST results, the lift remains about the same but the drag is increased by 3 drag counts, which is also closer to matching the experimental value.These experimental values are uncorrected for aeroelastic effects.

- **Grid and Code Assessment Conclusions**
  - **C-O topology, rather than O-C topology, preferred for this configuration**
  - **Detail of geometric modeling of the blunt to sharp leading-edge transition at the wing crank did not effect results**
  - **Distance function modification important, especially to Spalart-Allmaras and Menter's SST turbulence models**
  - **Single block C-O topology grid with a 1" full scale geometric transition from blunt to sharp wing leading edge was used for the turbulence model and Reynolds number effect studies**

The conclusions which were reached by this grid study were that the C-O topology, rather than the O-C topology, is preferred for this configuration. The detail of the geometric modeling of the blunt to sharp leading-edge transitions at the wing crank did not effect the results and the distance function modification was important, especially to the Spalart-Allmaras and Menter's SST turbulence model results. Therefore, the single block C-O topology grid with 1 inch full scale geometric transition from blunt to sharp wing leading edge was used for the turbulence model study and the Reynolds number effect study.

Spanwise Wing Pressure Distributions, M=0.90, α=1.0 deg, Re_c=30x10^6

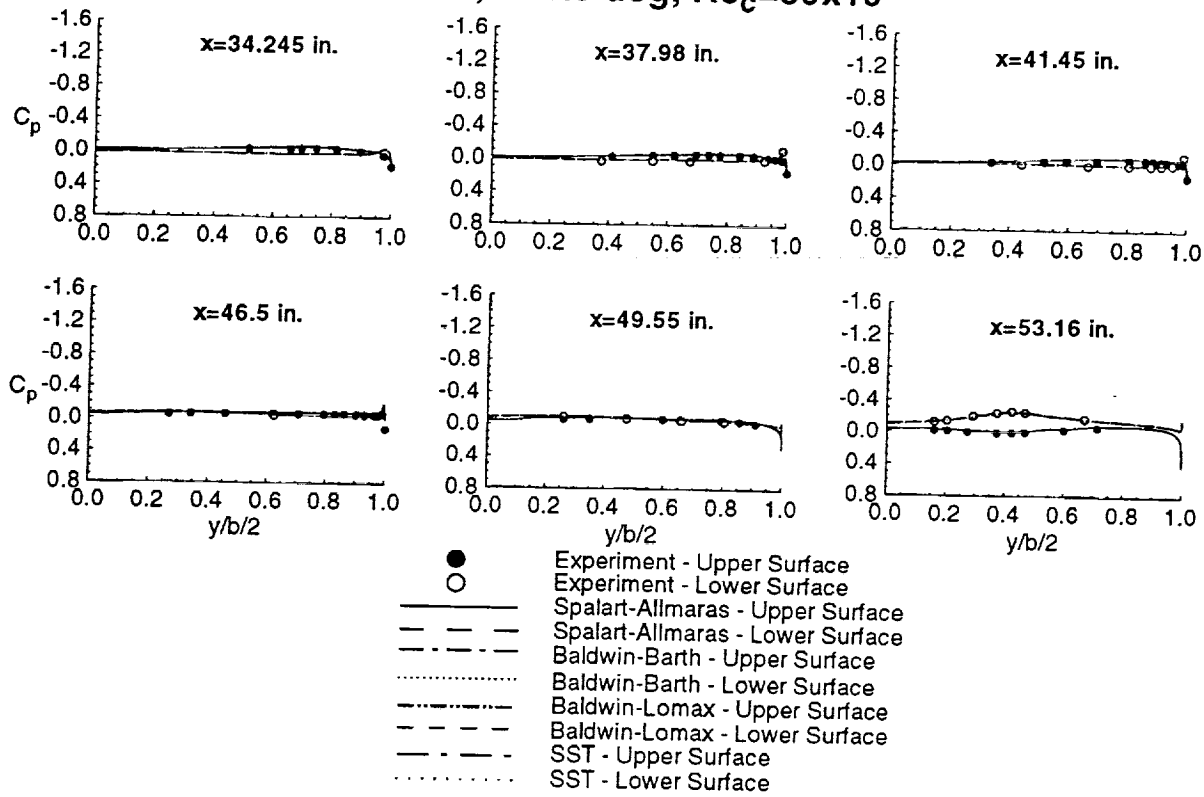

The next three figures show the spanwise pressure distribution comparisons for all three angles-of-attack.This figure indicates that at a Mach number of 0.90, a Reynolds number of 30 million and an angle-of-attack of 1.0 deg, all of the turbulence models agreed well with experiment at all of the pressure stations.

Spanwise Wing Pressure Distributions, M=0.90, α=5.0 deg, Re_c=30x10^6

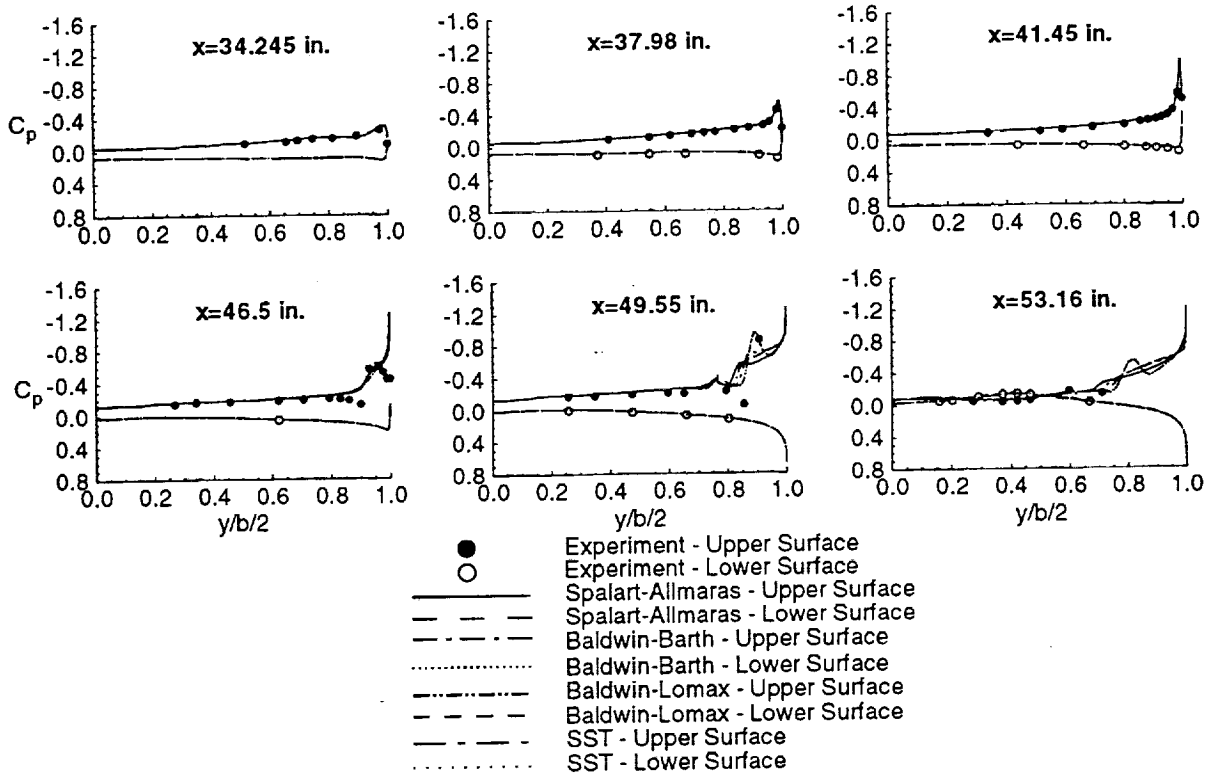

The spanwise pressure distributions for the α=5.0 deg case shown in this figure indicate that up to the crank in the wing, all of the turbulence models predict the flow characteristics very well. At the crank region, i.e. x=46.5 inches, none of the models pick up the detail seen in the outboard 20% span in the experimental data. At an x station of 49.55 inches, Baldwin-Lomax is the only model that picks up the apparent suction peak at 95% span in the experimental data. At the x=53.16 inches station, all of the models perform equally well, with Baldwin-Lomax showing a suction peak at approximately 85% span. The experimental pressures do not extend this far outboard; therefore it is difficult to say if the suction peak is real.

Spanwise Wing Pressure Distributions, M=0.90, α=10.0 deg, Re_c=30x10^6

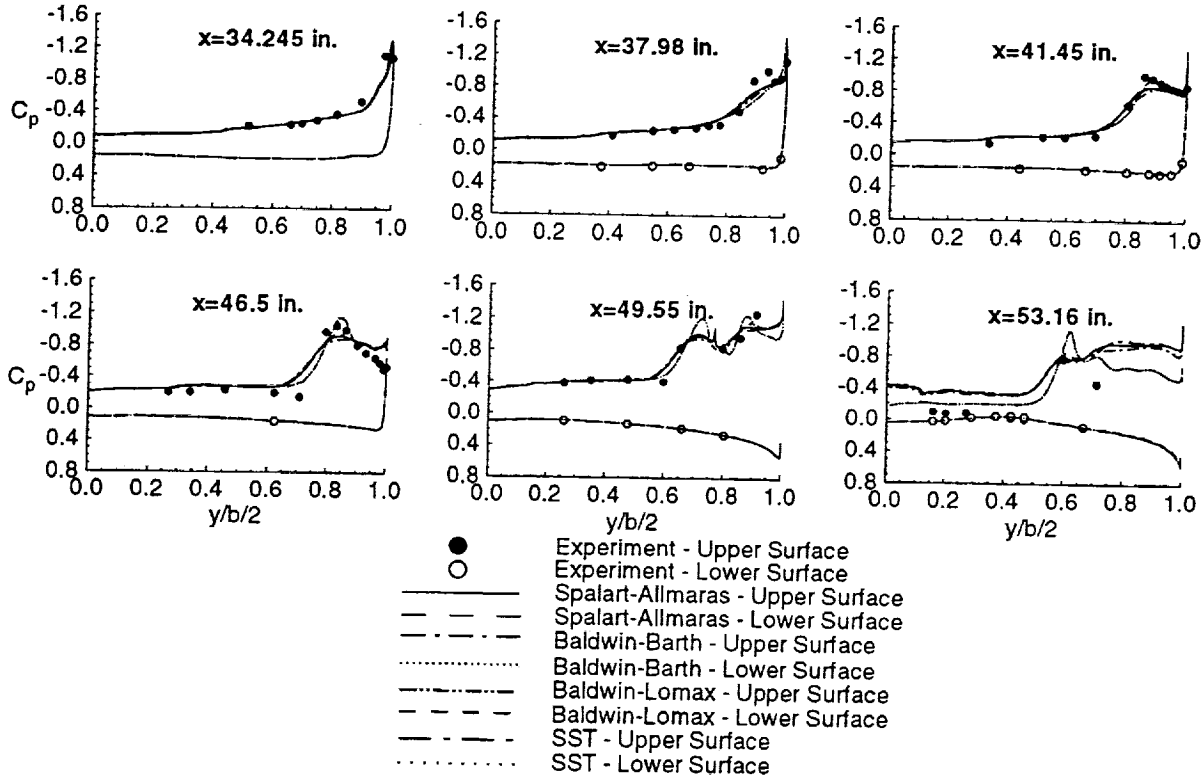

The spanwise pressure distributions for the α=10.0 deg case shown in this figure indicate that at the x station of 34.245 inches, all of the models predict the flow characteristics very well. At the next station, x=37.98 inches, none of the models pick up the detail seen in the last 20% span. At the x=41.45 inches station, the Baldwin-Lomax model tends to pick up the magnitude of the suction peak seen at approximately 90% span in the experimental flow better than any of the other three models. At the crank region, i.e. x=46.5 inches, the Baldwin-Lomax model comes the closest of the four models to picking up the pressure increase seen at 75% span and the suction peak at 80% span in the experimental data. At an x station of 49.55 inches, Baldwin-Lomax comes the closest to matching the fluctuations in the experimental data. At the x=53.16 inches station, Baldwin-Lomax comes the closest of the four models to picking up the upper surface pressure distribution seen in the experiment.

Computational Surface Streamlines, M=0.90, α=1.0 deg, Re_c=30x10^6

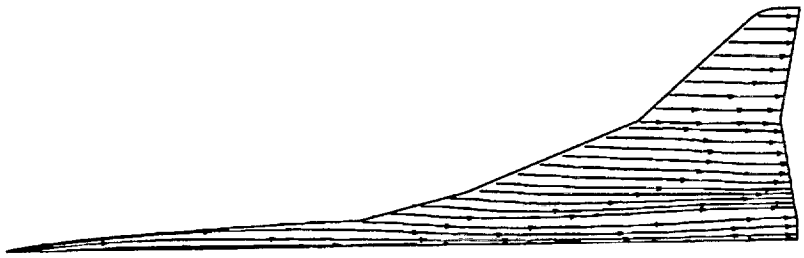

Baldwin-Lomax

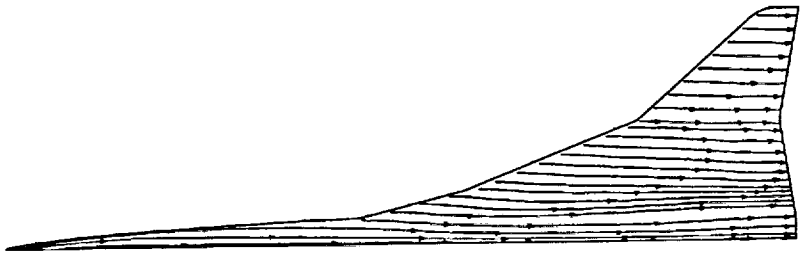

Baldwin-Barth

In the following six figures a separation line is indicated by the streamlines coalescing to a line while an attachment line is a line from which the streamlines are flowing out.

This figure shows the computational surface streamlines for the Baldwin-Lomax and Baldwin-Barth turbulence models for the α=1.0 deg case. The computational surface streamlines are aligned with the freestream flow on both the outboard and inboard wing sections for these two turbulence models at α=1.0 deg.

Computational Surface Streamlines, M=0.90, α=1.0 deg, Re_c=30x10^6

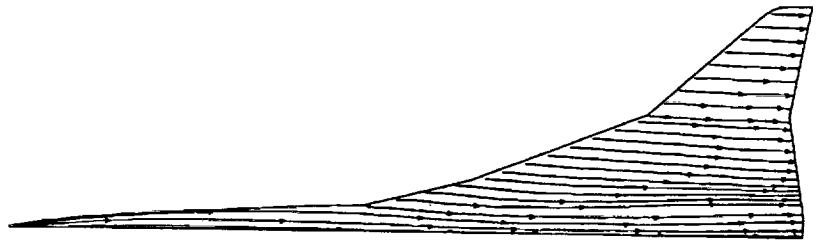

Spalart-Allmaras

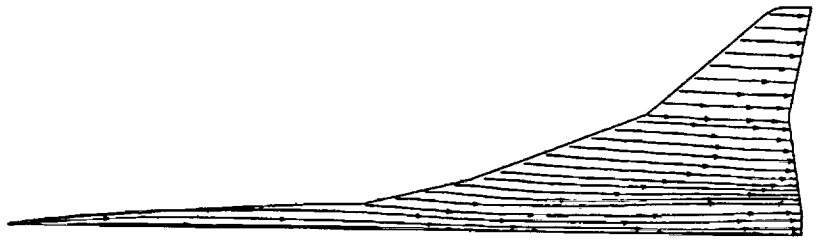

SST

This figure shows the computational surface streamlines for the Spalart-Allmaras and the SST turbulence models for the α=1.0 deg case. The computational surface streamlines are aligned with the freestream flow on both the outboard and inboard wing sections for these two turbulence models at α=1.0 deg.

Computational Surface Streamlines, M=0.90, α=5.0 deg, Re_c=30x10^6

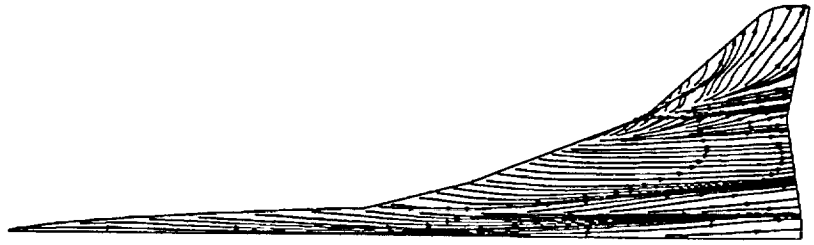

Baldwin-Lomax

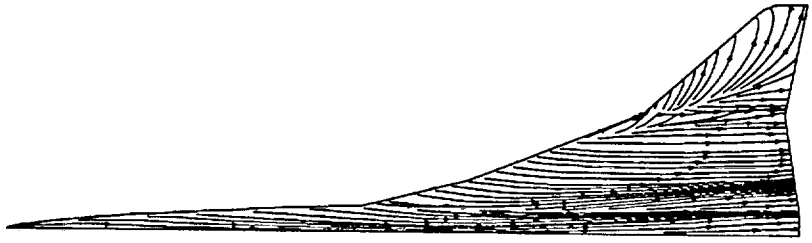

Baldwin-Barth

The computational streamlines for the Baldwin-Lomax and Baldwin-Barth turbulence models are shown for the α=5.0 deg case. Both show separations at the trailing edge wing/fuselage juncture and at the inboard trailing edge of the wing. They also both show a separation at the crank with an attachment near the outboard wing leading edge. The Baldwin-Lomax solution shows an extra separation and reattachment at the outboard wing leading edge that the other model does not show.

Computational Surface Streamlines, M=0.90, α=5.0 deg, Re_c=30x10^6

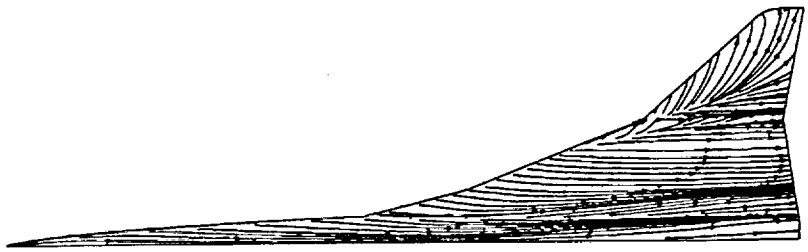

Spalart-Allmaras

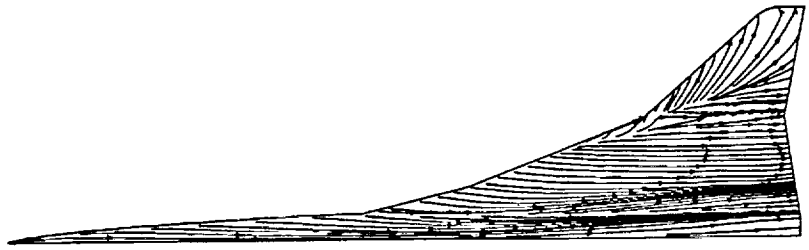

SST

The computational streamlines for the Spalart-Allmaras and SST turbulence models are shown for the α=5.0 deg case. Both show separations at the trailing edge wing/fuselage juncture and at the inboard trailing edge of the wing. They also both show a separation at the crank with an attachment near the outboard wing leading edge.

Computational Surface Streamlines, M=0.90, α=10.0 deg, Re_c=30x10^6

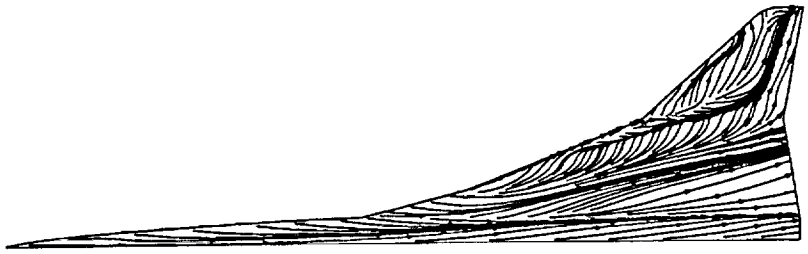

Baldwin-Lomax

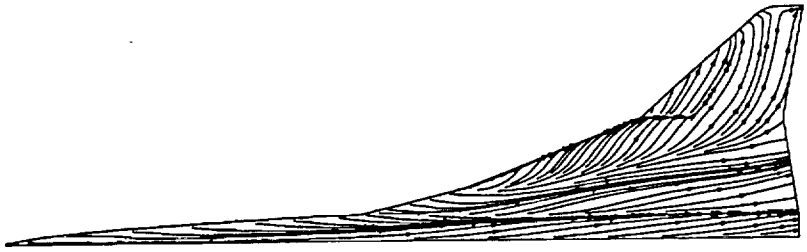

Baldwin-Barth

The computational streamlines for the Baldwin-Lomax and Baldwin-Barth turbulence models are shown for the α=10.0 deg case. Both cases show a separation at the wing/fuselage juncture, at the inboard trailing edge of the wing and at the crank region of the wing. They both also show a reattachment line in the inboard center of the wing. The Baldwin-Lomax case, however, also shows a separation at the inboard leading edge of the wing and at the outboard leading edge of the wing with a reattachment line also seen in the outboard region of the wing.

Computational Surface Streamlines, M=0.90, α=10.0 deg, Re_c=30x10^6

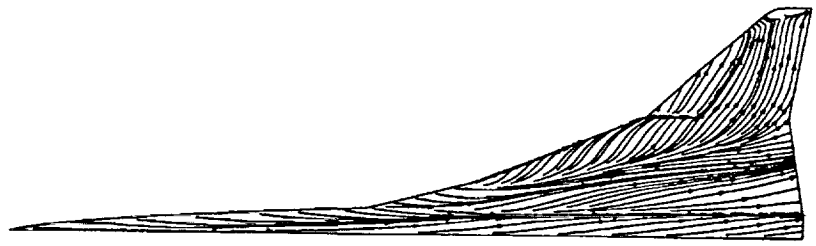

Spalart-Allmaras

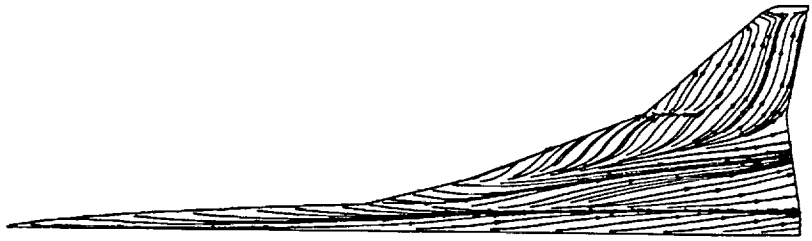

SST

The computational streamlines for the Spalart-Allmaras and SST turbulence models are shown for the α=10.0 deg case. Both cases show a separation at the wing/fuselage juncture, at the inboard trailing edge of the wing and at the crank region of the wing. They both also show a reattachment line in the inboard center of the wing.

Drag Polars
M=0.90, Re_c=30x10^6

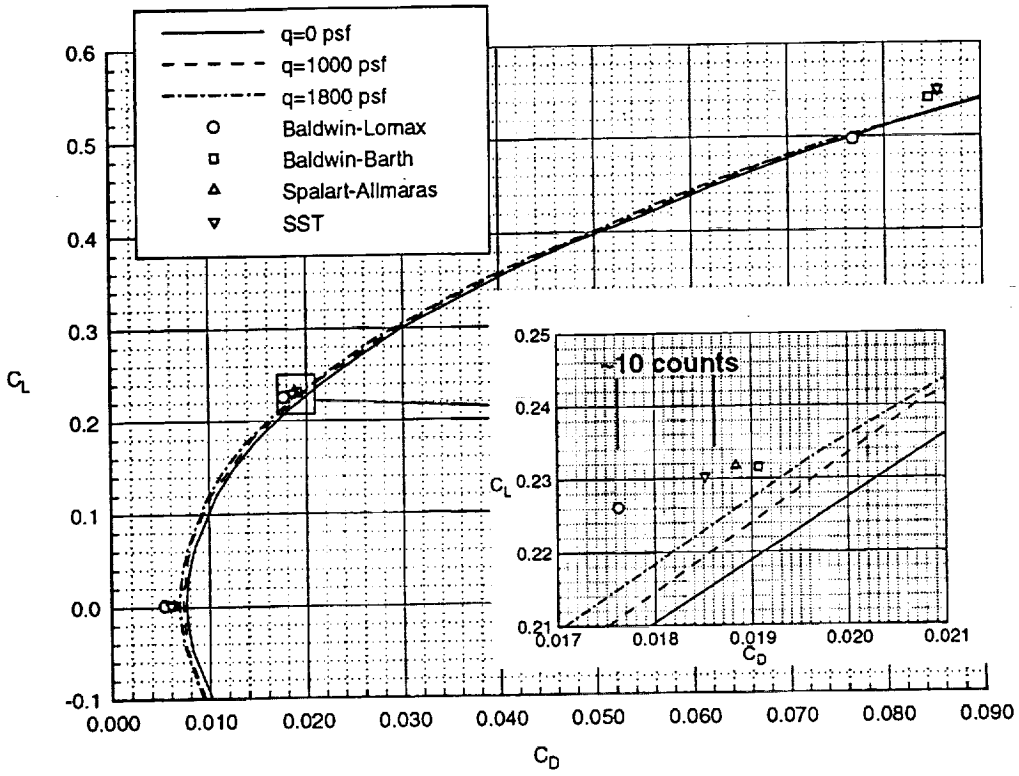

There are three experimental curves shown on the next four figures; the first is the experimental data corrected for aeroelastics to a q=0 psf, the second is the low q (q=1000 psf) data and the third is the high q (q=1800 psf) data taken in the NTF experiment.

This figure shows the drag polar for the four different turbulence models and the experimental data. The experimental data shows a decrease in lift at a given drag value and an increase in drag at a given lift value as the q levels are decreased. At α=1.0 deg, all of the models predict the drag lower than the experimental data. At the design point, α=5.0 deg, Baldwin-Barth comes the closest to matching the experimental data; the Baldwin Barth data is approximately four drag counts lower than the high q data, while the Spalart-Allmaras, SST, and Baldwin-Lomax models are 6, 7 and 12 drag counts lower than the high q data, respectively. At α=10.0 deg, Baldwin-Lomax predicts lift and drag lower than the other three models, but it does come the closest to the experimental curve.

	α, deg	Baldwin-Lomax	Baldwin-Barth	Spalart-Allmaras	Menter's SST
C_{Dp}	1	0.0004	0.0005	0.0005	0.0005
	5	0.0130	0.0135	0.0133	0.0131
	10	0.0723	0.0789	0.0800	0.0801
C_{Dv}	1	0.0049	0.0057	0.0058	0.0054
	5	0.0046	0.0056	0.0055	0.0053
	10	0.0045	0.0057	0.0055	0.0052

The computational wing pressure distributions discussed earlier in this paper indicated that Baldwin-Lomax agreed the best with the experimental data while this drag polar indicates that the Baldwin-Barth model agrees best with experiment. This discrepancy is believed to be caused by a difference in the viscous drag components of the turbulence model results. The Baldwin-Lomax turbulence model viscous drag component results are approximately 10 drag counts lower than the other three models at all three angles-of-attack. At α=10.0 deg, the pressure component of drag for Baldwin-Lomax is approximately 60 drag counts lower than the other three models, which can account for the results seen at this angle-of-attack.

Lift-to-Drag Ratios
$M=0.90, Re_c=30x10^6$

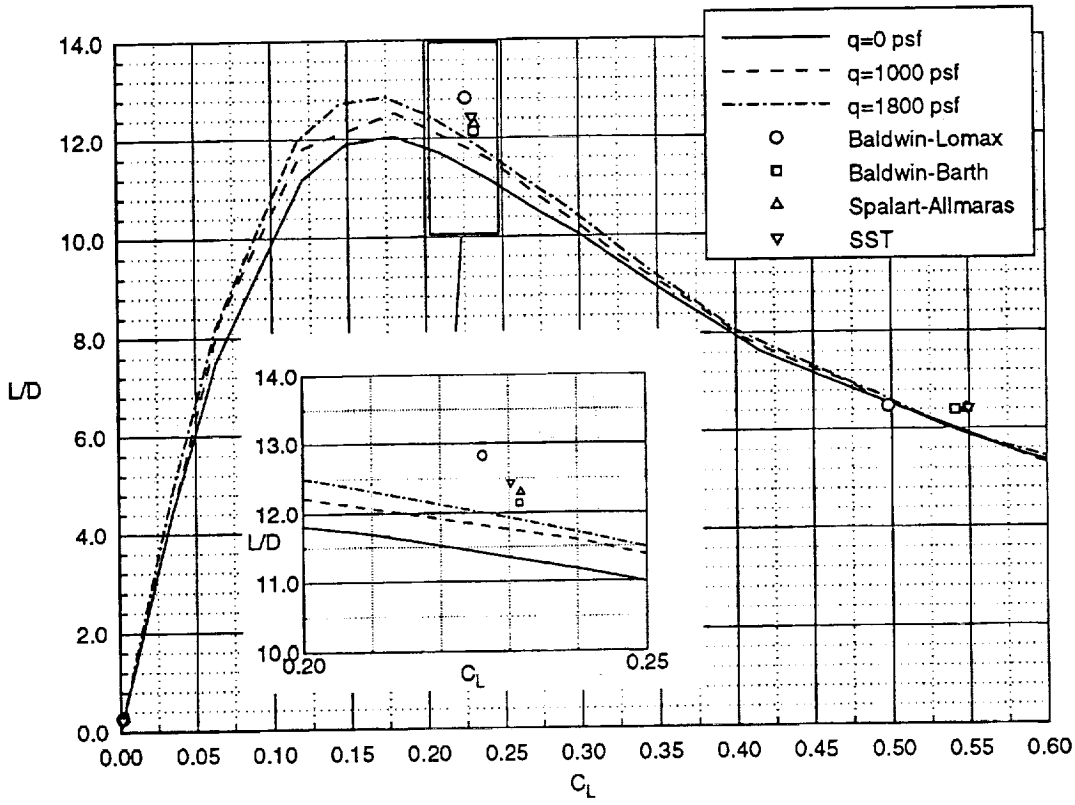

The lift-to-drag ratios for the four turbulence models versus the experimental data are shown in this figure. This figure shows that at α=1.0 deg, all four of the models predict approximately the same L/D value, which agrees well with the experimental values. At α=5.0 deg, Baldwin-Barth comes the closest to matching the high q data. At α=10.0 deg, Baldwin-Lomax predicts the experimental L/D level closer than the other three models. As mentioned earlier, the discrepancies between the pressure data examined earlier and the force data shown here are due to differences in the viscous and pressure drag components of the four turbulence models.

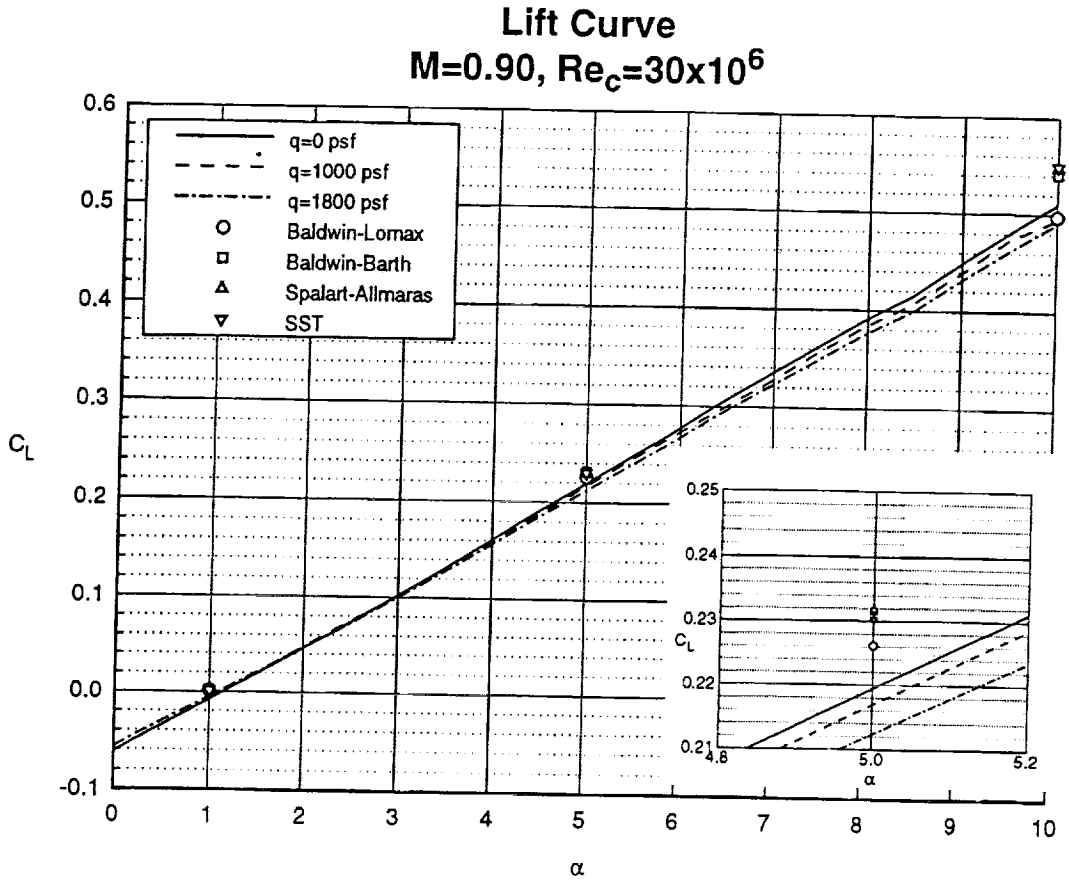

This figure shows the lift curve for the four turbulence models and the experimental data. At an α=1.0 deg, all of the models are slightly higher than the experimental data. At the design point, α=5.0 deg, Baldwin-Lomax is closer to the experimental lift curves than the other three models and at α=10.0 deg, Baldwin-Lomax underpredicts the corrected experimental curve but falls on the uncorrected curves. The other three models all overpredict the lift at α=10.0 deg.

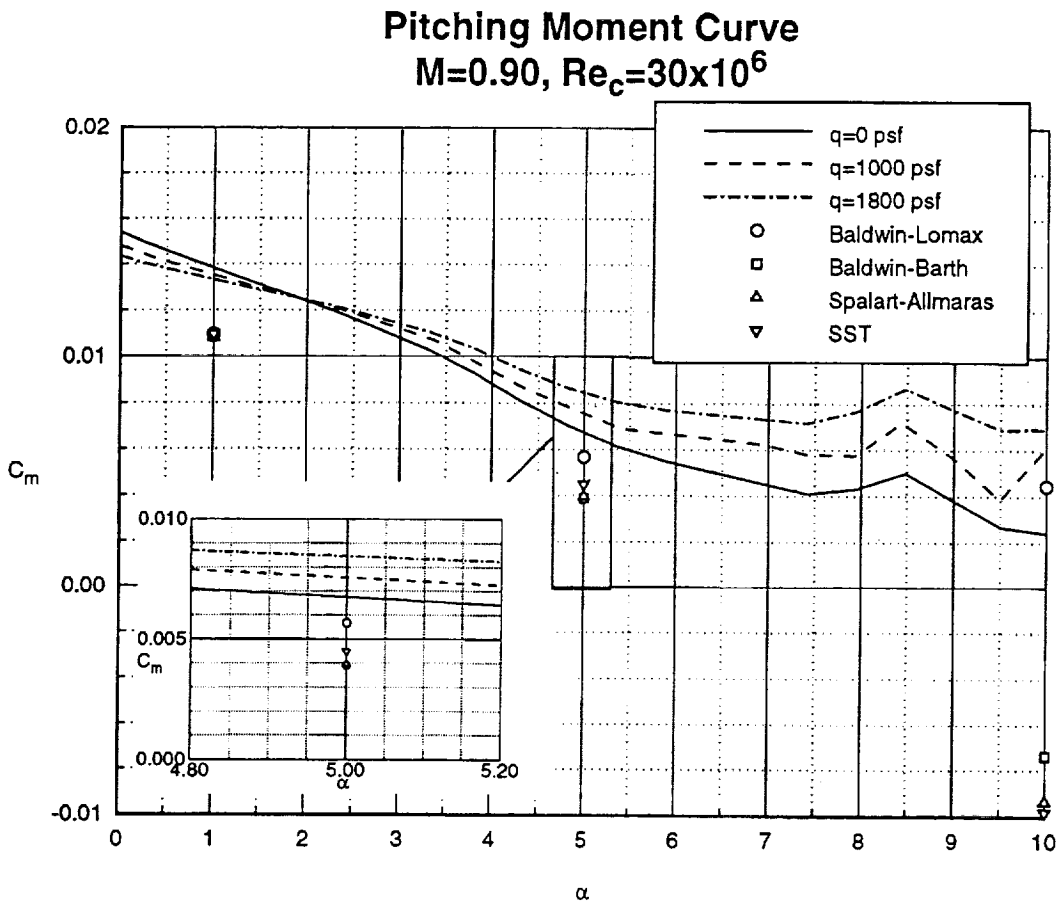

This figure shows the pitching moment curves for the four turbulence models and the experimental data. At an α=1.0 deg, all of the models underpredict the pitching moment. At α=5.0 deg, all of the models again underpredict the pitching moment, but Baldwin-Lomax comes the closest to the experimental values. At α=10.0 deg, Baldwin-Barth, Spalart-Allmaras, and SST all underpredict the pitching moment values but Baldwin-Lomax overpredicts the corrected values and underpredicts the uncorrected values, but not to the same extent as the other models.

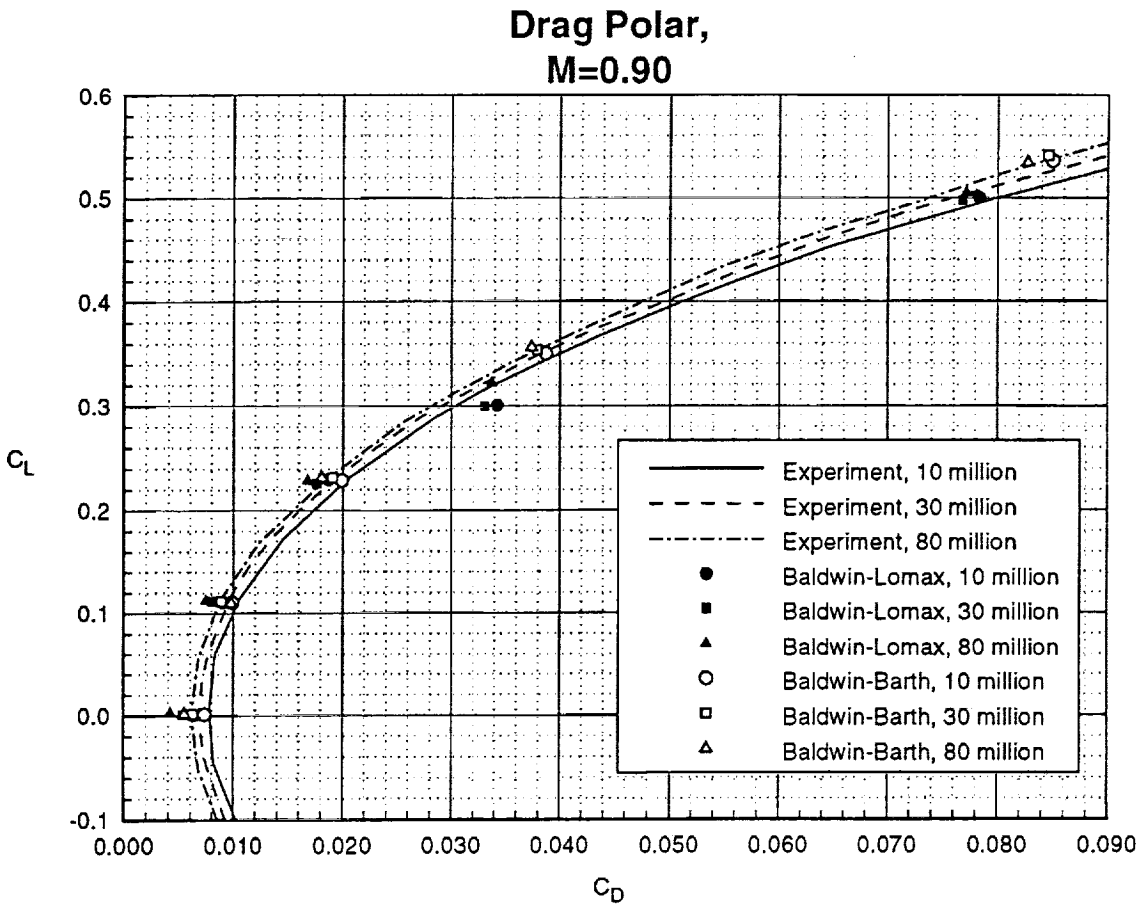

A Reynolds number effect study was also performed on the NTF 2.2% HSR geometry. These preliminary calculations were performed at a Mach number of 0.90, at angles-of-attack ranging from 1.0 to 10.0 degrees and at Reynolds numbers ranging from 10 to 80 million. Also, two turbulence models were tested during the course of this study, the algebraic Baldwin-Lomax model and the one equation Baldwin-Barth model.

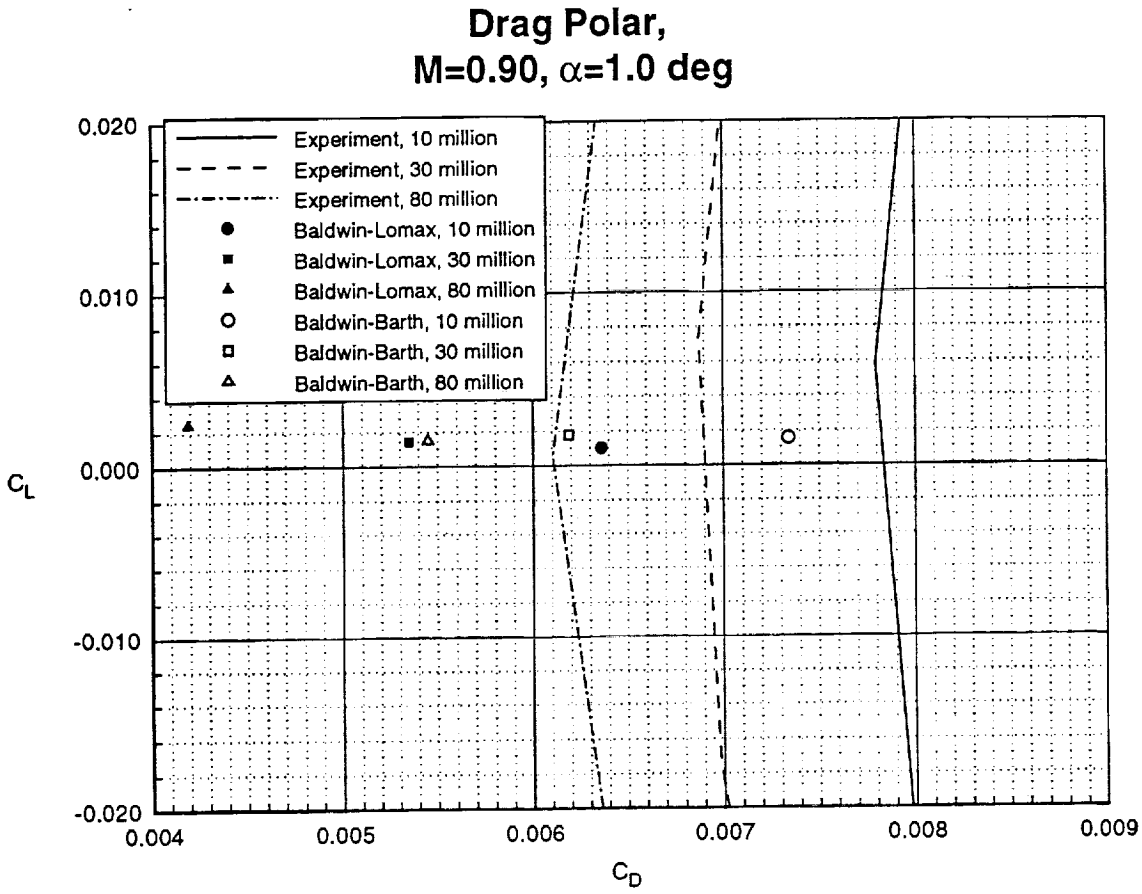

This figure shows that at α=1.0 deg, both of the turbulence models pick up the same Reynolds number effect trend as the experimental data, which is that the drag level decreases as the Reynolds number increases. Neither model predicts the same lift or drag levels as the experimental data, however. For the Re_c=10 million cases, the Baldwin-Lomax model is 15 drag counts low and the Baldwin-Barth model is 5 drag counts low. For the Re_c=30 million cases, the Baldwin-Lomax and Baldwin-Barth cases are 15 and 7 drag counts low, respectively and for the Re_c=80 million case, the Baldwin-Lomax case is 19 drag counts low while the Baldwin-Barth case is 7 drag counts low.

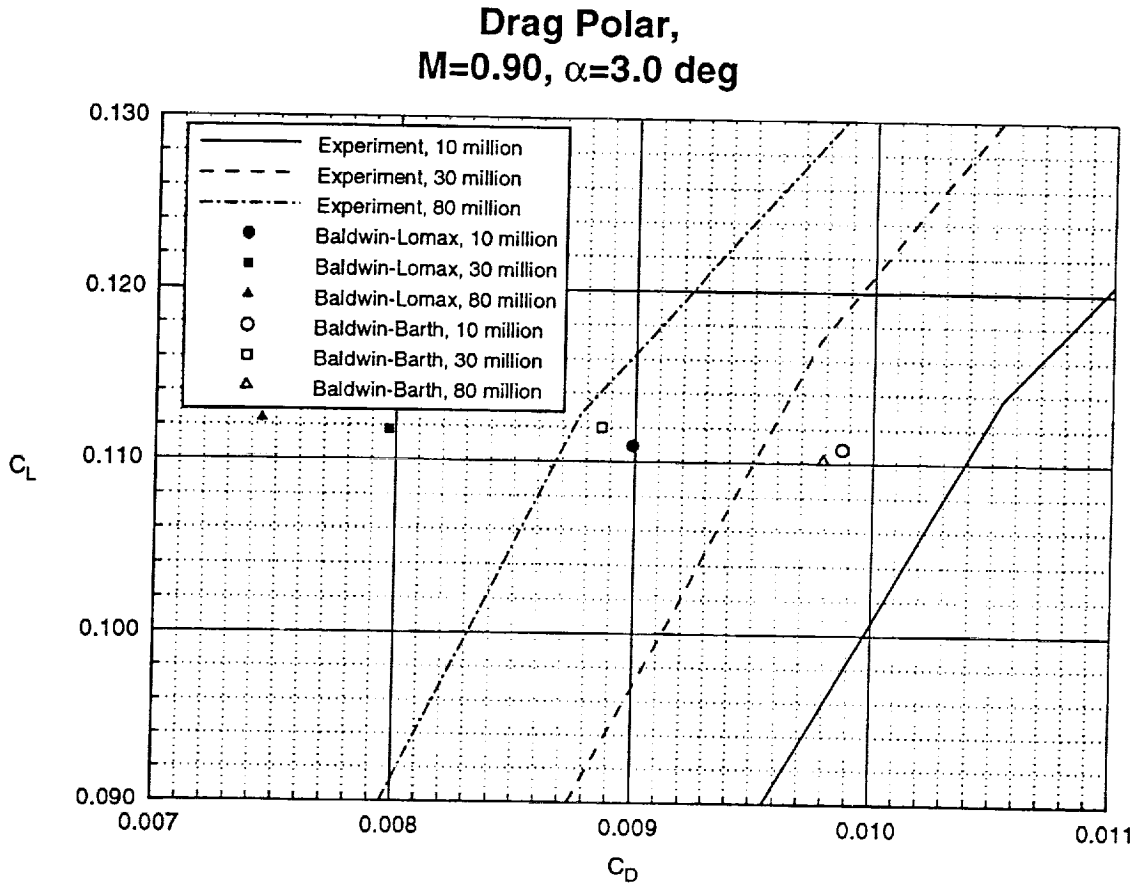

This figure shows that at α=3.0 deg, the Baldwin-Lomax turbulence model does predict the same Reynolds number effect trend as the experimental data, which is that the drag level decreases as the Reynolds number increases, but the Baldwin-Barth case does not predict the correct trend. Neither model predicts the same lift or drag levels as the experimental data. For the Re_c=10 million cases, the Baldwin-Lomax model is 14 drag counts low and the Baldwin-Barth model is 5 drag counts low. For the Re_c=30 million cases, the Baldwin-Lomax and Baldwin-Barth cases are 16 and 7 drag counts low, respectively and for the Re_c=80 million case, the Baldwin-Lomax case is 13 drag counts low while the Baldwin-Barth case is 11 drag counts high.

Drag Polar, M=0.90, α=5.0 deg

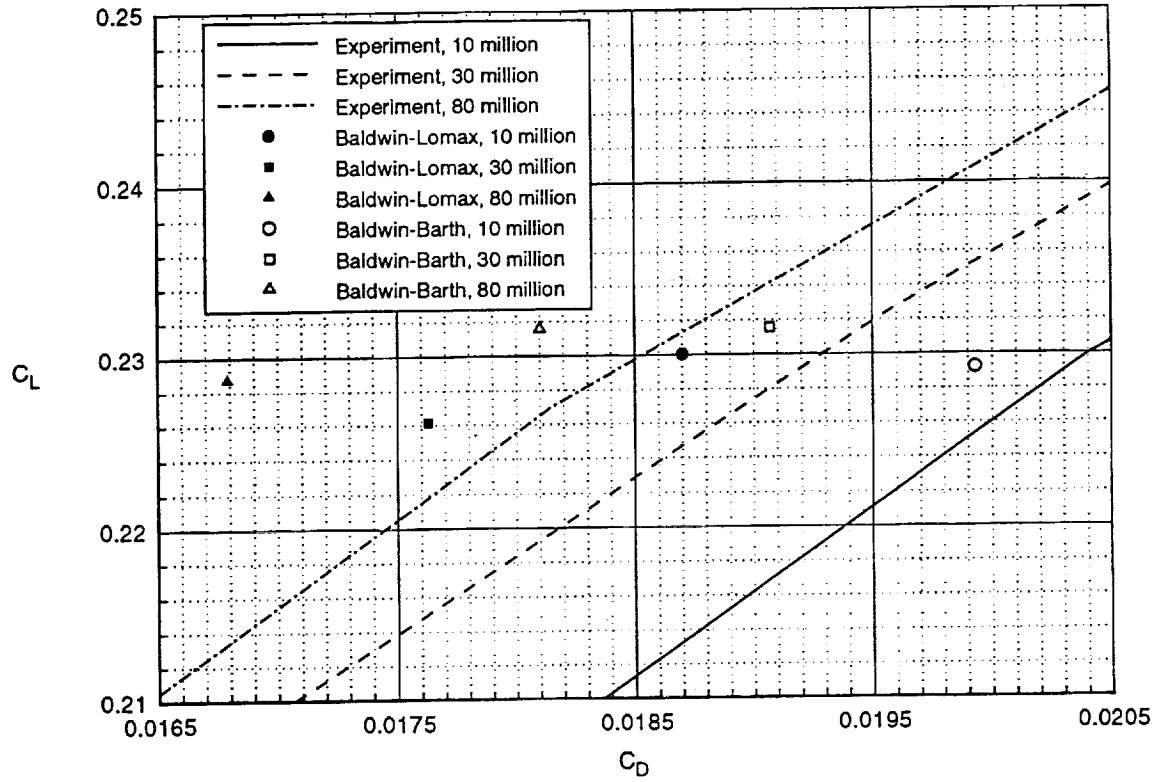

This figure shows that at α=5.0 deg, both of the turbulence models pick up the same Reynolds number effect trend as the experimental data, which is that the drag level decreases as the Reynolds number increases. Neither model predicts the same lift or drag levels as the experimental data, however. For the Re_c=10 million cases, the Baldwin-Lomax model is 17 drag counts low and the Baldwin-Barth model is 4 drag counts low. For the Re_c=30 million cases, the Baldwin-Lomax and Baldwin-Barth cases are 12 and 4 drag counts low, respectively and for the Re_c=80 million case, the Baldwin-Lomax case is 16 drag counts low while the Baldwin-Barth case is 6 drag counts low

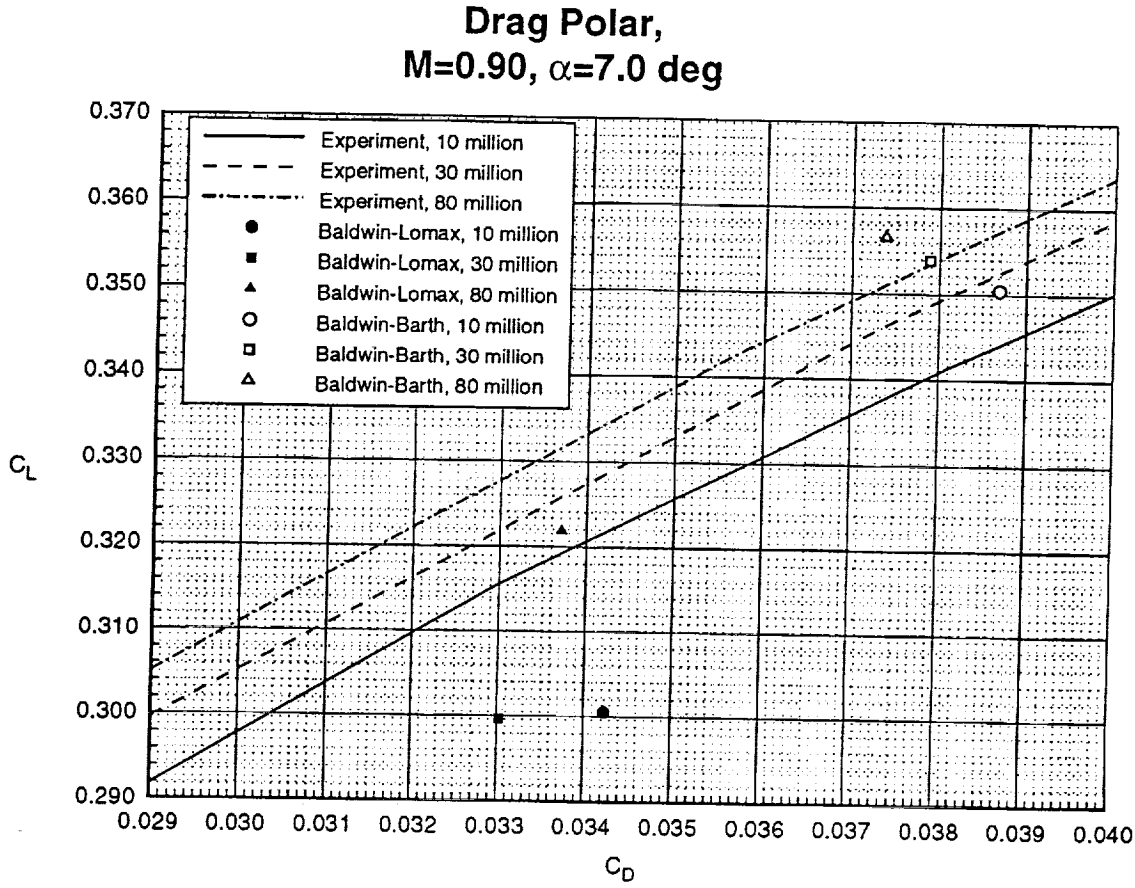

This figure shows that at α=7.0 deg, the Baldwin-Barth turbulence model does predict the same Reynolds number effect trend as the experimental data, which is that the drag level decreases as the Reynolds number increases, but the Baldwin-Lomax case does not predict the correct trend. Neither model predicts the same lift or drag levels as the experimental data. For the Re_c=10 million cases, the Baldwin-Lomax model is 38 drag counts high and the Baldwin-Barth model is 12 drag counts low. For the Re_c=30 million cases, the Baldwin-Lomax and Baldwin-Barth cases are 40 drag counts high and 12 drag counts low, respectively and for the Re_c=80 million case, the Baldwin-Lomax case is 17 drag counts high while the Baldwin-Barth case is 11 drag counts low.

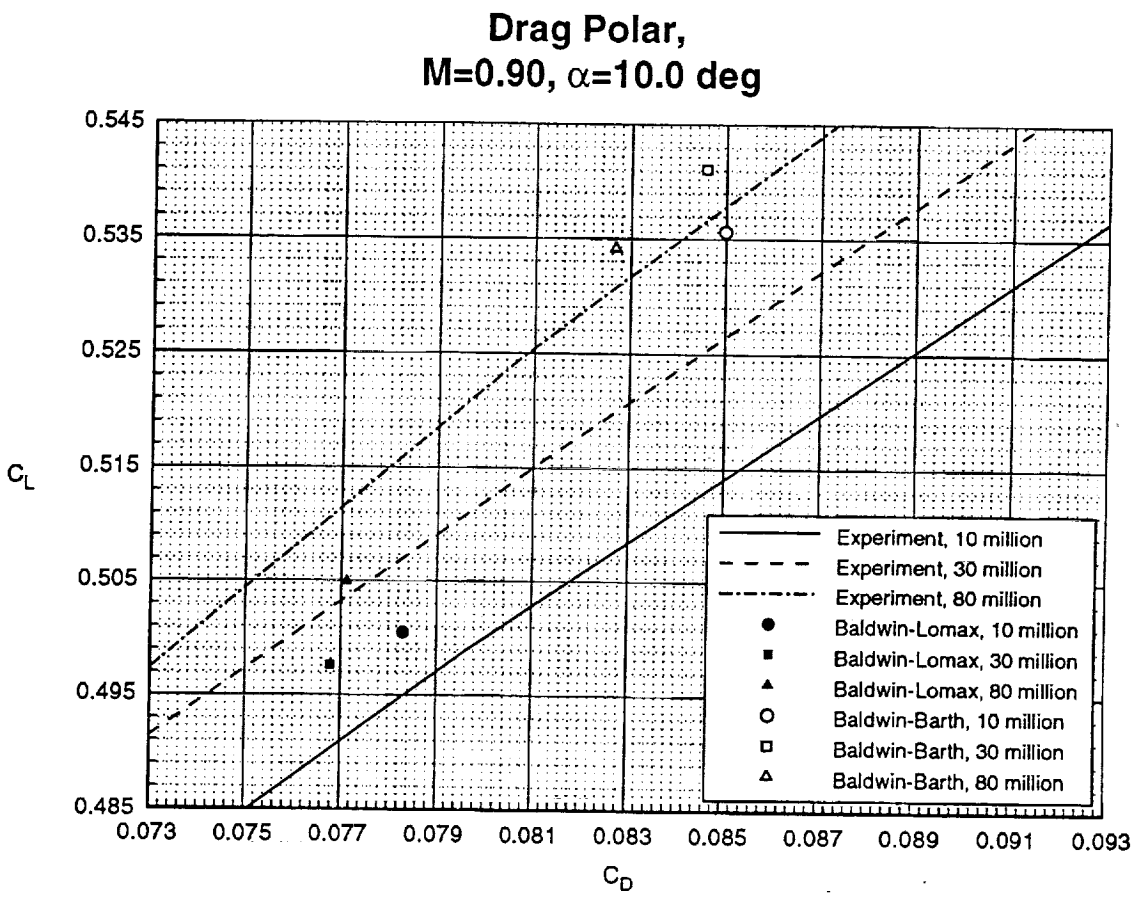

This figure shows that at α=10.0 deg, the Baldwin-Barth model predicts the same Reynolds number effect trend as the experimental data, which is that the drag level decreases as the Reynolds number increases; however, neither model predicts the same lift or drag levels as the experimental data. For the Re_c=10 million cases, the Baldwin-Lomax model is 18 drag counts low and the Baldwin-Barth model is 76 drag counts low. For the Re_c=30 million cases, the Baldwin-Lomax and Baldwin-Barth cases are 16 drag counts high and 56 drag counts low, respectively and for the Re_c=80 million case, the Baldwin-Lomax case is 20 drag counts high while the Baldwin-Barth case is 10 drag counts low.

Conclusions

- **Grid and Code Assessment Study**
  - **C-O topology, rather than O-C topology, preferred for this configuration**
  - **Detail of geometric modeling of the blunt to sharp leading-edge transition at the wing crank did not effect results**
  - **Distance function modification important, especially to Spalart-Allmaras and Menter's SST turbulence models**
- **Turbulence Model Study**
  - **Computed forces and pressures for the turbulence model study compared reasonably well with experiment, with Baldwin-Lomax and Baldwin-Barth showing best agreement**
- **Reynolds Number Effect Study**
  - **More work needs to be done to accurately determine the ability of CFL3D to predict the Reynolds number effects for this configuration**

In conclusion, the grid and code assessment study indicated that the C-O topology, rather than the O-C topology, is preferred for this configuration. The detail of the geometric modeling of the blunt to sharp leading-edge transition at the wing crank did not effect the results and the distance function modification was important, especially to the Spalart-Allmaras and Menter's SST turbulence models. The turbulence model study showed that the computed forces and pressure compared reasonably well with the experimental data, with the Baldwin-Lomax and Baldwin-Barth models showing the best agreement. The Reynolds number effect study indicated that more work needs to be done to accurately determine the ability of CFL3D to predict the Reynolds number effects for this configuration.

Critical Stability and Control Issues in High-Speed Aerodynamics for the HSCT

Douglas L. Wilson
Principal Engineer
HSCT Aerodynamics-Stability and Control
Boeing Commercial Airplane Group

Norman H. Princen
Senior Engineer
Stability, Control, and Flying Qualities Technology
Flight Performance
McDonnell Douglas Aerospace

Oran C. Harris
Sr. Specialist Engineer
Flight Control Group Technical Leader
Lockheed Martin Aeronautical Systems Co.

Abstract:

The stability and control issues in high speed aerodynamics of most significance for the development of a viable HSCT are identified, aned the status of the Ref. H configuration with respect to these issues is discussed. The interdependence between aerodynamic requirements and assumptions about airplane system functions such as Envelope Protection and Integrated Flight/Propulsion Control is highlighted.

The conclusions presented draw on results from the Ref. H Assessment and Alternate Control Concepts Assessment performed under Configuration Aerodynamics Subtask 5 during 1995.

Outline:

- **Role of Stability and Control in HSR and Configuration Aerodynamics**
- **General Observations on S&C Issues**
- **S&C Issues Specific to HSCT**
- **Implications for TCA**
- **Major Aerodynamic Technology Needs for S&C**
- **Specific Results of Ref. H Assessment**

Role of Stability and Control in HSR and Configuration Aerodynamics

Stability and Control Responsibilities Typically Include:

Flight Characteristics - Static and Dynamic (bare airframe)
Bare Airframe Stability Characteristics and Control Effectiveness
Stability and Control Requirements
Control Configuration
Control Surface Aerodynamic Hinge Moments
Aeroelastics ("Quasi-Steady") affecting Stability and Control characteristics
Propulsion Effects affecting Controllability
Handling Qualities (pilot-in-loop) (including "outer-loop" control laws)
Certification of Handling Qualities, Stability, and Control
Development of:
    6-DOF Aerodynamic/Elastic Database for Simulation
    (used for Flight Characteristics, Control Laws, & Handling Qualities)
Contribute to:
    Envelope Protection/Stall Warning
    Ice Effects
    Systems Design

Stability and Control Issues span many HSR Elements

In the HSR program these responsibilities are spread among 5 TMT's and 6 ITD's:

TMT's	ITD's
Aeroperformance	Config Aero
	High Lift
Flight Deck	Guidance & Flight Controls
Technical Integration	Technical Integration
Structures	Aeroelasticity & Structural Dynamics
Propulsion (CPC)	Propulsion Controls

Stability and Control Advisory Working Group (SCAWG) created to coordinate these activities

Members:

Dave Hahne	Nasa Langley	(HL ITD member)
Oran Harris	Lockheed Martin	
Paul Kubiatko *	McDonnell Douglas	
Naomi McMillin *	Nasa Langley	
Norm Princen	McDonnell Douglas	(GFC ITD member)
A. Tom Stephens	Boeing	(GFC ITD member)
Doug Wilson	Boeing	(CA ITD member)

* Associate members

General Observations on S&C Issues

Stability and Control Issues tend to be Constraints, not Optima

- Airplane must have safe flight characteristics and be certificable (constraints)
- Within these constraints, optimize economic utility by minimizing
  - Drag
  - Weight
  - Noise
  - Cost

Stability and Control "Design Points" tend to be at the corners of the envelope and in non-normal conditions.

- Large Angle-of-Attack
- Large Sideslip Angle
- High Speed/High "q" (Vd/Md)
- Low Speed (Cl max/Stall)
- Transonic Speeds
- Maneuver Conditions
- Ground Effect Conditions
- Crosswind/Windshear/Turbulence
- Aft or Fwd. c.g. limit, at Max or Min Weight
- Engine Failure / Inlet Unstart
- Reversionary Control States
- Failure Cases
- Emergency Procedures

For example, longitudinal stability requirements, which affect Cmo constraints, will probably be most critical in a lowest reversionary flight control mode at high transonic conditions.

--> **1-g cruise is generally not a critical design condition!**

S&C Issues Specific to HSCT

Aeroelastic Effects are more critical for HSCT than for Subsonic Transport

- Some control surfaces reverse elastically (including elevator)
- Basic stability (CM/CL) changed significantly due to aeroelastics--
  a.c. shift can be greater than allowable c.g. range

--> **Elastic effects MUST be considered--rigid aerodynamic results are not meaningful by themselves for high speed conditions.**

Structural Dynamics Influence Handling Qualities and Control Laws

- First body bending mode is at low frequency ~ 1.3 Hz (TBV)
- Interacts with pilot, control system
- May require greater "quasi-static" stability (more forward c.g.) from airframe for control system to perform as required.
- Handling Qualities assessment and Control Law analysis MUST include structural modes.
- Limits of instability not yet determined in presence of dynamic modes (PCD2 work)

--> **We don't yet know the limits on Cm/Cl or Cmo**

Heavy Dependence on "Flight Systems" in baseline HSCT

- Flight-critical stability augmentation in 3 axes
- Flight-critical envelope protection
- Flight-critical c.g. control (slow)
- Integrated flight/propulsion control
- Programmed flaps (function of M, alpha, ...?)

--> **If these functions are not feasible, aerodynamic solutions will be required, causing performance impact.**

S&C Implications of TCA Configuration

TCA Controls are sized for low-speed criteria, not high-speed stability

- High AoA Recovery
- Takeoff Rotation
- Go-Around
- Tip-Up (nosegear liftoff)
- Vmcg
- Cross-wind landing

--> **Acceptability of TCA for high-speed stability and control is unknown.**

TCA is generally "Worse" for S&C than Ref. H

- Higher outboard sweep causes greater aeroelastic losses
- Longer body causes greater aeroelastic losses and lowers frequency of bending modes.
- Larger inboard wing causes more pitchup (TBV)
- Ailerons & spoilers are thinner, more swept, less effective

--> **Ref. H results should be viewed as "optimistic" with respect to TCA**

Major Aerodynamic Technology Needs for Stability and Control

Improved CFD Capability for "Off-Cruise" Conditions

- Dependence on wind tunnel creates long design cycle-time, limits understanding
- Current CFD tools do not efficiently address many S&C design areas:
  - high alpha & beta
  - control effectiveness
  - lateral-directional characteristics
  - unsteady aerodynamics
  - dynamic stability derivatives
- Many current CFD development/application efforts (multi-block grids, adaptive grids,...) are moving toward meeting these needs.

Reduced Cycle Time for Aeroelastic Predictions

- Faster turn around in aeroelastic analysis is needed to design for acceptable high-speed S&C characteristics.
- Improvements needed in cycle time for structural modelling and interface with aerodynamic codes
- ACE efforts will help address these needs

BHN, 12 Feb 96

Model TCA

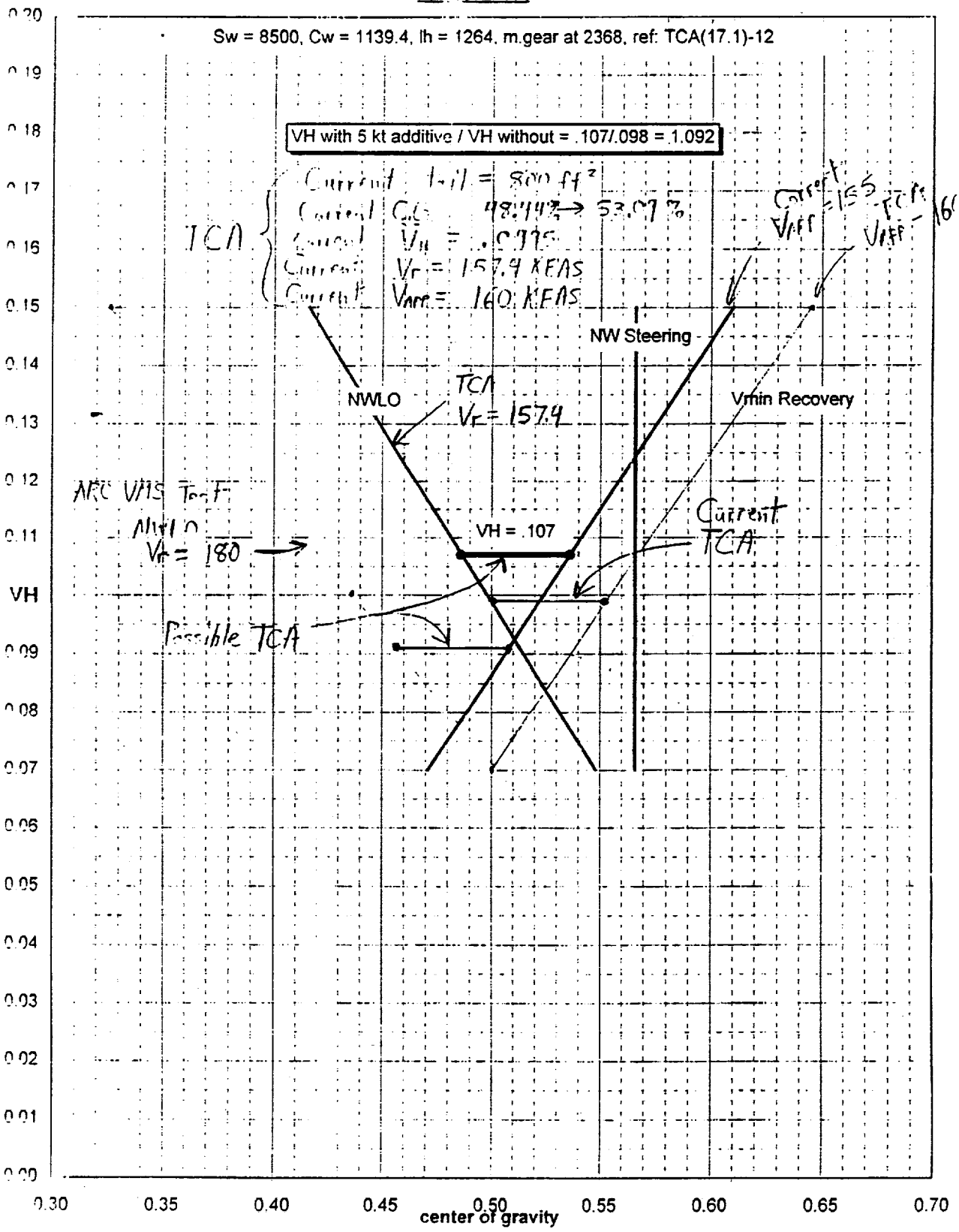

UPWT RESULTS
Alternate Control Concepts

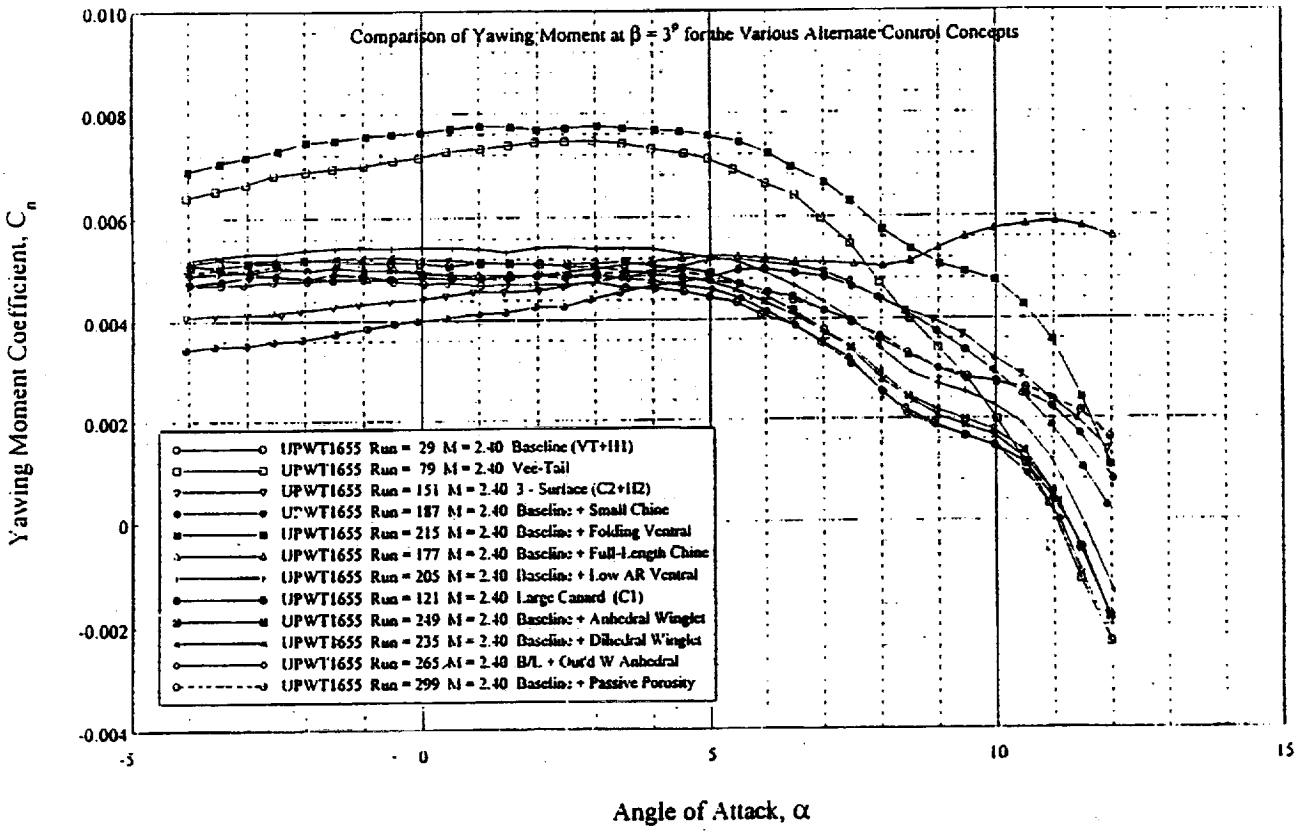

UPWT RESULTS
Alternate Control Concepts

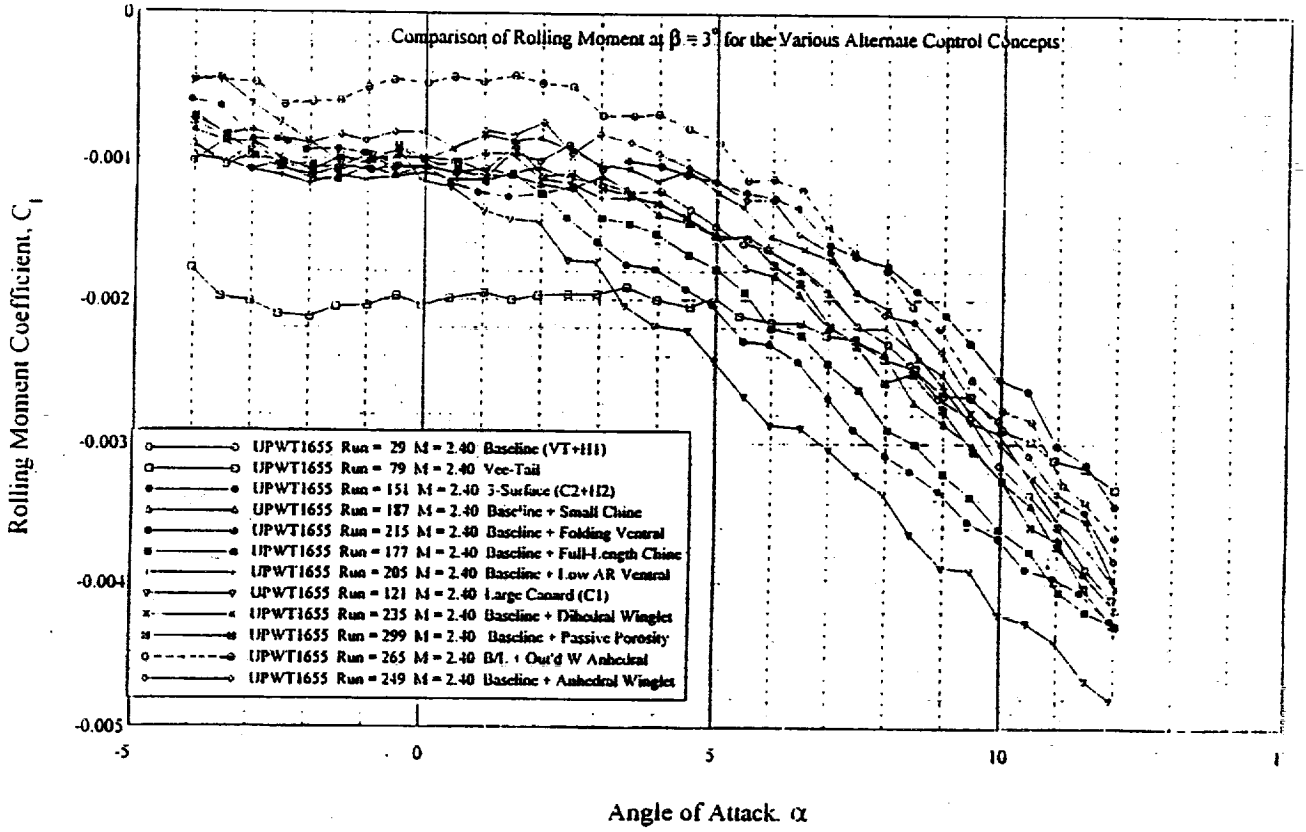

Trim with Maximum Thrust

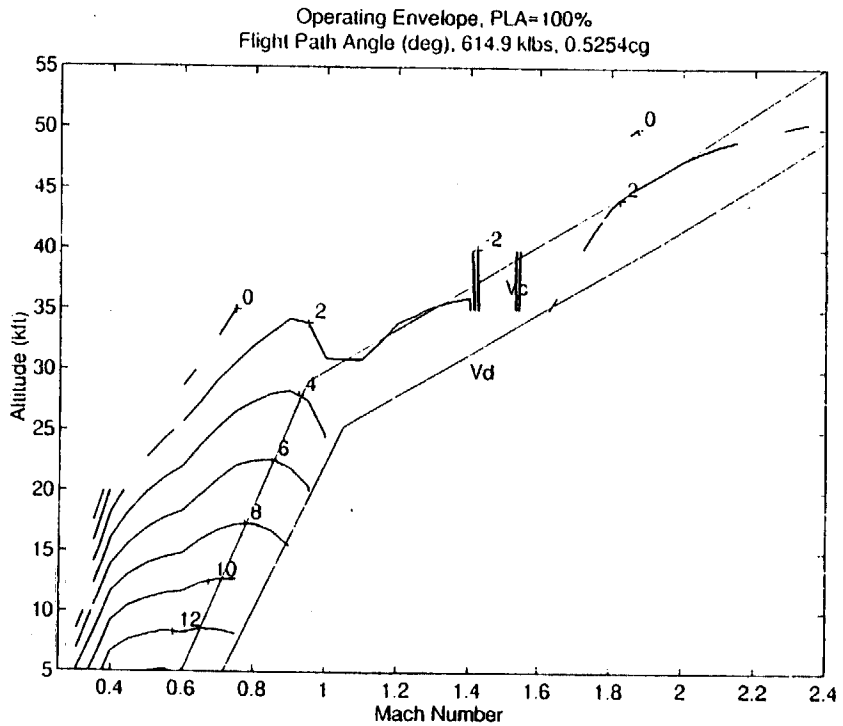

- There is an engine model singularity at M = 1.5.

Speed Brake Capability

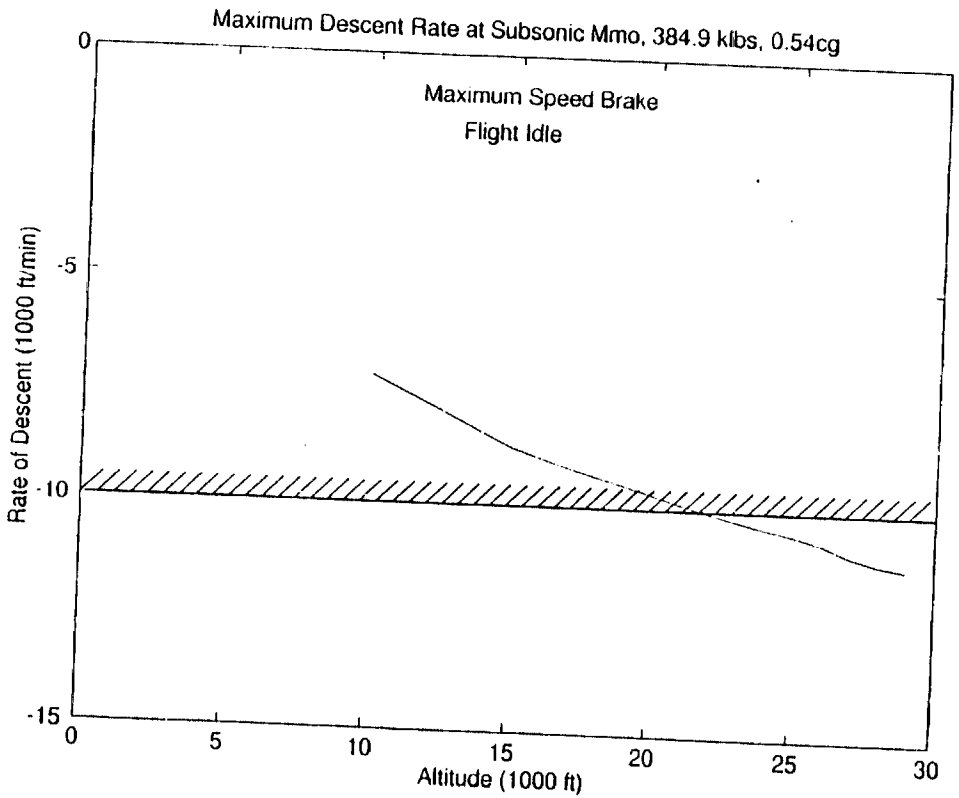

- 10,000 ft/min descent rate requirement **NOT** met.

Crosswind Landing

- At landing condition, must be able to decrab with a 35 knot crosswind.
- Case checked:
  - End of cruise weight = 384.9 klbs
  - Aft C.G. = 53.2%
  - Automatic approach LE/TE flaps = 35.5/9.0
- Results:
  - Sideslip = 12.2 degrees, Bank Angle = 5.8 degrees
  - Rudder = 7.8 degrees, Not rudder limited
  - Ailerons = $\pm$30 degrees, No maneuvering authority
- Does **NOT** meet requirement.

Roll Performance

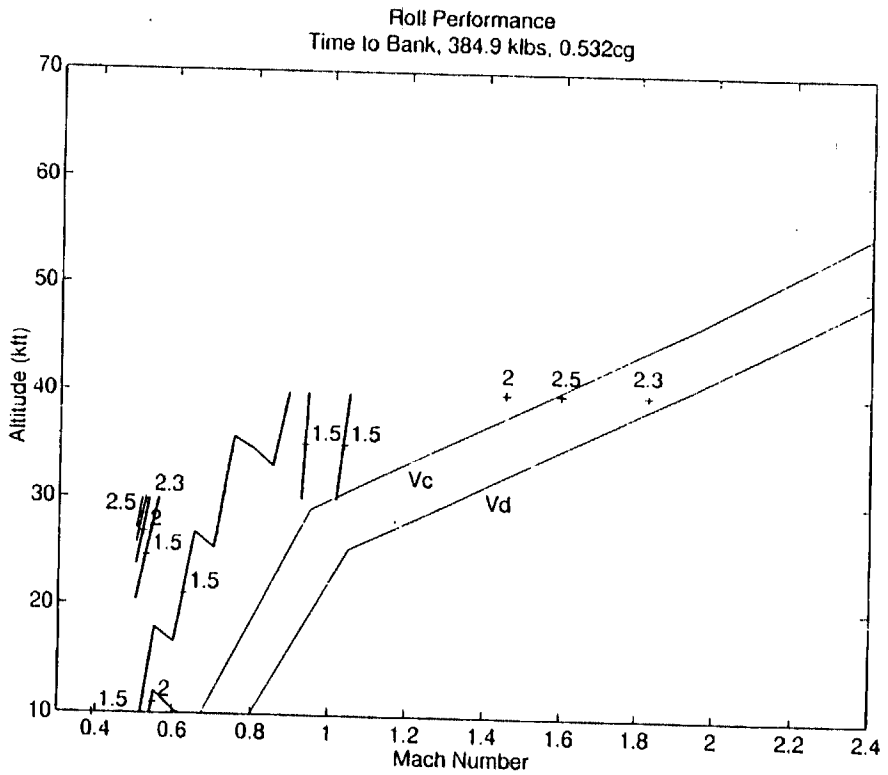

- Requirement of < 2.3 sec time to bank **NOT** met.

HDR-AT-[illegible]
Attachment 1

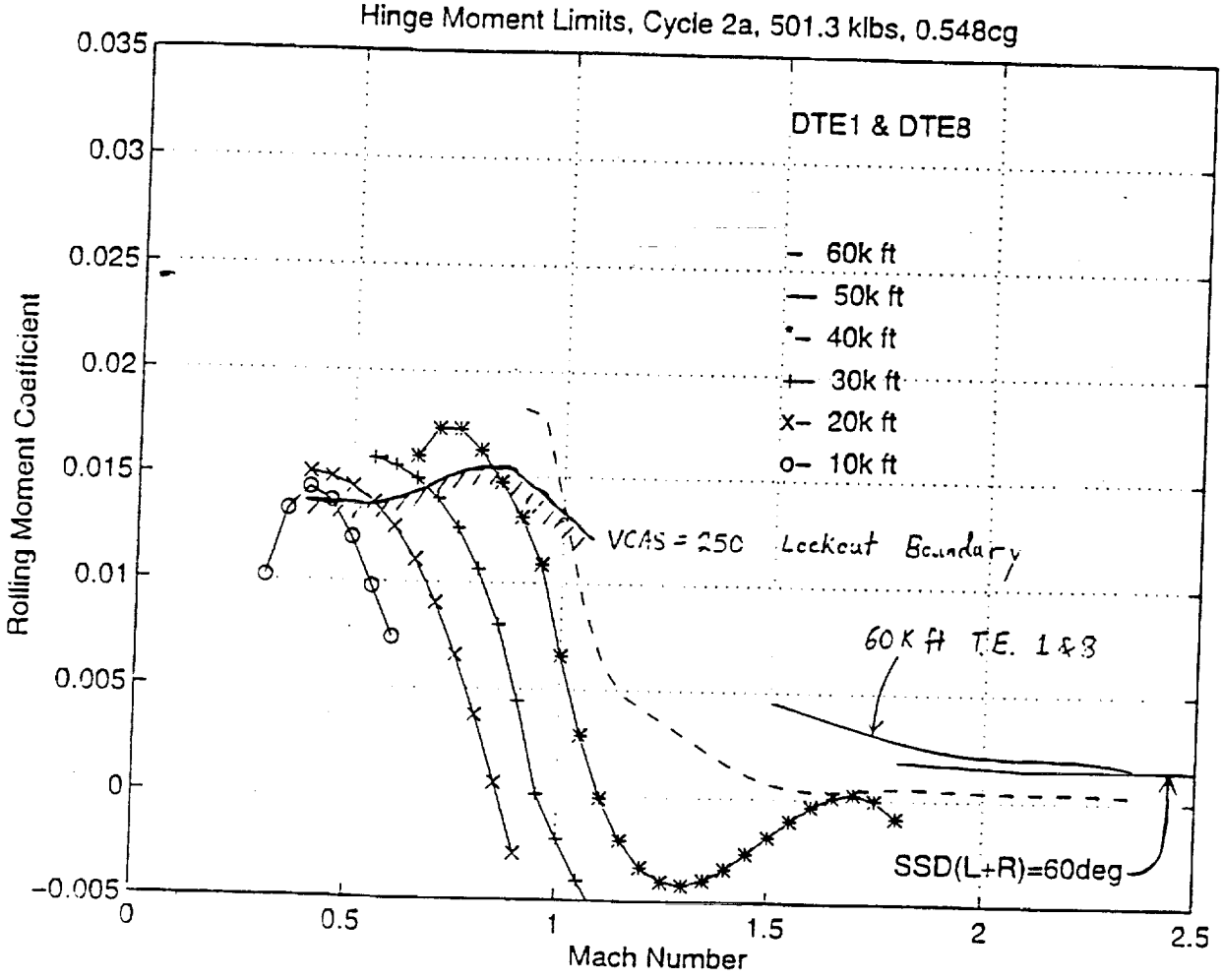

HSR-HT-TO-016
Attachment 3

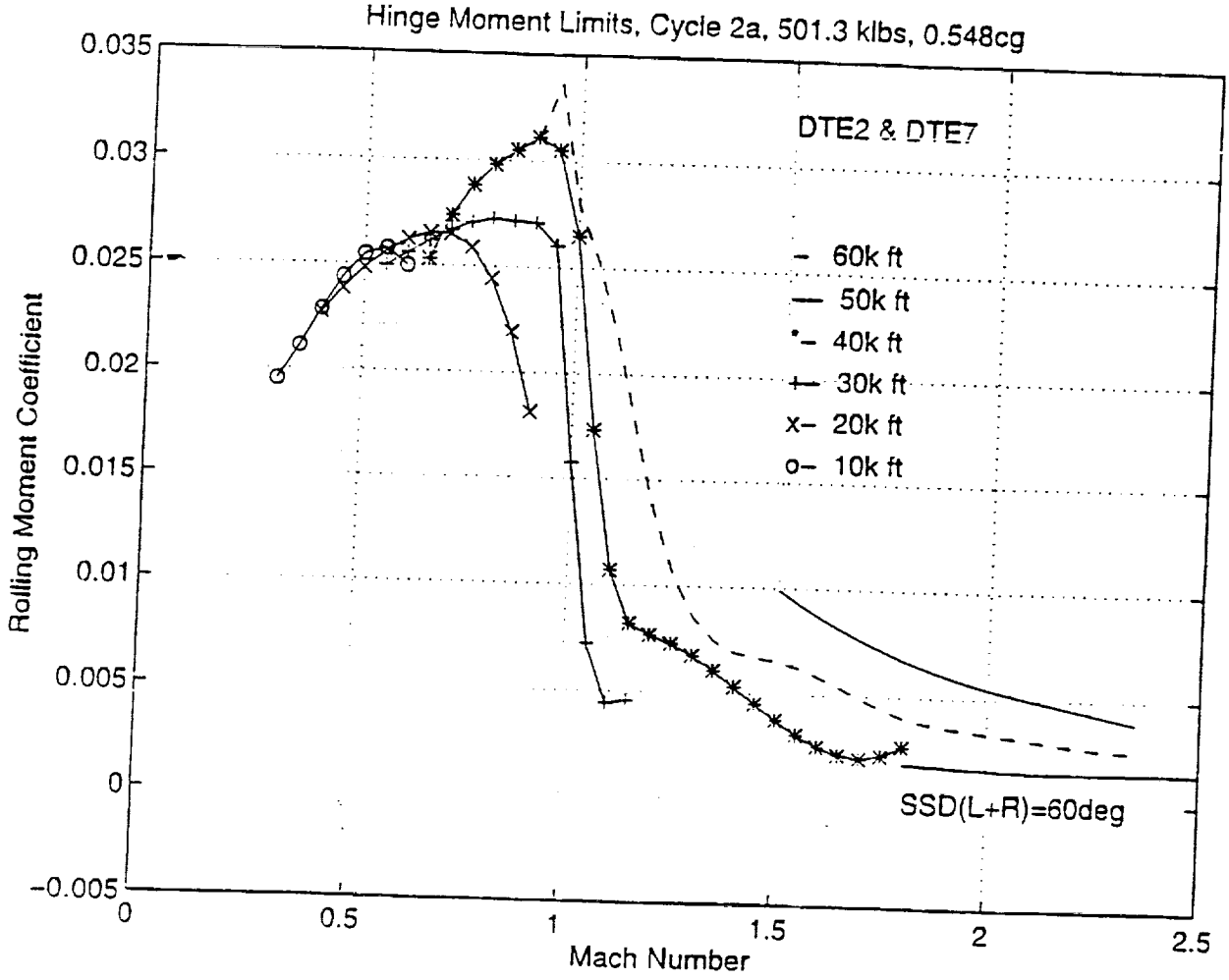

Recommendations

- Drag devices on the HSCT must be increased in size, not decreased, as they were on the TCA.
- Pitch control must be increased for adequate Vmin Recovery and may need to be even larger to meet the Pitch Recovery Requirement.
- Roll control must be increased over the Ref. H baseline.
- The engines must increase in size so there is an adequate thrust margin throughout the operational flight envelope.
- Engine sensitivity to maneuver transients must be decreased to prevent unstart.
- Future assessments should decouple assessing the basic airframe from assessing the engines.
- Future assessments should assess fixes to problems.

An Experimental Database for Conventional and Alternate Control Concepts on the HSR 1.675% Reference H Model

Naomi McMillin, Jerry Allen, Gary Erickson, Jim Campbell, Mike Mann
NASA Langely Research Center

Paul Kubiatko and David Yingling
McDonnell Douglas Aerospace

Charlie Mason
Lockheed/Martin

High-Speed Research Configuration Aerodynamics Workshop
NASA Langley Research Center
February 27-29, 1996

Objective

The objective was to experimentally evaluate the longitudinal and lateral-directional stability and control characteristics of the Reference H configuration at supersonic and transonic speeds. A series of conventional and alternate control devices were also evaluated at supersonic and transonic speeds. A database on the conventional and alternate control devices was to be created for use in the HSR program.

Objectives

- To experimentally evaluate the longitudinal and lateral-directional stability and control characteris tics of the Reference H configuration at supersoni and transonic speeds.
- To experimentally evaluate a series of conventiona and alternate control devices at supersonic and transonic speeds.
- To develop a stability and control database on conventional and alternate control devices for us in the HSR program.

Approach

To experimentally evaluate the stability and control characteristics of the Reference H configuration, the 1.675% HSR Ref H model was tested in the Langley Unitary Plan Wind Tunnel (UPWT) and the Langley 16 Ft. Transonic Tunnel (16' TT). The UPWT testing was conducted at M = 1.8, 2.1, 2.4, and 2.7, Re = 3 x 106 /ft., $\alpha = -4^{\circ}$ to 12°, and $\beta = -6^{\circ}$ to 6°. The 16' TT testing was conducted at M = 0.6, 0.85, 0.9, 0.95, 0.98, and 1.20, Re = 3.1 x 10^6 to 3.98 x 10^6 /ft., $\alpha = -4^{\circ}$ to 12°, and $\beta = -6^{\circ}$ to 6°. The Reference H model with a cylindrical aftbody, horizontal and vertical tails, and wing mounted engine nacelles was the baseline configuration. A component build-up was conducted to evaluate mutual interference effects. Testing was conducted in two phases - conventional control concepts and alternate control concepts.

Approach

- **Langley Unitary Plan Wind Tunnel (UPWT)**
  - **M = 1.8, 2.1, 2.4 and 2.7**
  - **Re = 3 x 10^6 /ft**
  - **$\alpha = -4^{\circ}$ to 12°, $\beta = -6^{\circ}$ to 6°**
- **Langley 16 FT Transonic Tunnel (16' TT).**
  - **M = 0.6, 0.85, 0.90, 0.95, 0.98, 1.2**
  - **Re = 3.1 x 10^6 to 3.98 x 10^6 /ft**
  - **$\alpha = -4^{\circ}$ to 12°, $\beta = -6^{\circ}$ to 6°**
- **Baseline configuration was the Ref H model with a cylindrical aftbody, horizontal and vertical tails, and wing mounted engine nacelles.**
- **A component build-up was conducted to evaluate mutual interference effects.**
- **Testing was conducted in two phases - Conventional Controls and Alternate Controls.**

Conventional Control Concepts

The HSR 1.675% Reference H Controls model was tested to evaluate conventional control concepts. The baseline configuration was the cylindrical extended aftbody, vertical and horizontal tails, and wing mounted engine nacelles.The wing mounted engine nacelles were removable and capable of being blocked with plugs. The model had two aftbodies - a truncated aftbody an a cylindrical extended aftbody. The control devices available on the model were the rudder (δ_r = 0°, 10°, and 20°), horizontal tail incidence (δ_{H1} = -15° to 15° in 3 increments), elevators $\delta_{e,H1}$ = 0°, ±10°, and ±20°), outboard wing leading-edge flaps (δ_{LE} = 0°, 4°, 8°, and 10°), trailing-edge flaps (δ_{TE} = 0°, ±3°, ±6°, ±10°, ±20° and ±40°), and spoiler/slot/deflectors (δ_{SSD} = 0°, ±20°/±30°, and ±40°/±60°).

Conventional Control Concepts

HSR 1.675% Ref H Controls Model

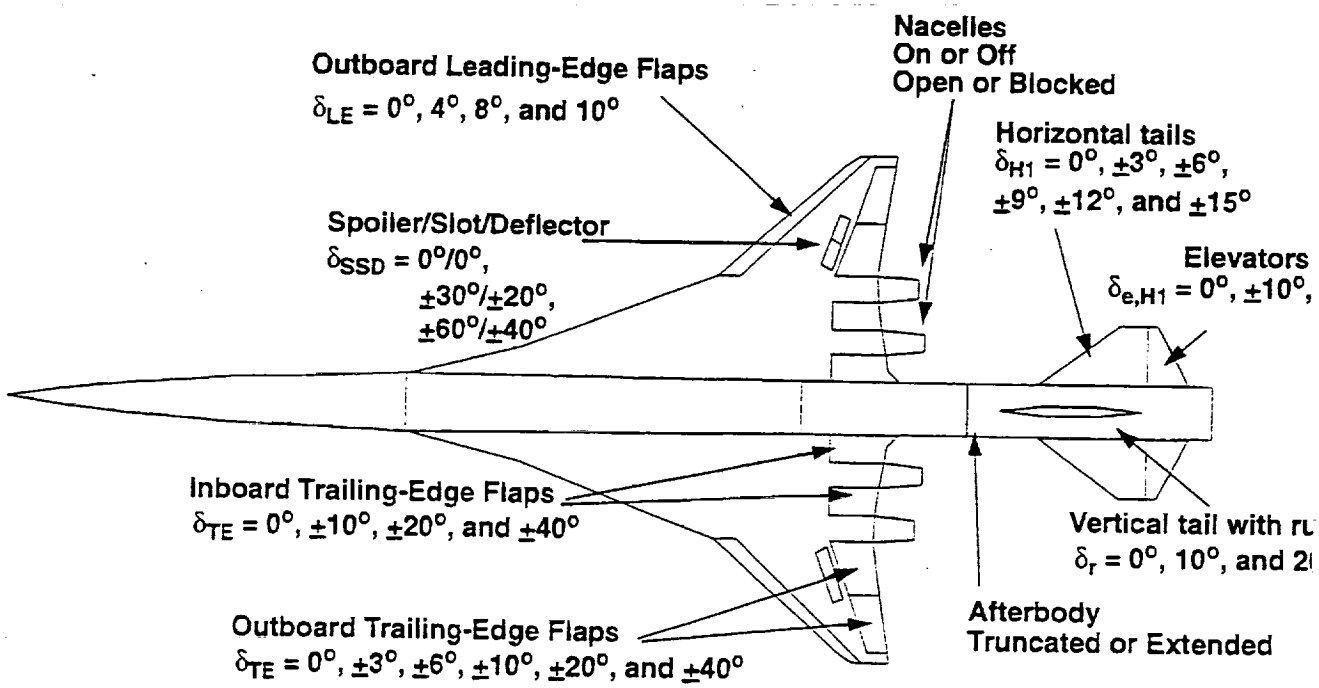

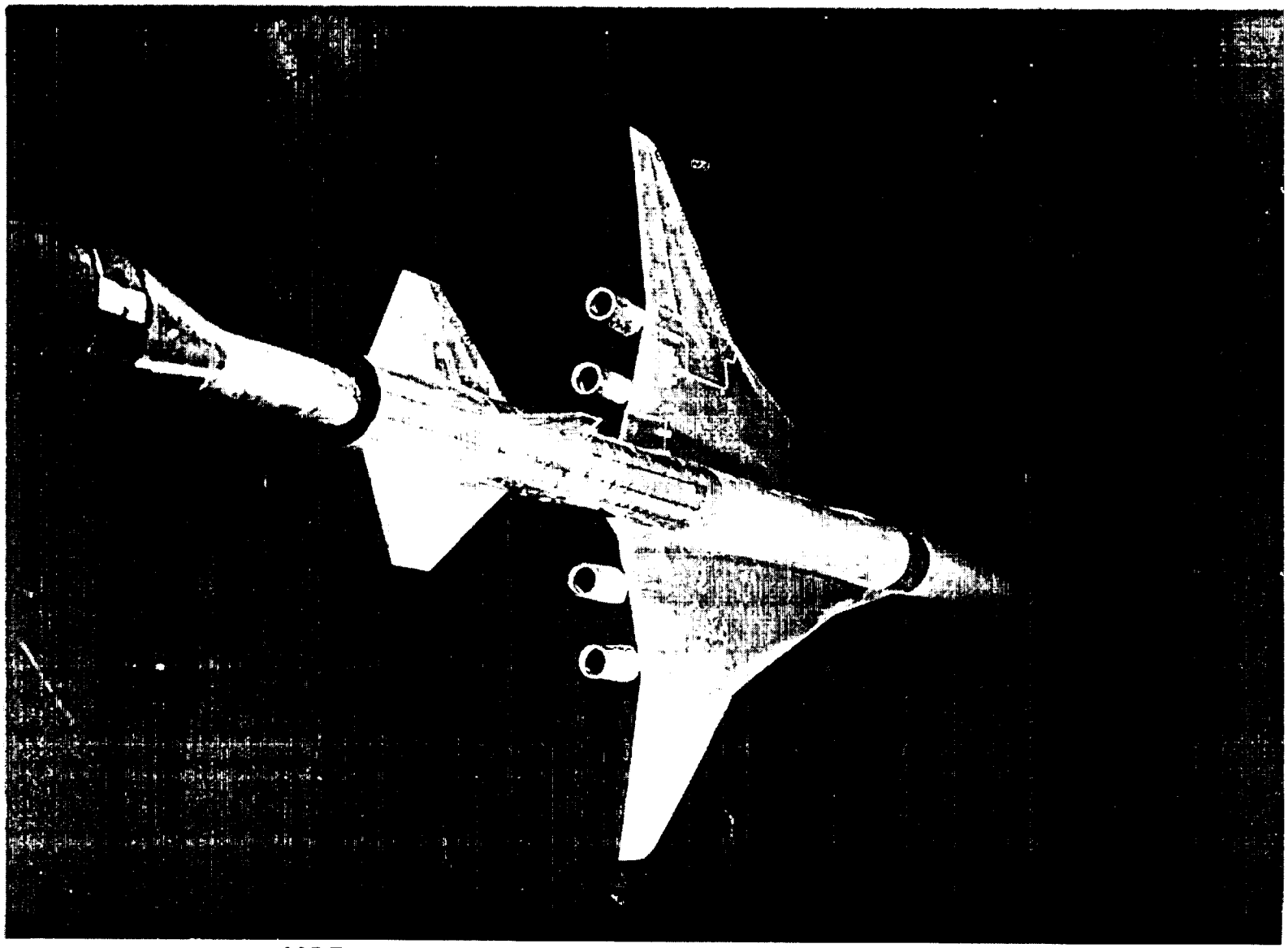

HSR 1.675% Reference H Controls Model - 16' TT

The HSR 1.675% Reference H Controls model installed in the Langley 16 Ft. Transonic Tunnel. The photograph shows the baseline configuration - extended aftbody, vertical and horizontal tails, and wing mounted engine nacelles.

Data Summary for the HSR 1.675% Reference H Controls Model

Data was collected on twelve concepts on the HSR 1.675% Reference H Contrc model in the Langley UPWT and 16' TT. The twelve concepts examined were tl truncated aftbody, baseline, component build-up, blocked nacelles, blocked nacelles with various control devices, symmetrical trailing-edge flaps, differentia trailing-edge flaps, leading-edge flaps, stabilizer (horizontal tail incidence), elevators, rudder, and spoiler/slot/deflector. In UPWT 464 polars were obtained c 77 configurations. In 16' TT, 323 polars were obtained on 44 configurations. No data was obtained on blocked nacelles or spoiler/slot/deflectors in the 16' TT.

Data Summary for the HSR 1.675% Ref H Controls Model

Concept	UPWT M = 1.8, 2.1, 2.4, 2.7 Re = 3 x 10^6 /ft			16' TT M = 0.6, 0.85, 0.9, 0.95, 0.98, 1.2 Re = 3.1 x10^6 to 3.98 x10^6 /ft		
	α Polars	β Polars	# of config.	α Polars	β Polars	# of config.
Truncated Afterbody	Nac. On, δ_{TE} = 0°, 3°, δ_{LE} = 0°, 4°			Nac. Off, δ_{TE} = 0°,3°, δ_{LE} =0°, 4°, 8°, 10°		
	16 (13)	6 (2)	4	28 (29)	0	5
Baseline	Nac. On, Extended Aftbody, Vertical and Horizontal Tails On					
	10 (8)	12 (8)	1	12 (19)	18 (13)	1
Component Build-up	Nacelles On/Off, Tails On/Off			Nacelles On, Tails Off		
	24	24	4	6	18	1
Blocked Nacelles	RHS Inbd, Outbd, or Both Blocked, Tails On/Off			No Data		
	16	26	4			
Blocked Nacelles With Various Control Devices	RHS Inbd, Outbd, or Both Blocked, Tails On/Off			No Data		
	36	14	10			
Symmetrical Trailing-Edge Flaps	Nac. On/Off,Tails On/Off, δ_{TE} = 10°			Nac. On, Tails On/Off, δ_{TE} = 10° and 20°		
	28 (4)	30	4	21	0	4
Differential Trailing-Edge Flaps	Tails On/Off, δ_{TE} = ±10°			Tails On, δ_{TE} = ±10°, ±40°		
	72	0	18	102 (1)	0	17
Leading-edge Flaps	Tails On/Off, δ_{LE} = 10°,δ_{TE} = 0°, 10°			Tails On/Off, δ_{LE} = 10°,δ_{TE} = 0°, 3°		
	16	0	5	24	0	4
Stabilizer	δ_{H1} = ±6°, ±15°, δ_{LE} = 0°, δ_{TE} = 0° and 10°			δ_{H1} = ±6°, ±9°, δ_{LE} = 0°, 10°, δ_{TE} = 0°, 3°,10°, 20°		
	38	12	10	49	0	8
Elevator	$\delta_{e,H1}$ = ±20°			$\delta_{e,H1}$ = ±20°		
	8	0	2	12	0	2
Rudder	δ_r = 20°			δ_r = 10° and 20°		
	8	12	1	9	27	2
Spoiler/Slot/Deflector	δ_{SSD}=0°, 30°/20°,60°/40°			No Data		
	46	10	14			
Total	318 (25)	146 (10)	77	263 (49)	63 (13)	44

Repeatability of the Longitudinal Coefficients Obtained on the HSR 1.675% Reference H Controls Model

Data obtained on the baseline configuration (extended aftbody/nacelles/tails) were used to determine the repeatability of the longitudinal coefficients in the testing conducted on the conventional control concepts. The repeatability numbers obtained are based on data scatter between 3 to 5 polars at $-0.10 \leq C_L \leq 0.25$. The UPWT data show that for $1.8 \leq M \leq 2.7$, the repeatability of C_D was less than one drag count, the repeatability of $C_L < 0.0008$, and the repeatability of $C_m < 0.0008$. The 16' TT data show that for $0.6 \leq M \leq 1.2$, the repeatability of C_D varied from ± 0.0002 to ± 0.00035 dependent on Mach number with the higher repeatability number occurring at M = 0.98 where the tunnel flow is more unsettled. Similarly, the repeatability of C_L varied from ± 0.0015 to ± 0.003. The repeatability of C_m was ± 0.0005 across the Mach number range in 16' TT.

HSR 1.675% Ref H Controls Model
Repeatability* of the Longitudinal Coefficients at $-0.10 \leq C_L \leq 0.25$

Based on the Extended Aftbody/Nacelles/Tails Configuration

M	C_D	C_L	C_m
Langley 16' TT			
0.60	±0.0003	±0.0015	±0.0005
0.85	±0.0002	±0.002	±0.0005
0.9	±0.0003	±0.002	±0.0005
0.95	±0.0003	±0.002	±0.0005
0.98	±0.00035	±0.003	±0.0005
1.2	±0.0003	±0.002	±0.0005
Langley UPWT			
1.8	±0.00008	±0.0008	±0.0008
2.1	±0.00005	±0.0005	±0.0005
2.4	±0.00005	±0.0005	±0.0005
2.7	±0.00008	±0.0008	±0.0005

* Based on observed data scatter between 3 to 5 polars

Selection of Alternate Control Concepts

The selection of the alternate control concepts to be tested was conducted through a team effort with personnel from NASA Langley Research Center, Boeing, McDonnell Douglas, and Lockheed/Martin. The team agreed to a rating process involving the categories of longitudinal control, lateral control, directiona control, longitudinal stability, lateral stability, directional stability, angle of attack range, Mach number range, Reynolds number sensitivity, elasticity, design maturity, and effectiveness. Through group consensus, each concept was given a rating of 1, 2, or 3 in each category. A rating of 3 indicated that the concept yielde large benefits in that category. Each rating was multiplied by a weight factor (shown in the viewgraph) and then all ratings for a given concept were summed.

Selection of Alternate Control Concepts

- The various concepts were selected through a rating process.
- Several categories were selected for consideration.
- Each concept was given a rating of 1, 2, or 3 in each category. A rating of 3 indicated that the concept yielded large benefits in that category.
- Each rating was reached by consensus between the HSR participants.
- Each rating was multiplied by a weight factor and then all ratings for a given concept were summed.

Category	Weight Factor	Category	Weight Factor
Longitudinal Control	3	Angle of Attack Range	3
Lateral Control	3	Mach Number Range	3
Directional Control	3	Reynolds Number Sensitive	2
Longitudinal Stability	1	Elasticity	2
Lateral Stability	3	Design Maturity	2
Directional Stability	2	Effectiveness	3

Prioritized Alternate Control Concepts

The ten alternate control concepts selected are given in prioritized order: butterfly tails, all-flying vertical tail, canards, 3-surface (canard/horizontal/vertical tail), ventrals (low aspect ratio and folding), chines (small and full-length), winglets, outboard wing with 5° anhedral, 10o split trailing-edge flaps, and passive porosity forebody.

Prioritized Alternate Control Concepts

1. **Butterfly Tails**
2. **All-Flying Vertical Tail**
3. **Canards**
4. **3-Surface (Canard/Horizontal Tail/Vertical Tail)**
5. **Ventrals - Low Aspect Ratio and Folding**
6. **Chines - Small and Full-length**
7. **Winglets**
8. **Outboard Wing with 5° Anhedral**
9. **10° Split Trailing-Edge Flaps**
10. **Passive Porosity Forebody**

Alternate Control Concepts

The HSR 1.675% Reference H Alternate Controls Model was built to accommodate all ten alternate control concepts. This model is a modification to the Controls Model. A new aftbody was built to accommodate the all-flying vertical tail, the butterfly tails, and the ventrals. A new forebody was built with removable side panels so as to accomodate the canards, the 3-surface concept, the chines, and the porous forebody. The outboard wing panel was already removable such that new panels could be built to accommodate the winglets, the 10° split trailing-edge flaps, and the 5° anhedral wing.

Alternate Control Concepts
HSR 1.675% Ref H Alternate Controls Model

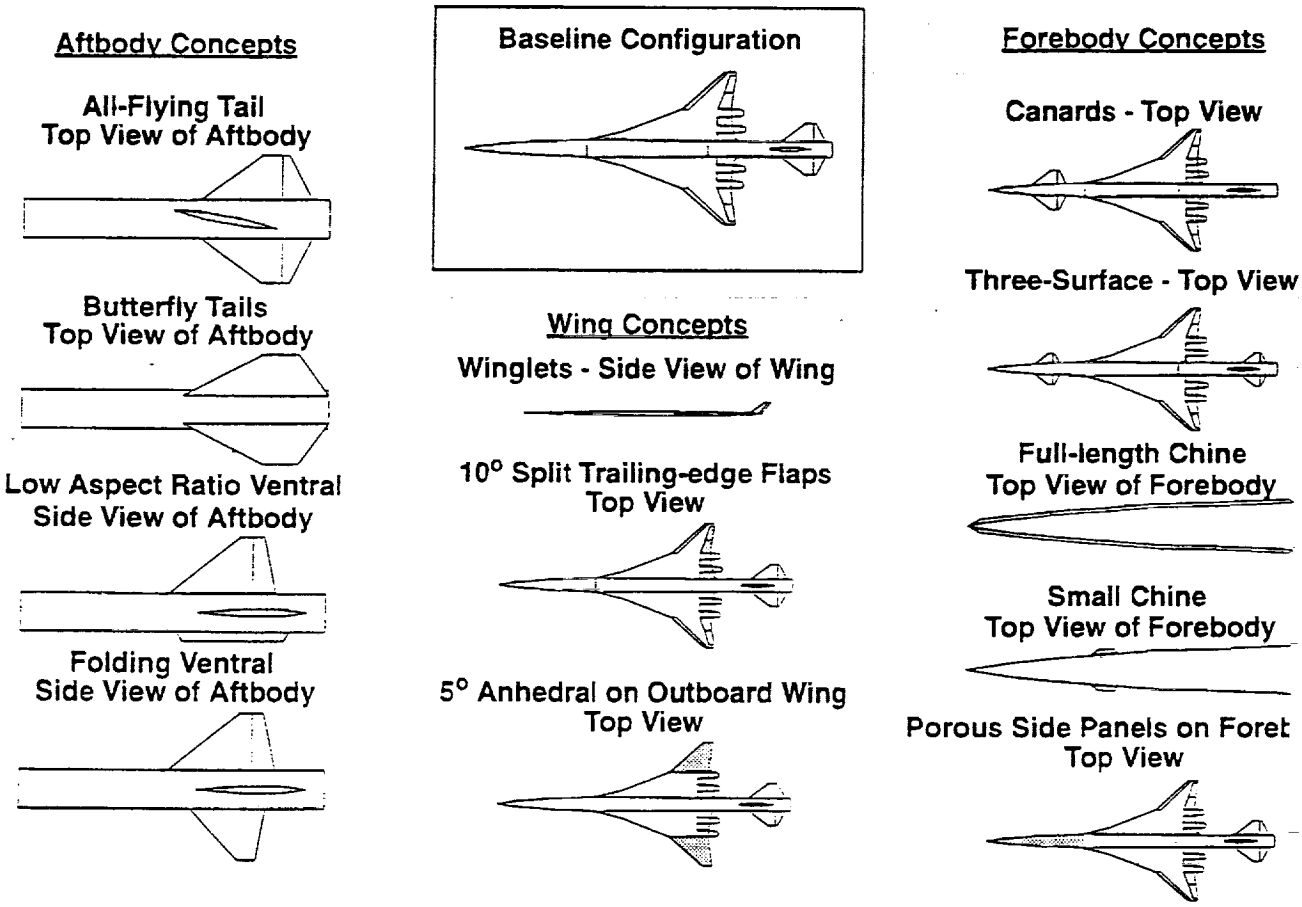

HSR 1.675% Reference H Alternate Control Model Aftbody Concepts

The three alternate control concepts employed on to the aftbody of the model are the all-flying tail, the butterfly tails, and the ventrals. The all flying vertical tail had incidence settings of 0°, ±5°, and ±10°. The butterfly tails were canted at 45° on the aftbody. The butterfly tails had incidence settings of 0°, ±5°, and ±10°. The butterfly tails also had elevators with deflection angles of 0° and ±10°. Two designs were chosen for the ventral concepts. The first was a low aspect ratio ventral which is small compared to the vertical tail. The second was a folding ventral that when folded out in flight would be much larger than the low aspect ratio ventral.

HSR 1.675% Ref H Alternate Controls Model - Aftbody Concepts

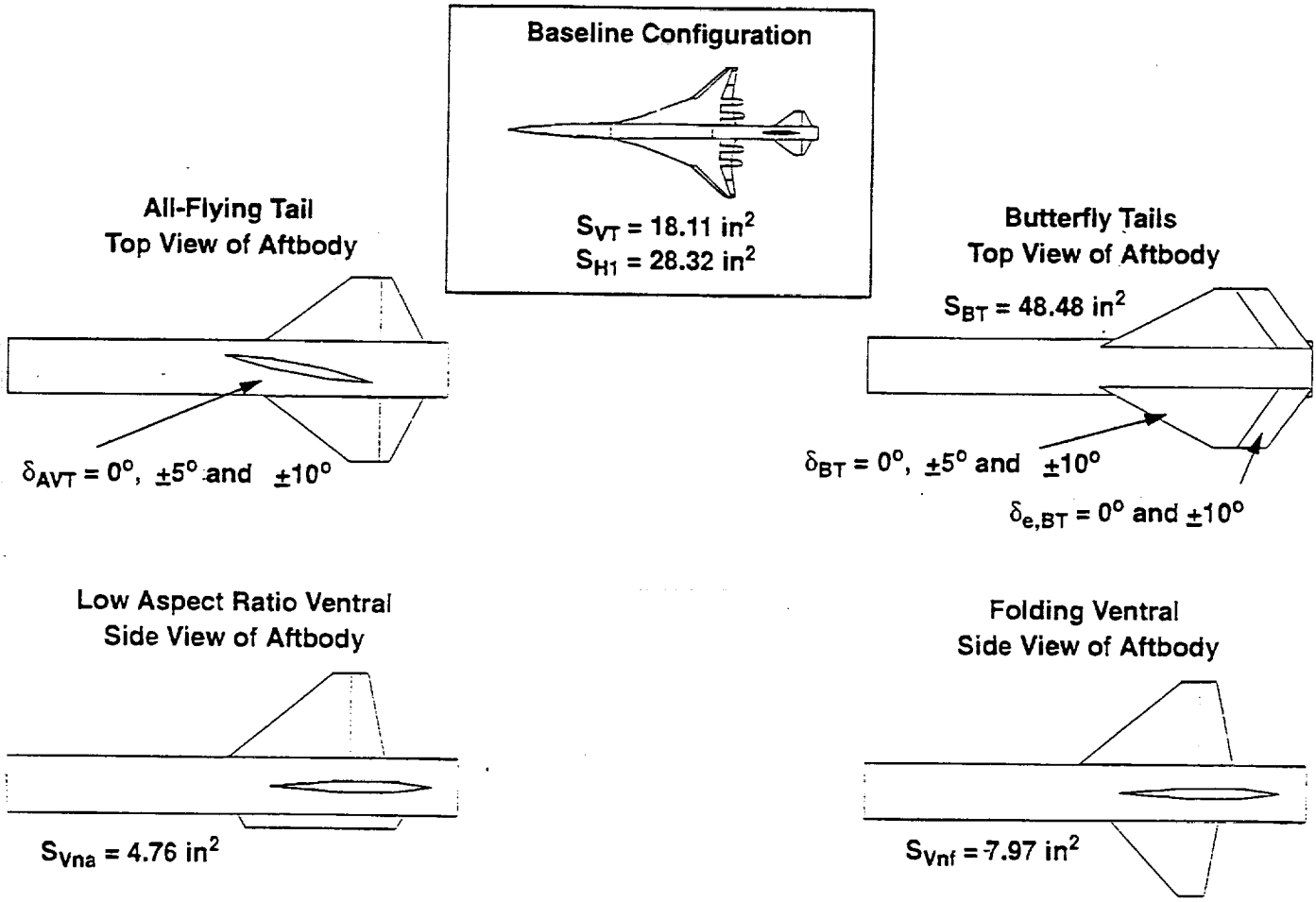

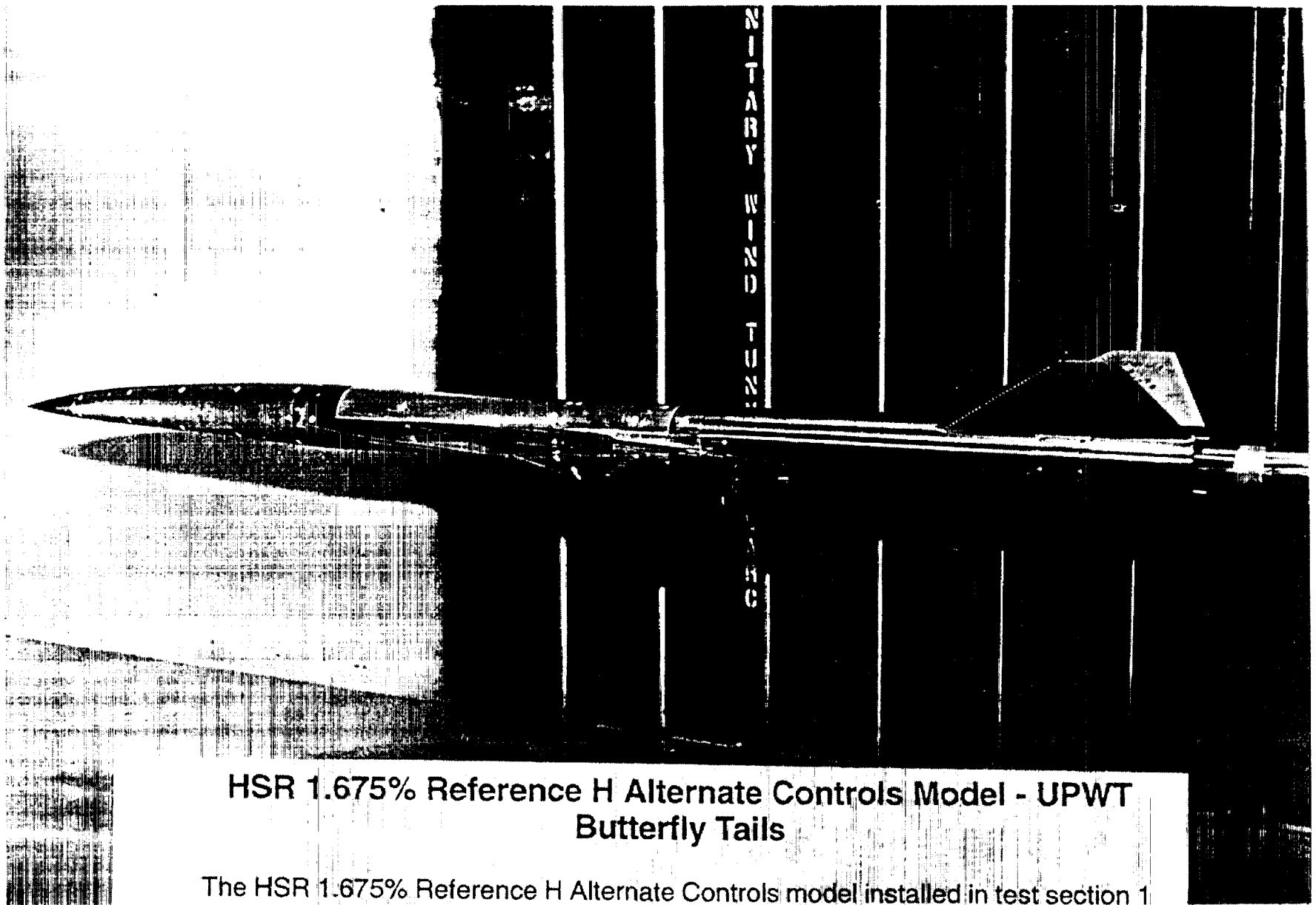

HSR 1.675% Reference H Alternate Controls Model - UPWT Butterfly Tails

The HSR 1.675% Reference H Alternate Controls model installed in test section 1 of the Langley Unitary Plan Wind Tunnel. The photograph shows the butterfly tails configuration with the butterfly tails at 0^{o} incidence.

HSR 1.675% Reference H Alternate Control Model Forebody Concepts

The three alternate control concepts employed on to the forebody of the model are the canards, 3-surface, chines, and porous forebody. The canards had an area comparable to the baseline horizontal tails, were employed without any horizontal tails, and had wiping surfaces. The canards had incidence settings of 0°, -10°, and -20° and elevators with deflection angles of 0° and $\pm 20^{\circ}$. The 3-surface concept was a small canard/small horizontal tail/vertical tail arrangement. The small canard is approximately 1/2 the size of the canard on the canards only concept. The small canards had incidence settings of 0°, 5°, -10°, and -20° and elevators with deflection angles of 0° and $\pm 20^{\circ}$. The small horizontal tail is approximately 1/2 the size of the baseline horizontal tail. The small horizontal tail had incidence settings of 0°, $\pm 6^{\circ}$, $\pm 9^{\circ}$, and $\pm 15^{\circ}$ and elevators with deflection angles of 0° and $\pm 20^{\circ}$. Two designs were chosen for the chines concept. The first was a full-length chine extending from the body nose to the inboard wing leading-edge. The second design was a small chine. The porous forebody concept consisted on porous side panels with 22% porosity. A plenum is present with this concept.

HSR 1.675% Ref H Alternate Controls Model - Forebody Concepts

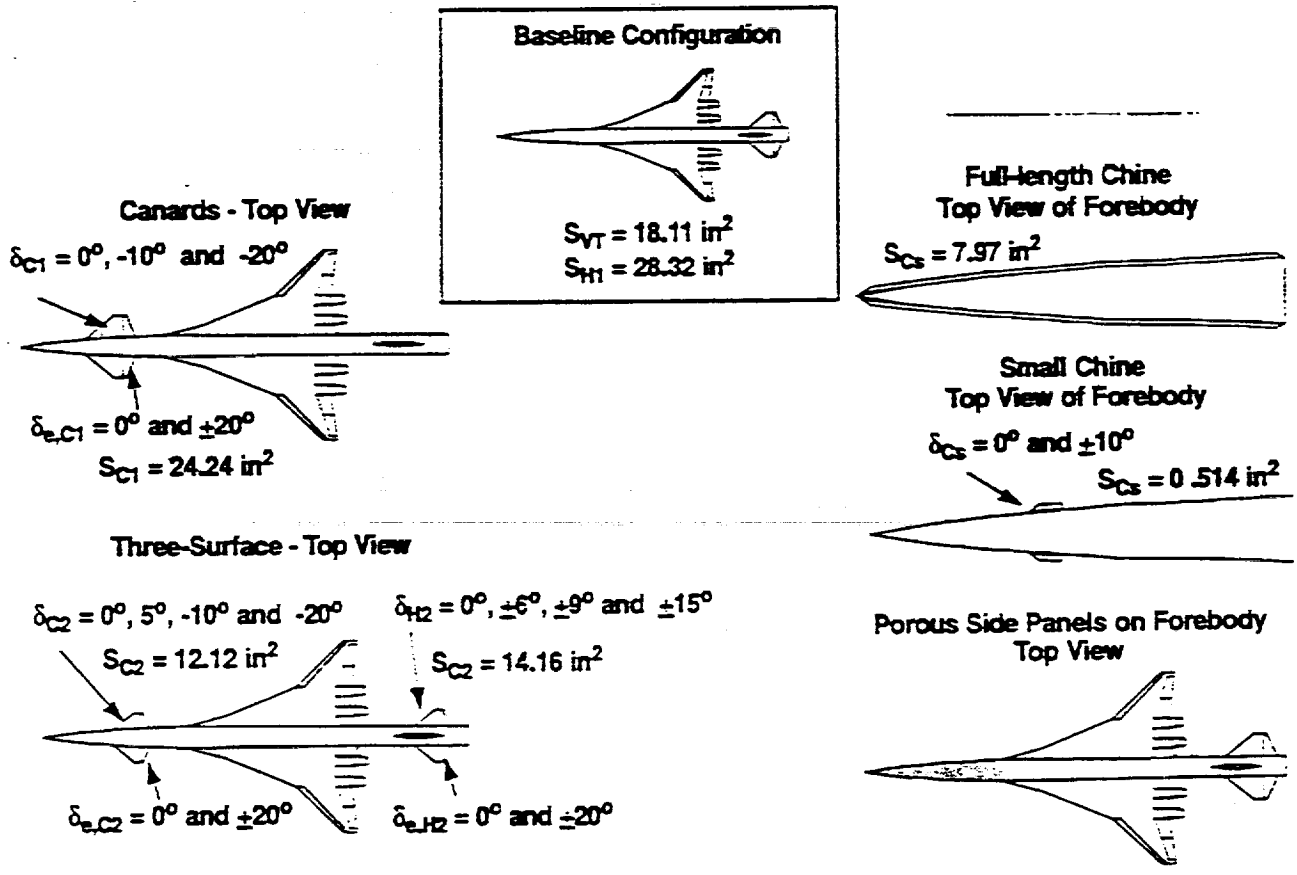

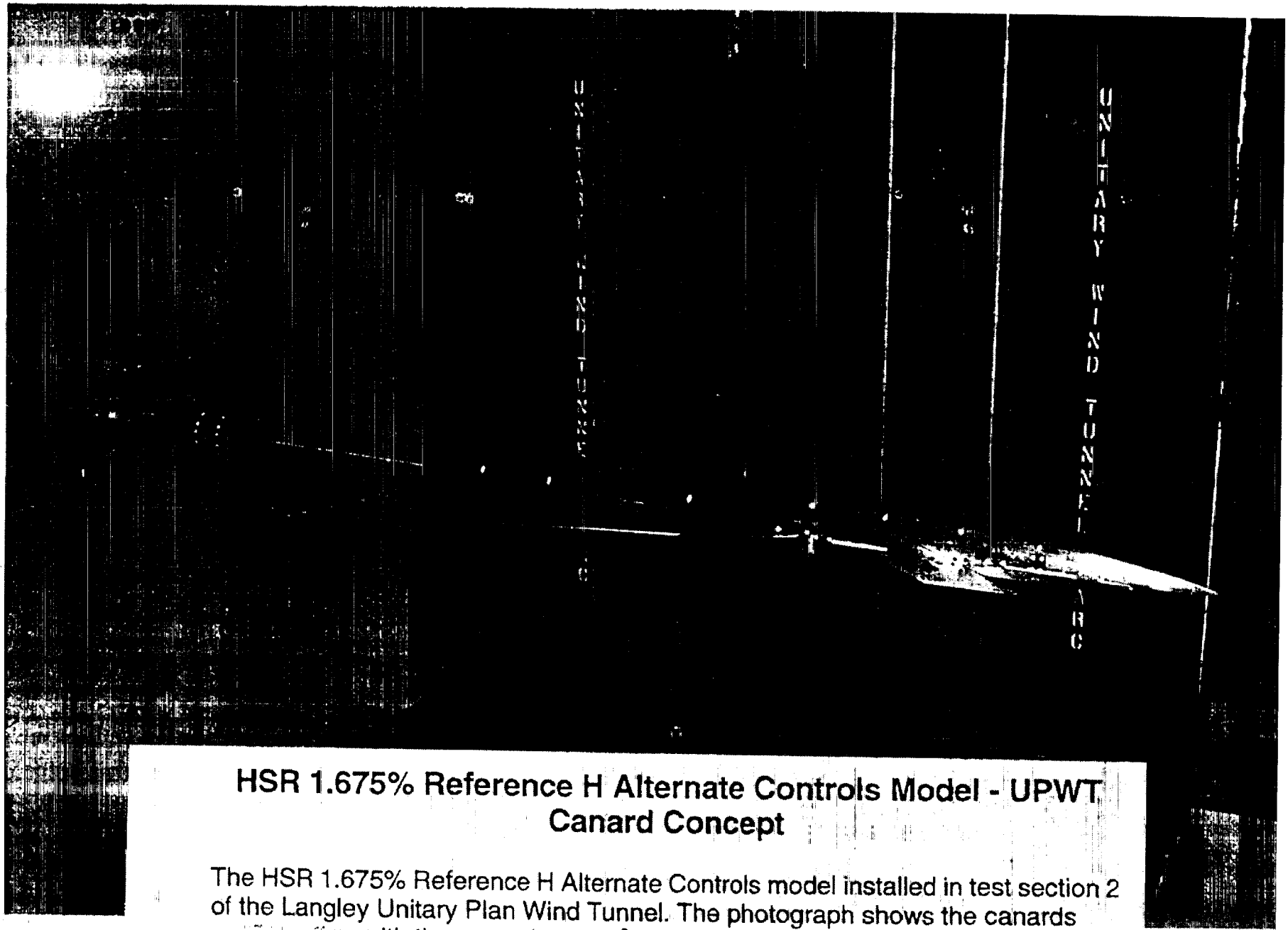

HSR 1.675% Reference H Alternate Controls Model - UPWT Canard Concept

The HSR 1.675% Reference H Alternate Controls model installed in test section 2 of the Langley Unitary Plan Wind Tunnel. The photograph shows the canards

HSR 1.675% Reference H Alternate Control Model Wing Concepts

The three alternate control concepts employed on to the wing of the model are the 5° anhedral wing, 10° split trailing-edge flaps, and winglets. The 5° anhedral wing concept is the outboard wing with 5° anhedral. The 10° split trailing-edge flaps were employed on the two outboard flaps on the right hand side. The winglets were designed with 0° anhedral and 0° dihedral. The winglets also had a rudder with deflection angles of 0° and 20°.

HSR 1.675% Ref H Alternate Controls Model - Wing Concepts

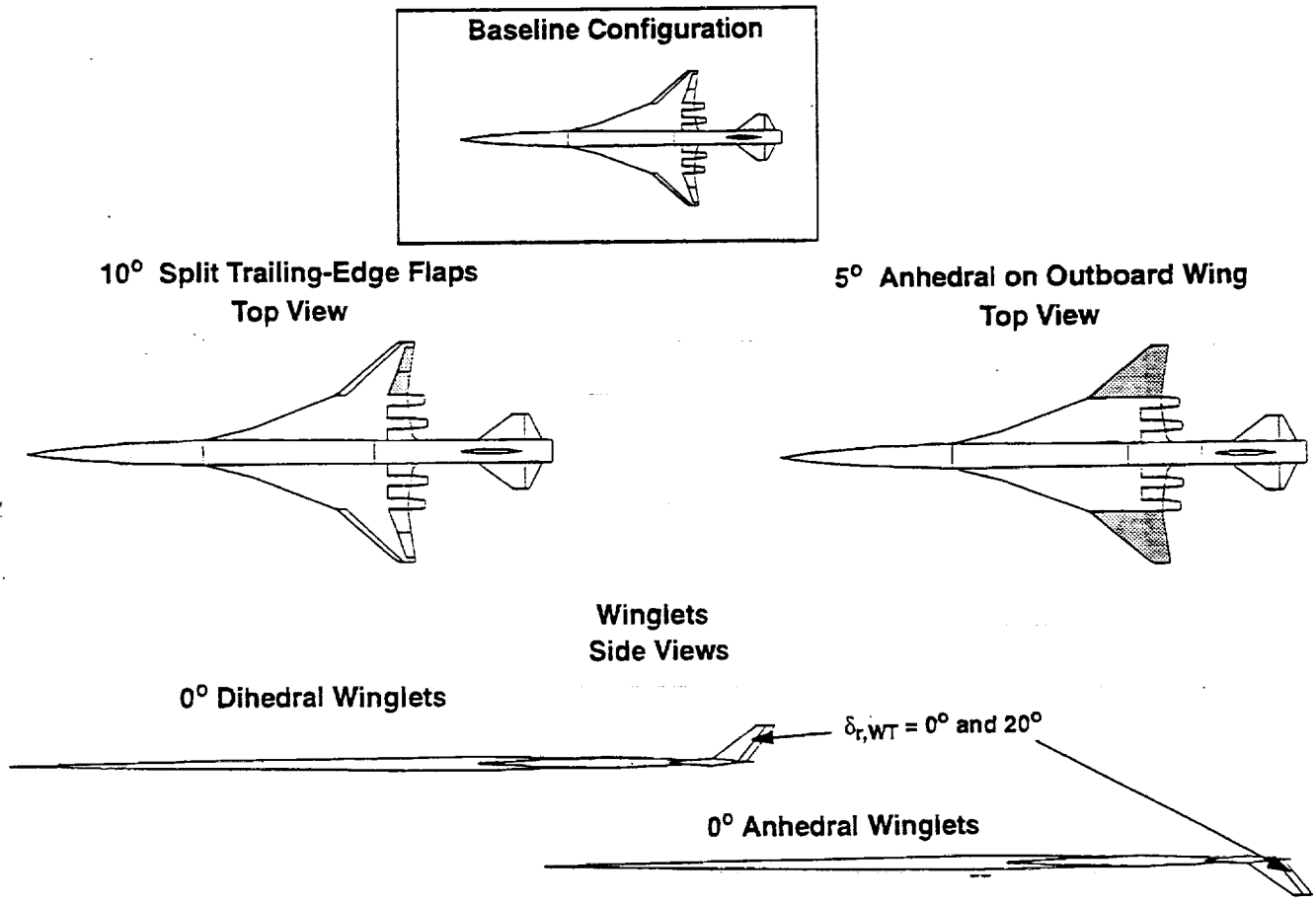

Data Summary for the HSR 1.675% Reference H Alternate Controls Model

Data was collected on 10 alternate control concepts on the HSR 1.675% Reference H Alternate Controls model in the Langley UPWT and 16' TT. The te concepts examined were the all-flying vertical tail, butterfly tails, canards, 3-surface, ventrals, chines, anhedral wing, winglets, split trailing-edge flaps, and porous forebody. Data was also obtained on the baseline configuration and on component buildup configurations. In UPWT 602 polars were obtained on 80 configurations. In 16' TT, 277 polars were obtained on 18 configurations. No da was obtained on winglets, split trailing-edge flaps, or porous forebody in the 16 TT.

Data Summary for the HSR 1.675% Ref H Alternate Controls Model

Concept	UPWT M = 1.8, 2.1, 2.4, 2.7 Re = 3 x 10^6 /ft			16' TT M = 0.6, 0.85, 0.9, 0.95, 0.98, 1.2 Re = 3.1 x 10^6 to 3.98 x 10^6 /ft		
	α Polars	β Polars	# of config.	α Polars	β Polars	# of config.
Baseline	Nac. On, Extended Aftbody, Vertical and Horizontal Tails On					
	8 (37)	12 (10)	1	12 (26)	18 (12)	1
Component Build-up	Nacelles On, Tails On/Off			Nacelles On, Tails On		
	24 (2)	36	3	36 (6)	24	3
All-flying Vertical Tail	δ_{AVT} = 5°, 10°			δ_{AVT} = 5°		
	20 (2)	18	2	18	6	1
Butterfly Tails	δ_{BT} = 0°, ±5°, ±10°, $\delta_{\Phi,BT}$ = 0°, ±10°			δ_{BT} = 0°, ±5°		
	34 (26)	36 (10)	9	24	18	3
Canards	δ_{C1} = 0°, -10°, -20°, $\delta_{\Phi,C1}$ = 0°, ±20°, δ_{TE} = 0°, 10°			δ_{C1} = 0°, -10°		
	34 (4)	24	11	18	2	2
3-Surface	δ_{C2} = Off, 0°, 5°, -10°, -20°, $\delta_{\Phi,C2}$ = 0°, ±20°, δ_{H2} = Off, 0°, ±15°, $\delta_{\Phi,H2}$ = 0°, ±20°, δ_{TE} = 0°, 10°			δ_{C2} = 0°, δ_{H2} = Off, 0°		
	96 (9)	32 (1)	38	18	11	2
Ventrals	Low aspect ratio, Folding			Folding		
	16 (1)	24	2	12	6	1
Chines	Full-length, Small, δ_{Cs} = 0°, ±0°			Full-length, Small, δ_{Cs} = 0°		
	20	28	4	24	12	2
Anhedral Wing	5° Anhedral on Outboard Wing			5° Anhedral on Outboard Wing		
	12 (2)	18	2	12	6	1
Winglets	δ_{WT} = Off, 0° Anhedral, 0° Dihedral, $\delta_{r,WT}$ = 0°, 20°			No Data		
	26	34	5			
Split Trailing-edge Flaps	δ_{STE} = 5°			No Data		
	8	12	1			
Passive Porosity On Forebody	Porosity - Both Sides, Right Hand Side Only			No Data		
	12	18	2			
Total	310 (81)	292 (21)	80	174 (32)	103 (12)	16

( ) - Repeat Runs

Repeatability of the Longitudinal Coefficients Obtained on the HSR 1.675% Reference H Alternate Controls Model

Data obtained on the baseline configuration (extended aftbody/nacelles/tails) were used to determine the repeatability of the longitudinal coefficients in the testing conducted on the alternate control concepts. The repeatability numbers obtained are based on data scatter between 3 to 5 polars at $-0.10 \leq C_L \leq 0.25$. The UPWT data show that for M= 2.4 and 2.7, the repeatability of C_D was ± 0.0001, the repeatability of C_L was less than or equal to ± 0.001, and the repeatability of C_m ± 0.0004. However, for M = 1.8 and 2.1, the repeatability was significantly worse where repeatability for C_D was ± 0.0006, the repeatability of C_L was ± 0.006, and the repeatability of C_m was from ± 0.0008 to ± 0.002. The 16' TT data show that for M = 0.90 and 1.2, the repeatability of C_D was ± 0.0002. The repeatability of C_L varied from ± 0.002 to ± 0.003 and the repeatability of C_m was ± 0.0003 to ± 0.0005.

HSR 1.675% Ref H Alternate Controls Model
Repeatability* of the Longitudinal Coefficients at $-0.10 \leq C_L \leq 0.25$

Based on the Extended Aftbody/Nacelles/Tails Configuration

M	C_D	C_L	C_m
Langley 16' TT			
0.9	±0.0002	±0.002	±0.0003
1.2	±0.0002	±0.003	±0.0005
Langley UPWT			
1.8	±0.0005	±0.006	±0.0008
2.1	±0.0006	±0.006	±0.002
2.4	±0.0001	±0.001	±0.0004
2.7	±0.0001	±0.0008	±0.0004

* Based on observed data scatter between 3 to 5 polars

Concluding Remarks

Supersonic and transonic aerodynamic data has been obtained on the Referen H configuration and various conventional and alternate control devices. The da is be used in a simulation package for the Reference H configuration. Also the data is to be used to compare the stability and control characteristics of the Reference H configuration against the HSCT Flight Controls Requirements Specifications. The data has already been used to make recommendations on control devices for the Technology Concept Airplane.

Concluding Remarks

- Data to be used in a simulation package for the Reference H configuration.
- Data to be used in comparing the stability and control characteristics of the Reference H configuration against the HSCT Flight Controls Requirments Specifications.
- Data was used to make recommendations on controls for the Technology Concept Airplane.

Future Directions

Future work in this area includes furthering the application of CFD methods for control effector design and assessments of stability and control characteristics. Also the data set will be characterized with respect to control authority and stability augmentation for use in future stability and control design activities.

Future Directions

- **Mature the application of CFD methods for control effector design and stability and control assessments.**
- **Characterize the data set with respect to control authority and stability augmentation for use in future stability and control design activities.**

HIGH REYNOLDS NUMBER EFFECTS ON HSCT STABILITY & CONTROL CHARACTERISTICS

NASA/Industry High Speed Research Configuration Aerodynamics Workshop

Michael B. Elzey
Principal Engineer
HSCT Stability and Control
The Boeing Company

Lewis R. Owens, Jr.
Aerospace Engineer
Subsonic Aerodynamics Branch
NASA Langley Research Center

Dr. Richard A. Wahls
Aerospace Engineer
Transonic/Supersonic Branch
NASA Langley Research Center

Dr. Douglas L. Wilson
Principal Engineer
HSCT Stability and Control
The Boeing Company

Introduction

Two wind tunnel tests during 1995 in the National Transonic Facility (NTF 070 and 073) served to define Reynolds number effects on longitudinal and lateral-directional stability and control. Testing was completed at both high lift and transonic conditions. The effect of Reynolds number on the total airplane configuration, horizontal and vertical tail effectiveness, forebody chine performance, rudder control and model aeroelastics was investigated. This paper will present pertinent stability and control results from these two test entries. Note that while model aeroelastic effects are examined in this presentation, no corrections for these effects have been made to the data.

HSCT Reynolds Number Testing in the NTF
1990 - 1995

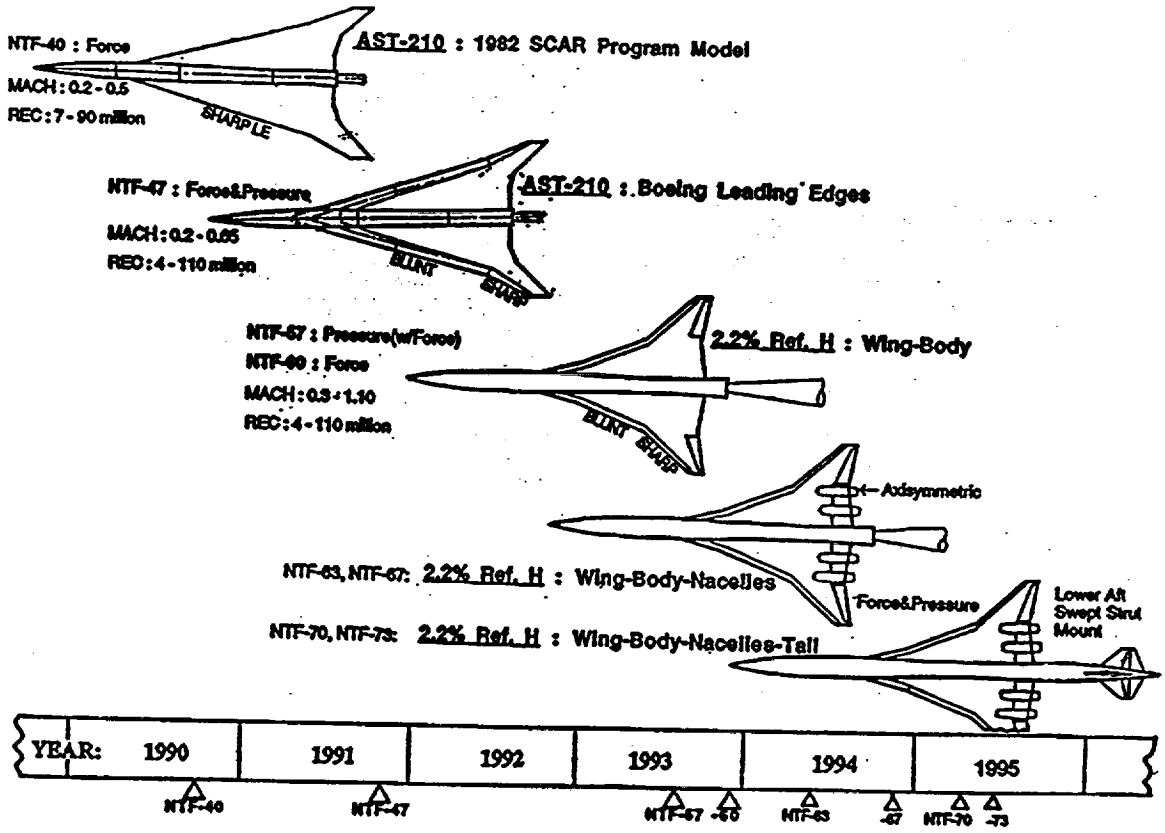

HSCT high Reynolds number testing in the National Transonic Facility has included AST and Ref H straight sting mounted, empennage removed configurations from 1990 through 1994. During 1995, two tests were completed on a lower swept strut mounted, full aft body with empennage available (NTF 070 and 073). These tests included a significant amount of stability and control, Reynolds number investigations.

TEST OBJECTIVES
STABILITY AND CONTROL
NTF 070/073

HSCT Stability and Control test objectives for the high Reynolds number entries in the NTF during 1995 included the following:

- The effect of Reynolds number on longitudinal and lateral-directional stability and control for both high lift and high speed conditions. Included are Reynolds number trends on the baseline total airplane configuration, the horizontal and vertical tails, the forebody chines and rudder effectiveness.
- Model aeroelastic effects on longitudinal stability and control levels.
- Forebody trip strip effects.
- Lower swept strut/aft body seal development.

Stability and control test objectives which were not met during 1995 and for which test time still needs to be scheduled in the NTF include Reynolds number effects on:

- Wing trip strips.
- Elevator effectiveness.
- Additional leading edge/trailing edge flap deflections (50°/30° and 30°/10°).

Reference H Configuration
HSCT

BOEING HIGH SPEED CIVIL TRANSPORT
(HSCT)
REFERENCE H CONFIG.

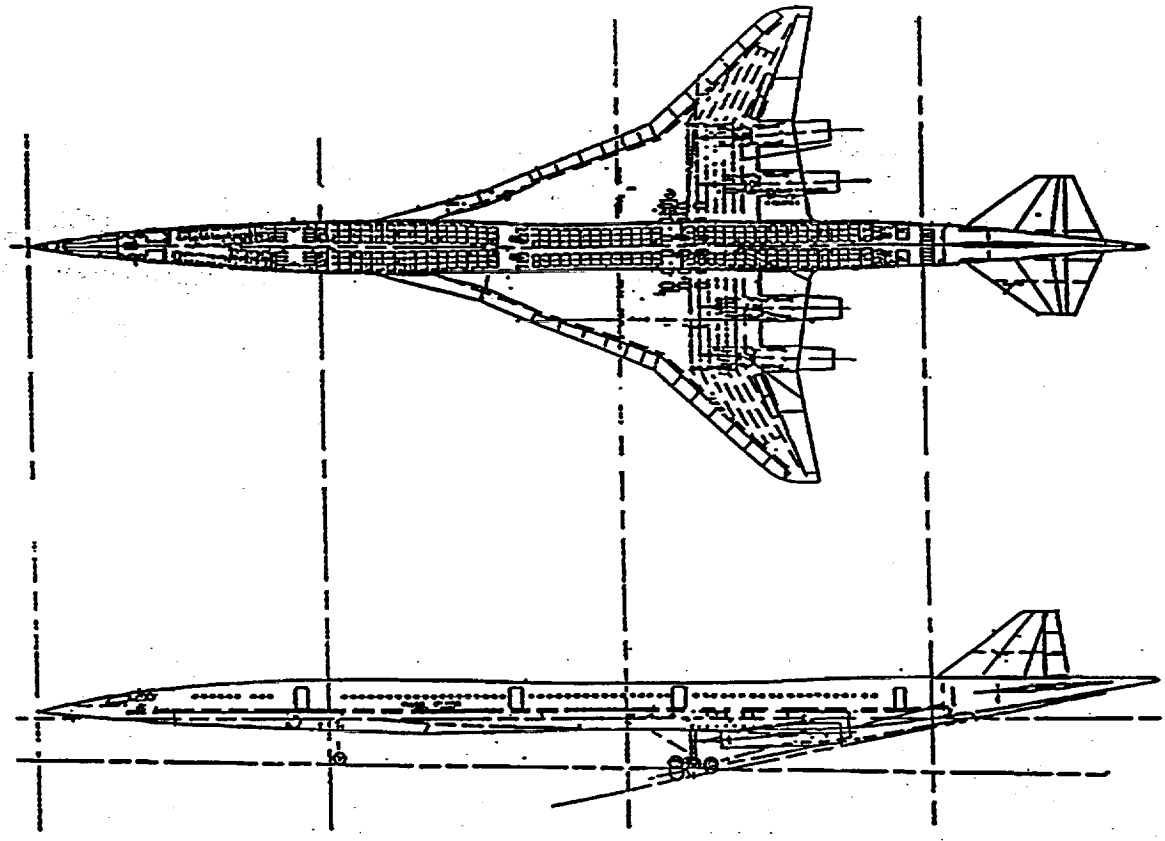

The Reference H HSCT configuration shown is the base for the wind tunnel results presented.

The Effect of Reynolds Number on Low Speed Longitudinal Stability M = 0.30

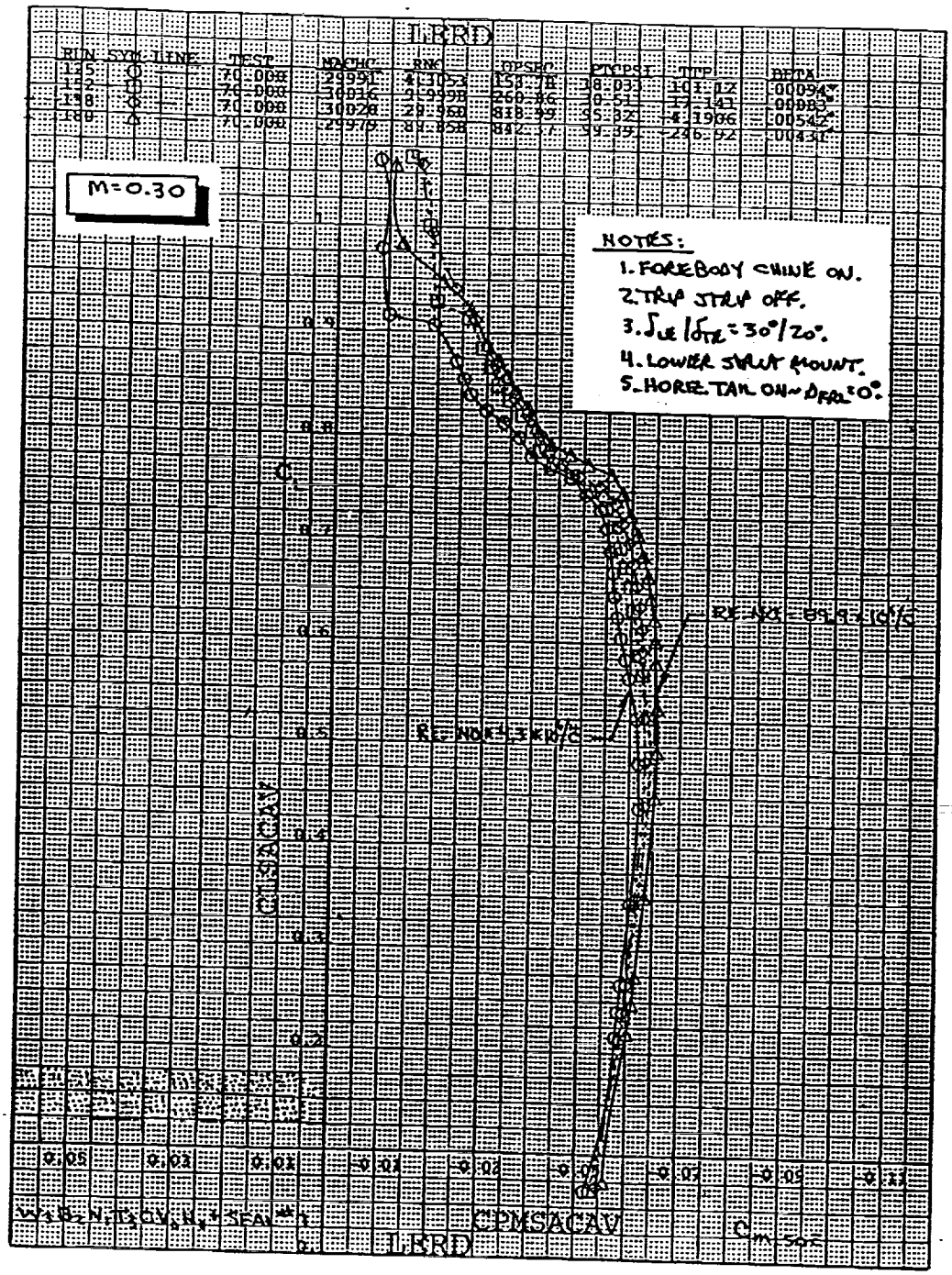

This chart shows that increasing Reynolds number provides a slight increase (approximately 1% $\bar{c}$) in longitudinal stability at M = 0.30. The horizontal tail was on.

The Effect of Reynolds Number on Low Speed Downwash and Stabilizer Effectiveness M = 0.30

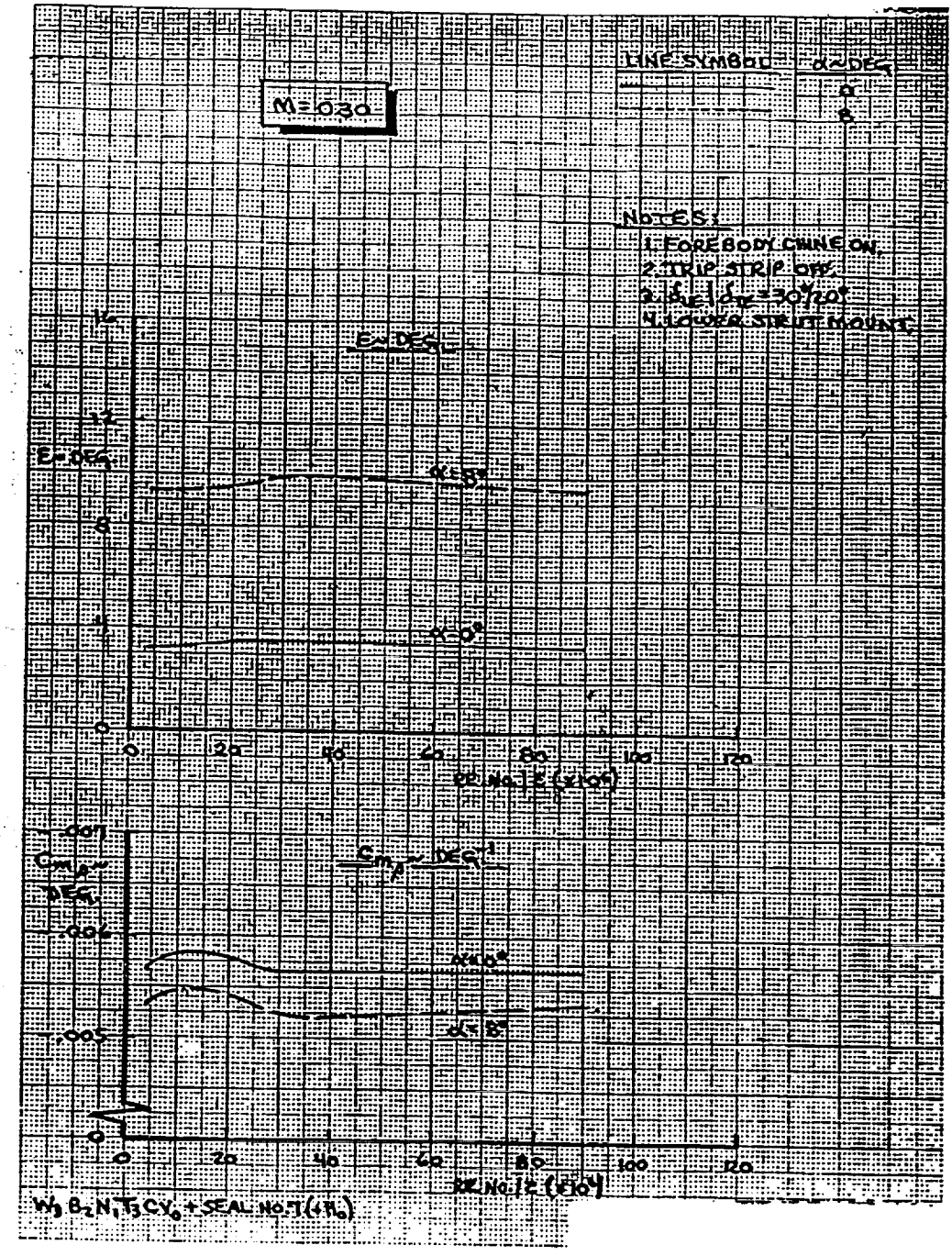

Downwash (ε) and stabilizer effectiveness at low speeds (M = 0.30) are relatively invariant with increasing Reynolds number taken at a constant angle-of-attack.

The Effect of Reynolds Number on High Speed Longitudinal Stability M = 0.95

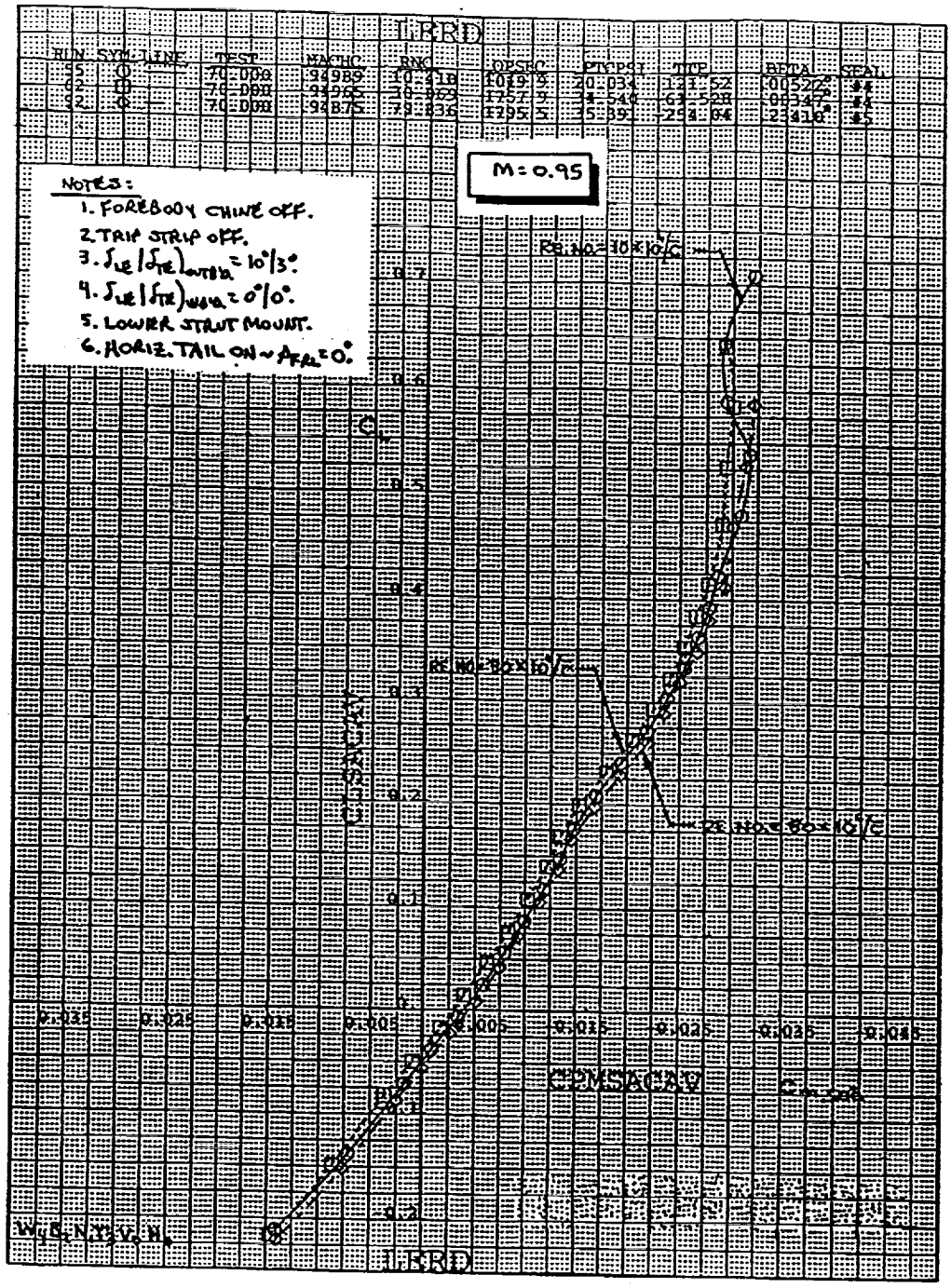

This chart demonstrates that the high speed (M = 0.95) longitudinal stability is relatively insensitive to increasing Reynolds number. The horizontal tail is on.

M = 0.30

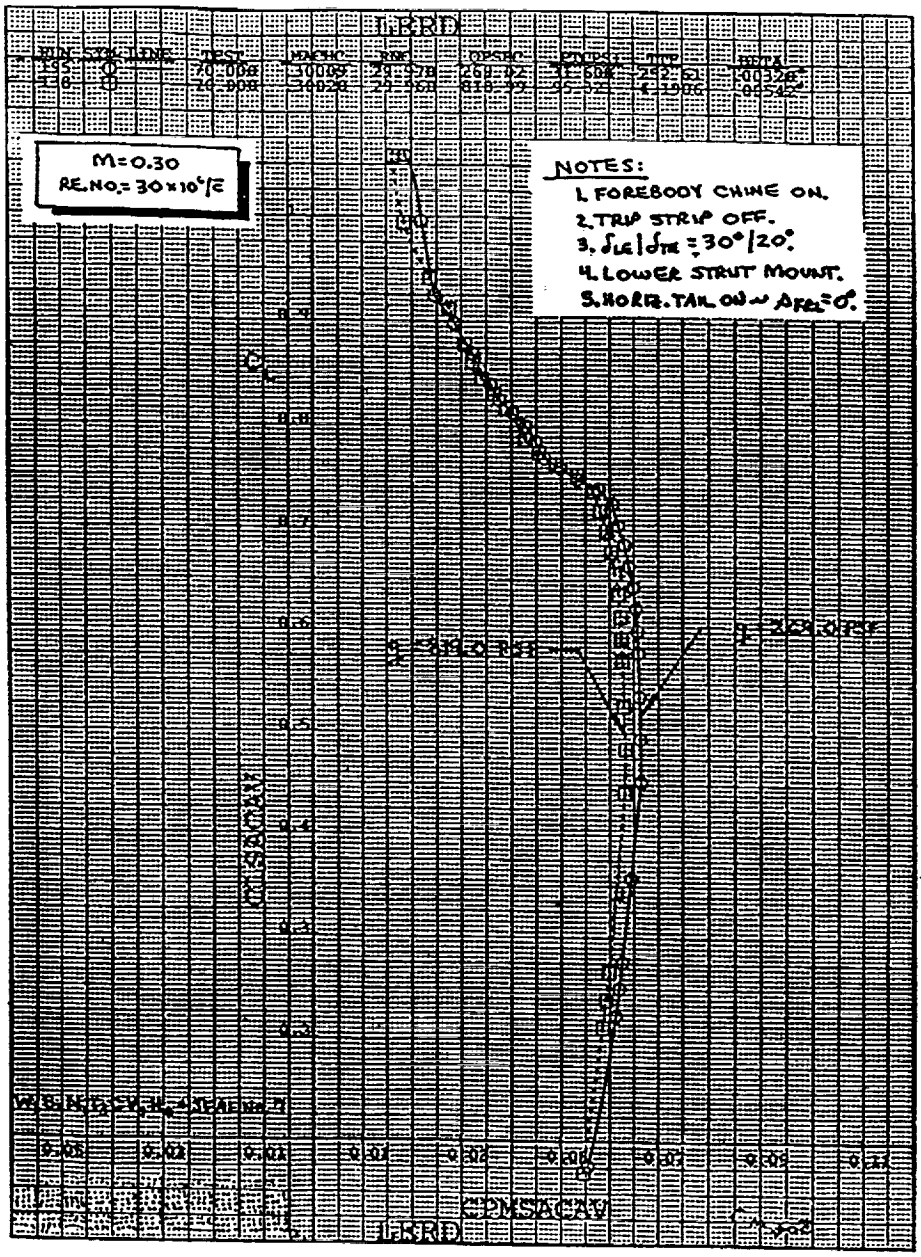

Model aeroelastic effects on longitudinal stability in the high lift configuration, at M = 0.30, are demonstrated in the Figure above. It will be seen that increasing the dynamic pressure (q) from 269 to 819 psf at a constant Reynolds number of 30 x $10^6/\bar{c}$ produces a small, positive shift in the linear range of data. Note that above C_L = 0.75, results tend to collapse. A constant Reynolds number is maintained in the above two sets of data by varying temperature as well as dynamic pressure.

Model Aeroelastics
Re. No. = 30 x $10^6/\bar{c}$ ~ Horizontal Tail Off
M = 0.95

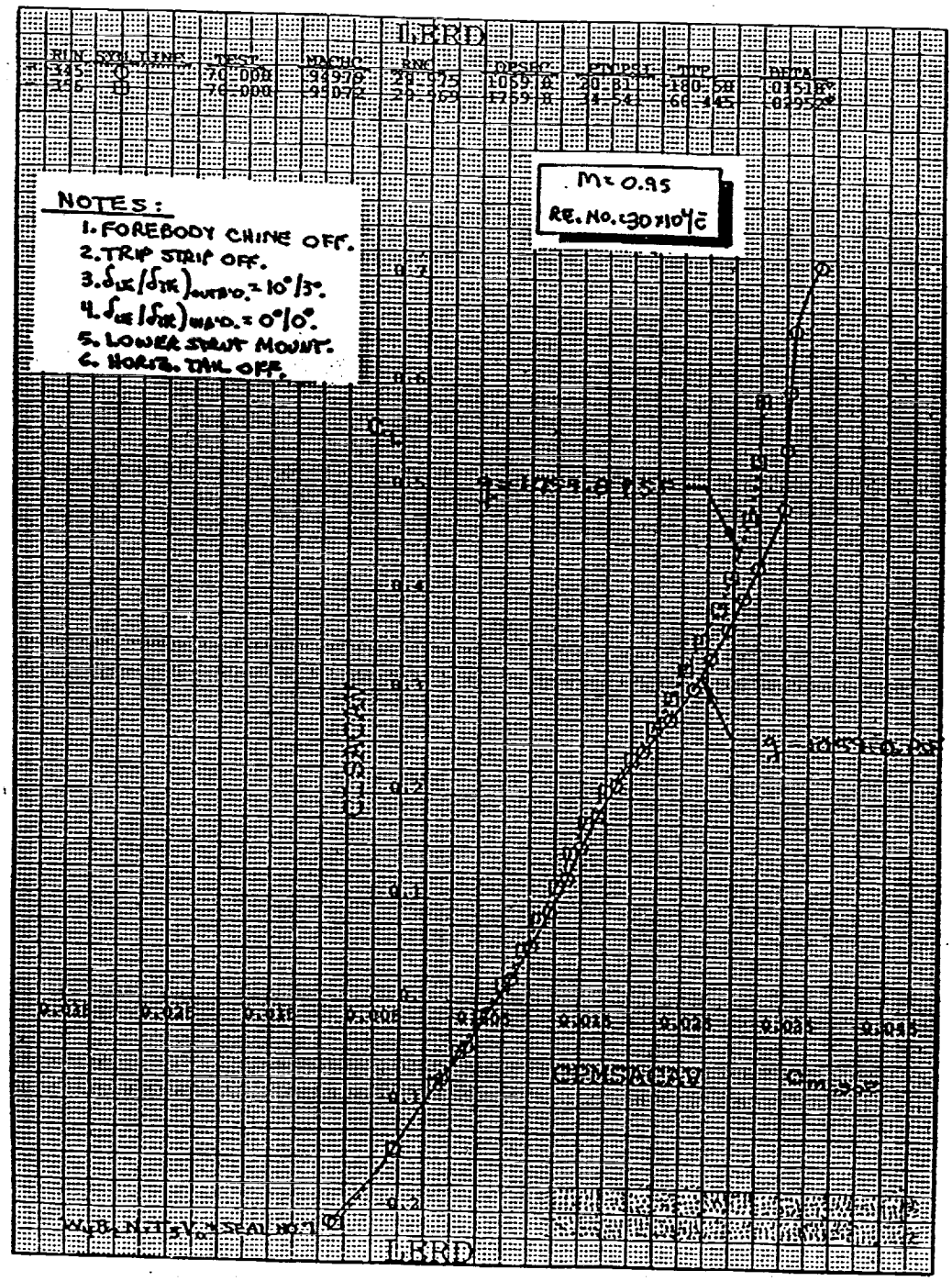

Model aeroelastic effects on longitudinal stability in the transonic configuration, at M = 0.95, are shown above. In this high speed case, there is a loss in longitudinal stability of approximately 0.4%$\bar{c}$ going from 1059 to 1759 psf.

Model Aeroelastics
Re. No. = 30 x $10^6/\bar{c}$ ~ Horizontal Tail Off
M = 0.95

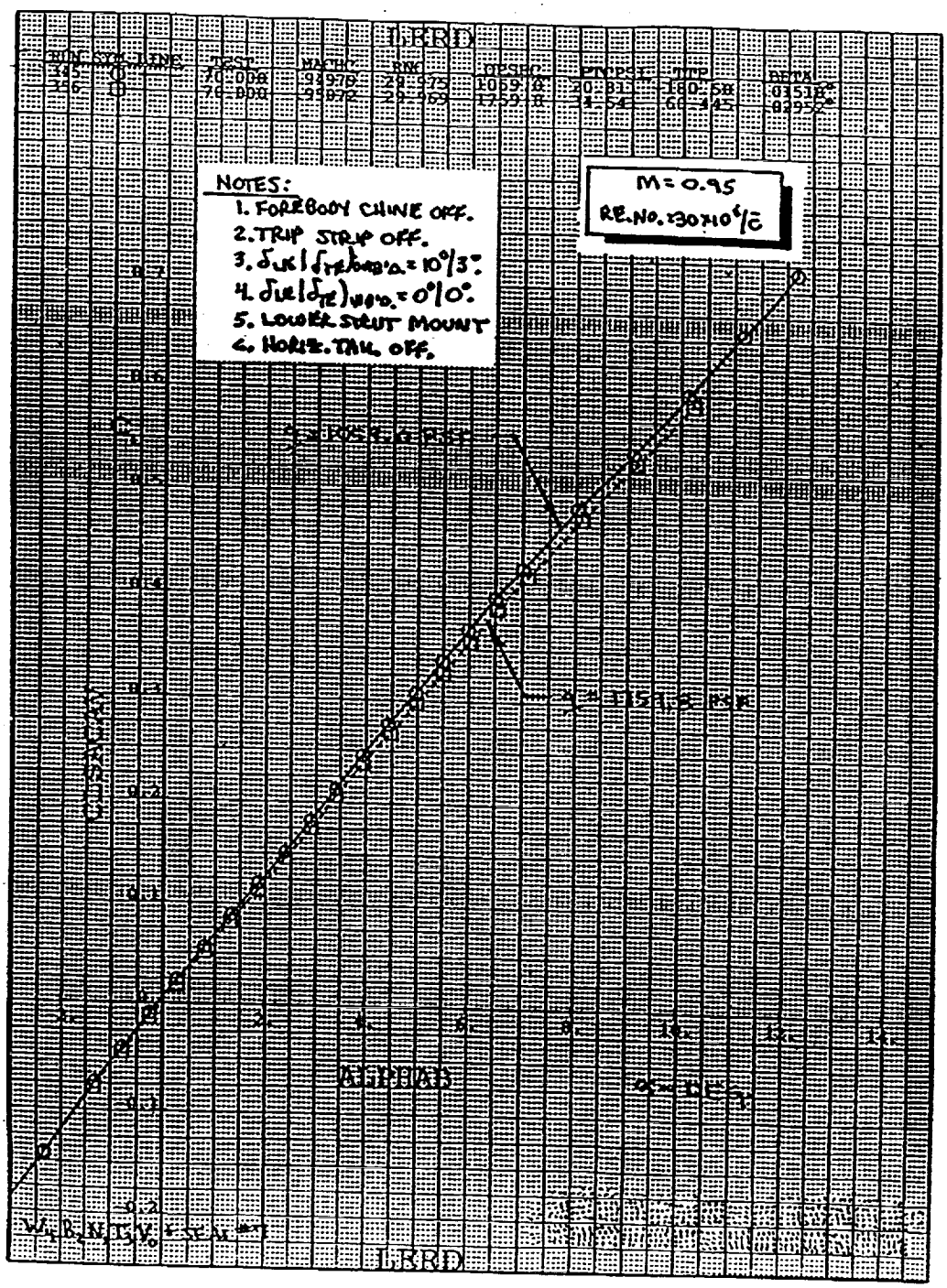

The change in lift curve slope due to model aeroelastics in the transonic mode at M = 0.95 is demonstrated above. This 3.5% loss in lift curve slope, coupled with the stability loss exhibited on the previous page, is consistent with an outboard wing twist change.

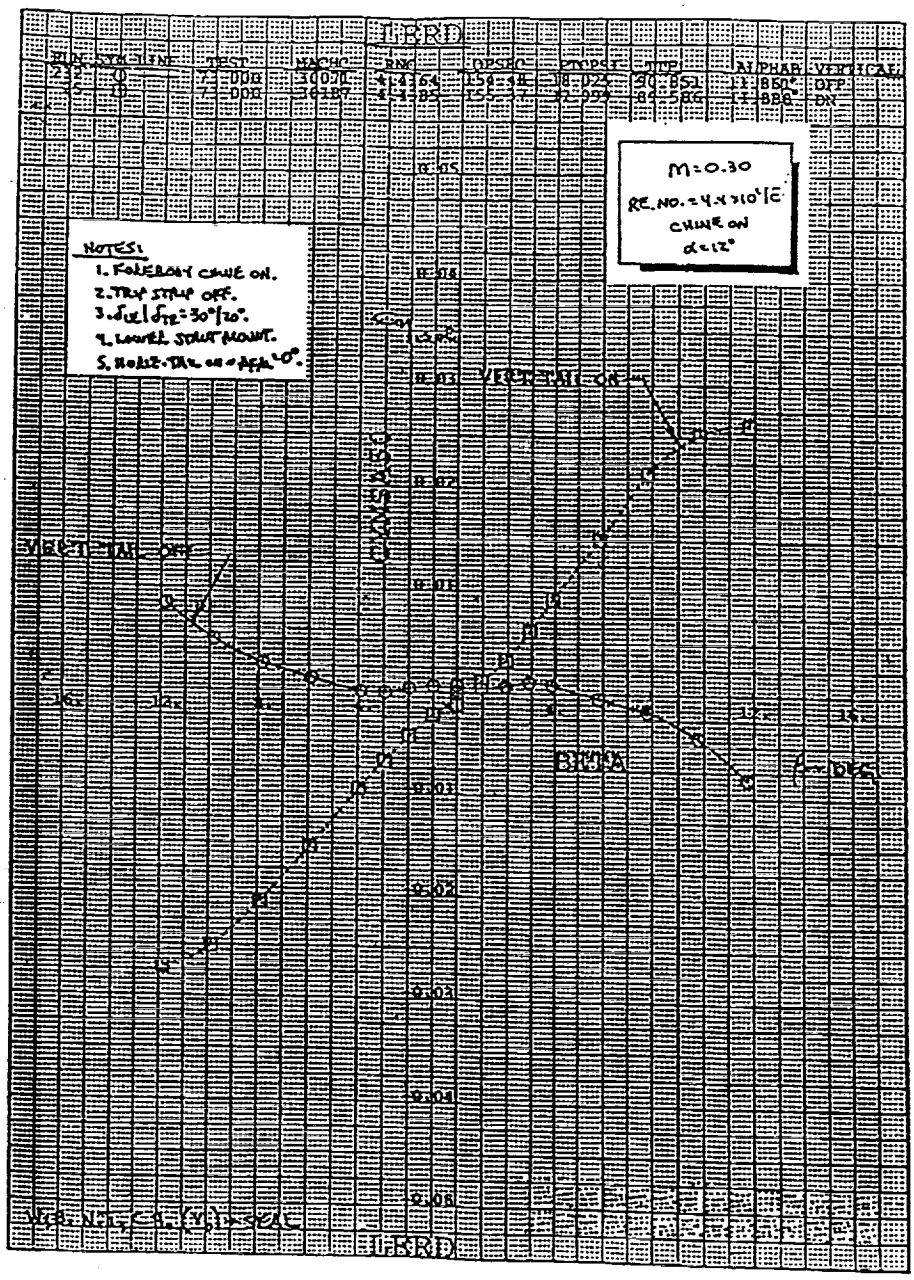

These data indicate that the vertical tail, at M = 0.30, $\alpha = 12°$, Reynolds number = 4.4 x $10^6/\bar{c}$, with the forebody chine on, provides significant directional stability. Note that from $\beta = -4°$ to $\beta = 4°$, the vertical tail off data has essentially neutral directional stability. Outside of these sideslip boundaries, the vertical tail off directional stability levels are unstable. Higher Reynolds number data look similar for this condition.

Vertical Tail Effectiveness
Forebody Chine On ~ Reynolds Number = 4.4 x $10^6/\bar{c}$ ~ α = 20°
M = 0.30

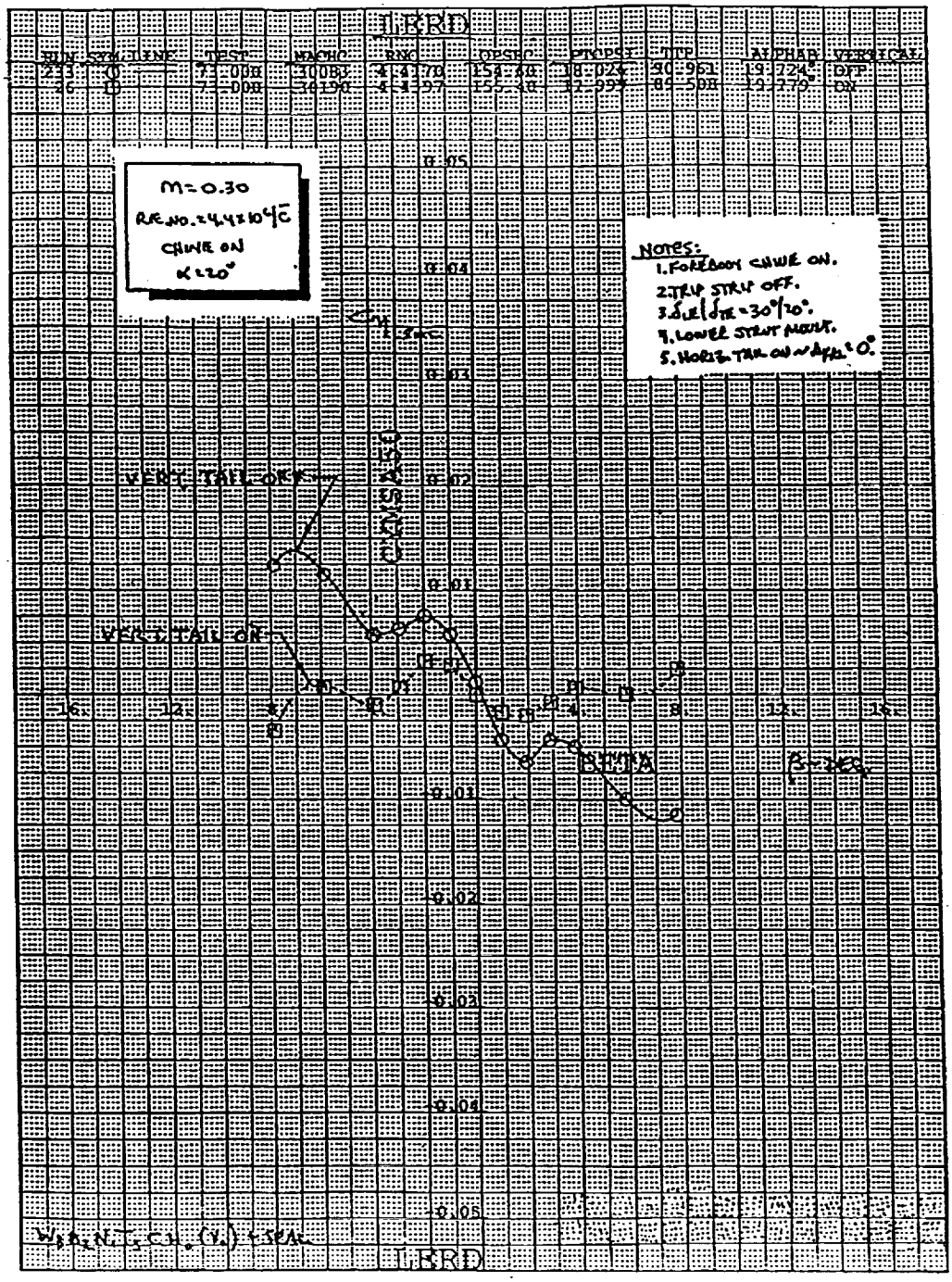

The dramatic loss in directional stability at α = 20°, compared to the α = 12° data shown on the previous page is evident. The Reynolds number and Mach number are still 4.4 x $10^6/\bar{c}$ and 0.30, respectively. The vertical tail increment is still stabilizing, but provides a much smaller ΔC_η at this higher attitude. The vertical tail on level is approximately neutrally stable.

Vertical Tail Effectiveness
Forebody Chine Off ~ Reynolds Number = 10.5 x $10^6/\bar{c}$ ~ $\alpha = 4°$
M = 0.95

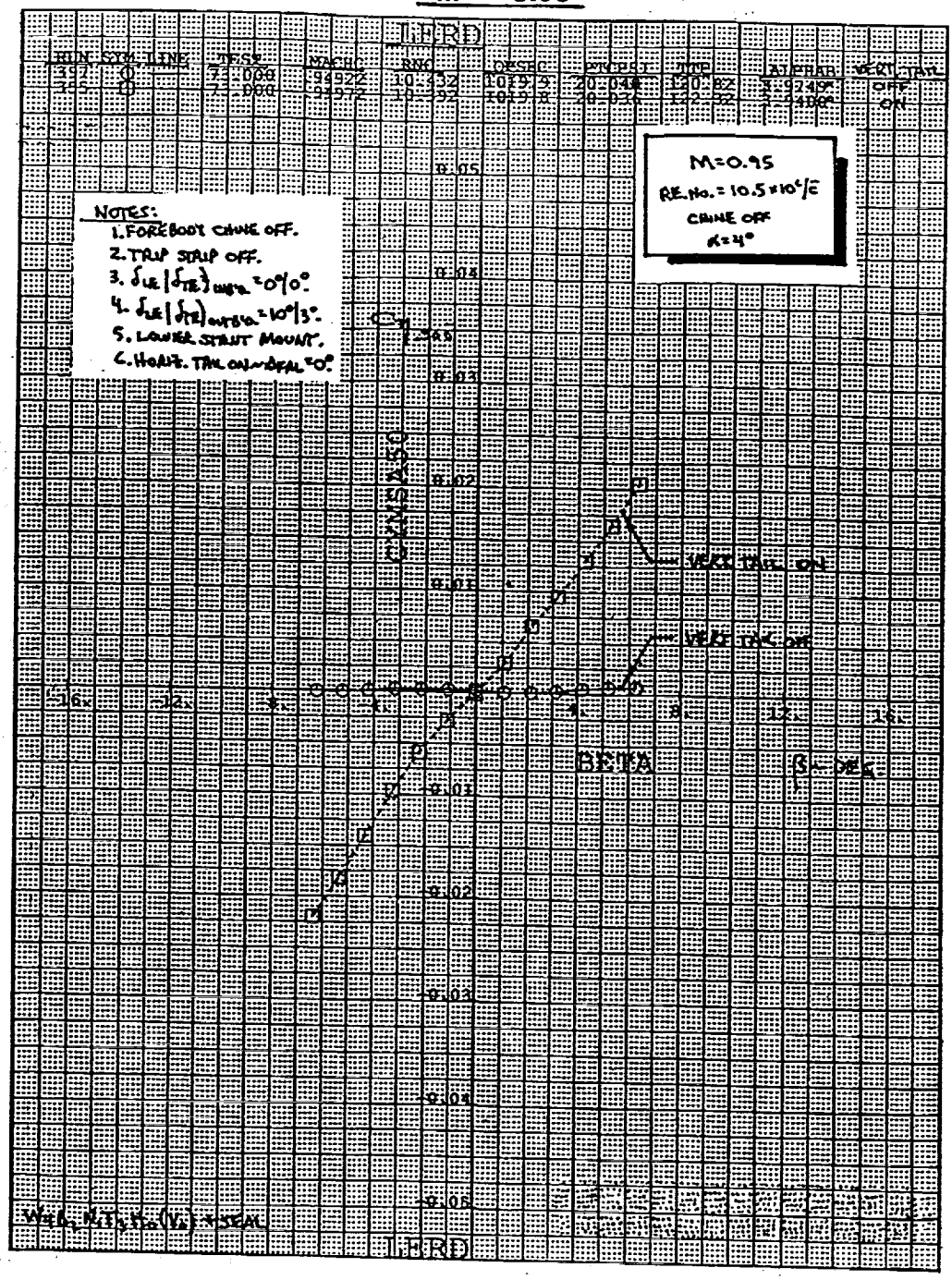

High speed, the forebody chine is removed. The vertical tail provides a considerable input to C_{n_β}. The vertical tail off level shows neutral directional stability.

Forebody Chine Effectiveness
Vertical Tail On ~ Reynolds Number = 4.4 x $10^6/\bar{c}$ ~ α = 12°
M = 0.30

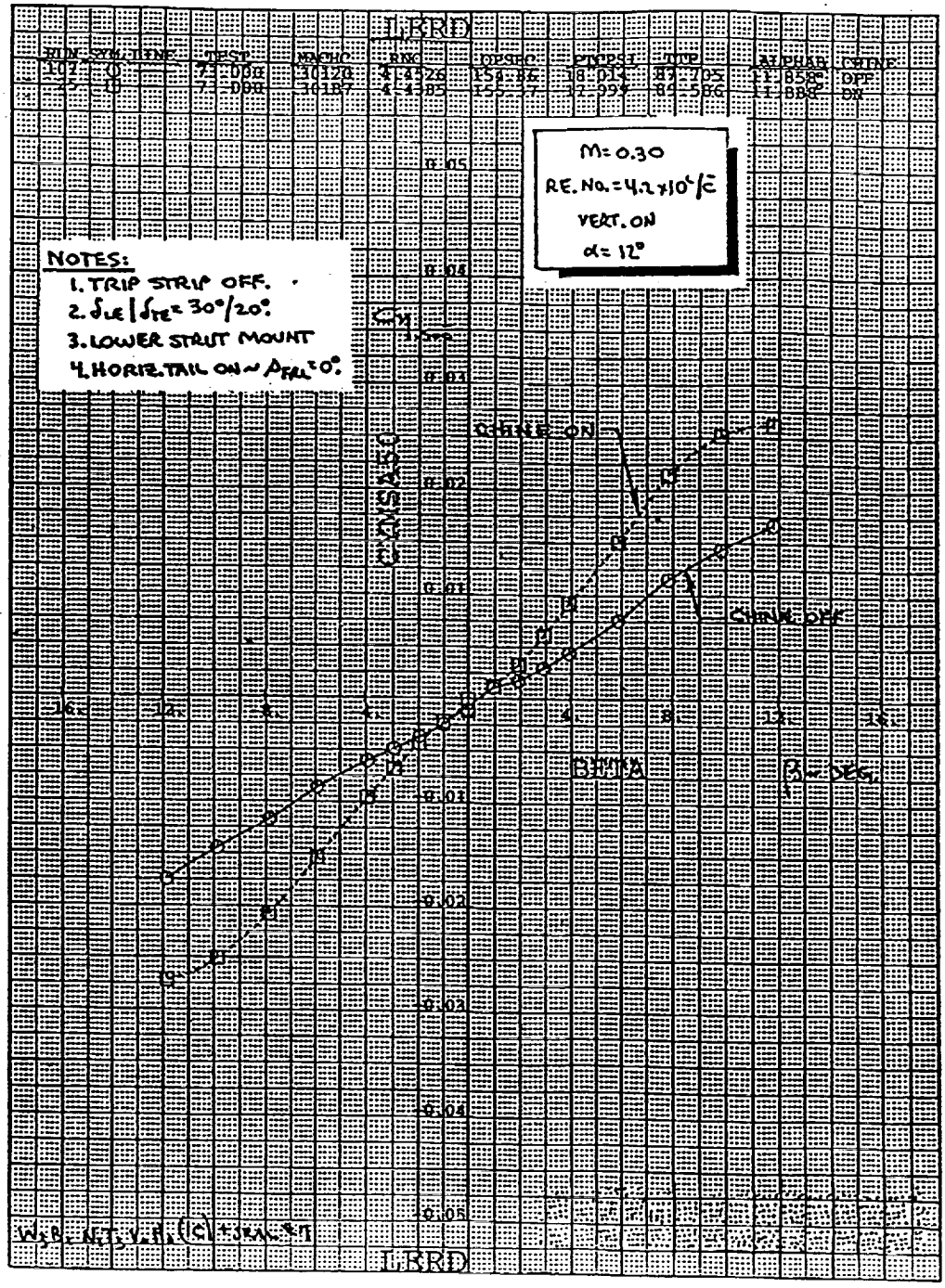

The forebody chine provides a significant increment to directional stability (C_{n_β}) at α = 12° with a chord Reynolds number of 4.4 x 10^6 at M = 0.30. The vertical tail is on. C_{n_β} is nearly doubled with the forebody chine on.

Forebody Chine Effectiveness
Vertical Tail On ~ Reynolds Number = 4.4 x $10^6/\bar{c}$ ~ α = 20°
M = 0.30

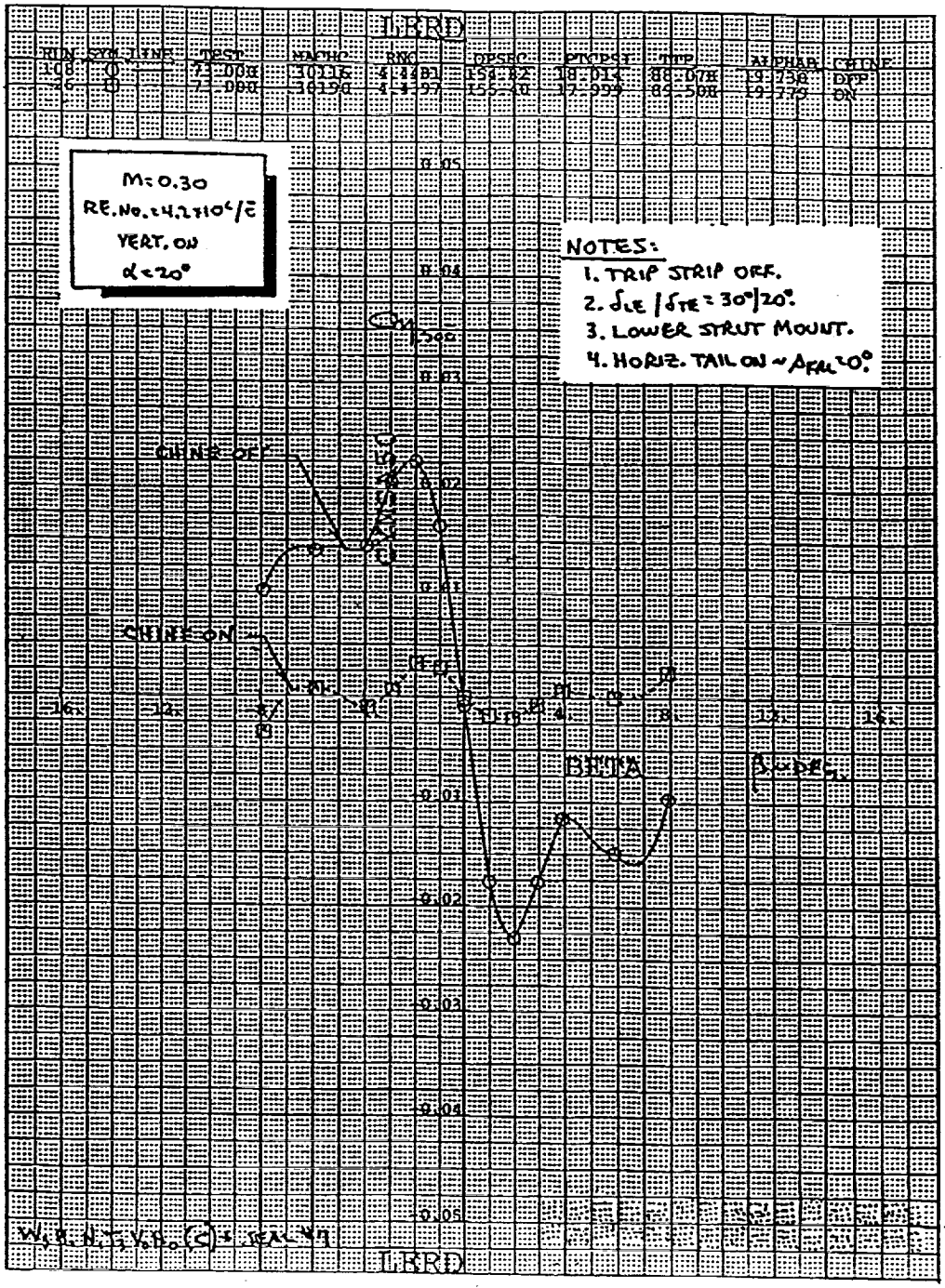

At α = 20°, the forebody chine continues to provide a strong increment to directional stability, particularly between $\beta = \pm 2°$. Forebody chine on data demonstrate essentially neutral directional stability. Mach number and Reynolds number are still 0.30 and 4.4 x $10^6/\bar{c}$, respectively.

Forebody Chine Effectiveness
Vertical Tail On ~ Reynolds Number = 4.4 x $10^6/\bar{c}$ ~ β = 0°
M = 0.30

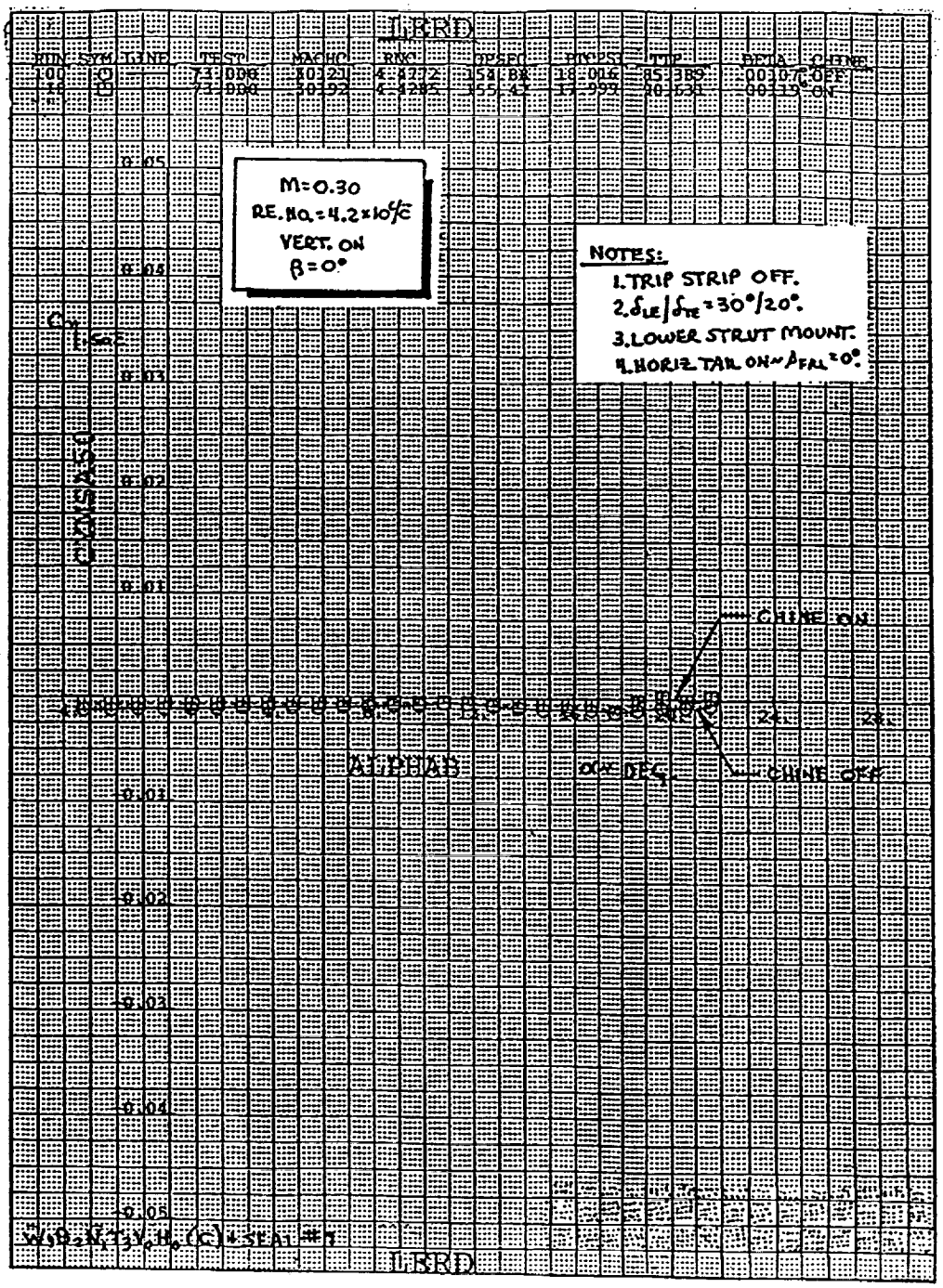

Note that there is no increment in the directional data at β = 0°, M = 0.30 and a Reynolds number of 4.4 x $10^6/\bar{c}$.

Forebody Chine Effectiveness
Vertical Tail On ~ Reynolds Number = 90.5 x $10^6/\bar{c}$ ~ $\beta = 0°$
M = 0.30

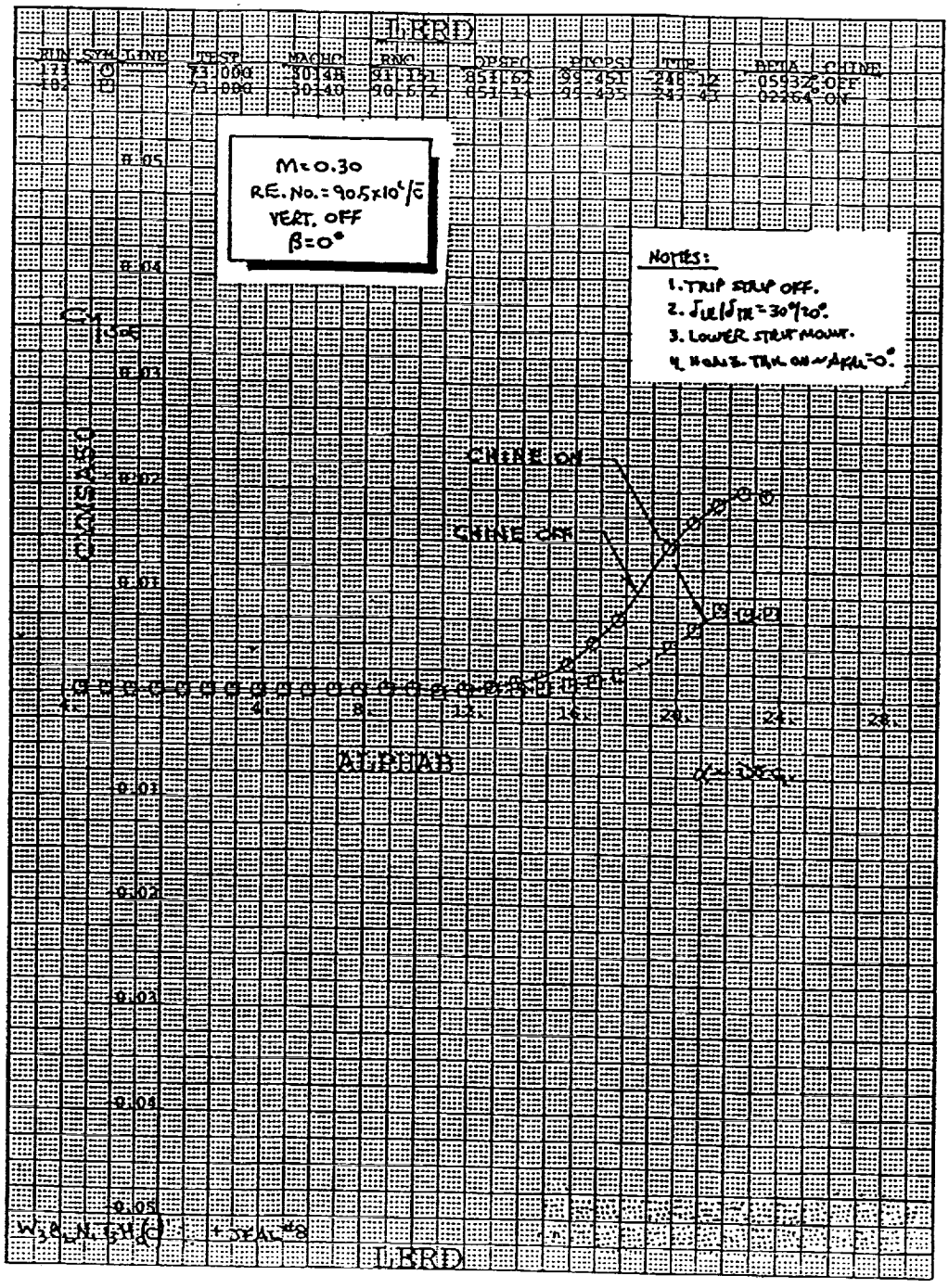

In general, Reynolds number effects are not large on chine effects. However, at $\beta = 0°$, Reynolds number = 90.5 x 10^6, M = 0.30, a large yawing moment develops above $\alpha = 15°$. The forebody chine alleviates this phenomenon.

Effect of Reynolds Number on Directional Stability
Angle-of-Attack = 0°, 8°, 12° and 20°
Vertical Tail On/Forebody Chine On ~ M = 0.30

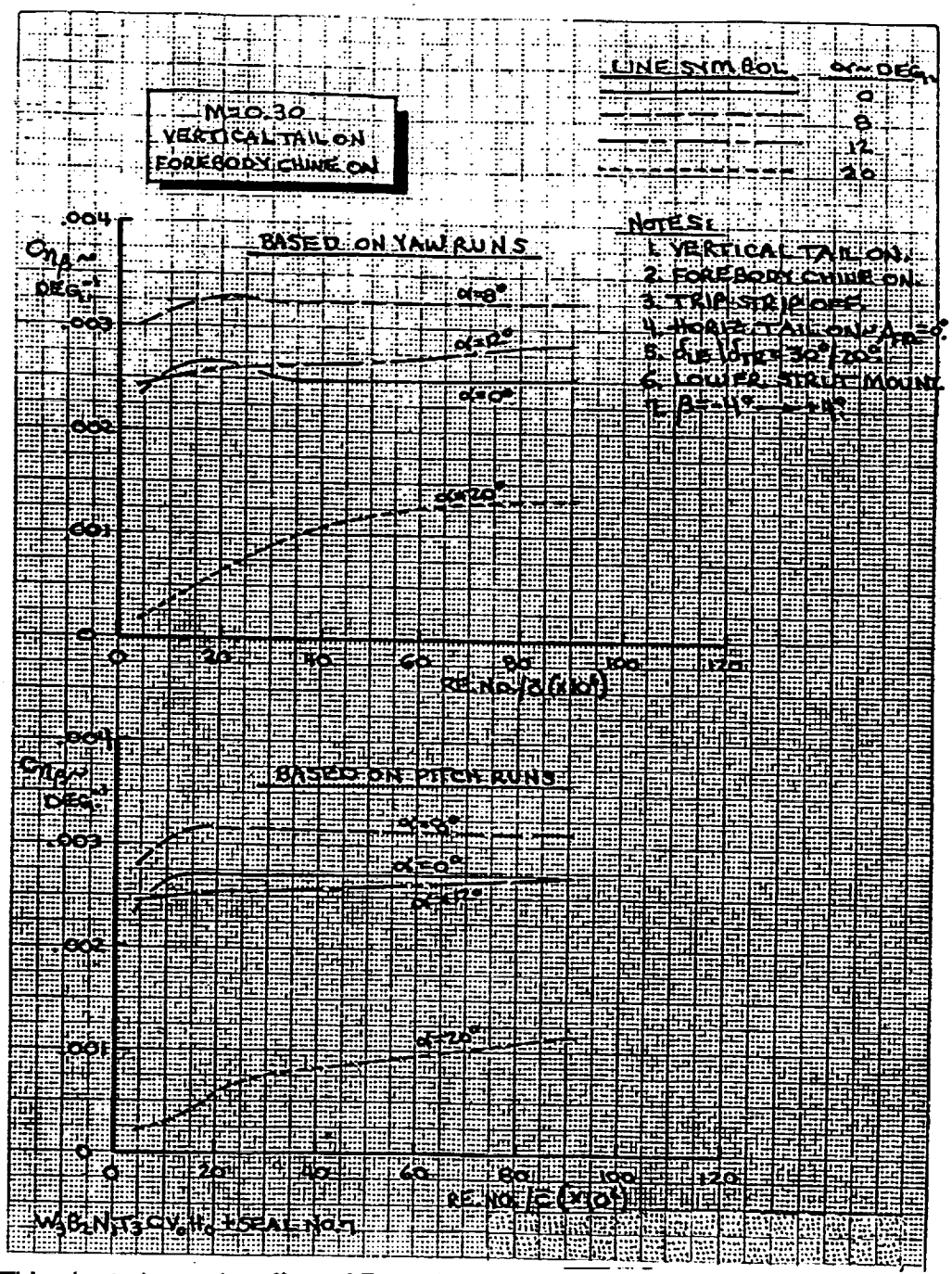

This chart shows the effect of Reynolds number on low speed directional stability (C_{n_β}) at several angles-of-attack for a constant vertical tail on, forebody chine on configuration. Note that at all angles-of-attack and Reynolds numbers, a favorable (positive) C_{n_β} level is achieved. Reynolds number effects are relatively linear for low attitudes. There is a strong Reynolds number effect at the high (20°) angle-of-attack. Also note that the directional stability based upon the pitch runs compares quite favorably with the C_{n_β} acquired from yaw runs.

Effect of Reynolds Number on Directional Stability
Angle-of-Attack = 0°, 8°, 12° and 20°
Vertical Tail On/Forebody Chine Off ~ M = 0.30

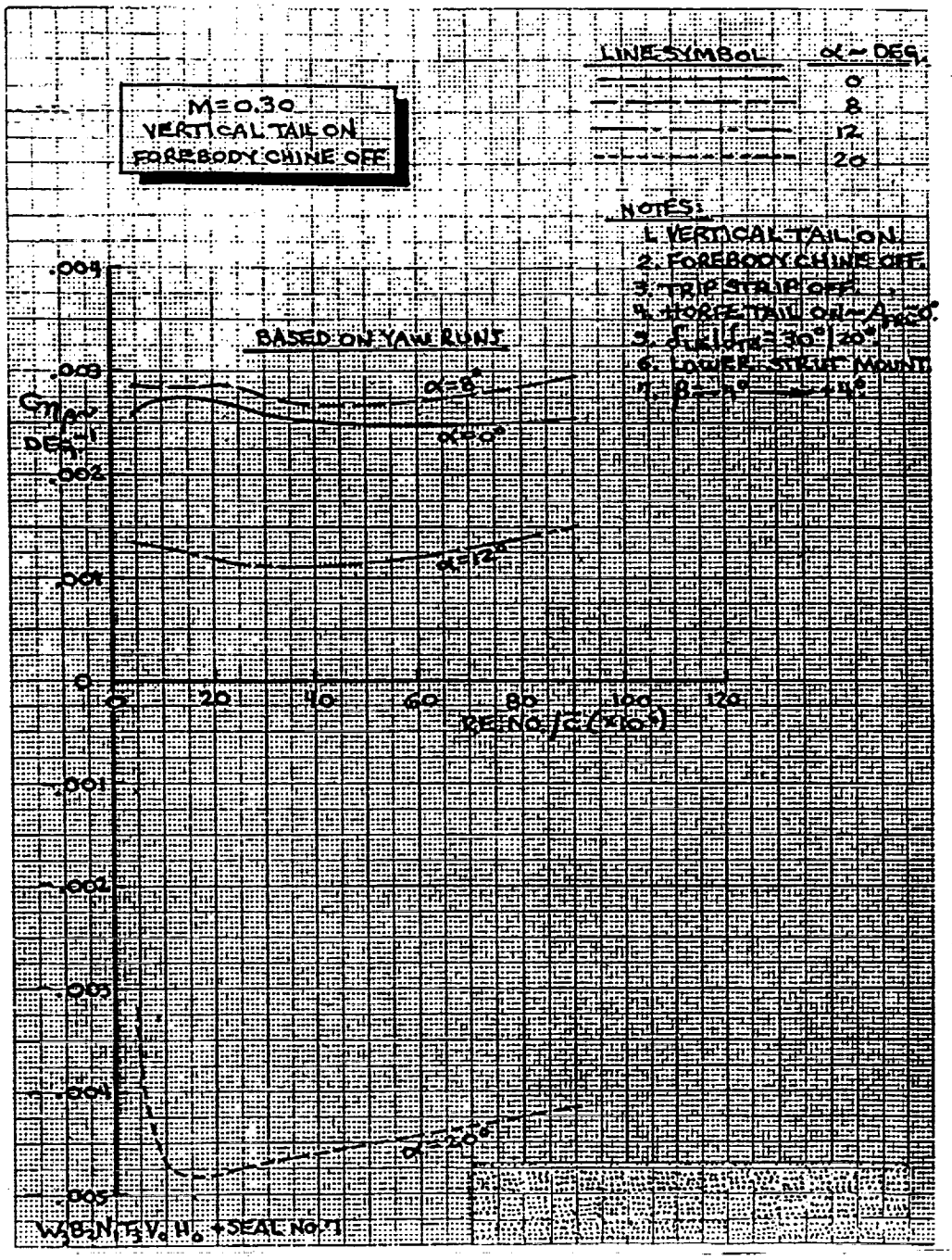

Removal of the forebody chine, while leaving the vertical tail on, produces the directional stability data shown above. There is some reduction in level at $\alpha = 12°$, and a large degradation for 20° attitude chine off. The $\alpha = 20°$ directional stability is particularly non-linear with Reynolds number increase.

Effect of Reynolds Number on Directional Stability
Angle-of-Attack = 0°, 8°, 12° and 20°
Vertical Tail Off/Forebody Chine On ~ M = 0.30

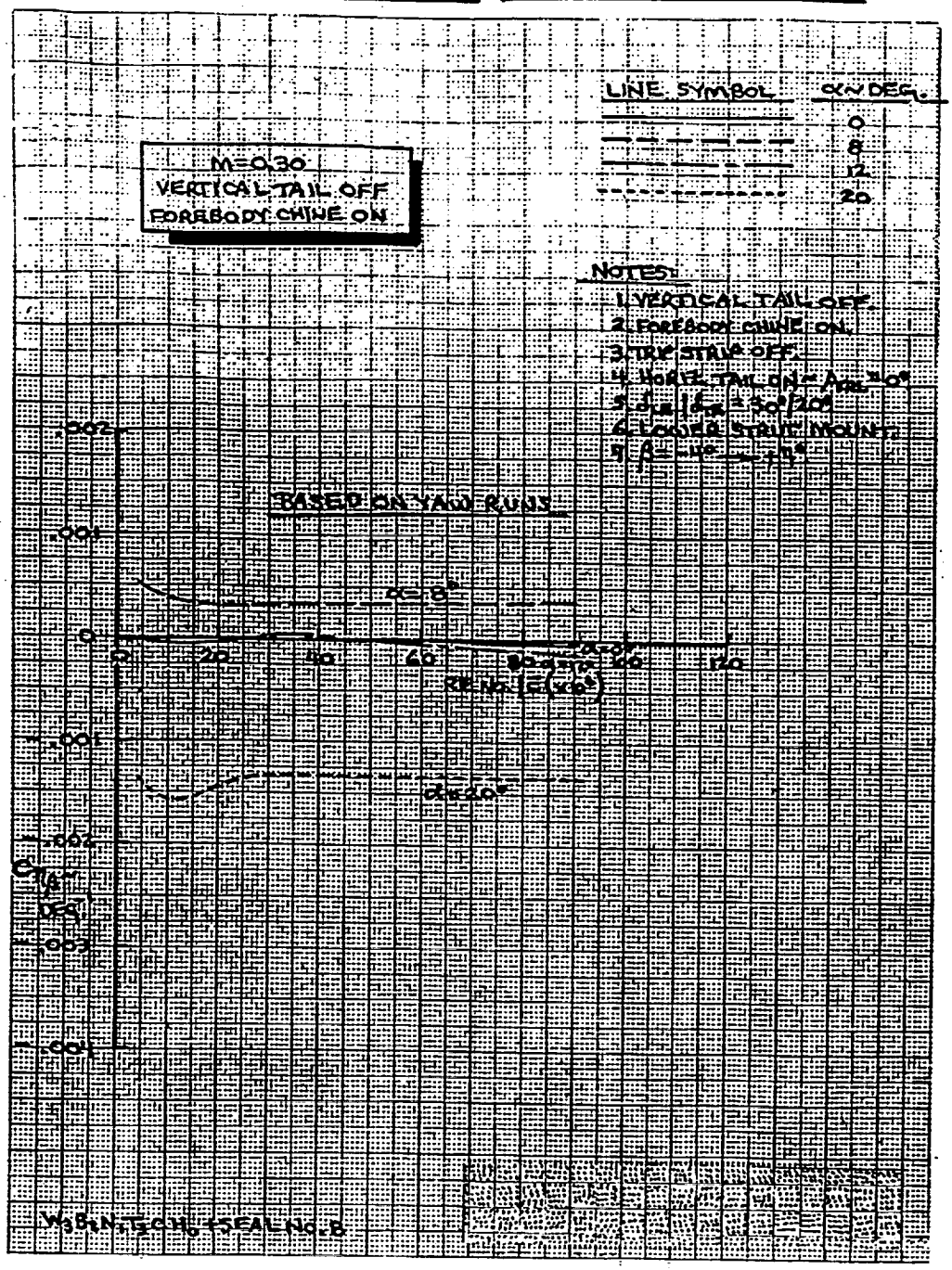

Taking off the vertical tail, while putting on the forebody chine tend to collapse the directional stability for the various angles-of-attack. The model tends to exhibit near neutral C_{n_β} at the lower attitudes.

Effect of Reynolds Number on Directional Stability
Angle-of-Attack = 0°, 8°, 12° and 20°
Vertical Tail Off/Forebody Chine Off ~ M = 0.30

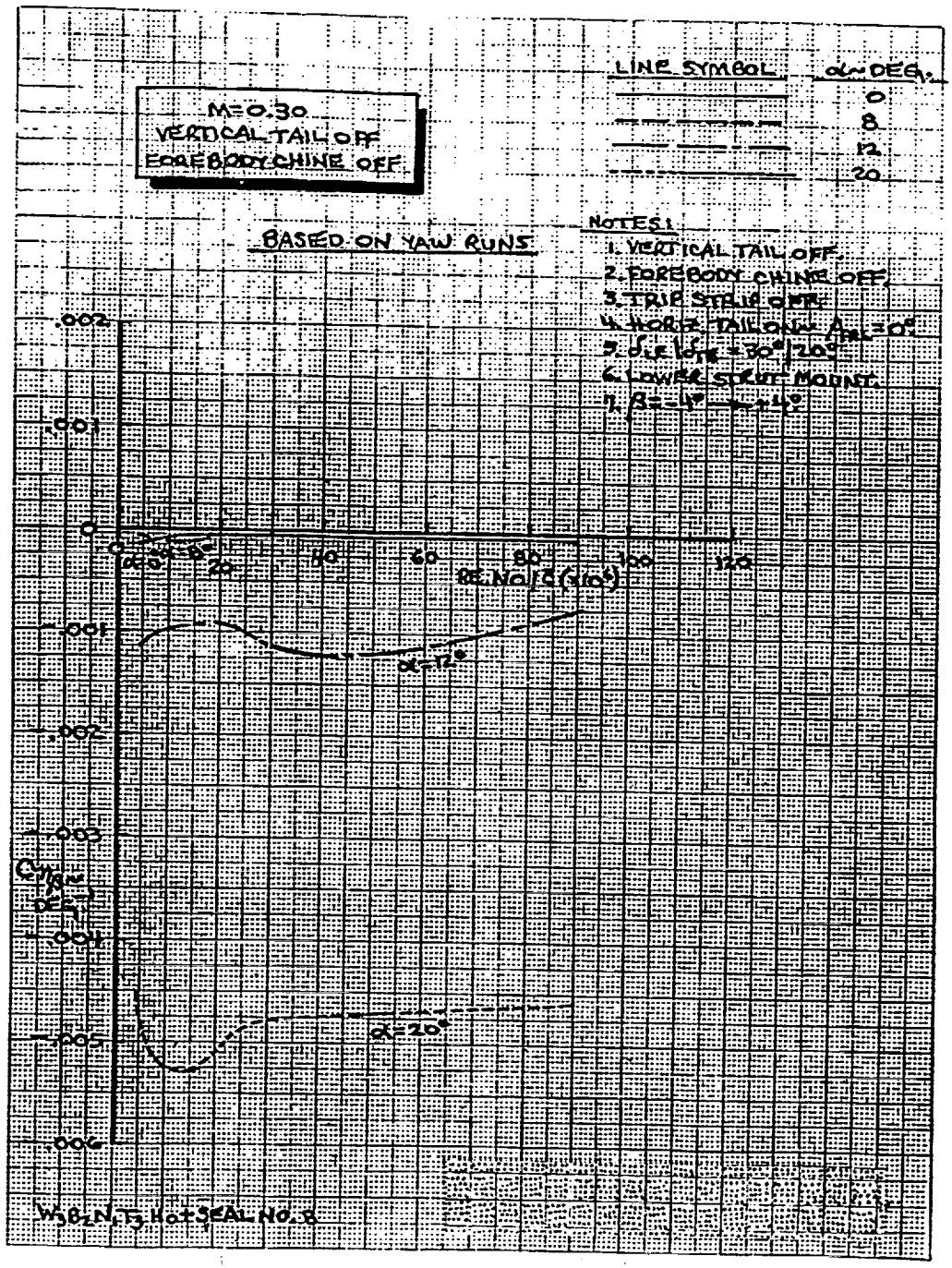

The directional stability levels shown above are for the vertical tail and forebody chine off configuration. At low attitudes, this model condition displayed neutral C_{n_β}, and was relatively invariant with Reynolds number growth. The higher attitude data tended to be more non-linear and more unstable.

Effect of Reynolds Number on Directional Stability
Vertical Tail On and Off/Forebody Chine On and Off
$\alpha = 0° \sim M = 0.30$

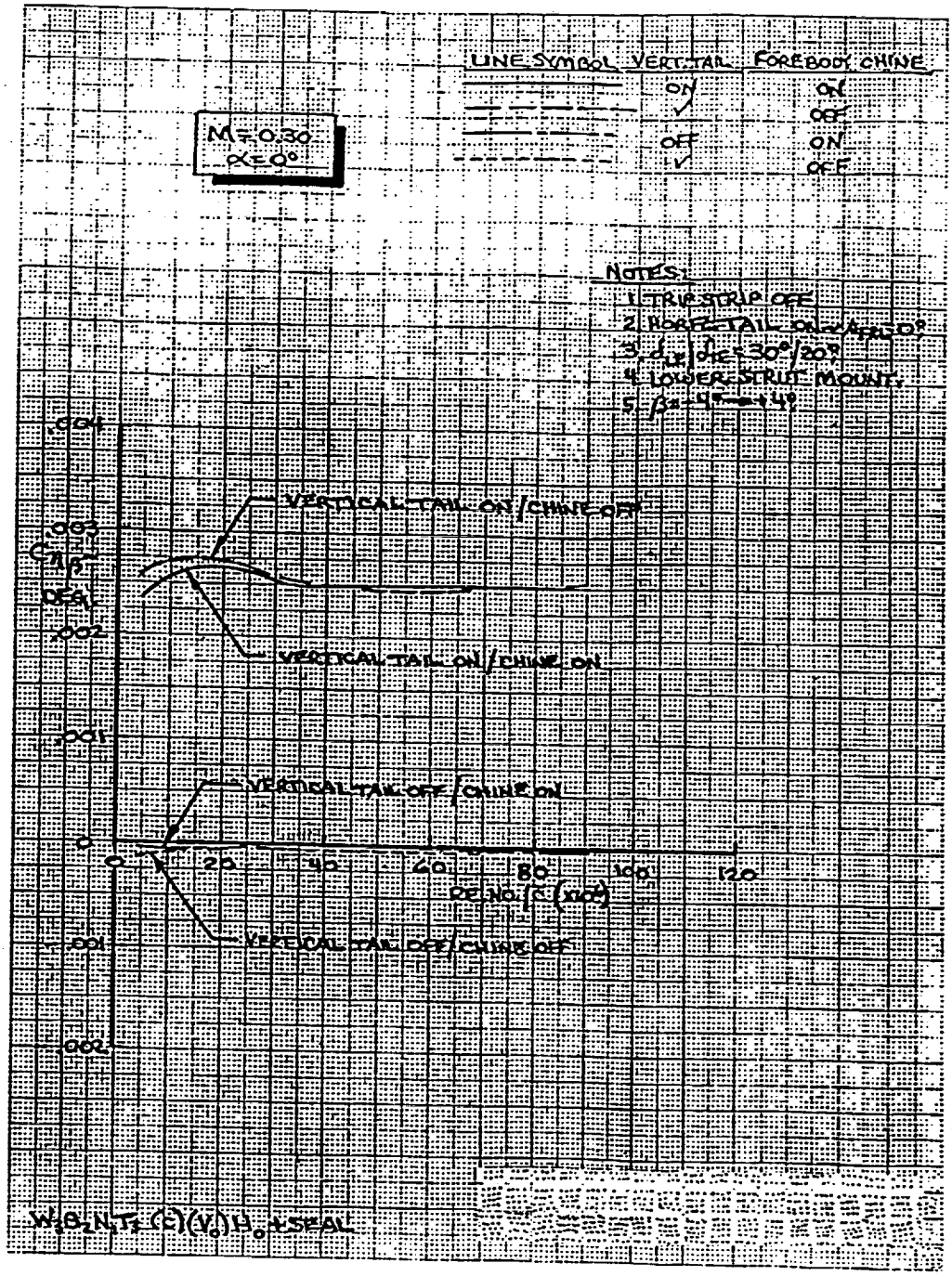

This chart shows that at low attitudes ($\alpha = 0°$), the high lift directional stability does not dramatically change with increasing Reynolds number. Also apparent is the fact that for these conditions, the forebody chine increment is negligible, and the vertical tail increment (chine on or off) is large.

Effect of Reynolds Number on Directional Stability Vertical Tail On and Off/Forebody Chine On and Off

$\alpha = 8° \sim M = 0.30$

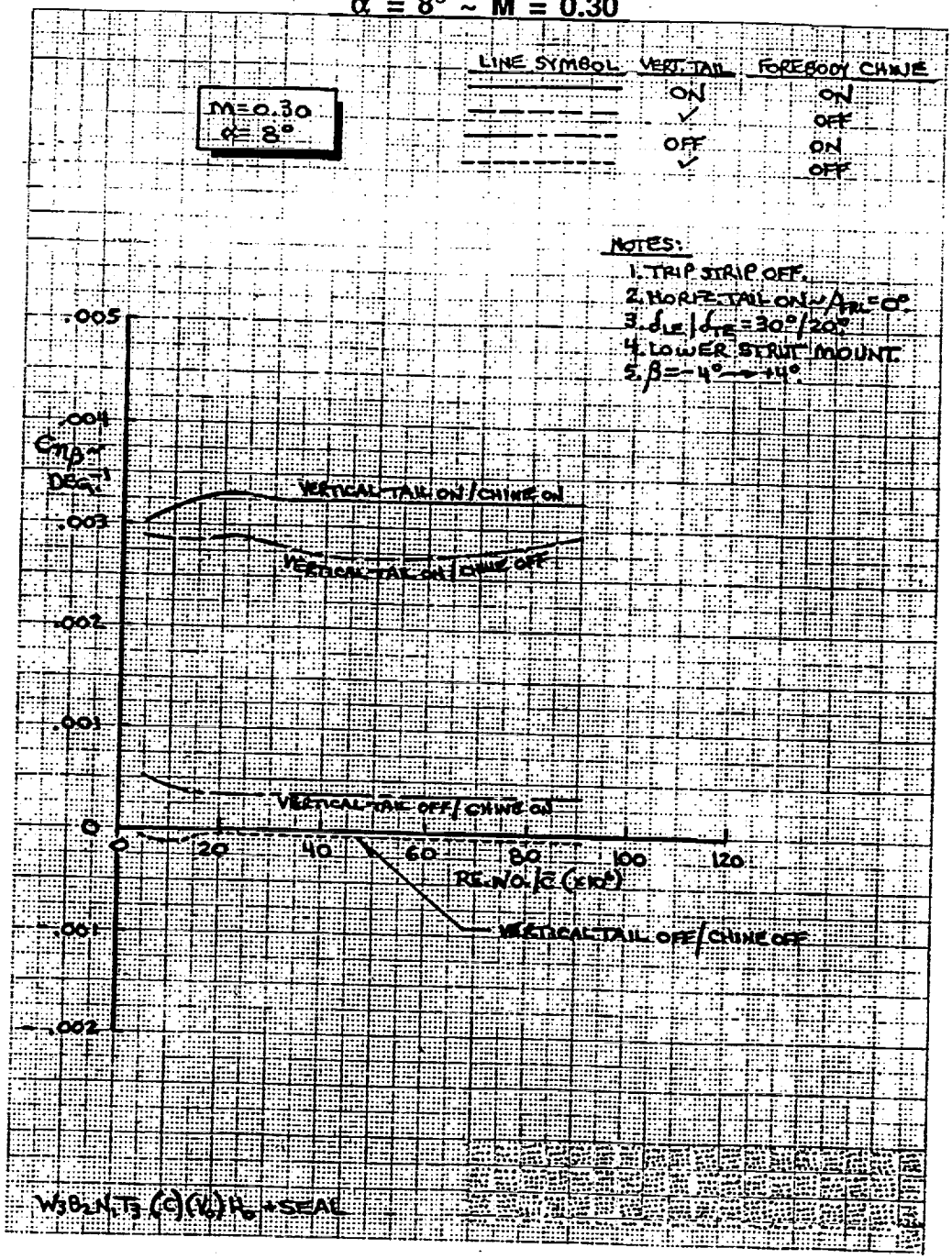

The chine increment grows somewhat with an increase in the angle-of-attack to 8°. Once again, the directional stability (C_{n_β}) is relatively linear with increasing Reynolds number.

Effect of Reynolds Number on Directional Stability
Vertical Tail On and Off/Forebody Chine On and Off
α = 12° ~ M = 0.30

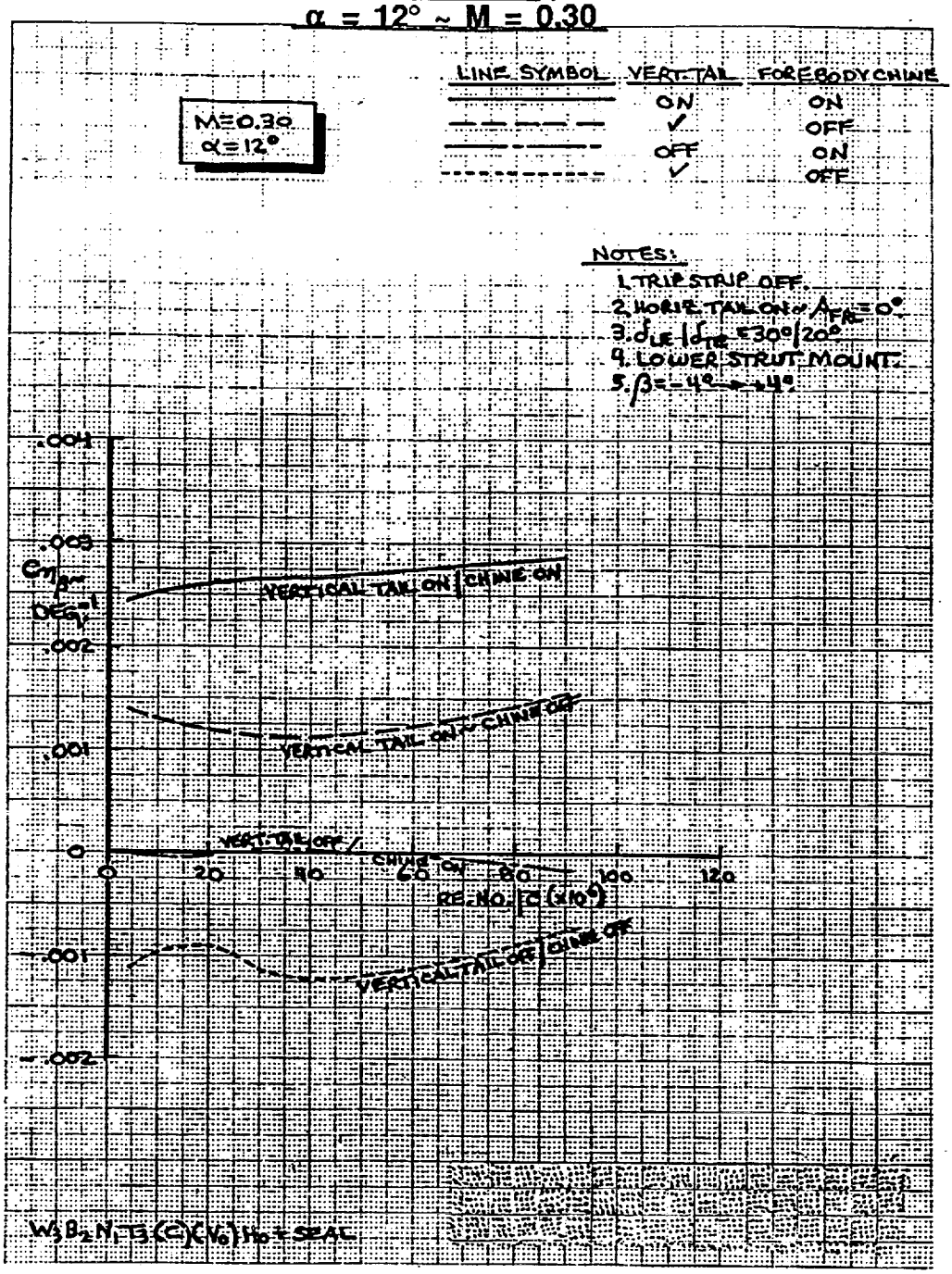

The forebody chine increment becomes larger by the time 12° angle-of-attack is reached. Directional stability change with Reynolds number is not as linear at this attitude.

Effect of Reynolds Number on Directional Stability Vertical Tail On and Off/Forebody Chine On and Off $\alpha = 20° \sim M = 0.30$

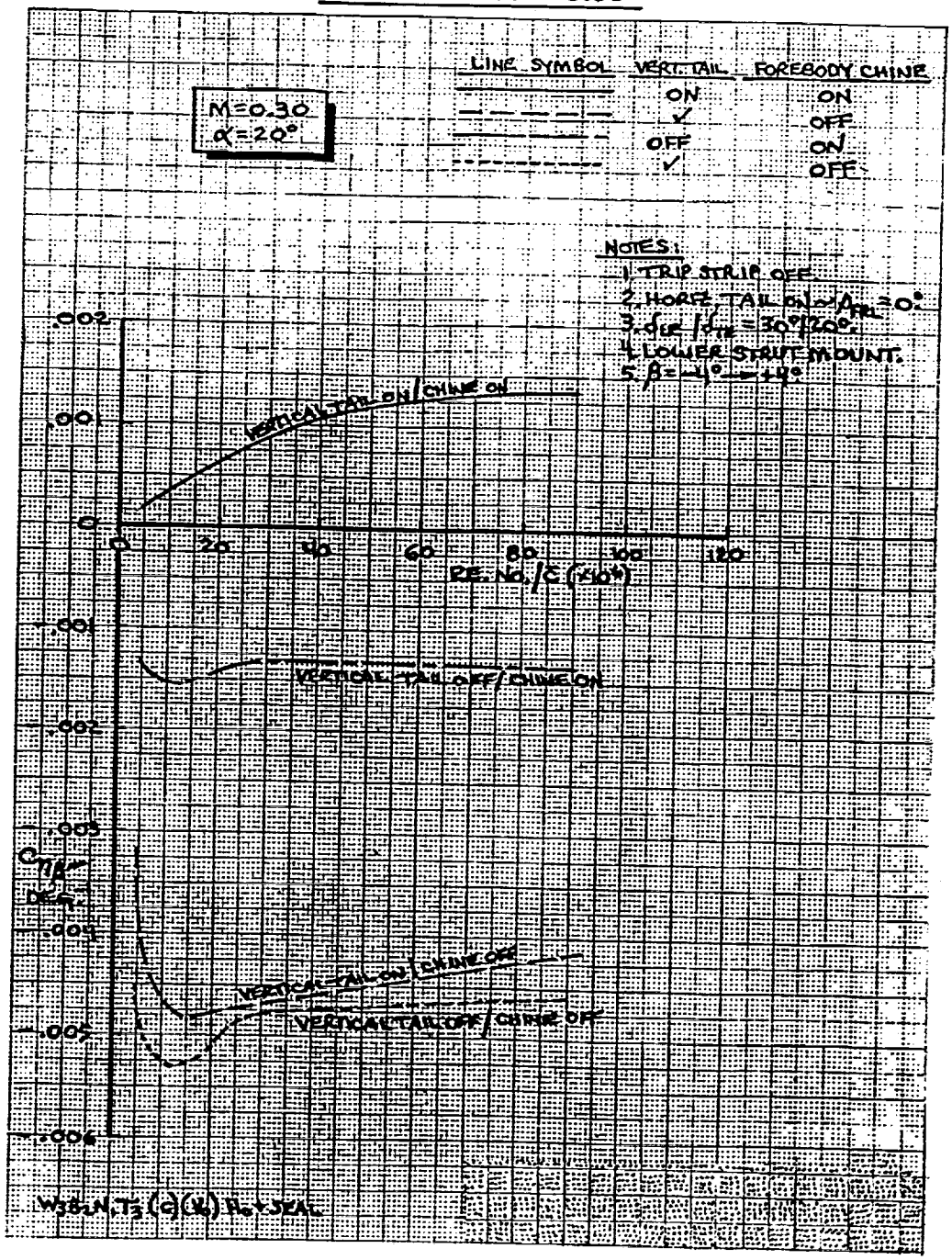

At $\alpha = 20°$, the chine influence on C_{n_β} is powerful. There is a significant change in directional stability as a function of Reynolds number for three of the four configurations. The vertical tail influence is still strong with the chine on. However, this is not true with the chine removed.

Effect of Reynolds Number on Directional Stability
Angle-of-Attack = 0°, 4°, and 8°
Vertical Tail On/Forebody Chine Off ~ M = 0.95

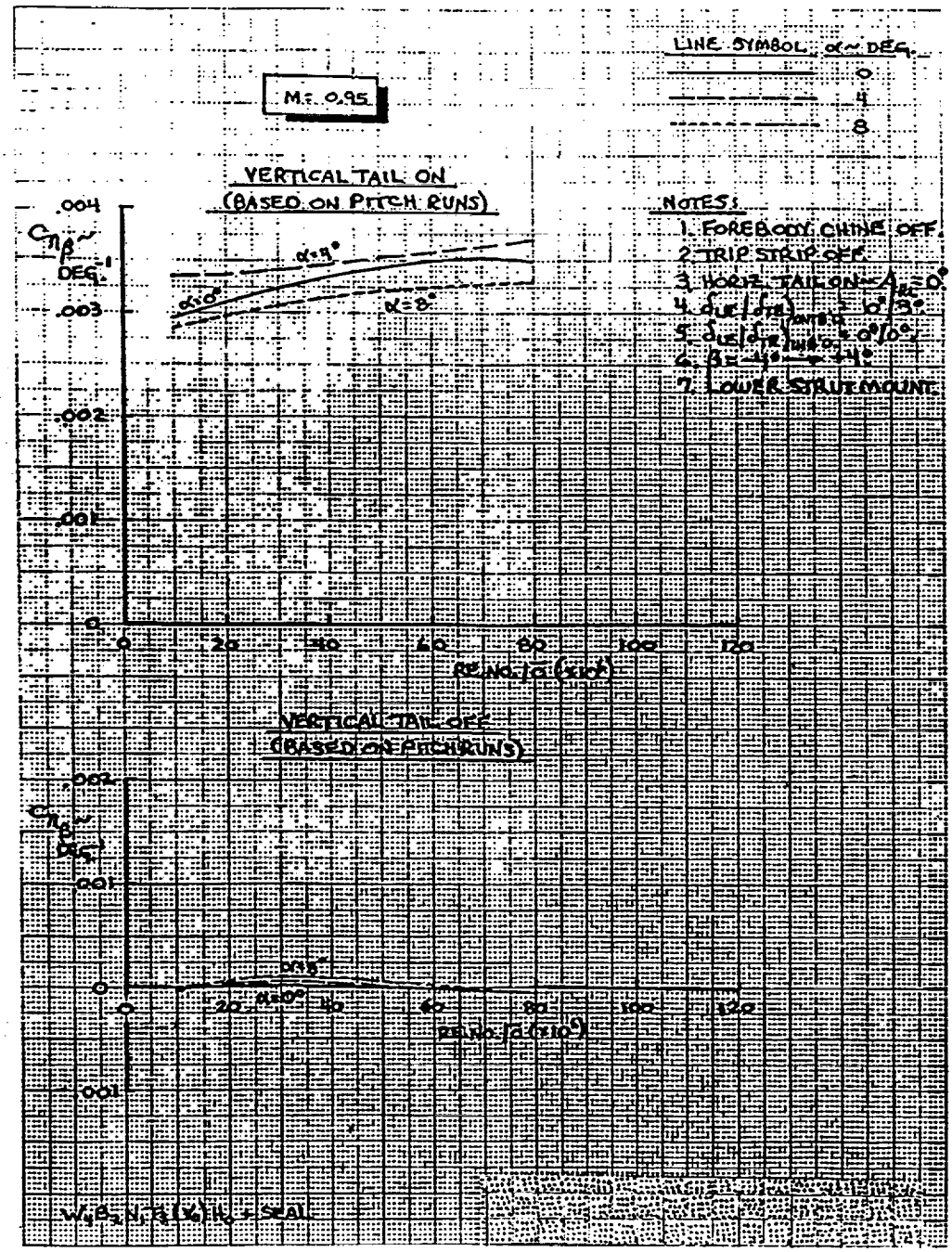

Transonic (M = 0.95) directional stability results are shown above. Vertical tail on and off data are shown. The forebody chine was removed. Vertical tail on Reynolds number growth provides a 10% to 20% increase in C_{n_β}. The directional stability with the vertical tail off had a near neutral stability level and was relatively invariant with increasing Reynolds number.

Effect of Reynolds Number on Directional Stability
Vertical Tail On and Off
α = 0° and 8° ~ M = 0.95

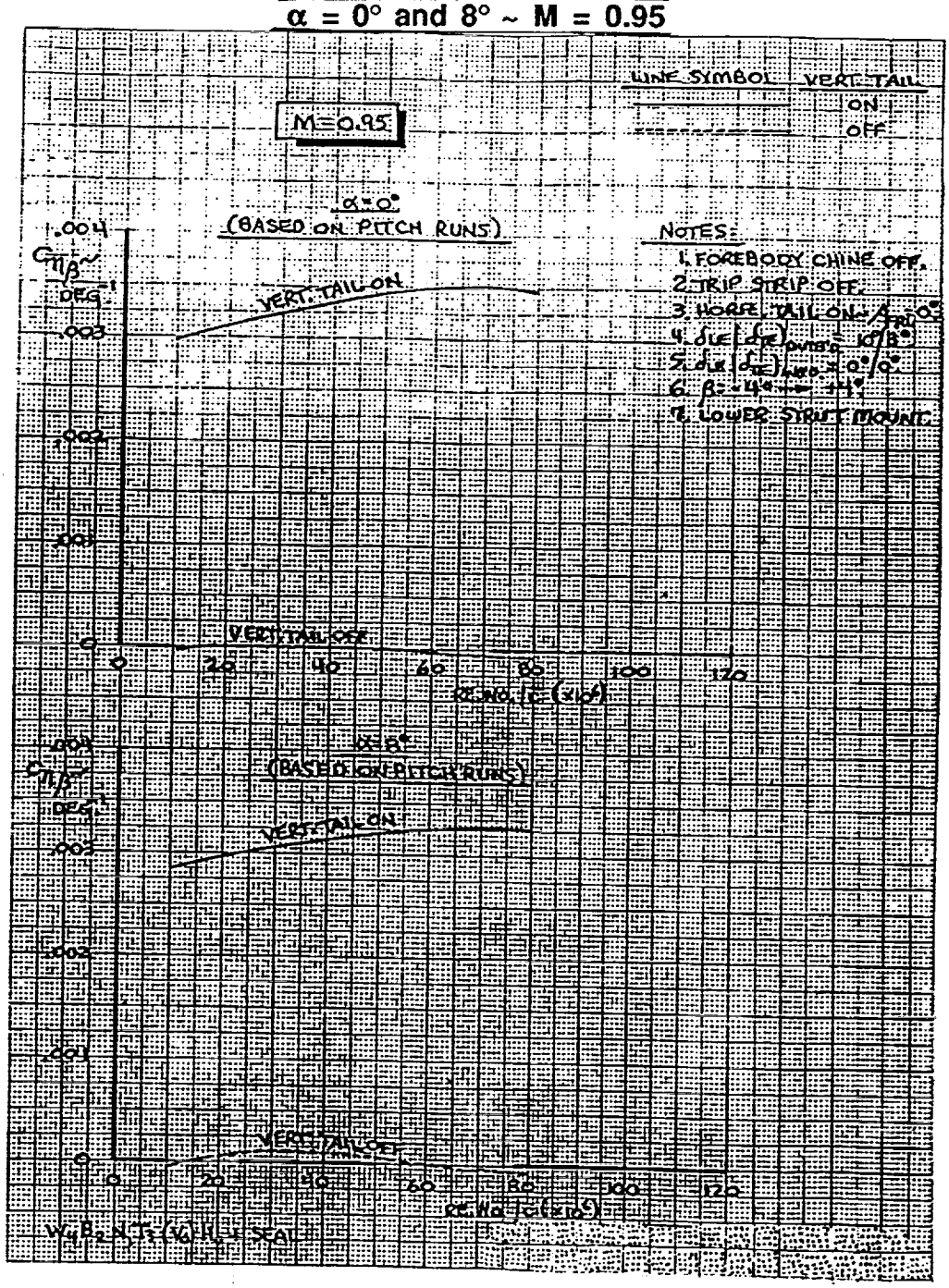

The above chart shows that directional stability, vertical tail on, for the transonic case (M = 0.95) at α = 0° and 8°, increases by 15% due to a chord Reynolds number growth from 10 to 80 million. This is not true for the vertical tail off condition, which remains at a near neutral stability level independent of Reynolds number.

Rudder Effectiveness in Sideslip

M = 0.30 ~ Reynolds Number = 4.4 x $10^6/\bar{c}$ ~ α = 8°

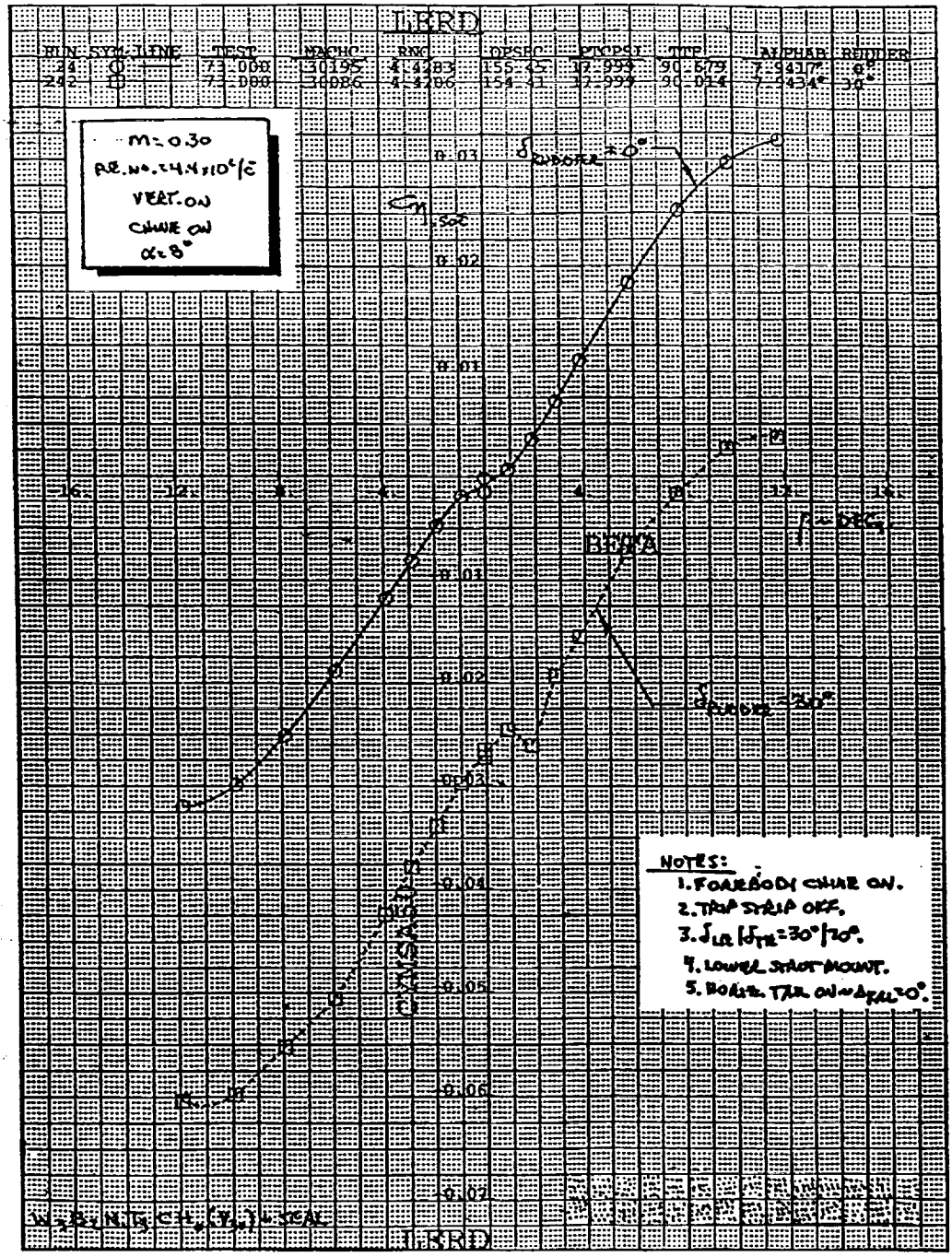

This chart presents the effect of rudder deflection on yawing moment as a function of sideslip angle at M = 0.30, with a chord Reynolds number of 4.4 x 10^6 and an angle-of-attack of 8°. Notice that with the rudder deflected 30°, directional stability is actually reversed between β = +1° and +2°. It is also evident that there is a significant loss in C_{n_β} from β = -1° to +1° with the rudder undeflected.

Rudder Effectiveness in Sideslip

M = 0.30 ~ Reynolds Number = 90.5 x $10^6/\bar{c}$ ~ α = 8°

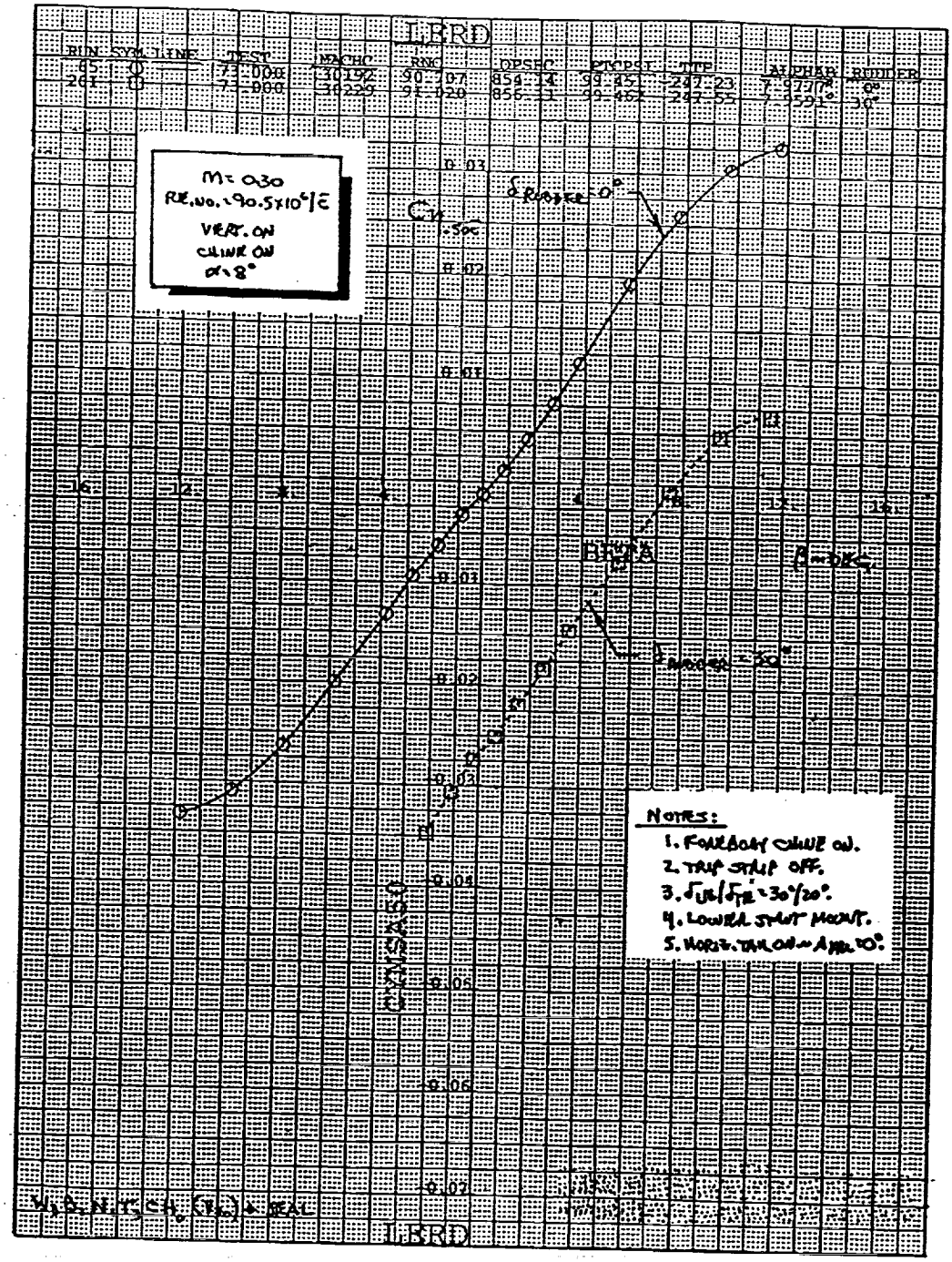

This figure gives the same information as on the previous page, except the Reynolds number has been increased from 4.4 x $10^6/\bar{c}$ to 90.5 x $10^6/\bar{c}$. Note that the non-linparities in directional stability have been virtually eliminated.

Effect of Reynolds Number on Directional Stability
M = 0.30 ~ δ_{Rudder} = +30° ~ α = 12°

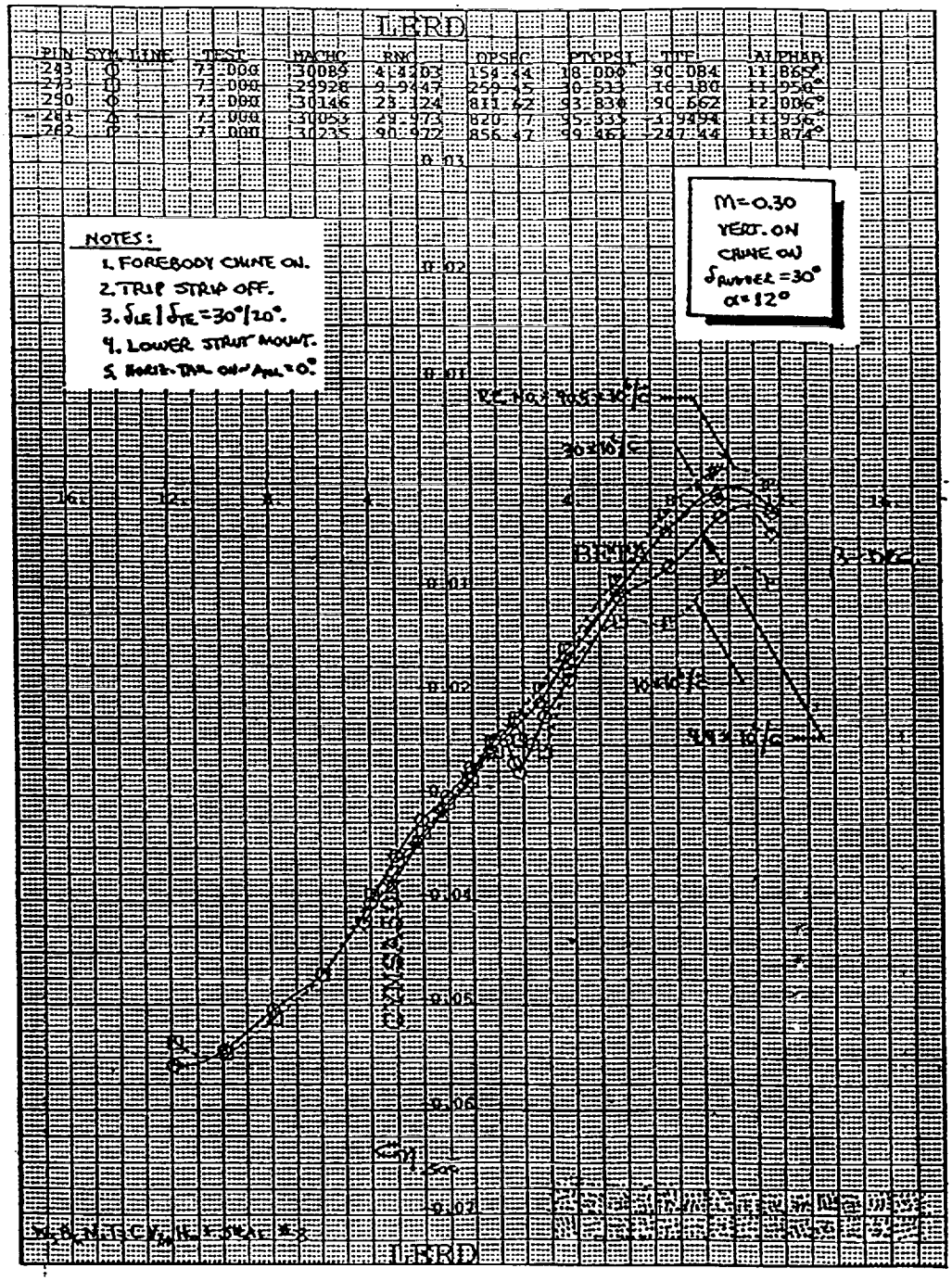

The data above show the effect of Reynolds number on directional stability and control at M = 0.30, α = 12° with the rudder deflected +30°. It will be observed that the non-linearity experienced between β = +1° and +2° disappears with increasing Reynolds number. Also not to be overlooked is the fact that, at low Reynolds numbers with full rudder deflection, maximum sideslip full rudder trim capability is not achieved. However, high Reynolds number testing mitigates this condition.

Conclusions

- Longitudinal stability increased slightly with higher Reynolds numbers for the high lift condition.
- Reynolds number increase had little effect on longitudinal characteristics high speed.
- Longitudinal model aeroelastics are small. An outboard wing twist change was evidenced high speed.
- The vertical tail provided a solid input to directional stability, particularly at lower attitudes, both in the high lift and high speed conditions.
- The forebody chine supplied a strong increment to C_{n_β} at higher attitudes in the high lift configuration.
- Increasing chord Reynolds number had little effect on C_{n_β} for the high lift condition at lower angles of attack. This Reynolds number increase did help directional stability at $\alpha = 20°$ with both the vertical tail and forebody chine on. When the chine was removed and the vertical tail left on, Reynolds number growth caused a loss in C_{n_β} in an already unstable state.
- As the Reynolds number level was extended, high speed C_{n_β} increased between 10% and 20%.
- Directional stability in the high lift configuration was somewhat non-linear in sideslip with the rudder undeflected and reverses near $\beta = 0°$ at $4.4 \times 10^6/\bar{c}$ Reynolds number for $\alpha = 8°$. This non-linearity is eliminated at the highest Reynolds number tested.
- At low Reynolds numbers, maximum sideslip full rudder trim is not achieved. However, trim is achieved at high Reynolds number.
- Future near term stability and control high Reynolds number testing should include:
    - Elevator effectiveness at low speeds.
    - Additional leading and trailing edge deflections with the empennage on.
    - Trip strip effects.

Simulated Inlet Unstart and Nacelle/Diverter Effects for the Boeing Reference H Configuration

Susan E. Cliff, Timothy J. Baker, Scott D. Thomas, Ernest D. Aguayo

1 Abstract

The Boeing Reference H configuration was tested in the NASA Ames 9x7 Supersonic Wind Tunnel. A simulated unstarted inlet was evaluated as well as the aerodynamic performance of the configuration with and without nacelle and diverter components. These experimental results were compared with computational results from the unstructured grid Euler flow solver *AIRPLANE*. The comparisons between computational and experimental results were good, and demonstrated that the Euler code is capable of efficiently and accurately predicting the changes in the aerodynamic coefficients associated with inlet unstart and the effects of the nacelle and diverter components.

2 Introduction

Inlet unstart can cause drastic changes in the aerodynamic forces and moments acting on an aircraft, often resulting in severe controllability problems. Inlet unstart can arise from a rapid maneuver, a sudden change in atmospheric temperature (Mach number), or an engine induced disturbance. Any of these conditions can alter the shock system in an mixed compression inlet and cause the normal shock to propagate forward of the nacelle. Wind tunnel tests are usually performed to determine the severity of the controllability problem associated with an inlet unstart by measuring changes in the forces and moments with one or more unstarted inlets. Such tests are expensive and time consuming, consequently an efficient computational method to predict changes in force and moment coefficients due to inlet unstart would be a great benefit to the aircraft designer.

In this report, *AIRPLANE* computational predictions are compared with experimental results for the Boeing Reference H configuration obtained during a test in the NASA Ames 9x7 Supersonic Wind Tunnel. Comparisons are presented for the configuration without nacelles, with fully started captive nacelles, fully started non-captive nacelles, as well as unstarted non-captive nacelles. In the next section we describe the experimental configuration and test conditions. This is followed by a brief description of the computational method and details about the simulations that were carried out. The remainder of the report provides a detailed comparison of the computational and experimental results, showing how the computer simulations can provide considerable insight into the aerodynamic effects of an inlet unstart.

3 Experimental Model and Instrumentation

A 2.7% scale model of the Boeing Reference H configuration was tested in the NASA Ames 9x7 Supersonic Wind Tunnel. The fuselage was truncated a short distance downstream of the wing trailing edge and bored to accept a six component balance and sting assembly. The model had a total of 370 pressure taps on the wing, body, and nacelles. Flow-through five-component balances were installed within the right hand nacelles to measure individual nacelle forces. The left hand nacelles were pressure instrumented. The non-captive nacelles were mounted on a remotely controlled support system which provided a three- dimensional nacelle position capability. This instrumentation is further described in [1]. A mass-flow control plug and pressure instrumentation were incorporated into each nacelle sting to control and measure the mass-flow through each nacelle. An installation photograph of the model is shown in Fig. 1. The mass-flow characteristics of each nacelle/sting assembly were determined by static calibrations prior to installation in the wind tunnel. The data presented in this report were taken at Mach 2.4 and a Reynolds number 3 million per foot. All aerodynamic forces and moments on the wing/body and individual nacelles were measured for a range of mass-flow ratios for the right- hand outboard nacelle. The outboard nacelle was selected for unstart since it produces the larger change in the lateral and directional moment coefficients.

Force and pressure data on the various components were obtained for the following four configurations: wing/body alone, captive flow-through nacelles, non-captive flow-through nacelles, and non-captive nacelles

with an unstarted right-hand outboard nacelle.

4 Computational Method

All computations were carried out with the *AIRPLANE* code [2, 3]. This computational method uses a vertex based finite volume method to solve the Euler equations on an unstructured tetrahedral mesh. The mesh generator employs a Delaunay triangulation algorithm [4, 5] to create a tetrahedral mesh throughout the flowfield. *AIRPLANE* has proven to be very reliable and capable of handling a variety of complex geometries. It has been used extensively in several investigations of supersonic transport configurations [6, 7, 8]. These studies have been undertaken as part of a successful program of research at NASA Ames to reduce sonic boom, improve aerodynamic performance, and analyze nacelle/airframe integration. Use of the *AIRPLANE* code to study the inlet unstart problem, however, represents a different application of the method which warranted a careful validation with experimental data.

An unstructured tetrahedral mesh was developed for the complete baseline Reference H configuration including the wing, body, tails, nacelles and diverters. A close up view of the *AIRPLANE* surface geometry in the vicinity of the nacelles is shown in Fig. 2. The surface is colored by local pressure coefficient for the captive flow-through nacelle case. The thin boundary layer diverters make it challenging to obtain a high quality surface mesh in the region of the nacelles, diverters and wing lower surface. The rapid transition from the blunt inboard wing to the sharp outboard wing was accurately modelled in the *AIRPLANE* computation. The configuration was meshed in a modular fashion so that components could easily be removed or interchanged, and meshes for different configurations could be generated in a straight forward manner. Each nacelle and diverter comprised one component in the data set which could be easily modified to generate a mesh for the wing/body configuration with or without the nacelle/diverter assembly. To obtain meshes for the non-captive nacelle cases, the isolated nacelles were simply added as separate components to the wing/body data set and these meshes were quickly generated.

For the unstart cases, the mass-flow within the nacelle was controlled by the use of a mass-flow plug. The plug was translated along the nacelle axis into the aft portion of the nacelle to change the nacelle exit area. The aft portion of the outboard nacelle was extended nearly two diameters downstream to ensure that the interference from the mass-flow plug would not alter the pressure distributions on the forward part of the nacelles. This modified outboard nacelle was treated as a separate component and replaced the original outboard nacelle in the data set. The axisymmetric mass-flow plug was defined by attaching two 30 degree cones to a smooth transitionary surface which imposed tangency along the base of each cone. A drawing of the nacelle and plug is shown in Fig. 3. The small included cone angles and the smooth transitionary surface on the plug were designed to produce an attached bow shock wave for started cases, and also to limit the expansion on the aft portion of the plug. For each new plug position, the translated plug definition simply replaced the previous plug data set and a complete mesh was automatically generated.

The *AIRPLANE* flow solver usually requires between 1,000 and 2,000 iterations to achieve convergence at supersonic Mach numbers for configurations with started nacelles. For the unstarted nacelle cases, the convergence was slowed significantly because the terminal shock had to propagate internally from the nacelle exit to the inlet, before the external flow field could develop. The normal shock wave was still inside the nacelle after 2,000 iterations. The shock position depends on the nozzle back pressure which is affected by overall changes in the flow field. However, it takes several iterations for a small change in shock position to influence the nozzle back pressure and thus initiate a further adjustment of the shock strength and position. A total of 20,000 iterations was required to achieve a fully converged solution which could only be attained after the normal shock had propagated through the nacelle to a position in front of the inlet.

The computations were carried out on the IBM SP2 at NASA Ames. This computer system consists of 160 IBM 590 processors running in parallel. The parallelized version of the *AIRPLANE* code has been shown to give linear speed up [9] as the number of processors is increased. Converged solutions for these cases (20,000 iterations) were achieved in 6 hours using 64 nodes for meshes with approximately 459,000 points and 2.77 million tetrahedral cells. This exceptional speed-up in computational time permitted several computations for this problem to be obtained within a reasonable turnaround time.

5 Corrections to Experimental and Computational Results

The lift, drag, and pitching moments on the individual nacelles were measured experimentally using 5-component flow-through balances. The balances were intended to measure the forces on the external surfaces of the nacelles. However, several corrections to the balance data were necessary to isolate the exterior forces. A total of five corrections were applied to the measured axial-force data. Four pressure-area corrections were

made, these include corrections for: the forward and aft balance cavities, the forward lip of the balance, and the rubber seal which was used to prevent flow through the balance cavity and maintain a uniform pressure within the cavity. The fifth correction was a skin friction correction on the forward interior portion of the nacelle.

To obtain the forces and moments of just the external surfaces of the nacelles in the computational results, several auxiliary programs were developed and used to isolate surface triangles not on the exterior of the nacelles and obtain the aerodynamic coefficients of these parts. The algorithm which computes the force and moment coefficients by integration of the surface pressures was removed from the *AIRPLANE* code to run independently on a workstation. In addition, three auxiliary programs were used to isolate the surface triangles covering the aft extension used on the unstarted nacelle, the surface triangles on the nacelle interior, and those at the base of the nacelle. The first program was used to eliminate all triangles behind a plane lying at the true aft end of the actual nacelle. This program was only applied to the outboard nacelle where the nacelle surface in the computational model had been extended to eliminate any interference effects from the plug. The second program was used to obtain all triangles with aft facing surface normals in order to isolate the nacelle base from the rest of the nacelle. The base pressures were integrated separately and then the drag from the base was subtracted from the computations. This program was not needed for the plugged nacelle, since the aft portion was removed by the application of the first program, and also the extended aft surface of the nacelle closed smoothly to a circle. The third program was used to isolate all triangles on the interior of the nacelle. This program makes use of the fact that the nacelles are nearly aligned with the x-axis. By determining the included angle between the surface normal vector and a position vector which extends perpendicularly from the line through the center of the nacelle to the surface face, the interior triangles can be identified as those with included angles between 90 and 180 degrees. The interior nacelle forces were then obtained and the drag subtracted from the computations. A calculated flat plate skin friction value of 0.19 counts (per nacelle, based on the wing reference area) was added to the nacelle drag to permit realistic comparisons with the wind tunnel results.

6 Determination of Mass-Flow Ratio for Computed Results

Mass-flow ratio (MFR) is a nondimensional quantity that measures the amount of mass flux passing through a surface S relative to free-stream values. It is defined as the integral over S of the inner product of the local momentum vector, $\rho\mathbf{V}$, and an element of area, $d\mathbf{A}$, divided by free-stream momentum and reference area A.

$$\mathrm{MFR} = \frac{\int_S \rho\mathbf{V}\cdot d\mathbf{A}}{\rho_\infty \|\mathbf{V}_\infty\| A}$$

The surface of integration is the interior of the circle contained inside the nacelle, in a plane oriented perpendicular to the axis. The surface S becomes annular when the nose of the plug is moved forward of the aft most cutting plane. For converged steady state flow, the computed value of MFR was found to be the same, to two decimal places, inside the nacelle independent of position along the axis.

When used in conjunction with the *AIRPLANE*/flow solver the MFR is computed based on the unstructured tetrahedral mesh and node-based solution. For each surface of integration, S, a planar slice is derived from the mesh and solution files. The slice consists of triangles and flow values (density, momentum, and energy) at the vertices. The slicing algorithm treats each tetrahedron that touches S, creating one or two triangles apiece. Triangle vertices and flow values are found by linear interpolation along the edges of the tetrahedron. Two triangles are created when the intersection of a tetrahedron with the plane is a quadrilateral.

The integral is approximated by the sum over the slice triangles of the inner product of $\rho\mathbf{V}$ and the triangular element area vector. The value $\rho\mathbf{V}$ for each triangle is the average of the values at the three vertices, and the area vector is half the cross product of two edge vectors. Care is taken to orient the surface vectors the same way, streamwise, and to accumulate values with 64-bit real precision. The reference area, A, is the sum of the magnitudes of the triangle element areas. The mesh spacing is small enough to make this value nearly the same as the area of a circle of the same radius as the interior of the nacelle.

7 Computational Results

The starting position of the nacelle plug was estimated using quasi-one dimensional analysis to obtain a mass-flow ratio in the outboard nacelle near the experimental value of 0.385. This was the smallest measured MFR in the experimental data set and represented a data point where the outboard nacelle was definitely unstarted. The actual value of MFR obtained from the computation was 0.447 for this initial plug position. An adjustment of the position gave the experimental value to 3 decimal places. The computational plug was

subsequently moved to 5 other positions to provide a range of MFR data from 0.385 to 1.124.

The *AIRPLANE* computations were obtained at the same Mach number and angle of attack as experiment (M = 2.41, α = 4.53 deg). However, the experimental model could not be positioned at precisely zero degrees yaw and the experimental data was, in fact, taken at a yaw angle of -0.56 deg. This primarily affected the yawing moment and had little impact on the other forces and moments. Since the option to compute the flow at non-zero yaw angles has not yet been implemented in *AIRPLANE*, all computations are presented at zero degrees yaw and were derived from solutions for the right hand side of the configuration, assuming lateral symmetry. Two solutions were required to achieve results for the non- symmetric cases, one with flow-though nacelles and one with the outboard nacelle unstarted. The lift, drag, and pitching moment coefficients could easily be obtained by adding the flow-through and unstart results and dividing by 2 to adjust the reference area. The rolling and yawing moment coefficients were obtained by subtracting the unstarted results from the started results and dividing by four, to adjust the reference area and span.

A view of the computational surface pressure coefficient contours for the unstarted case with MFR of 0.39 is shown in Fig. 4. The dramatic bow shock generated by the unstarted nacelle is readily apparent on the wing lower surface. The inboard nacelle shocks are benign in comparison, but are evident by the increased shock strength on the wing between the nacelles. The C_p contours computed by *AIRPLANE* are shown for a started case, with the plug moved aft, using the same color map used in Fig. 5. The shocks off the outboard nacelle are now of the same magnitude as the inboard. Lower surface planform views of the configuration with started and unstarted nacelle are shown in Fig. 6.

A vertical slice through the flow field which intersects the axis of the outboard nacelle is shown in Fig. 7. The Mach contours calculated by *AIRPLANE* are displayed. The stand off distance for the detached bow wave is evident; the non-smooth shape is due to a non-uniform grid. The subsonic flow within the duct appears to be fairly uniform, indicating that the solution has converged. Velocity vectors colored by Mach number through this vertical slice are shown in Fig. 8. The velocity vectors upstream of the inlet turn away from the unstarted nacelle. The flow enters the nacelle asymmetrically and appears to be diverted downward (away from the wing). This is a result of the high pressure in the region between the nacelle and wing, forcing the flow to turn downward.

Seven cuts normal to the nacelle axis were used to compute mass-flow ratio within the nacelle duct. These seven computations were averaged to determine a single value. The variation between cuts was small, on the order of 0.25 percent. A view of the slices colored by Mach number for the unstart case is shown in Fig. 9. The lower portion of the forward cuts exhibit slightly lower Mach number than the aft cuts due to the downward pointing velocity vectors at the inlet (compare with Fig. 8). The small hole in the aft-most cut is from the intersection of the plug with the slice. A started case is shown in Fig. 10. Here, the flow is near free-stream, and the shocks reflecting within the nacelle result in color reversals of the Mach contours along the duct.

8 Wing/Body Pressure Distribution Comparisons

Experimental and computational pressure distributions on the wing/body are compared for the following four cases: wing/body alone, captive flow-through nacelles, non-captive flow-through nacelles, and non-captive nacelles with an unstarted right-hand outboard nacelle. The streamwise and spanwise cut locations are superimposed on the lower surface pressure contours predicted by *AIRPLANE* for the unstarted case in Fig. 11. Similarly, the started captive and non-captive nacelle pressure coefficient contours are displayed in Figs 12 and 13. These three figures can be used to identify the source of shocks when studying the wing-body pressure distributions where the flow from the nacelles causes rapid variations in the wing pressures.

The pressure distributions for a streamwise cut near the fuselage (Y=124.56) are shown for the four configurations in Figs. 14a-d. The comparisons for wing/body alone agree fairly well, with a small disagreement in the upper surface pressures near the mid chord. This disagreement is reduced in the captive nacelle cases (Fig. 14 b), due to a closer match in the computational and experimental lift coefficients. The computational shocks from the inboard nacelle and diverter lie aft of experiment and are of weaker strength. The aft shift in shock location is expected from inviscid computations, because in a viscous flow the shock pressure rise is propagated upstream in the subsonic region of the boundary layer. The comparison of the non-captive started nacelles case is similar to the captive started case (compare Figs. 14b and 14c).

The comparisons for the unstarted nacelle (Fig. 14d) show discrepancies in the pressure distributions near the nacelle shocks. The experimental shock is stronger than that predicted by *AIRPLANE*. The single experimental shock results from the intersection of the outboard and inboard nacelle shocks, whereas the *AIRPLANE* computations show two distinct shocks. The upstream shock emanates from the inboard nacelle, and the aft shock from the outboard nacelle. The source of the shocks can easily be identified in Fig. 11.

For station Y=181.93, the pressure taps right adjacent to the inboard nacelle could not be incorporated

into the model and hence are not available for comparison. The available data, presented in Figs. 15a-d, compare well with the computational results. The strength of the computational nacelle shocks has increased as expected with reduced distance from the nacelles (compare with previous figure).

The pressure distributions for the next streamwise station (Y=252) are shown in Figs. 16a-d. This station is located between the nacelles very near the inboard nacelle. The wing-body results compare well, particularly on the lower surface. The upper surface pressures are in slightly better agreement for the captive nacelle cases (compare Figs. 16a and 16b). The computed nacelle shocks are weaker and aft of experiment (Figs. 16b and 16c). *AIRPLANE* shows two distinct shocks for the unstarted case (Fig. 16d); the upstream shock originates from the outboard nacelle, and the aft shock from the inboard nacelle. The outboard nacelle shock is of sufficient strength to be forward of the inboard nacelle shock even though the data are sampled much closer to the inboard nacelle (see Fig. 11). The experimental data also indicate that two shocks are present, but it is too sparse to determine the strength of the shocks.

The comparisons for the second streamwise cut between the nacelles (Y=323.79) are shown in figures 17a-d. The *AIRPLANE* results show one large shock for the unstarted case, whereas the experimental data suggests that the shocks from the inboard and outboard nacelles are distinct.

The next cut (Y=473) is located outboard of the outboard nacelle. The pressure comparisons are shown in Figs. 18a-d. The unstarted nacelle shock creates a broad region of high pressures on the outboard wing lower surface in both the computational and experimental results (Fig. 18d). The computational shock is slightly aft of experiment but the magnitudes of the shocks are in good agreement.

The pressure comparisons for the remaining streamwise cut on the outboard wing are shown in Figs. 19a-d. The comparison for the unstarted case (Fig. 19d) shows poorer agreement than the previous span station (Fig. 18d) due to the growing displacement between the computed and measured shock waves.

The pressure distributions in the spanwise direction for the four configurations are shown in Figs. 20-24. The comparisons are made at slightly different angles of attack resulting in small differences between the results upstream of the nacelles (Figs. 20-21). The leading edge pressure spike is under predicted by *AIRPLANE*. It seemed likely that this discrepancy arose from an inadequate rendering of the wing leading edge curvature. In order to test this possibility, the leading edge was refined by adding three additional span sections between each pair of the original sections. However, even with this refinement, the experimental pressure peak at the leading edge was still under predicted. The shock on the upper surface in Fig. 20 is accurately predicted by *AIRPLANE*. Similar good comparisons are shown in Fig. 21. Here, the leading edge is sharp but no experimental taps were available to compare the leading edge pressure distributions.

The next cut slices through the outboard nacelle, which is depicted in the geometrical representation in Fig. 22. Excellent comparisons are shown for the wing-body and captive nacelle cases (Figs. 22a and b). The *AIRPLANE* results for the non-captive unstarted case correlate well with the experimental data. The unstarted case depicts the computational bow shock as two large pressure spikes symmetrically located on either side of the outboard nacelle. The bow shock is not as easily identified in the experimental data due to the lack of pressure taps at this station.

The computational and experimental pressure comparisons for the next spanwise cut sliced through both nacelles (Fig. 23). The wing/body results correlate well. The wing/body/nacelle/diverter results do not correlate very well, especially between the nacelles and on the inboard side of the inboard nacelle. In general, the computational shocks are stronger and located a smaller distance from the nacelle center than experiment. The four nacelle shocks predicted by *AIRPLANE* can easily be identified by the four rapid increases in wing pressures. The non-captive started nacelle case (Fig. 23c) shows very good correlations between experiment and *AIRPLANE*. The unstarted case shows the large spread of the bow shock indicative of the large distance of the nacelle shock to this wing station. The strength and location of the inboard portion of the bow shock is in close agreement with experiment. The lack of outboard experimental taps makes it impossible to compare the outboard half of the bow shock.

The pressures for the final cut near the trailing edge of the wing are shown in Fig. 24. As before, the wing/body results are very good. The captive nacelle comparison is fair in the vicinity of the nacelles and the non-captive solution shows very good agreement. This may be a consequence of a larger discrepancy in the shock strength for the diverters which are deeply submerged in the boundary layer rather than due to the shocks from the nacelles which lie outside of the boundary layer. The lower surface pressures correlate well outboard of the outboard nacelle, but poor comparisons are shown inboard for the unstarted nacelle case. This poor agreement may be a result of the shock angle differences being accentuated by the large distance from the leading edges of the nacelles to this station.

9 Aerodynamic Coefficients for the Wing/Body and Started Nacelle Configurations

The *AIRPLANE* force and moment coefficients for the wing/body configuration near the cruise flight condition are compared with three experimental runs in Fig. 25a. The results are in very good agreement. The enlarged scale shows that the computations predict more lift than experiment, although the slopes of the curves compare well. The drag comparisons are excellent; the drag difference is less than two drag counts. An axial force skin friction correction of 61.6 counts was added to the computations for realistic comparisons with the experimental data. The correction was applied to the axial force computations, and the lift and drag were recomputed at the computational angle of attack. The correction was derived from a flat plate skin friction value of 59.6 counts plus an additional 2.0 counts to account for the drag of the trip dots used to fix transition on the wind tunnel model. The pitching moment data comparisons are also in excellent agreement near the cruise condition. The full range of data is compared in Fig. 25b. The differences between the computational and experimental data is not evident at this scale, except for in the pitching moment curves, where the computations are predicting more stability than experiment.

The force and moment comparisons for the complete configuration including boundary layer diverters and flow-through nacelles are shown in Fig. 26a. The magnitude of the computational lift coefficients is in better agreement with experiment, than the wing/body results (compare with Fig. 34a). A very slight difference in lift curve slopes is evident. The computational and experimental drag polars correlate very well. The computational drag coefficients are shown with the base and internal duct drag removed. The correction to the computational axial force coefficient was 69.4 counts which consisted of a flat plate skin friction value of 67.4 counts and 2.0 drag counts of trip dot drag. The pitching moment comparisons are very good, the computations indicate slightly more positive moments with increased stability than experiment. The full range of experimental data is compared with the *AIRPLANE* computations in Fig. 26b. Here, the only differences seen are in the pitching moment data, where the *AIRPLANE* results again indicate more stability than experiment (compare with Fig. 25b).

The force and moment comparisons for the wing/body configuration with non- captive nacelles near cruise are shown in Fig. 27a. The computations are predicting more lift for a given angle of attack than experiment. Note that the lift coefficient comparisons with the diverters present are in better agreement than the wing/body and wing/body/nacelle cases (compare Figs. 25a, 26a, and 27a). The computational axial force correction was 69.3 counts, 67.3 skin friction and 2.0 counts trip dot drag. The drag comparisons are excellent, the computational and experimental drag differences are within 0.5 counts. The pitching moment data are also in excellent agreement. The comparisons for the full range of angles of attack indicate a small discrepancy in the pitching moments at the lower lift coefficients (Fig. 27b).

10 Aerodynamic Coefficients with Nacelle Unstart for the Wing/Body

The computational and experimental changes in wing/body rolling and yawing moment coefficients as a function of mass-flow ratio are compared in Fig. 28. The magnitudes and slopes of the rolling moment curves correlate well. The additional lift on the wing from the high pressures from the nacelle shocks cause the rolling moment to become negative (lifting right wing) as the mass-flow ratio decreases. The slopes of the computational and experimental yawing moment curves are also in good agreement. The non-zero yawing moment seen in the experimental data with started nacelles is due to the data being taken with the model at a yaw angle of -0.56. The magnitude of the yawing moments would be in agreement if the the experimental data were obtained at a yaw angle of 0.

The comparisons of lift and drag on the wing/body as functions of the MFR of the right-hand outboard nacelle are shown in Fig. 29. The lift coefficient correlations of *AIRPLANE* and experiment are excellent. The magnitude of the lift and the changes in lift due to unstart are nearly matched. The increase in pressure on the lower surface of the wing from the nacelle shocks increases the lift on the aft portion of the wing.

The comparisons of drag coefficient as a function of MFR are in good agreement, the difference between *AIRPLANE* and experiment being approximately one drag count. A flat plate skin friction coefficient of 59.6 counts was obtained for the wind tunnel Reynolds number of 3 million per foot and added to the inviscid drag computed by *AIRPLANE* to obtain the computed drag values shown here. The drag on the wing/body decreases with decreasing MFR due to the nacelle being placed aft of the maximum thickness/chord ratio on the wing. The positive pressures acting on a positive wing slope will result in a localized thrust on the wing.

The pitching moment comparison is shown in Fig. 30a. The slope of the pitching moment curve is accurately predicted, but the experimental data show a slightly more pronounced nose down pitching moment.

The computational MFR is plotted as a function of the ratio of exit area divided by the inlet area for the plugged nacelle (Fig. 30b). The abrupt change in the MFR indicates unstart, where a normal shock is located

outside of the nacelle inlet.

11 Aerodynamic Coefficients with Nacelle Unstart for the Individual Nacelles

Comparisons of the computational and experimental lift coefficients for the inboard and outboard nacelles as a function of the MFR in the right-hand outboard nacelle are shown in Fig. 31. The lift coefficients on the individual nacelles obtained by *AIRPLANE* are slightly larger (approximately 0.0005) than the experimental results. The slope of the computational and experimental lift curves correlate well. The change in the lift on the individual nacelles with unstart is predicted to be small by both *AIRPLANE* and experiment.

The individual nacelle drag coefficients are compared in Fig. 32. The computational and experimental data compare within approximately 0.1 to 1 count for the inboard nacelle. The outboard nacelles differ between 0 and 1.5 counts. The computational drag on the inboard nacelle increases slightly with reduced mass-flow, indicating unfavorable interference from the strong bow shock from the outboard nacelle. However, the experimental data indicate that essentially no change in drag occurs for the inboard nacelle. The drag on the outboard nacelle decreases with reduced mass-flow in both the computational and experimental data. However, the computations only indicate a quarter count decrease and the experimental data show approximately a 2.5 count decrease.

The pitching moment data comparisons are shown in Fig. 33. Both the computational and experimental data indicate no change in pitching moment with nacelle unstart. The *AIRPLANE* results show more nose-down pitching moment, but the difference is small on both nacelles.

12 Aerodynamic Coefficients with Nacelle Unstart for the Wing/Body/Nacelles

The forces on the wing, body, and nacelles are shown in Figs 34-36. The correlation of the lift on this composite configuration is poorer than the wing/body results, due to the lift differences on the individual nacelles being accentuated with 4 nacelles (compare Fig. 34 with 29a and 31). The computational drag of the composite configuration is 4 drag counts larger than the experimental drag (Fig. 35). The slopes of the curves are in good agreement, but the discrepancy again stems from the nacelle drag differences. The pitching moment comparison for the composite configuration is in excellent agreement. This, however, is fortuitous since it results from the compensating differences in the wing/body and individual nacelle contributions (compare Fig. 36 with 30 and 33).

13 Concluding Remarks

AIRPLANE is an ideal tool to evaluate nacelle unstart behavior. The unstructured tetrahedral mesh generator can model complete configurations and obtain flow field grids for different plug positions automatically. The flow solver is also well suited for this problem because it has been thoroughly validated for several supersonic transport configurations by comparing the computational results with experimental data and has proven to be extremely accurate in its ability to predict performance increments. It also has the ability to run on multiple platforms, with almost perfect scalability with multiple processors on the parallel IBM SP2 machine.

The excellent results shown in this study have clearly demonstrated that the *AIRPLANE* code is capable of accurately determining the changes in the aerodynamic force and moment coefficients associated with nacelle unstart. Even the magnitudes of the force and moment coefficients were fairly accurately predicted. The discrepancies that have been found are due primarily to the lack of viscosity in the computations. A Navier-Stokes solution may offer improved results, but the extra computational expense and time required to obtain a Navier- Stokes solution for this problem do not appear justified given the exceptionally good results demonstrated by the inviscid *AIRPLANE* code.

14 Acknowledgments

The authors would like to acknowledge the contributions of Gelsomina Cappuccio and Ronald Smith who are primarily responsible for obtaining the high quality wind tunnel data shown in this report.

References

[1] Bencze, Daniel P. — Experimental evaluation of nacelle-airframe interference forces and pressures at Mach numbers of 0.9 to 1.4, *NASA TM X-3321*, March, 1977.

[2] Jameson, A., Baker, T.J. and Weatherill, N.P. — Calculation of inviscid transonic flow over a complete aircraft, *AIAA 24th Aerospace Sciences Meeting*, Reno, AIAA Paper 86-0103, January 1986.

[3] Jameson, A. and Baker, T.J. — Improvements to the aircraft Euler method, *AIAA 25th Aerospace Sciences Meeting*, Reno, AIAA Paper 87-0452, January 1987.

[4] Baker, T.J. — Three dimensional mesh generation by triangulation of arbitrary point sets, *AIAA 8th Computational Fluid Dynamics Conference*, AIAA Paper 87-1124-CP, Hawaii, June 1987.

[5] Baker, T.J. — Automatic mesh generation for complex three-dimensional regions using a constrained Delaunay triangulation, *Engineering with Computers*, Vol. 5, pp. 161–175 (1989).

[6] Cliff, S.E., Reuther, J.J., Baker, T.J., Hicks, R.M. and Mann, M.J. — Supersonic wing design by numerical optimization with superimposed nacelle pressures, *Proc. NASA Workshop on Propulsion Airframe Integration*, Cleveland, Ohio, October 1993.

[7] Cliff, S.E., Baker, T.J. and Hicks, R.M. — Design and computational/experimental analysis of low sonic boom configurations, *Proceedings of High Speed Research: 1994 Sonic Boom Workshop*, NASA/CP-1999-209699, December 1999.

[8] Cliff, S.E. and Baker, T.J. — Nacelle integration studies for HSCT Configurations using *AIRPLANE*. Unpublished.

[9] Jameson, A., Cliff, S.E., Thomas, S.D., Baker, T.J. and Cheng, W. — Supersonic transport design on the IBM parallel system SP2, *Proc. Computational Aerosciences Workshop*, Sunnyvale, CA, March 1995.

Fig 1. Installation photograph of a 2.7% scale model of the Boeing Reference H configuration in the NASA Ames 9x7 Foot Supersonic Wind Tunnel.

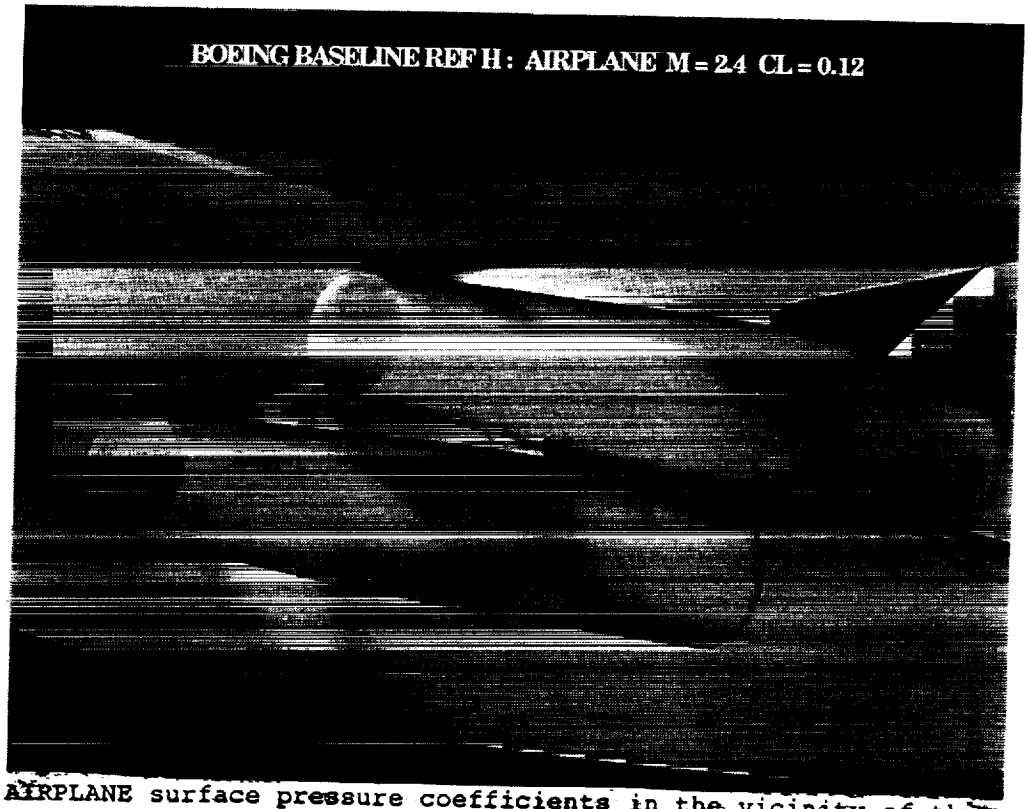

Fig 2. AIRPLANE surface pressure coefficients in the vicinity of the nacelles, M=2.4, CL = 0.12.

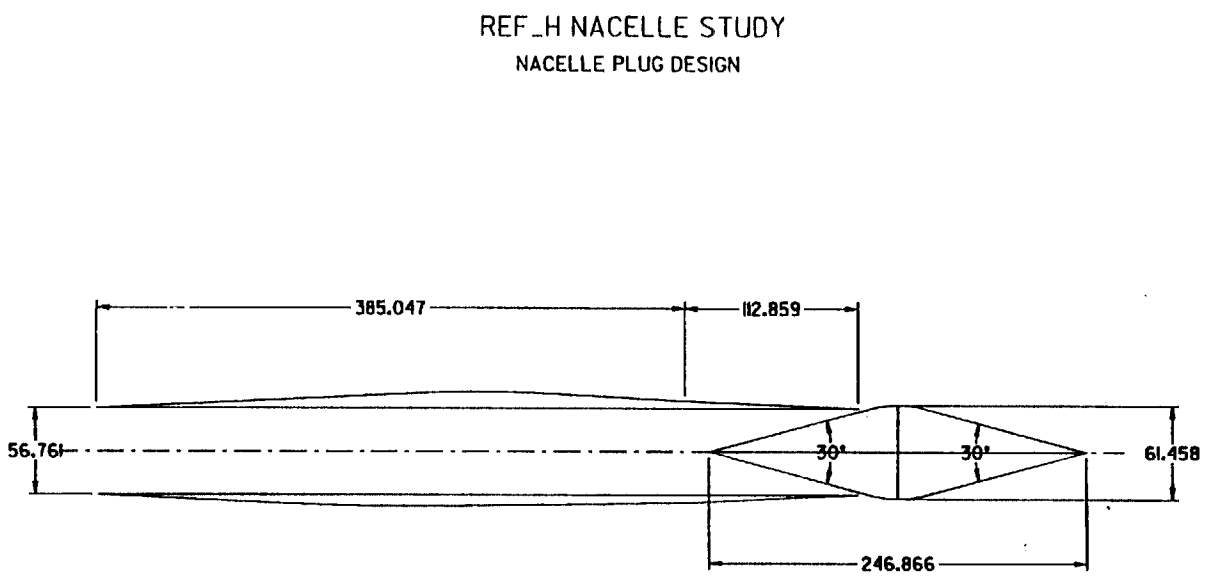

Fig 3. Drawing of outboard nacelle and supersonic plug.

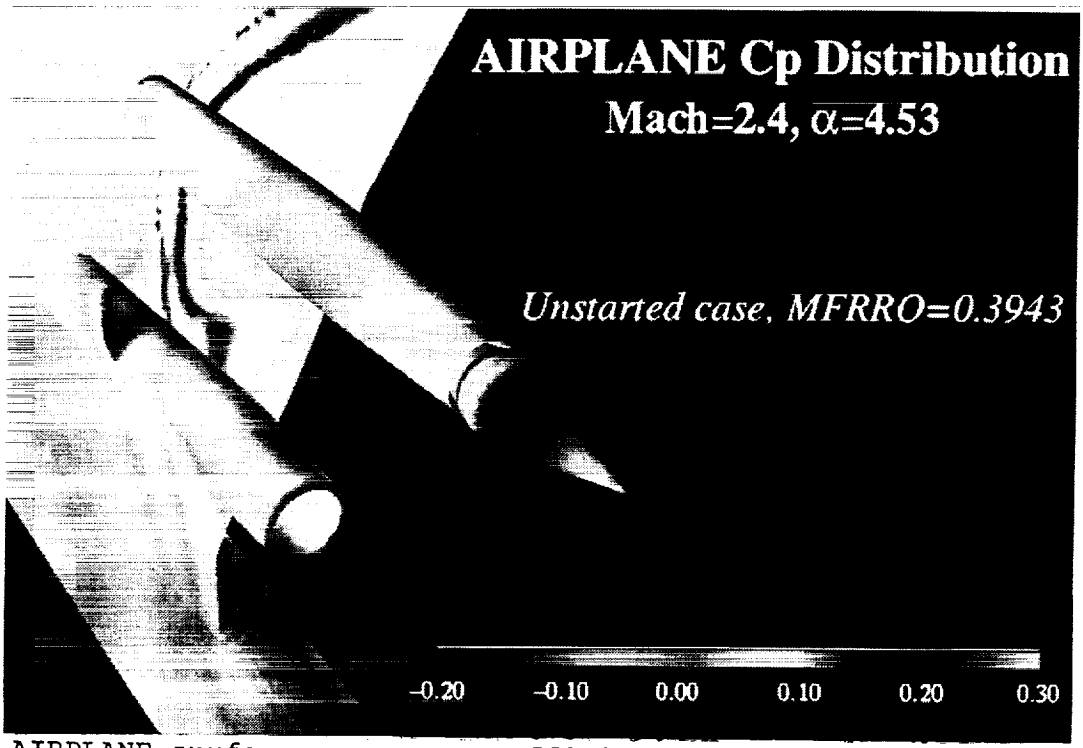

Fig 4. AIRPLANE surface pressure coefficients for the unstarted right-ha outboard nacelle with MFR = 0.39, M=2.4, alpha = 4.53.

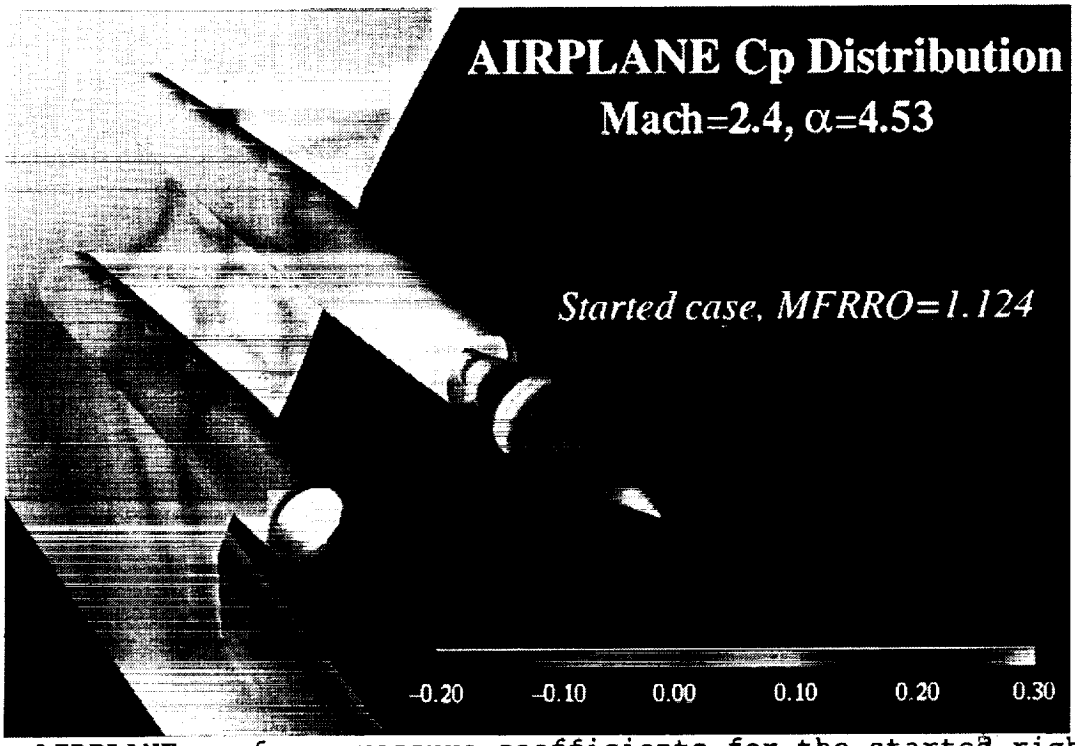

Fig 5. AIRPLANE surface pressure coefficients for the started right-hand outboard nacelle with MFR = 1.124, M=2.4, alpha = 4.53.

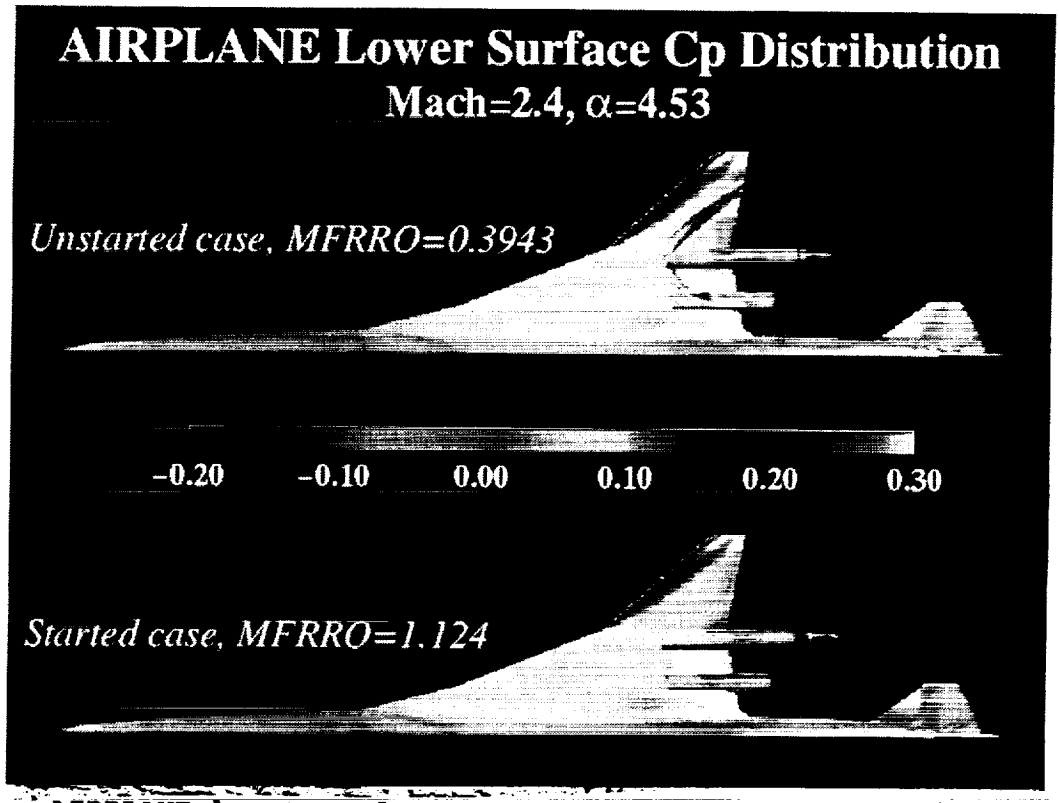

Fig 6. AIRPLANE lower surface pressure coefficients for the started and unstarted cases. M=2.4, alpha = 4.53.

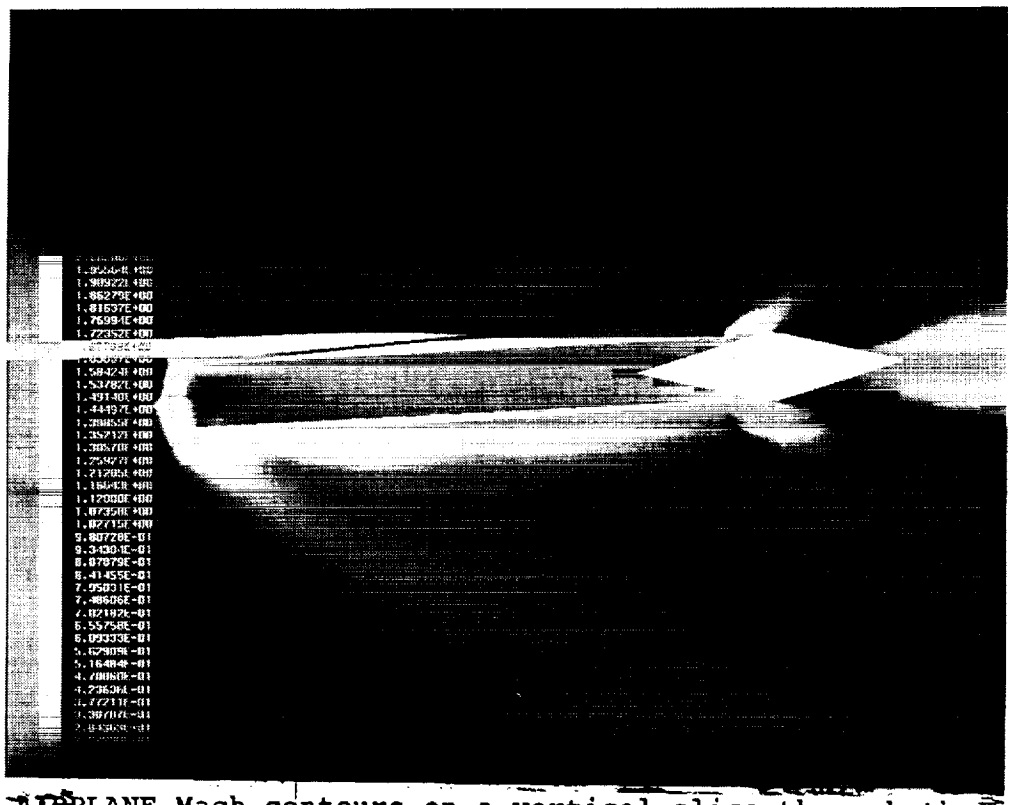

Fig 7. AIRPLANE Mach contours on a vertical slice through the axis of the unstarted nacelle with MFR = 0.39, M=2.4, alpha = 4.53.

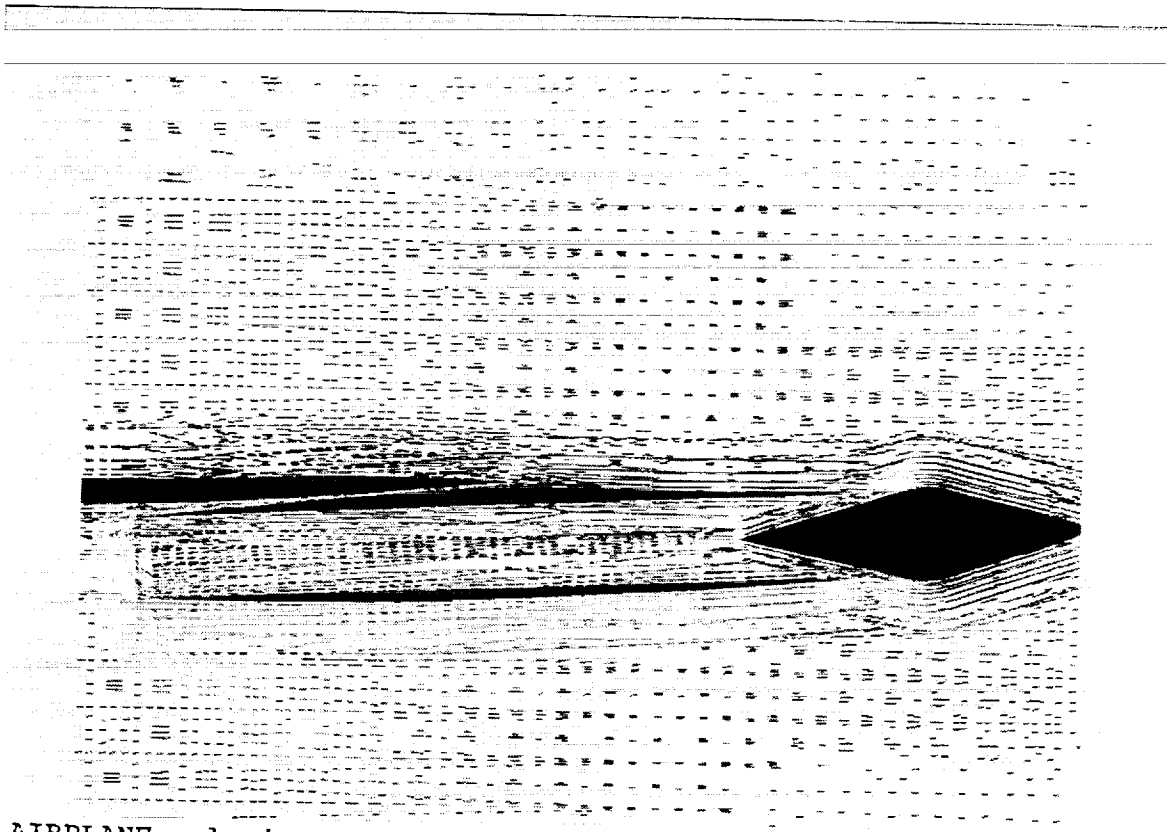

Fig 8. AIRPLANE velocity vectors colored by Mach number on a vertical slice through the unstarted nacelle with MFR = 0.39, M = 2.4, alpha = 4.53

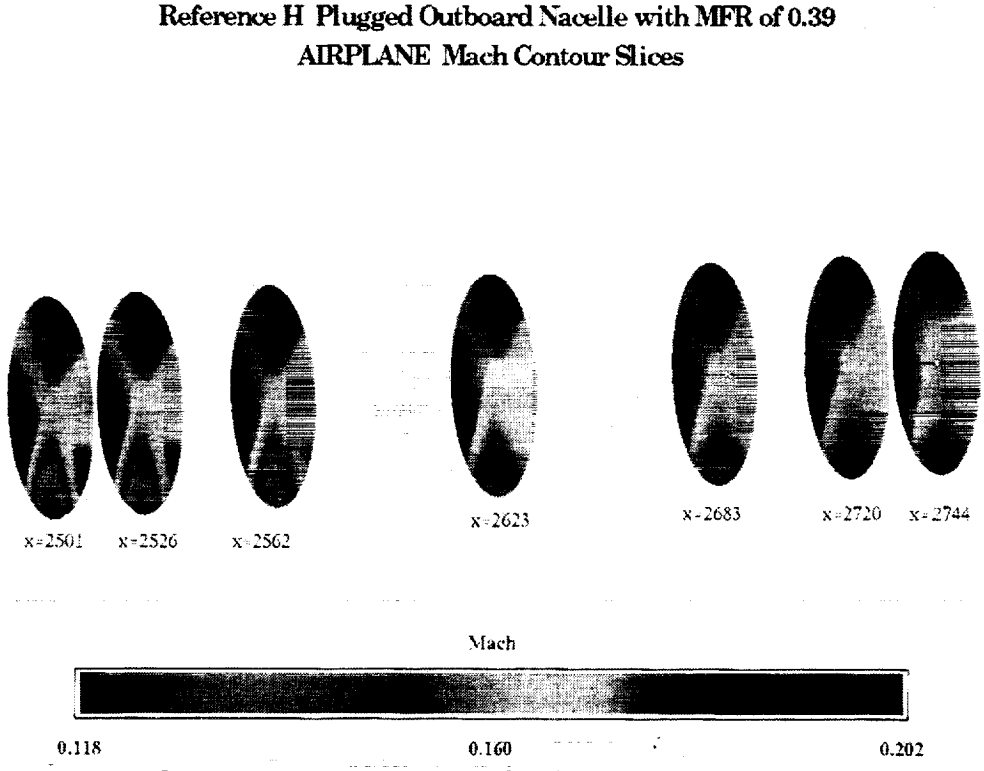

Fig 9. AIRPLANE Mach contours on interior nacelle cuts normal to the nacelle axis for the unstarted nacelle with MFR = 0.39.

Reference H Plugged Outboard Nacelle with MFR of 1.124
AIRPLANE Mach Contour Slices

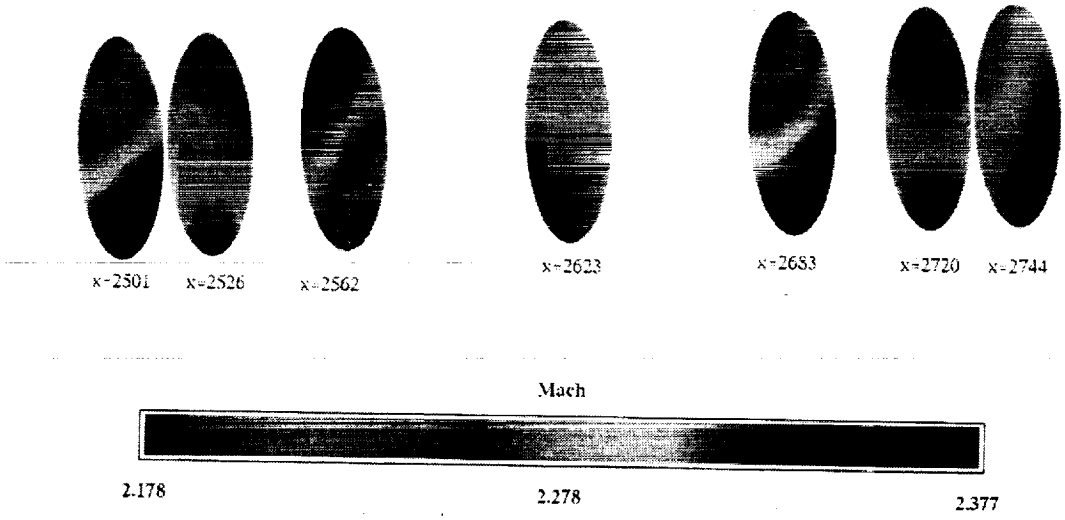

Fig 10. AIRPLANE Mach contours on interior nacelle cuts normal to the nacelle axis for the started nacelle with MFR = 1.12.

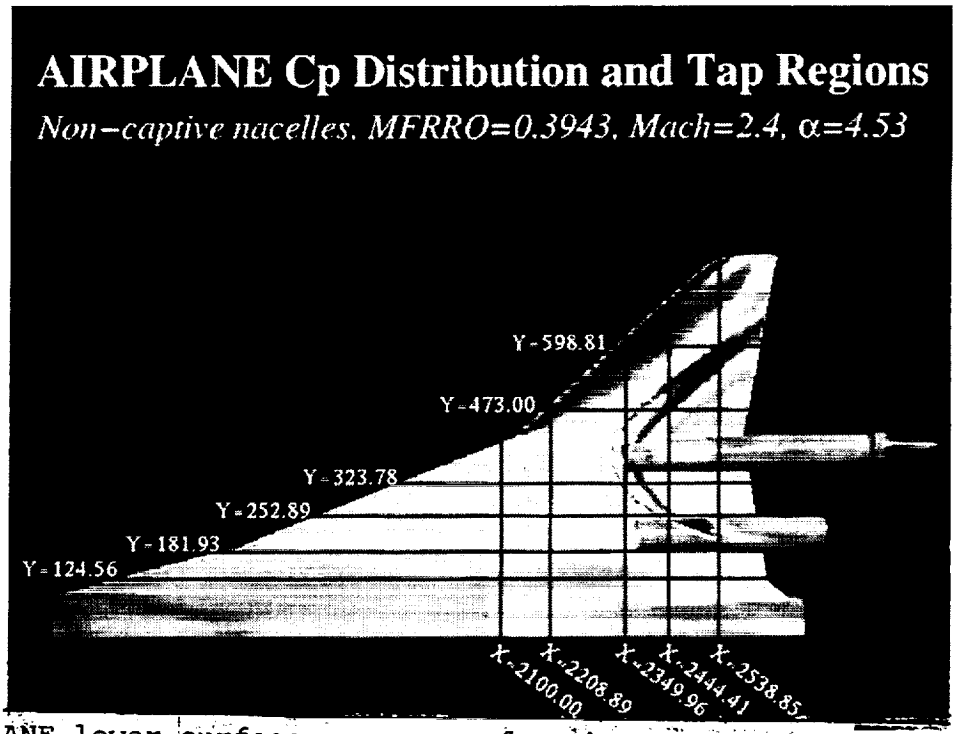

ig 11. AIRPLANE lower surface pressures for the unstarted non-captive nacelle case with streamwise and spanwise cut locations, MFR = 0.39, M = 2.4, alpha = 4.53.

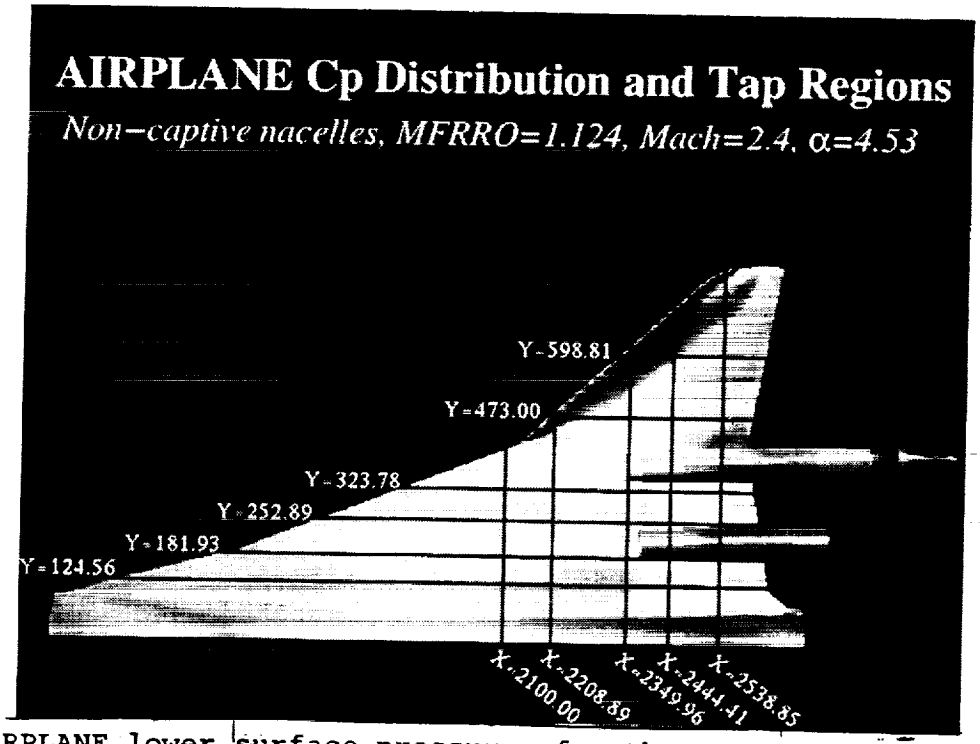

Fig 12. AIRPLANE lower surface pressures for the started non-captive nace case with streamwise and spanwise cut locations, MFR = 1.12, M = alpha = 4.53.

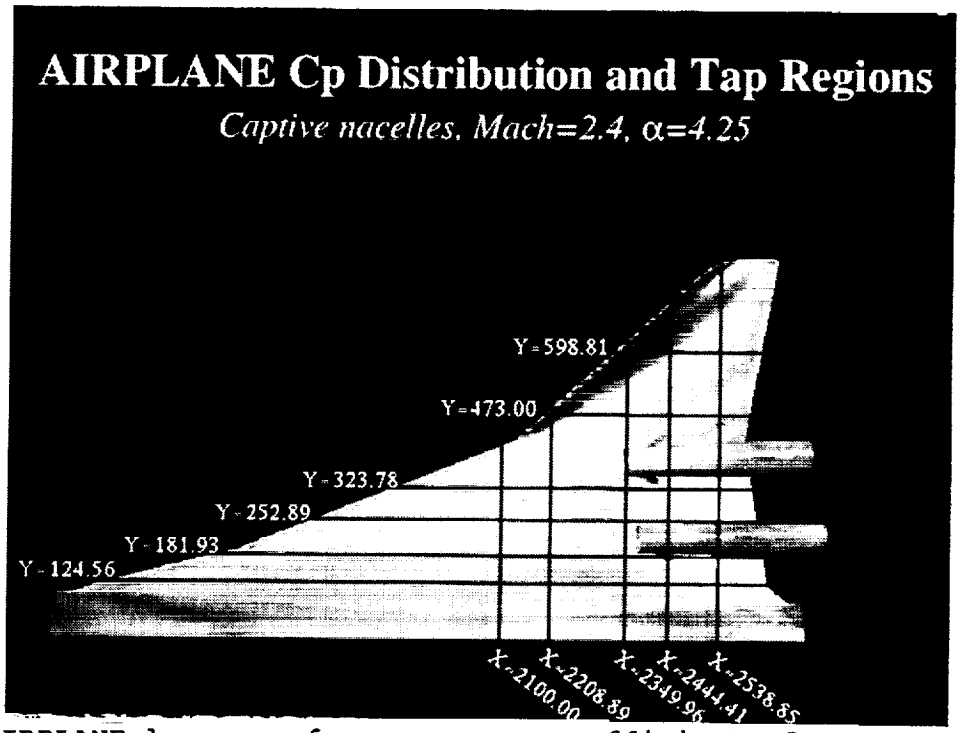

Fig 6. AIRPLANE lower surface pressure coefficients for the started and unstarted cases. M=2.4, alpha = 4.53.

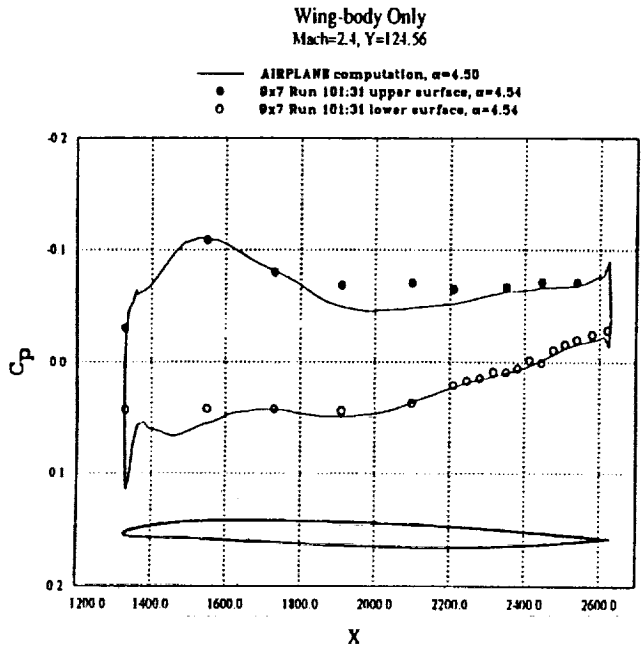

a) Wing-body only

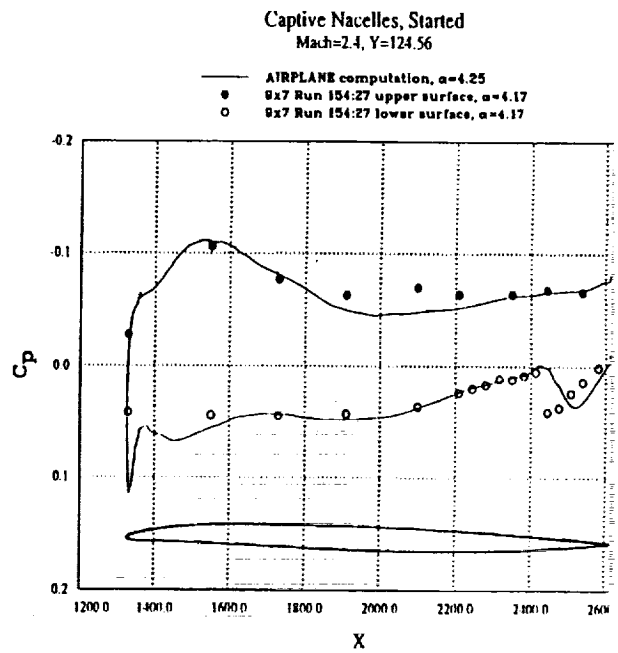

b) Captive nacelles, started

Fig 14. Streamwise computational/experimental pressure distributions on the wing-body, M = 2.4, CL = 0.12, Y = 124.56.

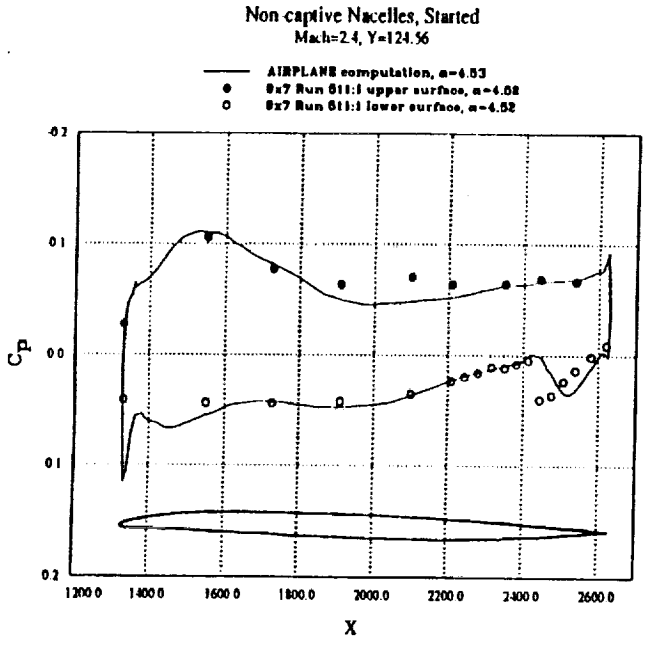

c) Non-captive nacelles, started

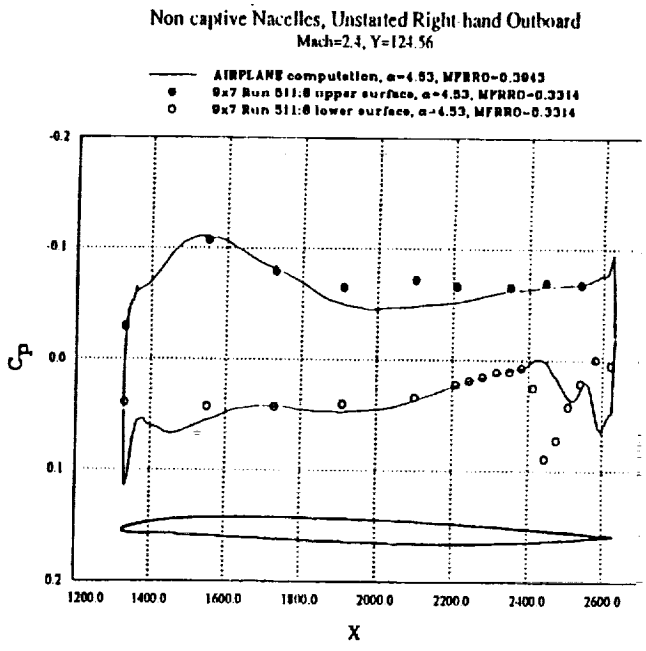

d) Non-captive nacelles, unstarted right-hand ou

Fig 14. Concluded.

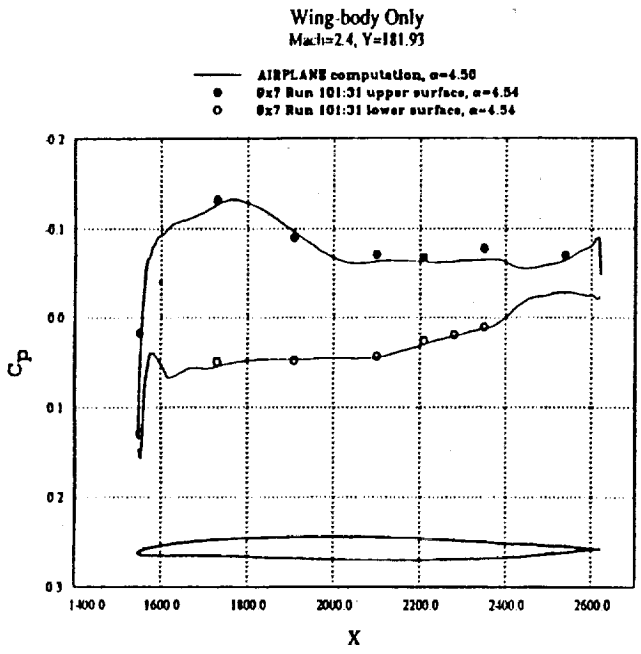

a) Wing-body only

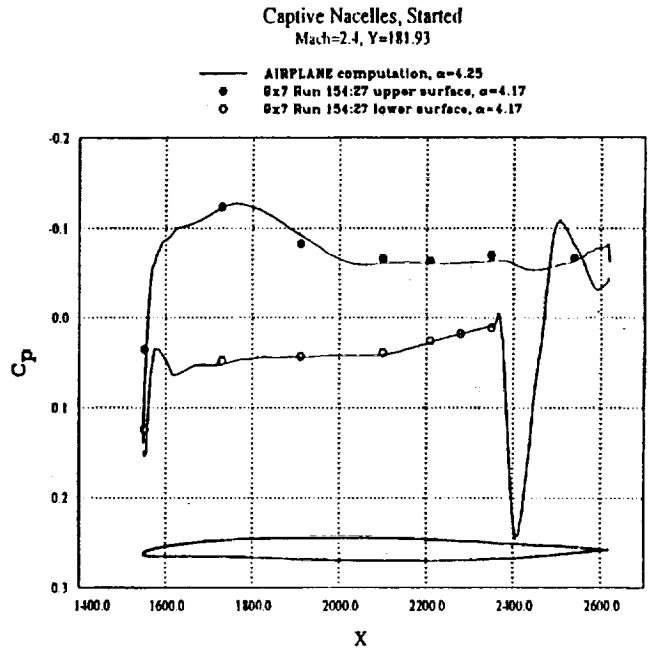

b) Captive nacelles, started

Fig 15. Streamwise computational/experimental pressure distributions on the wing-body, M = 2.4, CL = 0.12, Y = 181.93.

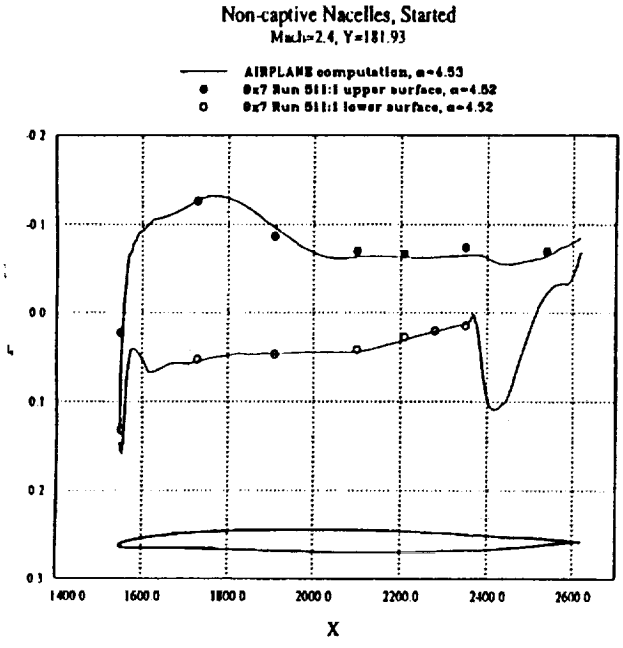

c) Non-captive nacelles, started

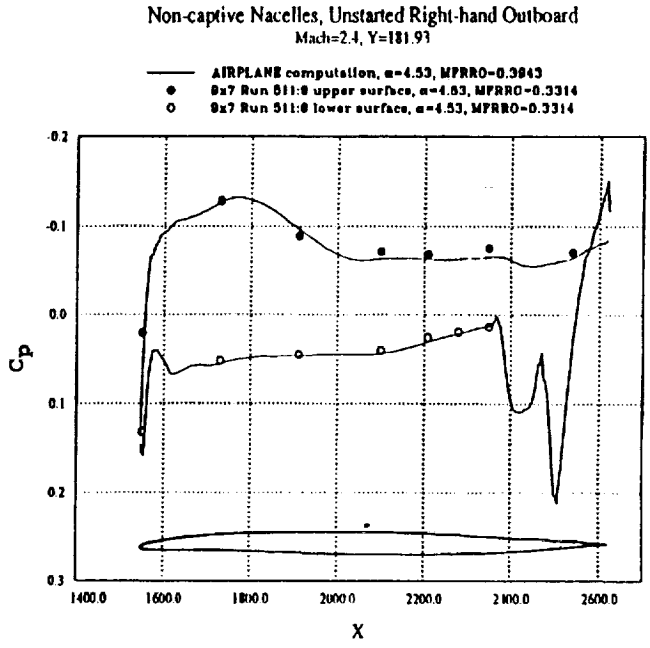

d) Non-captive nacelles, unstarted right-hand outboar

Fig 15. Concluded.

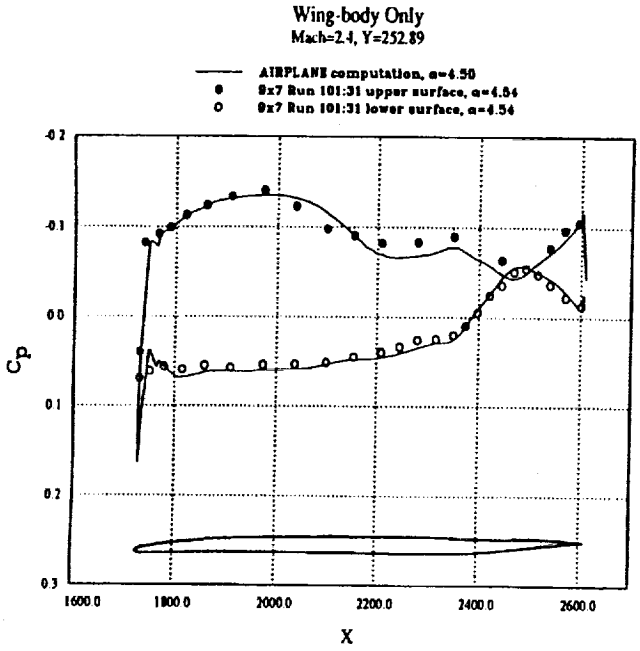

a) Wing-body only

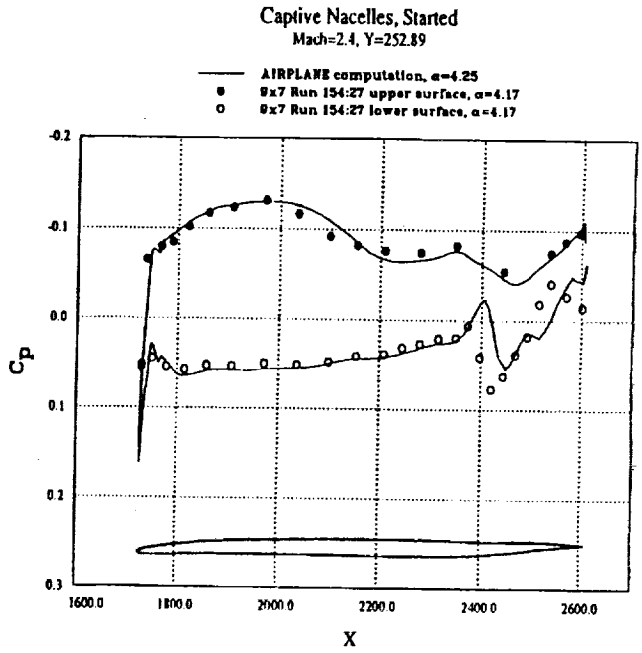

b) Captive nacelles, started

Fig 16. Streamwise computational/experimental pressure distributions on the wing-body, M = 2.4, CL = 0.12, Y = 252.89.

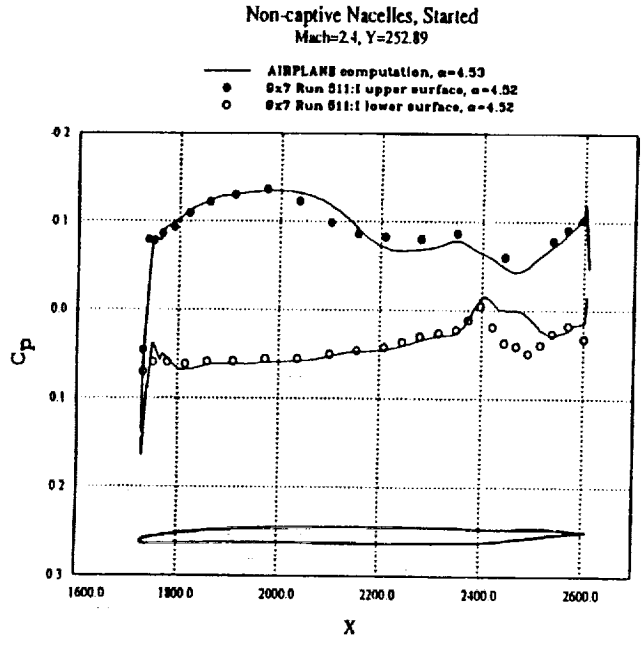

c) Non-captive nacelles, started

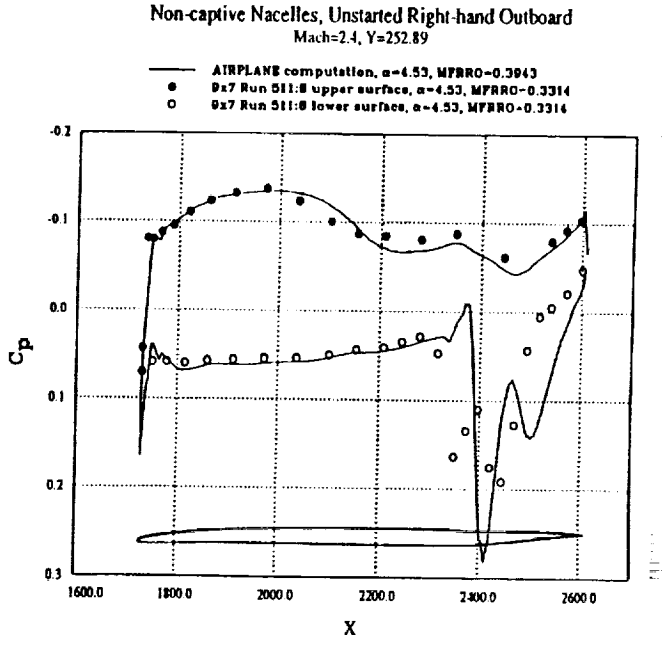

d) Non-captive nacelles, unstarted right-hand out

Fig 16. Concluded.

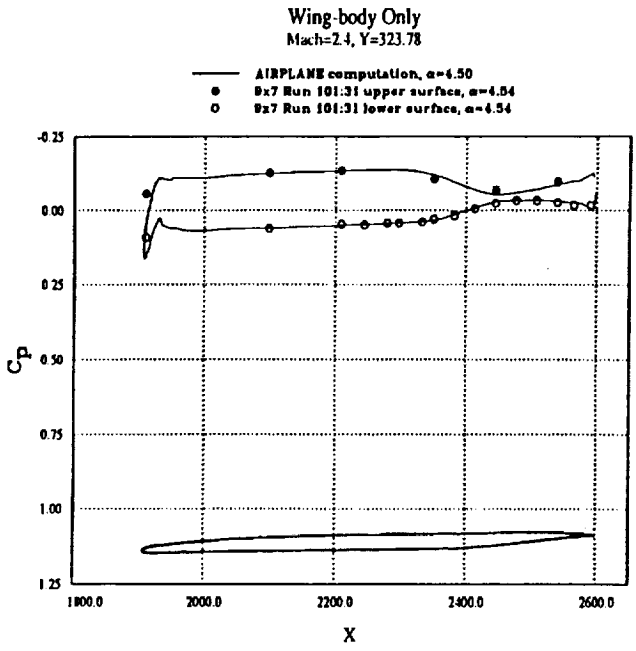

a) Wing-body only

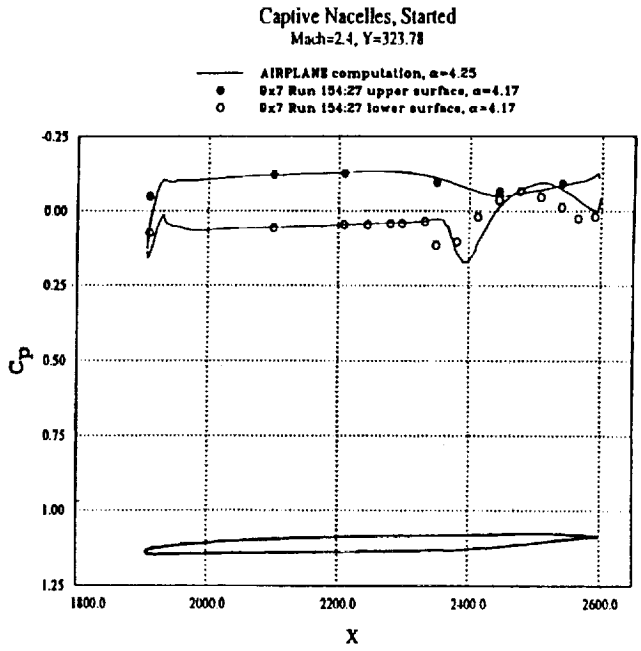

b) Captive nacelles, started

Fig 17. Streamwise computational/experimental pressure distributions on the wing-body, M = 2.4, CL = 0.12, Y = 323.78.

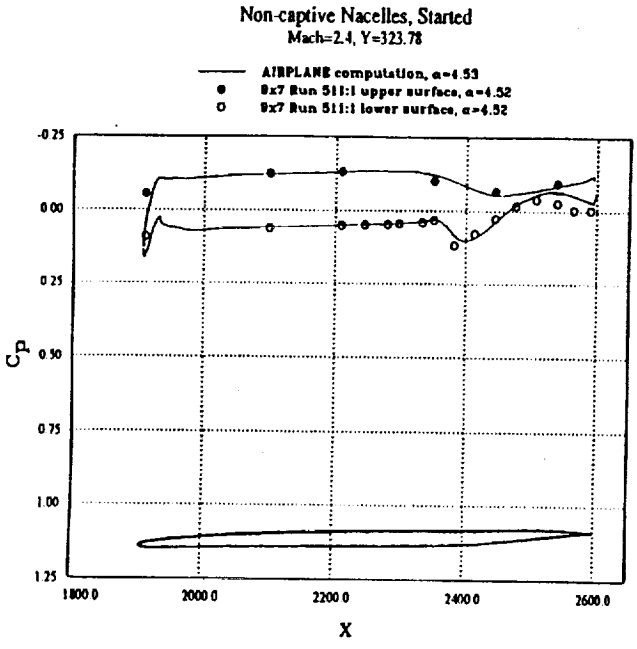

c) Non-captive nacelles, started

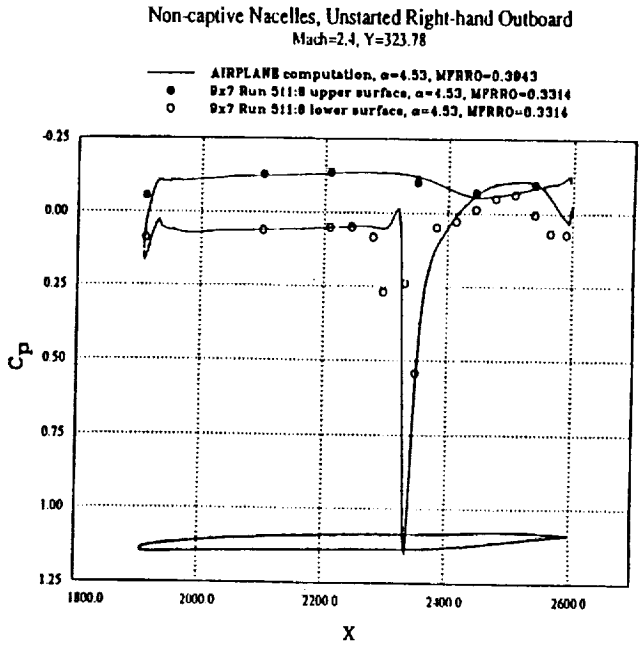

d) Non-captive nacelles, unstarted right-hand outboard

Fig 17. Concluded.

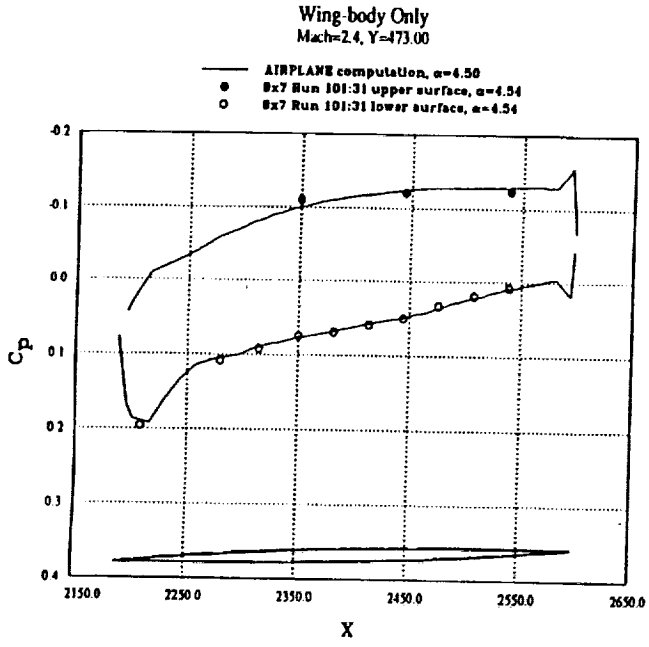

a) Wing-body only

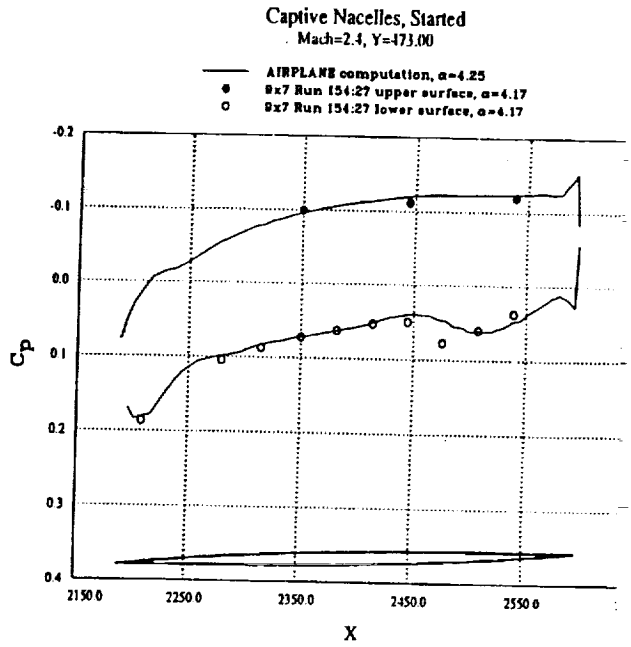

b) Captive nacelles, started

Fig 18. Streamwise computational/experimental pressure distributions on the wing-body, M = 2.4, CL = 0.12, Y = 473.00.

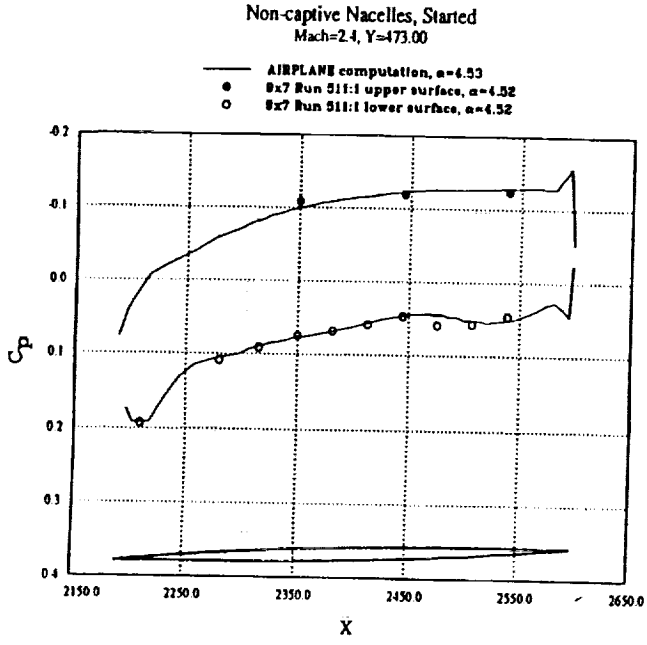

c) Non-captive nacelles, started

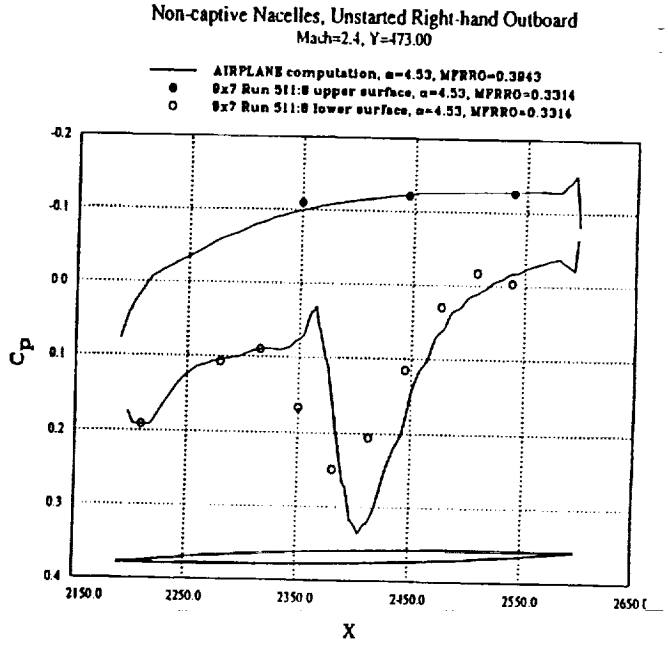

d) Non-captive nacelles, unstarted right-hand outbc

Fig 18. Concluded.

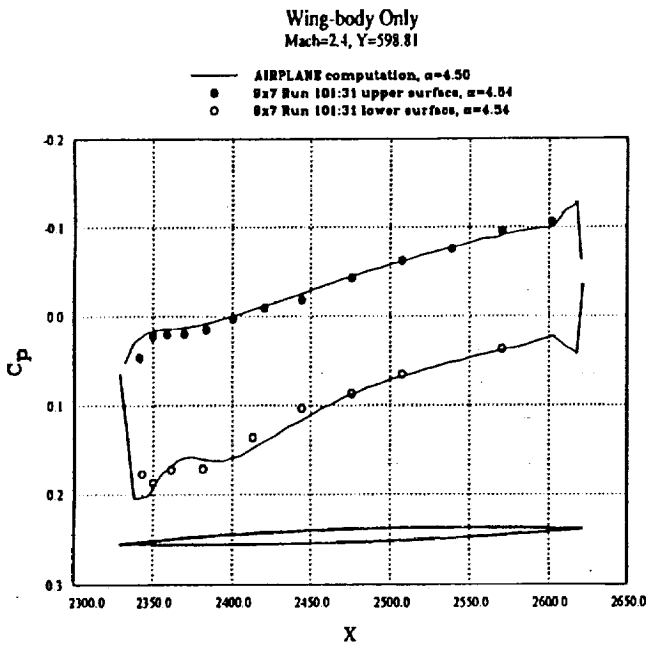

a) Wing-body only

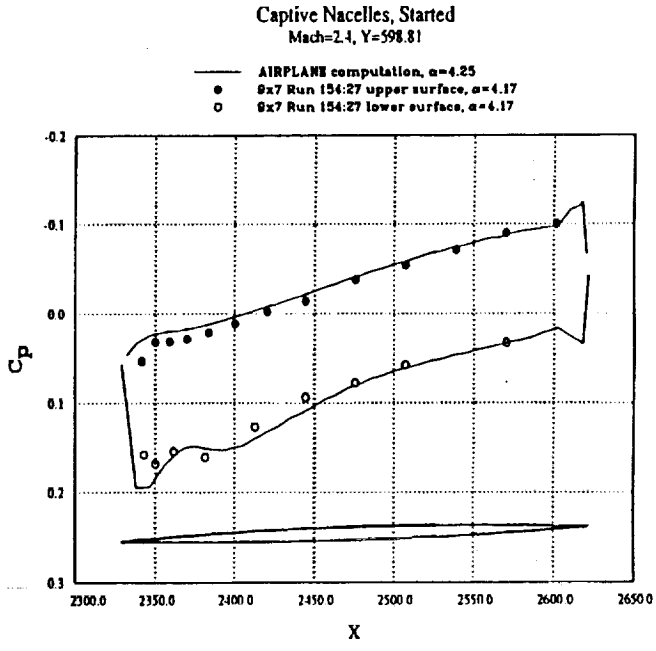

b) Captive nacelles, started

Fig 19. Streamwise computational/experimental pressure distributions on the wing-body, M = 2.4, CL = 0.12, Y = 598.81.

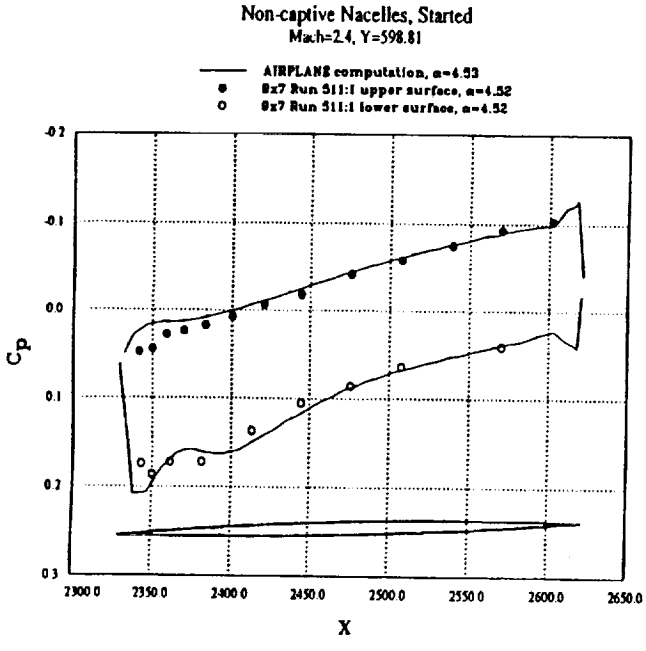

c) Non-captive nacelles, started

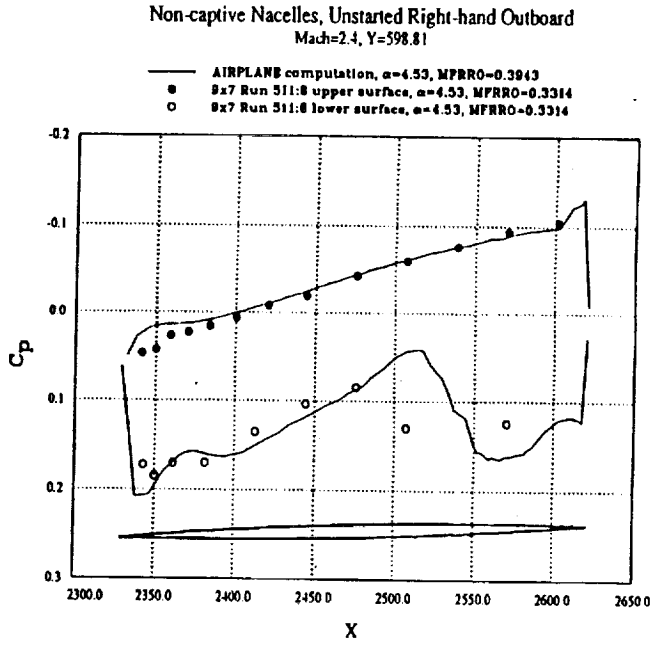

d) Non-captive nacelles, unstarted right-hand outboard

Fig 19. Concluded.

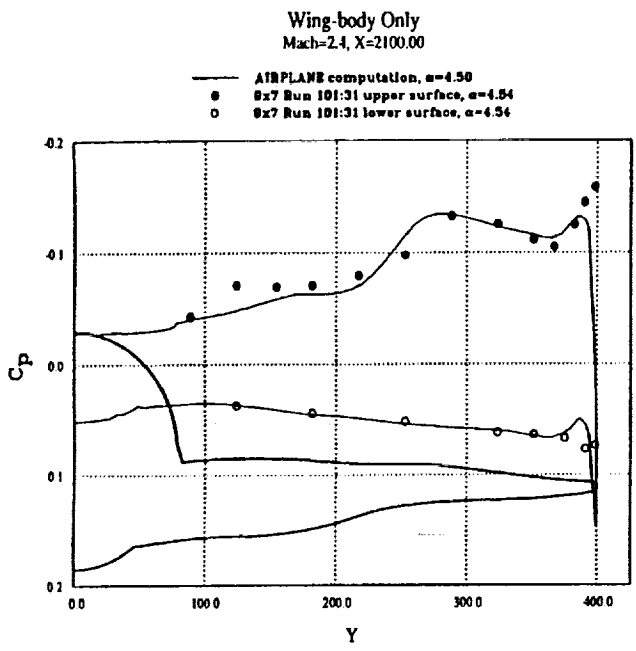

a) Wing-body only

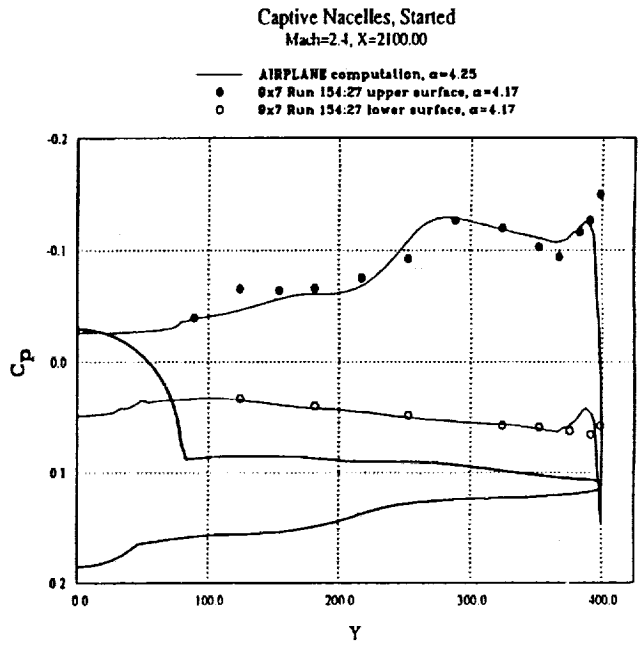

b) Captive nacelles, started

Fig 20. Spanwise computational/experimental pressure distributions on the wing-body, M = 2.4, CL = 0.12, X = 2100.00.

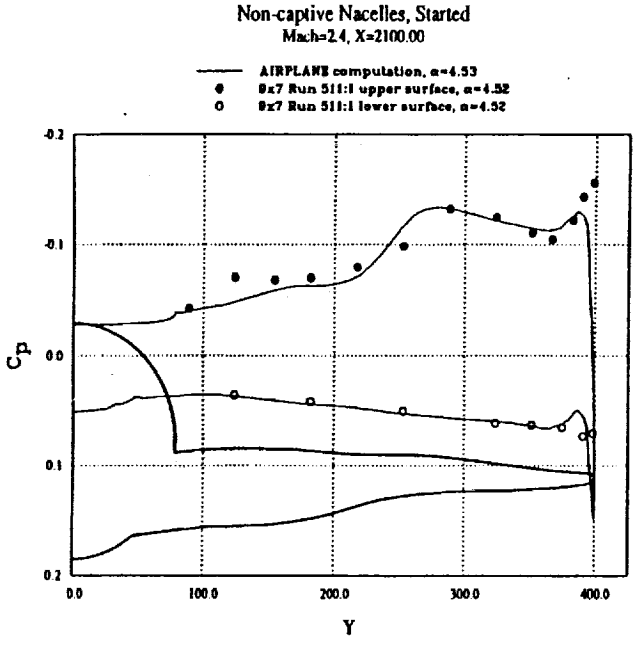

c) Non-captive nacelles, started

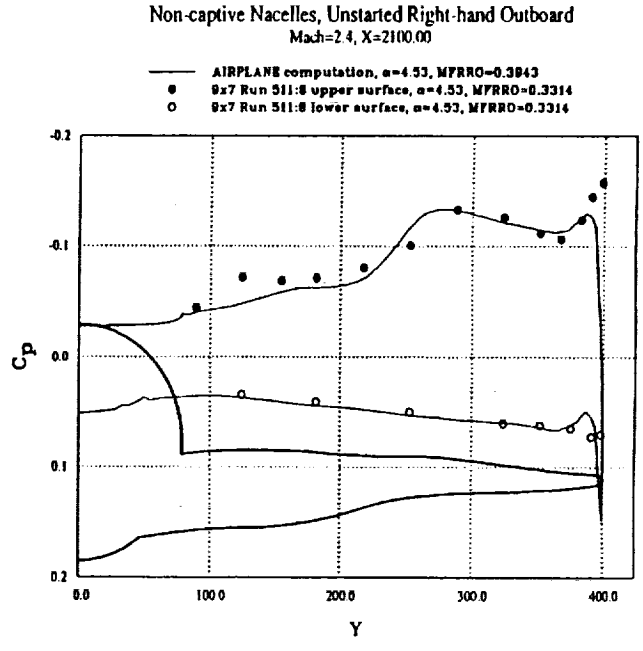

d) Non-captive nacelles, unstarted right-hand outbc

Fig 20. Concluded.

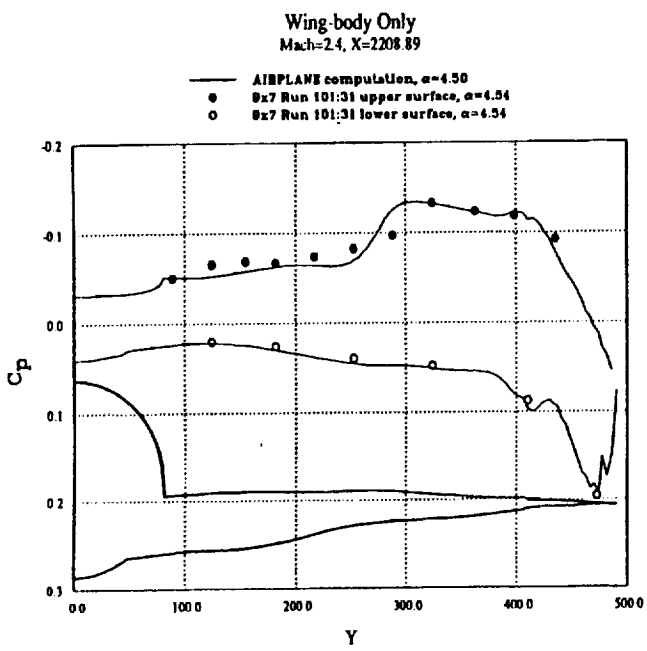

a) Wing-body only

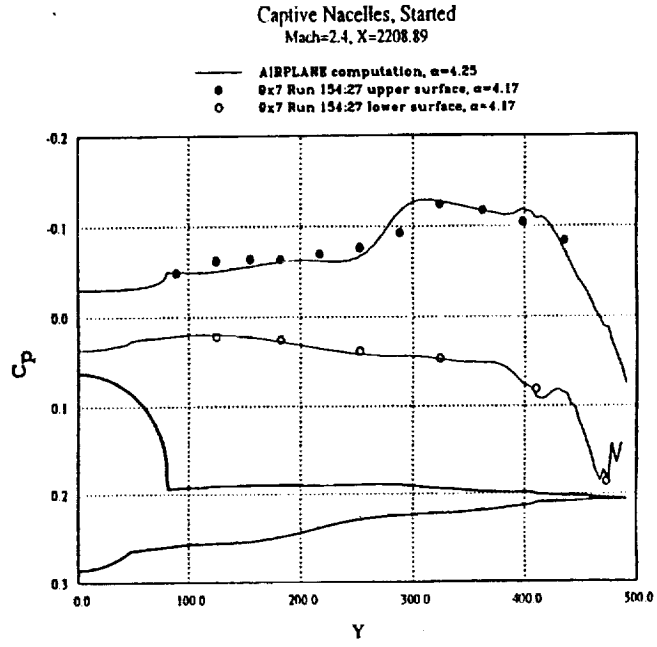

b) Captive nacelles, started

Fig 21. Spanwise computational/experimental pressure distributions on the wing-body, M = 2.4, CL = 0.12, X = 2208.89.

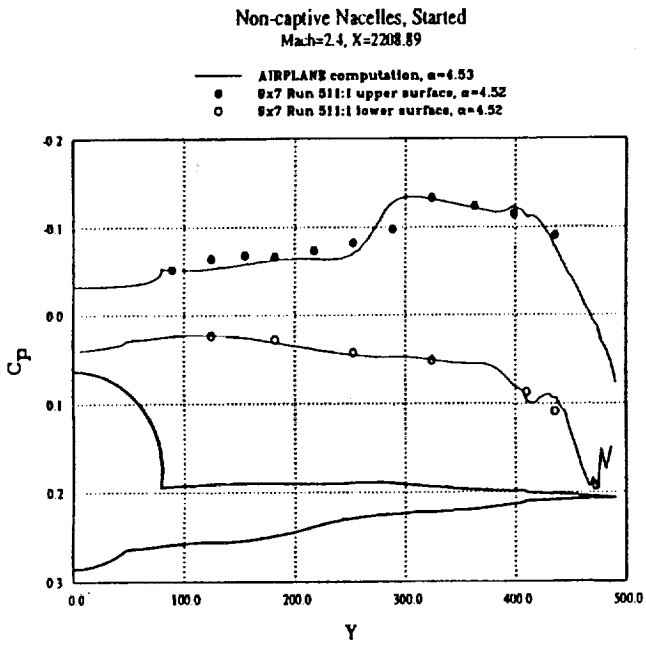

c) Non-captive nacelles, started

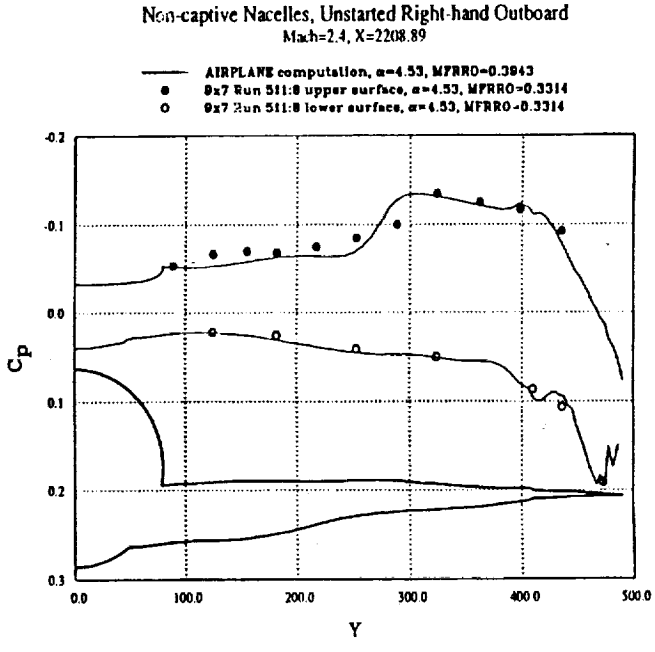

d) Non-captive nacelles, unstarted right-hand outboar

Fig 21. Concluded.

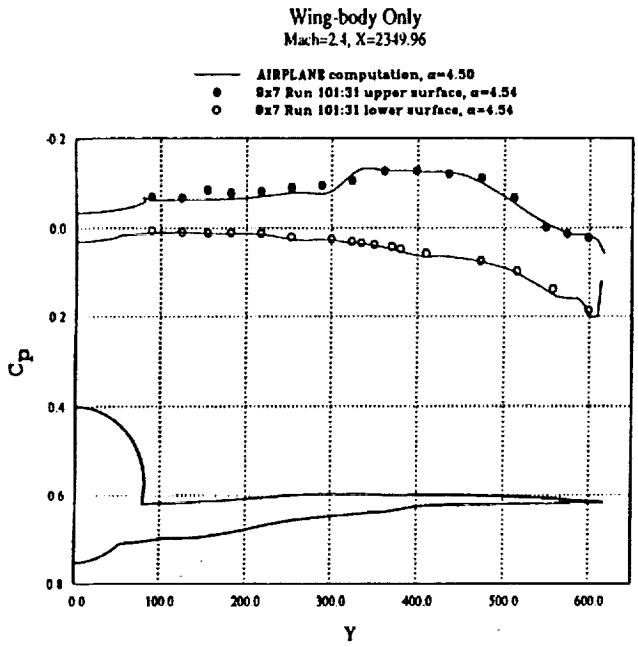

a) Wing-body only

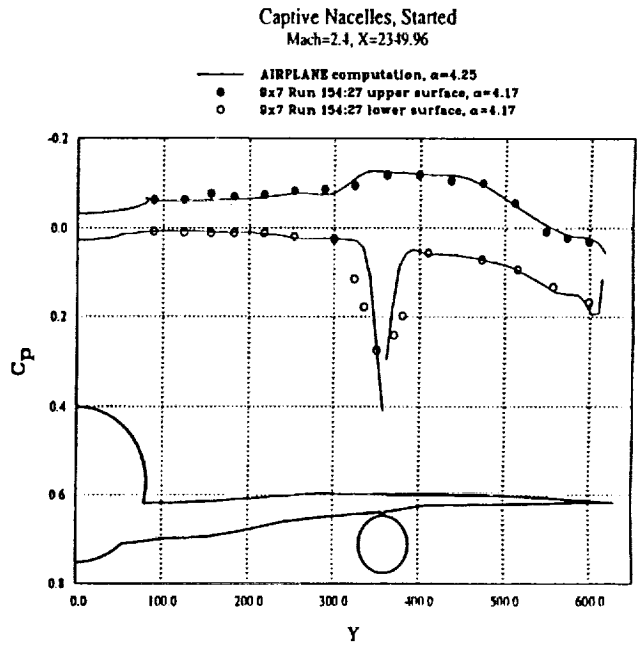

b) Captive nacelles, started

Fig 22. Spanwise computational/experimental pressure distributions on the wing-body, M = 2.4, CL = 0.12, X = 2349.96.

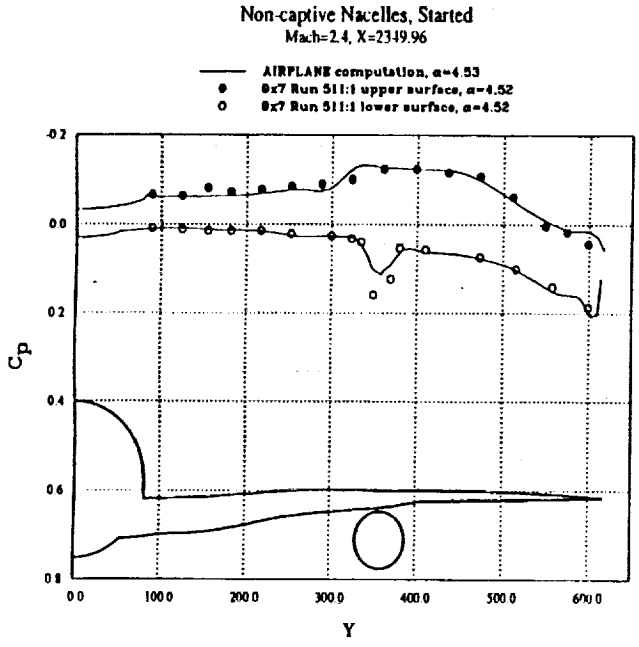

c) Non-captive nacelles, started

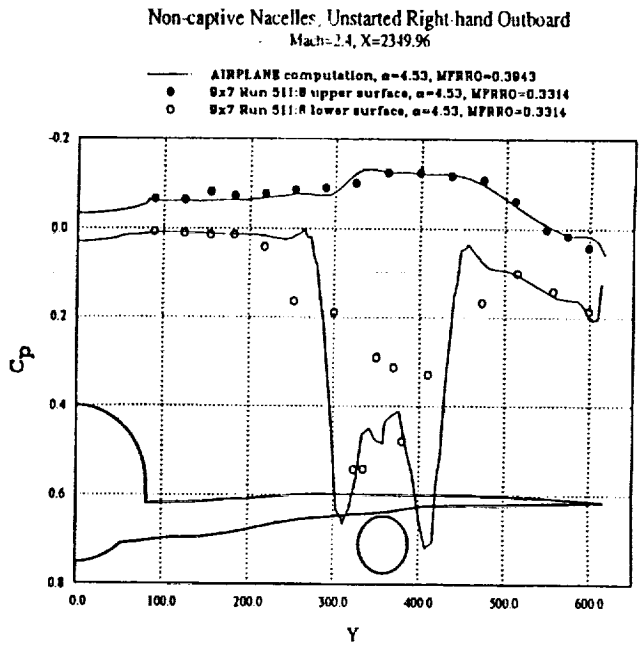

d) Non-captive nacelles, unstarted right-hand outbo

Fig 22. Concluded.

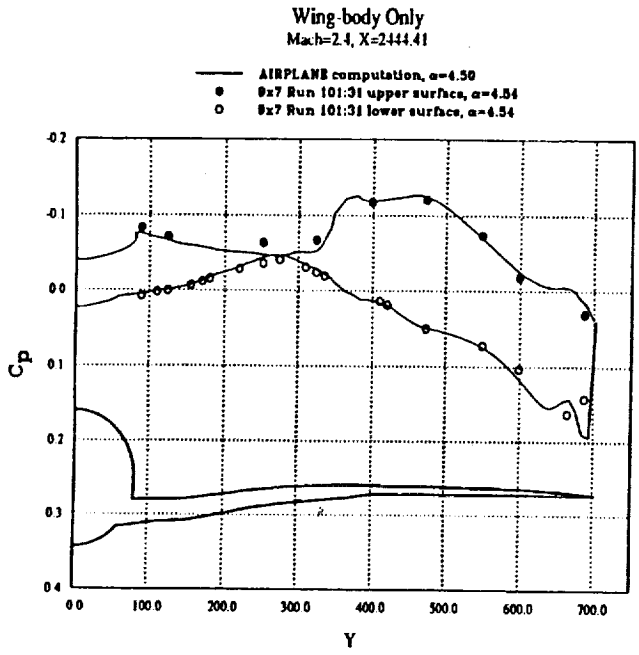

a) Wing-body only

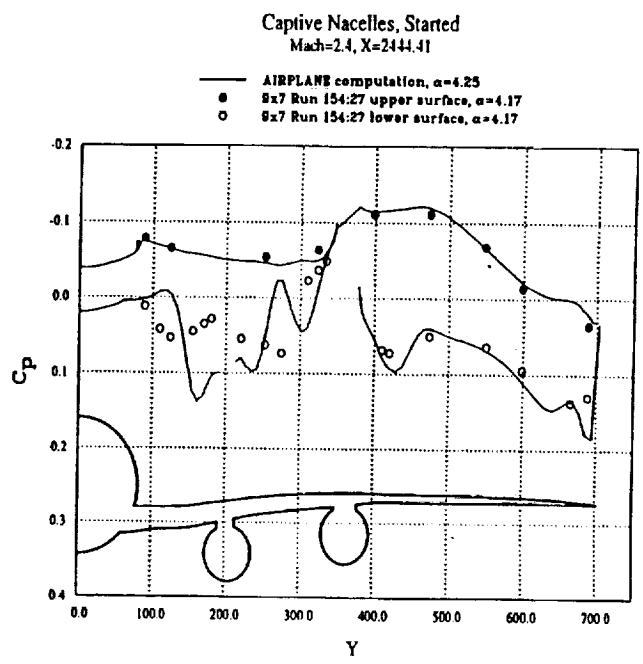

b) Captive nacelles, started

Fig 23. Spanwise computational/experimental pressure distributions on the wing-body, M = 2.4, CL = 0.12, X = 2444.41.

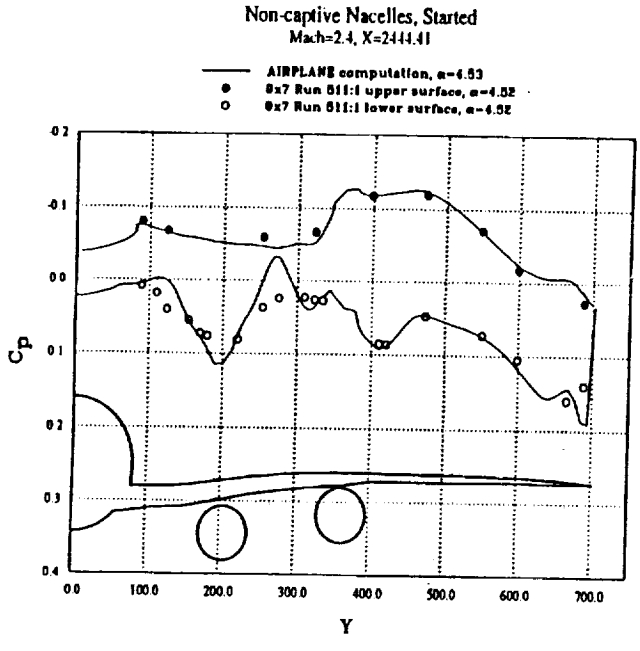

c) Non-captive nacelles, started

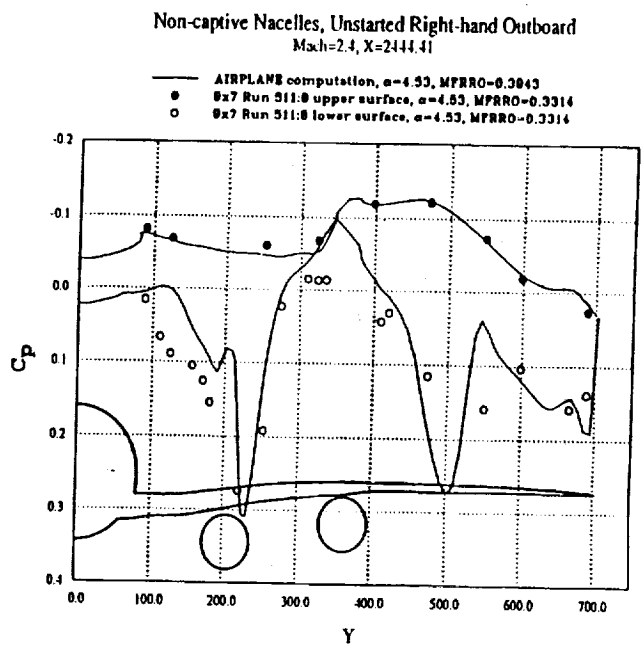

d) Non-captive nacelles, unstarted right-hand outboar

Fig 23. Concluded.

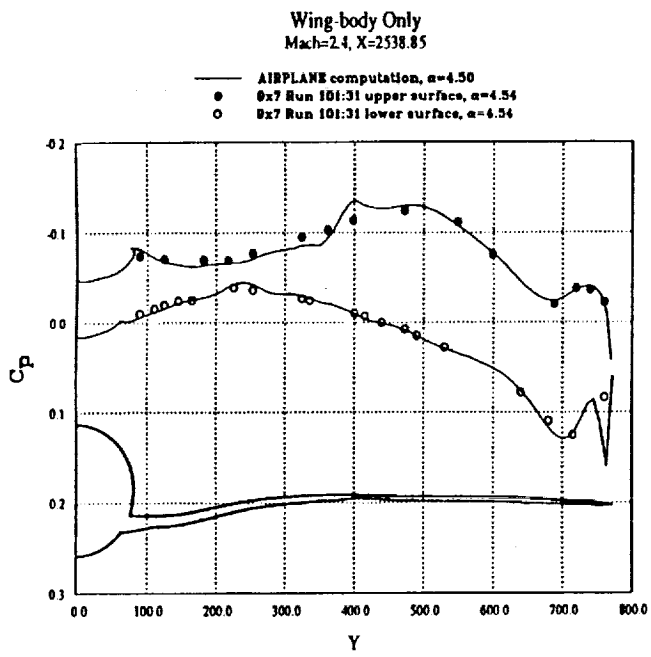

a) Wing-body only

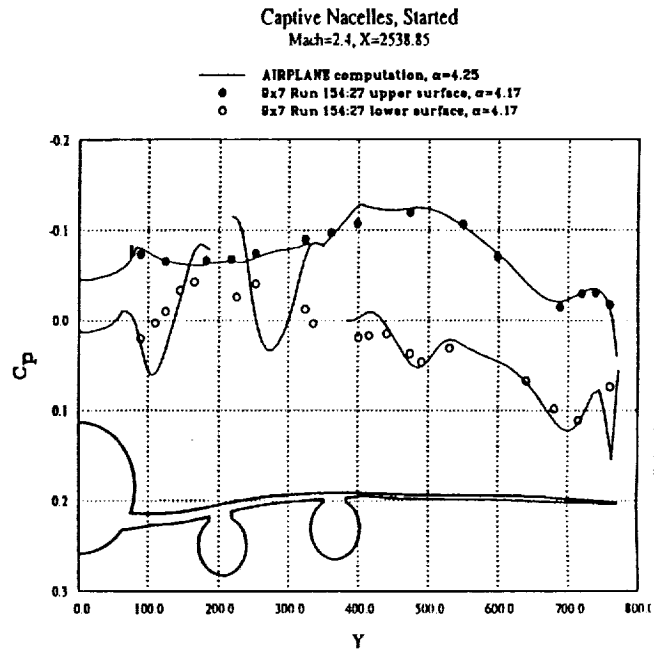

b) Captive nacelles, started

Fig 24. Spanwise computational/experimental pressure distributions on the wing-body, M = 2.4, CL = 0.12, X = 2538.85.

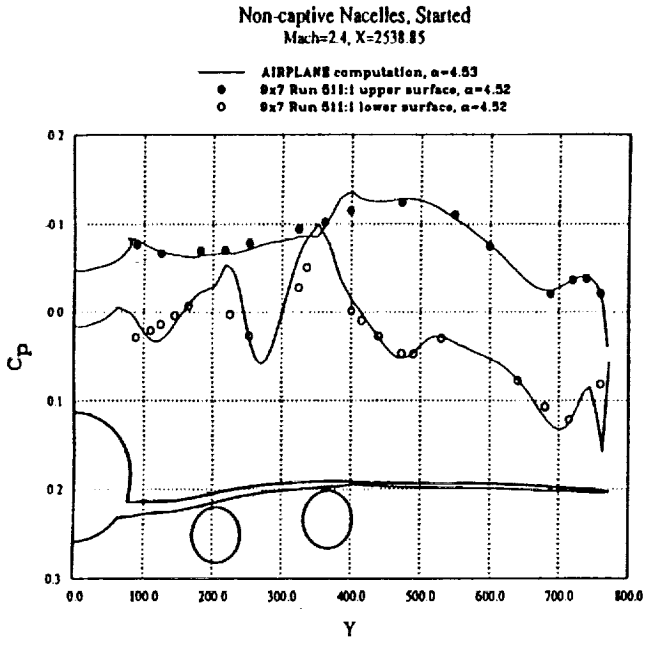

c) Non-captive nacelles, started

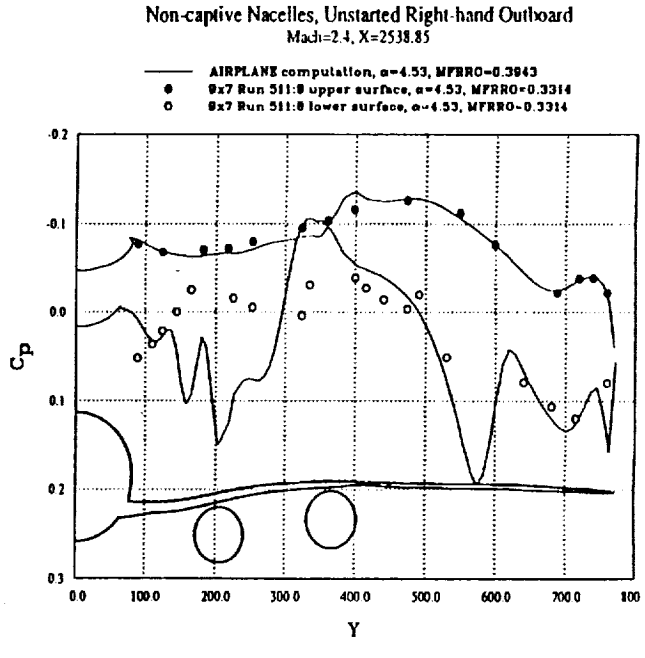

d) Non-captive nacelles, unstarted right-hand outbc

Fig 24. Concluded.

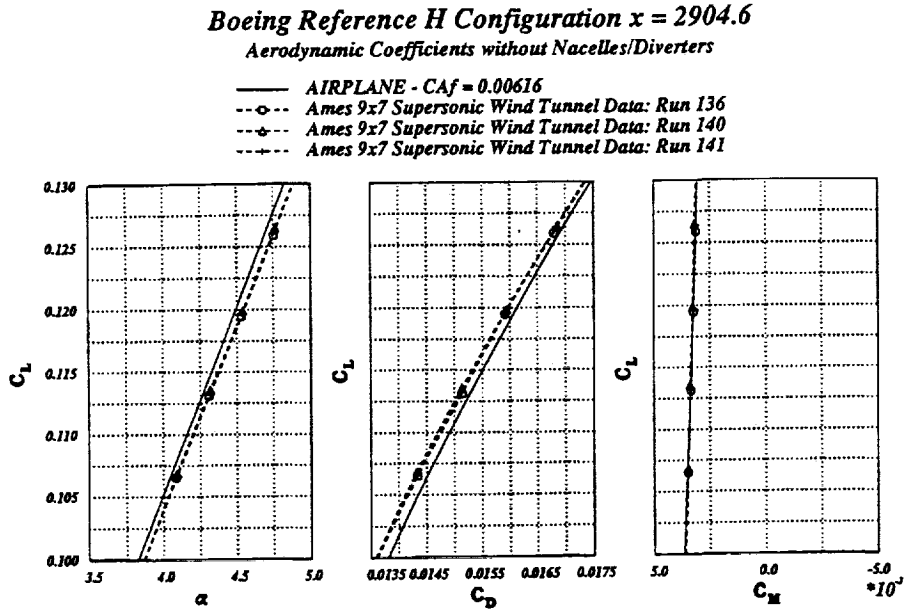

a) near the cruise flight condition

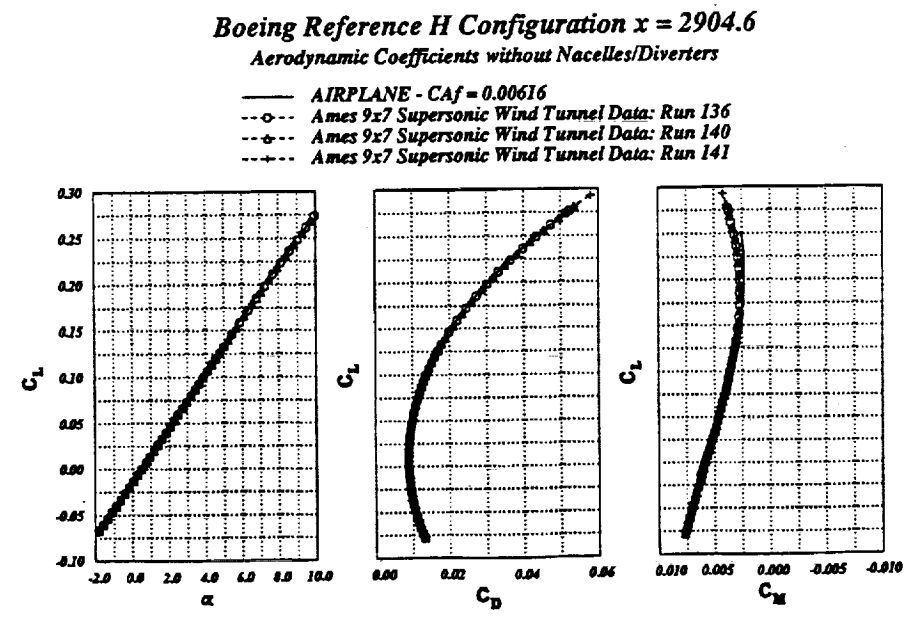

b) full range of data

Fig 25. Computational and experimental force and moment coefficients for the wing/body configuration, M = 2.4.

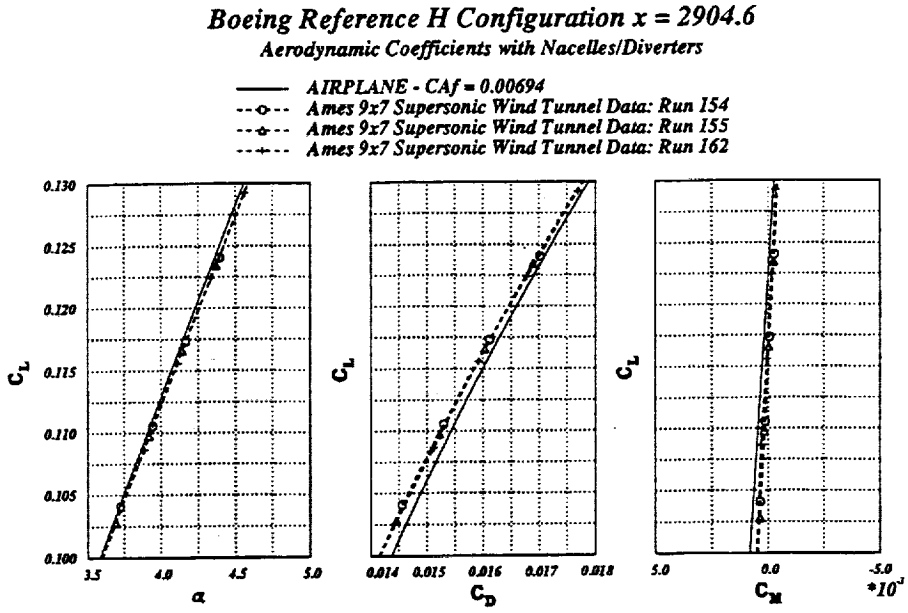

a) near the cruise flight condition

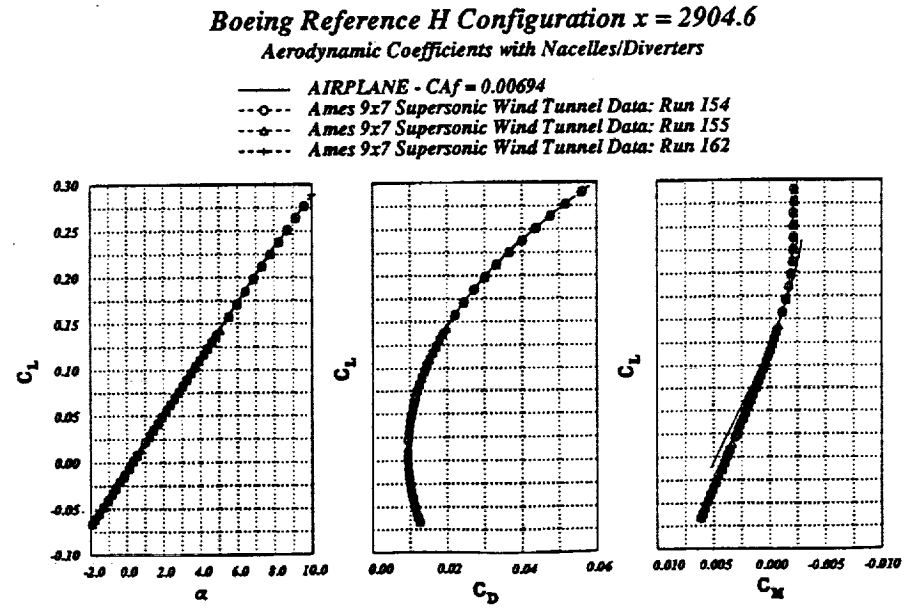

b) full range of data

Fig 26. Computational and experimental force and moment coefficients for the complete configuration with captive nacelles, M = 2.4.

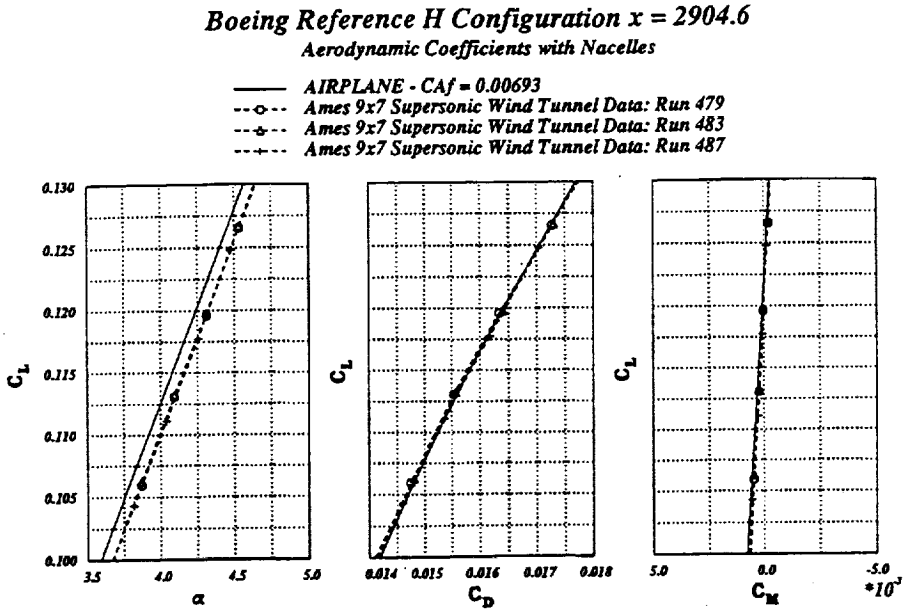

a) near the cruise flight condition

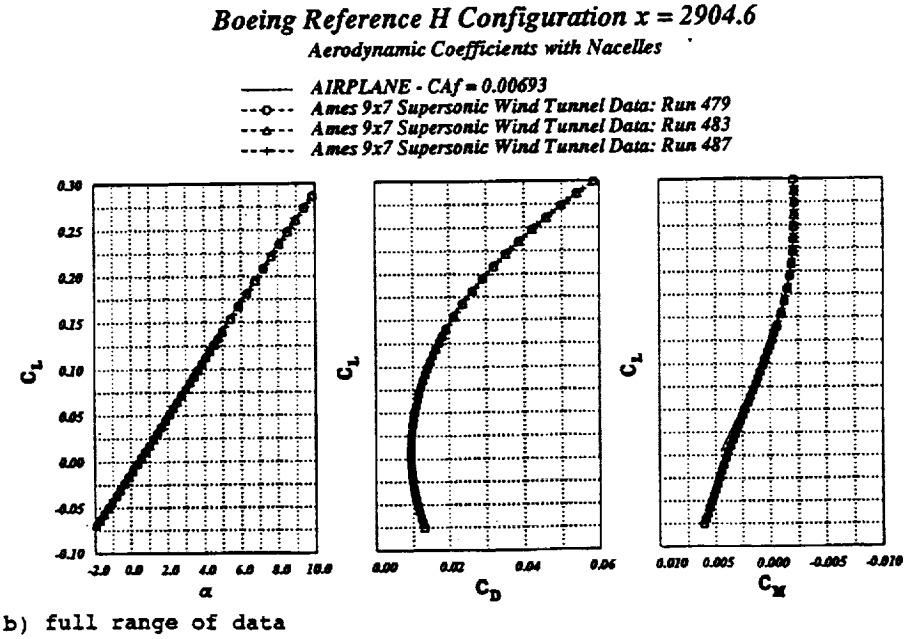

b) full range of data

Fig 27. Computational and experimental force and moment coefficients for the wing/body configuration with non-captive nacelles, M = 2.4.

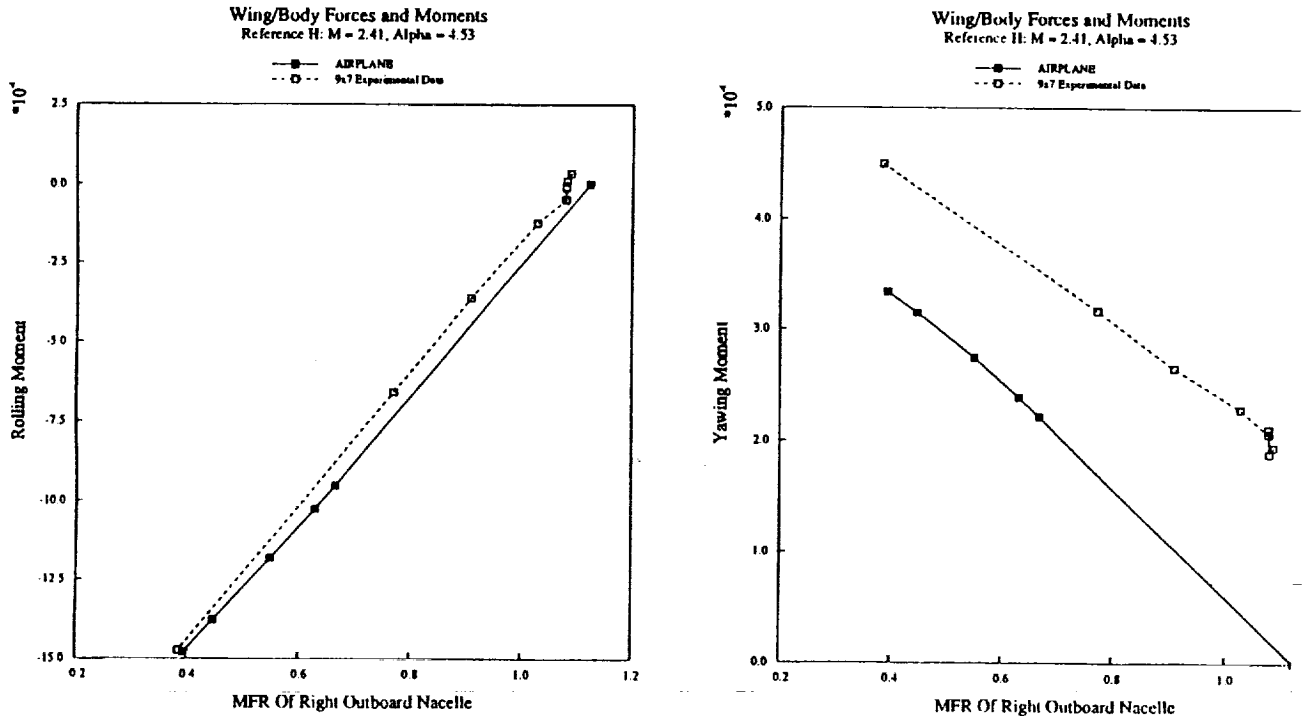

Fig 28. Computational and experimental rolling and yawing moment coefficients for the wing/body configuration as function of mass flow ratio of the right-hand outboard nacelle, M = 2.41, alpha = 4.53 degrees.

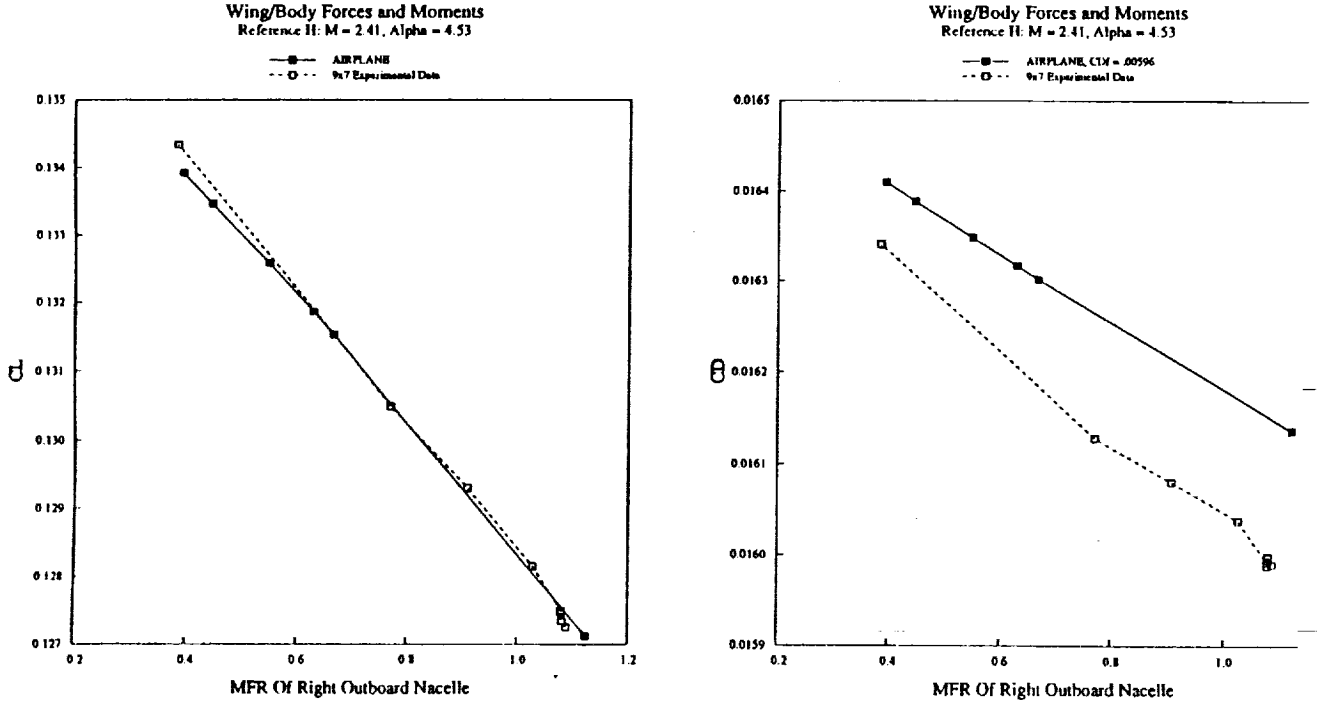

Fig 29. Computational and experimental lift and drag coefficients for the wing/body configuration as function of mass flow ratio of the right-hand outboard nacelle, M = 2.41, alpha = 4.53 degrees.

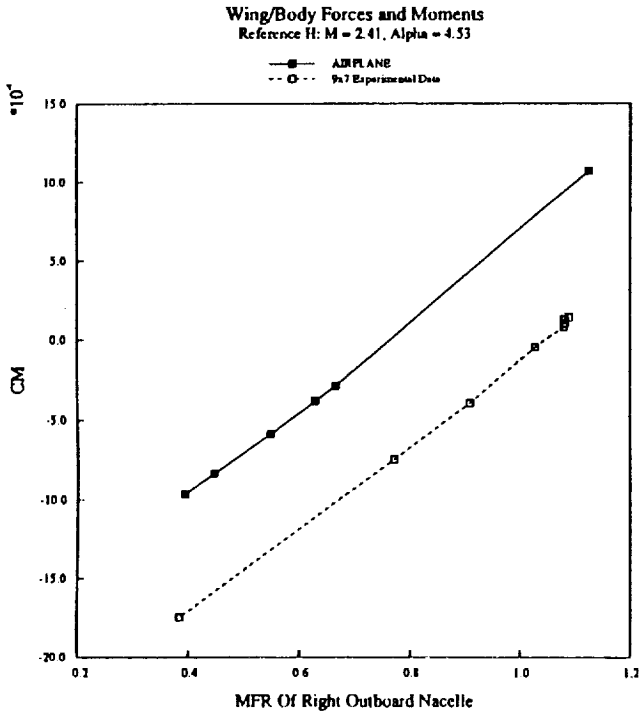

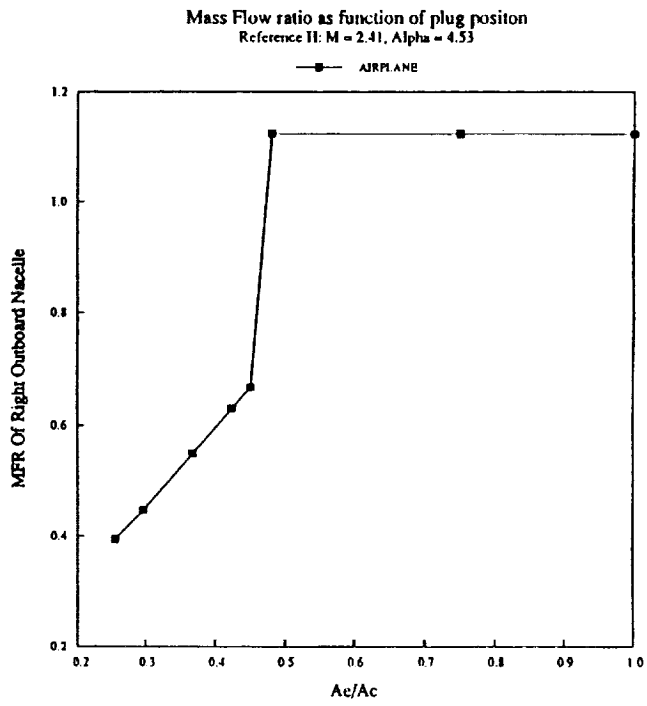

Fig 30. Computational and experimental pitching moment coefficients for the wing/body configuration as function of mass flow ratio of the right-hand outboard nacelle and mass flow ratio as a function of exit-/inlet- area ratio, M = 2.41, alpha = 4.53 degrees.

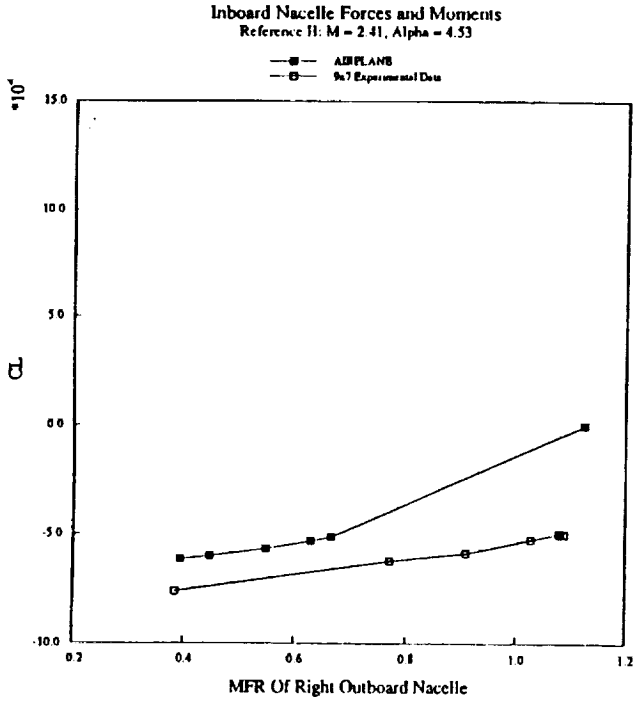

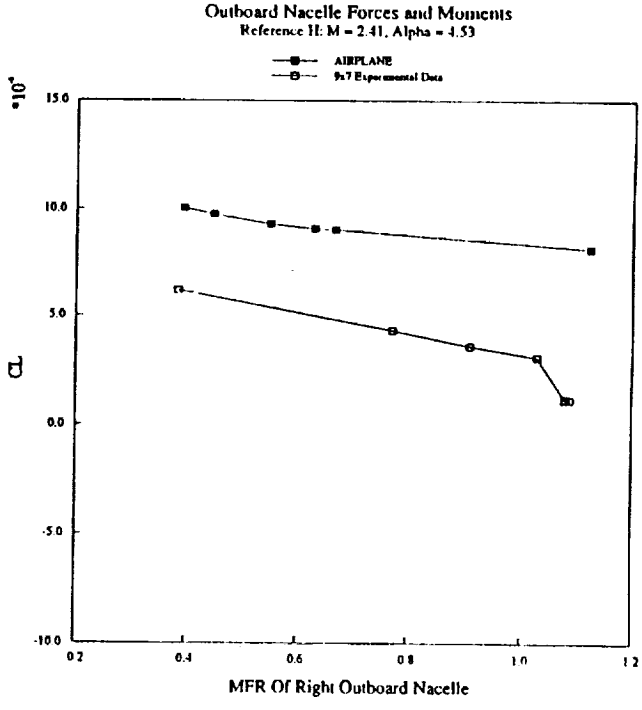

Fig 31. Computational and experimental lift coefficients for the inboard and outboard nacelles as function of mass flow ratio of the right-hand outboard nacelle, M = 2.41, alpha = 4.53 degrees.

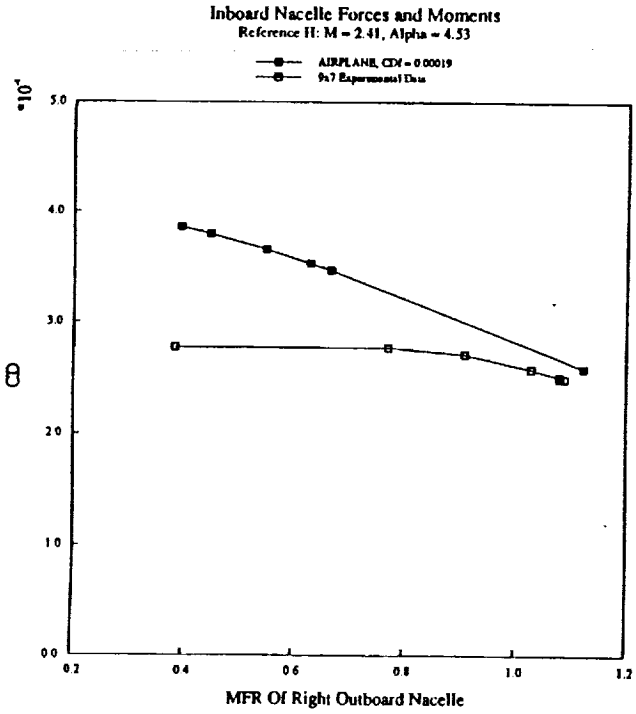

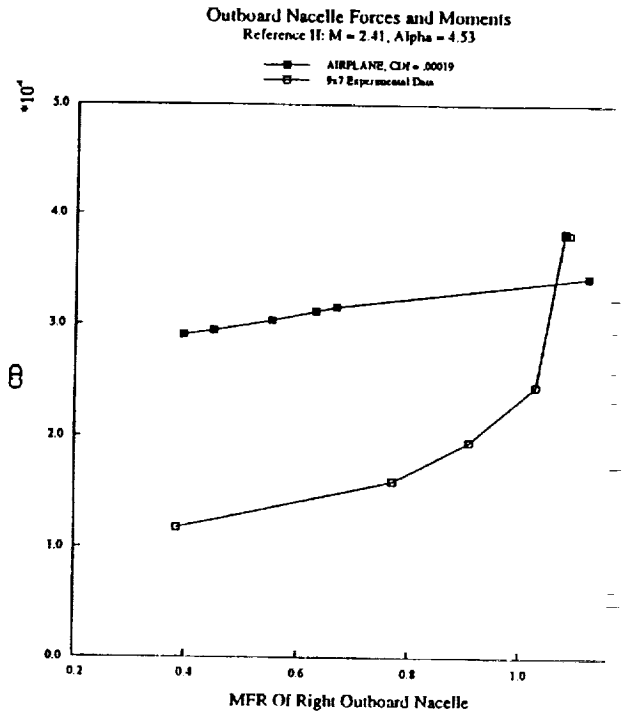

Fig 32. Computational and experimental drag coefficients for the inboard and outboard nacelles as function of mass flow ratio of the right-hand outboard nacelle, M = 2.41, alpha = 4.53 degrees.

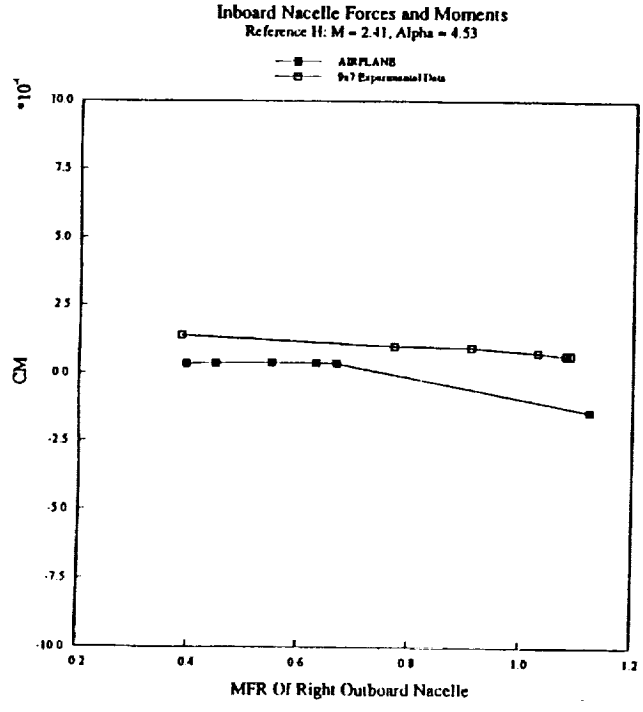

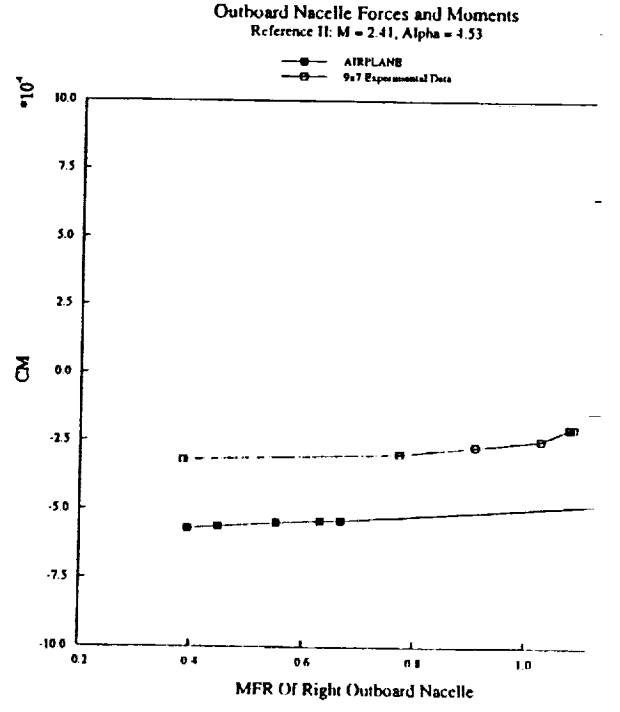

Fig 33. Computational and experimental pitching moment coefficients for the inboard and outboard nacelles as function of mass flow ratio of the right-hand outboard nacelle, M = 2.41, alpha = 4.53 degrees.

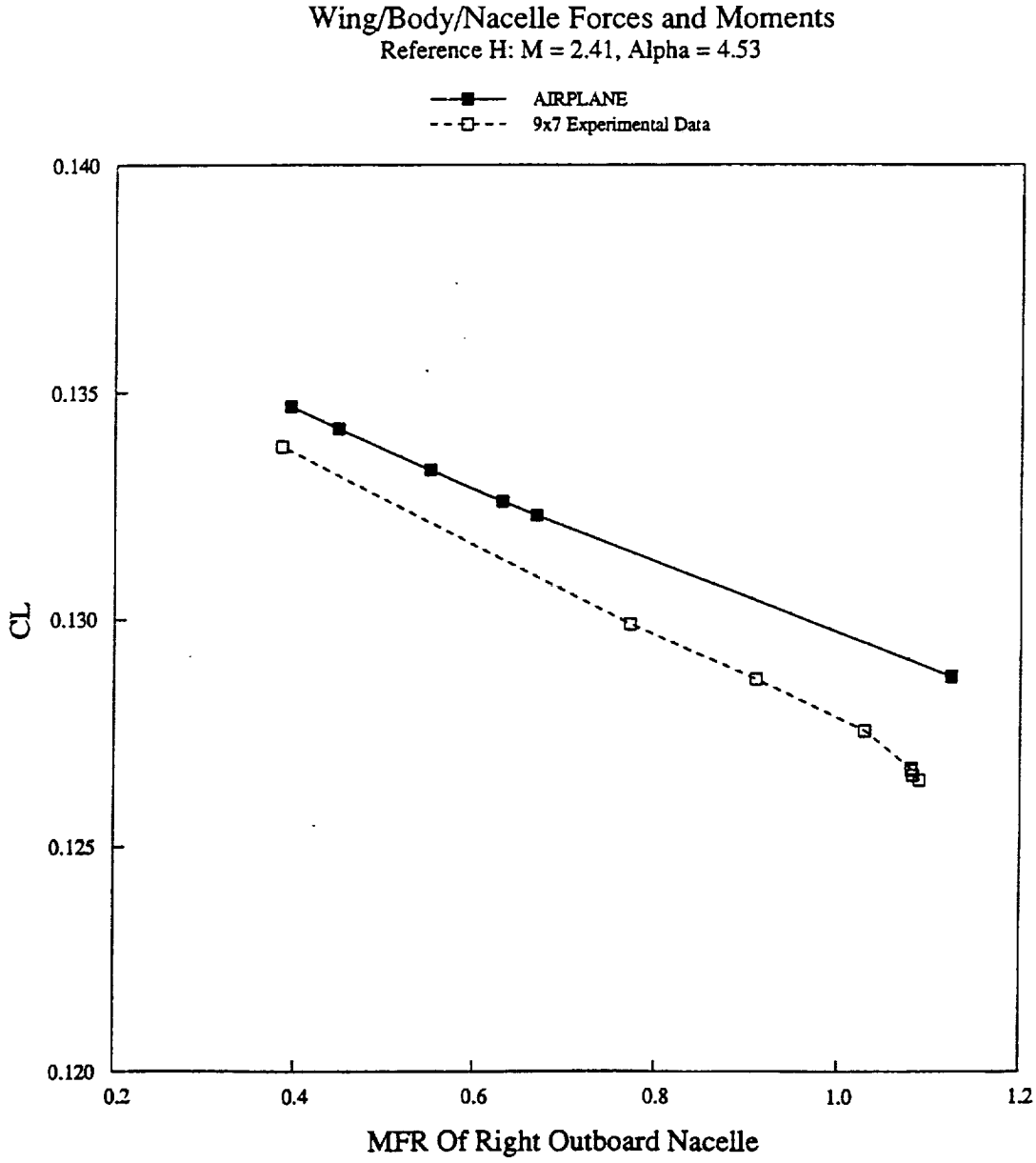

Fig 34. Computational and experimental lift coefficients for the wing/body non-captive nacelle configuration as function of mass flow ratio of the right-hand outboard nacelle, M = 2.41, alpha = 4.53 degrees.

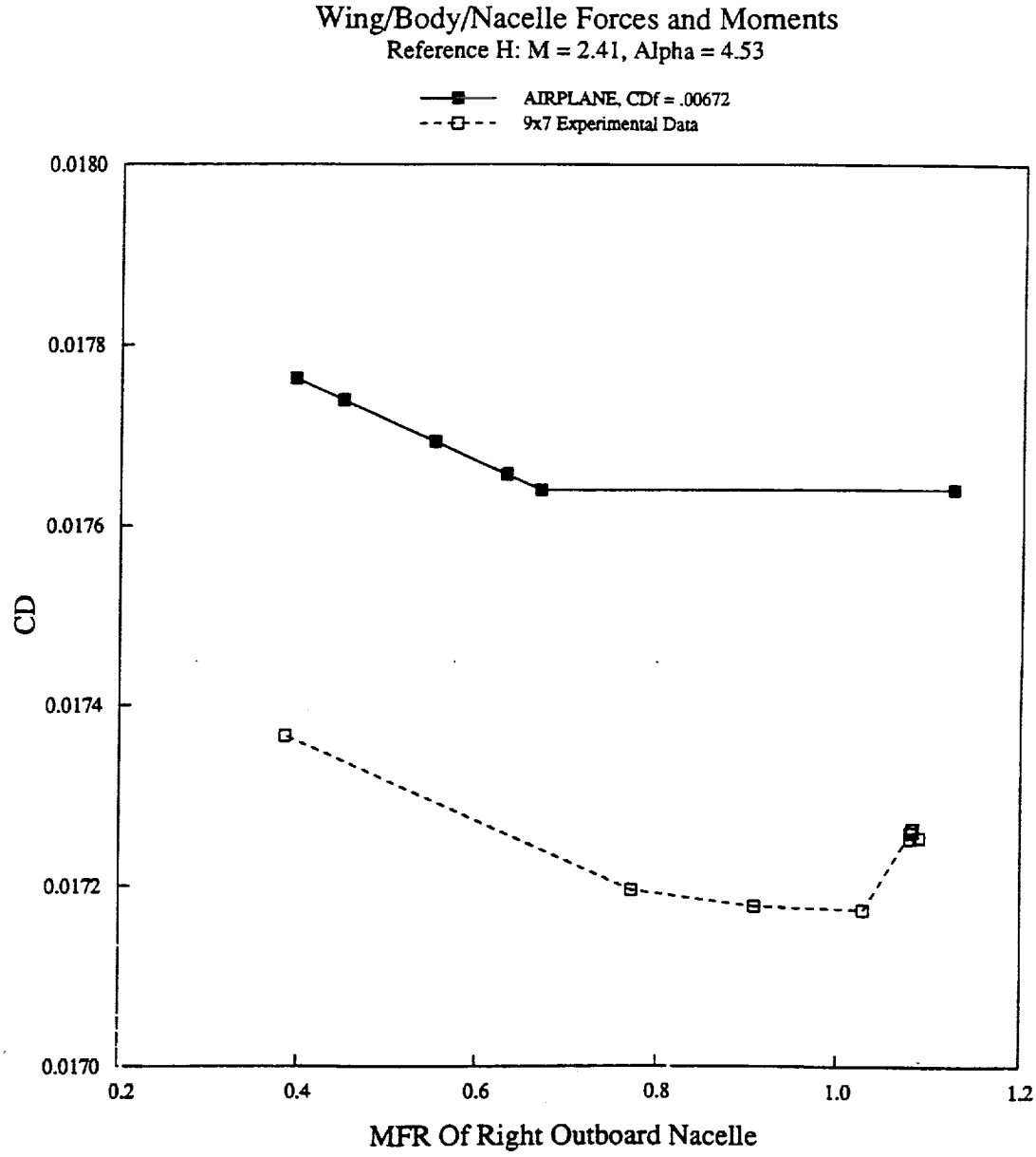

Fig 35. Computational and experimental drag coefficients for the wing/body non-captive nacelle configuration as function of mass flow ratio of the right-hand outboard nacelle, M = 2.41, alpha = 4.53 degrees.

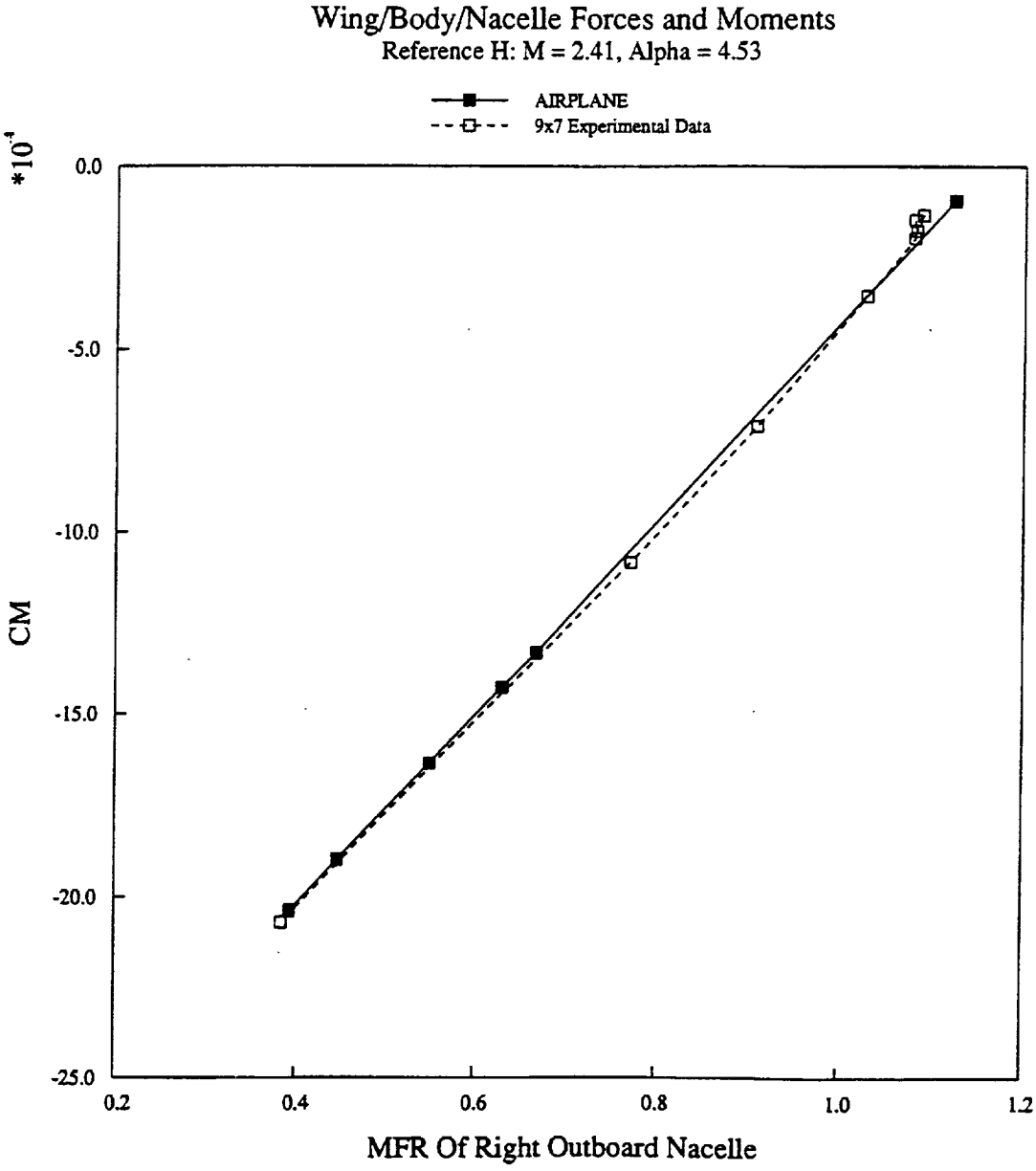

Fig 36. Computational and experimental pitching moment coefficients for the wing/body non-captive nacelle configuration as function of mass flow ratio of the right-hand outboard nacelle, M = 2.41, alpha = 4.53 degrees.

Wing Leading-Edge Geometry Effects on High-Lift Performance

David L. Hoyle and Marvine Hamner
McDonnell Douglas Aerospace
Long Beach, California 90807-5309

The purpose of this study was to gain insight into how wing geometries optimized for high-speed cruise performance performed at low-speed, high-lift conditions. The highly-swept HSR planforms attempt to maximize L/D by using simple-hinged leading-edge flaps to maintain attached flow over the wing during takeoff and landing. Wing leading edge parameters such as leading-edge radius and thickness distribution are typically defined to maximize high-speed cruise performance. This study shows that these parameters also play a crucial role in achieving the high-lift L/D's needed to meet minimum noise requirements.

Wind tunnel test data recently obtained on an arrow wing configuration yielded a maximum trimmed high-lift L/D of only 6.9. The current trimmed high-lift L/D metric for this planform is 8.2. Much of the deficiency in L/D was believed to arise from the wing leading edge definition. Wing geometry modifications to both the leading-edge radius and thickness have been analyzed using higher-order CFD methods. It is estimated that implementing these simple changes could increase the high-lift L/D's obtained by 1.0 to 1.5. This would correspond to a noise decrease of over 1.5 dB at engine cutback. Additional work needs to be done to determine the trade-offs in wing leading-edge design to maximize both the high-speed cruise and the high-lift performance.

MCDONNELL DOUGLAS — HIGH-SPEED CIVIL TRANSPORT — HSCT

Wing Leading-Edge Geometry Effects on High-Lift Performance

Roger W. Clark
Marvine P. Hamner
David L. Hoyle
Ryan C. Polito
Yoram Yadlin

February 29, 1996

This document describes the contract work performed by the Advanced Systems and Technology-Phantom Works Division of McDonnell Douglas Aerospace (MDA) under the High Speed Research Airframe Program, Phase II, NAS1-20220 (Purchase Order AZ0204), Task 4. This contract is part of the overall effort to develop technologies for an advanced supersonic transport aircraft, supported by NASA through its Langley Research Center.

4.0% MDC M2.4-7A Opt 2a Arrow Wing Wind Tunnel Model

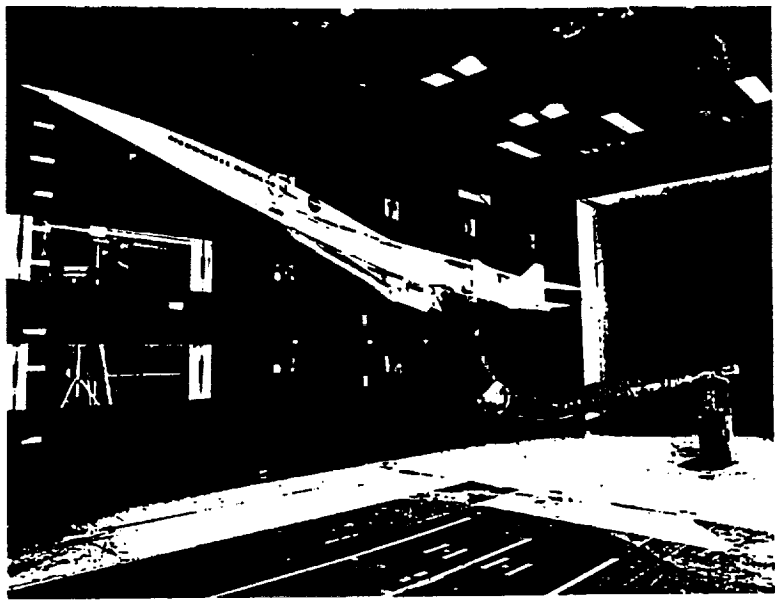

This study on the effects of the wing leading-edge geometry on high-lift performance was undertaken as a result of the findings that the wind tunnel data obtained on the 4% Arrow Wing model showed significantly less performance than was expected. The team thought at the time that this deficit was a result of the wing leading-edge definition, rather than either the wing leading-edge sweep or the aspect ratio. This study was then conducted to determine the sensitivity of the configuration's high-lift performance to wing leading-edge geometry.

This figure shows the 4.0% McDonnell Douglas M2.4-7A Arrow Wing model installed on a lower-swept blade support during its initial entry in the NASA Langley 14x22-ft wind tunnel, test LaRC 428 (August 1995). The model tested represents the Opt 2a configuration of the M2.4-7A, and was tested in both pitch and yaw at approximate Mach and Reynolds numbers of 0.3 and 8.0 million, respectively.

The high-lift configuration shown has both the nacelles and the empennage installed and has the leading- and trailing-edge flaps deflected to the 40°/10° configuration.

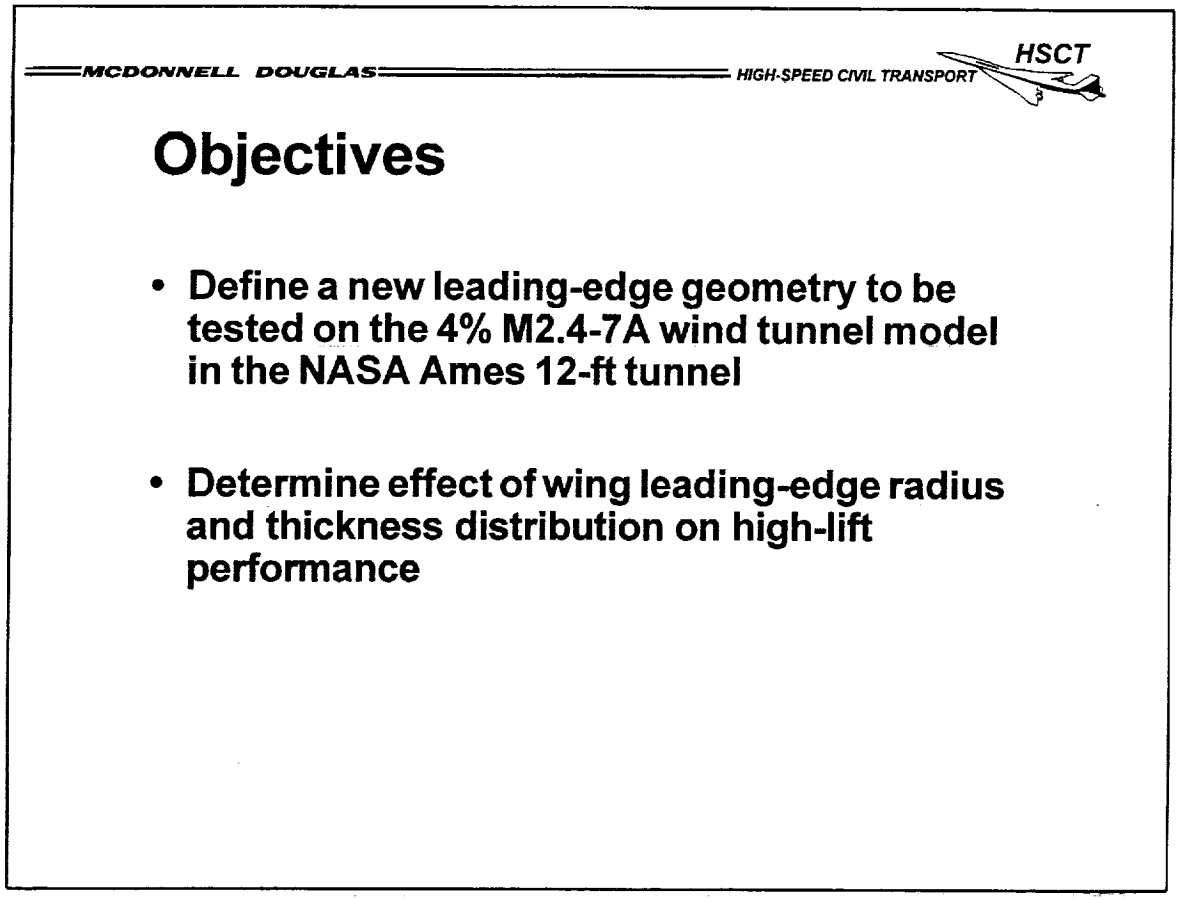

The objective of this paper is to present the findings of a study to determine the effects of wing leading-edge radius and thickness distribution on high-lift performance. The ultimate goal of this study was to define a new set of leading-edge flaps for the 4% Arrow Wing model which will be tested in the NASA Ames 12-ft tunnel in the latter part of this year. These flaps would incorporated changes in the leading-edge definition in order to achieve the level of performance previously expected from this configuration.

Outline

- **Wind tunnel data results on the M2.4-7A and Reference H -- predicted versus measured**
- **Geometry comparison of M2.4-7A with Ref H**
- **Discussion of CFD codes used for analysis**
- **Thickness distribution study for arrow wing planform**
- **M2.4-7A leading-edge geometry modifications and CFD analysis**
- **Conclusions**
- **Recommendations**

This paper will first provide a comparison of the measured wind tunnel performance of the 4% M2.4-7A Arrow Wing model relative to both the predicted levels and the performance of the 6% Reference H model. Comparisons of the geometry for these two configurations will be made to explain why the wing leading-edge definition on the Arrow Wing model was thought to be the cause of its diminished performance levels.

A discussion of the two CFD codes used for this study will then be made, showing the relative strengths and weakness of each as they apply to this study. Basic comparisons of the CFD data and the wind tunnel test data for the clean wing-body (WB) configuration will also be made for the M2.4-7A.

Next, geometry and performance comparisons will be made between the M2.4-7A and a second configuration with an identical arrow wing planform, the 1406 model from the planform study. This comparison will show the effects of thickness distribution on performance.

Finally, results of modifications to the leading-edge geometry of the M2.4-7A will be presented. This will be followed by the conclusions of the study and recommendations for the future.

Comparison of Wind Tunnel Test Results to Predicted Value

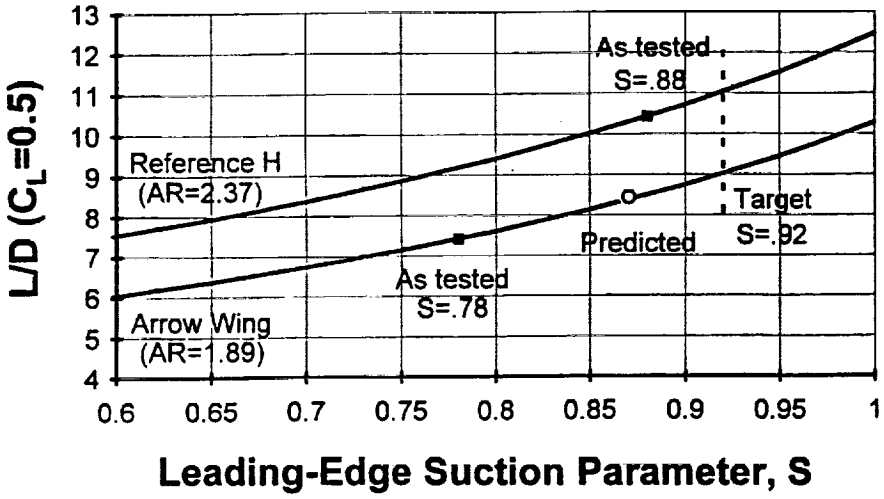

This figure shows the lift-to-drag ratio, L/D, at a lift coefficient of 0.5 as a function of leading-edge suction parameter. Curves for both the Arrow Wing and the Reference H are shown. (The Reference H data is based wind tunnel data obtained on the 6% Reference H model, also tested in the Langley 14x22 -ft tunnel.)

Wing leading-edge suction parameter is a comparison of the drag of a configuration at a given lift level relative to its theoretical maximum and minimum values. A value of 1.0 (100%) would correspond to the wing operating at its maximum theoretical efficiency (minimum induced drag), while a value of 0.0 (0%) would correspond to full wing leading-edge separation with no subsequent flow reattachment.

Because of its lower aspect ratio, the Arrow Wing was expected to give lower L/D's than the Reference H (as shown in the chart). This should have no effect, however, on the wing's performance. As indicated, the predicted performance level for the Arrow Wing is 87% leading-edge suction at C_L=0.5; the value measured during the test, however, resulted in a level of only 78%. For comparison, the measured efficiency value for the Reference H came in at 88%. There has been some speculation that the reduced performance of the M2.4-7A is a result of the increased wing leading-edge sweep (71° relative to 68°)--this will be shown to be clearly not the case.

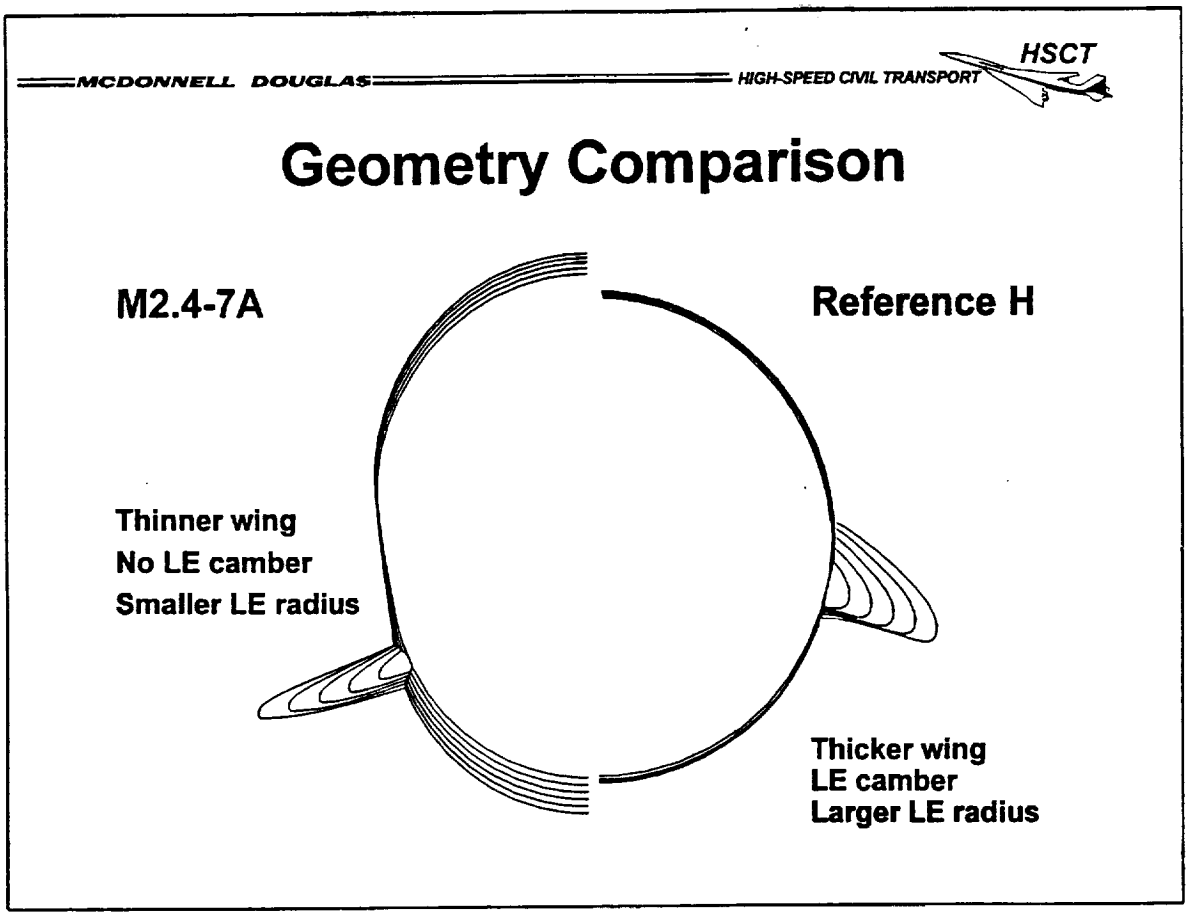

This figure shows several cross-sectional cuts through the wing and fuselage at a point near the wing apex for the Arrow Wing and Reference H geometries. This figure serves to show the major differences between the leading-edges definitions of the two wings: (1) the Reference H has a thicker wing--the M2.4-7A has a thin wing, (2) the Reference H has leading-edge camber--the M2.4-7A does not, (3) the Reference H has a large leading-edge radius--the M2.4-7A has a smaller leading-edge radius.

All of these items contribute directly to wing performance, i.e., maintaining attached flow at the leading edge. A thicker wing, leading-edge camber, and a larger leading-edge radius--all help to maintain attached flow. The performance of the M2.4-7A can clearly be improved by increasing these parameters, and as will be shown later, the Arrow Wing planform *can* meet its predicted performance levels by doing this.

Sensitivity of AERO2S to Input Leading-Edge Radius

High-Lift WB Configuration

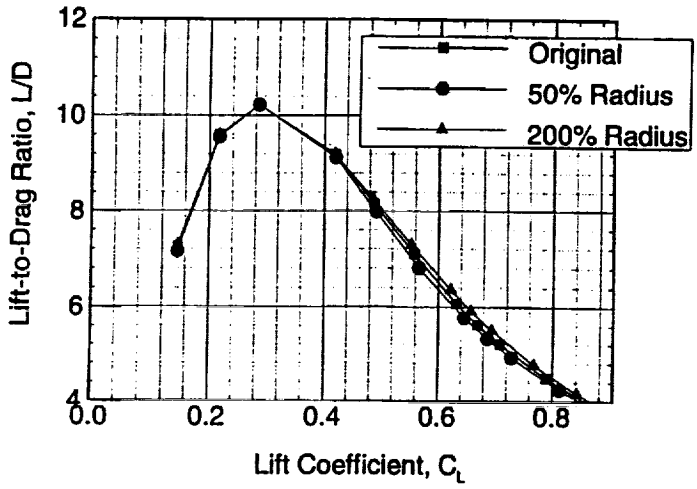

AERO2S is a vortex lattice method often used to assess the performance of HSCT-type configurations during preliminary design. AERO2S is easy to use, runs reasonably fast on virtually any platform, and can give decent predictions. It was hoped to use AERO2S in this study, since it allows the user to *specify* the leading-edge radius it uses during its calculations. Unfortunately, as this figure shows, AERO2S is rather insensitive to leading-edge radius.

This figure shows the AERO2S lift-to-drag performance of the Arrow Wing geometry for the 40°/10° configuration as a function of input leading-edge radius. These results show that by both halving and doubling the leading-edge radius, we only managed to change the resulting L/D by about 0.1 at C_L=0.5. Reducing the leading-edge radius all of the way to zero forces the AERO2S data to match the wind tunnel data quite well, but this is obviously not the correct way to run the code. This limitation of the AERO2S code made us have to go to higher-order methods.

M2.4-7A CFD Results
AERO2S and CFL3D

Clean WB Configuration

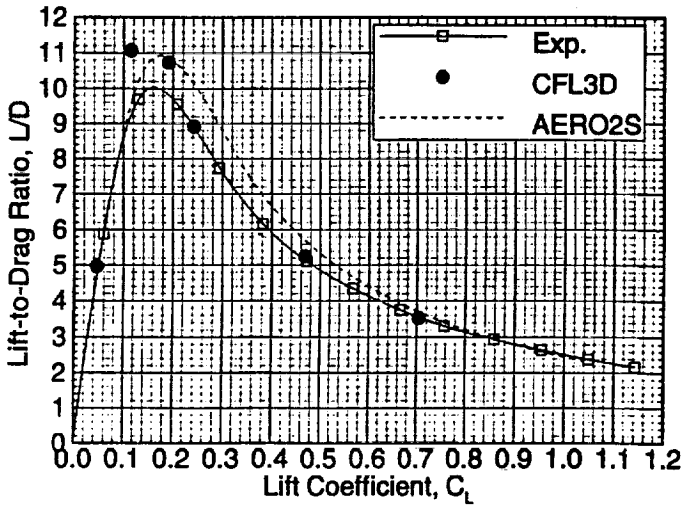

This figure shows a comparison of the CFD predictions with the measured test data for the M2.4-7A. Solutions for both AERO2S and CFL3D (Navier-Stokes) are shown. The test data are taken from test 428 for clean wing-body configuration. The AERO2S solution over-predicts the performance from C_L's of 0.1 to 0.7. CFL3D, however, falls right on the test data except for over-predicting the peak.

At the present, we have only done our analysis on the leading-edge geometry effects for the clean wing case, i.e., undeflected leading- and trailing-edge flaps. This was done to simplify the study. The idea is that any performance improvements which can be obtained on the clean wing will also show up for the deflected-leading-edge case.

A result of having an undeflected high-lift system, however, is that the climbout C_L of 0.5 is no longer a useful lift level at which to look at L/D. With the leading-edge flaps undeflected, the M2.4-7A begins to experience leading-edge separation at approximately 4° angle of attack. So, it was decided that our analysis would be performed at a C_L of 0.24, or about 5° angle of attack.

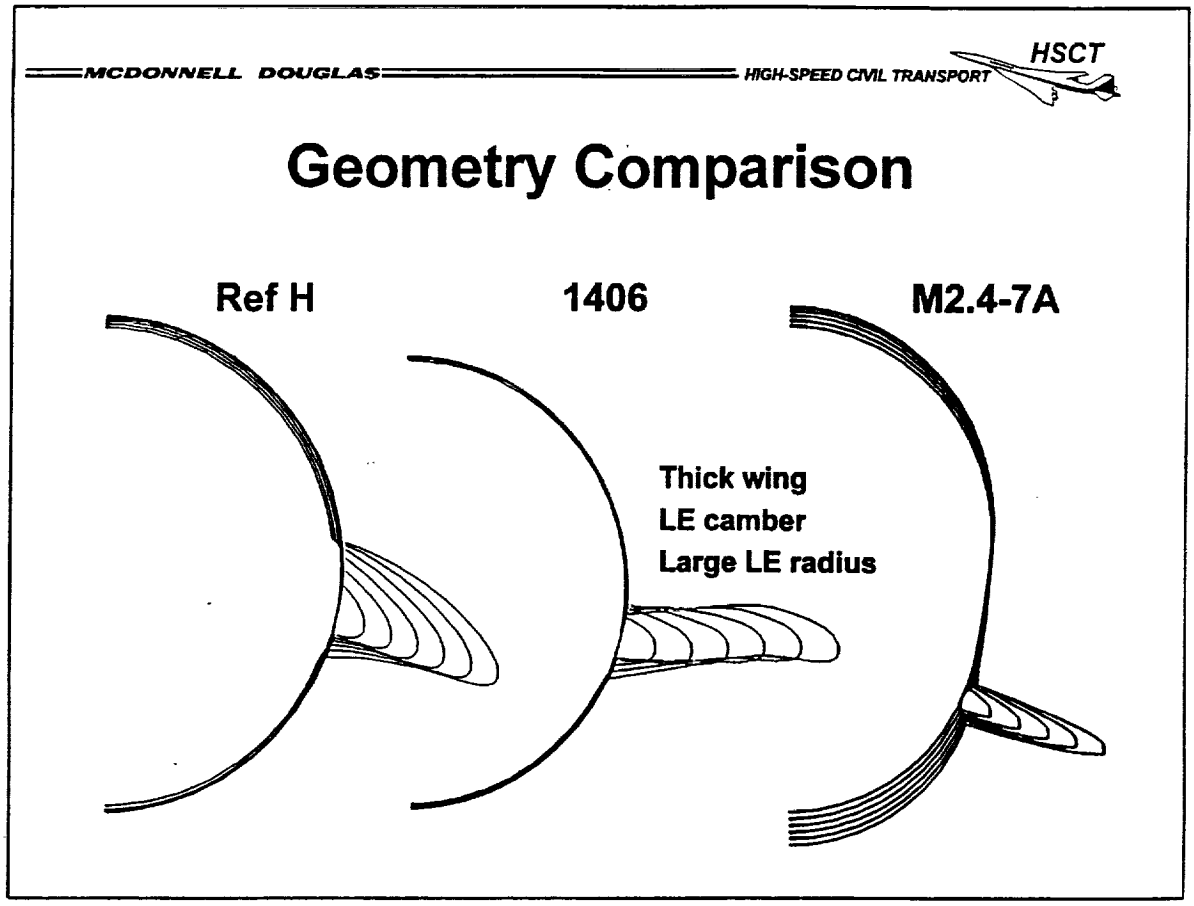

In this figure, a third geometry has been added to the comparison shown earlier--the 1406 model from the planform study. The 1406 model has an arrow wing planform identical to that of the M2.4-7A. As shown in the figure above, however, its airfoils are quite different. The 1406's wing is significantly thicker than that of the M2.4-7A, it has more leading-edge camber, and its leading-edge radius is also larger. Comparing the performance of the 1406 with the M2.4-7A will show the effects of these differences without changing the planform.

Performance Comparison
M2.4-7A and 1406

CFL3D

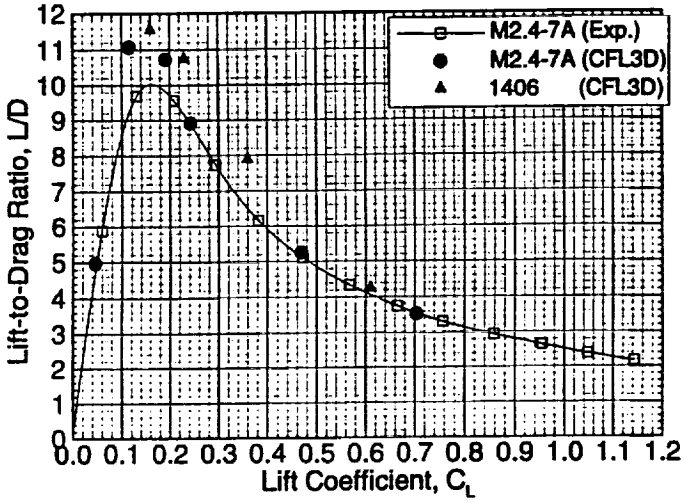

This figure shows a comparison of the CFL3D results for the 1406 and M2.4-7A along with test data for the M2.4-7A. As expected, the 1406 results show much higher L/D's at C_L's of 0.24 and 0.38. By C_L=0.6, the 1406 results collapse down onto those of the M2.4-7A. This comparison shows that the arrow wing planforms can achieve the high levels of wing suction parameter predicted for the M2.4-7A.

MCDONNELL DOUGLAS — HIGH-SPEED CIVIL TRANSPORT — HSCT

Geometry Comparison
M2.4-7A Modifications

Mod 2

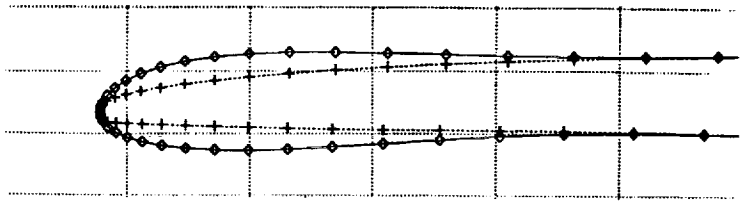

Mod 3

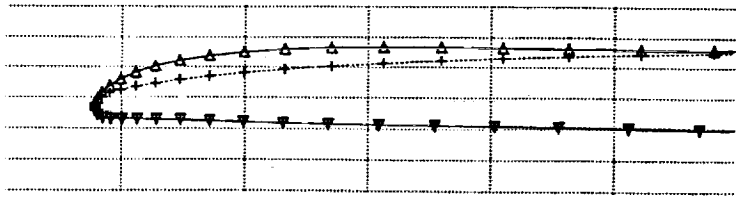

Analysis of several modifications to the M2.4-7A was done in CFL3D. This figure shows two of these geometry modifications.

The first modification, Mod 1, was an attempt to improve the leading-edge performance by "cleaning up" the leading-edge geometry. The small-radius corner on the lower surface was removed. The difference in the chordwise airfoils is not enough to be seen here. As seen on the next figure, a small amount of improvement was obtained.

The second modification, Mod 2, was an attempt to see how much leading-edge performance improvement could be obtained if the constraint to keep the resulting airfoils realistic was removed. The result was the "q-tipped" shaped airfoil shown. Mod 2 increases both the leading-edge radius and thickness distribution of the basic airfoil but does not change the mean camber line. A large increase in L/D was obtained for this geometry.

Mod 3, the next modification, attempted to remove the "q-tippishness" of the Mod 2 while keeping a large leading-edge radius. In this modification, the contraint to not change the camber was also remove. The resulting airfoil has an upper surface similar to that of Mod 2 (but with only a very slight amount inflection) and a lower surface close to that of the original airfoil. The lower surface has been modified, however, to accept the larger leading-edge radius.

Performance Comparison
M2.4-7A LE Geometry Modifications

CFL3D

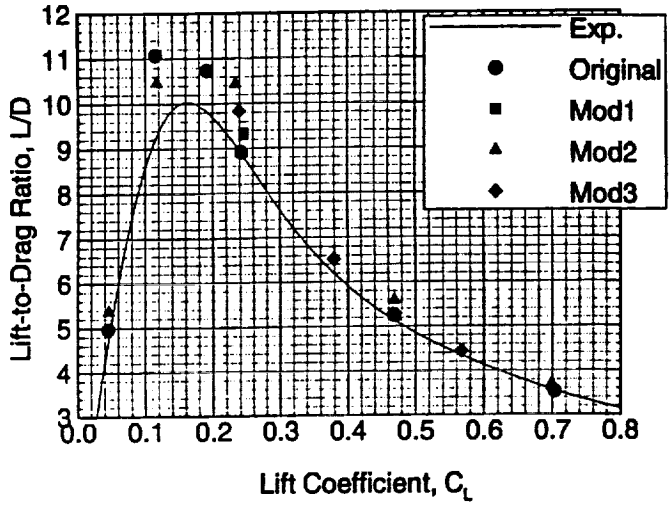

This figure shows the L/D performance of the various geometry modifications relative to the baseline geometry and the wind tunnel data from the LaRC 428 test of the 4% model.

At a C_L of 0.24 (corresponding to 5° degrees angle of attack), the Mod 1 geometry shows a very slight improvement, about 0.3 in L/D. The Mod 2 geometry, however, shows an improvement on the order of 1.6 in L/D. The Mod 3 geometry loses much of this improvement but still ends up with an increase over the baseline of about 1.0. The reduced leading-edge radius is thought to be the cause.

MCDONNELL DOUGLAS — HIGH-SPEED CIVIL TRANSPORT — HSCT

Performance Comparison
M2.4-7A Mod 3 and 1406 Geometry

CFL3D

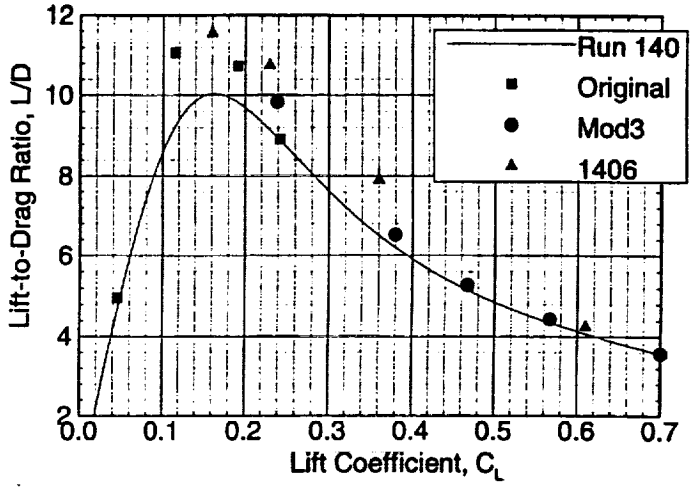

This figure shows a comparison of the Mod 3 results with those from the 1406 model and the original M2.4-7A. Test data for the M2.4-7A is also shown to help define the curve shape for the various results.

M2.4-7A Mod 2 CFD Results
AERO2S and CFL3D

Clean WB Configuration

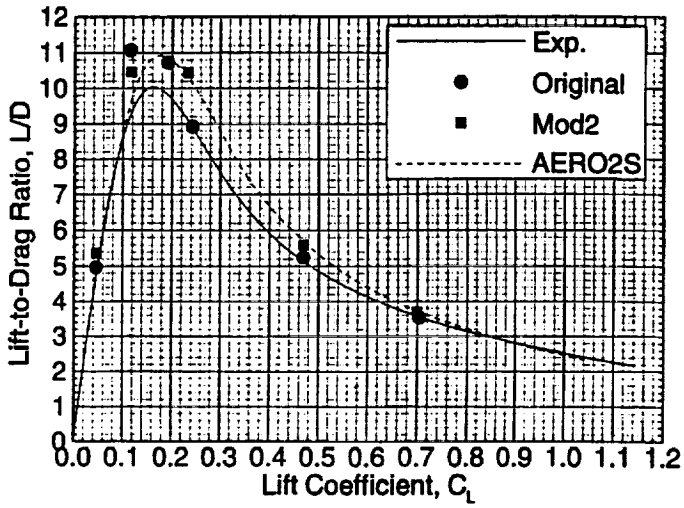

An interesting comparison between the CFL3D and AERO2S results for the Mod 2 wing is shown in this figure. When the M2.4-7A wing is sufficiently modfied that it can maintain relatively good leading-edge attachment, its performance predictions from AERO2S and CFL3D match *extremely* well. Since the camber line remains unchanged, the only modification to the original AERO2S input file was to increase the input leading-edge radius. We have not run any geometries with leading-edge radii larger than Mod 2 through CFL3D, so we cannot say whether or not this result is merely coincidental.

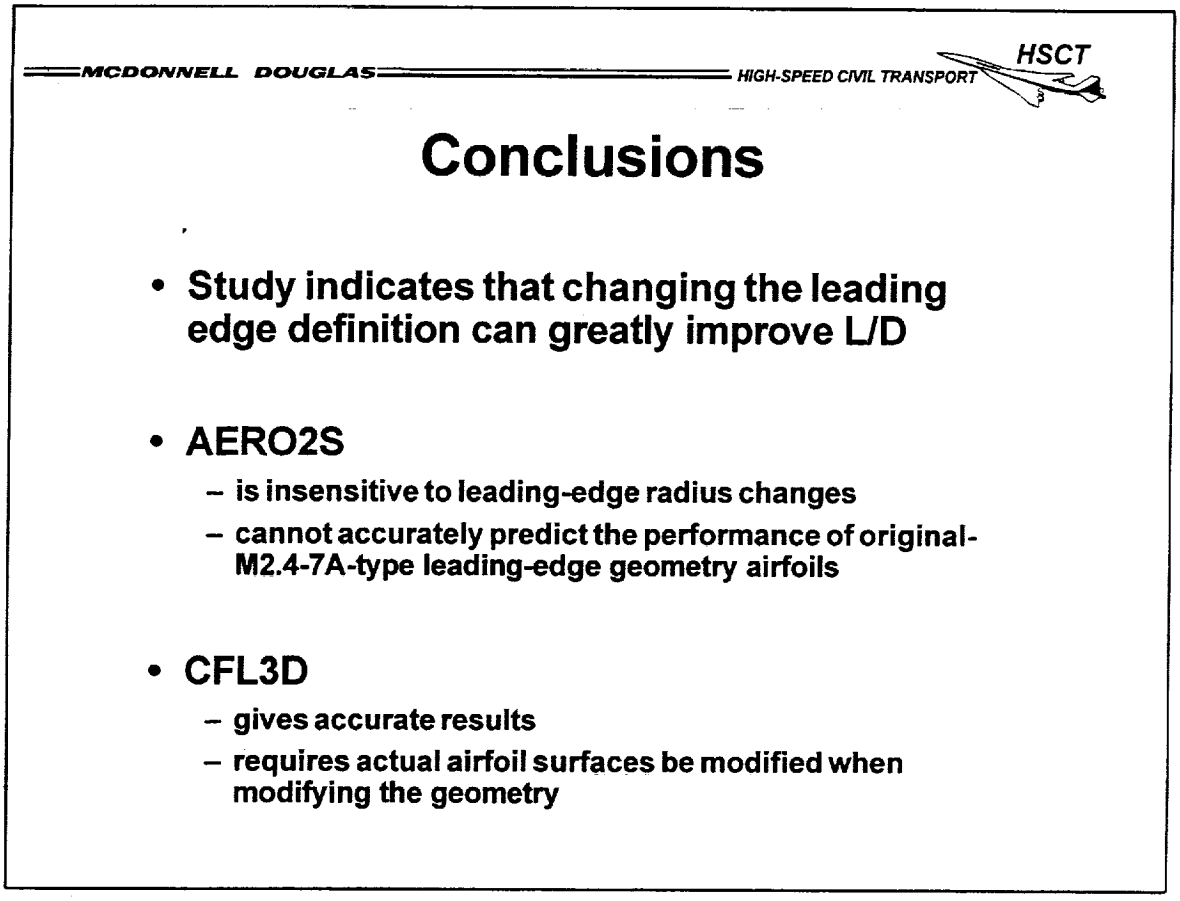

In conclusion, it has been shown that changes to the leading-edge definition can greatly improve L/D. Increasing the wing thickness also contributes to increased performance and allows for incorporation of an increased leading-edge radius.

AERO2S, on the whole, was found to be somewhat lacking in its ability to accurately model wing leading-edge performance. Comparison of the Mod 2 results indicates that it *might* be able to accurately predict the performance of certain airfoils, but this has not yet been proven and it looks like the only way to know whether its predictions for a given airfoil are accurate or not is to run the airfoil through a higher-order code (or wind tunnel test).

CFL3D proved to be quite accurate in modelling the performance of the M2.4-7A wing. Making geometry modifcations for input into this code, however, can be quite time-consuming since it requires that the actual surface definitions be changed.

Recommendations

- **CFD analysis required for high-lift configuration**
- **Testing of the modified leading-edge geometry on the 4% M2.4-7A in the NASA Ames 12-ft wind tunnel**
- **Trade studies need to be done to asses the impact of improved high-lift leading-edge geometries on cruise performance**

To date, all analysis has been done on the clean wing configuration. Additional analysis needs to be done on actual high-lift configurations with the leading- and trailing-edge flaps deflected. Testing of the best leading-edge design should then be included in the upcoming 12-ft entry of the 4% M2.4-7A model to verify the results. Finally, trade studies should be done to assess the trade-offs and impacts of wing leading edges designed for high-lift performance relative to those designed for high-speed cruise performance.

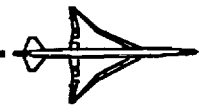

NASA LaRC Configuration Aerodynamics Workshop
Session 12
High Lift

Impact of Alternate Concepts for Wing Planform, Leading Edge Flaps, and Trim Configuration on the High Lift Performance of the Ref H HSCT

G. H. Wyatt and K. D. Visser
Boeing Commercial Airplane Company

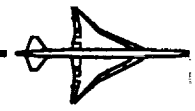

Introduction

This report will cover:

1. High lift aerodynamics overview.
2. The Technology Concept Airplane baseline, its sizing criteria, sensitivity of L/D to noise, and cutback L/D projections for the TCA.
3. A description of the 6% Ref H high lift model and mounting in the 14x22 facility.
4. Results of alternate planform testing.
5. Results of leading edge flap optimization testing.
6. Results of alternate trim concept testing.

High lift aerodynamics - what we do.

- Generate full scale flight lift and drag estimates for airplane sizing.
- Along with other HRS partners we plan, organize, and conduct wind tunnel tests to obtain necessary data.
- CFD code evaluation and appropriate use of results to better understand the wind tunnel data and flow physics.
- Multi-disciplinary trade studies and configuration development with the goal of developing the simplest high lift system which meets performance requirements.

TCA-4 December 1995 Baseline Airplane Sizing

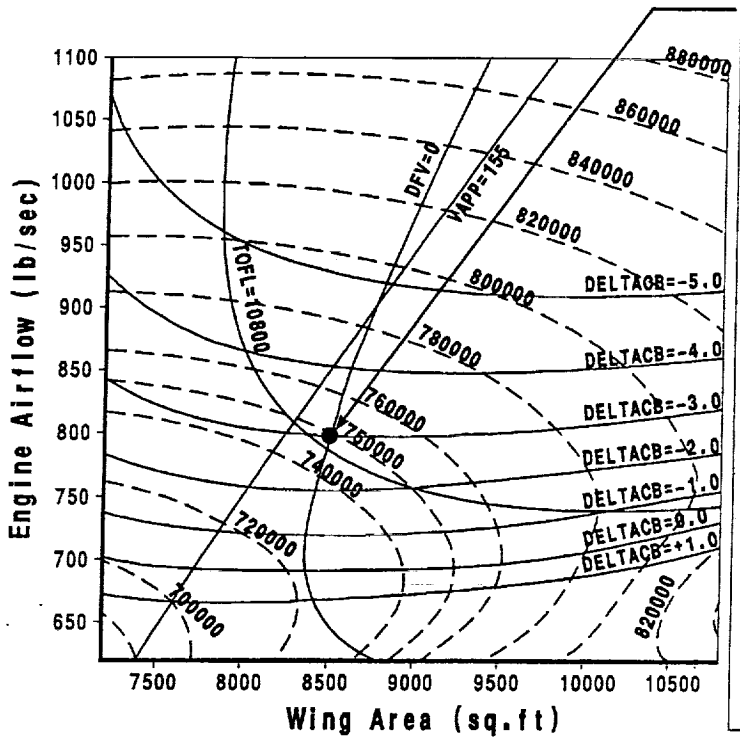

MTOW.....lb	749035
Sw.....sq.ft	8496
Wa.....lb/sec	798
Range.....nm	5000.0
Payload.....lb	63210
SLST/eng.....lb	55004
OEW.....lb	318703
Block Fuel....lb	326111
Reserve Fuel..lb	43560
Block Time....hr	5.28
Climb Time...min	50.47
TOFL.....ft	10716
1st Seg Grad....	0.052
2nd Seg Grad....	0.069
Vappr.....keas	153.2
CLappr.....	0.63
SL Margin...(dB)	-1.0
CB Margin...(dB)	-3.0

ASAP Ver A08 13-Nov-95

- This figure shows the December 1995 TCA cycle 4 sizing thumbprint. This cycle of the TCA is sized by required fuel volume and cutback noise, Stage III - 3 db. The resulting airplane weights 749,035 lb. Other mission sizing constraints that come close to effecting airplane sizing are the takeoff field length to meet second 1st and 2nd segment gradients and 60 minute climb time.
- Shown on this thumbprint are lines of constant Stage III noise. Note, the sensitivity of the TCA to noise, if Stage III - 5 db is required then the sized airplane would follow the fuel volume line up to the approach speed line (VAPP=155) then on up to DELTACD = -5 db line. This airplane would weigh 792,000 lb.

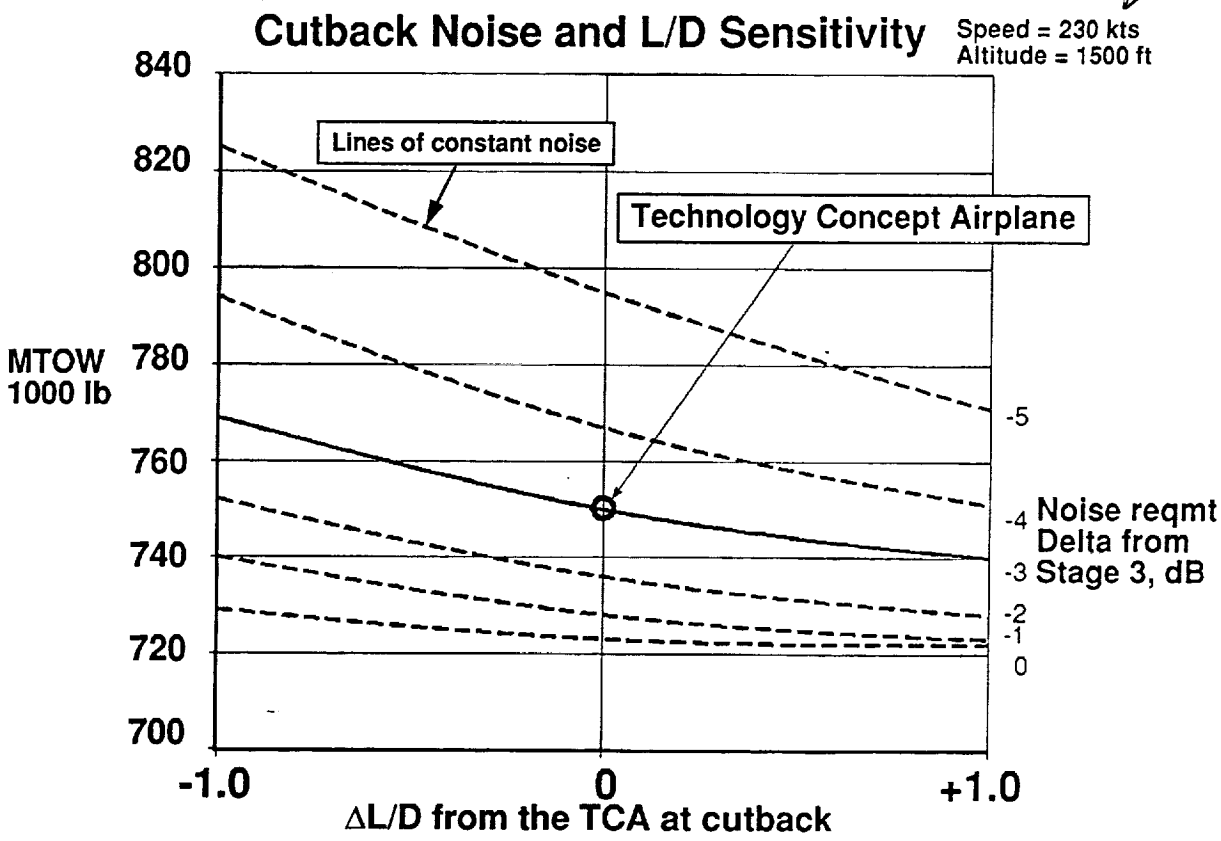

- This figure shows the sensitivity of the TCA baseline airplane to noise sizing criteria and L/D increments away from the performance which went into the baseline TCA. From this chart we see that the baseline TCA sizes to 750,000 lb at Stage III -3dB.
- Notice how the sensitivity of MTOW to noise increases with increasing noise regulations. Likewise the sensitivity of MTOW to L/D increases when L/D decreases.
- This chart illustrates the inter-dependance of noise and L/D at cutback.

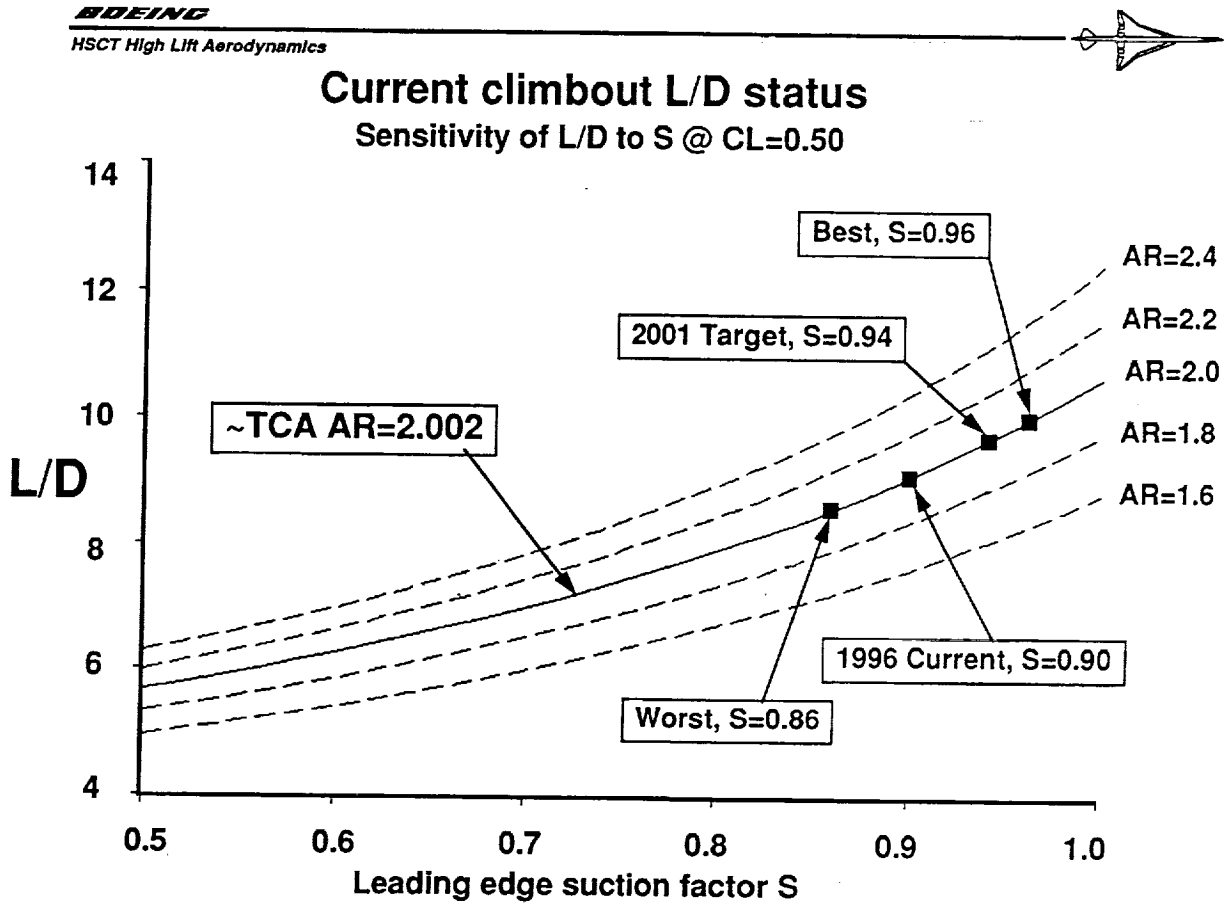

- This figure shows the sensitivity of L/D to leading edge suction at CL=0.50. Several lines of constant wing aspect ratio are shown to illustrate the effect of changing wing planform on L/D.
- The solid line in the middle represents the TCA. Several points at different S factors are noted along this curve. These points represent what the HSR high lift community currently thinks are the ranges of possible outcomes for trimmed L/D at cutback for a 2001 airplane.
- The target value of S=0.94 is the L/D technology goal for 2001. The current status, S=.90 is what can be demonstrated today. The best and worst cases represent the uncertainty for the TCA airplane.

6% Ref H high lift model in 14x22 facility

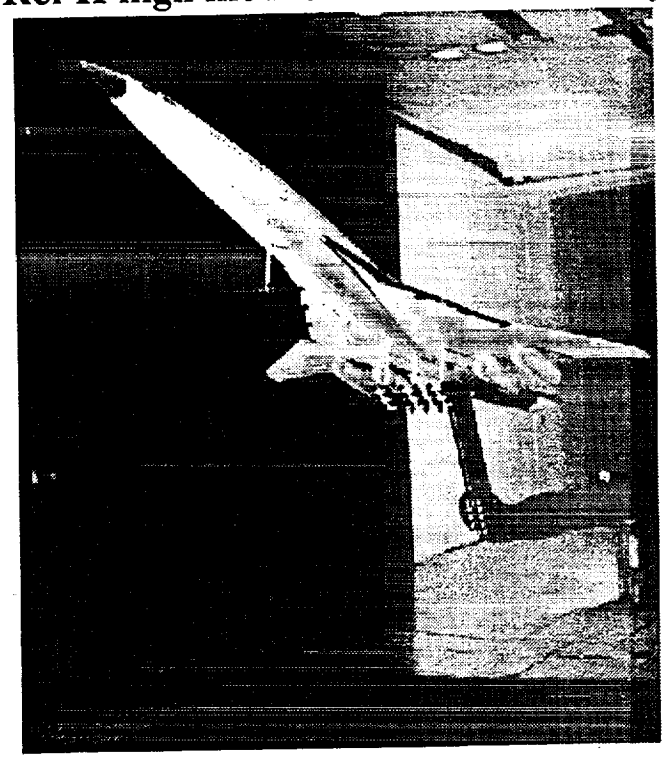

- This is the 6% Ref H high lift model shown installed in the LaRC 14x22 facility. This photo was taken during the first model entry in June of 1993. The first entry was swept strut mounted as shown. We have conducted a total of four entries with this model in the 14x22 tunnel. The three tests following the first one were mounted on a vertical post.
- All of the wind tunnel data contained in this report has been acquired by testing this model in this facility. All data presented herein was acquired at a Mach number of 0.24, q=85. This condition matches the approach speed. The Reynolds number based on model CBAR at these conditions is 8.4 million.

6% Ref H Model in 14x22 Test Section

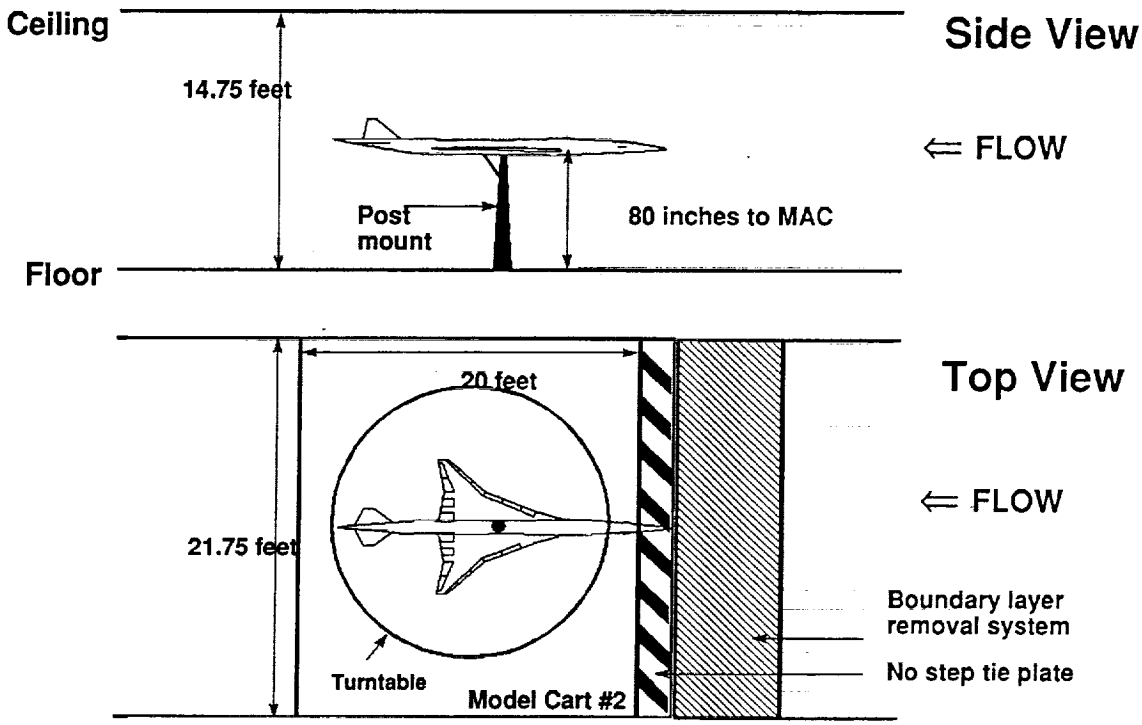

- This figure shows a side and top view of the 6% Ref H model post mounted in the 14x22 facility. Some items to note:
- All the test data analyzed in this report were acquired at the nominal height shown of 80 inches.
- The proximity of the model with respect to the boundary layer removal system was a concern. (See figure) This could not be avoided without major modifications to the model or the facility cart system.
- The post location is approximately 2 feet forward of the yaw turntable's center. As a result when the model was yawed it moved away from tunnel lateral center along an arc with a 2 foot radius.

Baseline Planform and Reference Areas of the 6% Ref H Model

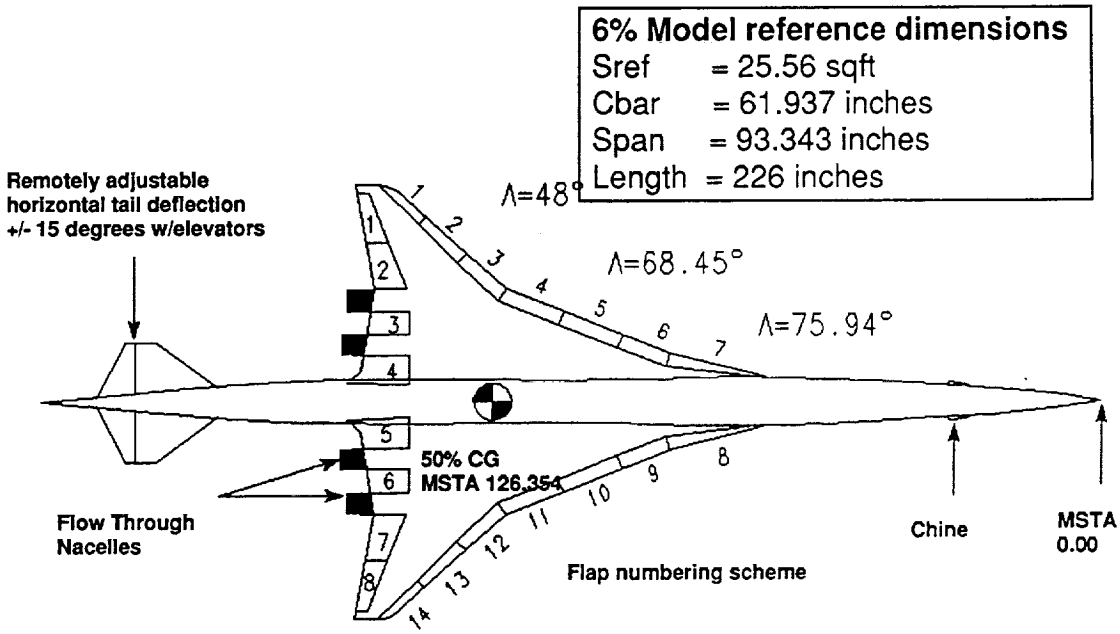

- This figure shows the planform, reference areas, and flap numbering scheme of the 6% Ref H model.
- Not shown on this figure is an important piece of the Ref H geometry. The inboard leading edge radius is as generous as possible given the constraints of wing thickness. This large radius delays leading edge separation on the inboard wing to higher angles of attack. For this reason the requirement for leading edge flap coverage on the inboard wing has been reduced.

Alternate planforms tested

All planforms have common aspect ratio, span, and area.
AR = 2.367
span = 93.34 inches
Sref = 25.56 sqft

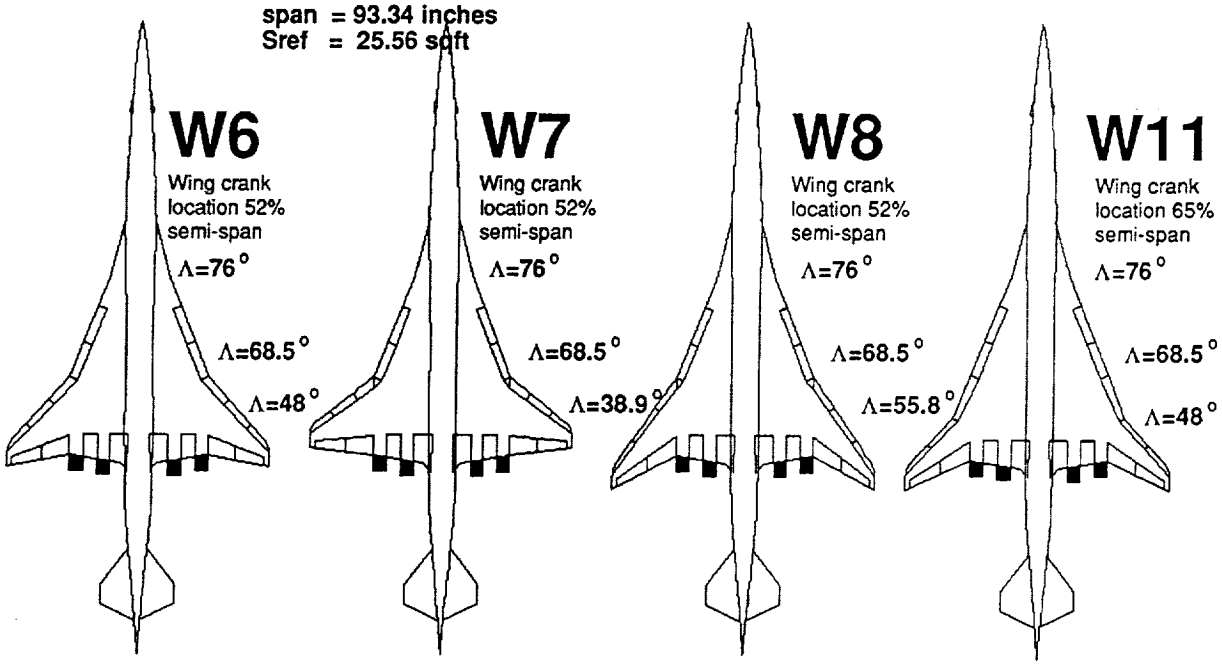

- This figure shows the four planforms tested.
- W6 is the baseline Ref H. W6 has outboard panel leading edge sweep =48 degrees. Wing crank location = 52% semi-span.
- W7 has an outboard panel leading edge sweep of 38.9 degrees. Wing crank location = 52% semi-span.
- W8 has an outboard panel leading edge sweep of 55 degrees. Wing crank location = 52% semi-span.
- W11 has an outboard panel leading edge sweep of 48 degrees, the same as Ref H, but the wing crank location is moved outboard to 65% of semi-span. This alternate planform is an attempt to match as closely as possible the M2.4-7A arrow wing planform given the constraints of the 6% model.

Trimmed Angle of Attack Characteristics of Alternate Planforms at CLTRIM=0.55

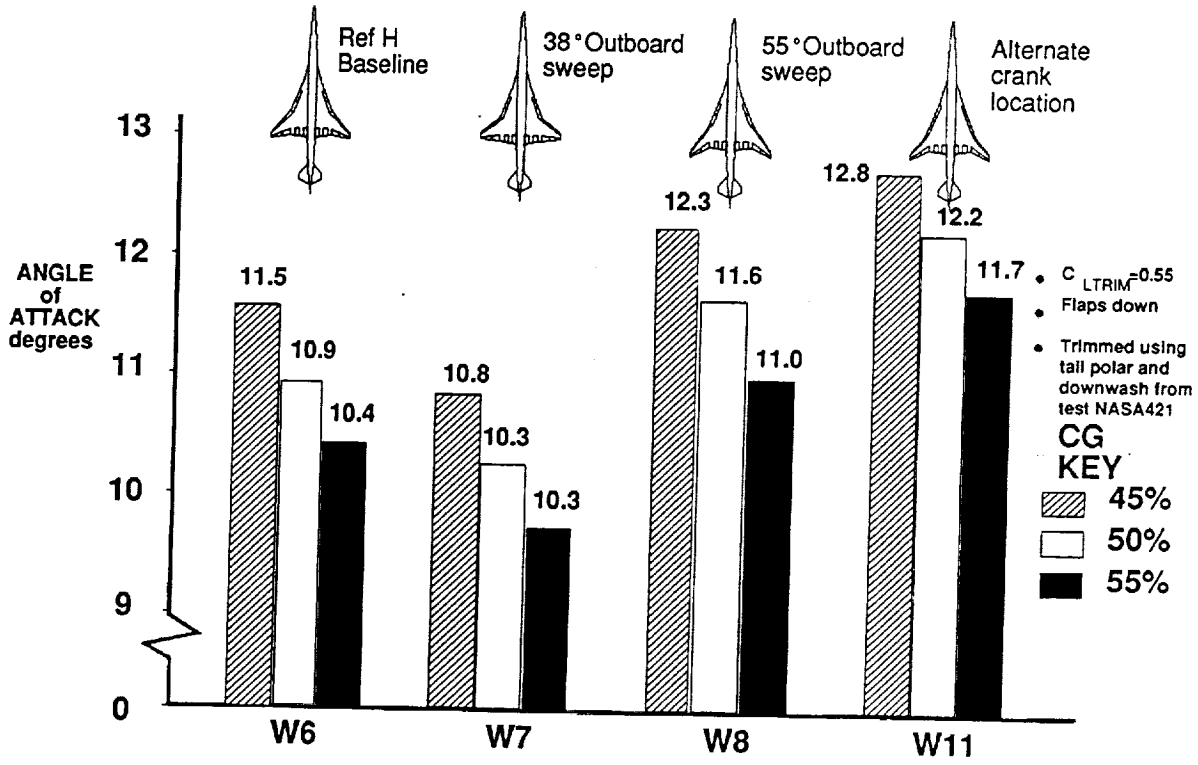

This chart shows the trimmed angle of attack variation of the four planforms as CG location is varied at CL=0.55.

- CL of 0.55 represents the cutback noise lift coefficient of the Ref H.
- The three bars under each planform represent trimmed angle of attack for CG positions of 45, 50, and 55% MAC.
- A lower angle of attack is preferred as that will promote attached flow and reduce drag due to separation.
- The best planform based on lowest trimmed angle of attack is the planform with the 38 outboard leading edge sweep. The baseline W6 is a close second to W7 with just slightly lower trimmed angles of attack.
- The other two planforms, W8 and W11, both exhibited much increased trimmed angles of attack.

Trimmed L/D Characteristics of Alternate Planforms at CL=0.55

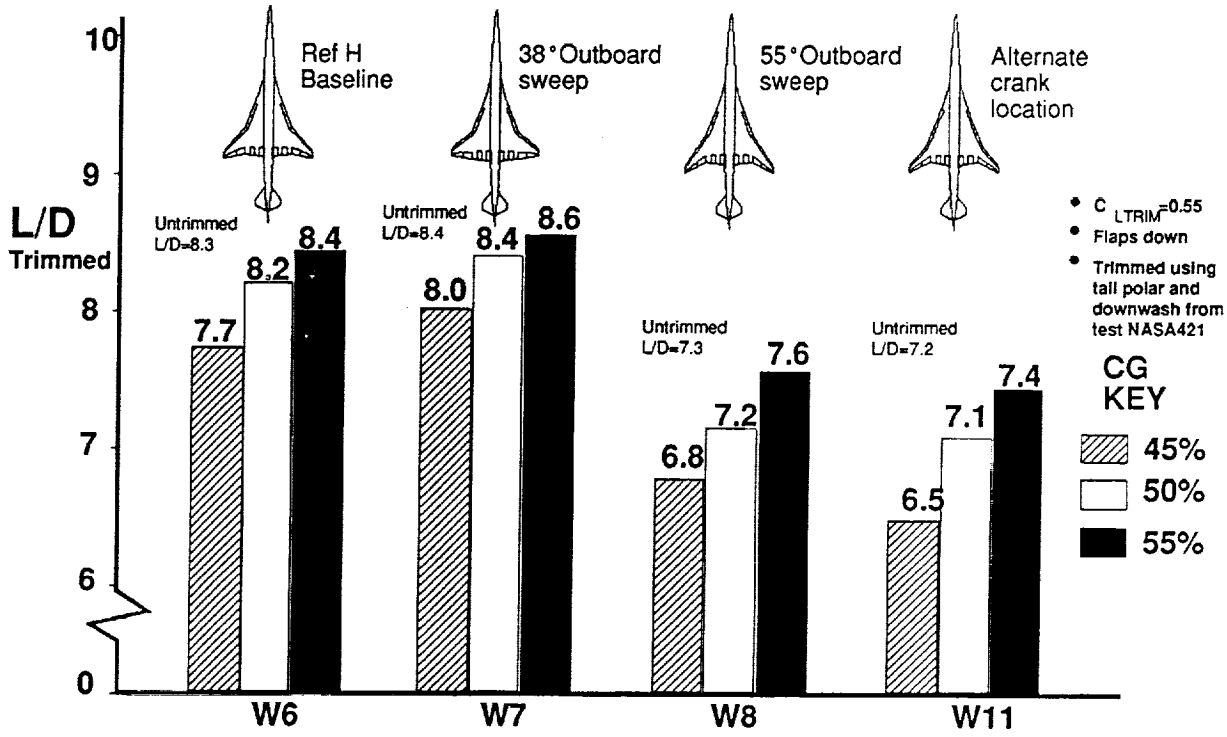

This chart shows trimmed L/D at CL=0.55 for the four planforms tested.

- CL of .55 represents the cutback noise lift coefficient.
- The three bars under each planform represent trimmed L/D for CG positions of 45, 50, and 55% MAC.
- Also shown on this Figure are the untrimmed L/D levels for each planform.
- The best planform based on highest trimmed L/D is W7 which is the planform with the 38 outboard leading edge sweep. W7 was expected to be the best planform since it has the lowest overall wing sweep angle. The baseline W6 is a close second to W7 with just slightly lower trimmed L/D's.
- The other two planforms, W8 and W11, both exhibited much decreased trimmed L/D's. This is not an unexpected result. W8 has increased outboard leading edge and trailing edge sweep which should theoretically hurt low speed performance. W11 has the same leading edge sweep angles as the baseline W6 but the crank location is moved outboard from 52% to 65% of span. W11 also has an increased trailing edge sweep which hurts trailing edge flap performance. W11 is a close approximation to the McDonnell Douglas M2.4-7A arrow wing planform.

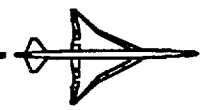

Alternate Planform Conclusions

- Wing planform is a powerful driver to increase low speed trimmed L/D and reduce noise at takeoff, climbout and approach. Lower sweep angle, higher aspect ratio, or more span is preferred.
- As wing leading edge sweep increases trimmed L/D can be expected to decrease even for the same aspect ratio.
- CG location is a powerful driver when analyzing trimmed performance for low speed operations.

Leading edge flap variations tested

Inboard leading edge treatments

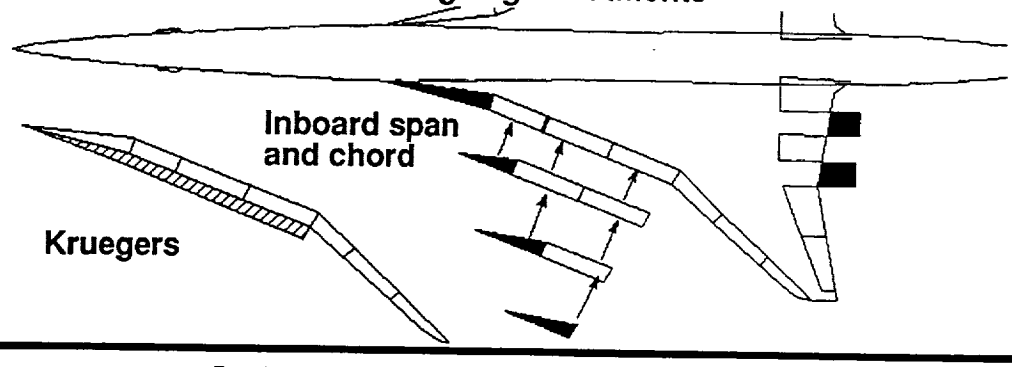

Outboard leading edge treatments

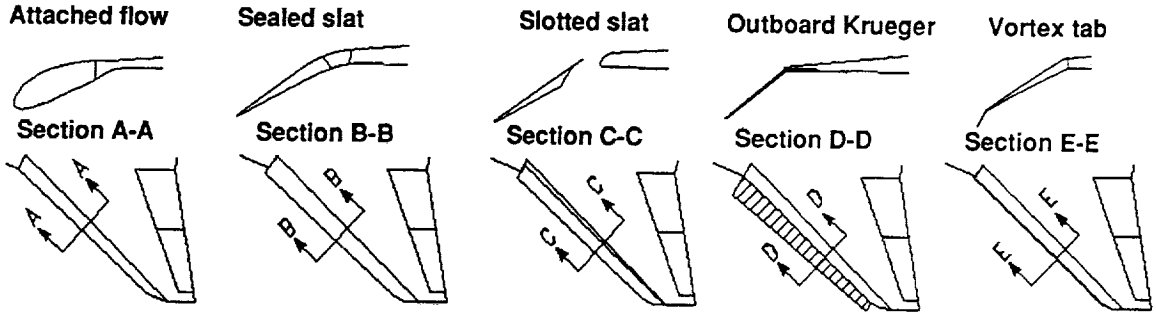

In addition to baseline plain flaps these variations were tested on the 6% Ref H model.

Inboard flap variations included:

- Inboard wing krueger flaps are designed to initiate a leading edge vortex and trap it on the upper surface of the krueger. The premise is that the vortex would simulate a large leading edge radius and incoming streamwise flow would flow over the trapped vortex and reattach aft.
- Flap span variations were tested to determine how much coverage flap coverage is required on the inboard wing.

Outboard flap variations included:

- An attached flow concept to investigate what could be expected if completely attached flow could be obtained.
- A sealed and a slotted slat concept.
- Krueger flaps similar to the inboard concept.

Effect of leading edge flap variations on L/D

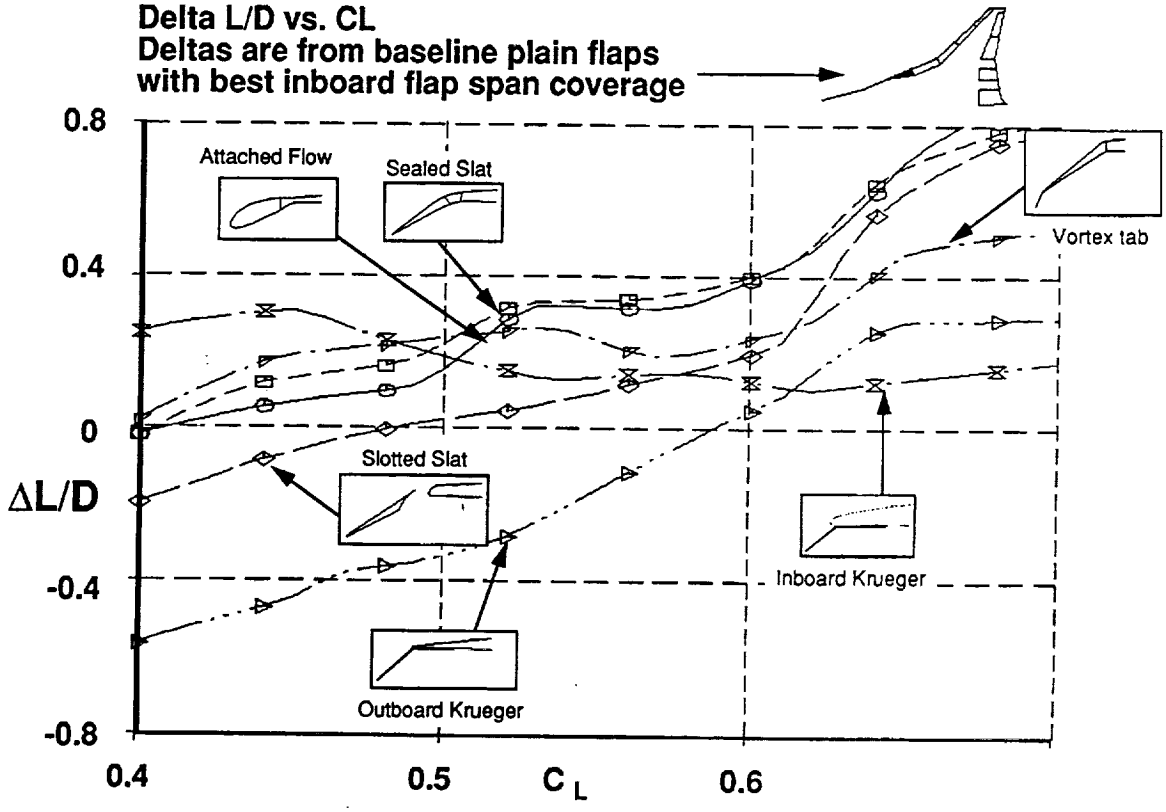

This figure shows the effect on L/D of each alternate leading edge flap tested. The data is presented as delta L/D from the baseline plain flap with the best inboard span flap coverage.

- Both the attached flow and the sealed slat concept performed the best over CL's of interest, .5 to .6. The attached flow concept was intended to provide us with an estimate of what is the best we could expect if fully attached flow were achieved. The sealed slat performed equal to the attached flow flap, it has an advantage of some fowler motion which adds wing area. However, it looks like the most promising concept. Delta L/D's of about 0.3 can be achieved with a sealed slat concept.
- The vortex tab although a small device worked quite well in improving L/D. This type of device will be a challenge to integrate.
- The slotted slat improved L/D only slightly and is not worth the mechanical complication.
- The inboard krueger provided delta L/D improvement of 0.2 over the CL range of interest.
- Outboard kruegers are only worth using at higher CL's.

Leading Edge Flap Conclusions

- When the TCA high lift wind tunnel models are tested we should continue to investigate variations in leading edge devices.
- We should focus on variations of the sealed slat, vortex tab, and inboard krueger flaps as they show the most promise.

Alternate Trim Configurations

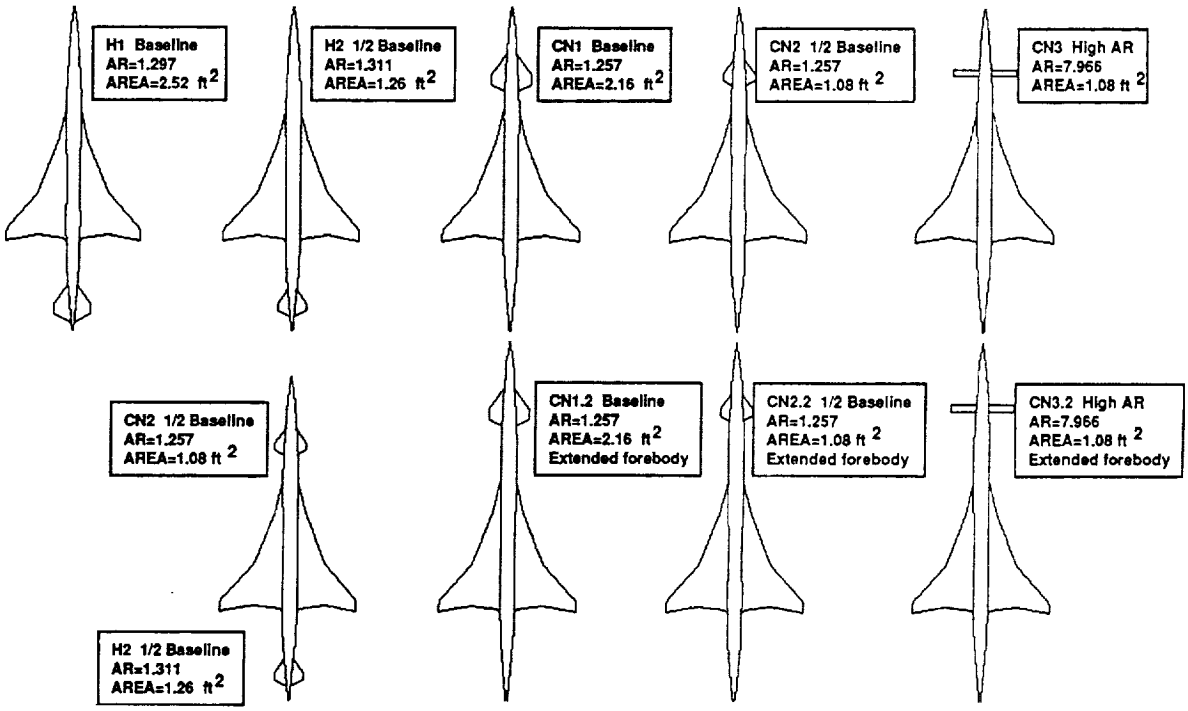

This figure illustrates new and existing model parts designed and built for the alternate trim and control test.

H1 - Baseline horizontal tail.
H2 - 1/2 size horizontal tail.
CN1 - Baseline canard mounted on baseline forebody.
CN2 - 1/2 size canard mounted on baseline forebody.
CN3 - High aspect ratio canard, same reference area as CN2.
3 Surface - H2 and CN2 mounted on the baseline body.
CN1.2 - Baseline canard mounted on the 2 foot extended forebody.
CN2.2 - 1/2 size canard mounted on the 2 foot extended forebody.
CN3.2 - High aspect ratio canard mounted on the 2 foot extended forebody.

Other parts not shown on this figure include:

- Canard high mount.
- Canard remote drive mechanism, allowing remote control deflection of canards from two positions on the forebody, low and high.
- Two canard wiping surfaces - fairings which provide a flat surface for the canards to wipe against and minimize unporting when the canards are deflected. These were made for both the high and low positions.
- Forebody plugs - to move the canards away from the wing to simulate an aft wing shift, two plugs were fabricated both 1 foot in length.
- New post mount system to allow high alpha and beta testing.

Canard Configurations

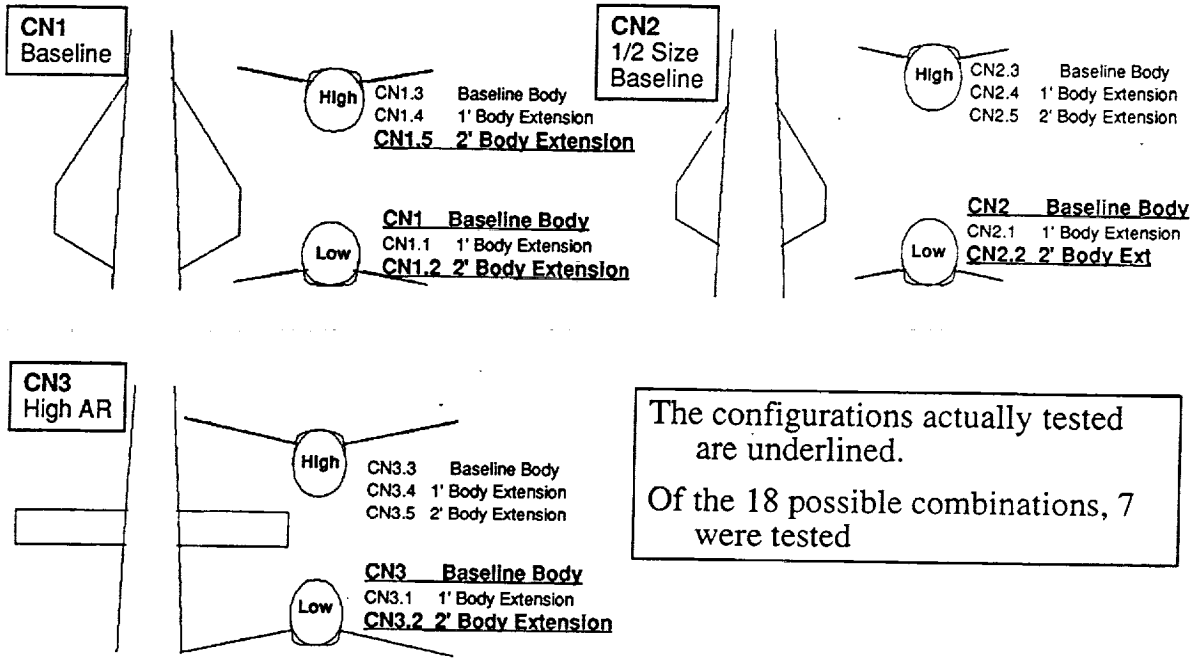

The configurations actually tested are underlined.

Of the 18 possible combinations, 7 were tested

This chart shows front views illustrating the different canard locations and orientations for the high and low positions

H1 - Baseline Horizontal Tail Trimmed L/D versus CG Location

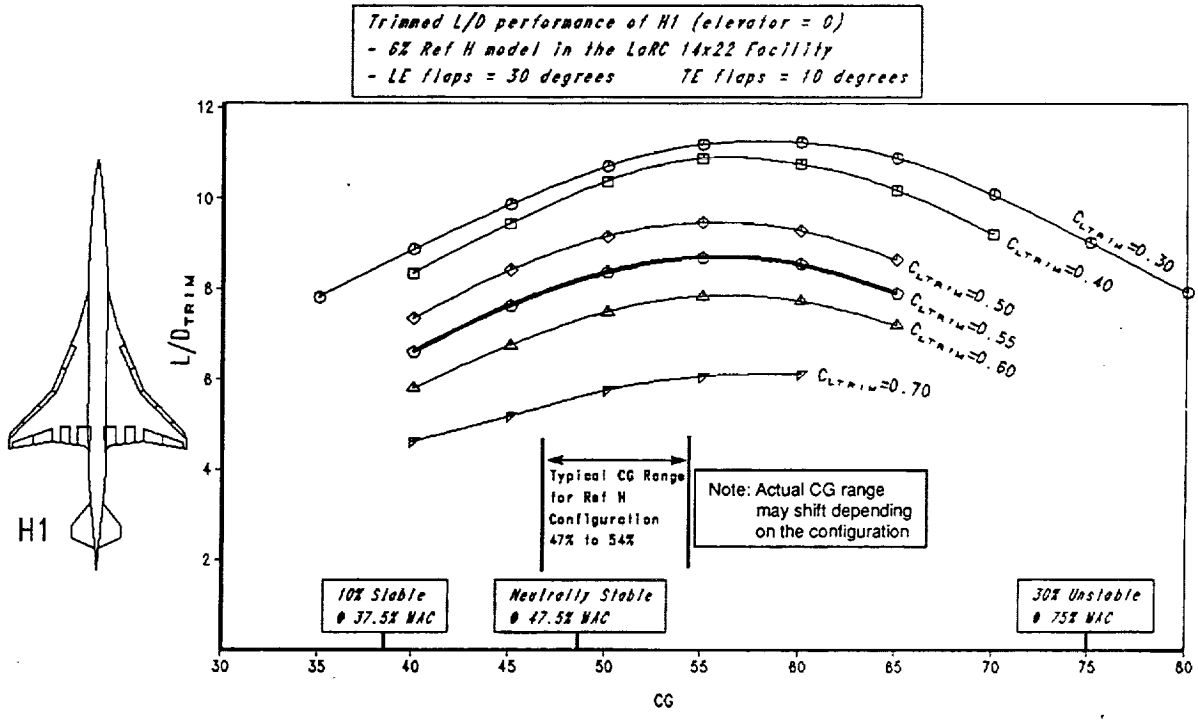

This figure shows trimmed L/D versus CG location for the baseline horizontal tail, H1. Each curve is for constant CLTRIM. For climbout noise abatement the CLTRIM of interest is 0.55.

- Also shown on this plot is the typical CG range for a Ref H type of configuration, CG 45% to 55%.
- Notice the trimmed L/D for the horizontal tail has a higher value at aft CG's. This is because at aft CG's the pitching moment characteristics tend to require tail upload to trim which helps the overall airplane L/D.

CN1.2 - Baseline Canard Mounted Low on Extended Forebody Trimmed L/D versus CG Location

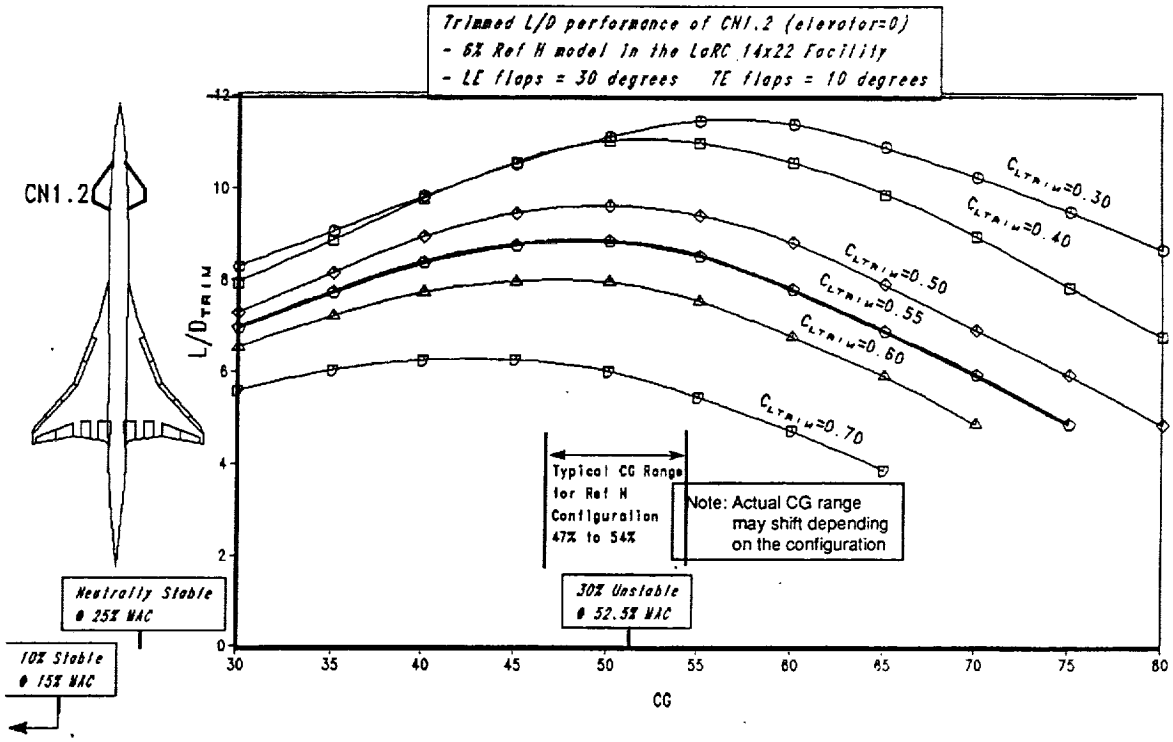

This figure shows trimmed L/D versus CG location for the baseline canard CN1 mounted low on the 2 foot extended forebody.

- Each curve is for constant CLTRIM. For climbout noise abatement the CLTRIM of interest is 0.55. Also shown on this plot is the typical CG range for a Ref H type of configuration, CG 45% to 55%.
- The trimmed L/D characteristics of canard CN1.2 are similar to that of the same canard on the short forebody. CN1.2 is less sensitive to CG position than CN1.
- Keep in mind that once the canard surface has been added, the CG may have to be shifted to yield the same amount of stability; ie the airplane may have to be reconfigured.

CN1.5 - Baseline Canard Mounted High on Extended Forebody Trimmed L/D versus CG Location

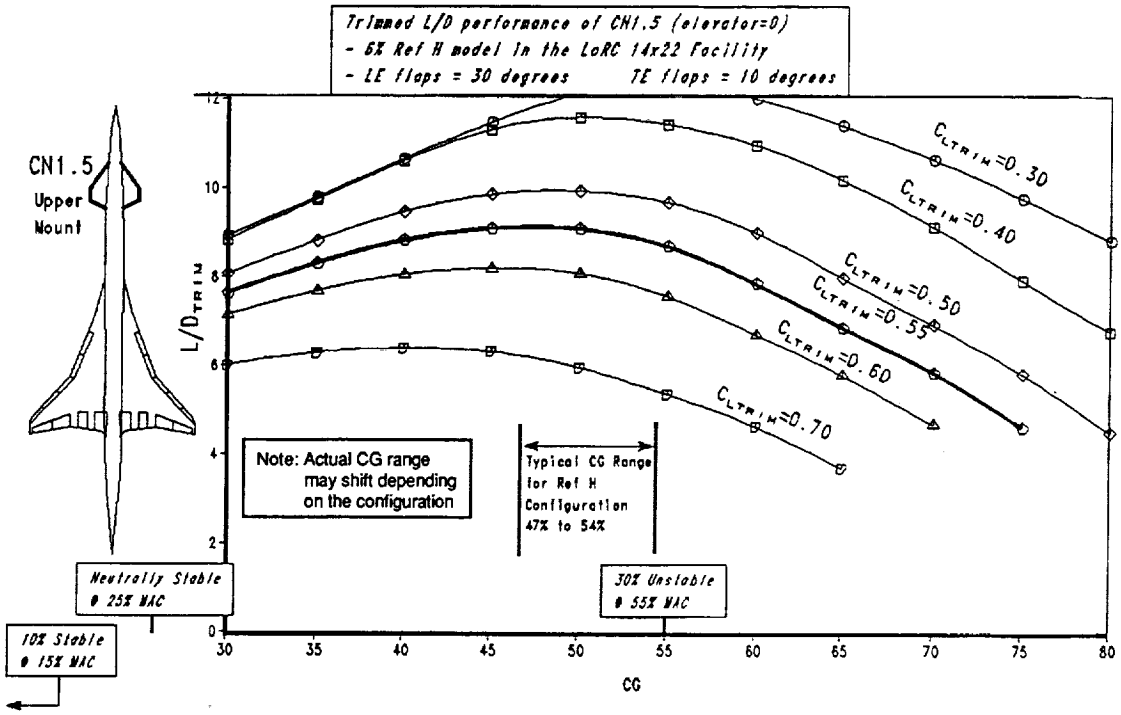

This figure shows trimmed L/D versus CG location for the baseline canard CN1.5 mounted high on the 2 foot extended forebody.

- Each curve is for constant CLTRIM. For climbout noise abatement the CLTRIM of interest is 0.55. Also shown on this plot is the typical CG range for a Ref H type of configuration, CG 45% to 55%.
- The trimmed L/D characteristics of canard CN1.5 are similar to the low mounted canard CN1.2, except that trimmed L/D is improved and sensitivity to CG position is less. This could be due to the high mount reducing the interference wake with the wing.
- CN1.5 has noticeable trimmed L/D improvement over CN1.2 at the more forward CG's.
- Keep in mind that when a canard surface is, the CG may have to be shifted to yield the same amount of stability; ie the airplane may have to be reconfigured.

CN3.2 - High Aspect Ratio Canard Mounted Low on Extended Forebody Trimmed L/D versus CG Location

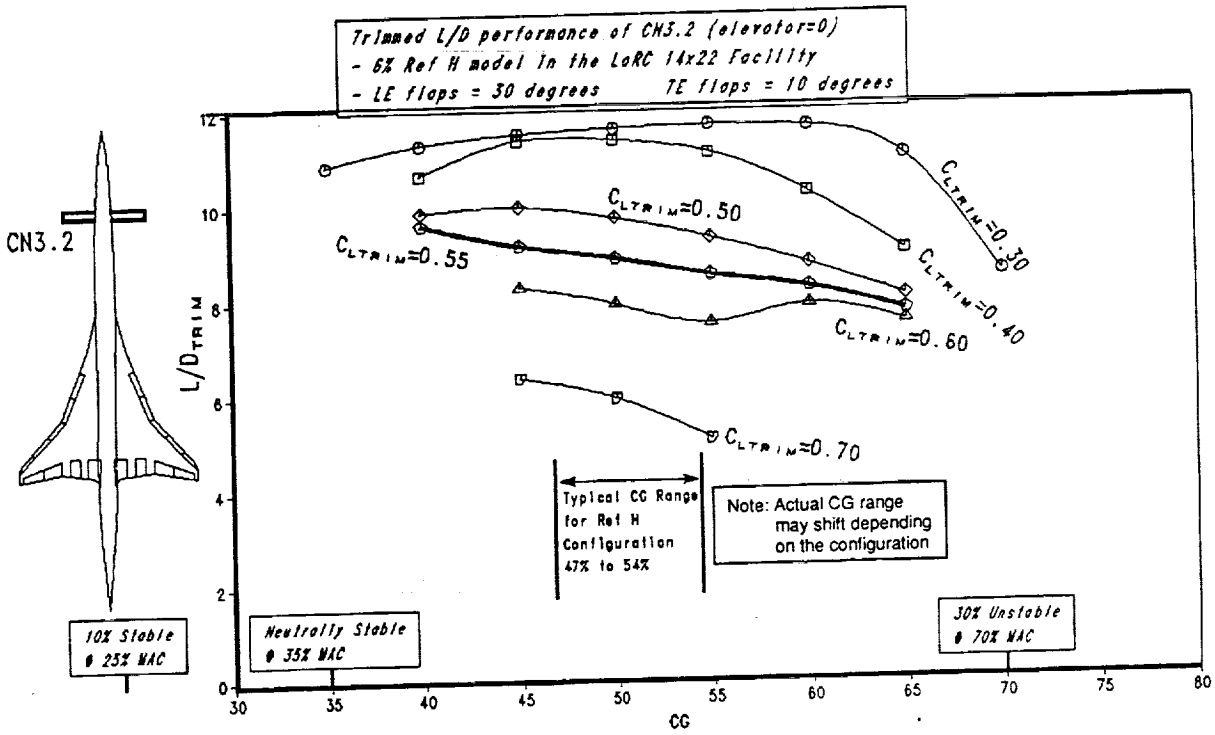

This figure shows trimmed L/D versus CG location for the high aspect ratio canard CN3 mounted low on the 2 foot extended forebody.

- Each curve is for constant CLTRIM. For climbout noise abatement the CLTRIM of interest is 0.55. Also shown on this plot is the typical CG range for a Ref H type of configuration, CG 45% to 55%.
- The most noticeable feature of this canard is that it exhibits the best trimmed L/D performance with a CG sensitivity that is much more flat over the range tested than the low aspect ratio canards. This is due to the high lift curve slope of this canard. The CLTRIM condition of 0.55 shows no signs of drop-off with forward CG shift, however the canard may be on the verge of stalling abruptly.
- Keep in mind that once the canard surface has been added, the CG may have to be shifted to yield the same amount of stability; ie the airplane may have to be reconfigured.

3 Surface - Trimmed L/D versus CG Location

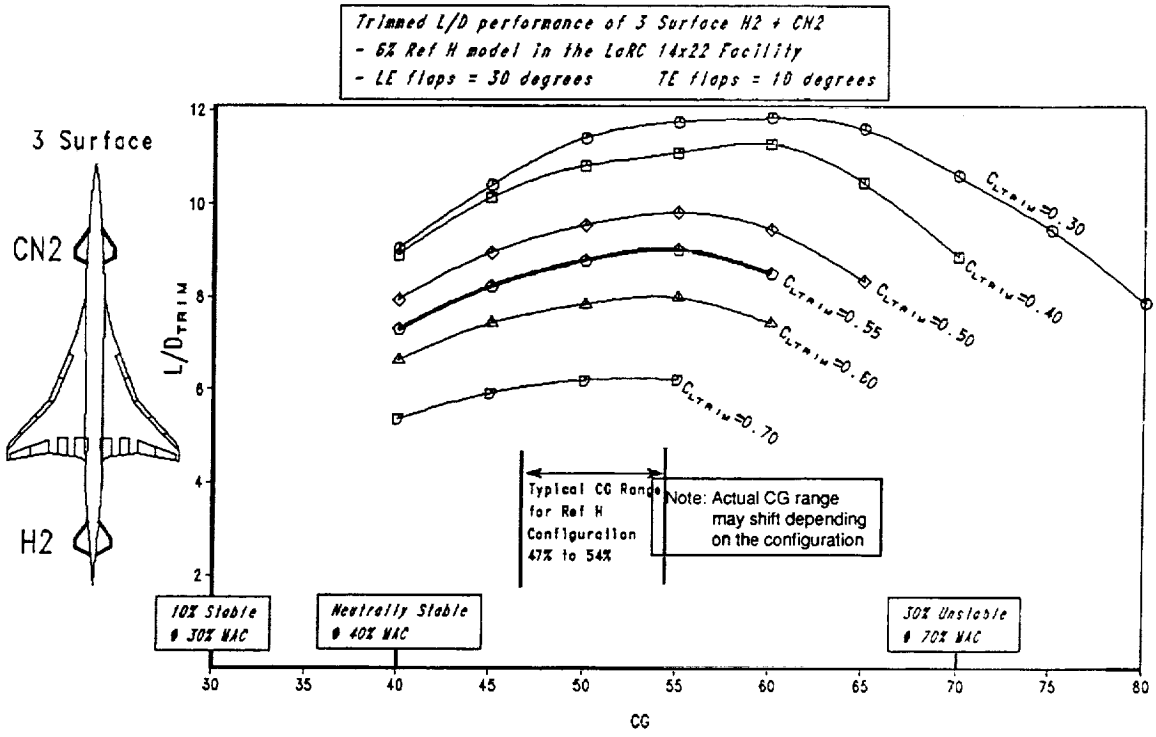

This figure shows trimmed L/D versus CG location for the three surface configuration. The three surface configuration used the baseline forebody.

- Each curve is for constant CLTRIM. For climbout noise abatement the CLTRIM of interest is 0.55. Also shown on this plot is the typical CG range for a Ref H type of configuration, CG 45% to 55%.
- The three surface configuration gives good trimmed L/D performance with little CG sensitivity. Generally the three surface is better than the aft tail and better than most canard configurations at aft CG's.
- Keep in mind that once the canard surface has been added, the CG may have to be shifted to yield the same amount of stability; ie the airplane may have to be reconfigured.

Trimmed L/D Comparison - Tailless, Baseline Tail and Canard

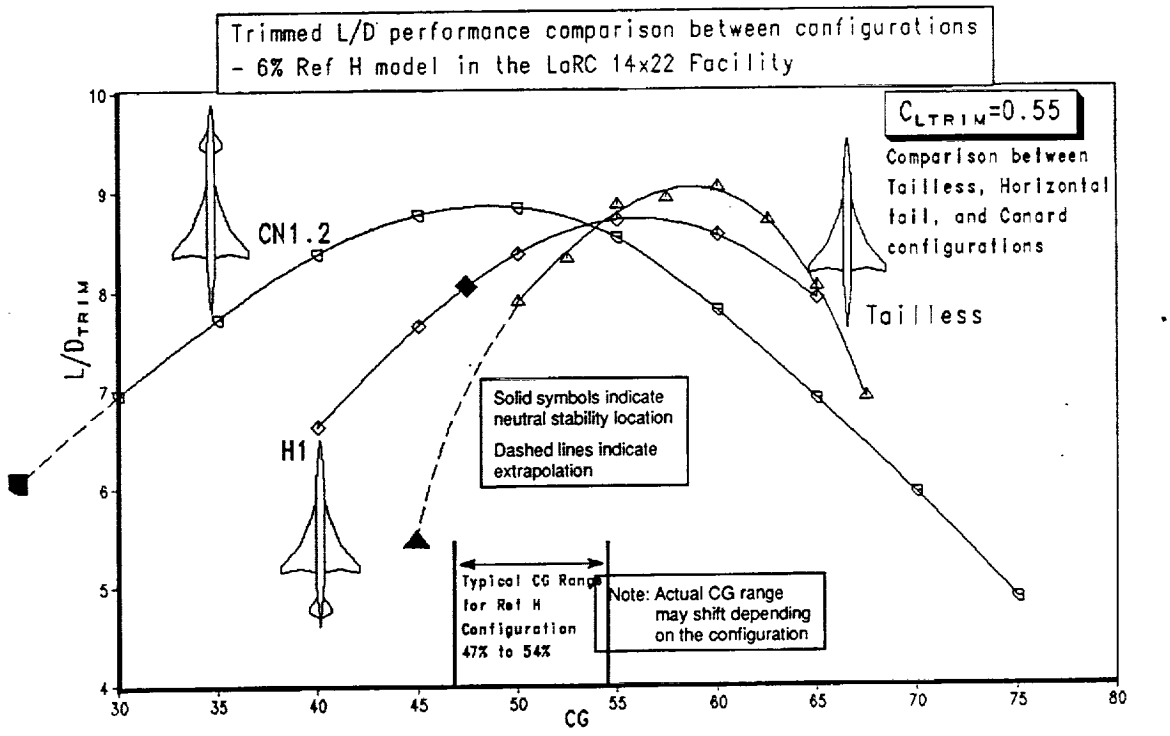

This figure shows a summary of the trimmed L/D characteristics of the tailless, H1, and CN1.2 configuration at CLTRIM=0.55.

- The tailless configuration in the CG range of interest is the worse. The canard is the best except at the far aft CG's.
- The SOLID symbols indicate the location of the neutral stability location. The dashed lines indicate an extrapolation of the data and should be taken with a grain (or two) of salt.

Trimmed L/D Comparison - Canards

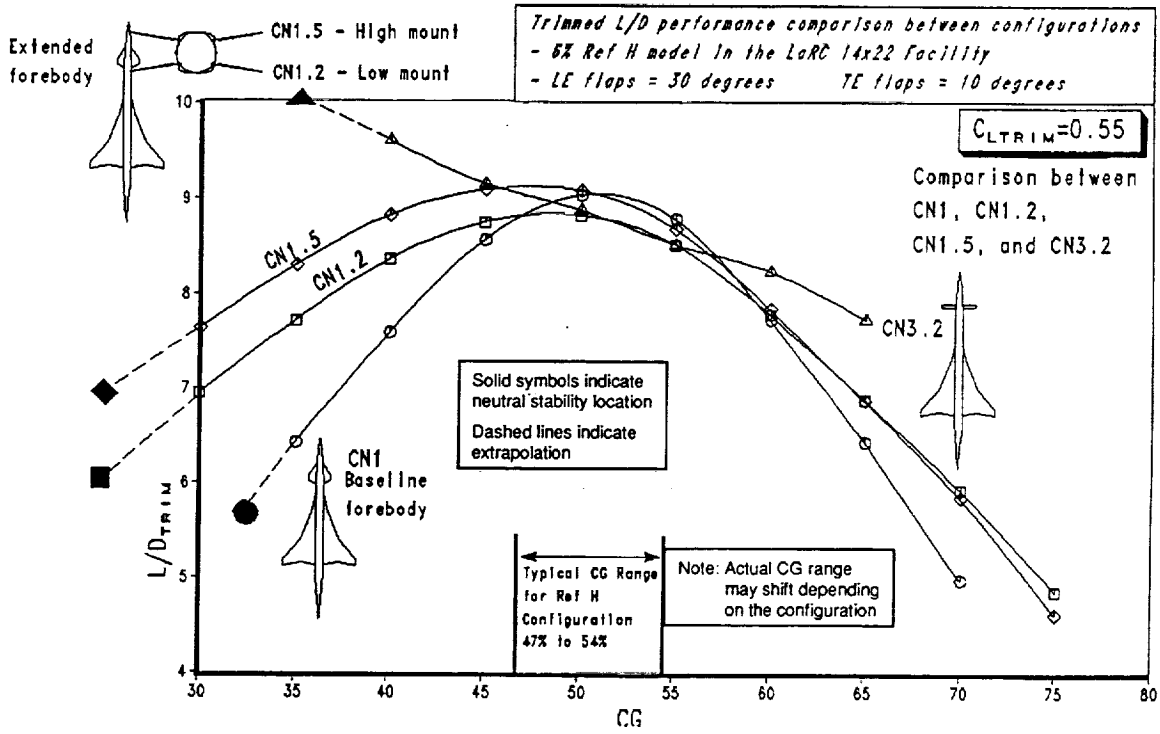

This figure shows the trimmed L/D characteristics at CLTRIM=0.55 of location of the baseline canard in different positions on the forebody. The high aspect ratio canard, CN3.2, has also been plotted for comparison.

- The longer forebody flattens out the CG sensitivity of the canard and the higher mount improves L/D at forward CG's for the baseline canard. Based on this, a high mount position on the baseline forebody of thebaseline canard could be an even better performer.
- The high aspect ratio canard does not provide the same L/D values in thetypical Ref H CG range as the CN1 or CN1.5 configuration, but performs better with the CG shifted forward. In addition the slope indicates this behavior to increase for more stable configurations, although it is suspected that the airfoil would stall abruptly
- The SOLID symbols indicate the location of the neutral stability location. The dashed lines indicate an extrapolation of the data and should be taken with a grain (or two) of salt.

Trimmed L/D Comparison - Baseline Tail, Canard, and 3 Surface

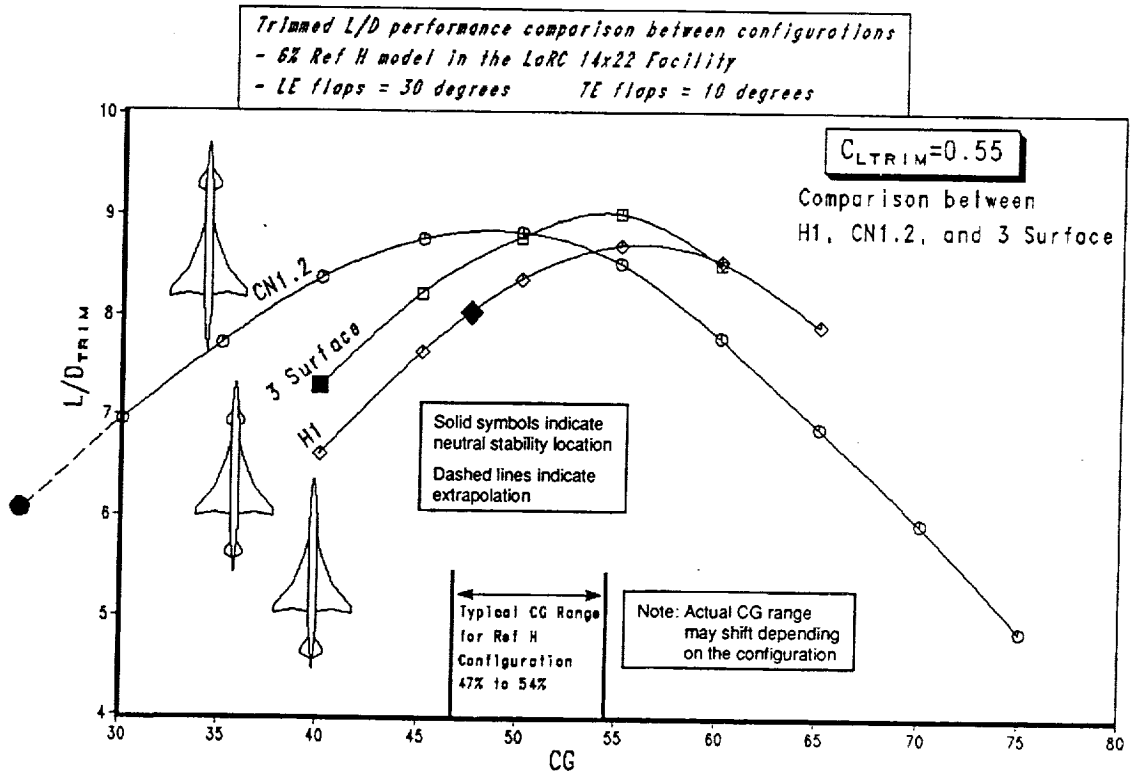

This figure compares trimmed L/D at CL=0.55 for the baseline tail H1, the baseline canard CN1.2, and the three surface configuration.

- The canard is the best performer at forward CG's and the 3 surface at aft CG's.
- The SOLID symbols indicate the location of the neutral stability location. The dashed lines indicate an extrapolation of the data and should be taken with a grain (or two) of salt.

Trimmed L/D Comparison at Common Stability Levels

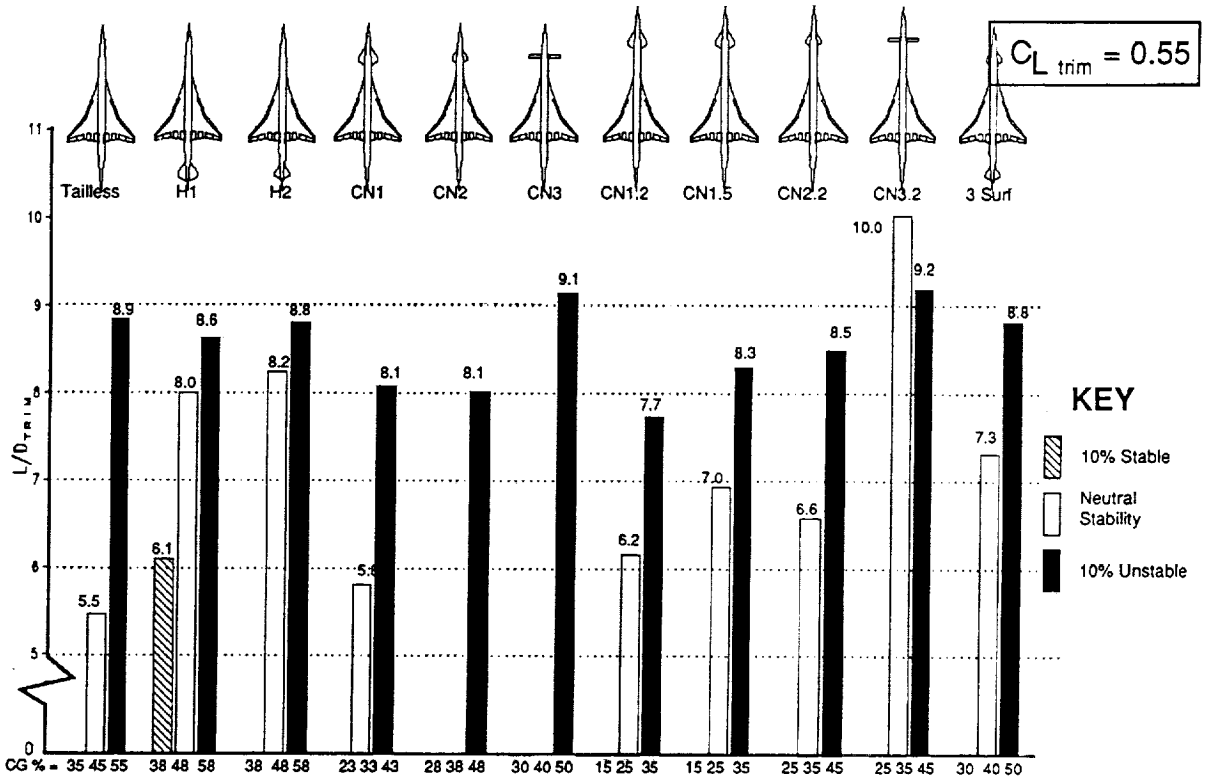

This figure illustrates a trimmed L/D comparison of all the trim devices at a common stability level.

- Data is shown for stability levels of 10% stable, neutral stability and 10% unstable. Note that there is no data for some of the configurations, particularly at more stable CG's
- On a common stability level the baseline tail H1 outperforms most of the canards. The three surface configuration does present a slight advantage for the 10% unstable case, but still not as much as the tailless configuration.
- The most significant results are from the high aspect ratio canard. Two important aspects stand out:

  First the configuration performs better than any other for the same stability levels.

  Secondly, the configuration shows a drop in the performance for the 10% unstable case. This is in contrast to the other planforms which continue to show performance gains for decreases in stability. The implication is that this configuration has the potential to have even greater performance capabilities if the CG is shifted forward for a more stable condition provided the canard does not stall. Of course a high lift device on the canard would help alleviate this potential problem....which leads to a possible conclusion arrived at many years ago.....Kudos to the Russians!

Alternate Trim Conclusions

Determine allowable or required stability levels for HSCT configurations. If we are constrained to a stable airplane then our trim and control options are limited to the tail, but if the configuration can be flown unstable then we have more options that can increase the overall configuration trimmed L/D.

The data indicates potential benefits can be achieved by further testing to:

- Optimize canard position with respect to the wing. This includes testing the three surface configuration with the high aspect ratio canard in the high positions. The high position canard may improve trimmed L/D by up to 0.2 over the low position.
- Further optimize the 3 surface configuration by testing more combinations of tail and canard deflections and elevators.
- Optimize the entire configuration for trimmed L/D by testing additional trailing edge flap settings and by span load optimization of the individual trailing edge flaps.

Final Remarks

- The most powerful way to increase low speed L/D is by changing the planform. Aspect ratio alone may not do the trick, leading edge sweep angle is also important.
- Choice of trim configuration can be as powerful as a planform change, but some stability risks may be required to obtain them. The small retractable high aspect ratio canard mounted high on the forebody looks to be the choice trim configuration from a low speed performance perspective.
- Our current high lift system is pretty good. We have demonstrated leading edge suction factors in the 85-90% range with the Ref H model. L/D increases greater than 0.5 units due to more efficient leading edge flaps may be difficult to obtain.
- The trimmed L/D difference between forward and aft CG's is ~0.5 units.

ASSESSMENT OF CFD CODES FOR HSCT REF. H HIGH LIFT AERODYNAMICS

Anthony J. Saladino and Ross D. Sheckler
Dynacs Engineering Co., Inc.
Renton, WA 98055

One of the high lift aerodynamics tasks for 1995 was to assess the applicability of using various CFD codes in predicting wind tunnel data for the Ref. H configuration at high speed and low speed conditions. Both the Euler and the Navier-Stokes methodologies have been utilized and the lift, drag, moment and pressure coefficients have been compared with the NASA Langley 14x22 wind tunnel data, test 404, run 195. The conditions that were tested correspond to a 6% Ref. H wing/body at a Reynolds number of 8.8 million, with flap settings of LE 30°/outboard TE 20°, Mach number of 0.24 and angle-of-attack of 10°.

Five CFD codes were chosen for this study: the structured grid codes are CFL3D, TNSMB, INS3D, and OVERFLOW; the unstructured grid code is USM3D. Separate Euler and viscous grids were used in the structured code runs. Two unstructured grids with different hinge line radius, leading and trailing edge detail were developed for the inviscid USM3D code.

The wind tunnel data base includes pressure coefficients at seven spanwise cuts and five chordwise cuts, the aerodynamic coefficients C_L, C_D and C_M, and mini-tuft data. Comparisons between CFD and wind tunnel data will be shown for one spanwise cut (X=2389.75 inches) and two chordwise cuts (Y=286.50 and 481.75 inches), along with comparisons between mini-tuft data and CFD velocity vectors.

CFD RUN MATRIX

Code	Euler	Navier-Stokes
CFL3D	X	X (S-A)*
INS3D	X	
OVERFLOW	X	X (B-B)
TNSMB	X	X (S-A)
USM3D	X	

* S-A Spalart-Allmaras 1-eqn turb. model
B-B Baldwin-Barth 1-eqn turb. model

Dynacs Engineering Co., Inc.

The CFD run matrix lists all of the codes used in the computational analysis. A multi-grid convergence strategy was used in the solution to CFL3D and TNSMB; the multi-grid strategy is not available for either INS3D or OVERFLOW, so these were run with the single grid option. In addition, different turbulence models were used for the viscous solutions: the Spalart-Allmaras model was used for CFL3D and TNSMB; the Baldwin-Barth turbulence model was used for the OVERFLOW solutions since the Baldwin-Barth model was not available. In each case, the residual was converged to at least 2.5 orders, and the lift coefficient and the drag coefficient were converged to the fourth decimal place and one count, respectively. Note that a viscous INS3D solution could not be obtained. The solution encountered convergence problems at the wing tip region where the grid is collapsed to the wake; INS3D cannot increase the smoothing in this region.

Viscous O-H Grid

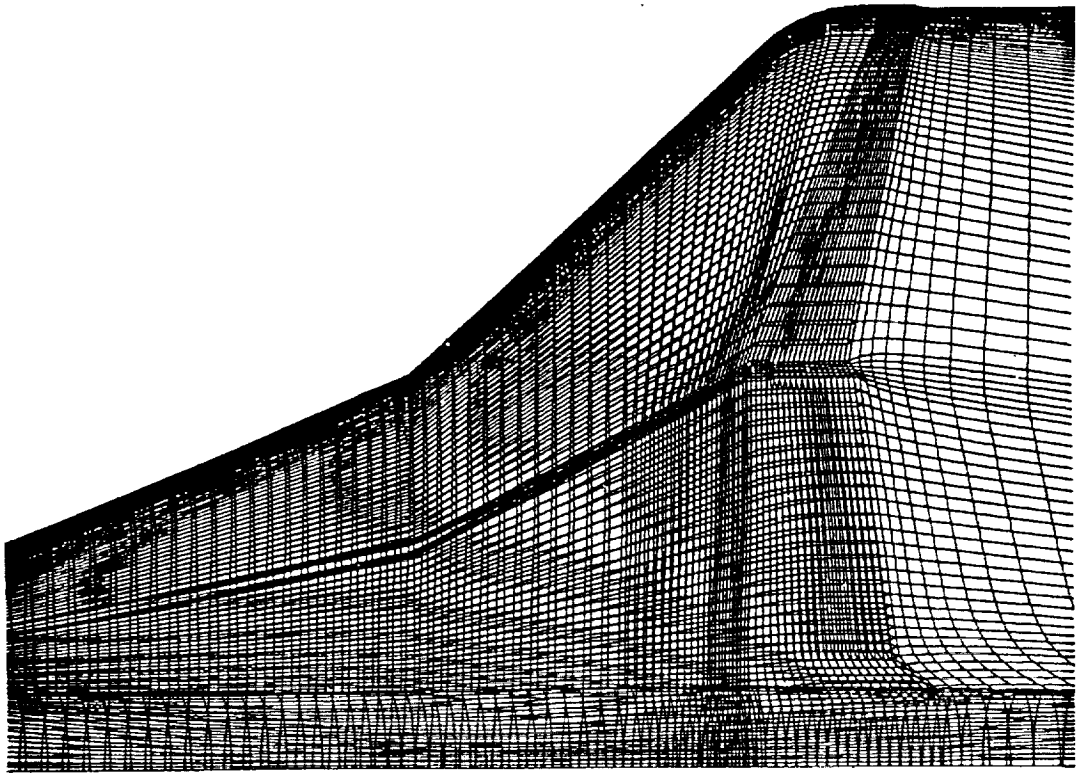

Dynacs Engineering Co., Inc.

Two different structured grids were used to obtain CFD results. The inviscid grid has dimensions 145x37x273 (not shown) and the viscous grid has dimensions 161x65x225. Both grids have an O-H topology and are single-block, and a wake region extends from the trailing edge to the outflow boundary. The wall spacing for the viscous grid is such that the value of y^+ is approximately 0.28. Two flow-through web regions separate the deflected and undeflected trailing edge flaps (16-inch inboard web, 13-inch outboard web).

Unstructured Grid (Case 1)

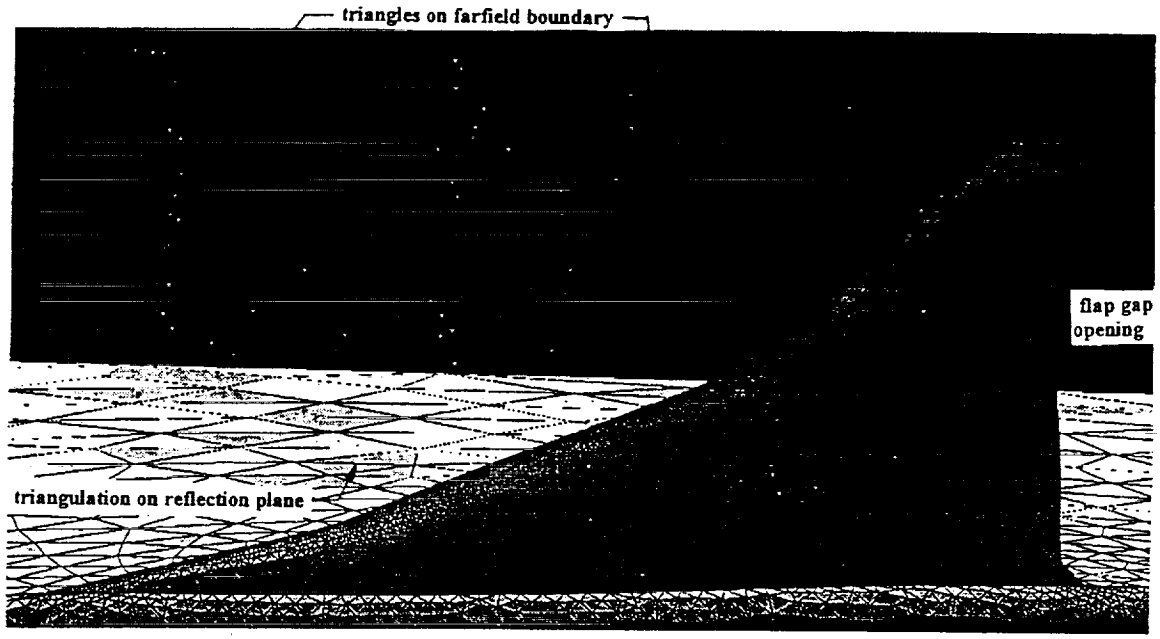

Dynacs Engineering Co., Inc.

Two unstructured grids were developed using Gridtool for the surface grid and Vgrid for the volume grid. In case 1, a total of 707,557 tetrahedra extend from the surface to the outflow boundary. The leading and trailing edge cell sizes are 3 inches and 12 inches, respectively. Case 1 models the surface with the two web regions added at the trailing edge.

Unstructured Grid (Case 2)

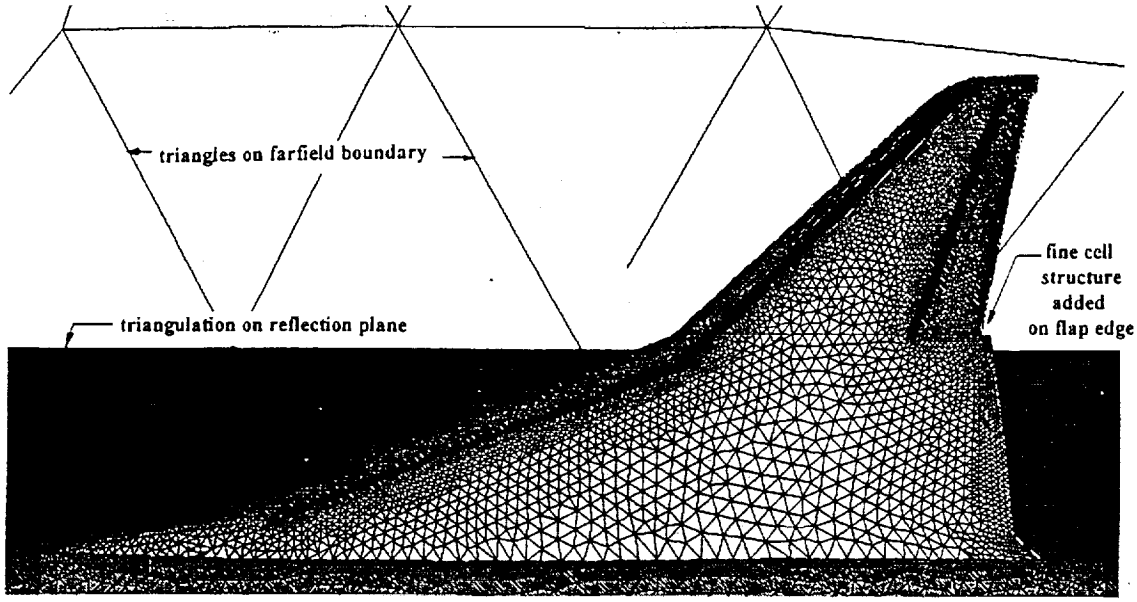

Dynacs Engineering Co., Inc.

Two unstructured grids were developed using Gridtool for the surface grid and Vgrid for the volume grid. For case 2, finer cell sizes were imposed on the hinge lines, the leading and trailing edges. The cell size at the trailing edge varies from 5 inches at the wing root to 1 inch at the wing tip, which is equivalent to 0.3% of the total chord at the root and 0.8% at the tip. The actual wind tunnel surface geometry was modeled in this case, where there is no web at the flap juncture. A fine cell size of 0.5 inch was added at the sides of the flap edges.

Inviscid Pressure Coefficient Comparisons at Y=286.50 inches Ref. H, W/B, Flaps LE 30/Outboard TE 20, Mach=0.24, Alpha=10° NASA Langley 14X22 Test 404, Run 195

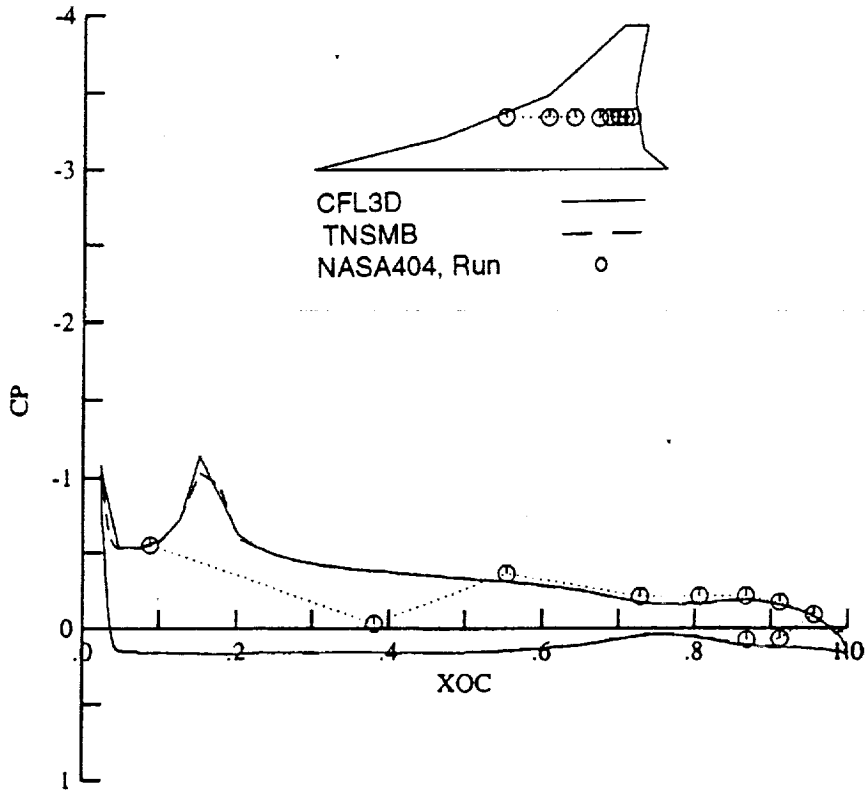

Dynacs Engineering Co., Inc.

Chordwise inviscid pressure coefficient comparisons are shown at Y=286.50 inches between CFL3D, TNSMB and data. No wind tunnel data was taken on the hinge line as this location was filled in by klax. There is a bad data point at X/C of approximately 0.38. The Kutta condition is satisfied at the trailing edge. The CFD results lie on top of each other except at the leading edge and hinge line. The suction pressure at the leading edge is almost equal to that at the hinge line.

Inviscid Pressure Coefficient Comparisons at Y=286.50 inches Ref. H, W/B, Flaps LE 30/Outboard TE 20, Mach=0.24, Alpha=10° NASA Langley 14X22 Test 404, Run 195

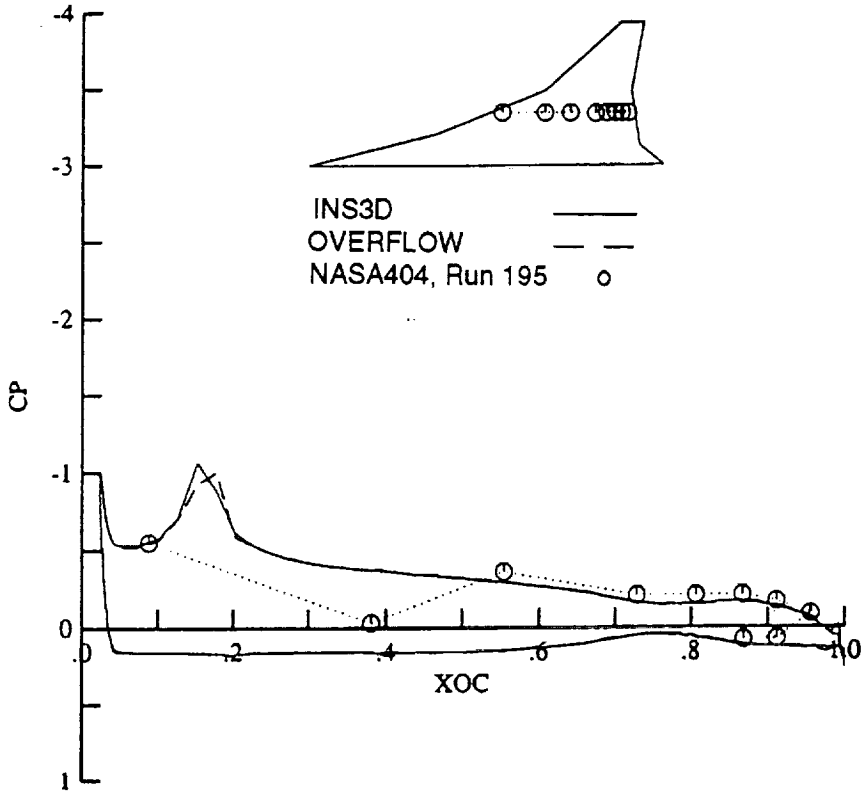

Dynacs Engineering Co., Inc.

Chordwise inviscid pressure coefficient comparisons are shown at Y=286.50 inches between INS3D, OVERFLOW and data. No wind tunnel data was taken on the hinge line as this location was filled in by klax. There is a bad data point at X/C of approximately 0.38. The Kutta condition is satisfied at the trailing edge. The CFD results lie on top of each other except at the hinge line, where the peak suction location predicted by OVERFLOW is further aft of that predicted by INS3D. The suction pressure at the leading edge is almost equal to that at the hinge line.

Inviscid Pressure Coefficient Comparisons at Y=481.75 inches Ref. H, W/B, Flaps LE 30/Outboard TE 20, Mach=0.24, Alpha=10° NASA Langley 14X22 Test 404, Run 195

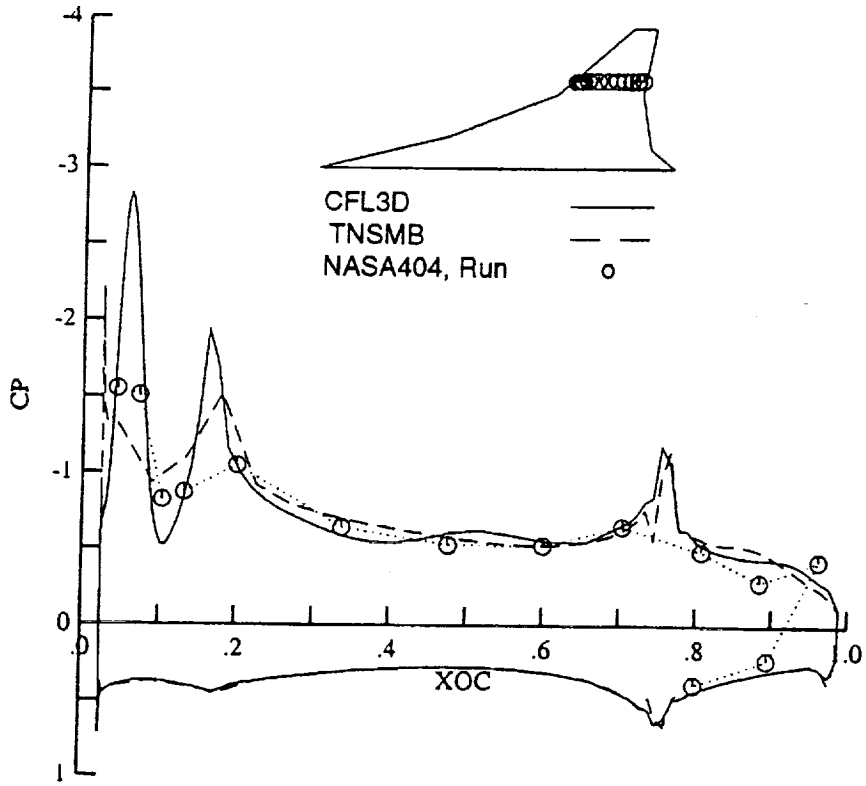

Dynacs Engineering Co., Inc.

Chordwise pressure coefficient cuts are compared with data at Y=481.75 inches for the inviscid CFL3D and TNSMB solutions. No wind tunnel data was taken on the hinge line as this location was filled in by klax. The Kutta condition is satisfied at the trailing edge. Postprocessing of the CFD results has resulted in some zigzags, due to interpolation in the longitudinal direction of the O-H grid. Suction peaks compare better among the codes at the trailing edge hinge than at the leading edge hinge line. A pressure increase on the lower surface occurs as a result of the deflected trailing edge flap. The data agrees reasonably well with the CFD results in the region between the leading and trailing edge hinge lines.

Inviscid Pressure Coefficient Comparisons at Y=481.75 inches Ref. H, W/B, Flaps LE 30/Outboard TE 20, Mach=0.24, Alpha=10° NASA Langley 14X22 Test 404, Run 195

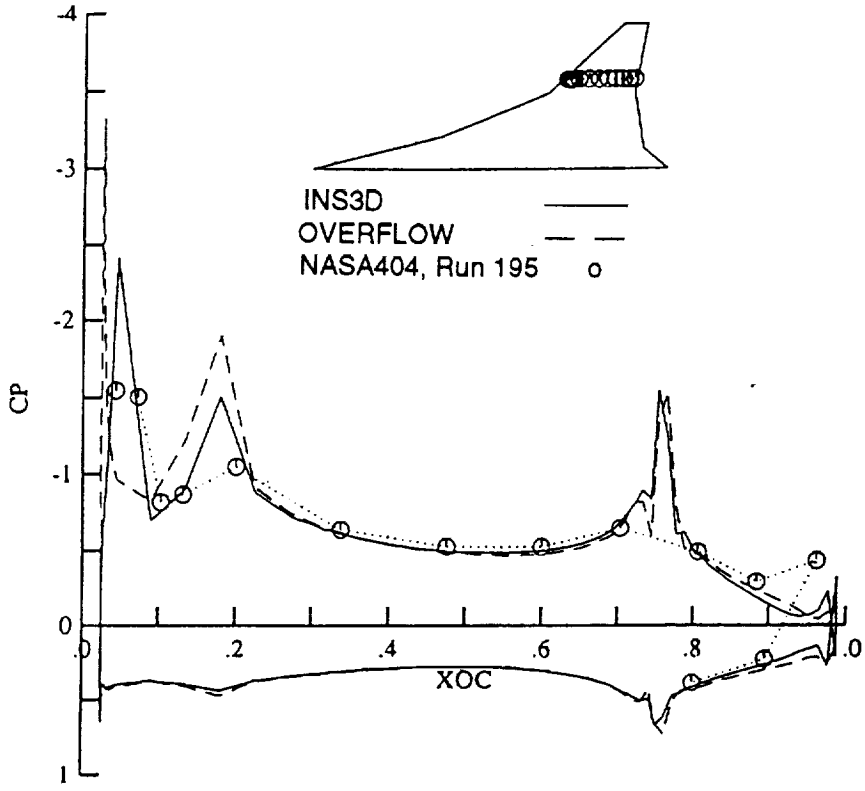

Dynacs Engineering Co., Inc.

Chordwise pressure coefficient cuts are compared with data at Y=481.75 inches for the inviscid INS3D and OVERFLOW solutions. No wind tunnel data was taken on the hinge line as this location was filled in by klax. The Kutta condition is satisfied at the trailing edge. Postprocessing of the CFD results has resulted in some zigzags, due to interpolation in the longitudinal direction of the O-H grid. Suction peaks compare better among the codes at the trailing edge hinge than at the leading edge hinge line. A pressure increase on the lower surface occurs as a result of the deflected trailing edge flap. The data agrees reasonably well with the CFD results in the region between the leading and trailing edge hinge lines.

Inviscid Pressure Coefficient Comparisons at X=2389.75 inches Ref. H, W/B, Flaps LE 30/Outboard TE 20, Mach=0.24, Alpha=10° NASA Langley 14X22 Test 404, Run 195

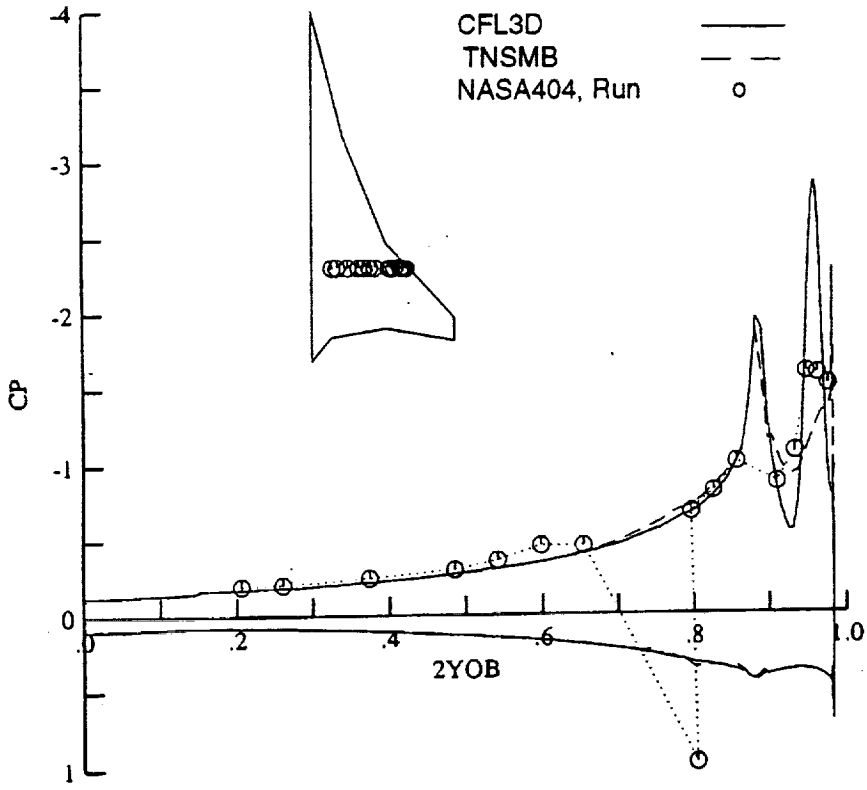

Dynacs Engineering Co., Inc.

Spanwise pressure coefficient cuts are compared with data at location X=2389.75 inches for CFL3D and TNSMB results. No wind tunnel data was taken on the hinge line as this location was filled in by klax. Comparison with data is good from the inboard to the outboard wing. However, each code predicts different suction peaks at the leading edge hinge lines as well as at the leading edge.

Inviscid Pressure Coefficient Comparisons at X=2389.75 inches Ref. H, W/B, Flaps LE 30/Outboard TE 20, Mach=0.24, Alpha=10° NASA Langley 14X22 Test 404, Run 195

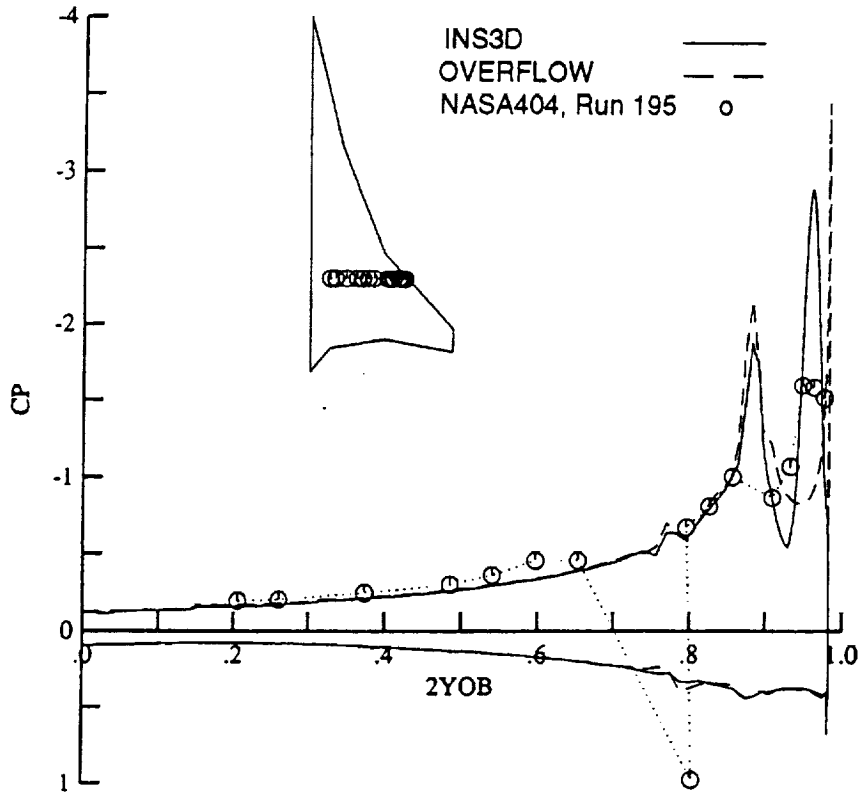

Dynacs Engineering Co., Inc.

Spanwise pressure coefficient cuts are compared with data at location X=2389.75 inches for INS3D and OVERFLOW results. No wind tunnel data was taken on the hinge line as this location was filled in by klax. Comparison with data is good from the inboard to the outboard wing. However, each code predicts different suction peaks at the leading edge hinge lines as well as at the leading edge.

Aerodynamic Coefficient Comparisons Between Inviscid CFD and Data Ref. H, W/B, Flaps LE 30/Outboard TE 20, Mach=0.24, Alpha=10° NASA Langley 14X22 Test 404, Run 195

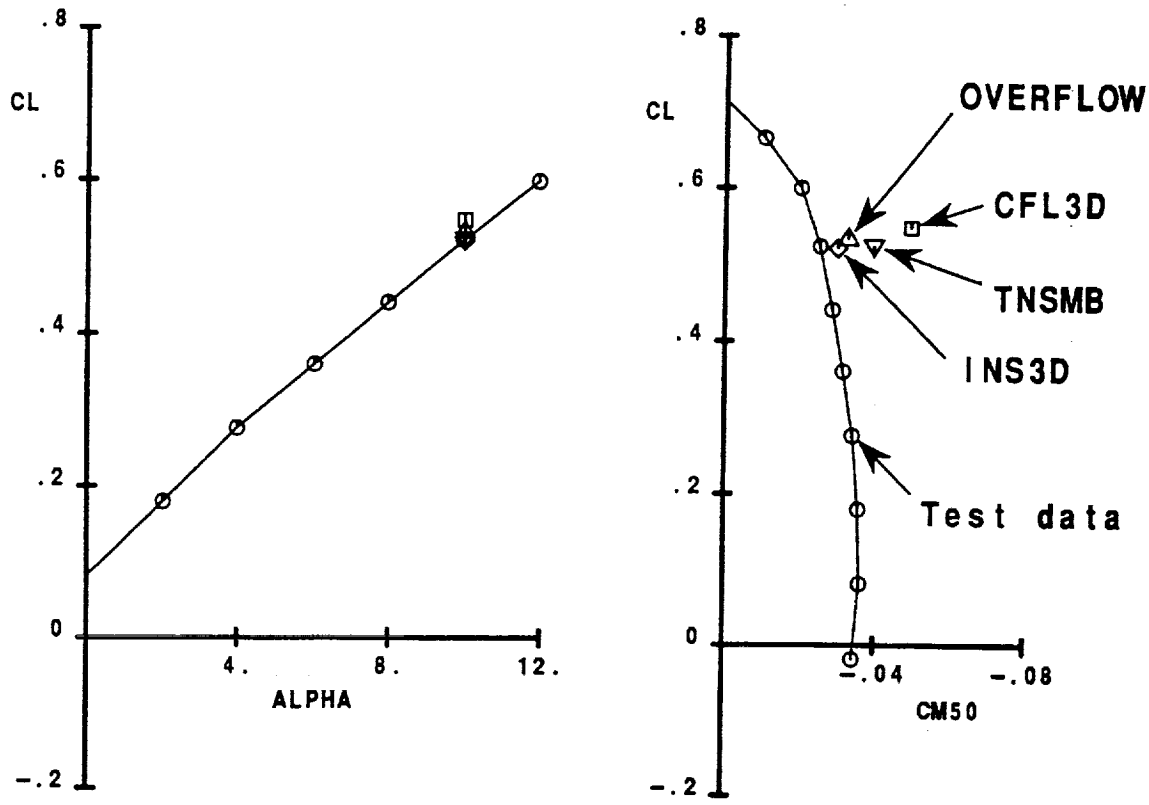

Dynacs Engineering Co., Inc.

Results for the lift and moment coefficients obtained from the structured Euler solutions are compared with the wind tunnel data. In general, the C_L vs. α comparison is good. CFD tends to overpredict the C_L data. There is a wider spread between the C_L vs C_M data and CFD. This is attributed to the inability of the inviscid codes to model the turbulent separation. It is also seen that the CFD values of C_M underpredict the data. The moment coefficient data compares the best with the incompressible INS3D code.

Aerodynamic Coefficient Comparisons Between Inviscid CFD and Data Ref. H, W/B, Flaps LE 30/Outboard TE 20, Mach=0.24, Alpha=10° NASA Langley 14X22 Test 404, Run 195

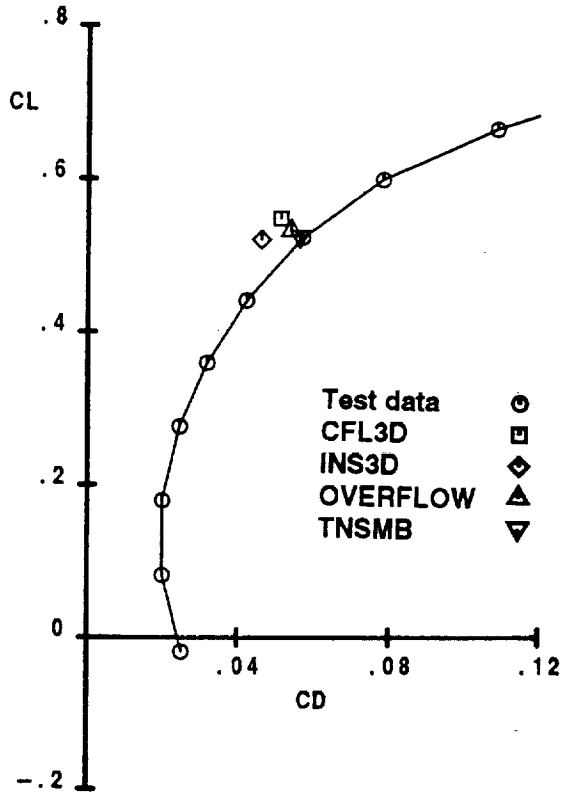

Dynacs Engineering Co., Inc.

Results for the drag coefficient obtained from the structured Euler solutions are compared with the wind tunnel data. The inviscid results are not expected to correlate with the drag data; however, TNSMB does provide close agreement with the C_D data. In all cases, the CFD values for C_D underpredict the data.

Inviscid Pressure Coefficient Comparisons at Y=286.50 inches Ref. H, W/B, Flaps LE 30/Outboard TE 20, Mach=0.24, Alpha=10° NASA Langley 14X22 Test 404, Run 195

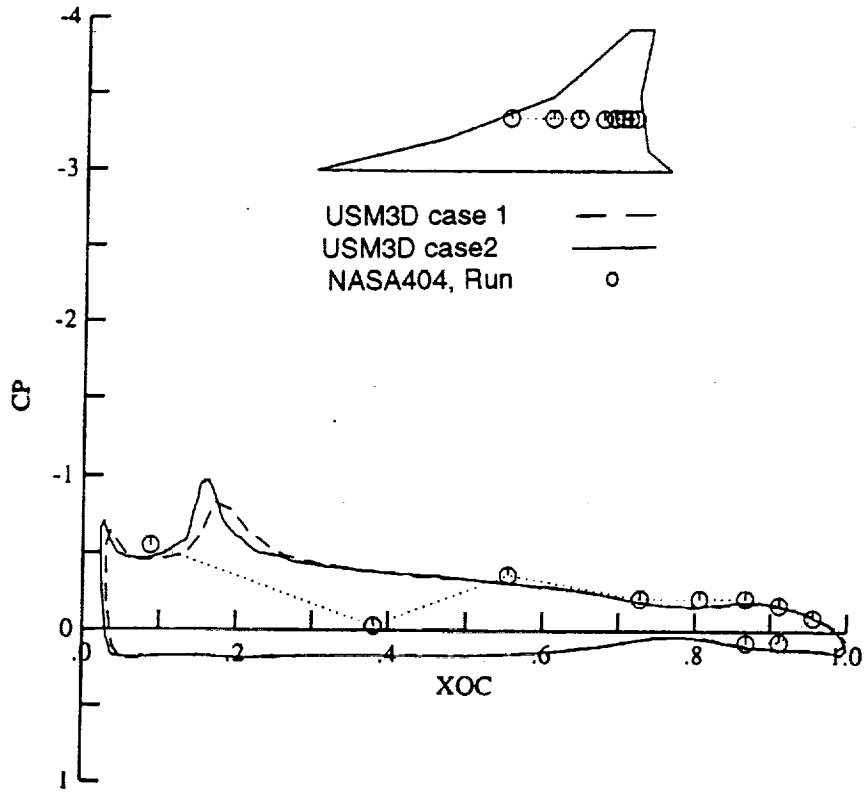

Dynacs Engineering Co., Inc.

Chordwise inviscid pressure coefficient comparisons are shown at Y=286.50 inches between both USM3D solutions and data. No wind tunnel data was taken on the hinge line as this location was filled in by klax. There is a bad data point at X/C of approximately 0.38. The Kutta condition is satisfied at the trailing edge. The CFD results lie on top of each other aft of the hinge line, but differ at the leading edge and hinge line. Refining the grid at these locations resulted in larger suction peaks that are shifted slightly upstream compared to the case 1 results. The suction pressure at the leading edge is almost equal to that at the hinge line.

Inviscid Pressure Coefficient Comparisons at Y=481.75 inches Ref. H, W/B, Flaps LE 30/Outboard TE 20, Mach=0.24, Alpha=10° NASA Langley 14X22 Test 404, Run 195

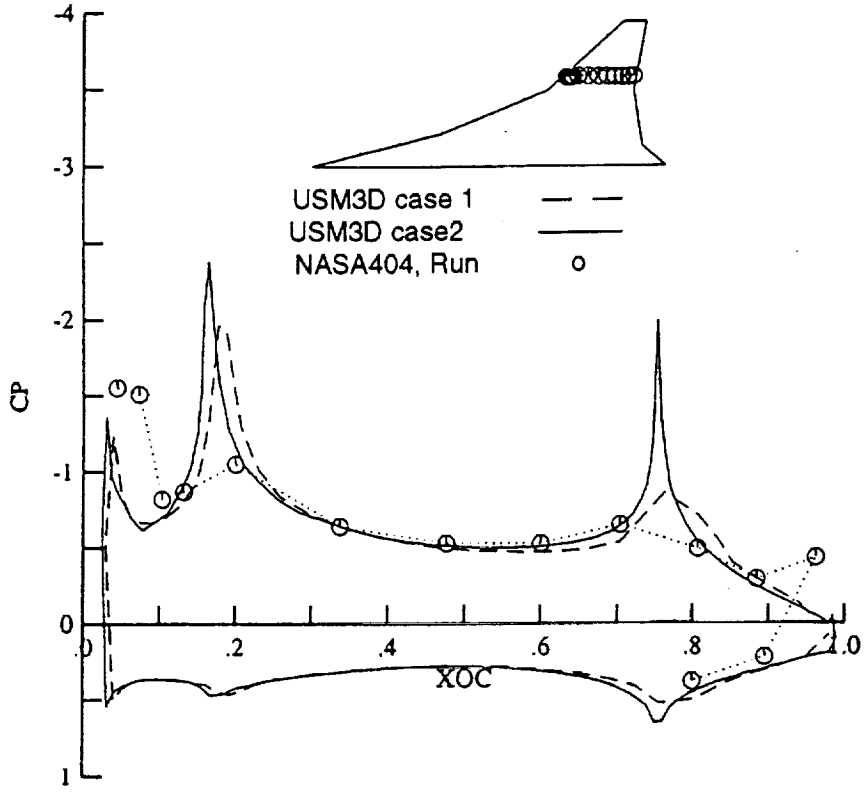

Dynacs Engineering Co., Inc.

The USM3D pressure coefficient cut at Y=481.75 inches compares reasonably well with data. No wind tunnel data was taken on the hinge line as this location was filled in by klax. The Kutta condition is satisfied at the trailing edge. The pressure difference between the upper and the lower surfaces are similar among the results except in the region of the hinge lines. The finer tetrahedral grid resulted in sharper and larger suction peaks, offset by a small spanwise location. There is also a slight mismatch on the lower surface between the two CFD cases. The trailing edge hinge suction peaks are much larger on the unstructured grid than shown previously on the structured grid.

Inviscid Pressure Coefficient Comparisons at X=2389.75 inches Ref. H, W/B, Flaps LE 30/Outboard TE 20, Mach=0.24, Alpha=10° NASA Langley 14X22 Test 404, Run 195

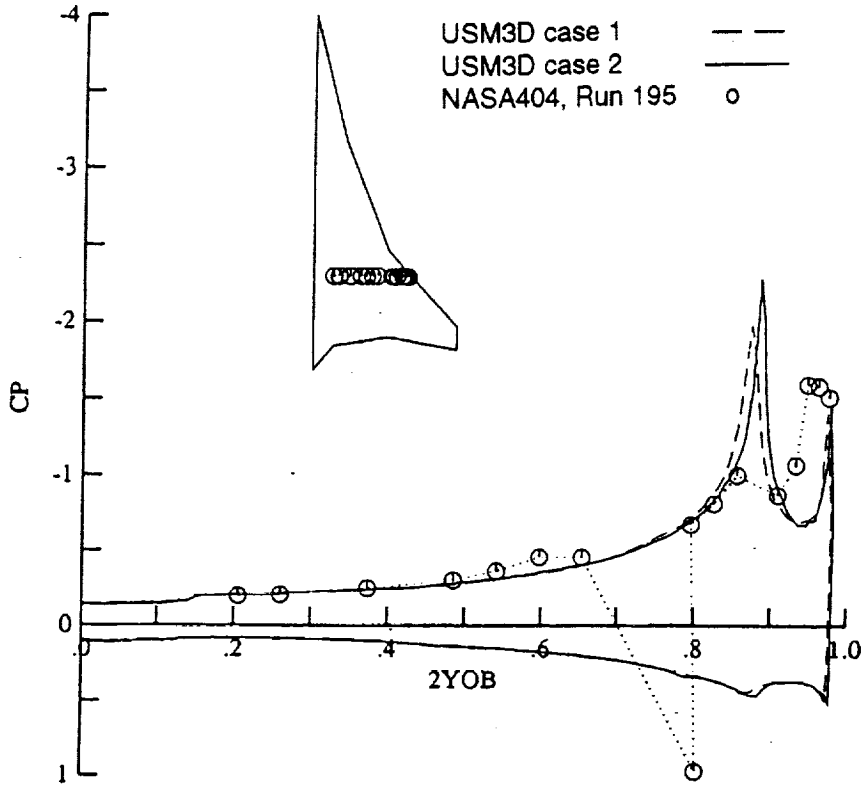

Dynacs Engineering Co., Inc.

The USM3D pressure coefficient cut at X=2389.75 inches compares reasonably well with data. No wind tunnel data was taken on the hinge line as this location was filled in by klax. The pressure difference between the upper and the lower surfaces are similar among the results except in the region of the hinge lines. Differences exist in the vicinity of the hinge lines; there is a large mismatch between CFD and data between the hinge line and leading edge. The finer tetrahedral grid resulted in sharper and larger suction peaks, and a slight difference in the spanwise location of these peaks.

Aerodynamic Coefficient Comparisons Between Inviscid CFD and Data Ref. H, W/B, Flaps LE 30/Outboard TE 20, Mach=0.24, Alpha=10° NASA Langley 14X22 Test 404, Run 195

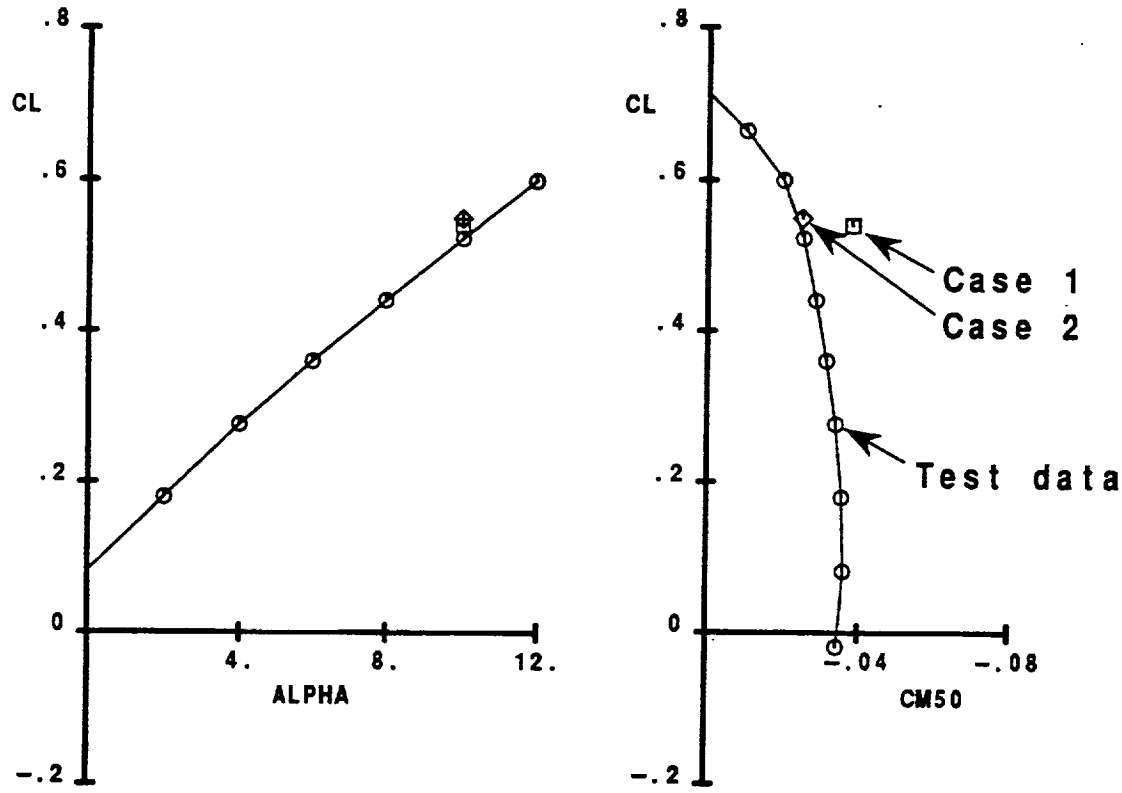

Dynacs Engineering Co., Inc.

Lift and moment coefficient test data are compared with results from two different Euler unstructured grids. The results indicate that lift for case 1 compared with the data better than for case 2, whereas the moment for case 2 came closer to the data than for case 1. This may be attributed to the finer grid resolution at the hinge lines and leading and trailing edges, as well as to the elimination of the web regions, in case 2.

Aerodynamic Coefficient Comparisons Between Inviscid CFD and Data Ref. H, W/B, Flaps LE 30/Outboard TE 20, Mach=0.24, Alpha=10° NASA Langley 14X22 Test 404, Run 195

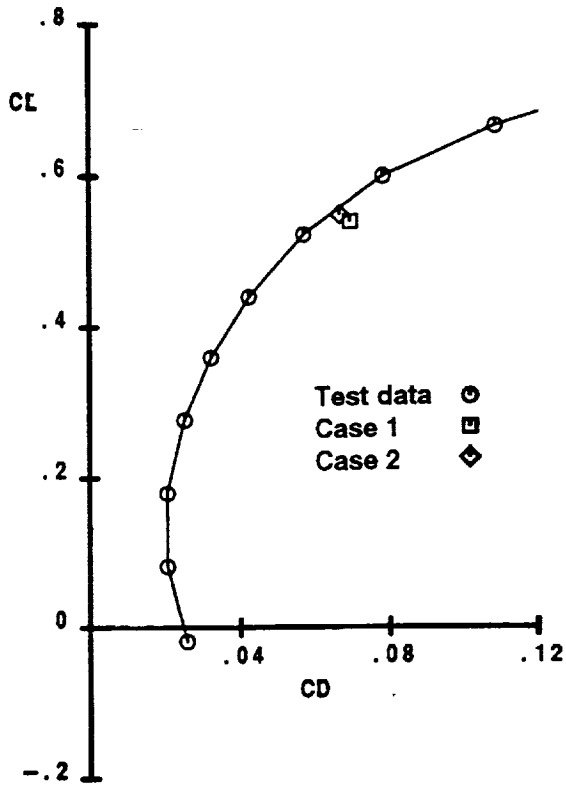

Dynacs Engineering Co., Inc.

Drag coefficient test data are compared with results from two different Euler unstructured grids. Although the lift was not predicted well with case 2 (see previous page for C_L- α curve), there was better drag prediction than for case 1. This may be attributed to the finer grid resolution at the hinge lines, leading and trailing edges, as well as to the elimination of the web regions, in case 2.

Viscous Pressure Coefficient Comparisons at Y=286.50 inches Ref. H, W/B, Flaps LE 30/Outboard TE 20, Mach=0.24, Alpha=10° NASA Langley 14X22 Test 404, Run 195

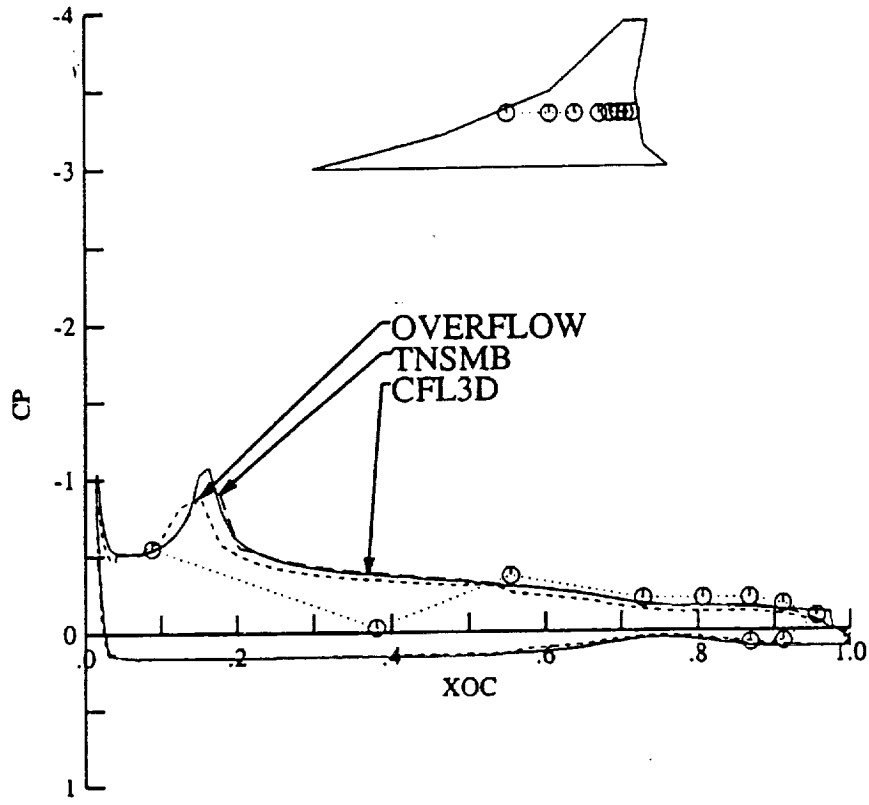

Dynacs Engineering Co., Inc.

A viscous pressure coefficient cut at Y=286.50 inches compares reasonably well with data. No wind tunnel data was taken on the hinge line as this location was filled in by klax. Good agreement exists in regions away from the hinge line. The pressure difference between the upper and the lower surfaces are similar among the results except in the region of the hinge lines.

Viscous Pressure Coefficient Comparisons at Y=481.75 inches Ref. H, W/B, Flaps LE 30/Outboard TE 20, Mach=0.24, Alpha=10° NASA Langley 14X22 Test 404, Run 195

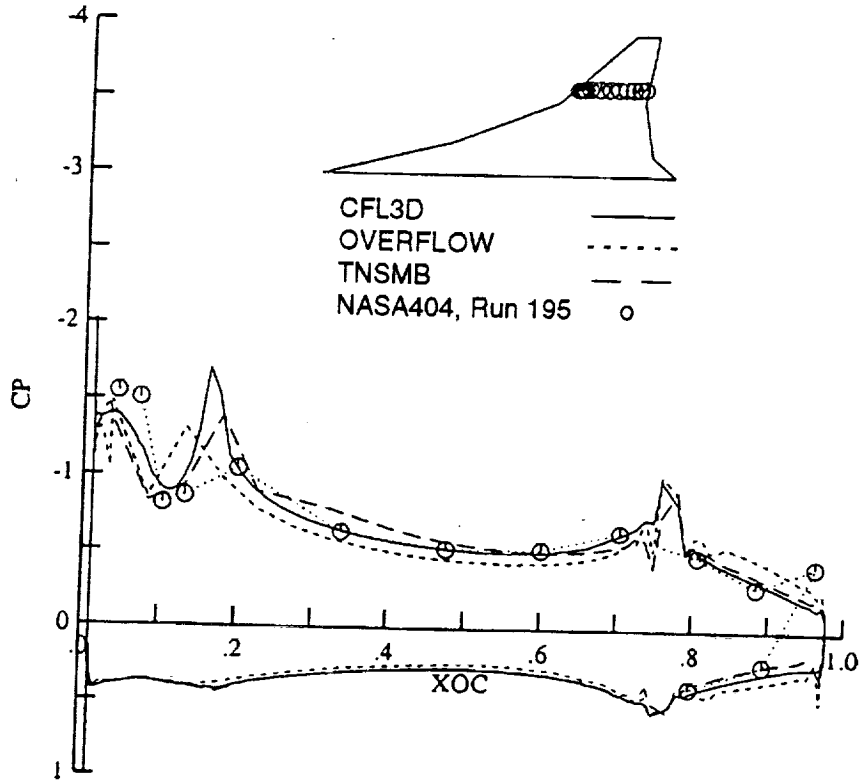

Dynacs Engineering Co., Inc.

A viscous pressure coefficient cut at Y=481.75 inches compares reasonably well with data. No wind tunnel data was taken on the hinge line as this location was filled in by klax. The leading edge pressures are dissimilar among the CFD results; the strong velocity gradients on the sharp outboard leading edge are affecting the results differently between the codes. There are noticeable variations in the values on the upper surface and with the location of the leading edge hinge line expansion. This is possibly related the different turbulence models used (Spalart-Allmaras for CFL3D and TNSMB, and Baldwin-Barth for OVERFLOW). Although TNSMB and CFL3D have the same turbulence models, there are obvious differences in the pressure in the boundary layer of the outboard wing.

Viscous Pressure Coefficient Comparisons at X=2389.75 inches Ref. H, W/B, Flaps LE 30/Outboard TE 20, Mach=0.24, Alpha=10° NASA Langley 14X22 Test 404, Run 195

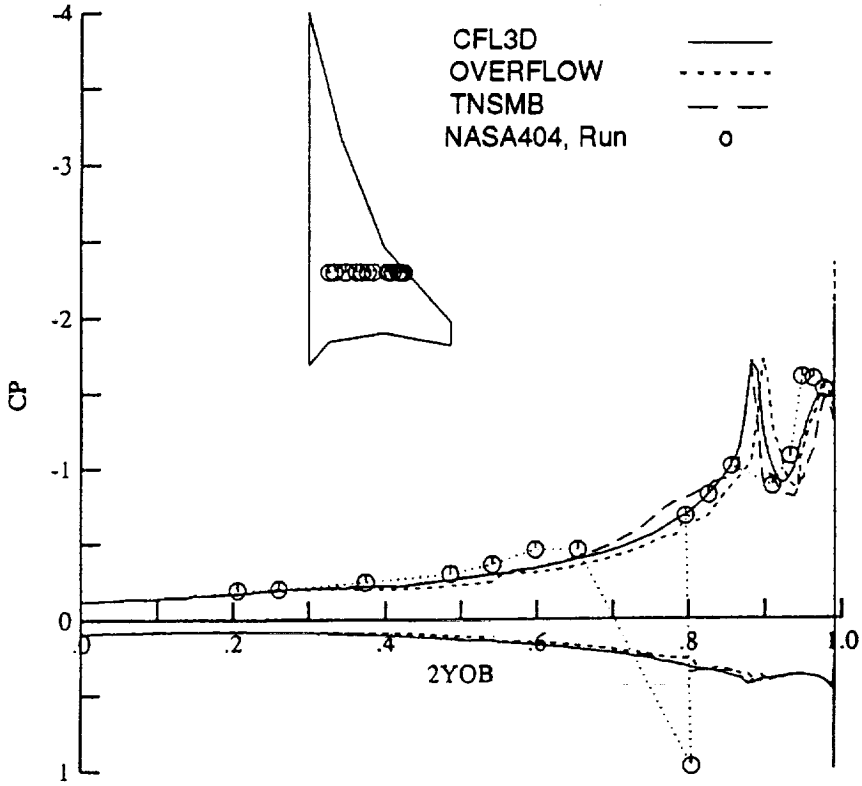

Dynacs Engineering Co., Inc.

A viscous pressure coefficient cut at X=2389.75 inches compares reasonably well with data. No wind tunnel data was taken on the hinge line as this location was filled in by klax. Compared with the Euler solutions presented previously, the leading edge and leading edge hinge line pressures are better predicted, due to the dissipative nature of the viscosity. Although TNSMB and CFL3D have the same turbulence models, there are obvious differences in the pressure in the separation region of the outboard wing.

Aerodynamic Coefficient Comparisons Between Viscous CFD and Data Ref. H, W/B, Flaps LE 30/Outboard TE 20, Mach=0.24, Alpha=10° NASA Langley 14X22 Test 404, Run 195

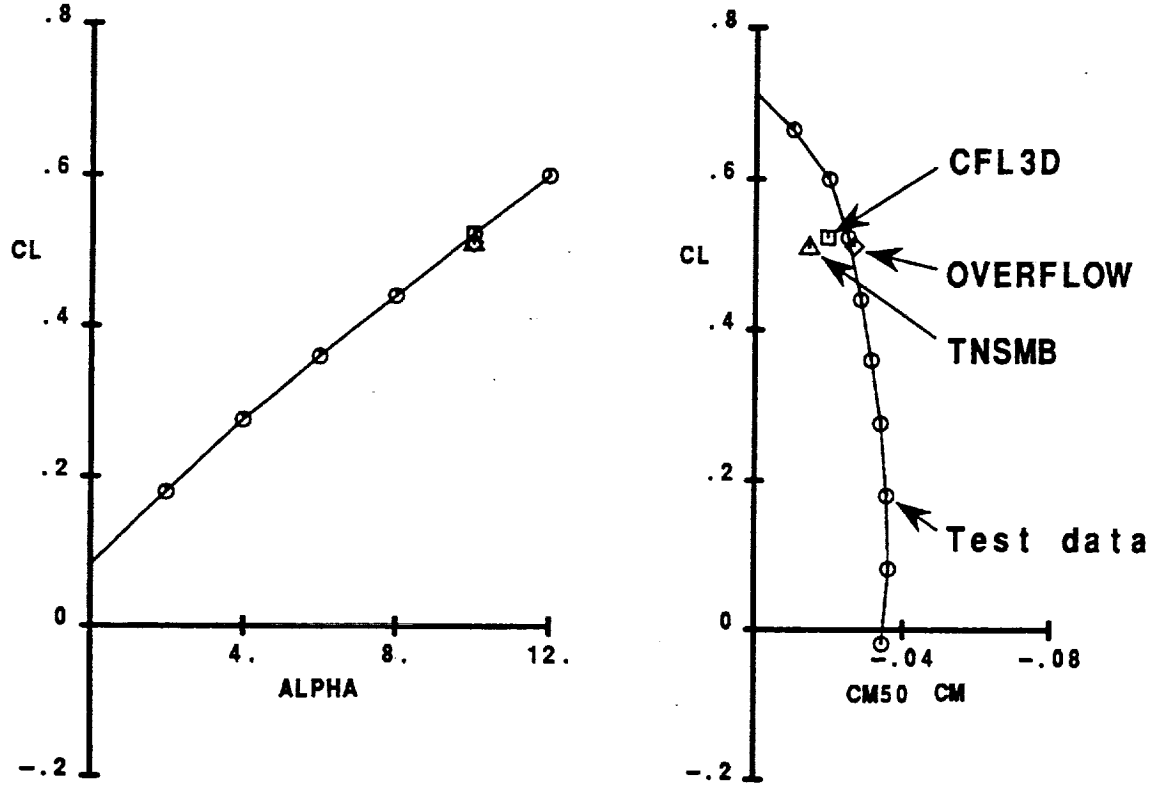

Dynacs Engineering Co., Inc.

The lift and moment coefficients are compared with wind tunnel aerodynamic coefficient data. All of the CFD lift coefficients underpredict the data, just the opposite to those found for the Euler results. Moment coefficient results indicate a nose-up trend for CFL3D and TNSMB compared with data, opposite to those of the Euler results; OVERFLOW predicts a slight nose-down moment compared with data. The moment is predicted more accurately with the viscous than for the inviscid results since the turbulent separation directly influences the location of the center of pressure.

Aerodynamic Coefficient Comparisons Between Viscous CFD and Data Ref. H, W/B, Flaps LE 30/Outboard TE 20, Mach=0.24, Alpha=10° NASA Langley 14X22 Test 404, Run 195

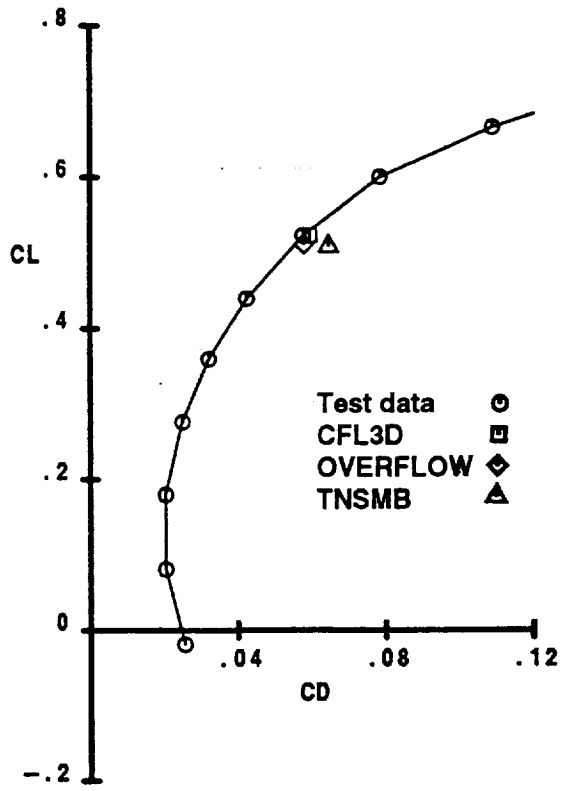

Dynacs Engineering Co., Inc.

Drag coefficient comparisons are made between viscous CFD and wind tunnel data. The CFD drag coefficient overpredicts the data, just the opposite to those found for the Euler results. However, the drag compares much better with the data due to the viscosity and the turbulence modeling. The larger values for drag is due to the addition of friction drag to the pressure drag that was computed in the inviscid solutions.

CFL3D Upper Surface Pressure Coefficient
Mach 0.24, Alpha 10, Flaps (30 LE/ Outboard TE 20), Re=8.8 milli

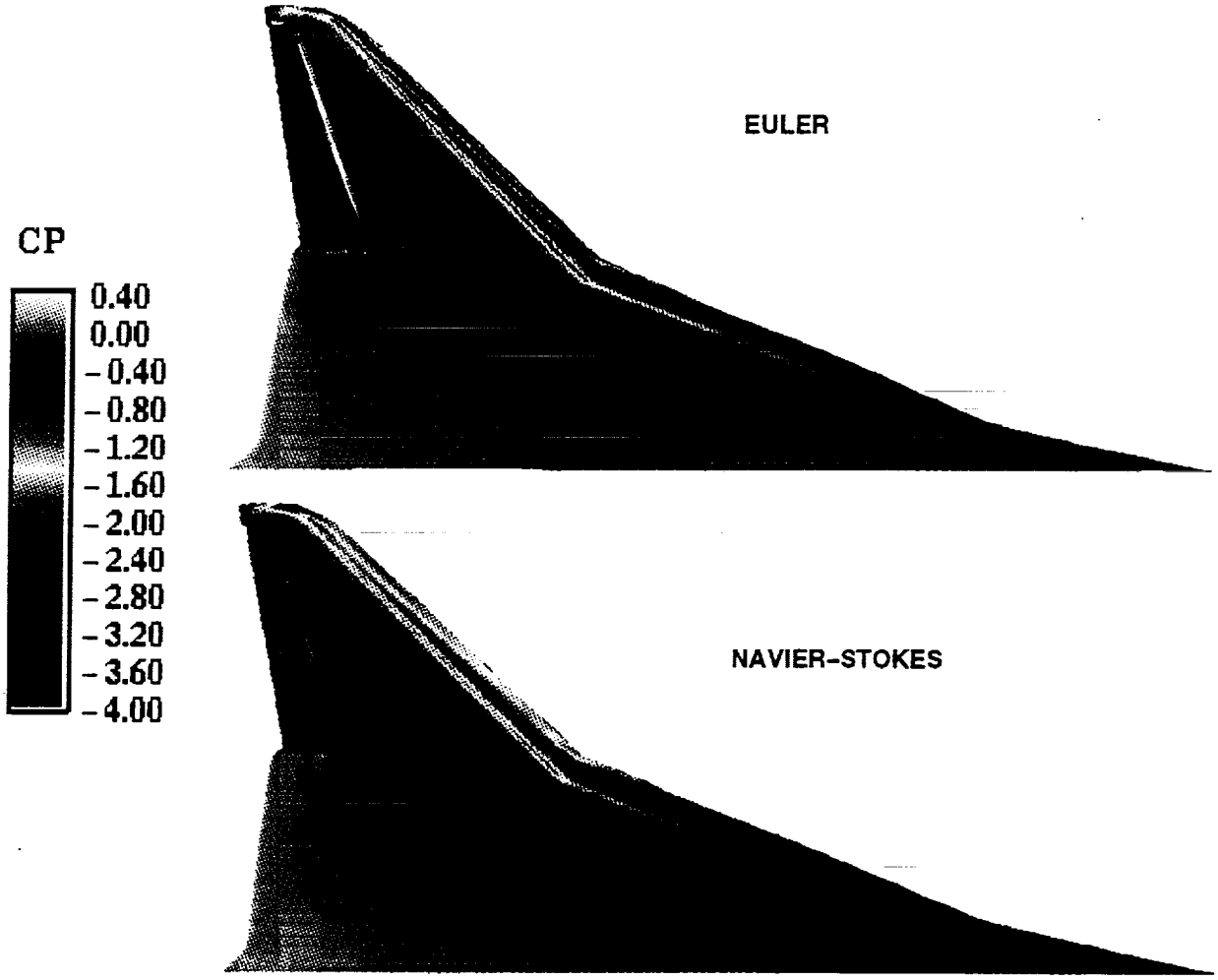

Dynacs Engineering Co., Inc.

To understand why the Navier–Stokes lift results are underpredicting the data, and why the Euler lift values, except for INS3D, are overpredicting the data, surface pressures are plotted. The case shown above compares the largest value of lift computed by all of the CFD codes (Euler) with an exact prediction (Navier–Stokes) compared to data. Greater expansion occurs on the outboard leading edge in the Euler solution. The sharp velocity gradients here may be generating leading edge vortices that are stronger for the inviscid case than for the viscous case.

Wind Tunnel Mini-Tuft Data

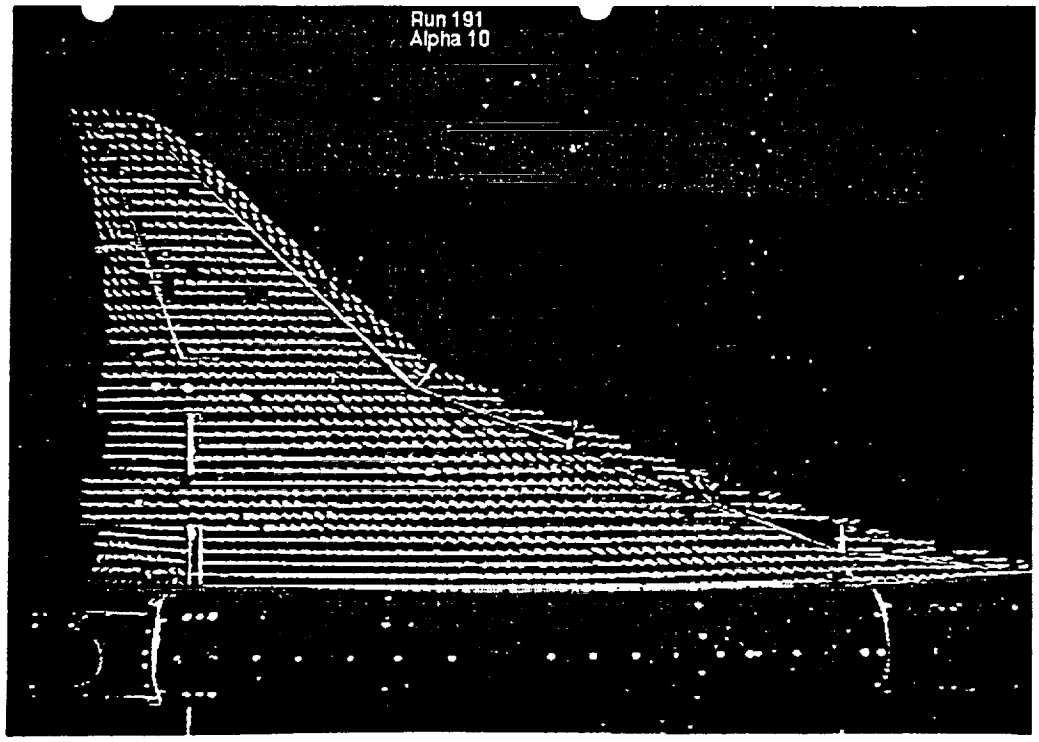

Dynacs Engineering Co., Inc.

Mini-tufts from the wind tunnel run is presented for the flap settings of LE 30 degrees and TE 20 degrees (some of the inboard TE flaps were also deflected). Separation has caused spanwise flow on the outboard wing as well as on the trailing edge flaps.

Viscous CFL3D Velocity Vectors (3 grid lines above surface)

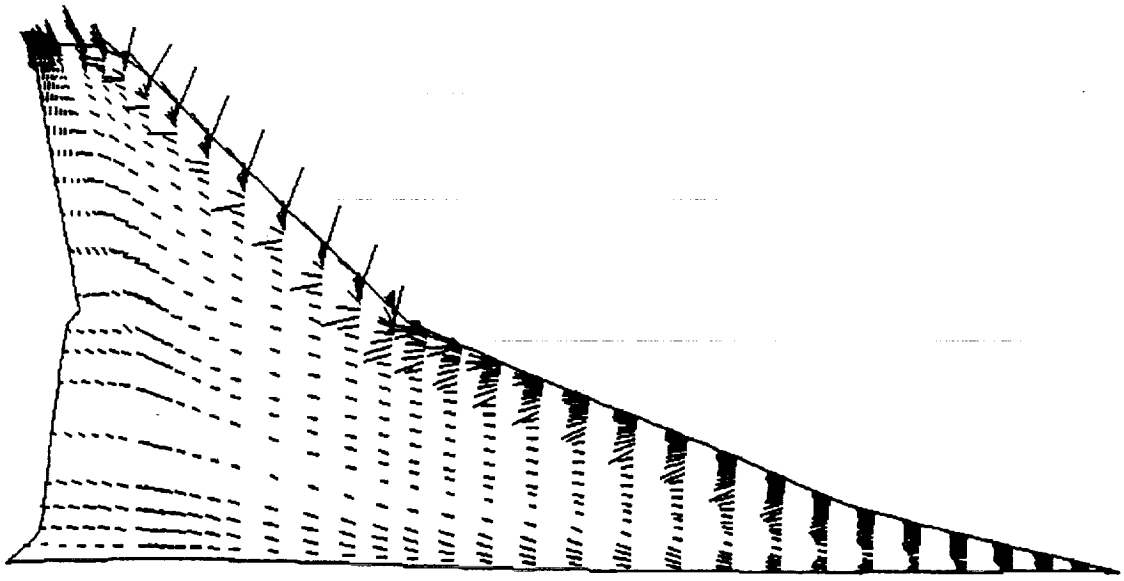

Dynacs Engineering Co., Inc.

Viscous CFL3D velocity vectors presented above are to be compared with the mini-tuft data on the previous page. The CFD vectors are plotted at three grid lines above the surface, and they are shown at every third station. Spanwise flow is evident on the outboard wing and the flow on the trailing edge flaps is predominantly spanwise. The mini-tufts show a similar region of spanwise flow on both the inboard and the outboard wing.

Viscous OVERFLOW Velocity Vectors (3 grid lines above surface)

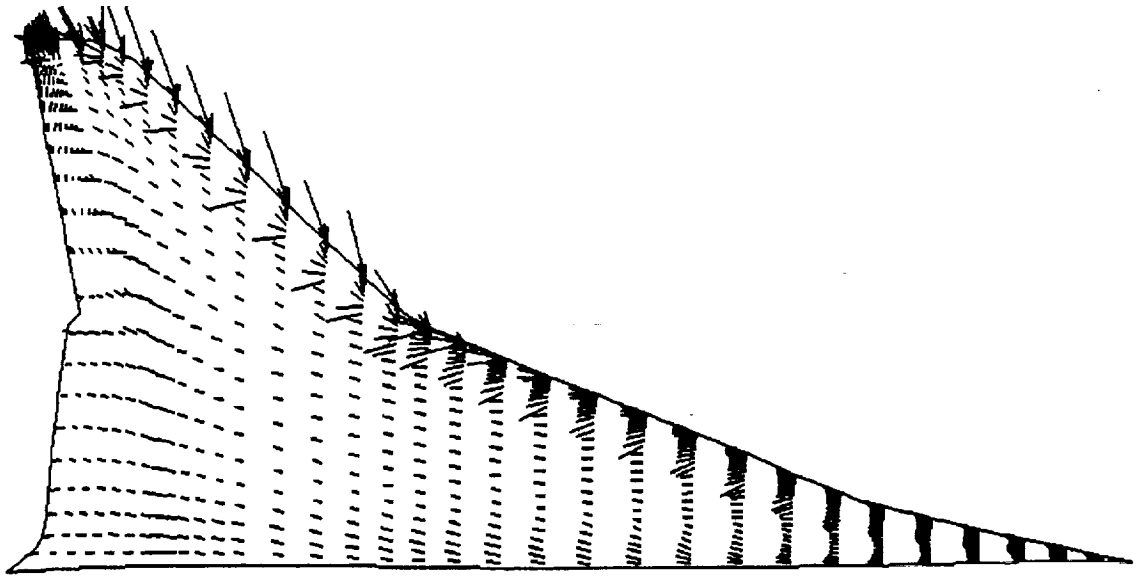

Dynacs Engineering Co., Inc.

Viscous OVERFLOW velocity vectors presented above are to be compared with the mini-tuft data on a previous page. The CFD vectors are plotted at three grid lines above the surface, and they are shown at every third station. Spanwise flow is evident on the outboard wing and the flow on the trailing edge flaps is predominantly spanwise. The mini-tufts show a similar region of spanwise flow on both the inboard and the outboard wing.

Viscous TNSMB Velocity Vectors (3 grid lines above surface)

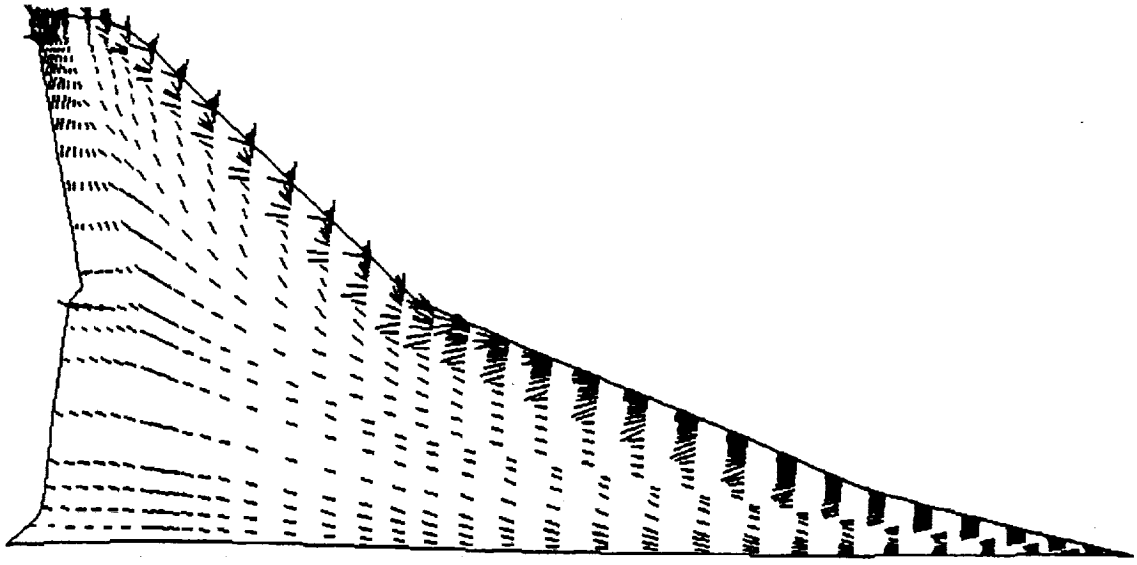

Dynacs Engineering Co., Inc.

Viscous TNSMB velocity vectors presented above are to be compared with the mini-tuft data on a previous page. The CFD vectors are plotted at three grid lines above the surface, and they are shown at every third station. Spanwise flow is evident on the outboard wing and the flow on the trailing edge flaps is predominantly spanwise. The mini-tufts show a similar region of spanwise flow on both the inboard and the outboard wing. There is greater turning on the outboard wing compared with those of the mini-tufts.

Viscous CFL3D Streamlines on the Upper Wing (one grid line above surface)

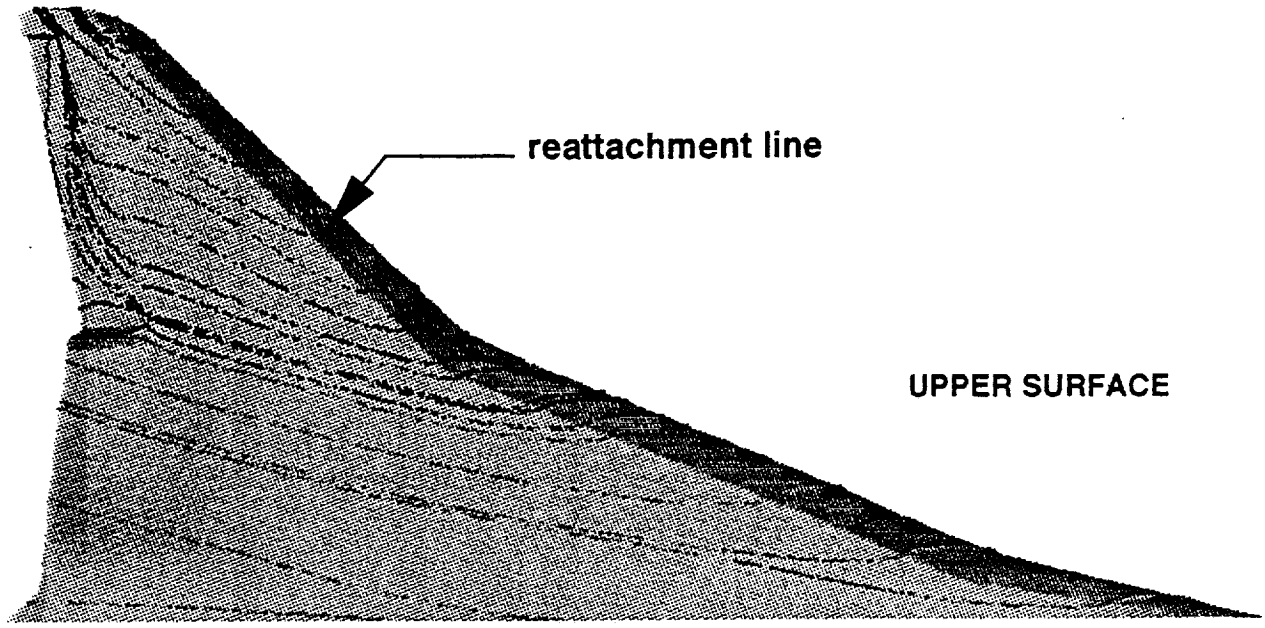

Dynacs Engineering Co., Inc.

To get some insight into the difference in the surface pressures between the viscous CFD results, some streamline traces were made. This figure shows streamline patterns for the viscous CFL3D solution. Each streamline was traced on the first grid line above the surface. The flow attaches on the lower surface of the leading edge flap (not shown) and then reattaches on the upper leading edge flap. The reattachment line extends from just inboard of the wing break to the outboard tip. The streamline patterns clearly show the spanwise flow in the boundary layer which is predominant on the outboard wing. Spanwise flow is strongest on the outboard wing. The Spalart-Allmaras turbulence model was used for this solution.

Viscous OVERFLOW Streamlines on the Upper Wing (one grid line above surface)

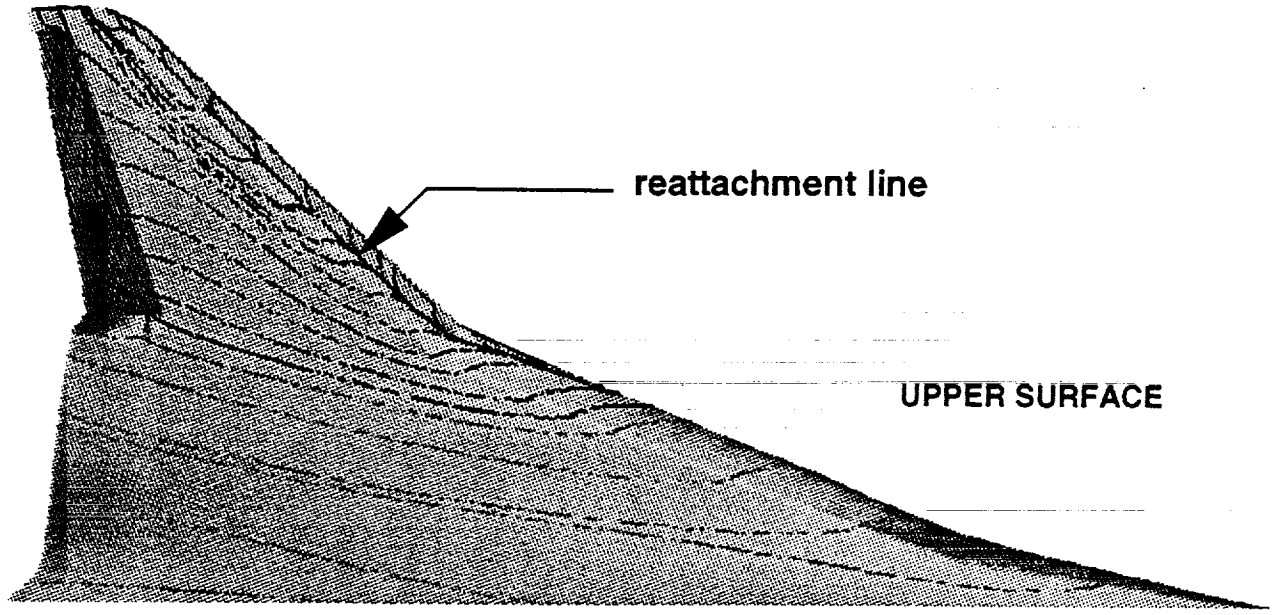

Dynacs Engineering Co., Inc.

To get some insight into the difference in the surface pressures between the viscous CFD results, some streamline traces were made. This figure shows streamline patterns for the viscous OVERFLOW solution. Each streamline was traced on the first grid line above the surface. The flow attaches on the lower surface of the leading edge flap (not shown) and then reattaches on the upper leading edge flap. The reattachment line extends from just inboard of the wing break to the outboard tip. The streamline patterns clearly show the spanwise flow in the boundary layer which is predominant on the outboard wing. Spanwise flow is strongest on the outboard wing. The Baldwin–Barth turbulence model was used for this solution.

Viscous TNSMB Streamline Traces on the Upper Wing (one grid line above surface)

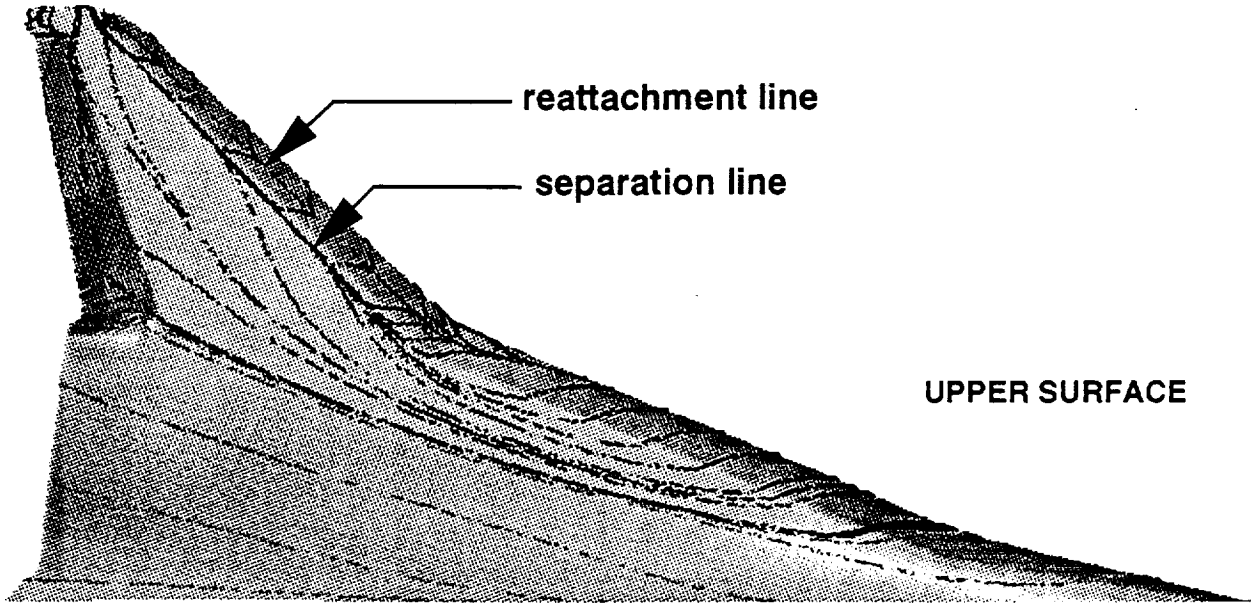

Dynacs Engineering Co., Inc.

To get some insight into the differences in the surface pressures between the viscous CFD results, some streamline traces were made. This figure shows streamline patterns for the viscous TNSMB solution. Each streamline was traced on the first grid line above the surface. The flow attaches on the lower surface of the leading edge flap (not shown) and then reattaches on the upper leading edge flap. The reattachment line extends from just inboard of the wing break to the outboard tip. The streamline patterns clearly show the spanwise flow in the boundary layer which is predominant on the outboard wing. Spanwise flow is strongest on the outboard wing. The Spalart-Allmaras turbulence model was used for this solution.

There is greater turning on the outboard wing for TNSMB that is not seen with the other codes. It is interesting to compare the leading edge reattachment and separation lines. In particular, there is a separation line just beyond the leading edge hinge line in the TNSMB solution; however, there does not appear to be a separation line in the CFL3D and OVERFLOW results. The Spalart-Allmaras turbulence model was used for the CFL3D and TNSMB solutions, whereas the Baldwin-Barth turbulence model was used for the OVERFLOW solution. The streamline behavior may be partly attributed to the different turbulence models used in the CFD codes.

Summary and Conclusions

Scheme	Code	C_L	C_D	C_M	Size (MW) on C-90	Cost (sec)
Euler	CFL3D	0.5407	0.0523	-0.0458	62	6200
	INS3D	0.5206	0.0462	-0.0298	52	28,800
	OVERFLOW	0.5323	0.05410	-0.0325	60	10,000
	TNSMB	0.5254	0.0564	-0.0393	91	10,000
	USM3D #1	0.5405	0.06961	-0.0379	125	8,000
	USM3D #2	0.5493	0.06670	-0.0247	225	45,700
Navier-Stokes	CFL3D	0.5235	0.05876	-0.0196	108	28,700
	OVERFLOW	0.5110	0.05730	-0.0266	89	28,000
	TNSMB	0.5090	0.06384	-0.0146	138	30,450
	TEST	**0.5235**	**0.0571**	**-0.0251**		

Dynacs Engineering Co., Inc.

A toolbox of results and methods has been developed that will be valuable for future studies. The computational and storage requirements on the C-90, the grid generation effort and the cost for a CFD run must be used to determine the best tool to use.

In general, there is a greater spread in the inviscid than for the viscous CFD aerodynamic coefficients. The larger lift predicted by the inviscid results compared with data, and vice versa for the viscous cases, may be caused by the generation of stronger leading edge vortices on the outboard leading edge in the Euler solutions. The best results for drag and moment are obtained with the Navier-Stokes solutions, due to the addition of viscosity and turbulence modeling. It is interesting to note that drag and moment are well predicted with the USM3D solution on the more refined grid of case 2. These results are better than those on the unstructured grid of case 1 due to the added grid refinement on the surface, and the elimination of the web between the inboard trailing edge flap and the wing in case 2. The more refined unstructured grid resulted in sharper hinge line pressure values; however, this degree of refinement overpredicted the suction peaks due to the lack of viscosity. The correct prediction of hinge pressures is very important; this is important for a Reynolds number study, for example, where the separation phenomenon needs to be modeled correctly.

Viscous CFD compares better than inviscid CFD at the hinge lines, leading and trailing edges, possibly due to differences in numerical dissipation between the Euler and the Navier-Stokes codes, and to differences in the grids. In addition, the differences in the C_p values between the viscous solutions can be attributed possibly to the different turbulence models used, especially in the separated regions of the outboard wing. The same supposition may be used to explain the different surface pressures among the viscous CFD results at the sharp outboard leading edge, where strong velocity gradients exist. In all cases the viscous results predicted more nose-up moments than the corresponding inviscid results.

NASA Ames Research Center
Low-Speed Aerodynamics Branch

Summary of HEAT 1 Aeroacoustics Installation Effects

Configuration Aerodynamics Workshop

Brian E. Smith, Paul T. Soderman, and Fanny A. Zuniga

February 27-29, 1996

Outline

I. Overview & background of Test Objectives

II. Acoustic Results

- Nozzle Pressure Ratio (NPR)
- Suppressor Performance
- ΔdB per % Thrust Loss

III. Aerodynamic Results

- Forces & Moments
- Wing & Nozzle Flowfields
- Surface Pressures

IV. Summary & Conclusions

V. Future Work

Potential HSCT Propulsion / Aerodynamic Interactions

High-Lift System and Wing Aerodynamics Influence

- Nozzle Entrainment and Installed Performance
- Mixer/Ejector Inflow Distortion
- Acoustic Signature

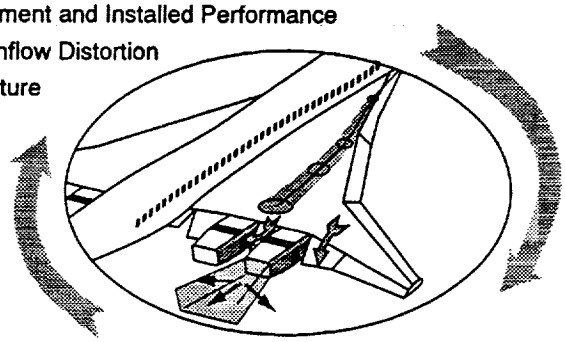

Nozzle Mixer/Ejector Entrainment Influences

- L.E. Vortex Trajectories and Wing Pressures
- T.E. Flap Flow Attachment and High-Lift System Performance

A critical part of the NASA High-Speed Research (HSR) program is the demonstration of satisfactory suppression of the jet noise present at low airspeeds. One scheme for reducing jet exhaust noise generated by a future High-Speed Civil Transport (HSCT) is the use of a mixer/ejector system which would entrain large quantities of ambient air into the exhaust flow from the powerplant in order to cool and slow the jet exhaust before it leaves the tailpipe. Of the variety of factors which can affect the noise suppression characteristics of the mixer/ejector system, the influence of the wing flow field and high-lift devices is not well understood. The effectiveness of the noise suppression device must be evaluated in the presence of the wing/high-lift system before definitive assessments can be made concerning HSCT noise. Of nearly equal importance is the evaluation of the performance of the high-lift system(s) in the presence of realistic propulsion units which feature high ambient flow entrainment rates and jet thrust coefficients. These noise suppressors must provide the required acoustic attenuation while not overly degrading the thrust efficiency of the propulsion system or the lift enhancement of the high-lift devices on the wing. The overall objective of the NASA High-lift Engine Aeroacoustics Technology program is to demonstrate satisfactory interaction between the jet noise suppressor and the high-lift system at airspeeds and angles of attack consistent with takeoff, climb, approach, and landing (see Figure 1).

In support of this program, an isolated aeroacoustic test of a 13.5%-scale, candidate mixer/ejector nozzle was performed in the Ames' Research Center 40- by 80-Foot Wind Tunnel. The purpose of the test was to measure the baseline aeroacoustic performance characteristics of this nozzle in isolation from the aerodynamic flowfield induced by an HSCT airframe. The test documented the acoustic signature of the nozzles with treated and hardwall ejector surfaces and with changes in the ratio of ejector-duct-to-jet-area over a wide range range of nozzle pressure ratios and freestream Mach numbers. The test also measured the thrust performance, ambient-flow aspiration ratio, and internal and external static pressures on the nozzles. The isolated aeroacoustic performance data has been compared with results obtained with this nozzle installed on a 13.5% Boeing Reference H HSCT configuration, semi-span model. The semi-span, aeroacoustics integration test documented the first-order effects of the airframe flowfield on the acoustic performance of the nozzle and the effect of the nozzle secondary inlet flows on the aerodynamic performance of the wing high-lift systems. This investigation is critical to understanding the mutual installation effects of mixer/ejector nozzles and wing high-lift systems.

HEAT 40- by 80-Foot Wind Tunnel Tests

HEAT image plane aero validation test
- 7x10 small-scale image plane
- Flow visualization & evaluation of trailing edge flap concepts
- Spring '93

GE AMEN isolated nozzle test
- Early generation mixer-ejector nozzle
- Validated acoustic measurement & hot jet test techniques
- December '93

GE 2DME HEAT Isolated Nozzle (HIN) test
- Gen 1 mixer-ejector nozzle
- Measured isolated aeroacoustic performance of nozzle for HEAT I model
- Summer '94

HEAT Semi-Span (HSS)
- 13.5% semi-span Boeing Reference H model
- Gen 1 suppressor nozzle
- Customer/Participants
  - Ames Research Center, Boeing, Douglas Aircraft Corporation, General Electric, Lockheed Georgia, Lewis Research Center
- Feb. - May 1995

HEAT 1A
- *13.5% semi-span Boeing Reference H model*
- *2 powered Gen ? nozzles*
- *Remotely actuated control surfaces*
- *early 1998*

40 x 80 Foot Wind Tunnel Isolated Nozzle Installation

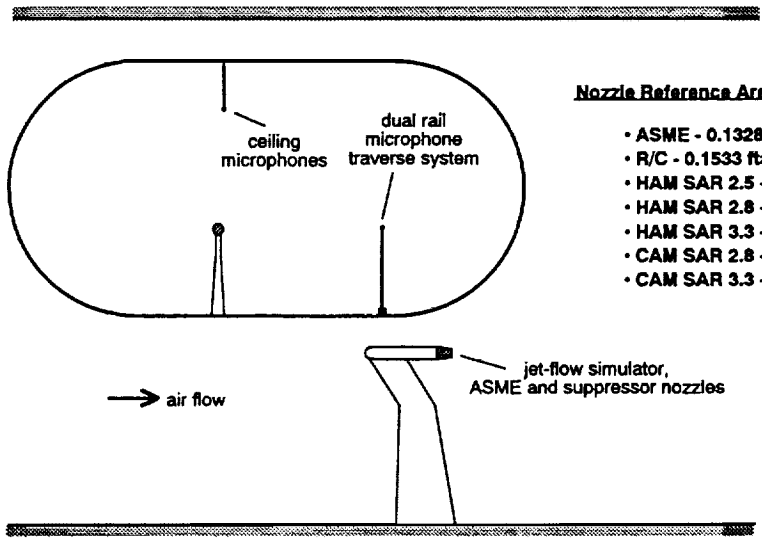

Nozzle Reference Areas, A8:

- **ASME - 0.1328 ft²**
- **R/C - 0.1533 ft²**
- **HAM SAR 2.5 - 0.1683 ft²**
- **HAM SAR 2.8 - 0.1508 ft²**
- **HAM SAR 3.3 - 0.1394 ft²**
- **CAM SAR 2.8 - 0.1549 ft²**
- **CAM SAR 3.3 - 0.1383 ft²**

HAM MODEL CROSS SECTION

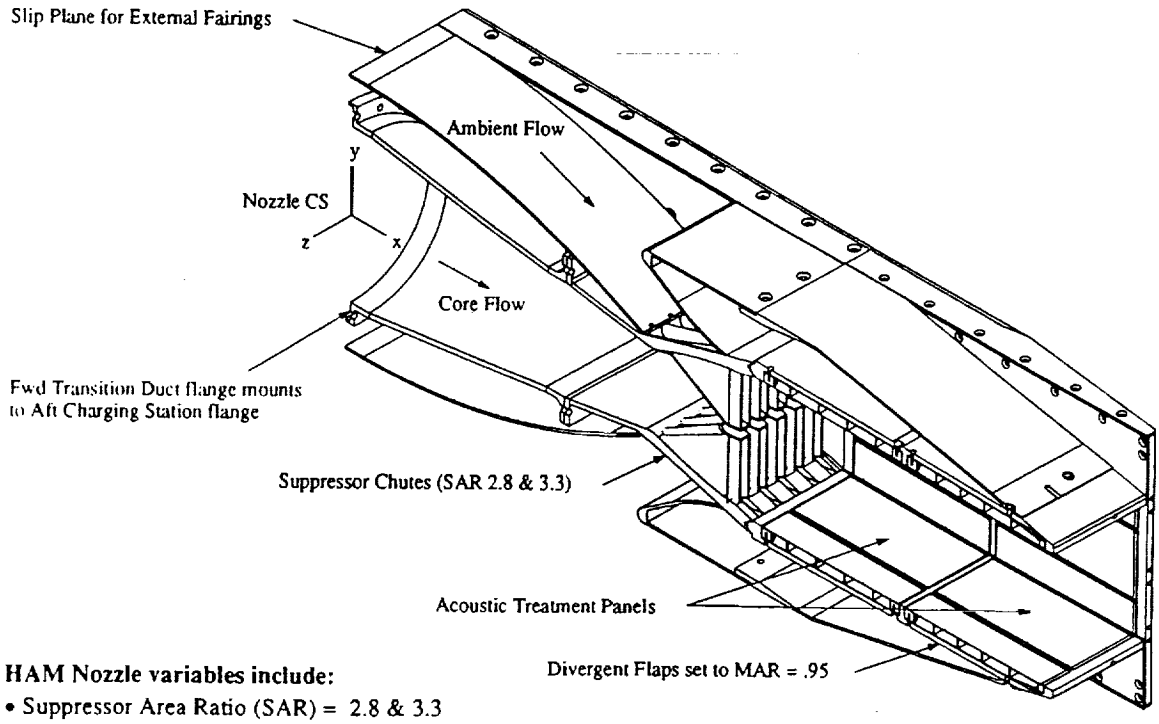

HAM Nozzle variables include:

- Suppressor Area Ratio (SAR) = 2.8 & 3.3
- Mixing Area Ratio (MAR) = .95 (Capable of MAR up to 1.4)
- Acoustic Treatment Panels and Hardwall Panels

Photo of Heat Isolated Nozzle (HIN) Test Installation

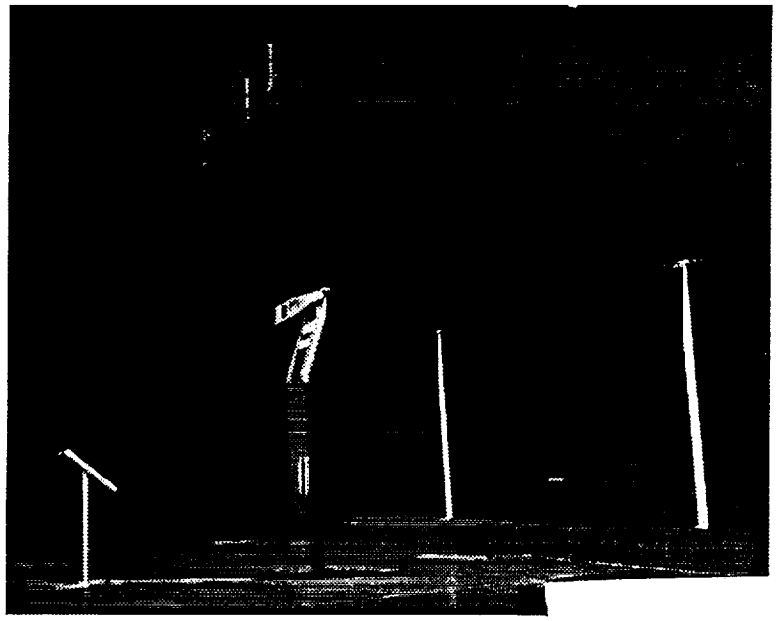

Close-Up of GE 2DCD Ejector Suppressor Nozzle

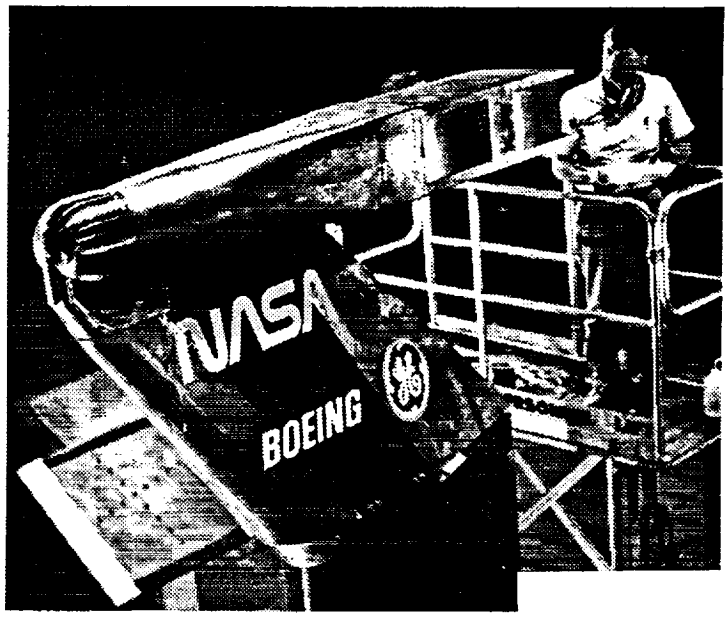

40- x 80- Foot Wind Tunnel Semi-Span Model Installation

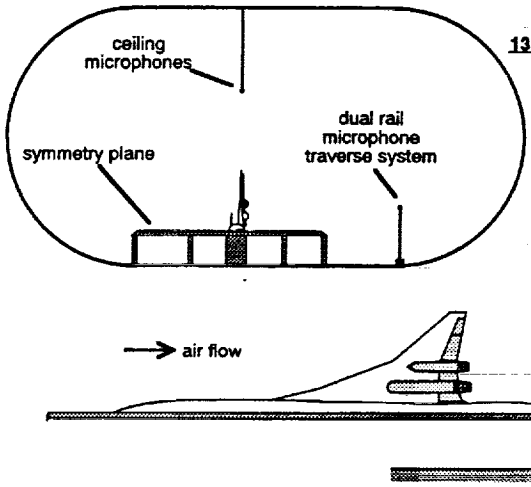

13.5% Boeing Ref H HSCT model:

- length - 42 ft
- semi-span - 8.7509 ft
- wing reference area - 64.699 ft²
- MAC - 11.613 ft
- mom ref ctr @ 50% MAC
- 19.6M<R_e<35.2M

HEAT I 40x80 Test

Primary Objectives

- Aerodynamic effects on installed noise suppressor performance
- Suppressor entrained-flow effects on high-lift system performance

Secondary Objectives

- Overwing pylon fin effects
- Acoustic fatigue & cabin noise measurements
- Horizontal tail effectiveness & plume impingement

Approach

- 13.5%-scale semi-span model of Boeing HSCT Ref H configuration
  - 0 & 35° deflection leading-edge flaps
  - 0, 10 & 20° trailing-edge flap deflection
  - adjustable incidence horizontal tail & elevator
- Inboard nacelle powered by propane-fueled jet flow simulator
  - 2.0 < NPR < 4.5
  - 715 to 1400°F
  - Suppressor area ratios: 2.5 (hot), 2.8 & 3.3 (hot & cold)
- Outboard flow-through nacelle
- Acoustically-treated plane of symmetry
- $0 < M < 0.4$
- $-2 < \alpha < 16°$

Schedule

February - May 1995 (385 runs)

Acoustics Results

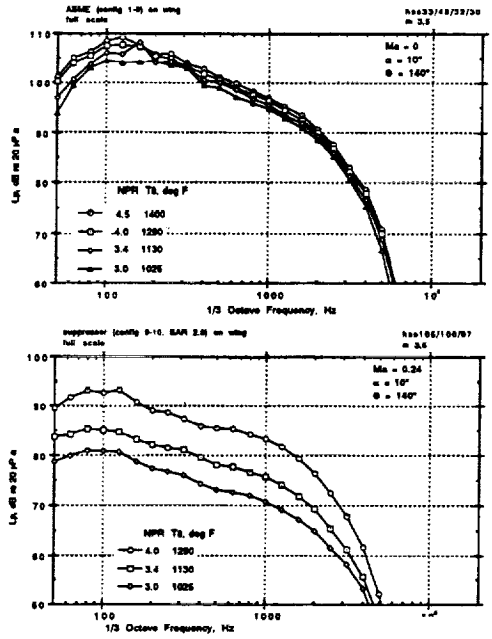

EFFECT of NOZZLE PRESSURE RATIO on THIRD-OCTAVE SPECTRA

The effect of nozzle pressure on ASME and suppressor full-scale third-octave spectra is shown below. The ASME nozzle and HAM suppressor were mounted on the HEAT semispan wing. The ASME data were acquired at zero flight speed, the suppressor data were acquired at flight Mach number of 0.25. The suppressor noise was much more sensitive to nozzle pressure ratio than was the ASME nozzle. For example, change pressure ratio from 3.0 to 4.0 caused the conical nozzle noise to increase from 2 to 6 dB depending on frequency, whereas the suppressor noise increased from 4 to 11 dB.

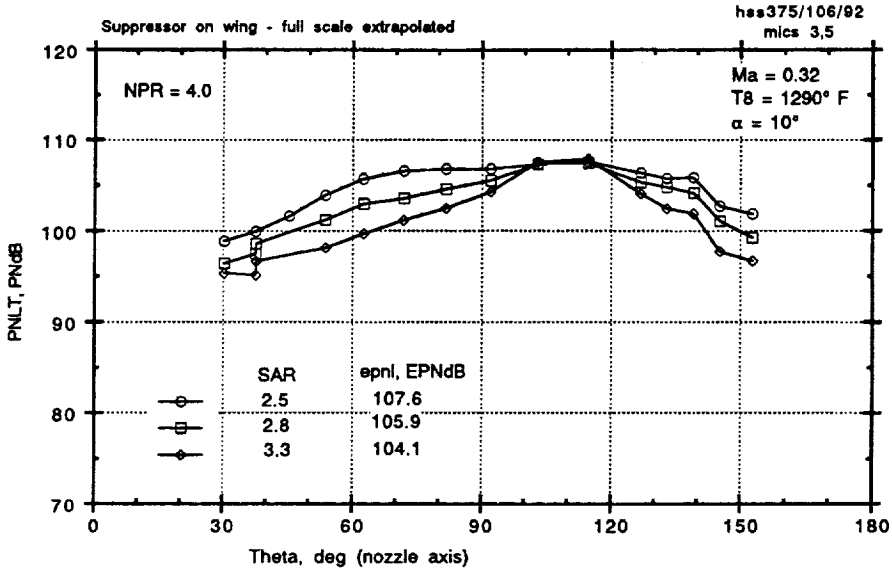
Suppressor on wing - full scale extrapolated
hss375/106/92
mics 3,5
NPR = 4.0
Ma = 0.32
T8 = 1290° F
α = 10°
PNLT, PNdB
SAR
epnl, EPNdB
2.5
107.6
2.8
105.9
3.3
104.1
Theta, deg (nozzle axis)

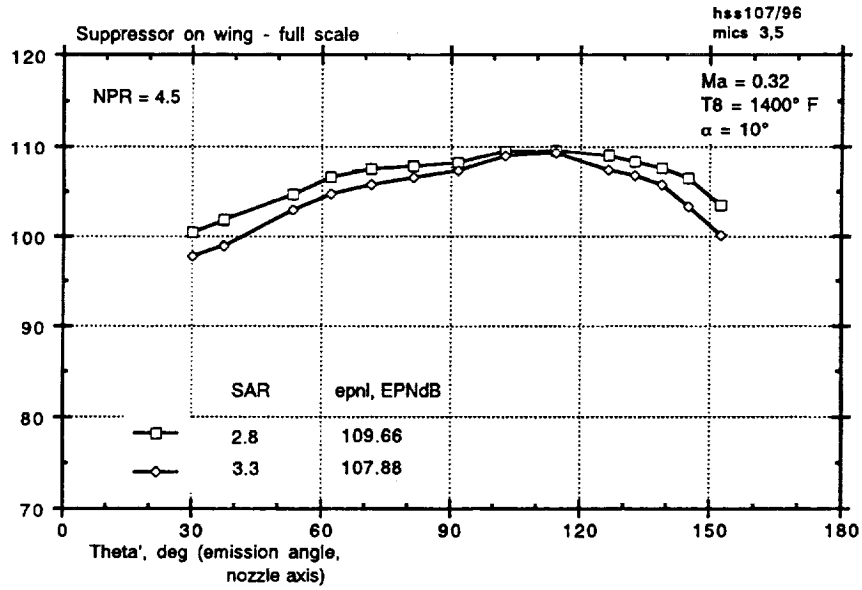
Suppressor on wing - full scale
hss107/96
mics 3,5
NPR = 4.5
Ma = 0.32
T8 = 1400° F
α = 10°
SAR
epnl, EPNdB
2.8
109.66
3.3
107.88
Theta', deg (emission angle,
nozzle axis)

EFFECT OF SUPPRESSOR AREA RATIO (SAR) - FULL SCALE PNL
Ma = 0.32

As shown in the previous figures, scaled and extrapolated data are plotted as Perceived Noise Levels versus directivity angle for three values of SAR: 2.5, 2.8, 3.3 and a higher nozzle pressure ratios of 4.0 and 4.5. At smaller angles, SAR 2.5 dominated the noise, but the data tend to merge at the peak noise. In both cases, the EPNL metric was maximum for the lowest SAR.

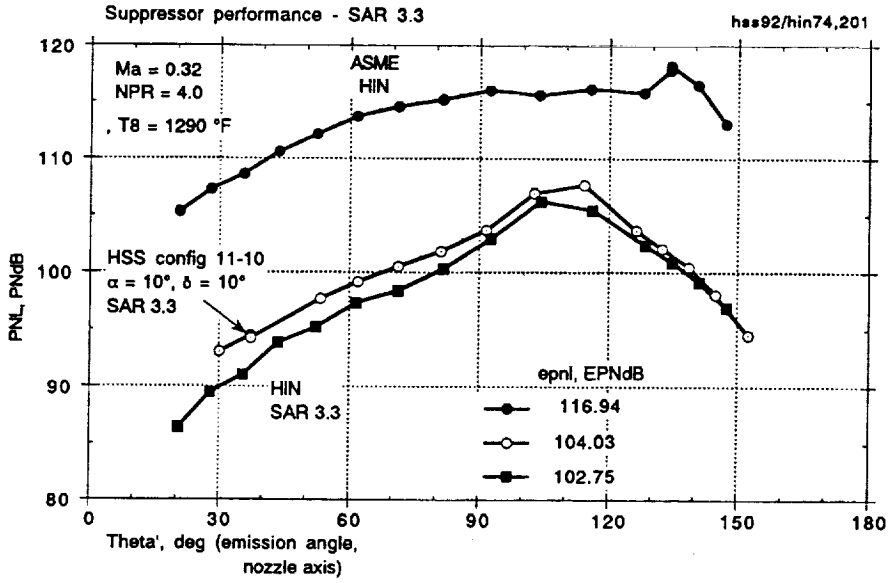
Suppressor performance - SAR 3.3
hss92/hin74,201
Ma = 0.32
NPR = 4.0
, T8 = 1290 °F
ASME
HIN
HSS config 11-10
α = 10°, δ = 10°
SAR 3.3
HIN
SAR 3.3
epnl, EPNdB
116.94
104.03
102.75
PNL, PNdB
120
110
100
90
80
0
30
60
90
120
150
180
Theta', deg (emission angle, nozzle axis)

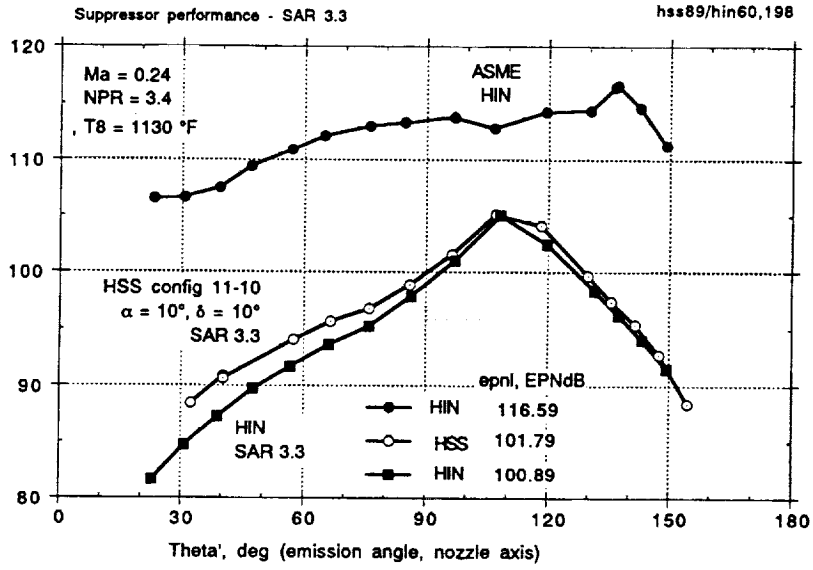
Suppressor performance - SAR 3.3
hss89/hin60,198
Ma = 0.24
NPR = 3.4
, T8 = 1130 °F
ASME
HIN
HSS config 11-10
α = 10°, δ = 10°
SAR 3.3
HIN
SAR 3.3
epnl, EPNdB
HIN 116.59
HSS 101.79
HIN 100.89
120
110
100
90
80
0
30
60
90
120
150
180
Theta', deg (emission angle, nozzle axis)

SUPPRESSOR PERFORMANCE - EPNL (SAR 3.3) and INSTALLATION EFFECT

This is the full-scale PNL flyover simulation for the ASME isolated nozzle, the isolated suppressor SAR 3.3, and the installed suppressor, both suppressors with acoustically treated ejectors. Two conditions are represented: flight Mach numbers of 0.24 and 0.32, and nozzle pressures ratios of 3.4 and 4.0. At the lower Mach number and nozzle pressure ratio, the suppression was 14.8 EPNdB; at the high Mach and pressure ratio, the suppression was only 12.91 EPNdB.

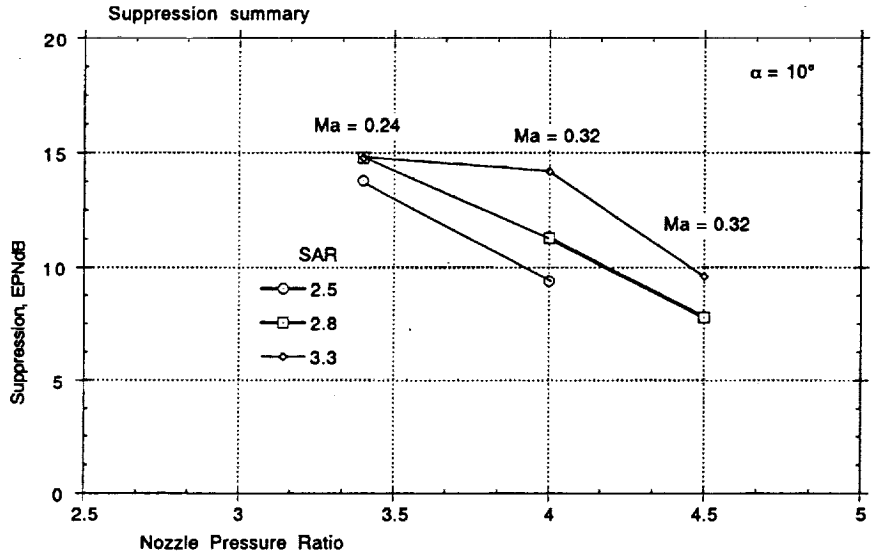

Suppression Summary

This figure summarizes the noise suppression measured during the HEAT Semi-Sapn test. The figure presents the suppression obtained with the three suppressor area ratio nozzles which were evaluated during the investigation. Although the jet exit areas are different for each of the nozzles. the results plotted here have been scaled and extrapolated to full-scale EPNdB values. The graph illustrates that the highest suppressor area ratio provided the most noise suppression. The acoustic suppression falls off as nozzle pressure ratio increases.

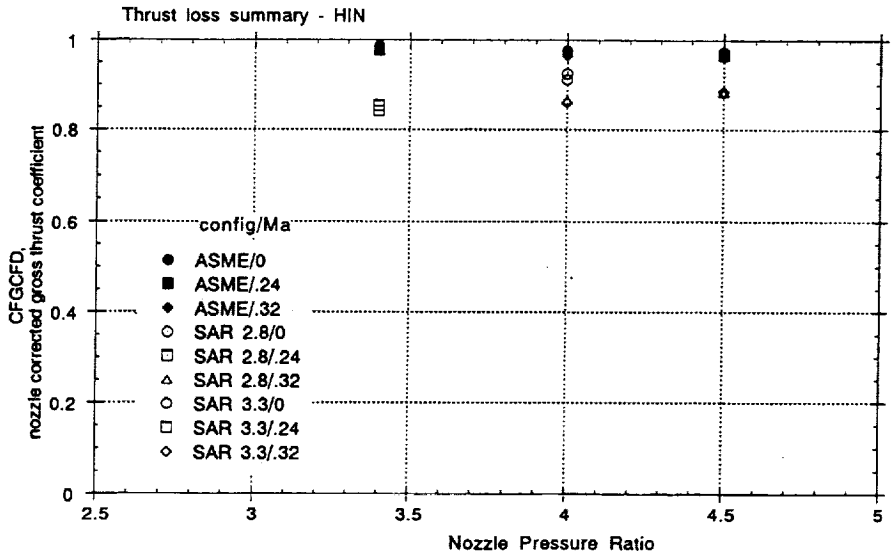
Thrust loss summary - HIN
CFGCFD,
nozzle corrected gross thrust coefficient
1
0.8
0.6
0.4
0.2
0
config/Ma
ASME/0
ASME/.24
ASME/.32
SAR 2.8/0
SAR 2.8/.24
SAR 2.8/.32
SAR 3.3/0
SAR 3.3/.24
SAR 3.3/.32
2.5
3
3.5
4
4.5
5
Nozzle Pressure Ratio

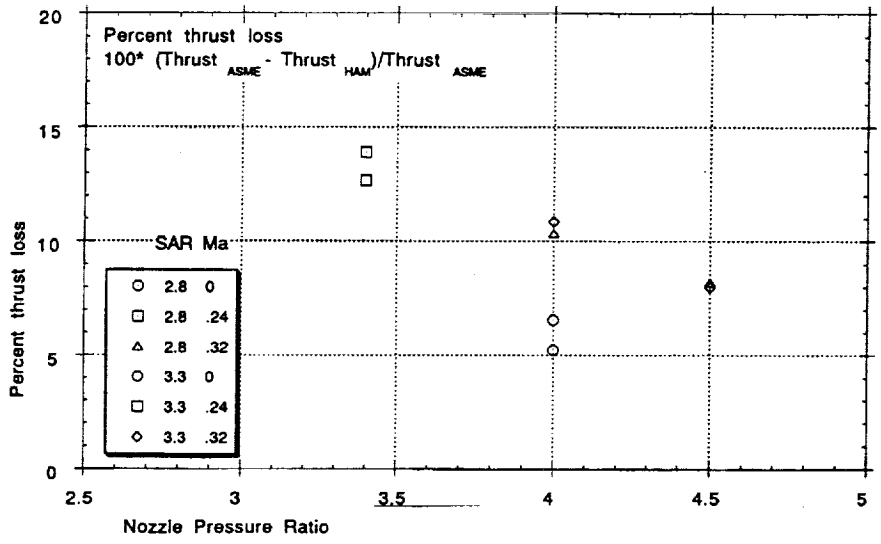
Percent thrust loss
100* (Thrust ASME - Thrust HAM)/Thrust ASME
Percent thrust loss
20
15
10
5
0
SAR Ma
2.8 0
2.8 .24
2.8 .32
3.3 0
3.3 .24
3.3 .32
2.5
3
3.5
4
4.5
5
Nozzle Pressure Ratio

Thrust Loss

The aerodynamic sessions in this workshop will cover installation effects on the performance of the jet flow simulator. However, the acoustic suppression is often linked to the simple jet thrust loss as shown here for the isolated nozzles. The parameter used is the corrected gross thrust coefficient, which is a ratio of the thrust corrected for nacelle drag divided by the predicted isentropic thrust (CFGCFD). The percent thrust loss due to the suppressor is shown for various operating conditions and is fairly high varying from 5 to 14 percent. Based on the suppression values shown on the previous page, the ratio of suppression to thrust loss (EPNdB / %TL) ranged from a minimum of 0.5 to a maximum of 1.9 for the isolated suppressors.

THRUST LOSS VS NOISE REDUCTION FOR HSCT NOZZLES
M0.32 SIDELINE CONDITIONS V_{ID}=2375 FT/S

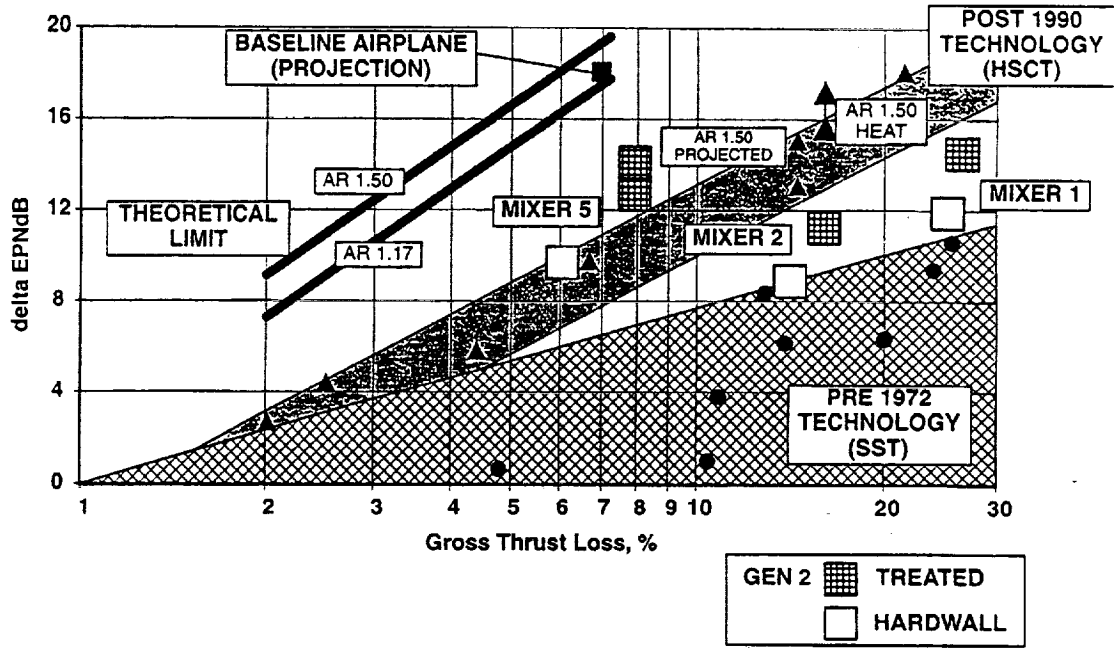

Aerodynamic Results

The following figures show comparisons in lift, drag and pitching moment coefficients for the 13.5% power-off semi-span test results with that of a 6% full-span Ref H model tested in Langley's 14x22 ft. wind-tunnel facility. Comparisons shown below were made at 3 different model configurations.

The lift curve figure shows excellent agreement between the lift coefficient results for the 13.5% semi-span and 6% full-span tests for 3 different configurations. The drag polar figure shows good agreement in drag coefficient for the 2 tests for the first 2 configurations. The largest differences in drag coefficient occurred for the configuration: leading-edge flap(LEF)=30° and trailing-edge flap(TEF)=10° at angles-of-attack less than 10°. The differences in drag may be due to the difference in leading-edge flap deflection. The results for the 13.5% model were made at LEF=35° and TEF=10° while the results for the 6% model were made at LEF=30° and TEF=10°. This 5° difference in leading-edge flap probably account for the differences in drag shown.

The lift-to-drag ratio (L/D) figure shows good agreement between L/D results for the 13.5% semi-span and 6% full-span tests at angles-of attack greater than 6° for all 3 different configurations. Finally, the last figure shows the differences in pitching moment coefficient for the semi-span and full-span tests.

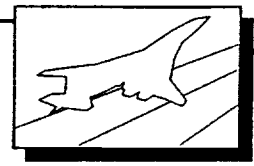

13.5% Ref H 40x80 ft. Semi-Span Results and Comparison to 6% Ref H 14x22 ft. LaRC Full-SpanTest Results

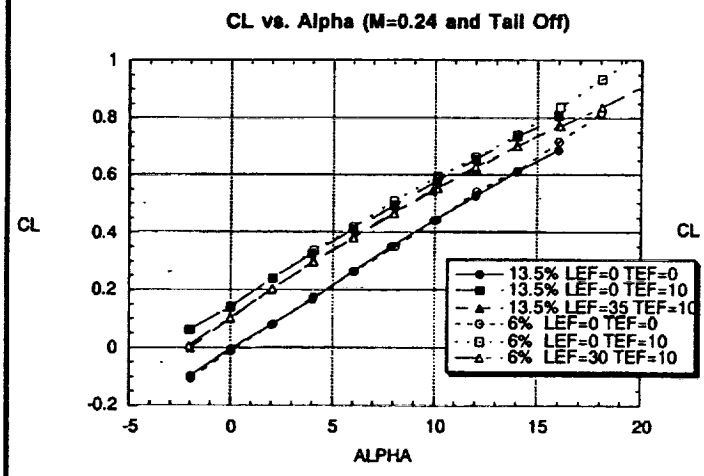

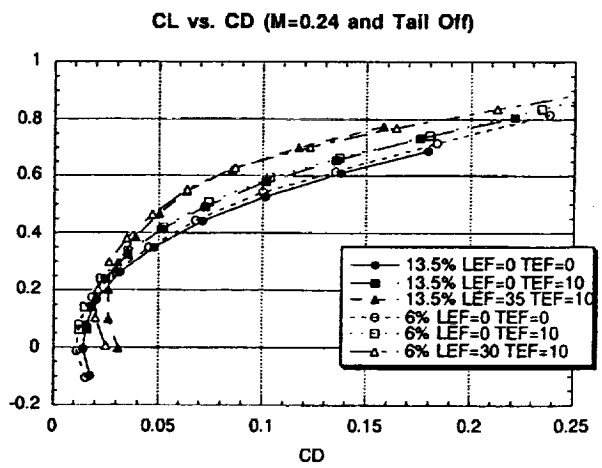

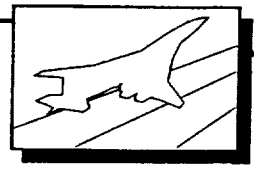

13.5% Ref H 40x80 ft. Semi-Span Results and Comparison to 6% Ref H 14x22 ft. LaRC Full-SpanTest Results

L/D vs. Alpha (M=0.24 and Tail Off)

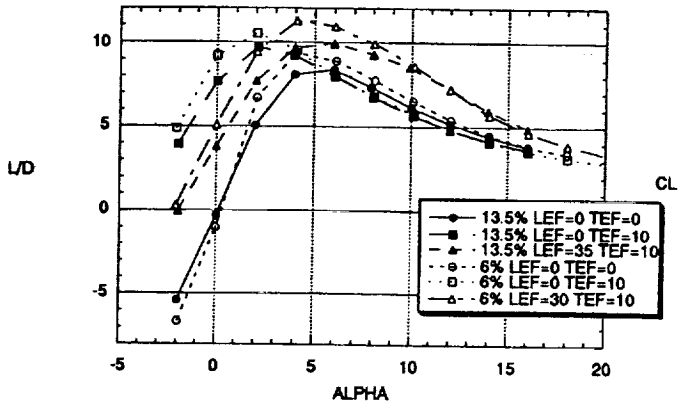

CL vs. CM (M=0.24 and Tail Off)

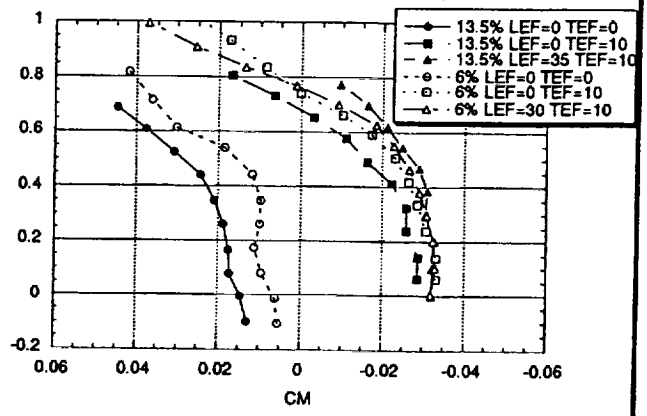

The figures below show the differences in lift, drag and pitching moment coefficients for simple-hinged and slotted flap configurations at power-off conditions. Results are shown for leading-edge flap at 35°, horizontal stabilizer at -5°, elevator at 0° and trailing-edge flaps at 20°/20°/10°/10°. Flap performance for Mach numbers 0.24 and 0.32 are also compared.

The lift curves show a slight loss in lift for the slotted flap configuration at both Mach numbers. The drag polar shows no measureable difference in drag coefficient for the simple-hinged and slotted flap configurations at Mach 0.24 and 0.32.

The last 2 figures show the differences in lift-to-drag ratio (L/D) and pitching moment coefficient for the two flap configurations. The figures show a decrease in L/D for the slotted flap configuration at angles-of-attack less than 10°. This decrease in L/D is greater at Mach 0.24. The final figure shows a reduction in pitching moment coefficient for the slotted flap configuration.

These results are consistent with results of previous wind-tunnel tests. In summary, the slotted flap configuration yields a reduction in lift-to-drag performance and a reduction in pitching moment coefficient.

SIMPLE-HINGED vs. SLOTTED FLAP

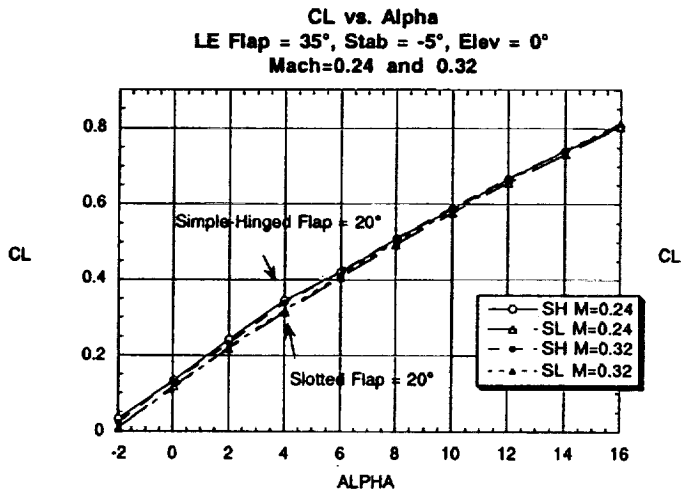

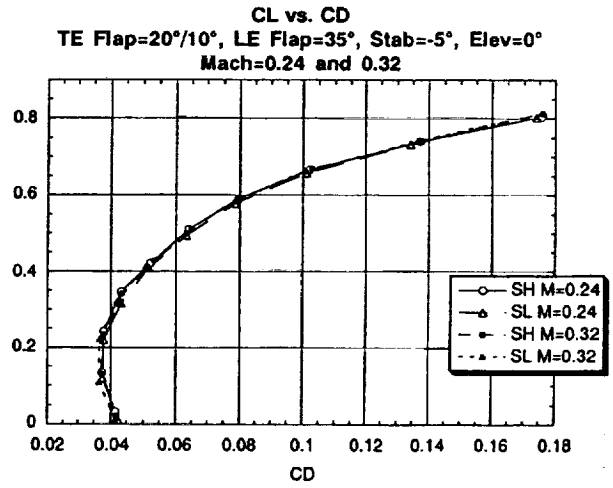

SIMPLE-HINGED vs. SLOTTED FLAP

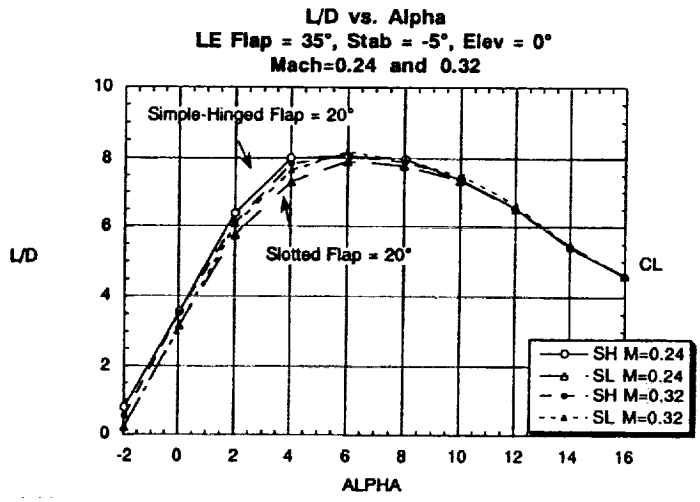

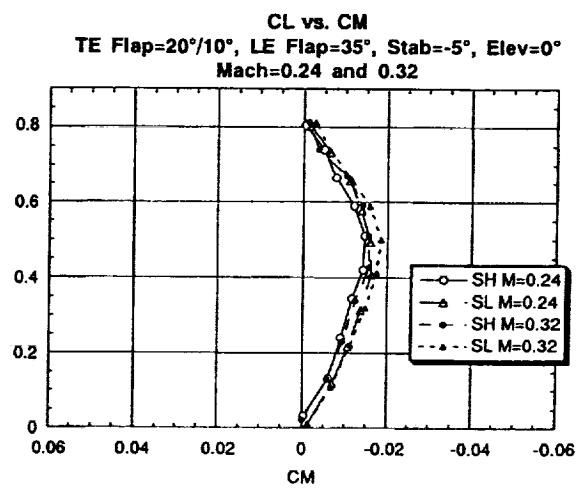

Wind-On Lift Drag Bookkeeping

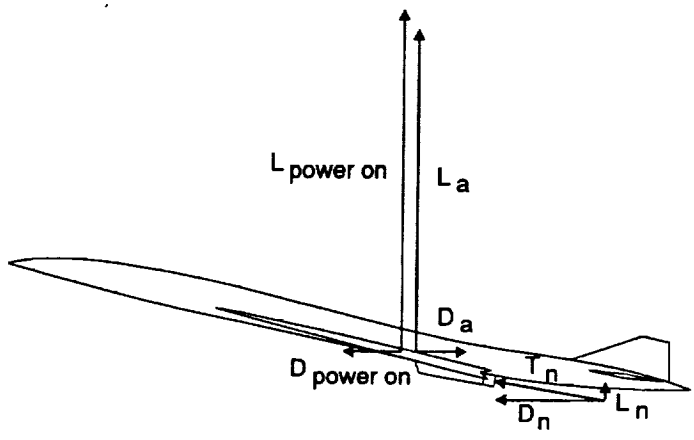

$L_{power\text{-}on}$ = gross lift measured power on

L_t = lift component of wind-on nozzle thrust measured during HIN

$D_{power\text{-}on}$ = gross drag measured power on

D_t = drag component of wind-on nozzle thrust measured during HIN

T_n = corrected wind-on nozzle thrust measured during HIN

L_a = aerodynamic lift = $L_{power\text{-}on} - L_t$

$C_{L_a} = L_a / (qS)$

D_a = aerodynamic drag = $D_{power\text{-}on} - D_t$

$C_{D_a} = D_a / qS$

aerodynamic pitching moment coefficients calculated using similar methodology

$L/D_a = L_a / D_a$

C_q = nozzle inlet suction coefficient = $mdot_{ejector\ inlets}/(V_{inf} * S)$

C_t = nozzle thrust coefficient (based on wind-on thrust from HIN) = $T_n/(qS)$

Comparison of Power Off and Power on (thrust removed) Lift Coefficients as a Function of Trailing Edge Flap Deflection
M=0.32, LEF=35°,tail off, NPR_{nom}=3.4, SAR 2.8, CAM, top-bottom inlets

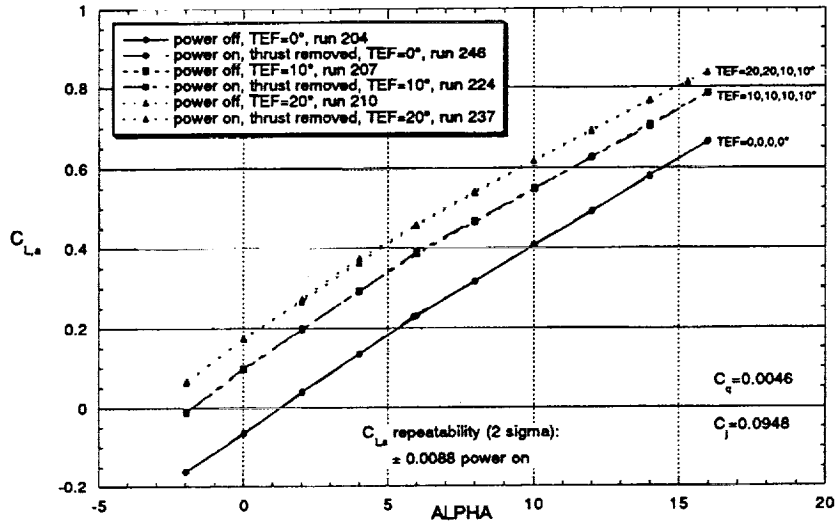

Comparison of Power Off and Power on (thrust removed) Drag Polars as a Function of Trailing Edge Flap Deflection
M=0.32, LEF=35°, tail off, NPR_{nom}=3.4, SAR 2.8, CAM, top-bottom inlets

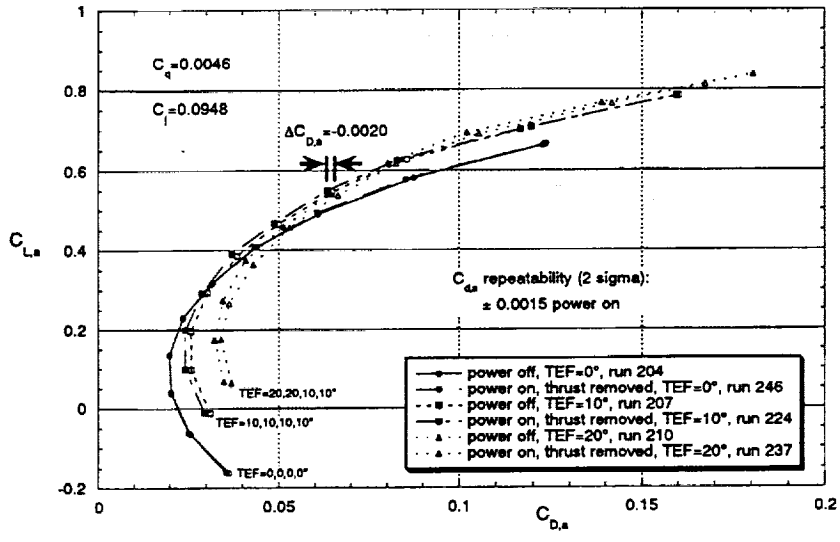

Comparison of Power Off and Power on (thrust removed) Pitching Moment Coefficients as a Function of Trailing Edge Flap Deflection
M=0.32, LEF=35°, tail off, NPR_{nom}=3.4, SAR 2.8, CAM, top-bottom inlets

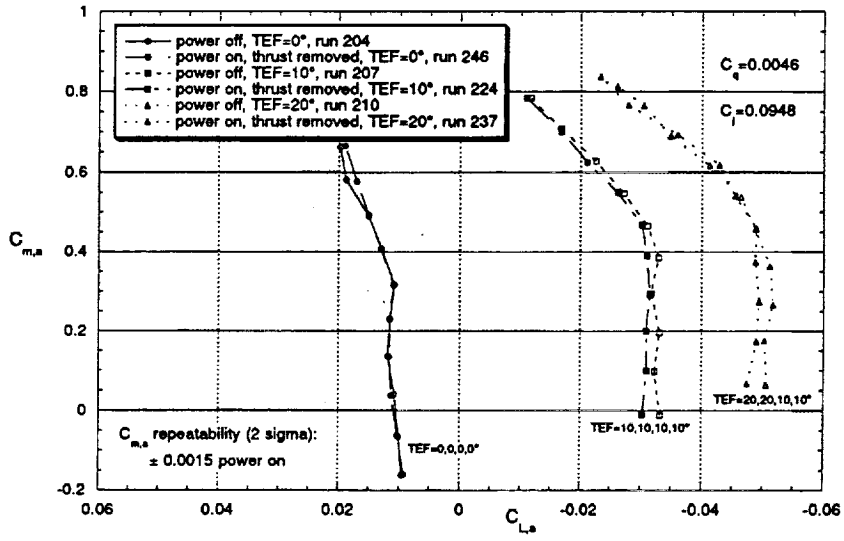

The previous figures present comparisons of power off and power on lift, drag, and pitching moment coefficients for three trailing edge flap deflection angles (ACONF =26, 13, and 29). The power on data were obtained using the CAM SAR 2.8 suppressor nozzle (NCONF=14, top-bottom ejector inlet orientation) operating at a nominal nozzle pressure ratio, NPR_{nom}=3.4. This condition corresponds to an ejector inlet suction coefficient, C_q=0.0046 and a jet thrust coefficient, C_j= 0.0948. The power on, thrust removed aerodynamic coefficients were calculated by subtracting the components of corrected, wind on thrust measured during the HEAT Isolated Nozzle (HIN) test from the measured lift, drag, and pitching moments prior to calculation of the aerodynamic coefficients.

The lift curves illustrate that the effects of nozzle inlet suction flows and the nozzle plume have very little effect on the lift of the Reference H model relative to the power off aerodynamic characteristics for the three flap deflections tested. The drag polars illustrate the favorable effect of inboard nozzle operation on the drag characteristics of the model. As the trailing edge flap angle is increased the difference between the power off and power on drag coefficients, $\Delta C_D = C_{D,a} - C_{D,power\ off}$, becomes progressively more negative. This favorable drag increment has a magnitude of approximately 20 counts at alpha=10° and a trailing edge flap deflection of 10°. The pitching moment curves illustrate that the power effect slightly increases the nose up pitching moment of the aircraft at the higher flap deflections.

Comparison of Power Off and Power On (thrust removed) L/D Ratios
M=0.32, LEF=35°, tail off, NPR_{nom}=3.4, SAR 2.8, top-bottom inlets

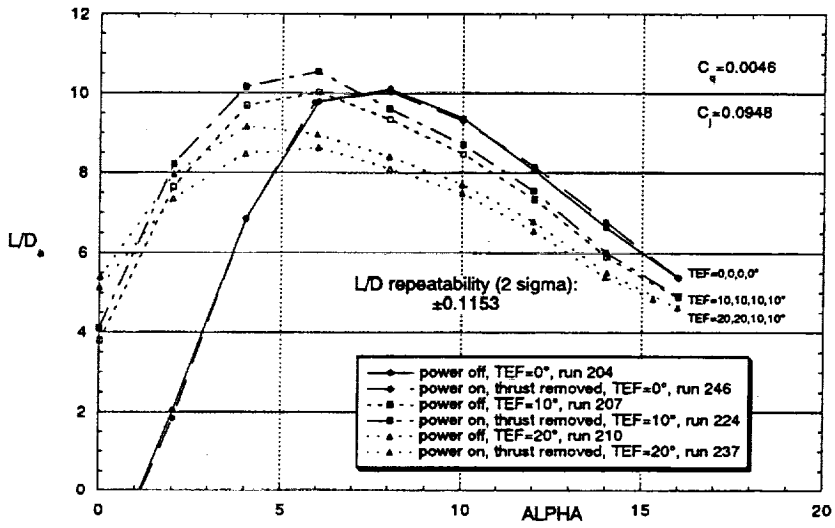

This figure presents the power off and power on, thrust removed L/D as a function of model angle of attack. At a trailing edge flap deflection of 0°, there is virtually no effect on vehicle L/D due to operation of the inboard nozzle. A deflection angles of 10° and 20°, operation of the nozzle has a beneficial effect on L/D. The magnitude of this effect is approximately +0.2 L/D at the nominal climbout angle of attack of 10° and trailing edge flap deflection of 10°.

The following figure shows the wing and flap upper surface pressure taps. In the following figures, pressure distributions will be presented for 2 rows on the inboard flap, 3 rows on the mid flap and 4 rows upstream of the ejector inlet (shown in the shaded area). Pressures from the lower surface will also be shown. Pressure distributions for the lower flap surface will also be shown which included 2 rows on the inboard flap and 3 rows on the outboard flap.

WING UPPER SURFACE PRESSURE TAPS

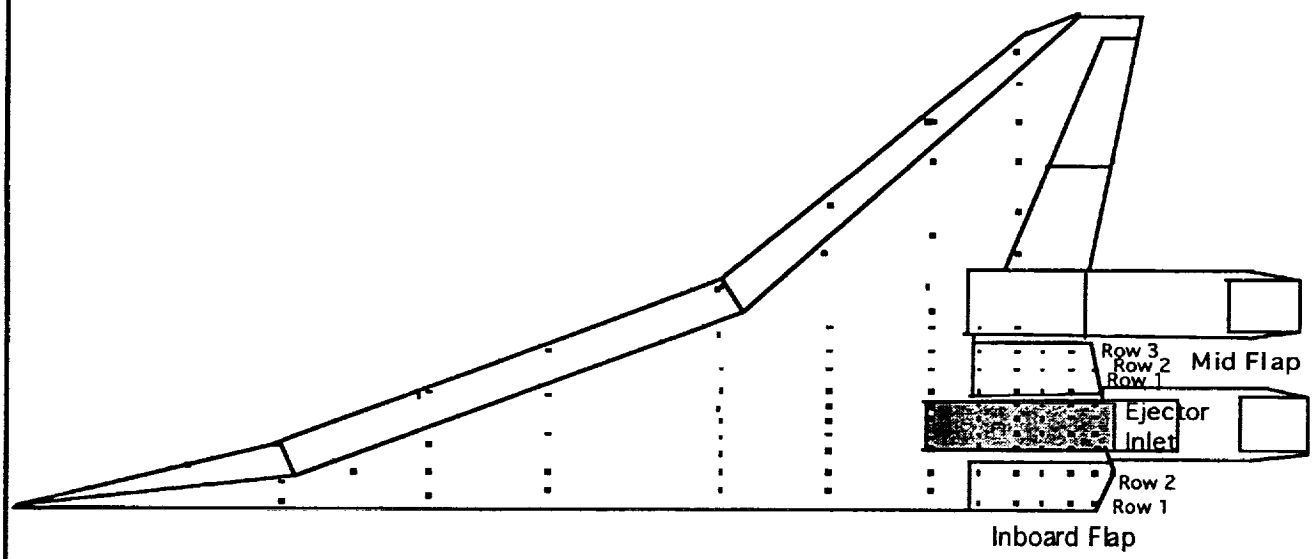

The following figures show power-on effects of the inlet flow on the pressure data for the inboard and outboard flaps and the region just upstream of the ejector inlet . The figures compare a power-off run with 2 power-on runs at Nozzle Pressure Ratios (NPR) 3.4 and 4.5. These NPR's were selected as key points of comparison since the nominal NPR for the power-on runs was 3.4 and maximum NPR tested was 4.5. The model configuration for all 3 runs was ACONF=29 (leading-edge flap=35°, trailing-edge flap=20°/20° and tail Off). For these comparisons, Mach number was held at 0.32 and Alpha was set at 14°. For the power-on runs, the Cold Aerodynamic Model (CAM) mixer/ejector nozzle was used with a Suppressor Area Ratio (SAR) of 2.8.

For the given configuration, the pressure distributions show the inlet flow effecting the local flowfield of the upper surface mid flap. All three pressure rows on the mid flap showed a reduction in pressure for NPR's=3.4 and 4.5. The second figure showed no effect on the data for the region upstream of the ejector inlet for this configuration.

This reduction in the pressure distributions supports the results of the power-induced aerodynamic effects where higher L/D ratios were reported for power-on conditions. In addition, the reductions in pressure distribtutions were the same for both power settings of NPR=3.4 and 4.5 indicating that the secondary inlet flows stay the same at these power settings.

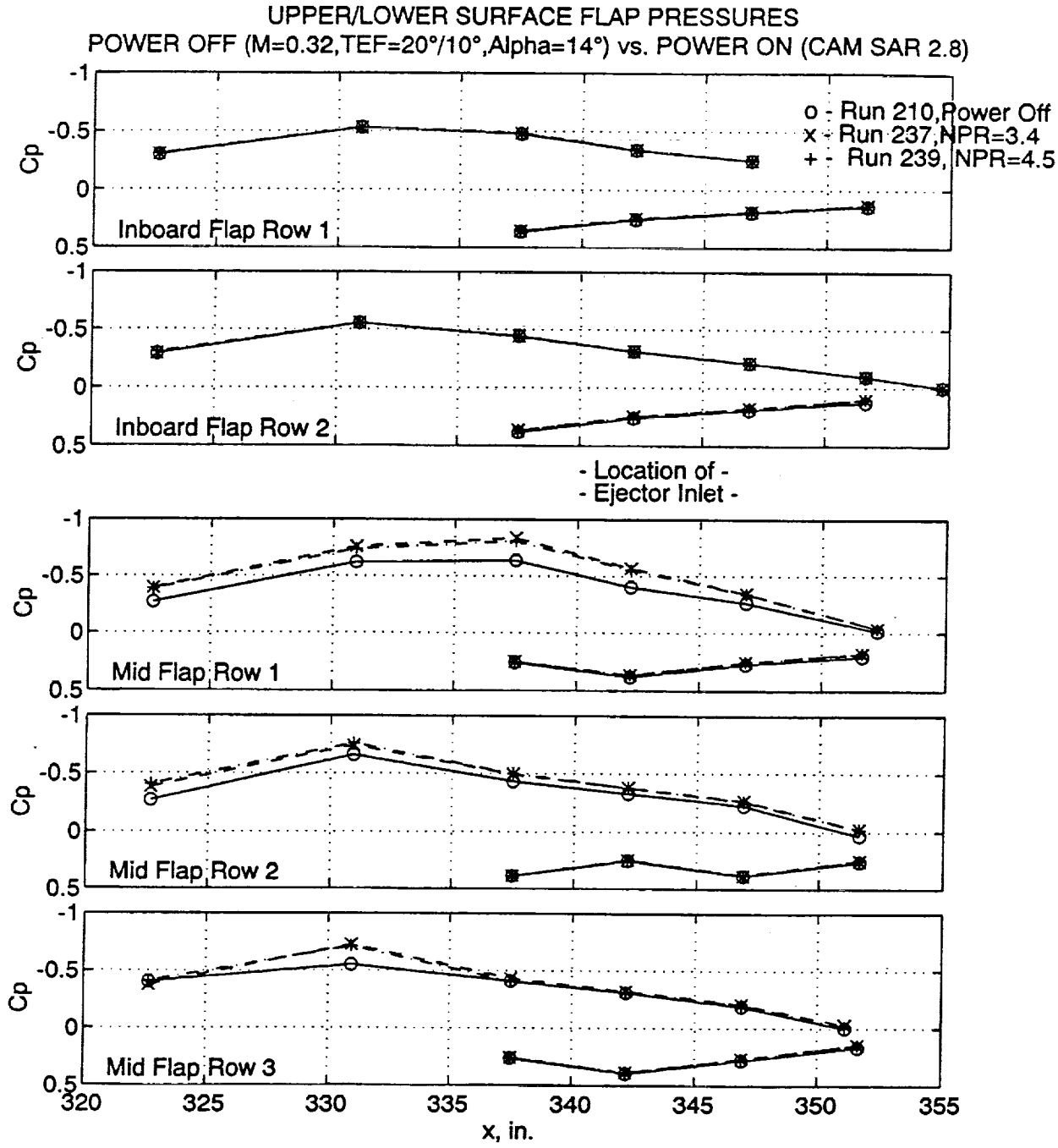
UPPER/LOWER SURFACE FLAP PRESSURES
POWER OFF (M=0.32,TEF=20°/10°,Alpha=14°) vs. POWER ON (CAM SAR 2.8)
o - Run 210,Power Off
x - Run 237,NPR=3.4
+ - Run 239, NPR=4.5
Inboard Flap Row 1
Inboard Flap Row 2
- Location of -
- Ejector Inlet -
Mid Flap Row 1
Mid Flap Row 2
Mid Flap Row 3
Cp
-1
-0.5
0
0.5
320
325
330
335
340
345
350
355
x, in.

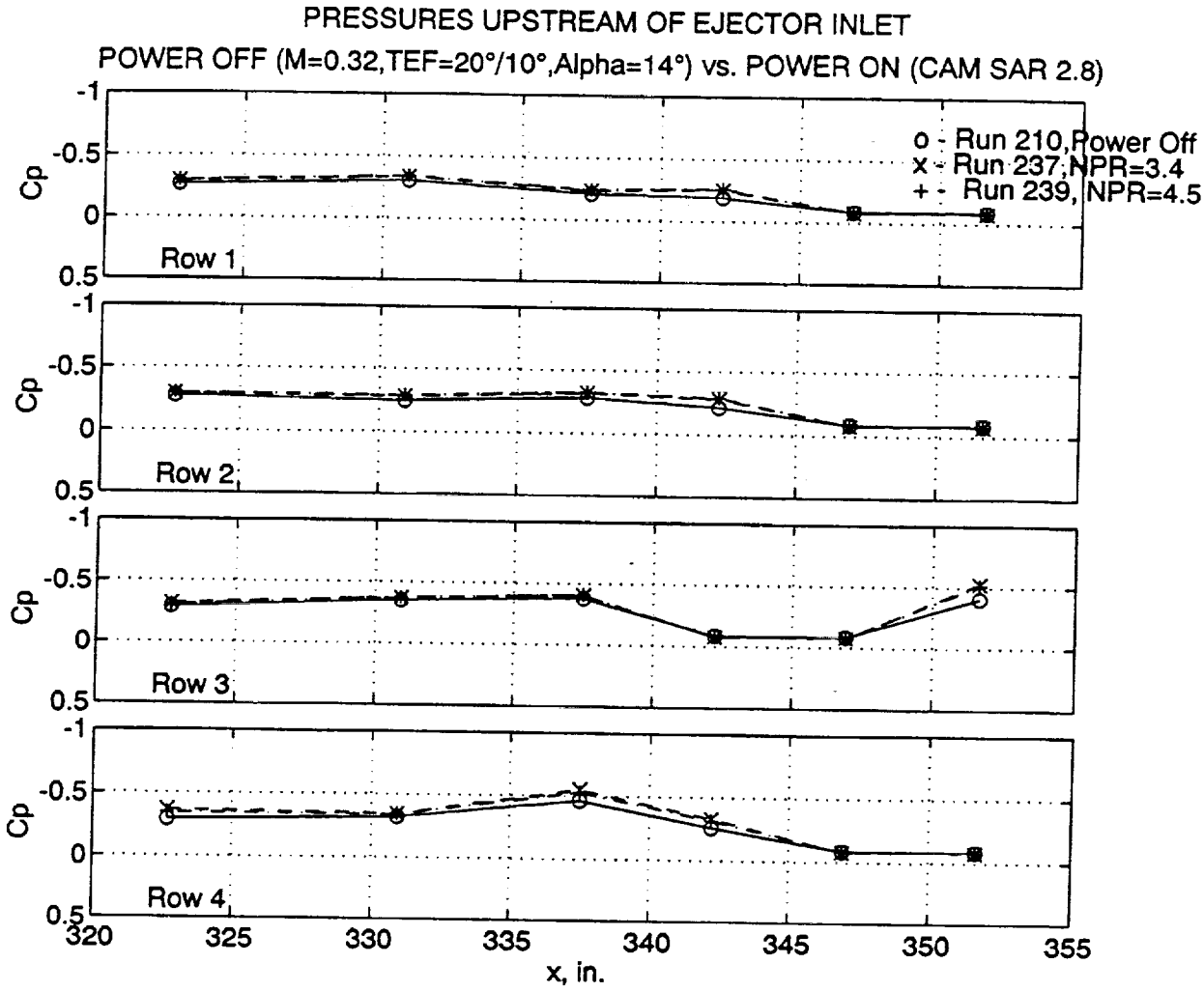
PRESSURES UPSTREAM OF EJECTOR INLET
POWER OFF (M=0.32,TEF=20°/10°,Alpha=14°) vs. POWER ON (CAM SAR 2.8)
o - Run 210,Power Off
x - Run 237,NPR=3.4
+ - Run 239, NPR=4.5
Cp
Row 1
Row 2
Row 3
Row 4
-1
-0.5
0
0.5
320
325
330
335
340
345
350
355
x, in.

Side View of Ejector Inlets on Sides of Nacelle and Relative Location of Trailing Edge Flaps

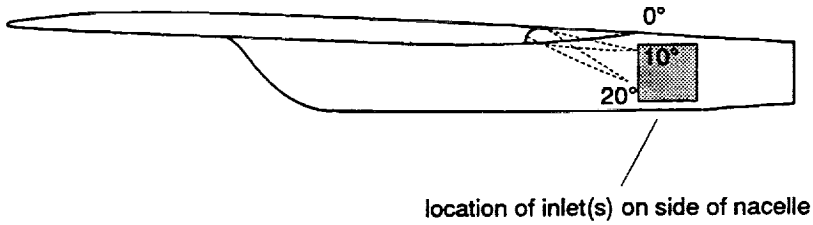

This figure illustrates the location of trailing edge flaps 1 and 2 relative to the longitudinal position of the ejector nozzle seconday inlets in the sides of the nacelle. The dotted lines depict the positions of the flaps when set at the 10° and 20° deflection angles. At 20° deflection, the pressure on the upper surfaces of the flaps is reduced by the suction of the ejector inlets.

Comparison of Power Off and Power on (thrust removed) Lift Coefficients as a Function of Trailing Edge Flap Deflection
M=0.32, LEF=35°, tail off, NPR_{nom}=3.4, SAR 2.8, CAM, SIDE-SIDE INLETS

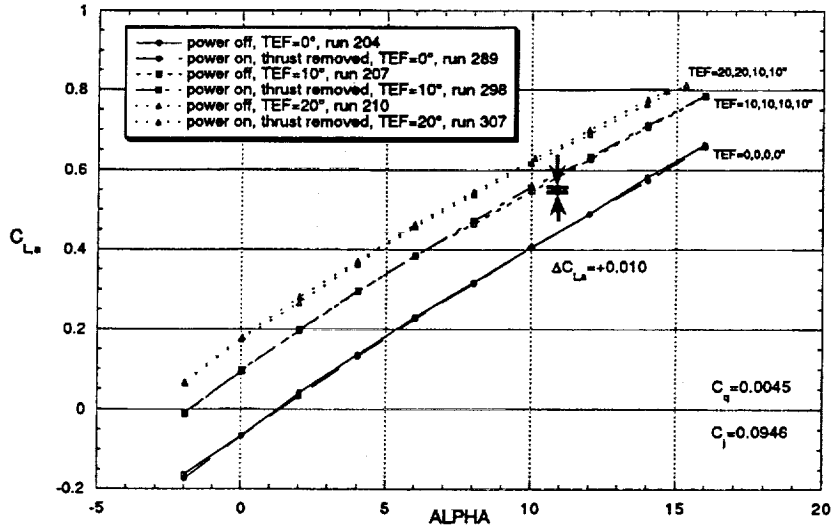

Comparison of Power Off and Power on (thrust removed) Drag Polars as a Function of Trailing Edge Flap Deflection
M=0.32, LEF=35°, tail off, NPR_{nom}=3.4, SAR 2.8, CAM, SIDE-SIDE INLETS

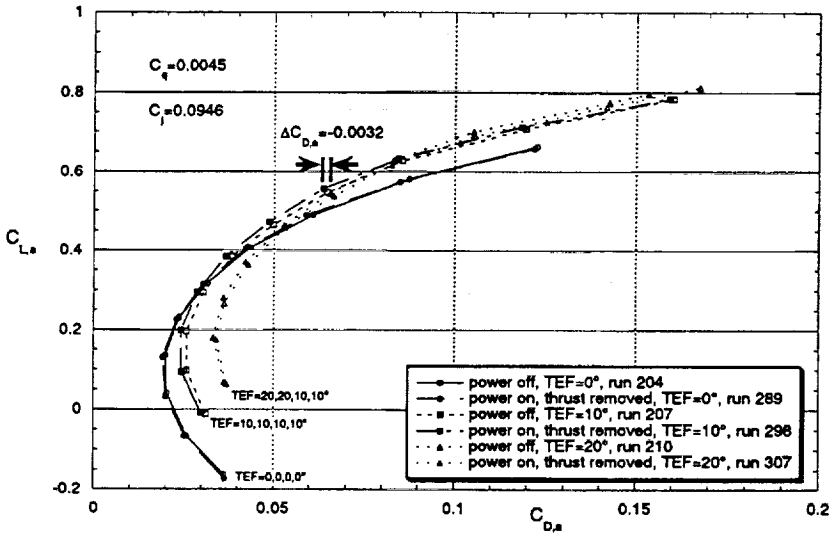

Comparison of Power Off and Power on (thrust removed) Pitching Moment Coefficients as a Function of Trailing Edge Flap Deflection
M=0.32, LEF=35°, tail off, NPR_{nom}=3.4, SAR 2.8, CAM, SIDE-SIDE INLETS

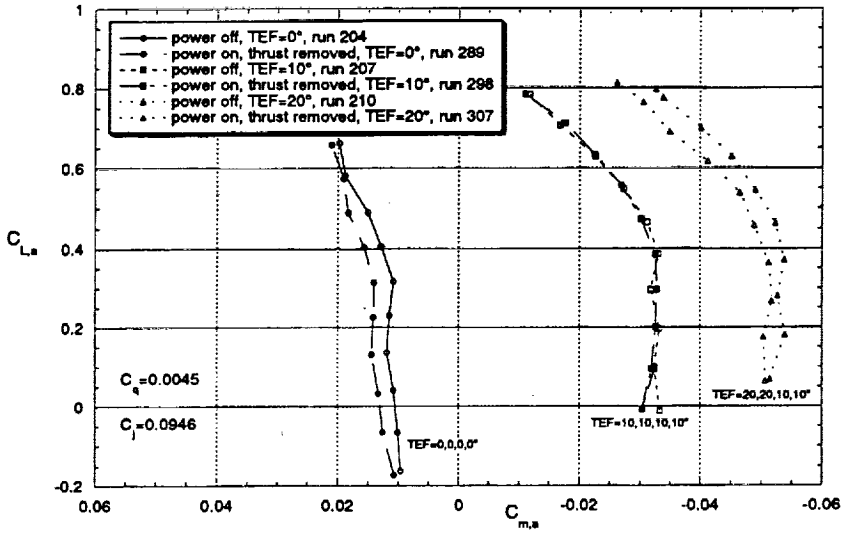

The previous three figures present comparisons of power off and power on lift, drag, and pitching moment coefficients for three trailing edge flap deflection angles (ACONF =26, 13, and 29). The power on data were obtained using the CAM SAR 2.8 suppressor nozzle (NCONF=16, *side-side ejector inlet orientation*) operating at a nominal nozzle pressure ratio, NPR_{nom}=3.4

The lift curves illustrate that the side-side inlet orientation has slightly beneficial effect on the lift of the model ($\Delta C_{L,a}$=+0.01) relative to the power off aerodynamic characteristics at trailing edge flap deflections of 10° and 20° especially in the range of the nominal climbout angle of attack, alpha= 10°. The drag polars illustrate that favorable propulsion induced drag effects with the side-side inlet configuration are larger than with the top-bottom arrangement. In the the side-side configuration, the propulsion induced drag increment, ΔC_D=-0.0032 compared with the value of -0.0020 in the top-bottom case at alpha=10° and a trailing edge flap deflection of 10 degrees. The pitching moment curves show that the side-side inlet orientation results in significant changes in overall model pitching moment as as flap deflection is changed. The magnitude of the propulsion induced change in pitching moment over the range 0°<alpha<16° is approximately equivalent to a 1° change in the incidence of the horizontal tail.

Comparison of Power Off and Power On (thrust removed) L/D Ratios
M=0.32, LEF=35°, tail off, NPR_{nom}=3.4, SAR 2.8, CAM, SIDE-SIDE INLETS

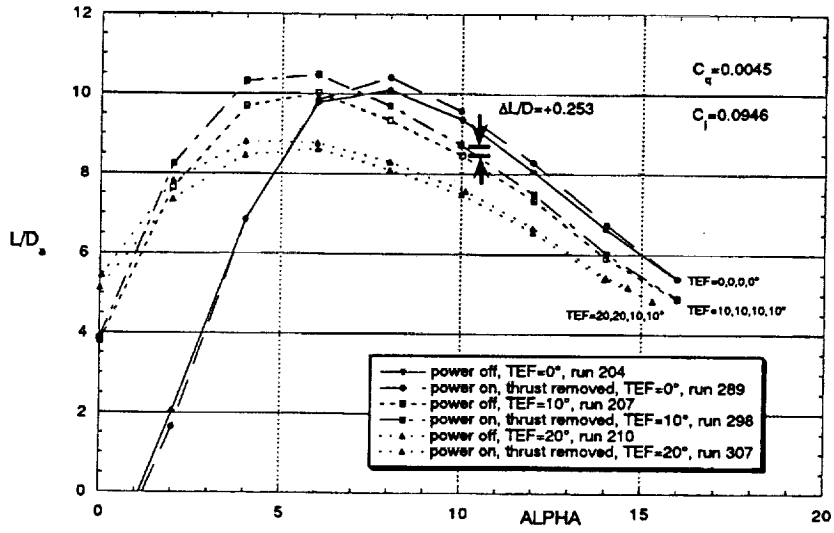

This figure presents comparisons of power off and power on L/D for three trailing edge flap deflection angles (ACONF =26, 13, and 29) with the ejector inlets in the *side-side orientation.* The combined effects of propulsion induced changes in lift and drag results in a favorable effect on L/D for all deflection angles of the trailing edge flaps within the range of 5°<alpha<15°. For the side-side inlet configuration (at the nominal climbout angle of attack of 10° and trailing edge deflection of 10°), the improvement in L/D is approximately 0.25 L/D. The beneficial effect falls off rather steelpy from 0.63 L/D at alpha=4° to essentially zero at alpha=16°.

The following figures show the effect of the ejector inlet flow for a rotated nozzle configuration with side/side inlets. The model configuration used for these runs was ACONF=29 (leading-edge flap=35°, trailing-edge flap=20°/20°, and tail off). The flow conditions for these comparisons were set at nominal takeoff conditions of Mach number=0.32 and alpha=10°. For the power-on runs, the same mixer/ejector nozzle as in the previous figures (CAM SAR 2.8) was used but at an orientation of 90° clockwise. This orientation moves the inlets from a top/bottom orientation to a side/side orientation.

The effect of the side/side inlets on the flap pressure distributions show a reduction in pressure data for both the inboard and mid flaps. As with the results of the top/bottom inlets, this reduction in pressure distribution supports the higher L/D results as reported in the power-induced aerodynamic effects section. Both the flap pressure distribution and power-induced aerodynamic results yield the same conclusion that the effects of the powered mixer/ejector nozzle improve the lift-to-drag performance of the high-lift system.

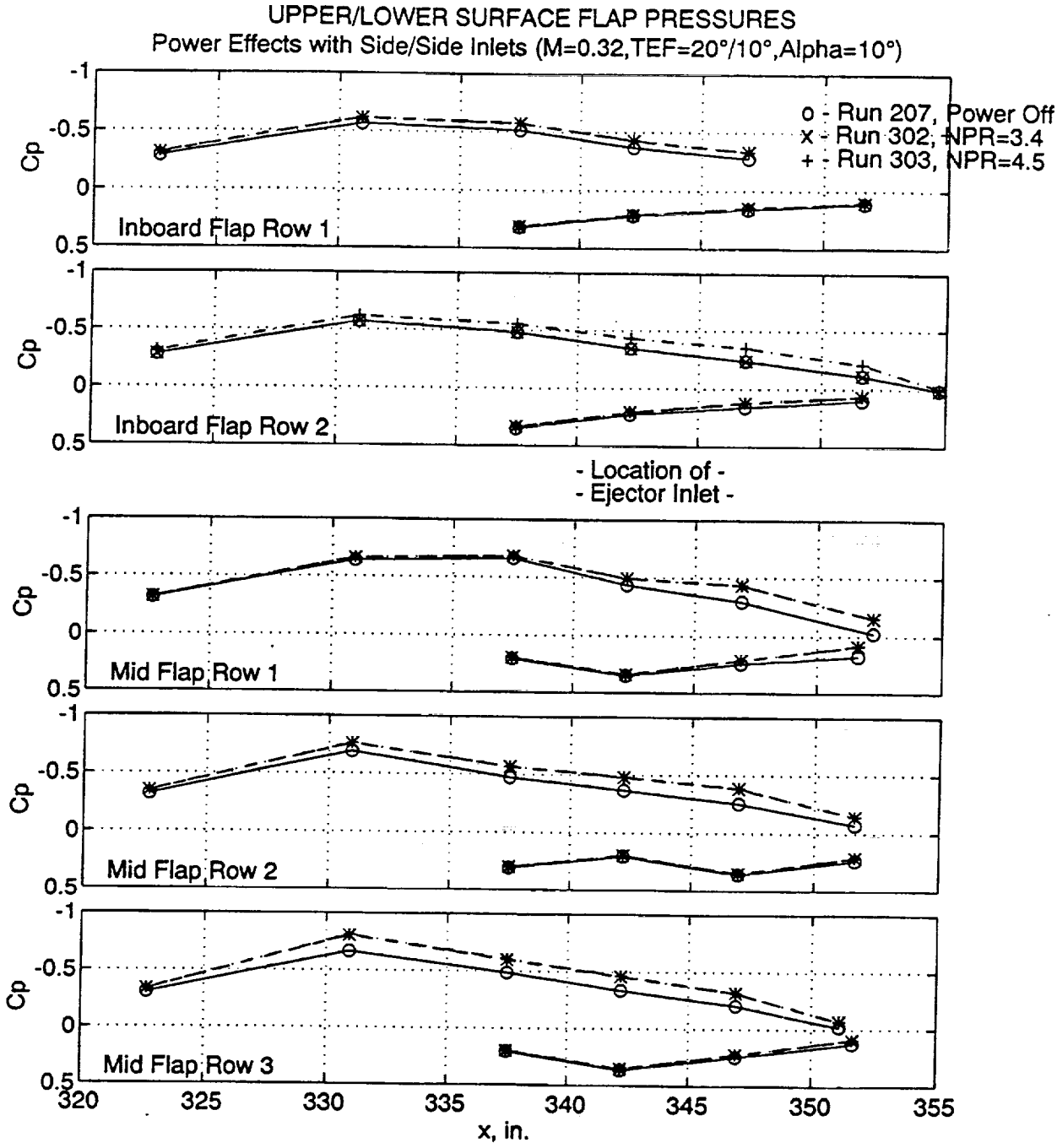
UPPER/LOWER SURFACE FLAP PRESSURES
Power Effects with Side/Side Inlets (M=0.32,TEF=20°/10°,Alpha=10°)
o - Run 207, Power Off
x - Run 302, NPR=3.4
+ - Run 303, NPR=4.5
Inboard Flap Row 1
Inboard Flap Row 2
- Location of -
- Ejector Inlet -
Mid Flap Row 1
Mid Flap Row 2
Mid Flap Row 3
Cp
-1
-0.5
0
0.5
320
325
330
335
340
345
350
355
x, in.

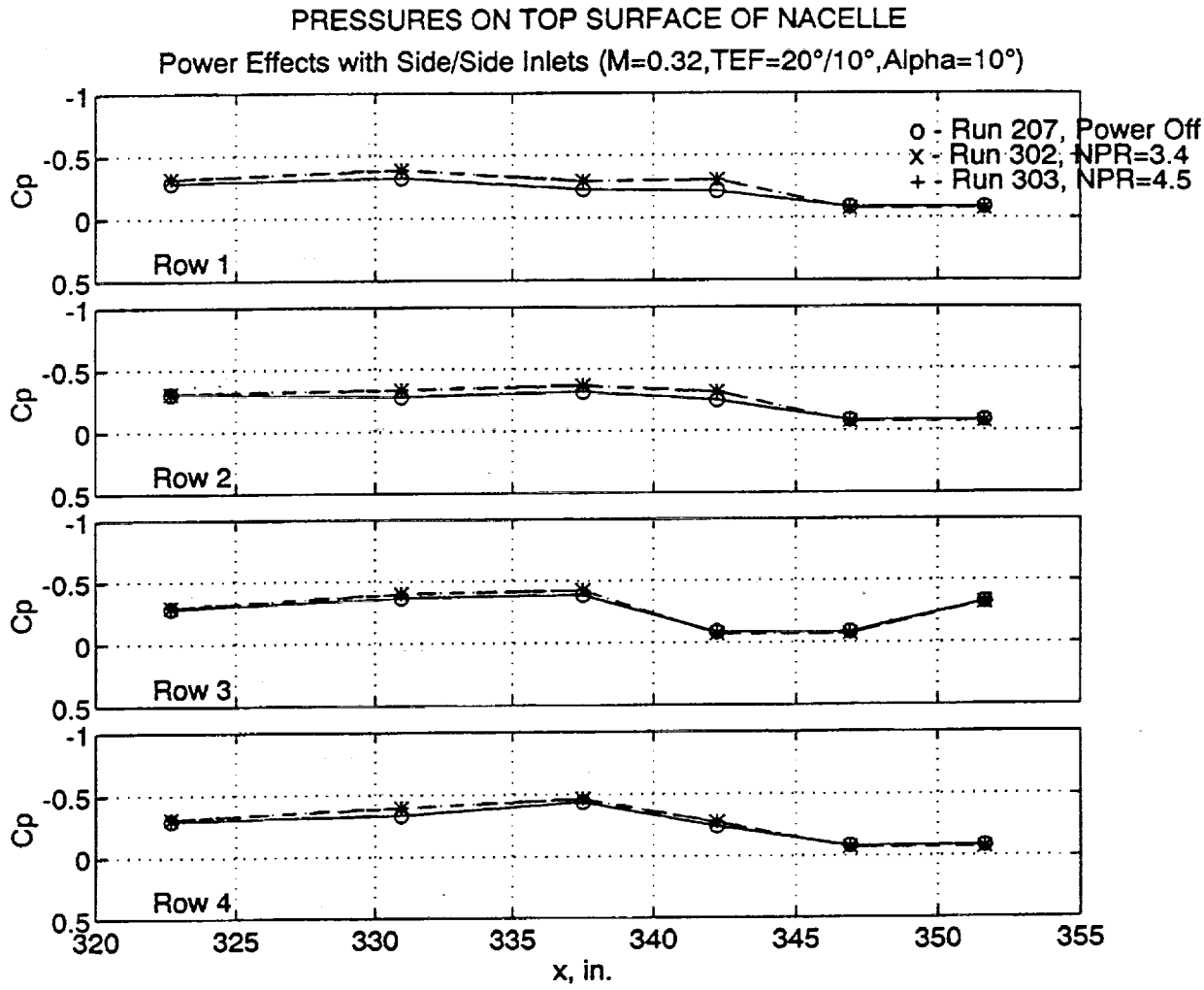
PRESSURES ON TOP SURFACE OF NACELLE
Power Effects with Side/Side Inlets (M=0.32,TEF=20°/10°,Alpha=10°)
o - Run 207, Power Off
x - Run 302, NPR=3.4
+ - Run 303, NPR=4.5
Cp
Row 1
Row 2
Row 3
Row 4
-1
-0.5
0
0.5
320
325
330
335
340
345
350
355
x, in.

Location of Overwing Support Pylon Fin Simulator Relative to Upper Ejector Inlet

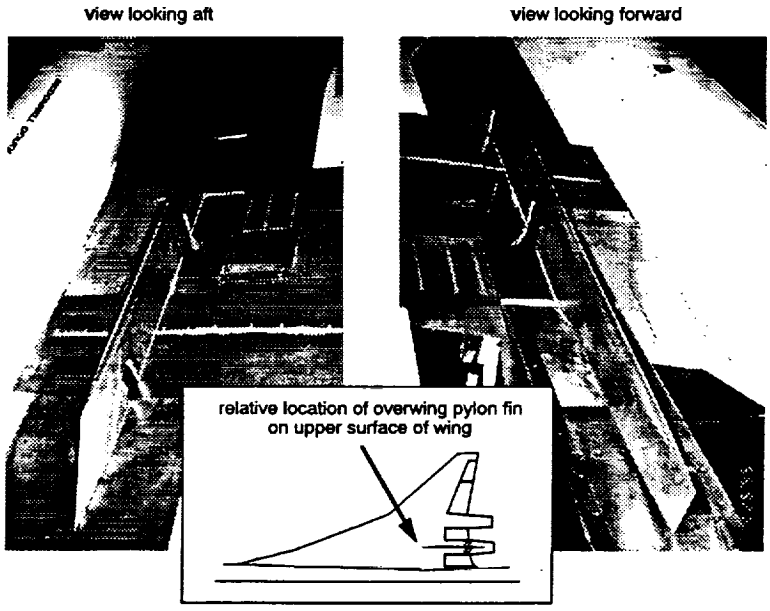

This figure shows photographs of the pylon fin simulator mounted over the inboard nozzle of the semi-span model. The primary purpose of the fin is to provide needed structural support for the outboard nozzle of the full scale aircraft. Although the fin is intended to mounted above the outboard station, its first order effects were evaluated on the inboard station of the HEAT model since only the inboard nozzle was powered. The fin covers approximately 11% of the width of the ejector inlet and the height of the fin is approximately 48% of the ejector inlet width. The fin is approximately six feet long (~3/8 of local wing chord).

Effect of Pylon Fin on Thrust-Removed L/D
M=0.32, LEF=35°, TEF=10°, tail off, NPR_{nom}=3.4, SAR 2.8, CAM, TOP-BOTTOM INLETS

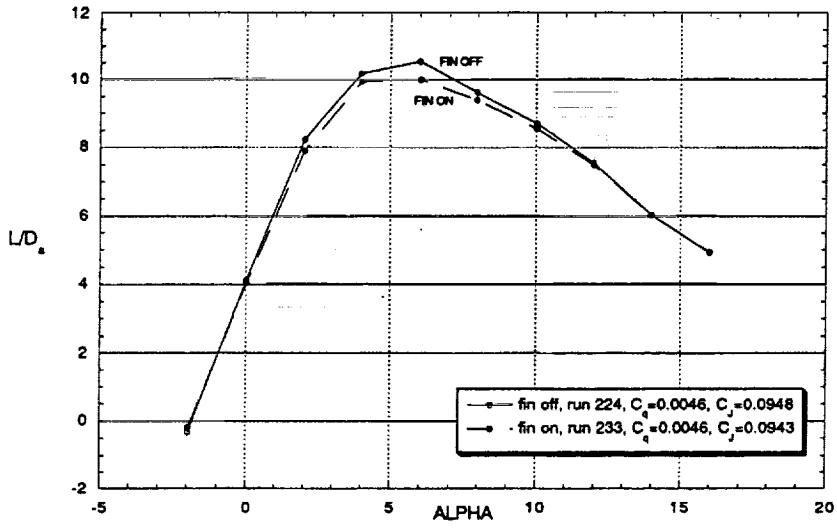

This figure presents comparisons of power off and power on L/D between the pylon fin off and pylon fin installed configurations. There is a consistent though small decrease in L/D when the fin is installed. The magnitude of this effect is less than approximately 0.2 L/D at alpha=10°. The relative effects of an overwing pylon fin may be different when installed at the outboard nozzle station because of the greater spanwise flows observed there.

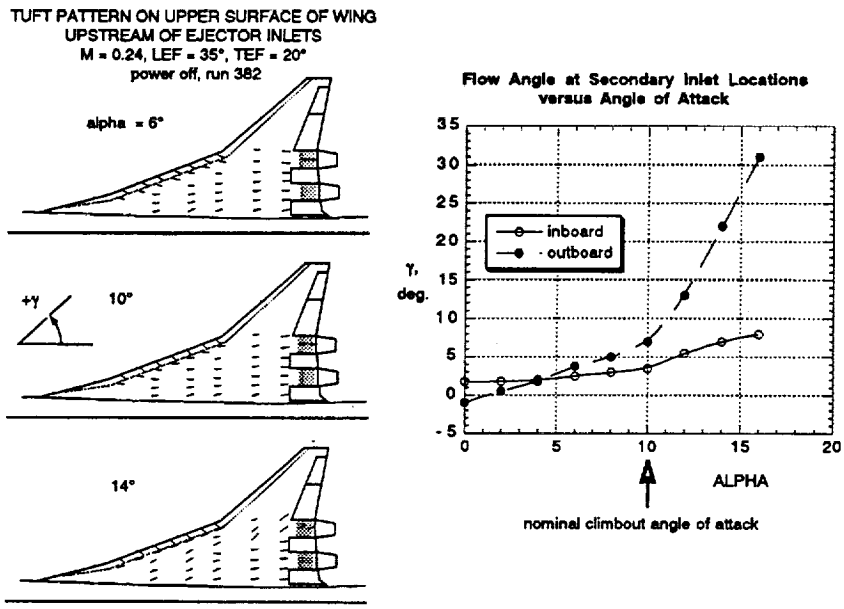

This figure illustrates the surface flow topology on the upper surface of the wing in which the upper inlet of the suppressor nozzle operated. The intent of this figure is to depict the environment in which the upper ejector inlets operate and to determine if any flow features would contribute to large changes in nozzle performance. The graphic on the left shows the surface flow pattern for three angles of attack bracketing the the flight regime of the aircraft at climbout/approach conditions. The patterns and flow angles were generated from video images of surface tufts taken during run 382. At alpha=6°, the flow on the upper surface appears to be fully attached. Between alpha=10° and 14°, flow separation occurs along the mid section of the leading edge immediately dowstream of the leading edge flap hinge line This separation and resulting vortical flow causes large changes in the surface flow angles. The lines of separation and attachment can be identified in the surface flow pattern. The plot on the right illustrates the variation in spanwise flow angularity over the full angle of attack range at the locations of the upper ejector inlets shown as shaded rectangles on the left hand sketch. The two curves on the plot show the differences in flow angularity at the location of the inboard and outboard nozzle secondary inlets. Flow from root to tip is expressed as a positive γ flow angle. The open symbols on the graph show that the spanwise flow at the inboard station transitions relatively smoothly from γ=2° at alpha=0° to a maximum value of γ=8° at alpha=16°. There is a small increase in slope of the curve at around alpha=10°. Over the range of 6<alpha<14°, the small changes in spanwise flows are probably not sufficient to cause large changes in nozzle performance. The solid symbols on the chart show the variation in flow angulatity at the location of the outboard nozzle inlet. Compared with the inboard inlet location, the curve shows larger spanwise flow angles at the outboard inlet location for alpha>4°. There is an abrupt increase in the slope of the curve at alpha=10°. This is probably due to onset of vortical flow at angles of attack greater that 10°. This phemomenon is highly planform and leading edge dependent and should be examined carefully in future investigations since the high spanwise flow angles could affect outboard nozzle performance. Because the flow visualization was performed power off, it is not known how the patterns change with nozzle operating.

Net Propulsive Force Bookkeeping

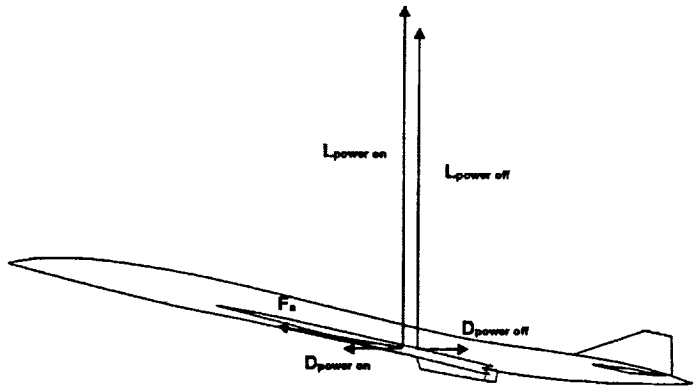

F_a = magnitude of vector sum of power on & power off lift and drag

= installed nozzle thrust *PLUS* induced aerodynamic effects

$C_{L,power\ on}$ = gross lift coefficient from power on runs

$C_{L,power\ off}$ = lift coefficient from power off runs corrected for drag tare plate pressure

$C_{D,power\ on}$ = gross drag coefficient from power on runs

$C_{D,power\ off}$ = drag coefficient from power off runs corrected for drag tare plate pressure

F_a = net propulsive force = $SQRT\{(C_{L,power\ on} - C_{L,power\ off})^2 + (C_{D,power\ on} - C_{D,power\ off})^2\} * q * S$

T_n = corrected wind-on nozzle thrust measured during HIN

C_{npl} = net propulsive force coefficient = F_a / T_n

where

q = corrected test section dynamic pressure

S = wing reference area (semi-span)

The net propulsive force parameter, F_a, is calculated by multiplying the square root of the sum of the squares of the differences between the power on and power off lift and drag coefficients by the power on dynamic pressure and wing reference area. This calculation yields a dimensional quantity with units of pounds force. This number represents the magnitude of the vector sum of the power on minus power off lift and drag. The magnitude of this parameter includes both changes in nozzle thrust performance due to the the wing/high lift systems flowfield as well as changes in the L/D performance of the airframe resulting from operation of the inboard nozzle. Since there was no force balance between the nozzle and the wing of the HEAT model, it is not possible to determine which of the two phenomena (nozzle thrust changes or airframe L/D changes) is the dominant factor in the establishing the magnitude of the force vector. The net force is non-dimensionalized by the wind on thrust of the nozzle, T_n, measured during the HEAT Isolated Nozzle (HIN) test for all subsequent plots of this parameter. This approach was used to permit the magnitude of the changes to be consistently compared with a known quantity.

Variation in Net Propulsive Force Coefficient as a Function of NPR
M=0.32, LEF=35°, TEF=10°, SAR 2.8, CAM, top-bottom inlets

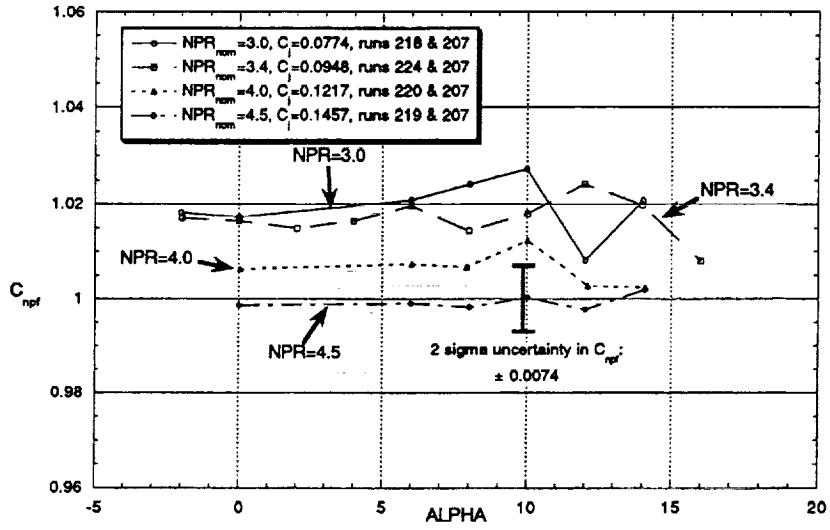

This figure presents comparisons of the ratio of the net propulsive force to the wind on thrust measured during the HEAT Isolated Nozzle (HIN) test for four nozzle pressure ratios 3.0<NPR<4.5. These conditions correspond to a range of jet thrust coefficients of 0.0074<C_j<0.1457. The power on data were obtained in the prime model configuration (ACONF=13) using the CAM SAR 2.8 suppressor nozzle (NCONF=14, top-bottom ejector inlet orientation). Uncertainties in the value of the net propulsive force ratio were determined by comparing the peak-to-peak values of the parameter calculated from the data of power on, alpha=10° repeat runs 98, 152, and 350 and the power off data of run 86. The value of the uncertainty in the coefficient, C_{npf}, is +/- 0.0074.

As nozzle pressure ratio increases, there is a decrease in the propulsive force coefficient. At NPR= 3.0 the average value of the net propulsive force coefficient over the full angle of attack range starts at about 1.02 and decreases to a value slightly less than 1.0 at NPR=4.5. At the prime test condition of NPR=3.4 and alpha=10°, the net propulsive force coefficient has a value of 1.018. The fact that the coefficients are greater than 1.0 for NPR's less than 4.5, is consistent with the favorable interaction effect (less drag, more lift) between the nozzle and wing flowfields noted earlier.

A possible explanation for this beneficial power on effect is that the presence of the nozzle plume effectively creates a solid body within the potential flow around the model which is not present during the power off condition. The plume makes the body appear to have a greater fineness ratio and hence less drag relative to the power off configuration. The plume may also reduce the adverse pressure gradient on aft facing surfaces of the wing and fuselage due to its displacement of the potential flow streamlines near the aft end of the configuration. Increasing the nozzle pressure ratio may result in greater entrainment of flow into the plume and increased flow velocities and drag on the configuration.

The jet thrust coefficient of the nozzle, C_j, is defined as

$C_j = T_N/(qS)$

Comparison of Spanwise Distribution of Total Pressure Recovery Between Upper and Lower Ejector Inlets as a Function of Trailing Edge Flap Deflection M=0.32, LEF=35°, NPr_{nom}=3.4, SAR 2.8, TOP-BOTTOM INLETS

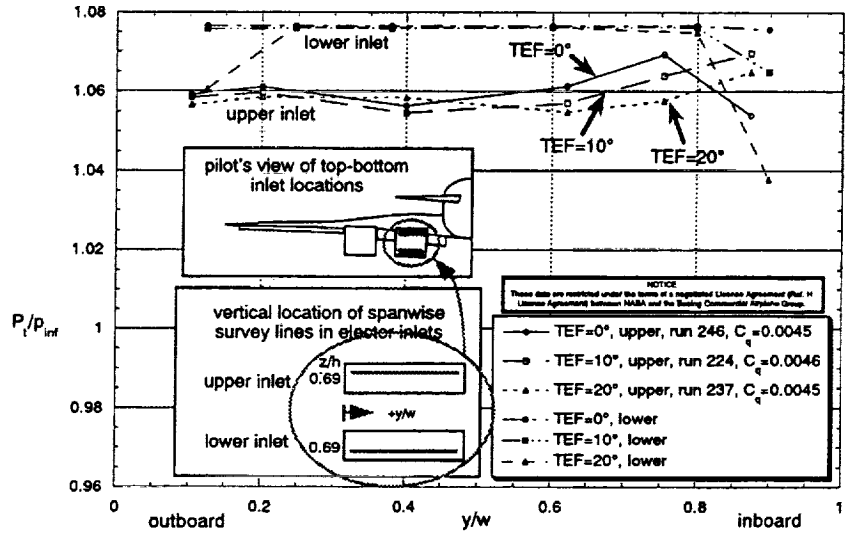

This figure illustrates the effect of trailing edge flap deflection on the spanwise distribution of total pressure recovery within the upper and lower ejector inlets. The spanwise total pressure recovery is shown as a fuction of the non-dimensional coordinate of the ejector inlet, y/w, at a single elevation within the ejector inlets corresponding to a non-dimensional position within the height of each inlet, z/h=0.69. The inset sketch shows the locations of the survey lines within the rectangular boundaries of the ejector inlet openings. The plot indicates that total pressure recovery of the upper ejector inlet is approximately 3-4% less than the values calculated for the lower inlet. This probably due to the thicker boundary layer on the upper surface of the wing relative to the boundary layer entering the lower inlet. The lower inlet total pressure recovery also shows much less spanwise sensitivity to changes in trailing edge flap deflection than the upper inlet. The recovery at the inboard edge of the lower inlet shows small decreases as the flap deflection is increased. In the region 0.5>y/w>0.75 the upper inlet pressure recovery decreases significantly with increasing flap deflection.

Comparison of Spanwise Distribution of Total Pressure Recovery Between Inboard and Outboard Ejector Inlets as a Function of Trailing Edge Flap Deflection M=0.32, LEF=35°, NPr_{nom}=3.4, SAR 2.8, SIDE-SIDE INLETS

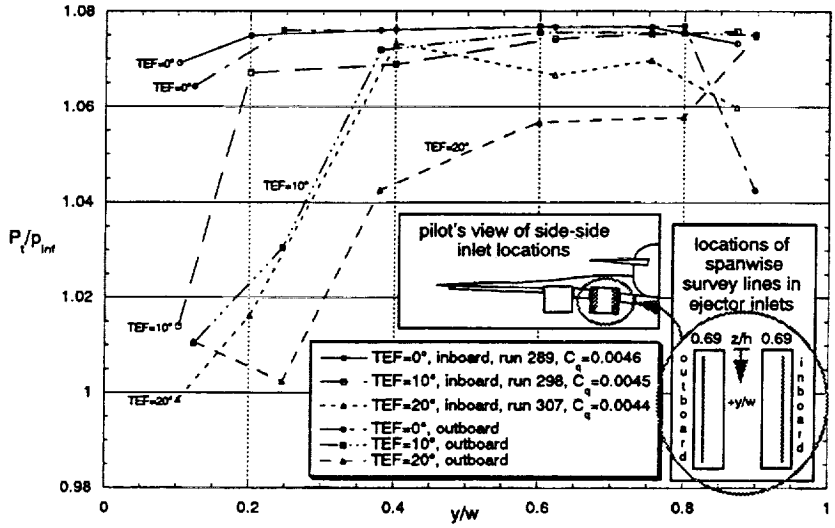

This figure illustrates the effect of trailing edge flap deflection on the spanwise distribution of total pressure recovery within the ejector inlets when oriented in the side-side configuration. At zero degrees flap deflection, both the magnitude and distribution of the pressure recovery are nearly identical for the inboard and outboard inlets. The plot shows that significant spanwise non-uniformity develops as the deflection of the trailing edge flaps is increased from 10° to 20°. Total pressure deficits as large as 7% are evident in the outboard inlet near y/w=0.25 for the 20° flap case. This is probably due to ingestion of the low energy wake from the trailing edge of the flaps. The side-side inlet configuration also shows a greater acoustic installation effect than the top-bottom orientation. This effect may be partially due to the non-uniformity in the inlet flow conditions.

Acoustics Summary and Conclusions

- ASME and RC nozzles generated similar acoustic spectra within 2 dB.
- Compared to static operation, ASME jet noise in flight was decreased downstream and increased upstream.
- Compared to a point source, distributed jet sources result in a small increase in extrapolated noise.
- ASME jet noise increased with nozzle pressure ratio at a faster rate than with the suppressor .
- The greater the suppressor area ratio (SAR), the better the noise suppression especially at NPR of 4.0 and above where the the SAR 2.5 was around 4 EPNdB louder than SAR 3.3.
- *The penalty due to installation of the suppressor on the HEAT model was only around 0.7 EPNdB for a baseline condition although this changed with off-design configurations.*

  For example, with the inboard flap angles set to 20°, the installation effect is around 1.6 EPNdB. With side-to-side inlets the installation effect was 2.8 EPNdB (see Allen, HEAT Workshop).
- The approach noise PNL values are increased up to 4 PNdB by installation on the HEAT wing.
- Suppression was effective over the entire audio range.
- Suppression never exceeded 15 EPNdB (NPR = 3.4) and decreased with either increases in nozzle pressure ratio or decrease in SAR. The least suppression (SAR 2.8, NPR = 4.5) was only 7 EPNdB.
- Thrust loss of the isolated suppressors varied from 5 percent (static operation) to 14 percent in flight. The ratio of suppression to percent thrust loss varied from 0.5 to 1.9 EPNdB / percent thrust loss.

Aero Summary and Conclusions

The propulsion-induced effects on a 13.5%-scale, half-span model of a representative HSCT configuration were measured during operation of a single, candidate ejector suppressor nozzle mounted on the inboard station of the wing. The results of the aerodynamic analyses of the induced effects of propulsion system can be summarized as follows:

Lift

Small favorable impact on lift for all configurations analyzed (0.01 to 0.02 C_{L_a}).
Largest favorable effect observed with side-side inlets at 20° flap deflection.

Drag

Favorable impact on drag for most configurations analyzed (20 to 32 counts less drag).
Pylon fin simulator causes small increase in model $C_{D,i}$ relative to fin off configuration.

Pitching Moment

Side-side inlet configuration shows small change in $C_{m,i}$ with trailing edge flap deflection.

L/D

Positive increments varying from approximately 0.5 to 0.15 L/D for prime model configuration.
Pylon fin causes reduction in L/D when mounted above inboard nozzle.

Wing & Nozzle Flowfield

Significant change in spanwise flow on upper surface of wing due to angle of attack.
Inlet orientation has dramatic effect on inlet total pressure distortion.

Wing/Flap Surface Pressures

Reduction in wing upper surface C_p near ejector inlets with TE flaps 1 & 2 at 20°:
- High alpha (~14°) and NPR = 3.4 &4.5
- Side-side inlet orientation

Directions for Future Aeroacoustics Testing

Aerodynamics (HEAT 1A):

- Evaluate effects of dual-nozzle operation on high-lift performance.
- Evaluate outboard wing spanwise flow effects on outboard nozzle aero performance.
- Single-nozzle HEAT 1 effects potentially twice as large w/two nozzles.
- Measurement of hinge moments on high-lift system components.

Acoustics (not currently part of HEAT 1A):

- Possible increased installation effects:
  - Plume-to-plume interactions
  - Dual aspirating ejector suppressor nozzles
  - Outboard wing spanwise flow effects on nozzle noise
  - Acoustic fatigue (structural) with two noise sources
- Azimuthal variation of noise:
  - Jet shielding and inboard nacelle shadowing
  - Wing flowfield effects on noise propagation
- Enhanced measurement capability:
  - Sideline EPNL measurements (ceiling mounted traverse)
  - Source location as f(Θ) (traversing phase-array antenna)
  - Airframe noise with full landing gear & high-lift simulation
  - Improved anechoic environment (40x80 acoustic mod)
  - Reduced JFS flow distortion

REPORT DOCUMENTATION PAGE

Form Approved
OMB No. 0704-0188

1. AGENCY USE ONLY *(Leave blank)*	2. REPORT DATE	3. REPORT TYPE AND DATES COVERED
	December 1999	Conference Publication

4. TITLE AND SUBTITLE
First NASA/Industry High-Speed Research Configuration Aerodynamics Workshop

5. FUNDING NUMBERS
WU 537-07-20-20

6. AUTHOR(S)
Richard M. Wood, Editor

7. PERFORMING ORGANIZATION NAME(S) AND ADDRESS(ES)
NASA Langley Research Center
Hampton, VA 23681-2199

8. PERFORMING ORGANIZATION REPORT NUMBER
L-17574C

9. SPONSORING/MONITORING AGENCY NAME(S) AND ADDRESS(ES)
National Aeronautics and Space Administration
Washington, DC 20546-0001

10. SPONSORING/MONITORING AGENCY REPORT NUMBER
NASA/CP-1999-209690/PT3

11. SUPPLEMENTARY NOTES

12a. DISTRIBUTION/AVAILABILITY STATEMENT
Unclassified–Unlimited
Subject Category 02 Distribution: Nonstandard
Availability: NASA CASI (301) 621-0390

12b. DISTRIBUTION CODE

13. ABSTRACT ***(Maximum 200 words)***

This publication is a compilation of documents presented at the First NASA/Industry High Speed Research Configuration Aerodynamics Workshop held on February 27–29, 1996 at NASA Langley Research Center. The purpose of the workshop was to bring together the broad spectrum of aerodynamicists, engineers, and scientists working within the Configuration Aerodynamics element of the HSR Program to collectively evaluate the technology status and to define the needs within Computational Fluid Dynamics (CFD) Analysis Methodology, Aerodynamic Shape Design, Propulsion/Airframe Integration (PAI), Aerodynamic Performance, and Stability and Control (S&C) to support the development of an economically viable High Speed Civil Transport (HSCT) aircraft. To meet these objectives, papers were presented by representative from NASA Langley, Ames, and Lewis Research Centers; Boeing, McDonnell Douglas, Northrop-Grumman, Lockheed-Martin, Vigyan, Analytical Services, Dynacs, and RIACS.

14. SUBJECT TERMS	15. NUMBER OF PAGES
High speed research; Aerodynamic design; Computational fluid dynamics; Aerodynamics; Stability and control; Performance; Propulsion airframe integration	624
	16. PRICE CODE: A99

17. SECURITY CLASSIFICATION OF REPORT	18. SECURITY CLASSIFICATION OF THIS PAGE	19. SECURITY CLASSIFICATION OF ABSTRACT	20. LIMITATION OF ABSTRACT
Unclassified	Unclassified	Unclassified	UL